Editor

R Nityananda
Raman Research Institute, Bangalore

Associate Editor

H R Krishnamurthy
Indian Institute of Science, Bangalore

Editorial Board

G S Agarwal, *University of Hyderabad, Hyderabad*
V Balakrishnan, *Indian Institute of Technology, Madras*
M Barma, *Tata Institute of Fundamental Research, Bombay*
P Chaddah, *Centre for Advanced Technology, Indore*
B M Deb, *Panjab University, Chandigarh*
P K Kaw, *Institute for Plasma Research, Gandhinagar*
H S Mani, *Indian Institute of Technology, Kanpur*
N Mukunda, *Indian Institute of Science, Bangalore*
T Padmanabhan, *Inter-University Centre for Astronomy and Astrophysics, Pune*
J C Parikh, *Physical Research Laboratory, Ahmedabad*
G Rajasekaran, *Institute of Mathematical Sciences, Madras*
V S Ramamurthy, *Institute of Physics, Bhubaneswar*
R Ramaswamy, *Jawaharlal Nehru University, New Delhi*
K R Rao, *Bhabha Atomic Research Centre, Bombay*
Probir Roy, *Tata Institute of Fundamental Research, Bombay*
A K Sood, *Indian Institute of Science, Bangalore*

Editor of Publications of the Academy

V K Gaur
C-MMACS, NAL, Bangalore

Subscription Rates
(Effective from 1989)

All countries except India	1 year	3 years	5 years
(Price includes AIR MAIL charges)	US$ 175	$ 470	$ 700
India	1 year	10 years (1989–1998 only)	
	Rs. 100	Rs. 500	

All correspondence regarding subscription should be addressed to the **Circulation Department** of the Academy

Editorial Office

Indian Academy of Sciences, C V Raman Avenue,
P.B. No. 8005, Bangalore 560 080, India

Telephone: 334 2546
Telex: 845-2178 ACAD IN
Telefax: 91-80-334 6094

© 1995 by the Indian Academy of Sciences. All rights reserved.

"Information for contributors" is printed in the last issue of every volume.

PRAMANA
— journal of
physics

© Printed in India

Vol. 45, No. 1,
July 1995
pp. 1–17

Diffusing wave spectroscopy of dense colloids: Liquid, crystal and glassy states

SUBRATA SANYAL† and AJAY K SOOD*
Department of Physics, Indian Institute of Science, Bangalore 560 012, India
†Present address: Department of Chemical and Nuclear Engineering, University of California at Santa Barbara, Santa Barbara, CA 93106, USA
*Also at Jawaharlal Nehru Centre for Advanced Scientific Research, Jakkur Campus, P O Jakkur, Bangalore 560 064, India

MS received 10 February 1995; revised 4 May 1995

Abstract. Using intensity autocorrelation of multiply scattered light, we show that the increase in interparticle interaction in dense, binary colloidal fluid mixtures of particle diameters 0·115 μm and 0·089 μm results in freezing into a crystalline phase at volume fraction ϕ of 0·1 and into a glassy state at $\phi = 0{\cdot}2$. The functional form of the field autocorrelation function $g^{(1)}(t)$ for the binary fluid phase is fitted to $\exp[-\gamma(6k_0^2 D_{\text{eff}} t)^{1/2}]$ where k_0 is the magnitude of the incident light wavevector and γ is a parameter inversely proportional to the photon transport mean free path l^*. The D_{eff} is the l^* weighted average of the individual diffusion coefficients of the pure species. The l^* used in calculating D_{eff} was computed using the Mie theory. In the solid (crystal or glass) phase, the $g^{(1)}(t)$ is fitted (only with a moderate success) to $\exp[-\gamma(6k_0^2 W(t))^{1/2}]$ where the mean-squared displacement $W(t)$ is evaluated for a harmonically bound overdamped Brownian oscillator. It is found that the fitted parameter γ for both the binary and monodisperse suspensions decreases significantly with the increase of interparticle interactions. This has been justified by showing that the calculated values of l^* in a monodisperse suspension using Mie theory increase very significantly with the interactions incorporated in l^* via the static structure factor.

Keywords. Colloids; dynamic light scattering; crystal and glass transitions.

PACS Nos 82·70; 64·70; 42·20; 05·40

1. Introduction

Charged stabilized aqueous colloidal suspensions of polystyrene particles (polyballs) and sterically stabilized nearly hard sphere colloids of polymethyl methacrylate particles have proved to be model condensed matter systems to study a rich variety of cooperative behaviour in equilibrium and non-equilibrium conditions [1]. These systems show liquid, crystal and even glassy states under suitable experimental conditions. Monodisperse polyball suspensions show either a body-centered cubic (BCC) phase at low volume fraction ϕ or a face-centered cubic (FCC) phase at high ϕ. Small-angle neutron scattering measurements [2] of the structure factors reveal a glassy phase in these systems for $\phi > 0{\cdot}2$. Monodisperse suspensions of polymethyl methacrylate particles have been studied extensively from the point of view of freezing of a liquid to an equilibrium crystalline phase or a metastable glassy state as a function of volume fraction ϕ [3–5].

In comparison with monodisperse suspensions, much less attention has been paid to the case of freezing of binary mixtures. The phase diagram becomes much richer

and complex with the introduction of two more parameters, namely, the diameter ratio $\sigma[=\sigma_A/\sigma_B, \sigma<1]$ and the relative number density of the small particles $x[=n_A/(n_A+n_B)]$, to characterize binary mixtures. Several compound crystalline structures have been identified [6, 7] in the optical microscopy of concentrated ($\phi \sim 0{\cdot}3$) aqueous suspensions of binary charged polystyrene spheres with diameters between 0·2 and 0·8 μm. The observed structures were similar to those found in the intermetallic compounds $MgCu_2$, AlB_2, $CaCu_5$, $NaZn_{13}$ and also of the type AB_4 with $P6_3/mmc$ symmetry, which has no counterpart in the conventional atomic systems. Bartlett *et al* [8] have studied the phase diagram of binary mixtures of nearly hard-sphere polyballs for some values of σ. These studies confirm the existence of AB_2 and AB_{13} superlattices in the (ϕ_A, ϕ_B) phase-diagram. In addition to the crystalline phase, glassy state has also been observed in polyball binary mixtures in measurements of shear modulus [9], static structure factor [10], diffusing wave spectroscopy [11] and Brownian dynamics simulations [12, 13]. The ease in the formation of glassy state in binary colloidal mixtures or charge-polydisperse colloids [12, 14] is similar to the fact that multicomponent solid solutions in conventional atomic systems are good glass formers [15].

Dynamics of the colloidal systems have been extensively studied by dynamic light scattering (DLS) experiments where the temporal fluctuations of the scattered light are analyzed in real time in terms of the intensity autocorrelation functions [16, 17]. In using the DLS technique, a stringent requirement is that the incident radiation should by scattered only once in the medium. Multiple scattering is avoided either by matching the refractive indices of the particles and the solvent [5] or by taking a low concentration of particles or thin sample cells. DLS measurements of the intermediate scattering functions have yielded valuable information on the non-ergodicity parameters across the kinetic glass transitions [4] allowing a direct comparison with the mode-coupling theory predictions [18].

The recently developed technique of the diffusing-wave spectroscopy (DWS) [19–22] has made it possible to study the particle dynamics from the intensity correlation functions in concentrated interacting suspensions. Subsequently, useful information about the polarization dependence in the freezing of monodisperse polyball suspensions [23] and also about the particle diffusion in the binary polyball mixtures are obtained by using DWS [24]. During the course of our studies, using DWS experiments on binary mixtures of strongly interacting polyballs, Meller and Stavans [11] have reported comprehensive phase diagrams (ϕ versus x) consisting of liquid, crystalline and glassy states for three values of σ, namely, $0{\cdot}54 \pm 0{\cdot}02$, $0{\cdot}78 \pm 0{\cdot}04$ and $0{\cdot}87 \pm 0{\cdot}03$. The different states of the system were confirmed from the presence or absence of Bragg-iridescence from the samples and the long-time temporal decay or saturation of the intensity autocorrelation functions. Our Brownian dynamics (BD) simulations [13] on binary mixtures, with $\sigma = 0{\cdot}495$ and $x = 0{\cdot}5$, reveal a liquid to crystal transition at $\phi \sim 0{\cdot}2$ and a liquid to glass transition at $\phi \sim 0{\cdot}3$. This is quite different from the results read from Meller and Stavans's [11] phase diagram with the parameters closest to our simulation, namely, $\sigma = 0{\cdot}54 \pm 0{\cdot}02$ and $x = 0{\cdot}5$. In their experiments [11], the mother samples of 10% volume fraction were treated with ion-exchange resins to reduce the impurity ion concentration n_i till these showed strong crystalline iridescence. The samples with different ϕ and x, on which the measurements were performed, were then made out of these mother samples. In the simulations, on the

preparations in the two cases, one must carry out DWS experiments and look for the liquid to crystal and the liquid to glass transitions on concentrated binary polyball mixtures, prepared similarly as in the simulation. This is the motivation of the present work. We indeed find, in accordance with our simulation [13], that a binary liquid mixture freezes into a crystalline phase at a lower volume fraction ($\phi = 0{\cdot}1$), while it forms a glassy state at $\phi = 0{\cdot}2$. Along the way, the DWS intensity autocorrelation functions of the binary liquid phase were analyzed in terms of effective diffusion constants [22], wherein the transport means free path, l^* [25], has been incorporated using the Mie scattering theory [26]. The slope parameter γ, to be explained in the following subsection [eq. (9)], shows a systematic dependence on the interaction between the particle. This has been understood by realizing that γ is inversely proportional to l^*, which increases with the interaction strength.

2. Theoretical background

DWS extends DLS to the optically turbid media and relates the temporal fluctuations of the multiply scattered light to the motion of the scatterers. The transport of photon is assumed to be diffusive with a diffusion constant $D_t = cl^*/3$, where c is the velocity of light in the medium. The transport mean free path l^* is related to the scattering mean free path l (the mean distance between successive scattering events) by $l^*/l = 2k_0^2/\langle q^2 \rangle$, where k_0 is the photon wave vector in the medium and $\langle q^2 \rangle$ is the mean squared scattering wave vector. The normalized temporal field autocorrelation function is defined by

$$g^{(1)}(q,t) = \frac{G^{(1)}(q,t)}{G^{(1)}(q,0)} \equiv \frac{\langle E_s(q,0)E_s^*(q,t)\rangle}{\langle |E_s|^2 \rangle}. \tag{1}$$

Within DWS, for the noninteracting monodisperse Brownian particles, it is given by [22]

$$g^{(1)}(q,t) = \int_0^\infty P(s)e^{(-2t/\tau_0)s/l^*}\,\mathrm{d}s, \tag{2}$$

where $P(s)$ is the distribution of path-lengths s for the random walk of photons and

$$\tau_0 = \frac{1}{Dk_0^2}. \tag{3}$$

Here D is the free particle diffusion coefficient.

For the "backscattering" geometry and the source at a fixed distance, $z_0 \sim l^*$, inside from the illuminated face at $z = 0$ of a slab of thickness L, one obtains [22]

$$G^{(1)}(t) = \frac{\sinh\left[\sqrt{\frac{6t}{\tau_0}}\left(\frac{L}{l^*} - \frac{z_0}{l^*}\right)\right] + \frac{2}{3}\sqrt{\frac{6t}{\tau_0}}\cosh\left\{\sqrt{\frac{6t}{\tau_0}}\left(\frac{L}{l^*} - \frac{z_0}{l^*}\right)\right\}}{\left(1 + \frac{8t}{3\tau_0}\right)\sinh\left[\frac{L}{l^*}\sqrt{\frac{6t}{\tau_0}}\right] + \frac{4}{3}\sqrt{\frac{6t}{\tau_0}}\cosh\left[\frac{L}{l^*}\sqrt{\frac{6t}{\tau_0}}\right]}. \tag{4}$$

For a sample of infinite thickness ($L \to \infty$), (4) simplifies to

$$G^{(1)}(t) = \frac{e^{-(z_0/l^*)(6t/\tau_0)^{1/2}}}{1 + \frac{2}{3}\sqrt{\frac{6t}{\tau_0}}}. \tag{5}$$

A distribution in the position z_0 of the source results in the replacement of z_0/l^* by $\langle z_0 \rangle / l^*$. It has been found experimentally that the $g^{(1)}(t)$ can be simply described using [19,20]

$$g^{(1)}(t) = \exp[-\gamma(6t/\tau_0)^{1/2}], \tag{6}$$

where $\gamma = \langle z_0 \rangle / l^* + 2/3$, i.e., $\gamma \propto 1/l^*$ [22]. When $l^*/l = 10$, then $\gamma \simeq 2$ for both polarized and depolarized scattering [27].

For the case of interacting particles, Mackintosh and John [27] have shown that $g^{(1)}(t)$ is related to the dynamic structure factor $S(q,t)$ such that $2t/\tau_0$ in (2) is replaced by $(l^*/l)[1 - S(q,t)/S(q,0)]$ where $S(q,t)$ is defined by

$$S(q,t) = \left\langle \frac{1}{N} \sum_{\alpha\beta} \exp[i\mathbf{q}\cdot(\mathbf{r}_\alpha(t) - \mathbf{r}_\beta(0))] \right\rangle \tag{7}$$

For short times, $S(q,t)$ can be expanded to linear power in t and hence it amounts to replacing t/τ_0 by t/τ_0' where $\tau_0'/\tau_0 = \langle q^2 S(q) \rangle / \langle q^2 \rangle$ [22]. Thus the time scale of the decay of $g^{(1)}(t)$ is modified and its functional form (i.e. square root singularity) for short times is not affected by interactions.

The form of $g^{(1)}(t)$ for all times has been obtained [27] only under the simplifying assumption that the interparticle spacing is larger than the wavelength and the particle size, so that the particle vibrations in a colloidal crystal or a glass, around their mean positions may be considered independent of each other. In addition, due to the viscosity of the fluid, phonon-like motions are strongly overdamped. They have also assumed large wavevector transfers q which correspond to distances smaller than the mean interparticle spacing. With these simplifying assumptions, for the long paths, for which the scattered light is still diffusive, the dynamic structure factor is replaced by its self-part $S_s(q,t)$ given by

$$S_s(q,t) = \left\langle \frac{1}{N} \sum_{\alpha} \exp[i\mathbf{q}\cdot(\mathbf{r}_\alpha(t) - \mathbf{r}_\alpha(0))] \right\rangle \tag{8}$$

$$\simeq \exp(-W(t)q^2)$$

where $W(t)$ is the mean square displacement (MSD) of a particle in time t. Then

$$g^{(1)}(t) = \exp[-\gamma(6k_0^2 W(t))^{1/2}], \tag{9}$$

Since $W(t)$ shows a non-decaying part at long-times in a solid, eq. (9) will predict a non-zero $g^{(1)}(t)$ at large times for both polarized and depolarized scattered light.

The MSD can be evaluated by considering a model for the interacting Brownian particles. For a one-dimensional harmonically bound Brownian particle of mass M and diameter $\sigma_p = 2a_p$, suspended in a solvent of viscosity η, the velocity auto-correlation

function in the strongly overdamped case ($\beta/\omega \gg 1$) is given by [16]

$$\Phi(t) \equiv \langle V(0)\, V(t)\rangle = \frac{k_B T}{M}\left[\exp(-\beta t) - \left(\frac{\omega^2}{\beta^2}\right)\exp\left(\frac{-\omega^2 t}{\beta}\right)\right], \tag{10}$$

where ω is the angular velocity associated with the harmonic potential, $\beta = \tau_v^{-1}$ with $\tau_v = M/6\pi\eta a_p$ as the Brownian velocity fluctuation time. This model applies strictly to the motion of a single particle in a colloidal crystal if the combined interparticle forces are treated in a harmonic approximation. It has been suggested [16] that the model can also be applied to the liquid-like ordering, if the similar form for the velocity autocorrelation function is retained, i.e.,

$$\Phi(t) = \frac{k_B T}{M}\exp\left(-\frac{t}{\tau_v}\right) - A\exp\left(-\frac{t}{\tau_I}\right), \tag{11}$$

where one expects that $A \ll k_B T/M$ and the fluctuation time associated with the interaction forces $\tau_I \gg \tau_v$. Within this model for times $t \gg \tau_v$, the MSD is given by

$$W(t) = Dt - A\tau_I(t + \tau_I \exp\{-t/\tau_I\} - \tau_I), \tag{12}$$

where the parameter A satisfies $A\tau_I < D$.

Let us now discuss DWS from a binary colloidal systems with species of different sizes. It has been shown that for noninteracting particles, the $g^{(1)}(t)$ is given by (2), where τ_0 [eq. (3)] is replaced by τ_{eff} [22],

$$g^{(1)}(t) = \exp(-\gamma(6t/\tau_{eff})^{1/2}), \tag{13}$$

where

$$1/\tau_{eff} = D_{eff} k_0^2,$$

$$D_{eff} = \left(\sum_i D_i/l_i^*\right)\Big/\left(\sum_i 1/l_i^*\right). \tag{14}$$

The effective diffusion constant D_{eff} is the weighted average of the individual diffusion coefficients of the pure species, the values of which are calculated via Stokes' law [28], i.e., $D_i = k_B T/(6\pi\eta a_i)$ where η is the viscosity of water (= 0·01089 P) and a_i are the radii of the particles. The weighting factors in (14), i.e., the inverse transport mean free paths $1/l_i^*$ for the individual pure species are summed to yield the optical analogue of the resistivity of the binary liquid alloy [29]

$$1/l_{eff}^* = \sum_i 1/l_i^*. \tag{15}$$

As stated above, the key quantity within the diffusion approximation of the photon transport is the photon random-walk step length l^*, which depends on the number of scattering events needed to randomize the direction of photon. The number of scattering events, in turn, depends on the scattering properties of the individual particles as well as the interparticle spatial correlations [21, 22]. A general expression for l^* for the monosized particles calculated [21, 30, 31] within the Mie theory [26] is summarized in the Appendix.

In the laboratory, one measures the normalized temporal intensity autocorrelation function $g_2(t)$ which is related to $g^{(1)}(t)$ by the Siegert's relation, i.e.,

$$g_2(t) \equiv g^{(2)}(t) - 1 = f|g^{(1)}(t)|^2] \tag{16}$$

The parameter f is fixed by the system optics and can be taken as a free parameter in fitting (6) and (16) to the relevant data.

3. Experiments

We use aqueous suspensions of charged polystyrene spheres (M/s Seradyn Inc., USA) of diameters $\sigma_B = 0{\cdot}115\,\mu m$ and $\sigma_A = 0{\cdot}089\,\mu m$. The quoted standard deviation of the diameters is less than 1%. Two sets of samples are prepared from these mother solutions. In one set, the samples of the small and the large spheres are obtained independently from their respective mother solutions by adding required amounts of triple-distilled, deionized water, so that the final volume-fraction of each of them becomes $\phi_A = \phi_B = 0{\cdot}05$. Equal volumes of these samples are then mixed to get total $\phi = 0{\cdot}1$ in a cylinderical quartz scattering cell of 8 mm inner-diameter containing a mixed-bed of ion-exchange resins [AG501–X8(D), M/s Bio-Rad Inc., USA] at the bottom of the cell to reduce the coion concentration n_i. The cell is then closed air-tight with properly cleaned teflon cap and parafilm. In the other set, the mother samples of the small and the large spheres with $\phi_A = \phi_B = 0{\cdot}1$ are mixed in 1:1 volume-ratio (total $\phi = 0{\cdot}2$) in a similar quartz sample cell with ion-exchange resins. The volume-fractions of the constituent solutions were confirmed to be within an experimental accuracy of 5% by drying a known volume of the suspension and weighing the solids. After an initial vigorous mixing of the samples with the resins, the cells are transferred into their respective quartz glycerin baths and left undisturbed for about an hour before the data accumulation begin. This is necessary to assure a proper gravitational settling down of the resins in the cell as well as uniformity of the glycerin without any air-bubbles surrounding the cell. A linearly polarized beam from Kr^+ laser ($\lambda = 647{\cdot}1$ nm) falls on one side of the sample and the scattered light of desired polarization is collected from the same side (scattering angle $\theta = 165°$). The normalized intensity autocorrelation $g_2(t)$ [eq. (16)] is measured using the Malvern correlator (model 7032CE). The laser light is vertically (V) polarized. The emergent multiply scattered light has, in general, a polarized (vertical) component with intensity $I_V(t)$ and a depolarized (horizontal) component with intensity $I_H(t)$. By setting the orientation of the analyzer, $g_2(t)$ was measured in either polarized, i.e., $C_{VV}(t) \equiv \langle I_V(t) I_V(0)\rangle / \langle I_V\rangle^2 - 1$ or depolarized, i.e., $C_{VH}(t) \equiv \langle I_H(t) I_H(0)\rangle / \langle I_H\rangle^2 - 1$ component. We note that although in normal isotropic systems the measured correlation functions $C_{VV}(t)$ and $C_{VH}(t)$ behave in qualitatively the same way, they give us access to different physical properties. While both respond to translational motion [23, 27, 32], only C_{VH} is sensitive to changes in the local dielectric anisotropy and hence contains information about the correlations of orientational fluctuations as well. The field autocorrelation $g^{(1)}(t)$ in the backscattering geometry is extracted using Siegart's relation eq. (16).

We note that since the system is in a frozen but disordered (i.e. non-ergodic) state, we are obliged to average over space as well as time to sample a representative fraction of all the configurations. To this end, we have averaged the correlation functions obtained

from ten spatially separated regions in the suspension. Each of these regions is achieved simply by rotating the sample cell in its position. The curves so obtained are labelled ensemble-averaged, while those from a single region are called time-averaged.

4. Results and discussions

Our fluid-phase data for the total $\phi = 0{\cdot}1$ mixtures of the small and the large polyballs, before putting in the ion-exchange resins, are shown by open symbols in figure 1. The measured $g_2(t)$ were non-linear least-square fitted by a simulated annealing Monte Carlo fitting method [33] using (16) and (13) with f and γ as fitting parameters. The values of D_i, l_i^* (as calculated [34] from the Mie theory) for the two constituent particle suspensions and also the values of D_{eff}, are presented in table 1. The τ_{eff} was calculated using (14). The values of the fitting parameters are given in the table 2. Given the fitted value of f, the data have been presented in the form of normalized $g^{(1)}(t)$ (experimental $g^{(1)}(t)/f$) in figure 1. The values of the parameter γ for the polarized and depolarized scattering are comparable with those in the monodisperse colloids [22, 23, 32]. The polarization dependence of γ can be simply understood as follows [22]. The autocorrelation

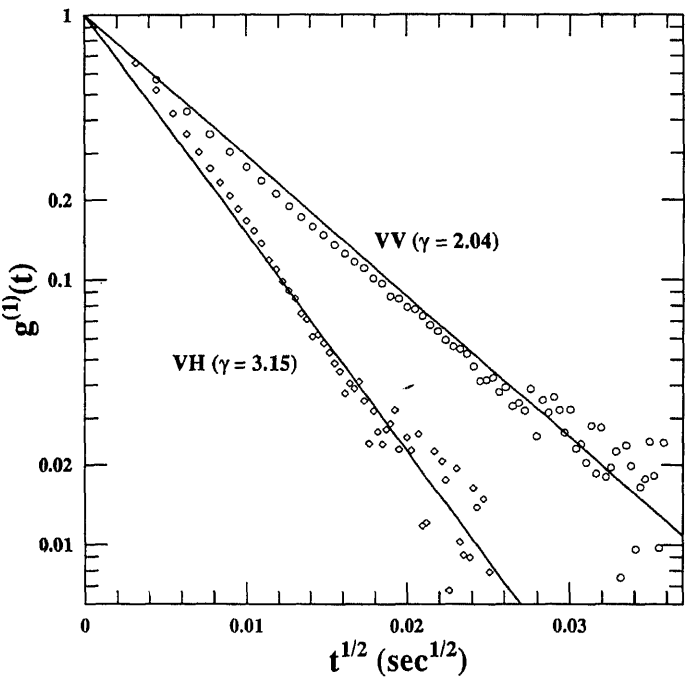

Figure 1. The fluid-phase time-averaged data for the polarized (VV) and the depolarized (VH) field autocorrelation functions $g^{(1)}(t)$ versus $t^{1/2}$ in the backscat-

Table 1. The parameters relevant to the Mie theory fits in figure 1 and the inset of figure 3, with $k_0 = 1297724\,\text{cm}^{-1}$. The parameters σ_i and l_i^* are in μm, while the D_i or D_{eff} are in $10^{-8}\,\text{cm}^2/\text{s}$.

σ_i	D_i	l_i^*	D_{eff}
0·089	3·17	232·77	3·58
0·115	4·10	295·82	

Table 2. The fitting parameters corresponding to figures 1 to 5, with $k_0 = 1{\cdot}29 \times 10^5\,\text{cm}^{-1}$. Samples I and II are 1:1 binary mixtures of 0·115 μm and 0·089 μm diameter particles with total $\phi = 0{\cdot}1$ and 0·2, respectively. The monodisperse sample III has $\phi = 0{\cdot}03$ and diameter 0·115 μm. The D_{eff} is in units of $10^{-8}\,\text{cm}^2/\text{s}$, A in units of 10^{-5}, τ_l in units of 10^{-3} s. Liquid: L, Crystal: C, Freezing: F and Glass: G, Pol: polarization.

Sample	State	Pol	D_{eff}	A	τ_l	f	γ
I	L	VV	3·578	—	—	0·9	2·0367
I	L	VH	3·578	—	—	0·9	3·1537
I	F	VV	3·578	1·116	3·204	0·118	0·0932
I	F	VH	3·578	0·4456	8·029	0·317	0·1072
I	C	VV	3·578	0·6348	5·526	0·145	0·0203
I	C	VV	3·578	5·217	6·822	0·196	0·0762
II	L	VV	3·217	—	—	0·8	2·332
II	L	VH	3·217	—	—	0·8	3·763
II	G	VV	3·217	0·1046	30·723	0·226	0·0018
II	G	VH	3·217	1·2492	2·349	0·237	0·0049
III	L	VV	3·473	—	—	0·99	1·89
III	L	VH	3·473	—	—	1·06	2·87
III	F	VV	3·473	1·816	1·912	0·7	0·988
III	C	VV	3·473	1·732	1·990	0·6	0·723
III	C	VH	3·473	5·926	0·5817	0·6	0·463

function for the perpendicular polarization (VH) decays more rapidly because the analyzer discriminates against the short photon paths which retain a high degree of their incident polarization. On the other hand, the autocorrelation function for the parallel polarization decays more slowly, due to the additional contributions of the low order scattering paths which have a longer decay time. In other words, for very short-times (shorter than that shown in figure), $g^{(1)}(t)$ is dominated by long paths for which the observed photons have lost their memory of their incident polarization and hence C_{VV} and C_{VH} will initially decay at the same absolute rate. This means $(C_{\text{VV}} - C_{\text{VH}})$ will be independent of time to first order in $\sqrt{t}$. Since the short paths tend not to alter the polarization of the incident light, I_{VV} is in general higher than I_{VH} [in our experiments $I_{\text{VV}}/I_{\text{VH}} \sim 3$].

After these initial measurements, the samples cells are left undisturbed. Typically about 2 days later, the $\phi = 0{\cdot}1$ mixture started showing Bragg-iridescence in the immediate vicinity of the ion-exchange resins-bed. The crystalline region started growing slowly till the whole of the sample in the cell showed the iridescence. Under this condition, the correlation functions measured for different polarization channels are presented in figure 2, for two cases namely, (a) in the region of 1·5 mm above the top of the resins-bed at around 174 h after the addition of resins (sample I, state C in table 2) and (b) at the height of 4 mm from the top of the resins-bed and time 194 h (sample I, state F in table 2). The temporal correlation functions for different polarization channels follow the similar trends in the crystallizing samples. The form of the correlation function $g^{(1)}(t)$ is same as predicted by (9). We note that the mean interparticle spacing is almost one third of wavelength of light and hence the assumption of retaining only the self part of the structure factor in deriving (9) is not fully satisfied. However, since (9) is the only closed form expression available for the $g^{(1)}(t)$ for the interacting colloids, we have chosen to use it to fit our experimental data to get some estimates of the parameters γ, f, A and τ_1. The solid lines show the fit to (9) and (12) by varying f, τ_1, γ and A. The values of the fitting parameters are provided in the respective figures as well as in table 2. Given the value of f, here too the data are presented in the normalized form $g^{(1)}(t)$. We note that the fits, though excellent at long times, are not

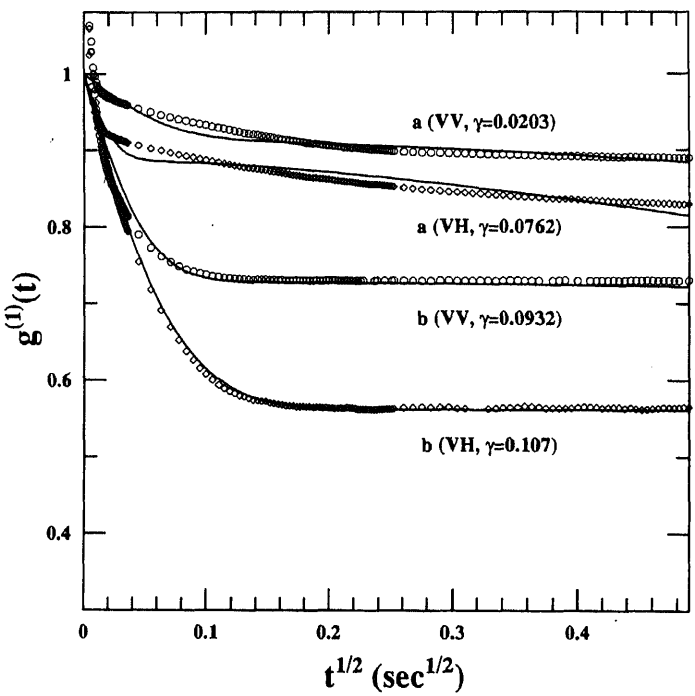

Figure 2. The normalized $g^{(1)}(t)$ versus $t^{1/2}$ for the different stages of crystallization in sample I ($\phi = 0{\cdot}1$) table 2. The data are shown in (a) the frozen state (state C, table 2) and (b) while freezing (state F, table 2). The solid lines are the fits to eqs (7) and (10). The fitted parameters are given in table 2.

than 1 at short times.

The situation is quite different with the total $\phi = 0{\cdot}2$ mixture. The sample does not Bragg-iridescence even a few weeks after the addition of resins. The autocorre functions measured after a week from the addition of resins (figure 3) show significan zero values at long time, similar to that shown in figure 2. The absence of Bragg-iride and non-decaying intensity autocorrelation functions show that the particles are trap a disordered state, as in a conventional glass. For comparison, the inset shows the state data for the sample (total $\phi = 0{\cdot}2$) but at a high impurity concentration. Here the solid lines are the best fits to the data using (13) with f and γ as fitting parameters f liquid state data in the inset and using (9) and (12) (by varying f, τ_1, γ and A) for the data. The relevant fitting parameters are listed in table 2. The quality of fit is poor at time and hence the extracted normalized $g^{(1)}(t)$ is again slightly higher than unity f glass data. Hence our experiments clearly show that the binary mixture with a total ϕ freezes into a crystalline state whereas for $\phi = 0{\cdot}2$, the interacting state of the mixture not show a crystalline phase even after a few months and is best described as a glass observation is similar to the predictions of our simulation work [13]. As mentioned e the difference between our results and those of Meller and Stavans [11] lies in th the interaction is allowed to build up in the samples.

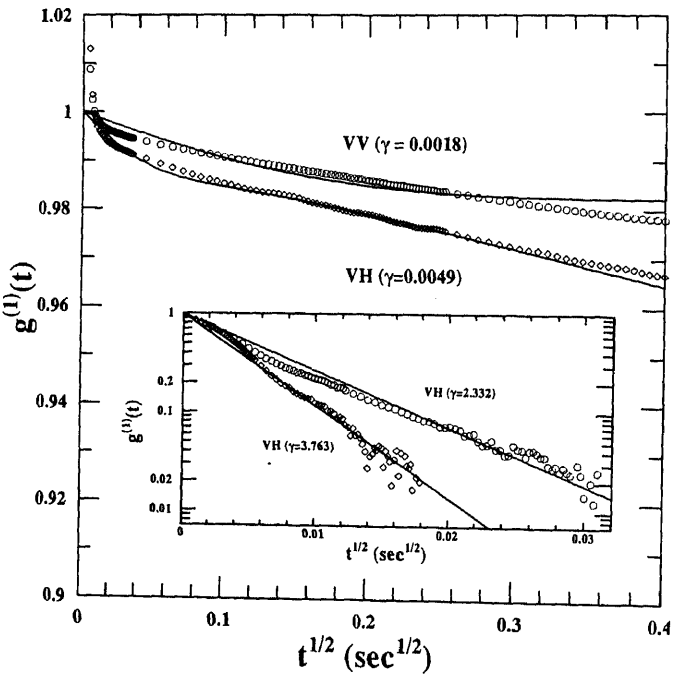

Figure 3. Same as in figure 2, but for the glass state with total $\phi = 0{\cdot}2$ at the h of 4 mm from the top of the resins-bed and 171 h after the addition of resins inset shows the data and the fits for the corresponding noninteracting limit.

It is interesting to compare the values of the parameter γ in table 2 obtained in the interacting colloids with the corresponding values in the noninteracting limit (figure 1 and the inset of figure 3). We note that γ (for a given scattering geometry) decreases as the interaction between the particles increases towards forming a crystal or a glass. To ascertain that this is a property of the freezing suspensions, we show the ensemble-averaged $g^{(1)}(t)$ for a monodisperse suspension (diameter $\sigma_p = 0{\cdot}115\,\mu$m and volume fraction $\phi = 0{\cdot}03$) in figure 4. The panel (a) shows the data for the parallel polarization channel (i.e. VV) of the system while freezing and the panel (b) shows both the parallel (VV) and the perpendicular (VH) channels in the state when the suspension has completely frozen into a crystalline order. In the state of freezing, as shown in figure 4(a), the sample shows the polarization dependence [23] of the correlation functions i.e., C_{VH} shows a liquid-like curve and hence the corresponding $g^{(1)}(t)$ is not plotted. The value of the parameter γ indeed decreases with the interaction as can be seen clearly by comparing figure 4 with the fluid-phase data shown by open circles and diamonds in figure 5 (see also table 2). In figure 5, we have also compared these with the initial part of the VV data in the crystallizing state (shown by +). We see clearly that as the interparticle interaction becomes important, the decay of $g^{(1)}(t)$ is different from

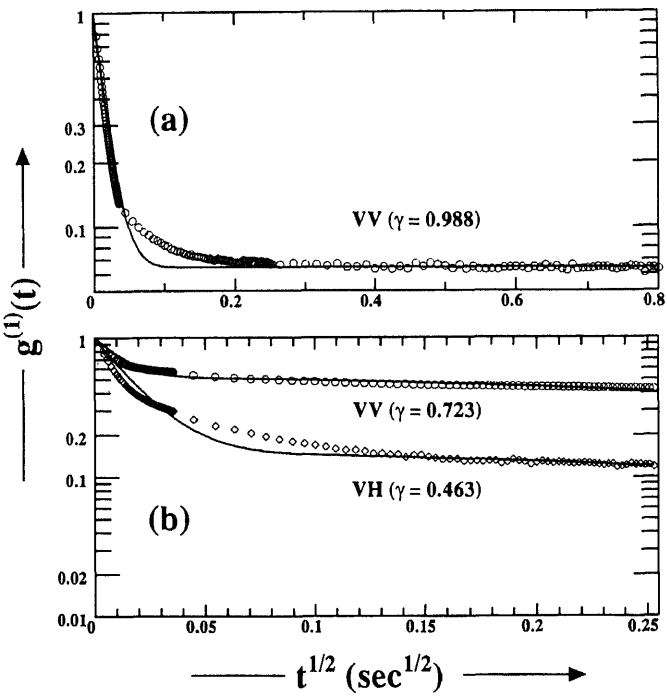

Figure 4. The semilog plots of the ensemble-averaged $g^{(1)}(t)$ versus $t^{1/2}$ (in $\sec^{1/2}$) of $0{\cdot}115\,\mu$m polyball suspension with $\phi = 0{\cdot}03$ (a) while freezing and (b) in the crystalline state alongwith the fits (solid lines) to a harmonic model as explained in the text, with parameters in table 2.

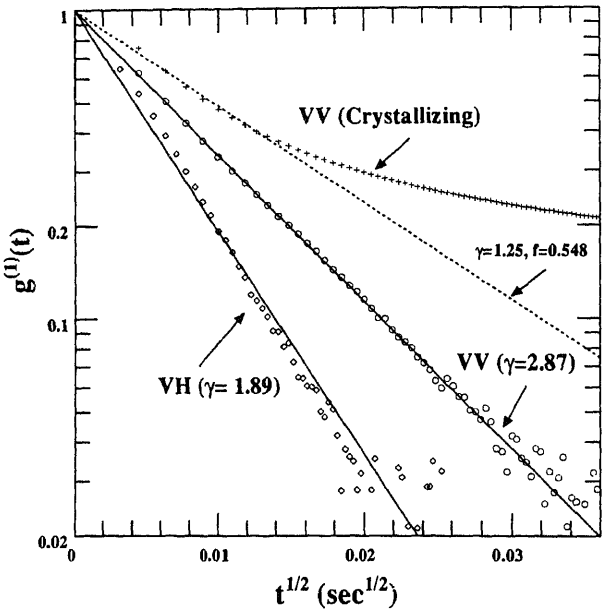

Figure 5. The fluid phase VV and VH time-averaged $g^{(1)}(t)$ versus $t^{1/2}$ (in $sec^{1/2}$) for $\phi = 0{\cdot}03$ is compared with the initial times data in the crystallizing state.

that without interaction, even at very early times. This is demonstrated by fitting (6) to the first 10 data points of the crystallizing suspension, shown by the dashed line and the corresponding parameters are given in table 2.

As we have mentioned before, the parameter γ is inversely proportional to the transport mean free path l^*, i.e., $\gamma \propto 1/l^*$ [22]. Therefore, the result that the magnitude of γ reduces with the growth of interaction in the system can be justified if we can show that l^* increases with the interaction. We do this only for the *monodisperse suspensions* (see Appendix for details). We calculate the l^* [eq. (17) of Appendix] by using the form factor $F(q)$ from the Mie scattering theory [eq. (18)] and incorporate the interparticle interaction through the structure factor $S(q)$ which can be calculated using either rescaled mean spherical approximation or Percus–Yevick approximation. For the present purpose, it suffices to note that the interacting charged colloids can be approximated to effective hard spheres by rescaling the volume fraction and therefore the Percus–Yevick approximation for the hard sphere system for which analytical results are known has been used as an input $S(q)$ in (17). The PY approximation, though not as good as mean spherical approximation for the $S(Q)$ of colloids, has been used because of the simple closed form expression [see (21) of the Appendix]. Our purpose is only to show qualitatively that l^* increases with the strength of interactions. In figure 6 we have shown the Percus–Yevick $S(q)$ for nine such different rescaled volume fractions ϕ^*. The height of the first peak of the structure factor, S_{max}, can be taken as a scale to measure the interparticle interaction. Figure 7 represents the calculated values of l^* for these $S(q)$ as a function of the interparticle interaction measured by S_{max}. We clearly see

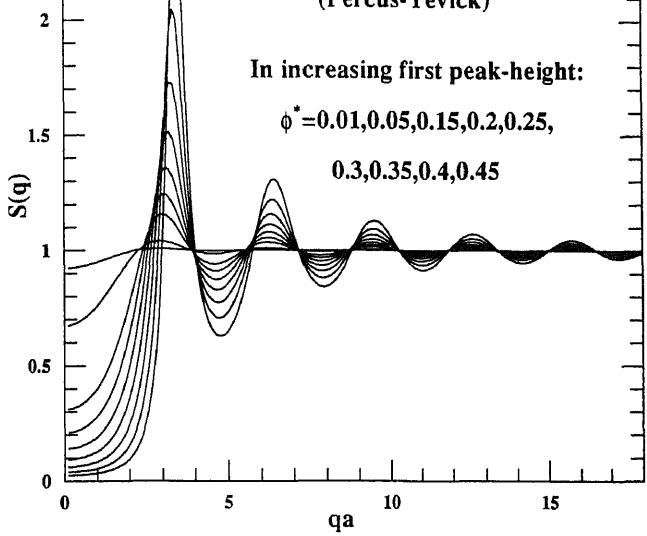

Figure 6. The static structure factor $S(q)$ in the Percus–Yevick approximation as a function for ten different values of the effective hard sphere volume-fraction ϕ^*.

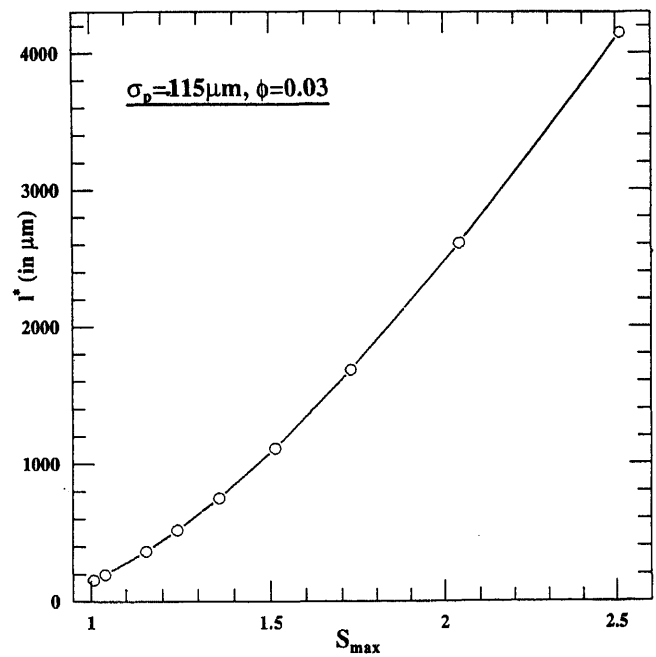

Figure 7. The calculated values of l^* (in μm) from the Mie theory (refer text) for different $S(q)$'s of figure 6 as a function of S_{max}, the first peak height of the $S(q)$.

that l^* increases almost linearly with the interaction. This qualitatively explains our results of the reduction of γ with the increase of the interaction strength.

5. Conclusions

In this paper, we have reported our observation of the formation of a crystalline phase when the interparticle interactions are increased in an equimolar binary mixture of polyball suspensions with a volume-fraction $\phi = 0{\cdot}1$. In comparison, the interactions in the same binary system with $\phi = 0{\cdot}2$ results in a metastable glassy state. This is in accord with our results in the BD simulations [13] of binary colloidal mixtures. We have also shown that the $g^{(1)}(t)$ of the binary mixture in the non-interacting fluid phases can be well-reproduced by replacing the τ_0 in the functional form of the correlation functions of the monodisperse suspensions by a properly weighted average τ_{eff} [eq. (13)], where l^* are calculated using Mie scattering theory. A model of the harmonically bound Brownian particle is used to calculate the root mean square displacements and the functional form of $g^{(1)}(t)$ suggested by MacKintosh and John [27] [eq. (9)] is shown to fit with a moderate success the results from the binary as well as monodisperse polyball suspensions while freezing into the crystalline or glassy states. These fits, though qualitative in nature due to the approximate form of (9), indicate that the parameter γ decreases as the particles in the suspensions start interacting with each other. This result is justified in the case of *monodisperse suspensions* by showing that the transport mean free path l^* which is inversely proportional to γ increases with the interaction between the particles. In conclusion, DWS has provided very interesting information on the dynamics of dense interacting colloids which can either form a crystalline state (at a low volume fraction) or a glassy state (at a high volume fraction). It could be worthwhile to carry out similar DWS experiments on binary colloids with different diameter ratios and relative volume fractions to map out the entire phase diagram.

Acknowledgements

We thank the Indo-French Centre for the Promotion of Advanced Research (IFCPAR project 607·1) for financial support. We thankfully acknowledge the participation of S Ramkumar in the initial phase of the experiments.

Appendix

Within the Mie scattering theory [26], a general expression of l^* for monodisperse particles, is given by [21, 30, 31]

$$l^* = \frac{k_0^6 a_p^4}{\pi n_p \int_0^{2k_0 a_p} I(Q) Q^3 \, dQ} = \frac{(k_0 \sigma_p)^6 \sigma_p}{96\phi \langle F(Q) S(Q) \rangle}. \tag{17}$$

Here n_p is the number density of particles and $\mathbf{Q} = (\mathbf{k}_0 - \mathbf{k}_f) a_p$ is the dimensionless momentum transfer for a single-scattering event. For monodisperse particles, we have replaced $I(Q)$ simply by the product of the form factor $F(Q)$ and the structure factor $S(Q)$. The angular brackets indicate an average over all the scattering paths. The form

factor $F(Q)$ for monodisperse systems is given by the Mie scattering theory as [26]

$$F(Qa_p) = Qa_p[A_1(\theta)A_1^*(\theta) + A_2(\theta)A_2^*(\theta)]. \tag{18}$$

where the dimensionless, single-scattering amplitudes $A_1(\theta)$ and $A_2(\theta)$ are related to the scattered far-fields E_ϕ and E_θ as

$$E_\phi = -\frac{ie^{ikr}}{kr} A_1(\theta)\sin\phi,$$

$$E_\theta = \frac{ie^{ikr}}{kr} A_2(\theta)\cos\phi,$$

$$A_1(\theta) = \sum_{n=1}^{\infty} \frac{2n+1}{n(n+1)}[a_n\pi_n(\cos\theta) + b_n\tau_n(\cos\theta)],$$

$$A_2(\theta) = \sum_{n=1}^{\infty} \frac{2n+1}{n(n+1)}[a_n\tau_n(\cos\theta) + b_n\pi_n(\cos\theta)], \tag{19}$$

with

$$\pi_n(\cos\theta) = \frac{P_n(\cos\theta)}{\sin\theta} \quad \text{and} \quad \tau_n(\cos\theta) = \frac{\mathrm{d}}{\mathrm{d}\theta}[P_n(\cos\theta)]. \tag{20}$$

The Mie scattering amplitudes are given by

$$a_n = \frac{\psi_n(\alpha)\psi_n^*(\beta) - m\psi_n(\beta)\psi_n^*(\alpha)}{\zeta_n(\alpha)\psi_n^*(\beta) - m\psi_n(\beta)\zeta_n^*(\alpha)},$$

$$b_n = \frac{m\psi_n(\alpha)\psi_n^*(\beta) - \psi_n(\beta)\psi_n^*(\alpha)}{m\zeta_n(\alpha)\psi_n^*(\beta) - \psi_n(\beta)\zeta_n^*(\alpha)},$$

where $\alpha = k_0 a_p$, $\beta = k_0 m a_p$, $\psi_n(x) = (\pi x/2)^{1/2} J_{n+1/2}(x)$ and $\zeta_n(x) = (\pi x/2)^{1/2} H^{(1)}_{n+1/2}(x)$ [$J_n(x)$ and $H_n(x)$ being the nth order Bessel function and Hermite polynomial, respectively] and $m^2 = \varepsilon_r = \varepsilon/\varepsilon_0$ is the relative dielectric constant of the sphere.

The static structure factor $S(Q)$ for the dense hard-spheres in the Percus–Yevick (PY) approximation is given in terms of the direct correlation function $c(Q)$ as [29, 35]

$$S(Q) = \frac{1}{1 - n_p c(Q)},$$

$$c(Q) = 4\pi \int_0^{\sigma_p} r^2 c(r) \frac{\sin(Qr)}{Qr} \mathrm{d}r,$$

$$c(r) = \alpha_0 + \alpha_1\left(\frac{r}{\sigma_p}\right) + \alpha_2\left(\frac{r}{\sigma_p}\right)^3, \tag{21}$$

$$\alpha_0 = -\frac{(1+2\phi)^2}{(1-\phi)^4},$$

$$\alpha_1 = \frac{6\phi(1+\phi/2)^2}{(1-\phi)^4},$$

$$\alpha_2 = \frac{1}{2}\phi\alpha_0.$$

References

[1] For a review, see A K Sood, in *Solid State Physics*, edited by H Ehrenreich and D T (Academic, New York, 1991) Vol. 45, p. 1

[2] E B Sirota, H D Ou-Yang, S K Sinha, P M Chaikin, J D Axe and Y Fujji, *Phys. Rev. L* 1524 (1989)

[3] P N Pusey, W van Megen, P Bartlett, B J Ackerson, J G Rarity and S M Underwoo *Rev. Lett.* **63**, 2753 (1989)

[4] W van Megen and P N Pusey, *Phys. Rev.* **A43**, 5429 (1991)
W van Megen, S M Underwood and P N Pusey, *Phys. Rev. Lett.* **67**, 1586 (1991)
W van Megen and S M Underwood, *Phys. Rev.* **E47**, 248 (1993)

[5] P N Pusey and W van Megen, *Nature* (*London*) **320**, 340 (1986)
P N Pusey and W van Megen, *Phys. Rev. Lett.* **69**, 2083 (1987)
S E Paulin and B J Ackerson, *Phys. Rev. Lett.* **64**, 2663 (1990)
P N Pusey, *J. Phys.* (Paris) **48**, 709 (1987)
W van Megen and S M Underwood, *Langmuir* **6**, 35 (1990)

[6] S Yoshimura and S Hachisu, *Prog. Colloid Polym. Sci.* **68**, 59 (1983); *Nature* (*Londo* 188 (1980)

[7] S Yoshimura and S Hachisu, *J. Phys. Colloq.* (Paris) **46**, C3-115 (1985)

[8] P Bartlett, R H Ottewill and P N Pusey, *J. Chem. Phys.* **93**, 1299 (1990); *Phys. Rev. L* 3801 (1992)

[9] H M Lindsay and P M Chaikin, *J. Chem. Phys.* **76**, 3774 (1982)

[10] R Kesavamoorthy, A K Sood, B V R Tata and A K Arora, *J. Phys.* **C21**, 4737 (19

[11] A Meller and J Stavans, *Phys. Rev. Lett.* **68**, 3646 (1992)

[12] H Löwen, J P Hansen and J N Roux, *Phys. Rev.* **A44**, 1169 (1991)

[13] S Sanyal and A K Sood, *Phys. Rev. E* (in press); S Sanyal, Ph.D Thesis (IISc, Ban India), Unpublished (1994)

[14] B V R Tata and A K Arora, *J. Phys. Condensed Matter* **4**, 7699 (1992)

[15] J F Sadoc and C N J Wagner, in *Glassy metals II*, edited by M Bech and H J Gunt (Springer-Verlag, Berlin, 1983), p. 53
M Kimura and F Yonezawa, in *Topological disorder in condense matter*, edi F Yonezawa and T Ninomiya (Springer-Verlag, Berlin, 1983) p. 80

[16] P N Pusey and R J A Tough, in *Dynamic light scattering: Applications of photon corr spectroscopy*, edited by R Pecora (Plenum, New York, 1985)

[17] B J Berne and R Pecora, *Dynamic light scattering* (Wiley, New York, 1976)

[18] For reviews on MCT, see, W Götze, in *Liquids, freezing and the glass transition*, Pr ings of the Les Houches Summer School, Session L1, edited by J P Hansen, D Le and J Zinn-Justin, (North-Holland, Amsterdam, 1991), p. 287
W Götze and L Sjögren, *Rep. Prog. Phys.* **55**, 241 (1992)

[19] G Maret and P E Wolf, *Z. Phys.* **B65**, 409 (1987)
M Rosenbluh, M Hoshen, I Freund, M Kaveh, *Phys. Rev. Lett.* **58**, 2754 (1987)
I Freund, M Kaveh and M Rosenbluh, *Phys. Rev. Lett.* **60**, 1130 (1988)

[20] M J Stephen, *Phys. Rev.* **B37**, 1 (1988)
A A Golubentsev, *Zh. Eksp. Theor. Fiz.* **86**, 47 (1984); *Sov. Phys. JETP* **59**, 26 (198

[21] D J Pine, D A Weitz, P M Chaikin and E Herbolzheimer, *Phys. Rev. Lett.* **6** (1988)

[22] D J Pine, D A Weitz, G Maret, P E Wolf, E Herbolzheimer and P M Chaikin in *Sca and localization of classical waves in random media*, edited by P Sheng, (World Sci Singapore, 1989)
D J Pine, D A Weitz, J X Zhu and E Herbolzheimer, *J. Phys. France* **51**, 2101 (19

[23] S Sanyal, A K Sood, S Ramkumar, S Ramaswamy and N Kumar, *Phys. Rev. Lett.* 7 (1994)

[24] P D Kaplan, A G Yodh and D J Pine, *Phys. Rev. Lett.* **68**, 393 (1992)

[25] Y Kuga and A Ishimaru, *J. Opt. Soc. Am.* **A8**, 831 (1984)
M P van Albada and A Lagendijk, *Phys. Rev. Lett.* **55**, 2692 (1985)

P E Wolf and G Maret, *Phys. Rev. Lett.* **55**, 2696 (1985)
E Akkerman, P E Wolf and R Maynard, *Phys. Rev. Lett.* **56**, 1471 (1986)
[26] A Ishimaru, *Wave propagation and scattering in random media* (Academic, New York, 1978), p. 29–30
H C van de Hulst, *Light scattering by small particles* (Dover, New York, 1957, 1981), p. 121–128, 176–177
[27] F C MacKintosh and S John, *Phys. Rev.* **B40**, 2383 (1989)
[28] G K Batchelor, *J. Fluid Mech.* **74**, 1 (1976); **131**, 155 (1983)
[29] N W Ashcroft and D C Langreth, *Phys. Rev.* **159**, 500 (1967)
J M Ziman, *Philos. Mag.* **6**, 1013 (1961)
[30] S Fraden and G Maret, *Phys. Rev. Lett.* **65**, 512 (1990)
[31] P D Kaplan, J L Rouke, A G Yodh and D J Pine, *Phys. Rev. Lett.* **72**, 582 (1994)
[32] F C MacKintosh, J X Zhu, D J Pine and D A Weitz, *Phys. Rev.* **B40**, 9342 (1989)
[33] S Sanyal *et al*, unpublished
[34] We thank Prof. A G Yodh for providing us with the computer program to calculate l^*
[35] W Hess and R Klein, *Adv. Phys.* **32**, 173 (1983) p. 181

PRAMANA
— journal of
physics

© Printed in India

Vol. 45, No. 1,
July 1995
pp. 19–24

A comparative dielectric relaxation study between hydrogen- and non-hydrogen-bonded liquids: Nitriles vs alcohols

S N HELAMBE, M P LOKHANDE, A C KUMBHARKHANE and
S C MEHROTRA
Department of Physics, Dr. Babasaheb Ambedkar Marathwada University, Aurangabad 431 004, India

MS received 2 March 1995; revised 22 May 1995

Abstract. Dielectric properties of nitriles have been studied using time domain reflectometry in the frequency range of 10 MHz to 10 GHz over the temperature range of 0°C to 45°C. The calculated dielectric relaxation parameters are compared with values for the corresponding n-alcohols. The dielectric behaviour in n-nitrile systems is quite different from the corresponding behaviour in n-alcohols. The dipoles in n-nitrile systems show a tendency to remain antiparallel, unlike in alcohol systems. The activation energy decreases with the increase of molecular size, whereas in hydrogen bonded liquid it increases.

Keywords. N-nitriles; dipoles; relaxation times-microwaves; dielectrics.

PACS No. 77·22

1. Introduction

Structural information about n-alcohols in the liquid state has been extensively studied through dielectric relaxation measurements [1–3]. Three features with respect to the number of carbon atoms N_C, in n-alcohols have been observed.

(1) An increase in the Kirkwood correlation factor with N_C: this indicates that the n-alcohols with larger N_C become more ordered in the liquid phase.
(2) Increase of the relaxation time with N_C: this indicates a slower rotation for the heavier molecules, and
(3) Increase of the activation energy with N_C: this indicates that the hydrogen bonded energy strengthens with increase in N_C.

The above features have been associated with hydrogen bonding. This study on the nitriles was undertaken to determine the role of dipole moment in the above mentioned features. Nitriles were studied because (1) many nitriles exist in the liquid state at room temperature, (2) these are not hydrogen bonded and (3) they have large dipole moments. The dielectric constant results are available only for acetonitrile [4] and butanenitrile [5]. The dielectric properties on seven n-nitriles with $N_C = 1$ to 5, 7, 9 and 10 are determined in this work.

In § 2, the experiment is described. The results and conclusions are given in § 3.

2. Experimental

The dielectric spectra were obtained by the time domain reflectometry (TDR) technique [6, 7]. In the TDR technique a fast rising step pulse of about 25 ps generated by S-52 pulse generator and was transmitted through 3·5 mm coaxial line with characteristic impedance 50 ohms. The sample cell has been placed at the end of the transmission line after the sampling head. The SMA (Standard Military Application) type cell was used for the work. The cell had outer and inner dimensions of 3·5 mm and 1·52 mm, respectively. The effective pin length of inner conductor was 1·35 mm. The Tektronix 7854 sampling oscilloscope was used to sample the reflected pulse. The time window used for the experiment was kept 5 ns. The reflected pulse was digitized with 1024 points in the selected time window and transferred to personal computer (PC/XT) through IEEE-488 card. The complex reflection function ρ^* of the sample liquids were determined through Fourier transforming the measured reflected pulse [7–10]. The spectra show the single Debye relaxation type as expected [11]. The complex dielectric spectra obtained are fitted to the Debye equation

$$\varepsilon^* = \varepsilon_0 + \frac{\varepsilon_0 - \varepsilon_\infty}{1 + j\omega\tau} \tag{1}$$

with ε_0 and τ as fitting parameters. In the fitting procedure, ε_∞ is not fitted and assumed to be 3·5. This is done because the data are not sensitive to ε_∞ in the frequency range under consideration. The details are given in an earlier paper [12].

3. Results and discussion

The values of static dielectric constant (ε_0) and relaxation time (τ) at different temperatures are given in tables 1 and 2 respectively. The static dielectric constants of acetonitrile [4] ($\varepsilon_0 = 35{\cdot}9$) and butanenitrile [5] ($\varepsilon_0 = 20{\cdot}2$) as reported earlier are in good agreement with the values reported here.

In general, ε_0 decreases with increase in the number of carbon atoms. This decrease can be ascribed to decrease of dipoles per unit volume with an increase in the size of the

Table 1. Static dielectric constant ε_0 for n-nitrile at different temperature.

	ε_0				
Nitrile	$t = 0\,^\circ C$	$t = 10\,^\circ C$	$t = 25\,^\circ C$	$t = 35\,^\circ C$	$t = 45\,^\circ C$
Acetonitrile	40·0 (1)	38·2 (1)	36·9 (1)	36·1 (1)	33·7 (3)
Butanenitrile	26·2 (1)	24·3 (4)	22·0 (2)	21·1 (1)	20·3 (1)
Pentanenitrile	23·0 (1)	21·5 (1)	21·0 (2)	19·1 (1)	11·3 (1)
Hexanenitrile	18·1 (1)	18·0 (1)	16·3 (1)	16·0 (1)	14·2 (1)
Octanenitrile	14·7 (1)	13·2 (1)	13·0 (1)	12·2 (1)	10·8 (2)
Decanenitrile	11·4 (1)	11·0 (1)	10·6 (1)	10·4 (1)	10·2 (1)
Undecanenitrile	*	11·0 (1)	10·3 (1)	9·1 (1)	9·1 (5)

*not studied.

Number in bracket denotes uncertainties in the last significant digits obtained by the least squares fit method. For ex. 40·1 (1) means 40·1 + 0·1. The realistic errors in the values is about 2% considering other experimental aspects.

Table 2. Relaxation time τ for n-nitrile at different temperature.

	τ(ps)				
Nitrile	$t=0\,^{\circ}C$	$t=10\,^{\circ}C$	$t=25\,^{\circ}C$	$t=35\,^{\circ}C$	$t=45\,^{\circ}C$
Acetonitrile	6·4 (7)	3·6 (1)	3·4 (1)	2·7 (1)	1·3 (8)
Butanenitrile	10·2 (3)	9·9 (5)	8·9 (7)	8·0 (4)	6·7 (5)
Pentanenitrile	16·8 (4)	14·4 (2)	13·0 (2)	11·3 (1)	10·9 (1)
Hexanenitrile	28·2 (3)	22·0 (3)	17·4 (4)	16·3 (2)	14·2 (3)
Octanenitrile	45·0 (4)	36·6 (3)	31·4 (3)	25·6 (2)	22·0 (3)
Decanenitrile	84·8 (13)	73·7 (3)	67·5 (8)	53·6 (2)	49·2 (4)
Undecanenitrile	*	76·8 (5)	64·6 (1)	62·6 (1)	58·7 (5)

* not studied

Table 3. Kirkwood correlation factor g at different temperatures.

	g				
Nitrile	$t=0\,^{\circ}C$	$t=10\,^{\circ}C$	$t=25\,^{\circ}C$	$t=35\,^{\circ}C$	$t=45\,^{\circ}C$
Acetonitrile	0·87 (5)	0·86 (5)	0·88 (5)	0·89 (5)	0·85 (5)
Butanenitrile	0·80 (4)	0·76 (4)	0·73 (4)	0·72 (4)	0·71(4)
Pentanenitrile	0·74 (4)	0·71 (4)	0·73 (4)	0·68 (4)	0·66 (4)
Hexanenitrile	0·72 (4)	0·74 (4)	0·70 (4)	0·71 (4)	0·64 (4)
Octanenitrile	0·72 (4)	0·66 (4)	0·68 (4)	0·66 (4)	0·59 (3)
Decanenitrile	0·65 (4)	0·65 (4)	0·65 (4)	0·66 (4)	0·66 (4)
Undecanenitrile	*	0·69 (4)	0·67 (4)	0·62 (3)	0·61 (3)

Number in brackets denote errors in least significant digits by assuming 2% error in the values of ε_0 and ε_∞.

molecules. Structural information can be obtained from the Kirkwood correlation factor [13], g, as

$$g\frac{4\pi N\mu^2}{9kTV}=\frac{(\varepsilon_0-\varepsilon_\infty)(2\varepsilon_0+\varepsilon_\infty)}{\varepsilon_0(\varepsilon_\infty+2)(\varepsilon_\infty+2)} \tag{3}$$

where μ is the dipole moment, N/V is number density and ε_∞ is the square of the refractive index. The values of ρ and ε_∞ have been taken at 25°C, from the Aldrich Catalog handbook of Chemical [14]. The values of g obtained by the Kirkwood Frohlich [13] equation is given in table 3. The values of g are less than one, indicating that the dipoles are oriented in antiparallel direction. As the size of the molecule increases, the values of g further decreases. The tendency to remain antiparallel increases with increase of chain size in the molecule. This tendency is due to dipole-dipole interactions between two molecules.

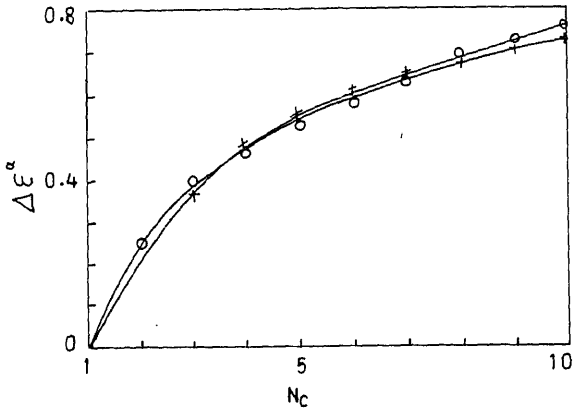

Figure 1. Plot of relative change in ε_0, $\Delta\varepsilon_0$ with number of carbon atoms in n-nitriles and n-alcohols at 25 °C. (○), OH; (+), CN

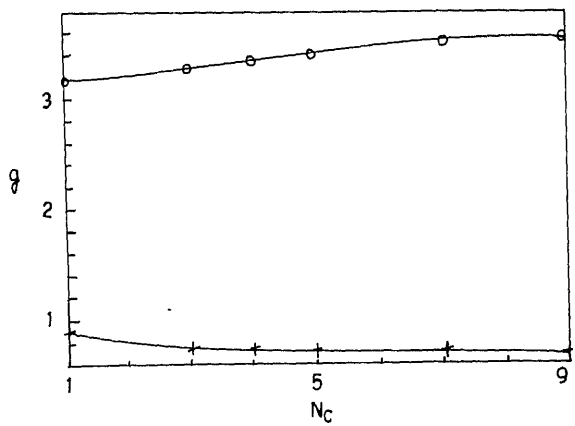

Figure 2. Plot of Kirkwood correlation factor vs number of carbon atoms for n-nitriles and n-alcohols at 25°C. (○), (OH); (+), CN

It will be interesting to compare the results with the corresponding results of hydrogen bonded liquids, like alcohols. The figure 1 shows the plot of change in $\Delta\varepsilon^a$ with the number of carbon atoms in n-nitriles and n-alcohols [3, 4].

The value of $\Delta\varepsilon^a$ is defined as

$$\Delta\varepsilon^a = \frac{(\varepsilon_0)^a_{N_{C=0}} - (\varepsilon_0)^a_{N_{C=0}}}{(\varepsilon_0)^a_{N_{C=0}}} \tag{4}$$

where $(\varepsilon_0)^a_N$ is the value of the static permittivity for the system with N carbon atoms. The g values are given in figure 2. It shows that the g values decrease with N_C in nitrile systems. It remains almost constant in alcohol systems.

The change in relaxation times, $\Delta\tau$, for alcohol and nitrile systems are shown in figure 3.

The value of $\Delta\tau$ is defined as

$$\Delta\tau = (\tau)^a_{N_{C=0}} - (\tau)^a_{N_{C=0}} \tag{5}$$

where $(\tau)^a_N$ is the relaxation time for the system a with N carbon atoms.

In figure 3, the change in relaxation in alcohols is larger than corresponding values in nitriles. This may be because of the –OH group in alcohol which is a hydrogen bonded liquid. As the chain is long and as there is the strong hydrogen bonding with neighbouring molecules, relaxation time tends to increase with number of carbon

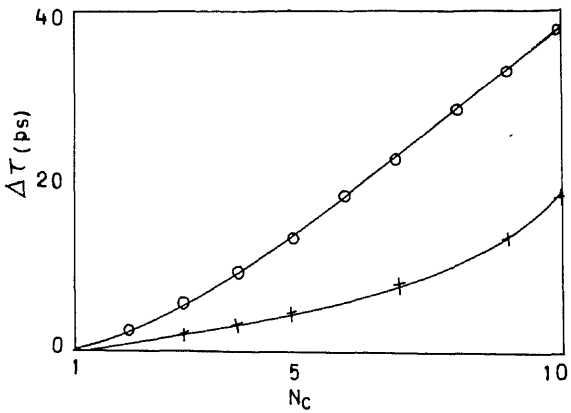

Figure 3. Plot of relative change in τ, $\Delta\tau$ with number of carbon atoms in n-nitriles and n-alcohols at 25°C. (○), (OH); (+), CN

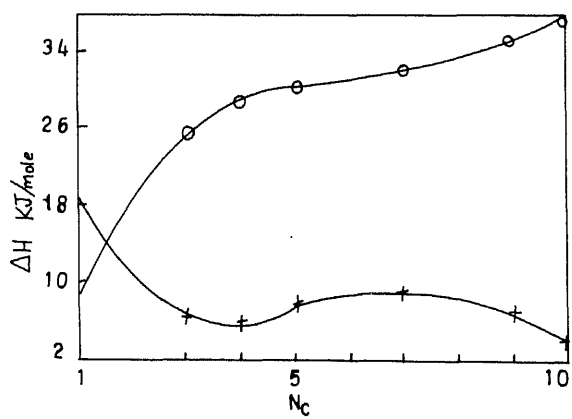

Figure 4. Plot of activation energies (ΔH) KJ/mole vs number of carbon. (○), (OH); (+), CN

atoms. In case of nitriles though chain is long, there is no such strong bonding with neighbouring molecules.

The activation energies were calculated from Eyring equation [15]. The activation energies are associated with dipole-dipole interaction. The results are shown in figure 4 along with the corresponding values for n-alcohol systems [2, 3]. It can be seen that nitrile system behave in a very different manner. This may be because of the fact that the activation energies in nitrile systems are due to the dipole-dipole interactions, whereas, in alochol systems it may be due to the hydrogen bonding. It is interesting to note that the trend in the activation energy is similar to the trend as observed in the (g) factor, related to the cooperative effect. The higher correlation factor leads to the higher value of the activation energy.

Acknowledgement

We are grateful to Dr P B Patil and G S Raju for discussion and helpful suggestions. Financial support from University Grants Commission, New Delhi is gratefully acknowledged.

References

[1] Mehrotra S C and Gestblom B, *Finn. Chem. Lett.* 34 (1985)
[2] Gestblom B and Sjoblom J, *Acta. Chem. Scand.* **A38**, 575 (1984)
[3] Gestblom B and Sjoblom J, *Acta. Chemica. Scand.* **A38**, 47 (1984)
[4] Moumouzlas G, Panopoulos D K and Ritzoulis G, *J. Chem. Engg. Data* **36**, 20 (1991)
[5] Janz G J and Tomkins R P T, *Nonaqueous Electrolytes Handbook* (Academic Press, New York, 1972)
[6] Cole R H, *Ann. Rev. Phys. Chem.* **28**, 283 (1977)
[7] Puranik S M, Kumbharkhane A C and Mehrotra S C, *J. Microwave Power and Electromagnetic Energy* **26**, 3 (1991)
[8] Kumbharkhane A C, Puranik S M and Mehrotra S C, *J. Faraday Trans.* **87**, 1569 (1991)
[9] Kumbharkhane A C, Puranik S M and Mehrotra S C, *J. Solution Chem.* **21**, 201 (1992)
[10] Cole R H, Berberian G J, Masshimo S, Chryssikos G, Burns A and Tombari E, *J. Appl. Phys.* **66**, 793 (1989)
[11] Hill N E, Vaughan W E, Price A H and Davies M, in *Dielectric properties and behaviour* (Van Nostrand, New York, 1949) p. 340
[12] Kumbharkhane A C, Helambe S N, Doraiswamy S and Mehrotra S C, *J. Chem. Phys.* **99**, 2405 (1993)
[13] Kirkwood J G, *J. Chem. Phys.* **7**, 911 (1939)
[14] Aldrich Chemical Company Inc. USA (1990)
[15] Eyring H, *J. Chem. Phys.* **4**, 283 (1936)

Phonon dispersion in quasiperiodic semiconductor superlattices

SUJATA RATH, PRAFULLA K JHA and SANKAR P SANYAL
Department of Physics, C V Raman Building, Bhopal University, Bhopal 462026, India

MS received 20 September 1993; revised 9 May 1995

Abstract. The phonon spectra of unstrained and strained quasiperiodic semiconductor superlattices (QSSL) have been calculated using one-dimensional linear chain model. We consider two types of quasiperiodic systems, namely cantor triadic bar (CTB) and Fibonacci sequences (FS), constituting of AlAs, GaAs and GaSb of which the latter two have a lattice mismatch of about 7%. The calculations have been made using transfer matrix method and also with and without the inclusion of strain. We present the results on phonon spectra of two component CTB and two as well as three component FS semiconductor superlattices (SSL), thickness and order dependence on LO mode of GaAs, effect of strain on LO frequency of GaAs. The calculated results show that the strain generated due to lattice mismatch reduces significantly the magnitudes of the confined optical phonon frequency of GaAs.

Keywords. Quasiperiodic; phonon; strained layer; transfer matrix.

PACS Nos 63·20; 63·90; 68·35

1. Introduction

In the recent years with the development of various crystal growth techniques, a great deal of interest has been generated towards the experimental as well as theoretical studies of the electronic and vibrational properties of semiconductor superlattices (SSL) [1–11]. This is mainly because of the potentiality of the applications of the SSL in various high speed semiconductor devices.

Although a lot has been studied on the binary SSL having perfect lattice matching between its components, only a few investigations have been reported on the periodic strained layer semiconductor superlattices (SLSL) [12–14]. The fabrication and study of the lattice vibrational properties of superlattices consisting of lattice mismatched materials are gaining interest because of their applications in various opto-electronic devices. The strain due to lattice mismatch of the constituting components of the SLSL is accommodated by each layer in such a way that the system is structurally and thermodynamically stable. The strain generated in such systems is isotropic in nature and in most of the cases, it changes the volume of each binary layer without affecting the crystal symmetry [15]. Due to this fact, it has now been possible to fabricate semiconductor heterostructures by avoiding misfit dislocations [14].

On the other hand, the discovery of icosahedral crystallographic symmetry has proved to be a new dimension to the study of the electronic and vibrational properties of quasi-periodic systems [16, 17]. Among the quasi-periodic superlattices, the Fibonacci superlattices (FSL) have been studied extensively both theoretically [18] as well as experimentally [19]. However, in the case of FSL, the main emphasis has been on the study of acoustic phonon propagation and their transmission [20–22]. Other types of quasi-periodic sequences are Thue-Morse, Cantor bar etc. Recently, some

theoretical efforts have been devoted to investigate the vibrational properti semiconductor quasi-periodic systems [20].

In a recent paper, we have reported the calculated results of vibrational pro $(GaAs)_{n_1}(GaSb)_{n_2}$ SSL [2]. In this investigation the effects of strain on the vi modes of a kind of quasiperiodic semiconductor superlattices, the cantor bar ductor superlattices (CBSSL) of one and three generations comprising of GaAs as its components. In addition to this, we have also calculated th spectra for two component GaAs, GaSb and three component GaAs, InAs a FSL of four generations. Also, we have studied the thickness dependence o phonon modes of GaAs. The main objective in investigating this problem ha understand the effect of strain on the phonon properties of quasiperiodic sup The lattice mismatch in GaAs and GaSb is quite large ($\approx 7\%$) and these mat ideal for observing the effects of strain on the vibrational properties of su periodic SSL. The phonon dispersion curves (PDC) in CBSSL have been c using a linear chain model [2] and the transfer matrix method. This method ha been applied to study the PDC in multicomponent SSL [1] and strai superlattice [2]. We present the structure and generation of the sequence of § 2 followed by a brief outline of the method of calculation of PDC. The res been discussed in § 3.

2. Model structure and dispersion relation

The one-dimensional quasiperiodic semiconductor superlattices under cons are generated recursively along Z-direction by two elementary media: med media B. The model structure prescribed in figure 1, maps the mathematic the cantor triadic bar sequence infinitely as follows [23], $C_1 =$ $C_2 = B_2A_2B_2, \ldots C_n = B_nA_nB_n = C_{n-1}A_nC_{n-1}$ where $B_n = C_{n-1}$, while A_n is medium as layer A_1 but with different thickness, $dA_n = (2+\alpha)^{n-1}dA_1$ w parameter α is the thickness ratio of dA_n to dB_n. The total thickness generation one-dimensional quasiperiodic semiconductor superlattice ($dC_n = (2+\alpha)^n dB_1$ where dB_1 is the thickness of the layer B in the first gener

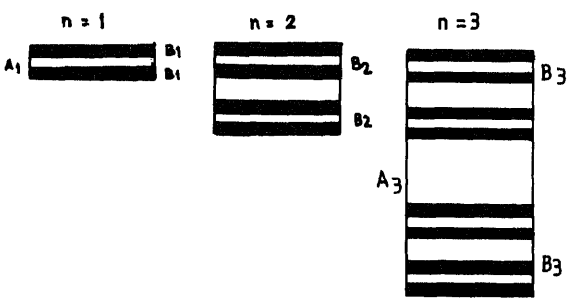

Figure 1. Geometry of a cantor bar triadic semiconductor superlattice three generations.

The fractal dimension of present model [23] is given by $D = \ln 2/\ln(2+\alpha)$. It is easy to find that when $\alpha = 1$, the QSSL becomes usual CBSSL with $D = \ln 2/\ln 3$; when $\alpha = \Lambda = (\sqrt{5}-1)/2$, the structure of QSSL is somewhat like the Fibonacci superlattice. If we substitute, A_n by C_{n-2} and B_n by C_{n-2}, it is just the usual Fibonacci superlattice. Hence, the physical meaning of the quantity α can be found from the fact that it governs the formation of various sequences.

A Fibonacci superlattice comprises of an arrangement of individual building blocks of type A (each of thickness d_A) and type B (each of thickness d_B) following a concatenation scheme determined by the Fibonacci sequence $G_1 = A$, $G_2 = AB$, $G_3 = ABA, \ldots$, $G_r = G_{r-1}G_{r-2}$ [17]. The rth generation FSL G_r consists of F_r type A blocks and F_{r-1} type B blocks, where F_r are the Fibonacci numbers given iteratively $F_r = F_{r-1} + F_{r-2}$ for $r > 2$ with $F_0 = 0$ and $F_1 = 1$. In order that phonons may recognize the distinct interfaces spaced in Fibonacci manner, each building block should be subdivided into two or more layers with different elastic properties. In this paper, we have considered that both type A and B blocks consist of two and three layers.

In order to calculate the phonon dispersion curves for these QSSL, we have adopted a linear chain model in one-dimension, details of which have been given in our previous papers [1, 2]. The general equation of motion of any atom in either of the components of the QSSL can be written as [1]

$$m_j\omega^2 u_n = -C_i(u_{n-1} + u_{n+1} - 2u_n) \tag{1}$$

where $C_i (i = A, B)$ are the nearest neighbour force constants, u_n are the displacements, and m_j are respective masses of the atoms. By using the transfer matrix method as in our earlier papers [1, 2], we get

$$\cos QD = 1/2 \operatorname{tr} T \tag{2}$$

where T is a unimodular (2×2) transfer matrix which has the property of relating the coefficients of the displacement vectors in one cell $(l+1)$ to those in the previous one (l) and is given by

$$T = \prod K_1^{-1} H_n K_n^{-1} H_{n-1} K_{n-1}^{-1} \ldots H_2 K_2^{-1} H_1 \tag{3}$$

where H_i and K_i $(i = 1, n)$ are (2×2) unimodular matrices and defined in ref. [1].

In the present paper, we have calculated the dispersion curves for diatomic one and three generation CBSSL and two and three component four generation FSL. The transfer matrix in the case of one generation CBSSL reduces to

$$T = K_1^{-1} H_3 K_3^{-1} H_2 K_2^{-1} H_1. \tag{4}$$

This equation is similar to that which has been reported earlier by us in the case of multicomponent SSL [2], where there are only two components, the middle one being different than the two adjacent neighbours. The dispersion relation for three generation CBSSL as well for two and three component four generation FSL have been calculated using (2) and (3) [24].

The effect of strain due to lattice mismatch at the interface of the two components has been considered in the usual manner, as discussed in our previous paper [2]. We have calculated the phonon dispersion relation by considering the effect of strain also, to reveal its role in the dispersion of phonons in such systems. Also we have investigated

the effect of change in layer thickness on the highest longitudinal optical mod by varying the value of α.

3. Results and discussion

We have calculated the phonon dispersion curves (PDC) of unstrained an one, three generation CBSSL and two, three component four generation constituents of CBSSL and two component FSL are GaAs and GaSb and th component FSL are GaAs, InAs and GaSb. The various parameters constants have been calculated in the usual way as explained in our earlier pap The calculated bulk dispersion curves (longitudinal modes) for GaAs a compared with the experimental values [25,26] have been reported in ref. [

In figures 2(a) and 2(b), we have plotted the PDC of one and three generatic with the components B and A as $(GaAs)_{n_1}$ and $(GaSb)_{n_2}$ respectively with the $n_1 = n_2 = 10$. In this calculation, we have not considered the effect of stra figures reveal that they adequately explain the usual features of the su vibrations. It is also seen from these figures that with the increase of the th GaSb from one to three generations, the number of confined modes of GaSb This fact is true in both one and three generation CBSSL. However, when th the components is reversed with a motivation to study the effect of increased of one of the constituents, the number of GaAs layers increases as the n generations increase resulting into the increase in the number of confine modes. It is observed from these figures that the self similarity nature incre increase in the generation number. In addition to this, we have also calcu

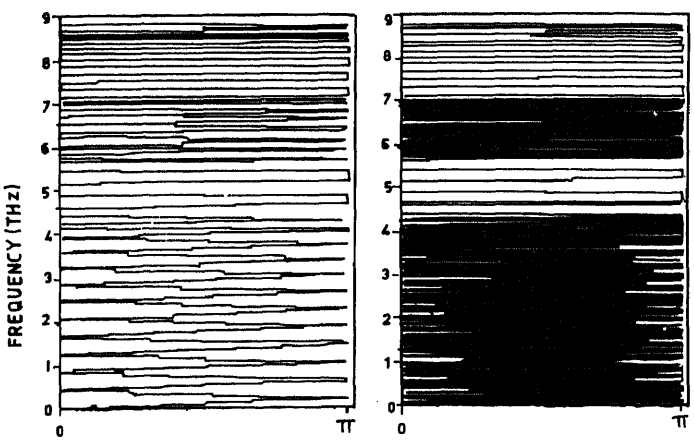

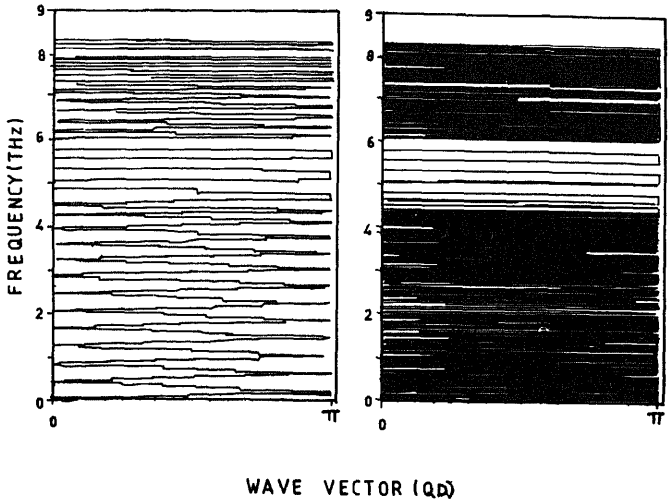

Figure 3. Phonon dispersion curves of strained CBSSL with components A and B as $(GaSb)_{10}$ and $(GaAs)_{10}$ respectively for (a) one and (b) three generations.

phonon dispersion curves in another quasiperiodic system, the two and multicomponent Fibonacci SSL. The results are quite similar to that of CBSSL.

In order to understand the effect of strain generated due to lattice mismatch, we have plotted in figures 3(a) and 3(b), the PDC of one and three generation CBSSL with the components GaSb and GaAs for the above mentioned order and thickness. It is observed from these figures, that in addition to the self similarity nature and other usual features observed in quasi-periodic SSL, there is a downward shift of the highest LO mode frequency of GaAs for both the cases and generations. This is attributed to the fact that the lattice mismatch is accommodated by tensile strain in GaAs and as compressive strain in GaSb. Thus, it reduces the lattice constant of GaSb and enhances that of GaAs. However, when the order of the components is reversed, the downward shift increases more because of the increase in the number of the GaAs layers. Our arguments can be justified from our earlier papers [1, 2] and Raman scattering measurements made on InGaAs/GaAs [13] and GaSb/AlSb [27] SLSL, respectively. To the best of our knowledge, we have calculated for the first time the PDC of a multicomponent four generation Fibonacci SSL without and with the effect of strain included. The FSL comprises of building blocks A as $(GaAs)_{10}(GaSb)_{10}(InAs)_{20}$ and that of B as $(GaAs)_{10}(GaSb)_{10}(InAs)_4$. The calculations here are carried out with the assumption that GaSb and InAs are perfectly lattice matched and there occurs a lattice mismatch between InAs and GaAs. The PDC have been plotted in figures 4(a) and 4(b). This figure reveals that there occurs a considerably large amount of frequency shift of the highest GaAs LO mode which is more prominent in this case than the two component FSL with all usual features observed in quasiperiodic systems.

To investigate the effects of strain on the LO phonon modes quantitatively, we plot in figure 5, the highest LO mode of GaAs for three generation CBSSL for cases

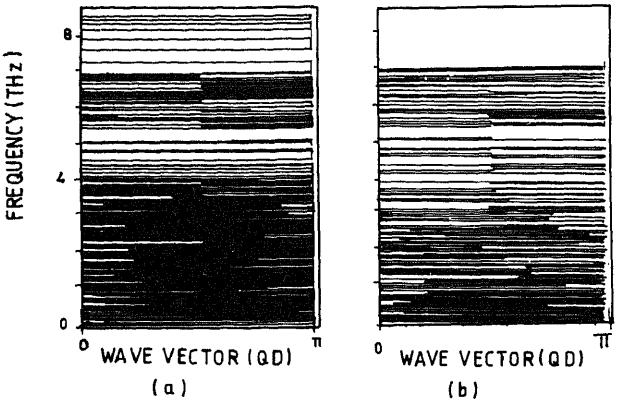

Figure 4. Phonon dispersion curves for FSSL of four generations with blocks $A = (GaSb)_{10}(InAs)_{20}(GaAs)_{10}$, $B = (GaSb)_{10}(InAs)_4(GaAs)_{10}$ for unstrained (a) and strained (b) systems.

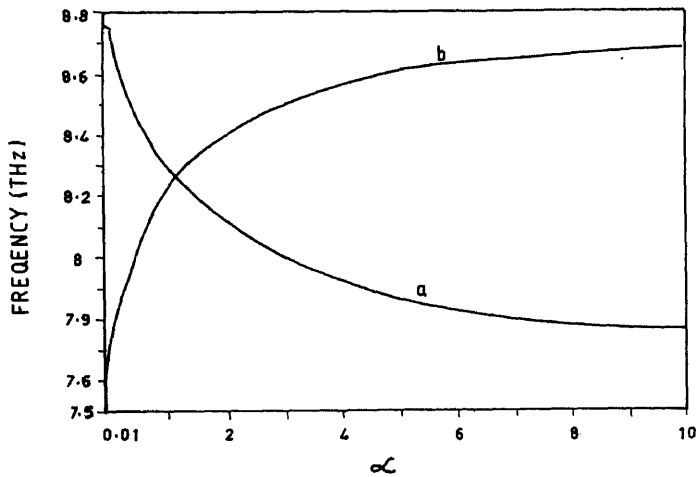

Figure 5. Thickness ratio α as a function of highest GaAs LO frequency of strained CBSSL for three generations with layers A and B as (a) $(GaSb)_{10}$ and $(GaAs)_n$; (b) $(GaAs)_{10}$ and $(GaSb)_n$ respectively.

(a) B = GaAs and A = GaSb, (b) B = GaSb and A = GaAs. Considering the first case in which the thickness of the GaSb layer is kept constant and that of GaAs is varied resulting into the variation of the parameter α from 0·01 to 10. It is observed that as the value of the parameter α increases from 0·01 to 10, the thickness of GaSb increases as compared to that of GaAs leading to the downward shift of the GaAs LO mode. At $\alpha = 10$, the system behaves as bulk GaSb and the frequency is very near to that of GaSb

LO mode. But as α decreases to 0·01, the strain induced effect on the LO modes of GaAs relaxes thereby saturating at a frequency quite close to that of experimental zone centre value. This is due to the fact that around $\alpha = 0{\cdot}01$, the thickness of GaAs layers is very large as compared to GaSb and hence the system behaves as bulk GaAs. Similar arguments hold good when the order is reversed (case (b)) thereby showing reverse nature.

In conclusion, we have investigated the effect of built-in strain on the PDC of quasiperiodic CBSSL and FSL thereby observing that the change in the in-plane lattice parameter subsequently, enhances (or suppresses) the highest LO mode of GaAs. However, so far no efforts have been made from the experimental point of view on the phonon properties of such systems. We emphasize the need of Raman measurement for such systems.

Acknowledgements

The authors are grateful to the Department of Science and Technology for financial assistance. SR and PKJ are grateful to CSIR for the award of senior research fellowship and research associateship respectively. One of us (SPS) acknowledges the career award of UGC.

References

[1] S Rath and S P Sanyal, *Phys. Status Solidi* **B176**, 63 (1993)
[2] S Rath and S P Sanyal, *Pramana – J. Phys.* **41**, 21 (1993)
[3] C Colvard, T A Gant, M V Klein, R Merlin, R Fischer, H Morkoc and A C Gossard, *Phys. Rev.* **B31**, 2080 (1985) and references therein
[4] B D Rouhani, A A Maradudin and R F Wallis, *Phys. Rev.* **B29**, 6454 (1984)
[5] L Esaki, *Physics and applications of quantum wells and superlattices*, edited by E E Mendez and K Von Kliltzing (Plenum Press, New York, 1989)
[6] A K Ramdas and S Rodriguez, *Semiconductor and semimetals*, edited by J K Furdyna and J Kossut (Academic Press, New York, 1988)
[7] J Sapriel and B D Rouhani, *Surf. Sci. Rep.* **10**, 189 (1989)
[8] M V Klein, *IEEE J. Quantum Electronics* **22**, 1780 (1986)
[9] M Cardona, *Spectroscopy of semiconductor microstructures*, (Plenum Press, New York, 1990)
[10] B Jusserand and M Cardona, *Light scattering in solids*, (Springer–Verlag, Heidelberg, 1989) Vol. V, p. 49
[11] M Cardona, *Superlattices and microstructures* **7**, 183 (1990)
[12] E Friess, K Eberl, U Menczigar and G Abstreiter, *Solid State Commun.* **73**, 203 (1990)
[13] F Iikawa, F Cerdeira, C Vazquez-Lopez, P Motisuke, M A Sacilotti, A P Roth and M A Masut, *Solid State Commun.* **68**, 211 (1988) and references therein
[14] P Voisin, *Semiconductor Physics*, edited by C E T Gonsalves da Silva, L E Oliveiza and J R Leile (World Scientific, Singapore, 1987) p. 46
[15] T P Pearsell, *Semiconductors and semimetals*, (Academic Press, New York, 1990) Vol. 32, p. 1
[16] H Bottger and G Kasner, *Quasicrystals*, Edited by M V Jaric and S Lundqvist, (World Scientific, Singapore, 1990)
[17] R Merlin, *IEEE J. Quantum Electron.*, **QE-24**, 1791 (1988)
[18] S Tamura and J P Wolfe, *Phys. Rev.* **B36**, 3491 (1987)
[19] D C Hurley, S Tamura, J P Wolfe, K Ploog and J Nagle, *Phys. Rev.* **B37**, 8829 (1988)
[20] S Tamura and F Nori, *Phys. Rev.* **B40**, 9790 (1989)

[21] S Tamura and F Nori, *Phys. Rev.* **B41**, 7941 (1990)
[22] N Nishigushi, S Tamura and F Nori, *Phys. Rev.* **B48**, 2515 (1993)
[23] B B Mandelbrot, *The fractal geometry of nature* (Freeman, New York, 1982)
[24] Sujata Rath, *Phonons in semiconductor superlattices* Ph.D. Thesis, Barkatullah University, Bhopal (1993)
[25] D Strauch and B Dorner, *J. Phys.* **C2**, 1497 (1990)
[26] M K Farr, J G Traylor and S K Sinha, *Phys. Rev.* **B11**, 1587 (1975)
[27] P V Santos, A K Sood, M Cardona, K Ploog, Y Ohmori, M Okamoto, *Phys. Rev.* **B37**, 6381 (1988)

Effect of crystal field on the spin density at the copper nucleus in copper complexes

V GOMATHY*, U S GHOSH and C BASU
Department of Solid State Physics, Indian Association for the Cultivation of Science, Jadavpur, Calcutta 700 032, India
*Department of Physics, Raja Peary Mohan College, Uttarpara 712 258, W.B., India

MS received 12 August 1994; revised 10 March 1995

Abstract. The role of lower symmetry component of the crystal field in causing a mixing of excited $3d^{x-1}4s$ with the ground $3d^x$ configuration and leading to spin density at the nucleus for iron group ions was suggested by Griffith and Orgel. This mechanism has been examined in detail for the two low-symmetry copper complexes, one square planar (D_{4h} symmetry) and the other distorted tetrahedron (D_{2d} symmetry) and the calculation has been performed using the powerful Racah method and tensor operator technique. It is found that for the two types of copper complexes, copper pthalocyanin (square planar, D_{4h} symmetry) and cesium copper chloride (distorted tetrahedron, D_{2d} symmetry) the contribution from this mechanism to the spin density at the nucleus vanishes identically.

Keywords. Spin density; configuration interaction.

PACS No. 31·20

1. Introduction

The problem dealt with in the present work is the result of a program which we initiated for studying the effect of configuration interaction on the various physical properties of iron group such as crystal field splittings [1–5], intensity of crystal field spectra [6, 7], reduction of orbital moment and s-o coupling [8] and finally on the spin density at the nuclear site of the ion. The configuration interaction in which we are interested in the said program concerns the mixing of the ground configuration $3d^x$ with the excited configurations $3d^{x-1}4l(4l \equiv 4s, 4p, 4d$ and $4f)$ in which a 3d electron is promoted to the 4s, 4p, 4d or 4f orbit.

For the explanation of spin density at the nulcear site of iron group ions Abragam *et al* [9] proposed a mechanism where the ground configuration $1s^22s^22p^63s^23p^63d^x$ gets admixed via interelectronic repulsion with the excited configuration $1s^22s^22p^63s3p^63d^xRs$ where Rs is a generalized higher s-orbital orthogonal to all the s-orbitals. The method of evaluating Rs using variational Hartree–Fock calculation has been illustrated by Abragam *et al* [9]. However, this mechanism yielded a result for the spin density equal to $-0{\cdot}3$ a.u. instead of the experimental value -3 a.u. approximately in the case of Mn^{2+}. Griffith and Orgel [10, 11] suggested a mechanism which is dependent on crystal field having a symmetry lower than the cubic and causing an admixture of the excited configuration $1s^22s^22p^63s^23p^63d^{x-1}4s$ with the ground configuration. To our knowledge the size of the contribution from this mechanism to the spin density, although, suggested long ago, was not quantitatively calculated and reported in the

which is now considered to be the most plausible and successful mechan
excellent agreement with the experiment. This mechanism is based on th
magnetic polarization of an atomic or ionic core of closed shells by ar
external shell having a total spin S. The radial functions of s-orbitals of a
with spin up and down are considered to be different because of their
coupling with the magnetic d-electrons and the density at the origin will be
for the two cases. Some details of the calculation can be found in the revie
[12,13]. The calculation of spin density involves quantities which are se
the precise form of electron wavefunctions. Further development involvin
forms of Hartree–Fock calculation and other rigorous techniques
correlation and relativistic correction may be found in excellent reviews
Recent works [16–20] with the highly sophisticated methods such as lar
configuration H–F technique, multireference configuration interaction te
many-body perturbation technique etc. are confined within the relativ
atoms. The complexity of these sophisticated calculations seems to indica
nued reliance on the more straightforward spin-polarized H–F technique fo
atoms or ions.

We would like to stress that the present paper does not aim at explaining
density of the two copper complexes, Cu-pthalocyanin (CuPc) and Cs_2CuCl_4
the size of the contribution from the crystal field dependent mechanism sug
Griffith and Orgel as a part of our program of studying the effect of confi
interaction on the various physical properties of iron group ions as stated ea
choose the above two particular ions since the deviation from pure cubic syn
large in these cases, a condition necessary for Griffith and Orgel mechanism to
significance. The first is a covalent square planar complex (D_{4h} symmetry) [21
a large deviation from cubic symmetry. In Cs_2CuCl_4, the Cu^{2+} ion deviates f
T_d as observed from X-ray [22, 23] and it is best described by D_{2d} symmetry
epr hyperfine structures from which the experimental values of spin density
extracted are also available for these two copper complexes [21, 25]. To our su
found that the contribution to the spin density from Griffith and Orgel me
vanishes identically in these two particular cases even though the symmetry
appreciably from pure cubic, a result considered to be worth reporting. The n
is evidently due to the particular symmetry of the copper ion. This, of course,
mean that in the case of other symmetries of the copper complex, the contribut
Griffith and Orgel mechanism will also vanish.

The central density χ of the unpaired spin is calculated from the followin
sion [9]

$$\chi = \frac{4\pi}{S} \langle \psi | \sum \delta(\mathbf{r}_t) s_{tz} | \psi \rangle_{S_z = S}$$

where S is the total spin of the ion in its ground configuration, the state ψ is t
state of the ground configuration $3d^x$ in a crystal field admixed with the states
configuration $3d^{x-1}4s$ via both crystal field and interelectronic repulsion co
together as the perturbation.

2. Method of calculation

The lowest state of the ground configuration $3d^9$ of Cu^{2+} ion in D_{2d} and D_{4h} symmetry is given by [24, 21]

$$\psi_g(3d^9) = (1/2)^{1/2}[|3d^9\,{}^2D\ 1/2\ 2\rangle \mp |3d^9\,{}^2D\ 1/2\ -2\rangle]$$
$$= (1/2)^{1/2}[|\psi_1\rangle \mp |\psi_2\rangle] \quad \text{(say)}. \tag{2}$$

The upper and lower signs correspond to $D_{2d}(Cs_2CuCl_4)$ and D_{4h}(CuPc) systems respectively. We consider the mixing of this lowest state as given by (2) with the various states of the excited configuration $3d^8 4s$ via the combined action of interelectronic repulsion and crystal field interaction i.e. through the operator

$$\sum_{i<j} (e^2/r_{ij}) + H_c \tag{3}$$

where $H_c = \Sigma_i - |e|\,V(i)$, and $V(i)$ is the crystal field potential of the ith electron and the summation extends over all the electrons of the unfilled shell. For Cs_2CuCl_4(D_{2d} symmetry)

$$V(i) = a_{20}\,V_0^{(2)}(i) + a_{40}\,V_0^{(4)}(i) + a_{44}[V_4^{(4)}(i) + V_{-4}^{(4)}(i)]$$
$$+ a_{32}[V_2^{(3)}(i) - V_{-2}^{(3)}(i)] + a_{52}[V_2^{(5)}(i) - V_{-2}^{(5)}(i)] \tag{4}$$

For CuPc (D_{4h} symmetry)

$$V(i) = a_{20}\,V_0^{(2)}(i) + a_{40}\,V_0^{(4)}(i) + a_{44}[V_4^{(4)}(i) + V_{-4}^{(4)}(i)] \tag{5}$$

In (4) and (5) a_{kq}'s are crystal field coefficients and $V_q^{(k)} = r^k\,Y_k^q$, Y_k^q being a spherical harmonic of order k and component q. In the present calculation we need only to consider the term $a_{20}\,V_0^{(2)}$ of the crystal field potential, for other terms of the potential the matrix elements of H_c between the states of $3d^9$ and $3d^8 4s$ vanish. The configurationally mixed lowest state becomes

$$\psi = \psi_g(3d^9) - (1/\Delta E)\sum_{\psi_e} \langle\psi_e(3d^8 4s)|\left[\sum(e^2/r_{ij}) + \sum - |e|a_{20}\,V_0^{(2)}(i)\right]$$
$$\times |\psi_g(3d^9)\rangle|\psi_e(3d^8 4s)\rangle \tag{6}$$

where the general form of the states of the excited configuration $3d^8 4s$ is written as $\psi_e = |3d^8(S_1 L_1)\ 4s\ S'L'M_S'M_L'\rangle$ and ΔE is the energy separation of the excited configuration $3d^8 4s$ from the ground $3d^9$ configuration. For the matrix elements of $\Sigma(e^2/r_{ij})$ in (6) we need to calculate only

$$\langle 3d^9\,{}^2D|\sum e^2/r_{ij}|3d^8(^1D)4s\,{}^2D\rangle$$

since the matrix of $\Sigma e^2/r_{ij}$ is diagonal in L, S. Here M_S and M_L values are omitted in the state symbol as the matrix element does not depend on them. Racah [26] has already given a very convenient formula for the evaluation of such matrix element which

reduces to the following (using eq. (79) of Racah [26])

$$\begin{aligned}\langle 3d^9\,{}^2D|\textstyle\sum e^2/r_{ij}|3d^8(^1D)4s^2D\rangle &= (9/14)^{1/2}[\langle d^9\,{}^2D||U^{(2)}||d^9\,{}^2D\rangle\langle d^9\,{}^2D\{|d^8(^1D)d^2D\rangle 5^{1/2}\\ &+ \langle d^9\,{}^2D\{|d^8(^1S)d^2D\rangle\langle d^8\,{}^1S||U^{(2)}||d^8\,{}^1D\rangle 5^{1/2}\\ &+ \langle d^9\,{}^2D\{|d^8(^1D)d^2D\rangle\langle d^8\,{}^1D||U^{(2)}||d^8\,{}^1D\rangle 5^{1/2}\\ &+ \langle d^9\,{}^2D\{|d^8(^1G)d^2D\rangle\langle d^8\,{}^1G||U^{(2)}||d^8\,{}^1D\rangle 5^{1/2}]R^{(2)}(3d\,3d,\,3d\,4s)\end{aligned} \tag{7}$$

where the various symbols and quantities have been explained in Racah's papers [26, 27]. Using eq. (74) of Racah [27]

$$\langle d^9\,{}^2D||U^{(2)}||d^9\,{}^2D\rangle = -\langle d||u^{(2)}||d\rangle = -1 \tag{8}$$

and

$$\langle d^8(S_1L_1)||U^{(2)}||d^8(S_1L_1')\rangle = -\langle d^2(S_1L_1)||U^{(2)}||d^2(S_1L_1')\rangle \tag{9}$$

The r.h.s. of (9) has been tabulated by Racah [27], eq. (103b).

Carrying out the calculation involved in (7) we finally get

$$\langle 3d^9\,{}^2D|\textstyle\sum e^2/r_{ij}|d^8(^1D)4s^2D\rangle = -(2/35)^{1/2}R^{(2)}(3d\,3d,\,3d\,4s)$$

where $R^{(2)}(3d\,3d,\,3d\,4s)$ is the interelectronic repulsion integral defined by Condon and Shortley [28]. The matrix element of $\Sigma V_0^{(2)}(i)$ that occurs in (6) is of the form

$$\langle 3d^9\,{}^2D\,1/2\,M_L|\textstyle\sum V_0^{(2)}|d^8(S_1L_1)4s^2L_1\,1/2\,M_{L_1}\rangle = A \quad \text{(say)} \tag{10}$$

which may be written as (using tensor operator formula [29])

$$\begin{aligned}A = 9^{1/2}\langle d^9\,{}^2D\{|d^8(S_1L_1)d^2D\rangle(-1)^{L_1-M_L}[5(2L_1+1)]^{1/2}\\ \begin{Bmatrix}2 & 2 & L_1\\ 0 & L_1 & 2\end{Bmatrix}\langle 3d||V^{(2)}||4s\rangle\begin{pmatrix}2 & 2 & L_1\\ -M_L & 0 & M_{L_1}\end{pmatrix}.\end{aligned} \tag{11}$$

Thus the admixed state ψ in (6) reduces to

$$\begin{aligned}\psi = (1/2)^{1/2}[|\psi_1\rangle \mp |\psi_2\rangle] - (\Delta E)^{-1}[-(1/35)^{1/2}R^{(2)}(3d\,3d,\,3d\,4s)\\ \times(|\phi_1\rangle \mp |\phi_2\rangle) + v_{20}\{(1/35)^{1/2}(|\phi_1\rangle \mp |\phi_2\rangle) - (3/20)^{1/2}(|\phi_3\rangle \pm |\phi_4\rangle)\\ + (3/140)^{1/2}(|\phi_5\rangle \mp |\phi_6\rangle)\}]\end{aligned} \tag{12}$$

where

$$\begin{aligned}v_{20} &= |e|a_{20}\langle 3d||V^{(2)}||4s\rangle\\ &= |e|a_{20}(5/4\pi)^{1/2}\begin{pmatrix}0 & 2 & 2\\ 0 & 0 & 0\end{pmatrix}\int R_{3d}^* r^2 R_{4s} r^2\,dr\end{aligned}$$

$$|\phi_1\rangle = |3d^8(^1D)4s^2D\,1/2\,2\rangle, \quad |\phi_2\rangle = |3d^8(^1D)4s^2D\,1/2\,-2\rangle$$

$$|\phi_3\rangle = |3d^8(^3F)4s^2F\,1/2\,2\rangle, \quad |\phi_4\rangle = |3d^8(^3F)4s^2F\,1/2\,-2\rangle$$

$$|\phi_5\rangle = |3d^8(^1G)4s^2G\,1/2\,2\rangle, \quad |\phi_6\rangle = |3d^8(^1G)4s^2G\,1/2\,-2\rangle$$

and the upper sign in (12) corresponds to Cs_2CuCl_4 and the lower sign to CuPc. The

Expanding ψ according to (12) χ ultimately comes out to be

$$\chi = \chi_C + \chi_R + \chi_{CR} \tag{13}$$

where

$$\chi_C = [(1/35)(\langle\phi_1|Q|\phi_1\rangle + \langle\phi_2|Q|\phi_2\rangle) + (3/20)(\langle\phi_3|Q|\phi_3\rangle + \langle\phi_4|Q|\phi_4\rangle) + (3/140)(\langle\phi_5|Q|\phi_5\rangle + \langle\phi_6|Q|\phi_6\rangle)](4\pi/S)(v_{20}/\Delta E)^2$$

$$\chi_R = (4\pi/S)(1/35)[(1/\Delta E)R^{(2)}(3d\,3d, 3d\,4s)]^2[\langle\phi_1|Q|\phi_1\rangle + \langle\phi_2|Q|\phi_2\rangle]$$

$$\chi_{CR} = (4\pi/S)(1/\Delta E)^2[-(1/35)^{1/2}v_{20}R^{(2)}(3d\,3d, 3d\,4s)] \times [\langle\phi_1|Q|\phi_1\rangle + \langle\phi_2|Q|\phi_2\rangle]$$

in which $Q = \Sigma\delta(\mathbf{r}_t)s_{tz}$; χ_C represents the contributions to the spin density at the nucleus arising through the admixture of ground $3d^9$ and excited $3d^8 4s$ configurations via crystal field alone as was suggested by Griffith and Orgel [10], χ_R stands for the contribution arising through the admixture of the two configurations via interelectronic repulsion alone and the contribution χ_{CR} arises from the cross terms like

$$\langle\phi_i|\sum e^2/r_{ij}|\psi_g(3d^9)\rangle \quad \langle\psi_g(3d^9)|H_C|\phi_i\rangle \quad \langle\phi_i|Q|\phi_i\rangle.$$

The type of matrix element $\langle\phi_i|Q|\phi_i\rangle$ that we now need is

$$\langle d^8(S_1 L_1)s^2 L_1\ 1/2\ M_{L_1}|\sum\delta(\mathbf{r}_t)s_{tz}|d^8(S_1 L_1)s^2 L_1\ 1/2\ M_{L_1}\rangle = B \quad \text{(say)}$$

where $M_{L_1} = 2$ or -2. Using (22) and (26) of Racah [26]

$$B = \langle d^8(S_1 L_1)s_t{}^2 L_1\ 1/2\ M_{L_1}|\delta(\mathbf{r}_t)s_{tz}|d^8(S_1 L_1)s_t{}^2 L_1\ 1/2\ M_{L_1}\rangle$$

$$= \begin{pmatrix} 1/2 & 1 & 1/2 \\ -1/2 & 0 & 1/2 \end{pmatrix}\langle S_1 4s\ 1/2||\delta(\mathbf{r})s_0^{(1)}||S_1 4s\ 1/2\rangle$$

$$= (-1)^s \cdot 6^{1/2}\begin{Bmatrix} 1/2 & 1 & 1/2 \\ 1/2 & S_1 & 1/2 \end{Bmatrix}|\psi_{4s}(0)|^2$$

where $\psi_{4s}(0)$ is the wave function of 4s electron at $r = 0$ (origin).

3. Results

Calculation yields

$$\chi_C = (4\pi/S)[v_{20}/\Delta E]^2(1/4\pi)\{(1/35)|\psi_{4s}(0)|^2 - (1/20)|\psi_{4s}(0)|^2 + (3/140)|\psi_{4s}(0)|^2\}$$

$$= 0$$

$$\chi_R = (\Delta E)^{-2}(1/35S)[R^{(2)}(3d\,3d, 3d\,4s)]^2|\psi_{4s}(0)|^2$$

$$\chi_{CR} = -(\Delta E)^{-2}S^{-1}(1/35)^{1/2}R^{(2)}(3d\,3d, 3d\,4s)v_{20}|\psi_{4s}(0)|^2$$

Thus χ_C is found to vanish identically in the present case showing that the crystal field through the mechanism suggested by Griffith and Orgel has no contribution to the spin

density at the nuclear site of the copper ion. However the crystal field indirectly gives a non-zero contribution χ_{CR} which involves the crystal field parameter through v_{20}. An estimate of χ_{CR} may be made from the knowledge of a correct radial wave function in the crystal which is difficult to obtain. However, a rough estimate may be made by considering Richardson's wave functions [30, 31].

The energy separation ΔE of the excited configuration $3d^8 4s$ from the ground $3d^9$ configuration for Cu^{2+} ion is obtained from Moore's table [32]

$$\Delta E = 0{\cdot}74 \times 10^5\,\mathrm{cm}^{-1} = 3{\cdot}371688 \times 10^{-1}\,\mathrm{a.u.}$$

Using Richardson's radial functions we have

$$|\psi_{4s}(0)|^2 = 36{\cdot}2232\,\mathrm{a.u.}$$

$$R^{(2)}(3d\,3d,\ 3d\,4s) = 0{\cdot}006833\,\mathrm{a.u.}$$

$$\int R^*_{3d} r^2 R_{4s} r^2 dr = 1{\cdot}3743\,\mathrm{a.u.} \tag{14}$$

As in our previous work [5] the value of v_{20} in the case of Cs_2CuCl_4 can be calculated from the knowledge of metal-ligand distance [22, 23], ligand charge ($= -|e|$) and the radial integral given in (14). The value is $v_{20} = 0{\cdot}0133$ a.u. for Cs_2CuCl_4.

The value of v_{20} is difficult to estimate in the case of Cu-pthalocyanin. A rough estimate in this case will be made considering v_{20} for the covalent compound CuPc larger than that for Cs_2CuCl_4 by a maximum of one order in magnitude. Thus using the above numerical values and the total spin $S = 1/2$ for Cu^{2+} ion we arrive at the following results

$$\chi_C = 0$$

$$\chi_R = 0{\cdot}85 \times 10^{-3}\,\mathrm{a.u.}$$

$$\chi_{CR} = -0{\cdot}165 \times 10^{-2}\,\mathrm{a.u.} \quad (\text{for } Cs_2CuCl_4)$$

$$= -1{\cdot}65 \times 10^{-2}\,\mathrm{a.u.} \quad (\text{for CuPc assuming that } v_{20} \text{ has a value 10 times that in the case of } Cs_2CuCl_4)$$

4. Discussion

The above calculation shows that χ_C, the contribution arising from the mechanism of Griffith and Orgel identically vanishes in the present case. Further, it is clear that χ_{CR} is of very little significance when compared with the experiment which gives a total value of about $-3{\cdot}2$ a.u. in Cu(Pc) [21] and $-2{\cdot}7$ a.u. in Cs_2CuCl_4 [25] for the spin density at the copper nucleus as derived from the epr hyperfine spectral data of these two copper complexes. Incidentally, we note that the magnitude of χ_R is even smaller than that of χ_{CR}. We conclude that the role of crystal field in contributing to the spin density at the site of copper nucleus in the case of copper pthalocyanin and cesium copper chloride is of very little importance although the symmetry of the copper ion largely deviates from cubic.

References

[1] C Basu, D Majumdar and U S Ghosh, *Solid State Commun.* **9**, 845 (1971)
[2] C Basu, D Majumdar and U S Ghosh, *J. Chem. Phys.* **57**, 62 (1972)
[3] C Basu and U S Ghosh, *Phys. Rev.* **B11**, 1847 (1975)
[4] C Basu and U S Ghosh, *Phys. Rev.* **B15**, 1307 (1977)
[5] V Gomathy, C Basu and U S Ghosh, *Phys. Status. Solidi* **B160**, 583 (1990)
[6] C Basu and U S Ghosh, *Phys. Status. Solidi* **B70**, K95 (1975)
[7] V Gomathy, C Basu and U S Ghosh, *Phys. Status. Solidi* **B86**, 379 (1978)
[8] C Basu, D Majumdar and U S Ghosh, *Phys. Status. Solidi* **B53**, 711 (1972)
[9] A Abragam, J Horowitz and M H L Pryce, *Proc. R. Soc. (London)* **A230**, 169 (1955)
[10] J S Griffith and L E Orgel, *Trans. Faraday Soc.* **53**, 601 (1957)
[11] J S Griffith, *The theory of transition metal ions* (Cambridge University Press, 1961) p. 328
[12] A J Freeman and R E Watson, *Magnetism*, edited by G T Rado and H Suhl (Academic Press, New York, 1965) Vol. II, p. 167
[13] R E Watson and A J Freeman, *Hyperfine interactions* (Academic Press, New York, 1967) p. 53
[14] L Armstrong Jr., *Theory of the hyperfine structure of free atoms* (Wiley-Interscience, 1971), Ch. IV and V
[15] A Hibbert, *Rep. Prog. Phys.* **38**, 1217 (1975)
[16] D Feller and E R Davidson, *J. Chem. Phys.* **88**, 7580 (1988)
[17] S A Blundell, W R Johnson, Z W Liw and J Sapirstein, *Phys. Rev.* **A40**, 2233 (1989)
[18] D Sundholm and J Olsen, *J. Chem. Phys.* **94**, 5051 (1991)
[19] J Carlsoson, P Johnsson and C F Fischer, *Phys. Rev.* **A46**, 2420 (1992)
[20] P Johnsson and C F Fischer, *Phys. Rev.* **A48**, 4113 (1993)
[21] D Kivelson and R Neiman, *J. Chem. Phys.* **35**, 149 (1961)
[22] L Helmholtz and R F Crue, *J. Am. Chem. Soc.* **74**, 1176 (1952)
[23] B Morosin and E C Lingafelter, *J. Phys. Chem.* **65**, 50 (1961)
[24] J Ferguson, *J. Chem. Phys.* **40**, 3406 (1964)
[25] M Sharnoff, *J. Chem. Phys.* **42**, 3383 (1965)
[26] G Racah, *Phys. Rev.* **63**, 367 (1943)
[27] G Racah, *Phys. Rev.* **62**, 438 (1942)
[28] E U Condon and G H Shortley, *Theory of atomic spectra* (University Press, Cambridge, 1953) p. 175
[29] B R Judd, *Operator techniques in atomic spectroscopy* (McGraw–Hill, New York, 1963) p. 72
[30] J W Richardson, W C Nieuwpoort, R R Powell and W F Edgell, *J. Chem. Phys.* **36**, 1057 (1962)
[31] J W Richardson, R R Powell and W C Nieuwpoort, *J. Chem. Phys.* **38**, 796 (1963)
[32] C E Moore, NBS circular no. 467 (US Dept. of Commerce, 1952) Vol. II

PRAMANA
— journal of
physics

© Printed in India

Vol. 45, No. 1,
July 1995
pp. 41–46

Triple differential cross sections for ionization of hydrogen atoms by positrons in a Schwinger variational calculation

J N DAS, A DEY and K CHAKRABARTI
Department of Applied Mathematics, University College of Science, 92, Acharya Prafulla Chandra Road, Calcutta 700 009, India

MS received 2 August 1994; revised 31 December 1994

Abstract. Schwinger variational principle has been used to calculate triple differential cross-sections for ionization of hydrogen atoms by positrons at intermediate and high energies for Ehrhardt type asymmetric geometry. The results agree in general with the calculations of Brauner *et al* [8] and with the second Born calculation.

Keywords. Cross section; collision; ionization; peak; scattering.

PACS No. 34·80

1. Introduction

The study of ionization collisions of atoms by incident charged particles has been an active field of research for the past few decades. Much emphasis has been laid on the study of triple differential cross sections (TDCS) for ionization of atoms by electrons. These studies focus light on various aspects of the ionization problem. In this connection the theoretical work of Byron *et al* [1, 2], Curran and Walters [3] and Curran *et al* [4], Schlemmer *et al* [5], Jones *et al* [6], McCarthy *et al* [7], Brauner *et al* [8], Das and Seal [9, 10] and Seal and Das [11] and the experimental works of Ehrhardt *et al* [12], Ehrhardt [13] and Lohmann *et al* [14] are noteworthy.

For a long time it has been known that positron is more efficient in ionization of atoms and molecules. Recent measurements of total cross sections for hydrogen atoms [15] and hydrogen molecules [16] by positron impact further confirm this. TDCS measured results for positrons are not available now. However, in near future, when such results will be available a new dimension will be added to the ionization studies. A few calculations for total cross sections for ionization of hydrogen atoms by positrons exist at present [17–20]. Brauner *et al* [8] also recorded TDCS results for ionization of hydrogen atoms by positrons along with those for ionization by electrons.

Recently we have made a Schwinger variational calculation (SVC) of TDCS for ionization of hydrogen atoms by electrons and obtained good results [21]. Here we want to report our TDCS results in certain cases for ionization by positrons obtained with the same variational method.

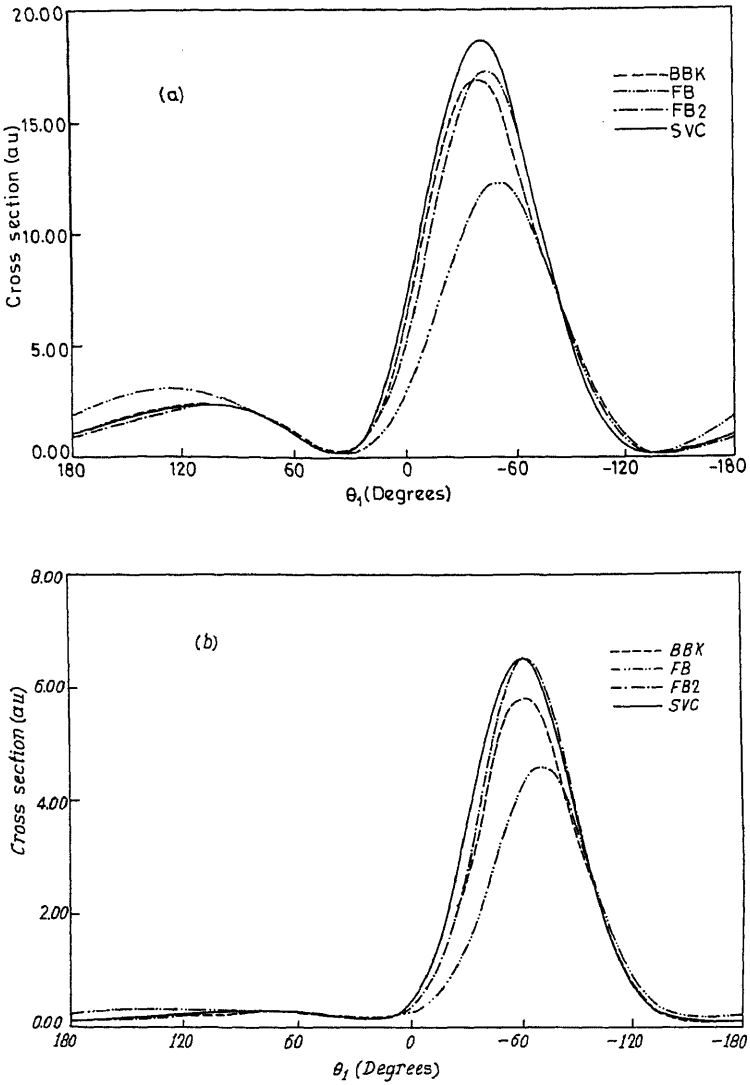

Figure 1. TDCS versus ejection angle θ_1 for ionization of hydrogen atoms by positrons at $E_i = 250\,\text{eV}$, $E_1 = 5\,\text{eV}$, $\theta_1 = 3°$ (**a**) $\theta_2 = 8°$ (**b**). Theory: —— present results (SVC); ——— results of Brauner *et al* (BBK); —·— FB2; —··— FB.

Joachain [22])

$$[T] = \frac{\langle \Phi_f | V | \Psi_i^+ \rangle \langle \Psi_f^{(-)} | V | \Phi_i \rangle}{\langle \Psi_f^{(-)} | V - VG^{(+)} V | \Phi_i \rangle}. \tag{1}$$

It is easily checked that this is stationary (to 1st order) under arbitrary variations

$$|\Psi^{(\pm)}\rangle \rightarrow |\Psi^{(\pm)}\rangle + \Delta |\Psi^{(\pm)}\rangle.$$

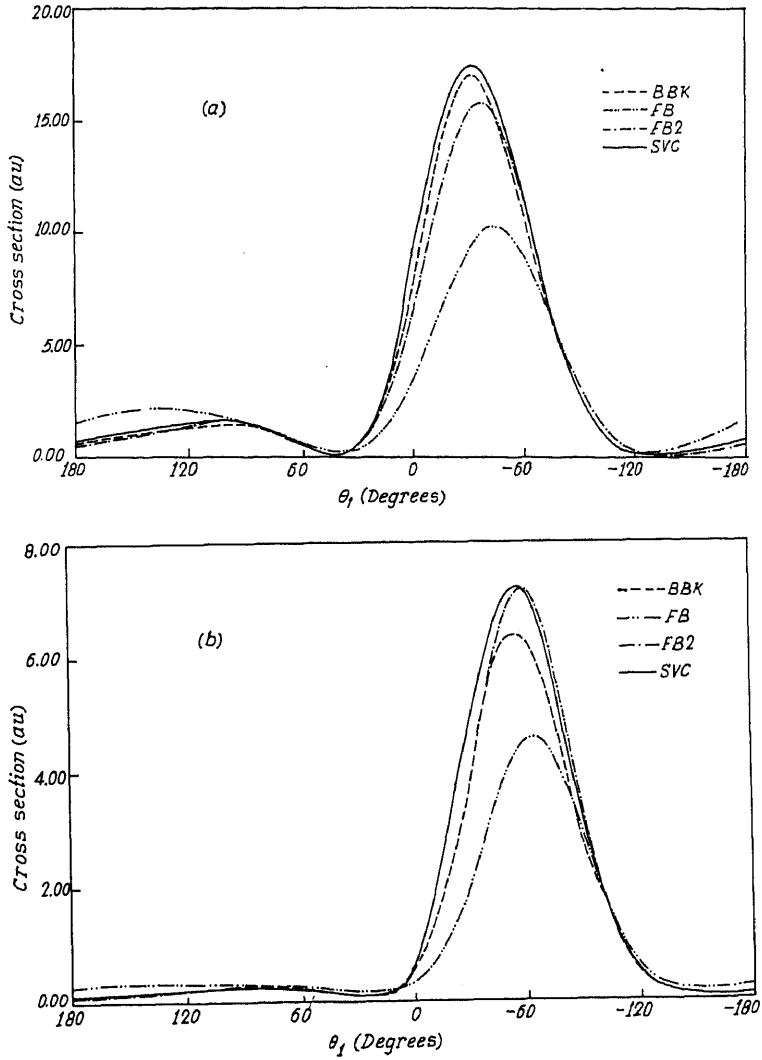

Figure 2. Same as figure 1 except for $E_i = 150\,\text{eV}$, $E_1 = 5\,\text{eV}$, $\theta_2 = 4°$ (**a**) and $\theta_2 = 10°$ (**b**).

This provides the variational principle. Here $|\Phi_i\rangle$ and $|\Phi_f\rangle$ are unperturbed initial and final states, $|\Psi_i^{(+)}\rangle$ and $|\Psi_f^{(-)}\rangle$ are the initial and final channel exact states respectively. V is the interaction potential and $G^{(+)}$ is the Green's function for the perturbed Hamiltonian in which the interaction V is omitted. It is reasonable at high energies to approximate $|\Psi_i^{(+)}\rangle$ and $|\Psi_f^{(-)}\rangle$ by $|\phi_i\rangle$ and $|\Phi_f\rangle$ respectively. The resulting scattering amplitude is then given by

When f_{B2} is small compared to f_B,

$$f \approx f_B + f_{B2}, \tag{3}$$

the second Born amplitude.

The present calculation is effectively same as our recent work [21] except for a change in sign in the interaction potential.

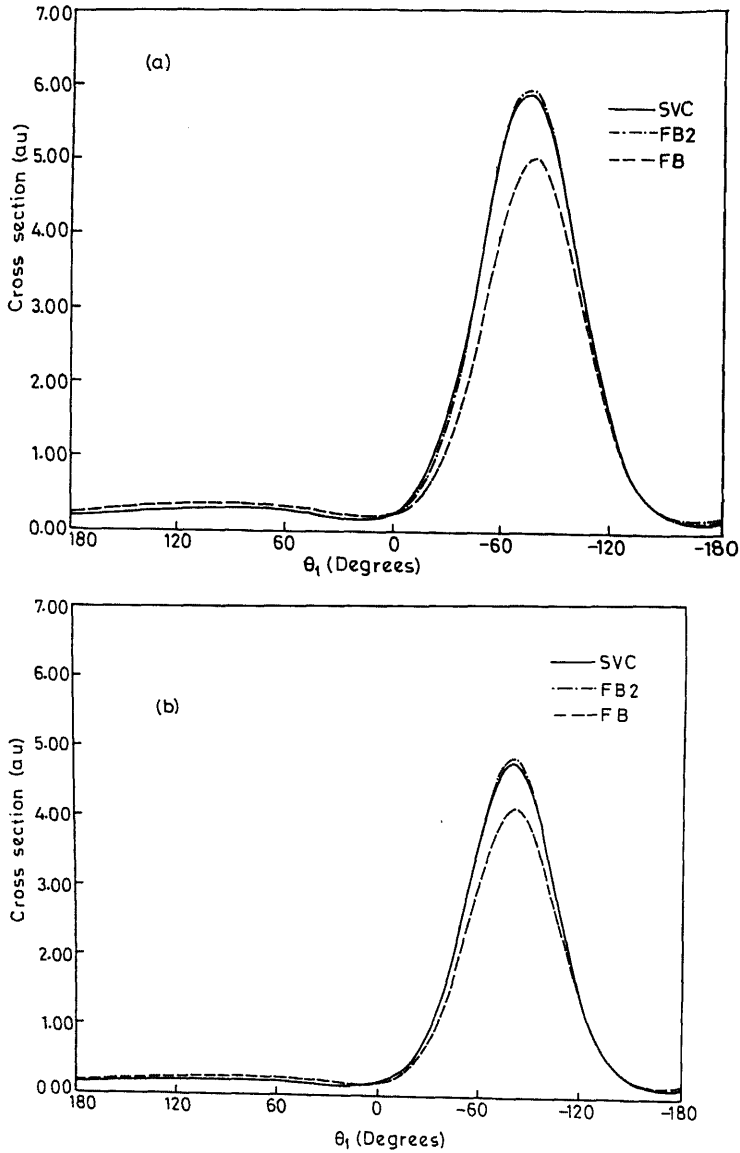

Figure 3a, b.

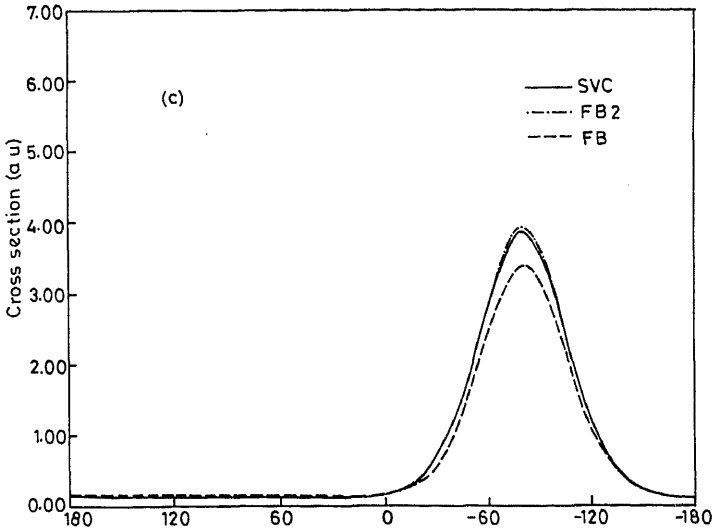

Figure 3c.

Figure 3. As in figure 1 with $E_1 = 5$ eV, $\theta_2 = 5°$, $E_i = 600$ eV (**a**), $E_i = 800$ eV (**b**) and $E_i = 1000$ eV. Theory — SVC; —·—· FB2; ———— FB.

3. Results and discussion

We have used here the usual notations: E for energy, p for momentum, θ for scattering angle (referred to incident particle momentum direction as polar axis). E_i, p_i refer to the incident particle, E_1, p_1, θ_1 to the ejected particle and E_2, p_2, θ_2 to the scattered particle. The scattering is considered in a plane.

Three representative sets of results are presented in figures 1(a), 1(b), 2(a), 2(b) and 3(a), 3(b), 3(c) respectively. Figures 1(a) and 1(b) correspond to $E_i = 250$ eV, $E_1 = 5$ eV, $\theta_2 = 3°$ (1(a)) and $\theta_2 = 8°$(1(b)). In figures 2(a) and 2(b) $E_i = 150$ eV, $E_1 = 5$ eV, $\theta_2 = 4°$ (2(a)) and $\theta_2 = 10°$, (2(b)), while in figures 3(a), 3(b) and 3(c), $E_1 = 5$ eV, $\theta_2 = 5°$; $E_i = 600$ eV (3(a)), $E_i = 800$ eV (3(b)), $E_i = 1000$ eV (3(c)).

As no experimental data for positron impact ionization are available, we compare our results with the theoretical results of Brauner *et al* [8] (see figures 1 and 2), second Born approximation (FB2) and the first Born approximation (FB). At intermediate energies (150 eV–200 eV), the agreement of the present results (SVC) with FB2 and those of Brauner *et al* are fairly good. Since these three results agree well, we may conclude that first Born approximation underestimates cross section in the binary peak region. This is plausible because it is a high energy approximation.

At high energies (600 eV, 800 eV, 1000 eV presented in figures 3) the present results and FB2 results agree remarkably. There is practically no difference between these two. Even at 1000 eV the first Born approximation results differ significantly from that of FB2 and the present results in the binary peak region, though a very slow convergence to the SVC results from 600 eV to 1000 eV is detectable. In the recoil peak region first Born approximation seems to work much better at these energies.

Certain points need to be noted for the present results. Binary peaks are shifted to smaller angles compared to first Born results and the peak heights are much larger. These are just opposite for ionization by electrons. The recoil peak heights are smaller for ionization by positrons compared to those by electrons. At large momentum transfers the present results tend to depart from those of Brauner *et al* [8].

4. Conclusions

It is interesting to note the good agreement between the Schwinger variational results and those of Brauner *et al*. However, at large momentum transfers these tend to depart from each other. Future experimental confirmation or otherwise of these results will be interesting. Schwinger variational calculation for ionization of hydrogen and helium atoms by electrons and positrons using more accurate wave functions such as that used by Das and Seal [9] may produce better results.

Acknowledgement

Research fellowships provided to the authors A Dey and K Chakrabarti by CSIR are gratefully acknowledged.

References

[1] F W Byron, C J Joachain and B Piraux, *J. Phys.* **B13**, L673 (1980)
[2] F W Byron, C J Joachain and B Piraux, *Phys. Lett.* **A99**, 427 (1983)
[3] E P Curran and H R J Walters, *J. Phys.* **B20**, 337 (1987)
[4] E P Curran, C J T Whelan and H R J Walters, *J. Phys.* **B24**, L19 (1991)
[5] P Schlemmer, M K Srivastava, T Rösel and H Ehrhardt, *J. Phys.* **B24**, 2719 (1991)
[6] S Jones, D H Madison, A Franz and P L Altic, *Phys. Rev.* **A48**, R22 (1993)
[7] I E McCarthy and X Zhang, *Aust. J. Phys.* **43**, 291 (1990)
[8] M Brauner, J S Briggs and H Klar, *J. Phys.* **B22**, 2265 (1989)
[9] J N Das and S Seal, *Phys. Rev.* **A47**, 2978 (1993)
[10] J N Das and S Seal, *Pramana – J. Phys.* **40**, 253 (1993)
[11] S Seal and J N Das, *Aust. J. Phys.* **47**, 49 (1994)
[12] H Ehrhardt, K Jung, G Knoth and P Schlemmer, *Z. Phys.* **D1**, 3 (1986)
[13] H Ehrhardt, Private communication (1991)
[14] B Lohmann, I E McCarthy, A T Stelbovics and E Weigold, *Phys. Rev.* **A30**, 758 (1984)
[15] A Schwab, *Nucl. Instrum. Methods Phys. Res.* **B56–57**, 586 (1991)
[16] D Fromme, G Kruse, W Raith and G Sinapius, *J. Phys.* **B21**, L261 (1988)
[17] A S Ghosh, P S Mazumdar and M Basu, *Can. J. Phys.* **69**, 621 (1985)
[18] K K Mukherjee, N R Singh and P S Mazumder, *J. Phys.* **B22**, 99 (1989)
[19] A Oshaki, T Watanbe, K Nakanishi and K Iguchi, *Phys. Rev.* **A32**, 2640 (1985)
[20] A E Wetmore and R E Olson, *Phys. Rev.* **A34**, 2122 (1986)
[21] J N Das, A Dey and K Chakrabarti, *Aust. J. Phys.* **47**, 751 (1994)
[22] C J Joachain, *Quantum collision theory*, (North Holland, New York, 1973) p. 413

journal of physics

July 1995
pp. 47–63

Bound state population and dissociation dynamics of a Morse oscillator with oscillating well-depth and driven by intense radiation: Perturbative and numerical studies

PRANAB SARKAR and S P BHATTACHARYYA
Department of Physical Chemistry, Indian Association for the Cultivation of Science, Jadavpur, Calcutta 700 032, India

MS received 12 September 1994; revised 28 February 1995

Abstract. Bound state population dynamics in a diatom modelled by an appropriate Morse oscillator with a time-dependent well-depth is investigated perturbatively both in the absence and presence of high intensity radiation. For sinusoidally oscillating well-depth, the population of the mth bound vibrational level, $P_{mm}(t)$, is predicted to be a parabolic function of the amplitude of the oscillation of the well-depth (ΔD_0) at a fixed laser intensity. For a fixed value of ΔD_0, $P_{mm}(t)$ is also predicted to be quadratic function of the field intensity (ε_0). Accurate numerical calculations using a time-dependent Fourier grid Hamiltonian (TDFGH) method proposed earlier corroborate the predictions of perturbation theory. As to the dissociation dynamics, the numerical results indicate that the intensity threshold is slightly lowered if the well-depth oscillates. Possibility of the existence of pulse-shape effect on the dissociation dynamics has also been investigated.

Keywords. Morse oscillator; time-dependent well-depth; photo dissociation.

PACS No. 33·80

1. Introduction

The quantum dynamics of a periodically forced Morse oscillator has attracted serious attention in view of its usefulness as a model for gaining insight into the response of molecular vibrations when interacting with intense radiation or laser fields [1–8]. Recent numerical studies on the dissociation dynamics of a hydrogen fluoride molecule by monochromatic sub-picosecond pulses have shown that the dissociation probability (P_d) is less than 10^{-5} when the laser intensity is below 10^{14} w/cm^2. Chelkowski *et al* [4–5] showed that the obtained rates of dissociation are sensitive to the shape of the excitation pulse and an appropriately chirped pulse can achieve very selective vibrational excitation with high efficiency. Brown and Wyatt [9] analyzed the bottlenecking problem in the multiphoton dissociation of a diatom modelled by a Morse oscillator under laser irradiation of high intensities. Recently, Gangopadhyay and Ray [10] proposed a theory of multiphoton excitation and dissociation of a Morse oscillator in the presence of dissipation and explored how the interplay of excitation and dissipation with the non-linearity could lead to observable effects. Adhikari *et al* [11–12] observed numerically, that the multiphoton dissociation process is characterized by the existence of a typical threshold intensity and an induction period in much the same way as the multiphoton ionization of atoms in strong laser fields [13–15]. Many more studies on different aspects of the multiphoton dissociation of molecules are also available in the current literature [16–19].

In all these studies, the Morse oscillator is characterized by a fixed time invariant well-depth which is an acceptable picture for an isolated oscillator. However, we can

the well-depth of the Morse oscillator about the mean or the unperturbed well-depth D_0^{AB}. How does the oscillating well-depth modify the dynamics of dissociation of the diatom under strong laser irradiation? Does it alter the bound state population dynamics or affect the intensity or time thresholds observed for isolated diatoms or for Morse oscillator with constant well-depths? We propose to probe some of these questions numerically by directly solving the time-dependent Schrödinger equation (TDSE) within the framework of the time-dependent Fourier grid Hamiltonian method (TDFGH). The numerical study has been backed up by a low order perturbative analysis wherever feasible. The plan of the paper is as follows. In § 2 we invoke the first order time-dependent perturbation theory to obtain the qualitative features of the bound state population dynamics for short-time scales. The time-dependent Fourier grid Hamiltonian method [11–12] is employed for obtaining more accurate and quantitative information on the bound state population as well as dissociation dynamics (§ 3). The main features of the perturbative and numerical results are analyzed in § 4 for both continuous and pulsed irradiation.

2. Perturbative bound state dynamics

Since the diatomic molecule is represented by a Morse potential, the unperturbed Hamiltonian (H_0) is given by

$$H_0 = \frac{p^2}{2m} + D_{AB}^0\{1 - \exp[-\beta(x - x_{eq})]\}^2. \tag{1}$$

The parameters of H_0 are so chosen as to describe the bound vibrational levels of hydrogen molecule [$D_0 = 0{\cdot}17440$ a.u., $\beta = 1{\cdot}02764$ a.u., $x_{eq} = 1{\cdot}40201$ a.u.].

Now let us suppose that the well-depth D_{AB}^t of the oscillator oscillates with time. If the time-dependent well-depth be represented by D_{AB}^t, the Hamiltonian becomes time-dependent.

$$H_t = \frac{p^2}{2m} + D_{AB}^t\{1 - \exp[-\beta(x - x_{eq})]\}^2 \tag{2}$$

where we have chosen $D_{AB}^t = D_{AB}^0 + \Delta D f(t)$, $f(t)$ being the temporal modulator of ΔD such that at $t = 0$, $H_t = H_0$. A simple choice for $f(t)$ is $f(t) = \sin \omega t$. As time proceeds, the well-depth D_{AB}^t therefore varies sinusoidally. The Hamiltonian H_t is manifestly phenomenological. But we may offer some rationalization in the following way. If the Morse oscillator (H_0) interacts weakly with the surrounding (H_s) through an interaction term V_{0s}, the equilibrated system eigenstates can be found by solving the following eigenvalue equation [20].

$$\begin{pmatrix} H_0 & V_{s0} \\ V_{s0}^+ & H_s \end{pmatrix} \begin{pmatrix} C_0 \\ C_s \end{pmatrix} = E \begin{pmatrix} C_0 \\ C_s \end{pmatrix}. \tag{2a}$$

Equation (2a) can be split into a pair of coupled eqs (2b) and (2c)

$$H_0 C_0 + V_{0s} C_s = E C_0 \tag{2b}$$

$$V_{s0}^{+} C_0 + H_s C_s = E C_s. \tag{2c}$$

Using the fact that $C_s = -(H_s - E)^{-1} V_{s0}^{+} C_0$, we can recast (2a) as

$$[H_0 - V_{0s}(H_s - E)^{-1} V_{s0}^{+}] C_0 = E C_0$$

which can be written as

$$[H_0 + V_{\text{eff}}] C_0 = E C_0$$

i.e.,

$$H_{\text{eff}} C_0 = E C_0.$$

Over a long-time scale V_{eff} may be replaced by a time-averaged interaction and be treated as a constant quantity. But while probing on a very short-time scale one would notice a time-varying V_{eff}. We have treated V_{eff} as a sinusoidally oscillating term so that $H_{\text{eff}} \to H_0$ as $t \to 0$ and V_{eff} averaged over a characteristic period of oscillation is zero. This simplifies the problem greatly.

The other perturbation present in the system is external and works on a faster time scale. The characteristics of the time-varying field which couples with the oscillator are as follows,

$$V'(x, t) = \varepsilon_0 S(t) x \sin \omega t;$$

where ε_0 is the electric field strength and ω the laser frequency, and $S(t)$ is a pulse shape function. When the field is continuous, $S(t) = 1$. For pulsed fields $S(t)$ can have many different forms. However, we shall make use of the following three forms only in the present study:

(i) $S(t) = \sin^2 \dfrac{\pi t}{t_p}$;

(ii) $S(t) = 1 - \left| 1 - \dfrac{2t}{t_p} \right|$;

(iii) $S(t) = \exp[-\gamma (t - t_p)^2]$

where t_p stands for the pulse duration. So the total Hamiltonian representing a Morse oscillator with oscillating well-depth and interacting with an external time-varying field is given by

$$H(t) = \frac{p^2}{2m} + \left[D_{AB}^0 + \Delta D \sin \frac{2\pi t}{\tau} \right] (1 - \exp[-\beta (x - x_{\text{eq}})])^2 + \varepsilon_0 S(t) x \sin \omega t \tag{3}$$

$$= \frac{p^2}{2m} - D_{AB}^0 (1 - \exp[-\beta (x - x_{\text{eq}})])^2 + \Delta D \sin \frac{2\pi t}{\tau} \times (1 - \exp[-\beta (x - x_{\text{eq}})])^2 + \varepsilon_0 S(t) x \sin \omega t$$

$$= H_0 + H_1(t) + H_2(t) \tag{4}$$

where

$$H_1 = \Delta D \sin\frac{2\pi t}{\tau}(1 - \exp[-\beta(x - x_{eq})])^2 \quad \text{and} \quad H_2 = \varepsilon_0 S(t) x \sin \omega t.$$

The zeroth order Hamiltonian (H_0) is clearly the free Morse oscillator Hamiltonian of constant well-depth D^0_{AB}.

Now we consider the different cases that may arise; for e.g. (i) when the external time-varying field is present but the well-depth does not oscillate, i.e., $\varepsilon_0 \neq 0$, but $\Delta D = 0$; (ii) when the well-depth oscillates but the field is absent, i.e., $\varepsilon_0 = 0$, but $\Delta D \neq 0$; (iii) when the well-depth oscillates and the applied field intensity is non-zero, i.e., $\varepsilon_0 \neq 0$ and $\Delta D \neq 0$. In what follows we make a perturbative estimate of the population of different levels, assuming a short-time interval and not too high fields.

(i) *when* $\varepsilon_0 \neq 0$, *but* $\Delta D = 0$:

If $\varepsilon_0 \neq 0$ and $\Delta D = 0$, the Hamiltonian of the system becomes

$$H(t) = H_0 + H_2(t)$$

where

$$H_2(t) = \varepsilon_0 S(t) x \sin \omega t. \tag{5}$$

For the sake of simplicity we consider that the field is continuous i.e. $S(t) = 1$. Thus,

$$H_2(t) = \varepsilon_0 x \sin \omega t.$$

Let the system be in the mth eigenstate of H_0, (Φ^0_m) at $t = 0$. The perturbation throws Φ^0_m into a linearly superposed state $\Psi(t)$ with

$$\Psi(t) = \sum_{k=1}^{N} a_k(t) \Phi^0_k \exp(-iE^0_k t/\hbar);$$

where

$$H_0 \Phi^0_k = E^0_k \Phi^0_k \text{ and}$$

$$i\hbar \frac{\delta \Psi}{\delta t} = (H_0 + H_2(t))\psi.$$

In the first order therefore the transition probability from an initial eigenstate (n) of the unperturbed Morse oscillator (H_0) to a state (m) caused by the applied field is given by

$$|a^1_m(t, \varepsilon_0)|^2 = \frac{\varepsilon_0^2 \langle m|x|n\rangle^2}{4\hbar^2}\left[\frac{4\sin^2(\omega_{mn} - \omega)t/2}{(\omega_{mn} - \omega)^2} - \frac{1}{(\omega^2_{mn} - \omega^2)}\right.$$

$$\times\left[2\sin(\omega + \omega_{mn})t/2 \sin(\omega_{mn} - \omega)t/2 + 4\sin^2(\omega_{mn} - \omega)t/2\right]$$

$$\left. + \frac{4\sin^2(\omega_{mn} + \omega)t/2}{(\omega_{mn} + \omega)^2}\right] = P^1_{mm}(t, \varepsilon)$$

where

$$a^1_m(t, \varepsilon_0) = \frac{\varepsilon_0 \langle m|x|n\rangle}{2i\hbar}\left[\frac{\exp i(\omega_{mn} - \omega)t - 1}{(\omega_{mn} - \omega)} - \frac{\exp i(\omega_{mn} + \omega)t + 1}{(\omega_{mn} + \omega)}\right] \tag{6}$$

and $\langle m|x|n\rangle = \langle \Phi_m^0|x|\Phi_n^0\rangle, \omega_{mn} = (E_m^0 - E_n^0)/\hbar$; and ε_0 is the electric field strength of the applied radiation, ω is its frequency which is supposed to be slightly off-resonance. $|a_m^1(t,\varepsilon)|^2$ or $P_{mm}^1(t,\varepsilon)$ is then the population of the mth state of the unperturbed Morse oscillator created by the applied off-resonance time-varying electric field of the radiation.

(ii) *when* $\varepsilon_0 = 0$ *but* $\Delta D \neq 0$

In this case,

$$H(t) = H_0 + H_1(t)$$

where

$$H_1(t) = \Delta D \sin(2\pi t/\tau)[(1 - \exp[-\beta(x - x_{eq})])^2].$$

Now expanding the exponential term and considering only terms up to $(x - x_{eq})^2$ we obtain,

$$H_1(t) = H_1^{(1)}(t) = \Delta D \sin(2\pi t)/\tau\, \beta(x - x_{eq})^2.$$

The first order transition amplitude $a_m^1(t)$ is therefore given by

$$a_m^1(t, \Delta D) = \frac{\Delta D \beta^2}{4i\hbar}\langle m|(x - x_{eq})^2|n\rangle \times \left[\frac{\exp i(\omega_{mn} - (2\pi/\tau))t - 1}{(\omega_{mn} - (2\pi/\tau))} - \frac{\exp i(\omega_{mn} + (2\pi/\tau))t - 1}{(\omega_{mn} + (2\pi/\tau))}\right].$$

The first order transition probability from the state n to the state m due to oscillations of the well-depth alone is therefore given by

$$|a_m^1(t, \Delta D)|^2 = P_{mm}^1(t, \Delta D) = \frac{(\Delta D)^2 \beta^4}{16\hbar^2}\langle m|(x - x_{eq})^2|n\rangle^2 \times \left[\frac{4\sin^2(\omega_{mn} - (2\pi/\tau))t/2}{(\omega_{mn} - (2\pi/\tau))^2} - \frac{1}{(\omega_{mn} - (4\pi^2/\tau))} \times \left(4\sin\left(\omega_{mn} + \frac{2\pi}{\tau}\right)t/2 - \sin\left(\omega_{mn} - \frac{6\pi}{\tau}\right)t/2 + 4\sin^2\left(\omega_{mn} + \frac{2\pi}{\tau}\right)t/2\right) + 4\frac{\sin^2(\omega_{mn} + (2\pi/\tau))t}{(\omega_{mn} + (2\pi/\tau))^2}\right] \quad (7)$$

$P_{mm}^{(1)}(t, \Delta D)$ in fact gives the population of the mth vibrational level of the unperturbed Morse oscillator of well-depth D_0^{AB} created by a sinusoidal temporal fluctuation of the well-depth with an amplitude ΔD.

(iii) *when both* $\varepsilon_0 \neq 0$ *and* $\Delta D \neq 0$

In this case

$$H(t) = H_0 + H_1(t) + H_2(t) = H_0 + H'(t)$$

$$H'(t) = \Delta D \sin(2\pi t/\tau)[1 - \exp[-\beta(x - x_{eq})]]^2 + \varepsilon_0 x \sin \omega t.$$

Now making approximations already introduced in (ii), we may write $H'(t)$ as

$$H'(t) = H^{(1)}(t)\Delta D \sin(2\pi t/\tau)\beta(x - x_{eq}^2)^2 + \varepsilon x \sin \omega t.$$

The first order transition amplitude for the oscillator with oscillating well-depth in the presence of the applied time-varying non-resonant field is then given by

$$a_m^1(t, \varepsilon_0 \Delta D) = \frac{\varepsilon_0 \langle m|x|n\rangle}{2i\hbar}\left[\frac{\exp i(\omega_{mn} - \omega)t - 1}{(\omega_{mn} - \omega)} - \frac{\exp i(\omega_{mn} + \omega)t + 1}{(\omega_{mn} + \omega)}\right]$$
$$+ \frac{\Delta D\beta^2}{4i\hbar}\langle m|(x - x_{eq})^2|n\rangle\left[\frac{\exp i(\omega_{mn} - (2\pi/\tau))t - 1}{(\omega_{mn} - (2\pi/\tau))}\right.$$
$$\left. - \frac{\exp i(\omega_{mn} + (2\pi/\tau))t - 1}{(\omega_{mn} + (2\pi/\tau))}\right].$$

The corresponding transition probability from an initial unperturbed state n to the final perturbed state m caused by the oscillating well-depth and time-varying electric field of the radiation that act in unison is therefore given by

$$|a_m^1(t, \varepsilon_0, \Delta D)|^2 = P_{mm}^1(t, \varepsilon_0, \Delta D) =$$
$$\frac{\varepsilon_0^2 \langle m|x|n\rangle^2}{4\hbar^2}\left[\frac{4\sin^2(\omega_{mn} - \omega)t/2}{(\omega_{mn} - \omega)^2} - \frac{1}{(\omega_{mn}^2 - \omega^2)}\left[2\sin(\omega + \omega_{mn})t/2\right.\right.$$
$$\left.\left. \times \sin(\omega_{mn} - \omega)t/2 + 4\sin^2(\omega_{mn} - \omega)t/2\right] + \frac{4\sin^2(\omega_{mn} + \omega)t/2}{(\omega_{mn} + \omega)^2}\right]$$
$$+ \frac{(\Delta D)^2\beta^4}{16\hbar^2}|\langle m|(x - x_{eq})^2|n\rangle|^2\left[\frac{4\sin^2(\omega_{mn} - (2\pi/\tau))t/2}{(\omega_{mn} - (2\pi/\tau))^2} - \frac{1}{(\omega_{mn} - (4\pi^2/\tau))}\right.$$
$$\times\left(4\sin\left(\omega_{mn} + \frac{2\pi}{\tau}\right)t/2 - \sin\left(\omega_{mn} - \frac{6\pi}{\tau}\right)t/2 + 4\sin^2\left(\omega_{mn} + \frac{2\pi}{\tau}\right)t/2\right)$$
$$\left. + \frac{4\sin^2(\omega_{mn} + (2\pi/\tau))t}{(\omega_{mn} + (2\pi/\tau))^2}\right] + \frac{\Delta D\beta^2\varepsilon_0\langle(x - x_{eq})^2\rangle_{mn}}{8\hbar^2}$$
$$+\left[\frac{2\cos(\omega - (2\pi/\tau))t - 2\cos(\omega_{mn} - (2\pi/\tau))t - 2\cos(\omega_{mn} - \omega)t + 2}{(\omega_{mn} - (2\pi/\tau))(\omega_{mn} - \omega)}\right.$$
$$- \frac{2\cos(\omega + (2\pi/\tau))t - 2\cos(\omega_{mn} - (2\pi/\tau))t - 2\cos(\omega_{mn} + \omega)t + 2}{(\omega_{mn} - (2\pi/\tau))(\omega_{mn} + \omega)}$$
$$- \frac{2\cos(\omega + (2\pi/\tau)t - 2\cos(\omega_{mn} + (2\pi/\tau))t - 2\cos(\omega_{mn} - \omega)t + 2}{(\omega_{mn} + (2\pi/\tau))(\omega_{mn} - \omega)}$$
$$\left. + \frac{2\cos(\omega - (2\pi/\tau))t - 2\cos(\omega_{mn} + (2\pi/\tau))t - 2\cos(\omega_{mn} + \omega)t + 2}{(\omega_{mn} + (2\pi/\tau))(\omega_{mn} + \omega)}\right]$$
$$= P'_{mn}(t, \varepsilon, \Delta D = 0) + P'_{mn}(t, \varepsilon = 0, \Delta D) + P'_{mm}(t, \varepsilon_0, \Delta D) \qquad (8)$$

$P'_{mm}(t, \varepsilon_0, \Delta D)$ represents the part of the time-dependent population of the mth state of the unperturbed Morse oscillator (H_0) that is created by the interference of the population excitation–deexcitation dynamics caused by well-depth oscillation and the applied time-varying field. The overall expression of $P'_{mm}(t, \varepsilon_0, \Delta D)$ suggests a parabolic dependence of the population on the electric field strength (ε_0) when all other system parameters viz., ΔD, β, etc., are fixed. The expression also reveals parabolic dependence of P'_{mm} on ΔD at fixed ε_0 and β. However, these are first order results and are therefore of limited validity. We therefore propose to calibrate these predictions against near exact solutions of the corresponding TDSE equation by invoking the TDFGH method proposed earlier by Adhikari *et al* [11–12] and later extensively applied by Sarkar *et al* [21–22]. Since the TDFGH method is not yet widely known, we would briefly discuss the salient features of the method.

TDFGH method

Let us start with the TDSE,

$$i\hbar \frac{\delta \Psi}{\delta t} = H\Psi \tag{9}$$

where

$$H = H_0 + V'(x, t) = \frac{p^2}{2m} + V(x) + V'(x, t). \tag{10}$$

We can employ the FGH method [23–24] to evaluate the eigenfunctions and eigenvalues of H_0 giving

$$H_0 |\Phi_i^0(x)\rangle = \varepsilon_i^0 |\Phi_i^0(x)\rangle, \quad i = 1, 2, \ldots N, \tag{11}$$

where N is the number of grid points used for representing $|\Phi_i^0\rangle$ in the co-ordinate space.

$$|\Phi_i^0\rangle = \sum_{i=1}^{N} |x_i\rangle \Delta x\, w_i^0 \tag{12}$$

$\{w_i^0\}$ in (12) represent the values of the co-ordinate representative of the state function $|\Phi_i^0(x)\rangle$ at the grid points, the values of which are obtained by the standard variational recipe [23–24]. The FGH method can be used to propagate the wave function on the same grid as shown by Adhikari *et al* [11–12]. Thus, when the perturbation is switched on, the state function $\Psi(x, t)$ is given by

$$|\Psi(x, t)\rangle = \sum_{i=1}^{N} |x_i\rangle \Delta x\, w_i(t). \tag{13}$$

The amplitudes ($w_i(t)$) are now time-dependent quantities and their evolution equations are as follows

$$w_j = \frac{1}{i\hbar} \sum_i [\langle x_j | H_0 | x_i\rangle + \langle x_j | V(x, t) | x_i\rangle] w_i(t). \tag{14}$$

Once initial values of $\{w_i\}$ are specified, (14) can be numerically integrated on the specified grid by Runge–Kutta or Bulirsch–Stoer method [25]. The matrix elements of

H_0 and V of (14) can be evaluated using the FGH method

$$\langle x_i|H_0|x_j\rangle = \frac{1}{\Delta x}\left[\sum_{l=-n}^{n}\frac{\exp[2\pi l(i-j)/n]}{N}\right]\{T_1\} + V(x_i,t)\delta_{ij} \tag{15}$$

where

$$T_1 = [\hbar^2/2m](l\Delta k)^2, \quad \Delta k = (2\pi/N\Delta x) \quad \text{and} \quad 2n = N-1$$

and

$$\langle x_i|V(x,t)|x_j\rangle = V(x_i,t)\delta(x_i - x_j) \tag{16}$$

Once $w_i(t)$ and hence $\Psi(x,t)$ are obtained, the projections of $\Psi(x,t)$ onto the eigenstates of H_0 generate time-dependent overlap amplitudes

$$S_i(t) = |\langle\Phi_i^0|\Psi(x,t)\rangle|^2, \quad i = 1,2,3,\ldots N. \tag{17}$$

The $S_i(t)$ essentially represent the population of the ith eigenstate of the unperturbed Hamiltonian at a time $\{t\}$ after the perturbation is switched on. If the system is initially in the unperturbed ground state, $S_1(0) = 1$ and $S_j(0) = 0\,(j \neq 1)$. For $t > 0$, $S_i(t)$ begin to change with time as the perturbation V causes excitations to occur with respect to the unperturbed system. $S_i(t)$s, therefore, provide a complete description of the dynamics of level population in terms of which changes in all observables can be calculated and interpreted. Once the oscillator is excited to an unbound level, dissociation takes place. Using the $S_i(t)$ values, we can therefore define the dissociation probability P_d as follows,

$$P_d(t) = 1 - \sum_{i}^{n_b}\langle|\Psi(x,t)|\Phi_i^0\rangle|^2 = 1 - \sum_{i} S_i(t). \tag{18}$$

In (18), n_b stands for the number of bound states supported by the unperturbed Hamiltonian (i.e. the free Morse oscillator of constant well-depth, in this case). In what follows, we discuss the numerical results obtained from TDFGH method and the expectations based on first order perturbation theory.

3. Results and discussion

(i) *Bound state population dynamics*

Figure 1(a) shows the growth and decay of the population of the ground and the first three excited vibrational levels of the Morse oscillator with constant well-depth ($\Delta D = 0$) computed numerically by the TDFGH recipe, as the electric field of the applied radiation interacts with it. Figure 1(b) shows the perturbatively computed population [eq. (6)] versus time profile of the first excited state. The population versus time profiles for other excited states have more or less identical features. The similarity of the nature of the population dynamics of the excited states calculated numerically and perturbatively establishes the validity of the first order TDPT over the time-scale of our analysis and for the strengths of the perturbations used. Figure 2 shows the numerically calculated population versus time profiles of the ground and the first three excited states of the Morse oscillator in the presence of radiation when the well-depth oscillates sinusoidally with time. The main features of the bound level population dynamics are identical with those observed for the constant well-depth case. The conclusion is therefore that the oscillating well-depth does not alter the gross dynamical

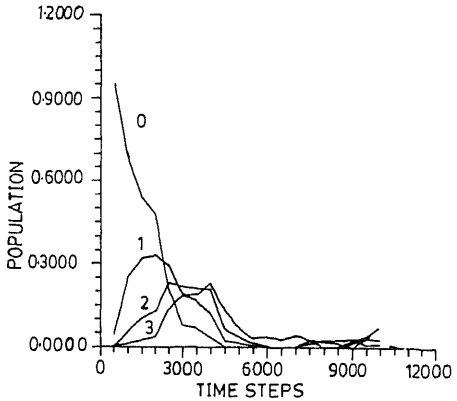

Figure 1(a). Growth and decay of level populations of the ground and the first three excited states of a Morse oscillator with constant well-depth as the electric field of the applied radiation interacts with it.

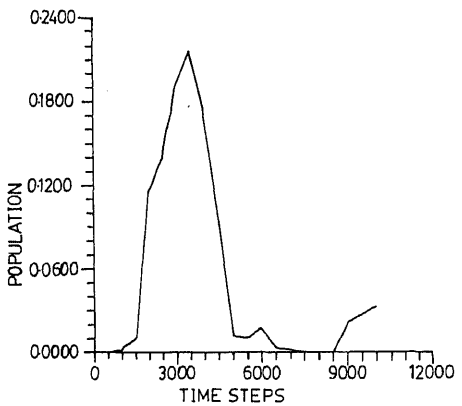

Figure 1(b). Perturbatively computed population versus time profile of the first excited state of the same system depicted in figure 1(a).

features of the population-time profiles, although the excitation or relaxation rates in the presence of the well-depth oscillation may be quite different from their constant well-depth counterparts (see later).

Figure 3(a) shows the numerically computed (by TDFGH method) population of a vibrational level ($k = 2$) of the Morse oscillator with oscillating well-depth ($\Delta D \neq 0$) as a function of the intensity (ε_0) of the applied field. The overall parabolic nature of the profile mirrors the prediction of the first order TDPT. Figure 3(b) shows the behaviour of the numerically computed population $P_{kk}(t) - \Delta D$ profile for a fixed value of 'ε_0', the applied field strength. From the figure it is seen that the population of the given state monotonically increases as ΔD increases. Thus, the perturbation theoretical prediction that the dependence of the population on ΔD would be parabolic for a fixed value of ε_0

population dynamics of the three highest bound vibrational levels for the $\Delta D \neq 0$ case which is basically similar to that observed for the lower states. From the observed population dynamics it appears that if the applied field intensity is below a certain threshold, excitation is the only process to reckon with and the dissociation probability is negligible. Once the threshold is crossed, rapid onset of dissociation of the diatomic molecule sets in. It would therefore be interesting to know how the dissociation

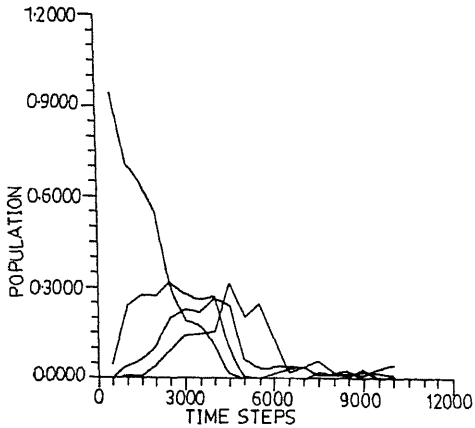

Figure 2. Growth and decay of level populations of the ground and the first three excited states of the Morse oscillator in the presence of the radiation when well-depth oscillates sinusoidally with time.

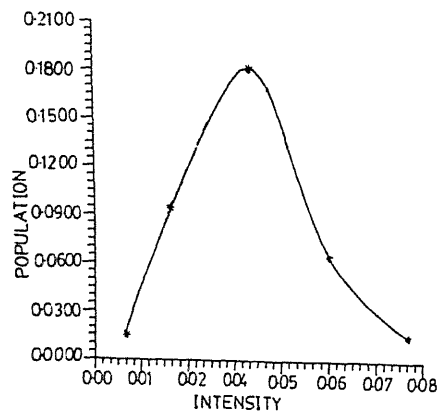

Figure 3(a). Numerically computed population (by the TDFGH method) of a vibrational level ($k = 2$) of a Morse oscillator with oscillating well-depth ($\Delta D \neq 0$) as a function of the intensity (ε) of the applied field.

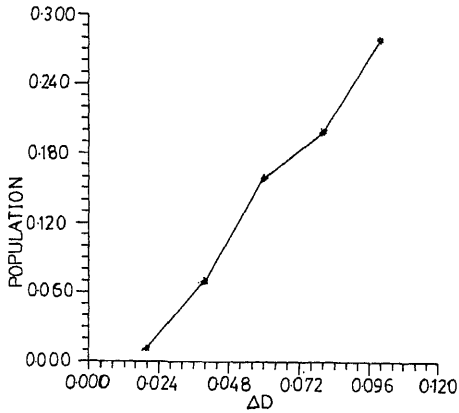

Figure 3(b). Numerically computed population of the $k = 2$ level shown as a function of ΔD for a fixed value of ε, the strength of the applied field.

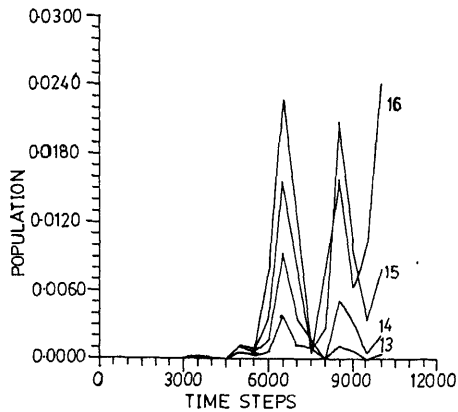

Figure 3(c). Numerically computed population versus time profiles of the three highest bound vibrational levels.

probability depends upon the applied field intensity, when the well-depth oscillates. The specific questions to be probed are the following. Does the well-depth oscillation alter the dissociation dynamics observed for a constant well-depth Morse oscillator? Is there any pulse-shape effect on the temporal characteristics of the dissociation process? Before focussing on these aspects of the problem, we would like to see whether an oscillating well-depth affects the excitation or relaxation rates induced by the field.

Let us suppose that we start with the system in the ground state of the unperturbed oscillator at $t = 0$. Figures 3(d) and (e) show the growth of the population of the first excited state as the applied field interacts with the Morse oscillator of (i) fixed, and (ii) oscillating well-depth, respectively. The limiting slopes of these curves give the total

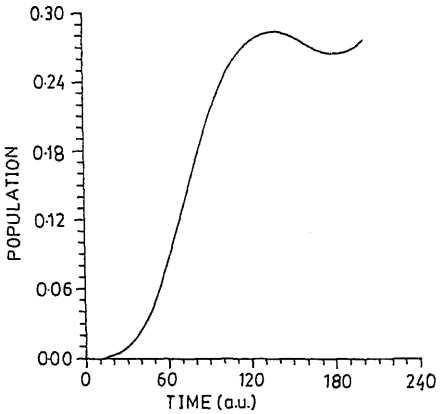

Figure 3(d). Growth of the population of the first excited state as the applie interacts with the Morse oscillator of fixed well-depth ($\varepsilon = 0{\cdot}06$, $\Delta D = 0{\cdot}0$).

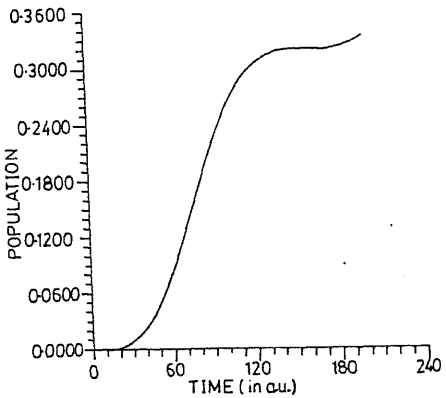

Figure 3(e). Growth of the population of the first excited state as the applie interacts with the Morse oscillator of oscillating well-depth ($\varepsilon = 0{\cdot}06$, $\Delta D =$

rate of excitation into the first excited state, which are recorded in table 1. For a M oscillator with a time-dependent well-depth, the excitation rate is larger sh constructive interference between the field-induced and the oscillating well- controlled excitations. If we start with the oscillator in an excited state, we can sim compute the rate of relaxation caused by the external field as well as by the in perturbation set up in the system due to oscillation in the well-depth. For $k = 1$ these rates are also reported in table 1 both when $\Delta D = 0$, $\varepsilon_0 \neq 0$ and $\Delta D \neq 0$, ε Thus, the well-depth oscillation is seen to enhance the excitation rates but depre relaxation rates in a Morse oscillator interacting with the radiation.

Table 1. Computed excitation and relaxation rates of a given vibrational level of a Morse oscillator in the absence and presence of well-depth oscillation.

System	Rate of excitation to the first excited state (ps^{-1})	Rate of relaxation of the first excited state (ps^{-1})
i) Morse oscillator with fixed well-depth	i) 1·79	i) 8·30
ii) Morse oscillator with oscillating well-depth	ii) 2·84	ii) 6·16

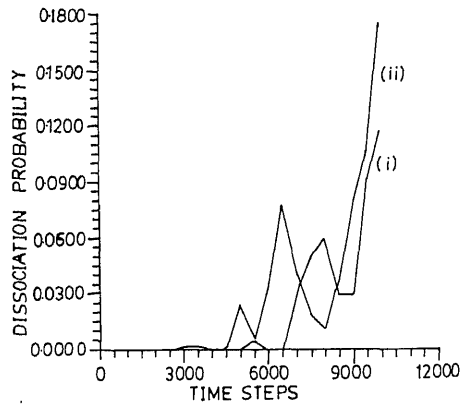

Figure 4(a). Dissociation probability versus time profile for the oscillator with (i) fixed well-depth (ii) oscillating well-depth, for a fixed value of ε_0.

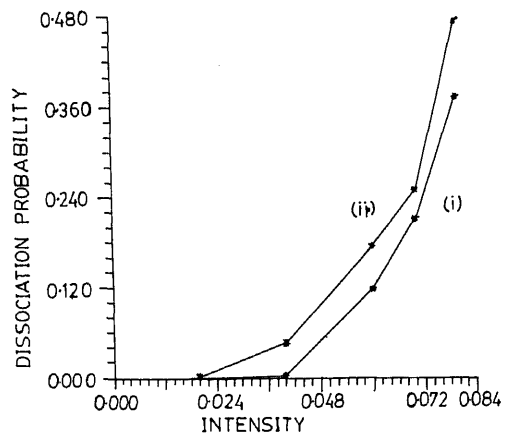

Figure 4(b). Computed dissociation probability P_d as a function of the intensity of the applied field of the laser for the oscillator with (i) time-invariant well-depth (ii) time-varying well-depth.

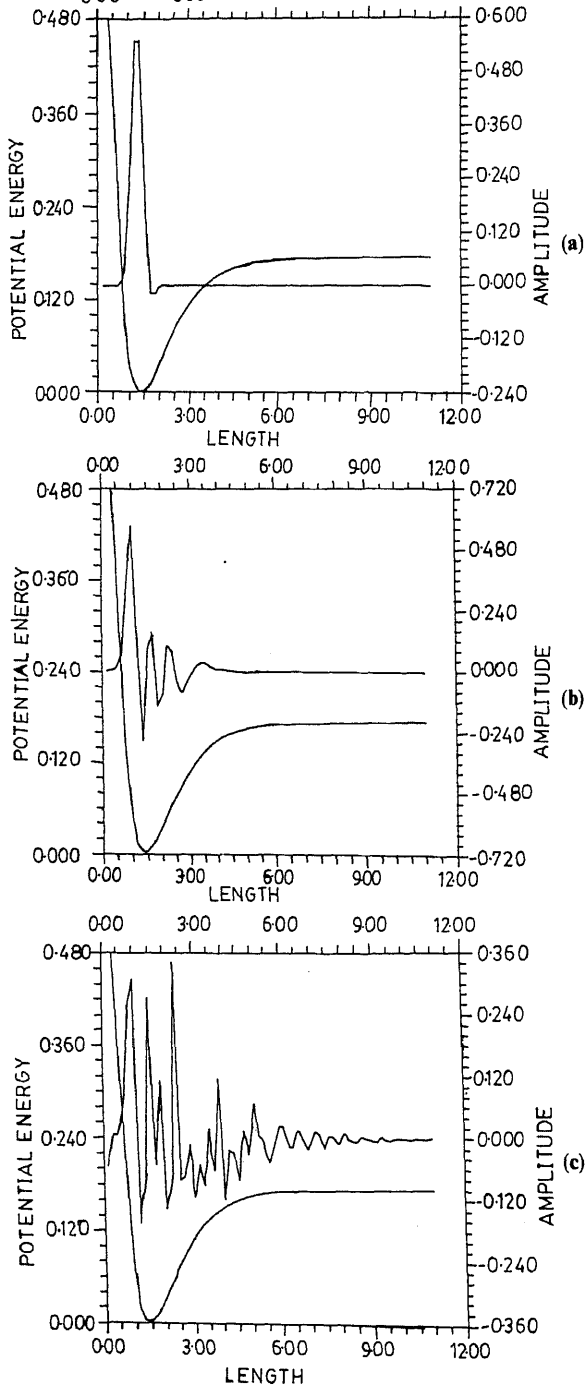

Figure 5(a–c). Profiles of the ground state vibrational wave function of H_2 (modelled by a morse oscillator) as it dissociates under laser irradiation. (a) $\Psi(x,t)$ at $t=0$; (b) $\Psi(x,t)$ at $t=10$ fs$(c)\Psi(x,t)$ at $t=25$ fs. The peak intensity of the pulse is $\varepsilon_0=0{\cdot}06$ a.u.

(ii) *Dissociation dynamics*

(a) *Dissociation probability, time and intensity thresholds*: We first consider the case, when the field is continuous. Figure 4(a) shows the P_d-time profile for the oscillator (i) with fixed well-depth (ii) with oscillating well-depth, for a fixed value of ε_0. The oscillating well-depth is seen to lower the time-threshold slightly with respect to the constant well-depth Morse oscillator.

Figure 4(b) shows how the computed dissociation probability of a Morse oscillator at a given time (t) varies with the intensity of the applied time-varying field with (i) time-invariant well-depth, (ii) time-varying well-depth. In both cases, a clear threshold intensity ($\varepsilon^0 = \varepsilon_0$) is seen to exist beyond which the dissociation probability rises sharply. From the figures, one would be tempted to conclude that, the oscillation of well-depth lowers the threshold intensity compared to that observed in the constant well-depth case, when illumination is continuous.

We have monitored at this point the wave function as the molecule dissociates. Figures 5(a–c) show the wavefunction at different stages of evolution after the field is switched on. As the system gains energy from perturbing field, more and more nodes appear in $\Psi(x, t)$ and the effective spatial extension of $\Psi(x, t)$ increases.

When a pulsed field is used, the picture that emerges from the continuous-field-oscillator model is seen to change a lot. Figure 6(a) shows how the dissociation probability varies with the field intensity ε_0 in (i) the fixed well-depth case, (ii) the oscillating well-depth case, when the intensity varies as $\sin^2(\pi t/t_p)$. From the figures a picture opposite to that observed in the continuous field case is seen to emerge i.e., the oscillating well-depth increases the threshold intensity of dissociation when a pulsed field is used. Figure 6(b) shows the dissociation probability versus time profile in (i) continuous laser field; (ii) pulsed laser field with $\sin^2$ dependence; (iii) triangularly pulsed laser field; (iv) laser with Gaussian pulse shape, when the peak intensity (ε_0) and laser frequency (ω) are the same in each case. From the figures it is seen that compared

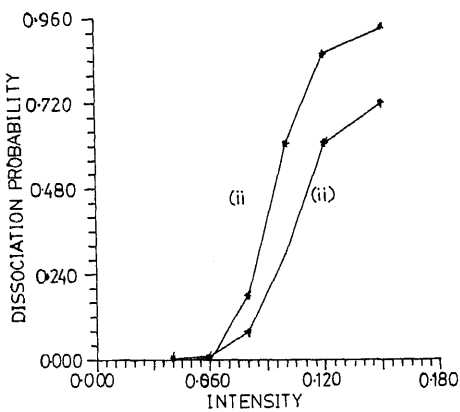

Figure 6(a). Dissociation probability versus intensity profile for the oscillator with (i) fixed well-depth (ii) oscillating well-depth for pulsed laser fields.

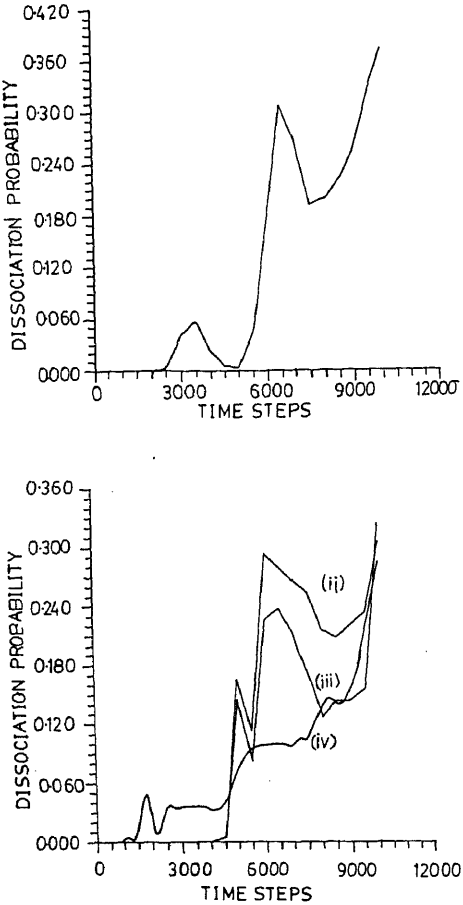

Figure 6(b). Dissociation probability versus time profile for (i) continuous laser field (ii) pulsed laser field with $\sin^2$ dependence (iii) triangularly pulsed laser field. (iv) Gaussian pulsed laser field.

to continuous irradiation, the pulsed laser field lowers the dissociation probability of the diatom at any given time. But the gross features of the P_d versus time profile for three different types of pulsed fields are not very different [4–5]. It would be interesting to analyze the kind of effects that a Morse oscillator with a randomly oscillating well-depth would bring about. We will address ourselves to this problem in a future communication.

4. Conclusions

By studying the bound state population and dissociation dynamics of a model diatomic species whose binding energy oscillates with time, we come to the following conclusions:

tions as long as the perturbation is small and short-time scales are considered.
(ii) When the well-depth oscillates slowly, which is the actual situation when the system interacts with the surrounding medium, the threshold intensity decreases to a small extent for dissociation under continuous irradiation; but, for pulsed fields, oscillating well-depth is predicted to increase the threshold intensity of dissociation.
(iii) The nature of the dissociation probability versus time profiles and the actual extent of dissociation appears to be almost the same for pulses of different shapes that we have studied. However, a different choice of V_{eff} could change the picture completely. The problems of microscopic derivation of V_{eff} and thus, H_{eff} and a fully quantum dynamical study of the processes of our interest are presently under way.

Acknowledgement

One of us (PS) wishes to thank the Council of Scientific and Industrial Research Government of India, New Delhi, for the award of a Junior Research Fellowship.

References

[1] A D Bandrauk, ed., *Atomic and molecular processes with short intense laser pulses* (Plenum New York, 1988)
[2] M Quack, In *Advances in chemical physics*, (Wiley, New York, 1982) Vol 50
[3] H P Breuer, K Dietz and M Holthaus, *Z. Phys.* **D8**, 349 (1988); **D11**, 1 (1989)
[4] S Chelkowski and A D Bandrauk, *Phys. Rev.* **A41**, 6480 (1990)
[5] S Chelkowski, A D Bandrauk and P B Corkum, *Phys. Rev. Lett.* **65**, 2355 (1990)
[6] M E Goggin and P W Milonni, *Phys. Rev.* **A37**, 796 (1988)
[7] V S Letokhov, In *Non-linear laser chemistry* (Springer, Berlin, 1988) ch. 5
[8] N Bloembergen and A H Zewail, *J. Phys. Chem.* **88**, 5459 (1984)
[9] R C Brown and R E Wyatt, *J. Phys. Chem.* **90**, 3590 (1986); *Phys. Rev. Lett.* **57**, 1 (1986)
[10] G Gangopadhyay and D S Ray, *J. Chem. Phys.* **97**, 4104 (1992)
[11] S Adhikari, P Dutta and S P Bhattacharyya, *Chem. Phys. Lett.* **199**, 574 (1992); *Int. J Quantum Chem.* (to appear, 1995)
[12] S Adhikari and S P Bhattacharyya, *Phys. Lett.* **A172**, 155 (1992); *Proc. Indian Acad. Sci (Chem. Sci.)* (1994)
[13] J Javanawnen, J H Eberly and Q Su, *Phys. Rev.* **A38**, 3430 (1988)
[14] J N Bardsley, A Szoke and M J Comella, *J. Phys.* **B21**, 3430 (1988)
[15] J N Bardsley and M J Comella, *Phys. Rev.* **A39**, 2252 (1989)
[16] B Just, J Nanz and G K Paramonov, *Chem. Phys. Lett.* **193**, 429 (1992)
[17] B Just, J Nanz and I Trisca, *Chem. Phys. Lett.* **193**, 423 (1992)
[18] G K Paramonov, *Chem. Phys. Lett.* **169**, 573 (1990)
[19] M Quack and E Sutcliffe, *Infrared Phys.* **25**, 163 (1985)
[20] R McWeeny, *Methods of molecular quantum mechanics* 2nd ed. (1989) A.P. (N.Y.)
[21] P Sarkar, S Adhikari and S P Bhattacharyya, *Chem. Phys. Lett.* **227**, 187 (1994)
[22] P Sarkar and S P Bhattacharyya, *Int. J. Quantum Chem.* 1995 (in press)
[23] C C Marston and G G Balint Kurti, *J. Chem. Phys.* **91**, 3571 (1989)
[24] G G Balint Kurti, C L Ward and C C Marston, *Comput. Phys. Commun.* **67**, 285 (1991)
[25] J Stoer and R Bulirsch, *Introduction to numerical analysis* (New York, Springer, 1980) sec 7.2.14

Electronegativity and hardness profiles of a chemical process: Comparison between quantum fluid density functional theory and *ab initio* SCF method

S NATH† and P K CHATTARAJ*
Department of Chemistry, Indian Institute of Technology, Kharagpur 721 302, India
*Author for correspondence
†Present address: Department of Physical Chemistry, Indian Association for Cultivation of Science, Jadavpur, Calcutta 700 032, India

MS received 7 May 1994; revised 4 April 1995

Abstract. Temporal evolution of electronegativity and hardness associated with a collision process between a Be atom and a proton has been studied within a quantum fluid density functional framework. In the presence of a third collisional partner to take away excess energy, this collision may lead to a chemical reaction producing a BeH^+ molecule. For comparison *ab initio* SCF level calculation (with 6–31G** basis set) on BeH^+ molecule with different geometries have been performed. Electronegativity equalization and maximum hardness principles are analyzed.

Keywords. Electronegativity; hardness; structure; dynamics.

PACS Nos 31·20; 34·50; 82·20; 82·40

Chemical concepts like electronegativity [1–4] and hardness [5–9] have been found to be important in understanding various physico-chemical processes. Electronegativity was first defined by Pauling [1] as the power of an atom in a molecule to attract electrons to itself and was shown to be related to chemical potential (μ) in density functional theory (DFT) as [3, 4]

$$-\chi = \mu = \left(\frac{\partial E}{\partial N}\right)_{v(r)} \tag{1}$$

where E, N, $v(r)$ are electronic energy, number of electrons and external potential respectively. The concept of hardness which was introduced by Pearson [5] has been defined, within DFT, as [6–9]

$$\eta = \frac{1}{2}\left(\frac{\partial \mu}{\partial N}\right)_{v(r)} = \frac{1}{2}\left(\frac{\partial^2 E}{\partial N^2}\right)_{v(r)}. \tag{2}$$

Using finite difference approximations and assuming Koopmans' theorem to be valid, μ and η become [7–10]

$$\mu \simeq -(I + A)/2 \simeq (\varepsilon_{\text{LUMO}} + \varepsilon_{\text{HOMO}})/2 \tag{3}$$

$$\eta \simeq (I - A)/2 \simeq (\varepsilon_{\text{LUMO}} - \varepsilon_{\text{HOMO}})/2. \tag{4}$$

Here I and A are ionization potential and electron affinity respectively and $\varepsilon_{\text{HOMO}}$ and $\varepsilon_{\text{LUMO}}$ are energies of highest occupied and lowest unoccupied molecular orbitals respectively.

In a chemical reaction, difference of electronegativity drives the electron transfer from a species of lower electronegativity to one with higher electronegativity until their electronegativity values become equal. According to Sanderson's electronegativity equalization (EE) principle [3, 11–15] this molecular electronegativity is equal to the geometric mean of isolated atoms' electronegativities. An important principle of molecular electronic structure theory associated with hardness concept is hard-soft-acid-base (HSAB) principle [5, 16] which states that hard acids will prefer to react with hard bases and soft acids with soft bases to form a stable molecule. This principle is closely related to maximum hardness principle (MHP) [17–19] which states that "there seems to be a rule of nature that molecules arrange themselves so as to be as hard as possible". Pearson [17] postulated MHP on the basis of his vast experience on chemical reactions. The first formal proof of it for a class of states (cf. eq. (14) of ref. 18) has been provided by Parr and Chattaraj [18]. Thus during molecule formation or in general in a chemical reaction, electronegativity of an atom changes until it attains the molecular electronegativity value and its hardness gets maximized which is the consequence of MHP. Therefore a chemical reaction dynamics can be envisaged in terms of temporal evolution of electronegativity and hardness during a chemical reaction. Several systems and processes have been studied in order to understand the implications of EE [13–15, 20, 21], MH [22–33] and HSAB [23, 25–27] principles. In this letter we study a collision process between a Be atom and a proton and study the temporal evolution of χ and η during the process within a quantum fluid density functional (QFDF) framework [37–40]. Since, in the presence of a third partner to take away the excess energy, this collision may lead to the formation of BeH^+, which is a stable closed shell molecule with $D_0 = 3{\cdot}14$ eV and $R_e = 1{\cdot}3122$ Å [34–36] we also supplement this calculation by *ab initio* SCF calculations [41]. In both the cases χ and η have been expressed as functions of internuclear distance (R) and hence have implicit temporal dependence. *Ab initio* calculations have been carried out at SCF level with 6–13 G** basis set for different internuclear distances of BeH^+. It should be noted here that the former calculation is within a dynamical context and hence the excited states get mixed during temporal evolution whereas the latter calculation refers to movement from one ground state to another.

In QFDF formalism [37–40] which is an amalgamation of quantum fluid dynamics (QFD) and time-dependent density functional theory (TDDFT), time-evolution of electron density (ρ) and current density (j) can be found by solving a generalized nonlinear Schrödinger equation (GNLSE). The electron density and current density in turn uniquely determine all other properties of the system [42, 43]. The GNLSE is given by [37–40],

$$[-\tfrac{1}{2}\nabla^2 + v_{\text{eff}}(r,t)]\phi(r,t) = i\frac{\partial\phi(r,t)}{\partial t} \tag{5}$$

with

$$\phi = \rho^{1/2}\exp(i\xi) \quad \text{and} \quad j = [\phi_{\text{re}}\nabla\phi_{\text{im}} - \phi_{\text{im}}\nabla\phi_{\text{re}}] = \rho\nabla\xi$$

where ξ is the velocity potential. In eq. (5) the effective potential v_{eff} is given by [20, 37–39]

$$v_{\text{eff}} = \frac{\delta T_{\text{NW}}}{\delta\rho} + \frac{\delta E_{\text{XC}}}{\delta\rho} + \int\frac{\rho(r',t)}{|r-r'|}dr' - \frac{Z}{r} + v_{\text{ext}}(r,t) \tag{6}$$

where T_{NW} and E_{XC} denote non-Weizsäcker part in kinetic energy (KE) and exchange correlation energy functionals respectively, explicit forms of which have been given earlier [20, 37, 38]. Although Hohenberg–Kohn theorems [44] assert the existence of these functionals, their exact forms are still not known even for the ground state and various approximations with respective merits and demerits have been proposed [45]. The external potential denoted by $v_{ext}(r, t)$ is as given below,

$$v_{ext}(r, t) = -\frac{1}{|R(t) - r|} \tag{7}$$

where $R(t)$ refers to the classical trajectory of two nuclei and has been calculated by standard straightline approximation [37]. Since $v_{ext}(r, t)$ vanishes at the boundary, the validity of TDDFT [42, 43] allows us to legitimately assume that the mappings $v_{ext}(r, t) \rightarrow \rho(r, t)$ and $v_{ext}(r, t) \rightarrow j(r, t)$ are uniquely invertible and accordingly the total time-dependent Hamiltonian is a unique functional of $\rho(r, t)$ and $j(r, t)$. Therefore, in this context one can define a time-dependent energy quantity, $E(t)$, as a density functional [46] and the corresponding definition for the time-dependent chemical potential can be given by [20]

$$-\chi(t) = \mu(t) = \frac{\delta E(t)}{\delta \rho} = \frac{1}{2}(\nabla \xi)^2 + \frac{\delta T}{\delta \rho} + \int \frac{\rho(r', t)}{|r - r'|} dr' - \frac{Z}{r} + \frac{\delta E_{XC}}{\delta \rho} + v_{ext}(r, t). \tag{8}$$

Since μ is constant over the whole space in a molecule, if at a distance r_μ, we get [20]

$$\frac{1}{2}(\nabla \xi)^2 + \frac{\delta T}{\delta \rho} + \frac{\delta E_{XC}}{\delta \rho} = 0, \tag{9}$$

the chemical potential becomes equal to total electrostatic potential at r_μ in that time step as

$$-\chi(t) = \mu(t) = \int \frac{\rho(r, t)}{|r_\mu - r|} dr - \frac{Z}{r_\mu} + v_{ext}(r_\mu, t). \tag{10}$$

At time $t = 0$, (9) and (10) become identical to that given by Politzer *et al* [47] considering principle of equalization of electronegativity and the distance r_μ was found to match well with the covalent radii of atoms.

Temporal evolution of η has been calculated at every time step from the following expression [48, 49]

$$\eta(t) = \int f(r, t) \eta(r, t) dr \tag{11}$$

where $\eta(r, t)$ is the local hardness at time t given by [48, 49]

$$\eta(r, t) = \frac{1}{2N} \int \frac{\delta^2 F[\rho(r, t)]}{\delta \rho(r, t) \delta \rho(r', t)} \rho(r') dr'. \tag{12}$$

Here $F[\rho]$ is the usual Hohenberg–Kohn functional explicit approximate form of which has been given elsewhere [20, 37]. The Fukui function, $f(r)$ has been given

by [50]

$$f(r)=\left(\frac{\partial \rho}{\partial N}\right)_{v(r)}. \tag{13}$$

This can be approximated [32, 33] by neglecting the smaller second term in the expression of Hellmann–Feynman force [48] written as the sum of forces acting on $f(r)$ and a term involving the product of the matrix elements of perturbation caused by small changes in external potential and local hardness. Thus $f(r)$ becomes [32, 33]

$$f(r,t)=\frac{\rho(r,t)}{N}. \tag{14}$$

Same approximate form of $f(r)$ has been found by Gázquez expressing density of charged species as the renormalized electron density of the neutral species [51].

It is important to note that exact forms for $T[\rho]$ and $E_{XC}[\rho]$ are not known even for the ground state [45]. As it has been done in all earlier time-dependent calculations within QFDF framework [37–40], in this paper also it has been assumed that $T[\rho]$

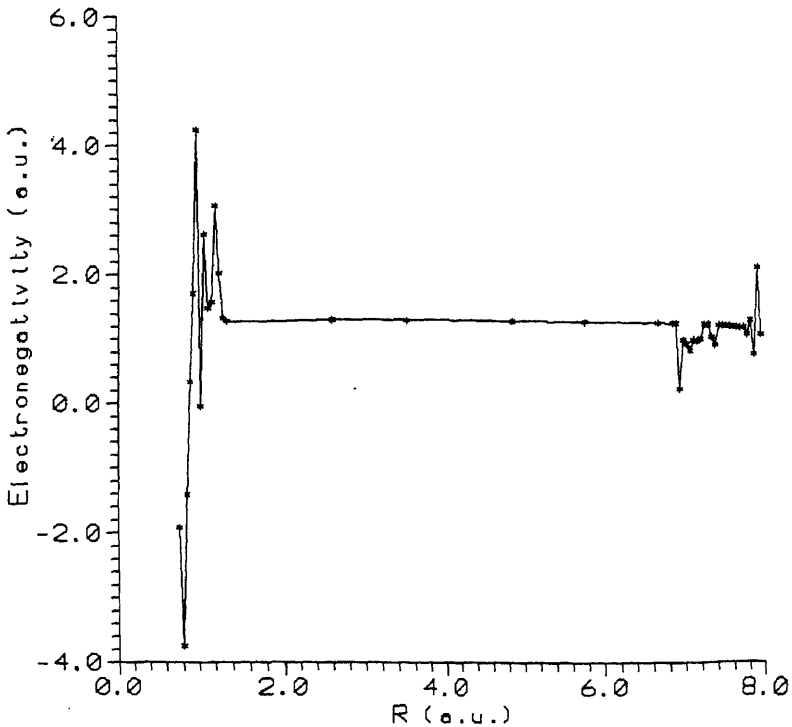

Figure 1. The plot of electronegativity (χ) versus internuclear distance (R) of BeH^+ (a supermolecule as in ref. 37) calculated within a quantum fluid density functional (QFDF) framework.

and $E_{xc}[\rho]$ have the same forms in ground and excited states. This assumption need not always be valid. The present state of knowledge of excited-state DFT does not leave any other alternative [38].

Time evolution of the system as well as its properties like electronegativity and hardness has been found by solving eq. (5) as an initial-boundary value problem. The numerical solution starts with a near Hartree–Fock [52] density of Be-atom in a ^1S state and a proton with a KE value of 5 keV approaching it for a head-on collision. A leap-frog finite difference scheme which is stable for quantum mechanical equations of motion due to the presence of $i(i^2 = -1)$ [53] has been adopted here to solve eq. (5). The numerical method has been reported in detail earlier [20, 38, 39]. In *ab initio* SCF calculations [41] χ and η have been calculated from (3) and (4) using energies of HOMO and LUMO obtained at different internuclear distances.

The electronegativity profiles obtained from QFDF and *ab initio* calculations have been presented in figures 1 and 2 respectively. The electronegativity profile obtained from QFDF calculation (figure 1) shows some initial transients as the electron density gets reoriented around the nucleus due to nonlinear effective potential field, v_{eff}. After elapse of certain time the electron density does not change appreciably which is akin to some sort of dynamic equilibrium. At this stage, χ attains a constant value over a range

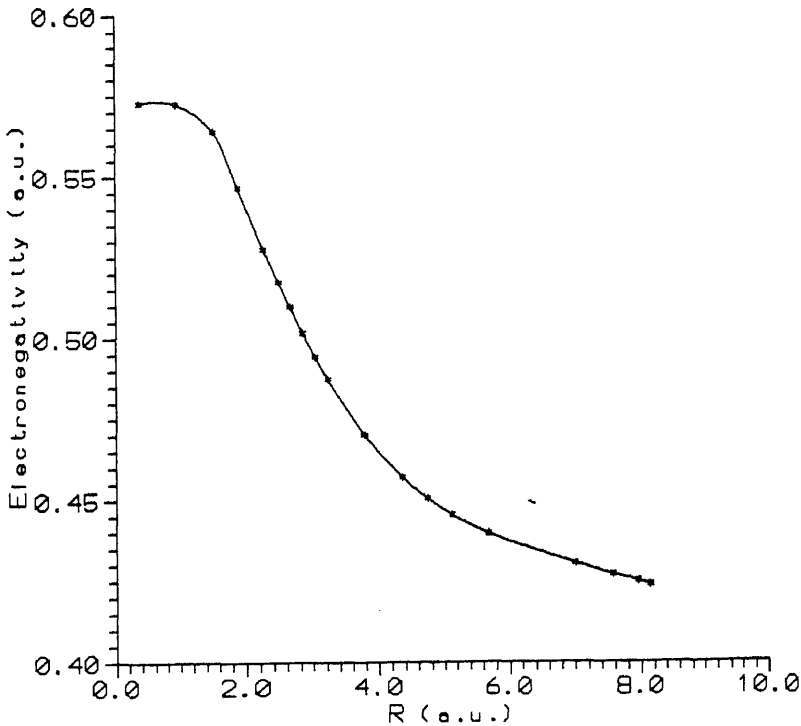

Figure 2. The plot of electronegativity (χ) versus internuclear distance (R) of BeH^+ obtained through an *ab initio* SCF calculation.

KE($\simeq$ 5 keV). Hence in the encounter regime where internuclear distance is too small, electronegativity profile shows sharp fluctuation due to rapid nonlinear charge oscillations at the vicinity of the two nuclei. On the other hand, the SCF results being associated with ground states of BeH^+ at different internuclear distances, the electronegativity profile does not show oscillations but increases monotonically in the process of molecule formation and reaches a plateau corresponding to the molecular electronegativity value (figure 2). It has been found in this SCF calculation that as the proton approaches Be atom, charge (Mulliken population) on Be atom decreases from 3·44 at $R = 4{\cdot}3$ Å to the minimum value of 3·06 at the equilibrium bond distance ($R_e = 1{\cdot}3122$ Å) and it increases again as BeH^+ molecule ion is squeezed beyond its equilibrium configuration.

Figures 3 and 4 present the hardness profiles obtained from QFDF and *ab initio* SCF calculations respectively. Both figures show rise in hardness as the two nuclei approach

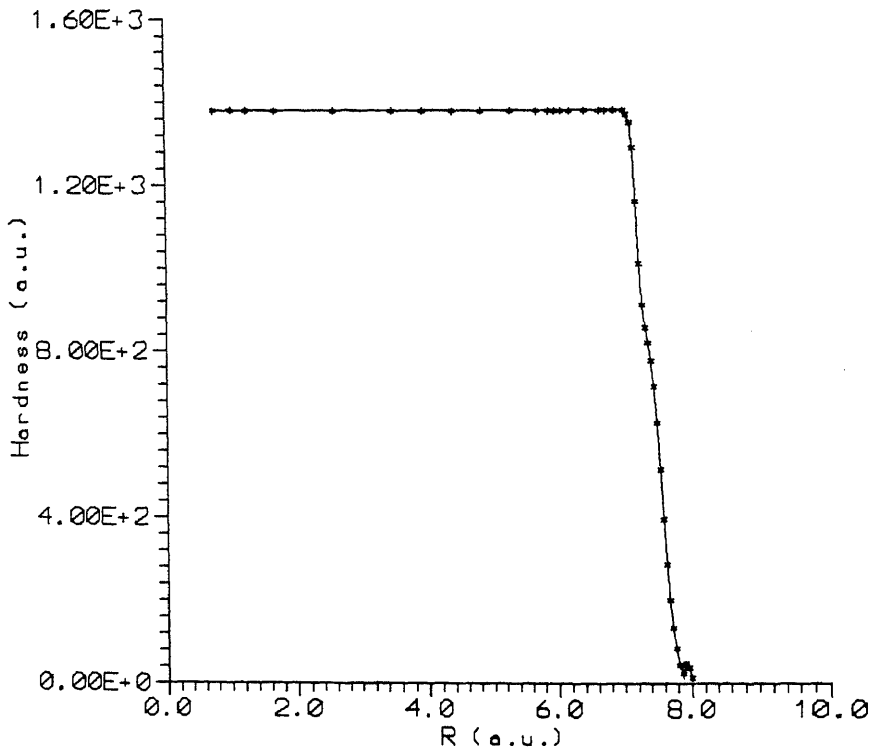

Figure 3. The plot of hardness (η) versus internuclear distance (R) of BeH^+ (a supermolecule as in ref. 37) calculated within a quantum fluid density functional (QFDF) framework.

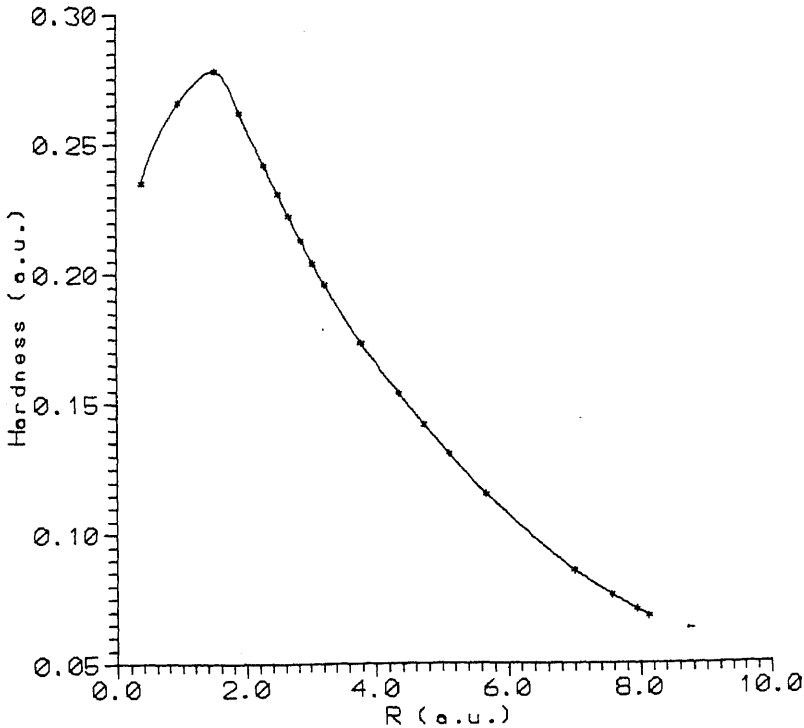

Figure 4. The plot of hardness (η) versus internuclear distance (R) of BeH^+ obtained through an *ab initio* SCF calculation.

each other. Hardness in figure 3 rises sharply as the proton approaches Be atom. In this dynamical process, as the electron density of Be atom gets accumulated near the nucleus and does not change appreciably in course of time, η becomes constant after attaining a high value which may be considered as the dynamical variant of maximum hardness principle [32, 33]. In SCF method, however, rise in η is not so sharp along the reaction path of formation of BeH^+ molecule. In this case η passes through a maximum which, however, is not at equilibrium bond distance of BeH^+ because the extrema for the electronic energy and the nuclear repulsion energy do not appear in the same point of the potential energy curve [19, 22, 31].

It may be noted that the major features in χ and η profiles obtained from structure and dynamics calculations do not match in general. The differences in numerical values as well as other features in the profiles are probably due to the following reasons. The dynamical formalism involves mixing of excited state densities with ground state density as is evidenced from nonvanishing current density, while, in *ab initio* SCF method, calculations were restricted to ground states with different internuclear geometries of BeH^+. The electron correlation has not been taken into account in *ab initio* SCF calculations. Exact forms for kinetic and exchange-correlation energy functionals of DFT are not known [45]. Hence approximate forms for these functionals

are used and their validity in excited states is tacitly assumed. It is in the spirit of Slater's transition state approach [54] where the ground state Hartree–Fock–Slater formalism is considered to be applicable to excited states as well. Straight-line approximation has been used for the calculation of classical trajectory of nuclei. Finally the expression for $f(r)$ given in (14) is an approximation which may be modified by incorporating appropriate inhomogeneity corrections.

This study compares the χ and η profiles generated through electronic structure and dynamics calculations. In SCF calculation, electronegativity increases from a small value corresponding to that of Be atom when proton is much away from it and increases monotonically as proton approaches and finally reaches an asymptote which may be identified as the electronegativity of BeH^+ molecule. This is a consequence of the electronegativity equalization principle. Hardness also increases as the internuclear distance decreases and passes through a maximum in the neighbourhood of equilibrium configuration, as expected from the maximum hardness principle. In the dynamical situation rapid charge oscillation is observed in the encounter zone and excited state densities get mixed with the ground state density.

Acknowledgements

PKC would like to thank CSIR, New Delhi for financial assistance and SN is thankful to CSIR, New Delhi for receiving research associateship. We are thankful to the referee for constructive criticism.

References

[1] L Pauling, *The nature of the chemical bond* (Cornell Univ. Press, Ithaca, New York, 1960) p. 88
[2] R P Iczkowski and J L Margrave, *J. Am. Chem. Soc.* **83**, 3547 (1961)
[3] R G Parr, R A Donnelly, M Levy and W E Palke, *J. Chem. Phys.* **68**, 3801 (1978)
[4] K D Sen and C K Jørgensen eds., *Electronegativity, structure and bonding*, (Springer, Heidelberg, 1987) Vol. 66
[5] R G Pearson, *J. Am. Chem. Soc.* **85**, 3533 (1963)
[6] R G Parr and R G Pearson, *J. Am. Chem. Soc.* **105**, 7512 (1983)
[7] R G Parr and W Yang, *Density functional theory of atoms and molecules* (Oxford University Press, New York, 1989)
[8] K D Sen and D M P Mingos eds., *Chemical hardness, structure and bonding*, (Springer–Verlag, Berlin, 1992) Vol. 80
[9] P K Chattaraj and R G Parr in reference 8
P K Chattaraj, *J. Indian Chem. Soc.* **69**, 173 (1992)
[10] R G Pearson, *Proc. Natl. Acad. Sci. USA*, **83**, 8440 (1986)
[11] R T Sanderson, *Science* **114**, 670 (1951); **116**, 41 (1952); **121**, 207 (1955)
[12] R T Sanderson, *J. Chem. Educ.* **29**, 539 (1952); **31**, 238 (1954)
[13] R A Donnelly and R G Parr, *J. Chem. Phys.* **69**, 4431 (1978)
[14] P Politzer and H Weinstein, *J. Chem. Phys.* **71**, 4218 (1979)
[15] R G Parr and L Bartolotti, *J. Am. Chem. Soc.* **104**, 3801 (1982)
[16] P K Chattaraj, H Lee and R G Parr, *J. Am. Chem. Soc.* **113**, 1855 (1991)
[17] R G Pearson, *J. Chem. Educ.* **64**, 561 (1987)
[18] R G Parr and P K Chattaraj, *J. Am. Chem. Soc.* **113**, 1854 (1991)
[19] R G Parr and J L Gázquez, *J. Phys. Chem.* **97**, 3939 (1993)
[20] P K Chattaraj and S Nath, *Int. J. Quantum Chem.* **49**, 705 (1994)

[21] S Nath, P K Nandi, A B Sannigrahi and P K Chattaraj, *J. Mol. Struct.* **279**, 207 (1993)
[22] R G Pearson and W E Palke, *J. Phys. Chem.* **96**, 3283 (1992)
[23] D Datta, *Inorg. Chem.* **31**, 2797 (1992)
[24] D Datta, *J. Phys. Chem.* **96**, 2409 (1992)
[25] P K Chattaraj and P v R Schleyer, *J. Am. Chem. Soc.* **116**, 1067 (1994)
[26] M Galván, A D Pino and J D Joannopoulos, *Phys. Rev. Lett.* **70**, 21 (1993)
[27] A D Pino, M Galván, T A Arias and J D Joannopoulos, *J. Chem. Phys.* **98**, 1606 (1993)
[28] P K Chattaraj, S Nath and A B Sannigrahi, *Chem. Phys. Lett.* **212**, 223 (1993)
P K Chattaraj, S Nath and A B Sannigrahi, *J. Phys. Chem.* **98**, 9143 (1994)
P K Chattaraj, and S Nath, *Indian J. Chem.* **A33**, 842 (1994)
[29] J L Gázquez, A Martínez and F Méndez, *J. Phys. Chem.* **97**, 4059 (1993)
[30] S Nath, A B Sannigrahi and P K Chattaraj, *J. Mol. Struct.* **306**, 87 (1994)
[31] S Nath, A B Sannigrahi and P K Chattaraj, *J. Mol. Struct.* **309**, 65 (1994)
[32] P K Chattaraj and S Nath, *Proc. Indian Acad. Sci. (Chem. Sci.)* **106**, 229 (1994)
[33] P K Chattaraj and S Nath, *Chem. Phys. Lett.* **217**, 342 (1994)
[34] S M Read and J T Vanderslice, *J. Chem. Phys.* **37**, 205 (1962)
[35] K E Banyard and G K Taylor, *J. Phys.* **B8**, L137 (1975)
[36] K P Huber and G Herzberg, *Molecular spectra and molecular structure*, Constants of diatomic molecules (Van Nostrand, New York, 1979) Vol. IV, p. 81
[37] B M Deb and P K Chattaraj, *Phys. Rev.* **A39**, 1696 (1989)
B M Deb and P K Chattaraj, *Chem. Phys. Lett.* **148**, 550 (1988)
[38] B M Deb, P K Chattaraj and S Mishra, *Phys. Rev.* **A43**, 1248 (1991)
[39] P K Chattaraj, *Int. J. Quantum Chem.* **41**, 845 (1992)
[40] B M Deb and P K Chattaraj, in *Solitons: Introduction and application*, edited by M Lakshmann (Springer, Berlin, 1988) pp. 11–25
P K Chattaraj in *Symmetries and singularity structures: Integrability and chaos in nonlinear dynamical systems*, edited by M Lakshmann and M Daniel (Springer–Verlag, Berlin 1990) pp. 172–182
[41] W J Hehre, L Radom, P v R Schleyer and J A Pople, *Ab initio molecular orbital theory* (Wiley, New York, 1986)
[42] E Runge and E K U Gross, *Phys. Rev. Lett.* **52**, 997 (1984)
[43] A K Dhara and S K Ghosh, *Phys. Rev.* **A35**, 442 (1987)
[44] P Hohenberg and W Kohn, *Phys. Rev.* **B136**, 864 (1964)
[45] P K Chattaraj and B M Deb, *J. Sci. Ind. Res.* **43**, 238 (1984)
[46] For the definition of a similar time-dependent energy quantity in the presence of a harmonic time-dependent perturbation see B M Deb and S K Ghosh, *J. Chem. Phys.* **77**, 342 (1982)
L J Bartolotti, *Phys. Rev.* **A24**, 1661 (1981). See Reference 42 for a general time-dependent situation
[47] P Politzer, R G Parr and D R Murphy, *J. Chem. Phys.* **79**, 3859 (1983)
[48] M Berkowitz, S K Ghosh and R G Parr, *J. Am. Chem. Soc.* **107**, 6811 (1985)
[49] M Berkowitz and R G Parr, *J. Chem. Phys.* **88**, 2554 (1988)
[50] R G Parr and W Yang, *J. Am. Chem. Soc.* **106**, 4049 (1984)
[51] J L Gázquez, in reference 9
[52] E Clementi and C R Roetti, *At. Data Nucl. Data Tables* **14**, 174 (1974)
[53] P K Chattaraj, K S Rao and B M Deb, *J. Comput. Phys.* **72**, 504 (1987)
[54] J C Slater, *Phys. Rev.* **81**, 385 (1951)

MANA
ournal of
physics

© Printed in India

Vol. 45, No. 1,
July 1995
pp. 75–80

e inversion potential for NH_3 and its isotopic species

AQUINO[1], A PALMA[2], J L LÓPEZ[3] and M A ROSALES[4]
partamento de Física, Universidad Autónoma Metropolitana-Iztapalapa, Apdo. Postal
34, México, D. F. 09340, México
iversidad Autónoma de Puebla, Instituto de Ciencias, Depto. de Física, Apdo. Postal J-48,
bla, Pue. 72570, México
ca de Física, Div. de CBI, Universidad-Autónoma Metropolitana-Azcapotzalco, Apdo.
al 16-306, México D. F. 02200, México
pto. de Física y Matemática, Esc. de Ciencias, Universidad de las Americas Puebla, Apdo.
al 100, Sta. Catarina, Mártir, Puebla 72820, México

received 30 June 1994; revised 9 January 1995

ract. Using *ab initio* data of the potential surface for the ground state of NH_3 a function is ined to represent, with a very high precision, the potential along the inversion coordinate. inversion spectra of NH_3, ND_3, NH_2D and NHD_2 are found by numerically solving the ödinger equation for this potential. Comparison is made of the calculated inversion uencies and the experimental values, and the molecular constants of NH_3 are also compared hose found in the literature.

words. Vibrational spectrum of NH_3; quartic anharmonic oscillator; double-well potential; ecular constants of NH_3.

CS Nos **31·20; 35·20**

ntroduction

e inversion of the NH_3 molecule, in which a nitrogen atom oscillates between both es of the plane defined by the hydrogen atoms (figure 1) is an old problem that has n extensively studied by means of experimental and empirical methods [1–12] while *ab initio* approaches have been rather scarce [13–15].

Several types of double-well potentials have been used [3, 8, 9, 12–14] to simulate the ersion barrier of NH_3, but perhaps the simplest analytical way to represent this ential is by means of a quartic anharmonic oscillator with a symmetrical double- l [15]:

$$V(x) = -\tfrac{1}{2}x^2 + \lambda x^4, \quad \lambda > 0$$

h an energy spectrum consisting of doublets, one member of each doublet belonging symmetrical state and the other to the antisymmetrical state. It is known [16] that Schrödinger equation for this potential is not solvable by perturbation theory, since perturbative series in powers of the parameter λ is divergent for any value of $\lambda > 0$. me years ago, Bunker *et al* [13] calculated the energy surface for NH_3 and showed t the inversion barrier can be predicted from the first principles. Palma *et al* [14] ose some points from the energy surface calculated by Bunker [13] and used the thod of least squares to find an eighth degree polynomial to represent the inversion

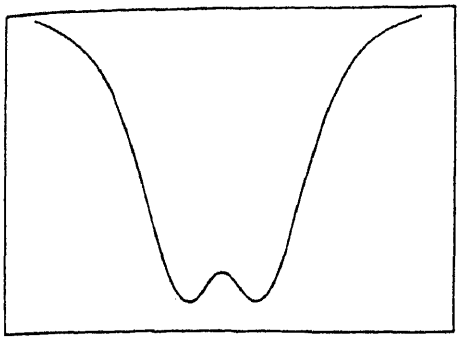

Figure 1. The double-well potential for the inversion of the NH_3 molecule.

proposed, from which the quartic anharmonic oscillator potential with double-well is found and the molecular constants and the inversion frequencies for NH_3 are determined.

2. The quartic anharmonic potential

If we assume that the inversion potential $V(x)$ can be represented by a fourth degree polynomial then the corresponding Hamiltonian can be written as:

$$H' = \frac{\hbar p^2}{2\mu} - \frac{1}{2}ax^2 + \frac{1}{2}bx^4 \tag{1}$$

where μ is reduced mass.

This Hamiltonian can be reduced to that of a quartic anharmonic oscillator with double-well

$$H = \tfrac{1}{2}P^2 - \tfrac{1}{2}Q^2 + \lambda Q^4 \tag{2}$$

by means of the transformations:

$$P = \left(\frac{\hbar^2}{\mu a}\right)^{1/4} p \quad \text{and} \quad Q = \left(\frac{\mu a}{\hbar^2}\right)^{1/4} x.$$

The energy unit ε and the anharmonic constant of (2) are expressed as:

$$\varepsilon = \hbar\nu_0 = \left(\frac{a\hbar^2}{\mu}\right)^{1/2}, \tag{3a}$$

$$\lambda = \frac{b\varepsilon}{2a}. \tag{3b}$$

3. The inversion frequencies for NH_3

The inversion of NH_3 may be treated, to a good approximation, as a problem of one particle in a one-dimensional potential $V(x)$, where x represents the inversion coordinate,

i.e., it measures the distance of the N atom to the plane of the hydrogen atoms. Both quantities, x and $V(x)$, are given in atomic units. If R stands for the distance of the N atoms to one of the H atoms and α is the angle between the H–N–H bonds, then the inversion coordinate will be given by:

$$x = [1 - \tfrac{4}{3}\sin^2(\alpha/2)]^{1/2} R = R \sin \beta.$$

where β is the angle between the N–H bond and the plane of the H atoms. If m and M are the masses of the H and N atoms, respectively, the reduced mass may be expressed as $\mu = 3m(M + 3m\sin^2\beta)/(M + 3m)$. Unlike other works [14, 15], in the present one the angle β is not taken as 21°49′, corresponding to the experimental equilibrium configuration [11], but it is calculated by interpolation from the data in table 1 of ref. [14], which determine an angle of 22°44′ for the theoretical equilibrium configuration.

As already mentioned, there exists a number of suggestions for the analytical form of $V(x)$, and in this work we propose the use of a fourth degree polynomial which satisfactorily reproduces the points of the potential surface. This is achieved by taking the same six points (table 1, ref. [14]) chosen by Palma *et al* [14] from the 54 point calculated by Bunker *et al* [13] using *ab initio* methods.

The fourth degree polynomial $V(x) = c_0 + c_1 x^2 + c_2 x^4$ which best reproduces the mentioned data has $c_0 = -56{\cdot}4064$, $c_1 = -3{\cdot}034493 \times 10^{-2}$ and $c_2 = 2{\cdot}666604 \times 10^{-2}$. With these values the energy unit ε, eq. (3a), the anharmonic constant λ, eq. (3b), and the other molecular constants are readily determined for NH_3. Some of these constants are summarized in table 1. Reference [10] is the best empirical calculation ever made, where a potential of the form $V(x) = aq^2/2 + bq^4/2 + d\exp(-cq^2)$ was used; the parameters β, a, b, c and d were varied until the value of the energy closest to the experimental value was obtained. The experimental values for the barrier height and the equilibrium distance [5] are $2020 \pm 12\,\mathrm{cm}^{-1}$ and $0{\cdot}382 \pm 0{\cdot}004$ Å, respectively.

As shown in § 2, the Hamiltonian associated with the fourth-degree polynomial potential, eq. (1) reduces to that of a double-well anharmonic oscillator, eq. (2). The corresponding Schrödinger equation was numerically solved for the NH_3 and its isotopic species. Two numerical methods were employed, the first being described in ref. [14, 19], while the second is mentioned in ref. [15, 17], and the results found were

Table 1. Values of the molecular constants for NH_3.

Molecular constant	This work	Ref. [10]
μ(g)	$4{\cdot}263 \times 10^{-24}$	$4{\cdot}263 \times 10^{-24}$
a(dynes/cm)	$9{\cdot}45 \times 10^{-4}$	$9{\cdot}42 \times 10^{4}$
b(dynes/cm^3)	$2{\cdot}96 \times 10^{21}$	$0{\cdot}47 \times 10^{21}$
c(cm^{-2})	0·00	$4{\cdot}269 \times 10^{16}$
d(ergs)	0·00	$2{\cdot}452 \times 10^{-12}$
ν_0(cm^{-1})	790·3	789·9
H(Barrier height, cm^{-1})	1894·5	2018
X_e(Equilibrium dist., A)	0·399	0·382
β(Equilibrium angle)	22°44′	22°12′

Table 2. Vibrational spectrum for NH_3 ($\lambda = 0{\cdot}02607$) along the inversion coordinate in cm^{-1}. (s = symmetrical, a = antisymmetrical).

State	Ref. [13]	Ref. [14]	Present work	Experiment [5]
O^s	0·0	0·0	0·0	0·0
O^a	1·02	0·995	0·969	0·793
1^s	986·7	924·12	928·92	932·51
1^a	1032·3	981·04	981·46	986·70
2^s	1682·0	1559·57	1561·41	1597·60
2^a	2011·6	1931·34	1913·56	1910·00
3^s		2473·40	2435·88	2383·46
3^a		3065·91	2998·67	2895·48

Table 3. Vibrational spectrum for ND_3 ($\lambda = 0{\cdot}01970$) along the inversion coordinate in cm^{-1}. (s = symmetrical, a = antisymmetrical).

State	Ref. [14]	Present work	Experiment [5]
O^s	0·0	0·0	0·0
O^a	0·048	0·047	0·053
1^s	756·01	757·55	745·7
1^a	760·84	761·91	749·4
2^s	1338·91	1344·31	1359
2^a	1442·98	1438·90	1429
3^s	1818·64	1811·33	1830
3^a	2151·52	2127·62	2106·6

identical. In table 2 we present the values of the vibrational spectrum of NH_3 predicted by this model, the experimental values [5], and the results obtained by Palma *et al* [14] and by Bunker *et al* [13].

Although we have taken only six points of the surface potential calculated by Bunker to determine $V(x)$ through a least squares fitting, from tables 2 and 3 it may be seen that the obtained results are very accurate.

4. Isotopic species of NH_3

From the Born–Oppenheimer approximation, the same potential curve for NH_3 may be used for the isotopic species ND_3, NH_2D and NHD_2 and the results must also be satisfactory since the deuterium nucleus is heavier than that of hydrogen. From table 3 it can be seen that our results are very similar to those obtained using an eight degree polynomial [14] as the inversion potential for ND_3.

The results obtained for the isotopic species NH_2D and NHD_2 are shown in table 4. In these cases, the motion is more complex but we will still assume that the potential surface is the same as for NH_3. In table 5, our results are compared to some experimental values, for example the ground state splitting $\Delta_0 = |O^a - O^s|$ and the first excited state splitting $\Delta_1 = |1^a - 1^s|$. Further, also in that table we show the value of k,

Table 4. Vibrational spectrum for NH_2D ($\lambda = 0{\cdot}02354$) and NHD_2 ($\lambda = 0{\cdot}02152$) along the inversion coordinate in cm^{-1}. (s = symmetrical, a = antisymmetrical)

State	NH_2D	NHD_2
O^s	0·0	0·0
O^a	0·342	0·133
1^s	854·16	799·17
1^a	877·32	809·58
2^s	1443·16	1379·14
2^a	1681·40	1536·35
3^s	2122	1930·49
3^a	2580·77	2313·36

Table 5. Splitting energies for NH_3, ND_3, NH_2D and NHD_2 in cm^{-1}. (s = symmetrical, a = antisymmetrical)

	Experiment	Calculated	Ref. [14]	Ref. [13]
		NH_3		
Δ_0	0·793	0·969	0·995	1·02
Δ_1	35·81	52·54	56·92	45·6
1^s	932·51	928·92	924·12	986·7
1^a	968·32	981·46	981·04	1032·3
k		1·0		
		ND_3		
Δ_0	0·053	0·047	0·048	
Δ_1	3·7	4·36	4·83	
1^s	745·7	757·55	756·01	
1^a	749·4	762·91	760·84	
k		1·323		
		NH_2D		
Δ_0	0·406	0·342		
Δ_1	19·7	23·16		
1^s	874	854·16		
1^a	894	877·32		
k		1·128		
		NHD_2		
Δ_0	0·1705	0·133		
Δ_1	9·84	10·41		
1^s	808	799·17		
1^a	818	809·58		
k		1·233		

the square root of the ratio of the reduced mass of a given species to the reduced mass of NH_3.

The experimental values of Δ_0 and Δ_1 for NH_2D and NHD_2 have been taken from refs. [10, 18]. From table 5 it can also be observed that the fourth degree potential

used in this work produces, in general, better results than the eight degree potentials [13, 14].

5. Conclusions

The energy levels for ND_3 are not particularly sensitive to the type of potential used to model the inversion, and this may be seen from table 4 where the results obtained using a fourth degree polynomial and those from ref. [14], where an eighth degree polynomial are practically the same; we believe that the NH_2D and NHD_2 molecules must behave similarly, whereas for the case of NH_3 a difference is indeed observed between our results and those of ref. [14], ours being closer to the experimental values.

The discrepancy between our calculated values (especially the higher energy levels) and the experimental values may be produced by the fact that the fourth degree polynomial increases indefinitely as the inversion coordinate x increases, while the true potential has a limit before molecular dissociation takes place (figure 1).

The points of the potential surface completely determine the observables of the problem (spectrum and molecular constants), so that in the present work it has not been necessary to rely on experimental values of the geometry or to use adjustable parameters, i.e., everything is determined from first principles.

The molecular constants found with this model are very similar to those obtained by Swalen and Ibers [10] with a totally empirical method, where five adjustable parameters were present. Finally, it must be pointed out that only experimental data for NH_2D and NHD_2 are available in the literature, whereas no theoretical data calculated from first principles can be found.

References

[1] H Y Sheng, E F Barker and D M Dennison, *Phys. Rev.* **60**, 786 (1941)
[2] M V Migeotte and E F Barker, *Phys. Rev.* **50**, 418 (1936)
[3] F T Wall and G Glocker, *J. Chem. Phys.* **5**, 314 (1937)
[4] W E Good, *Phys. Rev.* **70**, 213 (1946)
[5] W S Benedict and E K Plyer, *Can J. Phys.* **35**, 1235 (1957)
[6] C W Townes, *Phys. Rev.* **70**, 665 (1946)
[7] M T Weiss and M W P Strandberg, *Phys. Rev.* **83**, 567 (1951)
[8] M F Manning, *J. Chem. Phys.* **3**, 136 (1935)
[9] R R Newton and L H Thomas, *J. Chem. Phys.* **16**, 310 (1948)
[10] J D Swalen and J A Ibers, *J. Chem. Phys.* **36**, 1914 (1962)
[11] C H Townes and A L Schalow, *Microwave spectroscopy* (Dover, New York, 1975) p. 300
[12] C C Costain and G B B M Shuterland, *J. Phys. Chem.* **56**, 321 (1952)
[13] P R Bunker, W P Kraemer and V Spirko, *Can. J. Phys.* **62**, 1801 (1984)
[14] G Campoy, A Palma and L Sandoval, *Int. J. Quantum Chem.* (*Quantum Chem. Symp.*) **23**, 355 (1989)
[15] N Aquino, M. Sc. Thesis, A non-perturbative numerical solutions for Schrödinger equation, UNAM, Mexico (1992)
[16] K Banerjee and S P Bhatnagar, *Phys. Rev.* **D18**, 4767 (1978)
[17] N Aquino, M Berrondo and A Palma, (not published)
[18] M T Weiss and M W Strandberg, *Phys. Rev.* **83**, 567 (1951)
[19] N Aquino, *Int. J. Quantum Chem.* **54**, 107 (1995)

PRAMANA
— journal of
physics

© Printed in India

Vol. 45, No. 1,
July 1995
pp. 81–89

A low cost PC based card for heat-capacity measurements at low temperatures

R S SANNABHADTI, S RAMAKRISHNAN, K GHOSH, ARUN PATADE and GIRISH CHANDRA
Tata Institute of Fundamental Research, Bombay 400005, India

MS received 28 July 1994

Abstract. We describe a simple, low cost pc based card for the measurement of heat capacity using adiabatic calorimetry at low temperatures. This card provides the control pulse to the sample heater as well as trigger pulse to the nano-voltmeter which monitors the sensor voltage (Ge sensor, Lake Shore Inc., USA). We have also added a 12 bit DAC on this card and this is used for remote setting of the heater current of an old SHE (now Biomagnetic, Inc., USA, model CCS) analog constant current source. Although this card is used here for heat-capacity measurements, the same can also be used for thermo-power and thermal-conductivity measurements.

Keywords. Low temperature; automation; heat-capacity.

PACS No. 07·20

1. Introduction

Low temperature heat-capacity measurements are always very important to the solid state physicists [1, 2]. Many of the phase transitions (such as, magnetism or superconductivity) can be confirmed only after performing the heat-capacity measurements at low temperatures. Usually, the variation of the heat-capacity of solids with temperatures is very large at low temperatures. Depending on the nature of the samples, the mass of the sample used in the heat-capacity measurements may vary as much as two orders in magnitude. It is therefore essential that the apparatus used for this measurement should allow flexible control of the heating power applied to the sample at low temperatures. One normally uses a programmable current source (Keithley, model 220, USA) which has a GPIB interface and this is used to control the value of the heater current as well as the duration of the heater pulse in the heat-capacity measurements. In this paper, we describe a PC based (compatible with IBM PC) card which can be used along with the analog current source in place of the programmable current source which is generally used for heater current supply. Moreover, the card provides a trigger pulse for every nth ($n = 1$ to 999) second to the nanovoltmeter which monitor the sensor voltage within 10 μsec after the heater is turned off. This helps us to measure accurately the sample temperature as well as the time to determine its thermal relaxation time of the sample which is related to its heat-capacity at that temperature. Further, this circuit provides automatic control for current reversal for temperature sensor current which eliminates the use of another

2. Circuit details

Figure 1 shows how the card and relay drivers are connected in the system. We have used a commercial card (from M/s Dynalog Microsystems Ltd., India) which provides the basic *I/O* facilities like addresses, chip-select lines, read, write and other *I/O* control lines. This is connected to an *I/O* slot of an IBM compatible personal computer and uses the power supply of the host computer. On this card, we have built the necessary interfaces for the microvoltmeter HP, model 34401A, and the constant current sources (M/s Keithley model 225 and M/s Biomagnetic Inc., model CCS). However, one can use

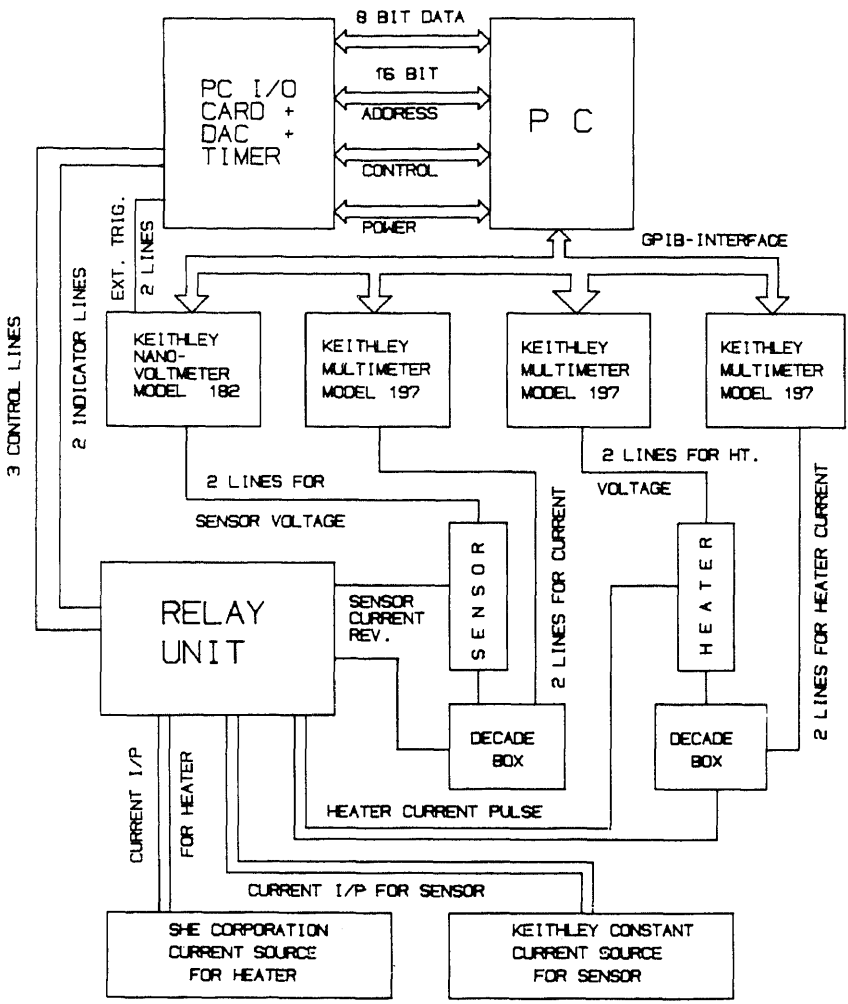

Figure 1. Schematic diagram of the connection of the interface card and relay unit to the host computer, microvoltmeter and the analog dc current source.

any IEEE-488 programmable microvoltmeter and any analog dc current source with voltage programmable facility with this interface card.

The voltage output from a calibrated Germanium sensor (M/s Lake Shore Inc., USA) is connected to the nanovoltmeter (Keithley, model 182, USA) for monitoring the temperature. The card provides a facility to measure the voltage for the forward and reverse current to eliminate the error due to thermo-emfs. The sensor voltage is monitored every two seconds (selectable through software) for a period of 2–3 min (programmable using software). After the sensor temperature is stabilized, a heat pulse is given using the timer and DAC built on the *I/O* card. At the end of the timer pulse to the heater, trigger pulses are generated from the card. The sensor voltage data are sent to the computer every one second by this external trigger pulse to the nanovoltmeter. The data are acquired by the PC using a IEEE-488 interface bus. There is a very short time delay ($< 10\ \mu$sec) between the first trigger pulse and the end of heater current pulse.

Figures 2 and 3 give the details about the timer interfaces of the card along with the DAC for heater current control and also the sensor current reversal. With the help of software (written in Quick Basic, 4.5, Microsoft, USA), a current reversal pulse is sent using the *C* port pin 10 of IC11 [3]. This IC is configured with all ports as output ports. The *A* and *B* ports are used for outputting 12 bit data to the DAC. The *C* port of the IC11 also provides a stop pulse option for switching off the current pulse. The timer gate is open for clock pulses with the start pulse for the heater current source. The clock frequency is 100 kHz. Along with the 0·1 s pulse from pin 16 of IC11, Q1 of IC2 goes high and Q2 of IC2 gives 0·1 s pulse. This opens one of the gates of IC3 and gives 100 kHz clock pulses to first counter in IC1 [3]. This IC1 has three 16 bit counters. The first and second counters are configured as rate generators. These clock pulses are used in generating the trigger pulses for nanovoltmeter and current pulse for the heater. These pulses are given to third counter in IC1 and this is configured as a monoshot. The period of the monoshot is preselectable. This period should have integer values in order to synchronize with trigger pulses and this period is obtained by loading the counter. The output of the monoshot goes low (negative pulse) with the first clock pulse provided the gate pulse is already received. The same gate pulse is used to reset the "divide by 2 counter" (first flip-flop of IC6). The input to IC6 is 1 s (selectable using software) pulses. The output of the IC6 (two second pulses) are prevented during the heater current pulse by the monoshot output of IC1. At the end of this current pulse, the two second pulses come out of one of the gates of IC3, which are given to the first monoshot of IC7. This monoshot gives two second negative pulses ($\bar{Q}1$) for triggering the voltmeter. The monoshot pulse of IC1 is inverted and used to drive the reed relays, which supply the heater current pulse. The relays have 2 NO (normally open) contacts. The relay RL1 is active with the monoshot pulse of IC1 and this gives current to the heater. The relay RL2 keeps the heater current source short circuited when IC1 monoshot pulse is absent. For sensor current reversal, we have another set of relay RL3 and RL4 as shown in figure 3. The driving pulses to all the relays are fed via two opto-isolators (MCT2E) and this ensures complete isolation for these pulses.

The heater current amplitude is controllable using an external dc voltage in an old SHE's (model CCS) constant current source. We have modified this current source so that the output current can be programmed using an external dc voltage. The unit requires 1 V dc for the full amplitude in any current range. However, one can use any

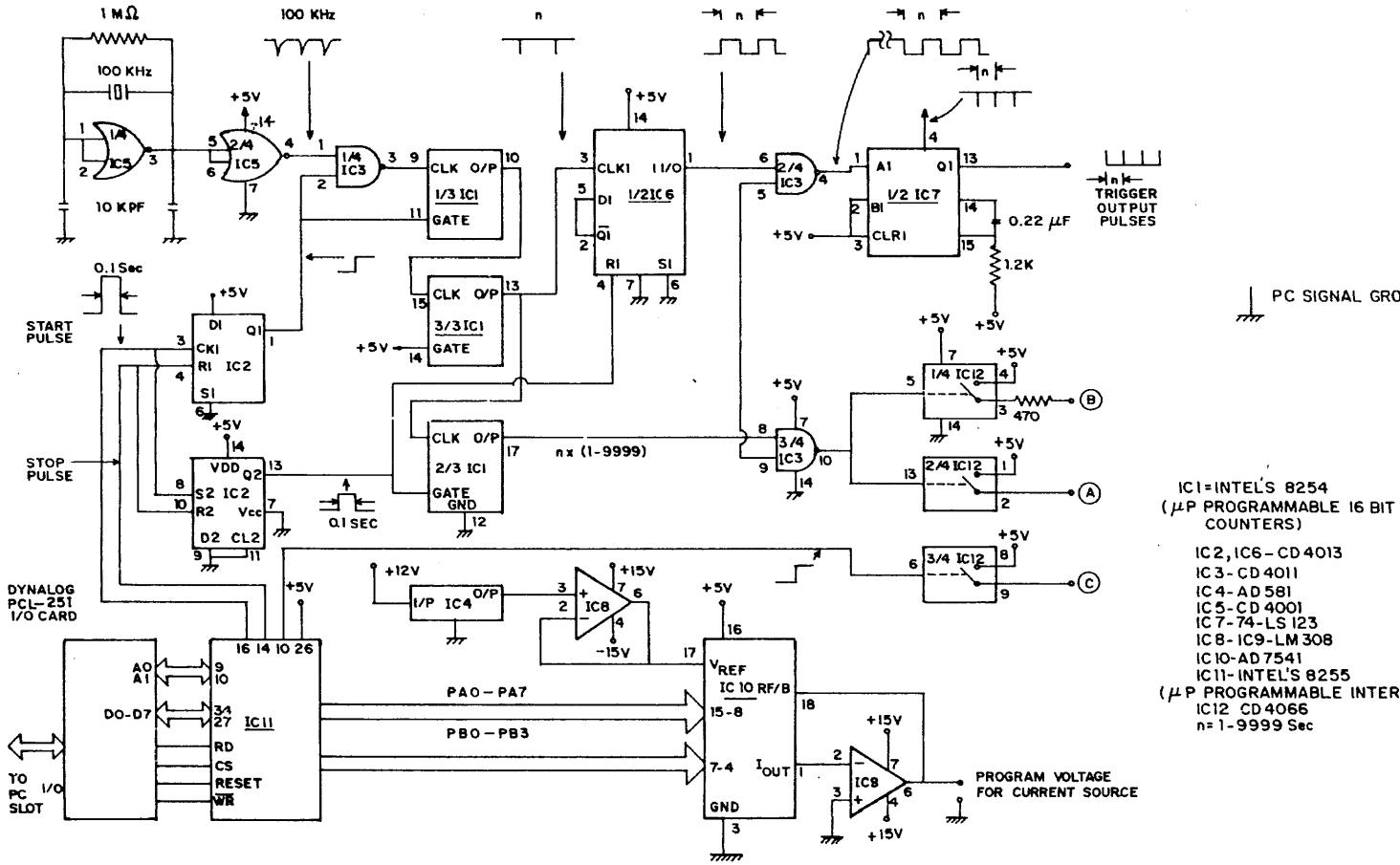

Figure 2. Circuit diagram of the interface card. The pulses are derived from 100 kHz quartz clock.

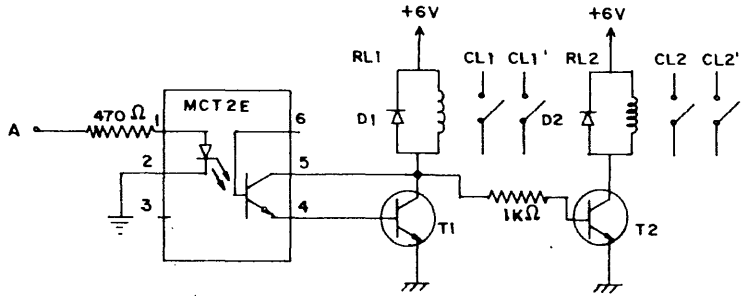

HEATER CURRENT PULSE

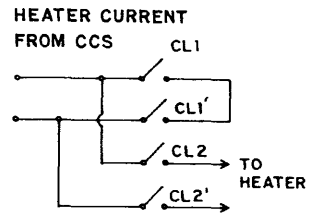

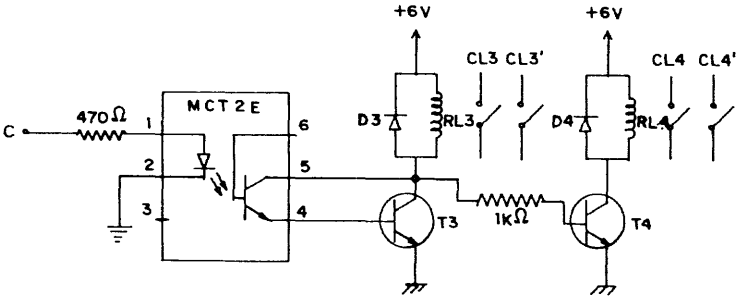

SENSOR CURRENT REVERSAL

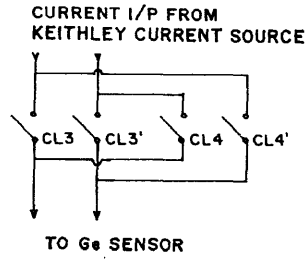

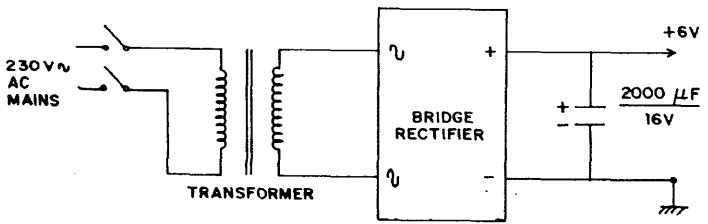

RELAY POWER SUPPLY

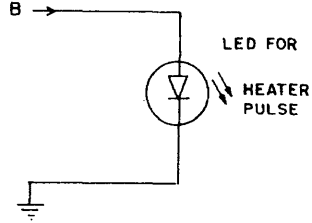

D1, D2, D3, D4 — IN 4001 DIODES

T1, T2, T3, T4 = BC 107C TRANSISTORS

RL1, RL2, RL3 RL4 = REED RELAYS

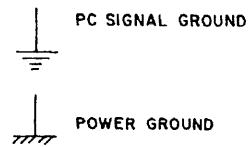

* INPUT SIGNAL A, B, C ARE COMING FROM PC-CARD

analog voltage programmable current source with this card. The DAC IC is AD from Analog Devices, USA [4]. The 12 bit binary O/P from A and B ports of I connected to this DAC. The external reference to this DAC is derived by using a 581 (Analog Devices) and a buffer which gives a 10 V reference. The DAC out connected to an operational amplifier LM308 [5] which gives a voltage outpu feedback path is completed by the resistors inside the DAC. This output is us heater current control.

3. Heat capacity measurements

Heat-capacity measurements are performed in a standard glass cryostat which co of outer liquid N_2 dewar and an inner dewar where liquid He is transferred. The t capacity of N_2 dewar is 3 litres and that of He is 1·3 litres. The hold time for He de 16 hours which is enough to perform heat-capacity measurements from 1·5 K to We have used adiabatic heat pulse technique to measure the heat-capacity of ma in the above mentioned temperature range. In this technique, the base temperatu is sampled via measuring the output from the nanovoltmeter (sensor voltage) eve second for 3 minutes and if the drift rate is less than 5 μK/sec, a heat pulse is app the sample. After a preselected time duration (software selectable) of this heater p a given temperature range, the nanovoltmeter is triggered every second to measu time vs temperature data for at least two minutes (software selectable) [7]. A triggering operations, current settings (heater and sensor currents) and current re (for sensor current) are preformed by the pc card. The heat-capacity is calculated the expression,

$$C_p\left(\frac{dT_S}{dt}\right) = P - k(T_S - T_0)$$

where P is the heating power of the heat pulse, T_S is the sample temperature a denotes the sample temperature in the absence of external heating and is determi extrapolating the pre-heating drift curve as shown in figure 4. It can be shown t the post-heating period, $U(t) = T_S - T_0$ is given by,

$$U(t) = \left(\frac{P}{C_p\beta}\right)[1 - e^{-\beta t_h}]e^{-\beta(t - t_h)}$$

where t_h denotes the heating time and $\beta = \tau^{-1}$ and the heating starts at $t =$ relaxation time is defined as $\tau = C/\kappa$ where C is the heat-capacity and κ is the t conductance of the heat leak. Figure 4 shows T vs t measurement cycle of the hea method, when τ is comparable to t_h. The pre- and post-heating drift curv measured during a time t_m. The post-heating drift curve is registered after a t delay time t_d following the heating interval t_h in order to allow for internal temp equilibrium of the sample and the sample holder assembly. The post-heating te ture drift curve is fitted to eq. (2). At low temperatures ($T < 20$ K), a linear ver eq. (2) is used (retaining only the first order terms) and at high temperatures, non-linear expression is used. The fitted expression is then extrapolated to the mi the heating period, $t = t_h/2$ to obtain $U(t_h/2)$. The heat-capacity itself is cal

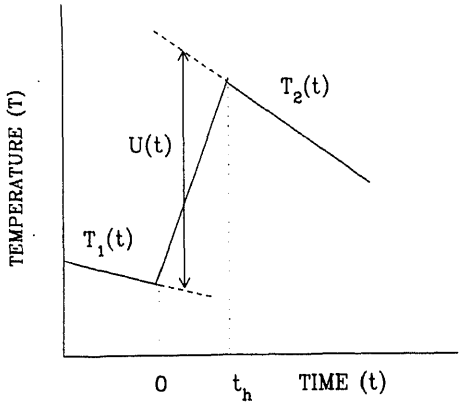

Figure 4. A schematic plot of temperature (T) vs time (t) in the pre- and post-heating interval of the heat-capacity measurements.

iteratively from the expression,

$$U(t_h/2) = \frac{2P}{C\beta} \sin h\left(\frac{1}{2}\beta t_h\right) = \frac{Pt_h}{C}\left[1 + \frac{1}{24}(\beta t_h)^2\right]. \tag{3}$$

The third term is used for the evaluation of C at low temperatures. A mixed language [6] (BASIC-FORTRAN-BASIC) has been used for controlling the instruments (via IEEE-488 interface) and real time evaluation of heat-capacity data.

4. Results

The pc card is used in a standard adiabatic calorimeter to measure the heat-capacity of single crystal copper. The temperature dependence of the heat-capacity (C_p) is shown in figure 5. The heat-capacity from 1·5 K to 10 K is fitted with the expression,

$$C_p = \gamma T + \beta T^3. \tag{4}$$

The inset shows the C_p/T vs T^2 plot at low temperatures. Our values (C_p and γ) agree with the literature values [7]. We have also studied the heat capacity of a superconductor $Y_5Os_4Ge_{10}$ and the data are shown in figure 6. The inset shows the superconducting transition at 8·9 K [8,9] in this compound. The heat-capacity of this sample is given by,

$$C_p = \gamma T + \beta T^3 + \delta T^5 \tag{5}$$

where the first term is due to electronic contribution, the second and third terms are lattice and anharmonic contribution to the heat capacity from 10 K to 30 K. The values of γ, β and δ for this sample and for single crystal copper are given in table 1.

This card can also be used in the measurement of thermo-power of metals and alloys. The onboard DAC and timer can be used for giving heater pulse to the auxiliary heater in standard thermo-power setup and the voltmeters can be triggered at the end of this

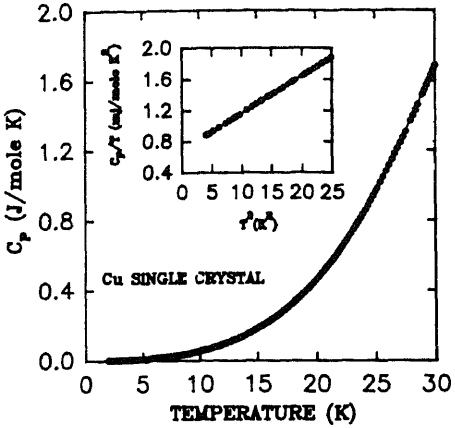

Figure 5. Temperature dependence of the heat-capacity of single crystal copper from 1·5 K to 30 K. The inset shows C_p/T vs T^2 at low temperatures. The solid line is a fit to the eq. (4) (see text).

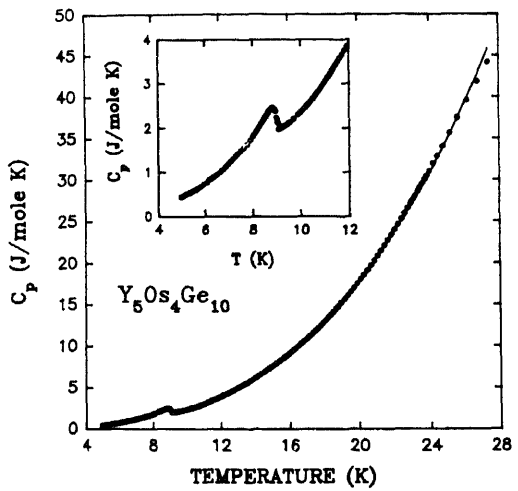

Figure 6. Temperature dependence of the heat-capacity of $Y_5Os_4Ge_{10}$ from 4·5 K to 25 K. The inset shows C_p vs T at low temperatures. The solid line is a fit to the eq (5) (see text).

heat pulse. The time dependence of the voltage (dV/dt) and the time dependence of temperature (dT/dt) can be computed and the ratio (dV/dT) yields the thermo-power. In the case of thermal-conductivity measurements, one gives known value of the heat pulse (selectable using software) to the auxiliary heater using this card and by noting th

Table 1. Heat-capacity data of single crystal copper and poly-crystalline $Y_5Os_4Ge_{10}$.

Sample	Range	γ	β	δ
	K	mJ/mole K^2	mJ/mole K^4	mJ/mole K^6
Copper	1·5–10	0·7	0·0476	—
$Y_5Os_4Ge_{10}$	10–30	24·4	2·1	0·00013

temperature difference across the sample. Then one can calculate the thermal-conductivity of the specimen.

5. Conclusion

We have described a simple substitute for a programmable/timer current source using PC based card in conjunction with an analog dc current source. The card eliminates the use of two such programmable current sources in the heat-capacity experiments. The simple design with accurate timer and very low cost ($<$ 200 US Dollars) are the main features of this interface card. Further, this card can also be used in other measurements like thermo-power which require both timer and programmable current sources.

Acknowledgements

We would like to thank Dr A K Nigam for the loan of single crystal copper and Mr Kristian Jonason for his help in taking the heat-capacity data at low temperatures. Finally, we would like to thank Mr S G Pawar for wiring some of the circuits used in this card.

References

[1] E S R Gopal, Specific heats at low temperatures (Plenum, New York, 1966)
[2] G R Stewart, *Rev. Sci. Instrum.* **54**, 1 (1982)
[3] IC11 and IC1 are 8255 and 8254 from Intel Corporation, Santa Clara, California 95051, USA
[4] Analog Devices, Norwood, Massachusetts 02062-9106, USA
[5] National Semiconductors, Santa Clara, California 95051, USA
[6] Mixed language program written using Microsoft Quick Basic version 4·1 and Microsoft Fortran version 5·0 and the software written in Quick Basic 4·1 to run the pc based card are available upon request from the authors.
[7] E Gmelin and P Roedhammer, *J. Phys.* **F14**, 223 (1981)
[8] K Ghosh, S Ramakrishnan and Girish Chandra, *Phys. Rev.* **B48**, 10440 (1993)
[9] K Ghosh, S Ramakrishnan, Arvind D Chinchure, Kristian Jonason, V R Marathe, S Shah and Girish Chandra, *Phys. Rev.* **B51**, 11656 (1995)

Pramana journal of physics Vol. 45 (No. 1), July 1995

Contents

Diffusing wave spectroscopy of dense colloids: Liquid, crystal and glassy states.....*Subrata Sanyal and Ajay K Sood* 1

A comparative dielectric relaxation study between hydrogen- and non-hydrogen-bonded liquids: Nitriles vs alcohols.....*S N Helambe, M P Lokhande, A C Kumbharkhane and S C Mehrotra* 19

Phonon dispersion in quasiperiodic semiconductor superlattices..... ..... *Sujata Rath, P K Jha and S P Sanyal* 25

Effect of crystal field on the spin density at the copper nucleus in copper complexes.....*V Gomathy, U S Ghosh and C Basu* 33

Triple differential cross sections for ionization of hydrogen atoms by positrons in a Schwinger variational calculation..... .....*J N Das, A Dey and K Chakrabarti* 41

Bound state population and dissociation dynamics of a Morse oscillator with oscillating well-depth and driven by intense radiation: Perturbative and numerical studies.....*Pranab Sarkar and S P Bhattacharyya* 47

Electronegativity and hardness profiles of a chemical process: Comparison between quantum fluid density functional theory and *ab initio* SCF method .....*S Nath and P K Chattaraj* 65

The inversion potential for NH_3 and its isotopic species..... .....*A N Aquino, A Palma, J L López and M A Rosales* 75

A low cost PC based card for heat-capacity measurements at low temperatures .....*R S Sannabhadti, S Ramakrishnan, K Ghosh, Arun Patade and Girish Chandra* 81

Indexed in CURRENT CONTENTS ISSN 0304-4289

Edited and published by V K Gaur for the Indian Academy of Sciences, Bangalore 560080. Typeset at Thomson Press (I) Ltd., New Delhi 110001 and printed at Macmillan India Press, Madras 600041.

PRAMANA

journal of physics

Vol. 45 No. 2
August 1995

NDIAN ACADEMY OF SCIENCES
ndian National Science Academy
ndian Physics Association

journal of physics

Editor

R Nityananda
Raman Research Institute, Bangalore

Associate Editor

H R Krishnamurthy
Indian Institute of Science, Bangalore

Editorial Board

G S Agarwal, *University of Hyderabad, Hyderabad*
V Balakrishnan, *Indian Institute of Technology, Madras*
M Barma, *Tata Institute of Fundamental Research, Bombay*
P Chaddah, *Centre for Advanced Technology, Indore*
B M Deb, *Panjab University, Chandigarh*
P K Kaw, *Institute for Plasma Research, Gandhinagar*
H S Mani, *Indian Institute of Technology, Kanpur*
N Mukunda, *Indian Institute of Science, Bangalore*
T Padmanabhan, *Inter-University Centre for Astronomy and Astrophysics, Pune*
J C Parikh, *Physical Research Laboratory, Ahmedabad*
G Rajasekaran, *Institute of Mathematical Sciences, Madras*
V S Ramamurthy, *Institute of Physics, Bhubaneswar*
R Ramaswamy, *Jawaharlal Nehru University, New Delhi*
K R Rao, *Bhabha Atomic Research Centre, Bombay*
Probir Roy, *Tata Institute of Fundamental Research, Bombay*
A K Sood, *Indian Institute of Science, Bangalore*

Editor of Publications of the Academy

V K Gaur
C-MMACS, NAL, Bangalore

Subscription Rates
(Effective from 1989)

	1 year	3 years	5 years
All countries except India (Price includes AIR MAIL charges)	US$ 175	$ 470	$ 700
India	1 year Rs. 100	10 years (1989–1998 only) Rs. 500	

All correspondence regarding subscription should be addressed to the **Circulation Department** of the Academy

---

Editorial Office

Indian Academy of Sciences, C V Raman Avenue,
P.B. No. 8005, Bangalore 560 080, India

Telephone: 334 2546
Telex: 845-2178 ACAD IN
Telefax: 91-80-334 6094

© 1995 by the Indian Academy of Sciences. All rights reserved.

"Information for contributors" is printed in the last issue of every volume

PRAMANA
— journal of
physics

© Printed in India

Vol. 45, No. 2,
August 1995
pp. 91–139

Generalized Fock spaces, new forms of quantum statistics and their algebras

A K MISHRA and G RAJASEKARAN
Institute of Mathematical Sciences, Taramani, Madras 600 113, India

MS received 4 March 1995

Abstract. We formulate a theory of generalized Fock spaces which underlies the different forms of quantum statistics such as 'infinite', Bose–Einstein and Fermi–Dirac statistics. Single-indexed systems as well as multi-indexed systems that cannot be mapped into single-indexed systems are studied. Our theory is based on a three-tiered structure consisting of Fock space, statistics and algebra. This general formalism not only unifies the various forms of statistics and algebras, but also allows us to construct many new forms of quantum statistics as well as many algebras of creation and destruction operators. Some of these are: new algebras for infinite statistics, q-statistics and its many avatars, a consistent algebra for fractional statistics, null statistics or statistics of frozen order, 'doubly-infinite' statistics, many representations of orthostatistics, Hubbard statistics and its variations.

Keywords. Fock spaces; quantum statistics; q-deformations; quantum groups; Hubbard model; orthostatistics.

PACS Nos 03·70; 05·30; 02·20; 71·27

1. Introduction

Recently, much effort has been devoted to q-deformations of oscillators. Both single oscillators [1–12] as well as systems of oscillators [13–33] have been studied. However, inspite of the larger literature which now exists, a unified picture of multioscillator systems covering the various q-deformations and algebras that have been proposed, has not emerged.

The aim of the present work is to construct a general formalism which may help one to develop such a unified picture. We construct a theory of generalized Fock spaces which has sufficient flexibility to encompass all types of oscillator algebras that have been proposed in the past as well as those that may be proposed in the future. Using this formalism, we are able to classify and clarify the interconnections that exist between different q-deformations and different algebras.

In another paper [34] we have pointed out that as far as a single-oscillator is concerned, q-deformation does not lead to anything fundamentally new, and is merely equivalent to a change of variable. A q-deformed oscillator is just a different representation of the usual oscillator. On the other hand, when we go to multioscillator systems, new things are possible; these are the new forms of statistics. However, even here, we find that many of the q-deformations for multioscillator systems proposed in the literature again belong to the category of substitution or change of variables and should be regarded only as different representations of the well-known Bose–Einstein or Fermi–Dirac statistics. Particular mention must be made of the work of Greenberg [13, 14] in this

nothing but Bose or Fermi statistics in disguise, Greenberg's proposal involves a new statistics, called infinite statistics and this statistics is infact based on a new Fock space which is much larger than the usual bosonic or fermionic Fock spaces.

In order to construct a unified theory, we find it convenient to start with the underlying space of the allowed states of the system. We construct the creation and destruction operators $c^\dagger$ and c as outer products of the state vectors. It is this device of starting with the set of state vectors of the system as the primary concept, that cuts through the jungle of different algebras which, *prima facie* look different, but on closer examination are found to be related. Two sets of creation and destruction operators which are related by substitution, operate on the same space of state vectors and hence describe essentially the same class of systems.

We first formulate the theory of the generalized Fock spaces. The key element is the notion of independence of the permutation-ordered states. The largest linear vector space constructed in this way is the super Fock space. The subsequent specification of a subset of states in this space as null states leads to many reduced Fock spaces. The general theory which applies to the super Fock space as well as to the reduced Fock spaces, all of which are to be called collectively as generalized Fock spaces, then allows us to construct annihilation, creation and number operators. Whereas the annihilation and creation operators and their algebras even for a particular Fock space are not unique and many representations are possible, a universal representation for the number operators valid for all forms of statistics and algebras exists.

We apply the formalism to the super Fock space as well as to the bosonic and fermionic Fock spaces, the latter being the most familiar examples of reduced Fock spaces. Super Fock space is characterized by a unique statistics named 'infinite statistics'. However, the same infinite statistics can be represented by different algebras of c and $c^\dagger$ and we give a number of representations of infinite statistics. In the bosonic and fermionic Fock spaces, many different forms of statistics can be defined and for each form of statistics many different representations of c and $c^\dagger$ are possible.

Although the main aim of the general framework presented here is to develop a unified picture of the various forms of statistics and algebras, the same formalism also allows us to construct a large number of new forms of quantum statistics as well as new algebras of c and $c^\dagger$. In fact there is no limit to the number of possibilities.

An important part of our work deals with two-indexed systems. Our general formalism for the single-indexed system applies to most multi-indexed systems also since in most cases a multiplet of indices can be mapped into a single index. But, we show that there exist certain situations where such a mapping is not possible. Consequently, we develop the general formalism for the two indexed system and discover an enormously rich variety of novel forms of quantum statistics and algebras.

The plan of the paper is as follows. The theory of the generalized Fock spaces is given in § 2. In § 3 we apply the general theory to the super Fock space and in § 4 we apply it to the reduced bosonic and fermionic Fock spaces. Section 4 also contains a new statistics called null statistics. The alternative approach of starting with $cc^\dagger$ algebras and deriving cc relations therefrom is presented in § 5. Two-indexed systems are treated in § 6 and Appendix. Section 7 is devoted to summary and discussion.

A quick overview of the paper may be obtained from the pictorial summaries given in figures 3 and 4 and the tabular information provided in tables 1–4.

Given a set of oscillators with indices $g, h, l \cdots m$, we construct the state vector

$$|n_g, n_h \cdots n_m; 1\rangle = |\underbrace{1_g \cdots 1_g}_{n_g} \underbrace{1_h \cdots 1_h}_{n_h} \cdots \underbrace{1_m \cdots 1_m}_{n_m}\rangle \tag{2.1}$$

On the r.h.s. of this equation, $1_g, 1_h \cdots 1_m$ appear $n_g, n_h \cdots n_m$ times respectively and $n_g \cdots n_m$ denote the number of quanta with indices $g \cdots m$ respectively. Together with the state (2.1) we consider the set of all states obtained through all distinct permutations of the entries on the r.h.s. of (2.1). Thus, we have

$$|n_g, n_h \cdots n_m; 2\rangle = |\underbrace{1_g \cdots 1_g}_{n_g - 1} 1_h 1_g \underbrace{1_h \cdots 1_h}_{n_h - 1} \cdots \underbrace{1_m \cdots 1_m}_{n_m}\rangle \tag{2.2}$$

$$\vdots$$

$$|n_g, n_h \cdots n_m; 35\rangle = |1_g 1_g 1_m 1_m \underbrace{1_h \cdots 1_h}_{n_h} \cdots \underbrace{1_m \cdots 1_m}_{n_m - 2}\rangle \tag{2.3}$$

$$\vdots$$

$$|n_g, n_h \cdots n_m; s\rangle = |\underbrace{1_m \cdots 1_m}_{n_m} \cdots \underbrace{1_h \cdots 1_h}_{n_h} \underbrace{1_g \cdots 1_g}_{n_g}\rangle \tag{2.4}$$

Here we have given examples of a few permutations. In (2.2), the positions of one g-quantum and one h-quantum has been interchanged and in (2.3), we have indicated a few more interchanges. Collectively, we shall denote the set of all these states as

$$|n_g, n_h \cdots n_m; \mu\rangle, \quad \mu = 1, 2, \ldots s \tag{2.5}$$

where s is the total number of distinct permutations and μ labels each of these states. It is easy to see that

$$s = \frac{(n_g + n_h + \cdots + n_m)!}{n_g! n_h! \cdots n_m!} \tag{2.6}$$

(In (2.3), μ has been put 35 rather arbitrarily). We assume the existence of a unique vacuum state corresponding to zero occupation number for all the oscillators:

$$|0\rangle \equiv |0, 0, 0 \ldots 0\rangle \tag{2.7}$$

We shall first consider the set of all the s states given in (2.5) as linearly independent. Although they are linearly independent, they may not be orthogonal to each other in general, nor are they normalized. However, a state in one sector characterized by the occupation numbers $(n_g, n_h \ldots n_m)$ is orthogonal to any state in another sector characterized by another set of occupation numbers $(n'_g, n'_h \ldots n'_m)$. We can summarize these statements by the equation:

$$\langle n'_g, n'_h \ldots n'_m; \alpha | n_g, n_h \ldots n_m; \beta\rangle = \delta_{n'_g n_g} \delta_{n'_h n_h} \ldots \delta_{n'_m n_m} M_{\alpha\beta} \tag{2.8}$$

Note in particular that the inner product vanishes even if a single occupation number does not match. Within the same sector, the inner product is given by

$$\langle n_g \ldots n_m; \alpha | n_g \ldots n_m; \beta\rangle = M_{\alpha\beta} \tag{2.8a}$$

dimensions, one corresponding to each sector $\{n_g \ldots n_m\}$. We choose all these matric to be positive definite. This set of inner-product matrices M plays an important role the general formalism.

From the set of linearly independent vectors given in (2.5), it is possible to constru an orthonormal set of vectors which we shall denote by a double-barred ket:

$$\|n_g \ldots n_m; \mu\rangle\rangle; \quad \mu = 1 \ldots s. \tag{2.}$$

These satisfy the orthonormality relation

$$\langle\langle n'_g \ldots n'_m; \alpha \| n_g \ldots n_m; \beta \rangle\rangle = \delta_{n'_g n_g} \ldots \delta_{n'_m n_m} \delta_{\alpha\beta}. \tag{2.1}$$

There is no unique way of doing this and the resulting orthonormal set is not uniqu One may use Gram–Schmidt orthogonalization procedure or calculate the eigenstat of the inner-product matrix M or follow any other method. Whatever may be t method, one can write the relation connecting the two sets of kets:

$$\|n_g \ldots n_m; \mu\rangle\rangle = \sum_{\nu} X_{\nu\mu} |n_g \ldots n_m; \nu\rangle \tag{2.1}$$

and the inverse relation:

$$|n_g \ldots n_m; \alpha\rangle = \sum_{\beta} (X^{-1})_{\beta\alpha} \|n_g \ldots n_m; \beta\rangle\rangle \tag{2.1}$$

where X is a non-singular matrix. Although X is not unique (since it depends on t particular orthogonalization procedure used), it is possible to show, usir (2.8), (2.1 (2.11) and (2.12), that $XX^\dagger$ is the inverse of the innerproduct matrix [34a].

$$M^{-1} = XX^\dagger \tag{2.1}$$

Thus, one simple way of ensuring positivity of the inner-product matrix is to choo a non-singular matrix X and then determine M using (2.13). Again it must be kept mind that we are dealing with an infinite set of matrices, X, one for each sect $\{n_g \ldots n_m\}$. Also the orthonormality relation holds between vectors from two differe sectors and we have already used this in writing (2.10).

The completeness relation for the orthonormal set of states $\|n_g \ldots n_m; \mu\rangle\rangle$ can written in the form:

$$I = \sum_{n_g \ldots n_m} \sum_{\mu} \|n_g \ldots n_m; \mu\rangle\rangle \langle\langle n_g \ldots n_m; \mu\| \tag{2.1}$$

where I is the identity operator. Substituting from (2.11) into (2.14) and using (2.13), v get the resolution of the identity operator in terms of the non-orthonormal set of state

$$I = \sum_{n_g \ldots n_m} \sum_{\lambda,\nu} |n_g \ldots n_m; \nu\rangle (M^{-1})_{\nu\lambda} \langle n_g \ldots n_m; \lambda| \tag{2.14}$$

It is convenient to define the projection operator

$$P(n_g \ldots n_m) = \sum_{\mu} \|n_g \ldots n_m; \mu\rangle\rangle \langle\langle n_g \ldots n_m; \mu\| \tag{2.1}$$

$$= \sum_{\lambda,\nu} |n_g \ldots n_m; \nu\rangle (M^{-1})_{\nu\lambda} \langle n_g \ldots n_m; \lambda| \tag{2.1}$$

so that we have

$$I = \sum_{n_g \ldots n_m} P(n_g \ldots n_m) \tag{2.17}$$

One can easily verify the following properties of the projection operators:

$$P(n_g \ldots n_m) \| n'_g \ldots n'_m; \mu \gg = \delta_{n_g n'_g} \ldots \delta_{n_m n'_m} \| n_g \ldots n_m; \mu \gg \tag{2.18}$$

$$P(n_g \ldots n_m) | n'_g \ldots n'_m; \mu \rangle = \delta_{n_g n'_g} \ldots \delta_{n_m n'_m} | n_g \ldots n_m; \mu \rangle \tag{2.19}$$

It is worth noting that $P(n_g \ldots n_m)$ projects out any single state not only from the orthonormal set $\| n_g \ldots n_m; \mu \gg$ but also from the non-orthonormal set $| n_g \ldots n_m; \mu \rangle$.

In terms of the above projection operators it is very easy to construct the number operators:

$$N_k = \sum_{n_g \ldots n_k \ldots n_m} n_k P(n_g \ldots n_k \ldots n_m) \tag{2.20}$$

which satisfy the following properties

$$N_k \| n_g \ldots n_k \ldots n_m; \mu \gg = n_k \| n_g \ldots n_k \ldots n_m; \mu \gg \tag{2.21}$$

$$N_k | n_g \ldots n_k \ldots n_m; \mu \rangle = n_k | n_g \ldots n_k \ldots n_m; \mu \rangle \tag{2.22}$$

$$[N_k, N_j] = 0 \quad \text{for any } k \text{ and } j \tag{2.23}$$

We now introduce the transition operators which connect states, lying in different sectors. Obviously it is enough to define the so-called annihilation and creation operators c_j and $c_j^\dagger$. We define

$$c_j^\dagger = \sum_{n_g \ldots n_j \ldots n_m} \sum_{\mu' \nu} A_{\mu' \nu} | n_g \ldots (n_j + 1) \ldots n_m; \mu' \rangle \langle n_g \ldots n_j \ldots n_m; \nu | \tag{2.24}$$

and c_j as the hermitian conjugate of $c_j^\dagger$, where $A_{\mu' \nu}$ are a set of arbitrary (complex) numbers. Note that the span of μ' is larger than that of ν and this is the reason for the prime on μ. Specifically,

$$\mu' = 1 \ldots s'; \quad s' = \frac{(n_g + \ldots (n_j + 1) + \ldots n_m)!}{n_g! \ldots (n_j + 1)! \ldots n_m!} \tag{2.25a}$$

$$\nu = 1 \ldots s; \quad s = \frac{(n_g + \ldots n_j + \ldots n_m)!}{n_g! \ldots n_j! \ldots n_m!} \tag{2.25b}$$

Hence A is a rectangular matrix. Since A is arbitrary in general, the relation (2.24) provides the most general definition of the creation operator. Even in this general case, it is possible to verify the following commutation relation between the number operator defined in (2.20) and the creation operator defined in (2.24)

$$[c_j^\dagger, N_k] = - c_j^\dagger \delta_{jk} \tag{2.26}$$

The projection property given in (2.19) plays a crucial role in the proof of (2.26).

So far we did not specify how the ordered state vectors $| n_g \ldots n_m; \mu \rangle$ are constructed. In fact, in general there is no need to specify any procedure for their explicit construction. The formalism given so far holds whatever may be the explicit form of their construction. However, once annihilation and creation operators c and $c^\dagger$ are

$c^\dagger$ and the vacuum state $|0\rangle$. This procedure has the advantage that the arbitrarines the matrix A introduced in (2.24) disappears and A in fact gets determined in terms M. Hence let us do it.

In terms of creation operators, the ordered state (2.2) for instance is constructed follows:

$$|\underbrace{1_g \ldots 1_g}_{n_g-1} 1_h 1_g \underbrace{1_h \ldots 1_h}_{n_h-1} \ldots \underbrace{1_m \ldots 1_m}_{n_m}\rangle = (c_g^\dagger)^{n_g-1} c_h^\dagger c_g^\dagger (c_h^\dagger)^{n_h-1} \ldots (c_m^\dagger)^{n_m}|0\rangle \quad (2.$$

and other states are constructed in a similar fashion. We may introduce the notati

$$|n_g \ldots n_m; \mu\rangle = (c_g^{\dagger n_g} \ldots c_m^{\dagger n_m}; \mu)|0\rangle \quad (2.$$

$$\langle n_g \ldots n_m; \mu| = \langle 0|(c_m^{n_m} \ldots c_g^{n_g}; \mu) \quad (2.$$

where $(c_g^{\dagger n_g} \ldots c_m^{\dagger n_m}; \mu)$ is a permutation of the creation operators similar to the permu tions defined in (2.1)–(2.5) and $(c_m^{n_m} \ldots c_g^{n_g}; \mu)$ is defined as the hermitian conjugate $(c_g^{\dagger n_g} \ldots c_m^{\dagger n_m}, \mu)$. For states constructed in this manner, there exists a simple formu connecting states in 'adjacent' sectors. For instance,

$$|1_j, \underbrace{1_g \ldots 1_g}_{n_g} \ldots \underbrace{1_m \ldots 1_m}_{n_m}\rangle = c_j^\dagger |\underbrace{1_g \ldots 1_g}_{n_g} \ldots \underbrace{1_m \ldots 1_m}_{n_m}\rangle \quad (2.3$$

More generally, we may write

$$c_j^\dagger |n_g \ldots n_j \ldots; \lambda\rangle = |1_j, n_g \ldots n_j \ldots; \lambda\rangle \quad (2.3$$

where $|1_j, n_g \ldots n_j \ldots; \lambda\rangle$ on the right is a subset of states in which one j quantum appea on the extreme left. Although the total number of states in the set $|n_g \ldots (n_j+1) \ldots; \lambda'\rangle$ s' given by (2.25a), the total number of states in the subset $|1_j, n_g \ldots n_j \ldots; \lambda\rangle$ is s given b (2.25b). Further the states in the subset $|1_j, n_g \ldots n_j \ldots; \lambda)$ are given the same ordin number λ as in the set $|n_g \ldots n_j \ldots; \lambda\rangle$. This is possible since the quanta $\{n_g \ldots n_j \ldots\}$ a permuted among themselves without disturbing the extra j-quantum sitting on t extreme left.

We now substitute the expression for $c_j^\dagger$ given by (2.24) into the l.h.s. of (2.31). We hav

$$\begin{aligned} & c_j^\dagger |n_g \ldots n_j \ldots; \lambda\rangle \\ & = \sum_{n_g' \ldots n_j' \ldots} \sum_{\mu' \nu} A_{\mu' \nu} |n_g' \ldots (n_j'+1) \ldots; \mu'\rangle \langle n_g' \ldots n_j' \ldots; \nu | n_g \ldots n_j \ldots; \lambda\rangle \\ & = \sum_{\mu' \nu} A_{\mu' \nu} M_{\nu \lambda} |n_g \ldots (n_j+1) \ldots; \mu'\rangle \end{aligned} \quad (2.3$$

where we have used (2.8). On comparing with (2.31), we get

$$\sum_\nu A_{\mu' \nu} M_{\nu \lambda} = \delta_{\mu' \lambda} \quad (2.33$$

From (2.33) we see that $\mu' = \lambda$. This means that in (2.24), only the subse $|1_j, n_g \ldots n_j \ldots; \lambda\rangle$ contributes and hence A is in fact a square matrix and is equal to th

inverse of M^{-1}:

$$A = M^{-1} \tag{2.34}$$

So, we may rewrite (2.24):

$$c_j^\dagger = \sum_{n_g \ldots n_j \ldots} \sum_{\lambda,\nu} (M^{-1})_{\lambda\nu} |1_j, n_g \ldots n_j \ldots; \lambda\rangle\langle n_g \ldots n_j \ldots; \nu|. \tag{2.35}$$

Thus, A and hence c and $c^\dagger$ are completely determined in terms of the set of M matrices.

Next, consider the expression for the number operator (eqs. (2.20), (2.15) and (2.16)):

$$N_k = \sum_{n_g \ldots n_k \ldots n_m} n_k \sum_{\mu} \|n_g \ldots n_k \ldots n_m; \mu\rangle\rangle\langle\langle n_g \ldots n_k \ldots n_m; \mu\| \tag{2.36}$$

$$= \sum_{n_g \ldots n_k \ldots n_m} n_k \sum_{\lambda\nu} |n_g \ldots n_k \ldots n_m; \lambda\rangle (M^{-1})_{\lambda\nu} \langle n_g \ldots n_k \ldots n_m; \nu| \tag{2.37}$$

One may try to express this in terms of c and $c^\dagger$. Using (2.28) and (2.29),

$$N_k = \sum_{n_g \ldots n_k \ldots n_m} n_k \sum_{\lambda\nu} (c_g^{\dagger n_g} \ldots c_k^{\dagger n_k} \ldots c_m^{\dagger n_m}; \lambda)|0\rangle$$

$$\langle 0|(c_m^{n_m} \ldots c_k^{n_k} \ldots c_g^{n_g}; \nu)(M^{-1})_{\lambda\nu} \tag{2.38}$$

Apart from $c^\dagger$ and c, the above expression contains the vacuum projector $|0\rangle\langle 0|$. Later we shall give examples where $|0\rangle\langle 0|$ is determined as products of $c^\dagger$ and c so that N_k can be expressed entirely in terms of $c^\dagger$ and c. However, in general, this does not lead to simple results, whereas (2.36) provides us with a universal representation of number operators which is valid in all cases.

So far, we regarded the set of state vectors $|n_g, n_h \ldots; \mu\rangle; \mu = 1 \ldots s$ (where s is given by (2.6)) to be linearly independent and the resulting generalized Fock space is the complete Fock space, which we shall call the *super Fock space.*

We shall now show how to construct reduced Fock spaces. The motivation for this is that many Fock spaces of physical interest such as the bosonic Fock space or fermionic Fock space are reduced Fock spaces. There are various ways of doing this. One may postulate relationships between states connected by permutations, or one may disallow certain permutations by equating them to null vectors. Yet another way to achieve this is to use the permutation group S_n acting on the n-particle state. The super Fock space we have constructed consists of all the representations of the permutation group. If we allow only certain representations of S_n, we get a reduced Fock space.

All these possibilities are contained in the statement that in the space of vectors $|n_g, n_h \ldots; \mu\rangle$, there are r null vectors ($r < s$)

$$\sum_{\mu} B_\mu^p |n_g, n_h \ldots; \mu\rangle = 0; \quad p = 1, 2, \ldots r; \quad r < s. \tag{2.39}$$

where B_μ^p are constants. So, the dimension of the vector space in the sector $\{n_g, n_h \ldots\}$ is reduced to d given by

$$d = s - r. \tag{2.40}$$

An important class of reduced Fock spaces

states connected by permutation of indices will be taken to be related to each other through equations of the type (2.39). In other words, the number of relations r in (2.39) is $s-1$. We shall call this space as the *bosonic Fock space*. If we impose the additional restriction: $n_a = 0$ or 1 only, the resulting space will be called *fermionic Fock space*. This restriction can also be stated in the form of (2.39):

$$|n_g, n_h \ldots; \mu\rangle = 0 \quad \text{for} \quad n_g, n_h \ldots \geqslant 2. \tag{2.41}$$

We can define a new reduced Fock space, also of dimension $d = 1$ in each sector, by taking the set of all the permuted states as null states except a single state (of a chosen order) which is taken to be the allowed state. We shall call this as the Fock space of frozen order.

Another important class of reduced Fock spaces are those associated with para-statistics [35–37], which we shall call parabosonic and parafermionic Fock spaces. For these, the number of relations r is smaller than for bosonic or fermionic Fock spaces, so that the dimension d satisfies

$$1 < d < s. \tag{2.42}$$

The formalism constructed in the present section is valid for all these reduced Fock spaces also. with the modification that all the summations over μ, ν etc. will now go over the range $1 \ldots d$ and correspondingly; X, M and A become $d \times d$ matrices. There is an arbitrariness in the choice of the d states. Any choice of d states will do, as long as they are non-null states.

All these Fock spaces, the super Fock space as well as the reduced ones will be collectively called generalized Fock spaces. To sum up this discussion we may note that a generalized Fock space is completely defined by stating what are the allowed states of the system.

We shall define statistics by the precise relationship linking states obtained by permutation. In general, many relationships can be envisaged and hence many different forms of statistics can reside within a particular reduced Fock space. However, in super Fock space, all the states obtained by permutation are independent and so there is a unique statistics associated with this Fock space, namely 'infinite statistics'. Similarly, in the Fock space of frozen order too, there exists only a single statistics, named 'null statistics'.

In this section we started with the generalized Fock space consisting of the set of allowed states of the system and constructed the creation, annihilation and number operators in terms of the outer products of state vectors. Do these c and $c^\dagger$ form an operator algebra? In general, c and $c^\dagger$ constructed in this way may not form a simple algebra, or even a closed algebra. Historically, it is the reverse route that has been followed; one postulates an algebra of c and $c^\dagger$ and then deduces the states allowed by the algebra. In this sense, a given relation involving c and $c^\dagger$ implicitly defines an inner product and through it specifies the allowed and the null states of the system. In practice, starting with an algebra is an easier procedure and we shall use it in the latter sections. Actually, it is complementary to the approach described in this section.

Therefore we have two equivalent ways of dealing with the generalized Fock spaces. In the first approach, which we have formulated in this section we construct c and $c^\dagger$ in terms of the allowed states of the system and the algebra of c and $c^\dagger$ is then a derived

consequence. This is the more fundamental approach and is of universal validity. In the second approach, which we have used in the latter sections, we start with an algebra of c and $c^\dagger$ and then determine the states of the system allowed by the $cc^\dagger$ algebra. Since the res···trictions on the allowed states of the system can generally be stated in the form of cc relations, the first approach can be characterized as $cc \rightarrow cc^\dagger$ while the second is $cc^\dagger \rightarrow cc$. Within the second approach, an elegant method to derive cc relations from $cc^\dagger$ algebras will be described.

For infinite statistics, there is no restriction on the allowed states and cc relations do not exist. Hence, for this statistics, the first approach should be interpreted as 'no cc relation' $\rightarrow cc^\dagger$ algebra while in the second approach, starting with any particular $cc^\dagger$ algebra describing infinite statistics one shows that there does not exist any cc relation. In those cases where the $cc^\dagger$ algebra depends on a continuous parameter q, one can determine the values of q where cc relation exists. Generally, these values of q correspond to the boundary of the region in the parameter space where infinite statistics with positive definite M exists. On this boundary, one or more eigenvalues of the M matrices become zero, thus leading to the emergence of the same number of null vectors in the Fock space which can equivalently be interpreted as the emergence of cc relations. Thus the formalism unifies infinite statistics residing on the super Fock space with the various forms of statistics residing on reduced Fock spaces.

It must be noted that the inner product matrices M occurring in (2.35) are quite arbitrary. Consequently, more than one realization or representation of creation and destruction operators is possible. In fact, it is this freedom to select arbitrary M which enables one to construct different algebras involving c and $c^\dagger$, all operating over the same Fock space.

To sum up, we construct a three-tiered structure consisting of Fock space, statistics and algebra. Fock space is specified by the set of the allowed states of the system. Statistics is defined by the nature of the symmetry of the allowed states under permutation. Algebra of the creation and destruction operators is determined by the choice of the inner product matrices M.

Different representations of infinite statistics are constructed in § 3. In the bosonic and fermionic Fock spaces, many forms of quantum statistics which include Bose and Fermi statistics are possible. These and the null statistics in the Fock space of frozen order are taken up in § 4.

3. Super Fock space and infinite statistics

3.1 *The standard representation* ($M = 1$)

Having taken all the s states to be independent, the simplest choice of the matrix X is the unit matrix which implies M and A also to be unit matrices (of appropriate dimensions) for all the sectors $\{n_g, n_h \ldots\}$:

$$X = M = A = 1. \tag{3.1}$$

For this choice, which we shall call the standard representation of infinite statistics, the ordered states (2.5) themselves form an orthonormal set:

$$\langle n_g, n_h \ldots; \mu | n_g, n_h \ldots; \nu \rangle = \delta_{\mu\nu}. \tag{3.2}$$

Further, the creation and annihilation operators are given by

$$c_j^\dagger = \sum_{n_g, n_h \ldots} \sum_{\mu} |1_j, n_g, n_h \ldots; \mu\rangle \langle n_g, n_h \ldots; \mu| \tag{3.3}$$

$$c_j = \sum_{n_g, n_h \ldots} \sum_{\mu} |n_g, n_h \ldots; \mu\rangle \langle 1_j, n_g, n_h \ldots; \mu| \tag{3.4}$$

From (3.3) and (3.4), using the orthogonality and completeness relations, one can derive the $cc^\dagger$ algebra:

$$c_i c_j^\dagger = \delta_{ij} \tag{3.5}$$

This algebra was first proposed by Greenberg [13], in an important paper on infinite statistics.

In the standard representation, we also have the useful identity:

$$\sum_i c_i^\dagger c_i = 1 - |0\rangle\langle 0| \tag{3.6}$$

Although this identity can be obtained from (3.3) and (3.4) that define $c^\dagger$ and c, it is important to note that within Fock space it follows from the $cc^\dagger$ algebra (3.5). We shall prove it by showing that (3.6) is valid, when applied on any state in the super Fock space. First applying on $|0\rangle$, we find that both sides are zero. Next we apply on the other states $c_k^\dagger c_l^\dagger \ldots |0\rangle$:

$$\left\{ \sum_i c_i^\dagger c_i - 1 + |0\rangle\langle 0| \right\} c_j^\dagger c_k^\dagger \ldots |0\rangle = 0 \tag{3.7}$$

Using (3.5) and noting $\langle 0| c_j^\dagger = 0$ we see that the left side of (3.7) infact vanishes, thus completing the proof of (3.6).

In a different context, Cuntz [38] had studied the algebra defined by (3.5) and by the relation:

$$\sum_i c_i^\dagger c_i = 1. \tag{3.8}$$

Cuntz algebra is inconsistent with Fock space, as can be seen by applying both sides of (3.8) on $|0\rangle$. In contrast, our (3.6), because of the inclusion of the vacuum projector term in it, is consistent with Fock space and is infact a consequence of the algebra of c and $c^\dagger$ in the standard representation of infinite statistics.

Putting $M = 1$, the number operator N_k given in (2.38) becomes

$$N_k = \sum_{n_g \ldots n_k \ldots n_m} n_k \sum_{\mu} (c_g^{\dagger n_g} \ldots c_k^{\dagger n_k} \ldots c_m^{\dagger n_m}; \mu) |0\rangle\langle 0| (c_m^{n_m} \ldots c_k^{n_k} \ldots c_g^{n_g}; \mu) \tag{3.9}$$

Substitution of $|0\rangle\langle 0|$ from (3.6) into this equation and a straightforward but tedious calculation finally leads to

$$N_k = \sum_{n_g \ldots n_k \ldots n_m} \sum_{\mu} (c_g^{\dagger n_g} \ldots c_k^{\dagger n_k} \ldots c_m^{\dagger n_m}; \mu) c_k^\dagger c_k (c_m^{n_m} \ldots c_k^{n_k} \ldots c_g^{n_g}; \mu) \tag{3.9a}$$

This expression is identical to Greenberg's formula for N_k [13], though it is written in a different form. This illustrates the derivation of the representation of N_k in terms of c and $c^\dagger$. As already mentioned, in general neither the procedure nor the result is simple

nd in any case one does not need it. The universal representation of N_k given in (2.36) is ufficient.

.2 *q-mutators with real q*

Many other choices of M are possible. A particularly interesting choice is the one in which M is given as a function of a real parameter q. Consider the inner product between the -particle state vectors with all occupation numbers unity: $|1_g, 1_h \ldots; \mu\rangle$. The inner product natrix M in this sector has dimension $n! \times n!$ and its matrix element is taken to be

$$\langle 1_g, 1_h \ldots; \mu | 1_g, 1_h \ldots; \nu\rangle = q^J, \tag{3.10}$$

where q is a real number lying in the range $-1 < q < +1$ and J is the number of nversions required to transform the state $|1_g, 1_h \ldots; \nu\rangle$ into the state $|1_g, 1_h \ldots; \mu\rangle$. Number of inversions is the minimum number of successive interchanges between djacent quanta that will take the state $|1_g, 1_h \ldots; \nu\rangle$ to $|1_g, 1_h \ldots; \mu\rangle$. For example,

$$\langle 1_h 1_g 1_k | 1_g 1_h 1_k\rangle = q \tag{3.11}$$

$$\langle 1_h 1_k 1_g | 1_g 1_h 1_k\rangle = q^2. \tag{3.12}$$

The positivity of the q-dependent M matrices defined above has been proved by Fivel 15] and Zagier [16]. In particular, Zagier has given the explicit form of the determi- ant of the $(n! \times n!)$ dimensional M matrix for arbitrary n:

$$\det M = \prod_{k=1}^{n-1} [1 - q^{k(k+1)}]^{(n-k)n!/k(k+1)} \tag{3.13}$$

At $q = 0$, M is the unit matrix and so is positive-definite. Hence, it will remain positive-definite in $-1 < q < 1$, if $\det M$ has no zeroes there. According to (3.13), for eal q, zeroes of $\det M$ occur only at $q = \pm 1$, thus proving the positive-definiteness of M in the range $-1 < q < 1$.

The inner product for states with occupation numbers larger than unity (which are he same as states with repeated indices) is obtained from the above inner product for tates with distinct indices by symmetrizing with respect to the repeated indices. For xample, consider

$$\langle 2_g 1_m | 1_g 1_m 1_g\rangle = \langle 1_g 1_g 1_m | 1_g 1_m 1_g\rangle \tag{3.14}$$

eplace one of the g's by h in both the initial and final states and thus get a matrix lement with distinct indices which can be calculated using (3.10). This replacement can e done in $(2!)^2$ ways. The sum of these $(2!)^2$ matrix elements divided by 2! is the required nswer. Thus,

$$\langle 1_g 1_g 1_m | 1_g 1_m 1_g\rangle = \tfrac{1}{2}[\langle 1_g 1_h 1_m | 1_g 1_m 1_h\rangle + \langle 1_g 1_h 1_m | 1_h 1_m 1_g\rangle + \langle 1_h 1_g 1_m | 1_g 1_m 1_h\rangle + \langle 1_h 1_g 1_m | 1_h 1_m 1_g\rangle] \tag{3.15}$$

$$= q + q^2 \tag{3.16}$$

is clear that the matrix M for repeated indices is obtained from the higher

It is worth noting that the norm for n-particle state with all the indices repeated

$$\langle n_g|n_g\rangle = [n_g!]_q = [n_g]_q[n_g-1]_q\ldots[2]_q[1]_q \tag{3.}$$

where the 'q-number' $[n]_q$ is defined by

$$[n]_q \equiv \frac{1-q^n}{1-q} = 1+q+q^2+\ldots q^{n-1} \tag{3.}$$

Inverting these M matrices and defining the creation operator through (2.35), c can derive the algebra of c and $c^\dagger$. This is more difficult than the reverse proced which is the way this subject really developed. Greenberg [14] proposed the q-muta algebra:

$$c_i c_j^\dagger - q c_j^\dagger c_i = \delta_{ij} \tag{3.}$$

The q-dependent M matrices defined through (3.10), (3.15) and (3.16) follow from t algebra. Fivel and Zagier then proved the positivity of these M matrices $-1<q<+1$. In spite of the fact that we have not derived (3.19) from the M matri defined here, we can assert its validity because the M matrices completely determi c and $c^\dagger$. It is in order to emphasize this point that we have presented the M matri first and the algebra of c and $c^\dagger$ as a derived consequence.

3.3 *New representations of infinite statistics*

First we briefly consider the 2-parameter algebra

$$c_i c_j^\dagger - q_1 c_j^\dagger c_i - q_2 \delta_{ij} \sum_k c_k^\dagger c_k = \delta_{ij} \tag{3.}$$

where q_1 and q_2 are real parameters. This may be regarded as another representation infinite statistics. Although the determination of the full region in the $\{q_1, q_2\}$ pa meter space for which M is positive definite is still an unsolved problem, one can sh [19] positivity of M on the straight line defined by $q_1 = 0$; $-1 < q_2 < \infty$. Infact i possible to map this whole line on to the point $q_1 = 0; q_2 = 0$ by a redefinition of c an so that we just get back the standard representation defined by (3.5).

We next present two new algebras:

$$c_i c_j^\dagger - c_j^\dagger c_i = \delta_{ij} p^{2\Sigma_{k<i} N_k} p^{N_i} \tag{3.}$$

and

$$\left.\begin{aligned} c_i c_j^\dagger - p^{-1} c_j^\dagger c_i = 0 \quad \text{for} \quad i \neq j \\ c_i c_i^\dagger - c_i^\dagger c_i = p^{N_i} \end{aligned}\right\} \tag{3.}$$

where p is a real parameter and N_i are number operators already written down in § 2. these two algebras, the first one (3.21) is based on ordered indices, that is, given any t indices i and j, one must be considered larger or smaller than the other. So, we may ta the indices to be the natural numbers $1, 2, 3\ldots$

Equations (3.21) and (3.22) are again representations of the same infinite statisti for it is possible to map both these algebras on to Greenberg's q-mutator algebra (3.19) with the following identification of the parameters: $p = q^{-1}$. Temporar renaming the $(c, c^\dagger)$ of (3.21) and (3.22) by $(b, b^\dagger)$ and $(d, d^\dagger)$ respectively, the mapping

ansformation equations are

$$b_i = p^{\Sigma_{k<i} N_k} p^{(1/2)N_i} c_i \tag{3.23}$$

$$d_i = p^{(1/2)N_i} c_i. \tag{3.24}$$

ence, it is clear that both the algebras of (3.21) and (3.22) lead to positive definite matrices for $p > +1$ and $p < -1$ (corresponding to $-1 < q < +1$).

An interesting feature of the algebra (3.21) is the validity of ordinary commutation lation between c_i and $c_j^\dagger$ for $i \neq j$ as in Bose statistics; nevertheless the full algebra (3.21) escribes infinite statistics!

In contrast to the situation for the q-mutator algebra of (3.19), where the number perators can be expressed in terms of c and $c^\dagger$ only after considerable algebraic anouvers [16, 17] and the resulting expressions are quite complicated, the corre-onding expressions for the algebras (3.21) and (3.22) are simple. For (3.21), we get aking $p > 0$)

$$\left.\begin{aligned} N_1 &= \frac{1}{\log p} \log(c_1 c_1^\dagger - c_1^\dagger c_1) \\ &\vdots \\ N_i &= \frac{1}{\log p} \log(c_i c_i^\dagger - c_i^\dagger c_i) - 2 \sum_{k<i} N_k \end{aligned}\right\} \tag{3.25}$$

or (3.22), the number operator is even simpler:

$$N_i = \frac{1}{\log p} \log(c_i c_i^\dagger - c_i^\dagger c_i) \quad \text{for all } i. \tag{3.26}$$

spite of our ability to write down such formal expressions for N_i in terms of c's and s, we must also point out that they are not of much use. All that one ever needs of the umber operators are the properties contained in (2.21)–(2.23) and (2.26) and as for xplicit representation, (2.36) and (2.37) will do.

4 *q-mutators with complex q*

'e now generalize Greenberg's q-mutator algebra to complex q. This generalized gebra is based on ordered indices and is defined by the following equations.

$$c_i c_j^\dagger - q c_j^\dagger c_i = 0 \quad \text{for} \quad i < j \tag{3.27}$$

$$c_i c_i^\dagger - p c_i^\dagger c_i = 1 \tag{3.28}$$

here q and p are complex and real parameters respectively and the indices i, j etc. refer any of the natural numbers $1, 2, 3, \ldots$. The relation for the opposite order $i > j$ is erivable from (3.27) by hermitian conjugation:

$$c_i c_j^\dagger - q^* c_j^\dagger c_i = 0 \quad \text{for} \quad i > j \tag{3.27'}$$

nd so it is not an independent relation.

Let us now calculate the inner product matrix for this algebra. For distinct indices, e find

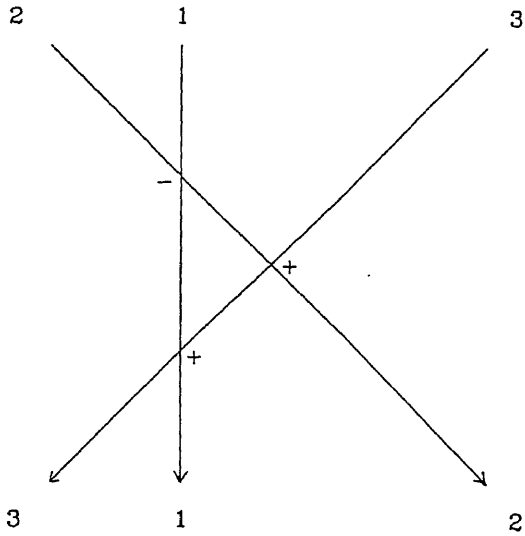

Figure 1. Inversion diagram for the permutation (213)→(312).
Positive inversions: (1, 3)→(3, 1) and (2, 3)→(3, 2).
Negative inversion: (2, 1)→(1, 2).

where J_+ and J_- are the number of positive and negative inversions in the permutation $\nu \to \mu$. The total number of inversions (the sum of positive and negative inversions) is the same as the number of inversions already defined below (3.10). We further define an inversion as positive if it is a transposition of indices from the ascending order to the descending order and as negative if it is the reverse transposition. For example, (1, 2)→(2, 1) is a positive inversion while (2, 1)→(1, 2) is a negative inversion. Thus we have

$$\langle 1_3 1_1 1_2 | 1_2 1_1 1_3 \rangle = (q^*)^2 q \tag{3.29'}$$

since the permutation (213)→(312) contains two positive and one negative inversions as shown in figure 1.

The relationship between the algebra defined by (3.27) and (3.28) with complex q (and $p = |q|$) and Greenberg's algebra defined by (3.19) with real q can be given. Calling the creation operators for the former and latter algebras as $c^\dagger(q)$ and $c^\dagger(|q|)$ respectively, the relationship is

$$c_i^\dagger(q) = e^{i\theta \Sigma_{k<i} N_k} c_i^\dagger(|q|) \tag{3.30}$$

where θ is the phase of q:

$$q = |q| e^{i\theta} \tag{3.31}$$

and N_k are the number operators defined in (2.37).

As a consequence, the inner product matrices for the two algebras are related by θ-dependent unitary matrices:

$$M(q) = T^\dagger(\theta) M(|q|)\, T(\theta) \tag{3.32}$$

We have already given in (3.13), Zagier's result for the determinant of M for real q. For our algebra with complex q, because of (3.32), the determinant of M for n particles with distinct indices is

$$\det M_n(q) = \prod_{k=1}^{n-1} (1 - |q|^{k(k+1)})^{(n-k)n!/k(k+1)} \tag{3.34}$$

Zeroes of $\det M_n(q)$ occur only on the circle $|q| = 1$. Hence, $M_n(q)$ for complex q is positive for $|q| < 1$, and we have thus extended the Fivel–Zagier result for positivity to complex q (for the case $p = |q|$).

In contrast to the situation for Greenberg's algebra, the inner product matrix M for states with repeated indices cannot be derived from that for states with distinct indices, for the present algebra. For n-particle states with all the indices repeated, the norm is the same as in (3.17) and (3.18), with q replaced by p:

$$\langle n_g | n_g \rangle = (1+p)(1+p+p^2)\ldots(1+p+p^2+\ldots p^{n_g-1}) \tag{3.35}$$

which is positive for $p > -1$. For states with only some indices repeated, M is a function of both q and p and the problem is more complicated; but we have verified positivity of the M's up to 3-particle states for $-1 < p < |q|^{-2}$.

If we choose $p = -1$, all states with repeated indices are forbidden. This is just Pauli's exclusion principle. Thus, the algebra defined by (3.27) and (3.28) with $p = -1$ leads to *infinite statistics with exclusion principle.*

Infact, we can restrict both (3.5) and (3.19) to $i \neq j$ and for $i = j$ replace them by

$$c_i c_i^\dagger + c_i^\dagger c_i = 1 \tag{3.36}$$

In all these cases, we have infinite statistics with exclusion principle.

A compilation of the various algebras all representing infinite statistics is given in table 1.

3.5 *Unitary transformations*

We must point out an important difference between the algebras described by (3.5), (3.19) and (3.20) on the one hand and the algebras of (3.21), (3.22), (3.27) and (3.28) on the other hand. It is easy to see that the former are covariant under the unitary transformations on the indices:

$$c_k \to \sum_m U_{km} c_m; \quad U^\dagger U = U U^\dagger = 1. \tag{3.37}$$

In fact, one can show [19] that under certain conditions (3.20) is the most general bilinear algebra of c_i and $c_j^\dagger$ invariant under this unitary transformation. This property is violated for the complex q-algebra of (3.27) and (3.28) as well as the algebras of (3.21) and (3.22). Covariance under the unitary transformation is desirable in a general context since it is closely connected to the superposition principle in quantum mechanics [3]. Nevertheless, algebras violating this requirement have been proposed in the recent literature, either because of the possibility of applications to specific

Table 1. Representations of infinite statistics.

Statistics	Representation	Algebra
Infinite	Standard representation	$c_i c_j^\dagger = \delta_{ij}$
,,	q-mutator (with real q)	$c_i c_j^\dagger - q c_j^\dagger c_i = \delta_{ij}$
,,	Two-parameter algebra	$\begin{cases} c_i c_j^\dagger - q_1 c_j^\dagger c_i \\ - q_2 \delta_{ij} \Sigma_k c_k^\dagger c_k = \delta_{ij} \end{cases}$
,,	q-mutator, transformed	$c_i c_j^\dagger - c_j^\dagger c_i = \delta_{ij} p^{2\Sigma_{k<i} N_k} p^{N_i}$
,,	q-mutator, transformed	$\begin{cases} c_i c_j^\dagger - p^{-1} c_j^\dagger c_i = 0, & \text{for } i \neq j \\ c_i c_i^\dagger - c_i^\dagger c_i = p^{N_i} \end{cases}$
,,	q-mutator (with complex q)	$\begin{cases} c_i c_j^\dagger - q c_j^\dagger c_i = 0, & \text{for } i < j \\ c_i c_i^\dagger - p c_i^\dagger c_i = 1 \end{cases}$
Infinite with Pauli principle	Standard representation	$\begin{cases} c_i c_j^\dagger = 0, & \text{for } i \neq j \\ c_i c_i^\dagger + c_i^\dagger c_i = 1 \end{cases}$
,,	q-mutator (with real q)	$\begin{cases} c_i c_j^\dagger - q c_j^\dagger c_i = 0, & \text{for } i \neq j \\ c_i c_i^\dagger + c_i^\dagger c_i = 1. \end{cases}$
,,	q-mutator (with complex q)	$\begin{cases} c_i c_j^\dagger - q c_j^\dagger c_i = 0, & \text{for } i < j \\ c_i c_i^\dagger + c_i^\dagger c_i = 1 \end{cases}$

systems in condensed matter physics or because of mathematical motivation. Hence we include such algebras in our investigation.

3.6 *Thermodynamics*

A detailed treatment of thermodynamic aspects is outside the scope of the presen paper. Nevertheless a brief statement is in order.

Consider the partition function for the canonical ensemble:

$$Z = Tre^{-\beta H} \tag{3.38}$$

where $\beta = (kT)^{-1}$ and H is the Hamiltonian of the system. If the system consists o non-interacting particles, we have

$$H = \sum_i \varepsilon_i N_i \tag{3.39}$$

where N_i are the number operators and ε_i are the single-particle energies. Hence, usin the orthonormal set $\|\ldots n_i \ldots; \mu\rangle\rangle$ in the evaluation of the trace in (3.38), we get

$$Z = \sum_{n_1, n_2, \ldots} d(\ldots n_j \ldots) e^{-\beta \Sigma_i \varepsilon_i n_i} \tag{3.40}$$

where $d(\ldots n_j \ldots)$ is the dimension of the sector $\{\ldots n_j \ldots\}$, defined in (2.40), and th summation is over all the allowed occupation numbers n_i for all i.

All the thermodynamics of the system can be derived from the partition functio Further, the set of $d(\ldots n_j \ldots)$ on the r.h.s. of (3.40) provide invariant characteristics o

he Fock space that are not dependent on the particular statistics or algebra living in hat Fock space. Hence, thermodynamics is the same for all forms of statistics and lgebras residing in a given Fock space.

For super Fock space and the associated infinite statistics, for which d is equal to defined by (2.6):

$$d = n!/\Pi_i n_i!; \quad n = \sum_i n_i, \tag{3.41}$$

he thermodynamics is independent of the particular representation or algebra of c and $c^\dagger$. In particular, if one uses the q-mutator algebra (3.19) to describe infinite statistics, he properties of the system in thermodynamic equilibrium are independent of q, provided q lies in the range $-1 < q < 1$. Greenberg [14] had originally envisaged small violations of Fermi or Bose statistics by choosing $q = \mp(1-\varepsilon)$, ε small and positive. We see that equilibrium thermodynamics will not manifest such small violations.

The expression for d given by (3.41) is the same as Boltzmann counting and hence Greenberg has called infinite statistics as 'quantum Boltzmann statistics'. However, since the Gibbs factor $1/n!$ is missing, the statistical mechanics of a system of free particles obeying infinite statistics with the index i in (3.40) interpreted as momentum will suffer Gibbs paradox [20]. Therefore, the super Fock space and the associated infinite statistics cannot be naively applied to familiar physical systems. In our approach, super Fock space plays the role of a mathematical template which can be used for carving out various physical systems.

As long as one takes the Hamiltonian to be of the form (3.39) which is the only correct form for non-interacting particles, the statistical mechanics and thermodynamics of the system are independent of the algebra of c and $c^\dagger$. One can then construct interaction terms involving c and $c^\dagger$ as in the usual many-body theory and their effect will of course depend on the algebra.

Recent literature contains many calculations on the statistical distributions or other thermodynamic quantities for the Hamiltonian

$$H = \sum_i \varepsilon_i c_i^\dagger c_i \tag{3.42}$$

with c and $c^\dagger$ satisfying some q-deformed algebra. Since $c_i^\dagger c_i$ is not a number operator in general, the physical meaning of the Hamiltonian (3.42) is not a priori clear, although one may suppose that it takes into account some type of interactions.

4. Statistics and algebras in bosonic, fermionic and frozen Fock spaces

We introduce two types of reduced Fock spaces in subsection 4.1. In one, we take any two states obtained by permutation to be related to each other and we allow all occupation numbers: $n_i = 0, 1, 2, \ldots$ for all i. In the other, any two states obtained by permutation are again related to each other but occupation numbers are restricted by exclusion principle: $n_i = 0$ and 1 only. We shall call the former as bosonic Fock space

bosonic and fermionic Fock spaces is to take

$$|n_1, n_2 \ldots; \mu\rangle = q^J |n_1, n_2 \ldots; 1\rangle \tag{4.1}$$

where q is a complex number and J is the number of inversions in the permutation: $1 \to \mu$. The number of inversions was already defined in § 3. Although J was defined there for the case in which the occupation numbers were restricted to unity, the same definition can be extended to larger occupation numbers. We assume $q \neq 0$. The case $q = 0$ will be considered separately. Many different forms of statistics as well as various algebras of c and $c^\dagger$ can be shown to be contained as particular cases of (4.1).

We first make some general remarks amplifying the meaning of (4.1). This equation can be obtained by repeated application of the elementary relation:

$$|\ldots 1_i 1_j \ldots\rangle = q|\ldots . 1_j 1_i \ldots\rangle, \quad \text{for} \quad i > j \tag{4.2}$$

where, except for the two adjacent quanta of indices i and j which are interchanged, all other quanta are left unchanged. In (4.2), we have used the same notation for the state vectors as on the r.h.s. of (2.1)–(2.4). It is clear that, for any q other than ± 1, (4.2) makes sense only if the indices i and j are ordered through an inequality (to be specific, $i > j$). Hence we have taken the indices to be the natural numbers $1, 2, 3 \ldots$ in writing (4.1).

The relationship among the state vectors given in (4.1) or (4.2) can be equivalently expressed as a quadratic relation between two creation operators or two annihilation operators. For any state $|\ldots\rangle$, using (2.30) or (2.31) we have

$$c_i^\dagger c_j^\dagger |\ldots\rangle = |1_i 1_j \ldots\rangle$$

$$c_j^\dagger c_i^\dagger |\ldots\rangle = |1_j 1_i \ldots\rangle$$

Comparing with (4.2), we get

$$c_i^\dagger c_j^\dagger |\ldots\rangle = q c_j^\dagger c_i^\dagger |\ldots\rangle, \quad \text{for} \quad i > j$$

Since this is valid for any state $|\ldots\rangle$, we can write

$$c_i^\dagger c_j^\dagger - q c_j^\dagger c_i^\dagger = 0 \quad \text{for} \quad i > j$$

or,

$$c_j c_i - q^* c_i c_j = 0 \quad \text{for} \quad i > j. \tag{4.3}$$

The above cc relation (eq. 4.3) is common to both bosonic and fermionic spaces. But for the fermionic space there exists the additional restriction:

$$c_i^\dagger c_i^\dagger = 0, \quad \text{or} \quad c_i c_i = 0. \tag{4.4}$$

All the states $|n_1, n_2 \ldots; \mu\rangle$ for fixed occupation numbers $(n_1, n_2 \ldots)$ but different values of μ being related to each other through (4.1), the dimension of the vector space in any sector $(n_1, n_2 \ldots)$ is reduced to unity. So, for each sector we choose one standard vector $|n_1, n_2 \ldots; 1\rangle$ which we rewrite as $|n_1, n_2 \ldots\rangle$, dispensing with μ completely.

The matrices X and M then become numbers related by

$$M^{-1} = XX^*. \tag{4.5}$$

Equation (2.11) becomes

$$\|n_1, n_2 \ldots\rangle\!\rangle = X(n_1, n_2 \ldots)|n_1, n_2 \ldots\rangle \tag{4.6}$$

and we have

$$\langle\!\langle n_1, n_2 \ldots \| n_1', n_2' \ldots\rangle\!\rangle = \delta_{n_1 n_1'} \delta_{n_2 n_2'} \ldots \tag{4.7}$$

From (2.35), we get

$$\begin{aligned} c_j^\dagger &= \sum_{n_1 \ldots n_j \ldots} |1_j, n_1, n_2 \ldots n_j \ldots\rangle\langle n_1, n_2 \ldots n_j \ldots| M^{-1}(n_1, n_2 \ldots) \\ &= \sum_{n_1 \ldots n_j \ldots} q^{\Sigma_{i<j} n_i} |n_1, n_2 \ldots (n_j + 1) \ldots\rangle\langle n_1, n_2 \ldots n_j \ldots| M^{-1}(n_1, n_2 \ldots) \end{aligned}$$

where we have pushed the j quantum to the right of all i quanta for $i < j$ using (4.2). Also using (4.5) and (4.6),

$$c_j^\dagger = \sum_{n_1 \ldots n_j} q^{\Sigma_{i<j} n_i} \frac{X(n_1 \ldots n_j \ldots)}{X(n_1 \ldots (n_j + 1) \ldots)} \|n_1, n_2 \ldots (n_j + 1) \ldots\rangle\!\rangle \langle\!\langle n_1, n_2 \ldots n_j \ldots\| \tag{4.8}$$

Equation (4.8) and its hermitian conjugate define the most general form of creation and destruction operators for the bosonic and fermionic Fock spaces.

If we assume factorization of the norm M as well as that of X:

$$X(n_1, n_2 \ldots) = \phi(n_1)\phi(n_2) \ldots, \tag{4.9}$$

then we get

$$c_j^\dagger = \sum_{n_1 \ldots n_j \ldots} q^{\Sigma_{i<j} n_i} \frac{\phi(n_j)}{\phi(n_j + 1)} \|n_1 \ldots n_j + 1 \ldots\rangle\!\rangle \langle\!\langle n_1 \ldots n_j \ldots\| \tag{4.10}$$

$$c_j = \sum_{n_1 \ldots n_j \ldots} (q^*)^{\Sigma_{i<j} n_i} \frac{\phi^*(n_j)}{\phi^*(n_j + 1)} \|n_1 \ldots n_j \ldots\rangle\!\rangle \langle\!\langle n_1 \ldots (n_j + 1) \ldots\| \tag{4.11}$$

We now construct the operator algebras for $c^\dagger$ and c given by (4.10) and (4.11). First of all, *for any form of* $\phi(n_i)$, we get

$$\left.\begin{aligned} c_i c_j^\dagger - q c_j^\dagger c_i &= 0 \quad \text{for} \quad i < j \\ c_i c_j^\dagger - q^* c_j^\dagger c_i &= 0 \quad \text{for} \quad i > j \end{aligned}\right\} \tag{4.12}$$

For $i = j$, the algebra depends on the choice of q and $\phi(n_i)$. We find

$$c_j c_j^\dagger = |q|^{2\Sigma_{i<j} N_i} \left| \frac{\phi(N_j)}{\phi(N_j + 1)} \right|^2 \tag{4.13}$$

$$c_j^\dagger c_j = |q|^{2\Sigma_{i<j} N_i} \left| \frac{\phi(N_j - 1)}{\phi(N_j)} \right|^2 \tag{4.14}$$

where $N_i, N_j \ldots$ are number operators and $\phi(N_i)$ is the function introduced in (4.9). So,

we can write the generalised commutation relation

$$\left.\begin{aligned} c_j c_j^\dagger - p c_j^\dagger c_j &= |q|^{2\Sigma_{i<j} N_i} f(N_j) \\ f(N_j) &= \left|\frac{\phi(N_j)}{\phi(N_j+1)}\right|^2 - p\left|\frac{\phi(N_j-1)}{\phi(N_j)}\right|^2 \end{aligned}\right\} \tag{4.15}$$

where p is any (complex) number. Equations (4.12) and (4.15) constitute the $cc^\dagger$ algebra for q-statistics defined by the cc algebra of (4.3).

What we have derived above can be regarded as the most general algebra of creation and annihilation operators for q-statistics, subject to the assumption of the factorization of the normalization factor implied by (4.9). In particular, since the function $\phi(N_j)$ occurring in (4.15) is arbitrary, we may regard our equations as constituting an infinite-parameter deformation of the algebra of c and $c^\dagger$. Exploiting the arbitrariness of $\phi(N_j)$ we can get many simpler forms of the algebra which we now describe.

(i) Choosing $\phi(n_j)$ to be a constant independent of n_j but noting that $\phi(-1)$ must vanish [38a], (4.15) becomes

$$c_j c_j^\dagger - p c_j^\dagger c_j = |q|^{2\Sigma_{i<j} N_i}\{1 - p(1-\delta_{N_j,0})\} \tag{4.16}$$

where $\delta_{N_j,0}$ is the Kronecker delta, which can also be represented as $\sin \pi N_j/\pi N_j$.

(ii) Putting $p = 0$ in (4.16) we get the simple algebra:

$$c_j c_j^\dagger = |q|^{2\Sigma_{i<j} N_i} \tag{4.17}$$

(iii) As a third possibility, we may choose $f(N_j)$ in (4.15) to be unity and p real so that we have the algebra:

$$c_j c_j^\dagger - p c_j^\dagger c_j = |q|^{2\Sigma_{i<j} N_i} \tag{4.18}$$

This choice requires that the function $\phi(n)$ must satisfy the equation

$$\left|\frac{\phi(n_j)}{\phi(n_j+1)}\right|^2 - p\left|\frac{\phi(n_j-1)}{\phi(n_j)}\right|^2 = 1 \tag{4.19}$$

The solution of this functional equation (with the constraints that $\phi(0)$ is finite and $\phi(-1)$ vanishes) is

$$|\phi(n)|^{-2} = [(n)!]_p \equiv [n]_p [n-1]_p \ldots [1]_p \tag{4.20}$$

where

$$[n]_p = \frac{p^n - 1}{p-1} = 1 + p + p^2 + \ldots + p^{n-1} \tag{4.21}$$

For $p = 1$, the 'p-numbers' in (4.20) and (4.21) become ordinary numbers.

(iv) As a final choice we put $p = |q|^2$ in (4.18)–(4.21). As a consequence of this choice, the r.h.s. of (4.18) becomes a bilinear function of c and $c^\dagger$. For, from (4.14), we can prove an identity:

$$(|q|^2 - 1) \sum_{k<j} c_k^\dagger c_k = \sum_{k<j} |q|^{2\Sigma_{i<k} N_i} \left|\frac{\phi(N_k - 1)}{\phi(N_k)}\right|^2 (|q|^2 - 1)$$

$$= \sum_{k<j} |q|^{2\Sigma_{i<k}N_i}(|q|^{2N_k} - 1)$$

$$= |q|^{2\Sigma_{i<j}N_i} - 1 \tag{4.22}$$

where we have used (4.20) and (4.21) with $p = |q|^2$. Hence (4.18) can be replaced by

$$c_j c_j^\dagger - |q|^2 c_j^\dagger c_j = 1 + (|q|^2 - 1) \sum_{k<j} c_k^\dagger c_k \tag{4.23}$$

Any one of (4.16), (4.17), (4.18) or (4.23) together with (4.12) constitute a $cc^\dagger$ algebra and one can construct many more examples of $cc^\dagger$ algebras, all of which correspond to the same q-statistics specified by (4.3). We have so far assumed that the occupation numbers are unrestricted: $n_j \geqslant 0$ and so these algebras are valid for the bosonic q-statistics, namely q-statistics in the bosonic space.

The fermionic q-statistics is defined by (4.3) and (4.4). In this case, n_j in (4.10) and (4.11) can take the value 0 only, while all the other occupation numbers will range over 0 and 1. So, the only arbitrary parameter that enters the definition of c and $c^\dagger$ is $r = \phi(0)/\phi(1)$. The $cc^\dagger$ relation for $i \neq j$ is still the same as in (4.12) while the $c_j c_j^\dagger$ relation of (4.15) can be simplified to

$$c_j c_j^\dagger - p c_j^\dagger c_j = |q|^{2\Sigma_{i<j}N_i} |r|^2 \{\delta_{N_j,0} - p\delta_{N_j,1}\} \tag{4.24}$$

Further, we can generally prove the fermionic analogue of the identity which was earlier proved in (4.22) for the bosonic case only for a special choice of $\phi(n)$:

$$\begin{aligned}(|q|^2 - 1) \sum_{k<j} c_k^\dagger c_k &= (|q|^2 - 1) \sum_{k<j} |q|^{2\Sigma_{i<k}N_i} |r|^2 \delta_{N_k,1} \\ &= \sum_{k<j} |q|^{2\Sigma_{i<k}N_i} (|q|^{2N_k} - 1)|r|^2 \\ &= (|q|^{2\Sigma_{i<j}N_i} - 1)|r|^2\end{aligned} \tag{4.25}$$

Hence, (4.24) can be rewritten as

$$c_j c_j^\dagger - p c_j^\dagger c_j = \{|r|^2 + (|q|^2 - 1) \sum_{k<j} c_k^\dagger c_k\}(\delta_{N_j,0} - p\delta_{N_j,1}) \tag{4.26}$$

Equations (4.12) and (4.26) constitute the general algebra for the fermionic q-statistics. In contrast to (4.15) of the bosonic case, the fermionic case does not have the freedom of infinite-parameter deformation.

On the r.h.s. of (4.26), apart from the curly bracket $\{\ \}$ which is bilinear in c and $c^\dagger$, there are Kronecker deltas which depend on the operator N_j. A simpler relation is obtained for the choice $p = -1$, since $\delta_{N_j,0} + \delta_{N_j,1} = 1$. We then have

$$c_j c_j^\dagger + c_j^\dagger c_j = |r|^2 + (|q|^2 - 1) \sum_{k<j} c_k^\dagger c_k \tag{4.27}$$

A further choice $|r|^2 = 1$ gives

$$c_j c_j^\dagger + c_j^\dagger c_j = 1 + (|q|^2 - 1) \sum_{k<j} c_k^\dagger c_k \tag{4.28}$$

which is the fermionic analogue of (4.23).

Table 2. Statistics and algebras in the bosonic Fock space.

Statistics	cc algebra	$c_ic_j^\dagger$ algebra for $i \neq j$	$c_jc_j^\dagger$ algebra	Remarks
q-statistics	$c_ic_j = q^* c_jc_i$ for $i<j$	$c_ic_j^\dagger = qc_j^\dagger c_i$ for $i<j$	$c_jc_j^\dagger - pc_j^\dagger c_j = \lvert q\rvert^{2\Sigma_{i<j}N_i} f(N_j)$	General representation
"	$c_ic_j = q^* c_jc_i$ for $i<j$	$c_ic_j^\dagger = qc_j^\dagger c_i$ for $i<j$	$c_jc_j^\dagger - pc_j^\dagger c_j = \lvert q\rvert^{2\Sigma_{i<j}N_i}\{1-p(1-\delta_{N_j,0})\}$	
"	$c_ic_j = q^* c_jc_i$ for $i<j$	$c_ic_j^\dagger = qc_j^\dagger c_i$ for $i<j$	$c_jc_j^\dagger = \lvert q\rvert^{2\Sigma_{i<j}N_i}$	
"	$c_ic_j = q^* c_jc_i$ for $i<j$	$c_ic_j^\dagger = qc_j^\dagger c_i$ for $i<j$	$c_jc_j^\dagger - pc_j^\dagger c_j = \lvert q\rvert^{2\Sigma_{i<j}N_i}$	
"	$c_ic_j = q^* c_jc_i$ for $i<j$	$c_ic_j^\dagger = qc_j^\dagger c_i$ for $i<j$	$c_jc_j^\dagger - \lvert q\rvert^2 c_j^\dagger c_j = 1 + (\lvert q\rvert^2 - 1)\sum_{k<j} c_k^\dagger c_k$	Covariant under $SU_q(n)$
bose statistics	$c_ic_j = c_jc_i$	$c_ic_j^\dagger = c_j^\dagger c_i$ for $i \neq j$	$c_jc_j^\dagger - pc_j^\dagger c_j = f(N_j)$	General representation
"	$c_ic_j = c_jc_i$	$c_ic_j^\dagger = c_j^\dagger c_i$ for $i \neq j$	$c_jc_j^\dagger - pc_j^\dagger c_j = \{1-p(1-\delta_{N_j,0})\}$	
"	$c_ic_j = c_jc_i$	$c_ic_j^\dagger = c_j^\dagger c_i$ for $i \neq j$	$c_jc_j^\dagger = 1$	Simplest representation

"	$c_ic_j = c_jc_i$	$c_ic_j^\dagger = c_j^\dagger c_i$ for $i \neq j$	$c_jc_j^\dagger - pc_j^\dagger c_j = 1; \quad p \neq -1$	Commuting deformed oscillators
"	$c_ic_j = c_jc_i$	$c_ic_j^\dagger = c_j^\dagger c_i$ for $i \neq j$	$c_jc_j^\dagger - c_j^\dagger c_j = 1$	Canonical rep. of bosons
fermi statistics	$c_ic_j = -c_jc_i$ for $i \neq j$	$c_ic_j^\dagger = -c_j^\dagger c_i$ for $i \neq j$	$c_jc_j^\dagger - pc_j^\dagger c_j = f(N_j)$	General representation
"	$c_ic_j = -c_jc_i$ for $i \neq j$	$c_ic_j^\dagger = -c_j^\dagger c_i$ for $i \neq j$	$c_jc_j^\dagger - pc_j^\dagger c_j = \{1 - p(1 - \delta_{N_j,0})\}$	
"	$c_ic_j = -c_jc_i$ for $i \neq j$	$c_ic_j^\dagger = -c_j^\dagger c_i$ for $i \neq j$	$c_jc_j^\dagger = 1$	
"	$c_ic_j = -c_jc_i$ for $i \neq j$	$c_ic_j^\dagger = -c_j^\dagger c_i$ for $i \neq j$	$c_jc_j^\dagger - pc_j^\dagger c_j = 1; \quad p \neq -1$	Anticommuting deformed oscillators
"	$c_ic_j = -c_jc_i$ for $i \neq j$	$c_ic_j^\dagger = -c_j^\dagger c_i$ for $i \neq j$	$c_jc_j^\dagger - c_j^\dagger c_j = 1$	Anticommuting bosons
fractional statistics	$c_ic_j = e^{-i\theta}c_jc_i$ for $i < j$	$c_ic_j^\dagger = e^{i\theta}c_j^\dagger c_i$ for $i < j$	Any one of the same $c_jc_j^\dagger$ relations given in bose or fermi statistics above	

Table 3. Statistics and algebras in the fermionic Fock space.

Statistics	cc algebra	$c_ic_j^\dagger$ algebra for $i \neq j$	$c_jc_j^\dagger$ algebra	Remarks
q-statistics	$c_ic_j = q^* c_jc_i$ for $i<j$ $c_ic_i = 0$	$c_ic_j^\dagger = qc_j^\dagger c_i$ for $i<j$	$c_jc_j^\dagger - pc_j^\dagger c_j = (\delta_{N_j,0} - p\delta_{N_j,1}) \times \left\{ \lvert r\rvert^2 + (\lvert q\rvert^2 - 1) \sum_{k<j} c_k^\dagger c_k \right\}$	General representation
,,	$c_ic_j = q^* c_jc_i$ for $i<j$ $c_ic_i = 0$	$c_ic_j^\dagger = qc_j^\dagger c_i$ for $i<j$	$c_jc_j^\dagger + c_j^\dagger c_j = \lvert r\rvert^2 + (\lvert q\rvert^2 - 1) \sum_{k<j} c_k^\dagger c_k$	
,,	$c_ic_j = q^* c_jc_i$ for $i<j$ $c_ic_i = 0$	$c_ic_j^\dagger = qc_j^\dagger c_i$ for $i<j$	$c_jc_j^\dagger + c_j^\dagger c_j = 1 + (\lvert q\rvert^2 - 1) \sum_{k<j} c_k^\dagger c_k$	Covariant under $SU_q(n)$
bose-statistics	$c_ic_j = c_jc_i$ $c_ic_i = 0$	$c_ic_j^\dagger = c_j^\dagger c_i$ for $i \neq j$	$c_jc_j^\dagger - pc_j^\dagger c_j = (\delta_{N_j,0} - p\delta_{N_j,1})\lvert r\rvert^2$	
,,	$c_ic_j = c_jc_i$ $c_ic_i = 0$	$c_ic_j^\dagger = c_j^\dagger c_i$ for $i \neq j$	$c_jc_j^\dagger + c_j^\dagger c_j = 1$	Commuting fermions

fermi-statistics	$c_ic_j=-c_jc_i$ for all i,j	$c_ic_j^\dagger=-c_j^\dagger c_i$ for $i\neq j$	$c_jc_j^\dagger-pc_j^\dagger c_j=(\delta_{N_j,0}-p\delta_{N_j,1})\lvert r\rvert^2$	
"	$c_ic_j=-c_jc_i$ for all i,j	$c_ic_j^\dagger=-c_j^\dagger c_i$ for $i\neq j$	$c_jc_j^\dagger+c_j^\dagger c_j=1$	Canonical rep. of fermions.
fractional statistics	$c_ic_j=e^{-i\theta}c_jc_i$ for $i<j$ $c_ic_i=0$	$c_ic_j^\dagger=e^{i\theta}c_j^\dagger c_i$ for $i<j$	$c_jc_j^\dagger-pc_j^\dagger c_j=(\delta_{N_j,0}-p\delta_{N_j,1})\lvert r\rvert^2$	
"	$c_ic_j=e^{-i\theta}c_jc_i$ for $i<j$ $c_ic_i=0$	$c_ic_j^\dagger=e^{i\theta}c_j^\dagger c_i$ for $i<j$	$c_jc_j^\dagger+c_j^\dagger c_j=1$	

The algebra given by (4.3), (4.12) and (4.23) (for real q) are covariant under *the quantum group* $SU_q(n)$ where n is the total number of indices. This is true of the fermionic algebra of (4.3), (4.12) and (4.28) also. (See refs. [21–31] for this relationship to the theory of quantum groups.) However, our approach based on states related by q-statistics (4.1) does not involve any notion of quantum group *per se* and so we shall not describe it. The formalism of the generalized Fock space appears to be capable of incorporating many general algebraic structures. In particular, the $c_j c_j^\dagger$ algebra of (4.15) constitutes a general infinite-parameter deformation while the quantum-group related algebra of (4.23) is only a particular case of this.

We have constructed the general algebras for arbitrary complex q. The choice of q defines the symmetry of the state under permutation. Hence we call the different choices of q as different forms of statistics. Particular values of q such as $q = \pm 1$ or $q = e^{i\theta}$ are of special interest, although these cases are all contained in the general formulae already given. We shall call the statistics obtained for $q = +1$, -1 and $e^{i\theta}$ as Bose statistics, Fermi statistics or 'fractional' statistics respectively. Either the bosonic or fermionic Fock space can be used to construct any one of the various forms of statistics. Thus, within our terminology, it is perfectly possible for instance to have Fermi statistics residing in bosonic Fock space or vice versa.

Within a particular statistics, different choices of M or ϕ correspond to different representations of c_j and $c_j^\dagger$, which in turn lead to different $cc^\dagger$ algebras. If we assume the factorization given in (4.9), for a given q, only the $i = j$ part of the $cc^\dagger$ algebra depends on the representation.

For the sake of clarity, all these forms of statistics and algebras are exhibited in tables 2 and 3 for the bosonic and fermionic spaces respectively.

Several comments are in order, concerning the contents of these tables. The algebra

$$c_i c_j - c_j c_i = 0, \quad \text{for} \quad i \neq j \tag{4.29}$$

$$c_i c_j^\dagger - c_j^\dagger c_i = 0, \quad \text{for} \quad i \neq j \tag{4.30}$$

$$c_i c_j^\dagger = 1 \tag{4.31}$$

provide the simplest representation for Bose statistics based on the simple choice of M or ϕ as unity. This is analogous to the standard representation (3.5) for infinite statistics but very different from it. In fact they live in entirely different Fock spaces. In recent literature, (4.31) has been sometimes confused with infinite statistics. Equation (4.31) coupled with (4.29) and (4.30) infact describes Bose statistics only, although in a noncanonical representation.

Attention may be drawn to the 'anticommuting bosons' and the 'commuting fermions' shown in tables 2 and 3 respectively. The commuting fermions have been called hard-core bosons in condensed-matter-physics literature. Our terminology seems more appropriate since they are really fermions in disguise, living in the fermionic Fock space.

The precise connection of our 'fractional' statistics to the exchange property of the wavefunctions proposed [39, 40] for one and two-dimensional systems needs further study. In particular, a suitable mapping of the ordered indices to coordinates in one and two-dimensions is necessary.

Among all the different algebras given in tables 2 and 3, only two of them, namely the canonical representations for the bosons and fermions have the distinction of being covariant under the unitary transformations that mix the indices (see (3.37)). All the other algebras violate this requirement, although, as we have already mentioned, two of them, one in the bosonic and the other in the fermionic Fock spaces, are covariant under the quantum groups $SU_q(n)$.

The examples contained in these tables can be called deformed-oscillator algebras on which many papers [1–12, 21–27, 32, 41, 42] have been written recently. In spite of the multiplicity of these deformed algebras, we must not ignore the basic fact that *they are all avatars of just two primary constructions which may be taken to be the canonical bosonic algebra for the bosonic Fock space and the canonical fermionic algebra for the fermionic Fock space.* All the different forms of statistics belonging to the bosonic Fock space as well as their various algebraic representations are related to each other and to the canonical bosonic algebra and similar is the situation for the fermionic Fock space. Given two different forms of statistics within the bosonic Fock space characterized by the statistics parameters q_1 and q_2 respectively, or/and two different representations characterized by the functions $\phi_1(n)$ and $\phi_2(n)$ respectively, it is easy to get from (4.10) the relationship

$$c_j^\dagger(2) = \left(\frac{q_2}{q_1}\right)^{\Sigma_{i<j} N_i} \frac{\phi_2(N_j - 1)}{\phi_2(N_j)} \frac{\phi_1(N_j)}{\phi_1(N_j - 1)} c_j^\dagger(1) \tag{4.32}$$

The corresponding equation for the fermionic Fock space is

$$c_j^\dagger(2) = \left(\frac{q_2}{q_1}\right)^{\Sigma_{i<j} N_i} \left(\frac{r_2}{r_1}\right) c_j^\dagger(1) \tag{4.33}$$

Hence, from the point of view of Fock space, there is nothing new in all these deformed oscillators.

In the above equations, the number operator N_i are given by

$$N_i = \sum_{n_1 \ldots n_i \ldots} n_i \| n_1 \ldots n_i \ldots \rangle\!\rangle \langle\!\langle n_1 \ldots n_i \ldots \| \tag{4.34}$$

and, written in this fashion in terms of the normalized states $\| \; \rangle\!\rangle$, N_i *is the same in all the different forms of statistics (within the bosonic or fermionic Fock spaces) and in all the different representations.*

Using (4.14) it is also possible to express the number operators in terms of c and $c^\dagger$ in any statistics or any representation within the bosonic or fermionic Fock space. Noting that for the canonical bosonic algebra

$$q = 1; \quad \phi(n) = \frac{1}{(n!)^{1/2}}, \tag{4.35}$$

we get from (4.14)

$$N_i = c_i^\dagger c_i. \tag{4.36}$$

For other statistics and representations also, the set of equations obtained from (4.14) starting with $j = 1$ and successively increasing j, can be seen to be implicit recursion

formulae for all N_j. Thus we have

$$\left.\begin{aligned} c_1^\dagger c_1 &= \left|\frac{\phi(N_1-1)}{\phi(N_1)}\right|^2 \\ c_2^\dagger c_2 &= |q|^{2N_1}\left|\frac{\phi(N_2-1)}{\phi(N_2)}\right|^2 \\ &\vdots \end{aligned}\right\} \tag{4.37}$$

By choosing $\phi(N_j)$ one then gets the desired explicit expressions for N_j. However, as already emphasized, such expressions are not of much use: the universal representation of N_j given in (4.34) is sufficient for all purposes.

The formalism of Fock space developed here has sufficient flexibility so as to allow many straightforward extensions or generalizations. For instance, the relationship between permuted states defined by (4.1) or (4.2) can be generalized further. Instead of (4.3), we may take

$$c_j c_i - q_{ij}^* c_i c_j = 0 \quad \text{for} \quad i > j, \tag{4.38}$$

where q_{ij} are complex parameters. This may be called *multiparameter q-statistics*. The algebras corresponding to such extensions as well as further generalizations can all be constructed essentially by the same procedure as given in this section. Details will be presented elsewhere. Suffices it to say that, once the relationship among the permuted states is specified through the *cc* relation, the rest of the story follows.

Special cases of such algebras have been reported in the literature on quantum groups [21–33]. We have already referred to the generality of our approach as compared to quantum groups. As further points of comparison between the two approaches we must mention the following. From the point of view of quantum groups, the whole set of relations among c and $c^\dagger$ are taken for granted. In contrast, our analysis based on the underlying Fock space reveals the *cc* relation as the key to the whole algebraic structure, although the normalization function $\phi(n)$ also plays a role in determining the actual representation of the operators. Hence, depending on the mode of expressing the *cc* relation and the choice of $\phi(n)$, one can generate any number of algebras of c and $c^\dagger$. Thus, our approach helps to demystify the quantum-group related algebras by reducing them to their basic essentials which are identified to be simple properties of state vectors in the Fock space. Reversing the procedure, one can probably reconstruct the whole edifice of the quantum group itself starting from the more elementary notions relating to states in the Fock space. This of course lies outside the purview of the present paper.

4.2 *Fock space of frozen order and null statistics*

In subsection 4.1 we had taken any two states obtained by permutation to be related to each other. We now consider a limiting situation in which the particles are frozen in a particular order, with no permutation allowed. This is the *Fock space of frozen states*

this may be obtained as the limit $q \to 0$ of the q-statistics, more properly, it must be regarded as an independent statistics. For, whereas the statistics for two (non-zero) values of q are related to each other through (4.32) or (4.33), the statistics for $q = 0$ cannot be related to statistics for $q \neq 0$. Hence, we shall construct the algebra of c and $c^\dagger$ for this system of frozen states directly from the definition. Again, depending on whether the particles obey exclusion principle or not, we have two different versions of the system which we shall call the fermionic and the bosonic versions respectively.

Let us first consider the bosonic version. Referring to (4.1) the Fock space of frozen states is obtained by taking $|n_1 n_2 \ldots; 1\rangle$ as the allowed state and requiring

$$|n_1 n_2 \ldots; \mu\rangle = 0 \quad \text{for} \quad \mu \neq 1 \tag{4.39}$$

Or, equivalently

$$|\ldots 1_j 1_i \ldots\rangle = 0 \quad \text{for} \quad i < j \tag{4.40}$$

and hence

$$c_i c_j = 0 \quad \text{for} \quad i < j \tag{4.41}$$

Assuming factorization of the norm as in (4.9), we can represent the creation operator in the form:

$$c_j^\dagger = \sum_{n_j, n_{j+1} \ldots} \frac{\phi(n_j)}{\phi(n_j + 1)} \| 0_1 \ldots 0_{j-1}, (n_j + 1), n_{j+1} \ldots \rangle\!\rangle \langle\!\langle 0_1, \ldots 0_{j-1}, n_j, n_{j+1} \ldots \| \tag{4.42}$$

The zeroes in the state vectors arise from the fact that $c_j^\dagger$ can create a quantum with index j only if indices $i < j$ are unoccupied. From (4.41) and the orthogonality of the states, we get

$$c_k c_j^\dagger = 0 \quad \text{for} \quad k \neq j \tag{4.43}$$

The $c_j c_j^\dagger$ algebra will depend on the choice of $\phi(n_j)/\phi(n_j + 1)$. We shall assume $\phi(n_j) = \phi(n_j + 1)$ for simplicity. Then, by using the completeness relation for the states, one can verify

$$c_j c_j^\dagger = 1 - \sum_{k<j} c_k^\dagger c_k \tag{4.44}$$

Equations (4.41), (4.43) and (4.44) together define the algebra for the bosonic version of the statistics of frozen order.

For the fermionic version, (4.41) is replaced by

$$c_i c_j = 0 \quad \text{for} \quad i \leqslant j \tag{4.45}$$

and one again gets

$$c_k c_j^\dagger = 0 \quad \text{for} \quad k \neq j \tag{4.46}$$

but, instead of (4.44), one finds

$$c_j c_j^\dagger = 1 - \sum_{k \leqslant j} c_k^\dagger c_k \tag{4.47}$$

Thus, the fermionic version of the statistics of frozen states is described by the algebra of (4.45)–(4.47). It is interesting to note that the replacement of the sign $<$ in the bosonic algebra by the sign $\leqslant$ yields the fermionic algebra.

Finally, we note that the expression for the number operators in terms of c and $c^\dagger$ for the above algebra of null statistics can be shown to be essentially the same as that for the standard representation of infinite statistics (eq. 3.9a), but because of (4.41) or (4.45), it can be simplified to read as

$$N_k = \sum_{n_1, n_2 \ldots n_k} c_1^{\dagger n_1} c_2^{\dagger n_2} \ldots c_k^{\dagger n_k} c_k^\dagger c_k c_k^{n_k} \ldots c_2^{n_2} c_1^{n_1} \tag{4.48}$$

where the sum over $n_1, n_2 \ldots n_k$ is unrestricted ($\geqslant 0$) for the bosonic version, but is restricted for the fermionic version: $n_1, n_2 \ldots n_{k-1}$ go over 0 and 1 while $n_k = 0$.

4.3 *Thermodynamic aspects*

For the bosonic and fermionic Fock spaces, (3.40) for the partition function becomes

$$Z = \sum_{n_1, n_2 \ldots} e^{-\beta \Sigma_i \varepsilon_i n_i} \tag{4.49}$$

where $n_i = 0, 1, 2, \ldots \infty$ for the bosonic space and $n_i = 0, 1$ for the fermionic space. This is a well-known result for the canonical Bose and Fermi statistics, but we emphasize the fact that *the partition function and the resulting thermodynamics is the same for all the various q-statistics and q-deformed algebras living in the same bosonic Fock space and similarly for the fermionic Fock space.* This point has been missed in much of the current literature and so considerable confusion has been created. Part of this confusion is due to the choice of the inappropriate Hamiltonian (eq. (3.42)) and the wrong emphasis placed on some particular algebra of c and $c^\dagger$.

We further note that the above Z in (4.49) is valid even for the Fock space of frozen order and null statistics since $d = 1$ in this case too.

To sum up, equilibrium thermodynamics of a system of free particles is determined entirely by the dimension d and spectrum of allowed occupation numbers which together characterize the Fock space and does not depend on the permutation properties of the multiparticle states or the algebras of c and $c^\dagger$.

5. Derivation of cc relations from $cc^\dagger$ algebras

In the last section construction of the bilinear algebra of c and $c^\dagger$ starting from states related by (4.1) was shown. In other words, $cc^\dagger$ algebra has been derived from the cc algebra given by (4.3). The converse is also true; the cc algebra can be derived from the $cc^\dagger$ algebra, as is shown in this section. Thus, within the framework of Fock space it is unnecessary to give both cc and $cc^\dagger$ relations. Either the cc relation or the $cc^\dagger$ relation can be used to define the Fock space and the other can be derived. But there are some caveats:

(i) Although the cc relation does define the Fock space, the $cc^\dagger$ algebra does not follow uniquely; as already pointed out, the operators $c, c^\dagger$ and their algebras depend on the choice of M.

(ii) In order to define the Fock space completely, the $cc^\dagger$ algebra must fulfill certain conditions. The $cc^\dagger$ algebra must be such that an arbitrary inner product $\langle 0|c_i c_j \ldots c_g^\dagger c_h^\dagger|0\rangle$ or infact the vacuum matrix element of any polynomial in the c's and $c^\dagger$'s arbitrarily ordered, can be calculated using the $cc^\dagger$ algebra and the definition of the vacuum state $|0\rangle$:

$$c_k|0\rangle = 0 \quad \text{for all } k. \tag{5.1}$$

A general form of the $cc^\dagger$ algebra that satisfies this requirement is:

$$c_i c_j^\dagger = A_{ij} + \sum_{k,m} B_{ijkm} c_k^\dagger c_m \tag{5.2}$$

where A_{ij} and B_{ijkm} can be constants, but more generally they can be functions of the number operators. All the $cc^\dagger$ algebras considered in this paper are of this form.

There exists an elegant method [19] to derive cc relations from the $cc^\dagger$ algebras. Restricting ourselves to relations quadratic in c, we define

$$Q_{ij} = c_i c_j - q' c_j c_i \tag{5.3}$$

where q' may be an arbitrary complex parameter. Suppose that, by using the given $cc^\dagger$ algebra, we are able to prove

$$Q_{ij} c_k^\dagger = \sum_{i'j'k'} F_{ijk;i'j'k'} c_{k'}^\dagger Q_{i'j'} \tag{5.4}$$

for all i, j and k where $F_{ijk;i'j'k'}$ may be a c-number or operator. Then, by applying this equation successively, we get

$$Q_{ij} c_k^\dagger c_m^\dagger \ldots = \sum_{i'j'k'} \sum_{i''j''m'} F_{ijk;i'j'k'} F_{i'j'm;i''j''m'} c_{k'}^\dagger c_{m'}^\dagger \ldots Q_{i''j''} \tag{5.5}$$

Allowing both sides of this equation to act on $|0\rangle$, the right side vanishes and so we see that Q_{ij} acting on any Fock state $c_k^\dagger c_m^\dagger \ldots |0\rangle$ gives zero. Hence we may write the operator identity:

$$Q_{ij} = 0 \tag{5.6}$$

which is the cc relation sought after. It may also be pointed out that often one finds

$$F_{ijk;i'j'k'} = f_{ijk} \delta_{ii'} \delta_{jj'} \delta_{kk'} \tag{5.7}$$

so that (5.4) is simplified to

$$Q_{ij} c_k^\dagger = f_{ijk} c_k^\dagger Q_{ij} \tag{5.8}$$

Thus, the form-invariance of Q_{ij} on being pushed to the right of $c_k^\dagger$, as explicitly given in (5.4) or (5.8) is the necessary and sufficient condition for the existence of the cc relation. We may now apply this method on various $cc^\dagger$ algebras discussed in the previous sections.

5.1 *q-mutator algebra with real q*:

The $cc^\dagger$ algebra is

$$c_i c_j^\dagger - q c_j^\dagger c_i = \delta_{ij}, \quad \forall i, j. \tag{5.9}$$

We define

$$Q_{ij} = c_i c_j - q' c_j c_i, \quad \forall i,j \tag{5.10}$$

From (5.9),

$$Q_{ij} c_k^\dagger = (1 - qq') c_i \delta_{kj} + (q - q') c_j \delta_{ki} + q^2 c_k^\dagger Q_{ij} \tag{5.11}$$

The form-invariance of Q_{ij} requires

$$q' = q = \pm 1. \tag{5.12}$$

So, we get the *cc* relations

$$c_i c_j \pm c_j c_i = 0 \tag{5.13}$$

corresponding to Bose and Fermi statistics at $q = \pm 1$. For $-1 < q < 1$, there are no *cc* relations and we have infinite statistics. The inner product matrix M which remains positive definite for $-1 < q < 1$, develops zero eigenvalues at $q = \pm 1$. (see eq. (3.13)) corresponding to the null states such as $(c_i^\dagger c_j^+ \pm c_j^\dagger c_i^\dagger)|0\rangle$ arising from (5.13).

5.2 *q-mutator algebra with complex q*

The $cc^\dagger$ relations are

$$c_i c_j^\dagger - q c_j^\dagger c_i = 0 \quad \text{for} \quad i < j \tag{5.14}$$

$$c_i c_i^\dagger - p c_i^\dagger c_i = 1 \tag{5.15}$$

We define

$$Q_{ij} = c_i c_j - q' c_j c_i \quad \text{for} \quad i < j \tag{5.16}$$

$$= c_i c_i \quad \text{for} \quad i = j \tag{5.17}$$

Using (5.14) and (5.15), we find

$$\left.\begin{aligned} Q_{ij} c_k^\dagger &= q^2 c_k^\dagger Q_{ij} \quad \text{for} \quad i \leqslant j < k \\ &= q^{*^2} c_k^\dagger Q_{ij} \quad \text{for} \quad k < i \leqslant j \\ &= |q|^2 c_k^\dagger Q_{ij} \quad \text{for} \quad i < k < j \\ &= (q^* - q') c_j + p q^* c_i^\dagger Q_{ij} \quad \text{for} \quad k = i < j \\ &= (1 - qq') c_i + pq c_j^\dagger Q_{ij} \quad \text{for} \quad i < j = k \\ &= (1 + p) c_i + p^2 c_i^\dagger Q_{ii} \quad \text{for} \quad i = j = \text{k}. \end{aligned}\right\} \tag{5.18}$$

The form-invariance of Q_{ij} for $i < j$ requires

$$q' = q^* = e^{-i\theta} \tag{5.19}$$

where θ is real. We thus get the *cc* relation corresponding to fractional statistics at the boundary $|q| = 1$ of the disc $|q| < 1$ in the complex plane.

We already know that the disc $|q| < 1$ corresponds to the region of positive-definite inner product matrix M for the complex q-mutator algebra of infinite statistics. At the boundary of this positivity region, we have fractional statistics living in a reduced Fock

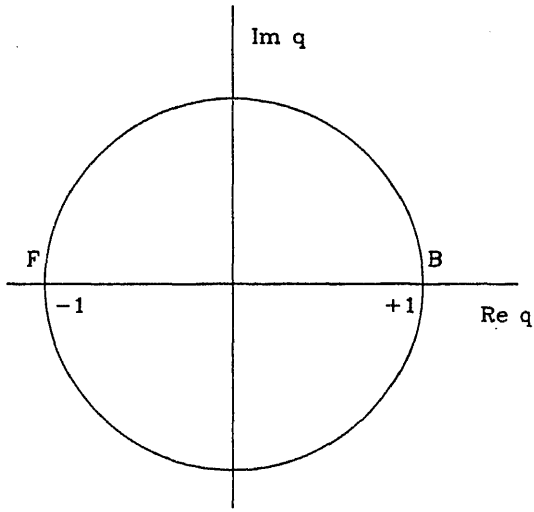

Figure 2. The complex q-plane of the q-mutator algebra. The disc $|q| < 1$ corresponds to infinite statistics and the circle $|q| = 1$ corresponds to fractional statistics. F and B are the Fermi–Dirac and Bose–Einstein points.

space (see figure 2). It is the states of vanishing norm of the form

$$(\ldots c_i^\dagger c_j^\dagger \ldots |0\rangle) \quad -e^{i\theta}(\ldots c_j^\dagger c_i^\dagger \ldots |0\rangle) \quad \text{for} \quad i<j \tag{5.20}$$

which contribute to the zeroes of $\det M_n$ in (3.34) at $|q| = 1$. Once we remove these states, we get the reduced Fock space of positive-definite norm.

The form-invariance of Q_{ij} for $i = j$ requires

$$p = -1 \tag{5.21}$$

with the corresponding cc relation

$$c_i c_i = 0 \tag{5.22}$$

This leads to the exclusion principle namely $n_i = 0$ or 1 only; equivalently, the norms of states with repeated indices are zero as seen by putting $p = -1$ in (3.35).

To sum up, we may note four possibilities all contained in the algebra of (5.14) and (5.15):

(a) Infinite statistics with multiple occupation

$$|q| \neq 1; \quad p \neq -1. \tag{5.23}$$

(b) Infinite statistics with exclusion principle

$$|q| \neq 1; \quad p = -1 \tag{5.24}$$

(c) Fractional statistics with multiple occupation

$$q = e^{i\theta}; \quad p \neq -1 \tag{5.25}$$

The $cc^\dagger$ relations are

$$c_i c_j^\dagger - q c_j^\dagger c_i = 0 \quad \text{for} \quad i<j \tag{5.27}$$

$$c_j c_j^\dagger - p c_j^\dagger c_j = |q|^{2\Sigma_{i<j} N_i} f(N_j) \tag{5.28}$$

We define

$$Q_{ij} = c_i c_j - q' c_j c_i \quad \text{for} \quad i>j \tag{5.29}$$

Using (5.27), (5.28) we get

$$\left.\begin{aligned} Q_{ij} c_k^\dagger &= q^2 c_k^\dagger Q_{ij} \quad \text{for} \quad i<j<k \\ &= q^{*^2} c_k^\dagger Q_{ij} \quad \text{for} \quad k<i<j \\ &= |q|^2 c_k^\dagger Q_{ij} \quad \text{for} \quad i<k<j \\ &= pq^* c_j^\dagger Q_{ij} + c_i |q|^{2\Sigma_{m<j} N_m} f(N_j)(1-q'q^*) \quad \text{for} \quad i>j=k \\ &= pq c_i^\dagger Q_{ij} + |q|^{2\Sigma_{m<i} N_m} f(N_i) c_j (q - q'|q|^2) \quad \text{for} \quad k=i>j \end{aligned}\right\} \tag{5.30}$$

Repeating the argument of form-invariance of Q_{ij}, we conclude

$$c_i c_j - q^{*^{-1}} c_j c_i = 0 \quad \text{for} \quad i>j \tag{5.31}$$

In this proof we have not used any particular form of $f(N_j)$, but have used only the standard commutation relations among N_k and c_i (eqs. (2.23) and (2.26)).

This derivation of the $c_i c_j$ relation for $i \neq j$ is valid for the bosonic as well as the fermionic Fock spaces. However, for the fermionic space, there exists the additional relation:

$$c_i c_i = 0 \tag{5.32}$$

To derive this, we now commute $c_k^\dagger$ through $c_i c_i$ using (5.27–5.28), we get

$$\left.\begin{aligned} c_i c_i c_k^\dagger &= q^{*2} c_k^\dagger c_i c_i \quad \text{for} \quad i>k \\ &= q^2 c_k^\dagger c_i c_i \quad \text{for} \quad k>i \\ &= p^2 c_i^\dagger c_i c_i + |q|^{2\Sigma_{m<i} N_m} c_i \{ p f(N_i - 1) + f(N_i) \} \quad \text{for} \quad i=k \end{aligned}\right\} \tag{5.33}$$

So, for the validity of (5.32), we require

$$c_i \{ p f(N_i - 1) + f(N_i) \} = 0 \tag{5.34}$$

Substituting the form of $f(N_i)$ for the fermionic Fock space (from eq. (4.24))

$$f(N_i) = |r|^2 (\delta_{N_i,0} - p \delta_{N_i,1}), \tag{5.35}$$

we see that (5.34) is satisfied, since in the fermionic Fock space, $\delta_{N_i,2} = 0$ and $c_i \delta_{N_i,0} = 0$.

One may also note that (5.34) is also satisfied for $p = -1$ and $f(N_i) =$ constant (which may be chosen to be unity). So, for bosonic Fock space, i.e. $c_i c_i \neq 0$, we must avoid $p = -1$ in (5.28) and (4.15).

The above derivations of cc relations have used the general $cc^\dagger$ algebra and hence includes the cases of quantum-group-covariant algebras, independent deformed oscillators, commuting fermions, anticommuting bosons etc. Further, it must be noted that the presence of the term with the factor $|q|^{2\Sigma_{i<j}N_i}$ in (5.28) is crucial for the validity of the cc relations; without this factor, there will be no cc relation and we will get infinite statistics.

6. Two-indexed systems

We have so far considered generalized Fock spaces consisting of states $|n_g, n_h, \ldots, ; \mu\rangle$ where the indices $g, h, \ldots$ may refer either to a single quantum number, or to a collection of quantum numbers, specifying the space, spin and other internal degrees of freedom. In the latter case, it may be supposed that one has mapped a collection of indices to a single index. What is envisaged in this section are situations where such mapping is not possible. This can happen in various ways. To be specific, let us consider oscillators with a pair of indices, a latin index $(g, h, \ldots)$ and a greek index $(\alpha, \beta \ldots)$. There exists a class of systems in which the occupation numbers with a single index n_g or n_α are defined, but occupation numbers with both the indices $n_{g\alpha}$ are not defined. Such systems cannot be mapped into single-indexed systems. In another class of systems, $n_{g\alpha}$ do exist, but the subsidiary conditions that define the reduced Fock space depend on the two indices g and α in such a way that prevents mapping of (g, α) into a single index. We consider these two classes of systems in subections 6.1 and 6.2 respectively.

In may also be mentioned that we first encountered such systems in the study of the Hubbard model in the limit of infinite Coulomb repulsion [43–46]. Although this was our original motivation, this has now opened the door to a more general framework encompassing novel forms of statistics and algebras.

6.1 *Systems in which $n_{g\alpha}$ do not exist*

We specify the states as $|n_g, n_h \ldots; n_\alpha, n_\beta \ldots; \mu\rangle$, where $n_g, n_h \ldots$ are the numbers of quanta with indices $g, h \ldots$ respectively, while $n_\alpha, n_\beta, \ldots$ are the numbers of quanta with indices $\alpha, \beta \ldots$ respectively and we have the constraint:

$$n_g + n_h + \ldots = n_\alpha + n_\beta + \ldots \tag{6.1}$$

We may regard n_g as the total number of quanta with index g whatever may be their greek index and similarly for n_α. In such a state, the occupancy number with both indices such as $n_{k\alpha}$ is not defined. The latin indices and the greek indices are independently permutated and this leads to a much enlarged space in each sector. Now μ goes over $1 \ldots s'$ where

$$s' = \frac{(n_g + n_h + \ldots)!}{n_g! n_h! \ldots} \times \frac{(n_\alpha + n_\beta + \ldots)!}{n_\alpha! n_\beta! \ldots} \tag{6.2}$$

$$s = \frac{}{n_{g\alpha}! n_{h\beta}! \ldots} \tag{6.3}$$

In general, s' is larger than s.

Let us consider the two-particle sector as an example. If we specify occupation numbers with both indices, we have the two states in the sector $(1_{k\alpha}, 1_{m\beta})$: $|1_{k\alpha}, 1_{m\beta}; \mu\rangle$ with $\mu = 1$ or 2 which correspond to $|1_{k\alpha}, 1_{m\beta}\rangle$ and $|1_{m\beta}, 1_{k\alpha}\rangle$ and another two states in the sector $(1_{m\alpha}, 1_{k\beta})$: $|1_{m\alpha}, 1_{k\beta}; \mu\rangle$ with $\mu = 1$ or 2 corresponding to $|1_{m\alpha}, 1_{k\beta}\rangle$ and $|1_{k\beta}, 1_{m\alpha}\rangle$. (Here we are not using $k\alpha, m\beta$ etc. in their generic sense; they are used to denote specific values of the indices). On the other hand, with the new type of states with decoupled indices for which occupation number with both indices do not exist, we have the two-particle states $|1_k, 1_m; 1_\alpha, 1_\beta; \mu\rangle$ and now μ goes over 1 to 4 corresponding to the four state vectors $|1_{k\alpha}, 1_{m\beta}\rangle$, $|1_{m\beta}, 1_{k\alpha}\rangle$, $|1_{m\alpha}, 1_{k\beta}\rangle$, $|1_{k\beta}, 1_{m\alpha}\rangle$. Thus, both the sectors considered earlier are combined to form a single enlarged sector. Such a regrouping of sectors with consequent enlargement occurs throughout the Fock space, in the case of the decoupled indices.

The construction of the orthonormal set as well as the other properties of the generalized Fock spaces given in § 2 goes through for the present case of decoupled indices also except that the matrices X, M etc. will be of higher dimensions. The creation and destruction operators $c^\dagger_{k\alpha}, c_{k\alpha}$ also can be constructed in the same way as in § 2. The relevant equations and formulae with the appropriate changes incorporated are given in Appendix A. They are self-explanatory.

Just as in the case of single-indexed systems (cf. § 2), we can again have a super Fock space in which all the states connected by independent permutation of the latin and greek indices are taken to be independent. We shall call the associated statistics as 'doubly-infinite' statistics since it is infinite statistics in latin and greek indices separately. By imposing relations among the permutated states, one can get many kinds of reduced Fock spaces. Because of the larger number of available states in each sector, many new types of statistics become possible. These can be discussed and the associated algebras can be constructed by the same procedure as in § 3, 4 and 5. However, we shall be brief and restrict ourselves to presenting some of the important results only. Some of these algebras and the new kinds of statistics implied by them have been discussed by us in greater detail in the earlier papers [18, 19, 46].

Doubly-infinite statistics

Consider the $cc^\dagger$ algebra described by

$$c_{k\alpha} c^\dagger_{m\beta} - q\delta_{\alpha\beta} \sum_{\gamma} c^\dagger_{m\gamma} c_{k\gamma} = \delta_{km}\delta_{\alpha\beta} \tag{6.4}$$

where q is a real parameter lying in the range

$$-1 < q < 1. \tag{6.5}$$

It is the second term on the left of (6.4) in which α and β have been dissociated from k and m respectively that leads to the decoupling of the latin and greek indices and

prevents the mapping of latin and greek indices to a single index. One can show [19] that the inner-product matrices following from this algebra are all positive-definite for $-1 < q < 1$. Further, one can show using arguments similar to those in § 5 that there is no *cc* relation for this algebra in the same parameter range and so all the states connected by *independent* permutation of the latin and greek indices are independent. The underlying Fock space is the full super Fock space of dimension given by (6.2) and we have infinite statistics in latin and greek indices separately, or doubly-infinite statistics.

For $q = 0$ in (6.4), the two indices can be mapped into a single index and the algebra reduces to the standard representation of single-indexed infinite statistics described in § 3.1.

The algebra of (6.4) is covariant under the unitary transformations on the latin indices:

$$d_{k\alpha} = \sum_m U_{km} c_{m\alpha}; \quad U^\dagger U = UU^\dagger = 1 \tag{6.6}$$

as well as under separate unitary transformations on the greek indices:

$$e_{k\alpha} = \sum_\lambda V_{\alpha\lambda} c_{k\lambda}; \quad V^\dagger V = VV^\dagger = 1. \tag{6.7}$$

But the algebra is not covariant under the enlarged unitary transformations involving both the latin and greek indices (for $q \neq 0$). A special case of the unitary transformations of (6.6) and (6.7) is the phase transformation. Equation (6.4) is covariant under either of the following phase transformations:

$$d_{k\alpha} = e^{i\phi_k} c_{k\alpha} \tag{6.8}$$

$$e_{k\alpha} = e^{i\phi_\alpha} c_{k\alpha} \tag{6.9}$$

As a consequence, the number operators N_k and N_α exist. However, (6.4) is not covariant under the transformation:

$$f_{k\alpha} = e^{i\phi_{k\alpha}} c_{k\alpha} \tag{6.10}$$

and correspondingly, $N_{k\alpha}'$ does not exist.

We can make q in (6.4) complex provided we order the latin indices and thus we get an algebra which is the analogue of the q-mutator algebra with complex q for the single-indexed systems (§ 3):

$$c_{i\alpha} c_{j\beta}^\dagger - q\delta_{\alpha\beta} \sum_\gamma c_{j\gamma}^\dagger c_{i\gamma} = 0 \quad \text{for} \quad i < j \tag{6.11}$$

$$c_{j\alpha} c_{j\beta}^\dagger - p\delta_{\alpha\beta} \sum_\gamma c_{j\gamma}^\dagger c_{j\gamma} = \delta_{\alpha\beta} \tag{6.12}$$

where q is complex, but p is real. This again describes the same doubly-infinite statistics; only the representation and algebra are different. This algebra is no longer covariant under the unitary transformations of (6.6) and (6.7), but is still covariant under the phase transformations of (6.8) and (6.9). Positivity of the inner-product matrices M requires $|q| < 1$. As for p, similar statements as in § 3 can be made.

Coming back to (6.4), at the boundary of the range of q given in (6.5), namely at $q = \pm 1$, we get two new forms of statistics called orthobose and orthofermi statistics [18, 19, 46] which reside in reduced Fock spaces defined by cc relations. The algebras for these are given below:

Orthobose statistics:

$$c_{k\alpha}c^{\dagger}_{m\beta} - \delta_{\alpha\beta}\sum_{\gamma} c^{\dagger}_{m\gamma}c_{k\gamma} = \delta_{km}\delta_{\alpha\beta} \tag{6.13}$$

$$c_{k\alpha}c_{m\beta} - c_{m\alpha}c_{k\beta} = 0. \tag{6.14}$$

Orthofermi statistics:

$$c_{k\alpha}c^{\dagger}_{m\beta} + \delta_{\alpha\beta}\sum_{\gamma} c^{\dagger}_{m\gamma}c_{k\gamma} = \delta_{km}\delta_{\alpha\beta} \tag{61.5}$$

$$c_{k\alpha}c_{m\beta} + c_{m\alpha}c_{k\beta} = 0. \tag{6.16}$$

The inner product matrices M for the reduced Fock spaces generated by these algebras (eqs. (6.13)–(6.16)) can be shown to be positive. In both these statistics, any two states obtained by permuting the greek indices are independent. On the other hand, states obtained by permuting the latin indices are either equal to each other, or related by $(-1)^J$ where J is the number of inversions in the permutation of the latin indices, for the orthobose or orthofermi statistics respectively. Thus, we have infinite statistics in the greek indices and Bose or Fermi statistics in the latin indices. For orthofermi statistics, we have the further condition:

$$n_k = 0 \text{ or } 1 \text{ only.} \tag{6.17}$$

It must be noted that the exclusion implied by (6.17) is stronger than the usual Pauli exclusion principle; (6.17) requires that there cannot be more than one particle with index k whatever may be its greek index.

We have constructed a local relativistic quantum field theory [47] based on orthostatistics. It may be worth mentioning that although orthostatistics does involve infinite statistics, the problems faced by finite statistics are avoided by associating the latin index (pertaining to Fermi or Bose statistics) with the conventional degrees of freedom such as momentum and spin and assigning the greek index (of infinite statistics) to a new degree of freedom.

Orthostatistics can be generalized to q-orthostatistics. We keep the infinite statistics in the greek indices but have q-bose or q-fermi statistics in the latin indices. More precisely, we must regard these as q-orthostatistics lying in orthobosonic and orthofermionic Fock spaces. We can call them q-orthobose or q-orthofermi statistics.

q-Orthobose statistics:

$$c_{i\alpha}c^{\dagger}_{j\beta} + q\delta_{\alpha\beta}\sum_{\gamma} c^{\dagger}_{j\gamma}c_{i\gamma} = 0 \quad \text{for} \quad i<j \tag{6.18}$$

$$c_{j\alpha}c^{\dagger}_{j\beta} - |q|^2\delta_{\alpha\beta}\sum_{\gamma} c^{\dagger}_{j\gamma}c_{j\gamma} = \delta_{\alpha\beta} + \delta_{\alpha\beta}(|q|^2 - 1)\sum_{k<j}\sum_{\gamma} c^{\dagger}_{k\gamma}c_{k\gamma} \tag{6.19}$$

$$c_{i\alpha}c_{j\beta} + q^* c_{j\alpha}c_{i\beta} = 0 \quad \text{for} \quad i<j \tag{6.20}$$

q-Orthofermi statistics:

$$c_{i\alpha}c^{\dagger}_{j\beta} + q\delta_{\alpha\beta}\sum_{\gamma} c^{\dagger}_{j\gamma}c_{i\gamma} = 0 \quad \text{for} \quad i<\mathrm{j} \tag{6.21}$$

$$c_{j\alpha}c^{\dagger}_{j\beta} + \delta_{\alpha\beta}\sum_{\gamma} c^{\dagger}_{j\gamma}c_{j\gamma} = \delta_{\alpha\beta} + \delta_{\alpha\beta}(|q|^2-1)\sum_{k<j}\sum_{\gamma} c^{\dagger}_{k\gamma}c_{k\gamma} \tag{6.22}$$

$$c_{i\alpha}c_{j\beta} + q^{*}c_{j\alpha}c_{i\beta} = 0 \quad \text{for} \quad i<j \tag{6.23}$$

$$c_{j\alpha}c_{j\beta} = 0 \tag{6.24}$$

In (6.18)–(6.24), q is an arbitrary complex parameter. For $q = e^{i\theta}$, and $q = 0$ we shall have fractional statistics and statistics of frozen order respectively, but in the latin indices only. Of course one can construct many other algebras corresponding to the same statistics, just as in the case of the single-indexed systems.

Further, these equations are analogous to (4.3), (4.12), (4.23) and (4.28) which are covariant under quantum groups. So, another direction is indicated here for the further generalization of quantum-group-theoretic structures to two-indexed systems.

6.2 *Systems in which $n_{g\alpha}$ exist*

We shall now consider a different kind of double-indexed systems. Here, the occupation numbers $n_{g\alpha}$ exist, nevertheless mapping to single-indexed systems is not possible because of the subsidiary conditions that define the reduced Fock space. We give below three examples of such double-indexed systems, described by the algebras:

(a)

$$c_{k\alpha}c^{\dagger}_{m\beta} + (1-\delta_{km})c^{\dagger}_{m\beta}c_{k\alpha} = \delta_{km}\delta_{\alpha\beta}\left(1 - \sum_{\gamma} c^{\dagger}_{k\gamma}c_{k\gamma}\right) \tag{6.25}$$

$$c_{k\alpha}c_{m\beta} + (1-\delta_{km})c_{m\beta}c_{k\alpha} = 0. \tag{6.26}$$

(b)

$$c_{k\alpha}c^{\dagger}_{m\beta} - (1-\delta_{km})c^{\dagger}_{m\beta}c_{k\alpha} = \delta_{km}\delta_{\alpha\beta}\left(1 + \sum_{\gamma} c^{\dagger}_{k\gamma}c_{k\gamma}\right) \tag{6.27}$$

$$(1-\delta_{km})(c_{k\alpha}c_{m\beta} - c_{m\beta}c_{k\alpha}) = 0. \tag{6.28}$$

(c)

$$c_{k\alpha}c^{\dagger}_{m\beta} - (1-\delta_{km})c^{\dagger}_{m\beta}c_{k\alpha} = \delta_{km}\delta_{\alpha\beta}\left(1 - \sum_{\gamma} c^{\dagger}_{k\gamma}c_{k\gamma}\right) \tag{6.29}$$

$$c_{k\alpha}c_{m\beta} - (1-\delta_{km})c_{m\beta}c_{k\alpha} = 0. \tag{6.30}$$

Each of these algebras is covariant under the unitary transformation on the greek indices defined by (6.7), but not covariant under the unitary transformation on the latin indices defined by (6.6). However, all of them are covariant under not only the phase transformations in (6.8) and (6.9) but also the $k\alpha$-dependent phase transformation of (6.10), hence all the occupation numbers n_k, n_α as well as $n_{k\alpha}$ exist.

Algebra (a) leads to states which are antisymmetric for simultaneous interchange of latin and greek indices as in Fermi–Dirac statistics, but the usual Pauli exclusion principle is replaced by the stronger or more exclusive exclusion principle, as in

orthofermi statistics (see eq. (6.17)):

$$n_k = 0 \text{ or } 1 \text{ only}, \tag{6.31}$$

where

$$n_k \equiv \sum_\alpha n_{k\alpha} \tag{6.32}$$

These are precisely the states that are allowed in the Hubbard model of strongly correlated electrons in the limit of infinite intrasite Coulomb repulsion if we interpret the latin index as the site and the greek index as the spin. Hence, this algebra and the statistics can be called Hubbard algebra and Hubbard statistics respectively. For more details, the reader is referred to [46]. Since $n_{k\alpha}$ exists, the states of the system can be

Table 4. Statistics and algebras for 2-indexed systems.

$N_{k\alpha}$	Statistics in latin indices	Statistics in greek indices	$cc^\dagger$ algebra
Do not exist	infinite	infinite	$c_{k\alpha}c^\dagger_{m\beta} - q\delta_{\alpha\beta}\sum_\gamma c^\dagger_{m\gamma}c_{k\gamma} = \delta_{km}\delta_{\alpha\beta}$ (real q)
"	"	"	$c_{k\alpha}c^\dagger_{m\beta} - q\delta_{\alpha\beta}\sum_\gamma c^\dagger_{m\gamma}c_{k\gamma} = 0$, for $k<m$ $c_{k\alpha}c^\dagger_{k\beta} - p\delta_{\alpha\beta}\sum_\gamma c^\dagger_{k\gamma}c_{k\gamma} = \delta_{\alpha\beta}$ (complex q and real p)
"	Fermi/Bose	"	$c_{k\alpha}c^\dagger_{m\beta} \pm \delta_{\alpha\beta}\sum_\gamma c^\dagger_{m\gamma}c_{k\gamma} = \delta_{km}\delta_{\alpha\beta}$
"	q-fermi/ q-bose	"	$c_{i\alpha}c^\dagger_{j\beta} - q\delta_{\alpha\beta}\sum_\gamma c^\dagger_{j\gamma}c_{i\gamma} = 0$ for $i<j$ $c_{j\alpha}c^\dagger_{j\beta} - x\delta_{\alpha\beta}\sum_\gamma c^\dagger_{j\gamma}c_{j\gamma}$ $= \delta_{\alpha\beta} + \delta_{\alpha\beta}(\lvert q\rvert^2 - 1)\sum_{k<j}\sum_\gamma c^\dagger_{k\gamma}c_{k\gamma}$ $x = \lvert q\rvert^2$ for q-bose; $x = -1$ for q-fermi
Exist	Antisymmetric for total exchange, but $n_k \leqslant 1$		$c_{k\alpha}c^\dagger_{m\beta} + (1-\delta_{km})c^\dagger_{m\beta}c_{k\alpha} = \delta_{km}\delta_{\alpha\beta}\left(1 - \sum_\gamma c^\dagger_{k\gamma}c_{k\gamma}\right)$
"	Symmetric for total exchange for $k \neq m$, but infinite statistics in greek indices for $k = m$		$c_{k\alpha}c^\dagger_{m\beta} - (1-\delta_{km})c^\dagger_{m\beta}c_{k\alpha} = \delta_{km}\delta_{\alpha\beta}\left(1 + \sum_\gamma c^\dagger_{k\gamma}c_{k\gamma}\right)$
"	Symmetric for total exchange but $n_k \leqslant 1$		$c_{k\alpha}c^\dagger_{m\beta} - (1-\delta_{km})c^\dagger_{m\beta}c_{k\alpha} = \delta_{km}\delta_{\alpha\beta}\left(1 - \sum_\gamma c^\dagger_{k\gamma}c_{k\gamma}\right)$

which can be rewritten in the form:

$$\sum_{\alpha} n_{k\alpha} = 0 \text{ or } 1 \text{ only} \tag{6.33}$$

this system cannot be mapped into a single-indexed system.

Algebra (b) can be regarded as the bosonic 'counterpoint' of algebra (a). States are symmetric under simultaneous exchange of latin and greek indices for quanta with different latin indices ($k \neq m$). But for quanta with identical latin indices ($k = m$), there is no restriction on the symmetry with respect to the greek indices. In other words, there is infinite statistics in greek indices if the corresponding latin indices are identical. Whereas algebra (a) leads to more exclusive states than allowed by Pauli, algebra (b) leads to 'more inclusive' states than allowed by Bose. For this reason we may call algebra (b) as the 'inclusive counterpoint' to algebra (a). Such a restriction on the allowed states of a two-indexed system which distinguishes $k = m$ from $k \neq m$ cannot be mapped into a condition for a single-indexed system.

Finally, algebra (c) leads to states that are symmetric for simultaneous exchange of latin and greek indices, but the stronger exclusion principle of (6.33) is also valid as in algebra (a). Hence, algebras (a) and (c) represent two forms of statistics which may be called antisymmetric and symmetric Hubbard statistics respectively both residing within the same reduced Fock space. On the other hand, algebra (b) and its statistics lie in a different reduced Fock space which is a Fock space with the new 'inclusion' principle.

A compilation of the algebras and statistics for two-indexed systems is given in table 4. The cc relations are not included since they can be shown to follow from the $cc^\dagger$ algebra, whenever they exist.

7. Summary and discussion

We have formulated a theory of generalized Fock spaces which is sufficiently general so as to encompass the well-known Fock spaces and many newer ones. We have shown that such a theory can be constructed without introducing creation and annihilation operators. The only requirements for constructing a generalized Fock space are to specify the set of allowed states, and to make it an inner product space. By freeing the notion of the underlying state space from c and $c^\dagger$, we are able to define different forms of quantum statistics in a representation independent manner. Subsequently, one can construct c and $c^\dagger$ and their algebras in any desired representation.

Our general formalism not only unifies the various forms of statistics and algebras proposed so far but also allows one to construct many new forms of quantum statistics as well as algebras of c and $c^\dagger$ in a systematic manner. Some of these are the following:

(a) Many new algebras for infinite statistics
(b) Complex q-statistics and a number of $cc^\dagger$ algebras representing them
(c) A consistent algebra of c and $c^\dagger$ for 'fractional' statistics
(d) Null statistics or statistics of frozen order
(e) 'Doubly-infinite' statistics and its representations
(f) q-orthobose and q-orthofermi statistics

(g) A statistics for two-indexed systems with a new 'inclusion principle'.
(h) A symmetric version of Hubbard statistics.

Our primary concept is that of generalized Fock space, of which many categories have been introduced in this paper. Next comes the notion of statistics which is defined by the type of symmetry or relationship among the state vectors residing in the particular type of Fock space. In a given Fock space, more than one type of symmetry can be postulated, the prime example of this being the symmetry, antisymmetry or q-symmetry in the bosonic and fermionic Fock spaces. For a given statistics, there can exist different representations of c and $c^\dagger$, leading to different $cc^\dagger$ relations. To summarize, a particular Fock space can admit different statistics, and a particular statistics can be represented by more than one $cc^\dagger$ algebra. But *the important point is that various statistics and algebras residing in a given Fock space are all interelated.*

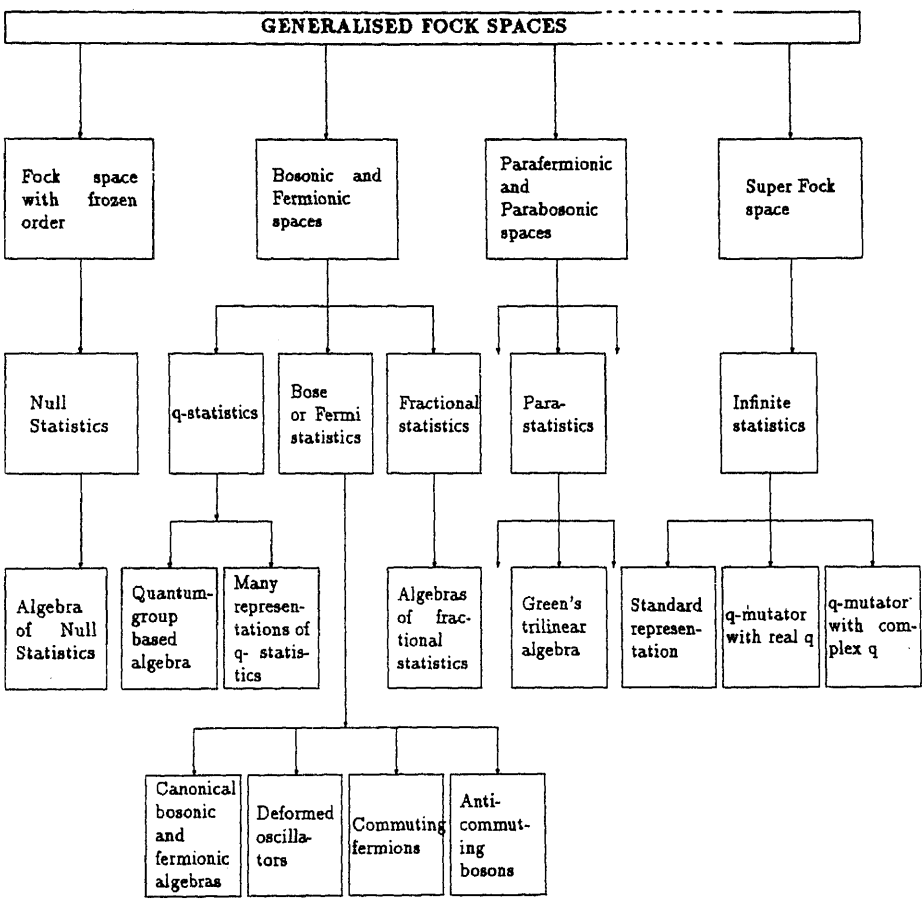

Figure 3. Generalized Fock spaces, quantum statistics, algebras and their inter-

These interconnections are given by generalized versions of the well-known Jordan–Wigner–Klein transformations. No such interconnections exist among statistics and algebras belonging to distinct Fock spaces. We must further add that equilibrium thermodynamics of a system of free particles is the same for all the different statistics and algebras within the same Fock space.

For the sake of clarity, the above-described logical order of concepts as well as their logical interconnections are presented in the form of flow charts or block diagrams in figures 3 and 4. The single-indexed systems are considered in figure 3. The Fock spaces of higher dimension are shown to the right of those of lower dimension. The Fock space of frozen order as well as the bosonic and fermionic Fock spaces have the lowest dimension $d = 1$ in any sector $\{n_g, n_h \ldots\}$. Next come the parafermionic and parabosonic Fock spaces which have $d > 1$. At the extreme right, we have the super Fock space which has the largest dimension $d = s$ in each sector with s given by (2.6). Null statistics and infinite statistics can be regarded as the opposite limiting cases of generalized statistics and hence these two forms of statistics along with their Fock spaces occupy the opposite ends of the diagram. Although not shown separately

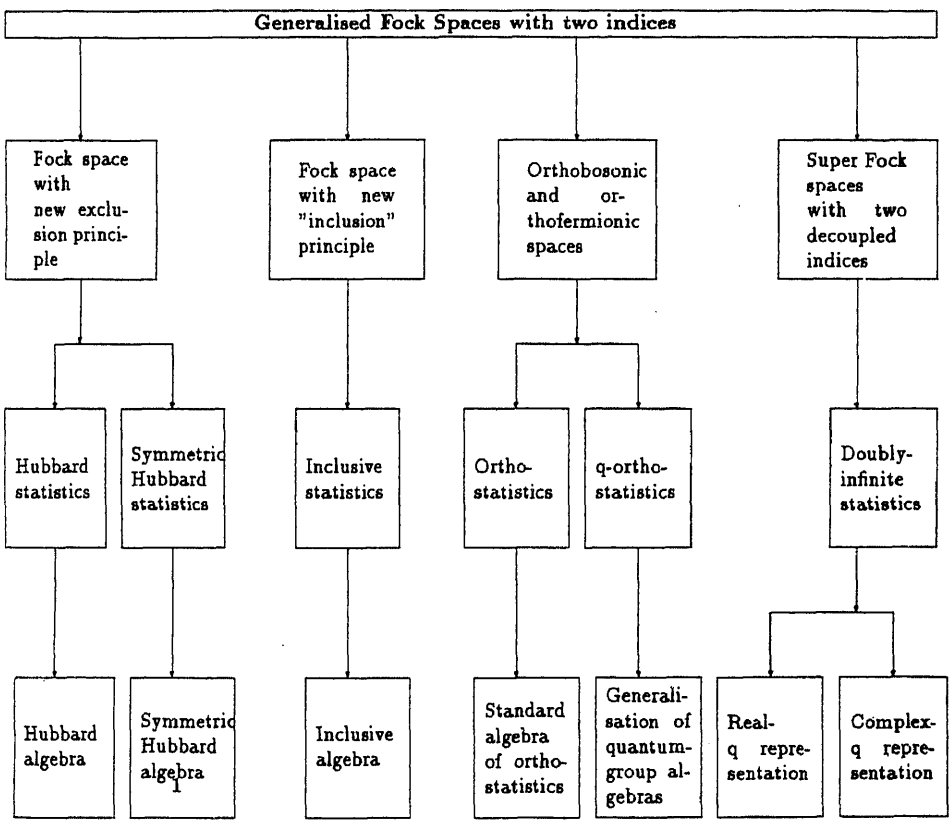

Figure 4. Same as figure 3 for systems with two indices that cannot be mapped into a single index.

in figure 3 because of lack of space, the bosonic and fermionic Fock spaces are distinct and each must be separately associated with the complete set of statistics and algebras shown. Same is true of the parabosonic and parafermionic Fock spaces. Further, there are two Fock spaces of frozen order, the bosonic and fermionic type. And finally, there exists another super Fock space with exclusion principle, which is not shown separately.

Within the parafermionic and parabosonic Fock spaces many 'deformations' of parastatistics and many other representations and algebras apart from Green's trilinear algebra [35] are possible. These are indicated by the hanging arrows in figure 3. Further, as shown by the dotted lines, there is enough room for many new varieties of Fock spaces and associated statistics and algebras. These possibilities may be pursued in the future.

Coming to figure 4 depicting the systems with two indices, here again Fock spaces of higher dimension generally lie to the right. Although shown together, the orthobosonic and orthofermionic Fock spaces must be regarded distinct. Here, one can envisage a richer harvest of new Fock spaces, statistics and algebras because of the two indices and this again is for the future.

We now conclude with some general comments:

1. We must once again repeat and emphasize the point that most of the q-deformations on oscillators discussed in the literature amount to only a change of variable and hence must be regarded as different avatars of bosonic or fermionic systems. However, one must clearly distinguish those deformations such as the q-mutator algebra of Greenberg that require the construction of new types of Fock spaces. Obviously, Greenberg-type of deformations can never be reduced to change of variables living within the bosonic or fermionic Fock space. Some degree of confusion prevails in recent literature since this distinction is not kept in mind. (see for instance [7, 32, 41, 42, 48]).
2. In §4, we have shown that algebras that are covariant under quantum groups are only a particular case of the more general class of algebras that can be derived from the formalism of generalized Fock spaces. This formalism is based on linear vector space and linear operators acting on this space; mathematically, no more sophistication is required. And yet it is capable of handling quantum-group related structures in a self-contained manner. It would seem that the basic concepts of quantum groups are contained in the theory of generalized Fock spaces and it must be possible to construct quantum group itself starting from this theory.
3. We have already referred to the desirability of covariance under unitary transformations that mix the indices as a requirement for the algebras of creation and annihilation operators. We shall call the algebras that statisfy this requirement as covariant algebras. This property stems from the superposition principle in quantum mechanics. Since the indices describe quantum states of a single particle, if we demand that, for any orthonormal set of quantum states obtained by superposition of the original set of quantum states, the algebra should retain the same form, then covariance under unitary transformations follows. Many of the algebras presented in this paper violate this requirement. Nevertheless, these algebras may be useful to describe specific systems in specific states such as those encountered in condensed matter physics.

Some of these noncovariant algebras do have other nice physical and mathematical properties. Under this category, we may include the algebras that are covariant under quantum groups or the algebras representing braid group statistics [49, 50].

Among the algebras for single-indexed systems that have been discussed, Greenberg's q-mutator algebra is the only q-deformation that is covariant under unitary transformations, but then one has to pay the price of the enlarged Fock space. Every other known q-deformation leads to a noncovariant algebra.

Greenberg's q-mutator algebra (including the case $q=0$ which is the standard representation), the canonical bosonic and fermionic algebras and Green's trilinear algebras for parabosons and parafermions are the covariant representatives living respectively in the super Fock space, bosonic and fermionic Fock spaces and the parabosonic and parafermionic Fock spaces. All the other algebras living in these three categories of Fock spaces, although noncovariant, can be transformed to these covariant algebras through equations such as (4.32). This is not the case for the algebra of null statistics or the algebra of infinite statistics with Pauli principle living respectively in the Fock space of frozen order and the super Fock space with Pauli principle. In these Fock spaces, covariant algebras do not exist.

4. Quantum mechanics is sometimes viewed as a deformation of classical mechanics since the commutator bracket of quantum mechanics can be related to the deformation of the classical Poisson bracket, the Planck's constant playing the role of the deformation parameter. Relying on similar reasoning it has been proposed that a deformation of canonical commutation relations will lead to fundamentally new mathematical or physical structures [51–53]. The analysis presented in this paper shows that nothing of this sort happens, if viewed within the framework of Fock space. The transition from classical to quantum mechanics requires the replacement of the notion of the phase space by that of the Hilbert space or Fock space. In contrast, we have seen that all the deformations of commutation relations can be formulated within the framework of Fock space. In fact most of the deformed structures proposed in the literature exist within the time-honoured bosonic and fermionic Fock spaces only. Even Greenberg's infinite statistics lives within a Fock space, although an enlarged one.

5. While remaining within the framework of quantum mechanics, the general theory of Fock spaces presented here throws light on the enlarged framework within which the familiar quantum field theory and statistical mechanics reside and hence may lead to newer forms of quantum field theory and statistical mechanics. This is infact the main motivation behind our work. Apart from earlier work on parastatistics [37], we may mention as examples of new forms of quantum field theories, Greenberg's construction [13, 14, 54] of a non-relativistic quantum field theory based on infinite statistics and our construction [47] of a local relativistic quantum field theory based on orthostatistics. Many other forms of quantum field theories based on the generalized Fock spaces may be possible. Their formulation and study is an agenda for the future.

6. One may not be able to construct local relativistic quantum field theories corresponding to many of the newer forms of statistics and algebras, since admissible statistics in relativistic systems is severely restricted by the axioms of local quantum physics [55]. However, nonrelativistic quantum field theories based on such 'inadmissible' statistics are still possible. Condensed matter physics is a rich field where

applications of such theories may be relevant. In fact there is no reason why the quasiparticles encountered in condensed matter systems should be bosons or fermions only. We have shown that any of the generalized Fock spaces provides a perfectly valid quantum-mechanical framework for many-particle systems. Hence, quasiparticles living in a generalized Fock space offer an important field of study.

Appendix A

Generalised Fock Spaces for Two-indexed Systems

Here we consider only those two-indexed systems in which $n_{g\alpha}$ do not exist. See §6.1.

The state vectors, inner products and orthonormal sets:

$$\langle n'_g, n'_h \ldots; n'_\alpha, n'_\beta \ldots; \mu | n_g, n_h \ldots; n_\alpha, n_\beta \ldots; \nu \rangle = \delta_{n'_g n_g} \delta_{n'_h n_h} \ldots \delta_{n'_\alpha n_\alpha} \delta_{n'_\beta n_\beta} \ldots M_{\mu\nu} \tag{A1}$$

$$\| n_g, n_h \ldots; n_\alpha, n_\beta \ldots; \mu \gg = \sum_\nu X_{\nu\mu} | n_g, n_h \ldots; n_\alpha, n_\beta \ldots; \nu \rangle \tag{A2}$$

$$\ll n'_g, n'_h \ldots; n'_\alpha, n'_\beta \ldots; \mu \| n_g, n_h \ldots; n_\alpha, n_\beta \ldots; \nu \gg = \delta_{n'_g n_g} \delta_{n'_h n_h} \ldots \delta_{n'_\alpha n_\alpha} \delta_{n'_\beta n_\beta} \ldots \delta_{\mu\nu} \tag{A3}$$

$$M^{-1} = XX^+ \tag{A4}$$

$$I = \sum_{\substack{n_g, n_h \ldots \\ n_\alpha, n_\beta \ldots}} \sum_\mu \| n_g, n_h \ldots; n_\alpha, n_\beta \ldots; \mu \gg \ll n_g, n_h \ldots; n_\alpha, n_\beta \ldots; \mu \| \tag{A5}$$

$$= \sum_{\substack{n_g, n_h \ldots \\ n_\alpha, n_\beta \ldots}} \sum_{\lambda, \nu} | n_g, n_h \ldots; n_\alpha, n_\beta \ldots; \nu \rangle (M^{-1})_{\nu\lambda} \langle n_g \ldots; n_\alpha \ldots; \lambda | \tag{A6}$$

Projection operators:

$$P(n_g, n_h \ldots; n_\alpha, n_\beta \ldots) = \sum_\mu \| n_g, n_h \ldots; n_\alpha, n_\beta \ldots; \mu \gg \ll n_g, n_h \ldots; n_\alpha, n_\beta \ldots; \mu \| \tag{A7}$$

$$= \sum_{\lambda, \nu} | n_g, n_h \ldots; n_\alpha, n_\beta \ldots; \nu \rangle (M^{-1})_{\nu\lambda} \langle n_g \ldots; n_\alpha \ldots; \lambda | \tag{A8}$$

$$I = \sum_{\substack{n_g, n_h \ldots \\ n_\alpha, n_\beta \ldots}} P(n_g, n_h \ldots; n_\alpha, n_\beta \ldots) \tag{A9}$$

$$P(n_g, n_h \ldots; n_\alpha, n_\beta \ldots) \| n'_g, n'_h \ldots; n'_\alpha, n'_\beta \ldots; \mu \gg = \delta_{n_g n'_g} \ldots \delta_{n_\alpha n'_\alpha} \ldots \| n_g \ldots; n_\alpha \ldots; \mu \gg \tag{A10}$$

$$P(n_g \ldots; n_\alpha \ldots) | n'_g \ldots; n'_\alpha \ldots; \mu \rangle = \delta_{n_g n'_g} \ldots \delta_{n_\alpha n'_\alpha} \ldots | n_g \ldots; n_\alpha \ldots; \mu \rangle \tag{A11}$$

Number operators:

$$N_k = \sum_{\substack{n_g \ldots n_k \ldots \\ n_\alpha \ldots}} n_k P(n_g \ldots n_k \ldots; n_\alpha \ldots) \tag{A12}$$

$$N_\beta = \sum_{\substack{n_g \ldots \\ n_\alpha, n_\beta \ldots}} n_\beta P(n_g \ldots; n_\alpha, n_\beta \ldots) \tag{A13}$$

$$N_k \| n_g \ldots n_k \ldots; n_\alpha, n_\beta \ldots; \mu \gg = n_k \| n_g \ldots n_k \ldots; n_\alpha, n_\beta \ldots; \mu \gg \tag{A14}$$

$$N_k | n_g \ldots n_k \ldots; n_\alpha, n_\beta \ldots; \mu \rangle = n_k | n_g \ldots n_k \ldots; n_\alpha, n_\beta \ldots; \mu \rangle \tag{A15}$$

$$N_\beta \| n_g \ldots n_k \ldots; n_\alpha, n_\beta \ldots; \mu \gg = n_\beta \| n_g \ldots n_k \ldots; n_\alpha, n_\beta \ldots; \mu \gg \tag{A16}$$

$$N_\beta | n_g \ldots n_k \ldots; n_\alpha, n_\beta \ldots; \mu \rangle = n_\beta | n_g \ldots n_k \ldots; n_\alpha, n_\beta \ldots; \mu \rangle \tag{A17}$$

$$[N_k, N_j] = [N_\alpha, N_\beta] = [N_k, N_\alpha] = 0 \quad \text{for any } k, j \text{ and any } \alpha, \beta \tag{A18}$$

Total number operator is

$$N = \sum_k N_k = \sum_\alpha N_\alpha \tag{A19}$$

Creation and destruction operators:

$$c^\dagger_{j\beta} = \sum_{\substack{n_g, n_j \ldots \\ n_\alpha, n_\beta \ldots}} \sum_{\mu' \nu} A_{\mu' \nu} | n_g \ldots (n_j + 1) \ldots; n_\alpha, n_\beta + 1 \ldots; \mu' \rangle \otimes \langle n_g \ldots n_j \ldots; n_\alpha, n_\beta \ldots \nu | \tag{A20}$$

$$[c^\dagger_{j\beta}, N_k] = - c^\dagger_{j\beta} \delta_{jk} \tag{A21}$$

$$[c^\dagger_{j\beta}, N_\alpha] = - c^\dagger_{j\beta} \delta_{\alpha\beta} \tag{A22}$$

For some particular μ,

$$|3_g, 2_h; 4_\alpha, 1_\beta; \mu \rangle = |1_{g\alpha} 1_{g\alpha} 1_{g\beta} 1_{h\alpha} 1_{h\alpha} \rangle = (c^\dagger_{g\alpha})^2 c^\dagger_{g\beta} (c^\dagger_{h\alpha})^2 |0\rangle \tag{A23}$$

$$c^\dagger_{j\beta} | n_g \ldots n_j \ldots; n_\alpha, n_\beta \ldots; \lambda \rangle = \underbrace{| 1_{j\beta}; n_g \ldots n_j \ldots; n_\alpha, n_\beta \ldots; \lambda \rangle}_{n_g \ldots n_j + 1 \ldots; n_\alpha, n_\beta + 1} \tag{A24}$$

$$\begin{aligned} c^\dagger_{j\sigma} | n_g \ldots n_j \ldots; n_\alpha \ldots n_\sigma \ldots; \lambda \rangle &= \sum_{\substack{n'_g \ldots n'_j \ldots \\ n'_\alpha \ldots n'_\sigma \ldots}} \sum_{\mu' \nu} A_{\mu' \nu} | n'_g \ldots (n'_j + 1) \ldots; n'_\alpha \ldots n'_\sigma + 1 \ldots; \mu' \rangle \\ &\quad \otimes \langle n'_g \ldots n'_j \ldots; n'_\alpha \ldots n'_\sigma \ldots; \nu | n_g \ldots n_j \ldots; n_\alpha \ldots n_\sigma \ldots; \lambda \rangle \end{aligned} \tag{A25}$$

$$= \sum_{\mu' \nu} A_{\mu' \nu} M_{\nu\lambda} | n_g \ldots (n_j + 1) \ldots; n_\alpha \ldots n_\sigma + 1 \ldots; \mu' \rangle \tag{A26}$$

$$\sum_\nu A_{\mu' \nu} M_{\nu\lambda} = \delta_{\mu'\lambda} \tag{A27}$$

$$A = M^{-1} \tag{A28}$$

$$c^\dagger_{j\sigma} = \sum_{\substack{n_g \ldots n_j \ldots \\ n_\alpha \ldots n_\sigma \ldots}} \sum_{\lambda \nu} (M^{-1})_{\lambda\nu} | 1_{j\sigma}; n_g \ldots n_j \ldots; n_\alpha \ldots n_\sigma \ldots; \lambda \rangle \otimes \langle n_g \ldots n_j \ldots; n_\alpha \ldots n_\sigma \ldots; \nu | \tag{A29}$$

References

[1] L C Biedenharn, *J. Phys.* **A22**, L873 (1989)
[2] A J Mcfarlane, *J. Phys.* **A22**, 4581 (1989)
[3] K Odaka, T Kishi and S Kamefuchi, *J. Phys.* **A24**, L591 (1991)
[4] R N Mohapatra, *Phys. Lett.* **B242**, 407 (1990)
[5] M Arik and D D Coon, *J. Math. Phys.* **17**, 705 (1976)
[6] S Chaturvedi and V Srinivasan, *Phys. Rev.* **A44**, 8024 (1992)
[7] S Chaturvedi, A K Kapoor, R Sandhya, V Srinivasan and R Simon, *Phys. Rev.* **A43**, 4555 (1991)
[8] R Parthasarathy and K S Viswanathan, *J. Phys.* **A24**, 613 (1991)
[9] K S Viswanathan, R Parthasarathy and R Jagannathan, *J. Phys.* **A25**, L335 (1992)
[10] M Arik, *Z. Phys.* **C51**, 627 (1991)
[11] T Brzezinski, I L Egusquiza and A J Macfarlane, *Phys. Lett.* **B311**, 202 (1993)
[12] R Chakrabarti and R Jagannathan, *J. Phys.* **A25**, 6393 (1992)
[13] O W Greenberg, *Phys. Rev. Lett.* **64**, 407 (1990)
[14] O W Greenberg, *Phys. Rev.* **D43**, 4111 (1991)
[15] D I Fivel, *Phys. Rev. Lett.* **65**, 3361 (1990)
[16] D Zagier, *Commun. Math. Phys.* **147**, 210 (1992)
[17] S Stanciu, *Commun. Math. Phys.* **147**, 147 (1992)
[18] A K Mishra and G Rajasekaran, *Pramana – J. Phys.* **38**, L411 (1992)
[19] A K Mishra and G Rajasekaran, *Pramana – J. Phys.* **40**, 149 (1993); *Phys. Lett.* **A188**, 210 (1994)
[20] R F Werner, *Phys. Rev.* **D48**, 2929 (1993)
[21] S L Woronowicz, *Commun. Math. Phys.* **111** 613 (1987); Publ. RIMS Kyoto University **23**, 117 (1987)
[22] W Pusz and S L Woronowicz, *Rep. Math. Phys.* **27**, 231 (1989)
[23] W Pusz, *Rep. Math. Phys.* **27**, 349 (1989)
[24] M Chaichian, P Kulish and J Lukierski, *Phys. Lett.* **B262**, 43 (1991)
[25] M Chaichian and P Kulish, in *Nonperturbative methods in low-dimensional quantum field theories* (Proc. 14th John Hopkins Workshop on Current Problems in Particle Theory, Debrecen, Hungary, 1990) (World Sci. Pub. Co., River Edge, NJ, 1991) p. 213
[26] R Jagannathan, R Sridhar, R Vasudevan, S Chaturvedi, M Krishnakumari, P Santha and V Srinivasan, *J. Phys.* **A25**, 6429 (1992)
[27] E G Floratos, *J. Phys.* **A24**, 4739 (1991)
[28] S K Soni, *J. Phys.* **A24**, L169 (1991)
[29] A Schirrmacher, *Z. Phys.* **C50**, 321 (1991)
[30] B Zumino, preprint (1991) LBL-30120, UCB-PTH-91/1
[31] A Shirrmacher, J Wess and B Zumino, *Z. Phys.* **C49**, 317 (1991)
[32] L Hlavaty, *Czek. J. Phys.* **42**, 1331 (1992)
[33] D B Fairlie and C K Zachos, *Phys. Lett.* **B256**, 43 (1991)
[34] A K Mishra and G Rajasekaran, Preprint IMSc/20-1993
[34a] Eq. (2.13) is analogous to the relation between the metric tensor and the vierbien in general relativity.
[35] H S Green, *Phys. Rev.* **90**, 270 (1953)
[36] O W Greenberg and A M L Messiah, *Phys. Rev.* **B136**, 248 (1964)
[37] Y Ohnuki and S Kamefuchi, *Quantum field theory and parastatistics*, (Springer-Verlag, Berlin–Heidelberg–New York, 1982)
[38] J Cuntz, *Commun. Math. Phys.* **51**, 173 (1977)
[38a] On applying both sides of (4.14) on the vacuum state, the left hand side vanishes and so for consistency, $\phi(-1) = 0$
[39] J M Leinass and J Myrheim, *Nuovo Cimento.* **B37**, 1 (1977)
[40] F Wilczek, *Phys. Rev. Lett.* **48**, 1144 (1982); **49**, 957 (1982)
[41] G S Agarwal and S Chaturvedi, *Mod. Phys. Lett.* **A7**, 2407 (1992)
[42] C R Lee and J P Yu, *Phys. Lett.* **A150**, 63 (1990)

[43] J Hubbard, *Proc. R. Soc.* (*London*) **A276**, 238 (1963)
[44] J Hubbard, *Proc. R. Soc.* (*London*) **A285**, 542 (1965)
[45] M Ogata and H Shiba, *Phys. Rev.* **B41**, 2326 (1990)
[46] A K Mishra and G Rajasekaran, *Pramana – J. Phys.* **36**, 537 (1991); **37**, 455 (E) (1991)
[47] A K Mishra and G Rajasekaran, *Mod. Phys. Lett.* **A7**, 3525 (1992)
[48] J W Goodison and D J Toms, *Phys. Rev. Lett.* **71**, 3240 (1993)
[49] Non-perturbative quantum field theory: mathematical aspects and applications (Selected papers of Jürg Fröhlich), Advanced Series in Mathematical Physics **15**, (World Scientific 1992)
[50] K Fredenhagen, M Gaberdiel, S M Rüger, Scattering states of plektons (particles with braid group statistics) in 2 + 1 dim. QFT, preprint Hamburg University and DAMTP Cambridge, 1994
[51] S V Shabanov, Preprint BuTP-92/94
[52] S Iida, *Phys. Rev. Lett.* **69**, 1833 (1992)
[53] T Suzuki, *J. Math. Phys.* **34**, 3453 (1993)
[54] O W Greenberg, *Physica* **A180**, 419 (1992)
[55] R Haag, *Local quantum physics* (Springer, Berlin 1992)

— journal of
physics

August 1995
pp. 141–148

Time dependent canonical perturbation theory I: General theory

B R SITARAM and MITAXI P MEHTA
Physical Research Laboratory, Navrangpura, Ahmedabad 380 009, India

MS received 27 April 1995

Abstract. In this communication, we reanalyze the causes of the singularities of canonical perturbation theory and show that some of these singularities can be removed by using time-dependent canonical perturbation theory. A study of the local and global properties (in terms of the perturbation parameter) is also undertaken.

Keywords. Canonical; perturbation; Hamiltonian systems; integrability.

PACS Nos 03·20; 05·45

1. Introduction

For almost a hundred years, it has been known [1] that canonical perturbation theory is generically singular. Later works, most notably the KAM theorem [2] have shown that in spite of the singularities, the perturbation series does make sense in certain regions of phase space (the irrational tori), and hence, the orbits of the perturbed system lie close to those of the unperturbed system. In the case of the rational tori, even an infinitesimal perturbation is adequate to completely destroy the integrability and the orbits of the unperturbed system. Our analysis of perturbation theory, in this paper, tries to determine the exact cause of the singularities and shows how time-dependent perturbation theory can be used to study Hamiltonian systems which are close to integrable systems.

Consider the Hamiltonian

$$H = H_0(I) + \varepsilon H_1(I, \theta), \tag{1}$$

where I denote the action variables and θ denote the angle variables of the unperturbed Hamiltonian, H_0. (It is assumed that H_0 defines compact orbits.) In the language of Lie transforms, the aim of canonical perturbation theory is to determine a generator $\mathscr{F}(I, \theta)$ which intertwines between the time evolutions generated by H_0 and H:

$$\mathscr{F} \exp(-tH_0) = \exp(-tH)\mathscr{F} \tag{2}$$

as operators acting on phase space. To calculate $\mathscr{F}$, we write

$$\mathscr{F} = \ldots \exp(\varepsilon^n F_n) \ldots \exp(\varepsilon F_1) \tag{3}$$

where the action of the F_i is through Poisson Brackets:

$$\exp(\varepsilon^n F_n) f = f + \varepsilon^n \{F_n, f\} + \frac{\varepsilon^{2n}}{2} \{F_n, \{F_n, f\}\} + \ldots \tag{4}$$

for any function f on phase space. To order ε, and in the limit of infinitesimal t, we get

$$\exp(\varepsilon F_1) H_0 = H + O(\varepsilon^2), \tag{5}$$

$$\{F_1, H_0\} = H_1. \tag{6}$$

We now recognize that the θ's represent angles; to make sense, all quantities, including H_1 and F_1 must be periodic in these angles. This motivates the Fourier expansions:

$$H_1 = \sum H_{1n}(I) \exp[i(n\cdot\theta)],$$
$$F_1 = \sum F_{1n}(I) \exp[i(n\cdot\theta)]; \tag{7}$$

Defining the frequencies of the unperturbed motion by $\omega = \partial H_0/\partial I$, we get the algebraic condition:

$$i(n\cdot\omega)F_{1n} = H_{1n}, \tag{8}$$

which leads to an obvious singularity whenever $(n\cdot\omega) = 0$ (the rational case).

1.1 *Reasons for singularities in the generator* F_1

It is worthwhile investigating at this stage the reason for this singularity. As we shall see, such an analysis will provide us with a way of circumventing the singularity.

A. Equation (6) can be considered as a partial differential equation for F_1. Using the method of characteristics, we see that the solutions of the characteristics are given by

$$\theta = \theta_0 + \omega t, \quad I = I_0, \tag{9}$$

where θ_0, I_0 represent the initial conditions. As can be seen, in the rational case, characteristics are closed; as a result, global solutions can be found only if suitable initial conditions can be formulated such that the value of F_1 on the initial surface matches with that obtained by integrating H_1 along the characteristic to the point where it reintersects the initial surface. This is possible iff the integral of H_1 along closed characteristics vanishes, i.e., iff $H_{1n} = 0$ whenever $(n\cdot\omega) = 0$. Thus, generically, the PDE has no global solutions.

B. Equivalently, (6) can be solved by using the formula

$$F_1 = \int \exp(-tH_0)H_1 \mathrm{d}t, \tag{10}$$

where the integral is to be computed along the solutions to the equations of motion using H_0 as the Hamiltonian. In general, H_1 is periodic in time on the H_0 orbits and can contain a piece which is constant in time. Such a piece, on integration gives rise to a term which is linear in t and hence to a term which is linear in θ's (an aperiodic term). From this point of view, the singularity in F_1 arises from an attempt to express a term linear in angles as a periodic series.

C. Equation (6) can also be considered as an operator equation in a Hilbert space of periodic functions; such an equation admits solutions iff the RHS of the equation is orthogonal to the null eigenvectors of the adjoint of the operator, a condition that can easily be seen to be equivalent to the condition that $H_n = 0$ whenever $(n\cdot\omega) = 0$.

D. From a general point of view, any canonical transformation that is well-defined (e.g., analytic) and is time-independent is dynamically trivial: If $\mathscr{F}$ generates such a canonical transformation, then H_0 and H have the same spectrum: there is a 1–1 map between corresponding orbits. If H_0 and H have distinct dynamical contents (as would be expected to be the case), then the canonical transformation has to be either ill-defined (by being singular, as in canonical perturbation theory or by being multiple-valued) or time-dependent.

From this analysis, it is clear that the solution to opt for is to have either aperiodic terms in $\mathscr{F}$ or to allow for time-dependent $\mathscr{F}$'s. We shall assume the latter in this paper.

1.2 *Derivation of the time-dependent generating function*

To derive the equation for F_1, assume that g satisfies the equation

$$\frac{\partial g}{\partial t} + \{g, H_0\} = 0 \tag{11}$$

and define $h = \exp(\varepsilon F_1) g = g + \varepsilon\{F_1, g\} + O(\varepsilon^2)$. Using the condition that h be an invariant under H, i.e., $(\partial h/\partial t) + \{h, \mathrm{H}\} = 0$ gives the equation determining F_1:

$$\frac{\partial F_1}{\partial t} + \{F_1, H_0\} = H_1, \tag{12}$$

whose solution is

$$F_1(t) = \sum H_{1n} \exp[i(n\cdot\theta_0)] \frac{(\exp[i(n\cdot\omega)t] - 1)}{i(n\cdot\omega)} + F_{10} \tag{13}$$

where F_{10} is an arbitrary function of I and θ_0, representing the value on the initial surface $t = 0$, and where $\theta_0 = \theta - \omega t$. Thus,

$$F_1 = \sum H_{1n} \exp[i(n\cdot\theta)] \frac{(1 - \exp[-i(n\cdot\omega)t])}{i(n\cdot\omega)} + F_{10}, \tag{14}$$

where F_{10} is now an arbitrary function of I and $\theta - \omega t$.

The above solution can also be written in a different form which is sometimes more useful:

$$F_1(I, \theta, t) = \int_0^t H_1(I, \theta + \omega(z - t), z)\mathrm{d}z + F_{10} \tag{15}$$

which follows easily from the characteristic equations of the PDE for F_1 (eq. 12).

As is clear, F_{10} corresponds to the fact that we can choose the canonical transformation arbitrarily at $t = 0$. It is also easy to see that the time-dependent canonical transformation where F_{10} is zero is equivalent to using the unperturbed Hamiltonian to go back in time and to go forward in time using the perturbed Hamiltonian. In what follows, we will choose $F_{10} = 0$.

Another motivation for considering time-dependent perturbation theory comes from Hamilton–Jacobi theory. Usually, while applying Hamilton–Jacobi theory, one considers the generating function to be linear in time and writes the Hamilton–Jacobi

equation in the form

$$H\left(\frac{\partial W}{\partial q}, q\right) = E \tag{16}$$

$$S = W - Et. \tag{17}$$

However, it is also possible to work with the full Hamilton–Jacobi equation: Assume,

$$H(I, \theta) = H_0(I) + \varepsilon H_1(I, \theta) \tag{18}$$

$$I = \frac{\partial S}{\partial \theta} \tag{19}$$

$$S(\theta, t) = S_0(\theta, t) + \varepsilon S_1(\theta, t) + \varepsilon^2 S_2(\theta, t) + \ldots \tag{20}$$

Using these equations in the Hamilton–Jacobi equation

$$\frac{\partial S}{\partial t} + H(I, \theta) = 0 \tag{21}$$

and equating equal powers of ε we get a series of equations determining S_i. It is then trivial to see that by allowing S to be explicitly dependent on time, we can derive an expression for S which is equivalent to the above Lie transform formalism.

To analyze the effect of such an F_1 and to draw conclusions about the integrability of the transformed system, it is convenient to replace the given dynamical system with one with an extra degree of freedom; the two extra phase space coordinates will be (t, T), and the new Poisson bracket is defined as,

$$\{f, g\}' = \frac{\partial f}{\partial t}\frac{\partial g}{\partial T} - \frac{\partial f}{\partial T}\frac{\partial g}{\partial t} + \{f, g\} \tag{22}$$

where the unprimed bracket refers to the original Poisson bracket. We also define

$$H_0' = H_0 + T, \quad H' = H + T \tag{23}$$

and use z to denote the (new) arc parameter. We notice that there is no change in the definition of H_1. It is then trivial to see that the equation determining F_1 is the same as (6), using primed PBs, and that the solution coincides with that given in (15). We can thus interpret F_1 as a genuine function on the extended phase space defined by (I, T, θ, t). This also allows us to establish the integrability of H' (to order ε): we have $n + 1$ invariants (I, T) for H_0' and their transforms under the canonical transformation define invariants for H'. It is also straightforward to derive the equations for higher order perturbation theory (i.e., for $F_n, n > 1$) in a similar fashion.

2. Analyticity properties of the perturbation series

We now consider the analyticity properties of the perturbation series that we have developed above. There are two aspects to this study: first, we consider the finiteness of each term in the perturbation theory, that is, we consider the behaviour of each of the generators F_i as a function on phase space. Secondly, we consider the convergence of the canonical transformation as a whole, $\mathscr{F}$, as a function of the perturbation parameter.

2.1 *Analyticity properties of* F_i

We note that the function F_1 has the property of being an entire function of the two variables t and $(n\cdot\omega)$ (and hence I, if ω's and H_n are entire functions of I). This important property persists to all orders of perturbation theory:

Lemma. Assume that H_0' *and* H_1 *are analytic in* I. *Define a sequence of canonical transformations through the equations*:

$$H^{(0)} = H_0',$$

$$\{F_1, H_0'\}' = H_1, \tag{24}$$

$$H^{(n+1)} = \exp(\varepsilon^{(n+1)} F_{n+1}) H^{(n)}, \quad n \geqslant 0,$$

$$-\{F_{n+1}, H_0'\}' = \text{coefficient of } \varepsilon^{n+1} \text{ in } H^{(n)}, \quad n \geqslant 1. \tag{25}$$

(Note that at the nth stage, $F_{(n)}$ is chosen to kill the term of order ε^n.) Then, F_n is an entire function of I and t and is periodic in θ for all $n = 1, 2, \ldots$ (In brief, we shall say that F_n is regular.)

Proof. The proof follows from induction, using the following facts:

(1) If $H^{(n)}$ is regular and F_n is regular, so is $H^{(n+1)}$: this follows from the fact that the computation of $H^{(n+1)}$ involves the computation of derivatives, which preserves regularity.
(2) The PDE $\{A, H_0'\}' = G$ has the property that if G is regular, then A is regular; in fact, if $G = \Sigma G_n \exp[i(n\cdot\theta)]$, where the Fourier coefficients are entire functions of I and t, then $A = \Sigma A_n \exp[i(n\cdot\theta)]$, where

$$A_n = \exp[-i(n\cdot\omega)t] \int_0^t \exp[i(n\cdot\omega)t]\, G_n \mathrm{d}t. \tag{26}$$

The RHS is an integral of an entire function of t and $(n\cdot\omega)$ along a contour which lies within the region of analyticity; hence the conclusion.

Thus, in contrast to canonical perturbation theory, each of the generators is finite. At this stage it is worthwhile examining points (A) and (B) once again from the new perspective.

A′. In the extended system, the characteristics are never closed (the equation for t is $t = t_0 + z$); thus, it is possible to choose as initial surface, the surface $t = 0$ and choose F arbitrarily on this surface.

B′. Constant terms under the integral are retained explicitly as functions of time, not replaced by (aperiodic) functions of θ.

2.2 *Convergence of perturbation theory*

As noted above, the full canonical transformation $\mathscr{F}$ is equivalent to transforming backwards in time using H_0 and then transforming forwards in time using H. Since the first step is independent of ε, the analyticity properties of $\mathscr{F}$ is decided by the analyticity properties of the time evolution operator H as a function of ε. In general, of course, the

analyticity properties of $\mathscr{F}$ as a function of ε will depend on t; this is in contrast to the time-independent case, where analyticity properties are independent of t. In general, it is not possible to derive general results regarding the analyticity properties of the transformation; however, there are two special results that are of interest:

1. We assume that there exists a time-independent canonical transformation $\mathscr{F}_{\mathrm{KAM}}$ (calculated using e.g., KAM theory) for a phase space point and for a certain value of ε. The following diagram shows the relation of $\mathscr{F}$ with the KAM generator.

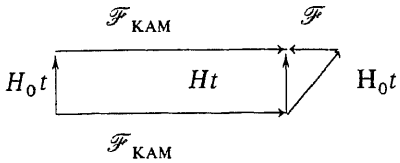

which translates into

$$\mathscr{F} = \mathscr{F}_{\mathrm{KAM}} \exp(-tH_0) \mathscr{F}_{\mathrm{KAM}}^{-1} \exp(tH_0). \tag{27}$$

Thus, $\mathscr{F}$ will exist provided the time evolution of $\mathscr{F}_{\mathrm{KAM}}$ under the unperturbed Hamiltonian is well-defined for real t. In particular, since $\mathscr{F}_{\mathrm{KAM}}$ will depend on I, θ and their evolution under H_0 is trivial, $\mathscr{F}$ will be analytic in ε provided $\mathscr{F}_{\mathrm{KAM}}$ is analytic in I, θ. Further, in such a case, $\mathscr{F}$ will be analytic in ε for all t.

2. For a class of Hamiltonian systems it is possible to relate the complex-time analytical structure of fully perturbed Hamiltonian systems to the complex-ε analytical structure of the canonical transformation which transforms the Hamiltonian with a small ε value to the Hamiltonian with a large ε value.

Take a Hamiltonian system where the unperturbed part is a homogeneous function of degree m in phase space variables (q_i, p_i) and the perturbation part is homogeneous function of degree n.

$$H(q_i, p_i) = H_0(q_i, p_i) + \varepsilon H_1(q_i, p_i); \tag{28}$$

assuming $n > m$, a scale transformation of the variables,

$$q_i' = q_i \varepsilon^{\alpha}, \quad p_i' = p_i \varepsilon^{\alpha} \tag{29}$$

where $\alpha = (1/(n-m))$, changes the Hamiltonian into,

$$H'(q_i', p_i') = \varepsilon^{-m\alpha}(H_0(q_i', p_i') + H_1(q_i', p_i')) \tag{30}$$

(Note that this transformation is not a canonical transformation, but it transforms the vector field of H at some ε to the vector field of H at $\varepsilon = 1$.) Reparametrizing the system by inserting $\varepsilon = (1 + \varepsilon')^{(1/m\alpha)}$ yields,

$$H'(q_i', p_i') = (1 + \varepsilon')(H_0(q_i', p_i') + H_1(q_i', p_i')). \tag{31}$$

This Hamiltonian represents the perturbation of the Hamiltonian $H_{\varepsilon=1}(q_i', p_i') = H_0(q_i', p_i') + H_1(q_i', p_i')$ by itself using the perturbation parameter ε'. i.e.

$$H'(q_i', p_i') = H_{\varepsilon=1}(q_i', p_i') + \varepsilon' H_{\varepsilon=1}(q_i', p_i'). \tag{32}$$

For this problem, $F_1 = H_{\varepsilon=1}(q_i', p_i')t$, and all the higher order generators vanish; thus F_1 alone is the generator of the canonical transformation and so it can be used as the Hamiltonian for the ε' evolution (except at $\varepsilon = 0$, because there the scaling transformation is ill-defined).

$$\frac{\partial q_i'}{\partial \varepsilon'} = \frac{\partial F_1}{\partial p_i'}; \quad \frac{\partial p_i'}{\partial \varepsilon'} = -\frac{\partial F_1}{\partial q_i'}. \tag{33}$$

Now F_1 is the same as $H(q_i, p_i)$ at $\varepsilon = 1$, but for an extra multiplier t. So above equations can be rewritten as,

$$\frac{\partial q_i'}{\partial \varepsilon' t} = \frac{\partial H_{\varepsilon=1}(q_i', p_i')}{\partial p_i}; \quad \frac{\partial p_i'}{\partial \varepsilon' t} = -\frac{\partial H_{\varepsilon=1}(q_i', p_i')}{\partial q_i}. \tag{34}$$

But these equations are the time evolution equations for the Hamiltonian $H_{\varepsilon=1}$. Thus if $H_{\varepsilon=1}$ has singularities in the complex t plane, then a canonical transformation defined by F_1 also will have singularities in the complex $\varepsilon' t$ plane, and hence in the complex ε plane for a fixed t. Also, the presence of a natural boundary in the complex t plane [3] for the Hamiltonian $H_{\varepsilon=1}$ will manifest itself as a natural boundary in the complex ε plane for $\mathscr{F}$. (A similar technique will work for $n < m$.)

In case the singularities of the time evolution operator $\exp(-tH)$ in the complex ε plane are isolated, it is possible to use analytic continuation to define F beyond the radius of convergence. However, as the above study shows, the existence of natural boundaries in the complex t plane may imply the existence of similar boundaries in the complex ε plane also. In applications to specific systems, it is possible to study the analyticity properties of F using standard tools for determining the analyticity properties of the solutions of the equations of motion using H as the Hamiltonian.

3. Conclusions

The following points can be noted regarding the canonical transformations derived above:

1. Because of the explicit time-dependence of $\mathscr{F}$, two points which lie on the same unperturbed orbit do not in general lie on the same perturbed orbit.
2. The spectra of the two Hamiltonians H_0 and H can be very different, even though they are related by a canonical transformation: this is because of the explicit time-dependence of $\mathscr{F}$.
3. It is trivial to see that time-dependent perturbation theory works satisfactorily in two situations where conventional perturbation theory is singular:
a. Let H_1 be a function of I alone. Conventional theory is singular in this case, as the only non-zero Fourier component corresponds to $n = 0$. Our theory allows for a regular solution, $F_1 = H_1 t$, which yields,

$$J = I; \quad U = T + \varepsilon H_1; \quad u = t; \quad \phi = \theta - \varepsilon \frac{\partial H}{\partial I}; \tag{35}$$

where (I, T, t, θ) denote the original canonical coordinates and (J, U, u, ϕ) the transforms of these coordinates.

b. Let H_1 be such that H_1 explicitly depends on θ and $\{H_0, H_1\} = 0$. (Note: this can happen only if the unperturbed frequencies ω are constant.) Once again, we have the solution $F = H_1 t$ and it is easy to check the correctness of the transformed invariants.

4. As the examples described above clearly show, the canonical transformation defined by $\mathcal{F}$ changes not only the (usual) canonical coordinates (I, θ) but also T. It is the motions defined by H'_0 and H' in the extended phase space defined by (I, θ, T, t) which are being mapped into one another. In principle, we could try to reduce the transformation to one on the usual phase space by eliminating t (using, e.g., the invariant corresponding to T); it is fairly straightforward to see that this results in recovering the singularities of canonical perturbation theory.

Numerical studies of the application of this theory will be studied in companion papers.

References

[1] M V Berry, in *Topics in nonlinear dynamics a tribute to Sir Edward Bullard*, edited by S Jorna (American Institute of Physics, New York, 1978) p. 37

[2] R Abraham and J E Marsden, *Foundations of mechanics* (The Benjamin/Cummings Publishing Company, Massachusetts, 1978)

[3] Y F Chang, M Tabor and J Weiss, *J. Math. Phys.* **23**, 531 (1982)

PRAMANA
— journal of
physics

© Printed in India

Vol. 45, No. 2,
August 1995
pp. 149–164

Time dependent canonical perturbation theory II: Application to the Henon–Heiles system

MITAXI P MEHTA and B R SITARAM
Physical Research Laboratory, Navrangpura, Ahmedabad 380 009, India

MS received 10 May 1995

Abstract. In this communication, we report the results of the application of time-dependent perturbation theory to the Henon–Heiles system. We show that the predictions of the perturbation theory hold good for short times, and try to explain the increase of error in the predicted results with the increase in energy.

Keywords. Canonical perturbation; Henon–Heiles

PACS Nos 05·45; 03·20

1. Introduction

One of the fundamental problems in canonical perturbation theory is, given a Hamiltonian

$$H = H_0 + \varepsilon H_1, \tag{1}$$

where ε is a parameter, to determine a canonical transformation which transforms H_0 to H, as a power series in ε. In a previous paper [1], this was attempted by allowing the canonical transformation to be time-dependent and it was shown that the approach removes some of the singularities of canonical perturbation theory. The method introduced a new degree of freedom, by using time as a canonical coordinate, with T as its conjugate variable, and replacing the original Hamiltonian H by $H + T$. The salient features of the results were:

1. The generators of the canonical transformation were finite at every order of perturbation theory.
2. The generators at nth order of perturbation theory were $O(\varepsilon^n)$.

In this communication, we study the application of the theory to the Henon–Heiles Hamiltonian. In general, perturbation theory can be tested via two approaches, namely, the predictions regarding invariants and the solutions of the equations of motion (EOM). Both these tests have been performed using third order perturbation theory for the system under study.

The plan of the paper is as follows: In § 2, we review the Henon–Heiles system. Section 3 contains the basic formulae for the generators of the canonical transformation, the invariants and the solutions. In § 4 we present the numerical results. Section 5 concludes with a discussion on the convergence properties of the perturbation series.

Henon and Heiles [2] to investigate the integrability of motion in an axisymmetric potential. The Hamiltonian is a truncation of the Toda-lattice Hamiltonian [3] up to third-order terms and it is a model for motion of a star in an axisymmetric gravitational field. The Hamiltonian is given by,

$$H = \frac{p_1^2 + p_2^2 + q_1^2 + q_2^2}{2} + \varepsilon\left(q_1^2 q_2 - \frac{q_2^3}{3}\right), \tag{2}$$

where ε is the perturbation parameter. ε can be rescaled using the transformation,

$$q_i \to \frac{Q_i}{\varepsilon}$$

$$p_i \to \frac{P_i}{\varepsilon}$$

$i = 1, 2$ under which,

$$H \to \frac{1}{\varepsilon^2} h$$

where,

$$h = \frac{Q_1^2 + Q_2^2 + P_1^2 + P_2^2}{2} + Q_1^2 Q_2 - \frac{Q_2^3}{3}.$$

Thus solving for motion of Henon–Heiles system for one value of ε and different values of energy is equivalent to solving for one value of energy and different values of ε. Our approach here has been the first one i.e. we have fixed the value of ε to 0·01 and studied the system for different values of energy. (For comparison with other results, energies are always quoted for the equivalent Hamiltonian, h.)

Further the system shows a transition from regular behaviour to chaotic behaviour with the change in energy [2]. The following characteristics are well-known: for $E < 1/12$ the Poincare sections indicate regular motion, i.e., the section is filled with closed curves and there is no exponential divergence of trajectories. In the range $1/12 < E < 1/6$ the motion shows a transition from regular to chaotic behaviour, becoming more and more chaotic with increase in E, i.e, the area which is covered by closed curves in the section becomes smaller with increase in E. Beyond $E = 1/6$, the motion becomes non-compact, with solutions escaping to infinity. (There are unbounded orbits for all energies, including for those with $E < 1/6$; these orbits do not play any role in our analysis, as a suitable choice of initial conditions ensures that the orbits remain bounded.)

Classical perturbation theory is known to be singular for this Hamiltonian because of resonances [3], which arise at second order in perturbation theory. The KAM theorem [4] cannot be applied directly to the system; the condition,

$$\det\left(\frac{\partial \omega_i}{\partial I_j}\right) \neq 0$$

is not satisfied, as the unperturbed frequencies are independent of the actions. Gustavson's method [5] give good results for small energies but does not predict the chaotic behaviour of Poincare sections.

3. Generating functions, solutions and invariants

We take the unperturbed Hamiltonian as the two-dimensional harmonic oscillator Hamiltonian,

$$H_0' = \frac{p_1^2 + p_2^2 + q_1^2 + q_2^2}{2} + T \tag{3}$$

with

$$H_0 = \frac{p_1^2 + p_2^2 + q_1^2 + q_2^2}{2}$$

and the full Hamiltonian as,

$$H' = H_0 + \varepsilon H_1 + T \tag{4}$$

where,

$$H_1 = q_1^2 q_2 - \frac{q_2^3}{3} \tag{5}$$

where (t, T) are extra phase space coordinates [1], and the new Poisson bracket is defined as

$$\{f,g\}' = \frac{\partial f}{\partial t}\frac{\partial g}{\partial T} - \frac{\partial f}{\partial T}\frac{\partial g}{\partial t} + \{f,g\},$$

with $\{f,g\}$ denoting the usual Poisson bracket.

In unperturbed action-angle coordinates we get,

$$H_0' = I_1 + I_2 + T, \tag{6}$$

$$H_1 = 2I_1 \cos^2\theta_1 \sqrt{2I_2}\cos\theta_2 - \frac{(\sqrt{2I_2}\cos\theta_2)^3}{3}. \tag{7}$$

The equations determining the generators are,

$$\{F_1, H_0'\}' = H_1 \tag{8}$$

$$\{F_2, H_0'\}' = -\frac{\{F_1, \{F_1, H_0'\}'\}'}{2} \tag{9}$$

$$\{F_3, H_0'\}' = -\frac{\{F_1, \{F_1, \{F_1, H_0'\}'\}'\}'}{3!} - \{F_2, \{F_1, H_0'\}'\}' \tag{10}$$

The F's were calculated using Mathematica programs. The expressions for the generating functions are given in the appendix.

Accordingly the constants of motion for H to third order are given by,

$$I_i' = I_i + \varepsilon\{F_1, I_i\}' + \frac{\varepsilon^2\{F_1, \{F_1, I_i\}'\}'}{2} + \frac{\varepsilon^3\{F_1, \{F_1, \{F_1, I_i\}'\}'\}'}{3!}$$
$$+ \varepsilon^2\{F_2, I_i\}' + \varepsilon^3\{F_2, \{F_1, I_i\}'\}' + \varepsilon^3\{F_3, I_i\}' \tag{11}$$

where $i = 1, 2$.

The solutions of the EOM for H can be obtained from those of H_0 using the equations

$$\xi_i = \xi_i' - \varepsilon\{F_1, \xi_i'\}' + \varepsilon^2 \frac{\{F_1, \{F_1, \xi_i'\}'\}'}{2} - \varepsilon^3 \frac{\{F_1, \{F_1, \{F_1, \xi_i'\}'\}'\}'}{3!}$$

$$- \varepsilon^2\{F_2, \xi_i'\}' + \varepsilon^3\{F_1, \{F_2, \xi_i'\}'\}' - \varepsilon^3\{F_3, \xi_i'\}' \qquad (12)$$

where $i = 1, 2, 3, 4$, $\xi_1 = I_1$, $\xi_2 = I_2$, $\xi_3 = \theta_1$, $\xi_4 = \theta_2$, $\xi_1' = I_1'$, $\xi_2' = I_2'$, $\xi_3' = \theta_1'$, $\xi_4' = \theta_2'$.

Here $I(t), \theta(t)$ represent the solutions of the EOM for the Henon–Heiles Hamiltonian, while $I'(t), \theta'(t)$ represent the solutions for the harmonic oscillator Hamiltonian.

4. Numerical results

Using a 4th-order Runge–Kutta–Gill adaptive ODE solver, the EOM for the Henon–Heiles system were solved and the invariants predicted by third order perturbation theory were computed. Figures 1(a) and 1(b) give the relative variation in one of the constants of motion (I_1') for two different energies: 1(a) for the regular regime of the perturbed Hamiltonian and 1(b) for the chaotic regime of the Hamiltonian, for first, second and third order perturbation theory. (In the figures, relative deviation in $I_1'(t)$ is calculated as $2*(I_1'(t) - I_1'(0))/(I_1'(t) + I_1'(0))$.) Figure 2 shows the third order prediction at different energy values. With increase in E the constancy becomes worse i.e., error increases but higher order results remain superior to lower order results for some time, at larger time the error become too large.

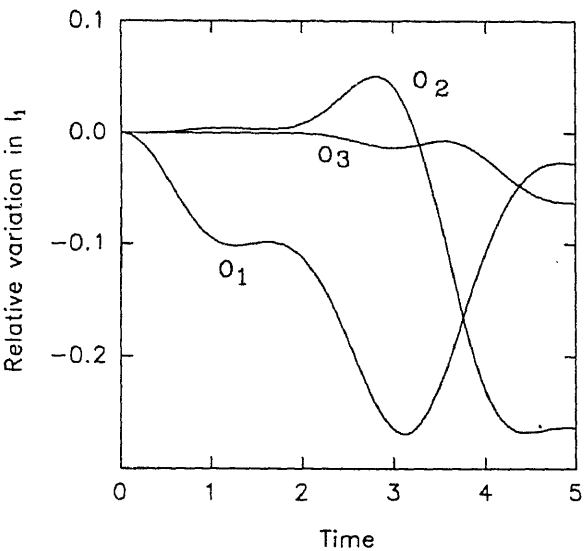

Figure 1a. Relative variation in predicted time-dependent constant of motion I_1' for $E = 0{\cdot}034$, O_1, O_2 and O_3 represent results of first, second and third order perturbation theory results respectively.

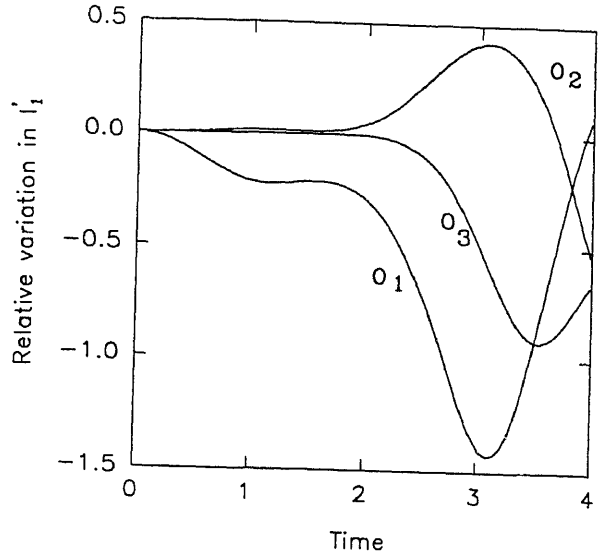

Figure 1b. Same as figure 1a for $E = 0{\cdot}112$.

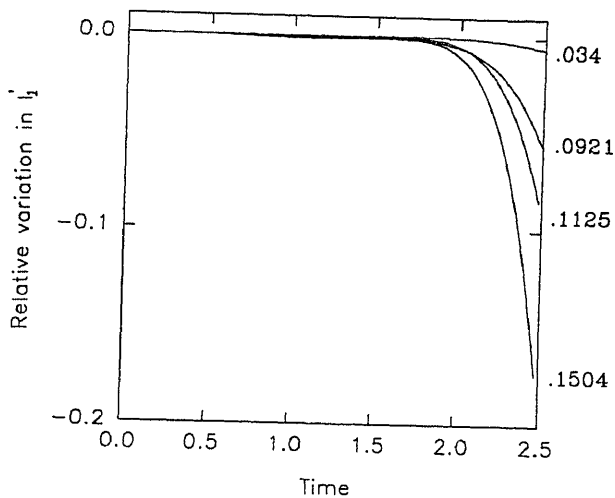

Figure 2. Relative variation in predicted constant of motion at third order, at different E values for the Henon–Heiles system.

For comparing the solutions, the same Runge–Kutta–Gill ODE solver was used and results were compared with the predictions of (12). These results are summarized in figures 3(a) and 3(b) (solid lines), which show the relative error in predicted solutions with respect to numerical solutions; for the first, second and third order perturbation theory. (The relative error in $I_1(t)$ is, $2(I_{1p}(t) - I_{1n}(t))/(I_{1p}(t) - I_{1n}(t))$ where I_{1p} is the predicted solution and I_{1n} is the numerical solution.) Figure 4 shows the results of

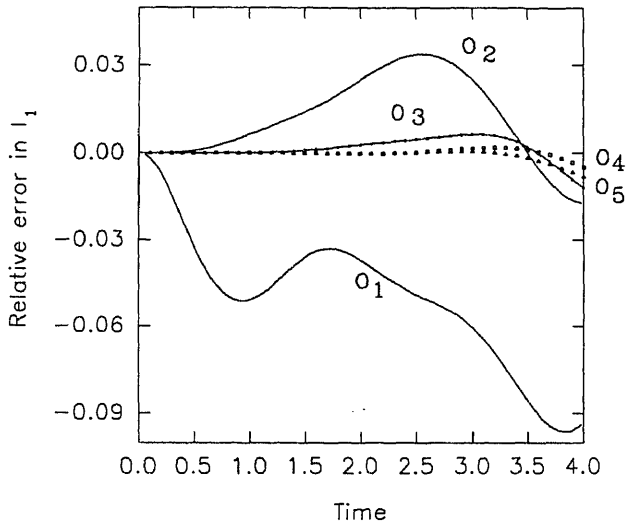

Figure 3a. Relative error in predicted solution for I_1 for the Henon–Heiles system at $E = 0{\cdot}034$. O_1, O_2 and O_3 represent results of first, second and third order perturbation theory results respectively. Dotted curves show numerically calculated higher orders.

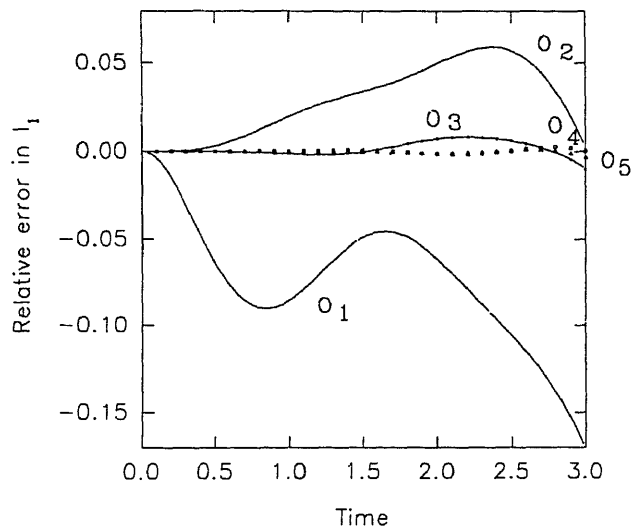

Figure 3b. Same as figure 3a for $E = 0{\cdot}112$.

application of the third order perturbation theory for a spectrum of energies ranging from the regular to the chaotic regime.

We also tested perturbation theory for two orbits of the Henon–Heiles system, one of which is known to be chaotic and the other regular (as seen from their Poincare

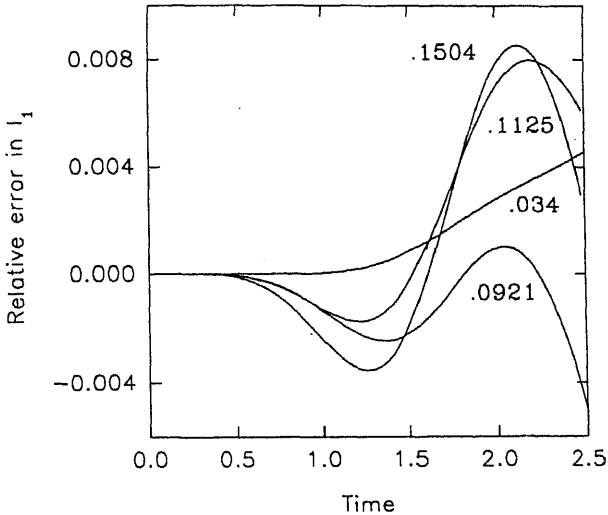

Figure 4. Relative error in third order predicted solution for I_1 for the Henon–Heiles system at different E values.

sections). Figure 5(a) shows the behaviour of the constants of motion for a chaotic trajectory and 5(b) shows the same for a regular trajectory at the same energy value. Figures 6(a) and 6(b) are the Poincare sections for the initial conditions of 5(a) and 5(b) respectively.

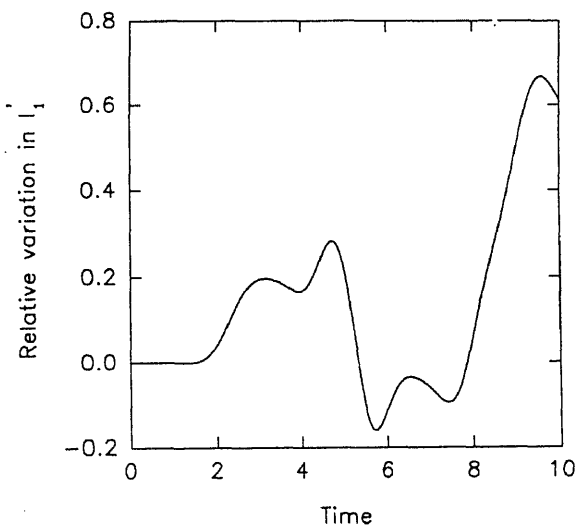

Figure 5a. Relative variation in third order predicted constant of motion I_1' for the Henon–Heiles system for a chaotic trajectory at $E = 0{\cdot}125$.

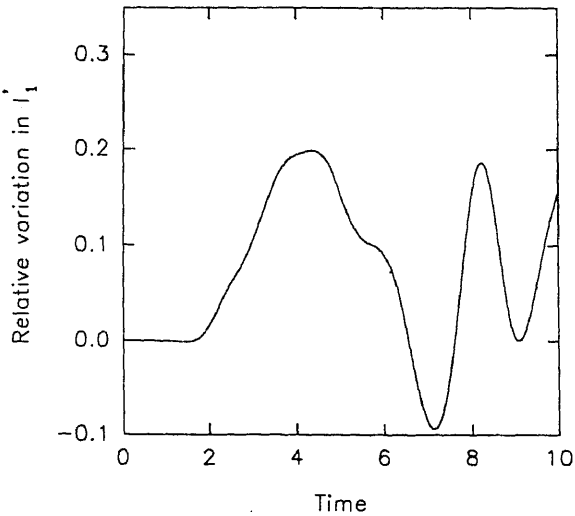

Figure 5b. Relative variation in third order predicted constant of motion I_1' for the Henon–Heiles system for a regular trajectory at $E = 0{\cdot}125$.

5. Convergence of the series

As it is obvious from the numerical results, the prediction of the perturbation theory does not seem to be in agreement with the numerical results. This may be due to two reasons,

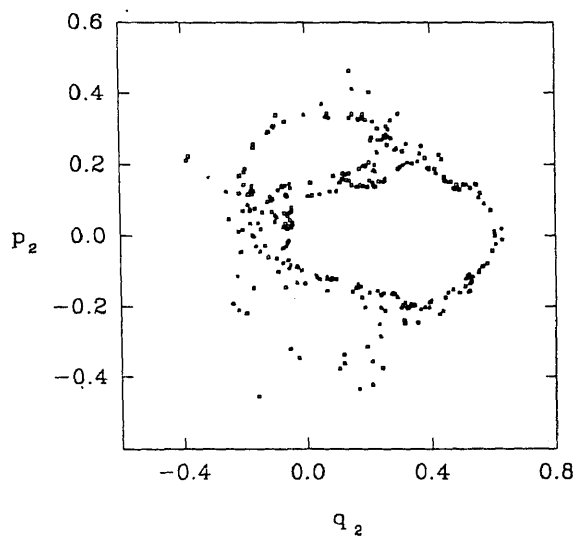

Figure 6a. Poincare section of the chaotic trajectory of figure 5a.

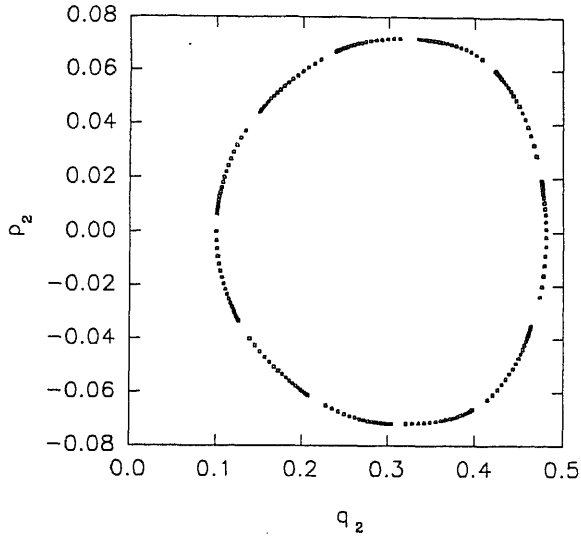

Figure 6b. Poincare section of the regular trajectory of figure 5b.

1. Only first few orders of the perturbation series are considered, in which case the perturbation theory should agree with the numerical results at higher energies, and larger times if enough number of terms in the perturbation series are considered.
2. Contrary to our assumption that the generating function is analytic in the complex ε plane, there exists a singularity; in that case one can expect the perturbation theory to converge only in the region where the distance of ε from origin is less than that of the radius of convergence.

To investigate which one of the former reasons is responsible for the disagreement of the perturbation theory with numerical calculations we analyzed the analytic structure of the system in complex ε real t space [1].

For the initial conditions selected for figure 2, the equations were integrated in real time for 100 different ε values lying on a circle with radius 0·01 and centre $\varepsilon = (0, 0)$. The failure of the integration subroutine was considered as existence of singularity. Three different subroutines drkgs (SSP; Runge-Kutta), d02baf (IMSL) and d02ebf (IMSL stiff equation solver) were used; the routine d02ebf fails with ihalf = 2, which indicates presence of singularity. The results of the calculations are shown in table 1. The smallest time at which one of the points on the circle becomes singular is given.

It is not expected for the above test to work for any general Hamiltonian because it does not detect branch point singularities, but in this specific case it turns out that a branch point in q_1 corresponds to a branch point in p_1 with negative exponent (this can be seen from Painleve analysis [6]) and same is true for q_2 and p_2. Thus even though there are singularities where the position variables remain finite, the corresponding momentum variables become infinite, hence the time at which one of the variables become infinity is the same at which another variable has a branch point with finite value.

Table 1. Complex-ε singularities in real time.

Initial conditions				Time for appearance of singularity		
q_1	q_2	p_1	p_2	drkgs	d02baf	d02ebf
4·47214	4·89898	0	0	$t > 200$		
14·1421	21·4476	0	0	111·6145	$111{\cdot}8 < t < 111{\cdot}9$	$111{\cdot}8 < t < 111{\cdot}9$
30	24·4949	0	0	27·0544	$27{\cdot}3 < t < 27{\cdot}4$	$27{\cdot}3 < t < 27{\cdot}4$
26·6648	31·9374	0	0	19·37	$19{\cdot}6 < t < 19{\cdot}7$	$19{\cdot}6 < t < 19{\cdot}7$
34·9285	34·9285	0	0	13·4095	$13{\cdot}6 < t < 13{\cdot}7$	$13{\cdot}6 < t < 13{\cdot}7$

This analysis indicate that the perturbation theory should be convergent for given initial conditions and ε for larger time values than what is seen in figure 2, thus the reason for disagreement should be truncation of the series rather than existence of a singularity. To verify this reasoning we did a numerical study as follows.

When one uses the generating functions for mapping of the solution for unperturbed Hamiltonian into the solution of the perturbed Hamiltonian, the result is the solution ξ of H in terms of solutions ξ' of H_0, t and a power series in ε. In this series for ξ the coefficient of a term ε^n is $(1/n!)(\mathrm{d}^n\xi/\mathrm{d}\varepsilon^n)$. We did numerical calculations for $\mathrm{d}^n\xi/\mathrm{d}\varepsilon^n$ using

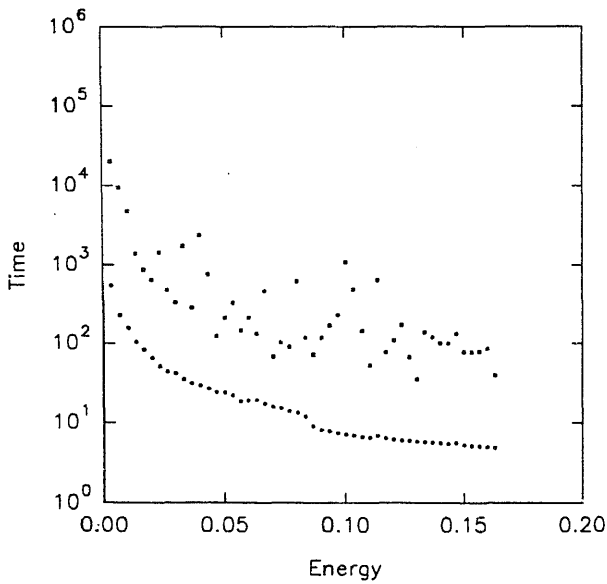

Figure 7. At fixed energy 100 different initial conditions are chosen randomly and each initial conditions is evolved in time with all the 100 different ε values equally spaced on a circle of radius 1 and centre (0, 0) in the complex-ε plane. The minimum time at which one of the points in complex-ε circle encounters a singularity is noted. From the minimum time thus found for each initial conditions at a fixed energy the minimum and maximum times are plotted against energy.

contour integral definition for derivatives and matched our numerical results with the analytical results predicted by perturbation theory. As can be seen from figure 3, where the dotted curves denote numerically calculated higher orders, the third order analytical predictions are well in agreement with numerical values and the fourth and fifth order numerical results show that a higher order analytical calculation would make the predictions better.

To explain the worsening of perturbation theory at higher energies, we did the following calculation. We selected 100 different initial conditions randomly for each of 49 different energies and for each set of initial conditions we fixed 100 points on the complex ε circle with radius 1 and centre (0, 0) and calculated the minimum value of time at which one of the points on the circle became singular. This value of time is the minimum real time at which there is a singularity in the complex ε plane and this singularity will decide the radius of convergence for the perturbation theory. Figure 7 shows the minimum and maximum values of the above minimum time from the 100 initial conditions at each energy value versus the energy. The minimum time value in the figure is the value up to which the perturbation theory will converge if enough number of orders are calculated, whereas the maximum at each energy shows that there are some initial conditions for which the perturbation theory will converge for very large time without any need for analytical continuation of the generator.

It thus appears from our analysis that the time-dependent canonical perturbation theory can be used for studying the Henon–Heiles system, the fact that the results show disagreement with numerical results is to be attributed to the low order of perturbation theory used.

Appendix A. Generating functions

We give below the form of the generating functions up to order ε^3.

$$F_1 = \frac{-(I_2^{3/2}\sin(3t-3\theta_2))}{9\sqrt{2}} + \sqrt{2}I_1\sqrt{I_2}\sin(t-\theta_2)$$
$$- \frac{I_2^{3/2}\sin(t-\theta_2)}{\sqrt{2}} + \frac{I_2\sqrt{I_2}\sin(3t-2\theta_1-\theta_2)}{3\sqrt{2}}$$
$$+ \frac{I_1\sqrt{I_2}\sin(2\theta_1-\theta_2)}{\sqrt{2}} + \sqrt{2}I_1\sqrt{I_2}\sin(\theta_2)$$
$$- \frac{I_2^{3/2}\sin(\theta_2)}{\sqrt{2}} - \frac{I_2^{3/2}\sin(3\theta_2)}{9\sqrt{2}}$$
$$+ \frac{I_1\sqrt{I_2}\sin(t-2\theta_1+\theta_2)}{\sqrt{2}} + \frac{I_1\sqrt{I_2}\sin(2\theta_1+\theta_2)}{3\sqrt{2}}$$

$$F_2 = \frac{-5I_1^2 t}{12} + \frac{I_1 I_2 t}{3} - \frac{5I_2^2 t}{12} - \frac{7I_1 I_2 t\cos(2\theta_1-2\theta_2)}{6}$$
$$+ \frac{3I_1^2\sin(t)}{8} - \frac{I_1 I_2\sin(t)}{2} + \frac{3I_2^2\sin(t)}{8} + \frac{I_1^2\sin(3t)}{72}$$

$$+\frac{I_1 I_2 \sin(3t)}{18}+\frac{I_2^2 \sin(3t)}{72}+\frac{I_1^2 \sin(t-4\theta_1)}{24}$$

$$-\frac{I_1^2 \sin(3t-4\theta_1)}{24}+\frac{I_1^2 \sin(4t-4\theta_1)}{48}-\frac{I_1^2 \sin(2t-2\theta_1)}{6}$$

$$-\frac{I_1 I_2 \sin(2t-2\theta_1)}{6}+\frac{I_1^2 \sin(3t-2\theta_1)}{12}+\frac{I_1 I_2 \sin(3t-2\theta_1)}{12}$$

$$-\frac{I_1^2 \sin(2\theta_1)}{6}-\frac{I_1 I_2 \sin(2\theta_1)}{6}+\frac{I_1^2 \sin(4\theta_1)}{48}$$

$$+\frac{I_1^2 \sin(t+2\theta_1)}{12}+\frac{I_1 I_2 \sin(t+2\theta_1)}{12}+\frac{I_2^2 \sin(t-4\theta_2)}{24}$$

$$-\frac{I_2^2 \sin(3t-4\theta_2)}{24}+\frac{I_2^2 \sin(4t-4\theta_2)}{48}-\frac{I_1 I_2 \sin(2t-2\theta_2)}{6}$$

$$-\frac{I_2^2 \sin(2t-2\theta_2)}{6}+\frac{I_1 I_2 \sin(3t-2\theta_2)}{12}+\frac{I_2^2 \sin(3t-2\theta_2)}{12}$$

$$+\frac{I_1 I_2 \sin(t-2\theta_1-2\theta_2)}{12}-\frac{I_1 I_2 \sin(3t-2\theta_1-2\theta_2)}{12}$$

$$+\frac{I_1 I_2 \sin(4t-2\theta_1-2\theta_2)}{24}+\frac{5I_1 I_2 \sin(t+2\theta_1-2\theta_2)}{8}$$

$$-\frac{I_1 I_2 \sin(3t+2\theta_1-2\theta_2)}{72}-\frac{I_1 I_2 \sin(2\theta_2)}{6}-\frac{I_2^2 \sin(2\theta_2)}{6}$$

$$+\frac{I_2^2 \sin(4\theta_2)}{48}+\frac{I_1 I_2 \sin(t+2\theta_2)}{12}+\frac{I_2^2 \sin(t+2\theta_2)}{12}$$

$$+\frac{5I_1 I_2 \sin(t-2\theta_1+2\theta_2)}{8}-\frac{I_1 I_2 \sin(3t-2\theta_1+2\theta_2)}{72}$$

$$+\frac{I_1 I_2 \sin(2\theta_1+2\theta_2)}{24}$$

$$F_3=\frac{-7I_1 I_2^{3/2} t\cos(2\theta_1-3\theta_2)}{2\sqrt{2}}-\frac{13I_1^2\sqrt{I_2}\,t\cos(2\theta_1-\theta_2)}{3\sqrt{2}}$$

$$+\frac{37I_1 I_2^{3/2} t\cos(2\theta_1-\theta_2)}{6\sqrt{2}}-\frac{7I_1^2\sqrt{I_2}\,t\cos(4\theta_1-\theta_2)}{18\sqrt{2}}$$

$$+\frac{11I_1^2\sqrt{I_2}\,t\cos(\theta_2)}{6\sqrt{2}}-\frac{13I_1 I_2^{3/2} t\cos(\theta_2)}{3\sqrt{2}}$$

$$+\frac{5I_2^{5/2} t\cos(\theta_2)}{6\sqrt{2}}-\frac{4\sqrt{2}I_1 I_2^{3/2} t\cos(3\theta_2)}{9}$$

$$+\frac{5I_2^{5/2}t\cos(3\theta_2)}{18\sqrt{2}}-\frac{2\sqrt{2}I_1^2\sqrt{I_2}t\cos(2\theta_1+\theta_2)}{9}$$

$$+\frac{I_1I_2^{3/2}t\cos(2\theta_1+\theta_2)}{3\sqrt{2}}+\frac{I_2^{5/2}\sin(t-5\theta_2)}{18\sqrt{2}}$$

$$-\frac{I_2^{5/2}\sin(2t-5\theta_2)}{216\sqrt{2}}-\frac{7I_2^{5/2}\sin(3t-5\theta_2)}{108\sqrt{2}}$$

$$+\frac{5I_2^{5/2}\sin(4t-5\theta_2)}{72\sqrt{2}}-\frac{2\sqrt{2}I_2^{5/2}\sin(5t-5\theta_2)}{135}$$

$$+\frac{I_2^{5/2}\sin(6t-5\theta_2)}{216\sqrt{2}}+\frac{5I_1I_2^{3/2}\sin(t-3\theta_2)}{9\sqrt{2}}$$

$$-\frac{7I_2^{5/2}\sin(t-3\theta_2)}{36\sqrt{2}}-\frac{I_1I_2^{3/2}\sin(2t-3\theta_2)}{18\sqrt{2}}$$

$$-\frac{13I_2^{5/2}\sin(2t-3\theta_2)}{72\sqrt{2}}+\frac{\sqrt{2}I_1I_2^{3/2}\sin(3t-3\theta_2)}{27}$$

$$+\frac{5I_2^{5/2}\sin(3t-3\theta_2)}{27\sqrt{2}}-\frac{I_1I_2^{3/2}\sin(4t-3\theta_2)}{18\sqrt{2}}$$

$$-\frac{I_2^{5/2}\sin(4t-3\theta_2)}{18\sqrt{2}}+\frac{I_1I_2^{3/2}\sin(6t-3\theta_2)}{162\sqrt{2}}$$

$$+\frac{I_2^{5/2}\sin(6t-3\theta_2)}{648\sqrt{2}}-\frac{I_1I_2^{3/2}\sin(t-2\theta_1-3\theta_2)}{9\sqrt{2}}$$

$$+\frac{I_1I_2^{3/2}\sin(2t-2\theta_1-3\theta_2)}{108\sqrt{2}}+\frac{7I_1I_2^{3/2}\sin(3t-2\theta_1-3\theta_2)}{54\sqrt{2}}$$

$$-\frac{5I_1I_2^{3/2}\sin(4t-2\theta_1-3\theta_2)}{36\sqrt{2}}+\frac{4\sqrt{2}I_1I_2^{3/2}\sin(5t-2\theta_1-3\theta_2)}{135}$$

$$-\frac{I_1I_2^{3/2}\sin(6t-2\theta_1-3\theta_2)}{108\sqrt{2}}-\frac{355I_1I_2^{3/2}\sin(2\theta_1-3\theta_2)}{216\sqrt{2}}$$

$$+\frac{49\sqrt{2}I_1I_2^{3/2}\sin(t+2\theta_1-3\theta_2)}{27}-\frac{13I_1I_2^{3/2}\sin(2t+2\theta_1-3\theta_2)}{18\sqrt{2}}$$

$$-\frac{I_1I_2^{3/2}\sin(3t+2\theta_1-3\theta_2)}{54\sqrt{2}}+\frac{7I_1I_2^{3/2}\sin(4t+2\theta_1-3\theta_2)}{216\sqrt{2}}$$

$$-\frac{\sqrt{2}I_1^2\sqrt{I_2}\sin(t-\theta_2)}{3}+\frac{23\sqrt{2}I_1I_2^{3/2}\sin(t-\theta_2)}{9}$$

$$-\frac{20\sqrt{2}I_2^{5/2}\sin(t-\theta_2)}{27}-\frac{I_1^2\sqrt{I_2}\sin(2t-\theta_2)}{2\sqrt{2}}$$

$$-\frac{2\sqrt{2}I_1I_2^{3/2}\sin(2t-\theta_2)}{3}+\frac{11I_2^{5/2}\sin(2t-\theta_2)}{18\sqrt{2}}$$

$$+\frac{5I_1^2\sqrt{I_2}\sin(3t-\theta_2)}{18\sqrt{2}}+\frac{I_1I_2^{3/2}\sin(3t-\theta_2)}{9\sqrt{2}}$$

$$-\frac{7I_2^{5/2}\sin(3t-\theta_2)}{54\sqrt{2}}-\frac{I_1^2\sqrt{I_2}\sin(4t-\theta_2)}{24\sqrt{2}}$$

$$+\frac{I_1I_2^{3/2}\sin(4t-\theta_2)}{36\sqrt{2}}+\frac{I_2^{5/2}\sin(4t-\theta_2)}{216\sqrt{2}}$$

$$-\frac{I_1^2\sqrt{I_2}\sin(t-4\theta_1-\theta_2)}{6\sqrt{2}}+\frac{I_1^2\sqrt{I_2}\sin(2t-4\theta_1-\theta_2)}{72\sqrt{2}}$$

$$+\frac{7I_1^2\sqrt{I_2}\sin(3t-4\theta_1-\theta_2)}{36\sqrt{2}}-\frac{5I_1^2\sqrt{I_2}\sin(4t-4\theta_1-\theta_2)}{24\sqrt{2}}$$

$$+\frac{2\sqrt{2}I_1^2\sqrt{I_2}\sin(5t-4\theta_1-\theta_2)}{45}-\frac{I_1^2\sqrt{I_2}\sin(6t-4\theta_1-\theta_2)}{72\sqrt{2}}$$

$$+\frac{I_1^2\sqrt{I_2}\sin(t-2\theta_1-\theta_2)}{3\sqrt{2}}-\frac{I_1I_2^{3/2}\sin(t-2\theta_1-\theta_2)}{6\sqrt{2}}$$

$$+\frac{I_1^2\sqrt{I_2}\sin(2t-2\theta_1-\theta_2)}{2\sqrt{2}}+\frac{5I_1I_2^{3/2}\sin(2t-2\theta_1-\theta_2)}{12\sqrt{2}}$$

$$-\frac{7\sqrt{2}I_1^2\sqrt{I_2}\sin(3t-2\theta_1-\theta_2)}{27}-\frac{2\sqrt{2}I_1I_2^{3/2}\sin(3t-2\theta_1-\theta_2)}{9}$$

$$+\frac{I_1^2\sqrt{I_2}\sin(4t-2\theta_1-\theta_2)}{6\sqrt{2}}+\frac{I_1I_2^{3/2}\sin(4t-2\theta_1-\theta_2)}{6\sqrt{2}}$$

$$-\frac{I_1^2\sqrt{I_2}\sin(6t-2\theta_1-\theta_2)}{162\sqrt{2}}-\frac{I_1I_2^{3/2}\sin(6t-2\theta_1-\theta_2)}{108\sqrt{2}}$$

$$+\frac{85I_1^2\sqrt{I_2}\sin(2\theta_1-\theta_2)}{36\sqrt{2}}-\frac{185I_1I_2^{3/2}\sin(2\theta_1-\theta_2)}{72\sqrt{2}}$$

$$+\frac{5I_1^2\sqrt{I_2}\sin(t+2\theta_1+\theta_2)}{3\sqrt{2}}-\frac{13I_1I_2^{3/2}\sin(t+2\theta_1-\theta_2)}{6\sqrt{2}}$$

$$-\frac{I_1^2\sqrt{I_2}\sin(2t+2\theta_1-\theta_2)}{9\sqrt{2}}-\frac{\sqrt{2}I_1I_2^{3/2}\sin(2t+2\theta_1-\theta_2)}{9}$$

$$+\frac{I_1 I_2^{3/2}\sin(3t+2\theta_1-\theta_2)}{9\sqrt{2}}+\frac{5I_1^2\sqrt{I_2}\sin(4\theta_1-\theta_2)}{54\sqrt{2}}$$

$$+\frac{I_1^2\sqrt{I_2}\sin(t+4\theta_1-\theta_2)}{6\sqrt{2}}-\frac{I_1^2\sqrt{I_2}\sin(3t+4\theta_1-\theta_2)}{324\sqrt{2}}$$

$$-\frac{5I_1^2\sqrt{I_2}\sin(\theta_2)}{24\sqrt{2}}+\frac{85I_1 I_2^{3/2}\sin(\theta_2)}{36\sqrt{2}}$$

$$-\frac{155I_2^{5/2}\sin(\theta_2)}{216\sqrt{2}}+\frac{5I_1 I_2^{3/2}\sin(3\theta_2)}{54\sqrt{2}}$$

$$-\frac{5I_2^{5/2}\sin(3\theta_2)}{27\sqrt{2}}+\frac{43I_2^{5/2}\sin(5\theta_2)}{1080\sqrt{2}}$$

$$-\frac{I_1^2\sqrt{I_2}\sin(t+\theta_2)}{2\sqrt{2}}+\frac{5I_1 I_2^{3/2}\sin(t+\theta_2)}{3\sqrt{2}}$$

$$-\frac{7I_2^{5/2}\sin(t+\theta_2)}{18\sqrt{2}}-\frac{I_1^2\sqrt{I_2}\sin(2t+\theta_2)}{3\sqrt{2}}$$

$$-\frac{I_1 I_2^{3/2}\sin(2t+\theta_2)}{9\sqrt{2}}+\frac{2\sqrt{2}I_2^{5/2}\sin(2t+\theta_2)}{27}$$

$$+\frac{I_1^2\sqrt{I_2}\sin(3t+\theta_2)}{9\sqrt{2}}-\frac{I_2^{5/2}\sin(3t+\theta_2)}{27\sqrt{2}}$$

$$+\frac{I_1^2\sqrt{I_2}\sin(t-4\theta_1+\theta_2)}{4\sqrt{2}}+\frac{I_1^2\sqrt{I_2}\sin(2t-4\theta_1+\theta_2)}{24\sqrt{2}}$$

$$-\frac{I_1^2\sqrt{I_2}\sin(3t-4\theta_1+\theta_2)}{27\sqrt{2}}+\frac{I_1^2\sqrt{I_2}\sin(6t-4\theta_1+\theta_2)}{648\sqrt{2}}$$

$$+\frac{23\sqrt{2}I_1^2\sqrt{I_2}\sin(t-2\theta_1+\theta_2)}{9}-\frac{26\sqrt{2}I_1 I_2^{3/2}\sin(t-2\theta_1+\theta_2)}{9}$$

$$-\frac{2\sqrt{2}I_1^2\sqrt{I_2}\sin(2t-2\theta_1+\theta_2)}{3}+\frac{5I_1 I_2^{3/2}\sin(2t-2\theta_1+\theta_2)}{6\sqrt{2}}$$

$$+\frac{I_1^2\sqrt{I_2}\sin(3t-2\theta_1+\theta_2)}{9\sqrt{2}}+\frac{I_1 I_2^{3/2}\sin(3t-2\theta_1+\theta_2)}{6\sqrt{2}}$$

$$+\frac{I_1^2\sqrt{I_2}\sin(4t-2\theta_1+\theta_2)}{36\sqrt{2}}-\frac{5I_1 I_2^{3/2}\sin(4t-2\theta_1+\theta_2)}{72\sqrt{2}}$$

$$+\frac{25I_1^2\sqrt{I_2}\sin(2\theta_1+\theta_2)}{54\sqrt{2}}+\frac{5I_1 I_2^{3/2}\sin(2\theta_1+\theta_2)}{18\sqrt{2}}$$

$$-\frac{I_1 I_2^{3/2}\sin(t+2\theta_1+\theta_2)}{3\sqrt{2}}+\frac{I_1^2\sqrt{I_2}\sin(3t+2\theta_1+\theta_2)}{81\sqrt{2}}$$

$$+\frac{I_1 I_2^{3/2}\sin(3t+2\theta_1+\theta_2)}{54\sqrt{2}}-\frac{43I_1^2\sqrt{I_2}\sin(4\theta_1+\theta_2)}{360\sqrt{2}}$$

$$+\frac{I_1^2\sqrt{I_2}\sin(t+4\theta_1+\theta_2)}{36\sqrt{2}}+\frac{2\sqrt{2}I_1 I_2^{3/2}\sin(t+3\theta_2)}{9}$$

$$-\frac{I_2^{5/2}\sin(t+3\theta_2)}{18\sqrt{2}}-\frac{I_1 I_2^{3/2}\sin(3t+3\theta_2)}{81\sqrt{2}}$$

$$-\frac{I_2^{5/2}\sin(3t+3\theta_2)}{324\sqrt{2}}+\frac{23I_1 I_2^{3/2}\sin(t-2\theta_1+3\theta_2)}{18\sqrt{2}}$$

$$+\frac{I_2 I_2^{3/2}\sin(2t-2\theta_1+3\theta_2)}{27\sqrt{2}}-\frac{I_1 I_2^{3/2}\sin(3t-2\theta_1+3\theta_2)}{27\sqrt{2}}$$

$$-\frac{43I_1 I_2^{3/2}\sin(2\theta_1+3\theta_2)}{540\sqrt{2}}+\frac{I_1 I_2^{3/2}\sin(t+2\theta_1+3\theta_2)}{54\sqrt{2}}$$

$$-\frac{I_2^{5/2}\sin(t+5\theta_2)}{108\sqrt{2}}.$$

References

[1] B R Sitaram and Mitaxi P Mehta, *Pramana – J. Phys.* **45**, 141 (1995)

[2] M Henon and C Heiles, *Astron. J.* **69**, 73 (1964)

[3] M V Berry, in Topics in nonlinear dynamics: A tribute to Sir Edward Bullard, *A conference proceedings*, edited by S Jorna (American Institute of Physics, New York, 19 p. 37

[4] M Tabor, *Chaos and integrability in nonlinear dynamics: An introduction* (John Wiley a Sons, New York, 1989) p. 106

[5] F A Gustavson, *Astron. J.* **71**, 670 (1966)

[6] Y F Chang, M Tabor and J Weiss, *J. Math. Phys.* **23**, 531 (1982)

— journal of
physics

August 1995
pp. 165–174

The Coulomb Green's function revisited

S S VASAN and M SEETHARAMAN
Department of Theoretical Physics, University of Madras, Guindy Campus, Madras 600 025, India

MS received 18 March 1995

Abstract. It is demonstrated how the energy-dependent Green's function for the Schrödinger–Coulomb problem can be deduced from a knowledge of the harmonic oscillator time-propagator. All the known results of the Coulomb system are shown to be elegantly derivable from such a connection.

Keywords. Coulomb-oscillator connection; Coulomb energy-Green's function.

PACS No. 03·65

1. Introduction

The purpose of this article is to show how the quantum mechanical Green's function for the Coulomb potential can be obtained from a knowledge of the Feynman propagator for the harmonic oscillator. The key ingredient in the analysis is a remarkably simple relation between the radial parts of the Green's functions for the oscillator and the Coulomb problems. This is an example of a general relation between the Green's functions for different potentials [1]. That there exists a connection between the oscillator and Coulomb systems is something known for a long time. What is more recent is the realization that this connection takes the most succinct and useful form when expressed in terms of the radial Green's function. It enables one to extract all the results pertaining to one physical system when the Green's function for a related system is known.

It is somewhat surprising that the Green's function for the Schrödinger equation with the Coulomb potential was not known completely until the sixties, given the fact that the exact treatment of the hydrogen atom was one of the early triumphs of quantum mechanics. The first general expression for the Coulomb Green's function appears to be a double integral representation due to Wichmann and Woo [2]. A one-parameter integral for the Green's function in momentum space was derived by Schwinger [3]. It was Hostler [4, 5] who obtained for the first time a closed form expression in coordinate space. Starting with the bilinear expansion of the Green's function in terms of energy eigenfunctions, he carried out the summation over the bound states and the integration over the continuum, and expressed the resulting one-parameter integral as a sum of products of Whittaker functions of different arguments. More recently, several authors [6–8] have computed the Coulomb Green's function in the context of solving the hydrogen atom problem by path integration.

The starting point of our method is the time-dependent propagator for the three-dimensional isotropic harmonic oscillator. By Fourier-transforming the radial part of the propagator, we derive first an expression for the radial part of the Green's function.

Invoking the relation referred to earlier, we go from the oscillator radial Green's function to the Coulomb radial Green's function. Once the latter is known, all the results of the Coulomb problem can be deduced: the discrete spectrum and the normalized eigenfunctions, the continuum and its δ-normalized eigenfunctions, as well as the completeness property of the eigenfunctions. By attaching spherical harmonics to the radial Green's function appropriately, and summing the resulting partial wave series, we obtain an expression for the complete Coulomb Green's function as an integral over a single variable.

The main advantage of our method is that there is no need to deal with the continuum and discrete states of the Coulomb potential separately. This is because we consider the partial wave expansion of the Green's function, rather than its eigenfunction expansion, and focus attention on the radial part which carries all the essential information, and contains so to speak both the discrete and continuum states. The angular degrees of freedom can thus be decoupled at the beginning and brought back at the end. Further, our method is simple and transparent, and leads to the final expression for the Green's function with much less labour.

2. Radial Green's function for the harmonic oscillator

The time-dependent propagator for a particle of unit mass moving from a position $\mathbf{r}'$ at time t' to a position $\mathbf{r}$ at time t in a potential V satisfies the equation ($\hbar = 1$)

$$\left[i\frac{\partial}{\partial t} + \frac{1}{2}\nabla^2 - V\right] K(\mathbf{r}t, \mathbf{r}'t') = i\delta(\mathbf{r}-\mathbf{r}')\delta(t-t'). \tag{1}$$

If the potential is time-independent the propagator depends on time only through $T = t - t'$, and if V is spherically symmetric, then it has also the partial wave expansion

$$K(\mathbf{r}, \mathbf{r}', T) = \sum_l \sum_m \frac{K_l(r, r', T)}{rr'} Y^*_{lm}(\theta, \phi)\, Y_{lm}(\theta', \phi'). \tag{2}$$

The function $K_l(r, r', T)$ defined by (2) is the radial propagator. For the isotropic harmonic oscillator with $V = \frac{1}{2}\omega^2 r^2$, the radial propagator is known to be given by the expression [9]

$$K_l^{\mathrm{osc}}(r, r', T) = \frac{\omega\sqrt{rr'}(-i)^{l+3/2}}{\sin\omega T} \exp\left[\frac{1}{2} i\omega(r^2 + r'^2)\cot\omega T\right] J_{l+1/2}\left(\frac{\omega rr'}{\sin\omega T}\right), \tag{3}$$

where $J_{l+1/2}$ is the Bessel function of the first kind.

The Green's function $G(\mathbf{r}, \mathbf{r}', E)$ which is a function of the energy E is related to the propagator by a Fourier transformation. For a central potential the angular dependence of G can be separated out exactly as in (2), with the radial part $g_l(r, r', E)$ replacing K_l on the rhs. For g_l we adopt the following definition:

$$g_l(r, r', E) = i\int_0^\infty \mathrm{d}T \exp(iET) K_l(r, r', T). \tag{4}$$

In (4) E is to be understood as $E + i\delta$ whenever necessary, together with the limit $\delta \to 0+$.

Our objective now is to obtain an expression for the oscillator Green's function g_l^{osc} using (3) and (4). To this end we consider the integral [10]

$$I = \int_0^\infty \left(\coth\frac{x}{2}\right)^{2\lambda} \exp(-\beta\cosh x) J_{2\mu}(\alpha\sinh x)\mathrm{d}x. \tag{5}$$

This integral exists provided the constants α, β, λ and μ satisfy the following two conditions:

$$\mathrm{Re}(\mu-\lambda) > -\tfrac{1}{2}, \quad \mathrm{Re}\,\beta > |\mathrm{Im}\,\alpha|. \tag{6}$$

It has the value

$$I = \frac{\Gamma(\frac{1}{2}-\lambda+\mu)}{\alpha\Gamma(2\mu+1)} M_{-\lambda,\mu}(\sqrt{\alpha^2+\beta^2}-\beta)\, W_{\lambda,\mu}(\sqrt{\alpha^2+\beta^2}+\beta) \tag{7}$$

where M and W are the Whittaker functions defined by the relations

$$M_{\lambda,\mu} = z^{(1/2)+\mu}\exp(-z/2)\Phi(\mu-\lambda+\tfrac{1}{2}, 2\mu+1; z), \tag{8}$$

$$W_{\lambda,\mu}(z) = \frac{\Gamma(-2\mu)}{\Gamma(\frac{1}{2}-\mu-\lambda)} M_{\lambda,\mu}(z) + \frac{\Gamma(2\mu)}{\Gamma(\frac{1}{2}+\mu-\lambda)} M_{\lambda,-\mu}(z). \tag{9}$$

In (8) $\Phi(a, c, z)$ is the confluent hypergeometric function which is regular at the origin.

We now change the variable in (5) by writing $\sinh x = \mathrm{cosech}\, t$. This transforms the integral into

$$I = \int_0^\infty \mathrm{d}t \exp(2\lambda t)\,\mathrm{cosech}\, t \exp[-\beta\coth t] J_{2\mu}(\alpha\,\mathrm{cosech}\, t). \tag{10}$$

The two conditions given in (6) ensure the convergence of the integral at the upper and lower limits respectively. Further, the first condition also ensures that the integrand in (10) [which we denote by $f(t)$] vanishes exponentially as $|t| \to \infty$ in the first quadrant of the complex t plane. Let us consider now a quarter circle of radius R in the first quadrant centred at the origin and bounded by the axes. Within this closed contour the function $f(t)$ has no singularities. Therefore an application of Cauchy's theorem yields, in the limit $R \to \infty$, the result

$$\int_0^\infty f(t)\mathrm{d}t = \int_0^{i\infty} f(t)\mathrm{d}t.$$

Using this in (10) and writing $t = i\tau$, we get

$$I = i\int_0^\infty \mathrm{d}\tau \exp(2i\lambda\tau)\,\mathrm{cosec}\,\tau \exp(i\beta\cot\tau) J_{2\mu}(-i\alpha\,\mathrm{cosec}\,\tau). \tag{11}$$

If we make the replacements

$$\tau = \omega T, \quad 2\lambda\omega = E, \quad \beta = \tfrac{1}{2}\omega(r^2+r'^2), \quad \alpha = i\omega r r', \quad 2\mu = l+\tfrac{1}{2} \tag{12}$$

in (11), the result is

$$I = \omega\int_0^\infty \mathrm{d}T \frac{\exp(iET)}{\sin\omega T} \exp\left[\frac{1}{2} i\omega(r^2+r'^2)\cot\omega T\right] J_{l+1/2}\left(\frac{\omega r r'}{\sin\omega T}\right). \tag{13}$$

It follows from (3), (4) and (13) that the oscillator radial Green's function is given by

$$g_l^{\text{osc}}(r,r',E) = (-i)^{l+1/2}\sqrt{rr'}\,I. \tag{14}$$

Using (7) to replace I on the rhs of (14), we finally arrive at the explicit expression

$$g_l^{\text{osc}}(r,r',E) = \frac{\Gamma\left(-\dfrac{E}{2\omega}+\dfrac{l}{2}+\dfrac{3}{4}\right)}{\omega\sqrt{rr'}\,\Gamma\left(l+\dfrac{3}{2}\right)} M_{\lambda,\mu}(\omega r'^2)\, W_{\lambda,\mu}(\omega r^2), \tag{15a}$$

$$\lambda = E/2\omega, \quad \mu = \tfrac{1}{2}(l+\tfrac{1}{2}). \tag{15b}$$

The above form holds for $r > r'$; for $r < r'$ the arguments of the two Whittaker functions must be interchanged. In obtaining (15), a phase factor $(-i)^{l+3/2}$ has been absorbed, by making use of the reflection property

$$(-z)^{-(1/2)-\mu} M_{-\lambda,\mu}(-z) = z^{-(1/2)-\mu} M_{\lambda,\mu}(z). \tag{16}$$

We note that whenever the argument of the gamma function in the numerator of (15) is a non-positive integer $-n_r$, g_l^{osc} has a pole in the energy plane at $E = (2n_r + l + 3/2)\omega$. These are the allowed energies of the oscillator for a fixed value of l. There are no other singularities because $M_{\lambda,\mu}$ and $W_{\lambda,\mu}$ are entire functions of λ. This follows from the definitions (8) and (9) and the fact that $\Phi(a,c,z)$ is an entire function of a.

3. Coulomb radial Green's function

The energy-dependent Green's function associated with the Coulomb potential $V(r) = -e^2/r$ (hydrogen atom) can be determined from a knowledge of g_l^{osc}. We have shown in an earlier work [1] that the radial part of the Coulomb Green's function is related in a remarkably simple manner to the oscillator radial Green's function. If we denote by $g_L^{\text{osc}}(r,r',\varepsilon,\omega)$ the latter, corresponding to an oscillator of frequency ω (indicated explicitly now), energy ε and angular momentum L, the precise connection between the two is

$$g_l^{\text{Cou}}(r,r',E) = 2(rr')^{1/4} g^{\text{osc}}_{2l+1/2}(\sqrt{r},\sqrt{r'},\varepsilon = 4e^2, \omega = \sqrt{-8E}). \tag{17}$$

In other words, the Coulomb radial Green's function for a given l and energy E is determined by the radial Green's function of an oscillator of frequency $\sqrt{-8E}$, energy $4e^2$ and angular momentum continued to the value $2l + 1/2$. Inserting (15) into (17), we obtain the expression

$$g_l^{\text{Cou}}(r,r',E) = \frac{2\Gamma(-\lambda+l+1)}{(2l+1)!\,\omega} M_{\lambda,\mu}(\omega r')\, W_{\lambda,\mu}(\omega r), \tag{18a}$$

with

$$\omega = \sqrt{-8E}, \quad \lambda = 2e^2/\omega, \quad \mu = l+\tfrac{1}{2}. \tag{18b}$$

Using (18) we can determine the complete Green's function for the Coulomb problem. Deferring this to a later section, we now consider how the Coulomb wave functions can be deduced from g_l^{Cou} which will be simply called g_l hereafter for convenience.

Energy eigenfunctions of the hydrogen atom

e singularities of the function g_l in the E plane constitute the spectrum of allowed ergies of the hydrogen atom. We see from (17) that g_l has simple poles when

$$-2e^2/\omega + l + 1 = -n_r, \quad n_r = 0, 1, 2, \ldots$$

ese correspond to bound states with energies (cf. 18b)

$$E = E_n = -e^4/2(n_r + l + 1)^2 = -e^4/2n^2, \tag{19}$$

ere $n = n_r + l + 1$ is the principal quantum number.

The bound state wave functions are given by the residue of g_l at its poles. If we denote u_{nl} the reduced radial wave function, we have

$$\mathrm{Res}[g_l(r, r', E)]_{E=E_n} = \lim_{E \to E_n} [(E_n - E) g_l] = u_{nl}(r) u_{nl}(r'). \tag{20}$$

the pole $\omega = \omega_n = 2/na$, where $a = e^{-2}$ is the Bohr radius, and

$$u_{nl}(r) u_{nl}(r') = \lim_{\omega \to \omega_n} \left[\frac{1}{8} (\omega^2 - \omega_n^2) g_l \right]. \tag{21}$$

so, $\lambda = -n$ in the limit; for this value of λ the Whittaker functions $M_{\lambda, l+1/2}$ and $_{,l+1/2}$ are both expressible in terms of Laguerre polynomials in a standard way. straightforward evaluation of the above limit yields the wave function

$$u_{nl}(r) = \left[\frac{(n-l-1)!}{n^2 a (n+l)!^3} \right]^{1/2} \left(\frac{2r}{na} \right)^{l+1} \exp(-r/na)\, L_{n+l}^{2l+1} \left(\frac{2r}{na} \right). \tag{22}$$

nay be noted that the wave function comes out with the correct normalization factor. e reason for this is to be traced ultimately to the normalization of the propagator which is specified by the inhomogeneous eq. (1).

In addition to the poles g_l has a branch point at $E = 0$. To see this we must consider e behaviour of the Green's function near $\omega = 0$. First, we note that the Whittaker nction $M_{\lambda, l+1/2}$ for $\lambda = 2e^2/\omega$ has the following behaviour as $\omega \to 0$:

$$M_{\lambda, l+1/2}(\omega r') \sim (\omega r')^{l+1} [A_0(r') + A_1(r')\omega + 0(\omega^2)].$$

is may be readily deduced from (8) on substituting the basic series representation of e confluent hypergeometric function Φ. Next we make use of an explicit series pansion of the Whittaker function $W_{\lambda, \mu}$ which is valid when $2\mu + 1$ is a positive eger [11]. This, coupled with the asymptotic expansion of $\Gamma(z + a)$, shows that for all ω

$$\Gamma(-\lambda + l + 1)\, W_{\lambda, l+1/2}(\omega r) \sim \omega^{-l} [B_0(r) + B_1(r)\omega + O(\omega^2)].$$

ence the behaviour of the Green's function is given by

$$g_l(r, r', E) \sim C_0(r, r') + C_1(r, r')\omega + O(\omega^2). \tag{23}$$

is result implies that g_l has a square-root branch point in the energy plane at the igin. The associated branch cut can be taken to run along the positive real axis. This rresponds to choosing the principal value for the argument of E: $-\pi < \arg E \leqslant \pi$.

The occurrence of the branch point singularity is indicative of a continuum of positive energy eigenvalues for the Coulomb potential. The corresponding eigenfunctions are determined by the discontinuity of g_l across the branch out. Denoting by $v_l(r, E)$ the continuum eigenfunction belonging to some $E > 0$, we have the relation

$$\begin{aligned}\operatorname{disc} g_l(r, r', E) &\equiv \lim_{\delta \to 0} [g_l(r, r', E + i\delta) - g_l(r, r', E - i\delta)] \\ &= 2\pi i v_l(r, E) v_l^*(r', E). \end{aligned} \tag{24}$$

Since for $E > 0$, $\omega(E \pm io) = \mp i|\omega|$, we introduce the asymptotic wave number $k = \sqrt{2E}$ and write $\omega(E \pm io) = \mp 2ik$, $k > 0$. Then the discontinuity can be written as

$$\begin{aligned}-ik(2l+1)!\operatorname{disc} g_l = &\Gamma(-\lambda' + \mu + \tfrac{1}{2}) M_{\lambda', \mu}(-2ikr')\, W_{\lambda', \mu}(-2ikr) \\ &+ \Gamma(\lambda' + \mu + \tfrac{1}{2}) M_{-\lambda', \mu}(2ikr')\, W_{-\lambda', \mu}(2ikr) \end{aligned} \tag{25}$$

where $\lambda' = ie^2/k$ and $\mu = l + 1/2$. In order to identify the eigenfunction v_l, we must cast the rhs of (25) in a factorized form. To this end, we first replace the W functions in (25) in terms of the M's, using the relation (9). The resulting expression is rewritten by invoking the reflection property (16) of the M function, and then simplified by using the standard property $\Gamma(z)\Gamma(1-z) = \pi \operatorname{cosec} \pi z$ of the gamma function. The entire calculation is best done keeping μ arbitrary, and putting $\mu = l + 1/2$ only at the end. The result is the product form

$$\begin{aligned}-ik(2l+1)!\operatorname{disc} g_l = &\frac{|\Gamma(\lambda' + l + 1)|^2}{(2l+1)!} \exp(-i\pi\lambda') M_{\lambda, l+1/2}(-2ikr') \\ &\times M_{-\lambda', l+1/2}(2ikr). \end{aligned} \tag{26}$$

From (26), (24) and (8), we get (apart from an over all phase factor) the continuum wave function:

$$\begin{aligned}v_l(r, E) = &\frac{\exp(\pi e^2/2k)}{\sqrt{2\pi k}(2l+1)!} \left| \Gamma\left(\frac{ie^2}{k} + l + 1\right) \right| (2kr)^{l+1} \exp(-ikr) \\ &\times \Phi\left(\frac{ie^2}{k} + l + 1, 2l + 2, 2ikr\right). \end{aligned} \tag{27}$$

This is the correct reduced radial wave function which is normalized according to

$$\int_0^\infty v_l^*(r, E) v_l(r, E) \mathrm{d}r = \delta(E - E'). \tag{28}$$

5. Completeness of the Coulomb eigenfunctions

The important property of completeness possessed by the Coulomb eigenfunctions can be deduced from the Green's function g_l as a direct consequence of its analytic properties in the energy plane. We present here an explicit demonstration.

For the present purpose it is more advantageous to consider g_l as a function of ω rather than of E. In the ω plane the only singularities are simple poles located on the

E plane, there is no singularity at $\omega = 0$, as shown by (23). As $\omega \to \infty$ in the half plane $\mathrm{Re}\,\omega > 0$, the Whittaker functions have the asymptotic behaviour

$$M_{\lambda,l+1/2} \to \frac{(2l+1)!}{l!} \exp\left(\frac{1}{2}\omega r'\right), \quad W_{\lambda,l+1/2} \to \exp\left(-\frac{1}{2}\omega r\right).$$

Therefore, the asymptotic form of g_l in the right half plane is

$$g_l \to \frac{2}{\omega} \exp\left[-\frac{1}{2}\omega(r-r')\right].$$

Consider now a contour in the ω plane made up of the imaginary axis from $\omega = iR$ to $\omega = -iR$ and a semicircle C_R lying in the right half plane with centre at the origin and radius $R > 2e^2/(l+1)$. All the poles of g_l lie within the contour. Integrating ωg_l around the contour, we have

$$\int_{C_R} \omega g_l(\omega)\mathrm{d}\omega + \int_{iR}^{-iR} \omega g_l(\omega)\mathrm{d}\omega = 2\pi i \sum (\text{residues of } \omega g_l). \tag{29}$$

The rhs can be immediately written down from (21):

$$\sum \text{residues} = \sum_{n=l+1}^{\infty} [(\omega - \omega_n)\omega g_l(\omega)]_{\omega=\omega_n}$$

$$= 4 \sum_{n=l+1}^{\infty} u_{nl}(r) u_{nl}(r'). \tag{30}$$

Evaluating the lhs in the limit $R \to \infty$, the integral over the semicircle becomes

$$\int_{C_R} \omega g_l(\omega)\mathrm{d}\omega \to \int_{C_R} 2\exp\left[-\frac{1}{2}\omega(r-r')\right]\mathrm{d}\omega$$

$$= \lim_{R\to\infty} 2\int_{-iR}^{iR} \exp\left[-\frac{1}{2}\omega(r-r')\right]\mathrm{d}\omega$$

$$= 8\pi i\delta(r-r'). \tag{31}$$

As for the other integral on the lhs, we can write it as

$$\int_{iR}^{-iR} \omega g_l(\omega)\mathrm{d}\omega = \int_{iR}^{0} \omega g_l(i|\omega|)\mathrm{d}\omega + \int_{0}^{-iR} \omega g_l(-i|\omega|)\mathrm{d}\omega.$$

In view of the relation $\omega = \sqrt{-8E}$, we can identify, as was done earlier, $g_l(\pm i|\omega|) = g_l(E \mp io)$ with $E > 0$. Thus we have

$$\int_{iR}^{-iR} \omega g_l \mathrm{d}\omega = \int_{R^2/8}^{0} (-4\mathrm{d}E) g_l(E - io) + \int_{0}^{R^2/8} (-4\mathrm{d}E) g_l(E + io).$$

Now, using (24) and proceeding to the limit $R \to \infty$, we get

$$\int_{i\infty}^{-i\infty} \omega g_l(\omega)\mathrm{d}\omega = -8\pi i \int_0^{\infty} \mathrm{d}E\, v_l(r,E) v_l^*(r',E). \tag{32}$$

Putting (30), (31) and (32) in (29), we have the completeness relation

$$\sum_{n=l+1}^{\infty} u_{nl}(r)u_{nl}(r') + \int_0^{\infty} dE\, v_l(r,E)v_l^*(r',E) = \delta(r-r'). \tag{33}$$

It may be noted that the above relation was also demonstrated by Mukunda [12] starting from the explicit expressions for the Coulomb wave functions.

6. The complete Green's function

The function g_l that we have considered so far is the radial part of the complete Green's function $G(\mathbf{r},\mathbf{r}',E)$, the connection between the two functions being given by the expansion

$$G(\mathbf{r},\mathbf{r}',E) = \sum_l \sum_m \frac{g_l(r,r',E)}{rr'} Y_{lm}(\theta,\phi)\, Y_{lm}^*(\theta',\phi'). \tag{34}$$

Making use of the relation

$$P_l(\cos\gamma) = \sum_m \frac{4\pi}{2l+1} Y_{lm}^*(\theta,\phi)\, Y_{lm}(\theta',\phi')$$

where γ is the angle between the two vectors $\mathbf{r}$ and $\mathbf{r}'$ and the explicit form (18) of g_l, we obtain the expression

$$G = \frac{1}{2\pi\omega rr'} \sum_l (2l+1) P_l(\cos\gamma) \frac{\Gamma(-\lambda+l+1)}{(2l+1)!} \times M_{\lambda,l+1/2}(wr')\, W_{\lambda,l+1/2}(\omega r). \tag{35}$$

Now the use of the formula [10]

$$\int_0^{\infty} \exp\left[-\frac{1}{2}(a+b)t\cosh x\right] \left(\coth\frac{x}{2}\right)^{2\lambda} I_{2\mu}(t\sqrt{ab}\sinh x)\,dx = \frac{\Gamma(\frac{1}{2}+\mu-\lambda)}{t\sqrt{ab}\,\Gamma(1+2\mu)} W_{\lambda,\mu}(at) M_{\lambda,\mu}(bt)$$

which holds when $\mathrm{Re}(1/2+\mu-\lambda)>0$, $\mathrm{Re}\, t>0$ and $a>b>0$, enables us to rewrite (35) as

$$G = \frac{1}{2\pi\sqrt{rr'}} \sum_l (2l+1) P_l(\cos\gamma) \int_0^{\infty} dx \exp\left[-\frac{1}{2}\omega(r+r')\cosh x\right] \times \left(\coth\frac{x}{2}\right)^{2\lambda} I_{2l+1}(\omega\sqrt{rr'}\sinh x). \tag{36}$$

Interchanging the order of the summation and the integration and applying the identity

$$\sum_l (2l+1) P_l(\cos\theta) I_{2l+1}(z) = \frac{1}{2} z I_0\left(z\cos\frac{\theta}{2}\right),$$

the summation in (36) can be performed. The result is

$$G=\frac{\omega}{4\pi}\int_0^\infty \mathrm{d}x \exp\left[-\frac{1}{2}\omega(r+r')\cosh x\right]\left(\coth\frac{x}{2}\right)^{2\lambda}\sinh x \times I_0\left(\omega\sqrt{rr'}\cos\frac{\gamma}{2}\sinh x\right). \tag{37}$$

By the change of variable $\operatorname{cosech} t=\sinh x$, (37) can be transformed into

$$G=\frac{\omega}{4\pi}\int_0^\infty \mathrm{d}t \exp\left[-\frac{1}{2}\omega(r+r')\coth t+2\lambda t\right]\operatorname{cosech}^2 t \times I_0\left(\omega\sqrt{rr'}\cos\frac{\gamma}{2}\operatorname{cosech} t\right). \tag{38}$$

In this expression, $\omega=\sqrt{-8E}$ and $\lambda=2e^2/\omega$.

Alternatively, we may proceed as follows. Starting with

$$G(\mathbf{r},\mathbf{r}',E)=\sum_l \frac{2l+1}{4\pi rr'} g_l(r,r',E)P_l(\cos\gamma)$$

we use (17), (14) and (13) to get

$$G=\frac{\omega}{2\pi\sqrt{rr'}}\sum_l (2l+1)P_l(\cos\gamma)(-i)^{2l+1} \times \int_0^\infty \frac{\mathrm{d}T\exp(i4e^2\,T)}{\sin\omega T}\exp\left[\frac{1}{2}i\omega(r+r')\cot\omega T\right]J_{2l+1}\left(\frac{\omega\sqrt{rr'}}{\sin\omega T}\right). \tag{39}$$

Using now the identity

$$\sum_l (2l+1)P_l(-\cos\theta)J_{2l+1}(z)=\frac{1}{2}zJ_0\left(z\cos\frac{\theta}{2}\right),$$

we obtain a different representation

$$G=\frac{\omega^2}{4\pi i}\int_0^\infty \mathrm{d}T\exp\left[4ie^2\,T+\frac{1}{2}i\omega(r+r')\cot\omega T\right] \times \operatorname{cosec}^2\omega T J_0\left(\omega\sqrt{rr'}\cos\frac{\gamma}{2}\operatorname{cosec}\omega T\right). \tag{40}$$

The above expression for the Coulomb Green's function is in agreement with those of Hostler [5] and Ho and Inomata [7] (modulo overall constant factors arising out of different definitions). At this point one can follow Hostler's steps to carry out the integration and express G in closed form in terms of Whittaker functions.

The logical end to the above analysis would be to compute the Coulomb propagator in closed form by Fourier-inverting the function G. This no one knows how to do as yet.

References

[1] S S Vasan, M Seetharaman and K Raghunathan, *Pramana – J. Phys.* **38**, 1 (1992)
[2] E H Wichmann and C-H Woo, *J. Math. Phys.* **2**, 178 (1961)
[3] J Schwinger, *J. Math. Phys.* **5**, 1606 (1964)
[4] L Hostler and R H Pratt, *Phys. Rev. Lett.* **10**, 469 (1963)
[5] L Hostler, *J. Math. Phys.* **5**, 591 (1964)
[6] H Duru and H Kleinert, *Phys. Lett.* **B84**, 185 (1979)
[7] R Ho and A Inomata, *Phys. Rev. Lett.* **48**, 231 (1982)
[8] F Steiner, *Phys. Lett.* **A106**, 363 (1984)
[9] D Peak and A Inomata, *J. Math. Phys.* **10**, 1422 (1969)
[10] I S Gradshteyn and I M Ryzhik, *Table of integrals, series and products* (Academic Press, New York. 1980) p. 729
[11] I S Gradshteyn and I M Ryzhik, *Table of integrals, series and products* (Academic Press, New York, 1980) p. 1063
[12] N Mukunda, *Am. J. Phys.* **46**, 910 (1978)

Gravitational and electromagnetic fields of a charged tachyon

K S VIRBHADRA
Physical Research Laboratory, Navrangpura, Ahmedabad 380 009, India
Present address: Theoretical Astrophysics Group, Tata Institute of Fundamental Research, Homi Bhabha Road, Bombay 400 005, India

MS received 3 October 1994

Abstract. An axially symmetric exact solution of the Einstein–Maxwell equations is obtained and is interpreted to give the gravitational and electromagnetic fields of a charged tachyon. Switching off the charge parameter yields the solution for the uncharged tachyon which was earlier obtained by Vaidya. The null surfaces for the charged tachyon are discussed.

Keywords. Einstein–Maxwell equations; tachyon.

PACS Nos 04·20; 04·40; 14·80

1. Introduction

The tardyons, the luxons, and the tachyons are the names given to particles which move, respectively, with velocities smaller than, equal to, and greater than the speed of light in vacuum [1–2]. Among these three classes of objects, tachyons have remained undetected. However, the subject of the superluminary objects have been fascinating many physicists' minds. Lucretius (50 B.C.) was probably the first scientist who mentioned such objects [3]. Few years before the special theory of relativity was given, Thomson, Heavyside, and Sommerfeld had investigated the questions arising from the assumptions that the superluminary objects exist in the nature [4]. However, with the outset of the special theory of relativity (STR), due to a misinterpretation by Einstein himself, a wrong idea prevailed that the non-existence of tachyons is a direct consequence of the STR [1,4]. To this end, Bilaumik *et al* (BDS) [4] reexamined this subject and found that it is rather the special theory of relativity that suggests a possibility for existence of superluminary objects. In order to have the energy and momentum (which are measurable quantities) real, BDS [4] hypothesized the tachyons to have their proper masses imaginary. Likewise, the proper lengths and the proper times of tachyons are also imaginary quantities. The velocity of a tachyon increases on the loss of its energy.

The causality problems (raised by Tolman, Schmidt, and Terletski) due to the assumption that the tachyons exist were resolved by Sudarshan and his co-workers [2,3]. BDS [4] suggested that the Cerenkov effect is likely to be an avenue for the detection of the faster-than-light objects if they carry electric charge. Many experimentalists [5–8] have put considerable effort to detect tachyons. Their experiments could not confirm the existence of tachyons. However, inspired by the Gell-Mann's totalitarian principle (which states that in physics anything which is not forbidden is compulsory) [2, 3], the subject of tachyons continued to be of interest to many researchers. Recami [3] presented a review on this subject.

Narlikar and Sudarshan [9] studied the propagation of tachyons in an expanding universe. They showed that the pre-mordial tachyons in a big-bang universe could not survive unless it had very large energy in the beginning. The trajectories of tachyons in the Schwarzschild background were studied by Narlikar and Dhurandhar [10]. These investigations were further extended by Dhurandhar [11] in the Kerr geometry. Vaidya [12] obtained a static, axially symmetric vacuum solution of the Einstein equations and interpreted it as describing the gravitational field of a tachyon. He found that there is a gravitational repulsion between a tachyon and a tardyon. Raychaudhuri [13] showed that there is an attraction between tachyons themselves. We [14] obtained the gravitational field of a tachyon (uncharged) in a de Sitter universe. The electromagnetic interactions between a charged tachyon and a charged tardyon, and between charged tachyons themselves have not been investigated. Therefore, it is of interest to obtain the gravitational as well as the electromagnetic fields of a charged tachyon. In the present paper, we obtain an axially symmetric exact solution of the Einstein–Maxwell equations and interpret it to give the gravitational and electromagnetic fields of a charged tachyon. We use the geometrized units ($G = 1, c = 1$) and follow the convention that the Latin indices run from 0 to 3.

2. Einstein–Maxwell equations

The Einstein–Maxwell equations are

$$R_i^k - \tfrac{1}{2} g_i^k R = 8\pi (T_i^k + E_i^k), \tag{1}$$

where

$$E_i^k = \frac{1}{4\pi}[-F_{im}F^{km} + \tfrac{1}{4} g_i^k F_{mn}F^{mn}], \tag{2}$$

$$\frac{1}{\sqrt{-g}}(\sqrt{-g}\,F^{ik})_{,k} = 4\pi J^i, \tag{3}$$

$$F_{ij,k} + F_{jk,i} + F_{ki,j} = 0. \tag{4}$$

R_i^k is the Ricci tensor. T_i^k and E_i^k are the energy-momentum tensors due to the matter and the electromagnetic field, respectively. J^i stands for the electric current density vector.

3. Solution for charged tachyon

By transforming the Reissner–Nordström solution, we have obtained a static and axially symmetric exact solution of the Einstein–Maxwell equations which is given by the line element,

$$\mathrm{d}\tau^2 = B\,\mathrm{d}t^2 - B^{-1}\mathrm{d}\rho^2 - \frac{\rho^2}{(1 - v\cos\theta)^2}(\mathrm{d}\theta^2 + \sin^2\theta\,\mathrm{d}\phi^2), \tag{5}$$

where

$$F_{\rho t} = -\frac{Q(1-v^2)}{\rho^2}. \tag{7}$$

The non-vanishing components of the energy-momentum tensor of the electromagnetic field are

$$E_t^t = E_\rho^\rho = -E_\theta^\theta = -E_\phi^\phi = \frac{Q^2}{8\pi\rho^4}(1-v^2)^2. \tag{8}$$

The current density vector and the energy-momentum tensor of matter are given by

$$J^i = 0, \quad T_i^k = 0. \tag{9}$$

We now proceed to show that the above solution gives the gravitational and electromagnetic fields of a charged tachyon.

Using the retarded time coordinate u given by

$$u = t - \int [B(\rho)]^{-1} \mathrm{d}\rho \tag{10}$$

in place of t, the above line element can be written as

$$\mathrm{d}\tau^2 = B\mathrm{d}u^2 + 2\mathrm{d}u\mathrm{d}\rho - \frac{\rho^2}{(1-v\cos\theta)^2}(\mathrm{d}\theta^2 + \sin^2\theta\,\mathrm{d}\phi^2) \tag{11}$$

and the non-vanishing component of the electromagnetic field tensor is given by

$$F_{\rho u} = -\frac{Q(1-v^2)}{\rho^2}. \tag{12}$$

Now by a coordinate transformation ρ going to r, where $\rho = r(1-v\cos\theta)$, the line element is

$$\mathrm{d}\tau^2 = D\mathrm{d}u^2 + 2\mathrm{d}u\,\mathrm{d}[r(1-v\cos\theta)] - r^2(\mathrm{d}\theta^2 + \sin^2\theta\,\mathrm{d}\phi^2), \tag{13}$$

where

$$D = 1 - v^2 + \frac{m}{r(1-v\cos\theta)} + \frac{Q^2(1-v^2)^2}{r^2(1-v\cos\theta)^2} \tag{14}$$

and the surviving components of the electromagnetic field tensor are

$$F_{ru} = -\frac{Q(1-v^2)}{r^2(1-v\cos\theta)}$$

$$F_{\theta u} = -\frac{Q(1-v^2)v\sin\theta}{r(1-v\cos\theta)^2}. \tag{15}$$

For $|v| < 1$, the solution can be transformed to the Reissner–Nordström solution given by the line element,

$$\mathrm{d}\tau^2 = B'\mathrm{d}u'^2 + 2\mathrm{d}u'\mathrm{d}r' - r'^2(\mathrm{d}\theta'^2 + \sin^2\theta'\mathrm{d}\phi^2), \tag{16}$$

where

$$B' = 1 - \frac{2M}{r'} + \frac{Q^2}{r'^2} \tag{17}$$

and

$$M = -\frac{m(1-v^2)^{-3/2}}{2}, \tag{18}$$

and the non-vanishing component of the electromagnetic field tensor

$$F_{r'u'} = -\frac{Q}{r'^2}, \tag{19}$$

by the coordinate transformations

$$\begin{aligned} u' &= u\sqrt{1-v^2}, \\ r' &= \frac{r(1-v\cos\theta)}{\sqrt{1-v^2}}, \\ \cos\theta' &= \frac{\cos\theta - v}{1 - v\cos\theta}. \end{aligned} \tag{20}$$

We obtained the axially symmetric solution by following the reverse process given here, i.e., we began with the Reissner–Nordström solution and obtained the axially symmetric solution by a complex transformation ($|v| > 1$). However, for convenience in presentation we have first written the axially symmetric solution (the line element in diagonal form) and then have shown that it transforms to the Reissner–Nordström solution for $|v| < 1$. The coordinate transformations expressed by (20) show that the origin of the frame S' moves with respect to the frame S with a uniform velocity v along the common Z-axis in the flat spacetime background [12]. The solution of the Einstein–Maxwell equations obtained by us has the following characteristics: (a) the gravitational field given by the line element (5) has all the geometrical characteristics of the Reissner–Nordström field, (b) the solution is axially symmetric which is required as there cannot be a tardyonic observer which can find a tachyon at rest, and (c) it contains a velocity parameter v, which is not possible to be transformed away for $|v| > 1$. However, for $|v| < 1$, the solution transforms to the Reissner–Nordström solution. Therefore, we interpret the solution to give the gravitational and the electromagnetic fields of a non-rotating charged tachyon. Switching off the charge parameter Q, one gets the solution for the uncharged (non-rotating) tachyon which was obtained by Vaidya [12].

4. Discussion

The solution given by us is singular at $r = 0$ and $\sec\theta = v$. The latter gives a right circular cone of semi-vertical angle arcsec(v) as the singularity surface. Again the null surfaces are given by the equation

$$(v^2-1)\rho^2 - m\rho - Q^2(v^2-1)^2 = 0. \tag{21}$$

This equation has two roots given by

$$\rho = \rho_{\pm}, \tag{22}$$

where

$$\rho_+ = \frac{m + \sqrt{m^2 + 4(v^2-1)^3 Q^2}}{2(v^2-1)},$$

$$\rho_- = \frac{m - \sqrt{m^2 + 4(v^2-1)^3 Q^2}}{2(v^2-1)}. \tag{23}$$

Using $\rho = r(1 - v\cos\theta)$, $r = (x^2 + y^2 + z^2)^{1/2}$, and $r\cos\theta = z$, the equations of null surfaces given by (22) can be written as

$$\left(z\sqrt{v^2-1} + \frac{v\rho_\pm}{\sqrt{v^2-1}}\right)^2 - (x^2+y^2) = \frac{\rho_\pm^2}{v^2-1} \tag{24}$$

which give two hyperboloids of revolution of two sheets in the three (spatial) space corresponding to ρ equals to ρ_+ and ρ equals to ρ_-. It is clear from (22)–(23) that the null surfaces for the charged tachyon are different from that of the uncharged tachyon. It is of interest to study the trajectories of the charged tardyons in the field of a charged tachyon.

After the completion of this work, a paper [15] came to our notice wherein the authors, using the complex tetrads, obtained a general Kerr–Schild class of solutions. They mentioned that a particular solution gives the charged rotating tachyon. The solution given by us has a clear physical interpretation. Dadhich brought to our notice his paper on charged tachyon [16]. Our method of obtaining the gravitational and electromagnetic fields of a charged tachyon is different from his.

Acknowledgements

This work is supported in part by the Basque government. Thanks are due to P C Vaidya for his guidance throughout the preparation of this work, and to J C Parikh and Alberto Chamorro for discussions.

References

[1] G Fienberg, *Phys. Rev.* **159**, 1089 (1967)
[2] O M P Bilaniuk and E C G Sudarshan, *Phys. Today* **5**, 43 (1969)
[3] E Recami, *Riv. del Nuovo Cimento* **9**, 1 (1986)
[4] O M P Bilaniuk, V K Deshpande and E C G Sudarshan, *Am. J. Phys.* **30**, 718 (1962)
[5] T Alväger and M N Kreisler, *Phys. Rev.* **171**, 1357 (1968)
[6] M V Davis, T Alväger and M N Kreisler, *Phys. Rev.* **183**, 1132 (1969)
[7] D F Bartlett and M D Lahana, *Phys. Rev.* **D6**, 1817 (1972)
[8] P V Ramana Murthy, *Lett. Nuovo Cimento* **1**, 908 (1971)
[9] J V Narlikar and E C G Sudarshan, *Mon. Not. R. Astron. Soc.* **175**, 105 (1976)
[10] J V Narlikar and S V Dhurandhar, *Pramana – J. Phys.* **6**, 388 (1976)
[11] S V Dhurandhar, *Phys. Rev.* **19**, 2310 (1979)
[12] P C Vaidya, *Curr. Sci.* **40**, 651 (1971)
[13] A K Raychaudhuri, *J. Math. Phys.* **15**, 856 (1974)
[14] K S Virbhadra, *Pramana – J. Phys.* **40**, 273 (1993)
[15] P V Bhatt and S K Vaidya, *Class. Quant. Gravit.* **8**, 1717 (1991)
[16] N Dadhich, *Indian J. Pure Appl. Math.* **7**, 151 (1976)

physics

pp. 181–187

A radiating dyon solution

A CHAMORRO and K S VIRBHADRA*

Departamento de Física Teórica, Universidad del País Vasco, Apartado 644, 48080 Bilbao, Spain

* Present address: Theoretical Astrophysics Group, Tata Institute of Fundamental Research, Homi Bhabha Road, Bombay 400 005, India

MS received 20 December 1994

Abstract. We give a non-static exact solution of the Einstein–Maxwell equations (with null fluid), which is a non-static magnetic charge generalization to the Bonnor–Vaidya solution and describes the gravitational and electromagnetic fields of a non-rotating massive radiating dyon. In addition, using the energy-momentum pseudotensors of Einstein and Landau and Lifshitz we obtain the energy, momentum, and power output of the radiating dyon and find that both prescriptions give the same result.

Keywords. Dyon; Einstein–Maxwell equations; energy-momentum pseudotensor.

PACS Nos 04·20; 04·40

There has been considerable interest in obtaining non-static solutions of Einstein's equations describing the gravitational field of a star radiating null fluid [1–3]. In 1953, Vaidya [2] obtained a nice form of non-static generalization to the Schwarzschild solution and it became well-known in the literature after the discovery of quasars. The quasars are high energy sources and therefore their gravitational field cannot be described by the Schwarzschild metric while the Vaidya metric is relevant to the study of such objects. Vaidya and others gave non-static generalizations to the Kerr solution [3]. Bonnor and Vaidya [4] obtained a non-static generalization to the Reissner–Nordström (RN) solution describing the emission of charged null fluid from a spherically symmetric charged radiating body. Mallett [5] gave an exact solution describing the radiating Vaidya metric [1] in a de Sitter universe. Patino and Rago [6] obtained a solution of the Einstein–Maxwell (EM) equations with null fluid for a spherically symmetric radiating massive charged (electric) object in a de Sitter universe.

The existence of magnetic monopoles is not yet confirmed, but it has been a subject of interest of many physicists (see in ref. 7). The Bonnor–Vaidya solution [4] is not enriched with a magnetic charge parameter. Therefore, it is of interest to obtain a non-static magnetic charge generalization to the Bonnor–Vaidya solution, characterized by three time-dependent parameters: mass, electric charge, and magnetic charge. Further we calculate the energy, momentum and power output of the radiating dyon in prescriptions of Einstein as well as Landau and Lifshitz (LL). Throughout this paper we use geometrized units where the gravitational constant $G = 1$ and the speed of light in vacuum $c = 1$. We follow the convention that Latin indices take values from 0 to 3 (x^0 is the time coordinate) and Greek indices take values from 1 to 3.

The EM equations with null fluid present are [4]

$$R_i^k - \tfrac{1}{2} g_i^k R = 8\pi(E_i^k + N_i^k), \tag{1}$$

$$\frac{1}{\sqrt{-g}}(\sqrt{-g}\,F^{ik})_{,k} = 4\pi J^i_{(e)}, \tag{2}$$

$$\frac{1}{\sqrt{-g}}(\sqrt{-g}\,{}^*F^{ik})_{,k} = 4\pi J^i_{(m)}, \tag{3}$$

where

$$E^k_i = \frac{1}{4\pi}\left[-F_{im}F^{km} + \frac{1}{4}g^k_i F_{mn}F^{mn}\right] \tag{4}$$

is the energy-momentum tensor of the electromagnetic field and

$$N^k_i = V_i V^k \tag{5}$$

is the energy-momentum tensor of the null fluid. V^k is the null fluid current vector satisfying

$$g_{ik} V^i V^k = 0. \tag{6}$$

${}^*F^{ik}$, the dual of the electromagnetic field tensor F^{ik}, is given by

$${}^*F^{ik} = \frac{1}{2\sqrt{-g}}\varepsilon^{iklm}F_{lm}. \tag{7}$$

ε^{iklm} is the Levi–Civita tensor density. R^k_i is the Ricci tensor. $J^i_{(e)}(J^i_{(m)})$ stands for the electric (magnetic) current density vector.

An exact solution of the above equations describing the gravitational and electromagnetic fields of a non-rotating radiating dyon is given, in coordinates $x^0 = u, x^1 = r, x^2 = \theta, x^3 = \phi$, by the metric,

$$ds^2 = Bdu^2 + 2dudr - r^2(d\theta^2 + \sin^2\theta\, d\phi^2), \tag{8}$$

where

$$B = 1 - \frac{2M(u)}{r} + \frac{q_e(u)^2 + q_m(u)^2}{r^2} \tag{9}$$

and the non-zero components of the electromagnetic field tensor,

$$F_{10} = \frac{q_e(u)}{r^2},$$

$$F_{23} = q_m(u)\sin\theta. \tag{10}$$

$M(u)$, $q_e(u)$, and $q_m(u)$ are mass, electric and magnetic charge parameters, respectively. These parameters depend on the retarded time coordinate u.

The surviving components of the Einstein tensor, $G^k_i \equiv R^k_i - \frac{1}{2}g^k_i R$, the energy-momentum tensor of the electromagnetic field, E^k_i, and the energy-momentum tensor of the null fluid, N^k_i, are

$$G^0_0 = G^1_1 = -G^2_2 = -G^3_3 = \frac{q_e^2 + q_m^2}{r^4},$$

$$G^1_0 = K^2, \tag{11}$$

$$E_0^0 = E_1^1 = -E_2^2 = -E_3^3 = \frac{q_e^2 + q_m^2}{8\pi r^4}, \tag{12}$$

$$N_0^1 = \frac{K^2}{8\pi}, \tag{13}$$

where

$$K^2 = \frac{2(q_e \dot{q}_e + q_m \dot{q}_m - \dot{M}r)}{r^3}. \tag{14}$$

The dot denotes the derivative with respect to the retarded time coordinate u. The null fluid current vector, the electric and magnetic current density vectors are

$$V^i = g_1^i \frac{K}{\sqrt{8\pi}}, \tag{15}$$

$$J^i_{(e)} = -\frac{\dot{q}_e}{4\pi r^2} g_1^i,$$

$$J^i_{(m)} = -\frac{\dot{q}_m}{4\pi r^2} g_1^i. \tag{16}$$

The radiating dyon solution given by us yields: (a) the Bonnor–Vaidya solution when $q_m = 0$, (b) the Vaidya radiating star solution [2] when $q_e = q_m = 0$, (c) the Reissner–Nordström solution when $q_m = 0$ and q_e and M are constants, (d) the Schwarzschild solution when $q_e = q_m = 0$ and M is constant and (e) the static dyon solution [8] when M, q_e, and q_m are constants.

Using the Tolman pseudotensor, Vaidya [9] calculated the total energy of a spherically symmetric radiating star and got $E = M$. Further Lindquist *et al* (LSM) [10], using the LL pseudotensor, obtained the energy, momentum, and power output for the Vaidya spacetime and found that the total energy and momentum components are $p^i = M; 0, 0, 0$ and the power output is $-\mathrm{d}M/\mathrm{d}u$. One of the present authors [11], using several energy-momentum pseudotensors, calculated the energy and momentum components for the Vaidya metric and found the same result as obtained by LSM. Now we obtain the energy, momentum and power output for the radiating dyon in prescriptions of Einstein as well as LL and show that both give the same result. The energy-momentum pseudotensors of Einstein [12] and LL [13] are

$$\Theta_i^k = \frac{1}{16\pi} H_i^{kl}{}_{,l}, \tag{17}$$

where

$$H_i^{kl} = -H_i^{lk} = \frac{g_{in}}{\sqrt{-g}} [-g(g^{kn} g^{lm} - g^{ln} g^{km})]_{,m}, \tag{18}$$

and

$$L^{mn} = L^{nm} = \frac{1}{16\pi} S^{mjnk}{}_{,jk}, \tag{19}$$

They satisfy the local conservation laws:

$$\frac{\partial \Theta_i^k}{\partial x^k} = 0, \tag{21}$$

$$\frac{\partial L^{mn}}{\partial x^m} = 0. \tag{22}$$

Θ_0^0 is the energy density. Θ_α^0 and Θ_0^α are the momentum and energy current density components, respectively. L^{00} and $L^{\alpha 0}$ give, respectively, the energy density and momentum (energy current) density components in LL prescription. The energy and momentum components in the prescription of Einstein are

$$P_i = \int\int\int \Theta_i^0 \mathrm{d}x^1 \mathrm{d}x^2 \mathrm{d}x^3, \tag{23}$$

whereas in the LL prescription are

$$P^i = \int\int\int L^{0i} \mathrm{d}x^1 \mathrm{d}x^2 \mathrm{d}x^3. \tag{24}$$

$i = 0$ gives the energy and $i = 1, 2, 3$ give the momentum components. One knows that the energy-momentum pseudotensors give the correct result if calculations are carried out in quasi-cartesian coordinates [9–14]. The quasi-cartesian coordinates are those in which the metric g_{ik} approaches the Minkowski metric η_{ik} at great distances. Therefore, one transforms the line element (8), given in u, r, θ, ϕ coordinates, to quasi-cartesian coordinates t, x, y, z according to

$$\begin{aligned} u &= t - r, \\ x &= r \sin\theta \cos\phi, \\ y &= r \sin\theta \sin\phi, \\ z &= r \cos\theta, \end{aligned} \tag{25}$$

and gets

$$\mathrm{d}s^2 = \mathrm{d}t^2 - \mathrm{d}x^2 - \mathrm{d}y^2 - \mathrm{d}z^2 - \left(\frac{2M(u)}{r} - \frac{q_\mathrm{e}(u)^2 + q_\mathrm{m}(u)^2}{r^2}\right) \times \left[\mathrm{d}t - \frac{x\mathrm{d}x + y\mathrm{d}y + z\mathrm{d}z}{r}\right]^2, \tag{26}$$

where,

$$r = (x^2 + y^2 + z^2)^{1/2}. \tag{27}$$

We are interested in calculating the energy-momentum components and the power output of the radiating dyon. Therefore, the required components of H_i^{kl} are

$$H_0^{01} = \frac{2x\Lambda}{r^4},$$

$$\frac{2y\Lambda}{}$$

$$H_0^{03} = \frac{2z\Lambda}{r^4},$$

$$H_1^{01} = \frac{x^2\Omega - Q^2r^2}{r^5},$$

$$H_2^{02} = \frac{y^2\Omega - Q^2r^2}{r^5},$$

$$H_3^{03} = \frac{z^2\Omega - Q^2r^2}{r^5},$$

$$H_1^{02} = H_2^{01} = \frac{xy\Omega}{r^5},$$

$$H_2^{03} = H_3^{02} = \frac{yz\Omega}{r^5},$$

$$H_3^{01} = H_1^{03} = \frac{zx\Omega}{r^5},$$

$$H_0^{12} = H_0^{23} = H_0^{31} = 0, \tag{28}$$

and those of S^{mjnk} are

$$S^{0101} = \frac{\Lambda(x^2 - r^2) - r^4}{r^4},$$

$$S^{0202} = \frac{\Lambda(y^2 - r^2) - r^4}{r^4},$$

$$S^{0303} = \frac{\Lambda(z^2 - r^2) - r^4}{r^4},$$

$$S^{0102} = \frac{\Lambda xy}{r^4},$$

$$S^{0203} = \frac{\Lambda yz}{r^4},$$

$$S^{0301} = \frac{\Lambda zx}{r^4},$$

$$S^{0221} = S^{0331} = \frac{\Lambda x}{r^3},$$

$$S^{0112} = S^{0332} = \frac{\Lambda y}{r^3},$$

$$S^{0113} = S^{0223} = \frac{\Lambda z}{r^3},$$

$$S^{0123} = S^{0231} = S^{0312} = 0, \tag{29}$$

where

$$\Lambda = 2Mr - Q^2,$$

$$\Omega = 3Q^2 - 4Mr,$$

$$Q^2 = q_e^2 + q_m^2. \tag{30}$$

We use (17) and (28) in (23), and (19) and (29) in (24), apply the Gauss theorem and evaluate the integrals over the surface of two-sphere of radius r_0. The energy and momentum components in both prescriptions (Einstein as well as LL) are

$$E(r_0) = M - \frac{q_e^2 + q_m^2}{2r_0} \tag{31}$$

and

$$P_x = P_y = P_z = 0. \tag{32}$$

Thus the total energy and momentum of the radiating dyon is $P^i = M; 0, 0, 0$ as expected. Now using (17)–(20) and (28)–(30) we calculate the energy current density components in both prescriptions and get

$$\Theta_0^1 = L^{01} = x\Delta, \tag{33}$$

$$\Theta_0^2 = L^{02} = y\Delta, \tag{34}$$

$$\Theta_0^3 = L^{03} = z\Delta, \tag{35}$$

where

$$\Delta = \frac{q_e \dot{q}_e + q_m \dot{q}_m - r\dot{M}}{4\pi r^4}. \tag{36}$$

Again we get the same result in both prescriptions. Switching off the electric and magnetic charge parameters we get the result for the Vaidya metric which were earlier obtained by one of the present authors [11]. Using the energy current density components, given by (33–36), we calculate the power output across a 2-sphere of radius r_0 and get,

$$W(r_0) = -\frac{\mathrm{d}}{\mathrm{d}u}\left[M - \frac{q_e^2 + q_m^2}{2r_0}\right]. \tag{37}$$

$q_e = q_m = 0$ in (37) gives the power output for the Vaidya spacetime [10]. The total power output (r_0 approaching infinity in (37)) is $-\mathrm{d}M/\mathrm{d}u$. Without using any energy-momentum pseudotensor, Bonnor and Vaidya [3] obtained the power output for the metric given by them. They got the same result as obtained by us.

Acknowledgements

This work has been partially supported by the Universidad del País Vasco under contract UPV 172.310-EA062/93 (AC) and by a Basque Government post-doctoral fellowship (KSV).

This work was presented in the seventh Marcel Grossmann Meeting (1994) and is to appear in the Proceedings in brief.

References

[1] P C Vaidya, *Proc. Indian Acad. Sci.* **A33**, 264 (1951)
A K Raychaudhuri, *Z. Phys.* **135**, 225 (1953)
W Israel, *Proc. R. Soc. (London)* **A248**, 404 (1958)
[2] P C Vaidya, *Nature (London)* **171**, 260 (1953)
[3] P C Vaidya and L K Patel, *Phys. Rev.* **D7**, 3590 (1973)
P C Vaidya, *Proc. Camb. Philos. Soc.* **75**, 383 (1974)
P C Vaidya, L K Patel and P V Bhatt, *Gen. Relativ. Gravit.* **16**, 355 (1976)
M Carmeli and M Kaye, *Ann. Phys. (NY)* **103**, 97 (1977)
[4] W B Bonnor and P C Vaidya, *Gen. Relativ. Gravit.* **1**, 127 (1970)
[5] R L Mallett, *Phys. Rev.* **D31**, 416 (1985)
[6] A Patino and H Rago, *Phys. Lett.* **A121**, 329 (1987)
[7] A S Goldhaber and W P Trower, *Am. J. Phys.* **58**, 429 (1990)
[8] I Semiz, *Phys. Rev.* **D46**, 5414 (1992)
[9] P C Vaidya, *J. Univ. Bombay* **21**, 1 (1952)
[10] R W Lindquist, R A Schwartz and C W Misner, *Phys. Rev.* **137**, B1364 (1965)
[11] K S Virbhadra, *Pramana – J. Phys.* **38**, 31 (1992)
[12] C Møller, *Ann. Phys. (NY)* **4**, 347 (1958)
[13] L D Landau and E M Lifshitz, *The classical theory of fields* (Pergamon Press, Oxford, 1985) p. 280
[14] K S Virbhadra, *Phys. Rev.* **D41**, 1086 (1990)
K S Virbhadra, *Phys. Rev.* **D42**, 2919 (1990)
F I Cooperstock and S A Richardson, in *Proc. 4th Canadian Conf. on General Relativity and Relativistic Astrophysics* (World Scientific, Singapore, 1991)
K S Virbhadra and J C Parikh, *Phys. Lett.* **B317**, 312 (1993)
K S Virbhadra and J C Parikh, *Phys. Lett.* **B331**, 302 (1994)

Static models of cosmic strings in general relativity

G P SINGH
Cosmology Group, Department of Mathematics, Indian Institute of Technology, Madras 600 036, India
Present Address: Department of Mathematics, Visvesvaraya Regional College of Engineering, Nagpur 440 011, India

MS received 22 September 1994; revised 9 May 1995

Abstract. Exact solutions to Einstein's equations for a cloud of massive strings with a general static metric representing spherical plane and hyperbolic symmetries are derived. Some properties of massive strings for different cases are also discussed.

Keywords. Cosmic strings; static models; cloud of massive strings.

PACS Nos 04·20; 98·80

1. Introduction

Cosmic strings have received considerable attention as they are believed to have served in the structure formation in the early stages of the universe. Cosmic strings may have been created during phase transitions in the early universe [1] and they could act as a source of gravitational field [2]. The existence of strings in the early universe can be used to introduce density fluctuations leading to the formation of galaxies [3–5]. A gauge-invariant model of a cloud of geometric strings with spherical, plane and cylindrical symmetries has been studied by Letelier [6]. He has suggested that the massive strings are being formed by geometric strings with particle attached to them along their extension. The general relativistic treatment of strings has been originally given by Letelier [6] and Stachel [7]. Relativistic models of cosmic strings in Bianchi type II, VI_0, VIII and IX space times have been studied by Krori *et al* [8]. Banerjee *et al* [10] have obtained Bianchi type I string cosmological models with magnetic field. Chakraborty [9] and Tikekar and Patel [11] have studied different cases of Bianchi type VI_0 string cosmology with and without magnetic field. Recently, Tikekar *et al* [12] have presented a new class of singularity free cylindrically symmetric models in string cosmology.

The study of static models of the universe is appealing not only for theoretical reasons, but also because, if there exists an explanation for the observed red shift other than the expansion of the universe, the static models could gain importance [13]. Gott [14] and Linet [15] had considered static cylindrically symmetric interior and exterior space-times of an extended cosmic strings with uniform and non-uniform energy densities. The metric of the static space-time describing infinite straight cosmic strings of linear mass density has been obtained by Letelier [16]. Recently, Krori *et al* have studied the field of a stationary cosmic string.

In this paper we are considering a more general static metric with spherical, plane and hyperbolic symmetries to study a cloud of massive strings in different cases.

2. Field equations

We consider the most general static line element for matter distribution given by

$$ds^2 = g^2(x)dt^2 - dx^2 - f^2(x)[dy^2 + F(y)dz^2] \tag{1}$$

which represents spherical $[F(y) = \sin^2 y]$, plane $[F(y) = 1]$ or hyperbolic $[F(y) = e^{2y}]$ symmetry.

The non-zero components of the Ricci curvature tensor are

$$\begin{aligned} R_{00} &= gg'' + 2\left(\frac{g}{f}\right)g'f' \\ R_{11} &= \frac{g''}{g} - \frac{2f''}{f} \\ R_{22} &= \frac{R_{33}}{F} = \varepsilon(F) - (f')^2 - ff'' - \left(\frac{f}{g}\right)g'f' \end{aligned} \tag{2}$$

with

$$\varepsilon(F) = \frac{\dot{F}}{2F} - \frac{\ddot{F}}{2F} = \begin{cases} 1 & \text{for } F = \sin^2 y \\ 0 & \text{for } F = 1 \\ -1 & \text{for } F = e^{2y} \end{cases}$$

and Ricci scalar

$$R = -\frac{2}{f^2}\varepsilon(F) + 2\frac{g''}{g} + 4\frac{f''}{f} + 2\left(\frac{f'}{f}\right)^2 + 4\frac{f'g'}{fg}. \tag{3}$$

The Einstein's equation for a cloud of strings is

$$R_{ij} - \tfrac{1}{2}g_{ij}R = -8\pi T_{ij} \tag{4}$$

where the energy-momentum tensor of a cloud of massive strings has been given by

$$T_{ij} = \rho u_i u_j - \lambda x_i x_j \tag{5}$$

with

$$u^i u_i = -x^i x_i = 1, \quad u^i x_i = 0.$$

Here ρ denotes the rest energy density of the strings with particles attached to them (P-strings) and λ is the string tension density. If we denote particle energy-density by ρ_p, then we have

$$\rho = \rho_p + \lambda. \tag{6}$$

The vector u^i describes the cloud four-velocity and x^i is a unit space-like vector representing the direction of the string.

If we assume that the space-like vector x^i is parallel to $\partial/\partial x$ (x^i must be taken along any one of the three directions $\partial/\partial x$, $\partial/\partial y$, $\partial/\partial z$) so that the energy-momentum tensor has the form

$$T_0^0 = \rho; \quad T_x^x = \lambda. \tag{7}$$

For the metric (1), the field (4) with the help of (2), (3) and (7), may be written as

$$2\frac{f''}{f}+\left(\frac{f'}{f}\right)^2-\frac{\varepsilon}{f^2}=8\pi\rho \tag{8}$$

$$\left(\frac{f'}{f}\right)^2+2\frac{f'g'}{fg}-\frac{\varepsilon}{f^2}=8\pi\lambda \tag{9}$$

$$\frac{f''}{f}+\frac{g''}{g}+\frac{f'g'}{fg}=0 \tag{10}$$

By combining (8)–(10), we have

$$\lambda'+(\lambda-\rho)\frac{g'}{g}+2\lambda\frac{f'}{f}=0. \tag{11}$$

3. Solutions of the equations

To solve the Einstein's equations we require one more relation between the variables because there are four variables in three independent equations.

Case I: Nambu strings

Consider the equation of state for a cloud of strings as

$$\rho=\lambda \quad (\rho_p=0) \tag{12}$$

then (11) gives the solution

$$\lambda=\frac{D}{f^2} \tag{13}$$

where D is a constant.
Using (12) and (13) in (8) and multiplying by f^2f' and integrating over x, we have

$$f=(8\pi D+\varepsilon)^{1/2}x+E \tag{14}$$

where E is an integration constant.

Substracting (9) from (8) and using (12), and then integrating over x, we get

$$g=K \text{ (constant)}. \tag{15}$$

From (12)–(14) we see that the rest energy density of the cloud of strings and the string tension density are decreasing as the field is moving along the x-axis in all the three cases viz., spherical, plane and hyperbolic symmetries.

Case II.

In this case we consider a relation between the metric coefficients as given by

$$f=g^n \tag{16}$$

Substituting this value of f in (10), we get

$$(n+1)\frac{g''}{g}+n^2\left(\frac{g'}{g}\right)^2=0 \tag{17}$$

for which the solution is

$$g=[Ax+B]^{(n+1)/(n^2+n+1)} \tag{18}$$

where A and B are arbitrary constants.

Using the value of f and g from (16) and (18) in (8) and (9), we have

$$8\pi\rho=\frac{n(n^2-1)(n+2)A^2}{(n^2+n+1)^2(Ax+B)^2}-\frac{\varepsilon}{(Ax+B)^{2n(n+1)/(n^2+n+1)}} \tag{19}$$

$$8\pi\lambda=\frac{n(n+1)^2(n+2)A^2}{(n^2+n+1)^2(Ax+B)^2}-\frac{\varepsilon}{(Ax+B)^{2n(n+1)/(n^2+n+1)}}. \tag{20}$$

From (6), (19) and (20) we get

$$8\pi\rho_p=-2\frac{n(n+1)(n^2+n-2)A^2}{(n^2+n+1)^2(Ax+B)^2}. \tag{21}$$

Substituting the value of $\varepsilon=0, 1, -1$ we can obtain the solutions of massive cosmic strings in plane, spherical and hyperbolic symmetric space-times respectively.

From (19)–(21) one can see that the rest energy density, tension density and particle density of the strings are decreasing as the field is moving along the x-axis in all the three symmetries and all the three densities vanish when $x\to\infty$.

Case III: Uniform density

If we consider the rest energy density of the cloud of strings to be uniform i.e., $\rho=\rho_0$ (constant), then (8) reduces to

$$2\frac{f''}{f}+\left(\frac{f'}{f}\right)^2-\frac{\varepsilon}{f^2}=8\pi\rho_0. \tag{22}$$

Multiplying (22) by f^2f' and integrating, we obtain

$$f'=\left(\frac{8\pi\rho_0}{3}f^2+\varepsilon\right)^{1/2}. \tag{23}$$

Now, we consider a plane symmetric space-time ($\varepsilon=0$). Substituting $\varepsilon=0$ in (23) yields the solution

$$f=b\exp\left(\left(\frac{8\pi\rho_0}{3}\right)^{1/2}x\right) \tag{24}$$

where b is an integration constant.

Using (24) in (10), one can obtain

$$g''+(8\pi\rho_0/3)^{1/2}g'+(8\pi\rho_0/3)g=0 \tag{25}$$

which has the solution

$$g = (d\cos(2\pi\rho_0)^{1/2}x) + c\sin((2\pi\rho_0)^{1/2}x))\exp[-(2\pi\rho_0)^{1/2}x] \tag{26}$$

where c and d are arbitrary constants.

From (9), (24) and (26), we have

$$\lambda = \frac{8\pi\rho_0}{(3)^{1/2}} \frac{(-d\sin((2\pi\rho_0)^{1/2}x) + c\cos((2\pi\rho_0)^{1/2}x))}{(d\cos((2\pi\rho_0)^{1/2}x) + c\sin((2\pi\rho_0)^{1/2}x))}. \tag{27}$$

Equations (6) and (27) give

$$\rho_p = \rho_0 - \frac{8\pi\rho_0}{(3)^{1/2}} \frac{(-d\sin((2\pi\rho_0)^{1/2}x) + c\cos((2\pi\rho_0)^{1/2}x))}{(d\cos((2\pi\rho_0)^{1/2}x) + c\sin((2\pi\rho_0)^{1/2}x))}. \tag{28}$$

From (27) it is clear that when x approaches $(2\pi\rho_0)^{-1/2}\tan^{-1}\left(\frac{c}{d}\right)$ the string tension density vanishes and the cloud of particles would attain uniform energy density. Thus in this model a cloud of strings with particles attached to them asymptotically tends to a cloud of particles.

Acknowledgements

The author thanks for the financial support from the National Board for Higher Mathematics (DAE) through the grant of a post doctoral fellowship. He also thanks Profs V B Johri, T Singh, P S Joshi, Dr Kalyani Desikan and Dr T P Singh for fruitful and stimulating discussions and the referee for valuable suggestions.

References

[1] T W B Kibble, *J. Phys.* **A9**, 1387 (1976)
[2] P S Letelier, *Phys. Rev.* **D28**, 2414 (1983)
[3] Ya B Zeldovich, *Mon. Not. R. Astron. Soc.* **192**, 663 (1980)
[4] A Vilenkin, *Phys. Rev.* **D23**, 852 (1981)
[5] A Vilenkin, *Phys. Rev. Lett.* **46**, 1169 (1981)
[6] P S Letelier, *Phys. Rev.* **D20**, 1294 (1979)
[7] J Stachel, *Phys. Rev.* **D21**, 2171 (1980)
[8] K D Krori, T Chaudhuri, C R Mahanta and A Mazumdar, *Gen. Relativ. Gravit.* **22**, 123 (1990)
[9] A Banerjee, A K Sanyal and S Chakraborty, *Pramana – J. Phys.* **34**, 1 (1990)
[10] S Chakraborty, *Indian J. Pure Appl. Phys.* **29**, 31 (1991)
[11] R Tikekar and L K Patel, *Pramana – J. Phys.* **42**, 483 (1994)
[12] R Tikekar, L K Patel and N Dadhich, *Gen. Relativ. Gravit.* **26**, 647 (1994)
[13] M S Berman, M M Som and F M Gomide, *Gen. Relativ. Gravit.* **21**, 287 (1989)
[14] J R Gott, *Astrophys. J.* **288**, 422 (1985)
[15] B Linet, *Gen. Relativ. Gravit.* **17**, 1109 (1985)
[16] P S Letelier, *Class. Quantum. Gravit.* **4**, 175 (1987)
[17] K D Krori, D Goswami and K Das, *Class. Quantum. Gravit.* **10**, 125 (1993)

— journal of physics

August 1995
pp. 195–208

Neutrino emissivity of quark matter at finite temperatures

V K GUPTA, A WADHWA* and J D ANAND
Department of Physics and Astrophysics, University of Delhi, Delhi 110007, India
*S.G.T.B. Khalsa College, University of Delhi, Delhi 110007, India

MS received 7 November 1994; revised 28 April 1995

Abstract. We evaluate the emissivity rates for d-decay and s-decay by exactly solving the angular integrals involved and without assuming the degeneracy of electrons. We have also studied the effects of QCD coupling constant as well as the s-quark mass on the emissivity rates. We find that these parameters are important in determining the threshold and extinction densities for d- and s-decays.

Keywords. Quark stars; bag model; emissivity rate; mean free path.

PACS Nos 12·38; 95·30; 97·60

1. Introduction

The possibility of dense stars having a core of essentially free quarks rather than nucleons has been studied for a long time now [1, 2]. If such stars do exist they have to be isolated observationally from other types of neutron stars. One distinguishing feature, as is well-known, is the surface emission of radiation which leads to stringent conditions on the temperature of the quark matter stars. Again, as is well-known, the neutrino emission plays an important role in the cooling of quark stars in the early stages of star evolution. The formalism for the neutrino emissivity rate by quark matter on the basis of β-equilibrium and charge neutrality condition has been given by Iwamoto [3]. The basic β-decay processes are

$$\begin{aligned} &\mathrm{s} \rightarrow u + e^- + \bar{\nu}_e \\ &\mathrm{d} \rightarrow u + e^- + \bar{\nu}_e \end{aligned} \tag{1.1}$$

along with their inverse reactions

$$\begin{aligned} &u + e^- \rightarrow \mathrm{s} + \nu_e \\ &u + e^- \rightarrow \mathrm{d} + \nu_e. \end{aligned} \tag{1.2}$$

Iwamoto has given a simple formula for neutrino emissivity rate from β-decay of quarks (see eq. (3.12) of ref. [3]) viz.

$$E_\nu(i) = 6V^3 \left(\prod_{j=1}^{4} \int \frac{\mathrm{d}^3 p_j}{(2\pi)^3} \right) E_2 \, W_{\mathrm{fi}} n(E_1)(1 - n(E_3))(1 - E_4)) \tag{1.3}$$

where $j = 1$ to 4 refers to s(or d), ν_e, u, e^- respectively and $i =$ s or d as the case may be, $n(E_j)$ is the distribution function of jth particle species and W_{fi} is the weak decay transition rate. Using the Weinberg–Salaam model, as extended to semi-leptonic processes to describe weak interactions, the transition rate for β-decay of s- or d-quark

is given by

$$W_{fi} = 64 G_i^2 (2\pi)^4 \delta^4(p_1 - p_2 - p_3 - p_4)(p_1 \cdot p_2)(p_3 \cdot p_4) \Big/ \prod_{j=1}^{4} (2E_j V) \qquad (1.4)$$

where $G_i^2 = G^2 \sin^2\theta_c$ for i = s-quark and $G_i^2 = G^2 \cos^2\theta_c$ for i = d-quark. Neglecting the neutrino momentum p_2 in the δ-function and by replacing the particle energies and momenta by their respective chemical potentials and fermi-momenta, Iwamoto has given the following formulas for neutrino emissivity rate (see eq. (3.21) and (4.11) of ref. [3])

$$E_{vd} = \frac{914}{315} G^2 \cos^2\theta_c \alpha_c p_f(d) p_f(u) p_f(e)\, T^6 \qquad (1.5)$$

$$E_{vs} = \frac{457\pi}{840} G^2 \sin^2\theta_c \mu_s p_f(u) p_f(e)(1 - \cos\theta_{34})\, T^6. \qquad (1.6)$$

Equation (1.5) is the emissivity rate for the massless d-quark decay while (1.6) is for the s-quark decay. In deriving these results, Iwamoto also assumes that electrons are completely degenerate and so their energies and momenta, like those of the quarks, are replaced by their chemical potentials and fermi-momenta. Burrows [4] improved upon this calculation by including the effects of neutrino momentum and obtained a T^7 behaviour for the emissivity rate instead of T^6. Duncan *et al* [5] (1983, paper I; 1984, paper II) studied in detail the dependence of emissivity on the QCD coupling α_c. They also show that the electron fraction in quark matter vanishes at a finite baryon density, $n_B = n_{ex}$ (extinction density) and so the emissivity becomes zero at $n_B \geq n_{ex}$. Also, recently Ghosh *et al* [6] have reported a calculation of the emissivity rate without making the assumptions of Iwamoto. They could, however, reduce (1.3) to a five-dimensional integral which they had to do numerically.

We, in this paper, have reanalyzed the emissivity rate and mean free path. Our starting point is, of course, again the same as (1.3). We have demonstrated that the angular integrals can be done exactly without requiring any assumptions to be made and leading to an expression for emissivity rate in terms of a three-dimensional integral. Further simplification requires one to assume electrons to be degenerate. However such an assumption is not valid at high temperatures, therefore we perform our calculations both with and without this assumption. For the thermodynamics of quark matter we retain terms to first order in α_c and include the effects of finite temperature and finite mass of the s-quark.

In § 2 we indicate the main steps involved in the derivation of emissivity rate and mean free path. The technical details are relegated to the Appendix. In § 3, we describe our results for emissivity rate and mean free path as functions of α_c, T, m_s and n_B. Finally, we compare these results with those of Iwamoto and Duncan *et al* and discuss their significance.

2. Formalism

We consider three-component quark matter (u, d, s) in β-equilibrium with a small fraction of electrons. The thermal equilibrium condition leads to the following relation

$$\mu_d = \mu_s = \mu_u + \mu_e \tag{2.1}$$

If one assumes that neutrinos escape freely from quark matter and hence do not take part in thermal equilibrium, the neutrino chemical potential, μ_ν, can be put equal to zero. Charge neutrality condition sets an additional constraint on the number densities $n_i (i = u, d, s, e)$ viz.

$$\frac{Q}{e} = \frac{2}{3}n_u - \frac{1}{3}n_d - \frac{1}{3}n_s - n_e = 0 \tag{2.2}$$

The total baryon density of quark matter is given by

$$n_B = \frac{1}{3}(n_u + n_d + n_s) \tag{2.3}$$

The above equations imply that only one parameter, say μ_u, is left free. Now consider the thermodynamics of the system. The pressure and energy are given by [2, 7]

$$P = -\sum_i \Omega_i - B \tag{2.4a}$$

$$E = -P + \sum_i \mu_i n_i - T\sum_i \frac{\partial \Omega_i}{\partial T} \tag{2.4b}$$

where the thermodynamic potentials are given by

$$\Omega_i = -(\mu_i^4/4\pi^2)[(1 - 2\alpha_c/\pi) + 2\pi^2(T/\mu_i)^2(1 - 2\alpha_c/3\pi)] \tag{2.4c}$$

$$\begin{aligned}\Omega_s = &-(\mu_s^4/4\pi^2)[(1 - 2{\cdot}5\lambda^2)(1-\lambda^2)^{0\cdot5} + 1{\cdot}5\lambda^4 \ln(1 + (1-\lambda^2)^{0\cdot5}/\lambda) \\ &+ 2\pi^2(1-\lambda^2)^{0\cdot5}(T/\mu_s)^2 - (2\alpha_c/\pi)(3((1-\lambda^2)^{0\cdot5} - \lambda^2 \ln(1 + (1-\lambda^2)/\lambda))^2 \\ &- 2(1-\lambda^2)^2 + 3\lambda^4(\ln(\lambda))^2 + \pi^2(T/\mu_s)^2((1 - 2/3\lambda^2) - \lambda^2 \\ &\times \ln(1 + (1-\lambda^2)^{0\cdot5}/\lambda)/(1-\lambda^2)^{0\cdot5}) - 6(\lambda^2(1-\lambda^2)^{0\cdot5} \\ &- \lambda^4(\ln(1 + (1-\lambda^2)^{0\cdot5})/\lambda) + (\pi^2/3)(T/\mu_s)^2\lambda^2/(1-\lambda^2)^{0\cdot5})\ln(\mu_0/\mu_s))].\end{aligned} \tag{2.4d}$$

Number densities of the particle species are obtained as

$$n_u = (\mu_u^3/\pi^2)(1 - 2\alpha_c/\pi) + \mu_u T^2(1 - 2\alpha_c/3\pi) \tag{2.4e}$$

$$n_d = n_u(u \leftrightarrow d) \tag{2.4f}$$

$$\begin{aligned}n_s = &[4(\mu^2 - m_s^2)^{1\cdot5} + 2\pi^2 T^2(2\mu^2 - m_s^2)/(\mu^2 - m_s^2)^{0\cdot5} - (8\alpha_c/\pi)\mu_s(\mu^2 - m_s^2) \\ &- (2\alpha_c/\pi)(-12m_s^2(\mu^2 - m_s^2)^{0\cdot5}\ln[(\mu_s + (\mu^2 - m_s^2)^{0\cdot5})/m_s] \\ &+ 6(m_s^4/\mu_s)\ln(m_s/\mu_s)) + (4\pi^2/3)\,T^2\mu_s - 6(m_s^2(\mu^2 - m_s^2)^{0\cdot5} \\ &+ (\pi^2/3)\,T^2(m_s^2/(\mu^2 - m_s^2)^{0\cdot5}) - (m_s^2/\mu_s)\ln[(\mu_s + (\mu^2 - m_s^2)^{0\cdot5})/m_s]) \\ &+ 6m_s^2(2(\mu^2 - m_s^2)^{0\cdot5} - (\pi^2/3)m_s^2\,T^2/(\mu^2 - m_s^2)^{1\cdot5})\end{aligned}$$

$$+\pi^2 T^2/(\mu^2 - m_s^2)((2\mu^2 - 5m_s^2)\mu/3$$

$$+(m_s^4/(\mu^2 - m_s^2)^{0.5})\ln[(\mu_s + (\mu^2 - m_s^2)^{0.5}/m_s)]](1/4\pi^2) \quad (2.4g)$$

$$n_e = (\mu_e^3/3\pi^2)(1 + \pi^2 T^2/\mu_e^2) \quad (2.4h)$$

where $i = \mathrm{u, d, s}$ in (2.4a), (2.4b) and $i = \mathrm{u, d}$ in (2.4c), $\alpha_c = g^2/4\pi$ and $\lambda = m_s/\mu_s$. Note that Iwamoto and Duncan *et al* define QCD coupling constant through $\alpha_c = g^2/16\pi$. In the above expressions the terms up to first order in α_c and to second order in temperature T have been retained.

The relation between fermi-momenta and the particle densities is given by

$$p_{fi} = (\pi^2 n_i)^{1/3} \quad (2.5)$$

for $i = \mathrm{u, d, s}, e^-$. For eqs (2.4e–2.4h) and (2.5) we then obtain relations between the chemical potentials and fermi-momenta of ith particle species. In the $T = 0$ limit these equations reduce to

$$\mu_i \simeq a p_{fi} \quad (2.6)$$

where $a = 1 + (2\alpha_c/3\pi)$ and $i = \mathrm{u, d}$. For the s-quarks, we obtain

$$\mu_s \cong m_s((1 + x^2)^{0.5} + (2\alpha_c/3\pi)[x - 3\ln\{(x + (1 + x^2)^{0.5})/(1 + x^2)^{0.5}\}]) \quad (2.7)$$

where $x = p_{fs}/m_s$. Equations (2.6) and (2.7) are identical to (8, 9) and (17a) of Duncan *et al* [5].

The stability of quark matter at finite temperature is determined by the value of energy per baryon, E/n_B. We consider the quark matter as stable so long as E/n_B stays below 930 MeV at zero pressure. For choosing the various parameters viz. α_c, B, μ_0 and m_s, the criterion is to determine the stability region discussed above. Once these values are chosen we are then left with one parameter, say $\mu_d = \mu_s = \mu$. This can be determined by fixing the baryon density n_B.

Substituting expression (1.4) in (1.3), the emissivity rate for the ith quark is given by

$$E_\nu(i) = \frac{24}{(2\pi)^8} G_i^2 \left(\prod_j^4 \int p_j \mathrm{d}E_j\right) E_2 n(E_1)(1 - n(E_3))(1 - n(E_4))$$

$$\delta(E_1 - E_2 - E_3 - E_4)\left(\prod_j^4 \int \mathrm{d}\Omega_j\right)(p_1 \cdot p_2)(p_3 \cdot p_4)\delta^3(\mathbf{p}_1 - \mathbf{p}_2 - \mathbf{p}_3 - \mathbf{p}_4). \quad (2.8)$$

The distribution function $n(E_j)$ of the jth particle species is given by (for $j = \mathrm{u, d, s}, e^-$)

$$n(E_j) = (\exp[(E_j - \mu_j)/T] + 1)^{-1}. \quad (2.9)$$

Defining the angular integrals in (2.8) by

$$I(E_1, E_2, E_3, E_4) = (p_1 p_2 p_3 p_4/128\pi^2)\left(\prod_j^4 \int \mathrm{d}\Omega_j\right)(p_1 \cdot p_2)(p_3 \cdot p_4)$$

$$\times \delta^3(\mathbf{p}_1 - \mathbf{p}_2 - \mathbf{p}_3 - \mathbf{p}_4).$$

The angular integrations involved in the above expression can be performed without recourse to any approximations. The rather complicated expression for $I(E_1, E_2, E_3, E_4)$ and some of the steps involved in the evaluation of angular integrals are given in the

Appendix. We can rewrite (2.8) as

$$E_\nu(i) = \frac{12G_i^2}{\pi^6} \int_{m_1}^{\infty} dE_1 \int_{m_2}^{\infty} dE_2 \int_{m_3}^{\infty} dE_3 \int_{m_4}^{\infty} dE_4 E_2 n(E_1)(1 - n(E_3)) \times (1 - n(E_4))\delta(E_1 - E_2 - E_3 - E_4) I(E_1, E_2, E_3, E_4) \quad (2.10)$$

At this stage this eq. (2.10) can be compared with (3.13), (3.15) and (3.18) of ref. [3]. Instead of the factor $p_f(d)p_f(u)p_f(e)E_2^2$ of Iwamoto, we obtain the function I, which is a function of all the four variables E_1, E_2, E_3 and E_4. The most crucial difference is that the function I is non-zero only for a certain range of values of these variables. We now introduce the following dimensionless parameters in expressions (2.9) and (2.10)

$$x_1 = (E_1 - \mu_1)/T,$$
$$x = E_2/T,$$
$$x_3 = (\mu_3 - E_3)/T,$$
$$x_4 = (\mu_4 - E_4)/T.$$

On substituting for the distribution function $n(E_j)$ from (2.9) into (2.10), the emissivity rate can be rewritten as

$$E_\nu(i) = \frac{12}{\pi^6} G_i^2 T^4 \int_0^{\infty} x dx \int_{l_1}^{\infty} dx_1 \int_{l_2}^{-\infty} dx_3 \int_{l_3}^{-\infty} dx_4 \delta(x_1 + x_3 + x_4 - x) \times I(E_1, E_2, E_3, E_4)/(1 + \exp(x_1))(1 + \exp(x_3))(1 + \exp(x_4)) \quad (2.11)$$

where

$$l_1 = (m_1 - \mu_1)/T,$$
$$l_2 = (\mu_3 - m_3)/T,$$
$$l_3 = (\mu_4 - m_4)/T.$$

Carrying out a similar analysis for the mean free path, we arrive at the following formula

$$\lambda^{-1} = \frac{24G_i^2}{\pi^4 x^2} \int_{l_1}^{\infty} dx_1 \int_{l_2}^{-\infty} dx_3 \int_{l_3}^{-\infty} dx_4 \delta(x_1 + x_3 + x_4 + x) \times I'(E_1, E_2, E_3, E_4)/(1 + \exp(x_1))(1 + \exp(x_3))(1 + \exp(x_4)) \quad (2.12)$$

where l_1, l_2, l_3 are the same as defined before for (2.11). The expression for I', which differs from that for I only in the sign of certain terms, is given in the Appendix.

Let us now look at the temperature dependence of emissivity rate. Since the chemical potentials of the quarks are a few hundred MeV for temperatures up to a few MeV, we can treat u, d and s quarks as completely degenerate. The limits of x_1 and x_3 integrals now go from $(-\infty, \infty)$ and two of the integrations can be performed exactly. The results are

$$E_\nu(i) = (3/2\pi^5) G_i^2 T^4 \int_0^{\infty} x dx \int_{-\infty}^{(\mu_4 - m_4)/T} dx_4 I(\mu_1, xT, \mu_3, \mu_4 - x_4 T) \times (x - x_4)/(1 + \exp(x_4))(\exp(x - x_4) - 1) \quad (2.13)$$

Similarly for the mean free path, λ, we obtain

$$\lambda_i^{-1} = (3/\pi^3) G_i^2 (T/x)^2 \int_{-\infty}^{(\mu_4 - m_4)/T} dx_4 I'(\mu_1, xT, \mu_3, \mu_4 - x_4 T)$$
$$\times (x + x_4)/(1 + \exp(x_4))(1 - \exp(-x - x_4)) \tag{2.14}$$

So far we have not assumed electrons to be degenerate as indeed they are not, particularly at higher densities. However, if we assume the degeneracy of electrons, the x_4 integral can also be performed leading to the following simple results

$$E_\nu(i) = (3/4\pi^5) G_i^2 \; T^4 \int_0^\infty dx \frac{x(x^2 + \pi^2)}{1 + \exp(x)} I(\mu_1, xT, \mu_3, \mu_4) \tag{2.15}$$

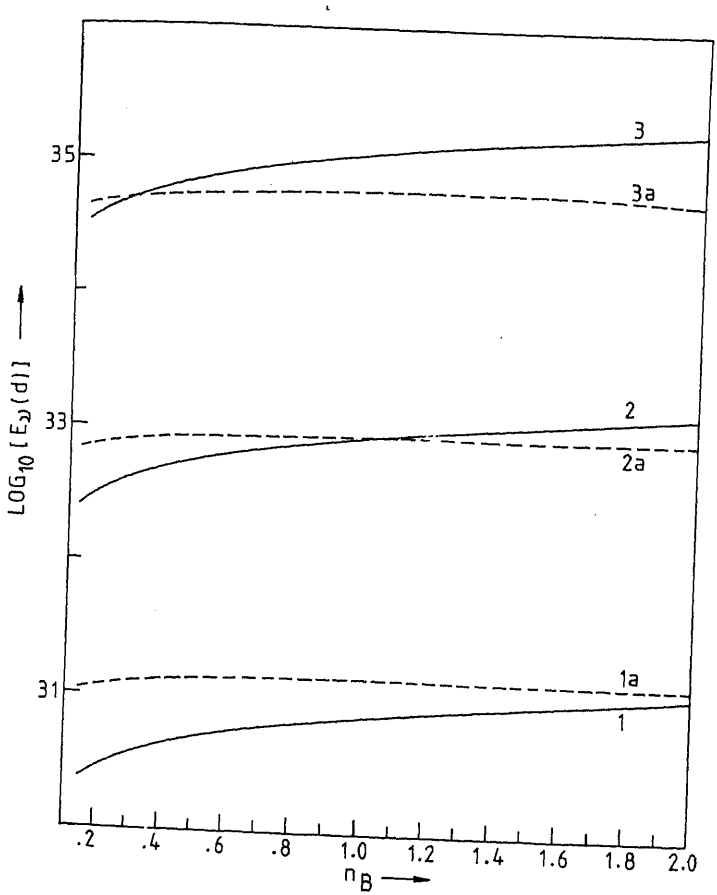

Figure 1a. Emissivity rate $E_\nu(d)$ (in erg/cm^{3}sec), for d-quark as a function of baryon density n_B (in fm^{-3}) at different temperatures for $\alpha_c = 0{\cdot}025$. Curves 1, 2, 3 correspond to $T = 1, 2, 4$ MeV respectively. Curves 1a, 2a, 3a refer to Duncan *et al* results for the same temperatures.

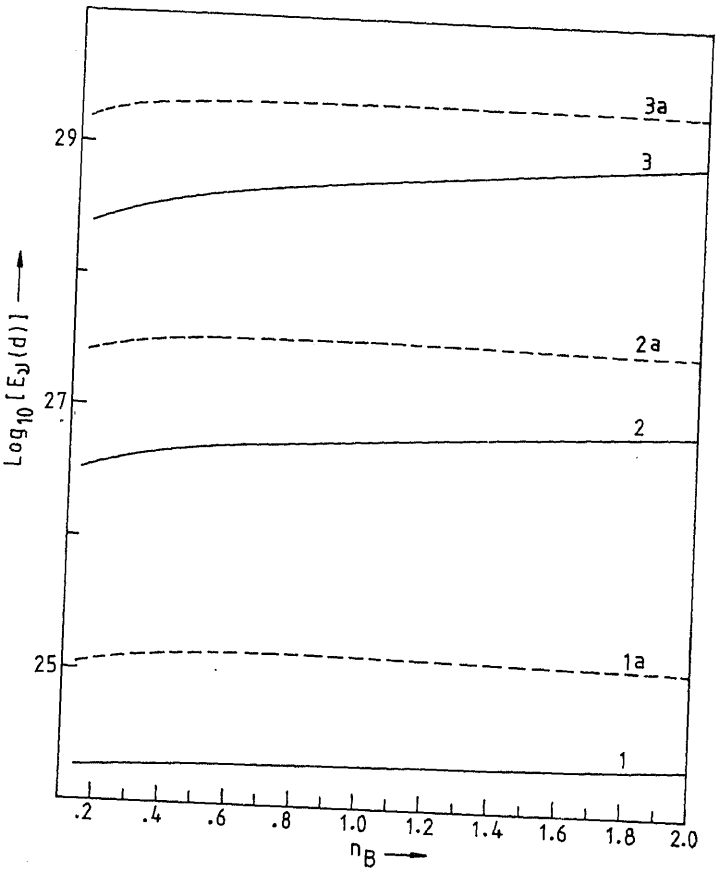

Figure 1b. Same as in figure (1a) but for temperatures $T = 0{\cdot}1$, $0{\cdot}25$ and $0{\cdot}5$ MeV. Curves 1, 2, 3 are our results and 1a, 2a, 3a refer to Duncan *et al* results.

$$\lambda_i^{-1} = (3/2\pi^3)G_i^2(T/x)^2\left(\frac{x^2+\pi^2}{1+\exp(-x)}\right)I'(\mu_1, xT, \mu_3, \mu_4) \tag{2.16}$$

esults and discussion

the actual numerical evaluation of emissivity rate and mean free path from eqs -2.16), one requires the numerical values of various parameters involved. For the ical potentials, we took a simple first order QCD model [2, 7] and expressed the ber densities in terms of chemical potentials, temperature and the QCD coupling ant α_c, (see eqs (2.4e) to (2.4h) of § 2). The values of constants α_c, B, m_s and μ_0 are n by demanding that the uds-quark matter be stable, that is to have its energy per en less than 930 MeV at some density while the ud-quark matter be unstable with its y per baryon greater than 940 MeV at the same density. One such choice of these ants, consistent with this requirement is [8]

$\alpha_c = 0{\cdot}025$, $B = 70\ \mathrm{MeV/fm^3}$ $m_s = 150\ \mathrm{MeV}$

We have computed the emissivity rate and the mean free path at different temperatures and densities. In figures 1a and 1b we plot $\log_{10}(E_\nu(d))$ as a function of the baryon density n_B, at temperatures $T = 1, 2, 4$ MeV and $T = 0{\cdot}1, 0{\cdot}25, 0{\cdot}5$ MeV respectively. Also drawn in these figures are the curves obtained by using the formalism of Duncan *et al* [5] and Iwamoto [3] at the same values of temperatures. We observe a reasonably close agreement in the two results at $T = 1, 2$ and 4 MeV while at lower temperatures there is a difference of up to one order of magnitude, our results being lower than those of Duncan *et al*.

In figures 2a and 2b we show the results for s-decay at temperatures $T = 1, 2, 4$ MeV and $T = 0{\cdot}1, 0{\cdot}25, 0{\cdot}5$ MeV respectively and compare with those of Duncan *et al*. We see that the two results agree broadly at higher densities for all temperatures. At lower densities, however, there is a marked difference in the two results. In our case the emissivity remains appreciable for all values of density, whereas in the case of Duncan *et al* there is a threshold

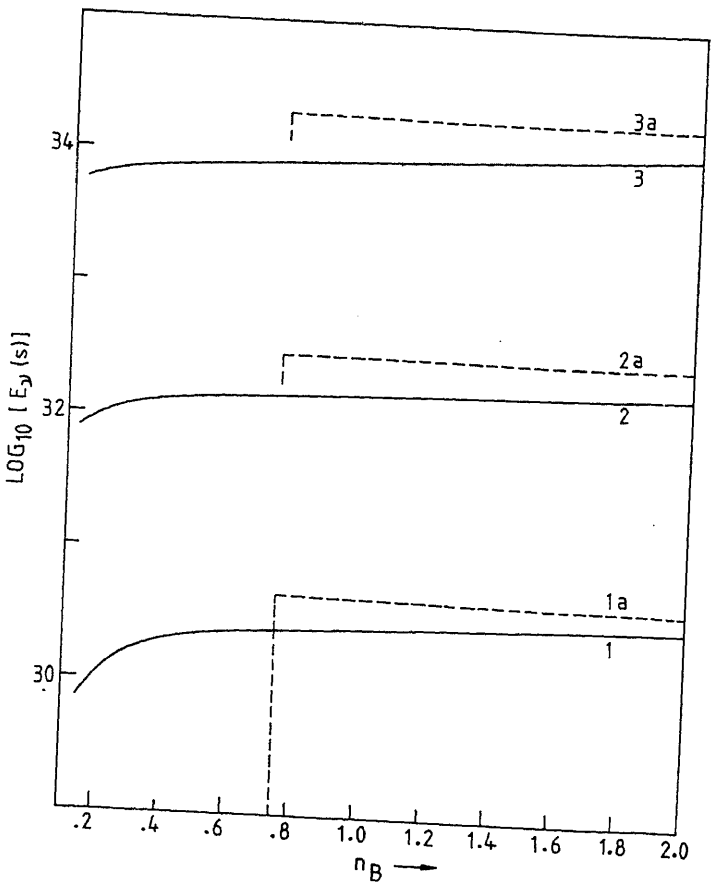

Figure 2a. Emissivity rate $E_\nu(s)$ (in erg/cm^3 sec), for s-quark as a function of baryon density n_B (in fm^{-3}) at different temperatures for $\alpha_c = 0{\cdot}025$. Curves 1, 2, 3 correspond to $T = 1, 2, 4$ MeV respectively. Curves 1a, 2a, 3a refer to Duncan *et al* results for the same values of temperatures

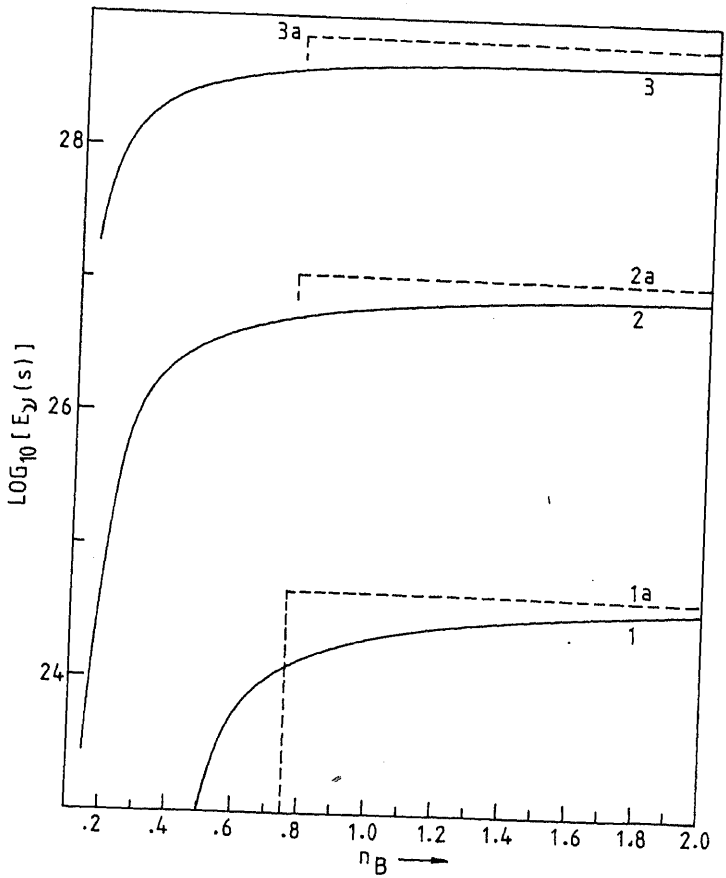

Figure 2b. Same as in figure 2a but for temperatures $T = 0{\cdot}1$, $0{\cdot}25$ and $0{\cdot}5$ MeV. Curves 1, 2, 3 are our results and 1a, 2a, 3a refer to Duncan *et al* results.

density below which the emissivity rate is zero. This threshold appears due to the kinematic restriction coming from an average over the angular integrations. In our case, the angular integrations are done exactly, as a result of which this threshold either disappears or is very low depending upon the temperature.

In figure 3a we show the effect of α_c on the emissivity rate $E_{\nu_i}(d)$, as a function of the baryon density n_B, at $T = 0{\cdot}1$ MeV and $m_s = 150$ MeV. The behaviour of emissivity with n_B changes altogether as α_c is increased. For small $\alpha_c (\leqslant 0{\cdot}05)$ the emissivity keeps on increasing with n_B (up to $2{\cdot}0\,\text{fm}^{-3}$). For higher values of α_c there is, however, an extinction density n_{ex}, beyond which the emissivity vanishes. This n_{ex} decreases with increasing α_c and is around $1{\cdot}25\,\text{fm}^{-3}$ at $\alpha_c = 0{\cdot}065$. Also reproduced, in the same figure, are the results obtained by Duncan *et al* for the same values of α_c. It can be seen that the two results are qualitatively similar, however, in the case of Duncan *et al*, the extinction density appears at higher values of α_c. To see the effect of strange quark mass on the extinction density we have shown in figure 3b, the emissivity rate, E_ν(d), as a function of baryon density n_B, at different values of α_c for $m_s = 300$ MeV and $T = 0{\cdot}1$ MeV. Figure 3

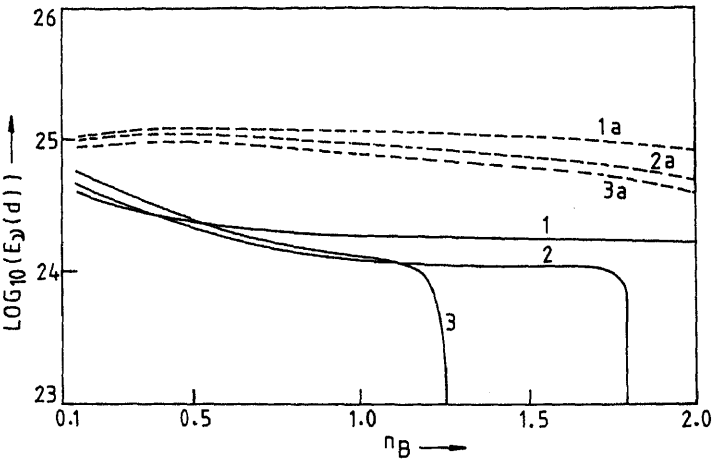

Figure 3a. Emissivity rate $E_\nu(d)$ (in erg/cm^{3}sec), for d-quark as a function of baryon density n_B(in fm^{-3}) at $T = 0{\cdot}1$ MeV for different values of α_c. Curves 1, 2, 3 refer to $\alpha_c = 0{\cdot}05$, $0{\cdot}6$ and $0{\cdot}065$ respectively. Curves 1a, 2a, 3a refer to the Duncan *et al* results for the same values of α_c.

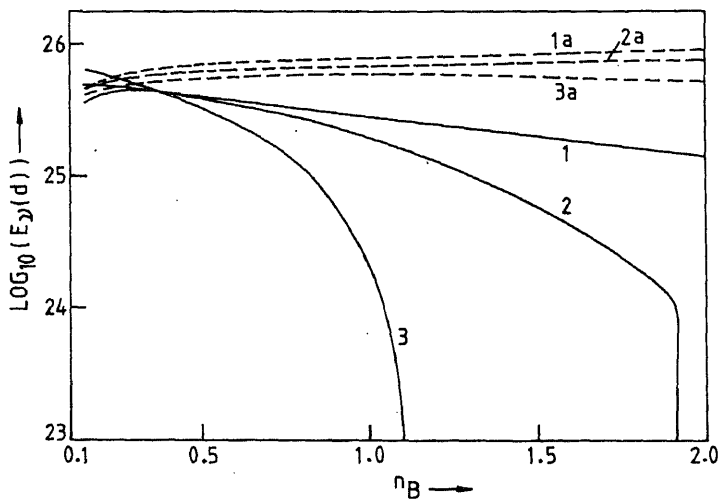

Figure 3b. Same as in figure 3a but for $m_s = 300$ MeV. Curves 1, 2, 3 correspond to our results at $\alpha_c = 0{\cdot}065$, $0{\cdot}08$ and $0{\cdot}1$ respectively. Curves 1a, 2a, 3a refer to Duncan *et al* results for the same values of α_c.

density remains much lower than that of Duncan *et al* as we increase α_c. This difference is

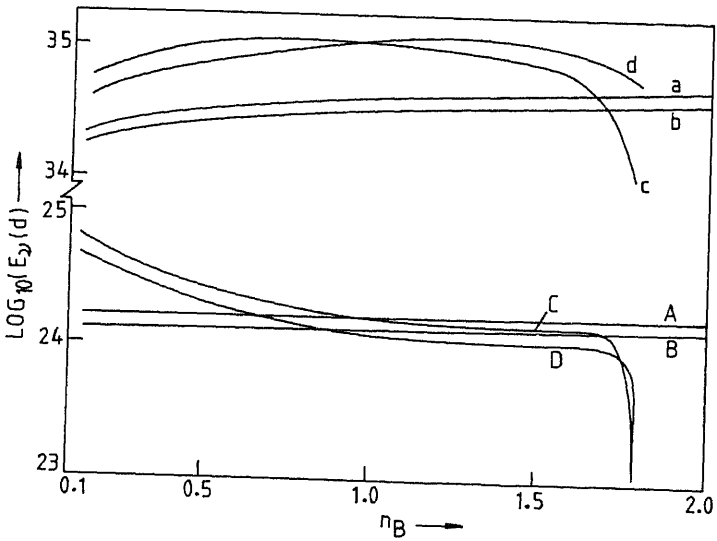

Figure 4. Emissivity rate $E_\nu(d)$ (in erg/cm^3 sec), for d-decay as a function of baryon density n_B (in fm^{-3}) at $T = 0{\cdot}1$ and 4 MeV. Curves A, B, C, D correspond to $T = 0{\cdot}1$ MeV and a, b, c, d to $T = 4$ MeV. Curves A, a and C, c refer to 1-dimensional integral results for $\alpha_c = 0{\cdot}025$ and 0·06 respectively. Curves B, b and D, d refer to the 2-dimensional integral results for $\alpha_c = 0{\cdot}025$ and 0·06 respectively.

In figure 4 we show the comparison of 1-dimensional (electrons degenerate case) and 2-dimensional (electrons non-degenerate case) results at $T = 0{\cdot}1$ and 4 MeV for d-decay. We observe a fairly close agreement of 1-dim. with the 2-dim. results for $\alpha_c = 0{\cdot}025$, whereas for $\alpha_c = 0{\cdot}065$ differences start appearing only at high densities for both $T = 0{\cdot}1$ and 4 MeV. Thus electron degeneracy has significant effect only at densities very close to the extinction density.

Finally, in figure 5 we show the mean free path λ, as a function of the baryon density n_B, at $T = 1$ and 4 MeV and for neutrino energies, $E_\nu = T$. We find that λ drops below the 10 km limit (approximate radius of a neutron star) at $T > 4$ MeV.

To summarize, in this paper we have calculated the emissivity and mean free path for the u, d, s-quark matter. We have followed the basic formalism of Iwamoto and others but we have done the various angular integrals involved exactly. As a consequence, the results obtained are not in terms of analytic expressions but in terms of certain integrals which are evaluated numerically. For d-decay, we find a reasonably close agreement with Duncan *et al* at higher temperatures while at lower temperatures there is a difference of up to one order of magnitude in the emissivity rate. For s-decay, our results agree broadly with those of Duncan *et al* particularly at higher densities. However in our case there is no threshold density below which the emissivity vanishes, unlike in their case where such threshold exists. The effect of QCD coupling constant α_c, and the strange quark mass m_s, on the emissivity rate has been studied in detail. Apart from the magnitude of emissivity rate, we find that the extinction density also depends critically on these parameters. As for the mean free path we have shown that it is less than the typical

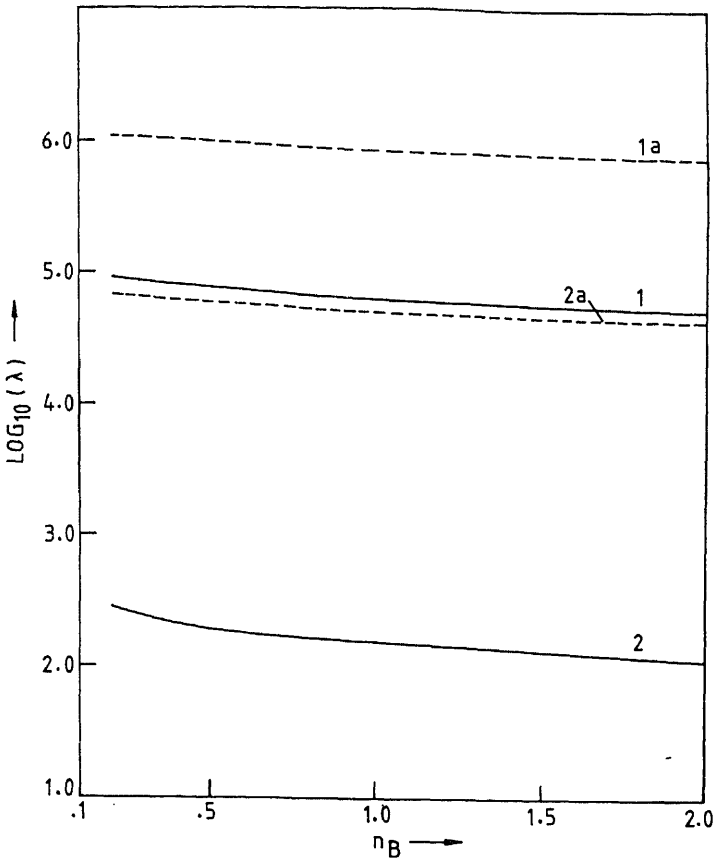

Figure 5. Mean free path, λ (in km), as a function of baryon density n_B (in fm^{-3}), at different temperatures and neutrino energies. Curves 1, 2 refer to $T = 1$ and 4 MeV respectively and $e_\nu = T$. Curves designated a refer to the results obtained using the Iwamoto expression for the same temperatures and neutrino energies.

chemical equilibrium is valid only for temperatures, $T \leqslant 4$ MeV. Though we have shown results for one choice of the parameters, quite similar results follow for any other suitable choice. The basic formalism for many other physical processes like bulk viscosity and cooling rates is similar. Calculations in this direction are in progress.

Appendix

In this we describe some of the steps involved in the evaluation of the angular integral $I(E_1, E_2, E_3, E_4)$, which is defined as

$$I(E_1, E_2, E_3, E_4) = (p_1 p_2 p_3 p_4 / 128\pi^2) \int \left[\prod_i d\Omega_i \right] (p_1 \cdot p_2)(p_3 \cdot p_4) \times \delta(\mathbf{p}_1 - \mathbf{p}_2 - \mathbf{p}_3 - \mathbf{p}_4). \quad \text{(A1)}$$

$$I(E_1, E_2, E_3, E_4) \equiv I$$

where

$$I = (p_1 p_2 p_3 p_4/128\pi^2) \int \left[\prod_i \mathrm{d}\Omega_i \right] [E_1 E_2 - \mathbf{p}_1 \cdot \mathbf{p}_2][E_3 E_4 - \mathbf{p}_3 \cdot \mathbf{p}_4] \times \delta(\mathbf{p}_1 - \mathbf{p}_2 - \mathbf{p}_3 - \mathbf{p}_4). \tag{A2}$$

Separating the three-dimensional δ-function into a delta function over the magnitude and one over the solid angles:

$$\delta(\mathbf{r} - \mathbf{r}_0) = \delta(r - r_0)\, \delta(\Omega - \Omega_0)/r^2 \tag{A3}$$

and using the latter to get rid of the integration over Ω_2, we obtain

$$I = (p_1 p_2 p_3 p_4/128\pi^2)(1/p_2^2) \int \mathrm{d}\Omega_3 \mathrm{d}\Omega_4 (E_3 E_4 - \mathbf{p}_3 \cdot \mathbf{p}_4) \int \mathrm{d}\Omega_1 \times [E_1 E_2 - p_1^2 + \mathbf{p}_1 \cdot (\mathbf{p}_3 + \mathbf{p}_4)] \delta[p_2 - (p_1^2 + (\mathbf{p}_3 + \mathbf{p}_4)^2 - 2\mathbf{p}_1(\mathbf{p}_3 + \mathbf{p}_4))^{1/2}]. \tag{A4}$$

Next, putting

$$\mathbf{p}_3 + \mathbf{p}_4 = \mathbf{P}; \quad \mathbf{p}_1 \cdot (\mathbf{p}_3 + \mathbf{p}_4) = \mathbf{p}_1 \cdot \mathbf{P} = p_1 P = p_1 P \cos\theta = p_1 P x$$

and using the remaining delta functions to perform the integration over x, we obtain

$$I = (p_1 p_2 p_3 p_4/128\pi^2)(2\pi/p_1 p_2) \int \mathrm{d}\Omega_3 \mathrm{d}\Omega_4 \theta(1 - |(p_1^2 + P^2 - p_2^2)/2p_1 P|) \times [E_3 E_4 + 0{\cdot}5(p_3^2 + p_4^2) - 0{\cdot}5P^2][E_1 E_2 - 0{\cdot}5(p_1^2 + p_2^2) + 0{\cdot}5P^2]/P. \tag{A5}$$

The theta function has made its appearance because the integration over x is performed only from -1 to $+1$. The remaining integrations over $\mathrm{d}\Omega_3 \mathrm{d}\Omega_4$ can now be performed easily because only the angle in $\mathbf{p}_3 \cdot \mathbf{p}_4$ is involved; one only has to be careful about the limits of integration which are determined by the theta function. This leads to the result

$$I = (\pi/8)[k_-^{12} k_+^{34} I_1(1,2;3,4) + (1/6)(k_+^{34} - k_-^{12}) I_2(1,2;3,4) - (1/20) \times I_3(1,2;3,4)] \tag{A6}$$

where

$$k_\pm^{ij} = E_i E_j \pm 0{\cdot}5(p_i^2 + p_j^2)$$

and

$$I_n(i,j;k,l) = (P_{ij}^{2n-1} - p_{ij}^{2n-1})\theta(P_{kl} - P_{ij})\theta(p_{ij} - p_{kl}) + (P_{ij}^{2n-1} - p_{kl}^{2n-1})\theta(P_{kl} - P_{ij})\theta(p_{kl} - p_{ij})\theta(P_{ij} - p_{kl}) + (P_{kl}^{2n-1} - p_{kl}^{2n-1})\theta(P_{ij} - P_{kl})\theta(p_{kl} - p_{ij}) + (P_{kl}^{2n-1} - p_{ij}^{2n-1})\theta(P_{ij} - P_{kl})\theta(p_{ij} - p_{kl})\theta(P_{kl} - p_{ij})$$

where

$$P_{ij} = p_i + p_j; \quad p_{ij} = |p_i - p_j|.$$

Similarly by considering expression (A1) for the mean free path and performing the angular integrations in the same way as for emissivity (except for taking care that in this case the integration over neutrino momentum is absent) we obtain (2·12) for the mean free path with the function $I'(E_1, E_2, E_3, E_4)$ given by

$$I'(E_1, E_2, E_3, E_4) = (\pi/8)[k_-^{12} k_+^{34} I_1(1, 2; 3, 4) + (1/6) \times (k_+^{34} + k_-^{12}) I_2(1, 2; 3, 4) + (1/20) I_3(1, 2; 3, 4)]. \quad \text{(A7)}$$

References

[1] E Witten, *Phys. Rev.* **D30**, 272 (1984)
[2] E Farhi and R L Jaffe, *Phys. Rev.* **D30**, 2379 (1984)
C Alcock, E Farhi and A Olinto, *Astrophys. J.* **310**, 261 (1986)
[3] N Iwamoto, *Phys. Rev. Lett.* **44**, 1637 (1980); *Ann. Phys.* **141**, 1 (1982)
[4] A Burrows, *Phys. Rev. Lett.* **44**, 1640 (1980)
[5] C Duncan, S L Shapiro and I Wasserman, *Astrophys. J.* **267**, 358 (1983); **278** 806 (1984)
[6] S K Ghosh, S C Pathak and P K Sahu, *Mod. Phys. Lett.* **A9**, 1717 (1994)
[7] D Freedman and L McLerran, *Phys. Rev.* **D42**, 1109 (1978)
[8] V K Gupta, A Wadhwa and J D Anand, in *Proceedings of international conference on quark-gluon plasma* (ICQGP 1993) held at Calcutta, India in January 1993. Published by World Scientific, Singapore (1994), 412
A Goyal and J D Anand, *Phys. Rev.* **D42**, 992 (1990)

Search for the χ_c' charmonium states as solution to the CDF ψ' puzzle

S F TUAN
Physics Department, University of Hawaii at Manoa, 2505 Correa Road, Honolulu, HI 96822, USA

MS received 17 April 1995

Abstract. The efforts of Roy–Sridhar–Close–Cho–Wise–Trivedi to resolve the CDF ψ' anomaly with cascades from above-threshold χ_c' states require well defined signatures [a small total width and a large branching fraction for $\chi_{cJ}' \to \gamma + \psi'$] for the solution to be viable. Here we estimate the production of such states from $\mathrm{BR}(B \to \chi_{cJ}' + X)\mathrm{BR}(\chi_{cJ}' \to \gamma\psi')$ and $\gamma\gamma$ production of χ_{c2}' at CLEO II, and comment on the feasibility of testing the hypothesis in terms of current experimental capabilities.

Keywords. CDF ψ' anomaly; χ_{cJ}' search.

PACS Nos 13·20; 13·65; 14·40

1. Introduction

The CDF measurement [1] of J/ψ and ψ' production at large transverse momentum (P_T) in 1·8 TeV $p\bar{p}$ collisions at the Tevatron has produced one of the most intriguing experimental results in recent times. At low transverse momentum the production of ψ's in $p\bar{p}$ in collisions is expected to proceed via the production of χ states followed by their decay [2], i.e. fusion process $g + g \to \chi \to \psi + X$. The analogous process at larger transverse momentum is $gg \to g\psi$. This process generates a cross-section that falls off at large P_T much faster than, say, the jet rate. This observation led to an expectation that ψ's produced at large P_T came almost exclusively from b-quark decay. By detecting whether or not the ψ's come from the primary event vertex, CDF has tested this expectation. The fraction of ψ's produced directly is almost independent of P_T and the rate of direct ψ production at large P_T is (substantially) larger than expected. Thus, this expectation is now known to be *false*.

The dominant production mechanism of J/ψ's at large transverse momentum is now believed to be the fragmentation of light (and charm) quark and gluon jets into χ_c mesons that subsequently decay to J/ψ [2] via the radiative mode as stressed by Cho *et al* [3] where the gluon fragmentation is found to be particularly important. When this J/ψ source is included, the theoretical prediction for $\mathrm{d}\sigma(p\bar{p} \to J/\psi + X)/\mathrm{d}P_T$ at $\sqrt{s} = 1{\cdot}8$ TeV agrees within a factor of 2 with recent CDF data [1].

While the rate for J/ψ production is in agreement with expectations, given the inherent theoretical uncertainties, the rate for ψ' production at CDF is at least a factor of 20 above theoretical expectations [4]. The calculation does not include the possibility of ψ' production from the decay of χ_c', 2P states. These 2P charmonium states are above $D\bar{D}$ threshold, however a branching ratio of a few % to ψ' could be sufficient to explain the deficit. Roy and Sridhar as well as others investigated this possibility quantitatively [3].

The basic premise is to recall that ψ' is the heaviest $c\bar{c}$ bound state which lies below the $D\bar{D}$ threshold. Therefore, $n=1$ χ_{cJ} states cannot radiatively decay to ψ' but their $n=2$ counterparts can. None of these χ'_{cJ} (or χ_{cJ} (2P)) states which lie above the $D\bar{D}$ threshold have been observed. Estimates of their masses yield $M(\chi_{c0}(2P))=3920$ MeV, $M(\chi_{c1}(2P)=3950$ MeV, and $M(\chi_{c2}(2P))=3980$ MeV [5]. These mass values taken literally would kinematically allow the S-wave transitions $\chi_{c0}(2P)\to D\bar{D}$ and $\chi_{c1}(2P)\to D^*\bar{D}$ to occur. We therefore expect that the $J=0$ and perhaps the $J=1$ excited $\chi_{cJ}(2P)$ states will be broad and have negligible branching fractions to lower $c\bar{c}$ bound states. However, angular momentum and parity considerations require the analogous decay $\chi_{c2}(2P)\to D\bar{D}$ and $\chi_{c2}(2P)\to D^*\bar{D}$ for the $J=2$ state to proceed via $L=2$ partial waves. Although we cannot readily compute by how much these D-wave decays will be suppressed, it is possible that the branching fractions for $\chi_{c2}(2P)$ states to charmonium states below $D\bar{D}$ threshold could be significant. Close [3] suggests that the $\chi_{c1}(2P)$ may also have suppressed hadronic widths due to quantum numbers or nodes in form factors manifested in decays near threshold, e.g. since ${}^3P_1\to\bar{D}D^*$ is near threshold the S- and D-waves present are affected by radial wave function nodes which can conspire to reduce the width. Hence in § 2 below we will consider the search for both $\chi_{c1}(2P)$ and $\chi_{c2}(2P)$. Although the ${}^1D_2$ and ${}^3D_2$ charmonium states may be present in the CDF data and detectable, they are unlikely to explain the $\psi'(3685)$ enhancement. For instance [3] ${}^1D_2$ production is suppressed, and it is expected to have a very small branching ratio to $\psi'\gamma$.

On a quantitative basis Page [6] has calculated the total widths of radial χ'_{cJ} states and found that they could be as small as 1–5 MeV. We need an estimate of the branching ratio $\mathrm{BR}(\chi'_{cJ}\to\gamma+\psi')$. A very rough estimate [7] can be obtained using the known experimentally measured branching ratio $\mathrm{BR}(\chi_{b2}(2P)\to\Upsilon(2S)+\gamma)\approx 16\%$ [8] as follows:

$$\mathrm{BR}(\chi_{c2}(2P)\to\gamma\psi')=\left(\frac{Q_c}{Q_b}\right)^2\left(\frac{k_c}{k_b}\right)^3\mathrm{BR}(\chi_{b2}(2P)\to\gamma\Upsilon(2S))\frac{\Gamma_{\mathrm{tot}}(\chi_{b2}(2P))}{\Gamma_{\mathrm{tot}}(\chi_{c2}(2P))} \quad (1)$$

Here $(Q_c/Q_b)^2=(4/9)/(1/9)=4$, and $(k_c/k_b)^3$ is the modification due to E_1 phase space; there will be some changes due to the actual size of $b\bar{b}$ relative to that of $c\bar{c}$ but this will be a factor of 2 or 3 and the estimate (1) may not be accurate to better than a factor of 5 to 10 anyway. For instance, taking $M(\chi_{c2}(2P))=3980$ MeV and $\Gamma_{\mathrm{tot}}(\chi_{b2}(2P))\approx\Gamma_{\mathrm{tot}}(\chi_{c2}(2P))$ gives $\mathrm{BR}(\chi_{c2}(2P)\to\gamma+\psi')\approx 100\%$! Thus the value $\mathrm{BR}(\chi_{c2}(2P)\to\gamma+\psi')\approx 10\%$ suggested by Roy and Sridhar [3] is by no means unreasonable. Another back of the envelope ansatz [7] is to take the $1P\to 1S$ charmonium data and *assume* the $2P\to 2S$ overlaps will have the same order of magnitude, then $B(\chi_{c2}(2P)\to\gamma+\psi')\approx B(\chi_{c2}(1P)\to\gamma+J/\psi)=13{\cdot}5\%$, with a measured $\Gamma_{c2}(1P)$ full width $=2$ MeV [8]. Hence if one of the $\chi_{cJ}(2P)$ states is calculated to have a total width in the range 1 MeV to 5 MeV [6], a branching ratio $B(\chi_{cJ}(2P)\to\gamma+\psi')>5\%$ can be expected (a value in the range 5–10% would be needed to explain the CDF ψ' anomaly [1, 3]). To summarize, the result is that, in order of magnitude, one expects the radiative transition to be $O(100\,\mathrm{KeV})$ and hence the BR is $O(1\text{–}10\%)$ if the hadronic width is $O(10\text{–}1$ MeV). It would be surprising if the branching ratio is less than 1% or much greater than 10%. To give an adequate spread for illustration, we shall take in § 2,

$$\mathrm{BR}(\chi_{cJ}(2P)\to\gamma+\psi(2S))=1,5,10\%. \quad (2)$$

The optimal method for accumulation of χ_{cJ} events at CLEO II is to take advantage of the inclusive decays of B mesons to charmonium. Hence we seek to estimate

$$B_J \equiv \mathrm{BR}[B \to \chi'_{cJ} + X]\,\mathrm{BR}[\chi'_{cJ} \to \gamma\psi'']. \tag{3}$$

The branching ratio $\mathrm{BR}[B \to \chi'_{cJ} + X]$ is given by Bodwin *et al* [9] as

$$R(\chi_{cJ}) \times 10{\cdot}7\% \times |R'_{\chi_c}(0)/R'_{\chi_c}(0)|^2 \tag{4}$$

where $R(\chi_{cJ}) = \Gamma(b \to \chi_{cJ} + X)/\Gamma(b \to e^- \bar{\nu}_e + X)$, 10·7% is the observed semileptonic branching ratio for the B meson, and multiplicative last term $|R'_{\chi_c}(0)/R'_{\chi_c}(0)|^2$ is Braaten's correction factor [10] for estimating $\mathrm{BR}(B \to \chi'_c + X)$ from $\mathrm{BR}(B \to \chi_c + X)$. The derivatives of the wave functions at the origin can be obtained from potential models. This procedure is certainly correct for the color-singlet matrix element (the $c\bar{c}$ contribution) and it may also be correct for the color-octet matrix element (the $c\bar{c}g$ contribution) if the latter is dominated by the radiation of soft gluons from the $c\bar{c}$ state. Whether or not this is the case remains to be seen [10].

The expression $R(\chi_{cJ})$ in (4) is given in terms of the non-perturbative parameters H_1 and H'_8 (proportional to the probabilities for a $c\bar{c}$ pair in a color-singlet P-wave and a color-octet S-wave state, respectively, to fragment into a color-singlet P-wave bound state) and takes the following form [9]

$$\begin{aligned} R(\chi_{c1}) &\cong 12{\cdot}4(2C_+ - C_-)^2 H_1/M_b + 9{\cdot}3(C_+ + C_-)^2 H'_8(M_b)/M_b \\ R(\chi_{c2}) &\cong 15{\cdot}3(C_+ + C_-)^2 H'_8(M_b)/M_b. \end{aligned} \tag{5}$$

Here C_+ and C_- are Wilson coefficients that arise from evolving the effective 4-quark interactions mediated by the W boson from the scale M_W down to the scale M_b. Numerically $C_+(M_b) \cong 0{\cdot}87$, $C_-(M_b) \cong 1{\cdot}34$, $H_1 \approx 15$ MeV, $H'_8(M_b) \cong 2{\cdot}5$ MeV, and $M_b = 5{\cdot}3$ GeV.

For the value $|R'_{\chi_c}(0)/R'_{\chi_c}(0)|^2$, we use a recent quark potential model [11] which takes into account that the value of $R'(0)$ for P-state charmonium is sensitive to the short distance behaviour of the potential, so that it is better to use values obtained from potentials whose short distance behaviour is more reliable. The potential [11] (an improved version of the Buchmüller–Grunberg–Tye potential) approaches the 2-loop QCD result at short distance, leads to energy spectra and leptonic widths in very good agreement with experiment. The values for $R'(0)$ for the P-wave charmonium states from this potential model Program [12] are

State	$R'(0)$ in $\mathrm{GeV}^{5/2}$
χ_c	0·20
χ'_c	0·23

(6)

For comparison, the value of $R'(0)$ for χ_c [10] obtained directly from the measured widths of χ_{c1} and χ_{c2} was about $0{\cdot}15\ \mathrm{GeV}^{5/2}$, hence one should ascribe an error of not less than 30% to any of these values. It is nevertheless reassuring that a recent compilation [13] of first non-vanishing derivative at zero $c\bar{c}$ separation for radial Schrödinger wave function of earlier potential models, give for $|R'_{\chi_c}(0)/R'_{\chi_c}(0)|^2$ values 1·36 (Buchmüller–Tye), 1·05 (Power-law), 0·97 (Logarithmic), and 1·42 (Cornell), quite

compatible with

$$\left|\frac{R'_{\chi_c}(0)}{R'_{\chi_c}(0)}\right|^2 = 1{\cdot}32 \tag{7}$$

of the recent potential model [11].

Assembling the pieces together from (3), (4), (5) and (7), we have for (3) and $J = 1$.

$$B_1 = 2{\cdot}89 \times 10^{-5}, 1{\cdot}45 \times 10^{-4}, 2{\cdot}89 \times 10^{-4} \tag{8}$$

for the respective values of $\mathrm{BR}|\chi'_{c1} - \gamma\psi'|$ given in (2). The corresponding values for $J = 2$ are

$$B_2 = 3{\cdot}77 \times 10^{-5}, 1{\cdot}89 \times 10^{-4}, 3{\cdot}77 \times 10^{-4}. \tag{9}$$

The world average (WA) and CLEO II measurement [14] for $\mathrm{BR}(B \to \chi_c + X)$ are

$$\mathrm{BR}(B \to \chi_{c1} + X) = 0{\cdot}42 \pm 0{\cdot}07\% \text{ (WA)}$$
$$\mathrm{BR}(B \to \chi_{c2} + X) = 0{\cdot}25 \pm 0{\cdot}10\% \text{ (CLEO)}. \tag{10}$$

For central values of (10), multiplying the above experimental numbers by correction factor (7), we have

$$\mathrm{BR}(B \to \chi'_{c1} + X) = 5{\cdot}54 \times 10^{-3}$$
$$\mathrm{BR}(B \to \chi'_{c2} + X) = 3{\cdot}30 \times 10^{-3}. \tag{11}$$

This compares with the values obtained by scaling the predictions of Bodwin *et al* [9] for $\mathrm{BR}(B \to \chi_{cJ} + X]$ using the correlation factor (7) of

$$\mathrm{BR}(B \to \chi'_{c1} + X) = 2{\cdot}8 \times 10^{-3}$$
$$\mathrm{BR}(B \to \chi'_{c2} + X) = 3{\cdot}77 \times 10^{-3}. \tag{12}$$

The agreement seems good for the χ'_{c2} case.

The final step is to estimate the number of observed events, N_J^{obs}. First we note that at CLEO II, the number of produced B mesons is given by

$$N_B^{\mathrm{produced}} = \left(\int \mathscr{L}\mathrm{d}t\right)\sigma(e^+e^- \to \Upsilon(4\mathrm{S}) \to B\bar{B})2 \tag{13}$$

where on a good year the integrated luminosity $\int \mathscr{L}\mathrm{d}t$ is $2\,\mathrm{fb}^{-1}$ of data on tape, the $\sigma(e^+e^- \to \Upsilon(4\mathrm{S}) \to B\bar{B})$ cross-section is about 1·07 nb, and the factor of 2 takes into account productions of pairs of B mesons in $\Upsilon(4\mathrm{S})$ decays. The number of observed events N_J^{obs} is then given by

$$N_J^{\mathrm{obs}} = N_B^{\mathrm{produced}} B_J B(\psi' \to J/\psi\pi^+\pi^-)\left(\sum_{l=e,\mu} B(J/\psi \to l^+l^-)\right)\varepsilon \tag{14}$$

where B_J is defined in (3), and ε is the efficiency for detecting $\psi' \to J/\psi\pi^+\pi^-$ in the dilepton mode (about 20% in the CLEO II detector [14]). Hence using theory (8), (9) or (12), we have

$$N_1^{\mathrm{obs}} = 0{\cdot}95, 4{\cdot}77, 9{\cdot}51 \text{ events}$$
$$N^{\mathrm{obs}} = 1{\cdot}24, 6{\cdot}22, 12{\cdot}40 \text{ events} \tag{15}$$

for the respective values of $\mathrm{BR}(\chi_{cJ}' \to \gamma\psi')$ given in (2). If we take advantage of the experimentally known branching ratios (10) in deducing (11), we have

$$N_1^{\mathrm{obs}} = 1{\cdot}82, 9{\cdot}11, 18{\cdot}23 \text{ events}$$

$$N_2^{\mathrm{obs}} = 1{\cdot}09, 5{\cdot}43, 10{\cdot}86 \text{ events} \tag{16}$$

for the respective values of $\mathrm{BR}(\chi_{cJ}' \to \gamma\psi')$. The theoretical mass estimates [5] $M(\chi_{c1}(2\mathrm{P})) = 3950\,\mathrm{MeV}$ and $M(\chi_{c2}(2\mathrm{P})) = 3980\,\mathrm{MeV}$ are also useful. The approximate locations of these resonances are needed to conduct the experimental search and reduce background.

At CLEO II, the χ_{c2}' state can also be searched for via the two photon production of this $J=2$ state. For instance, the number of events $N_{\chi_{c2}'}$ from $e^+e^- \to e^+e^-\gamma\gamma \to e^+e^-\chi_{c2}'$ is estimated to be

$$N_{\chi_{c2}'} = N_{\chi_{c2}} \frac{\sigma(\gamma\gamma \to \chi_{c2}')}{\sigma(\gamma\gamma \to \chi_{c2})} \frac{\mathrm{BR}(\chi_{c2}' \to \psi'\gamma)}{\mathrm{BR}(\chi_{c2} \to J/\psi\gamma)}$$

$$\times \sum_{l=e,\mu} \frac{\varepsilon(l^+l^-\pi^+\pi^-\gamma)}{\varepsilon(l^+l^-\gamma)} \frac{\mathrm{BR}(\psi' \to J/\psi\pi^+\pi^-)\mathrm{BR}(J/\psi \to l^+l^-)}{\mathrm{BR}(J/\psi \to l^+l^-)}. \tag{17}$$

In a recent paper on measurement of two-photon production of the χ_{c2}, Dominick *et al* [15], using $1{\cdot}5\,\mathrm{fb}^{-1}$ of data taken with beam energies near the $\Upsilon(4\mathrm{S})$, $25{\cdot}4 \pm 6{\cdot}9$ $N_{\chi_{c2}}$ events were obtained, with efficiency $\varepsilon(l^+l^-\gamma) = 0{\cdot}187 \pm 0{\cdot}003$. Taking into account that data accumulation is now $2\,\mathrm{fb}^{-1}$ on $\Upsilon(4\mathrm{S})$ and $1\,\mathrm{fb}^{-1}$ in the continuum, the number $N_{\chi_{c2}}$ can be doubled and we assume that $\varepsilon(l^+l^-\pi^+\pi^-\gamma) \cong \varepsilon(l^+l^-\gamma)/2$. For $\mathrm{BR}(\chi_{c2}' \to \psi'\gamma) = 10\%$ and taking central values for experimental numbers to illustrate, we have

$$N_{\chi_{c2}'} \cong 6 \times \frac{\sigma(\gamma\gamma \to \chi_{c2}')}{\sigma(\gamma\gamma \to \chi_{c2})} \text{events}. \tag{18}$$

The cross-section ratio is equal to the $\Gamma(\chi_{c2}' \to \gamma\gamma)/\Gamma(\chi_{c2} \to \gamma\gamma)$ and is not yet known since the total width $\Gamma(\chi_{c2}')$ has not yet been measured.

3. Conclusions

We have presented above in § 2 event rates for observing the $\chi_{cJ}'(J=1,2)$ in B decays at CLEO II. Though the event rates N_J^{obs} given by (15) and (16) are not large even with a year's accumulation of $B\bar{B}$, they can be steadily increased by extending the $B\bar{B}$ accumulation over a period of several years. Furthermore we have been surprised by how large the branching ratios $\mathrm{BR}(\chi_{cJ}' \to \chi\psi')$ can be in § 1, given the known and sizable [8] $\mathrm{BR}(\chi_{b1} \to \gamma + \Upsilon(2\mathrm{S})) \approx (21 \pm 4\%)$ and $\mathrm{BR}(\chi_{b2} \to \gamma + \Upsilon(2\mathrm{S})) \cong (16{\cdot}2 \pm 2{\cdot}4)\%$. Hence optimistically we can expect N_J^{obs} to be in the range of 10–20 events for an integrated luminosity of $2\,\mathrm{fb}^{-1}$, as needed to explain the CDF ψ' anomaly [1]. Estimates for 2γ production of χ_{c2}' are given in (17) and (18). At CDF the invariant mass spectrum of $\gamma\psi'$ combination can be studied. This possibility should be explored in parallel with the

Acknowledgements

The author thanks X Tata and T Browder for their comments and reading of the manuscript, and E Braaten, F E Close, Y P Kuang and P Page for helpful communications. This work was supported in part by the US Department of Energy under Grant DE-FG-03-94ER40833.

References

[1] CDF Collaboration, J/ψ, $\psi' \to \mu^+ \mu^-$ and $B \to J/\psi, \psi'$ cross-sections, Fermilab-Conf-94/136-E, contribution GLS0208 to the 1994, International Conference on High Energy Physics, Glasgow
[2] I Hinchliffe, "Current Issues in Perturbative QCD", LBL-36374; *Proc. of Division of particles and fields*, APS, August (1994) (to appear)
[3] D P Roy and K Sridhar, *Phys. Lett.* **B345**, 537 (1995)
F E Close, *Phys. Lett.* **B342**, 369 (1995)
Peter Cho, Mark B Wise and Sandip Trivedi, *Phys. Rev.* **D51**, R2039 (1995)
[4] E Braaten *et al*, *Phys. Lett.* **B333**, 548 (1994)
D P Roy and K Sridhar, *Phys. Lett.* **B339**, 141 (1994)
[5] S Godfrey and N Isgur, *Phys. Rev.* **D32**, 189 (1985)
[6] P R Page, OUTP-94-34P (bulletin board: hep-ph/9502204)
[7] F E Close, private communication
[8] Review of Particle Properties, *Phys. Rev.* **D50**, Part. I (August 1994)
[9] G T Bodwin, E Braaten, T C Yuan and G P Lepage, *Phys. Rev.* **D46**, R3703 (1992)
[10] E Braaten, private communication
[11] Y Q Chen and Y P Kuang, *Phys. Rev.* **D46**, 1165 (1992)
[12] E Braaten and Y Q Chen, private communication
[13] E J Eichten and C Quigg, Fermilab-Pub-95/045-T, CLNS95/1329 (bulletin board: hep-ph/9503356), March (1995)
[14] CLEO Collaboration, Inclusive decays of B mesons to charmonium, CLNS 94/1315, CLEO 94–26, December (1994)
[15] J Dominick *et al*, *Phys. Rev.* **D50**, 4265 (1994)

journal of physics

August 1995
pp. 215–219

Energy and momentum of cylindrical gravitational waves-II

K S VIRBHADRA
Physical Research Laboratory, Navrangpura, Ahmedabad 380 009, India
Present address: Theoretical Astrophysics Group, Tata Institute of Fundamental Research, Homi Bhabha Road, Bombay 400 005, India

MS received 3 October 1994; revised 27 March 1995

Abstract. Recently Rosen and the present author obtained the energy and momentum densities of cylindrical gravitational waves in Einstein's prescription and found them to be finite and reasonable. In the present paper we calculate the same in the prescriptions of Tolman as well as Landau and Lifshitz and discuss the results.

Keywords. Einstein–Rosen metric; energy-momentum pseudotensors.

PACS Nos 04·20; 04·40

1. Introduction

Long ago Scheidegger [1] raised doubts whether gravitational radiation has well-defined existence. To this end, Rosen [2] investigated whether or not the cylindrical gravitational waves have energy and momentum. He used the energy-momentum pseudotensors of Einstein and Landau and Lifshitz (LL) and carried out calculations in cylindrical polar coordinates and found that the energy and momentum density components vanish. The results obtained by him fit in with the conjecture of Scheidegger that a physical system cannot radiate gravitational energy. Two years later, Rosen [3] realized the mistake and carried out the calculations in "cartesian coordinates" and reported that the energy and momentum density are nonvanishing and reasonable. Though in the letter he remarked that he would publish the details elsewhere, it was not done until recently he and the present author [4] re-calculated the energy and momentum density components in "cartesian coordinates" in Einstein's prescription. They found finite and reasonable results.

The physical interpretation of Einstein's energy-momentum complex has been questioned by several physicists, notably by Weyl, Pauli and Eddington [5]. Their objections were that the energy-momentum complex of Einstein was neither a tensor nor was it symmetric. However, Palmer [6] discussed the importance of Einstein's energy-momentum complex in detail. Since the first energy-momentum complex of Einstein was given, a large number of prescriptions to obtain energy and momentum in a general relativistic system have been proposed by many authors [7]. Since there is no unique way of defining energy and momentum in a curved spacetime, and also the various energy-momentum complexes are not tensors, some researchers do not take them seriously. They even guess that the different energy-momentum complexes could give different and therefore unacceptable energy distribution in a given spacetime. However, we have shown that the energy-momentum pseudotensors of Einstein, Tolman and LL give the same result for energy distribution in the Kerr–Newman as

well as in the Vaidya spacetimes when calculations are carried out in "cartesian coordinates" [8–10]. We have already mentioned that Rosen and the present author obtained energy and momentum density for the cylindrical gravitational waves in "cartesian coordinates" in Einstein's prescription and found reasonable result. Therefore, it is of interest to investigate whether or not other energy-momentum complexes give the same result. This is the aim of this paper. We consider here the energy-momentum complexes of Tolman and LL. This paper is organized as follows. Section 2 gives the Einstein–Rosen metric describing the cylindrical gravitational waves. In § 3 and § 4, we obtain energy and momentum density of cylindrical gravitational waves in prescriptions of Tolman and LL. In § 5 we discuss the results obtained. We use the geometrized units such that $G = 1, c = 1$ and follow the convention that the Latin and Greek indices take values 0 to 3 and 1 to 3, respectively. x^0 is the time coordinate.

2. Einstein–Rosen metric

The Einstein–Rosen metric is a non-static vacuum solution of Einstein's field equations and it describes the gravitational field of cylindrical gravitational waves. It is given by the line element [11]:

$$ds^2 = e^{2\gamma-2\psi}(dt^2 - d\rho^2) - e^{-2\psi}\rho^2 d\phi^2 - e^{2\psi}dz^2, \tag{1}$$

where $\gamma = \gamma(\rho, t), \psi = \psi(\rho, t)$, and

$$\psi_{\rho\rho} + \frac{\psi_\rho}{\rho} - \psi_{tt} = 0, \tag{2}$$

$$\gamma_\rho = \rho(\psi_\rho^2 + \psi_t^2), \tag{3}$$

$$\gamma_t = 2\rho\psi_\rho\psi_t. \tag{4}$$

The subscripts on ψ and γ denote partial derivatives with respect to the subscripts. It is known that the energy-momentum complexes of Tolman and LL, like that of Einstein, give correct result if calculations are carried out in "cartesian coordinates" [12–17]. Therefore, one transforms the line element, given by (1), according to

$$x = \rho\cos\phi,$$

$$y = \rho\sin\phi, \tag{5}$$

and gets the line element in t, x, y, z coordinates [4],

$$ds^2 = e^{2(\gamma-\psi)}\left[dt^2 - \frac{(xdx + ydy)^2}{\rho^2}\right] - \frac{e^{-2\psi}}{\rho^2}(xdy - ydx)^2 - e^{2\psi}dz^2. \tag{6}$$

3. Energy and momentum of cylindrical gravitational waves in prescription of Tolman

The energy-momentum complex of Tolman is [13–14]

$$\mathcal{T}_k^i = \frac{1}{8\pi}U_{k,j}^{ij}, \tag{7}$$

$$U_k^{ij} = \sqrt{-g}[-g^{li}(-\Gamma_{kl}^j + \tfrac{1}{2}g_k^j\Gamma_{al}^a + \tfrac{1}{2}g_l^j\Gamma_{ak}^a) + \tfrac{1}{2}g_k^i g^{lm}(-\Gamma_{lm}^j + \tfrac{1}{2}g_l^j\Gamma_{am}^a + \tfrac{1}{2}g_m^j\Gamma_{al}^a)]. \quad (8)$$

is the energy density, $\mathscr{T}_\alpha^0$ are the momentum density components, and $\mathscr{T}_0^\alpha$ are the nponents of energy current density. The required nonvanishing components of U_k^{ij}

$$U_0^{01} = \frac{x(e^{2\gamma}-1)}{2\rho^2},$$

$$U_0^{02} = \frac{y(e^{2\gamma}-1)}{2\rho^2},$$

$$U_1^{01} = \frac{-2\psi_t\psi_\rho y^2}{\rho},$$

$$U_2^{02} = \frac{-2\psi_t\psi_\rho x^2}{\rho},$$

$$U_1^{02} = U_2^{01} = \frac{2\psi_t\psi_\rho xy}{\rho},$$

$$U_3^{03} = 2\psi_t(1-\rho\psi_\rho),$$

$$U_0^{11} = \frac{2e^{2\gamma}\psi_t\psi_\rho y^2}{\rho},$$

$$U_0^{22} = \frac{2e^{2\gamma}\psi_t\psi_\rho x^2}{\rho},$$

$$U_0^{12} = U_0^{21} = \frac{-2e^{2\gamma}\psi_t\psi_\rho xy}{\rho},$$

$$U_0^{33} = 2e^{2\gamma-4\psi}\psi_t(\rho\psi_\rho - 1). \quad (9)$$

ng (9) in (7) we obtain

$$\mathscr{T}_0^0 = \frac{e^{2\gamma}(\psi_\rho^2+\psi_t^2)}{8\pi},$$

$$\mathscr{T}_1^0 = \frac{x\psi_\rho\psi_t}{4\pi\rho},$$

$$\mathscr{T}_2^0 = \frac{y\psi_\rho\psi_t}{4\pi\rho},$$

$$\mathscr{T}_0^1 = -e^{2\gamma}\mathscr{T}_1^0,$$

$$\mathscr{T}_0^2 = -e^{2\gamma}\mathscr{T}_2^0,$$

$$\mathscr{T}_0^3 = \mathscr{T}_3^0 = 0. \quad (10)$$

4. Energy and momentum of cylindrical gravitational waves in prescription of LL

The energy-momentum complex of LL is [15]

$$L^{mn} = \frac{1}{16\pi} S^{mjnk}{}_{,jk}, \tag{11}$$

where

$$S^{mjnk} = -g(g^{mn}g^{jk} - g^{mk}g^{jn}). \tag{12}$$

L^{mn} is symmetric in its indices. L^{00} is the energy density and $L^{0\alpha}$ are the momentum (energy current) density components. S^{mjnk} has symmetries of the Reimann curvature tensor. The required nonvanishing components of S^{mjnk} are

$$S^{0101} = \frac{-(e^{2\gamma}y^2 + x^2)}{\rho^2},$$

$$S^{0102} = \frac{xy(e^{2\gamma} - 1)}{\rho^2},$$

$$S^{0202} = \frac{-(e^{2\gamma}x^2 + y^2)}{\rho^2},$$

$$S^{0303} = -e^{2(\gamma - 2\psi)}. \tag{13}$$

Making use of (13) in (11) we obtain energy and momentum (energy current) density components for the cylindrical gravitational waves in LL prescription

$$L^{00} = \frac{e^{2\gamma}(\psi_\rho^2 + \psi_t^2)}{8\pi},$$

$$L^{01} = \frac{-e^{2\gamma}\psi_\rho\psi_t x}{4\pi\rho},$$

$$L^{02} = \frac{-e^{2\gamma}\psi_\rho\psi_t y}{4\pi\rho},$$

$$L^{03} = 0. \tag{14}$$

5. Discussion

One can see from (10) and (14) that the energy-momentum complexes of Tolman and LL give the same energy and energy current densities as given by Einstein's prescription [4]. The momentum density components in the Tolman prescription are the same as in the Einstein prescription. The momentum density components in Tolman and LL prescriptions differ by a sign, as expected. The energy density of the cylindrical gravitational waves is finite and positive definite, and the momentum density components reflect the symmetry of the spacetime. Thus our investigations do not support the conjecture of Scheidegger [1].

Due to non-tensorial nature of energy-momentum complexes, some physicists do not take them seriously. They even conjecture that different energy-momentum complexes could give different energy distributions in a given spacetime. To this end we

ve shown that the well-known energy-momentum complexes of Einstein, Tolman d LL give the same and reasonable result for the Kerr–Newman, Vaidya, and nstein–Rosen spacetimes (see also ref. 4, 7–10).

cknowledgements

ne author thanks P C Vaidya, Nathan Rosen and Alberto Chamorro for careful ading of the manuscript, and to the Basque Government and the Tata Institute of ndamental Research for partial support for completion of this work. He also thanks e referee for suggestions.

ferences

] A E Scheidegger, *Rev. Mod. Phys.* **25**, 451 (1953)
] N Rosen, *Helv. Phys. Acta. Suppl.* **4**, 171 (1956)
] N Rosen, *Phys. Rev.* **110**, 291 (1958)
] N Rosen and K S Virbhadra, *Gen Relativ. Gravit.* **26**, 429 (1993)
] S Chandrasekhar and V Ferrari, *Proc. R. Soc. London* **A435**, 645 (1991)
] T Palmer, *Gen. Relativ. Gravit.* **12**, 149 (1980)
] K S Virbhadra, *Math. Today* **9**, 39 (1991)
] K S Virbhadra, *Phys. Rev.* **D41**, 1086 (1990)
] K S Virbhadra, *Phys. Rev.* **D42**, 2919 (1990)
] K S Virbhadra, *Pramana – J. Phys.* **38**, 31 (1992)
] M Carmeli, *Classical fields: General relativity and gauge theory* (John Wiley and Sons, 1982) p. 198
] C Møller, *Ann. Phys. (NY)* **4**, 347 (1958)
] P C Vaidya, *J. Univ. Bombay* **21**, 1 (1952)
] R C Tolman, *Relativity thermodynamics and cosmology* (Oxford Univ. Press, London, 1934) p. 227
] L D Landau and E M Lifshitz, *The classical theory of fields* (Pergamon Press, 1987) p. 280
] R W Lindquist, R A Schwartz and C W Misner, *Phys. Rev.* **137**, B1364 (1965)
] K S Virbhadra and J C Parikh, *Phys. Lett.* **B317**, 312 (1993)

te added in proof:

ng the Papapetrou pseudotensor we have obtained the energy and energy current (momen-) densities of the cylindrical gravitational waves (described by the Einstein–Rosen metric) have found them to be the same as given by the LL energy momentum complex.

Regd. No. KRN-A 64

Pramana journal of physics Vol. 45 (No. 2), August 1995

Contents

Generalized Fock spaces, new forms of quantum statistics and their algebras
.....*A K Mishra and G Rajasekaran* 91

Time dependent canonical perturbation theory I: General theory.....
.....*B R Sitaram and Mitaxi P Mehta* 141

Time dependent canonical perturbation theory II: Application to the Henon–Heiles system.....*Mitaxi P Mehta and B R Sitaram* 149

The Coulomb Green's function revisited.....
.....*S S Vasan and M Seetharaman* 165

Gravitational and electromagnetic fields of a charged tachyon.....
.....*K S Virbhadra* 175

A radiating dyon solution.....*A Chamorro and K S Virbhadra* 181

Static models of cosmic strings in general relativity.....*G P Singh* 189

Neutrino emissivity of quark matter at finite temperatures.....
.....*V K Gupta, A Wadhwa and J D Anand* 195

Search for the χ_c' charmonium states as solution to the CDF ψ' puzzle.....
.....*S F Tuan* 209

Brief Report

Energy and momentum of cylindrical gravitational waves.....
.....*K S Virbhadra* 215

Indexed in CURRENT CONTENTS ISSN 0304–4289

PRAMANA

journal of physics

Vol. 45 No. 3
September 1995

NDIAN ACADEMY OF SCIENCES
ndian National Science Academy
ndian Physics Association

Pramana – journal of physics

Editor

R Nityananda
Raman Research Institute, Bangalore

Associate Editor

H R Krishnamurthy
Indian Institute of Science, Bangalore

Editorial Board

G S Agarwal, *University of Hyderabad, Hyderabad*
V Balakrishnan, *Indian Institute of Technology, Madras*
M Barma, *Tata Institute of Fundamental Research, Bombay*
P Chaddah, *Centre for Advanced Technology, Indore*
B M Deb, *Panjab University, Chandigarh*
P K Kaw, *Institute for Plasma Research, Gandhinagar*
H S Mani, *Indian Institute of Technology, Kanpur*
N Mukunda, *Indian Institute of Science, Bangalore*
T Padmanabhan, *Inter-University Centre for Astronomy and Astrophysics, Pune*
J C Parikh, *Physical Research Laboratory, Ahmedabad*
G Rajasekaran, *Institute of Mathematical Sciences, Madras*
V S Ramamurthy, *Institute of Physics, Bhubaneswar*
R Ramaswamy, *Jawaharlal Nehru University, New Delhi*
K R Rao, *Bhabha Atomic Research Centre, Bombay*
Probir Roy, *Tata Institute of Fundamental Research, Bombay*
A K Sood, *Indian Institute of Science, Bangalore*

Editor of Publications of the Academy

V K Gaur
C-MMACS, NAL, Bangalore

Subscription Rates
(Effective from 1989)

All countries except India	1 year	3 years	5 years
(Price includes AIR MAIL charges)	US$ 175	$ 470	$ 700
India	1 year Rs. 100	10 years (1989–1998 only) Rs. 500	

All correspondence regarding subscription should be addressed to the **Circulation Department** of the Academy

---

Editorial Office

Indian Academy of Sciences, C V Raman Avenue,
P.B. No. 8005, Bangalore 560 080, India

Telephone: 334 2546
Telex: 845-2178 ACAD IN
Telefax: 91-80-334 6094

© 1995 by the Indian Academy of Sciences. All rights reserved.

"Information for contributors" is printed in the last issue of every volume.

Journal of physics

September 1995
pp. 221–226

Theoretical calculation of acoustic non-linearity parameter B/A of binary mixtures

J JUGAN, ROSHAN ABRAHAM and M ABDULKHADAR
School of Pure and Applied Physics, Mahatma Gandhi University, Priyadarshini Hill P.O., Kottayam 686 560, Kerala, India

MS received 13 March 1995; revised 21 June 1995

Abstract. Acoustic non-linearity parameter B/A is calculated for five binary liquid mixtures using Tong and Dong equation along with the Flory's statistical theory. Similar to other excess thermodynamical quantities an excess non-linearity parameter $(B/A)^E$ is defined for binary liquid mixtures. The interactions in the liquid mixtures are explained on the basis of the excess non-linearity parameter.

Keywords. Non-linearity parameter; excess non-linearity parameter; binary liquid mixture; ultrasonic velocity; isentropic compressibility.

PACS Nos 43·00; 43·25

1. Introduction

The non-linearity parameter B/A plays a significant role in non-linear acoustics and its determination is of increasing interest in a number of areas ranging from underwater acoustics to medicine. B/A of liquids can be obtained from the variation of sound velocity with temperature and pressure. A number of experimental and theoretical studies have been performed on the non-linearity parameter of liquids making use of phenomenological [1–3] or thermodynamic methods [4, 5]. Also some studies on B/A have been performed from the view point of theory of liquids [6]. B/A values for organic liquids [2, 3,7], liquid mixtures [6, 8, 9] and biological samples [10, 11] have been reported. Tong Jie *et al* [12] calculated the B/A values for pure liquids making use of Schaaff's equation [13] for sound velocity. Although detailed studies of the non-linearity parameter have been made for many pure liquids, such studies are sparse in the case of liquid mixtures.

In the present study, we have calculated the non-linearity parameter of five binary liquid mixtures of benzene, toluene, chlorobenzene, bromobenzene, nitrobenzene and methyl ethyl ketone (MEK), with MEK as a common component. We make use of the Tong and Dong equation [12] for pure liquids and Flory's statistical theory [14, 15] for calculating the B/A values. The thermodynamical parameters in Tong's equation are calculated for binary mixtures using Flory's theory. The variations of B/A with mole fraction of MEK are discussed. Also similar to other thermodynamical parameters, we define an excess non-linearity parameter $(B/A)^E$ for liquid mixtures.

2. Theory

Tong *et al* [12] applied Schaaff's equation for sound velocity in the basic equation for

where

$$J(o) = (1 - 1/\gamma)\frac{c^2 \rho K_T}{T\beta} \tag{2}$$

and

$$J(x) = \frac{2(3-2x)^2}{3(x-1)(6-5x)} \tag{3}$$

Here γ is the ratio of specific heat, ρ is the density, K_T is the isothermal compressibility, T is the temperature, β is the expansibility and x is the real volume of a molecule. x is the ratio of molecular weight to ρb, where b is the van der Waals' constant given by $b = (16/3)\pi r_o{}^3 N, r_o$ being the molecular radius and N the Avogadro number.

In the present study the thermodynamical parameters containing in (2) and (3) and which are required to calculate B/A values of binary mixtures are obtained as follows.

The characteristic and reduced parameters for pure components are obtained from Flory's statistical theory [14, 15] and those of mixtures are calculated by the procedure adopted by Pandey [16, 17]. The thermodynamical parameters β, K_T, C_P and γ for the mixtures which are necessary to calculate B/A for the mixtures are obtained by the relation suggested by Khanwalkar [18]. The van der Waals' constant b and x for the mixtures are calculated as

$$b = y_1 b_1 + y_2 b_2 \tag{4}$$

and

$$x = \frac{y_1 M_1 + y_2 M_2}{\rho_{12} b} \tag{5}$$

where y_1 and y_2 are the mole fractions and M_1 and M_2 are the molecular weights of first and second component respectively and ρ_{12} is the density of the mixture.

The excess properties of the mixtures are defined as the difference between the thermodynamic functions of mixing for a real solution in excess to those for an ideal solution. In studying liquid mixtures, excess properties are more important than thermodynamical properties [19]. Similar to excess thermodynamic functions for binary liquid mixtures we define an excess non-linearity parameter $(B/A)^E$ for binary mixtures as follows:

$$(B/A)^E = (B/A)_{mix} - (B/A)_{id} \tag{6}$$

where $(B/A)_{mix}$ is the theoretically calculated values and $(B/A)_{id}$ is that obtained from ideal components defined as

$$(B/A)_{id} = y_1(B/A)_1 + y_2(B/A)_2. \tag{7}$$

Here 1 and 2 refer to first and second components.

The sound velocity, density, adiabatic compressibility and molecular radius required for the present calculations are taken from the literature [20, 21].

3. Results and discussion

Acoustic non-linearity parameter B/A calculated for five binary mixtures at two

Table 1. Mole fraction (y_1) of methyl ethyl ketone, sound velocity (c), isentropic compressibility (K_s), and non-linearity parameter (B/A) of binary mixtures.

	303·15 K			313·15 K		
y_1	c(m/s)	K_s(TPa^{-1})	B/A	c(m/s)	K_s(TPa^{-1})	B/A
			Methyl ethyl ketone + Benzene			
0·0000	1276	707	10·76	1230	770	9·79
0·1126	1269	722	10·34	1226	783	9·52
0·2249	1260	739	9·97	1217	802	9·29
0·3113	1253	753	9·72	1210	817	9·14
0·4163	1244	771	9·46	1201	837	8·99
0·5232	1234	791	9·23	1191	859	8·88
0·6045	1225	809	9·08	1182	878	8·83
0·7148	1212	835	8·92	1169	908	8·81
0·8265	1197	865	8·83	1154	941	8·88
1·0000	1173	915	8·81	1128	1002	9·20
			Methyl ethyl ketone + Toluene			
0·0000	1291	699	11·62	1248	757	10·44
0·1367	1281	716	10·98	1240	773	9·99
0·2214	1274	728	10·61	1233	786	9·72
0·3435	1263	746	10·13	1222	807	9·39
0·4318	1255	761	9·81	1214	822	9·19
0·5406	1243	782	9·47	1202	846	8·98
0·6267	1232	801	8·85	1191	867	8·85
0·7122	1219	824	9·03	1178	893	8·78
0·8178	1203	855	8·86	1162	927	8·78
1·0000	1173	915	8·81	1128	1002	9·20
			Methyl ethyl ketone + Chlorobenzene			
0·0000	1245	589	12·02	1206	634	10·85
0·1068	1238	611	11·40	1197	660	10·41
0·1972	1235	629	10·97	1194	679	10·09
0·3202	1229	656	10·41	1188	709	9·68
0·4174	1224	680	10·01	1183	736	9·39
0·5576	1218	718	9·55	1177	776	9·06
0·6242	1213	740	9·37	1172	801	8·94
0·7288	1201	782	9·06	1160	848	8·81
0·8531	1187	840	8·84	1146	911	8·80
1·0000	1173	915	8·81	1128	1002	9·20
			Methyl ethyl ketone + Bromobenzene			
0·0000	1146	514	11·70	1109	554	10·80
0·1221	1144	542	11·10	1104	587	10·35
0·1917	1141	562	10·80	1101	609	10·09
0·2946	1139	591	10·41	1099	641	9·77
0·4069	1142	623	10·02	1102	676	9·46
0·5335	1146	665	9·59	1106	721	9·15
0·6748	1152	721	9·19	1112	782	8·89
0·8126	1155	796	8·90	1115	863	8·80
1·0000	1173	915	8·81	1128	1002	9·20

(*Continued*)

Table 1. (*Continued*)

	303·15 K			313·15 K		
y_1	c(m/s)	$K_s(TPa^{-1})$	B/A	c(m/s)	$K_s(TPa^{-1})$	B/A
			Methyl ethyl ketone + Nitrobenzene			
0·0000	1456	395	14·20	1408	426	12·71
0·0986	1426	424	13·15	1386	452	12·05
0·2098	1388	463	12·27	1348	494	11·31
0·3268	1154	506	11·42	1314	542	10·58
0·4182	1236	537	10·84	1296	575	10·08
0·5212	1312	579	10·24	1272	621	9·64
0·6458	1277	642	9·64	1239	691	9·15
0·7512	1241	715	9·19	1201	771	8·87
0·8119	1223	759	8·99	1183	819	8·78
1·0000	1173	915	8·81	1128	1002	9·20

different temperatures are given in table 1. The table also contains B/A of pure liquids. It is found that B/A values decrease as the mole fractions of MEK increases. The B/A for liquids has been interpreted as the quantity representing the magnitude of the hardness of the liquid [6] which may be considered to be true for the liquid mixtures as well. For all the five mixtures, as the mole fraction of MEK increases, the density and ultrasonic velocity decrease and hence the compressibility increases. Therefore as the mole fraction of MEK increases the bulk modulus, hence B/A must decrease.

Subramanyam Reddy [20] reported that the excess isentropic compressibility for all the five binary mixtures considered in the present study are negative. A plot of the calculated excess B/A, $(B/A)^E$, against mole fraction of MEK in the mixtures is shown in figure 1. It is interesting to note that $(B/A)^E$ values are all negative and show the same trend as that of the reported excess isentropic compressibility [20]. A negative compressibility is an indication of strong interaction in the liquid mixtures [22], which has been attributed to charge transfer, dipole-induced dipole and dipole-dipole interaction while a positive sign indicating weak interaction has been interpreted as due to dispersion forces [23]. In MEK-benzene system there is a dipole interaction between π electrons in the benzene ring and the carbonyl group $>$Co of MEK. Also in MEK-toluene there is dipole interaction between $>$CO and CH_2 group. In the other mixtures the same type of interactions are present between $>$CO and –Cl, –Br or $-NO_2$. The difference in the magnitude of $(B/A)^E$ for different mixtures is attributable to the difference in the extent of interactions present in them. It may be inferred that a more negative value of $(B/A)^E$ indicates a strong interaction between the different groups in the system. This is in accordance with the results of the study of excess isentropic compressibility values [20].

4. Conclusion

Acoustics non-linearity parameter B/A is calculated for five binary mixtures with methyl ethyl ketone as common component at two different temperatures. An excess

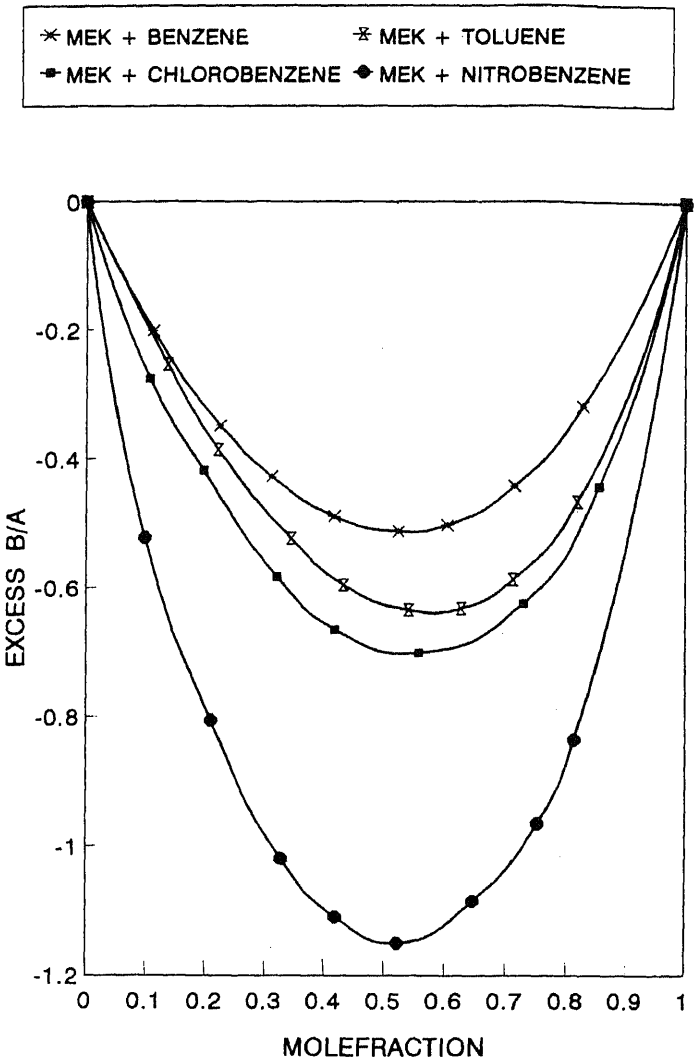

Figure 1. Variation of excess B/A with mole fraction of methyl ethyl ketone a
303·15 K.

non-linearity parameter $(B/A)^E$ which shows the same type of variation as isentropic compressibility with mole fraction has been defined. It is concluded that the $(B/A)^E$ is also an important quantity similar to other thermodynamic parameters useful to explaining the interaction in binary liquid mixtures.

References

[1] M Paul Hagelberg, *J. Acoust. Soc. Am.* **41**, 564 (1967)
[2] A B Coppens and Robert T Beyer, *J. Acoust. Soc. Am.* **38**, 797 (1965)

[3] Charles A Cain, *J. Acoust. Soc. Am.* **80**, 685 (1986)
[4] Harumi Endo, *J. Acoust. Soc. Am.* **71**, 330 (1986)
[5] B K Sharma, *J. Acoust. Soc. Am.* **73**, 106 (1983)
[6] Harumi Endo, *J. Acoust. Soc. Am.* **83**, 2043 (1988)
[7] Wesley N Cobb, *J. Acoust. Soc. Am.* **73**, 1525 (1983)
[8] Chandra M Sehgal and Burdett R Porter, *J. Acoust. Soc. Am.* **79**, 566 (1986)
[9] Laszlo Alter and E A Hiedemann, *J. Acoust. Soc. Am.* **34**, 410 (1962)
[10] A P Sarvazyan and T V Gnalikian, *J. Acoust. Soc. Am.* **88**, 1555 (1990)
[11] W K Law and L A Frizzell, *J. Acoust. Soc. Am.* **74**, 1295 (1983)
[12] Tong Jie and Dong Yanwu, *Kexue Togbao* **33**, 1511 (1988)
[13] W Schaaffs, *Z. Phys.* **115**, 69 (1940)
[14] P J Flory, *J. Am. Chem. Soc.* **87**, 1833 (1965)
[15] A Abe and P J Flory, *J. Am. Chem. Soc.* **87**, 1838 (1965)
[16] J D Pandey, *J. Chem. Soc. Faraday Trans. I* **75**, 2160 (1979)
[17] J D Pandey, *J. Chem. Soc. Faraday Trans. II* **76**, 1215 (1980)
[18] M S Khanwalkar, *Acoust. Lett.* **13**, 121 (1990)
[19] Shao-muMa and Henry Eyring, *J. Chem. Phys.* **42**, 1920 (1965)
[20] K Subramanyam Reddy, *J. Chem. Eng. Data* **31**, 238 (1986)
[21] S Ernst and J Glinski, *Acustica* **48**, 109 (1981)
[22] R J Fort and W R Moore, *Trans Faraday Soc.* **61**, 2102 (1965)
[23] K Sivanarayanan and S Prakash, *Acustica* **50**, 286 (1982)

Gyrotropic and piezoelectric coefficients and attenuation of elastic waves in $BaTiO_3$

B SUBRAMANYAM
Department of Physics, Indian Institute of Technology, Madras 600 036, India

MS received 12 May 1995

Abstract. Using Landau theory of phase transition, expressions for gyrotropic coefficients and piezoelectric coefficients are obtained for barium titanate in the tetragonal phase. Both coefficients vanish at the ferroelectric phase transition temperature. The piezoelectric coefficients tallied with the literature values. The attenuation coefficients for elastic waves propagating along the principal directions in tetragonal, orthorhombic and rhombohedral phases are derived based on Landau theory. It is predicted that there will be slight amplification for both longitudinal and transverse modes in the rhombohedral phase at a temperature close to the rhombohedral phase transition temperature.

Keywords. Gyrotropic and piezoelectric coefficients; attenuation; elastic waves; phase transition.

PACS Nos 64·70; 62·20; 64·60

1. Introduction

Barium titanate is a classical example of a substance undergoing a first order phase transition. It is paraelectric above Curie temperature (T_c), 120 °C, and has a cubic perovskite structure. At the Curie point the structure changes from cubic m3m (O_h) to tetragonal 4 mm (C_{4V}) with spontaneous polarization (SP) along (001) direction. Below 5 °C the SP points in the (011) direction and the crystal system is orthorhombic 2 mm (C_{2V}). On cooling below -70 °C it undergoes a further phase transition to rhombohedral 3 m (C_{3V}) with SP along (111) direction.

Considering the tetragonal, orthorhombic and rhombohedral phases as strained forms of cubic phase the author obtained expressions for elastic anomalies [1–3] using Landau theory of phase transitions. Using the second order elastic anomalies already published [1–3] expressions for the gyrotropic and piezoelectric coefficients for the barium titanate in the tetragonal phase are derived. Expressions are also obtained for the attenuation of elastic waves travelling along the principal directions (100), (110) and (111).

2. Gyrotropic coefficients

When spatial dispersion is present in a system the elastic constant matrix [4] acquires the structure.

$$C_{ij}(\Omega, \mathbf{k}) = C_{ij}(\Omega) + id_{ijl}(\Omega, \mathbf{k})\mathbf{k}_1 \tag{1}$$

where $\mathbf{k}$ denotes the wave vector of the acoustic wave, Ω its circular frequency. d_{ijl} are gyrotropic tensor components (5th rank). Their number depends on the crystal system and these have been worked out by Kumaraswamy and Krishnamurthy [4].

The free energy F of the crystal can be written as the sum of (i) elastic energy F_{ela} (ii) the Landau energy F_L (iii) the energy due to coupling between order parameter (in this case SP) and strains F_c (iv) the gyrotropic energy involving SP and elastic strains and also the spatial derivatives of SP and those of strains F_g.

$$F = F_{ela} + F_L + F_c + F_g \tag{2}$$

Since the term F_g is usually much smaller than F_c it can be neglected in the calculation of elastic anomalies and F_g should be taken into account while estimating gyrotropic coefficients. The expressions for F_{ela}, F_L and F_c are given in earlier publications on barium titanate [1–3].

F_g is chosen as equal to

$$\begin{aligned}
&B_1[(P_x(\partial\eta_1/\partial x) + P_y(\partial\eta_2/\partial y)) - (\eta_1(\partial P_x/\partial x) + \eta_2(\partial P_y/\partial y))] \\
&+ B_2[(P_x(\partial\eta_2/\partial x) + P_y(\partial\eta_1/\partial y)) - (\eta_2(\partial P_x/\partial x) + \eta_1(\partial P_y/\partial y))] \\
&+ B_3[(P_x(\partial\eta_5/\partial z) + P_y(\partial\eta_4/\partial z)) - (\eta_5(\partial P_x/\partial z) + \eta_4(\partial P_y/\partial z)] \\
&+ B_4[(P_x(\partial\eta_3/\partial x) + P_y(\partial\eta_3/\partial y)) - (\eta_3(\partial P_x/\partial x) + \eta_3(\partial P_y/\partial y))] \\
&+ B_5[(P_x(\partial\eta_6/\partial y) + P_y(\partial\eta_6/\partial x)) - (\eta_6(\partial P_x/\partial y) + \eta_6(\partial P_y/\partial x))] \\
&+ B_6[(P_z(\partial\eta_1/\partial z) + P_z(\partial\eta_2/\partial z)) - (\eta_1(\partial P_z/\partial z) + \eta_2(\partial P_z/\partial z))] \\
&+ B_7[P_z(\partial\eta_3/\partial z) - \eta_3(\partial p_z/\partial z)] \\
&+ B_8[(P_z(\partial\eta_5/\partial x) + P_z(\partial\eta_4/\partial y)) - (\eta_5(\partial P_z/\partial x) + \eta_4(\partial P_z/\partial y))]
\end{aligned} \tag{3}$$

where $B_i (i = 1 \text{ to } 8)$, $\eta_i (i = 1 \text{ to } 6)$ and $P_K (K = x, y, z)$ are constants, strains and components of SP respectively. F_g is chosen so that it is invariant under the transformation of the generating matrices of the tetragonal group 4 mm (C_{4v}). Each term in the square brackets in the expression for F_g given above is a difference of two terms which are individually invariant under the symmetry operations of the tetragonal groups. It is also necessary to choose equal but opposite coefficients (Bi's) for the two terms. This was warranted by the fact that the gyrotropic coefficients d_{ijl} must change sign [4] for any interchange of indices i and j. The following relations for the equilibrium values of the components of SP and their fluctuations for the tetragonal phase are taken from the earlier publications [1, 2].

$$P_{x0}^2 = P_{y0}^2 = 0 \tag{4}$$

$$P_{z0}^2 = -aP = 0{\cdot}284 \times 10^{12} a. \tag{5}$$

$$P_x^* = A\eta_5^* \tag{6}$$

$$P_y^* = A\eta_4^* \tag{7}$$

$$P_z^* = \sum_{i=1}^{6} \alpha_i \eta_i^* \tag{8}$$

where $a = a'(T - T_c)$ with a' a positive constant. P is a constant and η_i^* ($i = 1$ to 6) are fluctuations in strains about their equilibrium values.

$$A = -(\Gamma_1 g_{44} P_{z0})/P_1 = \frac{0{\cdot}502 \times 10^6}{\sqrt{a}(1 + i\Omega\pi)} \tag{9}$$

$$\alpha_1 = \alpha_2 = -(2\Gamma_3 g_{12} P_{z0})/P_3 = \frac{-0{\cdot}0227 \times 10^6}{\sqrt{a}(1 + i\Omega\tau)} \tag{10}$$

$$\alpha_3 = -(2\Gamma_3 g_{11} P_{z0})/P_3 = \frac{0{\cdot}320 \times 10^6}{\sqrt{a}(1 + i\Omega\tau)} \tag{11}$$

$$\alpha_4 = \alpha_5 = \alpha_6 = 0 \tag{12}$$

$$P_1 = \Gamma_1 8{\cdot}5a(1 + i\Omega\tau) \tag{13}$$

$$P_3 = \Gamma_3 37{\cdot}5a(1 + i\Omega\tau). \tag{14}$$

The relaxation time τ is defined as

$$\tau = \Gamma_j \left(\frac{\partial^2 F}{\partial P_K^2}\right)_0 \quad j = 1 \text{ to } 3 \quad \text{and} \quad K = x, y, z \tag{15}$$

The numerical values for P, A, $\alpha_1 = \alpha_2$, and α_3 are calculated using the values of elastic constants, g_{11}, g_{12} and g_{44} taken from Devonshire [5].

The cubic phase has inversion symmetry, hence all the d_{ijl} are zero in this phase. In the tetragonal phase d_{ijl} arises due to the absence of the inversion symmetry. By substituting $P_K = P_{K0} + P_K^*$ and $\eta_i = \eta_{i0} + \eta_i^*$ in the expression for F_g the gyrotropic coefficients are given by [6]

$$d_{ijl} = \frac{\partial^2 F}{\partial \eta_i^* (\partial \eta_j^* / \partial x_1)}. \tag{16}$$

The following gyrotropic coefficients can be obtained with the relations among them.

$$d_{133} = d_{233} = B_7 \alpha_1 = -\frac{B_7 0{\cdot}0227}{\sqrt{a}(1 + i\Omega\tau)} \times 10^6 \tag{17}$$

$$d_{142} = d_{251} = B_8 \alpha_1 = -\frac{B_8 0{\cdot}0227}{\sqrt{a}(1 + i\Omega\tau)} \times 10^6 \tag{18}$$

$$d_{151} = d_{242} = B_8 \alpha_1 = -\frac{B_8 0{\cdot}0227}{\sqrt{a}(1 + i\Omega\tau)} \times 10^6 \tag{19}$$

$$d_{342} = d_{351} = B_8 \alpha_3 = \frac{B_8 0{\cdot}320}{\sqrt{a}(1 + i\Omega\tau)} \times 10^6 \tag{20}$$

$$d_{461} = d_{562} = B_5 A = \frac{B_5 0{\cdot}502}{\sqrt{a}(1 + i\Omega\tau)} \times 10^6 \tag{21}$$

All the above five independent gyrotropic coefficients appropriate to C_{4v} are listed by Kumaraswamy and Krishnamurthy [4]. The coefficients are complex and proportional to $[(T - T_c)^{1/2}(1 + i\Omega\tau)]^{-1}$. The temperature variation of τ is given by Lemanov [7]

3. Piezoelectric coefficients

When the free energy is expressed in terms of strains and electric field, one o piezoelectric stress coefficients e_{mi} [8]. If free energy is expressed in terms of stress electric field, piezoelectric strain coefficients d_{mi} will result [8]. Using polari theory and by replacing electric field with polarization in the expression for free one can also get the a and b coefficients (a_{mi} and b_{mi}) as referred to by Cady [8]

The expression for the first thermodynamic potential is given by

$$\xi = 1/2C_{ij}^{p}\eta_i\eta_j + 1/2\chi_{km}^{s}P_K P_m + a_{mi}P_m\eta_i$$

where C_{ij}^{p} are elastic constants at constant polarization, χ_{km}^{s} are inverse suscepti at constant strain (clamped constants or high frequency values) P_K are compon polarization and η_i are strains. By introducing $P_K = P_{K0} + P_K^*$ and $\eta_i = \eta_{i0} + \eta_i^*$ expression for free energy $F = F_{ela} + F_L + F_c$ and comparing it with (23) the piez tric coefficients a_{mi} are the coefficients of $P_K^*\eta_i^*$. For the tetragonal phase of b titanate they are listed with their numerical values as

$$a_{33} = 2g_{11}P_{z0} = -11{\cdot}94\sqrt{a'(T - T_c)} \times 10^6$$

$$a_{32} = 2g_{12}P_{z0} = +0{\cdot}85\sqrt{a'(T - T_c)} \times 10^6$$

$$a_{15} = a_{24} = g_{44}P_{20} = -4{\cdot}26\sqrt{a'(T - T_c)} \times 10^6.$$

Devonshire [9] derived the following relations between C_{ij}^{P}, a_{mi}, b_{mi} and η_{mn}^{T} (s tibilities at constant stress) as

$$a_{mi} = b_{mj}C_{ji}^{P}$$

$$d_{mi} = b_{ni}\eta_{mn}^{T}$$

The values of d_{mi} are of the order 10^{-6} C_{ji}^{P}'s are of the order 10^{12}, b_{mi} are of the 10^{-7} and η_{mn}^{T} are of the order 10 to 100. The piezoelectric constants calculated author from Landau theory are of the order 10^6 and tally with the reported valu coefficients a_{33}, a_{32} and a_{15} vanish at $T = T_c$ and they vary as $\sqrt{T - T_c}$.

4. Attenuation

Lemanov obtained an expression for the attenuation coefficient (α) in terms of re imaginary parts of the elastic constants [7] as

$$\alpha = (\Omega/2)\mathrm{Im}aC_{ij}/\mathrm{Re}\,C_{ij}$$

The elastic anomalies reported by the author in different phases of barium titan complex [1–3]. Using (29) expressions for the attenuation coefficients (α's)

written in terms of $\Omega\tau = x$ for the longitudinal and transverse waves along the principal directions in tetragonal, orthorhombic and rhombohedral phases of barium titanate

Tetragonal

(100)

$$\alpha_{l_1} = \frac{0{\cdot}971x^3}{(1+x^2)^2} \times 10^8 \tag{30a}$$

$$\alpha_{t_1} = \frac{15{\cdot}873x^3}{(1+x^2)^2} \times 10^8 \tag{30b}$$

(110)

$$\alpha_{l_{11}} = \frac{6{\cdot}756x^3}{(1+x^2)^2} \times 10^8 \tag{31a}$$

$$\alpha_{t_{11}} = 0 \tag{31b}$$

(111)

$$\alpha_{l_{111}} = \frac{8{\cdot}141x^3}{(1+x^2)^2} \times 10^8 \tag{32}$$

$$\alpha_{t_{111}} = \frac{10{\cdot}417x^3}{(1+x^2)^2} \times 10^8 \tag{32b}$$

Orthorhombic

(100)

$$\alpha_{l_1} = \frac{x(0{\cdot}03 + 0{\cdot}02x^2)}{(0{\cdot}81+x^2)^2} 4{\cdot}854 \times 10^8 \tag{33a}$$

$$\alpha_{t_1} = \frac{x(0{\cdot}85 + 0{\cdot}6x^2)}{(0{\cdot}81+x^2)^2} 7{\cdot}937 \times 10^8 \tag{33b}$$

(110)

$$\alpha_{l_{11}} = \frac{x(0{\cdot}83 + 0{\cdot}75x^2)}{(0{\cdot}81+x^2)^2} 1{\cdot}672 \times 10^8 \tag{34a}$$

$$\alpha_{t_{11}} = \frac{x(0{\cdot}93 + 0{\cdot}52x^2)}{(0{\cdot}81+x^2)^2} 15{\cdot}152 \times 10^8 \tag{34b}$$

(111)

$$\alpha_{l_{111}} = \frac{x(1{\cdot}63 + 1{\cdot}48x^2)}{(0{\cdot}81+x^2)^2} 1{\cdot}010 \times 10^8 \tag{35a}$$

$$\alpha_{t_{111}} = \frac{x(1{\cdot}78 + 1{\cdot}14x^2)}{(0{\cdot}81+x^2)^2} 5{\cdot}208 \times 10^8 \tag{35b}$$

Rhombohedral

(100)

$$\frac{x(\ldots 0{\cdot}21 + 2{\cdot}93x^2 + 0{\cdot}63x^4 + 6{\cdot}14x^6)}{\ldots}$$

$$\alpha_{t_{11}} = \frac{x(-0{\cdot}45 + 8{\cdot}53x^2 + 17{\cdot}35x^4 + 8{\cdot}81x^6)}{(1 + 2{\cdot}6x^2 + 1{\cdot}44x^4)^2} 7{\cdot}937 \times 10^8$$

(110)

$$\alpha_{l_{111}} = \frac{x(-0{\cdot}45 + 8{\cdot}53x^2 + 17{\cdot}35x^4 + 8{\cdot}81x^6)}{(1 + 2{\cdot}6x^2 + 1{\cdot}44x^4)^2} 1{\cdot}672 \times 10^8 \quad (1$$

$$\alpha_{t_{111}} = \frac{x(-0{\cdot}26 + 3{\cdot}07x^2 + 8{\cdot}84x^4 + 6{\cdot}90x^6)}{(1 + 2{\cdot}6x^2 + 1{\cdot}44x^4)^2} 15{\cdot}152 \times 10^8 \quad (1$$

(111)

$$\alpha_{l_{111}} = \frac{x(-0{\cdot}7 + 13{\cdot}13x^2 + 25{\cdot}1x^4 + 11{\cdot}5x^6)}{(1 + 2{\cdot}6x^2 + 1{\cdot}44x^4)^2} 1{\cdot}010 \times 10^8 \quad (2$$

$$\alpha_{t_{111}} = \frac{x(-0{\cdot}41 + 4{\cdot}94x^2 + 12{\cdot}3x^4 + 8{\cdot}64x^6)}{(1 + 2{\cdot}6x^2 + 1{\cdot}44x^4)^2} 5{\cdot}208 \times 10^8 \quad (2$$

The variation of attenuation coefficients with $\Omega\tau = x$ along the principal directions the three phases are illustrated in figures (1a, b and c). The following observations c be inferred from the curves. 1) The attenuation is maximum for the rhombohed phase for the transverse mode along (110) direction. 2) Attenuation is minimum for t tetragonal phase for the longitudinal mode along (100) direction and vanishes for t transverse mode along (110) direction. 3) In the case of tetragonal and rhombohed phases maximum attenuation occurs around $\Omega\tau = 1{\cdot}75$ which corresponds $(T - T_c) \simeq 10^{-3}$ K 4) For the orthorhombic phase maximum attenuation occu around $\Omega\tau = 0{\cdot}75$ corresponding to $(T - T_c) \simeq 10^{-2}$ K. 5) Landau theory predicts f both modes in rhombohedral phase slight amplification for $\Omega\tau$ between 0 to 0·2 wi

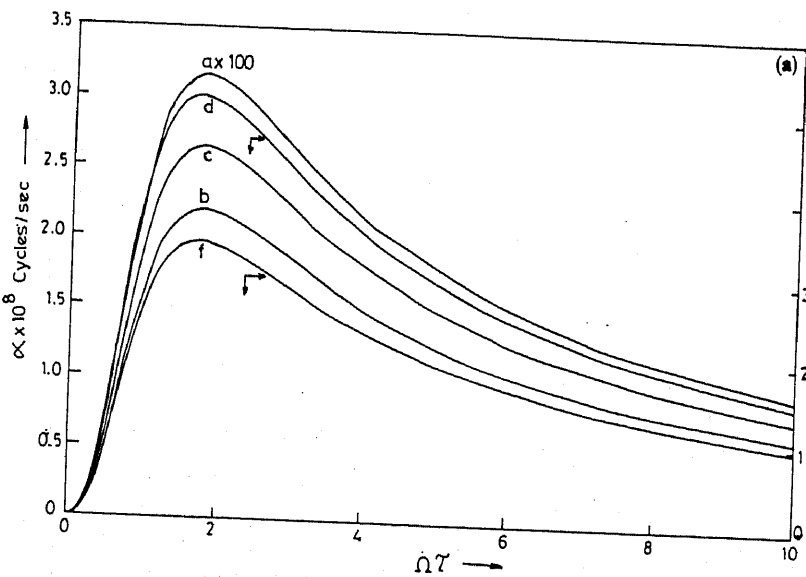

Figure 1. (*Continued*)

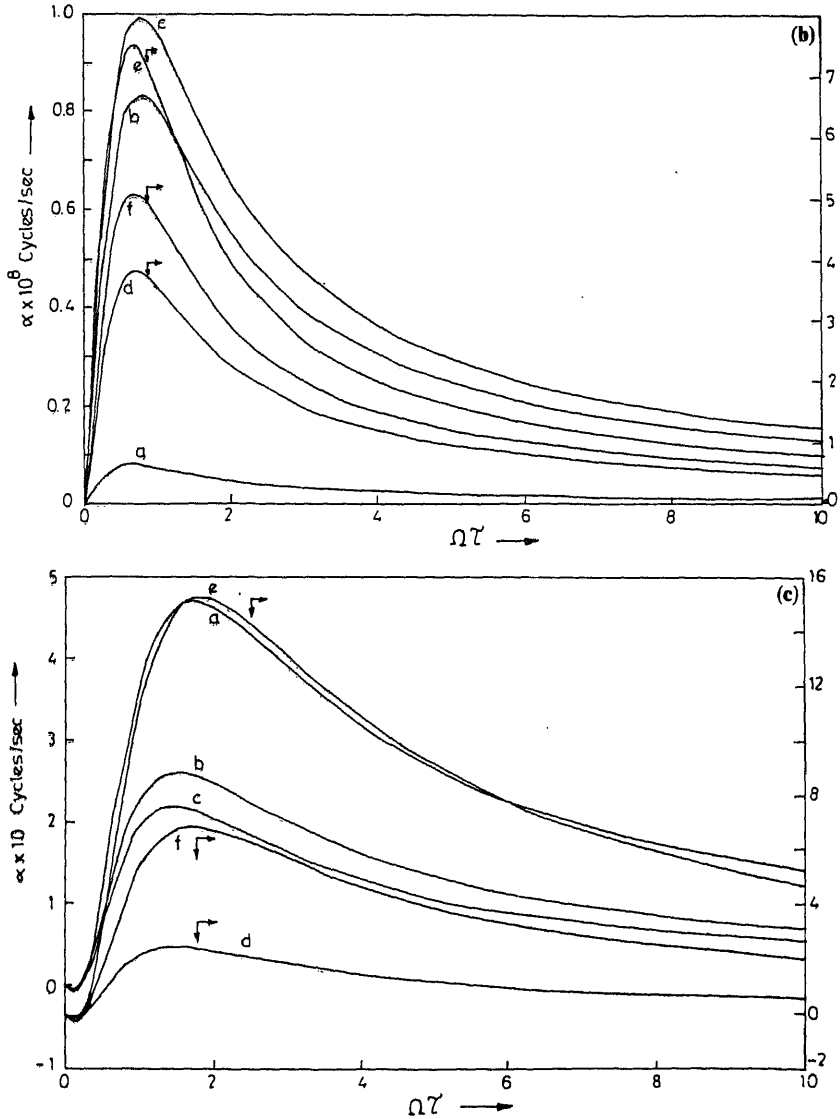

Figures 1(a)–(c). Represent variation of attenuation coefficients with the product of circular frequency and relaxation time ($\Omega\tau$) in tetragonal, orthorhombic and rhombohedral phases respectively. In each figure curve (a) α_{l_1} (b) $\alpha_{l_{11}}$ and (c) $\alpha_{l_{111}}$ represent attenuation coefficients of longitudinal mode along (100), (110) and (111) directions respectively. Curve (d) α_{t_1}, (e) $\alpha_{t_{11}}$ and (f) $\alpha_{t_{111}}$ represent attenuation coefficients of transverse mode along (100), (110) and (111) directions respectively.

maximum amplification for $\Omega\tau = 0{\cdot}1$ which corresponds to $(T - T_c) \simeq 0{\cdot}1$ K. Unfortunately, there are no experimental data available for comparison. It is hoped that the present work will stimulate experimental investigations to prove the validity of the theoretical predictions.

Acknowledgement

The author would like to thank Dr K S Viswanathan for the advice and discussi during the course of this work.

References

[1] B Subramanyam and K S Viswanathan, *Pramana – J. Phys.* **41**, 42 (1993)
[2] B Subramanyam and K S Viswanathan, *J. Appl. Phys.* **74**, 945 (1993)
[3] B Subramanyam, *Pramana – J. Phys.* **43**, 181 (1994)
[4] K Kumaraswamy and N Krishnamurty, *Acta Crystallogr.* **A36**, 760 (1980)
[5] A F Devonshire, *Philos. Mag.* **40**, 1040 (1949)
[6] B Subramanyam, and K S Viswanathan, *Pramana – J. Phys.* **41**, 208 (1993)
[7] V V Lemanov, *Proc. Second Inter. Conf. Condensed Matter Physics* edited by M Bri (Varna Bulgaria) (World Scientific, Singapore, 1982) 190–228
[8] W G Cady, *Piezoelectricity* (McGraw Hill Book, Co. Inc., 1946) p. 44, 252
[9] A F Devonshire, *Philos. Mag.* **42**, 1065 (1951)

Heat capacity and phonons in poly(L-leucine)

SEEMA SRIVASTAVA, POONAM TANDON, V D GUPTA*,
SHANTANU RASTOGI, S B KATTI† and L BURMAN
Physics Department, Lucknow University, Lucknow 226 007, India
*To whom all correspondence should be addressed
†Division of Biopolymers, Central Drug Research Institute, Lucknow 226 001, India

MS received 7 April 1995; revised 10 July 1995

Abstract. Poly(L-leucine) is one of the polyamino acids having a bulky hydrophobic side-chain. For want of full phonon dispersion curves and density-of-states on this biopolymer Roles *et al* have interpreted their specific heat data in a limited way. In the present communication we report an analysis of the normal modes and their dispersion for poly(L-leucine) which leads to a very good agreement of the specific heat calculations with experimental measurements. It is observed that the main contribution to specific heat comes from the coupling of the back-bone skeletal and side-chain modes. Several other assignments have been revised. A special feature of some dispersion curves is their tendency to bunch in the neighbourhood of helix angle. It has been attributed to the presence of strong intramolecular interactions. Repulsion between the dispersion curves is also observed.

Keywords. Conformation; phonon dispersion; α-helix; normal modes; poly(L-leucine); density-of-states; specific heat.

PACS No. 34·80

1. Introduction

In recent publication Wunderlich and Bu [1], Bu *et al* [2], Roles and Wunderlich [3] and Roles *et al* [4] have reported experimental and theoretical studies of heat capacities of a variety of polymeric systems, synthetic as well as biopolymeric. In most of the cases, their analysis is based on separation of the vibrational spectrum into group and skeletal vibrations. The former are taken from computations fitted to IR and Raman data and the latter by using the two parameter Tarasov model [1] and fitting to low temperature heat capacities. However in a few cases, where detailed dispersion curves of the vibrational spectrum are available [5–9], they have been used for obtaining group and skeletal vibrations and number of vibrators of each type. In some cases, dispersion curves for one polymeric system have been used to obtain the number of vibrators and frequencies of box oscillators for polymers with identical back-bone. This approach is OK when full dispersion curves are not available. However it has its own limitations, specially when the side-chain and back-bone modes are strongly coupled. In the present communication, we report for poly(L-leucine) (PLL), full dispersion curves, density-of-states and specific heat data which is found to be in good agreement with the experimental measurements. Vibrational spectroscopy is an important tool for probing conformation and conformationally sensitive modes of a polymer. In general, the infrared absorption, Raman spectra and inelastic neutron scattering from polymeric systems are very complex and cannot be unravelled without the full knowledge of

dispersion curves. One cannot appreciate without it the origin of both symm dependent and symmetry independent spectral features. Further the presence regions of high density of states which appear in all these techniques and play important role in thermodynamical behaviour are also dependent on the profile of dispersion curves. The lack of this information in many polymeric systems has b responsible for incomplete understanding of polymeric spectra. The advent of las and fast computers has eased these problems to a large extent. Dispersion curves a provide information on the extent of coupling along the chain together with understanding of the dependence of the frequency of a given mode upon the sequer length of the ordered conformation. Thus the study of phonon dispersion in polyme systems continues to be an important one. This group has earlier reported vibratio analyses and phonon dispersion for a variety of biopolymeric systems having α, β, and 3_{10} helical conformation [5–15]. As a part of this continuing programme, report here a study of normal modes of vibrations and their dispersions for PLL.

Poly(L-leucine) (figure 1) belongs to the class of polyamino acids having bull hydrophobic side-chains. In solid state, PLL adopts an α-helical conformation a molecular models demonstrate that the formation of α-helix reduces the side-chain

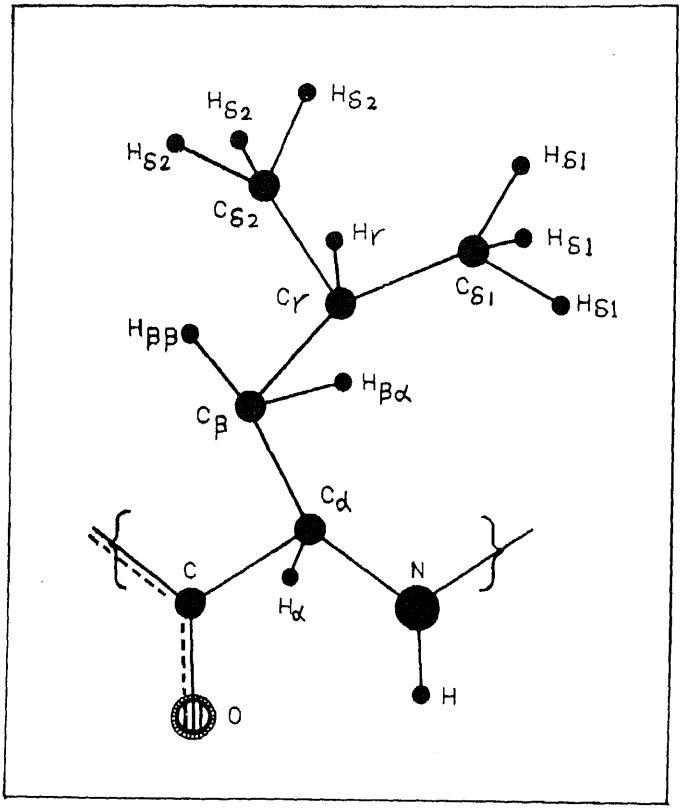

side-chain steric interference [16]. Infrared and Raman spectroscopic studies of PLL have been reported by Koenig and Sutton [17] and Itoh *et al* [18]. Their assignments are both incomplete and are based on qualitative considerations. It is, therefore, all the more important to carry out a complete normal mode analysis and their dispersion for PLL. It is through the dispersion curves that one can correlate microscopic behaviour of a crystal with its macroscopic properties such as specific heat.

2. Theory and experiment

2.1 *Normal mode analysis*

The calculation of normal mode frequencies has been carried out according to Wilson's G F matrix method [19] as modified by Higgs [20] for an infinite chain. The Wilson GF matrix method consists of writing the inverse kinetic energy matrix G and the potential energy matrix F in internal coordinates R. In the case of infinite isolated helical polymer, there are an infinite number of internal coordinates which lead to G and F matrices of infinite order. Due to the screw symmetry of the polymer a transformation similar to that given by Born and Von Karman can be performed which reduces the infinite problem to finite dimensions. The transformation consists of defining a set of symmetry coordinates.

$$S(\delta) = \sum_{s=-\infty}^{\infty} R^n \exp(is\delta)$$

where δ is the vibrational phase difference between the corresponding modes of the adjacent residue units.

The elements of the $G(\delta)$ and $F(\delta)$ matrices have the form:

$$G_{ik}(\delta) = \sum_{s=-\infty}^{\infty} G_{ik}^{s} \exp(is\delta)$$

$$F_{ik}(\delta) = \sum_{s=-\infty}^{\infty} F_{ik}^{s} \exp(is\delta)$$

The vibrational secular equation which gives normal mode frequencies and their dispersion as a function of phase angles has the form:

$$[G(\delta)F(\delta) - \lambda(\delta)I] = 0, \quad 0 \leqslant \delta \leqslant \pi$$

The vibrational frequencies $\nu(\delta)$ (in cm^{-1}) are related to eigenvalues $\lambda(\delta)$ by the following relation,

$$\lambda(\delta) = 4\pi^2 c^2 \nu^2(\delta) \tag{1}$$

For any given phase difference δ (other than 0 or π), the $G(\delta)$ and $F(\delta)$ matrices are complex. In order to avoid the difficulties involved in handling complex numbers, methods have been devised to transform the complex matrices into equivalent real matrices by constructing suitable linear combinations of coordinates. One method of

$$\begin{vmatrix} M & -N \\ N & M \end{vmatrix}.$$

In the present case, we can write $G(\delta) = G^R(\delta) + iG^I(\delta)$ and $F(\delta) = F^R(\delta) + i$ where $G^R(\delta)$, $F^R(\delta)$, $G^I(\delta)$, $F^I(\delta)$ are the real and imaginary parts of $G(\delta)$ and $F(\delta)$ product $H(\delta) = G(\delta)F(\delta)$ becomes

$$H(\delta) = \begin{vmatrix} G^R(\delta) & -G^I(\delta) \\ G^I(\delta) & G^R(\delta) \end{vmatrix} \times \begin{vmatrix} F^R(\delta) & -F^I(\delta) \\ F^I(\delta) & F^R(\delta) \end{vmatrix}$$

$$= \begin{vmatrix} H^R(\delta) & -H^I(\delta) \\ H^I(\delta) & H^R(\delta) \end{vmatrix}$$

where

$$H^R(\delta) = G^R(\delta)F^R(\delta) - G^I(\delta)F^I(\delta)$$

$$H^I(\delta) = G^R(\delta)F^I(\delta) + G^I(\delta)F^R(\delta)$$

The matrix $H(\delta)$ now has dimensions $2N \times 2N$. The eigenvalues, therefore, occ pairs of equal values. The difficulty of dealing with complex numbers is thus avo

2.2 *Force constant evaluation*

The force constants have been obtained by the least square fitting. In order to o the 'best fit' with the observed frequencies the following procedure is adopted. Init approximate force constants for back-bone are transferred from α Poly(L-alanine Thus starting with the approximate F matrix F_0 and the observed freque λ_{obs} (related through a constant), one can solve the secular matrix equation

$$GF_0 L_0 = L_0 \lambda_0$$

Let $\Delta\lambda i = \lambda i_{obs} - \lambda i_0$ in the above equation. It can be shown that in the first approximation

$$\Delta\lambda = J\Delta F$$

where J is computed from L_0. We wish to compute the corrections to F_0 so tha errors $\overline{\Delta\lambda}$ are minimized. We use the theory of least squares and calculate

$$J'P\overline{\Delta\lambda} = (J'PJ)\overline{\Delta F}$$

where P is a weighting matrix and J' is the transpose of J. The solution to this equ is obtained by inverting $(J'PJ)$ to give

$$\overline{\Delta F} = (J'PJ)^{-1}J'P\overline{\Delta\lambda}$$

If the number of frequencies is greater than the number of F matrix elements, the m $J'PJ$ should be non-singular and we obtain the corrections ΔF which will minimiz sum of the weighted squares of the residuals. If the corrections ΔF are fairly large, the l relation between force constant and frequency term in the matrix eq. (2) breaks d In such a situation , further refinement using higher order terms in the Taylor's s expansion of $\Delta\lambda_i$ is needed. This procedure has been developed by King *et al* [2

The poly(L-leucine) (Lot No. 81H5557, DP(vis)242, Mw 27,4000) was purchased from the Sigma Chemicals, USA. The FTIR spectra (3000–150 cm^{-1}) were recorded in CSI on Perkin-Elmer-1800 spectrophotometer and are shown in figures 2(a) and 2(b). Before running the spectra the equipment was well purged with dry nitrogen.

2.3 *Calculation of heat capacity*

One of the important uses of dispersion curves is that the microscopic behaviour of a crystal can be correlated with its macroscopic properties such as heat capacity. For a one dimensional system the density-of-state function or the frequency distribution function, which expresses the way energy is distributed among the various branches of normal modes in the crystal, is calculated from the relation,

$$g(\nu) = \sum_j (\partial \nu_j / \partial \delta)^{-1} \Big|_{\nu_j(\delta)=\nu}. \tag{3}$$

The sum is over all branches j. Considering a solid as an assembly of harmonic oscillators, the frequency distribution $g(\nu)$ is equivalent to a partition function. It can be used to compute thermodynamic quantities such as free energy, entropy, heat capacity and enthalpy [22]. The constant volume heat capacity is obtained using Debye's relation

$$C_v = \sum_j g(\nu_j) k N_A (h\nu_j/kT)^2 \frac{\exp(h\nu_j/kT)}{[\exp(h\nu_j/kT) - 1]^2} \tag{4}$$

with

$$\int g(\nu_j) \mathrm{d}\nu_j = 1.$$

The constant volume heat capacity C_v, given by (4) is converted into constant pressure heat capacity C_P using the Nernst–Lindemann approximation [23]

$$C_P - C_v = 3RA_o(C_P^2 T / C_v T_m^o) \tag{5}$$

where A_o is a constant often of a universal value [$3{\cdot}9 \times 10^{-3}$(°K mol)/J] and T_m^o is the estimated equilibrium melting temperature, which is taken to be 573 °K [4].

3. Results and discussion

In poly(L-leucine) there are 19 atoms per residue unit which give rise to 57 dispersion curves of vibrations. The vibrational frequencies were calculated for the values of δ ranging from 0 to π in steps of $0{\cdot}05\pi$. Assuming that ψ is the angle of rotation about the helix axis which separates the adjacent units, the modes corresponding to $\delta = 0$ and ψ are infrared as well as Raman active and $\delta = 2\psi$ gives only Raman active modes. Here ψ is the angle of rotation about the helix axis which separates the adjacent units. For α-helical PLL $\psi = 5\pi/9$. The calculated frequencies at $\delta = 0$ and $5\pi/9$ are compared with the observed ones. The force constants which gave best fit to the experimental data are given in table 1. Since the modes above 1350 cm^{-1} (except amide II) are non-dispersive, only the modes below this are shown in figure 3. Two lowest lying branches ($\delta = 0$ and $\delta = 5\pi/9$, $\nu = 0$) are the four acoustic modes which correspond to the rotation

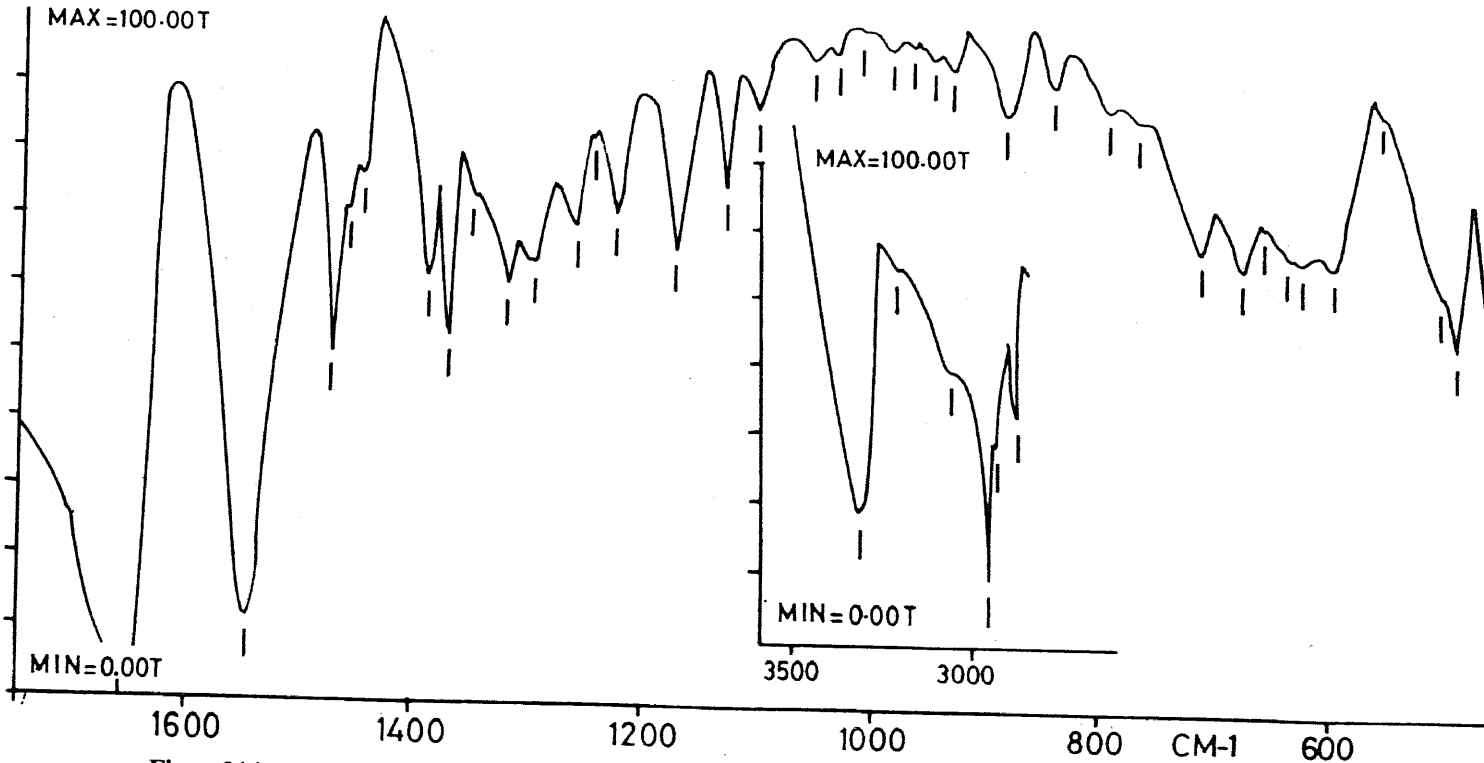

Figure 2(a). F.T.I.R. spectra of poly(L-leucine) (1700–450 cm^{-1}). The region 3500–2750 cm^{-1} is shown in inset.

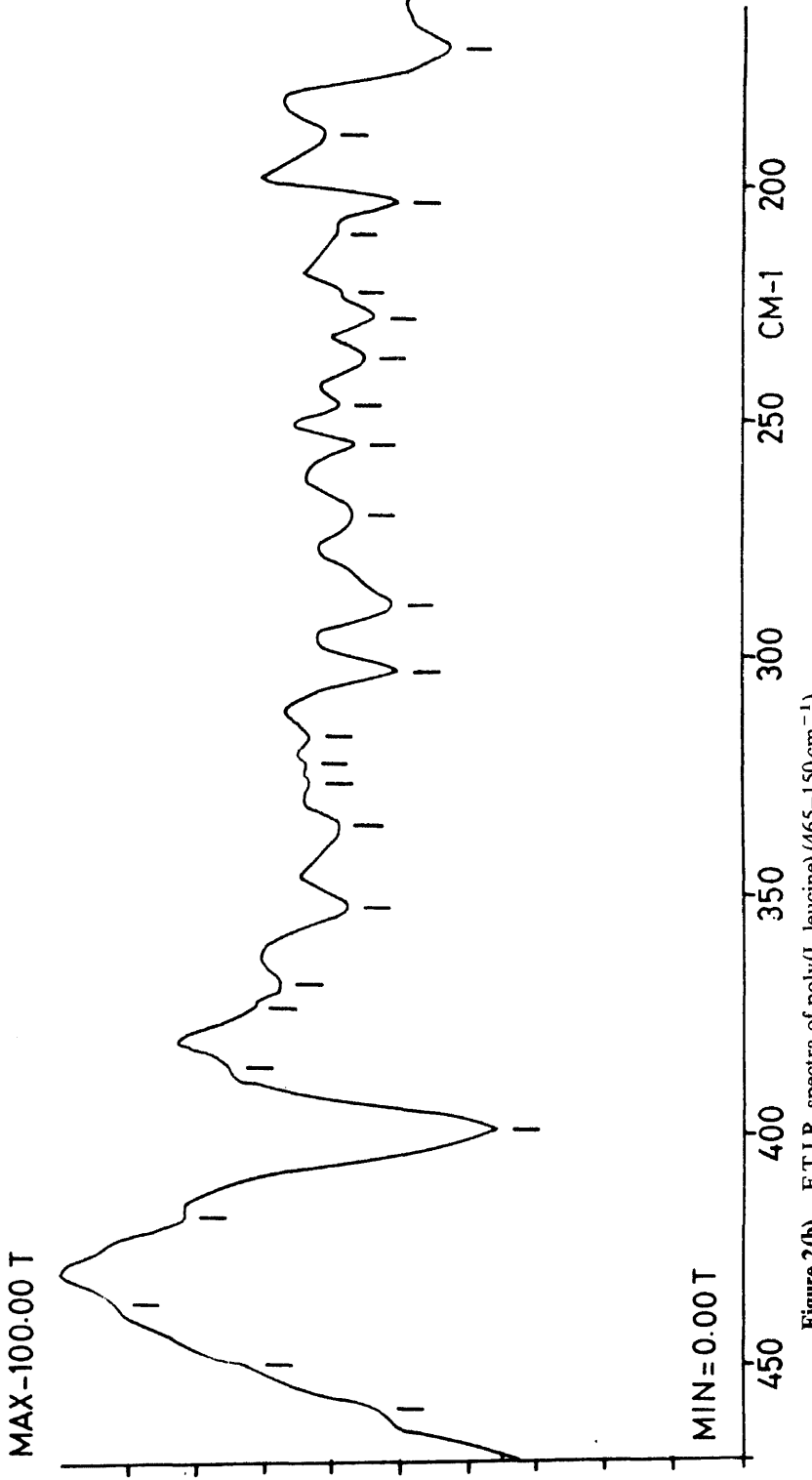

Figure 2(b). F.T.I.R. spectra of poly(L-leucine) (465–150 cm^{-1}).

ν(N–Cα)	2·850	ϕ(Cα–Cβ–Cγ)	0·550(0·18)
ν(Cα–Hα)	4·250	ϕ(Cβ–Cγ–Cδ_1)	0·515(0·18)
ν(Cα–C)	2·700	ϕ(Cβ–Cγ–Cδ_2)	0·515(0·18)
ν(C=O)	8·300	ϕ(Cβ–Cγ–Hγ)	0·523(0·22)
ν(C=N)	6·300	ϕ(Cδ_1–Cγ–Cδ_2)	0·515(0·18)
ν(H–N)	5·390	ϕ(Cδ_1–Cγ–Hγ)	0·500(0·22)
ν(Cα–Cβ)	2·550	ϕ(Cδ_2–Cγ–Hγ)	0·500(0·22)
ν(H$\beta\beta$–Cβ)	4·250	ϕ(Cγ–Cδ_1–Hδ_1)	0·445(0·21)
ν(H$\beta\alpha$–Cβ)	4·250	ϕ(Cγ–Cδ_2–Hδ_2)	0·445(0·21)
ν(Cβ–Cγ)	2·300	ϕ(Hδ_1–Cδ_1–Hδ_1)	0·421(0·24)
ν(Cγ–Cδ_2)	2·120	ϕ(Hδ_2–Cδ_2–Hδ_2)	0·421(0·24)
ν(Cγ–Cδ_1)	2·120	ϕ(Cα–Cβ–H$\beta\alpha$)	0·360(0·20)
ν(Cγ–Hγ)	4·340	ϕ(Cγ–Cβ–H$\beta\beta$)	0·360(0·20)
ν(Cδ_1–Hδ_1)	4·330	ϕ(Cγ–Cβ–H$\beta\alpha$)	0·360(0·20)
ν(Cδ_2–Hδ_2)	4·330	ϕ(Cα–Cβ–H$\beta\beta$)	0·360(0·20)
		ϕ(H$\beta\beta$–Cβ–H$\beta\alpha$)	0·422(0·25)
ω(C=O)	0·540	ϕ(N–Cα–Hα)	0·320(0·80)
ω(N–H)	0·120	ϕ(N–Cα–Cβ)	0·450(0·50)
		ϕ(Hα–Cα–C)	0·410(0·20)
τ(C–Cα)	0·010	ϕ(Hα–Cα–Cβ)	0·410(0·20)
τ(Cα–Cβ)	0·050	ϕ(C–Cα–Cβ)	0·520(0·18)
τ(Cβ–Cγ)	0·080	ϕ(N–Cα–C)	0·130(0·50)
τ(Cγ–Cδ_1)	0·016	ϕ(C=N–Cα)	0·530(0·35)
τ(Cγ–Cδ_2)	0·016	ϕ(N=C=O)	0·600(0·90)
τ(C=N)	0·030	ϕ(C=N–H)	0·200(0·65)
τ(N–Cα)	0·010	ϕ(H–N–Cα)	0·427(0·60)
		ϕ(Cα–C=O)	0·230(0·60)
		ϕ(Cα–C=N)	0·210(0·60)

Note: ν, ϕ, ω, τ denote stretch, angle bend, wag and torsion respectively. Non-bonded force constants are given in parentheses.

about the helix axis and and the translations $\parallel$ and two $\perp$ to the helix axis. The assignments of modes are made on the basis of potential energy distribution, line intensity, line profile, second derivative spectra and the presence/absence of modes in molecules having atoms placed in similar environment. For the sake of simplicity the modes are discussed under two separate heads viz. backbone modes and side-chain modes.

3.1 *Backbone modes*

Main-chain of PLL consists of amide groups joined together by Cα atoms. Modes involving the motions of main-chain atoms (–C(=O)–Cα(H)–N(H)–) are termed as backbone modes. Pure back-bone modes are given in table 2 and pure side-chain modes in table 3. The modes involving the coupling of back-bone and side-chain are given in table 4. All the amide modes except amide A and amide I are dispersive. A comparison of various amide modes of α PLL and α poly(L-alanine) [6] is given in table 5. Amide I, II and III modes fall nearly in the same region. It is clear that the frequency of amide

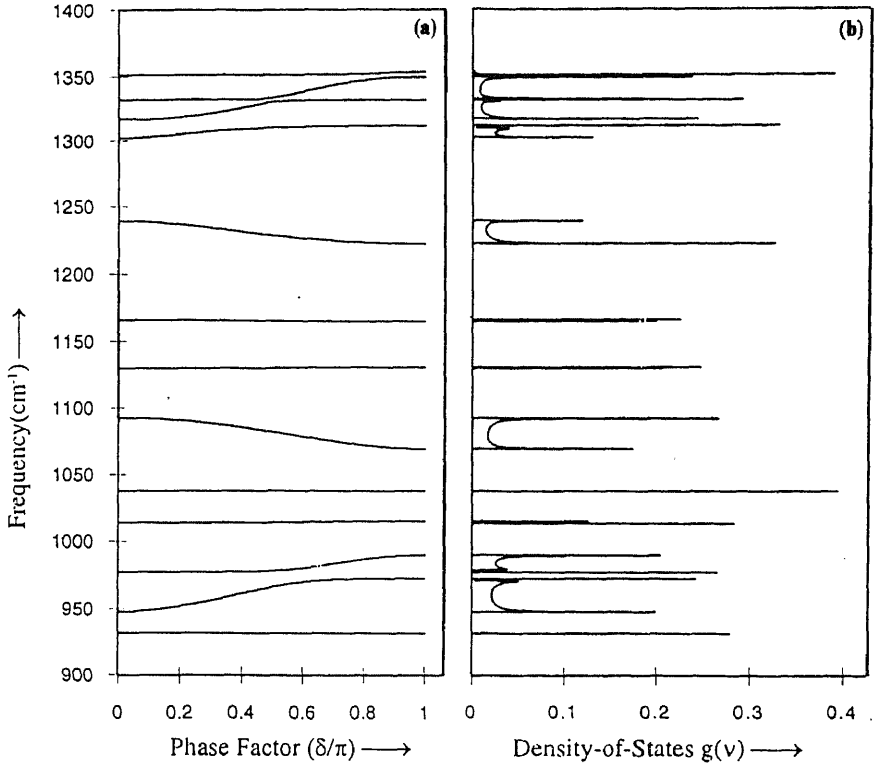

Figure 3. (a) Dispersion curves of poly(L-leucine) (1400–900 cm^{-1}); (b) Density-of-states $g(\nu)$ (1400–900 cm^{-1}).

V mode does not depend solely on main-chain conformation but side-chain structure in question also plays an important role in determining the frequency of this mode. The frequency of CO-in-plane-bend (amide IV), CO-out-of-plane bend (amide VI) and C–N torsion (amide VII) are also conformation dependent [24]. These modes mix strongly and very differently with the side-chain coordinates depending on the structure of the main and side-chains. In the spectra of PLL three bands have been observed at 614, 656 and 703 cm^{-1}. According to Koenig and Sutton [17] these bands are due to amide V in α, disordered and β sheet conformations respectively. The presence of all these modes in the spectra of PLL is said to be indicative of the coexistence of different conformational states. This does not appear to be correct. In α poly(L-alanine) [6] 656 cm^{-1} band has been assigned to amide VI which is calculated in PLL at 647 cm^{-1}. Amide V is calculated at 592 cm^{-1} at $\delta = 0$. On increasing the values of δ contribution of C=O wag increases and at zone boundary it becomes a mixture of amide V and amide VI. The 703 cm^{-1} band is a mixture of side-chain stretches and ω(N–H). Our assignments are further supported by the fact that these three bands are observed in poly(L-α-amino-n-butyric acid), poly(L-norvaline) and poly(L-norleucine) in α form and on N-deuteration the 703 and 656 cm^{-1} band do not change appreciably in intensities and

Table 2. Pure back-bone modes.

Cal.	Obs	Assignment (% P.E.D. at $\delta = 0{\cdot}0$)	Cal.	Obs.	Assignment (% P.E.D. at $\delta = 5\pi/9$)
3316	3313	ν(H–N)(99) {Amide A}	3316	3313	ν(H–N)(99) {Amide A}
1662	1657	ν(C=O)(57) + ν(C⋯N)(32) {Amide I}	1663	1657	ν(C=O)(55) + ν(C=N)(33) {Amide I}
1547	1546	ϕ(H–N–Cα)(42) + ϕ(C=N–H)26 + ν(C=N)(16) + ν(Cα–C)(5)(26) {Amide II}	1537	1518	ϕ(H–N–Cα)(45) + ϕ(C=N–H)(28) + ν(C=N)(12) {Amide II}
1302	1299	ν(C=N)(30) + ν(C=O)(19) + ν(Cα–C)(12) + ϕ(H–N–Cα)(12) + ϕ(N=C=O)(8) + ν(N–Cα)(7) {Amide III}	1311	1318	ϕ(N–Cα–Hα)(54) + ϕ(Hα–Cα–Cβ)(7) + ϕ(Hα–Cα–C)(7) + ν(C=N)(5)

Note: All frequencies are given in cm^{-1}.

Table 3. Pure side-chain modes.

Cal.	Obs.	Assignments (% P.E.D. at $\delta = 0{\cdot}0$)
2963	2960	$\nu(C\alpha\text{–}H\alpha)(99)$
2957		$\nu(C\delta_1 - H\delta_1)(99)$
2938	2938	$\nu(C\delta_2\text{–}H\delta_2)(98)$
2918	2916	$\nu(C\gamma\text{–}H\gamma)(24) + \nu(C\delta_1 - H\delta_1)(73)$
2917		$\nu(C\delta_1\text{–}H\delta_1)(98)$
2915	2913	$\nu(C\gamma\text{–}H\gamma)(65) + \nu(C\delta_1 - H\delta_1)(28)$
2910		$\nu(C\delta_2\text{–}H\delta_2)(98)$
2910		$\nu(C\delta_2\text{–}H\delta_2)(96)$
2906	2904	$\nu(H\beta\alpha\text{–}C\beta)(47) + \nu(H\beta\beta\text{–}C\beta)(48)$
2876	2874	$\nu(H\beta\beta\text{–}C\beta)(49) + \nu(H\beta\alpha - C\beta)(50)$
1466	1471	$\phi(H\delta_1\text{–}C\delta_1\text{–}H\delta_1)(92) + \phi(C\gamma - C\delta_1\text{–}H\delta_1)(6)$
1465		$\phi(H\delta_1\text{–}C\delta_1\text{–}H\delta_1)(94)$
1452	1454	$\phi(H\delta_2\text{–}C\delta_2\text{–}H\delta_2)(90) + \phi(C\gamma\text{–}C\delta_2\text{–}H\delta_2)(5)$
1452		$\phi(H\delta_2\text{–}C\delta_2\text{–}H\delta_2)(93)$
1444	1441	$\phi(H\beta\alpha\text{–}C\beta\text{–}H\beta\beta)(76)$
1393	1390	$\phi(C\gamma\text{–}C\delta_1\text{–}H\delta_1)(49) + \phi(H\delta_1\text{–}C\delta_1\text{–}H\delta_1)(45)$
1380	1370	$\phi(C\gamma\text{–}C\delta_2\text{–}H\delta_2)(48) + \phi(H\delta_2\text{–}C\delta_2\text{–}H\delta_2)(45)$
1351	1350	$\phi(C\delta_2\text{–}C\gamma\text{–}H\gamma)(49) + \phi(H\gamma\text{–}C\gamma\text{–}C\delta_1)(24)$
1333	1334	$\phi(C\beta\text{–}C\gamma\text{–}H\gamma)(47) + \phi(H\gamma\text{–}C\gamma\text{–}C\delta_1)(25)$
1038	1040	$\phi(C\gamma\text{–}C\delta_1\text{–}H\delta_1)(30) + \phi(C\gamma\text{–}C\delta_2\text{–}H\delta_2)(22) + \nu(C\beta\text{–}C\gamma)(11) + \nu(C\gamma\text{–}C\delta_2)(5) + \phi(C\delta_2\text{–}C\gamma\text{–}C\delta_1)(6)$
1014	1020	$\phi(C\gamma\text{–}C\delta_1\text{–}H\delta_1)(41) + \phi(C\gamma\text{–}C\delta_2\text{–}H\delta_2)(29)$
977	980	$\phi(C\gamma\text{–}C\delta_2\text{–}H\delta_2)(28) + \phi(C\gamma\text{–}C\delta_1\text{–}H\delta_1)(23) + \nu(C\gamma\text{–}C\delta_1)(10) + \nu(C\gamma\text{–}C\delta_2)(7) + \phi(C\alpha\text{–}C\beta\text{–}H\beta\alpha)(6) + \phi(C\alpha\text{–}C\beta\text{–}H\beta\alpha)(5)$
931	925	$\phi(C\gamma\text{–}C\delta_2\text{–}H\delta_2)(44) + \phi(C\gamma\text{–}C\delta_1\text{–}H\delta_1)(38)$
842	833	$\nu(C\beta\text{–}C\gamma)(35) + \phi(C\gamma\text{–}C\delta_2\text{–}H\delta_2)(25) + \phi(C\gamma\text{–}C\delta_1\text{–}H\delta_1)(11) + \nu(C\gamma\text{–}C\delta_1)(13)$
830		$\nu(C\gamma\text{–}C\delta_2)(30) + \nu(C\gamma\text{–}C\delta_1)(20) + \phi(C\gamma\text{–}C\delta_1\text{–}H\delta_1)(12) + \phi(H\beta\alpha\text{–}C\beta\text{–}C\gamma)(7) + \phi(C\gamma\text{–}C\delta_2\text{–}H\delta_2)(7) + \tau(C\alpha\text{–}C\beta)(6)$
328	323	$\phi(C\delta_1\text{–}C\gamma\text{–}C\delta_2)(64) + \phi(C\beta\text{–}C\gamma\text{–}C\delta_1)(8)$
282	289	$\tau(C\gamma\text{–}C\delta_2)(49) + \tau(C\gamma\text{–}C\delta_1)(48)$

Note: All frequencies are in cm^{-1}.

frequencies [18]. Only the band near 610 cm^{-1} shifts to about 450 cm^{-1} because it is due to amide V. One of the interesting features observed in the dispersion curves is the tendency of some curves to crowd or close in near the helix angle, which is indicative of the coupling between various modes. This phenomenon is observed in amide V and amide VI. Amide VI mode is most dispersive (23 cm^{-1}). It has 25% contribution from

Table 4. Mix modes.

Cal.	Obs.	Assignment (% P.E.D. at $\delta = 0{\cdot}0$)
1317	1318	ϕ(N–Cα–Hα)(63) + ϕ(Hα–Cα–C)(12)
1239	1241	ν(Cα–C)(9) + ϕ(Hα–Cα–C)(9) + ϕ(Hα–Cα–Cβ)(18) + ν(Cα–Cβ)(16) + ν(Cβ–Cγ)(8) + ϕ(Cα–Cβ–Hββ)(7) + ϕ(Hββ–Cβ–Cγ)(7) + ϕ(Cα–Cβ–Hβα)(6)
1166	1172	ϕ(Hα–Cα–Cβ)(22) + ϕ(Hα–Cα–C)(19) + ϕ(Hβα–Cβ–Cγ)(16) + ϕ(Cα–Cβ–Hβα)(10) + ϕ(Cα–Cβ–Hββ)(8) + ν(Cβ–Cγ)(7) + ϕ(Hββ–Cβ–Cγ)(6)
1130	1130	ν(N–Cα)(26) + + ν(Cα–C)(5) + ϕ(Cα–Cβ–Hβα)(15) + ϕ(Cα–Cβ–Hββ)(15) + ϕ(Hβα–Cβ–Cγ)(9) + ϕ(Hββ–Cβ–Cγ)(5)
1093	1099	ν(N–Cα)(32) + ν(Cα–C)(12) + ϕ(Hββ–Cβ–Cγ)(13) + ϕ(Hβα–Cβ–Cγ)(6)
948	943	ν(Cα–Cα)(5) + ϕ(Hα–Cα–Cβ)(8) + ν(Cα–Cβ)(47) + ϕ(Cγ–Cδ_2–Hδ_2)(5)
902	903	ν(Cα–C)(21) + ν(C=O)(6) + ϕ(N=C=O)(9) + ν(C=N)(6) + ϕ(C=N–Cα)(6) + ϕ(Hα–Cα–C)(5) + ϕ(Cγ–Cδ_2–Hδ_2)(7) + ϕ(Hβα–Cβ–Cγ)(7) + ϕ(Cγ–Cδ_1–Hδ_2)(6)
875	874	ϕ(N=C=O)(6) + ϕ(C=N–Cα)(6) + ν(N–Cα)(6) + ϕ(Cα–Cβ–Hββ)(9) + τ(Cβ–Cγ)(6) + ϕ(Cα–Cβ–Hβα)(7) + ϕ(Hββ–Cβ–Cγ)(5) + ϕ(Cγ–Cδ_1–Hδ_1)(5) + ϕ(Cγ–Cδ_2–Hδ_2)(5)
734	726	ω(C=O)(35) + ω(N–H)(25) + ν(Cγ–Cδ_1)(9) + ν(Cγ–Cδ_2)(5)
700	703	ω(N–H)(13) + ν(Cγ–Cδ_2)(20) + ν(Cβ–Cγ)(19) + ν(Cγ–Cδ_1)(14)
647	656	ω(C=O)(26) + ϕ(N–Cα–C)(12) + ϕ(Cα–Cβ–Cγ)(8) {Amide VI}
1332	1334	ϕ(Cβ–Cγ–Hγ)(38) + ϕ(Hγ–Cγ–Cδ_1)(19) + ϕ(N–Cα–Hα
1227	1224	ν(Cα–Cβ)(16) + ϕ(Hα–Cα–Cβ)(15) + ν(Cβ–Cγ)(9) + ϕ(Hα–Cα–C1)(9) + ϕ(Cα–Cβ–Hβα)(8) + ϕ(Hββ–Cβ–Cγ ϕ(Cα–Cβ–Hββ)(6) + ϕ(Hβα–Cβ–Cγ)(5)
1165	1172	ϕ(Hα–Cα–Cβ)(23) + ϕ(Hα–Cα–C)(19) + ϕ(Hβα–Cβ–Cγ ϕ(Cα–Cβ–Hβα)(10) + ϕ(Cα–Cβ–Hββ)(8) + ν(Cβ–Cγ)(6) ϕ(Hββ–Cβ–Cγ)(6)
1130	1130	ν(N–Cα)(20) + ϕ(Cα–Cβ–Hββ)(19) + ϕ(Cα–Cβ–Hβα)(16 ϕ(Hββ–Cβ–Cγ)(9) + ϕ(Hβα–Cβ–Cγ)(9)
1080	1076	ν(N–Cα)(38) + ϕ(Hββ–Cβ–Cγ)(10) + ν(Cα–C)(6) + ϕ(Hβα–Cβ–Cγ)(7)
969	960	ν(Cα–Cβ)(17) + ϕ(Cγ–Cδ_2–Hδ_2)(12) + ϕ(Cγ–Cδ_1–Hδ_1)(ν(Cα–C)(7)
896	899	ν(Cα–C)(16) + ν(Cα–Cβ)(13) + ϕ(Cγ–Cδ_2–Hδ_2)(7) + ϕ(Hβα–Cβ–Cγ)(6) + ϕ(Cγ–Cδ_1–Hδ_1)(7)
873	874	ϕ(Cα–Cβ–Hββ)(10) + ν(N–Cα)(7) + τ(Cβ–Cγ)(6) + ϕ(Cα–Cβ–Hβα)(6) + ν(Cα–Cβ)(5) + ν(Cγ–Cδ_2)(5) + ϕ(Cγ–Cδ_2–Hδ_2)(5) + ϕ(Cγ–Cδ_1–Hδ_1)(5)
751	756	ω(C=O)(35) + ω(N–H)(24) + ν(Cα–Cβ)(8)
699	703	ν(Cγ–Cδ_2)(25) + ν(Cγ–Cδ_1)(23) + ν(Cβ–Cγ)(20) + ω(N–H)
625	633	ϕ(N=C=O)(24) + ω(C=O)(10) + ϕ(Cα–Cβ–Cγ)(16) + ν(N–Cα)(5) + ϕ(Cα–C=O)(5) + ϕ(Cα–C=N)(5) + ϕ(C=N–Cα)(6) + ω(N–H)(6)

592	587	ω(N–H)(21) + τ(C=N)(14) + ω(C=O)(11) + ν(N–Cα)(6) + τ(N–Cα)(11) + ϕ(N=C=O)(6) + ϕ(C–Cα–Cβ)(5) {Amide V + Amide IV}	603	614	ω(N–H)(27) + ω(C=O)(25) + τ(C=N)(12) + τ(N–Cα)(12)
549	543	ϕ(Cα–C=N)(16) + ϕ(Cα–C=O)(13) + ϕ(N–Cα–Hα)(5) + ϕ(N–Cα–Cβ)(19) + τ(Cβ–Cγ)(7) + ϕ(Cα–Cβ–Cγ)(6) + ϕ(Cβ–Cγ–Cδ_2)(5)	501	506	ϕ(N–Cα–Cβ)(15) + ϕ(Cβ–Cγ–Cδ_2)(10) + τ(Cβ–Cγ)(9) + ϕ(Cα–C=N)(6) + ϕ(N–Cα–Hα)(6) + ϕ(Cα–Cβ–Cγ)(6) + ν(N–Cα)(5)
412	410	ϕ(Cα–C=O)(10) + ϕ(N=C=O)(8) + ν(Cα–C)(8) + ν(Cα–Cβ)(8) + ϕ(Cβ–Cγ–Cδ_2)(7) + ϕ(Cβ–Cγ–Cδ_1)(11) + ϕ(Cβ–Cγ–Hγ)(7) + ϕ(Cδ_2–Cγ–Hγ)(7) + ϕ(Hγ–Cγ–Cδ_1)(7)	438	452	ϕ(Cβ–Cγ–Cδ_1)(15) + ϕ(Cα–Cβ–Cγ)(8) + ν(Cα–C)(7) + ν(Cα–Cβ)(6) + ϕ(Cβ–Cγ–Cδ_2)(7) + ϕ(Cδ_2–Cγ–Hγ)(6) + ϕ(Cα–C=O)(6) + ϕ(Cβ–Cγ–Hγ)(5)
388	399	ϕ(Cα–C=O)(9) + (Cα–C=N)(5) + τ(Cβ–Cγ)(8) + ϕ(Cβ–Cγ–Cδ_1)(26) + ϕ(Cβ–Cγ–Cδ_2)(20) + τ(Cα–Cβ)(11)	372	368	ϕ(Cβ–Cγ–Cδ_1) + ϕ(Cβ–Cγ–Cδ_2)(16) + ϕ(Cα–C=O)(10) + ϕ(Cα–C=N) + τ(Cα–Cβ)(5)
300	302	ϕ(C=N–Cα)(10) + ϕ(N=C=O)(13) + ϕ(Cα–C=O)(6) + ϕ(C–Cα–Cβ)(8) + τ(Cγ–Cδ_2)(17) + τ(Cγ–Cδ_1)(15)	310	317	τ(Cγ–Cδ_2)(13) + ϕ(C=N–Cα)(11) + τ(Cγ–Cδ_1)(11) ϕ(N–Cα–C)(10) + ϕ(N=C=O)(8) + ϕ(Cα–C=O)(7) + ϕ(C–Cα–Cβ)(6)
268	271	ϕ(N=C=O)(5) + ϕ(C=N–Cα)(6) + ϕ(C–Cα–Cβ)(5) + τ(Cγ–Cδ_1)(32) + τ(Cγ–Cδ_2)(29)	271	271	τ(Cγ–Cδ_2)(37) + τ(Cγ–Cδ_1)(33)
217	227	ϕ(N–Cα–C)(22) + τ(C=N)(11) + τ(C–Cα)(7) + ϕ(C=N–Cα)(6) + τ(N–Cα)(5) + ϕ(Cα–C=O)(5) + ϕ(C–Cα–Cβ)(8) {Amide VII}	240	246	ϕ(N–Cα–Cβ)(23) + ϕ(Cβ–Cγ–Cδ_2)(22) + ϕ(Cα–C=N)(7) + ϕ(Cα–C=O)(5) + ϕ(N=C=O)(5) + ϕ(N–Cα–C)(6)
195	189	ϕ(C–Cα–Cβ)(19) + ϕ(N–Cα–Cβ)(12) + ϕ(Cβ–Cγ–Cδ_2)(15) + τ(Cβ–Cγ)(17) + τ(Cα–Cβ)(5)			τ(C=N)(7) + τ(C–Cα)(7) + ϕ(Cβ–Cγ–Cδ_2)(6)
148	144	ϕ(Cα–C=N)(9) + ϕ(Cα–Cβ–H$\beta\alpha$)(6) + ϕ(Cα–Cβ–H$\beta\beta$)(5) + ϕ(Cβ–Cγ–Cδ_2)(8) + ϕ(Cβ–Cγ–Cδ_1)(19) + τ(Cβ–Cγ)(17) + τ(Cα–Cβ)(5)	136	144	ϕ(Cα–Cβ–Cγ)(24) + ϕ(Cβ–Cγ–Cδ_1)(14) + τ(Cβ–Cγ)(6)
98	—	ϕ(C=N–Cα)(5) + ϕ(C–Cα–Cβ)(14) + ϕ(Cα–Cβ–Cγ)(40)	109	104	ϕ(C–Cα–Cβ)(26) + ϕ(N–Cα–C)(9) + ϕ(C=N–Cα)(6) + τ(C–Cα)(6) + τ(Cβ–Cγ)(7) + ω(C=O)(5)

(*Continued*)

Table 4. (*Continued*)

Cal.	Obs.	Assignment (% P.E.D. at $\delta = 0{\cdot}0$)	Cal.	Obs.	Assignment (% P.E.D. at $\delta = 5\pi/9$)
79	—	τ(C–Cα)(11) + ϕ(C=N–Cα)(6) + ϕ(N–Cα–Cβ)(17) + τ(Cβ–Cγ)(25) + τ(Cα–Cβ)(15)	87	—	ϕ(N–Cα–Cβ)(13) + ϕ(Cα–Cβ–Cγ)(16) + τ(Cβ–Cγ)(12) + τ(C–Cα)(11) + ϕ(Cα–Cβ–H$\beta\beta$)(6) + τ(Cα–Cβ)(5)
63	65	τ(C–Cα)(26) + τ(C=N)(6) + τ(N–Cα)(23) + ϕ(N–Cα–C)(9) + ϕ(N–Cα–Cβ)(9) + ϕ(Cα–Cβ–Cγ)(8)	60	65	τ(Cα–Cβ)(29) + τ(N–Cα)(11) + τ(C–Cα)(10) + τ(Cβ–Cγ) ω(N–H)(5)
39	—	ϕ(Cα–C=N)(13) + ϕ(Hα–Cα–C)(7) + ϕ(C=N–Cα)(6) + ϕ(N–Cα–Cβ)(8) + τ(Cα–Cβ)(34)	40	—	τ(Cα–Cβ)(14) + τ(C=N)(12) + τ(C–Cα)(10) + τ(N–Cα)(9) ϕ(N–Cα–Cβ)(8) + ϕ(Cα–C=N)(8) + ϕ(C–Cα–Cβ)(6) + ϕ(Cα–Cβ–Cγ)(5)

Note: All frequencies are in cm^{-1}.

Table 5. Comparison of amide modes of poly-L-leucine and poly-L-alanine.

	Poly-L-leucine		Poly-L-alanine	
	$\delta = 0{\cdot}0$	$\delta = 5\pi/9$	$\delta = 0{\cdot}0$	$\delta = 5\pi/9$
Amide A	3313	3313	3293	3293
Amide I	1657	1657	1659	1659
Amide II	1546	1518	1515	1540
Amide III	1299	1318	1270	1274
Amide IV	587	633	525	440
Amide V	587	617	595	610
Amide VI	656	633	685	656
Amide VII	227	171	238	190

Note: All frequencies are given in cm^{-1}.

ω(C=O). With increase in δ, the energy of this mode and the contribution of ω(C=O) decrease whereas ϕ(O=C=N) and ω(N–H) start mixing. At $\delta = \psi$ it becomes a mixture of amide IV and V. This characteristic feature has also been noticed in α poly(L-alanine) [6] and poly(α-aminoisobutyric acid) [15] (3_{10} helix) and can be attributed to strong intramolecular interactions stabilizing the helical structure. The dispersion curves of polyglycine II and other β sheet samples do not show this feature [7, 8]. The observed peak at 227 cm^{-1} has been assigned to amide VII and this mode has a lower value at $\delta = 5\pi/9$ in comparison to $\delta = 0$. The P.E.D. of this mode shows considerable mixing with Cα–N and Cα–C torsions. As in case of α poly(L-alanine) [6], in α PLL also, there is certain amount of mixing of the torsional modes with the angle bending modes. The peak at 543 cm^{-1} has been assigned to the mixture of (N–Cα–Cβ) bend (junction mode) and main-chain deformation. This mode shows maximum dispersion (64 cm^{-1}).

3.2 *Side-chain modes*

The side-chain [$-CH_2CH(CH_3)_2$] of PLL consists of a CH_2 attached to a gem dimethyl group. Pure side-chain modes are given in table 3. The CH_2 scissoring mode calculated at 1444 cm^{-1} corresponds to the observed band at 1441 cm^{-1} in PLL and at 1453 cm^{-1} in poly(γ-benzyl-L-glutamate) [17].

The peaks at 1334, 1318 and 1299 cm^{-1} have been assigned to (Cγ–Hγ) bend, (Cα–Hα) bend and amide III (back-bone mode) respectively. With increase in δ the contribution of (Cγ–Hγ) and (Cα–Hα) bend decrease in 1334 cm^{-1} and 1318 cm^{-1} mode respectively and the latter one starts mixing with the amide III. A repulsion takes place between 1334 and 1318 cm^{-1} modes in the neighbourhood of helix angle and at the point of inflexion there is a sudden jump in the density-of-states.

The observed band at 1172 cm^{-1} has been tentatively assigned to rocking of CH_3 group by Koenig and Sutton [17] but according to our normal mode calculations this mode is a mixture of (Cα–Hα) bend (40%) and CH_2 wag (25%). This is further supported by the fact that in poly(γ-benzyl-L-glutamate) which does not have any methyl group, the observed Raman band at 1183 cm^{-1} has been assigned to CH_2 wag

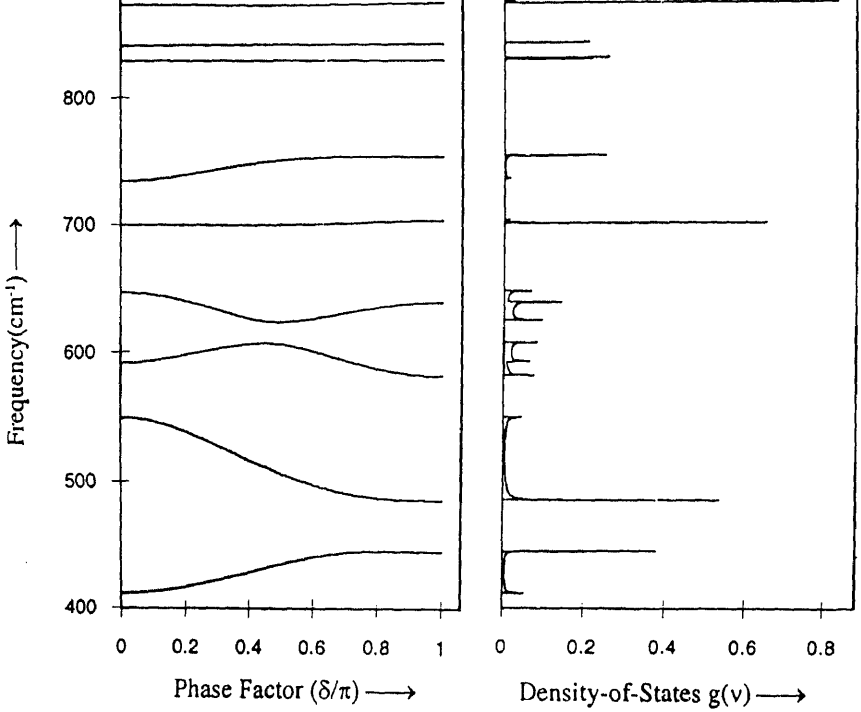

Figure 4. (**a**) Dispersion curves of poly(L-leucine) (950–400 cm^{-1}); (**b**) Density-of-states $g(\nu)$ (950–400 cm^{-1}).

[17]. This is consistent with our assignment. The CH_2 rocking mode is assigned to the peak at 875 cm^{-1} which is in accordance with the assignment of Koenig and Sutton [17]. All pure side chain modes are non-dispersive.

The modes calculated at 1130 and 1093 cm^{-1} ($\delta = 0$) correspond to the observed peaks at 1129 and 1099 cm^{-1}. They contain a mixture of side-chain CH_2 twist and skeletal (N–Cα) stretch. The 1130 cm^{-1} mode is non-dispersive. At $\delta = 0$ it has 34% contribution from CH_2 twist and as δ increases the contribution of (N–Cα) stretch decreases and that of CH_2 twist increases. The other one (1099 cm^{-1}) has 13% contribution from CH_2 twist (at $\delta = 0$) and shows a reverse behaviour later on. This mode is dispersive and with increase in δ the contribution of (N–Cα) stretch increases and that of CH_2 twist decreases. The modes at 948 and 1038 cm^{-1} (at $\delta = 0$) are mixtures of CH_3 rock and side-chain (C–C) stretch. The 1038 cm^{-1} mode is non-dispersive and has very little contribution from side-chain (Cβ–Cγ) stretch. The other one (948 cm^{-1}) has 47% contribution from side-chain (Cα–Cβ) stretch (at $\delta = 0$). In the 948 cm^{-1} mode the contribution of (Cα–Cβ) stretch decreases and that of CH_3 rock, (Cγ–Cδ_2) and (Cγ–Cδ_1) stretches increase with increase in δ and the frequency of this

mode increases and in the neighbourhood of helix angle ($\delta = \psi$) it exchanges its character with the 977 cm^{-1} mode (CH_3 rock at $\delta = 0$). After this, the 948 cm^{-1} mode becomes non-dispersive and 977 cm^{-1} mode is repelled upwards. They belong to the same symmetry species [25].

3.3 *Specific heat*

Recently, heat capacity measurements for a series of polyamino acids have been reported by Roles *et al* [3–4]. Their approach basically involves separation of vibrational spectra into group and skeletal spectrum and obtaining the number of vibrators for each case. These are obtained from the dispersion curves and spectra of polymers having the same skeletal structure (e.g. poly(L-glycine) and α poly(L-alanine) for poly(L-leucine)). As remarked earlier this approach has its own limitations specially when the back-bone and side-chain modes are heavily mixed up. This is very true in case of poly(L-leucine) below 1200 cm^{-1}. The density-of-states are shown in figures 3(b), 4(b) and 5(b). Modes which are purely skeletal, purely side-chain and mixture of

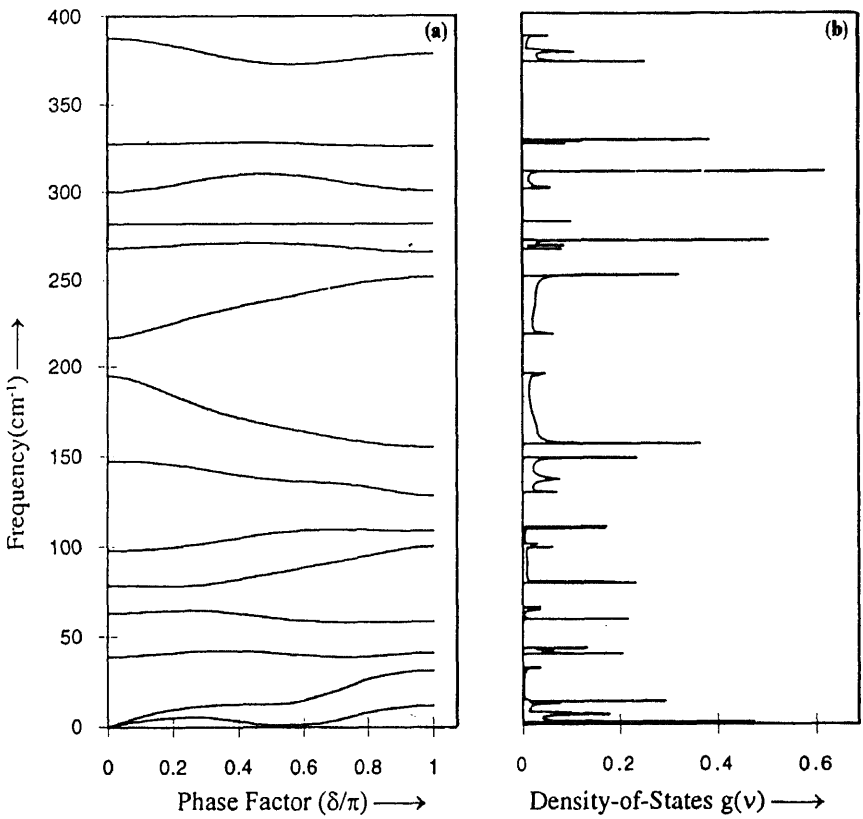

Figure 5. (**a**) Dispersion curves of poly(L-leucine) below 500 cm^{-1}, (**b**) Density-of-states $g(\nu)$ below 500 cm^{-1}.

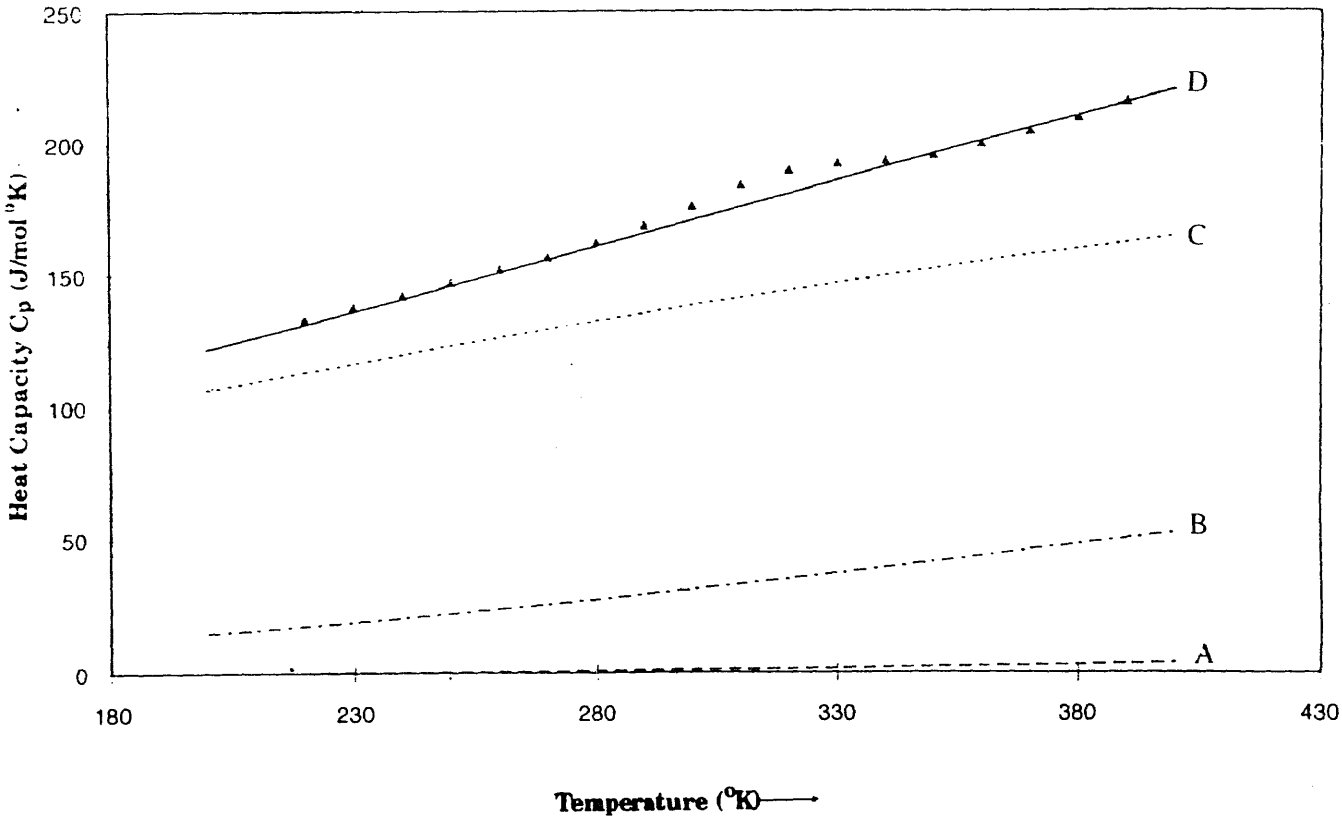

Figure 6. Variation of heat capacity C_P with temperature. [The contribution of back-bone modes (– – –), side-chain modes (—·—), mixed modes (- - -) and total heat capacity (———) are shown by curves A, B, C and D respectively. ▲ represents the experimental data].

these two are given in tables 2, 3 and 4 respectively. Their contributions to the heat capacities are shown in figure 6A, 6B and 6C respectively in the temperature range 220–390 K. Total heat capacity is shown in figure 6D and Δ's represent the experimental data of Roles *et al* [4]. The calculations are in very good agreement with the experimental measurements except in the region 300–330 K wherein experimental data show a bump. Although not explicitly mentioned, this bump could be due to some artifacts in experiments, such as presence of moisture. It should disappear on repeating measurements. Presence of any glass type transition is also not reported. Our methodology gives better agreement with experimental data substantiated by the r.m.s. deviation value which is 0·83% as compared with 1·09% of Roles *et al* [4].

The contribution from the lattice modes is bound to make an appreciable difference to the specific heat because of its sensitivity to these modes. At the moment, the calculation for dispersion curves for a unit cell are extremely difficult because even if we assume a minimum of two chains in unit cell then there would be 180 atoms leading to a matrix of 540 × 540. It would bring in an enormous number of interactions and make the problem almost intractable. Thus in-spite-of several limitations involved in the calculation of specific heat, the present work does provide a good starting point for further basic studies on thermodynamical behaviour of polypeptides and proteins which go into well-defined conformations.

Acknowledgement

Financial assistance to VDG from Council of Scientific and Industrial Research, New Delhi under the Emeritus Scientist Scheme is gratefully acknowledged.

References

[1] B Wunderlich and H S Bu, *Thermochimica Acta* **119**, 225 (1987)
[2] H S Bu, W Aycock, Z D Cheng Stephen and B Wunderlich, *Polymer* **29**, 1486 (1988)
[3] K A Roles and B Wunderlich, *Biopolymers* **31**, 477 (1991)
[4] K A Roles, A Xenopoulos and B Wunderlich, *Biopolymers* **33**, 753 (1993)
[5] V D Gupta, S Trevino and H Boutin, *J. Chem. Phys.* **48**, 3008 (1968)
[6] M V Krishnan and V D Gupta, *Chem. Phys. Lett.* **6**, 231 (1970)
[7] M V Krishnan and V D Gupta, *Chem. Phys. Lett.* **7**, 285 (1970)
[8] R D Singh and V D Gupta, *Spectrochim. Acta* **A27**, 385 (1971)
[9] A M Dwivedi and V D Gupta, *Chem. Phys. Lett.* **16**, 909 (1972)
[10] V D Gupta, R D Singh and A M Dwivedi, *Biopolymers* **12**, 1377 (1973)
[11] R B Srivastava and V D Gupta, *Biopolymers* **13**, 1965 (1974)
[12] L Burman, P Tandon, V D Gupta, S Rastogi, S Srivastava and G P Gupta, *J. Phys. Soc. Jpn.* **64**, 327 (1995)
[13] A Gupta, P Tandon, V D Gupta, S Rastogi and G P Gupta, *J. Phys. Soc. Jpn.* **64**, 315 (1995)
[14] L Burman, P Tandon, V D Gupta, S Rastogi and S Srivastava, *Polymer. J.* April (1995) (in press)
[15] O Prasad, P Tandon, V D Gupta, and S Rastogi, *J. Phys. Soc. Jpn.* **64**, (1995)
[16] E R Blout, C de Loze, S M Bloom and G D Fasman, *J. Am. Chem. Soc.* **82**, 3787 (1960)
[17] J L Koenig and P L Sutton, *Biopolymers* **10**, 89 (1971)
[18] K Itoh, T Shimanouchi and M Oya, *Biopolymers* **7**, 649 (1969)
[19] E B Wilson, J C Decuis and P C Cross, *Molecular vibrations: The theory of infrared and Raman vibrational spectra* (Dover Publications, New York, 1980)

[20] P W Higgs, *Proc. R. Soc.* (*London*) **A220**, 472 (1953)
[21] W T King, I M Mills and B L Crawford, *J. Chem. Phys.* **27**, 455 (1957)
[22] T H Benzinger, *Nature* (*London*) **229**, 100 (1971)
[23] R Pan, M Verma-Nair and B Wunderlich, *J. Therm. Anal.* **35**, 955 (1989)
[24] S Krimm and J Bandekar, *Adv. Protein Chem.* **38**, 181 (1986)
[25] D I Bower and W F Maddams, *The vibrational spectroscopy of polymers* (Cambridg University Press, 1989) 154–156

Streaming instability of a dusty plasma in the presence of mass and charge variation

B P PANDEY and C B DWIVEDI*
Indian Institute of Geomagnetism, Dr. Nanabhai Moos Marg, Colaba, Bombay 400 005, India
*Plasma Physics Division, Institute of Advanced Study in Science and Technology, Jawaharnagar, Khanapara, Guwahati 781 022, Assam, India

MS received 28 December 1994; revised 24 May 1995

Abstract. We study the effect of the mass and charge dynamics on the collective behaviour of a dusty plasma. It is shown that the finite non-zero streaming velocity of the dust grains leads to a novel coupling of the dust mass fluctuation with other dynamic variables of the plasma and the grains. The mass fluctuations causes a collisionless dissipation and provides an alternate channel for the beam mode instability to occur. Physically the negative energy wave associated with the beam mode couples to the mass fluctuation induced dissipative medium to produce the instability. We conclude that the higher value of the ion mass density to the dust mass density ratio reduces the threshold value for the onset of the instability. Its application in the astrophysical context is discussed.

Keywords. Dusty plasma; mass fluctuation; charge fluctuation.

PACS Nos 52·25; 52·35

1. Introduction

Dusty plasma is ubiquitous in the universe. Interstellar media, cometary tails, planetary rings, ionosphere, plasma processing, etc. are a few examples of the space and the laboratory plasmas where the dust plays an important role in determining the dynamical behaviour of the plasmas [1–4]. Dusty plasma is a three component plasma system consisting of the electrons, ions and the charged dust grains. The typical size of the dust grains is a few microns and these can carry ten to million times the electronic charge. In general, the size, mass, and charge on the grains may vary; for example, the mass may vary between 10^{-2} g to a few a.m.u. per dust charge [5, 6], the size may vary between a few micrometer to the molecular size i.e. there exists a smooth transition from dusty to a multi component plasma.

The dust grains in a plasma may be charged through the collisions, photoemission etc. We assume that the collisional process is primarily responsible for the grain charging (in this case the grains are negatively charged). As a result of the collisions, the ions stick to the grain surface and thus causes the variation of the grain charge, mass and radius. Generally, the effect of the mass variation of the grain is ignored since $m_i/m_d \ll 1$. In the light of the recent data of ASPERA for the matter ejected from Phobos [6], we carefully observe that even in the above mass limit, ion mass density may be comparable to the dust mass density leading thereby to an interesting consequence of a new wave instability.

Collective behaviour (waves, instabilities, etc.) of a dusty plasma in the absence of charge fluctuation has been studied by several authors [1–4]. Effect of the charge

variation on the collective modes has been ... mass on the grains has been assumed to be constant. However, in general, it is not true [12]. Actually the size (radius) of the grains should also be treated as a dynamical variable. But, for the simplicity, it is ignored as the time scale over which the radius varies is larger than that of the mass variation due to accretion [12]. Under these assumptions we find that when $v_{d0}/c_i > \eta_m^{1/2}(1+\delta)$, where $\eta_m = (m_{d\theta} n_{d0})/(m_1/n_{i0})$ is the dust mass density to ion mass density ratio and $\delta = n_{e0}/n_{i0}$ is the equilibrium electron to ion number density ratio, there exists a novel mode of instability. The paper is organized in the following fashion. In § 2, basic governing equations are given. Dispersion relation is derived in § 3. Section 4 includes the results and discussions.

2. Basic equations

We consider a three component plasma consisting of the electrons, ions and the electrically charged dust grains. It is assumed that the mass variation is solely due to the sticking of the ions on the grain surface and the other processes like photoionization, sputtering, etc. are ignored. The dust mass fluctuation equation is derived from the mass conservation relation. The basic linearized equations for the number conservation of the electrons, ions and the dust fluids are:

$$\partial_t n_{e1} + \nabla(n_{e1}\mathbf{v}_{e0} + n_{e0}\mathbf{v}_{e1}) = -\beta_{e0} n_{e1} - \beta_{e1} n_{e0}, \tag{1}$$

$$\partial_t n_{i1} + \nabla(n_{i1}\mathbf{v}_{i0} + n_{i0}\mathbf{v}_{i1}) = -\beta_{i0} n_{i1} - \beta_{i1} n_{i0}, \tag{2}$$

$$\partial_t n_{d1} + \nabla(n_{d1}\mathbf{v}_{d0} + n_{d0}\mathbf{v}_{d1}) = 0, \tag{3}$$

where the subscripts 0 and 1 represent the equilibrium and the perturbed quantities respectively; $n_a, \mathbf{v}_a$ (a = electron, ion and dust) are the number density and velocity of ath species. β_e and β_i denote the attachment frequencies of the electrons and the ions respectively.

Using (2) and (3) along with the mass conservation equation

$$\partial_t \rho + \nabla\cdot\mathbf{J} = 0, \tag{4}$$

where $\rho = \Sigma m_a n_a$ and $\mathbf{J} = \Sigma m_a n_a \mathbf{v}_a$, one obtains the required equation for the mass fluctuation as

$$\partial_t m_{d1} + (\mathbf{v}_{d0}\cdot\nabla) m_{d1} = (m_{d0}/n_{d0})(\beta_{i0} n_{i1} + \beta_{i1} n_{i0}). \tag{5}$$

In writing the above equation, the term proportional to the electron mass has been neglected. Using similar arguments, the dust charge fluctuation equation can be derived as

$$(\partial_t + \mathbf{v}_{d0}\cdot\nabla) Q_{d1} = -\frac{e}{n_{d0}}[\beta_{e0} n_{e1} + \beta_{e1} n_{e0}) - (\beta_{i0} n_{i1} + \beta_{i1} n_{i0})]. \tag{6}$$

Here the attachment frequencies for the electrons and the ions have been defined as $\beta_a = I_a n_d/q_a n_a$ with 'a' representing for the electron and ion. The expressions for the electron and ion currents are given in the refs [12, 13]. Using the above definition, and the equilibrium constraints $I_{e0} + I_{i0} = 0$, one finds

$$\beta_{a0} = (|I_{a0}| n_{d0})/(q_a n_{a0}) \tag{7}$$

and thus the charge and mass fluctuation equations can be written as:

$$d_t Q_{d1} + \eta q_{d1} = |I_{e0}| \left[\frac{n_{i1}}{n_{i0}} - \frac{n_{e1}}{n_{e0}} \right], \tag{8}$$

$$d_t m_{d1} + \eta \frac{m_i}{e} Q_{d1} = |I_{e0}| \frac{m_i}{e} \frac{n_{i1}}{n_{i0}}, \tag{9}$$

where $d_t = \partial_t + (\mathbf{v}_{d0} \cdot \nabla)$, $\eta = e|I_{e0}|C^{-1}(T_e^{-1} + w_0^{-1})$ and $\hat{\eta} = e|I_{e0}|C^{-1}w_0^{-1}$ with C as the capacitance of the grain and $w_0 = T_i - e\phi_{f0}$, T_i being the ion temperature and ϕ_{f0} the equilibrium floating potential of the grain surface. Equilibrium quasi neutrality $q_i n_{i0} + Q_{d0} n_{d0} - q_e n_{e0} = 0$ has been assumed.

Equation of motion for the electron, ion and dust grain fluids are

$$m_e n_e d_t \mathbf{v}_e = -\nabla P_e + q_e n_e \mathbf{E} - m_e n_e \nu_e (\mathbf{v}_e - \mathbf{v}_d). \tag{10}$$

$$m_i n_i d_t \mathbf{v}_i = -\nabla P_i + q_i n_i \mathbf{E} - m_i n_i \nu_i (\mathbf{v}_i - \mathbf{v}_d).$$

$$d_t (m_d \mathbf{v}_d) = Q_d \mathbf{E}. \tag{11}$$

In the equation of the motion of the dust, collisional terms are not included and the dust grains are assumed to be cold. The Poisson's equation closes the set of basic equations and is given as

$$\nabla^2 \phi = -4\pi e(n_i - n_e) - 4\pi Q_d n_d. \tag{12}$$

Now (8–12) form the basic set of equations for the study of the various wave phenomena in dusty plasma with dynamical behaviour of the dust mass and charge fluctuations.

3. Dispersion relation

We are interested in the low frequency response of the plasma i.e. $\omega \ll kv_{ti}, kv_{te}$. The equilibrium flow of the dust grains is non-zero i.e. $v_{d0} \neq 0$. Electrons and ions are assumed to follow the Boltzmann distribution;

$$n_e = n_{e0} \exp\left(-\frac{q_e \phi}{T_e} \right),$$

$$n_i = n_{i0} \exp\left(-\frac{q_i \phi}{T_i} \right), \tag{13}$$

where n_{e0}, n_{i0} are the equilibrium electron and ion number densities respectively. Considering the fluctuating quantities to vary as $\exp(-i\omega t + i\mathbf{k}\cdot\mathbf{r})$, (8–12) can be Fourier analyzed to yield the desired dispersion relation as

$$1 + \frac{1}{k^2 \lambda_e^2}\left(1 + \frac{i\beta}{\hat{\omega} + i\eta}\right) + \frac{1}{k^2 \lambda_i^2}\left(1 + \frac{i\beta\delta}{\hat{\omega} + i\eta}\right) + \frac{i\beta\omega_{cd}^2 v_{d0}}{k\hat{\omega}^2 c_i^2 \left[\frac{i\hat{\eta}(1+\tau)}{\hat{\omega} + i\eta} + 1\right]} - \frac{\omega_{pd}^2}{\hat{\omega}^2} = 0, \tag{14}$$

where $\omega_{ed}^2 = \dfrac{4\pi Ze^2 n_{e0}}{m_{d0}}$, $c_i^2 = \dfrac{T_i}{m_i}$, $\lambda_{e,i}^2 = \dfrac{T_{e,i}}{4\pi n_{e0,i0} e^2}$, $\delta = \dfrac{n_{e0}}{n_{i0}}$, $\tau = \dfrac{T_i}{T_e}$, $\omega_{pd}^2 = \dfrac{4\pi n_{d0} Q_{d0}^2}{m_{d0}}$, $\hat{\omega} = \omega - kv_{d0}$. Except for the 4th term in (14), rest of the terms are identical to the dispersion relation of Bhatt and Pandey [11]. The 4th term is caused by the mass fluctuation dynamics of the grains. We note that this term vanishes when the dust drift is zero. It is quite natural because in the absence of the finite flow velocity of the dust grains, the mass fluctuation equation becomes redundant and it does not get coupled with the other dynamic variables of the plasma and dust fluids. Defining $C_{ds}^2 = \lambda_{eff}^2 \omega_{pd}^2$ where $\lambda_{eff}^{-2} = \lambda_e^{-2} + \lambda_i^{-2}$; assuming $T_e \approx T_i \approx T$, $n_{e0} \approx n_{i0} \approx n_0$ (a situation relevant to the planetary rings [14]), eq. (14) in the limit of $k^2 \lambda_{eff}^2 \ll 1$ can be written as

$$(\hat{\omega}^2 - k^2 C_{ds}^2)(\hat{\omega} + i\eta) + i\beta\hat{\omega}^2(1+\delta) = \alpha\beta - i\beta\varepsilon(\hat{\omega} + i\eta), \tag{15}$$

where

$$\alpha = \varepsilon\hat{\eta}(1+\tau),\ \varepsilon = \frac{\omega_{ed}^2 \lambda_{eff}^2 k v_{d0}}{c_i^2}.$$

4. Results and discussion

We are interested in a physical situation where mass variation, charging and collision frequency satisfy the condition $\hat{\eta} \sim \eta, \beta < \omega$. Since in this limit, charge and mass dynamics can have appreciable effect and the damping effect on the wave is not very severe, the root of (15) can be calculated perturbatively. Accordingly the solution can be given as

$$\omega = k(v_{d0} - C_{ds}) + (\beta/2)\frac{\alpha + i\varepsilon k C_{ds} - ik^2 C_{ds}^2(1+\delta)}{k^2 C_{ds}^2}. \tag{16}$$

If one assumes that $\varepsilon > kC_{ds}(1+\delta)$ i.e. $\left(\dfrac{v_{d0}}{c_i}\right) > \eta_m^{1/2}(1+\delta)$, an instability sets in. Thus we see that the threshold condition for the onset of the beam driven instability is modified over the earlier condition $v_{d0}/c_i > 1$ as derived by Rosenberg [14]. Obviously the multiplicative factor $\eta_m^{1/2}$ in our threshold condition originates from the dust mass fluctuation dynamics.

In many astrophysical plasmas $\eta_m^{1/2} = \left(\dfrac{n_{d0} m_{d0}}{n_{i0} m_{i0}}\right)^{1/2} \gg 1$ owing to the large ratio of the dust to ion mass. Thus the mass fluctuation dynamics of the dust grains has a major role to play in deciding the onset condition for the beam driven mode instability in dusty plasmas. As we will see in the following discussions, the Mass Fluctuation Driven Streaming Instability (MFDSI) may have favourable conditions in many of the astrophysical systems.

(a) *Mars*: The formation of the dust belt around the mars is according to the present belief caused by the material ejected from its moon Phobos. Assuming that the grains initially move along the circular Keplerian orbit with $v_{d0} \approx v_k^{phobos} \sim 2{\cdot}64$ km/sec; for typical plasma parameters of the Mars, $n_{i0} \sim 0{\cdot}1\ cm^{-3}$, $T \sim 0{\cdot}1$ eV, $m_i = 10^{-24}$ g [15], one finds that $v_{d0}/c_i \sim 0{\cdot}2$. Taking $n_{d0} \sim 10^{-9} - 10^{-10}\ cm^{-3}$, $m_{d0} \sim 10^3 - 10^7$ a.m.u. [6], one finds the value of $\eta_m^{1/2} \sim 10^{-5} - 10^{-6}$. Thus the onset condition for the MIDIS is satisfied and its existence in Martian ring is possible.

(b) *Jovian ring*: Quasi periodic (~ 28 days) high speed (20–56 km/sec) streams of submicron ($0{\cdot}02 \leqslant a \leqslant 0{\cdot}1\ \mu$m) sized grains of the mass ($1{\cdot}6 \times 10^{-16} \leqslant m_{d0} \leqslant 1{\cdot}1 \times 10^{-14}$ g) were detected by 'Vlysses' mission to Jupiter [4]. Taking typical ring plasma parameters: $n_{i0} \sim 10^2\,\mathrm{cm}^{-3}$, $m_i \sim 10^{-22}$ g for a tenuous dust cloud $n_{d0} \sim 10^{-3}\,\mathrm{cm}^{-3}$ [16], one can calculate $v_{d0}/c_i \sim 3$ and $\eta_m^{1/2} \sim 1$. Obviously the instability condition holds good in the Jovian ring and hence the excitation of MFDSI may not be ruled out in the Jovian atmosphere.

(c) *Saturn ring*: For Saturn ring $v_{d0}/c_i \simeq \dfrac{R(\Omega_s - \Omega_k)}{c_i} \sim \mathrm{O}(1)$ [8] for different rings. Here R is the distance from the Saturn to ring and Ω_s, Ω_k represent rotational and Keplerian frequencies respectively. For typical plasma parameters $n_{i0} \sim 10\,\mathrm{cm}^{-3}$, $T \sim 50$ eV, $m_i \sim 10^{-23}$ g for the example for O^+ ions) and $n_{d0} m_{d0} \sim 1\,\mathrm{g/cm}^3$ [8], one gets $\eta_m^{1/2} \sim 10^{11}$. Very clearly the instability condition is not satisfied at all and hence the MFDSI is unlikely in Saturn ring.

(d) *Comets*: Havens [18] reports that the streaming instability may play an important role in interaction between cometary dust and solar wind plasma. Nappi [19] has also pointed out the interesting consequences for a streaming instability if dust is a dominant charge carrier. Considering the dust-plasma parameters inside the ionopause of the Halley's comet as described by Mendis and Rosenberg [4] i.e. $n_{i0} \sim 10^3 - 10^4\,\mathrm{cm}^{-3}$, $T_e \sim T_i = T \sim 0{\cdot}1$ eV, $n_{d0}, 10^{-3}\,\mathrm{cm}^{-3}, a \sim 0{\cdot}1\text{–}10\ \mu$m, v_{d0} (of the order of the solar wind speed) ~ 400 km/sec, $v_{d0}/c_i \sim 10^2$. Now considering the dust mass $m_{d0} \sim 10^{-16}$ g, the value of $\eta_m^{1/2} \sim 10^{-3}$. Thus it is concluded that the cometary environment may be susceptible to the MFDSI.

(e) *Interstellar media*: Most interesting region in the interstellar media is the star forming zones where one observes the molecular clouds [17]. The effect of the MHD shocks in such clouds have been studied in the recent past [3]. Assuming that the shock front moves with typical velocity $V_s \approx v_{d0}$; for the typical parameters [3] $T \sim 10$–20 K, $m_i \sim 10^{-22}$ g, one gets the shock speed $V_s \sim 10$ km/sec leading thereby $v_{d0}/c_i \sim 10^4$. For $Zn_{d0} \ll n_{i0}$, one finds that $\eta_m^{1/2} \sim 1$. Thus the interstellar media especially the star forming zones may become important locations for the existence of the MFDSI.

It is worth adding a few more comments in favour of the aforesaid instability. The inclusion of the mass and charge fluctuation dynamics requires that the time scale of the wave of interest ($\tau_\omega = 2\pi/\omega$) be of the order of the time scales of the mass fluctuation ($\tau = (a^2 w_i n_{i0} A \xi_i)^{-1}$) and charge fluctuation ($\tau_c = (\pi a^2 w_e n_{e0} e)^{-1}$) where πa^2 is the geometrical cross-section of the grains; w_i is the ion thermal velocity; A, ξ_i are the atomic mass number and sticking co-efficient of the ions respectively; w_e is the electron thermal velocity. These requirements restrict the scale size of the instability and is found that in the case of the above listed astrophysical systems the scale sizes are of the order of the size of the respective systems. Thus it is conjectured that the MFDSI could be a possible physical mechanism for the large scale structure formation. Furthermore, it could also be proposed as a triggering mechanism for the onset of the Jeans collapse.

In the light of the above discussions, it becomes clear that the MFDSI has a major role to play in most of the astrophysical situations. The dust mass to ion mass density ratio decides the threshold condition for the onset of the instability.

References

[1] C K Goertz, *Rev. Geophys.* **27**, 271 (1989)
[2] U de Angelis, *Phys. Scr.* **A45**, 465 (1992)
[3] W Hartquist, O Havens and G Morfill, *Fund. Cosmic. Phys.* **15**, 107 (1992)
[4] D A Mendis and M Rosenberg, *Annu. Rev. Astron. Astrophys.* **32**, 419 (1994)
[5] T Mukai, *International School of Physics "Enrico Fermi"* Varena, 1986 edited by J M Greenberg and S Aiellu (North-Holland, Amsterdam, 1989) 397
[6] S Barabash and R Lundin, *IEEE Trans. Plasma Sci.* **22**, 173 (1994)
[7] R K Varma, P K Shukla and V Krishan, *Phys. Rev.* **E47**, 3612 (1993)
[8] M R Jana, P K Kaw and A Sen, *Phys. Rev.* **E48**, 3930 (1993)
[9] F Melandso, T Aslaksen and O Havens, *J. Geophys. Res.* **96**, 13315 (1993)
[10] C Cui and J Goree, *IEEE Trans. Plasma Sci.* **22**, 151 (1994)
[11] J R Bhatt and B P Pandey, *Phys. Rev.* **E50**, 3980 (1994)
[12] L Spitzer Jr, *Physical Processes in the interstellar medium* (John Wiley, New York, 1978)
[13] B T Draine and E E Salpeter, *Astrophys. J.* **231**, 77 (1979)
[14] M Rosenberg, *Planet. Space Sci.* **41**, 229 (1993)
[15] M Horyani, J A Burns, M Tatrallyay and J G Luchmann, *Geophys. Res. Lett.* **17**, 853 (1990
[16] O Havnes and G E Morfill, *Adv. Space Res.* **4**, 85 (1984)
[17] F H Shu, F C Adams and S Lizano, *Annu. Rev. Astron. Astrophys.* **25**, 23 (1987)
[18] O Havnes, *Astron. Astrophys.* **193**, 309 (1988)
[19] C Nappi, *First Capri Workshop on Dusty Plasma*, Capri, 1989 edited by C Nappi (Institut di Cibernetica, Napoli)

Geometry effect on the nonlinear magnetic response of $YBa_2Cu_3O_{7-y}$

PARSHANT BATHAM[1], S B ROY[2], SHAILENDRA KUMAR[2], A K PRADHAN[2], A K GROVER[1], P CHADDAH[2], RAM PRASAD[3] and N C SONI[3]

[1] Centre of Advanced Study, Deparatment of Physics, Panjab University, Chandigarh 160 014, India

[2] Low Temperature Physics Group, Centre of Advanced Technology, Indore 452 013, India

[3] Metallurgy Division, Bhabha Atomic Research Centre, Bombay 400 085, India

MS received 22 June 1995

Abstract. Results are presented for study of nonlinear magnetization of a sintered $YBa_2Cu_3O_{7-y}$ pellet of different thickness of a sample subjected to very low magnetic field. On cooling the sample below T_c in zero field a change, in the oscillatory structure of harmonics in increasing dc field is observed in very low ac magnetic field. The effect of finiteness of the sample on the oscillatory structure and on the hysteresis of harmonics is also studied. The results are explained qualitatively.

Keywords. Nonlinear magnetization; critical current density; demagnetization factor.

PACS Nos 74·30; 74·60

1. Introduction

Nonlinear magnetization response of hard type II superconductors (including the high temperature superconductors) is a well studied phenomenon [1–7]. According to Bean's Critical State Model [1] the origin of the harmonics is hysteresis in magnetization and the nonlinear relation between magnetization and applied field due to pinning of the flux lines in hard type II superconductors. Bean's model assumes that a hard type II superconductors can carry a limiting macroscopic superconducting current density $J = J_c$ and further, that any electromotive force, however small, will induce the macroscopic superconducting current of density J_c to flow locally. Given the distribution of current that are set up and the applied field, one can calculate the flux density $B(r)$ at various point in the sample. The average magnetization induced by an applied field can be calculated by averaging the local flux density. If we apply an ac magnetic field $[H(t) = H_{ac}\cos wt]$, we have $M(wt) = -M(wt + \pi)$ i.e. magnetization which has time reversal symmetry. This is shown schematically in figure 1a and one observes only the odd harmonics in accordance with Bean's critical state model [1]. In the limit that critical current density is independent of applied field, this time reversal symmetry is maintained even when a static magnetic field is superimposed as depicted in figure 1b. The field dependence of critical current density leads to generation of even harmonics, when we superimpose the static magnetic field i.e. when $H(t) = H_{dc} + H_{ac}\cos wt$. It also breaks the time reversal symmetry of the magnetization loop as indicated in figures 1c–1e [8]. Ji *et al* [2] and Navarro *et al* [3] reported observation of the even harmonics when the dc field was superimposed on time varying magnetic field in high temperature superconductors. The amplitude of harmonics was calculated as a function of external

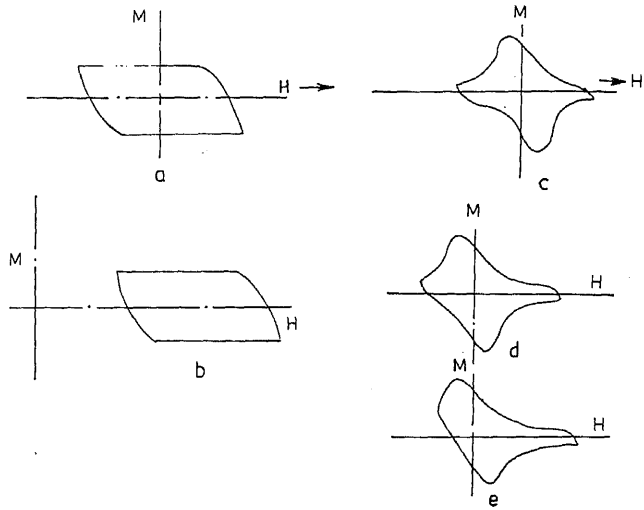

Figure 1. (a) ac magnetization as function of magnetic field; (b) ac magnetic field as function of magnetic field in presence of dc field where the current density does not depend upon magnetic field; (c)–(e) ac magnetization as function of field in increasing order of dc magnetic field where the current density depends upon magnetic field.

dc field and it was found that [4] magnitude of nth harmonics should show oscillatory structure with $(n-1)$ minima when the superimposed H_{app} field varies between $+H_{ac}$ and $-H_{ac}$. The history effect of the static magnetic field [6, 7] on the magnitude of harmonics in the case of ceramic samples of high temperature superconductors is a much more complicated phenomenon. The history effect is explained using the two component behaviour of ceramics ascribed to grains and intergrain boundaries. Further, the observation of a sharp structure of second harmonic in remnant state [9] can be explained in terms of flux trapping in grain and using this memory effect of magnetization in second harmonics, measurements can be made to estimate the field for first flux penetration into grains, viz. H_{clg}.

In the present investigation of harmonics generation, we have focused attention onto an aspect no specially studied in any detail so far, namely the effect of the sample shape (i.e. demagnetization factor) on the generation of harmonics in a given ceramic preparation of a compound. Magnetization studies in ceramic sample are routinely used to elicit informations of field dependence of intergrain and intragrain critical current density. Our present studies demonstrate that for the quantitative information on the current densities, the effect of demagnetization factor is necessary. We report the 2nd and 3rd harmonic as a function of static magnetic field in zero field cooled state of $YBa_2Cu_3O_{7-y}$ sintered pellet sample with different demagnetization factors with very low ac driving field at a temperature of 77 K. These samples with different demagnetization factors were obtained by progressive thinning of the same pellet.

2. Experimental

The results reported here are on a sintered pellet of $YBa_2Cu_3O_{7-y}$ which were prepared by standard solid state sintering process. Y_2O_3, $BaCO_3$ and CuO in appropriate proportion were calcinated in air at 900 °C for 15 hr, interspersed with grinding and mixing. The powder was compacted (at 10 tons/sq in) and sintered in oxygen at 940 °C for 15 h and was held at 400 °C during cooling. No second phase was detected in X-ray diffraction and oxygen was estimated by iodometry as 6·95. The sample has a resistive T_c of 90 K and this was confirmed by magnetization data as well. For measuring the ac magnetization a low field hysteresis loop tracer [10] with driving frequency of 317 Hz and driving field H_{ac} 1 to 2 Gauss was used. The field is applied perpendicular to the plane of the pellet to study the effect of the demagnetization factor of the pellet. A dc biasing field upto 45 G can be provided by a split pair of Helmholtz coils, coaxial to the coil of hysteresis loop tracer.

An AD3522 FET analyzer was used to measure the amplitude of harmonics in the AC magnetization. The possibility of spurious contribution at secondary coil (in absence of sample) from the driving frequency was checked. No contribution from higher harmonics signal was observed in the absence of the sample, or with the sample at $T > T_c$. The noise level was about 15 mV. For calculating the demagnetization factor we measure the ac magnetization at a low ac field value (1 G) such that no hysteresis was observable. With two different orientation that is field parallel to plane of pellet (of volume V) and field perpendicular to the plane of the pellet, we obtain values $M_{\parallel}$ *and* $M_{\perp}$ respectively [11].

$$M_{\parallel}/V = -H/(1-N_{\parallel}); \quad M_{\perp}/V = -H/(1-N_{\perp}) \tag{1}$$

We also not that the trace of demagnetization factor is one i.e.

$$N_{\perp} + 2N_{\parallel} = 1 \tag{2}$$

where $N_{\perp}$ and $N_{\parallel}$ are the demagnetization factors when applied field is perpendicular and parallel to the plane of the pellet. Using (1) and (2) and the observed $M_{\parallel}$ and $M_{\perp}$, we find that demagnetization factors are $N_1 = 0{\cdot}745$, $N_2 = 0{\cdot}792$ and $N_3 = 0{\cdot}842$ for three different pellets of thickness are $t_1 = 1{\cdot}61$ mm, $t_2 = 1{\cdot}41$ mm, and $t_3 = 0{\cdot}92$ mm, respectively, where the magnetic field is perpendicular to the plane of sample. Each of these sample had a diameter of 8·08 mm. We are interested in generation of harmonics in zero field cooled (ZFC) state. The sample is cooled to 77 K in absence of any dc bias (H_{dc}) and then the H_{dc} is switched on. Measurement are made for various H_{dc} field in small value of constant H_{ac} field.

3. Results and discussion

3.1. *Structural change in oscillatory behaviour of harmonics*

In figure 2, we present the magnitude of third harmonic signal (3f) as a function of H_{dc} with H_{ac} fixed at 1, 1·5, 2 and 3 Gauss for sintered pellet $YBa_2Cu_3O_{7-y}$ with demagnetization factors $N_1 = 0{\cdot}74$. Figures 3 and 4 show the same data for sample with demagnetization factors $N_2 = 0{\cdot}792$ and $N_3 = 0{\cdot}842$ respectively. In figure 2, the magnitude of third harmonic shows a minimum as H_{dc} varies from zero to maximum

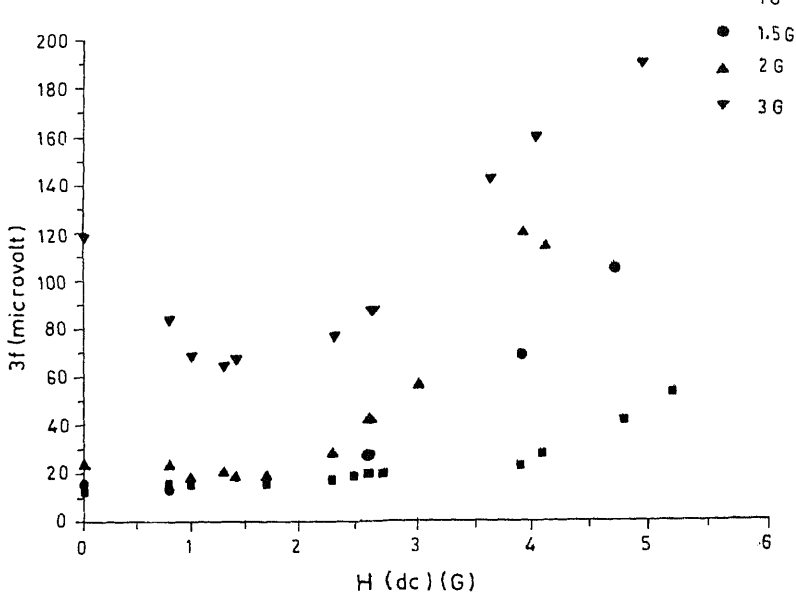

Figure 2. Third harmonic amplitude (3f) as a function of dc magnetic field, the ac field being fixed at 1, 1·5, 2 and 3 G for demagnetization factor $N_1 = 0{\cdot}745$.

value (5 G) at driving field $H_{ac} = 3$ G. But, at driving fields $H_{ac} = 1{\cdot}5$ and 1 G, the 3f signal increases monotonically on varying the dc bias from 0 to maximum value 5 G which is quite unusual. The observation of one minimum in 3f signal for $H = 3$ G is consistent with theory given by Ji *et al* [2] in which they have calculated that the magnitude of nth harmonic should show oscillatory behaviour with $(n-1)$ minima on varying the H_{dc} from $-H_{ac}$ to H_{ac}. This discussion is, however, valid only for $H_{ac} > H^*$, where H^* is the field for full penetration of the sample. In our observation of the M–H loops on this sample, the field for full penetration is about 2·0 G. The change in the oscillatory behaviour for demagnetization factor $N_1 = 0{\cdot}74$ shown in figure 2 appears to be at driving field at $H_{ac} = 2\,\text{G} = H^*$. For driving field $H_{ac} < H^*$, we observe a behaviour different from that predicted in ref. [2] in that 3f signal has only one minimum and that is at $H_{dc} = 0$. This is also seen from the calculation of ref. [4] when $H_{ac} \ll H^*$. The change in the oscillatory structure in 3f signal for demagnetization factors $N_2 = 0{\cdot}79$ and $N_3 = 0{\cdot}84$ is measured to be at field values $H = 1{\cdot}5$ and 1 G, as shown in figures 3 and 4 respectively. These results are new and call for further refinement in the existing theoretical models.

3.2 *Effect of geometry on the harmonics*

From figures 2 to 4, the change in oscillatory behaviour of 3f vs H_{dc} shifts to lower field values on increasing the demagnetization factor. This confirms the fact that on

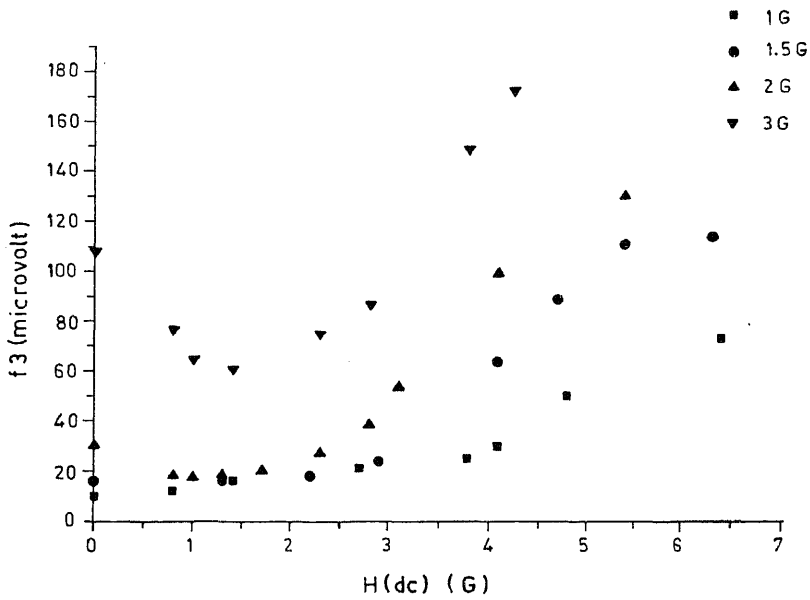

Figure 3. Third harmonic amplitude (3f) as a function of dc magnetic field, the ac field being fixed at 1, 1·5, 2 and 3 G for demagnetization factor $N_2 = 0{\cdot}792$.

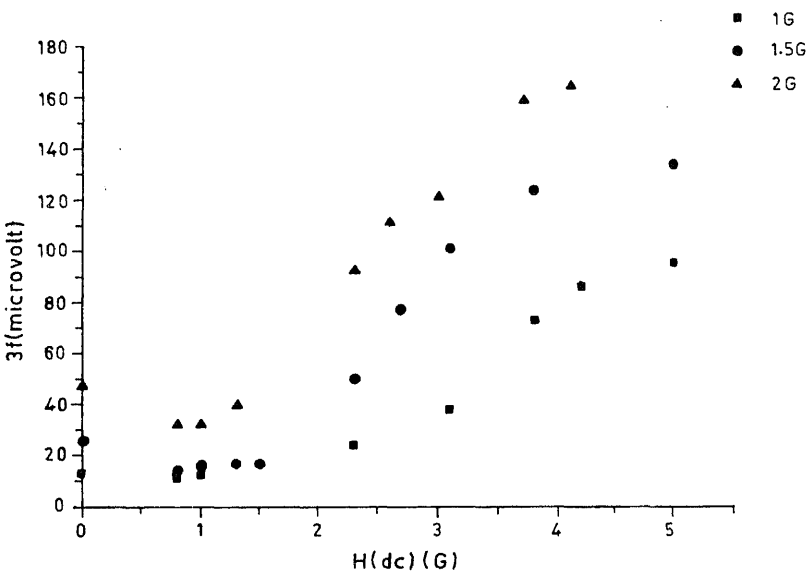

Figure 4. Third harmonic amplitude (3f) as a function of dc magnetic field, the ac field being fixed at 1, 1·5, and 2 G for demagnetization factor $N_3 = 0{\cdot}89$.

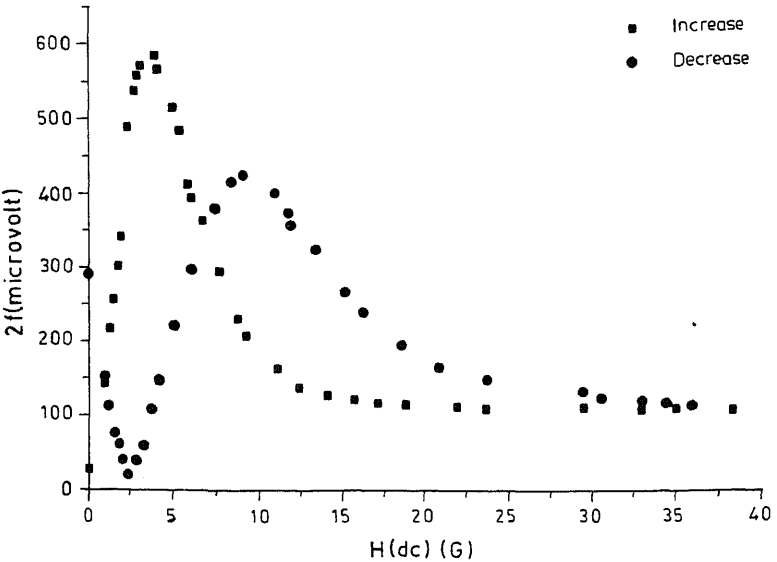

Figure 5. The hysteresis in the amplitude of second harmonic (2f) of a ZFC as function of H_{dc} raised to 39 G and lowered to zero value in $H_{ac} = 4$ demagnetization factor $N_1 = 0{\cdot}745$.

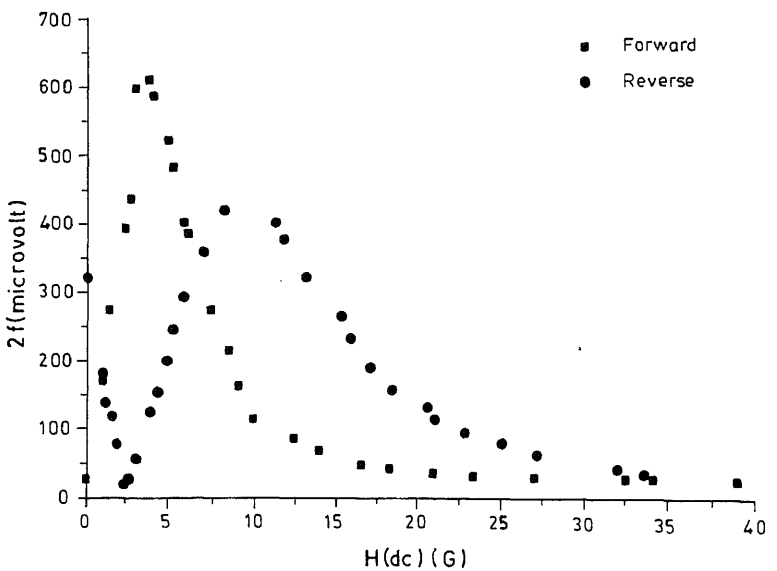

Figure 6. The hysteresis in the amplitude of second harmonic (2f) of a ZFC as function of H_{dc} raised to 39 G and lowered to zero value in $H_{ac} = 4$ demagnetization factor $N_2 = 0{\cdot}792$.

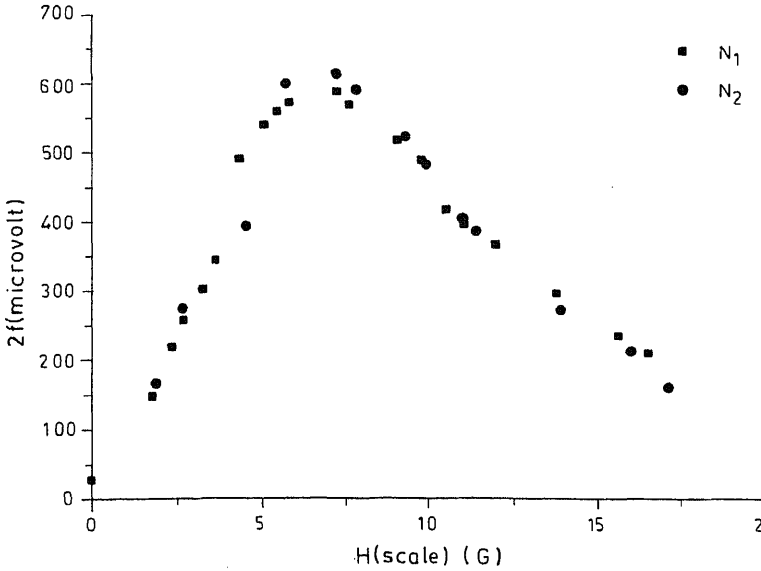

Figure 7. Unique functional dependence of amplitude of second harmonic a function of scaled field (H_{scl}). (■) curve denote scaling of applied fi demagnetization factor $N_1 = 0{\cdot}745$ and (●) curve signifies the scaling of fi demagnetization factor $N_2 = 0{\cdot}792$ for the unidirectional increase of the a field.

increasing the demagnetization factor, the effective field experienced b sample increases. The generation of even harmonics is the consequences field dependence of the critical current density [2–6]. The irreversible beha of the nonlinear response of the $YBa_2Cu_3O_{7-y}$ is attributed to the two ponent network of sample i.e. integrain and intragrain region. In figures 6, we observe that 2f signal shows a history effect with the applied ma field due to its ceramic nature [5,6] for demagnetization factors N_2 and $N_3 = 0{\cdot}79$. We have used a large ac field $H_{ac} = 4\,G$ and we observe a ficant difference in the amplitude and in the field dependence of 2f for di demagnetization factors.

However, scaling the applied field with the demagnetization factor H_s $\{1 - N(1 - V_f)\}$ [12], where N is demagnetization factor and V_f is ef volume of sample into which flux is able to penetrate. This scaling be useful once the flux starts penetrating the intergrain region and our eq. longer holds. We observe in figure 7 2f signal show a unique functional depe on scaled field for unidirectional increase in applied field and in figur unidirectional decrease in applied field, where following ref. [12], V_f is to be 0·4. Therefore, for quantitative measurement of critical current from magnetization studies, demagnetization correction is very important. Our show that when this is taken into account, a unique dependence on applied obtained.

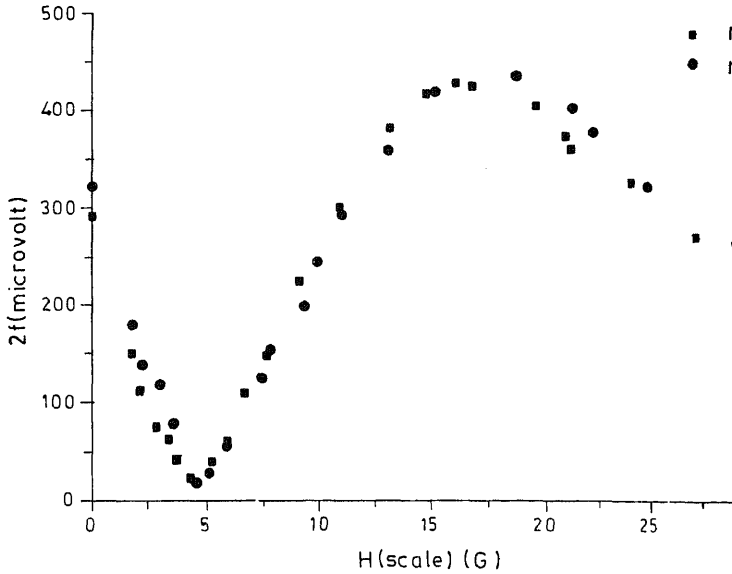

Figure 8. Unique functional dependence of amplitude of second harmo a function of scaled field (H_{scl}). (■) curve denote scaling of applied demagnetization factor $N_1 = 0{\cdot}745$ and (●) curve signifies the scaling o demagnetization factor $N_2 = 0{\cdot}792$ for the unidirectional decrease of th field.

4. Conclusion

In conclusion, we observed that the 3f shows consistent behaviour as theories p ac field $H_{ac} > H^*$. However at field smaller than H^*, 3f increases monotonicall field at which the shift in structure observed also decreases on thinning th progressively i.e. on increasing the demagnetization factor. We measured th cant difference in the second harmonics at different demagnetization facto sample. But, scaling the applied field with demagnetization factor and the tota experiencing the field, the 2f shows a unique field dependence.

Acknowledgements

One of us (PB) is thankful to CSIR, New Delhi for providing the financial su carrying out this work.

References

[1] C P Bean, *Rev. Mod. Phys.* **36**, 31 (1964)
[2] L Ji, R H Shon, G G Spalding, C J Lobb and M Tinkham, *Phys. Rev.* **B40**, 109
[3] R Navarro, F Lera, C Rillo and J Bartolomi, *Physica* **C167**, 127 (1989)
[4] P Chaddah, S B Roy, Shailendra Kumar and K V Bhagwat, *Phys. Rev.* **B46**, 11
[5] T Ishida and R B Goldfrab, *Phys. Rev.* **B41**, 9837 (1990)
[6] Shailendra Kumar, S B Roy, P Chaddah, Ram Prasad and N C Soni, *Phys* 450–459 (1990)

[7] S B Roy, Shailendra Kumar, P Chaddah, Ram Prasad and N C Soni, *Physica* **C198**, 383–388 (1990)
[8] S B Roy, Shailendra Kumar, A K Pradhan, P Chaddah, Ram Prasad and N C Soni, *Physica* **C218**, 476 (1994)
[9] Shailendra Kumar, S B Roy, A K Pradhan, P Chaddah, Ram Prasad and N C Soni, *J. Apl. Phys.* **73**, 1539 (1993)
[10] C Radhakrishnamurthy, S D Likhite and P W Sahasrabudhe, *Proc. Indian Acad. Sci.* **A87**, 245 (1978)
[11] A K Grover, C Radhakrishnamurthy, P Chaddah, G Ravi Kumar and G V Subba Rao, *Pramana – J. Phys.* **30**, 569 (1988)
[12] A M Campbell and F J Blunt, *Supercond. Sci. Tech.* **3**, 450–453 (1990)

Two photon absorption spectrum of *p*-dichlorobenzene

I B SINGH, S B RAI and D K RAI
Laser and Spectroscopy Laboratory, Department of Physics, Banaras Hindu University, Varanasi 221 005, India

MS received 28 November 1994; revised 23 May 1995

Abstract. Two photon absorption spectrum of *p*-dichlorobenzene has been studied in the spectral region 497–552 nm (one photon wavelength). Bands involving several frequencies of the excited electronic state not detected in the one photon absorption are seen. The observed two photon spectrum indicates that the electronic transition retains, to a large extent, the salient features of the two photon absorption spectrum of benzene and thus confirms chlorine as weak perturber (in the sense of Goodman and Rava [1]).

Keywords. Two photon absorption spectrum; *p*-dichlorobenzene; weak perturber; molecular spectra.

PACS No. 30·10

1. Introduction

Two photon absorption studies enable the observation of several features not accessible to direct observation in the usual one photon absorption spectrum [1]. Substituted benzenes, wherein one or more hydrogen atoms are replaced by other atoms or group of atoms, form a related class of molecules whose systematic study has led to a better understanding of many aspects of molecular spectra and hence such molecules have continued to draw the attention of molecular spectroscopist. Recently, we have reported an analysis of a part of the two photon electronic absorption spectrum of *o*-dichlorobenzene (ODCB) in the wavelength region 485–540 nm (one photon wavelength). In the present communication we report the results obtained in a similar study on *p*-dichlorobenzene (PDCB).

Earlier one photon absorption studies on PDCB have been carried out by Wollman [2] and by Conrad-Billroth [3] in the liquid phase and by Sponer [4], Joshi [5] and Anno and Matubara [6] in the vapour phase at low resolution. Rai [7] reported the one photon absorption spectrum of PDCB at a moderately high resolution which enabled him to identify several hitherto unobserved vibrational features. Even though two photon electronic absorption corresponding $^1B_{2u} \leftarrow {}^1A_{1g}$ transition of benzene has been investigated for several mono- and di-substituted benzenes (Goodman and his colleagues [1]), no work on dichlorobenzene has been reported prior to present study.

2. Experimental

The experimental set up used for recording the two photon spectrum of *p*-dichlorobenzene is essentially the same as described in our earlier paper [8]. In brief it consists of a pyrex cell 4 cm in diameter and 20 cm in length. A small bulb is attached in the middle of the tube to hold sample while the ends are closed with flat glass windows. An outlet is

also provided to connect a vacuum pump to create a proper vacuum in the cell. The electrodes are circular discs of stainless steel 1 cm in diameter and are mounted in the cell facing each other at a mutual separation of 1 cm. The electrodes are at a distance 5 cm from one of the windows. The experimental set up used is shown in figure 1.

A freshly purified sample of *p*-dichlorobenzene (reported purity 99·9%) is kept in the bulb of the cell which is dipped into a container of liquid nitrogen while the cell was evacuated to a residual gas pressure of approximately 10^{-2} torr. The liquid nitrogen container is then removed and the *p*-dichlorobenzene vapour fills the cell at a pressure appropriate to the ambient temperature. A DC voltage of 110–150 V was applied across the electrodes from a stabilized power supply (Bertan model No. 205A-O1R). The laser radiation from a dye laser (Quanta Ray model PDL-2 with coumarine 500 dye) pumped by the third harmonic of a Nd:YAG laser (Quanta Ray model DCR-2) was focused at a spot between the two electrodes with the help of a 5 cm focal length convergent lens. The repetition rate of the laser was 10 Hz and pulse width of the dye laser was ~ 7 ns. The dye laser peak output power at 510 nm was 10 mJ/pulse.

Under conditions of tight focusing, the photon density in the region becomes large enough to cause multiphoton absorption. Since the wavelength of the dye laser is appropriate for two photon absorption to the lowest lying singlet excited state of *p*-dichlorobenzene a substantial fraction of these molecules are excited to the excited state. Such excited molecules can be ionized by the absorption of an additional photon resulting in the creation of electron ion pairs. These ions and electrons are collected at the respective electrodes and give rise to an ionization signal. The A.C. signal thus generated was filtered from D.C. by using a capacitance resistance combination. The signal thus obtained is processed through a boxcar averager (EG and G model 164) with a gate width of 5 ns. The bias voltage, laser power and the focusing of the lens were adjusted so that the signal for one of the absorption peaks (near the middle of the tuning

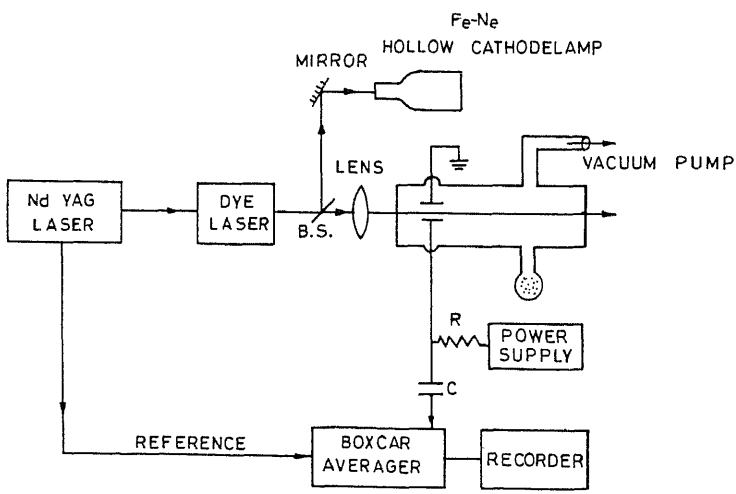

Figure 1. Experimental set up used for recording the two photon absorption spectrum of *p*-dichlorobenzene.

range) was optimum. The resulting absorption spectrum was then recorded with a double pen recorder. The resolution achieved in the experiment is 1–2 cm^{-1}. A small part of the dye laser beam was sent into a Fe–Ne hollow cathode lamp and the optogalvanic signal of Ne was used to provide standard lines for wavelength calibration of the spectrum. A part of the spectrum along with noise level is shown in figure 2. The measured wavelengths, the frequencies and the relative intensities of the various bands are listed in table 1. We also monitored the signal by varying the laser power. It is marked that the signal is varying linearly with the square of the laser power. This clearly indicates that the signal is due to simultaneous absorption of two photons.

3. Results

The reduced point group symmetry D_{2h} of PDCB results in the transition analogous to the $^1B_{2u} \leftarrow {}^1A_{1g}$ transition of benzene becoming an allowed transition. This results in the appearance of a strong (O–O) band along with intense bands involving the totally symmetric vibrations, namely 1, 2, 6a, 8a and 9a (in Wilson notation). The one photon absorption spectrum of PDCB vapour analyzed by Anno and Matubara [6], Joshi [5] and Rai [7] clearly demonstrates the correctness of this interpretation. The origin band as identified by these authors is at 35742 cm^{-1}. Since the longest wavelength available with the present dye is 552·0 nm, we could not observe bands with energy less than 36240 cm^{-1} and we have taken the value reported by Rai [7] for the position of the (O–O) band.

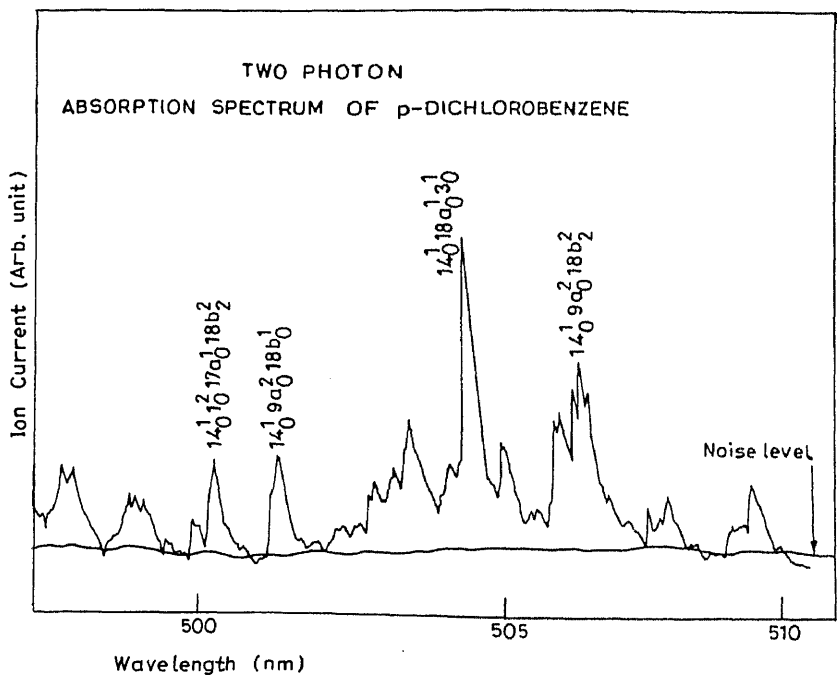

Figure 2a. A part of the two photon absorption spectrum of *p*-dichlorobenzene.

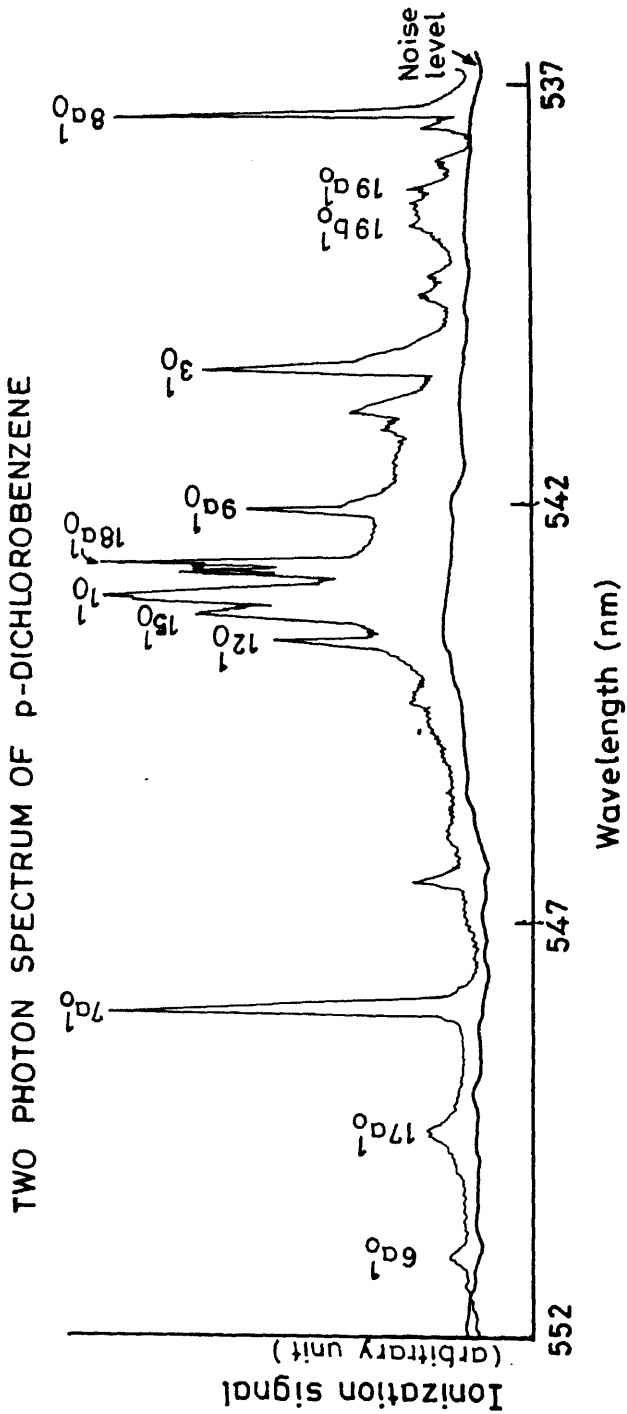

Figure 2b. A part of the two photon absorption spectrum of *p*-dichlorobenzene.

Table 1. Prominent two photon bands in *p*-dichlorobenzene and their assignment.

Wavelength of the bands (Å)	2ν in cm^{-1}	$\Delta\nu$ in cm^{-1}	Intensity	Assignment
5512·6	36280	538	W	$6a_0^1$
5499·6	36366	624	W	$17a_0^1$
5482·7	36478	736	VS	$7a_0^1$
5469·5	36566	824	MW	$17a_0^1 17b_0^1 6a_1^1$
5440·5	36761	1019	MS	$12a_0^1$
5436·9	36785	1043	MS	15_0^1
5436·2	36790	1048	VS	1_0^1
5433·0	36803	1061	S	$9a_0^1$
5432·7	36814	1072	VS	$18a_0^1$
5426·2	36858	1116	MS	$6a_0^1 17a_0^1$
5414·7	36936	1194	M	$7a_0^1 16b_0^1$
5409·7	36970	1228	S	3_0^1
5401·9	37024	1282	W	$7a_0^1 6b_0^1$
5399·4	37082	1340	W	$19b_0^1$
5389·8	37107	1365	W	$19a_0^1$
5381·4	37165	1423	VS	$8a_0^1$
5358·3	37325	1583	VS	14_0^1
5309·8	37666	1924	W	$14_0^1 18b_0^1$
5254·2	38064	2322	W	$14_0^1 7a_0^1$
5224·8	38278	2536	M	$14_0^1 18b_0^1 17a_0^1$
5174·7	38651	2909	W	$9a_0^2 7a_0^1 18b_1^1$
5141·5	38898	3156	S	$14_0^1 1_0^1 6a_0^1$
5128·1	39000	3258	M	$14_0^1 19a_0^1 18b_0^1$
5115·7	39095	3353	M	$14_0^1 1_0^1 7a_0^1$
5097·1	39237	3495	MS	$14_0^1 7a_0^2 16b_0^1$
5081·9	39355	3613	W	$14_0^1 1_0^1 10b_1^1$
5078·0	39385	3643	W	$14_0^1 1_0^2 6a_1^1$
5066·2	39477	3735	S	$14_0^1 9a_0^2 18b_2^2$
5052·1	39588	3846	M	$7a_0^2 19b_0^1 6a_0^2$
5048·7	39614	3872	S	$14_0^1 18a_0^1 3_0^1$
5038·2	39696	3954	MS	$14_0^1 9a_0^2 17b_0^2 10b_1^1$
5016·5	39868	4127	MS	$14_0^1 9a_0^2 18b_0^1$
5005·2	39958	4216	M	$14_0^1 1_0^2 17a_0^1 18b_2^2$
4990·0	40079	4337	MW	$14_0^1 9a_0^2 6a_0^1$
4977·5	40180	4438	MW	$14_0^1 9a_0^2 7a_0^1 10b_1^1$

It is well-known that in the corresponding transition in benzene vapour the longest wavelength band observed at the lowest temperature is the one involving the excitation of one quantum of a C–C–C in-plane bending vibration of e_{2g} symmetry. The ground state magnitude of this frequency is 608 cm^{-1} (mode 6a in Wilson notation) while the excited ($^1B_{2u}$) state magnitude is 538 cm^{-1}. This vibration is not expected to change drastically when some of the hydrogen atoms in benzene are replaced by chlorine atoms as in PDCB. Moreover, though the transition is now electronically allowed the charge cloud of the molecule does retain to a great extent the same features as in benzene so that the excitation of a single quantum of this vibration could be expected to give rise to a false origin and band structure loaded on to it. This is actually observed.

The weak band at a separation of 538 cm^{-1} (on the shorter wavelength side) from the (O–O) band is ascribed to the excitation $6a_0^1$. This mode is the Raman active component of the above mentioned e_{2g} vibration of benzene. The other component of this doubly degenerate vibration (in benzene) is seen as another weak band at a separation of 624 cm^{-1} from the (O–O) band. This is ascribed to the 17a mode and is infrared active.

A relatively intense band is seen at $0 + 736\ cm^{-1}$. This frequency is ascribed to the 7a mode involving the C–Cl stretching. The corresponding frequency (748 cm^{-1}) in the ground state of the molecule is seen prominently in Raman spectrum.

A group of five bands is seen at 36761, 36785, 36790, 36803 and 36814 cm^{-1} with separation from the O–O band of 1019, 1043, 1048, 1061 and 1072 cm^{-1}, respectively. The bands are assigned as $0 + 12_0^1$, $0 + 15_0^1$, $0 + 1_0^1$, $0 + 9a_0^1$ and $0 + 18a_0^1$. Of these the bands at a separation of 1048 cm^{-1} is the most prominent and is ascribed to the excitation of the totally symmetric ring breathing frequency (some of these bands may also involve sequence bands buried under the succeeding bands).

The band observed at 37325 cm^{-1} has the largest intensity in the whole spectrum. Its separation from the O–O band is 1583 cm^{-1}. This frequency is one of the characteristic features in the two photon spectrum of benzene derivatives and is assigned as 14_0^1. It is due to C–C stretching vibration. This frequency being the most active is involved in a large number of bands, in combination with several other frequencies, which dominate the whole structure. Some of the strong combination bands where this ν_{14} fundamental is involved are $14_0^1 1_0^1 6a_0^1$ at 38898 cm^{-1}, $14_0^1 9a_0^1 18b_0^1$ at 39477 cm^{-1} $14_0^1 18_0^1 3_0^1$ at 39614 cm^{-1} etc. Some other fundamental vibrations which appear with slightly lower intensity have the magnitude 1228 cm^{-1}, 1340 cm^{-1}, 1365 cm^{-1} and 1427 cm^{-1}. These bands are assigned to 3_0^1 (of b_{3g} species), $19a_0^1$ (of b_{2u} species), $19b_0^1$ (of

Table 2. Intensity of different vibrations with respect to ν_{14} in *o*- and *p*-dichlorobenzenes.

Vibration ν_x	ODCB Molecule $I(\nu_x)/I(\nu_{14})$	PDCB Molecule $I(\nu_x)/I(\nu_{14})$
7a	1/6	1/2·2
18a	1/2·5	1/2·2
1	1/2·5	1/2·2
12	1/6	1/4

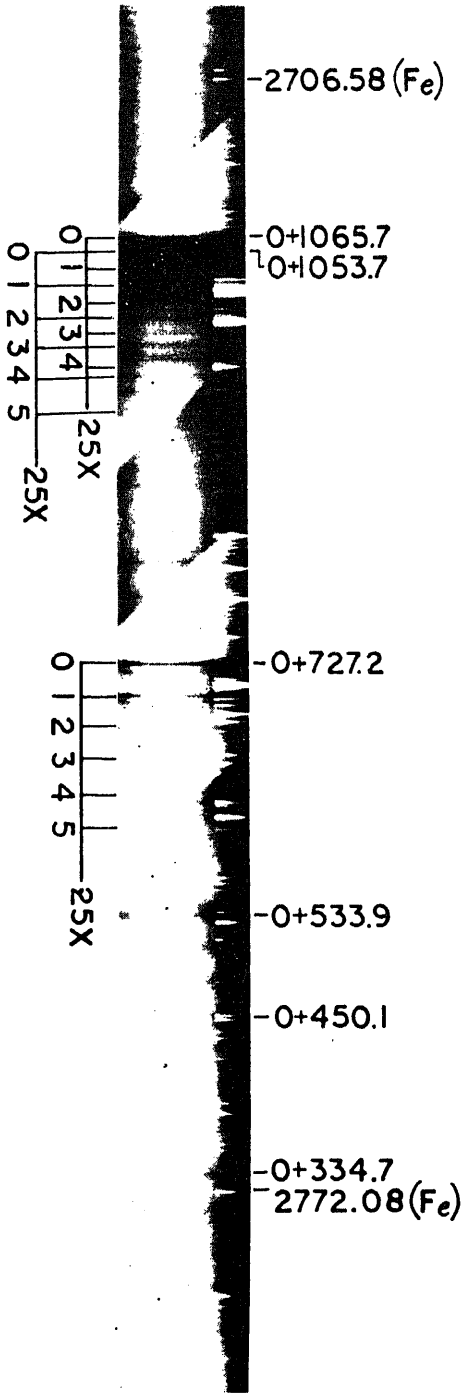

Figure 3. A part of the one photon absorption spectrum of *p*-dichlorobenzene

b_{1u} species) and $8a_0^1$ (of a_g species) modes respectively. Sequence bands are seen to accompany several of the main bands with separation -26, -31 and $-86\,cm^{-1}$. Table 1 gives the complete assignment of the observed bands. Some of the bands appear prominently in the two photon spectra of *o*- as well as in *p*-dichlorobenzene. The intensities of these bands with respect to ν_{14} in the two molecules are compared in table 2.

We have also compared our two photon spectrum with one photon spectrum reported by Rai [7]. A part of the one photon spectrum is also given in figure 3. Some of the prominent bands observed in our two photon spectrum (viz. $O_0^0 + 1061\,cm^{-1}$; $O_0^0 + 1048\,cm^{-1}$, $O_0^0 + 736\,cm^{-1}$, $O_0^0 + 538\,cm^{-1}$ etc) are clearly seen in one photon spectrum also.

Acknowledgement

Authors are grateful to CSIR for financial assistance.

References

[1a] L Goodman and R P Rava, *Adv. Chem. Phys.* **54**, 177 (1983)
[1b] L Goodman and R P Rava, *J. Chem. Phys.* **74**, 4826 (1981)
[2] W Wollman, (Unpublished work quoted in reference 5)
[3] H Conrad Billroth, *Z. Phys. Chem.* **1319**, 76 (1932)
[4a] H Sponer, *Rev. Mod. Phys.* **14**, 224 (1942)
[4b] H Sponer and J S Kirby Smith, *J. Chem. Phys.* **9**, 667 (1941)
[5] B D Joshi, *J. Sci. Res.* **6**, 133 (1955–56)
[6] T Anno and I Matubara, *J. Chem. Phys.* **23**, 796 (1955)
[7] J N Rai, Ph D thesis, Banaras Hindu University, India, (1967)
[8] I B Singh, S B Rai and D K Rai, *J. Mol. Spectrosc.* **163**, 364 (1994)

PRAMANA
— journal of
physics

© Printed in India

Vol. 45, No. 3,
September 1995
pp. 279–290

Picosecond time-resolved laser emission of coumarin 102: Solvent relaxation

S R INAMDAR, K CHANDRASEKHAR, D C PATIL, N N MATH and M I SAVADATTI*
Laser Spectroscopy (DRDO/KU), Department of Physics, Karnatak University, Dharwad 580003, India
*Mangalore University, Mangalore 574199, India

MS received 25 October 1994; revised 19 June 1995

Abstract. The time-resolved laser emission of coumarin 102 was investigated in various aprotic and protic solvents at picosecond resolution by frequency upconversion technique. The spectral shift of the transient emission spectrum is attributed to solvent reorientation and the results are discussed.

Keywords. Frequency upconversion; phase matching; solvent-relaxation.

PACS Nos 33·80; 42·65; 78·47

1. Introduction

Following the original experiment of Halliday and Topp [1], the frequency conversion technique has been applied by a number of workers to the investigation of charge transfer processes, energy transfer processes, isomerization reactions, vibrational relaxations and solvent relaxations [2]. As demonstrated by Moore *et al* [3] the use of multichannel detection with upconversion technique can provide more spectral information which cannot be obtained by other standard techniques such as streak camera and time correlated single photon-counting. This technique is attractive because the time-resolution achievable by this method is determined solely by the duration of the excitation pulse and not by the sample lifetimes and also the upconverted emission is free from background noise. As a part of our programme on picosecond processes in aminocoumarins, we present the preliminary investigation of solvation dynamics in protic and aprotic solvents using C 102 as a probe molecule and the frequency upconversion technique developed in our laboratory. Although the experimental and theoretical studies in solvation dynamics in solution has undergone a dramatic revolution in the past decade, yet the situation is not very clear as witnessed by discrepancies between theoretical and experimental results [4, 5].

When a molecule is excited to higher electronic state, several processes compete to deactivate the excited state during its lifetime. These processes can arise from either Franck–Condon state or relaxed excited state. The evolution of the excited state is controlled by the relative rates of different deactivation processes. The main processes which usually compete with the radiative deactivation of Franck–Condon excited state are vibrational relaxation, solvent relaxation, formation of charge transfer complexes, isomerization, energy transfer between like molecules and intersystem crossing (ISC) to the triplet state. For large molecules such as C 102, we expect

vibrational relaxation in S_1 state to be a very fast process which escapes our instrumental resolution. For coumarins, the ISC yields by triplet counting technique have been reported to be less than 0·05 for ethanol [6] at room temperature. The rate constant for ISC calculated using $\tau(S_1) = 4{\cdot}36$ ns is so low that the process takes place on a time scale much longer than the time delay. Intermolecular energy transfer processes between like molecules via Forster mechanism are relatively fast at high concentrations and slow at normal concentrations. In the present system this process was minimized by keeping the concentration of the solute at 1×10^{-3} mol dm^{-3}. Our probe molecule is a rigid one and structural considerations show that isomerization is quite unlikely. Although, discrete charge transfer complex via hydrogen transfer has been reported for C 102 in water [7], protonation of C 102 is not possible in protic and aprotic solvents. Our previous studies [8] have shown that dipole moment of C 102 changes from 5·016 D to 6·849 D upon excitation from S_0 to S_1 state. Also, our luminescence studies of C 102 as function of temperature reveals that the fluorescence of C 102 at room temperature (293 K) occurs at longer wavelength ($\lambda_{max} = 468$ nm) than the one obtained at 77 K ($\lambda_{max} = 456$ nm). There is no broadening of the emission at intermediate temperatures and no spectral shift is observed below 77 K (figure 1). Such characteristics of dye solution are generally the reflections of solvent-relaxation [9].

Immediately after laser excitation, the probe molecule will be in a 'Franck–Condon' (FC) excited state (a transitory excited state), possessing an altered electron distribution

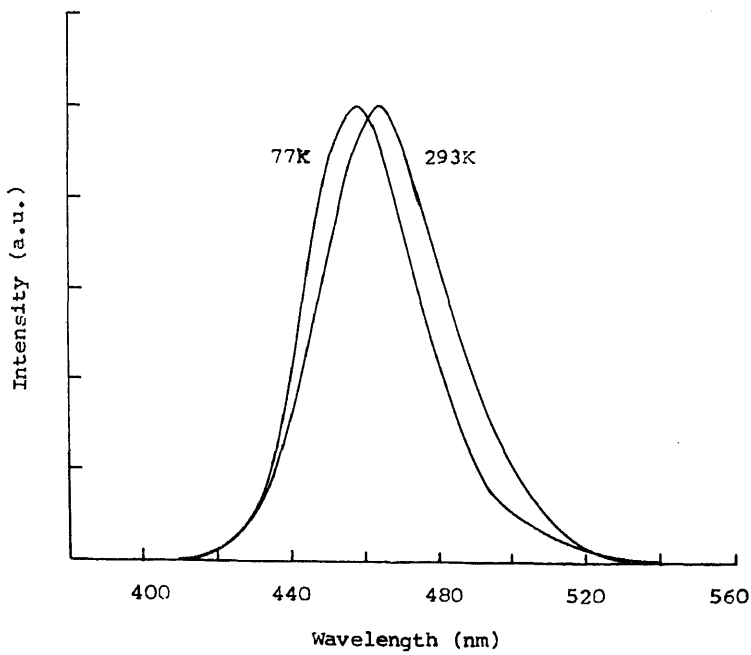

Figure 1. Normalized fluorescence spectra of C 102 (1×10^{-3} mol dm^{-3}) at 77 K and 293 K.

but the ground state geometry. The excited molecule is initially surrounded by equilibrium ground state solvent cage. During the lifetime of the excited state (S_1), the solvent cage adopts orientation consistent with the new excited state charge distribution of the probe molecule. As the solvent orientation changes continuously with time, the energy of the solute-solvent configuration changes correspondingly leading to the time-dependent spectral shift in the emission peak of the probe molecule. The solvation dynamics of C102 in non-associating solvents such as acetonitrile has been investigated earlier by Kahlow *et al* [10] from sub-picosecond fluorescence spectroscopy and the measured solvent-relaxation time was reported to be 0·9 ps. However, the time scale of solvation process at room temperature is expected to be in the picosecond domain for the associating solvents such as alcohols. In the present work, we focus our attention on the measurements of time-dependent superradiant laser emission on picosecond time scale in both polar aprotic and protic (alcohols) solvents to evaluate solvent-relaxation and compare its time scale relative to orientational relaxation time of solute molecule determined previously [8] in the ps time domain. The superradiant laser emission is nothing but amplified spontaneous emission (ASE) which shortens the S_1 state lifetime from τ_f to τ_{ASE}. According to the relation derived by Penzkofer and Blau [11] for the ratio of these two lifetimes, for a given dye, the lifetime of S_1 in the presence of ASE can be altered by suitably adjusting the solid angle of effective ASE and the position of maximum gain. Therefore, when the conversion efficiency of the mixing crystal is very poor to upconvert the fluorescence, one can use the superradiant emission as a probe by adjusting the excitation conditions properly. This study is also important in view of the current interest [12] on the influence of rotational motions of solvent and probe molecules on the dye laser performance.

2. Theoretical description

When two optical fields of frequencies ω_1 and ω_2 are mixed in a phase matched non-linear crystal, the output optical field with frequencies $\omega_1 + \omega_2$ and $\omega_1 - \omega_2$ is generated. The time-resolved spectra can be measured at a given time after excitation either by tuning the laser frequency or by tuning the crystal at a fixed laser frequency to select the fluorescence wavelength. The phase matching condition for frequency conversion is that $k_3 = k_1 + k_2$, where k_1, k_2 and k_3 are the fluorescence, gating laser and output signal wave vectors, respectively. The conversion efficiency of the crystal is proportional to the intensity of the gating pulse:

$$\frac{I(\omega_1 + \omega_2)}{I(\omega_1)} \propto I(\omega_2). \tag{1}$$

The instantaneous power of the sum-frequency in a crystal of length L is given approximately by [13]

$$P_\omega(L) = L^2 P_1 P_2 \omega_3/\omega_1 \tag{2}$$

where subscripts on the frequency ω and the power/unit area P refer to the fluorescence, gating pulse, and the sum-frequency respectively. If the power of the laser remains constant to within a few per cent, the upconverted signal at a particular delay is proportional to the fluorescence intensity.

3. Experimental

The schematic of the upconversion experiment is shown in figure 2. The laser system was passively and actively mode-locked Nd:YAG laser (Continuum, USA) which provided 1064 nm pulse of 35 ps duration at a repetition rate of 10 Hz with energy of 70 mJ. It was frequency doubled to 532 nm in a KDP crystal. Subsequently, mixing up of 1064 nm and 532 nm lights in another KDP crystal provided a sum-frequency at 355 nm (35 ps, 15 mJ).

The solutions of C 102 (Eastman Kodak and Exciton, USA) prepared at 1×10^{-3} mol dm^{-3} in various solvents were contained in a 10 mm pathlength quartz cell and excited by a 355 nm pulse. The unwanted feedback from the cell walls was avoided by careful alignment of the pump beam and the cell. A typical dye laser output for ethanolic solution of C 102 had nearly 5 mrad divergence and bandwidth of 13 nm (fwhm) as compared with 43 nm (fwhm) for fluorescence (figure 3). The thermal effects in the solution were minimized by circulating the dye solution. The superradiant laser emission collected by the lens was focussed onto the KDP type II crystal (4 mm path length) where it was mixed collinearly with the 1064 nm gating pulse. Our attempts to upconvert the fluorescence were in vain probably due to low conversion efficiency of the crystal used. The arrival time of the excitation pulse on the mixing crystal was controlled by adjusting the distance travelled by pump pulse using variable optical delay. By angle-tuning the crystal and adjusting the relative convergence of the input pulses in the crystal, we were able to upconvert the laser emission from 455–485 nm (spectral coverage: 30 nm; fwhm: 13 nm) to 318–333 nm (spectral coverage: 15 nm; fwhm: 5 nm). In addition to the upconverted signal, the output from the crystal consisted of the fundamental and its second harmonic which were cut off by using appropriate filters.

The upconverted signal was collected by the optical fibre and measured with a 0·5 m polychromator (Spectroscopy Instruments, Germany, 600 g/mm) and double intensified photodiode array which were controlled by a microcomputer. The signal was recorded as a function of delay. The spectral data were averaged over multiple measurements. The time-resolved spectra were obtained with no/little distortion.

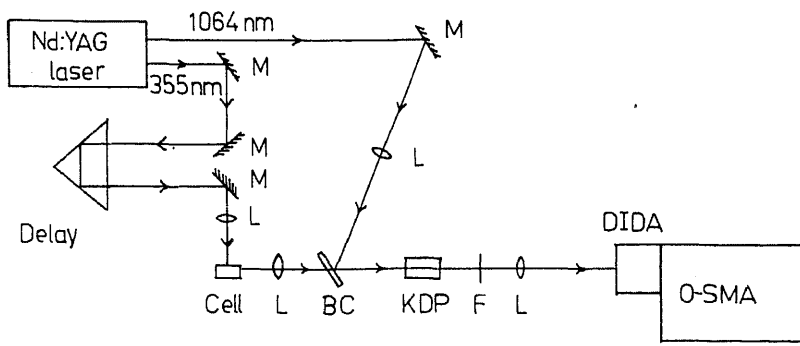

Figure 2. Schematic of upconversion experiment:
M: Mirror; L: Lens; BC: Beam combiner; F: Filter.

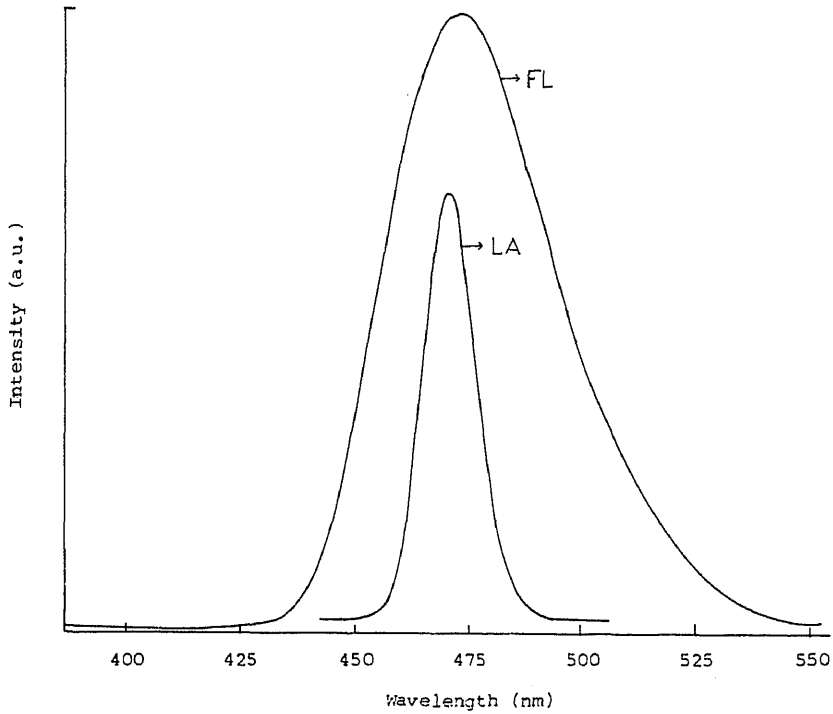

Figure 3. Static fluorescence (FL) and dye laser spectra (LA) of C 102 in ethanol at 1×10^{-3} Mol dm^{-3}

Absorption spectra at various concentrations for all the solvents were recorded using Hitachi (Model 3200) UV/Vis spectrophotometer and steady-state fluorescence emissions were measured using a 400 Watt Hg lamp, a scanning monochromator (Oriel), a photomultiplier (RCA 931A) and an X-Y recorder (Riken Denshi). Low temperature luminescence studies were made using closed cycle refrigerator (RMC Cryosystems, USA).

4. Results and discussion

Steady-state spectral characteristics of C 102 in various solvents at optimum concentrations along with the properties of the solvents are shown in table 1. We find that compared to dioxane solution, all other selected solutions exhibit red-shift both in absorption and fluorescence maxima which correlate reasonably with solvent polarity calculated according to Lippert [14]. Such spectral shifts are generally the reflections of solute-solvent interactions which may be of general or specific type such as hydrogen bonding. The C 102 is a planar molecule in the ground state and its dipole moment as stated earlier changes after excitation, indicating that C 102 should be solvated relatively larger in S_1 compared to ground state. In the general type of solvent effect, the Stokes shift depends on dielectric constant and refractive index of solvents, while

specific effects are associated with n-donor, π-donor and hydrogen bonding abilities of the solvents. For polar solutes like C 102, the interaction with non-polar solvents like dioxane depends on the dipole-induced-dipole forces, while with aprotic (polar but non-hydrogen bonding) solvents, the solute-solvent interaction depends on the stronger dipole-dipole forces. In protic solvents (alcohols), in addition to dipole-dipole

Table 1. Steady-state absorption and fluorescence characteristics of C 102 in various solvents and calculated values of polarity functions of solvents using Lippert's expression (1957).

Solvent	Dielectric constant (ε)	Refractive index (n)	Solvent polarity* (Δf)	λ_{ab} nm	λ_{fl} nm
Dioxane	02·21	1·4200	0·0215	372	427
DMSO	48·90	1·4770	0·2645	380	440
Acetonitrile	38·80	1·3442	0·3053	382	441
DMF	37·06	1·4305	0·2746	384	443
Ethanol	23·40	1·3611	0·2885	388	463
Methanol	32·04	1·3288	0·3080	391	471

*$\Delta f = (\varepsilon - 1)/(2\varepsilon + 1) - (n^2 - 1)/(2n^2 + 1)$

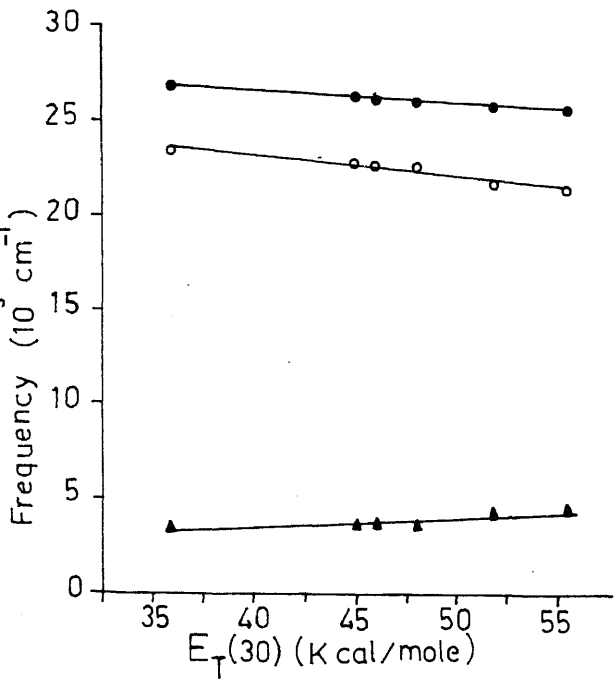

Figure 4. Absorption maxima (●), Static emission maxima (○) and Stokes shift (▲) as a function of E_T (30).

interaction, specific interaction such as H-bonding may be effective as the intramolecular charge transfer (ICT) character of C 102 is favourable for H-bonding with hydroxy group in alcohols. The dependence of Stokes shift, $\nu_a - \nu_f$ (cm^{-1}), on solvent polarity accordng to Lippert's expression seems to be less regular within polar solvents. This trend may perhaps be due to the fact that the Lippert's relation ignores the molecular aspect of solvation. It is therefore useful as pointed out by others also [15, 10] to use E_T (30) function, the empirical measure of solvent polarity [16] for understanding the polarization dependence of spectral characteristics. Figure 3 shows the steady-state absorption and emission maxima and Stokes shift as a function of E_T (30). As seen from figure 4, the absorption and static emission maxima are linearly related to E_T (30), the slope of the plot for emission being greater than that for absorption, implying that the solvation in S_1 is consistent with the finding that $\mu_e > \mu_g$. The linear E_T(30) dependence of Stokes shift indicates the existence of general type of solute-solvent interaction.

Transient emission spectra recorded in protic solvents (ethanol and n-butanol) were found to be red-shifted almost continuously on longer time scales available with the set up, while in aprotic solvents (AN and DMSO), the shift though being continuous is

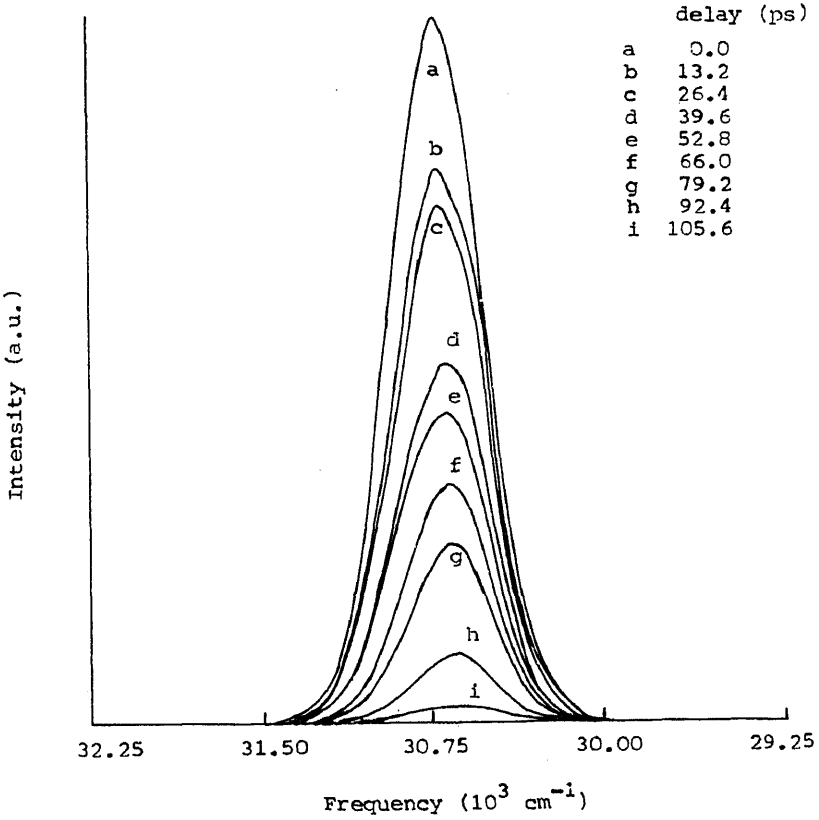

Figure 5. Time resolved spectra of C 102 at 20 °C.

complete at early times (nearly 45 ps), indicating that solvent relaxation in aprotic solvents is very fast and falls within the time-resolution of the instrument. The observed continuous red-shift can be ascribed to a continuously evolving solvent-relaxation. The FC (S_1) state is a quasi-continuum state consisting of discrete orientational levels corresponding to solute-solvent configurations. The transient spectra thus correspond to an elementary emission (almost continuous) originating from all possible orientational levels located between non-relaxed FC state and equilibrated excited state. Typical time-resolved spectra for ethanolic solutions is given in figure 5. The temporal profiles obtained from plots of intensity of the upconverted signal versus time (figure 6) yielded 1/e times (τ_{ASE}) of 45 ps and 60 ps respectively for n-butanol and ethanol which were found to be independent of wavelength. Consequently, the transient solvation phenomena is not apparent in the intensity decay profiles. The wavelength independence of decay in the present time-resolved experiment may be due to the narrow spectral coverage of the upconverted signal. Such a behaviour has been reported earlier [17]. For AN and DMSO the decay falls within the time response of the system. The τ_{ASE} values correspond to reduced lifetimes of S_1 state by amplified spontaneous emission via stimulated emission. Since lifetimes of S_1 are very much reduced, we believe that other non-radiative process probably that involving rearrangement of solute molecules hindered by solvent may be operative since these lifetimes approximately correlate with the viscosity of the solvent. During the course of solvation the degree of charge transfer in S_1 state may change continuously and the interconversion

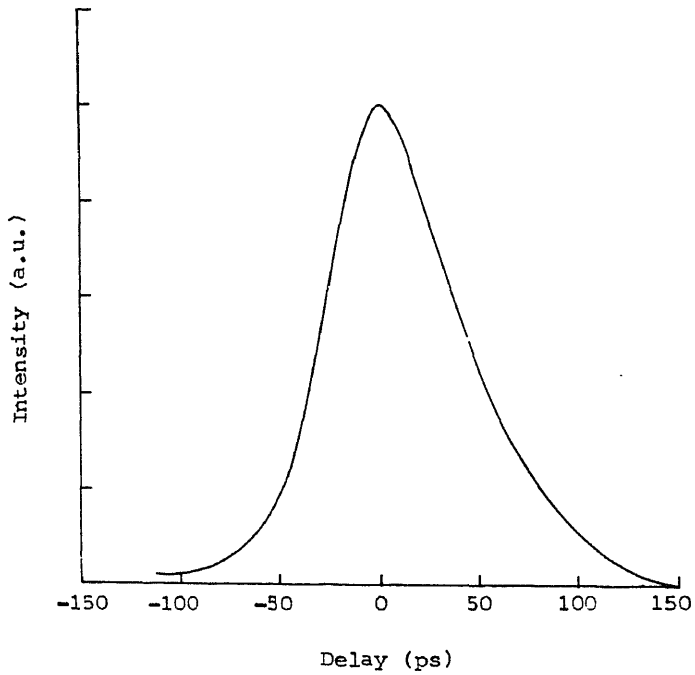

Figure 6. Decay profile of the upconverted signal of C 102 in ethanol

kinetics of charge transfer transient species is modulated by solvent motion. We also notice that these lifetimes are in reasonable agreement with τ_S values derived from Stokes shift correlation functions. However, it is important to note that τ_{ASE} obtained from $I(t)$ decay curve is concentration dependent while τ_S derived from $C(t)$ decay curve is concentration independent.

Solvation dynamics in polar liquids with a variety of probe/solvents combinations have been examined by different workers to experimentally verify the prediction, from dielectric continuum theory [18, 19] that the solvent orientational relaxation time, τ_S, as measured by the fluorescence spectral shift of a probe solute, should proceed exponentially in time equal to solvent's longitudinal relaxation time, τ_l, defined as

$$\tau_l = (\varepsilon_\infty/\varepsilon_0)\tau_d \tag{3}$$

where ε_∞ and ε_0 are infinite frequency and static dielectric constants, respectively and τ_d is the bulk dielectric relaxation time. The time evolution of the solvent-relaxation is usually quantified by the correlation function $C(t)$ [20] defined as

$$C(t) = \frac{\nu_{max}(t) - \nu_{max}(\infty)}{\nu_{max}(0) - \nu_{max}(\infty)} \tag{4}$$

in which $\nu_{max}(0)$, $\nu_{max}(\infty)$ and $\nu_{max}(t)$ are the optical frequencies that correspond respectively, to the wavelength maxima of emission spectrum of the probe at times zero, infinity (when the solute solvent system is at equilibrium), and at intermediate time t (during the relaxation). In the absence of specific interactions $C(t)$ provides a solute-independent measure of solvation dynamics as described by Castener and Fleming [19]. If the solvent orientation is described by continuum model, $C(t) = \exp(-t/\tau_S)$, i.e., $C(t)$ decays exponentially with a time constant equal to τ_S.

For extracting accurate $C(t)$ functions one should use the correct shapes of the transient emission spectra and the peak frequencies. The description of the method of analysis has appeared in many references [15, 10, 19]. The method of measurement in the present system was simplified by measuring the peak frequencies $\nu(t)$ directly from the normalized transient spectra (figure 7) and $\nu(\infty)$ was taken to be the limiting frequency beyond which spectral shift did not occur. Typical normalized time evolving spectra for ethanolic solutions is displayed in figure 6. In case of alcohols, $C(t)$ functions determined from relation (4) were found to decay non-exponentially. Nevertheless, the decays were fitted well by a single exponential dependency with time constants of $\tau_S = 55$ ps for ethanol and 65 ps for n-butanol (figure 8). In order to test the validity of dielectric continuum model (DCM) the longitudinal relaxation times from relation (3) were calculated using the available dielectric parameters at 293 K [$\varepsilon_0 = 26{\cdot}00$; $\varepsilon_\infty = 1{\cdot}85$; $\tau_d = 130$ ps, $n_0 = 1{\cdot}359$ for ethanol [21], $\varepsilon_0 = 17{\cdot}8$; $\varepsilon_\infty = 3{\cdot}5$; $\tau_d = 613$ ps, $n_0 = 1{\cdot}399$ for n-butanol [19] and the values are collected in table 2. In case of n-butanol agreement between τ_S (65 ps) and τ_l (110 ps) is sensible, while in case of ethanol τ_S (55 ps) is about six times greater than τ_l (9 ps) are agrees with the value of $\tau_S = 40$ ps reported earlier by Struve *et al* [22] who used DMABN as a probe molecule. As argued by Sumi and Marcus [23] the better relation for evaluating the longitudinal relaxation time for alcohols should be $\tau_l = (n_0^2/\varepsilon_0)\tau_d$ where n_0 is the refractive index of the solvent and this relation yields $\tau_l = 65$ ps which is in excellent agreement with our experimental value. Interestingly, our experimental value of τ_S is in close agreement

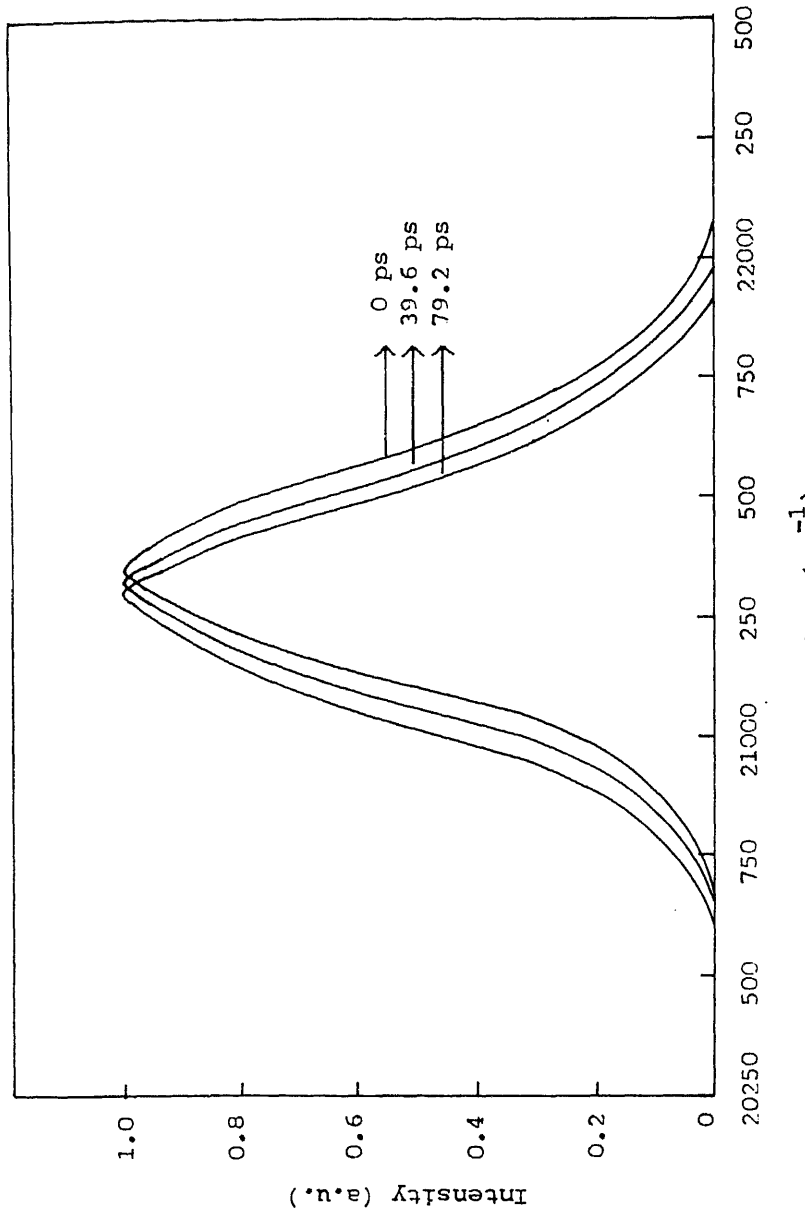

Figure 7. Normalized time-evolving spectra of C 102 in ethanol.

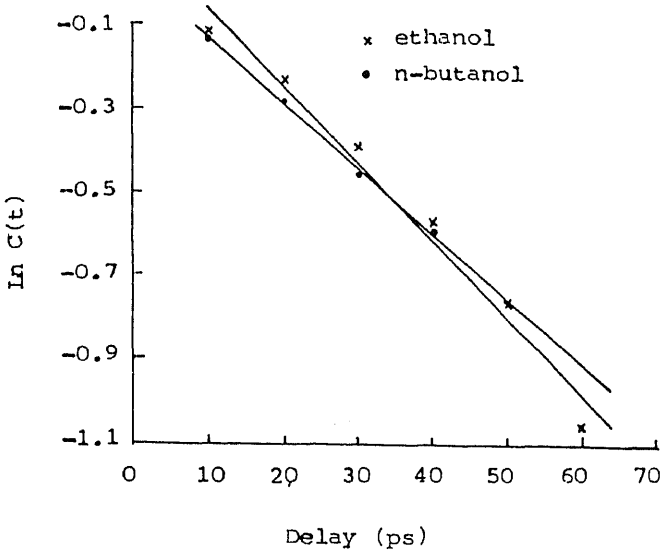

Figure 8. Stokes shift correlation function $C(t)$ for ethanol and n-butanol.

Table 2. Dielectric parameters and solvation times.

Solvent	τ_d (ps)	$\tau_l = (\varepsilon_\infty/\varepsilon_0)\tau_d$ (ps)	$\tau_l = (n_0^2/\varepsilon_0)\tau_d$ (ps)	τ_S(obs) (ps)
n-butanol	613	120	67	65(66[a])
ethanol	130	9	9	55(40[b])

[a] Castener *et al* 1987; [b] Struve *et al* 1973

with earlier reported values of $\tau_S = 66$ ps for n-butanol with LDS–750 as a probe molecule [19]. We therefore feel confident that our simplified extraction of $C(t)$ function from transient laser emission spectra are good enough for the description of solvation dynamics in n-butanol except the non-exponential behaviour of $C(t)$. However, with regard to ethanol, the agreement between experimental and theoretical results is obviously not good. These findings show that the continuum approach is not sufficient for the description of actual dynamics in the present systems. As pointed out by previous workers [24, 25, 26] the overall solvation dynamics according to molecular based models should show continuous range of times between τ_l and τ_d, with the shortest being τ_l and the longest τ_d. It is, therefore, concluded that the observed deviation from DCM model particularly for ethanol may result from the molecular aspect of solvents which is not included in the continuum description. In actual situation, the solute-solvent interaction becomes complicated due to the change in the intramolecular charge transfer and μ_e of S_1 state during solvation process. The basic difference in the two solvents may be associated with the importance of time-dependent changes in effective dipole moments and varying degree of polarization dependence of

applying refined theoretical models. As it is well-known, each time scale has a significance in the upconversion technique. However, the present system utilizing the superradiant laser emission as a probe can reveal the solvation dynamics and is better suited for selecting dyes as luminescence probes required for many applications [27].

Orientational relaxation time of 78 ps for C 102 in ethanol obtained from induced dichroism technique is greater than the solvent-relaxation time of 55 ps. This shows that rotational motion of the solute does not influence greatly that of the solvent.

Acknowledgement

The authors are grateful to the Defence Research and Development Organisation, New Delhi for funding the Picosecond Laser Spectroscopy Programme.

References

[1] L A Halliday and M R Topp, *Chem. Phys. Lett.* **46**, 8 (1977)
[2] A M Brearley, A J E Strandjord, S R Flom and P F Barbara, *Chem. Phys. Lett.* **113**, 43 (1985)
[3] R Moore, F E Doany, E J Heilweil and R M Hochstrasser, *J. Phys. Chem.* **88**, 876 (1984)
[4] G Zwan van der and J T Hynes, *J. Chem. Phys.* **89**, 4181 (1985)
[5] C Rulliere, A Declemy and Ph Kottis, *Ultrafast phenomena V* (Springer-Verlag Berlin 1986) 312
[6] G Jones II, W R Jackson, Chol Yoo Choi and W R Bergmark, *J. Phys. Chem.* **89**, 294 (1985)
[7] A J Campillo, J H Clark, S L Shapiro, K R Winn and P K Woddbridge, *Chem. Phys. Letts.* **67**, 218 (1979)
[8] K Chandrasekhar, S R Inamdar, D C Patil, N N Math and M I Savadatti, *Spectrosc. Lett.* **28**, 153 (1995)
[9] V Wintgens, J Pouliquen, P Valat, J Kossanyi, S Canonica and P G Wolynes, *J. Chem. Phys.* **86**, 5133 (1987)
[10] M A Kahlow, Jong Kang Tai and P F Barbara, *J. Chem. Phys.* **88**, 2372 (1988)
[11] A Penzkofer and W Blau, *Opt. Quant. Electron.* **15**, 325 (1983)
[12] V A Gaisenok, G G Krylov and S V Sergeev, *J. Appl. Spectrosc.* **58**, 57 (1993)
[13] A Yariv, *Quantum electronics* (Wiley, New York, 1975) 454
[14] E Z Lippert, *Z. Electrochem.* **61**, 962 (1957)
[15] V Nagarajan, A N Brearley, T J Kang and P F Barbara, *J. Chem. Phys.* **86**, 3183 (1987)
[16] C Reichardt (ed), *Molecular interactions* (Wiley, New York, 1982) Vol. 3 241
[17] T Okamura, M Sumitani and K Yoshihara, *Chem. Phys. Lett.* **94** 339 (1983)
[18] M Maroncelli and G R Fleming, *J. Chem. Phys.* **86**, 6221 (1987)
[19] E W Castner Jr, M Maroncelli and G R Fleming, *J. Chem. Phys.* **86**, 1090 (1987)
[20] B Bagchi, D W Oxtoby and G R Fleming, *Chem. Phys.* **86**, 257 (1984)
[21] C J F Bottcher, *Theory of Electrical polarization* (Elsevier Publishing Company, New York, 1952)
[22] W S Struve, P M Rentzepis and J Jortner, *J. Chem. Phys.* **59**, 5014 (1973)
[23] H Sumi and R A Marcus, *J. Chem. Phys.* **84**, 4272 (1986)
[24] D F Calef and P G Wolynes, *J. Chem. Phys.* **78**, 4145 (1983)
[25] P G Wolynes, *J. Chem. Phys.* **86**, 5133 (1987)
[26] I Rips, J Klafter and J Jortner, *J. Chem. Phys.* **88**, 3246 (1988)
[27] D M Gakamskii, N A Nemkovica and A M Rubinov, *Opt. Spectrosc.* **54**, 183 (1991)

MANA
rnal of
physics

© Printed in India

Vol. 45, No. 3,
September 1995
pp. 291–304

velopment of an experimental facility for studying atomic-field, msstrahlung from keV electrons interacting with atoms and lecules

GOEL, M J SINGH and R SHANKER
nic Physics Laboratory, Department of Physics, Banaras Hindu University,
nasi 221 005, India

received 15 May 1995; revised 3 August 1995

ract. A dedicated working setup for studying the process of atomic-field bremsstrahlung its dependence on various parameters for keV electrons incident on a solid or a gaseous et has been indigenously developed. The setup consists of a high vacuum scattering chamber ched with a rotatable X-ray photon detector, a home-built high voltage electron gun with placeable tungsten-filament cathode, an isolated floating high voltage system, high vacuum ping units, various signal processing electronic modules and an IBM PC/XT based multichannel analyzer. A brief description of the facility is presented. The performance of the ty has been tested by recording the bremsstrahlung spectra from 7·0 keV electrons on thin Ag, nd 7·5 keV electrons on Hf targets; the corresponding spectra are presented and discussed. The can operate in the range of 0–8·0 kV accelerating voltage in the present configuration. Other ble experiments that can be performed on the setup are also briefly mentioned.

words. Atomic-field bremsstrahlung; electron gun; isolated floating high voltage system.

CS Nos 34·80; 79·20

ntroduction

ctron bremsstrahlung (also called, atomic-field bremsstrahlung (AFB)) is common-nderstood to be the radiation of a photon in the scattering of an electron from an m or an ion under its respective screened nuclear Coulomb field. It is one particular sequence of the general coupling of the electromagnetic field and the matter fields. process is closely related both to elastic electron scattering and to direct radiative mbination in which the incident electron does not scatter but is captured by the m. Electron bremsstrahlung can teach us about many fundamental aspects of the pling of radiation and matter fields in addition to an application as a probe for lying the atomic structures.

lectron bremsstrahlung is of immense practical interest and importance for a iety of applications; for example, application in astrophysics (interpretation of ophysical spectra) and for modelling hot-plasmas, in plasma programmes – both in gnetic confinement and inertial confinement (determination of plasma-tempera-es, prediction of plasma properties, estimation of plasma heating). Other applica-ns concern transport and energy-loss of charged particle beams, shielding and iation damage both to materials and biological tissues. The current understanding

acquisition system. Many experiments have been performed over the years to measure the dependence of the radiation process on a variety of parameters, such as, the incident electron energy, the atomic number of the target material, the photon emission angle and the photon energy. Most of the previous experiments were performed in the high energy range (above 50 keV) of the incident electrons with solid targets [2]. Only recently, experimental data have become available on AFB process in low impact energies with gaseous targets [3].

To study the process of AFB generation, mostly thin solid foils are used as targets however, in some recent experiments, gaseous targets were also employed. In the ideal case, the target should be so thin that the incident electron undergoes only one single collision on the way through it so that the bremsstrahlung process is not disturbed by additional (elastic or inelastic) scattering processes. The advantage in the use of thin targets is that the effect of one single interaction is much easier to calculate theoretically than the corresponding multiple electron scattering problem. Hence, such experiments can be compared much more directly with theory. However, the problems involved in measurements with small counting rates from very thin target foils without destroying them are considerable.

The subject matter of the present paper is concerned mainly with the developmental aspect of an experimental facility for investigating the AFB process as a function of its relevant parameters. Design, fabrication and description of various components of the setup are given. Few typical examples of the recorded spectra of electron bremsstrahlung process are also presented from test runs on the developed facility. The major motivation to develop the said facility for studying the AFB process with solid and gaseous targets originates from three-fold reasons: (i) no such experimental facility is operative anywhere in the country, (ii) there is a great need of experimental data for AFB at keV energies for testing the existing theories and (iii) it is today's demand and concern to develop the indigenous components of the setup in the laboratory itself and to create a culture of designing and fabricating the equipments for use in research and training areas. As a matter of fact, these objectives have invited a challenging task to any researcher in the country. Our effort has been directed to achieve the same within the constraints of our infra-structural facility and funds availability.

2. Design and fabrication of AFB set up

The AFB setup consists of the following major parts:

- a high vacuum scattering chamber
- a high voltage electron gun
- an isolated floating high voltage system
- high vacuum pumping units
- signal processing and data acquisition system

Description of each part is given in the respective subsections as under:

2.1 *High vacuum scattering chamber*

The high vacuum scattering chamber comprises the following components:

(1) main scattering chamber

subsections:

2.1.1 *Main scattering chamber*: The high vacuum scattering chamber is a cylindrical stainless steel pipe of 190 mm height and 44 mm inner diameter as shown in figure 1a. It has two collinear ports each fitted with a KF 10 coupling; one adopts a high voltage electron gun and the collimating slits S_1 and S_2 (see, figure 2b), the other couples an insulated Faraday cup (see, subsection 2.1.2). Two slots of height 8·0 mm are cut in the cylinder on both sides of the collinear ports in a horizontal plane containing the electron-beam, the target and the axis of photon detector. Slots are covered with a 6 μ thick hostaphan foil which is strong enough to withstand the pressure in the chamber and transparent enough to transmit the X-ray photons of 2·0 keV energy up to 70%. The top flange of the chamber adopts a movable target holder in the centre which permits the positioning of targets in place without cycling the vacuum of the system.

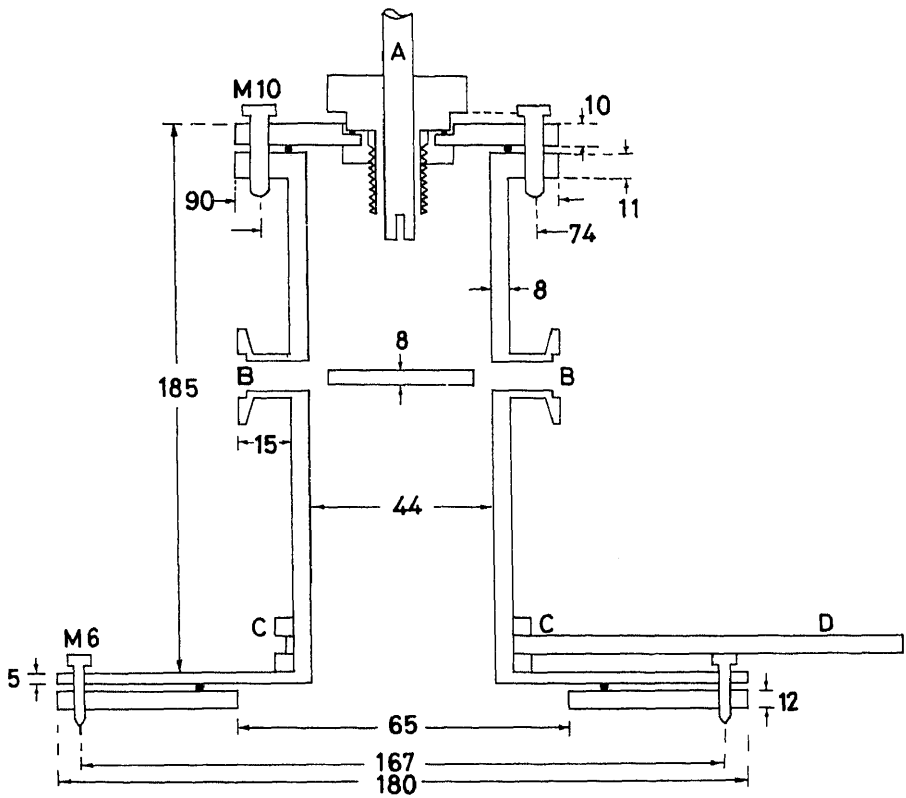

Figure 1a. Cross-section view of the main scattering chamber. A: ϕ 10 mm rotational vacuum feedthrough; B: KF 10; C: SS-collar; D: Al-rotatable platform.

2.1.2 *Faraday cup*: Faraday cup is a device to collect the charge of the transmitted electron beam through the target. In our setup, it consists of two coaxial hollow-Al-cylinders; the length/diameter of the inner and outer cylinders are 25 mm/7 mm and 56 mm/16 mm, respectively. The outer electrode is negatively biased to prevent secondary electrons produced in the inner cylinder from escaping, while the monitoring of the collected charge is made on the latter. The two electrodes are mounted on a perspex flange which has BNC connectors to provide for biasing and current monitoring outputs. The two electrodes mounted on the perspex flange are coupled to an aluminium enclosure (not shown in figure 1b) through a KF 10 coupling at its other end. The current is measured and integrated by a current integrator (ORTEC 439). Figure 1b shows a cross-section view of the Faraday cup with dimensions.

2.1.3 *Target device*: Thin foils of solid targets are mounted on the aluminium frame having 4-consecutive holes each of 12·0 mm diameter. The frame is attached on an insulated SS-shaft which enables the positioning of foils at a desired place and at a chosen angle in the centre of the chamber using a vacuum seal device (see, figure 1c). The gaseous targets are introduced in the collision zone through a tube attached with a hypodermic needle (ϕ 0·5 mm) or with a multicapillary tube with pore size 100 μ (not shown in figure). The effusing gas is finally pumped down by a diffusion pump placed underneath. The adjustment of the input gas pressure in the chamber is done by a fine needle valve (FCV 10 K, L H Alliston, England) in such a way that a single collision condition is maintained. The pressure of the gas in the vicinity of the collision zone is measured by a MKS capacitance manometer (Model 127aa–00001D). The single collision condition is ensured by measuring a linear dependence of the gas pressure as a function of bremsstrahlung photon counts in a chosen energy window (Δk) per incident electron for a given impact energy of the electrons. The target gas pressure measured by the capacitance manometer under this condition has been found to be typically of the order of 3×10^{-3} mbar. The gas density relative to this pressure is estimated to be about 10^{13} atom/cm^3 in the interaction zone. This 'thin' target ensures that multiple scattering events are negligible.

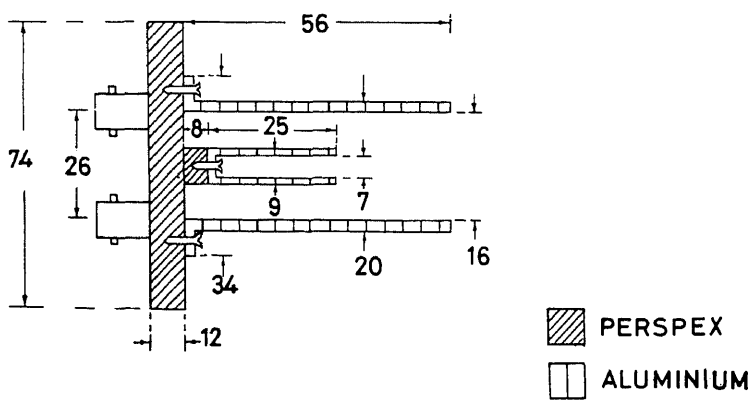

Figure 1b. Cross-section view of the Faraday cup assembly.

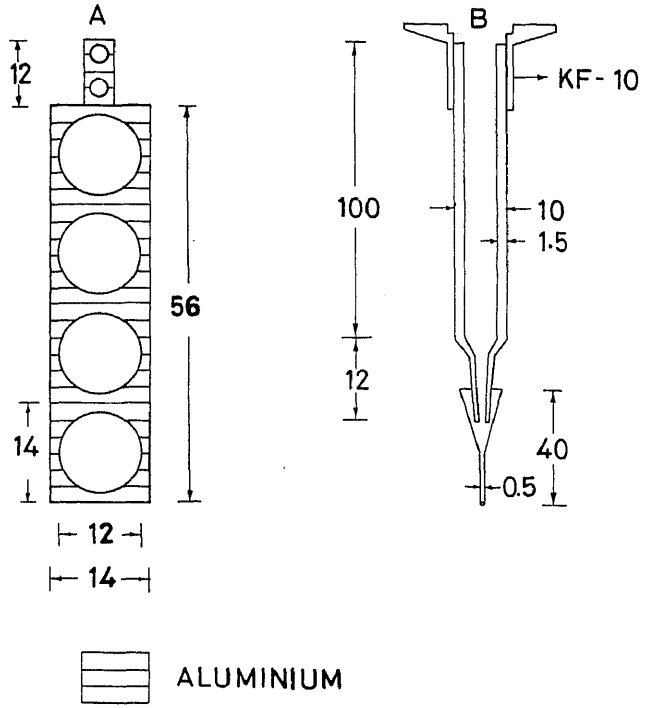

Figure 1c. Solid and gas target devices. A: solid target holder; B: gaseous target device.

2.1.4 *Rotatable Si(Li) X-ray detector*: An aluminium platform (530 mm × 250 mm × 10 mm) is coupled with the main chamber at its one end and rotates about the collision centre (see, D in figure 1a). A Canberra Si(Li) X-ray photon detector (Model SL80175, Cryostat Model 7905–7·5) is placed on this platform with its Be-window facing the 8·0 mm slot. The detector can be positioned at any angle between 30° and 150° on one side and between 210° and 270° on the other side of the collinear ports with a precision of $\pm$ 1°. Alignment of the cryostat with respect to the centre of collision can be made manually on the platform. The bottom of the platform is attached with three metallic supports which rest on the ground. These supports are fitted with an arrangement to adjust their heights as well (not shown in figure 1a).

2.2 *High voltage electron gun*

In the present setup, we have used an electron gun taken out from one of the discarded cathode ray oscilloscopes. Its indirectly heated oxide-coated cathode assembly was removed and it was replaced by an arrangement containing a hair-pin tungsten filament (ϕ 0·15 mm) and a pair of voltage/current feedthroughs as shown in figure 2a. This arrangement with a 'replaceable-filament' is desirable because it allows us to operate the gun with frequent exposures to atmosphere. The tungsten filament is more rugged and resistant to oxidation contrary to the oxide-coated cathodes. The arrangement is made snuggly-fitted to the grid cylinder (G) of the gun (see, figure 2b). The other main

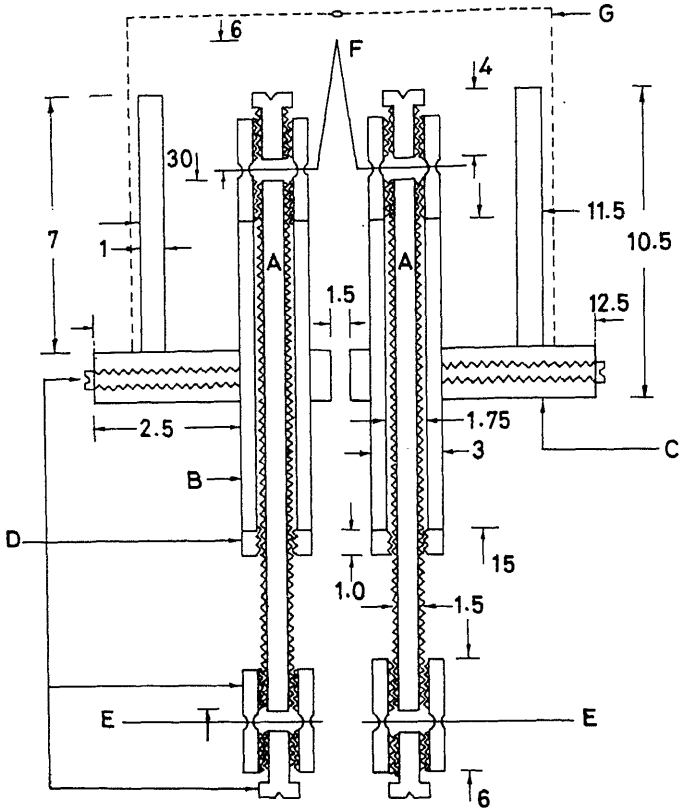

Figure 2a. Cross-section view of the replaceable filament-assembly of the high voltage electron gun. A: copper screw; B: ceramic tubing; C: Al-cylinder; D: Brass nut/bolt; E, E: Filament connecting leads; F: Tungsten filament; G: Grid cylinder.

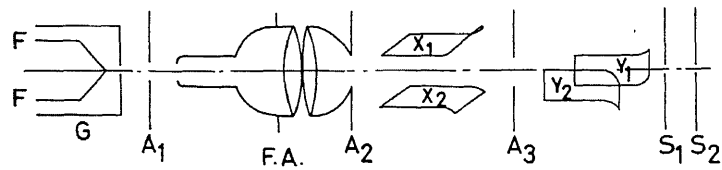

Figure 2b. Schematic sketch of the electron gun with different electrodes. FF: Filament; G: Grid: A_1, A_2, A_3: Anodes; FA: Focussing anode; X_1–X_2, Y_1–Y_2: Deflector plates; S_1, S_2: Collimating slits.

components of the electron gun, namely, control grid, anode, focussing electrode, X- and Y-deflector plates, etc. are shown in figure 2b. The input voltages to each electrode of the gun are provided by pins mounted on a perspex flange having a diameter 100·0 mm and a thickness 12·0 mm. The complete electron gun is made to rest vertically on the perspex flange with three aluminium pillars (ϕ 3·0 mm) attached to the base of the gun. An enclosure for the electron gun has been fabricated out of aluminium which

is coupled with the main scattering chamber through a KF 10 coupling. The other two ports fitted with KF 10 and KF 25 couplings of the enclosure, respectively, provide the facility to connect a Penning gauge and a differential pumping system (VS-114D). A collimating slit assembly S_1 and S_2 having carbon-apertures of 3·0 mm on a copper pipe of length 50·0 mm is fitted between the main scattering chamber and the electron gun enclosure. This arrangement facilitates the alignment of the beam on the target more precisely on one hand and cuts down the background radiation considerably on the other. Various voltages applied to gun-electrodes are discussed in § 2·3.

2.3 *Isolated floating high voltage system*

An isolated floating high voltage system for grid and filament power supplies has been developed. This was necessary in order to keep the anode at earth potential and the cathode/grid at a high negative voltage. A 20 kV isolation transformer (M/s Sairam, Bombay) was used to fulfil this job. Necessary grounding for high voltage and for other units is derived from a common earthing terminal. All units floating on high voltages are enclosed in a cage consisting of 12 mm thick perspex sheets covered with a grounded metallic net. The regulation of voltage/current is made from outside of the cage using the insulator shafts attached to the power supplies. A block diagram showing the electrical connections for the isolated floating high voltage system is given in figure 3.

Two regulated high voltage dc power supplies (0–20 kV, 0–1·5 mA) purchased from M/s FUG GmbH, Germany, were used to provide accelerating and focussing voltages in the gun. The voltage uncertainty of these power supplies is about 1%. The tungsten filament (6 watt) was heated by a constant current power supply (0–15 V, 0–15 A) and the grid voltage was kept slightly negative to the cathode voltage by a separate power supply. A typical set of values for voltage/current on different electrodes for obtaining a well collimated beam (ϕ 3·0 mm) of 6·0 nA on a Ag-target with 6·0 keV electrons is

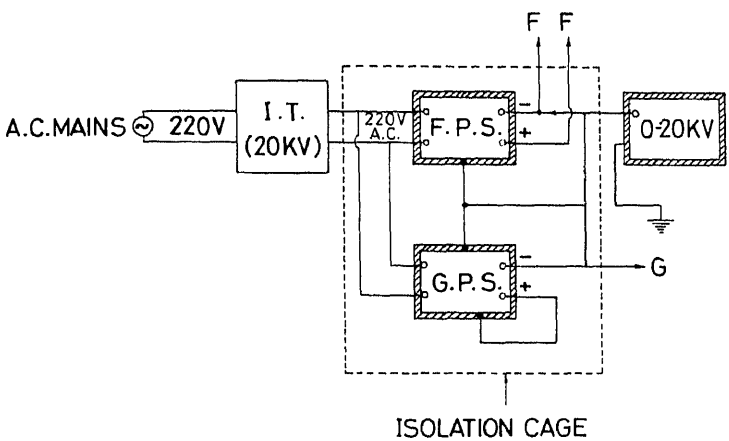

Figure 3. Electrical controls for an isolated floating high voltage system. FPS: Filament power supply; GPS: Grid power supply; IT: Isolation transformer; FF: Leads to filament; G: Lead to grid.

Table 1. Typical values of various voltages and currents applied to gun-electrodes for a beam of 6·0 nA, diameter of 3·0 mm on the target for 6·0 keV electrons incident on a thin Ag foil (157 μgm/cm^2).

Filament voltage	2·1 V
Filament current	3·0 A
Cathode voltage	− 6·0 kV
Emission current	0·007 mA
Focussing voltage	− 5·92 kV
Emission current	0·000 mA
Grid voltage	− 0·5 V
X_1-deflector plate	0·0 V
X_2-deflector plate	100·0 V
Y_1-deflector plate	0·0 V
Y_2-deflector plate	100·0 V
Beam current	6·0 nA

presented in table 1. A visual check of the dimensions of beam spot was made on a ZnS screen placed at the target position.

2.4 *High vacuum pumping system*

The main scattering chamber is evacuated by a 2·5″ oil-diffusion pump (VS-65D, 100 l/s) and the electron gun enclosure by a 4·5″ oil-diffusion pump (VS-114D, 300 l/s); both pumping units are purchased from M/s Hind High Vacuum Co. Pvt. Ltd., Bangalore. The pressures maintained by rotary and diffusion pumps are measured by a Pirani and a Penning gauge respectively. The base pressure attained in the scattering chamber and that in the electron gun enclosure is better than 2×10^{-6} mbar without using a liquid nitrogen trap.

2.5 *Signal processing and data acquisition system*

A block diagram of various electronic modules used for processing the photon and electron signals is shown in figure 4. Standard NIM modules have been used to process the photon signals generated by the Si(Li) detector. A Canberra Si(Li) X-ray photon detector, preamplifier (PA, Model 2008), H.V. power supply (Canberra, Model 30020) and spectroscopy amplifier (Canberra, Model 2020) constitute an integral part of the X-ray photon detection and corresponding signal processing system. An IBM PC/XT based 4K-Multichannel Analyzer (MCA) (M/s Nucleonix, Hyderabad) is interfaced with the photon signals through an ADC (see, figure 4). Data acquisition, stripping and plotting, etc. are carried out on this unit. Monitoring of the beam current is accomplished by a picoammeter (UNIBI, Bielefeld) and integration of which is done by a current integrator (ORTEC 439). All spectra are recorded in the pulse-height analysis (PHA) mode of the MCA and stored in the hard disc/floppy disc of the computer. The spectroscopy amplifier (SA) has a built-in facility to switch the pulse-pile-up rejection on or off while recording the spectra. This provision facilitates the rejection of pulse-pile-up events during acquisition of the data. The shaping time of the SA was chosen to be 12 μs in order to obtain the best resolution of the Si(Li) detector

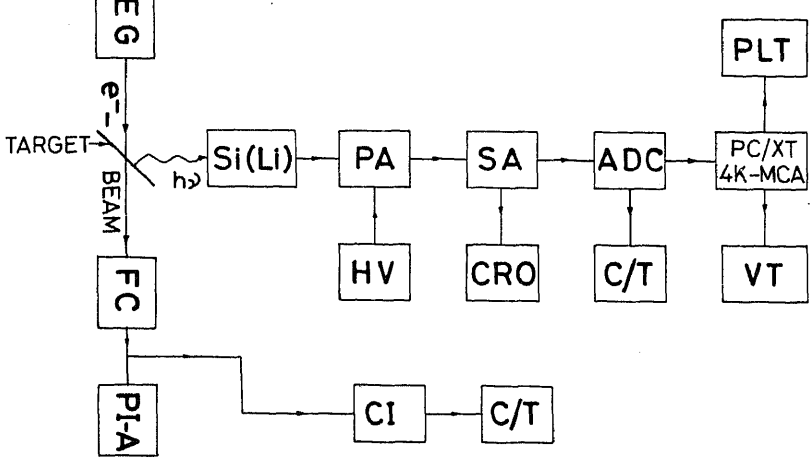

Figure 4. Signal processing and data acquisition system. PA: Preamplifier; SA: Spectroscopy amplifier; ADC: Analog to digital converter; HV: High voltage power supply; CRO: Cathode ray oscilloscope; C/T: Counter timer; VT: Video terminal; PLT: Plotter, CI; Current integrator; PI-A: Pico ammeter; FC: Faraday cup; EG: Electron gun.

(FWHM = 250 eV at 5·9 keV). Emulation software of 4K-MCA is used to accumulate, strip and analyze the data.

3. Operation, test runs and energy calibration

A successful operation of the developed facility essentially involves simultaneous smooth functioning of the vacuum system maintaining the base pressure of the system better than 2×10^{-6} mbar, a stable output of the collimated beam from the electron gun, a photon detector optimized for a high signal to noise-ratio and properly shaped and amplified photon-signals as input to ADC. When all of these are made functional with their optimized values, accumulation of the desired AFB spectra for a chosen target and incident energy is carried out on an IBM PC/XT based MCA in PHA mode (see, figure 4). As AFB intensity depends on Z^2 (Z = atomic number of the target), accumulation time of the AFB spectra depends on the target and beam current used in the experiment. For targets having Z between 40 and 80, data collection times with 1–3 nA beam current are found to be 20–30 minutes more than sufficient for a 2–3% counting statistics. The background radiation arises due to elastic and inelastic scattering of the incident electrons from materials in the neighbourhood of the target used, in particular, the radiation originated in the zone being away from the beam-target interaction region and seen by the detector in a given geometrical configuration contributes maximum. This problem of background radiation can be circumvented by collimating the incident beam with narrow slits and by employing a limited solid angle of the detector. The latter part can be readily achieved by using a narrow aperture on the detector's window. We have investigated the background radiation as a function of

impact energy of the electrons. We found that it increases almost by a factor of two by changing the incident energy of electrons from 2·5 keV to 7·0 keV. However, having considered the above points, one must make note that mere presence of the foreign materials in the vicinity of target can cause background radiation, for example, the materials of the frame on which the targets are mounted are the main source of background radiation. In order to reduce the intensity of the background radiation, it is always preferred to use a low-Z material for constructing the target-frame. Generally, the background radiation is recorded by introducing the empty frame in front of the beam. Nevertheless, this method is good enough as long as there exists a small probability of the incident electrons that are elastically scattered from the target. In AFB spectra, the background subtraction is a serious and important task while analyzing the data for determination of the AFB cross-sections.

A few test runs for AFB spectra produced from 7·0 and 7·5 keV electrons on thin Ag (157 μgm/cm^2), Au (193 μgm/cm^2) and Hf (6·6 mg/cm^2) targets have been carried out on the present facility and displayed in figures 5(a–c) respectively. The spectra have been recorded by placing the photon detector at an angle of 90° and the foil tilted at 45° with respect to the incident beam direction. The channel numbers of the MCA are calibrated for corresponding photon energies by using a standard ^{55}Fe radioactive source. The source is placed at the target position and the characteristic Mn-K_α and K_β

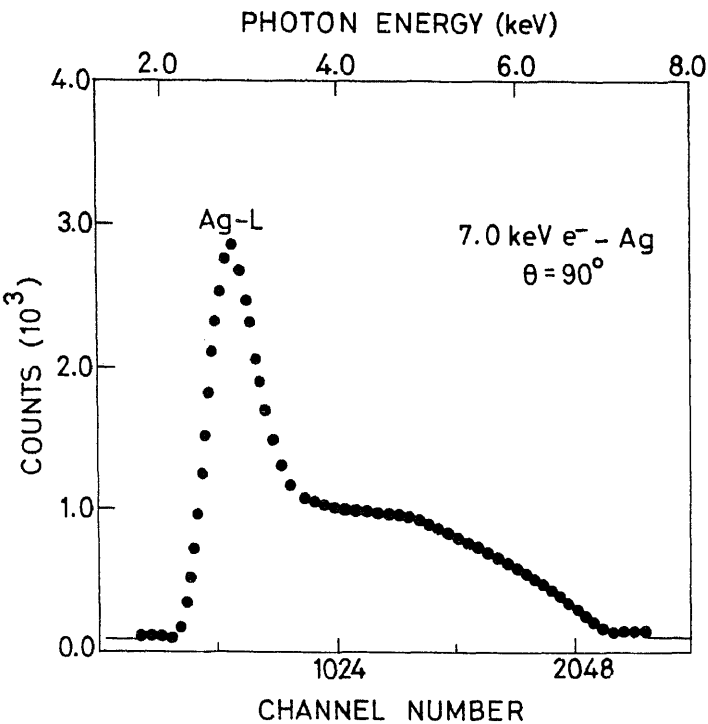

Figure 5a. Electron bremsstrahlung photon energy spectrum for 7·0 keV electrons on a thin Ag target.

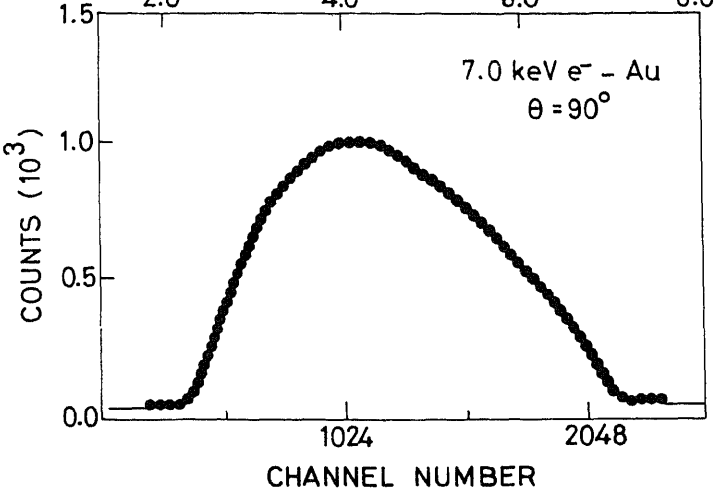

Figure 5b. Electron bremsstrahlung photon energy spectrum for 7·0 keV electrons on a thin Au target.

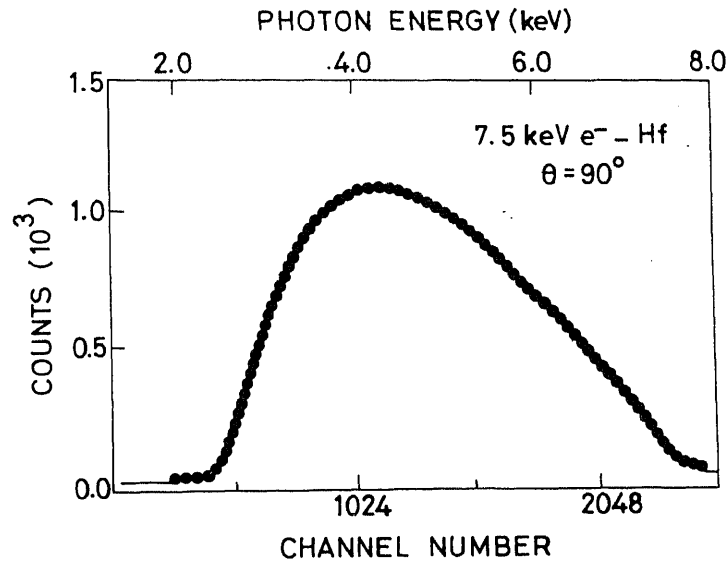

Figure 5c. Electron bremsstrahlung photon energy spectrum for 7·5 keV electrons on a thin Hf target.

lines appearing at 5·9 keV and 6·492 keV respectively are recorded using the identical electronic setup which was employed for accumulating the AFB spectra of different targets. A typical spectrum of ^{55}Fe radioactive source as recorded is shown in figure 6. The relative efficiency of the Si(Li) detector $\varepsilon(k)$ was determined by recording the

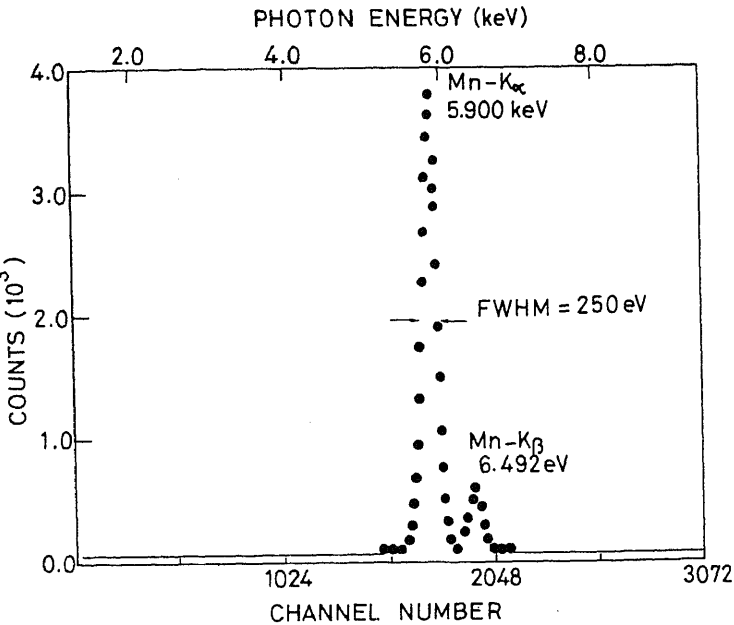

Figure 6. A typical photon energy spectrum from a ^{55}Fe radioactive source.

bremsstrahlung radiation emitted from 7·0 keV e^--Au collision in the photon energy range of 2·0–7·0 keV following the procedure given in ref. [4]. The efficiency was placed on an absolute scale by the measurement of Mn K_α-line from a calibrated ^{55}Fe radioactive source. The corrections for electron back-scattering, energy loss and X-ray absorption were taken into account. The geometrical efficiency of our detector was experimentally determined to be $1{\cdot}71 \times 10^{-4}$ at $k = 5{\cdot}9$ keV while its value from the theoretical AFB cross-section was found to be $1{\cdot}38 \times 10^{-4}$. Both results are found to agree with each other within the uncertainty of the target thickness of 20%. The electron bremsstrahlung spectra produced from gaseous targets are similar and the work in this direction is in progress.

4. Typical results and discussion

Figures 5a–c display the bremsstrahlung photon-energy spectra produced from 7·0 keV and 7·5 keV electrons on thin foils of Ag, Au and Hf respectively. These spectra exhibit a continuous radiation of photons with a well-defined high energy 'tip' appearing at the maximum energy of the incident electrons. In figure 5a, the energy spectrum shows a well-pronounced characteristic Ag-L peak around 3·0 keV over a continuous bremsstrahlung spectrum. Ag-L line could not be resolved into its constituent components due to insufficient resolution of the Si(Li) detector. The cut-off of the low energy photons in all spectra below about 2·0 keV arises due to partial absorption of X-rays in the dead layers of silicon and gold of the detector at Si-K and Au-M edges and partials in the target. Our recent results for the ratio of double

differential cross-sections for the bremsstrahlung photon emission from Ag and Au thin targets when bombarded with 7·0 keV electrons yield an excellent agreement with the theoretical predictions on the relative shape of the spectrum [5].

5. Other feasible experiments with the facility

The present setup as it is and one with some further modification, can be used for other feasible experiments as mentioned below:

1. Angular distribution measurements of the bremsstrahlung spectra as a function of the incident electron energy (T) and the atomic number (Z) of the target.
2. Innershell ionization cross-section of gaseous and solid targets at keV electron energies as a function of Z and T.
3. Measurement of bremsstrahlung photons detected in coincidence with decelerated electrons scattered in a fixed direction; thus information on the elementary radiation process can be obtained and a more stringent test of theoretical work is possible.
4. Multiple ionization of free atoms by using a parallel plate electrostatic analyzer and a time-of-flight spectrometer.

The investigations on problems (3) and (4) above are under active plan which will be taken up in the next phase of the development.

Conclusions

In this work, we have presented the description of a dedicated experimental setup developed indigenously for investigating the atomic-field bremsstrahlung process for keV electrons on a solid or a gaseous target. The design and fabrication of various components of the setup has been given. The high voltage electron gun can operate in the range of 0–8 kV accelerating voltage in the present configuration. The performance of the facility has been tested by recording the electron bremsstrahlung spectra for collisions of 7·0–7·5 keV electrons with thin solid targets and shown that the aimed objectives are fulfilled with satisfaction. It may be mentioned that the estimated cost of our indigenously built high voltage electron gun system is about 5–6 times lesser than that of the custom-built unit. The work with gaseous targets is in progress. Further, other possible experiments on the facility in the area of electron-atom/molecule collisions at keV energies are also mentioned.

Acknowledgements

The work was financially supported by Department of Science and Technology, New Delhi and in part by University Grants Commission, New Delhi. The authors wish to thank all the personnel involved with the fabrication work, specially Shri R M Singh.

References

[1] R H Pratt, *Comm. Atom. Mol. Phys.* **10**, 139 (1981)
R H Pratt, in *Innershell and X-ray Physics of atoms and solids*, edited by D Fabian, H Kleinpoppen and L Watson (Plenum, New York, 1981)

[2] C A Quarles and D B Heroy, *Phys. Rev.* **A24**, 48 (1981) and references therein
[3] M Semaan and C A Quarles, *Phys. Rev.* **A24**, 2280 (1981)
R Hippler, K Saeed, I McGregor and H Kleinpoppen, *Phys. Rev. Lett.* **48**, 1622 (1981)
[4] J Palinkas and B Schlenk, *Nucl. Instrum. Methods.* **169**, 493 (1980)
[5] S K Goel, M J Singh and R Shanker, *Phys. Rev.* **A52** (1995)

Regd. No. KRN-A 64

Pramana journal of physics Vol. 45 (No. 3), September 199

Contents

Theoretical calculation of acoustic non-linearity parameter B/A of binary mixtures.....*J Jugan, Roshan Abraham and M Abdulkhadar* 22

Gyrotropic and piezoelectric coefficients and attenuation of elastic waves in $BaTiO_3$.....*B Subramanyam* 22

Heat capacity and phonons in poly (L-leucine).....
.....*Seema Srivastava, Poonam Tandon, V D Gupta, Shantanu Rastogi, S B Katti and L Burman* 23

Streaming instability of a dusty plasma in the presence of mass and charge variation.....*B P Pandey and C B Dwivedi* 25

Geometry effect on the nonlinear magnetic response of $YBa_2Cu_3O_{7-y}$.....
.....*Parshant Batham, S B Roy, Shailendra Kumar, A K Pradhan, A K Grover, P Chaddah, Ram Prasad and N C Soni* 26

Two photon absorption spectrum of *p*-dichlorobenzene.....
.....*I B Singh, S B Rai and D K Rai* 27

Picosecond time-resolved laser emission of coumarin 102: Solvent relaxation
.....*S R Inamdar, K Chandrasekhar, D C Patil, N N Math and M I Savadatti* 27

Development of an experimental facility for studying atomic-field, bremsstrahlung from keV electrons interacting with atoms and molecules
.....*S K Goel, M J Singh and R Shanker* 29

Indexed in CURRENT CONTENTS ISSN 0304-428

Edited and published by V K Gaur for the Indian Academy of Sciences, Bangalore 560080. Typeset
Thomson Press (I) Ltd., New Delhi 110001 and printed at

PRAMANA

journal o
physi

Vol. 45 No
October 19

INDIAN ACADEMY OF SCIENCES
Indian National Science Academy
Indian Physics Association

Editor

R Nityananda
Raman Research Institute, Bangalore

Associate Editor

H R Krishnamurthy
Indian Institute of Science, Bangalore

Editorial Board

G S Agarwal, *Physical Research Laboratory, Ahmedabad*
V Balakrishnan, *Indian Institute of Technology, Madras*
M Barma, *Tata Institute of Fundamental Research, Bombay*
P Chaddah, *Centre for Advanced Technology, Indore*
B M Deb, *Panjab University, Chandigarh*
P K Kaw, *Institute for Plasma Research, Gandhinagar*
H S Mani, *Indian Institute of Technology, Kanpur*
N Mukunda, *Indian Institute of Science, Bangalore*
T Padmanabhan, *Inter-University Centre for Astronomy and Astrophysics, Pune*
J C Parikh, *Physical Research Laboratory, Ahmedabad*
G Rajasekaran, *Institute of Mathematical Sciences, Madras*
V S Ramamurthy, *Department of Science and Technology, New Delhi*
R Ramaswamy, *Jawaharlal Nehru University, New Delhi*
K R Rao, *Bhabha Atomic Research Centre, Bombay*
Probir Roy, *Tata Institute of Fundamental Research, Bombay*
A K Sood, *Indian Institute of Science, Bangalore*

Editor of Publications of the Academy

V K Gaur
C-MMACS, NAL, Bangalore

	Subscription Rates (1996)
All countries except India	1 year
(Price includes AIR MAIL charges)	US$ 200
India	1 year Rs. 200

Annual subscriptions for **individuals** for India and abroad are Rs. 75/- and $50 respectiv

All correspondence regarding subscription should be addressed to the **Circulation Depart** of the Academy

---

Editorial Office

Indian Academy of Sciences, C V Raman Avenue,
P.B. No. 8005, Bangalore 560 080, India

Telephone: 334 2546
Telex: 845-2178 ACAD
Telefax: 91-80-334 6094

© 1995 by the Indian Academy of Sciences. All rights reserved.

"Information for contributors"

PRAMANA
— journal of
physics

© Printed in India

Vol. 45, No. 4,
October 1995
pp. 305–309

Painlevé analysis and integrability of the damped anharmonic oscillator equation

S PAUL RAJ and S RAJASEKAR*
Department of Physics, St. Xavier's College, Tirunelveli 627 002, India
*Department of Physics, Manonmaniam Sundaranar University, Tirunelveli 627 002, India

MS received 24 April 1995; revised 9 August 1995

Abstract. The Painlevé analysis is applied to the anharmonic oscillator equation $\ddot{x} + d\dot{x} + Ax + Bx^2 + Cx^3 = 0$. The following three integrable cases are identified: (i) $C = 0$, $d^2 = 25\ A/6$, $A > 0$, B arbitrary, (ii) $d^2 = 9A/2$, $B = 0$, $A > 0$, C arbitrary and (iii) $d^2 = -9A/4$, $C = 2B^2/(9A)$, $A < 0$, $C < 0$, B arbitrary. The first two integrable choices are already reported in the literature. For the third integrable case the general solution is found involving elliptic function with exponential amplitude and argument.

Keywords. Anharmonic oscillator; Painlevé analysis; exact solution.

PACS No. 02·90

1. Introduction

In this paper we study the integrability of the nonlinear system

$$\ddot{x} + d\dot{x} + Ax + Bx^2 + Cx^3 = 0, \tag{1}$$

where an overdot denotes differentiation with respect to time t, d is the damping coefficient, B and C are quadratic and cubic nonlinearities coefficients, and A is the square of the natural frequency of the system. Very recently, chaotic behaviour in (1) subjected to a harmonic parametric excitation is studied [1]. The anharmonic oscillator equation (1) arises in many situations in physics and engineering [2] apart from the application to a classical anharmonic oscillator. The addition of an external periodic forcing term to (1) with $B = 0$ results in the Duffing oscillator and with $C = 0$ gives mechanical oscillator. System (1) with external periodic force and parametric perturbation exhibits complex dynamics [1, 3–5]. Some special analytical solutions of (1) are reported in [2]. The integrability of (1) with $B = 0$ is studied by Euler *et al* [6], Duarte *et al* [7], Parthasarathy and Lakshmanan [8] and Estevez [9].

Our motivation in the present paper is to investigate the integrability of (1) for nonzero values of d, A, B and C. Particularly by applying the Painlevé analysis [10, 11] we show that the system (1) is integrable for the specific choice of the parameter values $d^2 = -9A/4$, $C = 2B^2/(9A)$, $A < 0$ and B arbitrary in addition to the two other integrable choices reported in the literature for special form of (1). For this choice we then give the analytical solution.

2. Painlevé analysis of the damped anharmonic oscillator

The P-property requires that the solutions of (1) may be written as Laurent series

expansion in the complex variable [10, 11] $\tau = t - t_0$ with leading order

$$x \sim a_0 \tau^p, \tag{2}$$

where p is yet determined. Inserting the dominant term (2) in (1) one finds two possibilities

(i) $p = -2, \quad a_0 = -6/B, \quad C = 0.$
(ii) $p = -1, \quad a_0^2 = -2/C.$

Now to find higher order terms we write

$$x = a_0 \tau^p + \alpha \tau^{p+r} \tag{3}$$

and substitute in (1) to obtain resonances, that is, conditions such that arbitrary constants may enter in the expansion (3). For the case $p = -2$ resonance condition is $(r+1)(r-6) = 0$. In other words, the resonances occur at $r = -1, 6$. For the case (ii) $(p = -1)$ the resonance values become $r = -1, 4$. The root -1 corresponds to the arbitrariness of t_0.

To verify the occurrence of sufficient number of arbitrary constants we introduce the series expansion

$$x = a_0 \tau^p + \sum_{k=1}^{r} a_k \tau^{p+k} \tag{4}$$

in (1) and equate the coefficients of various powers of τ to zero.

Case (i): Here the resonances are $r = -1, 6$. The values of the coefficients a_i, $i = 1, 2, \ldots, 5$ are given by

$$a_1 = 6d/(5B), \quad a_2 = (d^2 - 25A)/(50B), \quad a_3 = d^3/(250B),$$
$$a_4 = (7d^4 - 125A^2)/(5000B), \quad a_5 = (79d^5 - 1375dA^2)/(75000B).$$

For a_6 we obtain

$$a_6(0) = 25A - 6d^2.$$

Hence, case(i) possesses P-property for

$$C = 0, \quad d^2 = 25A/6, \quad A > 0, \quad B \text{ arbitrary}. \tag{5}$$

Case (ii): Here $p = -1, r = -1, 4$. From the coefficients of $\tau^{-3}, \tau^{-2}, \tau^{-1}, \tau^0$ we obtain

$$a_0^2 = -2/C, \quad a_1 = -(2B + Cda_0)/6C, \quad a_2 = a_0(6AC - 2B^2 - Cd^2)/36C,$$
$$a_3 = da_0(9AC - 3B^2 - 2d^2C)/(108C) + B(2B^2 - 9AC)/(108C^2), \tag{6}$$

respectively. From the coefficients of τ^1 in (1) we get

$$a_4(0) = -2da_3 - 2a_0a_3(B + 3Ca_1) - 3Ca_0a_2^2$$
$$- a_2(A + 2Ba_1 + 3Ca_1^2).$$

Simple manipulation of the above equation yields $a_3 = 0$. From (6) we note that a_3 becomes zero either for $da_0\alpha_1/(108C) + \alpha_2 = 0$ with $\alpha_1 \neq 0$, $\alpha_2 \neq 0$ or for $\alpha_1 = \alpha_2 = 0$

where

$$\alpha_1 = 9AC - 3B^2 - 2d^2C, \quad \alpha_2 = B(2B^2 - 9AC)/(108C^2). \tag{7}$$

In the next section we show that analytical solution exists for $\alpha_1 = \alpha_2 = 0$, that is, for

$$2B^2 - 9AC = 0, \quad 9AC - 3B^2 - 2d^2C = 0. \tag{8}$$

From (8) the integrable conditions are

$$d^2 = -9A/4, \quad C = 2B^2/(9A), \quad A < 0, \quad B \text{ arbitrary}. \tag{9}$$

Further from (7), the conditions $\alpha_1 = 0$, $\alpha_2 = 0$ with $B = 0$ gives

$$d^2 = 9A/2, \quad B = 0, \quad A > 0, \quad C \text{ arbitrary}. \tag{10}$$

Thus we find that (1) possesses P-property for three parametric restrictions given by (5), (9) and (10). The third integrable choice (10) is reported in [6, 8, 9]. To the best of our knowledge the integrable choice (9) has not been listed in the literature.

3. Analytical solution for the integrable choice (9)

Analytical solution for the integrable choices (5) and (10) are given in [12, 2, 8]. In this section we obtain the exact solution of (1) for the parametric restrictions (9). For nonlinear differential equations, at present, no general methods are available to find analytical solutions. However, exact analytical solution is reported in the literature for certain form of second-order ordinary differential equation. For example in ref. [12] analytical solution is given for the equation

$$\ddot{W} + AW + BW^3 = 0, \tag{11}$$

where A and B are arbitrary. Since the above equation is a special case of (1), we check the possibility of reducing (1) into (11) by a suitable transformation. This may be possible for specific parametric choices.

First we write

$$x = uV \tag{12}$$

and find V so that no first derivative in u appears. We obtain $V = V_0 e^{-d/2t}$. For convenience we choose $V_0 = 1$. Equation (1) now becomes

$$\ddot{u} + (A - d^2/4)u + Be^{d/2t}u^2 + Ce^{-dt}u^3 = 0. \tag{13}$$

Then we use the transformation linear in W of the form

$$u = \alpha e^{at} + \beta W(Z)e^{gt}, \tag{14a}$$

$$Z = be^{ft}. \tag{14b}$$

When (14a) is substituted in (13) exponential time dependence in the second term of (14a) gives a first derivative in W. To eliminate the first derivative of W the transformation (14b) is introduced. Now we get a differential equation in W. To determine the constants of (14), we substitute (14) in (13) and equate the coefficients of W^0, W^2 and dW/dZ to zero. In the reduced differential equation all the terms contain exponential time dependence except the coefficient of W. So we equate the coefficient of W to zero.

Further when $f = -2g$ the exponential time dependent terms disappear and we obt

$$d^2W/dZ^2 = W^3. \tag{}$$

The constants in (14) are found to be

$$a = d/2, \quad f = -d/3, \quad g = d/6, \quad \alpha = -B/3C, \quad \beta = 2d^2/3B, \quad b = \sqrt{2} \tag{1}$$

and further we require

$$d^2 = -9A/4, \quad C = 2B^2/9A. \tag{16}$$

We note that the conditions given by (16b) are the parametric choices obtained f
P-analysis (clarify eq. (9)). More precisely equation (1) under the transformation

$$x(t) = (2d^2/3B)(1 + W(Z)e^{-(d/3)t}), \tag{17}$$

$$Z = \sqrt{2}e^{-(d/3)t} \tag{17}$$

together with the conditions (16b) reduces to (15) which is (11) when $A = 0$.

The first integral of (15) is

$$(dW/dZ)^2 = W^4/2 + c_0, \tag{18}$$

where c_0 is an integration constant. We consider two cases in which $c_0 = 0$ and $c_0 \neq$
separately. For $c_0 \neq 0$ with $W(0) = W_0 = (-2c_0)^{1/2}$ and $dW/dZ|_{Z=0} = 0$ real solution
of (15) exist only for $c_0 < 0$ and are given by

$$W = W_0/cn(W_0 v; k), \quad k^2 = 1/2, \quad v = Z - Z_0, \tag{19}$$

where Z_0 is a second integration constant so that the solution of (1) becomes

$$x(t) = (2d^2/3B)[1 + W_0 \exp(-dt/3)/cn(W_0 Z; k)],$$

$$Z = \sqrt{2}\exp(-dt/3) - Z_0. \tag{20}$$

The solution (20) for $d > 0$ exponentially decays to the stable fixed point (node) in the limit $t \to \infty$ for the range $0 < |W_0 Z_0| < \{\pi/2F(1/2; 1/2; 1; 1/2) - 2\}$. (The other two fixed points are saddle.) However, for $c_0 = 0$ the solution given by (20) becomes simple. In this case, straightforward integration of (18) gives the solution of (1) as

$$x(t) = (2d^2/3B)[1 \pm 1/(1 + c_1 \exp(dt/3))],$$

where c_1 is the integration constant.

Acknowledgement

The authors would like to thank the referee for several suggestions. This work forms part of UGC minor research project.

References

[1] J M Malasoma, C H Lamarque and L Jezequel, *Int. J. Nonlinear Dynamics* **5**, 153 (1994)
[2] J M Dixon, J A Tuszynski and M Otwinowski, *Phys. Rev.* **A44**, 3481 (1991)
[3] R H Plaut and J C Hsiech, *J. Sound Vib.* **120**, 73 (1987)

[4] L D Zavodney and A H Nayfeh, *J. Sound Vib.* **120**, 86 (1988)
[5] W Szemplinska-Stupnicka, R H Plaut and J C Hsieh, *J. Appl. Mech.* **56**, 947 (1989)
[6] N Euler, W H Steeb and K Cyrus, *J. Phys.* **A22**, L195 (1989)
[7] L G S Duarte, N Euler and I C Moreira, *J. Phys.* **A23**, 1457 (1990)
[8] S Parthasarathy and M Lakshmanan, *J. Sound Vib.* **137**, 523 (1990)
[9] P G Estevez, *J. Phys.* **A24**, 1153 (1991)
[10] M J Ablowitz, A Ramani and H Segur, *J. Math. Phys.* **21**, 715 (1980)
[11] A Ramani, B Grammaticos and T Bountis, *Phys. Rep.* **180**, 159 (1989)
[12] T Davis, *Introduction to nonlinear differential and integral equations* (Dover Publ., New York, 1962)

PRAMANA
— journal of
physics

© Printed in India

Vol. 45, No. 4,
October 1995
pp. 311–317

The particle in a box problem in q-quantum mechanics

G VINOD, K BABU JOSEPH and K M VALSAMMA
Department of Physics, Cochin University of Science and Technology, Kochi 682 022, India

MS received 23 February 1995; revised 20 July 1995

Abstract. A q-deformed, q-Hermitian kinetic energy operator is realised and hence a q-Schrödinger equation (q-SE) is obtained. The q-SE for a particle confined in an infinite potential box is solved and the energy spectrum is found to have an upper bound.

Keywords. q-calculus; q-quantum mechanics; particle in a box.

PACS Nos 01·55; 02·90; 03·65

1. Introduction

The study of q-deformations of Lie algebras and ordinary calculus has grown into a major area of research in mathematical physics. The q-deformed calculus, when applied to quantum mechanics with its fundamental postulates preserved, gives rise to q-quantum mechanics. Several years ago Janussis *et al* [1, 2] discussed q-quantization and the eigenvalue problem of q-differential operators. Quantum mechanics is usually deformed in two different ways: one may either replace the canonical commutation relation by a q-commutation relation or the momentum operator in the Schrödinger equation (SE) by a q-deformed one. Most of the work in this area is based on the former approach [3–5]. Minahan [6] has considered a q-extension of SE (q-SE) and obtained the spectrum of q-harmonic oscillator. The energy spectrum of a q-analog of hydrogen atom has been obtained by Yang and Xu [7]. In this paper, following the q-SE method, we determine the spectrum of a particle in a one dimensional infinite potential well.

The infinite potential well is characterized by a constant potential in a finite region outside which the potential is infinite. Particles subject to such a potential are trapped inside the constant potential region. This model potential has been used in the free electron model of metals. Study of any problem in q-quantum mechanics is of interest not only for pedagogic reasons but also for comprehending the uniqueness of standard ($q = 1$) quantum mechanics. One cannot also rule out the possible existence of q-systems in nature.

2. Elements of q-calculus

The mathematical idea of q-deformation has deep roots running down to the middle of the last century. Further developments were achieved mainly due to the works of

As $q \to 1, [n] \to n$. The q-factorial is

$$[n]! = [n][n-1][n-2]\ldots[2][1].$$

The q-difference operator D_x is defined by

$$D_x f(x) = \frac{f(qx) - f(x)}{x(q-1)}.$$

If $q \to 1$, then the ordinary derivative $df(x)/dx$ is obtained, if it exists. The produ and quotient rule for q-difference operators are

$$D_x\{u(x)v(x)\} = \{v(x)D_x u(x) + u(qx)D_x v(x)\}$$

$$D_x\{u(x)/v(x)\} = \frac{v(x)D_x u(x) - u(x)D_x v(x)}{v(qx)v(x)}.$$

The q-analogue of integration in the case of finite limits a, b is defined as:

$$S_a^b f(x)d(qx) = (1-q)\left\{b\sum_{r=0}^{\infty} q^r \phi(q^r b) - a\sum_{r=0}^{\infty} q^r \phi(q^r a)\right\}.$$

The product rule for q-integration is

$$Sv(x)D_x u(x)d(qx) = u(x)v(x) - Su(qx)D_x v(x)d(qx).$$

The q-analogues of exponential function and trigonometric functions have als constructed

$$E_q(x) = \sum_{n=0}^{\infty} \frac{x^n}{[n]!}$$

$$\sin_q x = \frac{1}{2i}\{E_q(ix) - E_q(-ix)\}$$

$$\cos_q x = \frac{1}{2}\{E_q(ix) + E_q(-ix)\}.$$

3. q-quantum mechanics

Even though it is customary [8] to take the q-commutation relation

$$D_x x - qxD_x = 1$$

as the starting point of q-quantum mechanics, the D_x operator is neither q-Her nor q-skew Hermitian (Appendix 1). Therefore it is not possible to define a simp straightforward realisation of the momentum operator which is q-Hermitian. Hc this difficulty can be circumvented in an approach based on the q-Schrödinger eq which is written as

$$H_q \psi_q = E_q \psi_q$$

where the q-deformed Hamiltonian $\mathbf{H}_q$ is the sum of a q-deformed kinetic

operator and a potential energy operator. Since in one dimension the kinetic energy operator contains d^2/dx^2 in the undeformed ($q = 1$) SE, we expect the q-deformed kinetic energy operator to contain $\mathbf{D}_x^2$. Besides, we demand that H_q is a q-Hermitian operator (Appendix 1). The q-adjoint operation is defined as

$$S\phi_q^*(x)\mathbf{A}\psi_q(x)d(qx) = S(\mathbf{A}^\zeta\phi_q(x))^*\psi_q(x)d(qx) \tag{12}$$

where the q-integration is over the q-line segment. Using (12) we can prove that

$$(\mathbf{D}_x)^\zeta = -\mathbf{D}_x\mathbf{q}^{-x\partial_x} \tag{13}$$

where the action of $q^{x\partial_x}$ is given by

$$q^{\pm x\partial_x}f(x) = f(q^{\pm 1}x)$$

So $\mathbf{D}_x^2\mathbf{q}^{-x\partial_x}$ serves as a q-hermitian operator (Appendix 1). We rewrite the q-SE as

$$\left\{\frac{-\hbar^2}{2m}\mathbf{D}_x^2\mathbf{q}^{-x\partial_x} + \mathbf{V}(\mathbf{x})\right\}\psi_q(x) = E_q\psi_q(x) \tag{14}$$

where E_q is a q-deformed energy eigenvalue.

In q-deformed space we can take $d(q\mathbf{x})$ as the elementary volume, or in the one dimensional problem $d(q\mathbf{x})$ serves as the elementary length. So $|\psi_q(x)|^2$ is the probability that a measurement performed on the system will locate it in the element $d(q\mathbf{x})$ of the q-line. Therefore, if we q-integrate $|\psi_q(x)|^2$ over the q-line segment of finite length, we will get unity

$$S|\psi_q(x)|^2 d(qx) = 1. \tag{15}$$

This probability interpretation demands $\psi_q(x)$ to be single valued and finite everywhere, as in the standard case. Also $\psi_q(x)$ and $D_x\psi_q(x)$ should vanish at endpoints of the q-line segment.

4. The particle in a box

In this problem,

$$V(x) = 0 \text{ for } 0 \leqslant x \leqslant a,$$
$$= \infty \text{ otherwise.} \tag{16}$$

We can write the q-SE for this potential as

$$(\mathbf{D}_x^2\mathbf{q}^{-x\partial_x} + k_q^2)\psi_q(x) = 0 \tag{17}$$

where

$$k_q^2 = \frac{2mE}{\hbar^2}. \tag{18}$$

Solution of the q-SE is

$$\psi_q(x) = N\sum_{r=0}^{\infty}\frac{(-1)^r q^{r(r+2)}(k_q x)^{2r+1}}{[2r+1]!} \tag{19}$$

N is the normalization constant. Since $\psi_q(0) = \psi_q(a) = 0$, the admissible solutions are those which satisfy

$$\sum_{r=0}^{\infty} \frac{(-1)^r q^{r(r+2)} (k_q a)^{2r+1}}{[2r+1]!} = 0.$$

Only numerical solutions of this equation are possible. From (18), the energy values are given by

$$E_q = \frac{\hbar^2 (k_q a)^2}{2ma^2}.$$

The q-normalization constant N is evaluated from

$$S_{-\infty}^{\infty} \psi_q^*(x) \psi_q(x) d(qx) = 1$$

which follows from the assumption that the particle is confined between $\mathbf{x} = \mathbf{x} = \mathbf{a}$. Let $\psi_q^* \psi_q$ be expressed as

$$\psi_q^*(x) \psi_q(x) = \sum_{r=0}^{\infty} b_r (k_q r)^{2r}$$

for even values of r,

$$b_r = -2 \sum_{s=0}^{(r-2)/2} \frac{q^{(r-s-1)(r-s+1)+s(s+2)}}{[2s+1]![2r-2s-1]!}$$

and for odd values of r,

$$b_r = 2 \sum_{s=0}^{(r-1)/2} \frac{q^{(r-s-1)(r-s+1)+s(s+2)}}{[2s+1]![2r-2s+1]!} - \frac{q^{(r-1)(r+3)/2}}{[r]![r]!}.$$

Since the series expansion of $\psi_q^*(kx)\psi_q(kx)$ is convergent, we may q-integrate each in the expansion (24) employing the identity

$$Sx^n d(qx) = \frac{x^{n+1}}{[n+1]}$$

which gives

$$N^2 \sum_{r=0}^{\infty} b_r \frac{k_q^{2r} a^{2r+1}}{[2r+1]} = 1$$

or,

$$N = \left\{ a \sum_{r=0}^{\infty} \frac{b_r (C_n)^{2r}}{[2r+1]} \right\}^{-1/2}$$

where C_n are the solutions of ka given by (20).

5. Analytic solutions for $q \approx 1$

Analytic solutions exist when q is close to unity. Let us take $q = 1 - \delta$, δ being

small quantity. The following approximations are valid

$$[n] = n\{1-(n-1)\delta/2\} \tag{26}$$

$$[n]! = n!\{1-n(n-1)\delta/2\}. \tag{27}$$

The wavefunction is approximated by

$$\psi_q(kx) = N \sin_q k_q x + N \sum_{r=0}^{\infty} \frac{(-1)^{r+1}(kx)^{2r+1}}{(2r+1)!} \left\{\frac{3r\delta}{2-r(2r+1)}\right\}. \tag{28}$$

The coefficients b_r take the form

$$b_r = \begin{cases} -2\Sigma_{s=0}^{(r-2)/2}\Delta_{r,s} & \text{for even } r \\ 2\Sigma_{s=0}^{(r-1)/2}\Delta_{r,s} - \dfrac{1}{(r!)^2}\left\{1-\dfrac{(r-1)(2r+3)\delta}{1+r(r-1)\delta}\right\} & \text{for odd } r \end{cases}$$

where $\Delta_{r,s}$ is given by

$$\Delta_{r,s} = \frac{1}{(2s+1)!(2r-2s-1)!}\left\{1+\frac{(r-1)(2r+3)\delta}{1+r(r-1)\delta}\right\}.$$

6. Numerical results and discussion

Here we have deformed the SE by giving a nonstandard realization of the kinetic energy operator, which coincides with the corresponding operator in the standard SE when

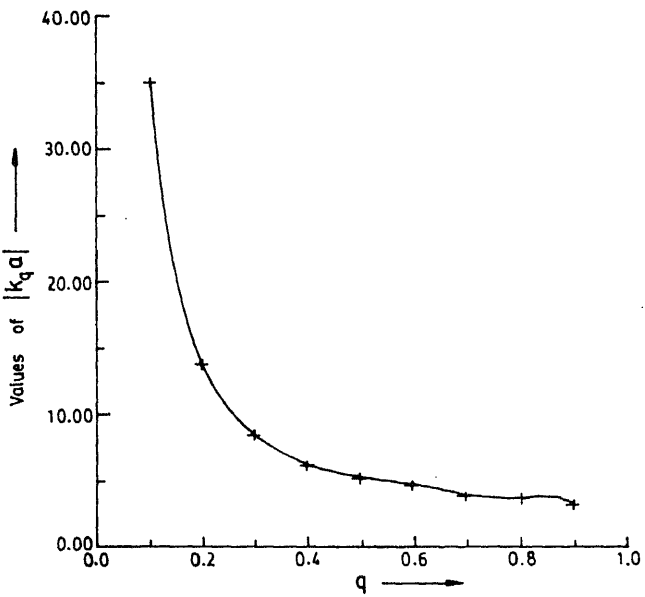

Figure 1. Variation of $|k_q a|$ (corresponding to the ground state) with q.

Table 1. Allowed values of $\pm k_q a$.

$q \downarrow n \rightarrow$	1	2	3	4
0·1	35·11869			
0·2	13·91709	69·87712		
0·3	8·564421	28·97956		
0·4	6·335347	16·46896	41·17533	
0·5	5·319289	10·92827	22·82981	45·21165
0·6	4·822798	8·039686	15·5551	24·57137
0·7	4·044871	7·795353	11·70577	15·03165
0·8	3·770396	7·872589	13·08165	14·74317
0·9	3·394796	6·803214	8·21286	

$q \rightarrow 1$. Numerical solutions of the q-SE for a particle in a box are obtained for ranging from 0 to 1. It is observed that for lower values of q, higher energy le forbidden. This is due to the rapidly converging nature of the wavefunction fo values of q. The numerical solutions are tabulated and the solution correspon the ground state of the system is plotted against q which is best fitted for a poly in q. The numerical solutions show that for $q \neq 1$, the energy eigenvalues have ar bound even in systems which possess an infinite number of energy eigenvalue $q = 1$.

Appendix 1

As the problem discussed in the text is a one dimensional one, all q-integrations a a segment of finite length. The q-adjoint operation is defined as

$$S\phi_q^*(x)\Omega\psi_q(x)d(qx) = S(\Omega\phi_q(x))^*\psi_q(x)d(qx)$$

where the functions $\phi_q(x)$ and $\psi_q(x)$ are assumed to vanish at the end points segment.

So a q-Hermitian operator Ω satisfies

$$S\phi_q^*(x)\Omega\psi_q(x)d(qx) = S(\Omega\phi_q(x))^*\psi_q(x)d(qx).$$

A q-Hermitian operator has the following properties:

(i) The eigenvalues of a q-Hermitian operator are real.
Let $\Omega\psi_q(x) = \omega\psi(x)$ from (A2),

$$(\omega - \omega^*)S\psi_q^*(x)\psi_q(x)d(qx) = 0$$

which implies $\omega^* = \omega$.
(ii) The eigenvectors of a q-Hermitian operator belonging to different eigenvalu q-orthogonal.

Suppose that $\psi_{q1}(x)$ and $\psi_{q2}(x)$ are two eigenvectors of Ω with eigenvalues ω_1 a respectively.

$$S\psi_{q1}^*(x)\Omega\psi_{q2}(x)d(qx) = S(\Omega\psi_{q1}(x))^*\psi_{q2}(x)d(qx)$$

or,

$$(\omega_1 - \omega_2) S\psi_{q1}(x)\psi_{q2}(x)d(qx) = 0 \text{ } (q\text{-orthogonality}).$$

Here we wish to show that $\mathbf{D}_x^2\mathbf{q}^{-x\partial_x}$ is q-Hermitian:

$$\begin{aligned} S\phi_q^*(x)\mathbf{D}_x^2\mathbf{q}^{-x\partial_x}\psi_q(x)d(qx) &= S\phi_q^*(x)\mathbf{D}_x(\mathbf{D}_x\psi_q(q^{-1}x))d(qx) \\ &= |\phi_q^*(x)\mathbf{D}_x\psi_q(q^{-1}x)| - S\mathbf{D}_x\phi_q^*(x)q^{1/2}\mathbf{D}_x\psi_q(x)d(qx) \\ &= -q^{1/2}S\mathbf{D}_x\phi_q^*(x)\mathbf{D}_x\psi_q(x)d(qx) \end{aligned}$$

where we have employed the product rule for q-integration given by (7). Similarly,

$$S(\mathbf{D}_x^2\mathbf{q}^{-x\partial_x}\phi_q(x))^*\psi_q(x)d(qx) = -q^{1/2}S\mathbf{D}_x\phi_q^*(x)\mathbf{D}_x\psi_q(x)d(qx)$$

Thus $\mathbf{D}_x^2\mathbf{q}^{-x\partial_x}$ is a q-Hermitian operator.

Acknowledgements

One of the authors (GV) thanks University Grants Commission for awarding a Research Fellowship. KMV would like to thank National Board of Higher Mathematics for awarding a post-doctoral fellowship.

References

[1] A Jannussis, L C Papaloucas and P D Sifarkas, *Hadronic J.* **3**, 1622 (1980)
[2] A Jannussis, G Brodinas and D Sourlas, *Lett. Nuovo Cimento* **30**, 123 (1981)
[3] L C Biedenharn, *J. Phys.* **A22**, L875 (1980)
[4] A J Macfarlane, *J. Phys.* **A22**, 4581 (1989)
[5] S Chaturvedi, A K Kapoor, R Sandhya, V Srinivasan and R Simon, *Phys. Rev.* **A43**, 4555 (1991)
[6] J A Minahan, *Mod. Phys. Lett.* **A5**, 2625 (1990)
[7] Yang Qin-Gzhu and Xu Bo-Wei, *J. Phys.* **A26**, L365 (1993)
[8] H Exton, *q-Hypergeometric functions and applications* (Chichester Ellis-Horwood, 1983)

— journal of physics

October 1995
pp. 319–326

Polarized light

G RAMACHANDRAN, A R USHA DEVI and
N S SAANDEEP KANNADAVARDHANA
Department of Studies in Physics, University of Mysore, Manasagangotri, Mysore 570 006, India

MS received 27 April 1995

Abstract. Following the recent work of Chandler *et al* on quasi probability distributions for spin-1/2 particles, we show that polarized light can be interpreted in terms of trivariate probability distributions in two different ways by choosing the variates to correspond to (i) the co-ordinates on the Poincare sphere, (ii) the components of the spin operator of the photon. In either case, it is shown that the Margenau–Hill procedure leads to probability mass functions while the Wigner–Weyl approach leads to probability density functions and the well-known Stokes parameters are also realised as appropriate averages with respect to these distribution functions.

Keywords. Density matrix; polarization; Stokes parameters; quasi-probability distributions.

PACS Nos 14·80; 03·65; 02·50; 07·60

1. Introduction

The subject of polarization of light [1] is an ancient one going back, according to Born and Wolf [2], to Huygens [3] of the seventeenth century. The state of polarization was characterized by Stokes [4] in terms of a set of four parameters s_0, s_1, s_2, s_3, named after him. Poincare [5] developed a geometrical representation for all states of polarization in terms of points on a sphere known by his name. It is well-known [6] that photons, the quanta associated with light, are spin-1 particles which are massless and hence deprived of the $|10\rangle$ or longitudinal state. The review articles by Fano [7] and McMaster [8] show how a partially polarized state of light can be represented in terms of a 2×2 hermitian and positive semidefinite matrix ρ employing the concept of the density matrix [9]. What is the composition in a partially polarized beam of light? If ρ has eigen values λ_1 and λ_2 with corresponding eigen states $|\varepsilon_1\rangle$ and $|\varepsilon_2\rangle$ respectively, one can say that the beam consists of $N\lambda_1$ photons with polarization $|\varepsilon_1\rangle$ and $N\lambda_2$ photons with polarization $|\varepsilon_2\rangle$, where N denotes the total number of photons which is proportional to the Stokes parameter $s_0 \geqslant (s_1^2 + s_2^2 + s_3^2)^{1/2}$ representing the total intensity I of the beam. The equality corresponds to completely polarized or pure states characterized by one of the eigenvalues being zero. The recent work of Chandler *et al* [10] on spin-1/2 particles shows that one can interpret the contents of a 2×2 density matrix for spin-1/2 particles in probabilistic ways based on the correspondence rules of Margenau and Hill [11] on one hand and Weyl [12] and Wigner [13] on the other. More recently Usha Devi *et al* [14] have adduced arguments following Margenau and Hill to show that an aligned spin-1 system can be viewed in terms of bivariate probability distribution by identifying the associated characteristic function. It is interesting to note that a beam of photons is akin to an aligned spin-1 system when the

Stokes parameter s_3 is zero. It is interesting to investigate whether a joint probability distribution interpretation can be given to an arbitrarily polarized beam of light. In this paper, we extend the Margenau–Hill procedure to provide a probabilistic interpretation for partially polarized light, in terms of a trivariate probability distribution even in the general case when $s_3 \neq 0$. We find, in fact, that there are two convenient ways in which this extension can be carried out viz., using the operators representing

(i) the co-ordinates on the Poincare sphere
(ii) the components of the spin of the photon

as the variates. This leads to a probability mass function where the variates assume discrete values. On the other hand a probability density function can be obtained using the Wigner-Weyl correspondence rule where once again the variates may be chosen in two alternative ways (i) and (ii).

2. States of polarization and the density matrix for photons

Our notations are as follows: Using a right handed co-ordinate system where the z-axis is chosen parallel to the momentum vector **k** of the photon, all possible states of polarization can be represented by [15]

$$|\varepsilon_{\alpha\beta}\rangle = (\cos\beta\cos\alpha - i\sin\beta\sin\alpha)|\varepsilon_x\rangle + (\cos\beta\sin\alpha + i\sin\beta\cos\alpha)|\varepsilon_y\rangle \quad (1)$$

where $|\varepsilon_x\rangle, |\varepsilon_y\rangle$ denote linear states of polarization along x, y axes respectively. Here $0 \leqslant \alpha < \pi$ and $-\pi/4 \leqslant \beta \leqslant \pi/4$ are angles such that $\theta = \pi/2 - 2\beta$ and $\phi = 2\alpha$ designate points on the Poincare sphere where the north pole corresponds to right circular polarization and the south pole corresponds to left circular polarization. Clearly, $|\varepsilon_{\alpha\beta}\rangle$ and $|\varepsilon_{\alpha+\pi/2-\beta}\rangle$ are orthogonal states in a two dimensional complex vector space and correspond geometrically to diametrically opposite points on the Poincare sphere. We choose the circular polarisation states

$$|\varepsilon_L\rangle = |\varepsilon_{0-\pi/4}\rangle = (|\varepsilon_x\rangle - i|\varepsilon_y\rangle)/\sqrt{2} \quad (2)$$
$$|\varepsilon_R\rangle = |\varepsilon_{0\pi/4}\rangle = (|\varepsilon_x\rangle + i|\varepsilon_y\rangle)/\sqrt{2}$$

as our basis with respect to which the density matrix ρ assumes the form

$$\rho = \frac{\mathrm{Tr}\rho}{2}[1 + \boldsymbol{\sigma}\cdot\mathbf{P}] \quad (3)$$

where $\sigma_1, \sigma_2, \sigma_3$ denote the standard Pauli matrices, $I = \mathrm{Tr}\,\rho = s_0$ denotes the intensity of the light beam. Moreover,

$$s_0 P_1 = s_1 = \mathrm{Tr}(\rho\sigma_1) = I_x - I_y \quad (4)$$
$$s_0 P_2 = s_2 = \mathrm{Tr}(\rho\sigma_2) = I_{x'} - I_{y'}$$
$$s_0 P_3 = s_3 = \mathrm{Tr}(\rho\sigma_3) = I_L - I_R$$

where x', y' denote linearly polarized states with $\beta = 0$ and $\alpha = \pi/4$ and $3\pi/4$ respectively. Note that s_1, s_2, s_3 are expectation values of the operators $\sigma_1, \sigma_2, \sigma_3$ respectively and hence we could identify $\sigma_1, \sigma_2, \sigma_3$ as operators representing the co-ordinates of a point on the Poincare sphere. On the other hand, considering photon as a spin-1 particle, the

density matrix can be expressed in terms of the Fano statistical tensors [7] t_q^k through

$$\rho = \frac{\mathrm{Tr}\rho}{3} \sum_{k=0}^{2} \sum_{q=-k}^{k} (-1)^q t_{-q}^k \tau_q^k(\mathbf{J}) \tag{5}$$

where $\tau_q^k(\mathbf{J})$ are spherical tensor operators constructed out of the spin operators $\mathbf{J}$ of the photon and are normalized such that

$$\langle 1m' | \tau_q^k(\mathbf{J}) | 1m \rangle = c(1k1; mqm') \sqrt{2k+1} \tag{6}$$

where $c(1k1; mqm')$ are Clebsch–Gordan coefficients. An explicit 3×3 matrix form for ρ is given by (1) of [16]. Observing that the basis states $|1m\rangle$ are such that $|11\rangle = -|\varepsilon_R\rangle$ and $|1-1\rangle = |\varepsilon_L\rangle$ leads to the identification,

$$t_0^0 = 1 \tag{7}$$

$$t_0^1 = -\left(\frac{3}{2}\right)^{1/2} \frac{s_3}{s_0}$$

$$t_0^2 = \frac{1}{\sqrt{2}}$$

$$\mathrm{Re}(t_2^2) = -\frac{\sqrt{3}}{2} \frac{s_1}{s_0}$$

$$\mathrm{Im}(t_2^2) = \frac{\sqrt{3}}{2} \frac{s_2}{s_0}$$

$$t_{\pm 1}^2 = t_{\pm 1}^1 = 0.$$

Clearly the system is aligned [17] if $s_3 = 0$ and an unitary transformation

$$U = \begin{pmatrix} e^{-i\theta/2} & 0 & 0 \\ 0 & 1 & 0 \\ 0 & 0 & e^{+i\theta/2} \end{pmatrix} \tag{8}$$

with $\tan\theta = s_2/s_1$ takes the photon density matrix into its principal axes of alignment frame (PAAF) [17],

$$\rho_{\mathrm{PAAF}} = \frac{1}{2} \begin{pmatrix} s_0 & 0 & (s_1^2 + s_2^2)^{1/2} \\ 0 & 0 & 0 \\ (s_1^2 + s_2^2)^{1/2} & 0 & s_0 \end{pmatrix}. \tag{9}$$

The conclusions drawn by Usha Devi *et al* [14] apply in toto here, together with the identification,

$$\Pi_x = \frac{1}{2}[s_0 - (s_1^2 + s_2^2)^{1/2}] \tag{10}$$

$$\Pi_y = \frac{1}{2}[s_0 + (s_1^2 + s_2^2)^{1/2}]$$

$$\Pi_z = 0$$

and we can explain the polarization in terms of the bivariate joint probabilit with any two of the spin components of the photon as variates. To describe th general situation i.e., when $s_3 \neq 0$ we need a trivariate probability distribution w have to treat all the three components of photon spin as variates.

3. Margenau–Hill probabilities for photons

The Margenau–Hill trivariate characteristic function for three non-commutin ators $\hat{X}_1, \hat{X}_2, \hat{X}_3$ is defined by,

$$\begin{aligned}\phi_{\mathrm{MH}}(I_1, I_2, I_3) = \frac{1}{3!}\mathrm{Tr}[\rho\{&\exp(i\hat{X}_1 I_1)\exp(i\hat{X}_2 I_2)\exp(i\hat{X}_3 I_3) \\ &+ \exp(i\hat{X}_1 I_1)\exp(i\hat{X}_3 I_3)\exp(i\hat{X}_2 I_2) \\ &+ \exp(i\hat{X}_2 I_2)\exp(i\hat{X}_3 I_3)\exp(i\hat{X}_1 I_1) \\ &+ \exp(i\hat{X}_2 I_2)\exp(i\hat{X}_1 I_1)\exp(i\hat{X}_3 I_3) \\ &+ \exp(i\hat{X}_3 I_3)\exp(i\hat{X}_1 I_1)\exp(i\hat{X}_2 I_2) \\ &+ \exp(i\hat{X}_3 I_3)\exp(i\hat{X}_2 I_2)\exp(i\hat{X}_1 I_1)\}].\end{aligned}$$

Choosing $\hat{X}_1, \hat{X}_2, \hat{X}_3$ to be $\sigma_1, \sigma_2, \sigma_3$ and ρ as given in (3), we can simplify (11) to

$$\begin{aligned}\phi^{(\sigma)}_{\mathrm{MH}}(I_1, I_2, I_3) = {} & s_0 \cos I_1 \cos I_2 \cos I_3 + i s_1 \sin I_1 \cos I_2 \cos I_3 \\ & + i s_2 \cos I_1 \sin I_2 \cos I_3 + i s_3 \cos I_1 \cos I_2 \sin I_3.\end{aligned}$$

Simplifying (12) further, $\phi^{(\sigma)}_{\mathrm{MH}}(I_1, I_2, I_3)$ could be cast into the form

$$\phi^{(\sigma)}_{\mathrm{MH}}(I_1, I_2, I_3) = \sum_{m_1, m_2, m_3 = -1, +1} f^{(\sigma)}_{\mathrm{MH}}(m_1, m_2, m_3)\exp(i(m_1 I_1 + m_2 I_2 +$$

where $f^{(\sigma)}_{\mathrm{MH}}(m_1, m_2, m_3)$ could be identified as the Margenau–Hill trivariate prob mass function for photons and is given by

$$f^{(\sigma)}_{\mathrm{MH}}(m_1, m_2, m_3) = \frac{1}{8}[s_0 + m_1 s_1 + m_2 s_2 + m_3 s_3].$$

m_1, m_2, m_3 are the classical random variables representing the operators $\sigma_1, \sigma_2,$ the Stokes parameters could be identified as first moments of the distri $f^{(\sigma)}_{\mathrm{MH}}(m_1, m_2, m_3)$ i.e.,

$$s_k = \mathrm{Tr}(\rho\sigma_k) = \sum_{m_1, m_2, m_3 = -1, +1} m_k f^{(\sigma)}_{\mathrm{MH}}(m_1, m_2, m_3), \quad k = 1, 2, 3.$$

On the other hand $\hat{X}_1, \hat{X}_2, \hat{X}_3$ in (11) could be chosen as J_1, J_2, J_3, the photo components and the density matrix ρ is then given by (5). To simplify the charac function $\phi^{(J)}_{\mathrm{MH}}(I_1, I_2, I_3)$ we follow the approach outlined in [14] where we ident the unitary matrices

$$U_1 = \frac{1}{2}\begin{pmatrix} 1 & \sqrt{2} & 1 \\ \sqrt{2} & 0 & -\sqrt{2} \\ 1 & -\sqrt{2} & 1 \end{pmatrix}, \quad U_2 = \frac{1}{2}\begin{pmatrix} 1 & -i\sqrt{2} & -1 \\ \sqrt{2} & 0 & \sqrt{2} \\ 1 & i\sqrt{2} & -1 \end{pmatrix}$$

$$\exp(iJ_1I_1) = U_1\exp(iJ_1I_1)U_1^{\dagger}, \exp(iJ_2I_2) = U_2\exp(iJ_2I_2)U_2^{\dagger} \quad (17)$$

in (11) where J_1^d and J_2^d are diagonal matrices with diagonal elements $1, 0, -1$. We can now simplify the characteristic function further to yield

$$\phi_{\mathrm{MH}}^{(\mathrm{J})}(m_1, m_2, m_3) = \sum_{m_1,m_2,m_3=-1,0,+1} f_{\mathrm{MH}}^{(\mathrm{J})}(m_1, m_2, m_3) \times \exp(i(m_1I_1 + m_2I_2 + m_3I_3)) \quad (18)$$

where

$$f_{\mathrm{MH}}^{(\mathrm{J})}(m_1, m_2, m_3) = \frac{1}{3}\mathrm{Re}[(\rho U_1^{\dagger})_{m_3m_1}(U_1U_2^{\dagger})_{m_1m_2}(U_2)_{m_2m_3} + (U_2\rho)_{m_2m_3}(U_1^{\dagger})_{m_3m_1}(U_1U_2^{\dagger})_{m_1m_2} + (U_2\rho U_1^{\dagger})_{m_2m_1}(U_2^{\dagger})_{m_3m_2}(U_1)_{m_1m_3}]. \quad (19)$$

Explicitly it may be seen that $f_{\mathrm{MH}}^{(\mathrm{J})}(m_1, m_2, m_3)$ assumes the simple form

$$f_{\mathrm{MH}}^{(\mathrm{J})}(m_1, m_2, m_3) = \frac{1}{48}\{2m_1m_2s_2 - m_3s_3\} \quad (20)$$

if $m_1, m_2, m_3 = \pm 1$;

$$f_{\mathrm{MH}}^{(\mathrm{J})}(m_1, m_2, m_3) = \frac{1}{24}\{m_1m_2s_2 + 3m_3^2[s_0 - (m_1^2 - m_2^2)s_1] - 2m_3s_3\} \quad (21)$$

if one of the variables m_1, m_2, m_3 assumes the value 0 and

$$f_{\mathrm{MH}}^{(\mathrm{J})}(m_1, m_2, m_3) = -\frac{1}{12}m_3s_3 \quad (22)$$

if more than one of m_1, m_2, m_3 take the value 0. Consequently the Stokes parameters could now be realised as the classical averages,

$$s_1 = \mathrm{Tr}[\rho(J_2^2 - J_1^2)] = \sum_{m_1,m_2,m_3=-1}^{1} f_{\mathrm{MH}}^{(\mathrm{J})}(m_1, m_2, m_3)(m_2^2 - m_1^2)$$

$$s_2 = \mathrm{Tr}[\rho(J_1J_2 + J_2J_1)] = \sum_{m_1,m_2,m_3=-1}^{1} f_{\mathrm{MH}}^{(\mathrm{J})}(m_1, m_2, m_3)(2m_1m_2)$$

$$s_3 = -\mathrm{Tr}[\rho J_3] = -\sum_{m_1,m_2,m_3=-1}^{1} f_{\mathrm{MH}}^{(\mathrm{J})}(m_1, m_2, m_3)m_3 \quad (23)$$

4. Wigner–Weyl probabilities for photons

The Wigner–Weyl characteristic function is defined by

$$\phi_{\mathrm{WW}}(I_1, I_2, I_3) = \mathrm{Tr}[\rho\exp(i(\hat{X}_1I_1 + \hat{X}_2I_2 + \hat{X}_3I_3))]. \quad (24)$$

Substituting $\hat{X}_1 = \sigma_1, \hat{X}_2 = \sigma_2, \hat{X}_3 = \sigma_3$ and ρ given by (3) in (24), we get

$$\phi_{\mathrm{WW}}^{(\sigma)}(I_1, I_2, I_3) = s_0\left[\cos I + \mathbf{P}\cdot\mathbf{I}\frac{\sin I}{I}\right] \quad (25)$$

where $I = (I_1^2 + I_2^2 + I_3^2)^{1/2}$.

Fourier transform of the characteristic function $\phi^{(\sigma)}_{WW}(I_1, I_2, I_3)$ yields the W
Weyl trivariate probability density function $f^{(\sigma)}_{WW}(x_1, x_2, x_3)$:

$$f^{(\sigma)}_{WW}(x_1, x_2, x_3) = (2\pi)^{-3} \iiint d^3 I \phi^{(\sigma)}_{WW}(I_1, I_2, I_3) \exp(-i(x_1 I_1 + x_2 I_2 + x_3 I_3))$$

$$= (2\pi)^{-3} s_0 \int_0^{\infty} \int_0^{\pi} \int_0^{2\pi} I^2 \mathrm{d}I \sin\theta_I \mathrm{d}\theta_I \mathrm{d}\phi_I \left[\cos I + i(\mathbf{P}\cdot\mathbf{I}) \frac{\sin I}{I} \right]$$

$$\times \exp(-i(x_1 I_1 + x_2 I_2 + x_3 I_3)).$$

Carrying out the integration over the solid angle $\mathrm{d}\Omega_I = \sin\theta_I \mathrm{d}\theta_I \mathrm{d}\phi_I$, we obta

$$f^{(\sigma)}_{WW}(x_1, x_2, x_3) = (2\pi^2 x)^{-1} \left[\int_0^{\infty} \mathrm{d}I \, I \cos I \sin Ix - \mathbf{P}\cdot\nabla_x \int_0^{\infty} \mathrm{d}I \sin I s \right.$$

where $\nabla_x = \left(\frac{\partial}{\partial x_1}, \frac{\partial}{\partial x_2}, \frac{\partial}{\partial x_3} \right)$, $x = (x_1^2 + x_2^2 + x_3^2)^{1/2}$. We can simplify (27) furthe

$$f^{(\sigma)}_{WW}(x_1, x_2, x_3) = s_0 [F_0(x) + F_1(x) \mathbf{P}\cdot\mathbf{x}]$$

where

$$F_0(x) = -\frac{1}{4\pi x} \frac{\mathrm{d}}{\mathrm{d}x} [\delta(1+x) + \delta(1-x)]$$

$$F_1(x) = -\frac{1}{4\pi} \frac{\mathrm{d}}{\mathrm{d}x} \left[\frac{\delta(1+x) - \delta(1-x)}{x} \right].$$

Now the quantum mechanical expectation values could be obtained in te
$f^{(\sigma)}_{WW}(x_1, x_2, x_3)$ as,

$$s_k = \mathrm{Tr}(\rho\sigma_k) = \iiint \mathrm{d}^3 x f^{(\sigma)}_{WW}(x_1, x_2, x_3) x_k, \quad k = 1, 2, 3.$$

Alternatively we can replace $\hat{X}_1, \hat{X}_2, \hat{X}_3$ in (20) by J_1, J_2, J_3 in which case

$$\phi^{(J)}_{WW}(I_1, I_2, I_3) = \mathrm{Tr}(\rho \exp(i\mathbf{J}\cdot\mathbf{I})).$$

We now express

$$\exp(i\mathbf{J}\cdot\mathbf{I}) = R^{\dagger}(\phi_I, \theta_I, 0) \exp(iJ_3 I) R(\phi_I, \theta_I, 0)$$

where $R(\alpha, \beta, \gamma)$ denote rotations through Euler angles α, β, γ. Making use of (5)
and the transformation properties of the spherical tensor operators $\tau^k_q(\mathbf{J})$
rotations viz.,

$$R(\alpha, \beta, \gamma) \tau^k_q(\mathbf{J}) R^{\dagger}(\alpha, \beta, \gamma) = \sum_{q'=-k}^{k} \tau^k_{q'}(\mathbf{J}) D^k_{q'q}(\alpha, \beta, \gamma)$$

where D^k denotes the standard $(2k+1)$ dimensional irreducible representa

rotations [18], we obtain

$$\phi^{(J)}_{WW}(I_1, I_2, I_3) = \Bigg[s_0 - \frac{3}{2}\frac{s_3 I_3}{I} \sum_{m=-1,0,1} m \exp(imI) + \frac{1}{4I^2}\{s_0(3I_3^2 - I^2) + 3s_1(I_2^2 - I_1^2) - 6s_2 I_1 I_2\} \times \sum_{m=-1,0,1} (3m^2 - 2)\exp(imI) \Bigg]. \tag{34}$$

Fourier transform of $\phi^{(J)}_{WW}(I_1, I_2, I_3)$ could now be carried out by generalising the techniques used in (26) to (29) to yield the Wigner–Weyl probability density function,

$$f^{(J)}_{WW}(x_1, x_2, x_3) = \Bigg[s_0 \mathscr{F}_0(x) - \mathscr{F}_1(x) s_3 x_3 + \mathscr{F}_2(x) \times \left\{ \frac{s_0}{3}(3x_3^2 - x^2) + s_1(x_2^2 - x_1^2) + 2s_2 x_1 x_2 \right\} \Bigg] \tag{35}$$

where

$$\mathscr{F}_0(x) = -\frac{1}{6\pi x} \sum_m \frac{\mathrm{d}}{\mathrm{d}x} \delta(x - m)$$

$$\mathscr{F}_1(x) = \frac{1}{4\pi x} \sum_m m \frac{\mathrm{d}}{\mathrm{d}x} \left[\frac{\delta(x-m)}{x} \right]$$

$$\mathscr{F}_2(x) = \frac{1}{24\pi} \sum_m (3m^2 - 1) \left[\frac{1}{x}\frac{\mathrm{d}}{\mathrm{d}x} \left\{ \frac{1}{x}\frac{\mathrm{d}}{\mathrm{d}x} \left(\frac{\varepsilon(m-x)}{x} \right) \right\} \right] \tag{36}$$

Here $\varepsilon(m - x)$ denotes the step function

$$\varepsilon(a) = \frac{1}{2\pi i} \int_{-\infty}^{\infty} \frac{\mathrm{e}^{iat}}{t} \mathrm{d}t = \begin{cases} 1 & \text{if } a > 0 \\ 0 & \text{if } a < 0 \end{cases} \tag{37}$$

Making use of the Weyl correspondence rule

$$x_1^l x_2^m x_3^n \to S\{J_1^l J_2^m J_3^n\} \tag{38}$$

where S stands for the symmetrizer, the Stokes parameters could be realised as the classical averages,

$$s_1 = \mathrm{Tr}[\rho(J_2^2 - J_1^2)] = \iiint f^{(J)}_{WW}(x_1, x_2, x_3)(x_2^2 - x_1^2)\mathrm{d}^3x$$

$$s_2 = \mathrm{Tr}[\rho(J_1 J_2 + J_2 J_1)] = \iiint f^{(J)}_{WW}(x_1, x_2, x_3)(2x_1 x_2)\mathrm{d}^3x$$

$$s_3 = -\mathrm{Tr}[\rho J_3] = -\iiint f^{(J)}_{WW}(x_1, x_2, x_3) x_3 \mathrm{d}^3x \tag{39}$$

Acknowledgement

One of us (ARU) thanks the CSIR for financial assistance throu
a Research Fellowship.

References

[1] G N Ramachandran and S Ramaseshan, *Crystal optics in Handbuch de*
S Flugge (Springer Verlag, Berlin, 1961)
[2] M Born and E Wolf, *Principles of optics*, Third edition, (Pergamon Pr
[3] C Huygens, *Traite' de La Lumiere* (Completed in 1968 and published in L
[2])
[4] G G Stokes, *Trans. Cam. Philos. Soc.* **9**, 399 (1852)
[5] H Poincare, *Theorie Mathematique de Lumiere* (Georges Carre, Paris, 1
[6] S S Schweber, *An Introduction to relativistic quantum field theory* (Row
ston. III, 1961)
A I Akhieser and V B Berestetsky, *Quantum electrodynamics* (Interscience,
[7] U Fano, *Rev. Mod. Phys.* **29**, 74 (1957)
[8] W H McMaster, *Rev. Mod. Phys.* **33**, 8 (1961)
[9] P A M Dirac, *Proc. Camb. Philos. Soc.* **25**, 62 (1929)
Von Neumann, *Nachr. Akad. Wiss Goettingen* **1**, 245 (1927)
L D Landau, *Z. Phys.* **64**, 629 (1930)
[10] C Chandler, L Cohen, C Lee, M Scully and K Wodkiewicz, *Found. Phys.*
[11] H Margenau and R N Hill, *Prog. Theor. Phys.* **26**, 722 (1961)
[12] H Weyl, *Z. Phys.* **46**, 1 (1927)
[13] E P Wigner, *Phys. Rev.* **40**, 749 (1932)
[14] A R Usha Devi, Swarnamala Sirsi, G Devi and G Ramachandran, *J. Phys.* G
[15] G Ramachandran, M V N Murthy and K S Mallesh, *Pramana – J. Phys.*
[16] G Ramachandran and K S Mallesh, *Phys. Rev.* **C40**, 1641 (1989)
[17] G Ramachandran , K S Mallesh and V Ravishankar, *J. Phys.* **G10**, L163 (
[18] M E Rose, *Elementary theory of angular momentum* (John Wiley, New Yor

PRAMANA
— journal of
physics

© Printed in India

Vol. 45, No. 4,
October 1995
pp. 327–331

On the Dirac equation with anomalous magnetic moment term in a beam of electromagnetic wave

N D SEN GUPTA
Tata Institute of Fundamental Research, Homi Bhabha Road, Bombay 400 005, India

MS received 24 April 1995

Abstract. The object of the paper is to obtain the solution of the Dirac equation with the Pauli-term in an electromagnetic field depending on the single variable $(ct - \mathbf{nr})$ along the direction $\mathbf{n}$.

Keywords. General; quantum theory; quantum mechanics.

PACS No. 03·65

1. Introduction

Recently, in a short paper by Salamin [1], an attempt was made to solve the Dirac equation with anomalous magnetic moment in the presence of a plane electromagnetic wave. Apart from the fact that the exact nature of the electromagnetic field is not stated clearly, the solution presented in the paper does not satisfy the equation which is proposed to be solved. The object of the present paper is to investigate the same problem for a general class of electromagnetic field considered in [1].

The field we consider is a function of a single variable

$$\theta = R^\mu x_\mu = Rx, \quad x^\mu \equiv (x^0 = ct, \mathbf{r}).$$

We use the notation $ab = a^\mu b_\mu$ for any two vectors a and b. The Lorentz potential for the external electromagnetic field is $A^\mu = A^\mu(\theta)$. For the wave field,

$$RR = R^\mu R_\mu = 0. \tag{1}$$

So that, without any loss of generality, with the choice of the gauge and the Lorentz condition,

$$A_0 = 0, \quad \frac{\partial A^\mu}{\partial x^\mu} = R\frac{dA}{d\theta} = 0. \tag{1'}$$

In general the electric and magnetic fields in these cases are always in the plane normal to the fixed direction $\mathbf{R}/R_0$, and the most general form of this class of field may be written as,

$$\mathbf{A} = \int_{-\infty}^{\infty} \{\mathbf{e}_1 a_1(R_0) f_1(\theta) + \mathbf{e}_2 a_2(R_0) f_2(\theta)\} dR_0 \tag{2}$$

where

$$\mathbf{e}_i \cdot \mathbf{R} = 0, \quad \mathbf{e}_i \cdot \mathbf{e}_j = \delta_{ij} \quad (i, j = 1, 2). \tag{2'}$$

In the case of radiation, it is not necessarily monochromatic, R_0 is proportional to the frequency. The Dirac equation without the Pauli-term for some special class of fields

belonging to this category was first solved by Volkov [2] and later by others [3- the investigation of the scattering of electromagnetic radiation and other pl problems.

In the following sections we proceed to construct the solution. The prob reduced to the solution of a second order ordinary differential equation. It n emphasized that the problem, in general, cannot be reduced to quadrature w further specification of the nature of the functions $f_1(\theta)$ and $f_2(\theta)$. The last sec devoted to discussion of nature of the solution for various special cases.

2. The equation and the solution

The Dirac equation with the Pauli-term may be written as

$$\left\{ i\gamma^\mu \frac{\partial}{\partial x^\mu} + \varepsilon\gamma^\mu A_\mu + M + i\frac{\lambda}{2}\gamma^\mu\gamma^\nu \frac{\partial A_\mu}{\partial x^\nu} \right\} \Psi = 0,$$

$$\gamma^\mu\gamma^\nu + \gamma^\nu\gamma^\mu = 2g^{\mu\nu},$$

$g^{\mu\nu} \equiv (1, -1, -1, -1)$ and $\varepsilon = e/\hbar c$, $M = mc/\hbar$, e and m are the charge and mass particle and λ is the parameter depending on the strength of the anomalous ma moment of the particle. Since $\partial/\partial v$, $\partial/\partial v_1$ and $\partial/\partial v_2$, where $v = R_0 x_0 + \mathbf{R}\cdot\mathbf{r}$ and v_i commute with the operator on Ψ (eq. (3)) they are constants. Hence, one can wri solution in the form,

$$\Psi(x_0, \mathbf{r}) = e^{-i(p.x + S(\theta))}\Phi(\theta),$$

where p^μ is an arbitrary vector and $S(\theta)$ is a scalar function of θ. Substituting this one gets,

$$\{\gamma(p + \varepsilon A) + M\}\Phi + \left\{ \frac{dS}{d\theta} + i\frac{\lambda}{2}\gamma\frac{dA}{d\theta} + i\frac{d}{d\theta} \right\}\gamma R\Phi = 0.$$

By virtue of eq. (1′)

$$(\gamma R)^2 = 0.$$

Again fron eqs (1′) and (2)

$$(RA) = 0 \text{ and } \gamma R\gamma A + \gamma A\gamma R = 0.$$

Hence multiplying eq. (5) by γR from left,

$$2(pR)\Phi = \{\gamma(p + \varepsilon A) - M\}\gamma R\Phi,$$

i.e.,

$$2(pR)\{\gamma(p + \varepsilon A) + M\}\Phi = \{(p + \varepsilon A)(p + \varepsilon A) - M^2\}\gamma R\Phi.$$

We choose p and S such that

$$pp = M^2,$$

$$2(pR)\frac{dS}{d\theta} + 2\varepsilon pA + \varepsilon^2 AA = 0$$

Finally from (5) and (8),

$$\left(\frac{\mathrm{d}}{\mathrm{d}\theta}+\frac{\lambda}{2}\gamma\frac{\mathrm{d}A}{\mathrm{d}\theta}\right)(\gamma R)\Phi=0. \tag{11}$$

In the absence of the Pauli-term i.e., for $\lambda=0$, Φ is constant and the problem reduces to that of the usual Dirac equation which has been already mentioned. From (9) $\hbar p$ is the free particle momentum. It is important to note that eq. (10), hence the expression for S is independent of λ.

3. Special cases

Although eq. (11) is linear, the determination of Φ cannot be, in general, reduced to quadrature, because it contains at least two mutually anti-commuting matrices. We consider special cases:

a) One of the functions f_1 and f_2 in (2) is zero, or equivalently the ratio f_1/f_2 is a constant, i.e.,

$$\mathbf{A}=\mathbf{e}f(\theta). \tag{12}$$

In this case the electric and magnetic fields **E** and **H** are given by,

$$\mathbf{E}=\mathbf{e}\cdot R_0\frac{\mathrm{d}f}{\mathrm{d}\theta}$$

and

$$\mathbf{H}=\mathbf{e}\times\mathbf{R}\frac{\mathrm{d}f}{\mathrm{d}\theta} \tag{13}$$

(*i*) If f is a linear function of θ, the field consists of constant mutually perpendicular electric and magnetic field of same magnitude.

and

(*ii*) If f is a periodic function, e.g., $f=F\cos(\theta+\delta)$ the field is due to plane polarized radiation, not necessarily monochromatic, along a fixed direction $\mathbf{R}/R_0$. Both these types of fields are important for applications in physical problems. From (11), one gets directly

$$(\gamma R)\Phi=\exp-\frac{\lambda}{2}(\gamma A)\Phi_0 \tag{14}$$

where Φ_0 is a constant spinor. This case has been discussed by Chakrabarti [6].

b) In the general case eq. (11) cannot be directly integrated. But the solution can be expressed in terms of solutions of second order linear differential equations. We may write

$$\mathbf{A}=F(\mathbf{e}_1\cos\mu+\mathbf{e}_2\sin\mu)$$

where

$$F^2=f_1^2+f_2^2 \quad \text{and} \quad \tan\mu=f_2/f_1 \tag{15}$$

Let $u_{\pm}$ be eigenspinors of $i(\mathbf{e}_1\cdot\gamma)(\mathbf{e}_2\cdot\gamma)$ with eigenvalues ± 1, i.e.,

$$i(\mathbf{e}_1\cdot\gamma)(\mathbf{e}_2\cdot\gamma)u_{\pm} = \pm u_{\pm}$$

$$(\mathbf{e}_2\cdot\gamma)u_{\pm} = \mp i(\mathbf{e}_1\cdot\gamma)u_{\pm},$$

and

$$i(\mathbf{e}_1\cdot\gamma)u_{\pm} \equiv u_{\mp},$$

$$\tilde{u}_{\pm}\cdot u_{\mp} = 0, \quad \tilde{u}_{\pm}\cdot u_{\pm} = 1.$$

Let

$$\gamma\cdot R\Phi = g_+(\theta)u_+ + g_-(\theta)u_-.$$

Substituting these in eq. (11), one is lead to two simultaneous first order equations,

$$\frac{dg_+}{d\rho} = i\lambda e^{-i\mu}g_-$$

$$\frac{dg_-}{d\rho} = -i\lambda e^{i\mu}g_+$$

where $d\rho = Fd\theta$. It is clear that g_+ and g_- are mutually complex conjugate o other. It follows from above that

$$\frac{d^2g}{d\rho^2} + i\frac{d\mu}{d\rho}\frac{dg_+}{d\rho} - \lambda^2 g_+ = 0$$

$$\frac{d^2g_-}{d\rho^2} - i\frac{d\mu}{d\rho}\frac{dg_-}{d\rho} - \lambda^2 g_- = 0.$$

Thus the problem ultimately reduces to solving the second order linear diffe equation. It must be emphasized that one has to restrict to only those solutions which satisfies the first order (18). One cannot proceed further without kn explicitly the nature of functions f_1 and f_2. We can consider some of the par cases of physical importance; namely the case of circular and elliptic pol radiation field. For monochromatic radiation

$$\mathbf{A} = \mathbf{e}_1 a_1\cos(\theta+\delta_1) + \mathbf{e}_2 a_2\sin(\theta+\delta_2).$$

Introducing suitable rotation in the plane of $\mathbf{e}_1$ and $\mathbf{e}_2$ one can write

$$\mathbf{A} = \mathbf{e}'_1 a'_1\cos\theta + \mathbf{e}'_2 a'_2\sin\theta,$$

where $\mathbf{e}'_1, \mathbf{e}'_1$ are the new mutually orthogonal unit vectors in the same plane and a a'_2 depend on a_1, a_2, δ_1 and δ_2. The radiation is, in general, elliptically polarized, particular for $a'_1 = a'_2 = a$ (say) the polarization is circular and the expressions and g_- take the simple form,

$$g_+ = e^{-ia(\theta/2)}\{B_+ e^{i(1-\lambda^2/2)^{1/2}a_{\parallel}} + B_- e^{-i(1-\lambda^2/2)a_{\parallel}}\}$$

$$= g^*_-$$

where B_+ and B_- depend on λ and a. They are to be so choosen that the simultaneous equation for g_+ and g_- (eqs (18)) are satisfied.

Finally, once the solution of eq. (11) is obtained, (for the special cases considered they are given by eqs (14) and (20)), one can finally obtain Φ from (8). Thus

$$\Phi(p, x) = \frac{1}{2(pR)} \{\gamma(p + \varepsilon A) - M\} \Phi_0', \tag{21}$$

where Φ_0' stands for the solution eq. (11), so that

$$\Psi(p, x) = e^{-i(p \cdot x + S(\theta))} \Phi(p, x). \tag{22}$$

It should be noted that each of the spinors $u_{\pm}$ introduced by (18) is two dimensional and $u_{\pm}$ arbitrary unit spinor in the respective subspaces. This degeneracy is removed by the operator (γA) which also changes $u_{\pm}$ to $u_{\mp}$. Again the part $(\gamma \mathbf{p}_1)$ of (γp) where $\mathbf{p}_1$ is a vector in the plane perpendicular to $\mathbf{R}$, changes $u_{\pm}$ to $u_{\mp}$. The subspace is invariant with respect to the remaining part of γp, namely $\gamma_0^0 p_0 - \gamma \cdot \mathbf{p}_{\parallel}$ ($\mathbf{p}_{\parallel}$ along $\mathbf{R}$), but the degeneracy may be removed.

4. Remarks

Since, eq. (2) is linear the most general solution is obtained by suitable superposition of the solutions given by (22). The most general solution is obtained in the form

$$\Psi(x) = \int_{-\infty}^{\infty} K(\mathbf{p}) \Psi(\mathbf{p}, x) d\mathbf{p}. \tag{23}$$

The function $K(\mathbf{p})$ is to be obtained by the given initial and/or boundary condition. There is no need of appeal for the field to vanish at infinity. Again, we want to emphasize that the radiation field need not be monochromatic but it should be unidirectional. One can also similarly investigate the class of fields for which R is not a null vector, $R, R \neq 0$. This encompases a wider class of fields which we hope to consider in future.

It can be easily checked in the absence of the anomalous magnetic moment, i.e., $\lambda = 0$, the solution given by eq. (22) reduced to known solution [3–5]. On the other hand for particles with no charge but anomalous magnetic moment, i.e., $e = 0$ but $\lambda \neq 0$, which may be of importance in astrophysical problem is obtained from (21) and (22) putting $\varepsilon = 0$ and hence $S = 0$.

References

[1] Salamin Yousef I, *J. Phys.* **26**, 6067 (1993)
[2] D M Volkov, *Z. Phys.* **94**, 250 (1935)
[3] P A M Dirac, *Comm. Dublin Inst. Adv. Studies Ser.* **A3**, (1946)
[4] N D Sen Gupta, *Bull. Calcutta Math. Soc.* **39**, 147 (1947), **44**, 132, 175 (1952); *Z. Phys.* **200**, 13 (1961); **201**, 222 (1961)
[5] X Ehlotsky, *Opt. Commun.* **13**, 1 (1975)
[6] A Chakrabarti, *Nuovo Cimento* **A56**, 604 (1968)

Fermilab top mass and modified Fritzsch mass matrices

P S GILL* and MANMOHAN GUPTA
Department of Physics, Panjab University, Chandigarh 160014, India
*Permanent Address: S.G.G.S. College, Chandigarh 160026, India

MS received 23 June 1995; revised 28 August 1995

Abstract. Fritzsch like mass matrices with non-zero 22-elements both in U sector and D sector have been investigated in the context of latest data regarding m_t^{phys}, $|V_{ub}|$, $|V_{cb}|$, $|V_{td}|$ and $|V_{ts}|$. Unlike several other phenomenological models, the present model not only accommodates the value of m_t^{phys} in the range 150–240 GeV, encompassing the CDF and D0 values, but is also able to reproduce $|V_{cb}| \cong 0{\cdot}040$ and $|V_{ub}/V_{cb}| = 0{\cdot}08 \pm 0{\cdot}02$ and $|V_{td}|$ is predicted to lie in the range 0·005–0·014. Further, the angles of the unitarity triangle, related to the CP-violating asymmetries, are calculated to be in the ranges $-1{\cdot}0 \leqslant \sin 2\alpha \leqslant -0{\cdot}1$, $0{\cdot}6 \leqslant \sin 2\alpha \leqslant 1{\cdot}0$ and $0{\cdot}48 \leqslant \sin 2\beta \leqslant 0{\cdot}56$, which are in agreement with other recent calculations.

Keywords. Quark mass matrices; quark mixing matrix; unitarity triangle; CP violation; fermion masses.

PACS Nos 12·15; 13·25; 13·20; 11·30

1. Introduction

The recently observed evidence for the top quark in $p\bar{p}$ collisions at Fermilab [1, 2] has added another success to the standard model's (SM) already long list of achievements. This, however, is certainly going to accelerate the search for discovering physics beyond the standard model. To this end, a peep into the physics beyond the SM is provided by the fermion mass matrices and mixing angles which essentially enter as free parameters in the SM. In the absence of a dynamical theory for quark mass matrices, several phenomenological models [3–14] have been considered with fair degree of success. The most widely studied as well as the most economical model is that of Fritzsch which, unfortunately, has been ruled out by the data [1, 2, 15]. The observation of rather high $m_t^{\text{phys}} = 176 \pm 13$ GeV [1] as well as $m_t^{\text{phys}} = 199 \pm 30$ GeV [2] at Fermilab has further complicated the situation regarding phenomenological mass matrices. In fact, rather high value of m_t^{phys}, although in agreement with limits on m_t^{phys} expected from radiative corrections within the SM, has posed serious challenge to some of the phenomenological models for mass matrices.

In the absence of a viable dynamical theory for quark mass matrices, it is perhaps desirable to develop phenomenological models which are simple as well as predictive. If such models, while remaining in tune with the data, are able to generate simple relations amongst Cabibbo–Kobayashi–Maskawa (CKM) matrix elements, then these models may provide vital clues for formulating a dynamical theory. We feel that in the formulation of a viable phenomenological scheme, ideas such as the hierarchical structure of mass matrices, relative smallness of CP violation, etc., may play a vital role.

At present we do not attempt to go into the origin of mass matrices, rather try to see the implications of these for the CKM matrix (V_{CKM}) phenomenology. In fact, we shall

mass matrices accommodate recently found value of m_t^{phys} along with the refinements in the measurements of V_{CKM} elements. Further, it would be interes investigate the implications of such mass matrices for hitherto unknown CKM elements, $|V_{td}|$ and $|V_{ts}|$ as well as the different angles of the unitarity triangle [

The plan of the paper is as follows. In § 2 we present the essential details phenomenological quark mass matrices considered here. In § 3, we present defi as well as relations of angles of the unitarity triangle with the asymmetries in B In § 4, we present the details of our calculations and results. Section 5 summari principal findings.

2. Mass matrices

For the sake of completeness and readability we reproduce some of the essential of Gill and Gupta [16]. To begin with, we consider hermitian mass matrices following form

$$M^i = \begin{bmatrix} 0 & A^i & 0 \\ A^{*i} & D^i & B^i \\ 0 & B^{*i} & C^i \end{bmatrix}, \quad [i = u, d],$$

where

$$A^i = |A^i| \exp(i\alpha_i),\ B^i = |B^i| \exp(i\beta_i)$$

and the elements of M^i are supposed to follow the hierarchical structur $|A^i| \ll |B^i| \approx D^i < C^i$.

The above matrices M^i can be expressed as

$$M^i = P^i \bar{M}^i P^{i\dagger},$$

where real matrices $\bar{M}^i$ are

$$\bar{M}^i = \begin{bmatrix} 0 & |A^i| & 0 \\ |A^i| & D^i & |B^i| \\ 0 & |B^i| & C^i \end{bmatrix},$$

and

$$P^i = \text{diag}\{1, \exp(-i\alpha_i), \exp(-i(\alpha+\beta)_i)\}.$$

The matrices $\bar{M}^i$ can be diagonalized exactly by orthogonal transformatic example,

$$\bar{M}^i = O^i M^i_{\text{diag}} (O^i)^\dagger$$

where

$$M^i_{\text{diag}} = \text{diag}(m_1, -m_2, m_3),$$

with subscripts 1, 2, 3 referring to u, c, t in U sector and d, s, b in D sector.

Using $\mathrm{tr}(M^i)$, $\mathrm{tr}(M^i)^2$, $\det(M^i)$, the values of matrix elements A^i, B^i, C^i are expressed in terms of quark masses as

$$C^i = (m_1 - m_2 + m_3 - D^i),\ A^i = (m_1 m_2 m_3 / C^i)^{1/2}$$
$$B^i = (-(A^i)^2 + C^i D^i + m_1 m_2 + m_2 m_3 - m_1 m_3)^{1/2}. \tag{7}$$

The diagonalising transformations O^i can be expressed as

$$O^i = \begin{bmatrix} (m_2 m_3 f_1/\Delta_1)^{1/2} & -(m_1 m_3 f_2/\Delta_2)^{1/2} & (m_1 m_2 f_3/\Delta_3)^{1/2} \\ (C^i m_1 f_1/\Delta_1)^{1/2} & (C^i m_2 f_2/\Delta_2)^{1/2} & (C^i m_3 f_3/\Delta_3)^{1/2} \\ -(m_1 f_2 f_3/\Delta_1)^{1/2} & -(m_2 f_1 f_3/\Delta_2)^{1/2} & (m_3 f_1 f_2/\Delta_3)^{1/2} \end{bmatrix} \tag{8}$$

where

$$f_1 = m_3 - m_2 - D^i; f_2 = m_3 + m_1 - D^i;\ f_3 = m_2 - m_1 + D^i;$$
$$\Delta_i = C^i(m_3 - m_1)(m_2 + m_1);\ \Delta_2 = C^i(m_3 + m_2)(m_2 + m_1)$$
$$\Delta_3 = C^i(m_3 + m_2)(m_3 - m_1). \tag{9}$$

To facilitate comparison with other similar approaches as well as for better physical understanding of the structure of V_{CKM}, we present here the approximate form of O^u. For example, by considering $m_u \ll m_c < D^u < m_t$ as well as $m_d \ll m_s < D^d < m_b$, the structure for O^u can be simplified and expressed as

$$O^u \cong \begin{bmatrix} 1 & -a_0 & a_0 d_0^2 R_u \\ a_0(1-R_t)^{1/2} & (1-R_t)^{1/2} & R_t'^{1/2} \\ -a_0 R_t'^{1/2} & -R_t'^{1/2} & (1-R_t)^{1/2} \end{bmatrix} \tag{10}$$

where

$$a_0^2 = (m_u/m_c),\ d_0^2 = (m_c/m_t),\ R_t = D^u/m_t,\ R_t' = \left(\frac{m_c + D^u}{m_t}\right)$$

and

$$R_u = \left(\frac{m_c + D^u}{m_t - D^u}\right)^{1/2}.$$

The matrix O^d can be obtained simply by changing $u \to d$, $c \to s$, $t \to b$ with $a_0 \to b_0$ and $d_0 \to c_0$ where $b_0^2 = (m_d/m_s)$ and $c_0^2 = (m_s/m_b)$.

The mixing matrix V_{CKM} in terms of $O^{u,d}$ can be expressed as

$$V_{\mathrm{CKM}} = O^{u\dagger} P^{ud} O^d, \tag{11}$$

where

$$P^{ud} = \mathrm{diag}\{1, \exp(i\phi_1), \exp(i\phi_2)\};\quad \phi_1 = \alpha_u - \alpha_d \text{ and } \phi_2 - \phi_1 = \beta_u - \beta_d.$$

Using (10) and retaining terms of leading order, (11) can be simplified and written as

$$V_{\mathrm{CKM}} \equiv \begin{bmatrix} V_{ud} & V_{us} & V_{ub} \\ V_{cd} & V_{cs} & V_{cb} \\ V_{td} & V_{ts} & V_{tb} \end{bmatrix}$$
$$\cong \begin{bmatrix} 1 + a_0 b_0 g_1 & -b_0 + a_0 g_1 & b_0 c_0^2 R_d + a_0 g_2 \\ -a_0 + b_0 g_1 & a_0 b_0 + g_1 & g_2 \\ a_0 d_0^2 R_u + b_0 g_4 & g_4 & g_3 \end{bmatrix} \tag{12}$$

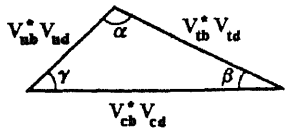

Figure 1. The CKM unitarity triangle in the complex plane.

where

$$g_1 = ((1-R_t)(1-R_b))^{1/2}\exp(i\phi_1) + (R_t' R_b')^{1/2}\exp(i\phi_2), \tag{13}$$

$$g_2 = (R_b'(1-R_t))^{1/2}\exp(i\phi_1) - (R_t'(1-R_b))^{1/2}\exp(i\phi_2), \tag{14}$$

$$g_3 = g_1(\phi_1 \Leftrightarrow \phi_2) \tag{15}$$

and

$$g_4 = -g_2(\phi_1 \Leftrightarrow \phi_2). \tag{16}$$

The above expressions for V_{CKM} are approximate, however, for the purpose of calculations, we have employed exact expressions.

3. Unitarity triangle

The unitarity of CKM matrix leads to six relations involving complex CKM matrix elements. These six relations represent six triangles in the complex plane with their angles constituting weak observable phases. Out of the six triangles, there is one triangle where all the three angles are naturally large and is expressed as

$$V_{ud} V_{ub}^* + V_{cd} V_{cb}^* + V_{td} V_{tb}^* = 0, \tag{17}$$

which is represented in figure 1. Interestingly, the sides of this triangle correspond to the decays $B_d \to \pi\pi$, $B_d \to D\pi$ and $B_d - \bar{B}_d$ mixing represented by $(V_{ud} V_{ub}^*)$, $(V_{td} V_{tb}^*)$ and $(V_{cd} V_{cb}^*)$ respectively. The three angles of the triangle in terms of CKM matrix elements are defined as [18]

$$\alpha \equiv \arg(-V_{td} V_{tb}^* / V_{ud} V_{ub}^*), \tag{18}$$

$$\beta \equiv \arg(-V_{cd} V_{cb}^* / V_{td} V^*{}_{tb}), \tag{19}$$

$$\gamma \equiv \arg(-V_{ud} V_{ub}^* / V_{cd} V_{cb}^*). \tag{20}$$

Table 1. CP violating asymmetry parameter, ImΛ, for different decay modes and its corresponding relations to angles of unitarity triangle.

Quark subprocess	Decay mode	ImΛ
$\bar{b} \to \bar{u}u\bar{d}$	$B_d^0 \to \pi^+\pi^-$	$\sin 2\alpha$
$\bar{b} \to \bar{c}c\bar{s}$	$B_d^0 \to \psi K_s$	$-\sin 2\beta$
$\bar{b} \to \bar{u}u\bar{d}$	$B_s^0 \to \rho K_s$	$-\sin 2\gamma$

The CP violating asymmetry parameter Λ, for the respective decays, is related to the angles of the unitarity triangle [18], expressed in table 1. However, the relation of the asymmetry parameter for the respective decays in terms of V_{CKM} elements is given as

$$\text{Im}\,\Lambda(B_d^0 \to \pi^+\pi^-) = \text{Im}\left(\frac{V_{tb}^* V_{td} V_{ub} V_{ud}^*}{V_{tb} V_{td}^* V_{ub}^* V_{ud}}\right) = \frac{2\bar{\eta}[\bar{\eta}^2 + \bar{\rho}(\bar{\rho}-1)]}{[\bar{\eta}^2 + (1-\bar{\rho})^2][\bar{\eta}^2 + \bar{\rho}^2]}; \tag{21}$$

$$\text{Im}\,\Lambda(B_d^0 \to \psi K_s) = \text{Im}\left(\frac{V_{tb}^* V_{td} V_{cb} V_{cd}^*}{V_{tb} V_{td}^* V_{cb}^* V_{cd}}\right) = \frac{2\bar{\eta}(\bar{\rho}-1)}{[\bar{\eta}^2 + (1-\bar{\rho})^2]}; \tag{22}$$

and

$$\text{Im}\,\Lambda(B_s^0 \to \rho K_s) = \text{Im}\left(\frac{V_{tb}^* V_{ts} V_{cd} V_{cs}^* V_{ub} V_{ud}^*}{V_{tb} V_{ts}^* V_{cd}^* V_{cs} V_{ub}^* V_{ud}}\right) = -\frac{2\bar{\eta}\bar{\rho}}{[\bar{\eta}^2 + \bar{\rho}^2]}. \tag{23}$$

In (21)–(23) we have also shown relations in terms of modified Wolfenstein parameters ($\bar{\rho} = \rho(1 - \lambda^2/2)$, $\bar{\eta} = \eta(1 - \lambda^2/2)$) of CKM matrix as suggested by Buras *et al* [19].

4. Results and discussion

Before we present our results, a brief discussion about various inputs which have gone into the analysis is perhaps in order. As a first step, we have considered quark masses at 1 GeV [20], for example, $m_u = 0{\cdot}0051 \pm 0{\cdot}0015$ GeV, $m_d = 0{\cdot}0089 \pm 0{\cdot}0026$ GeV, $m_s = 0{\cdot}175 \pm 0{\cdot}055$ GeV, $m_c = 1{\cdot}35 \pm 0{\cdot}05$ GeV, $m_b = 5{\cdot}3 \pm 0{\cdot}1$ GeV. Further, in order to simplify the analysis, we have fixed the two phases, viz., $\phi_1 = \phi_2 = 90°$ in accordance with the values considered elsewhere [14, 15]. Noting the fact that the CKM matrix elements $|V_{us}|$ and $|V_{cb}|$ are well known and have weak dependence on m_3's and D^i's, we have restricted the parameter space by first reproducing $|V_{us}| \cong 0{\cdot}22$ and $|V_{cb}| \cong 0{\cdot}040$ [18], ignoring the spread in the values of $|V_{cb}|$ as the calculated quantities hardly show any dependence on these. After having fixed the values of $|V_{us}|$ and $|V_{cb}|$, we have calculated $|V_{ub}|$, $|V_{td}|$, $|V_{ts}|$ and other phenomenological quantities related to V_{CKM}, for different values of R_t and m_t (1 GeV), however, for the purpose of discussion we have converted m_t (1 GeV) values into m_t^{phys} values. The values of R_b are constrained by the relation,

$$|V_{cb}| = (R_b'(1 - R_t))^{1/2} - (R_t'(1 - R_b))^{1/2}. \tag{24}$$

In order to have a better appreciation of the significance of our results, we first discuss our results when (i) $R_t \neq 0$, $R_b = 0$ (ii) $R_b \neq 0$, $R_t = 0$, corresponding to 22-element being nonzero in U and D sectors respectively. Keeping in mind that V_{CKM} can be characterized by any of the four elements [17], in table 2 we have presented our results pertaining to $|V_{ub}|$ and $|V_{td}|$. This is primarily to examine whether in the above mentioned cases the present form of mass matrices can accommodate m_t^{phys} in the range 150–240 GeV and the latest data regarding $R_{ub}(= |V_{ub}/V_{cb}|)$ which is in the range 0·06–0·10 [18]. From table 2, it is evident that 0·07 is the maximum value of R_{ub} for m_t^{phys} in the range 150–240 GeV in agreement with the conclusions of other similar calculations [14, 15]. Further, one can easily check that the above value of R_{ub} cannot be increased beyond 0·07 by any variation of R_t (or R_b), m_t^{phys}, ϕ_1, ϕ_2 and other quark

Table 2. Calculated values of $|V_{cb}|$, R_{ub} and $|V_{td}|$ when (i) $R_b = 0, R_t \neq 0$ and (ii) $R_t = 0$ and $R_b \neq 0$ for certain representative values of the sets (R_t, m_t^{phys}) and (R_b, m_t^{phys}), m_t^{phys} in GeV units. In ascending order, the corresponding m_t (1 GeV) values in GeV units are 250, 300, 350 and 400.

	$R_b = 0$			$R_t = 0$			
(R_t, m_t^{phys})	$\|V_{cb}\|$	R_{ub}	$\|V_{td}\|$	(R_b, m_t^{phys})	$\|V_{cb}\|$	R_{ub}	$\|V_{td}\|$
(−0·030, 150)	0·036	0·07	0·008	(0·012, 150)	0·043	0·06	0·011
(−0·020, 150)	0·037	0·06	0·009	(0·014, 150)	0·036	0·06	0·009
(−0·017, 150)	0·045	0·06	0·011	(0·042, 150)	0·041	0·07	0·008
(−0·020, 180)	0·038	0·06	0·010	(0·013, 180)	0·039	0·06	0·010
(−0·031, 210)	0·042	0·07	0·009	(0·041, 180)	0·039	0·07	0·007
(−0·021, 210)	0·039	0·06	0·009	(0·013, 210)	0·045	0·06	0·011
(−0·020, 210)	0·043	0·06	0·010	(0·015, 210)	0·038	0·06	0·009
(−0·031, 240)	0·038	0·06	0·008	(0·044, 240)	0·045	0·07	0·008
(−0·023, 240)	0·035	0·07	0·008	(0·016, 240)	0·036	0·07	0·009
(−0·021, 240)	0·045	0·07	0·010	(0·044, 240)	0·043	0·07	0·008

masses. Therefore, when $R_b = 0$ (or $R_t = 0$), it is clear that it is not possible to achieve simultaneously $m_t^{\text{phys}} > 150\,\text{GeV}$ as well as R_{ub} in the entire range 0·06–0·10. From a cursory look at table 2, it is clear that the value of $|V_{td}|$, for the considered range of parameters, is predicted in a narrow range of 0·008–0·011, therefore, a precise measurement of $|V_{td}|$ will have an important consequence for the mass matrices wherein either $R_b = 0$ or $R_t = 0$.

In tables 3(a, b) we have presented the results of calculations where in general $R_b \neq 0$ for different R_t values. For the sake of uniformity, we have presented in the tables the ratios of V_{CKM} matrix elements, e.g., R_{ub}, $R_{td} = |V_{td}/V_{cb}|$, $R_{ts} = |V_{ts}/V_{cb}|$. A general survey of the tables brings out easily that we are able to obtain R_{ub} from 0·06–0·10 by varying R_t for various values of m_t^{phys}. This can also be checked from the expressions of $|V_{ub}|$ and $|V_{cb}|$. An important prediction of the model is that $|V_{ts}| \lesssim |V_{cb}|$ for the entire range of m_t^{phys} and R_t. This is in accordance with expectations from the unitarity of V_{CKM}. Similarly the results of $|V_{td}|$ can encompass the presently expected range [18]. Coming to the angles of unitarity triangle, α and β, we find that the present values are in accordance with similar calculations by other authors [19, 21, 22]. In the tables 3(a, b), we have not shown values of J-rephasing invariant measure of CP-violation [17]. However, one can easily show that J, related to the area of the unitarity triangle, lies in the range $(1{\cdot}7\text{–}2{\cdot}8) \times 10^{-5}$, which is in agreement with the data and other similar calculations [14, 15, 23].

A closer scrutiny of our results reveals several interesting points. One finds that tables 3(a) correspond to positive values of $\sin 2\alpha$ whereas 3(b) correspond to the negative values. This sign ambiguity is in fact reflection of the uncertainty regarding the quadrant of the phase of the CKM matrix. This is also reflected in the fact that $|V_{td}|$ has essentially two corresponding ranges, e.g., negative values of $\sin 2\alpha$ correspond to $|V_{td}| < 0{\cdot}009$ whereas positive values correspond to $|V_{td}| \geq 0{\cdot}009$. This ambiguity, however, in the present formulation, arises from (24) wherein corresponding to a given value of R_t there are two values of R_b which can reproduce $|V_{cb}|$. Therefore, a measure-

Table 3a. Calculated values of $R_{ub}, R_{td}, R_{ts}, S_{2\alpha}(=\sin 2\alpha)$ and $S_{2\beta}(=\sin 2\beta)$ for different m_t^{phys} and R_t values when $|V_{cb}| = 0{\cdot}040$ with $S_{2\alpha}$ taking positive values.

	$m_t^{\text{phys}}(\text{GeV}) = 150$						$m_t^{\text{phys}}(\text{GeV}) = 180$						$m_t^{\text{phys}}(\text{GeV}) = 210$						$m_t^{\text{phys}}(\text{GeV}) = 240$					
R_t	R_b	R_{ub}	R_{td}	R_{ts}	$S_{2\alpha}$	$S_{2\beta}$	R_b	R_{ub}	R_{td}	R_{ts}	$S_{2\alpha}$	$S_{2\beta}$	R_b	R_{ub}	R_{td}	R_{ts}	$S_{2\alpha}$	$S_{2\beta}$	R_b	R_{ub}	R_{td}	R_{ts}	$S_{2\alpha}$	$S_{2\beta}$
0·00	−0·02	0·06	0·24	0·97	0·63	0·51	−0·02	0·06	0·24	0·97	0·60	0·51	−0·02	0·06	0·24	0·97	0·58	0·51	−0·02	0·06	0·24	0·97	0·56	0·51
0·01	−0·00	0·07	0·25	0·97	0·82	0·50	−0·01	0·07	0·25	0·97	0·81	0·50	−0·01	0·07	0·25	0·97	0·80	0·51	−0·01	0·07	0·25	0·97	0·79	0·51
0·02	0·01	0·07	0·26	0·97	0·90	0·50	0·01	0·07	0·26	0·97	0·90	0·50	0·01	0·07	0·26	0·97	0·89	0·50	0·01	0·07	0·26	0·97	0·89	0·50
0·03	0·02	0·08	0·27	0·97	0·95	0·50	0·02	0·07	0·26	0·97	0·95	0·50	0·02	0·07	0·26	0·97	0·95	0·50	0·02	0·07	0·26	0·97	0·94	0·50
0·04	0·03	0·08	0·27	0·97	0·98	0·50	0·03	0·08	0·27	0·97	0·98	0·50	0·03	0·08	0·27	0·97	0·98	0·50	0·03	0·08	0·27	0·97	0·97	0·50
0·05	0·05	0·08	0·28	0·97	0·99	0·49	0·04	0·08	0·28	0·97	0·99	0·50	0·04	0·08	0·28	0·97	0·99	0·50	0·04	0·08	0·28	0·97	0·99	0·50
0·06	0·06	0·08	0·28	0·97	1·00	0·49	0·06	0·08	0·28	0·97	1·00	0·50	0·06	0·08	0·28	0·97	1·00	0·50	0·05	0·08	0·28	0·97	1·00	0·50
0·07	0·07	0·09	0·28	0·96	1·00	0·49	0·07	0·08	0·28	0·96	1·00	0·49	0·07	0·08	0·28	0·96	1·00	0·50	0·07	0·08	0·28	0·96	1·00	0·50
0·08	0·08	0·09	0·29	0·96	0·99	0·49	0·08	0·09	0·29	0·96	1·00	0·49	0·08	0·09	0·29	0·96	1·00	0·50	0·08	0·09	0·29	0·96	1·00	0·50
0·09	0·09	0·09	0·29	0·96	0·99	0·49	0·09	0·09	0·29	0·96	0·99	0·49	0·09	0·09	0·29	0·96	0·99	0·49	0·09	0·09	0·29	0·96	0·99	0·50
0·10	0·10	0·09	0·30	0·96	0·98	0·49	0·10	0·09	0·30	0·96	0·98	0·49	0·10	0·09	0·30	0·96	0·98	0·49	0·10	0·09	0·30	0·96	0·98	0·49
0·11	0·11	0·09	0·30	0·96	0·97	0·49	0·11	0·09	0·30	0·96	0·97	0·49	0·11	0·09	0·30	0·96	0·97	0·49	0·11	0·09	0·30	0·96	0·97	0·49
0·12	0·13	0·10	0·30	0·96	0·95	0·49	0·12	0·10	0·30	0·96	0·96	0·49	0·12	0·10	0·30	0·96	0·96	0·49	0·12	0·10	0·30	0·96	0·96	0·49
0·13	0·14	0·10	0·31	0·96	0·94	0·49	0·14	0·10	0·31	0·96	0·95	0·49	0·14	0·10	0·31	0·96	0·95	0·49	0·13	0·10	0·31	0·96	0·95	0·49

Table 3b. Same as in table 3(a) with $S_{2\alpha}$ taking negative values.

m_t^{phys}(GeV) = 150						m_t^{phys}(GeV) = 180						m_t^{phys}(GeV) = 210						m_t^{phys}(GeV) = 240					
R_b	R_{ub}	R_{td}	R_{ts}	$S_{2\alpha}$	$S_{2\beta}$	R_b	R_{ub}	R_{td}	R_{ts}	$S_{2\alpha}$	$S_{2\beta}$	R_b	R_{ub}	R_{td}	R_{ts}	$S_{2\alpha}$	$S_{2\beta}$	R_b	R_{ub}	R_{td}	R_{ts}	$S_{2\alpha}$	$S_{2\beta}$
−0·03	0·06	0·21	0·98	−0·16	0·52	−0·03	0·06	0·22	0·98	−0·12	0·52	−0·03	0·06	0·22	0·98	−0·10	0·52	−0·03	0·06	0·22	0·98	−0·07	0·52
−0·02	0·06	0·20	0·98	−0·43	0·52	−0·02	0·06	0·20	0·98	−0·42	0·52	−0·03	0·06	0·21	0·98	−0·41	0·52	−0·03	0·06	0·21	0·98	−0·39	0·52
−0·02	0·07	0·20	0·98	−0·59	0·53	−0·02	0·07	0·20	0·98	−0·58	0·52	−0·02	0·07	0·20	0·98	−0·57	0·52	−0·02	0·06	0·20	0·98	−0·57	0·52
−0·01	0·07	0·19	0·98	−0·70	0·53	0·00	0·07	0·19	0·99	−0·78	0·53	−0·01	0·07	0·19	0·98	−0·69	0·53	−0·01	0·07	0·19	0·98	−0·69	0·52
0·00	0·07	0·19	0·99	−0·78	0·53	0·01	0·07	0·18	0·99	−0·83	0·53	0·00	0·07	0·19	0·99	−0·77	0·53	0·00	0·07	0·19	0·99	−0·77	0·53
0·01	0·07	0·18	0·99	−0·84	0·54	0·02	0·07	0·18	0·99	−0·88	0·53	0·01	0·07	0·18	0·99	−0·83	0·53	0·01	0·07	0·18	0·99	−0·83	0·53
0·02	0·07	0·17	0·99	−0·88	0·54	0·02	0·08	0·18	0·99	−0·91	0·54	0·02	0·07	0·18	0·99	−0·88	0·53	0·01	0·07	0·18	0·99	−0·88	0·53
0·03	0·08	0·17	0·99	−0·91	0·54	0·03	0·08	0·17	0·99	−0·94	0·54	0·02	0·08	0·18	0·99	−0·92	0·53	0·02	0·08	0·18	0·99	−0·92	0·53
0·03	0·08	0·17	0·99	−0·94	0·54	0·04	0·08	0·17	0·99	−0·96	0·54	0·03	0·08	0·17	0·99	−0·94	0·53	0·03	0·08	0·17	0·99	−0·94	0·53
0·04	0·08	0·17	0·99	−0·96	0·54	0·05	0·08	0·17	0·99	−0·97	0·54	0·04	0·08	0·17	0·99	−0·96	0·54	0·04	0·08	0·17	0·99	−0·96	0·53
0·05	0·08	0·16	0·99	−0·97	0·55	0·06	0·08	0·16	0·99	−0·99	0·54	0·05	0·08	0·17	0·99	−0·98	0·54	0·05	0·08	0·17	0·99	−0·98	0·54
0·06	0·09	0·16	0·99	−0·98	0·55	0·07	0·09	0·16	0·99	−0·99	0·55	0·06	0·08	0·16	0·99	−0·99	0·54	0·06	0·08	0·16	0·99	−0·99	0·54
0·07	0·09	0·16	0·99	−0·99	0·55	0·08	0·09	0·16	0·99	−1·00	0·55	0·07	0·09	0·16	0·99	−0·99	0·54	0·07	0·09	0·16	0·99	−0·99	0·54
0·08	0·09	0·16	0·98	−0·99	0·55	0·09	0·09	0·15	0·99	−1·00	0·55	0·08	0·09	0·16	0·99	−1·00	0·54	0·08	0·09	0·16	0·99	−1·00	0·54
0·09	0·09	0·15	0·99	−0·99	0·53	0·10	0·09	0·15	0·99	−1·00	0·55	0·09	0·09	0·15	0·99	−1·00	0·54	0·09	0·09	0·15	0·99	−1·00	0·54
0·10	0·09	0·15	0·99	−1·00	0·56	0·11	0·10	0·15	0·99	−1·00	0·55	0·10	0·09	0·15	0·99	−1·00	0·55	0·10	0·09	0·15	0·99	−1·00	0·54
0·11	0·10	0·15	0·99	−1·00	0·56	0·12	0·10	0·14	0·99	−1·00	0·56	0·11	0·10	0·15	0·99	−1·00	0·55	0·11	0·09	0·15	0·99	−1·00	0·54
0·12	0·10	0·14	0·99	−1·00	0·56	0·13	0·10	0·14	1·0	−0·99	0·56	0·12	0·10	0·14	0·99	−1·00	0·55	0·12	0·10	0·14	0·99	−1·00	0·55

the present as well as other similar calculations [19, 21, 22], a measurement of the decay $B_d^0 \to \psi K_s$ would provide a good test of present form of mass matrices as well as the CKM mechanism in general.

It needs to be brought out clearly that the present analysis is crucially dependent on D^u and D^d. In the V_{CKM} matrix elements, however, these manifest through R_t and R_b. Such mass matrices, in the language of Ramond *et al* [24], correspond to texture 4 zeros. Also, it seems that the analysis of Ramond *et al* finds it difficult to accommodate $|V_{cb}| \cong 0{\cdot}04$ as well as $R_{ub} = 0{\cdot}08 \pm 0{\cdot}02$ with texture 5 and 6 zeros mass matrices. Therefore, texture 4 zeros mass matrices seem to be essential for fitting the V_{CKM} phenomenology. It may be of interest to mention that such mass matrices have been shown, by Joyce and Turok [25], to maintain their basic structure as they evolve from GUT scale to the low energy scale.

5. Conclusions

Fritzsch like mass matrices, with non-zero 22-elements in both U and D sectors, have been considered to accommodate current experimental constraints on m_t^{phys} and CKM matrix elements. We have shown that such mass matrices can accommodate CDF and D0 m_t^{phys} values, e.g., 176 ± 13 GeV and 199 ± 30 GeV respectively, apart from reproducing $|V_{us}|$, $|V_{cb}|$ and $|V_{ub}/V_{cb}| = 0{\cdot}08 \pm 0{\cdot}02$. Further, $|V_{td}|$ is predicted to lie in the range 0·005–0·014, in agreement with the latest conclusions of Buras [26]. The calculated values of the angles of unitarity triangle, α and β, are also in agreement with other authors [19, 21, 22], however two different ranges for these highlight the ambiguity regarding the quadrant of CP-violating phase of CKM matrix.

Acknowledgements

The authors gratefully acknowledge useful discussions with Prof. M P Khanna.

References

[1] F Abe *et al* (CDF Collab.), *Phys. Rev.* **D50**, 2966 (1994); *Phys. Rev. Lett.* **73**, 225 (1994); *Phys. Rev. Lett.* **74**, 2626 (1995)
[2] S Abachi *et al* (DO Collab.), *Phys. Rev. Lett.* **74**, 2632 (1995)
[3] H Fritzsch, *Phys. Lett.* **B73**, 317 (1978); **B166**, 423 (1986); *Nucl. Phys.* **B155**, 189 (1979)
[4] B Stech, *Phys. Lett.* **B130**, 189 (1983)
[5] M Shin, *Phys. Lett.* **B145**, 285 (1984)
[6] M Gronau, R Johnson and J Schechter, *Phys. Rev. Lett.* **54**, 2176 (1985)
[7] L Lavoura, *Phys. Lett.* **B228**, 245 (1989)
E Ma, *Phys. Rev.* **D43**, R2761 (1991)
[8] C H Albright Preprint No. FERMILAB-CONF-90/196-T(1990); FERMILAB-PUB-89/258-T(1989)
[9] X-G He and W S Hou, *Phys. Rev.* **D41**, 1517 (1990)
[10] M Tanimoto, *Phys. Rev.* **D41**, 1586 (1990)
[11] M T Yamawaki and W W Wada, *Phys. Rev.* **D43**, 2432 (1991)
[12] E Ma, *Phys. Rev.* **D43**, R2761 (1991); T V Duong and E Ma, *J. Phys.* **G19**, 339 (1993)
[13] Suraj N Gupta and James M Johnson, *Phys. Rev.* **D44**, 2110 (1991)
[14] R E Shrock, *Phys. Rev.* **D45**, R10 (1992)

[15] F Abe *et al*, *Phys. Rev. Lett.* **64**, 142 (1990)
[16] P S Gill and M Gupta, PU-PHY-REPORT No. 1/93 (Unpublished)
[17] C Jarlskog (ed), in *CP Violation* (World Scientific, Singapore, 1989) p. 3
[18] Particle Data Group, *Phys. Rev.* **D50**, 1315 (1994)
[19] A J Buras, M E Lautenbacher and G Ostermaier, *Phys. Rev.* **D50**, 3433 (1994)
[20] J Gasser and H Leutwyler, *Phys. Rep.* **87**, 77 (1982)
S Narison, *Phys. Lett.* **B197**, 405 (1987)
[21] G Buchalla and A J Buras, MPI-PhT/94-19 (1994)
[22] A Ali, CERN-TH 7123/93
A Ali and D London, DESY-022/93 (1993)
I Bigi, CERN-TH 7207/94 (1993)
Y Nir and Uri Sarid, *Phys. Rev.* **D50**, 2818 (1993)
[23] C Jarlskog, *Phys. Rev. Lett.* **55**, 1039 (1985) and *Z. Phys.* **C29**, 491 (1985)
J F Donoghue, T Nakada, E A Paschos and D Wyler, *Phys. Lett.* **B195**, 285 (1987)
G Bélanger, E Boridy, C Hamazaoui and G G Jakimov, *Phys. Rev.* **D48**, 4275 (1993)
[24] P Ramond, R G Robert and G G Ross, *Nucl. Phys.* **B406**, 19 (1993)
[25] M Joyce and M Turok, Princeton University Preprint-TH-1374 (1993)
[26] A J Buras, *Acta Phys. Pol.* **B26**, 755 (1995)

Vacuum structure, chiral symmetry breaking and electric dipole moment of neutron

A R PANDA* and K C ROY
Physics Department, Kendrapara College, Kendrapara 754211, India
*Present address: Physics Department, Anandapur College, Anandapur 758021, India

MS received 23 January 1995; revised 22 July 1995

Abstract. Considering a CP-violating QCD interaction, the electric dipole moment of neutron (EDMN) is estimated in a quark model of light mesons with a dynamical breaking of chiral symmetry through a non-trivial vacuum structure. Pion and kaon, being treated consistently within the model, yield to the constituent quark wave functions as well as the dynamical quark masses and thus determine the constituent quark field operators with respect to light quark flavors. Using the translationally invariant hadronic states and these constituent quark field operators, the EDMN estimated here remains well within the recent experimental bound of $D_n < 11 \times 10^{-26}$ e-cm with the CP-violation parameter $|\theta| = 10^{-8}$, which in fact accounts for a strong CP-violation.

Keywords. Strong CP-violation; vacuum structure; chiral symmetry breaking; quark model.

PACS Nos 14·20; 13·40; 12·38; 11·30

1. Introduction

Though electric dipole moment of neutron (EDMN) has been of great interest to physicists since its discovery [1] yet it has drawn much attention of theoreticians as well as of experimentalists after the discovery of CP-violation in $K^0 - \bar{K}^0$ system [2]. Amongst many theoretical models [3] to explain this CP-violation when applied to estimate EDMN, the valency quark model estimates EDMN by adding the valency quark contributions. In the standard model, though one has a non-vanishing contributions towards EDMN due to quarks still it is very much suppressed [4] at the level of three generations [5] and with four generations it does not enhance much. However, when one studies EDMN in QCD it has been observed that due to instanton effects the total divergence term has non-vanishing physical effects [6]. These in turn yield to a CP-violating piece [7] in the QCD Lagrangian due to an equivalent chiral rotation in the quark space which we consider here to describe the strong interaction between quarks in the neutron and hence to estimate its EDMN. However, this being a low energy phenomenon, its study requires a consideration of non-perturbative regime of QCD where one has solutions specifically in the lattice gauge theory [8] or in QCD sum rules [9]. But they have also their own limitations such as non-availability of better computer capabilities in case of former and consideration of non-perturbative vacuum structure through the relationship with perturbative QCD calculations in case of latter.

Recently, an alternative scheme [10] for considering low energy phenomena has been proposed where one realizes, using a variational method [11] the existence of

a nontrivial vacuum structure through quark and gluon condensates in the non-perturbative regime [11]. Such a non-trivial vacuum structure has also yielded to a dynamical breaking of chiral symmetry [12] through which it has become possible to determine pion and kaon wave functions and subsequently the constituent quark field operators [13, 14]. The quark field operators obtained here when applied to explain electromagnetic and weak properties of pion, kaon and nucleon [13, 14] and static properties of baryons in general [15], have shown a reasonable amount of success. Further, such a formalism through the extremization of gap function [16] also generated dynamically the quark masses [17]. We may note that the method applied presently is non-perturbative with respect to the use of the equal time algebra for the constituent quark field operators and was also earlier applied to solvable cases in high energy physics [11, 12, 18, 19] and nuclear physics [20] with a reasonable amount of success. In view of its success in a wide ranging phenomena in the present investigation we will be further using these constituent quark field operators as well as the quark masses to estimate the electric dipole moment of neutron (EDMN).

The present article is organized as follows. In § 2, we briefly describe the vacuum structure and XSB used to estimate the constituent quark field operators and fix up our notations to apply them in later sections. In § 3, we estimate EDMN considering the CP-violating fundamental QCD-interaction Lagrangian [7, 21, 22] whereas in § 4, we discuss our results and compare them with the available experimental measurements as well as other model calculations.

2. Chiral symmetry breaking and vacuum structure

Considering the chiral symmetry breaking (XSB) arising from gluon condensates [12] and including such an effect one writes the constituent quark fields as [23]

$$\psi(\mathbf{x}) = \frac{1}{(2\pi)^{3/2}} \int [U(\mathbf{k}) q_I(\mathbf{k}) + V(-\mathbf{k}) \tilde{q}_I(-\mathbf{k})] \exp(i\mathbf{k}\cdot\mathbf{x}) \mathbf{dk}, \tag{2.1}$$

where the spinors are written as [24, 25]

$$U(\mathbf{k}) = \begin{pmatrix} \cos\dfrac{\phi(\mathbf{k})}{2} \\ (\boldsymbol{\sigma}\cdot\hat{\mathbf{k}})\sin\dfrac{\phi(\mathbf{k})}{2} \end{pmatrix} \quad \text{and} \quad V(-\mathbf{k}) = \begin{pmatrix} -(\boldsymbol{\sigma}\cdot\hat{\mathbf{k}})\sin\dfrac{\phi(\mathbf{k})}{2} \\ \cos\dfrac{\phi(\mathbf{k})}{2} \end{pmatrix}, \tag{2.2}$$

and the two component quark fields $q_I(\mathbf{k})$ and $\tilde{q}_I(\mathbf{k})$ are

$$q_I(\mathbf{k}) = \sum_r q_{Ir}(\mathbf{k}) u_{Ir} \quad \text{and} \quad \tilde{q}_I(\mathbf{k}) = \sum_r \tilde{q}_{Ir}(\mathbf{k}) v_{Ir} \tag{2.3}$$

with u_{Ir} and v_{Ir} being explicitly written as

$$u_{I\frac{1}{2}} = \begin{pmatrix} 1 \\ 0 \end{pmatrix}, \quad u_{I-\frac{1}{2}} = \begin{pmatrix} 0 \\ 1 \end{pmatrix}; \quad v_{I\frac{1}{2}} = \begin{pmatrix} 0 \\ -i \end{pmatrix} \quad \text{and} \quad v_{I-\frac{1}{2}} = \begin{pmatrix} i \\ 0 \end{pmatrix}. \tag{2.4}$$

The function $\phi(\mathbf{k})$ describing the spinors in (2.2) is arbitrary and can be derived in principle from the extremization of the energy functional. The quark field operator $\psi(\mathbf{x})$

in (2.1), through (2.2)–(2.4) is found to satisfy the equal time algebra and also becomes free chiral one when $\phi(\mathbf{k}) = \pi/2$.

Further, associating the quark field operators as in (2.1) with the presence of quark condensates through the quark–antiquark pair creation operator [13]

$$B_Q^\dagger = \int h(\mathbf{k}) q_I^\dagger(\mathbf{k})(\boldsymbol{\sigma}\cdot\hat{\mathbf{k}})\tilde{q}_I(-\mathbf{k})\mathrm{d}\mathbf{k} \tag{2.5}$$

and a unitary transformation

$$U_Q = \mathrm{e}^{B_Q^\dagger - B_Q} \tag{2.6}$$

one obtains with $\tilde{\psi}(\mathbf{k}) = U_Q^\dagger \tilde{\psi}_0(\mathbf{k}) U_Q$ the relationship between the arbitrary function $\phi(\mathbf{k})$ and the correlation function $h(\mathbf{k})$ as [13, 18]

$$\frac{\phi(\mathbf{k})}{2} = \frac{\phi_0}{2} - h(\mathbf{k}), \tag{2.7}$$

where $\tilde{\psi}_0(\mathbf{k})$ is the chiral field operator. Thus, the form of quark field operator in (2.1) with (2.2) corresponding to XSB can have an interpretation of destabilizing the chiral vacuum or perturbative vacuum $|\mathrm{vac}\rangle$ (i.e. the vacuum state associated with the expansion of free field operators) through (2.6) when $\phi_0 = \pi/2$. Such a destabilization also leads to the possibility of a non-perturbative vacuum $|\mathrm{vac}'\rangle$ (i.e. the vacuum state obtained via minimization of energy density) [9] obtained through the unitary transformation in (2.6) as

$$|\mathrm{vac}'\rangle = U_Q|\mathrm{vac}\rangle. \tag{2.8}$$

Such a non-perturbative vacuum is also found to be at a lower energy than the perturbative or chiral vacuum [10–12, 13, 18]. Such a change of basis from $|\mathrm{vac}\rangle$ to $|\mathrm{vac}'\rangle$ is also corresponding to the change of parameters of the theory and can be treated as a vacuum realignment [10].

Further, with the quark field operators (2.1) one also obtains the expectation value for flavor 'i' as,

$$\langle \mathrm{vac}'|\bar{\psi}_i(\mathbf{x})\psi_i(\mathbf{y})|\mathrm{vac}'\rangle = \frac{6}{(2\pi)^3}\int \cos\phi_i(\mathbf{k})\exp[i\mathbf{k}\cdot(\mathbf{x}-\mathbf{y})]\mathrm{d}\mathbf{k}. \tag{2.9}$$

where the factor 6 is due to color and spin summation. One also has here from (2.7) a relationship between the function $\phi_i(\mathbf{k})$ and the quark–antiquark correlation function $h_i(\mathbf{k})$ as $\cos\phi_i(\mathbf{k}) = \sin(2h_i(\mathbf{k}))$ which in fact is an explicit description of the vacuum structure or vacuum realignment [10, 11, 13, 18].

As noted earlier, though in principle the function $\phi(\mathbf{k})$ can be obtained from the extremization of energy functional still, one does not have a closed form for it. However, one uses here a phenomenological Gaussian function, for its simplicity as

$$\sin(2h_i(\mathbf{k})) = \cos\phi_i(\mathbf{k}) = \exp(-R_i^2\mathbf{k}^2/2) \tag{2.10}$$

which has been earlier useful to consider hadronic phenomena associated with the vacuum structure [13, 18].

Next the function $\phi_i(\mathbf{k})$ can also be related to the pion wave function using Goldstone theorem [13], where one considers the chiral charge operator for pion (say π^+) as

$$Q_5^{\pi^+} = \int \psi_1^\dagger(\mathbf{x})\gamma^5\psi_2(\mathbf{x})d\mathbf{x} \tag{2.11}$$

with the fields $\psi_1(\mathbf{x})$ and $\psi_2(\mathbf{x})$ written for u and d quarks respectively. With the help of such a chiral charge operator one also has chiral symmetry and its breaking through $Q_5^{\pi^+}|\text{vac}\rangle = 0$ and $Q_5^{\pi^+}|\text{vac}'\rangle \neq 0$ respectively. One may also note here that such a XSB corresponds to a pion state of zero momentum and zero energy as a Goldstone mode, and is also written explicitly as

$$|\pi^+(\mathbf{0})\rangle = \frac{N_\pi}{\sqrt{6}}\int d\mathbf{k}\left(\cos\frac{\phi_1(\mathbf{k})}{2}\cos\frac{\phi_2(\mathbf{k})}{2} - \sin\frac{\phi_1(\mathbf{k})}{2}\sin\frac{\phi_2(\mathbf{k})}{2}\right)$$
$$\times\, u_1^\dagger(\mathbf{k})\tilde{d}_I(-\mathbf{k})|\text{vac}'\rangle \tag{2.12}$$

with N_π as the normalization constant. Further, assuming the initial $SU(2)_L \times SU(2)_R$ chiral symmetry breaking into custodial symmetry $SU(2)_V$ one has here $R_1 = R_2 = R$ and hence $\phi_1(\mathbf{k}) = \phi_2(\mathbf{k}) = \phi(\mathbf{k})$ which when substituted in (2.12) yields to it as

$$|\pi^+(\mathbf{0})\rangle = N_\pi\frac{1}{\sqrt{6}}\int d\mathbf{k}\cos\phi(\mathbf{k})u_I^\dagger(\mathbf{k})\tilde{d}_I(\mathbf{k})|\text{vac}'\rangle. \tag{2.13}$$

The normalization constant N_π also, one obtains here, from the relation

$$N_\pi^2\int\cos^2\phi(\mathbf{k})d\mathbf{k} = 1 \tag{2.14}$$

which with the $\cos\phi(\mathbf{k})$ as in (2.10) becomes

$$N_\pi = \left(\frac{R_\pi^2}{\pi}\right)^{3/4}, \tag{2.15}$$

where $R_\pi^2 = R^2$ for the pion has been used. The estimation of R_π^2 as $23{\cdot}58\,\text{GeV}^{-2}$ [13] through the pionic properties such as pion decay constant has in fact led to a determination of the vacuum structure for u or d constituent quark through $R_1^2 = R_2^2 = R_\pi^2$ [13]. Such a vacuum structure has also estimated pion charge radius in reasonable agreement with its experimental measurement [13].

Next, in a similar manner, defining the chiral charge generator $Q_5^{K^+}$ for K-meson as [14]

$$Q_5^{K^+} = \int \psi_1^\dagger(\mathbf{x})\gamma^5\psi_3(\mathbf{x})d\mathbf{x} \tag{2.16}$$

with $\psi_3(\mathbf{x})$ being taken for s-quark, one evaluates from it using (2.1) the K^+ state as [14]

$$|K^+(\mathbf{0})\rangle = \frac{N_K}{\sqrt{6}}\int u_1^\dagger(\mathbf{k})\tilde{s}_I(-\mathbf{k})$$
$$\times\left(\cos\frac{\phi_1(\mathbf{k})}{2}\cos\frac{\phi_3(\mathbf{k})}{2} - \sin\frac{\phi_1(\mathbf{k})}{2}\sin\frac{\phi_3(\mathbf{k})}{2}\right)d\mathbf{k}|\text{vac}'\rangle, \tag{2.17}$$

where N_K is the normalization constant for K-meson with the functions $\phi_1(\mathbf{k})$ and $\phi_3(\mathbf{k})$ taken for u and s quarks respectively. One may note here that with $s \to d$ (i.e. $\phi_3(\mathbf{k}) \to \phi_2(\mathbf{k})$) the kaon state in (2.17) reduces to the pion state of zero momentum in (2.12).. However, (2.17) has two unknown parameters N_K and R_3^2 (through $\cos\phi_3(\mathbf{k})$) related to each other. Thus, the estimation of them requires two relations which are taken to be the normalization condition for K-meson state as described in (2.17) and the kaon decay constant through Van Royen and Weisskopf relations [26]. The normalization condition for K-meson as

$$N_K^2 \int \left(\cos\frac{\phi_1(\mathbf{k})}{2} \cos\frac{\phi_3(\mathbf{k})}{2} - \sin\frac{\phi_1(\mathbf{k})}{2} \sin\frac{\phi_3(\mathbf{k})}{2} \right)^2 d\mathbf{k} = 1 \tag{2.18}$$

and the Van Royen and Weisskopf relation for K-meson in momentum space as [14].

$$\frac{N_K}{(2\pi)^{3/2}} \int \left(\cos\frac{\phi_1(\mathbf{k})}{2} \cos\frac{\phi_3(\mathbf{k})}{2} - \sin\frac{\phi_1(\mathbf{k})}{2} - \sin\frac{\phi_3(\mathbf{k})}{2} \right) d\mathbf{k}$$

$$= \frac{f_K (m_K)^{1/2}}{\sqrt{6}} \tag{2.19}$$

yields to

$$\frac{1}{(2\pi)^{3/2}} \frac{1}{N_K} = \frac{f_K (m_K)^{1/2}}{\sqrt{6}} \tag{2.20}$$

which in fact with the experimentally measured value of f_K gives N_K as [14]

$$N_K = 1{\cdot}9935\,\text{GeV}^{3/2}. \tag{2.21}$$

Now a substitution of this value of N_K in (2.21) and the earlier obtained $\phi_1(\mathbf{k})$ through $R_1^2 = 23{\cdot}58\,\text{GeV}^{-2}$ in (2.18) yields to R_3^2 *as*

$$R_3^2 = 4{\cdot}084\,\text{GeV}^{-2}. \tag{2.22}$$

Thus such an estimation of R_3 or R_s determines $\phi_3(\mathbf{k})$ and hence the vacuum structure for s-quark. Such a vacuum structure when applied to estimate the kaon charge radius is also found [14] to estimate in reasonable agreement with its experimental measurement.

Further, through such a formalism, on extremization of the gap function, one can generate dynamically the quark masses as [16, 17]

$$m_i = \lim_{k \to 0} |\mathbf{k}| \tan(2h_i(\mathbf{k})) \tag{2.23}$$

which with (2.10) yields to

$$m_i = \frac{1}{R_i}, \tag{2.24}$$

which, in fact, with the quark radii as mentioned earlier gives $m_u = m_d = 0{\cdot}206\,\text{GeV}$ and $m_s = 0{\cdot}495\,\text{GeV}$.

We, in fact, will use the field operators and the masses of the constituent quarks obtained in this section to obtain the EDMN in later sections.

In this section we consider the 'strong' CP-violation present in the fundamental QCD Lagrangian to estimate the electric dipole moment of neutron. In QCD, consideration of a total divergence term constructed from the gluon field strength tensor $G_{\mu\nu}$ as $(1/2)\varepsilon_{\mu\nu\alpha\beta}G^{\alpha\beta}G^{\mu\nu}$ has been found to have some non-vanishing physical effects due to instanton effects [6]. Further, it is parameterized in terms of a constant parameter as $-\theta g^2 \tilde{G}_{\mu\nu}G^{\mu\nu}/32\pi^2$, with θ being zero or non-zero means no CP-violation or CP-violation. Also, through appropriate global rotations of the quark fields the effect of $\tilde{G}_{\mu\nu}G^{\mu\nu}$ is transferred to the quark sector and thus yielding to a CP-violating Lagrangian upto first order in θ, written as [7, 22]

$$\delta\mathscr{L}_{\mathrm{CP}}(x) = i\theta\tilde{m}\bar{\psi}_q(x)\gamma^5\psi_q(x), \tag{3.1}$$

where

$$\tilde{m} = \frac{m_u m_d m_s}{(m_u m_d + m_d m_s + m_s m_u)}, \tag{3.2}$$

with m_u, m_d and m_s being the masses of u, d and s quarks respectively. Thus with the CP-violating interaction in (3.1) and the electromagnetic current $J_\mu(x)$ one has from current algebra an expression involving EDMN (D_n) as [21]

$$T\langle n_{1/2}(\mathbf{P}_f)|J_\mu(0)i\int \mathrm{d}^4x\,\delta\mathscr{L}_{\mathrm{CP}}(x)|n_{1/2}(\mathbf{P}_i)\rangle$$

$$= -D_n(\bar{u}_{1/2}(\mathbf{P}_f)\sigma_{\mu\nu}k^\nu\gamma^5 u_{1/2}(\mathbf{P}_i) + O(\mathbf{k}^2), \tag{3.3}$$

where $\mathbf{k} = \mathbf{P}_f - \mathbf{P}_i$ and is the momentum carried by the electromagnetic current J_μ. Thus we estimate D_n through (3.3), and to do so, we consider the matrix element in (3.3) as

$$T\sum_x \langle n_{1/2}(\mathbf{P}_f)|J_\mu(0)|X\rangle\langle X|i\int \mathrm{d}^4x\,\delta\mathscr{L}_{\mathrm{CP}}(x)|n_{1/2}(\mathbf{P}_i)\rangle, \tag{3.4}$$

where $|X\rangle$ indicates intermediate states arising due to $\delta\mathscr{L}_{\mathrm{CP}}(x)$ and is an admixture of opposite parity states consistent with the quantum numbers of neutron which may be a pion-nucleon system in the ground state. Thus of the two possible intermediate states in this regard i.e. $|p\pi^-\rangle$ and $|n\pi^0\rangle$; only $|p\pi^-\rangle$ one contributes as π^0 at an elementary level does not couple to photon at low momenta. Further, $|X\rangle$ being an odd parity state, the space part of the electromagnetic current $J_\mu(0)$ only contributes to the matrix element which when used in (3.4) yields in the Breit frame the expression as [21]

$$T\sum_X \langle n_{1/2}(-\mathbf{p})|J_i(0)|X\rangle\langle X|i\int \mathrm{d}^4x\,\delta\mathscr{L}_{\mathrm{CP}}(x)|n_{1/2}(\mathbf{p})\rangle$$

$$= -D_n\bar{u}_{1/2}(-\mathbf{p})\sigma_{iv}k^\nu\gamma^5 u_{1/2}(\mathbf{p}), \tag{3.5}$$

where in the r.h.s., terms of $O(\mathbf{k}^2)$ and higher have been neglected due to the small momentum transfer. Further, replacing the possible intermediate states $|X\rangle$ by $(\sqrt{2/3})|p_{1/2}(\mathbf{p}')\pi^-(p'')\rangle$ with $\sqrt{2/3}$ as the appropriate C.G. factor, and simplifying the

r.h.s., (3.5) becomes,

$$2\cdot\frac{2}{3}\int M_{\rm em}(\mathbf{p};\mathbf{p}'',\mathbf{p}')M_{\rm CP}(\mathbf{p}',\mathbf{p}'',\mathbf{p})\,d\mathbf{p}'\,d\mathbf{p}''=D_n(2i/m_n)p_z p_i, \tag{3.6}$$

where in (3.6) the energy conservation $k^0=p_f^0=p_i^0$ has been used. The matrix elements due to electromagnetic and CP-violating interactions as $M_{\rm em}(\mathbf{p};\mathbf{p}'',\mathbf{p}')$ and $M_{\rm CP}(\mathbf{p}',\mathbf{p}'',\mathbf{p})$ respectively are explicitly written as

$$M_{\rm em}(\mathbf{p};\mathbf{p}'',\mathbf{p}')=\langle n_{1/2}(-\mathbf{p})|J_i(0)|p_{1/2}(\mathbf{p}')\pi^-(\mathbf{p}'')\rangle \tag{3.7}$$

and

$$M_{\rm CP}(\mathbf{p}',\mathbf{p}'';\mathbf{p})=\langle p_{1/2}(\mathbf{p}')\pi^-(\mathbf{p}'')|i\int d^4x\,\delta\mathscr{L}_{\rm CP}(x)|n_{1/2}(\mathbf{p})\rangle. \tag{3.8}$$

The factor '2' in (3.6), has in fact arisen due to the interchange of the two vertices i.e. electromagnetic and CP-violating ones. However, the estimations of the matrix elements in (3.7) and (3.8) need the translationally invariant states for proton and neutron which we write in consistent with their SU(6) quantum numbers as

$$\begin{aligned}|p_{1/2}(\mathbf{p})\rangle=&\frac{\varepsilon_{ijk}}{3\sqrt{2}}\int d\mathbf{k}_1\,d\mathbf{k}_2\,d\mathbf{k}_3\,\delta(\mathbf{k}_1+\mathbf{k}_2+\mathbf{k}_3)\tilde{u}_p(\mathbf{k}_1,\mathbf{k}_2,\mathbf{k}_3)\\&\times[u^{i\dagger}_{I_3^+}(\mathbf{k}_1+\mathbf{p}/3)u^{j\dagger}_{I_3^+}(\mathbf{k}_2+\mathbf{p}/3)d^{k\dagger}_{I_3^-}(\mathbf{k}_3+\mathbf{p}/3)\\&-u^{i\dagger}_{I_3^-}(\mathbf{k}_1+\mathbf{p}/3)u^{j\dagger}_{I_3^+}(\mathbf{k}_2+\mathbf{p}/3)d^{k\dagger}_{I_3^+}(\mathbf{k}_3+\mathbf{p}/3)]|\text{vac}'\rangle\end{aligned} \tag{3.9}$$

and

$$\begin{aligned}|n_{1/2}(\mathbf{p})\rangle=&\frac{\varepsilon_{ijk}}{3\sqrt{2}}\int d\mathbf{k}_1\,d\mathbf{k}_2\,d\mathbf{k}_3\,\delta(\mathbf{k}_1+\mathbf{k}_2+\mathbf{k}_3)\tilde{u}_n(\mathbf{k}_1,\mathbf{k}_2,\mathbf{k}_3)\\&\times[u^{i\dagger}_{I_3^+}(\mathbf{k}_1+\mathbf{p}/3)d^{j\dagger}_{I_3^+}(\mathbf{k}_2+\mathbf{p}/3)d^{k\dagger}_{I_3^-}(\mathbf{k}_3+\mathbf{p}/3)\\&-u^{i\dagger}_{I_3^-}(\mathbf{k}_1+\mathbf{p}/3)d^{i\dagger}_{I_3^+}(\mathbf{k}_2+\mathbf{p}/3)d^{k\dagger}_{I_3^+}(\mathbf{k}_3+\mathbf{p}/3)]|\text{vac}'\rangle,\end{aligned} \tag{3.10}$$

where the wave functions $\tilde{u}_{n,p}(\mathbf{k}_1,\mathbf{k}_2,\mathbf{k}_3)$ for neutron and proton are described by normalized harmonic oscillator wave functions as

$$\tilde{u}_{n,p}(\mathbf{k}_1,\mathbf{k}_2,\mathbf{k}_3)=(3R^4_{n,p}/\pi^2)^{3/4}\exp\left[(-R^2_{n,p}/6)\sum_{i<j}(\mathbf{k}_i-\mathbf{k}_j)^2\right] \tag{3.11}$$

with $R^2_{n,p}$ as their harmonic oscillator radii. However, in the earlier applications of the present formalism to explain the static properties of nucleons the two radii were taken to be the same [13], and here also we take them to be the same i.e. $R_n^2=R_p^2=R_N^2$. Thus, with the pion state as described in (2.3) and the electromagnetic current as $J_i(0)=\sum_{q,\alpha}e_q\bar{\psi}^\alpha_q(0)\gamma^i\psi^\alpha_q(0)$, we estimate the matrix element (3.7) to be

$$\begin{aligned}M_{\rm em}(\mathbf{p};\mathbf{p}'',\mathbf{p}')=&\langle n_{1/2}(-\mathbf{p})|\sum_{q,\alpha}e_q\tilde{q}^\alpha(0)\gamma^i q^\alpha(0)|p_{1/2}(\mathbf{p}')\pi^-(\mathbf{p}'')\rangle\\=&-\frac{e_u}{(2\pi)^3}\frac{1}{3\sqrt{6}}\left(\frac{3R_N^4}{\pi^2}\right)^{3/2}\left(\frac{R_\pi^2}{\pi}\right)^{3/4}\int d\mathbf{k}_1\,d\mathbf{k}_3\end{aligned}$$

$$\times \exp\left[-\frac{R_\pi^2}{2}\left(\mathbf{k}_2^2-\mathbf{k}_2\cdot\mathbf{p}''+\frac{\mathbf{p}''^2}{4}\right)\right]$$

$$\times \exp\left[-2R_N^2(\mathbf{k}_2^2+\mathbf{k}_3^2+\mathbf{k}_2\cdot\mathbf{k}_3+\frac{\mathbf{k}_2\cdot\mathbf{p}'}{2}+\frac{\mathbf{p}'^2}{6}\right)\Bigg]$$

$$\times [4V^\dagger_{-1/2}(\mathbf{k})\alpha_i U_{1/2}(\mathbf{k}')+V^\dagger_{1/2}(\mathbf{k})\alpha_i U_{-1/2}(\mathbf{k}')]$$

$$\times \frac{1}{|-\mathbf{k}_2+\mathbf{p}''||\mathbf{k}_2+\mathbf{p}'|}\sin\frac{\phi(\mathbf{k}_2+\mathbf{p}')}{2}\sin\frac{\phi(-\mathbf{k}_2+\mathbf{p}'')}{2},$$

(3

where $\mathbf{k}=-\mathbf{k}_2+\mathbf{p}''$ and $\mathbf{k}'=\mathbf{k}_2+\mathbf{p}'$ have been substituted, and with a fur simplification of the spinor part (3.12) becomes

$$M_{em}(\mathbf{p};\mathbf{p}'',\mathbf{p}')=\frac{5e_u}{(2\pi)^3 3\sqrt{6}}\frac{4ip_zp_i}{9}\left(\frac{3R_N^4}{\pi^2}\right)^{3/2}\left(\frac{R_\pi^2}{\pi}\right)^{3/4}$$

$$\times\int d\mathbf{k}_2 d\mathbf{k}_3 \sin\frac{\phi(\mathbf{k}_2+\mathbf{p}')}{2}\sin\frac{\phi(-\mathbf{k}_2+\mathbf{p}'')}{2}$$

$$\times\frac{1}{|-\mathbf{k}_2+\mathbf{p}''||\mathbf{k}_2+\mathbf{p}'|}\exp\left[-\frac{R_\pi^2}{2}(\mathbf{k}_2^2-\mathbf{k}_2\cdot\mathbf{p}''+\frac{\mathbf{p}''^2}{4}\right]$$

$$\times\exp\left[-2R_N^2\left(\mathbf{k}_2^2+\mathbf{k}_3^2+\mathbf{k}_2\cdot\mathbf{k}_3+\frac{\mathbf{k}_2\cdot\mathbf{p}'}{2}+\frac{\mathbf{p}'^2}{6}\right)\right],\quad (3$$

The matrix element (3.8) involving CP-violating interaction $\delta\mathscr{L}_{CP}(x)$ with the us the time translational invariance becomes,

$$M_{CP}(\mathbf{p}',\mathbf{p}'';p)=-\frac{1}{E_\pi(\mathbf{p}'')}\langle p_{1/2}(\mathbf{p}')\pi^-(\mathbf{p}'')|i\int d\mathbf{x}\,\delta\mathscr{L}_{CP}(\mathbf{x},0)|n_{1/2}(\mathbf{p})\rangle,$$

(3

with the pion energy $E_\pi(\mathbf{p}'')=(\mathbf{p}''^2+m_\pi^2)^{1/2}$. However, a substitution of the violating Lagrangian (3.1) in (3.14) yields it as,

$$M_{CP}(\mathbf{p}',\mathbf{p}'';p)=-\frac{i\theta\tilde{m}}{E_\pi(\mathbf{p}'')}\langle p_{1/2}(\mathbf{p}')\pi^-(\mathbf{p}'')|\int d\mathbf{k}\bar{q}^\alpha(\mathbf{k})\gamma^5 q^\alpha(\mathbf{k})|n_{1/2}(\mathbf{p})\rangle.\ (3$$

which in fact with the proton, neutron and pion states described earlier yields to

$$M_{CP}(\mathbf{p}',\mathbf{p}'';p)=\frac{i\theta\tilde{m}}{E_\pi(\mathbf{p}'')}\frac{1}{6\sqrt{6}}\left(\frac{3R_N^4}{\pi^2}\right)^{3/2}\left(\frac{R_\pi^2}{\pi}\right)^{3/4}\exp\left[-\frac{R_\pi^2 p'^2}{8}\right]$$

$$\times\exp\left[-\frac{R_N^2}{24}(5\mathbf{p}'^2+9\mathbf{p}''^2-6\mathbf{p}'\cdot\mathbf{p}'')\right]\int d\mathbf{k}_3'$$

$$\times\exp\left[-2R_N^2\left(\mathbf{k}_3'+\frac{\mathbf{p}'+3\mathbf{p}''}{12}\right)^2\right]$$

$$\times[4U^\dagger_{1/2}(\mathbf{k})\gamma^0\gamma^5 V_{-1/2}(\mathbf{k})+U^\dagger_{-1/2}(\mathbf{k})\gamma^0\gamma^5 V_{1/2}(\mathbf{k})],\quad (3$$

where, $\mathbf{k}$ has been substituted for $(\mathbf{p}'+\mathbf{p}'')/2$. Thus, after some simplifications and integration in (3.16) we obtain it as,

$$M_{CP}(\mathbf{p},\mathbf{p}'',\mathbf{p}) = -\frac{\theta\tilde{m}}{E_\pi(\mathbf{p}'')}\frac{1}{2\sqrt{6}}\left(\frac{3R_N^4}{\pi^2}\right)^{3/2}\left(\frac{R_\pi^2}{\pi}\right)^{3/4}\left(\frac{\pi}{2R_N^2}\right)^{3/2}$$
$$\times \exp\left[-\frac{5R_N^2+3R_\pi^2}{24}\mathbf{p}'^2-\frac{3R_N^2}{8}\mathbf{p}''^2+\frac{R_N^2}{4}\mathbf{p}'\cdot\mathbf{p}''\right]\cos\phi(\mathbf{k}). \tag{3.17}$$

The substitution of (3.17) along with (3.13) in the l.h.s. of (3.6) when compared with its r.h.s. gives rise to an expression for electric dipole moment of neutron after $\mathbf{k}_3$ integration as,

$$D_n = \frac{20}{729}\theta\tilde{m}m_n e(2\pi)^{-3}\left(\frac{3R_N^2}{2\pi}\right)^3\left(\frac{R_\pi^2}{\pi}\right)^{3/2}2\pi I, \tag{3.18}$$

where the integral 'I' is written as,

$$I = \int |\mathbf{k}_2|^2\,d|\mathbf{k}_2||\mathbf{p}'|^2\,d|\mathbf{p}'||\mathbf{p}''|^2\,d|\mathbf{p}''|\,d\phi'\,d\phi''\,d\cos\theta'\,d\cos\theta''$$
$$\times\left(\frac{\left[1-\exp\left[-\frac{R_\pi^2}{2}(\mathbf{k}_2^2+\mathbf{p}''^2-2k_2p''\cos\theta'')\right]\right]^{1/2}\left[1-\exp\left[-\frac{R_\pi^2}{2}(\mathbf{k}_2^2+\mathbf{p}'^2+2k_2p'\cos\theta')\right]\right]^{1/2}}{|\mathbf{k}_2-\mathbf{p}''||\mathbf{k}_2+\mathbf{p}'|(\mathbf{p}''^2+m_\pi^2)^{1/2}}\right)$$
$$\times\exp\left[-R_N^2\left(\frac{3\mathbf{k}_2^2}{2}+K_2p'\cos\theta'+\frac{\mathbf{p}'^2}{3}\right)\right]\exp\left[-\frac{R_\pi^2}{2}\left(\mathbf{k}_2^2-K_2p''\cos\theta''+\frac{\mathbf{p}''^2}{4}\right)\right]$$
$$\times\exp\left[-\frac{R_\pi^2-R_N^2}{4}(\sin\theta'\sin\theta''\cos(\phi''-\phi')+\cos\theta'\cos\theta'')p'p''\right]$$
$$\times\exp\left[-\frac{5R_N^2+6R_\pi^2}{24}\mathbf{p}'^2+\frac{R_\pi^2+3R_N^2}{8}\mathbf{p}''^2\right], \tag{3.19}$$

where $k_2=|\mathbf{k}_2|$, $p'=|\mathbf{p}'|$ and $p''=|\mathbf{p}''|$. However, the integral 'I' in (3.19) is to be evaluated numerically. Thus, in the following section we will be using (3.18) to estimate D_n, where also we will discuss and compare it with other theoretical estimations as well as the experimental measurements.

4. Results and discussion

The estimation of EDMN from (3.18) of the earlier section primarily requires the radius parameters R_n^2, R_p^2 and R_π^2 for the neutron, proton and pion wave functions in addition to the quark masses and neutron mass. However, they were obtained from the earlier

$I = 1{\cdot}300547 \times 10^{-3}\,\mathrm{GeV}^6$,

which when substituted in (3.18) along with the dynamically generated quark ma described in (2.24) and the neutron mass from its experimental measuremen determines the EDMN as

$$D_n = -7{\cdot}46 \times 10^{-8}|\theta|\text{e-cm}.$$

Thus, with a value of the parameter $|\theta| = 10^{-8}$ [7,21,22] the EDMN becomes

$$D_n = -7{\cdot}46 \times 10^{-26}\text{e-cm},$$

which lies within the uncertainty of its recently measured value of $(3 \pm 5) \times 10^{-2}$ [28] and well within the most recent experimental upper bound of $|D_n| < 11 \times 10^{-}$ [27].

We now compare our result with the other model estimations. In standard EDMN comes out to be within the range of 10^{-30} to 10^{-32}e-cm [4] which is s compared to experiments. Even with four generations in such a model, the estir does not go beyond 10^{-29}e-cm [29]. On the other hand, the result of Weinberg- model of spontaneous CP-violation [30] with dominant hadronic loops is 10^{-2} which is larger than experimental upper bound [27]. But, in the Left–Right Syn model EDMN is found to be in the range of 10^{-27} to 10^{-25}e-cm [31] in which a present estimation lies. However, in bag model, with the QCD interaction valency quark core level with the add parity N^{*-} states EDMN was obtaine $2{\cdot}7 \times 10^{-16}|\theta|$ e-cm [7] whereas the same in a current algebra analysis with violating πN-interaction was estimated to be $-3{\cdot}8 \times 10^{-16}|\theta|$e-cm [21]. Bu these estimations when compared with the experimental measurement [2 pointing to a rather weaker CP-violation. In the framework of CBM, Morg Miller [22], taking both valency quark core and pionic contributions, have est EDMN as $-4 \times 10^{-17}\theta$ e-cm, which also with the experimental measureme yields to a weaker CP-violation, though it is relatively stronger than the earli estimations [7,21]. Further, in some recent attempts [32–34] in the context of re of $U(1)$ anomaly problem; under certain approximations θ has also been predi QCD to be vanishing. In view of these diverse model predictions we believe an a measurement in this regard can provide the actual dynamics concerned with the E and thus be in a position to distinguish different theoretical models as well approximations involved in them. Nevertheless, we observe that the present inv tion in its attempt to explain EDMN has an agreement with the Left–Right Syn model and has a more reasonable explanation for the same compared to the st model. However, the present nonperturbative mechanism has yielded a limited a bility with respect to light flavors only and we believe when the same is exter heavier flavors can be able to describe hadron dynamics in a unified manner.

Acknowledgements

The authors are thankful to Profs S P Misra and N Barik for valuable discussion also thank A Nath, P Das and R K Sahoo for discussions.

ferences

] N F Ramsay, *Ann. Rev. Nucl. Part. Sci.* **32**, 211 (1982) and references therein
] J H Christenson, J W Cronin, V L Fitch and R Turley, *Phys. Rev. Lett.* **13**, 138 (1964)
] X G He, B H J McKeller and S Pakvasa, *Int. J. Mod. Phys.* **A4**, 5011 (1989) and references therein
] E P Shabalin, *Sov. J. Nucl. Phys.* **28**, 75 (1978); **31**, 864 (1980); **32**, 228 (1980) and references therein
] J O Eeg and I Picek, *Phys. Lett.* **B130**, 508 (1983); *Nucl. Phys.* **B244**, 77 (1984)
] S M Bar and A Zee, *Phys. Rev. Lett.* **55**, 2253 (1985)
A A Belavin, A M Polyakov, A S Schwartz and Yu S Tyupkin, *Phys. Lett.* **B59**, 85 (1975)
R Jackiw and C Rebii, *Phys. Rev. Lett.* **37**, 172 (1976)
C G Callan Jr., R F Dashen and D J Gross, *Phys. Lett.* **B63**, 334 (1976)
] V Baluni, *Phys. Rev.* **D19**, 2227 (1979)
] K G Wilson, *Phys. Rev.* **D10**, 2445 (1974)
J B Kogut, *Rev. Mod. Phys.* **51**, 659 (1979); **55**, 775 (1983)
M Creutz, *Phys. Rev. Lett.* **45**, 313 (1980); *Phys. Rev.* **D21**, 2308 (1980)
] M A Shifman, A I Vainstein and V I Zakharov, *Nucl. Phys.* **B147**, 365, 448, 519 (1979)
R A Bertlman, *Acta. Phys. Aust.* **53**, 305 (1981)
] S P Misra, *Phys. Rev.* **D35**, 2607 (1987)
] H Mishra, S P Mishra and A Mishra, *Int. J. Mod. Phys.* **A3**, 2331 (1988)
A Mishra, H Mishra, S P Mishra and S N Nayak, *Phys. Lett.* **B251**, 541 (1990)
] A Mishra, H Mishra, S P Misra and S N Nayak, *Pramana – J. Phys.* **37**, 59 (1991); *Z. Phys.* **C57**, 241 (1993)
] A Mishra and S P Misra, *Z. Phys.* **C58**, 325 (1993)
A Mishra, H Mishra and S P Misra, *Z. Phys.* **C57**, 241 (1983)
] S P Misra, Preprint IP/BBSR/94-90; hep-ph/9405402
] A R Panda and K C Roy, Submitted for publication
] S L Adler and A C Davis, *Nucl. Phys.* **B244**, 469 (1984)
M G Mitchard, A C Davis and A J Macfarlane, *Nucl. Phys.* **B325**, 470 (1989)
] H Mishra and S P Misra, *Phys. Rev.* **D48**, 5376 (1993)
] A Mishra, H Mishra, S P Misra and S N Nayak, *Phys. Rev.* **D44**, 110 (1990)
] A Mishra, H Mishra and S P Misra, *Int. J. Mod. Phys.* **A5**, 3391 (1990)
H Mishra, S P Misra, P K Panda and B K Parida, *Int. J. Mod. Phys.* **E1**, 405 (1992)
] P K Panda, R Sahu and S P Misra, *Phys. Rev.* **C45**, 2079 (1992)
] R J Crewther, P Di-Vecchia, G Veneziano and E Witten, *Phys. Lett.* **B88**, 123 (1979)
] M G Morgan and G A Miller, *Phys. Lett.* **B179**, 379 (1986)
] S P Misra, *Phys. Rev.* **D18**, 1661, 1673 (1978)
] A Le Yaouanc *et al*, *Phys. Rev. Lett.* **54**, 506 (1986)
] S P Misra and S Panda, *Pramana – J. Phys.* **27**, 523 (1985)
] R Van Royen and V F Weisskopf, *Nuovo Cimento* **A51**, 617 (1965)
] Particle Data Group, *Phys. Rev.* **D50**, 1173 (1994)
] Smith *et al*, *Phys. Lett.* **B234**, 192 (1990)
] A Barroso, R Chalabi, N Dombey and C Hanzaoui, *Phys. Lett.* **B196**, 269 (1987)
] S Weinberg, *Phys. Rev. Lett.* **37**, 657 (1976)
H Y Cheng, *Phys. Rev.* **D42**, 2329 (1990)
] K Babu and R N Mohapatra, Preprint Ud Mp PP 89–063
] A Abada *et al*, *Phys. Lett.* **B234**, 191 (1990)
] S Aoki and T Hatsuda, *Phys. Rev.* **D45**, 2427 (1992)
] H Banerjee, P Mitra and D Chatterjee, *Z. Phys.* **C62**, 511 (1994)

Controlling chaos: Stabilization of unstable orbits using exponential control for maps and flows

SANGEETA D GADRE and V S VARMA
Department of Physics and Astrophysics, University of Delhi, Delhi 110007, India

MS received 3 April 1995; revised 11 August 1995

Abstract. We demonstrate that chaos can be controlled using multiplicative exponential feedback control. Unstable fixed points, unstable limit cycles and unstable chaotic trajectories can all be stabilized using such control which is effective both for maps and flows. The control is of particular significance for systems with several degrees of freedom, as knowledge of only one variable on the desired unstable orbit is sufficient to settle the system onto that orbit. We find in all cases that the transient time is a decreasing function of the stiffness of control. But increasing the stiffness beyond an optimum value can increase the transient time. We have also used such a mechanism to control spatiotemporal chaos is a well-known coupled map lattice model.

Keywords. Controlling chaos; unstable orbits; Lyapunov exponents; transient time; spatiotemporal chaos.

PACS No. 05·45

1. Introduction

The problem of controlling chaos has recently received much attention [1–13]. A chaotic system in general cannot be made to converge to a freely evolving desired trajectory, whether periodic or chaotic, because of the inherent unpredictibility of the system. The control of chaos in this context consists of forcing the system to evolve along the desired trajectory. This can be achieved by different methods [1,4,7,10–13]. Though the problem of controlling chaos in low dimensional systems has been the main focus of interest till now, recently controlling chaos in spatiotemporal system, which is of greater practical importance, has begun to receive attention [14]. For instance, plasma devices, laser systems, chemical reactions, etc show both spatial and temporal chaos.

We have shown recently [15], that use of multiplicative exponential feedback control on a parameter of the system, with the argument of the exponential being proportional to the feedback response of the system, i.e. the difference between the desired value and the actual value of a suitably chosen variable of the system can stabilize unstable fixed points of 1-D maps. Besides, we also created new stable attractors which are not the natural attractors of the unmodulated system, depending on our requirement and use, using the discrete map. However, exponential control cannot stabilize any arbitrary orbit of the system. The functional form of the map and the control criterion decide which orbit can be forced onto the system. Our method is a combination of variable and parametric control as it achieves its goal by controlling the parameter through the variable. The motivation of using an exponential form of control is to have faster convergence to the desired orbit.

unstable orbits—namely unstable fixed points, limit cycles and chaotic trajectories. We demonstrate that it works effectively both for maps and flows. Besides controlling chaos in low-dimensional systems, we have demonstrated control of spatiotemporal chaos in a well-known coupled map lattice (CML) model [16–20] using exponential control. Exponential feedback pinnings are used to control chaos in the system by stabilizing a chosen unstable reference state.

Consider a general N-dimensional dynamical system

$$\mathbf{X} = \mathbf{F}(\mathbf{X}; \mu; t) \tag{1}$$

where $\mathbf{X} \equiv (X_1, X_2, \ldots, X_N)$ are variables and $\mu \equiv (\mu_1, \mu_2, \ldots, \mu_K)$ are parameters whose values determine the nature of the dynamics. We demonstrate that the stabilization of a desired unstable orbit or a chaotic trajectory of such a system is possible by multiplying a suitably chosen parameter say μ_r in (1) by an exponential feedback control involving only one suitably chosen variable say X_l, with the form of control being given by

$$\exp[\varepsilon(X_l - X_l^s)]. \tag{2}$$

Here X_l is the actual value of the chosen variable of the system after applying control, X_l^s is the desired value of that variable and ε is the "stiffness" of the control which can take both positive and negative values.

The dynamics of the modulated system in the presence of control is given by

$$\mathbf{X} = \mathbf{F}(\mathbf{X}; \mu_1, \mu_2, \ldots, \mu_r \exp[\varepsilon(X_l - X_l^s)], \ldots, \mu_K; t). \tag{3}$$

One of the important features of the control is that it does not change the solution of (1) corresponding to the orbit $\mathbf{X}_l = \mathbf{X}_1^s$. However, it changes the Lyapunov exponents of the controlled orbit, i.e. $\mathbf{X}_l^s$. This can be demonstrated by considering the logistic map as it is simplest to analyse. The expression for the Lyapunov exponent, for stabilizing the fixed point $X^* = 1 - 1/(4\lambda^*)$ in the presence of control is $\ln|4\mu(1 - 2X^*) + \varepsilon X^*|$ whereas the expression in the absence of control is $\ln|4\mu(1 - 2X^*)|$. However, in both cases X^* is a fixed point of the map. This argument can easily be extended for higher periods of maps as well as for flows.

The control works for those combinations of controlling parameters and variables of the system for which the largest real part of the Lyapunov exponent of the modulated system, represented by (3), is negative. The feedback function in the control involves only one suitably chosen variable X_l to convert the desired repellor—whether a fixed point, a limit cycle or a chaotic orbit, into an attractor. Thus, knowledge of only one suitably chosen variable on the desired unstable orbit is sufficient to settle the system onto that orbit. This makes the control particularly useful for systems with several degrees of freedom. For example, a desired unstable fixed point of the Lorenz system [21] can be stabilized using control with feedback depending on any one of the X, Y or Z variables whereas an unstable limit cycle or a chaotic trajectory of the Lorenz system can be converted into an attractor by using feedback depending on the Z variable only. For stabilizing most repellors, it is sufficient to multiply one chosen parameter by the exponential control; but sometimes, as in the case of one of the two fixed points of the Hénon map [22], both the parameters a and b of the system have to be multiplied by the

ponential control. Although in all the cases we have studied only one variable on the ired orbit was sufficient to make all the Lyapunov exponents of the system negative, s may not always be possible for arbitrary systems and it may turn out that for some tems control using more than one variable is required for the stabilization of an stable orbit. However, the fact remains that the control uses only a subset of the iables and the parameters for controlling chaos.

A quantity of obvious interest in the context of controlling chaos is the time required the system to settle onto the desired orbit. This of course depends upon the stiffness control ε. For a given ε we study the time τ required for the system to approach within istance ω of the desired orbit starting from some initial point. If ω_0 is the initial tance from the desired orbit, then it is clear that the length of the transient τ and ω are ated by $\omega = \omega_0 \exp(\lambda\tau)$, where λ is the largest Lyapunov exponent. The slope of the t of τ against $\ln(\omega/\omega_0)$ is nothing but $1/\lambda$. This of course has to be negative for nvergence. These values of the Lyapunov exponents are found to be in good eement with those obtained either numerically (using the method given in [23]) or, erever possible, analytically. We have studied the transient time τ required for tling onto a desired orbit, within a given accuracy ω, as a function of ε and found that general is a decreasing function of ε. But there exists an optimum stiffness of control ond which increase in ε increases τ. This behaviour of τ is found to be the same as t of λ with ε for a given orbit.

There is one drawback. The form of the control is such that for a given system an stable fixed point which is represented by a null vector cannot be stabilized. The son is obvious. The Jacobian of the modulated system given by (3) evaluated at such oint in the presence of the control is the same as that of the unmodulated system (1). the eigenvalues of the system remain unchanged in the presence of control and xed point represented by a null vector remains unstable even under control. Such nts may, however, get stabilized in the process of stabilizing other fixed points, ulting in the coexistence of more than one attractor. The fact that null vectors can be bilized in the process of stabilizing desired orbit can be illustrated by taking an mple of unstable fixed points of the logistic map. The map has two fixed points $= 0$ and $X^* = 1 - 1/(4\mu)$. X_2^* is stable for $0 < \mu < 1/4$ and unstable otherwise. In the cess of controlling X^*, the equation representing the modulated logistic map is

$$X_{n+1} = 4\mu \exp(\varepsilon(X_n - X^*)) X_n (1 - X_n) \equiv f.$$

th the fixed points i.e., X_n^* and X^*, of the unmodulated map are also the fixed points he modulated map. In order to test the stability of a fixed point of a modulated tem (i.e., logistic map in the presence of control), we have to find derivative of f w.r.t t that point. The general expression for $\mathrm{d}f/\mathrm{d}X$ in the case of the modulated logistic p is

$$\frac{\mathrm{d}f}{\mathrm{d}X} = 4\mu \exp(\varepsilon(X - X^*))(\varepsilon X(1 - X) + 1 - 2X).$$

erefore

$$\left.\frac{\mathrm{d}f}{\mathrm{d}X}\right|_{X=0} = 4\mu \exp(-\varepsilon X^*).$$

above mentioned range for μ becomes $0 < \mu < \exp(\varepsilon X^*)/4$. This shows that X_z^* c stabilized for values of μ not lying in the range (0, 1/4), by choosing suitable val ε for a given X^*.

The organization of this paper is as follows. In § 2 we study exponential contr stabilizing an unstable fixed point. In § 3.1 we extend the control algorithm to sta unstable closed orbits for flows. We suggest a more effective control for the stabiliz of higher orbits of a discrete dynamical system in § 3.2. In § 4 we discuss the stabiliz of chaotic orbits. We use our control for controlling spatiotemporal chaos in a model in § 5. We conclude with a summary of our results in § 6.

2. Exponential control for stabilizing an unstable fixed point

We have studied Lorenz system [21] as an example of a continuous dynamical s which is governed by the following equations

$$\dot{X} = \sigma(Y - X)$$

$$\dot{Y} = -XZ + rX - Y$$

$$\dot{Z} = XY - bZ$$

where X, Y, Z are the variables and σ, r, b the controlling parameters of the systen system has three critical points viz $X' = 0$, $Y' = 0$, $Z' = 0$; $X'' = \sqrt{b(r}$ $Y'' = \sqrt{b(r-1)}$, $Z'' = r - 1$ and $X''' = -\sqrt{b(r-1)}$, $Y''' = -\sqrt{b(r-1)}$, $Z''' =$ We choose the parameters σ, r and b so that the system is in a chaotic regime; i.e. w $\sigma = 10$, $b = 8/3$ and $r = 60$ in which case all the three critical points are unstable first critical point (X', Y', Z') which is represented by a null vector cannot be a stable fixed point using this form of control. This has been discussed i introduction. The second and third critical points can be converted into attracto multiplying the parameter b by $\exp[\varepsilon(Z - Z'')]$ and $\exp[\varepsilon(Z - Z''')]$ respectivel also possible to stabilize these points using other combinations of parameter variables, provided the control criterion i.e., the largest real part of the Lyap exponent, λ, is negative, is satisfied. Such combinations, with the corresponding of λ are listed in table 1 for $\varepsilon = -0{\cdot}001$, $-0{\cdot}01$ and $-0{\cdot}1$. Similarly, λ can be w out for positive values of ε also. Table 1 shows that the r-X, r-Y and b-Y for control work for suitably chosen negative values of ε. On the other hand, it is th b-X and b-Z forms of control which are effective for suitably chosen positive valu For the rest of the forms viz σ-X, σ-Y and σ-Z, the values of λ remain positive ε (the Lyapunov exponents with these forms of control are independent of ε and a same as that of the unmodulated Lorenz system) thereby implying that these for exponential control cannot stabilize the unstable fixed points of the Lorenz sys

For a fixed ω the transient τ, using different forms of exponential control, is fou be a decreasing function of ε. However there exists an optimum value of ε beyond increasing ε increases τ. This behaviour of τ is similar to that observed in the c discrete 1-D maps [15].

Table 1. The largest Lyapunov exponent λ for the Lorenz attractor while stabilizing (X'', Y'', Z'') with $\sigma = 10$, $b = 8/3$, $r = 60$ using exponential control with different combinations of parameters and variables for different values of the stiffness of control ε.

	λ for $\varepsilon =$		
Control form	$-0{\cdot}001$	$-0{\cdot}01$	$-0{\cdot}1$
r-X	0·616	−0·267	−3·950
r-Y	0·394	−2·381	−7·180
r-Z	0·767	1·117	2·250
b-X	0·739	0·927	2·425
b-Y	0·707	0·611	−0·113
b-Z	0·786	1·403	7·884
σ-X	0·717	0·717	0·717
σ-Y	0·717	0·717	0·717
σ-Z	0·717	0·717	0·717

The stable control region i.e. the range of values of ε for which an unstable orbit becomes stable is the range of ε for which the largest Lyapunov exponent of a given system for a given orbit in the presence of control is negative (i.e. the control criterion is satisfied). This range of ε can be obtained by using the condition that the real parts of the eigenvalues of the Jacobian matrix about a given orbit be less than zero for flows or lie in the range $(-1, 1)$ for maps. When a non-zero fixed point of the Lorenz system becomes unstable then the J matrix has one real (α) and two complex conjugate eigenvalues $(\beta \pm i\gamma)$. The real eigenvalue is always negative but the real parts of the complex eigenvalues are positive. In the presence of b-Z control, the lower limit of the stable control region of ε can be obtained by using the condition that $\mathrm{Re}(\lambda) \leqslant 0$. Using this constraint we obtain the following expression for ε:

$$\varepsilon \geqslant -\frac{B}{bZ^*} - \frac{1}{Z^*}$$

where

$$B = \frac{2 + 3\sigma + \sigma^2 + X^{*2} - [-4(1-\sigma)(2+\sigma)X^{*2} - 2 - 3\sigma - \sigma^2 - X^{*2}]^{1/2}}{2(2+\sigma)}.$$

The upper limit is ∞ in this case. For the given values of the controlling parameters the range of values of ε for which the non-zero unstable fixed points become stable is $0{\cdot}009568\cdots \leqslant \varepsilon \leqslant \infty$.

The Lyapunov exponents obtained analytically for the second and third critical points in the presence of the control have the same value. The variation of λ with ε shows the same behaviour as that of τ with ε. The optimum value of ε for which τ is minimum also corresponds to the most negative value of λ (minimum value of λ) and is 0·2 for the given values of the parameters with b-Z control. The value of λ obtained analytically is $-6{\cdot}8993\ldots$ for $\varepsilon = 0{\cdot}2$. We plot the transient τ, as a function of $\ln(\omega/\omega_0)$

for this value of ε and find that the reciprocal of the slopes for the second and third critical points are $\approx -6{\cdot}916$, which is in good agreement with the value obtained analytically.

We intend to compare the transient times and the basin of attractions, which is of great practical importance, for exponential control with those controls which show the following features:

(1) The control is continuous,
(2) it depends only on the variable(s) of the desired orbit,
(3) is independent of the previous value of the controlling parameters μ, if the values of the parameters are changing in the presence of control,
(4) and does not increase the dimensionality of the original system.

The reason for restricting the choice of controls for comparison to those possessing these properties is because the exponential control has all the above features.

To compare our control with that of Pecora and Carroll, both for X-drive and Y-drive, we consider the control where the parameter r is multiplied by the exponential feedback function involving the X variable for the same set of parameter values (such a choice of the control is made because Pecora and Carroll's method uses variables X and Y as drives). We find that the value of λ with this form of the control is $-4{\cdot}536$ for

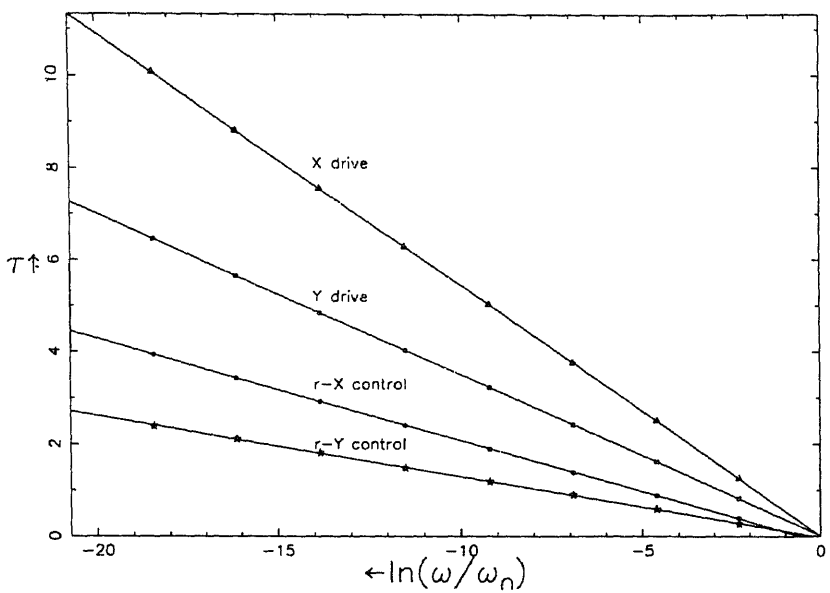

Figure 1. Plot of the transient time τ vs $\ln(\omega/\omega_0)$ for the Lorenz attractor with $\sigma = 10$, $b = 8/3$ and $r = 60$ while stabilizing the unstable fixed point $(\sqrt{b(r-1)}, \sqrt{b(r-1)}, r-1)$. Values of τ for Pecora and Carroll's method with X-drive (triangles) and Y-drive (squares) are compared with those obtained by using exponential control involving the parameter r and the variable X (circles) and also r and Y (stars).

1·7. We also find that λ for the control involving the parameter r and the variable
s $-7{\cdot}593$ for $\varepsilon = -0{\cdot}05$ for the same set of parameter values. The corresponding
ues of λ for Pecora and Carroll's method are $-1{\cdot}83$ for the X-drive and $-2{\cdot}85$ for
Y-drive [24]. Our values of λ are less than both these values and hence exponential
trol can be considered to be more effective.

To verify this we find the transient time τ, required to stabilize the second unstable
ed point of the Lorenz system for the same set of parameter values, for different
ues of ω using Pecora and Carroll's method (both for the X-drive and the Y-drive)
l also for exponential control involving the parameter r and the variables X and
or $\varepsilon = -1{\cdot}7$ and $\varepsilon = -0{\cdot}05$ respectively. We plot the variation of τ with $\ln(\omega/\omega_0)$ in
ire 1, which shows that our control stabilizes the unstable fixed point faster than
ora and Carroll's control. This is not surprising in view of the fact that our control
an exponential form.

We have also compared our control with the methods suggested by Singer *et al* [10],
l Chen and Chou [13]. For the first method, we find that the basin of attraction,
ile stabilizing non-zero fixed points of the Lorenz system, is smaller than the one
ained using exponential control. Also, the transient time is of the order $\sim 10^5$ which
igher as compared to that with exponential control ($\sim 10^3$). The method of Chen
l [13] shows the same transient time for stabilizing the unstable fixed points of the
enz map but the basin of attraction is smaller than that obtained with exponential
trol.

These comparisons should not be taken to imply that the exponential control will
ays be the better choice. They only show that the performance of exponential
trol is different from other controls and may be more efficient for some systems.

Exponential control for stabilizing unstable higher period orbits

Stabilization of unstable closed orbits for flows

unstable limit cycle of a continuous system can be converted into a stable limit cycle
multiplying one of the suitably chosen parameters, say μ_l, (or more depending on the
tem) by the exponential feedback function which depends only on one of the variable
X_r, i.e.

$$\mu_l \rightarrow \mu_l \exp[\varepsilon(X_r - X_r^u)]$$

ere X_r is the actual value of the variable of the given system with the feedback control
ler consideration and X_r^u is the value of the X_r coordinate on the desired unstable
it cycle which is required to be stabilized. The X_r^u is obtained after allowing the
tem to evolve freely for the same parameters without imposing the control.

We have implemented this idea for controlling unstable limit cycles of the Lorenz
tem. We choose parameter values $\sigma = 10$, $b = 8/3$ and $r = 28$. For these values the
rdinates of one point on one of the unstable limit cycles are $(-12{\cdot}786189$,
$9{\cdot}364189, 24{\cdot}00)$ [25]. The λ of the system is found to be positive. Since the limit
le is unstable, even on starting from an initial state very close to the limit cycle, the
tem trajectory will diverge away from the limit cycle. On implementation of the
trol, in which the parameter b is multiplied by $\exp[\varepsilon(Z - Z^u)]$, the Lyapunov

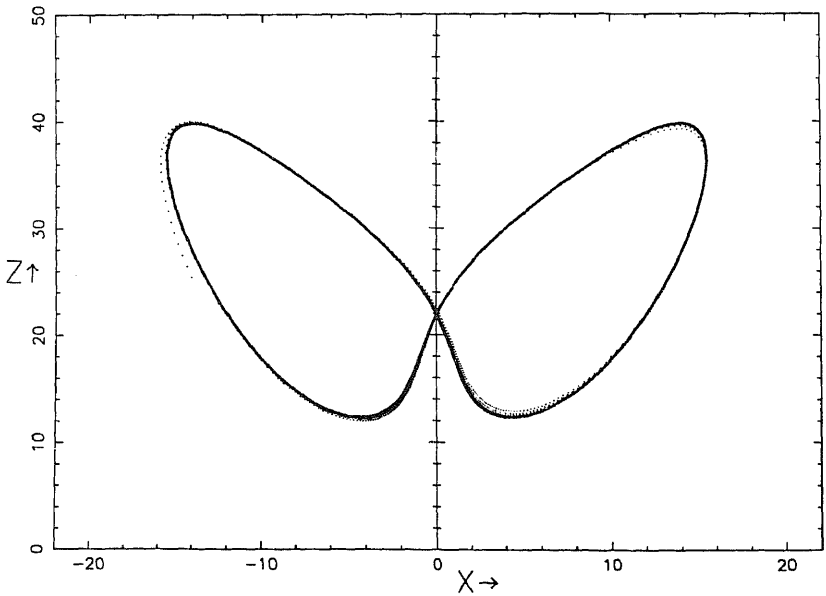

Figure 2. The dotted trajectory shows the convergence under exponential control of a nearby trajectory to the unstable closed orbit, represented by the bold curve, projected onto the (X, Z) plane of the Lorenz system with $\sigma = 10$, $b = 8/3$, and $r = 28$ starting from a point with coordinates $(-12{\cdot}786189, -19{\cdot}364189, 24{\cdot}00)$ for $\varepsilon = 0{\cdot}032$.

exponents of the system are found to become dependent on ε and for a certain range of values of ε, the real parts of all the Lyapunov exponents become negative thereby implying the stabilization of the limit cycle. Now, nearby trajectories are found to converge to the desired limit cycle as shown in figure 2. The transient τ shows a similar dependence on ε as in the previous sections. But for a given accuracy ω, the minimum value of τ corresponding to the optimal ε is much higher as compared to the case of the unstable fixed point of the Lorenz system. Moreover, the variation of τ with ε for a given ω is not as rapid as in the case of the unstable fixed point. With the result τ vs ε plot is quite flat displaying a shallow minimum.

We have also tested the control for another limit cycle of the Lorenz attractor. For the same parameter values, the coordinates of a point on a different limit cycle are $(-13{\cdot}917865, -21{\cdot}919412, 24{\cdot}00)$ [25]. The control is found to work effectively, and with similar features, in this case as well.

3.2 *Stabilization of higher period orbits of a discrete dynamical system*

We can extend the above control to convert unstable fixed points of higher period say $(\mathbf{X}^{*1}, \mathbf{X}^{*2}, \ldots, \mathbf{X}^{*k})$ to the stable fixed points for given values of the controlling parameters. What is required is a feedback that encodes as much information about a periodic orbit as is necessary for its unique characterization. But there is a problem of practicality. Since in this case the form of the control given by eq. (2) requires the

vergence of the chosen variable to one of the k values of that variable, the trolling technique diminishes in utility with increase in period. For higher period its of a discrete dynamical system a more effective control is one which employs gical OR structure in the feedback function. So in order to stabilize unstable fixed nts of period k *i.e.* $\{\mathbf{X}^{*i}\}$ one of the parameters μ_r in (1) is multiplied by

$$\exp\left(\varepsilon \prod_{i=1}^{k} (X_l(n) - X_l^{*i})\right) \tag{5}$$

ere $X_l(n)$ is the value of the chosen variables X_l at time n of the modulated map after lying control and $(X_l^{*1}, X_l^{*2}, \ldots, X_l^{*k})$ is the set of k values of X_l on the desired table period k orbit.

We had implemented this in the case of the logistic map for stabilizing a period rbit and found it to work effectively [15].

Stabilization of chaotic orbit

I have also tried to make different trajectories converge to a particular desired otic trajectory using our control. Again taking the Lorenz system as an example we ose the parameter values as $\sigma = 16, b = 4$ and $r = 40$. The real parts of the Lyapunov onents are (1·37, 0·0, −22·37) [26] indicating that this is a chaotic regime. We ose a chaotic trajectory starting with an initial point (10·0, 0·0, 30·0). We apply our

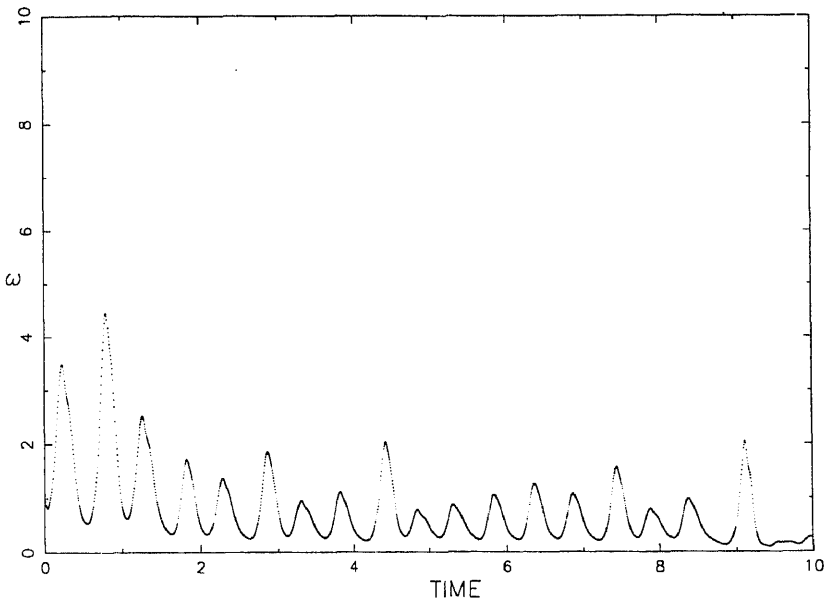

Figure 3a. The distance between the desired trajectory, starting with an initial point (10·0, 0·0, 30·0) and a trajectory started from a point away from the desired trajectory, for the Lorenz system with the parameter values as $\sigma = 16$, $b = 4$ and $r = 40$ for $\varepsilon = 0{\cdot}028$ is plotted against time.

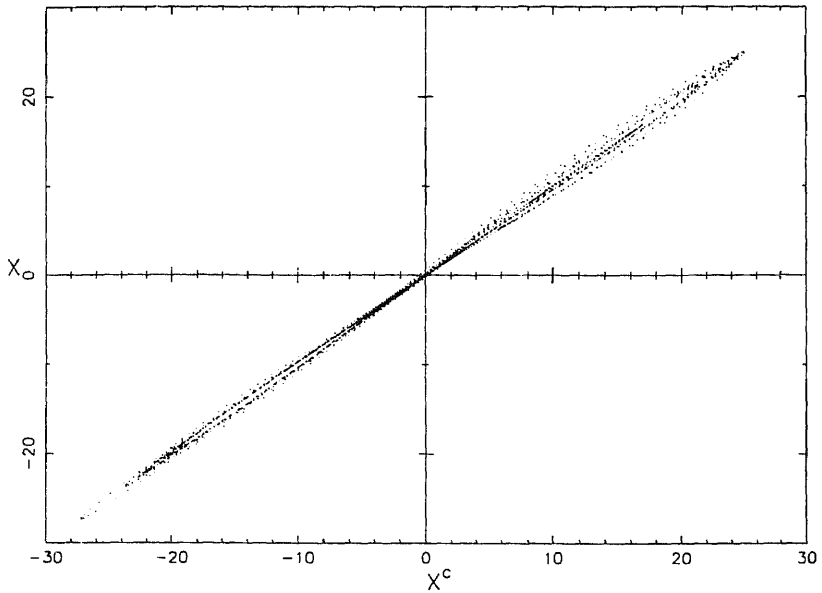

Figure 3b. Plot of X^c vs X for the Lorenz systems of figure 3a.

control by multiplying b by $\exp[\varepsilon(Z - Z^c)]$, where Z^c is the Z-coordinate of a point on the freely evolving chaotic trajectory. We find that the real parts of all the Lyapunov exponents of the modified Lorenz system become negative for a certain range of values of ε, showing that the desired chaotic trajectory has become a stable trajectory and different close by trajectories starting from different initial states converge to the desired trajectory. For a given ε in this range, the reciprocal of the slope of τ vs $\ln(\omega/\omega_0)$ is in good agreement with the numerically obtained minimum value of λ. It has been verified numerically that the system settles down onto the desired trajectory in the presence of the control. In figure 3(a) we plot the distance between the desired trajectory and a trajectory started from a point away from the desired trajectory, for $\varepsilon = 0{\cdot}028$. We also plot X^c vs X in figure 3(b) for the case in figure 3(a). The other features of the control remain unchanged. We have also tested our control for other chaotic trajectories and found it to work effectively.

5. Controlling spatiotemporal chaos

With exponential control it is also possible to control spatiotemporal chaos. A spatiotemporal system can be described by a coupled map lattice (CML) model [16–20]. Feedback pinnings [14] are used to control chaos of the system by stabilizing a certain unstable reference state. We use exponential feedback pinnings to control such a system. Here we consider the one-dimensional CML model [17–20], given by

$$X_{n+1}(i) = (1-\alpha) f[X_n(i)] + 0{\cdot}5\alpha\{f[X_n(i-1)] + f[X_n(i+1)]\}$$
$$\equiv F \qquad (6)$$

where $i = 1, 2, \ldots, L$ label the lattice sites and L is the system size. We assume periodic boundary conditions, $X_n(i + L) = X_n(i)$. Moreover, we take $f(X) = \mu X(1 - X)$. For a single site ($L = 1$), model (6) reduces to the well-known logistic map. The dynamical behaviour of model (6) with $L > 1$ is quite well understood [16–20]. The coupling term in (6) introduces very rich spatiotemporal patterns and the system displays homogeneous stationary solutions, inhomogeneous stationary solutions (spatial patterns), homogeneous periodic solutions and inhomogeneous periodic solutions (running or standing waves). In a chaotic state, all these patterns are unstable. We take $L = 60$, $\alpha = 0{\cdot}8$ and $\mu = 4$. The initial condition is prepared by choosing random numbers uniformly distributed in the interval [0, 1]. The motion of the system is fully turbulent at the chosen parameter values [17].

To control this system, we use pinnings defined by

$$X_{n+1}(i) = F \sum_{k=1}^{L/I} \delta(i - Ik - 1) \exp[\varepsilon(X_n(i) - \bar{X}_n(i)] \tag{7}$$

where I is the distance between two neighbouring pinnings, $\bar{X}_n(i)$ is the reference state to be stabilized and $\delta(j) = 1$ for $j = 1$ and $\delta(j) = 0$ otherwise.

The homogeneous stationary state of the system (6) is

$$\bar{X}_n(i) = X^* = 1 - 1/\mu \tag{8}$$

and an inhomogeneous stationary state is given by

$$\bar{X}_n(2j - 1) = \frac{B + \sqrt{B^2 - 4C}}{2\mu(2\alpha - 1)}$$

$$\bar{X}_n(2j) = \frac{B - \sqrt{B^2 - 4C}}{2\mu(2\alpha - 1)} \tag{9}$$

where $j = 1, 2, \ldots, L/2$, $B = 1 - \mu + 2\mu\alpha$ and $C = \alpha - \mu\alpha + 2\mu\alpha^2$. Both states are unstable for $\alpha = 0{\cdot}8$ and $\mu = 4$.

We control the unstable homogeneous stationary state (8) using (7) with $I = 2$ and $3{\cdot}36 < \varepsilon < 3{\cdot}78$ and the unstable inhomogeneous stationary state (9) with $I = 2$ and $0{\cdot}69 < \varepsilon < 0{\cdot}8$. These ranges for ε are obtained numerically. Although the initial values at the lattice sites are randomly distributed between 0 and 1, the system finds the desired patterns i.e. eqs (8) and (9) in less than 10^4 iterations. We show the effects of our control to state (8) for $I = 2, \varepsilon = 3{\cdot}5$ in figure 4(a), and to state (9) for $I = 2, \varepsilon = 0{\cdot}75$ in figure 4(b).

At the parameter values $\alpha = 0{\cdot}3$ and $\mu = 4$, system (6) has a running wave solution of time-period-two and space-period-four. Starting from initial conditions very near the running wave state, the system approaches the goal state in a small interval of time. If the initial values on the lattice sites are randomly distributed over the interval [0, 1], the transient time to the stable running wave state increases with increase in L. For $L = 60$ the average transient time is of order 10^{13} iterations or more [20]. Using (7) with $I = 4$ and $\varepsilon = 1{\cdot}0$ for the sites with $\bar{X}_n(i) = 0{\cdot}45841379\ldots$ and $\varepsilon = 2{\cdot}0$ for those with $\bar{X}_n(i) = 0{\cdot}89872907\ldots$, the average transient time is of order 10^3, (shown in figure 5), which is much shorter than that without control. We have considered different random initial configurations of the kind described above and found that the system always finds the same attractor possibly with a few defects. However no defects exist in figure 5.

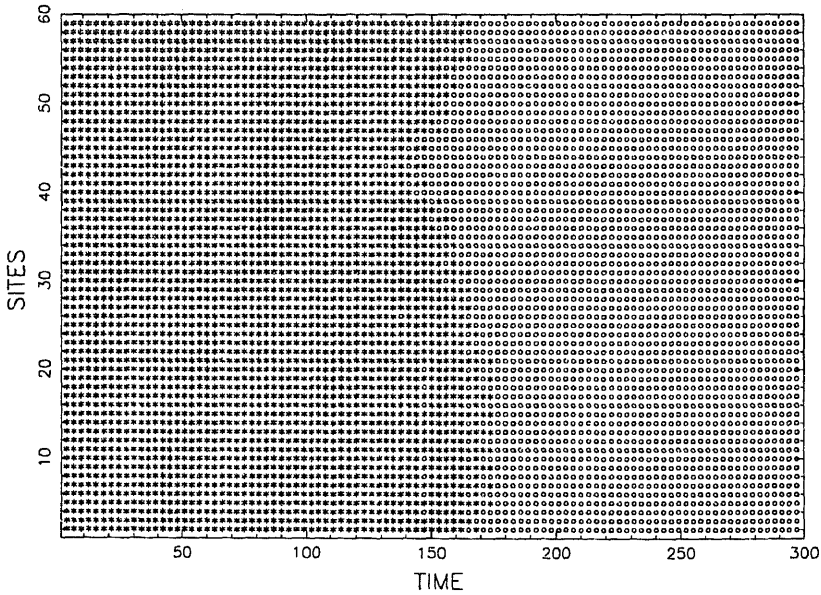

Figure 4a. The homogeneous unstable stationary state of eq. (6) with $\alpha = 0{\cdot}8$, $\mu = 4$ and $L = 60$ is controlled using exponential control at sites $i = 1, 3, 5, \ldots, 59$ with $\varepsilon = 3{\cdot}5$. Circles represent the state $X_n(i) = X^* = 0{\cdot}75$ while stars represent other states.

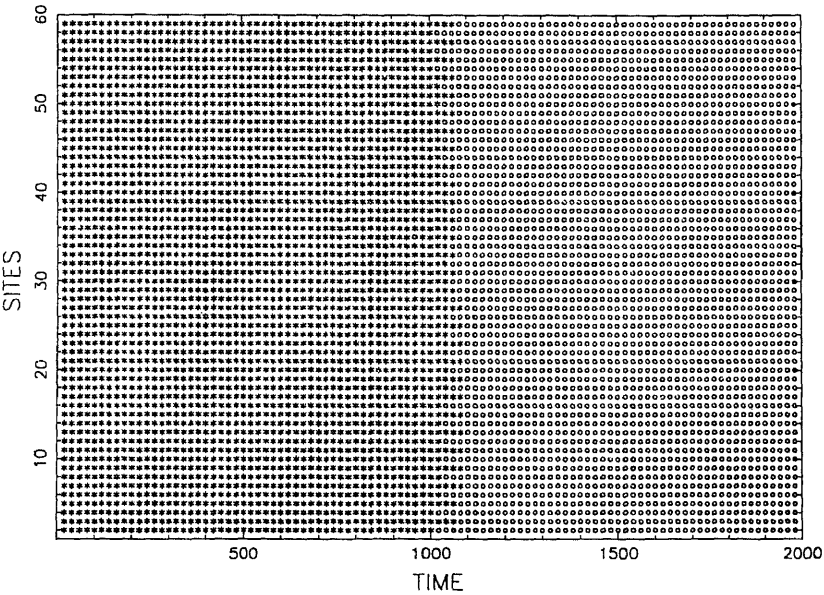

Figure 4b. The inhomogeneous unstable stationary state of (6) with $\alpha = 0{\cdot}8$, $\mu = 4$ and $L = 60$, which is $\bar{X}_n(2j-1) = 0{\cdot}536537\ldots$, $\bar{X}_n(2j) = 0{\cdot}880129\ldots$, is controlled using exponential control at sites $i = 1, 3, 5, \ldots, 59$ with $\varepsilon = 0{\cdot}75$. Circles represent that $X_n(i)$ has achieved the desired value while other values are represented by stars.

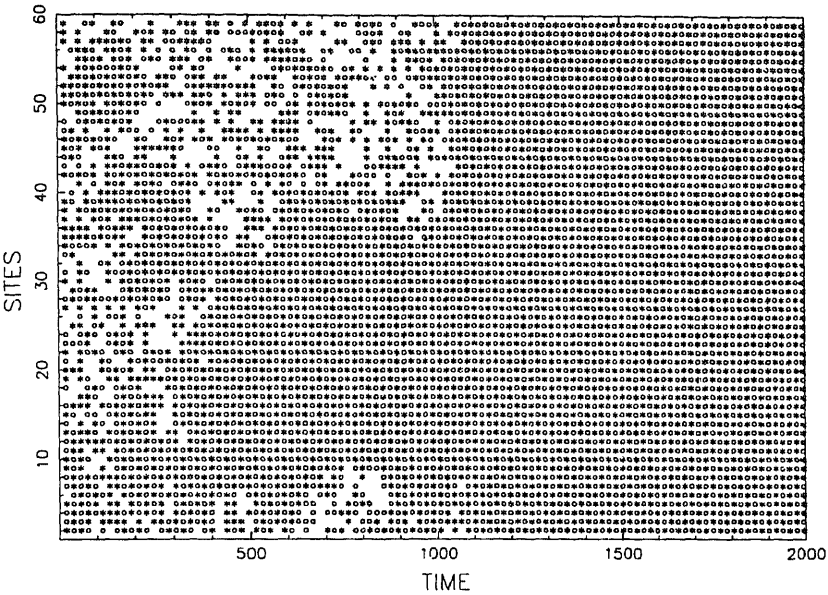

Figure 5. The transient process of the system evolution under controlling time-period-two and space-period-four running wave for $\alpha = 0{\cdot}3$ and $\mu = 4$. The initial state is prepared using random numbers uniformly distributed in $[0, 1]$. Circles represent the state $|X_n(i) - 0{\cdot}89| \leqslant 0{\cdot}15$, stars represent $|X_n(i) - 0{\cdot}45| \leqslant 0{\cdot}15$ while blank spaces represent other states. Exponential control is applied at sites $i = 1, 5, 9, \ldots, 57$; $\varepsilon = 1{\cdot}0$ for the sites with $\bar{X}_n(i) = 0{\cdot}45841379...$ and $\varepsilon = 2{\cdot}0$ for those with $\bar{X}_n(i) = 0{\cdot}89872907....$ We plot data once every 19 iterations.

e average relaxation time increases with increase in I. It is found to be of order 10^5 for 12 with more defects as compared to $I = 4$.

Conclusion

r exponential control given by (2) is found to work effectively both for maps as well or flows. Since the knowledge of only a subset of variables on the desired unstable it is sufficient to settle the system onto that orbit, this makes the control particularly ful for systems with several degrees of freedom. In the presence of the control, there sts a range of values of the stiffness constant ε for which a repellor —whether it be xed point, limit cycle or a chaotic trajectory, can be converted into an attractor. Both nd τ are found to be decreasing functions of ε. However there exists an optimum fness control for which both λ and τ go through a minimum. Such behaviour is racteristic of different types of orbits and for a variety of systems.

n the case of a CML model we find that control can be effected by pinning alternate tice sites using exponential feedback. We have succeeded in stabilizing various stable spatiotemporal patterns like an unstable homogeneous stationary state, an

Acknowledgements

We would like to thank Dr Neelima M Gupte for her invaluable comments and suggestions. We also thank the Inter University Center for Astronomy and Astrophysics (IUCAA) for allowing the use of their computing facility. One of the authors (SDG) also thanks Kirori Mal College, University of Delhi, Delhi, for grant of study leave.

References

[1] L M Pecora and T L Carroll, *Phys. Rev. Lett.* **64**, 821 (1990)
[2] L M Pecora and T L Carroll, *Phys. Rev. Lett.* **67**, 645 (1991)
[3] L M Pecora and T L Carroll, *Phys. Rev.* **A44**, 2374 (1991)
[4] E Ott, C Grebogi and J A Yorke, *Phys. Rev. Lett.* **64**, 1196 (1990)
[5] T Shinbrot, E Ott, C Grebogi and J A Yorke, *Phys. Rev. Lett.* **65**, 3215 (1990)
[6] W L Ditto, S N Rauseo and M L Spano, *Phys. Rev. Lett.* **65**, 3211 (1990)
[7] S Sinha, R Ramaswamy and J S Rao, *Physica* **D43**, 118 (1990)
[8] E R Hunt, *Phys. Rev. Lett.* **67**, 1953 (1991)
[9] C Reyl, L Flepp, R Badii and E Brun, *Phys. Rev.* **E47**, 267 (1993)
[10] J Singer, Y Z Wang and H H Bau, *Phys. Rev. Lett.* **66**, 1123 (1991)
[11] S Rajasekar and M Lakshmanan, *Physica* **D67**, 282 (1993)
[12] K Murali and M Lakshmanan, *Phys. Rev.* **E48**, R1624 (1993)
[13] Y H Chen and M Y Chou, *Phys. Rev.* **E50**, 2331 (1994)
[14] G Hu and Z Qu, *Phys. Rev. Lett.* **72**, 68 (1994)
[15] S D Gadre and V S Varma, *Pramana – J. Phys.* **43**, 431 (1994)
[16] T Bohr and O B Christensen, *Phys. Rev. Lett.* **63**, 2161 (1989)
[17] K Kaneko, *Prog. Theor. Phys.* **74**, 1033 (1985); *Physica* (Amsterdam) **D23**, 437 (1986); **D34**, 1 (1989); **D37**, 60 (1989)
[18] J P Crutchfield and K Kaneko, in *Directions in chaos*, edited by Hao Bai-Lin (World Scientific, Singapore, 1987); *Phys. Rev. Lett.* **60**, 2715 (1988)
[19] J D Keeler and J D Farmer, *Physica* (Amsterdam) **D23**, 413 (1986)
[20] E J Ding and Y N Lu, *J. Phys.* **A25**, 2897 (1992)
[21] E N Lorenz, *J. Atoms. Sci.* **20**, 130 (1976)
[22] M Hénon, *Commun. Math. Phys.* **50**, 69 (1976)
[23] C Sparrow, *The Lorenz equations, bifurcations and chaos* (Springer Verlag, New York, 1982)
[24] N Gupte and R E Amritkar, *Phys. Rev.* **E48**, R1620 (1993)
[25] J H Curry, in *Global theory of dynamical systems,* Lecture Notes in Mathematics, Edited by Z Nitecki and C Robinson (Springer Verlag, Berlin, 1980) **819**, 111–120
[26] I Shimada and T Nagashima, *Prog. Theor. Phys.* **69**, 1605 (1979)

physics
October 1995
pp. 369–376

acroscopic equation of motion in inhomogeneous media: microscopic treatment

M JAYANNAVAR and MANGAL C MAHATO
itute of Physics, Sachivalaya Marg, Bhubaneswar 751 005, India

received 10 May 1995; revised 16 August 1995

tract. The dynamical evolution of a Brownian particle in an inhomogeneous medium with tially varying friction and temperature field is important to understand conceptually. It uires to address the basic problem of relative stability of states in nonequilibrium systems ch has been a subject of debate for over several decades. The theoretical treatments adopted ar are mostly phenomenological in nature. In this work we give a microscopic treatment of problem. We derive the Langevin equation of motion and the associated Fokker–Planck ation. The correct reduced description of the Kramers equation in the overdamped limit oluchowski equation) is obtained. Our microscopic treatment may be helpful in under- nding the working of thermal ratchets, a problem of much current interest.

words. Brownian particle; diffusion; inhomogeneous systems; relative stability of states; kker–Planck equation.

CS Nos **05·60; 05·40; 05·90; 02·50**

Introduction

ermodynamic equilibrium states are ideal limiting cases and are convenient and en theoretically amenable to study with relative ease. However, one commonly ounters systems that are away from equilibrium. All nonequilibrium systems relax urally toward their respective equilibrium or stationary states. In nature, evolution n ongoing and dominant process. Naturally, the process of relaxation of the nequilibrium systems is of great interest in all branches of natural science, be it sics, chemistry or biology. Moreover, one comes across nonuniform systems more en than uniform systems. Uniform systems are characterized by a constant (space ependent) diffusion coefficient throughout the system and having the same tempera- e in all parts of the system. There are well established theoretical formalisms for form systems to describe their evolution towards equilibrium or steady states [1]. wever, the same is not true for nonuniform systems. There exist phenomenological criptions but often without microscopic foundations. The ad hoc nature of these criptions have led to some controversies, too, in the past. For instance, should the usion equation of a Brownian particle in the absence of external potential have the n [2–8]

$$\frac{\partial P}{\partial t} = \frac{\partial^2}{\partial q^2} D(q) P$$

$$\frac{\partial P}{\partial t} = \frac{\partial}{\partial q} D(q) \frac{\partial P}{\partial q} ?.$$

nonuniform systems self-consistent [2, 4, 8, 10].

In this work, we seek to clarify some of the issues pertaining to this important case of nonuniform systems in a systematic manner. We derive, from microscopic theory, the Kramers equation for the joint probability distribution of position and velocity of a Brownian particle in an inhomogeneous, nonisothermal medium. We then proceed to find the correct Smoluchowski limit to the Kramers equation. This, however, is not a mathematical problem alone; the underlying conceptual development is quite appealing and, as mentioned earlier, is subject to ongoing controversies for over several decades [2–8].

The evolution of a Brownian particle in condensed media is the most familiar example of a nonequilibrium process. The process is accompanied by frictional dissipation but aided by associated fluctuations. Nonequilibrium behaviour of macroscopic uniform systems is described well by linear-response theory when the initial state of the system is close to equilibrium. The fluctuation-dissipation theorem relating the power absorbed by the system to the intrinsic fluctuations in the system in equilibrium has foundations in the linear response theory. But, when the system is far from equilibrium the linear response theory cannot be relied upon. In most of the physical systems, whether close to or far from equilibrium, the approach to equilibrium can, however, be likened to one kind or other of a diffusion process; it may be translational diffusion of particles, rotational diffusion of macromolecules, spin diffusion of spin systems, heat or thermal diffusion in solids, energy diffusion in excitonic motion in semiconductors, and so on. The diffusion process in inhomogeneous systems, therefore, calls for added attention.

In the case of uniform systems the diffusion constant $D = \eta^{-1} k_B T$, where η is the friction coefficient and T the temperature. However, for nonuniform systems the space, q, dependence of the diffusion comes separately through $\eta(q)$ and $T(q)$. The origin of $\eta(q)$ and $T(q)$ and the manner in which they influence the relaxation of the nonequilibrium system are entirely different. The variation of $\eta(q)$ (in the absence of spatial variation of temperature) influences the dynamics of particle in a potential field and helps the system to approach towards its equilibrium or steady states. The relative stability of the competing states is generally governed by the usual Boltzmann factor in the local neighbourhood of the corresponding (representative) potential wells. A change in the potential barrier between two potential well minima changes the relaxation rate but leaves the relative stability of the two well states unchanged. This simple fact, however, may not apply for more general systems when the temperature is nonuniform along the potential surface (or spatial coordinate).

Landauer, in a series of papers [2–5], argues that for systems with nonuniform temperature the relative stability of two states will be affected by the detailed kinetics all along the pathways (on the potential surface) between the two states under comparison. It is the effect of thermal fluctuations that plays a crucial role and the resulting effective potential surface may have completely different nature from that of uniform temperature. With the help of his blowtorch theorem Landauer [3] shows that a change of temperature away from uniformity even at very unlikely positions of the system on the potential surface may cause probability currents to set in moving the system towards a new steady state situation changing thereby the relative stability of the otherwise locally stable states. This known important fact, however, has received much less attention in the literature

than it deserves. This effect can have important consequences on the particle motion in nonuniform systems, for instance, the kinetics of growth of crystalline nuclei in the melt around its critical size. The latent heat generation being, in this example, responsible for the creation of nonuniform temperature field across the surface of the nucleus. Nonuniform temperature field can also be generated by shining light on semiconductors. One can have nonuniform temperature field also because of nonuniform distribution of electrons and of phonons (or of quasiparticles in general) with different characteristic temperatures in a solid. It has been suggested that the nonuniform temperature field can produce current in a closed ring [3, 6, 9]. There has been a lot of theoretical work reported in recent times on thermal ratchets [10]. These works are inspired by the observed predominantly unidirectional protein (macromolecule) motion in biological systems even in the absence of obvious external forces and thermal gradients. The idea of relative stability of states in nonuniform temperature systems can help to understand the working of the thermal ratchets better [11, 12]. These are but few examples where nonuniform temperature field can have important bearing on the dynamical evolution. A systematic formalism to deal with such a situation is, therefore, essential.

In the following sections we proceed systematically to set up a formalism from microscopic theory. We derive the Kramers equation for space dependent friction coefficient and nonuniform temperature field. We then go over to obtain the correct Smoluchowski limit of the Fokker–Planck equation. Before concluding we also give the correct Langevin equation in the overdamped limit that is approximated properly to order $\eta(q)^{-1}$.

2. Microscopic derivation of Langevin equation in a space dependent friction field

To obtain Langevin equation in a space dependent friction field we consider the motion of a subsystem (Brownian particle) described by its coordinate Q and momentum P and subjected to an external potential field $V(Q)$ of the system. We assume the subsystem to be in contact with a thermal (phonon) bath. The bath oscillators are described by coordinates q_α and momentum p_α with characteristic frequencies ω_α. For our calculation we consider the total Hamiltonian

$$\mathscr{H} = \frac{P^2}{2M} + V(Q) + \sum_\alpha \left[\frac{p_\alpha^2}{2m_\alpha} + \frac{m_\alpha \omega_\alpha^2}{2} \left(q_\alpha - \lambda_\alpha \frac{A(Q)}{m_\alpha \omega_\alpha^2} \right)^2 \right], \tag{1}$$

where M is the Brownian particle mass and m_α are the masses of the bath oscillators. The interaction of the subsystem with the thermal bath [13] is through the linear coordinate–coordinate coupling term $\lambda_\alpha q_\alpha A(Q)$. From (1) one obtains the following equations of motion

$$\dot{Q} = \frac{P}{M}, \tag{2a}$$

$$\dot{P} = -V'(Q) + \sum_\alpha \lambda_\alpha A'(Q) \left[q_\alpha - \lambda_\alpha \frac{A(Q)}{m_\alpha \omega_\alpha^2} \right], \tag{2b}$$

$$\dot{q}_\alpha = \frac{p_\alpha}{m_\alpha}, \tag{2c}$$

and

$$\dot{p}_\alpha = -m_\alpha \omega_\alpha^2 q_\alpha + \lambda_\alpha A(Q), \tag{2d}$$

where $A'(Q)$ is the derivative of $A(Q)$ with respect to Q. After solving (2c) and (2d) for q_α using the method of Laplace transform and substituting its value in (2b), we obtain the Langevin equation of motion for Q and P.

$$\dot{Q} = \frac{P}{M}, \tag{3a}$$

$$\dot{P} = -V'(Q) - \eta[A'(Q)]^2 \frac{P}{M} + A'(Q) f(t). \tag{3b}$$

Thus, the effect of interaction of the Brownian particle with the thermal bath is to introduce a friction term and a fluctuating term $f(t)$ in the equation of its motion. The fluctuating term is given by

$$f(t) = \sum_\alpha \lambda_\alpha \left[q_\alpha(0)\cos(\omega_\alpha t) + \frac{\dot{q}_\alpha(0)}{\omega_\alpha} \sin(\omega_\alpha t) \right], \tag{4a}$$

where $q_\alpha(0)$ and $\dot{q}_\alpha(0)$ are the initial positions and velocities of the bath variables. The force $f(t)$ is fluctuating in character because of the associated uncertainties in these initial conditions of the bath variables. However, as the thermal bath is characterized by its temperature T, the equilibrium distribution of bath variables is given by the Boltzmannian form, so that $f(t)$ follows the following statistics

$$\langle f(t) \rangle = 0 \tag{4b}$$

and

$$\begin{aligned} \langle f(t) f(t') \rangle &= \sum_\alpha \frac{\lambda_\alpha^2 k_B T}{m_\alpha \omega_\alpha^2} \cos(\omega_\alpha (t - t')) \\ &= 2 k_B T \eta \delta(t - t'). \end{aligned} \tag{4c}$$

To arrive at equations (3b) and the last term of (4c) we have assumed [13, 14, 15] ohmic spectral density for the bath oscillators, i.e.,

$$\rho(\omega) = \frac{\pi}{2} \sum_\alpha \frac{\lambda_\alpha^2}{m_\alpha \omega_\alpha} \delta(\omega - \omega_c) = \eta \omega \exp(-\omega/\omega_c).$$

The upper cut-off frequency ω_c is assumed to be much larger than the characteristic frequencies of the system. Equations (3b) and (4c) correspond to the well known Markovian limit and are valid for time scales $t > 1/\omega_c$, which can be made arbitrarily small by appropriately choosing ω_c. For details we refer to [14, 15]. It should be noted that the transient terms have been neglected at time scales $t > \omega_c^{-1}$ to arrive at (3b), and is perfectly valid under Markovian approximation [15]. It is noted that $A'(Q) =$ constant corresponds to a uniform friction coefficient. Redefining, $\eta[A'(Q)]^2 = \eta(Q)$ and $f(t)/\sqrt{T\eta} \to f(t)$, and putting $M = 1$, we get,

$$\dot{Q} = P, \tag{5a}$$

$$\dot{P} = -V'(Q) - \eta(Q) P + \sqrt{\eta(Q)\, T} f(t), \tag{5b}$$

$\langle f(t) f(t') \rangle = 2k_B \delta(t - t')$. (5c)

s instructive to note that one could take $\eta(Q)$ to be constant piecewise along Q; in h piece of these Q segments (5b) would correspond to a constant friction coefficient with the same statistical character of $f(t)$ as in any other Q intervals.

Microscopic Markovian Langevin equation with space dependent friction and temperature

have so far derived the Langevin equation of motion (from a microscopic miltonian) of a Brownian particle with space dependent friction keeping the perature constant. We, now, consider a system for which the temperature too is ce dependent $T(Q)$. At this point it is pertinent to note the following important fact, vever. It is quite well known that when a charged Brownian particle is subjected to electric field charge current results. Similarly, when it is subjected to a thermal dient thermal current flows in the system. However, in the former case the effect of electric field can be incorporated in the particle Hamiltonian as a potential term ereas temperature gradient cannot be incorporated as the potential term in the miltonian formalism. Therefore, in order to incorporate the effect of the temperature omogeneity we reason as follows. The Brownian particle comes in contact with ntinuous sequence of independent temperature baths as its coordinate Q changes in e. Equivalently, each space point of the system is in equilibrium with a thermal bath haracteristic temperature $T(Q)$. In what follows we accept this idea and incorporate perature inhomogeneity into the equations of motion (5). Henceforth, for nota- al simplicity, the coordinate Q and momentum P are replaced by the corresponding er case letters q and p, respectively, reserving P for probability distribution.

For the sake of argument we consider, for the time being, the system to be subdivided pace q into several small segments and represent the segments Δq around q by ces i. Each segment is connected to an independent thermal bath at temperature T_i corresponding random forces $f_i(t)$. The last term on the right hand side of (5b), is efore replaced by $\sqrt{\eta(q)\, T_i} f_i(t)$ for the segment i. As the two different segments are coupled to an independent temperature bath we have $\langle f_i(t) f_j(t') \rangle = 2k_B \delta_{ij} \delta(t - t')$. ause $f(t)$ is δ-correlated in time, as the particle evolves dynamically the fluctuation e $f_i(t)$ experienced by the Brownian particle while in the space segment i at time ll have no memory about the fluctuating force experienced by it at some previous e t' while in the space segment $j \neq i$. Hence the space-dependent index i in $f_i(t)$ can be ored. Now, taking a continuum limit, the stochastic equations of motion of the wnian particle, in an inhomogeneous medium with space dependent friction and uniform temperature, are given by,

$$\dot{q} = p, \tag{6a}$$

$$\dot{p} = -V'(q) - \eta(q) p + \sqrt{\eta(q)\, T(q)} f(t), \tag{6b}$$

$$\langle f(t) f(t') \rangle = 2k_B \delta(t - t'). \tag{6c}$$

also important to note and repeat that as long as the random force is delta correlated

in $f(t) \to f(q,t)$ such that $\langle f(q,t) f(q',t') \rangle = 2g(q-q')\delta(t-t')$ with $g(0) = \Gamma$.

4. Derivation of Kramers and Smoluchowski equations

It is, now, a straightforward exercise to derive the corresponding Fokker–Planck equation. We put $M = 1$ so that $p = v$, the velocity of the Brownian particle. The stochastic differential equations (6a) and (6b) can be converted into an equation for probability density $P(q, v, t)$ using the well-known van Kampen lemma [16]. To this end, we consider a cloud of initial phase points of density $\rho(q, v, t)$ in (q, v) phase space each point (q, v) of which is evolving in time according to (6a) and (6b). The phase fluid evolves according to the stochastic Liouville equation (continuity equation)

$$\frac{\partial \rho}{\partial t} = -\nabla_q(\dot{q}\rho) - \nabla_v(\dot{v}\rho). \tag{7}$$

In order to obtain the equation for the evolution of $P(q, v, t)$ we ensemble average ($\langle \cdots \rangle$) eq. (7) over all realizations of the random force of given statistics and use the well-known result (van Kampen lemma) [16]

$$\langle \rho \rangle = P(q, v, t). \tag{8}$$

The averaging procedure is carried out after substituting for $\dot{q}$ and $\dot{v}$ in (7) from (6). A term like $\langle \rho f(t) \rangle$ appears which is evaluated using the Novikov theorem [17]. For details see refs [18, 19]. From this we obtain the desired Fokker–Planck equation

$$\frac{\partial P(q,v,t)}{\partial t} = -v\frac{\partial P(q,v,t)}{\partial q} - V'(q)\frac{\partial P(q,v,t)}{\partial v} + \eta(q)\frac{\partial}{\partial v}\left\{vP(q,v,t) + k_B T(q)\frac{\partial}{\partial v}P(q,v,t)\right\}. \tag{9}$$

This is the Kramers equation for space dependent friction coefficient $\eta(q)$ and nonuniform temperature $T(q)$, derived from microscopic theory. It should be noted that van Kampen had assumed (9) as the model Kramers equation to start with to study the diffusion of a Brownian particle in a ring due to the combined effect of space dependent friction coefficient and the temperature inhomogeneity [6]. Equations (6) and (9) are valid for all friction coefficients, low as well as high. It is, however, hard to slove (9) in general cases. Moreover, in many of the practical situations one does not need the detailed motion of the Brownian particle at time scales much smaller than the characteristic time scales of order η^{-1}. Therefore, sometimes it is unnecessary to retain the fast variables v.

In most of the problems of physical interest (overdamped case) the marginal distribution $P(q, t)$ suffices to describe the motion of a Brownian particle. In the case of uniform systems, that is, when η = constant and T = constant, the reduction of $P(q, v, t)$ to $P(q, t)$ is well known and goes by the name of adiabatic elimination. One simply sets $\dot{p} = 0$ in (6b) to obtain the overdamped Langevin equation. From these one obtains the Fokker–Planck equation for $P(q, t)$. The overdamped Langevin equation so obtained is correct to order η^{-1}. For inhomogeneous systems, however, the integration of (7) to

btain the equation for $P(q,t)$ is not easy. Moreover, simply ignoring the p term in (6b) s not correct. For instance, the resulting marginal distribution function so obtained oes not conform to the correct equilibrium distribution. However, Sancho *et al* [20] ave given a systematic procedure to go over to the overdamped Langevin equation for system with space dependent friction coefficient but at uniform temperature. The verdamped Langevin equation obtained by Sancho *et al* is correct to order $[\eta(q)]^{-1}$ nd leads to physically valid equilibrium distribution function.

Following the prescription of Sancho *et al* [20], we obtain the overdamped Langevin quation for an inhomogeneous system with nonuniform temperature field $T(q)$ and is iven as

$$\dot{q} = -\frac{V'(q)}{\eta(q)} - \frac{1}{2[\eta(q)]^2}\{T(q)\eta'(q) + \eta(q)\,T'(q)\} + \left(\frac{T(q)}{\eta(q)}\right)^{1/2} f(t), \tag{10}$$

ith

$$\langle f(t)f(t')\rangle = 2k_B\delta(t-t').$$

he corresponding Fokker–Planck equation for the overdamped case (the Smolu- owski equation), with k_B set equal to 1, is

$$\frac{\partial P(q,t)}{\partial t} = \frac{\partial}{\partial q}\frac{1}{\eta(q)}\left[\frac{\partial}{\partial q}T(q)P(q,t) + V'(q)P(q,t)\right]. \tag{11}$$

As pointed out earlier by van Kampen, the diffusion equation (11) in the absence of xternal potential has neither the form $\partial P/\partial t = (\partial^2/\partial q^2)D(q)P(q)$, nor $\partial P/\partial t = (\partial/\partial q)$ $(q)(\partial/\partial q)P(q)$. It is clear that $T(q)$ and $\eta(q)$ influence the motion of the Brownian article in different ways and their combined effect cannot be plugged together as the ffect of an effective diffusion coefficient $D(q)$. We note that our equation (11) agrees ith one of the forms obtained by van Kampen [6–8].

As already mentioned earlier the friction coefficient $\eta(q)$ only affects the relaxation rocess and not the equilibrium distribution function in a constant temperature field. iven enough time the system finds its equilibrium state. In contrast, the case of onuniform temperature field changes the concept of steady states. It can be readily erified that if the external potential is unbounded at infinity, i.e., $V(q) \to \infty$ as $q \to \pm\infty$, en the system evolves to a steady state $P_s(q)$ obtained by setting the probability urrent equal to zero

$$P_s(q,t) = \frac{C}{T(q)}\exp\left(-\int^q (V'(q)/T(q'))dq'\right) \tag{12}$$

here C is a normalization constant. The solution in no way resembles the distribution ecided by the usual Boltzmann factor alone. P_s is not a local function of $V(q)$. The on-local dependence of $P_s(q)$ on $T(q)$ and $V(q)$ forces the relative stability of the system two different local minima to depend sensitively on the temperature profile along the tire pathway connecting the two minima [2–5]. Moreover for particular choices of (q) it may so happen that $P_s(q)$ may show extrema at positions completely unrelated the minima of the external potential $V(q)$. Such a system with nonuniform tempera- re field is inherently nonequilibrium and $P_s(q)$ describes distribution of nonequilib- um steady states.

5. Conclusion

We have given a systematic microscopic derivation of Kramers equation of motion of a Brownian particle in a medium where friction coefficient is space dependent and having nonuniform temperature. We further obtain the Smoluchowski limit of the Kramers equation following the procedure given by Sancho *et al* [20]. We thus arrive at the correct overdamped Langevin equation for such a system. The microscopic treatment followed in this work helps resolve the controversy regarding the correct form of the diffusion equation followed by a Brownian particle in an inhomogeneous medium. We argue that the microscopic derivation of the equations makes their application to systems such as the thermal ratchets self-consistent [10–12]. Moreover, in many cases the numerical solution of the Langevin equation is much more transparent to appreciate physically, and the derived overdamped Langevin equation could thus be of some practical use.

Acknowledgements

One of us (AMJ) thanks Professor N Kumar for continued discussions on this subject and related problems.

References

[1] N G van Kampen, *Stochastic processes in physics and chemistry* (North Holland, Amsterdam, 1981)
C W Gardiner, *Handbook of stochastic methods* (Springer Verlag, Berlin, 1983)
[2] R Landauer, *Helv. Phys. Acta* **56**, 847 (1983); *J. Stat. Phys.* **53**, 233 (1988), and references therein
[3] R Landauer, *Physica* **A194**, 551 (1993), and references therein
[4] R Landauer, *Physics Today* **31**, 23 (November 1978)
[5] R Landauer, *Ann. NY Acad. Sci.* **316**, 433 (1979)
[6] N G van Kampen, *IBM J. Res. Develop.* **32**, 107 (1988)
[7] N G van Kampen, *Z. Phys.* **B68**, 135 (1987)
[8] N G van Kampen, *J. Maths. Phys.* **29**, 1220 (1988)
[9] M Buettiker, *Z. Phys.* **B68**, 161 (1987)
[10] M M Millonas, *Phys. Rev. Lett.* **74**, 10 (1995), and references therein
[11] A M Jayannavar and M C Mahato, unpublished
[12] A M Jayannavar, unpublished
[13] A O Caldeira and A J Leggett, *Physica* **A121**, 587 (1983); *Ann. Phys.* **149**, 374 (1983)
[14] K Lindenberg and V Seshadri, *Physica* **A109**, 483 (1981)
[15] A M Jayannavar, *Z. Phys.* **B82**, 153 (1991)
[16] N G van Kampen, *Phys. Rep.* **C24**, 172 (1976)
[17] E A Novikov, *Zh. Eksp. Teor. Fiz.* **47**, 1919 (1964); *Sov. Phys. JETP* **20**, 1290 (1965)
[18] A M Jayannavar and N Kumar, *Phys. Rev. Lett.* **48**, 553 (1982)
[19] A M Jayannavar, *Phys. Rev.* **E48**, 837 (1993)
[20] J M Sancho, M San Miguel and D Duerr, *J. Stat. Phys.* **28**, 291 (1982)

Pramana journal of physics Vol. 45 (No. 4), October 1995

Contents

Painlevé analysis and integrability of the damped anharmonic oscillator equation ..... *S Paul Raj and S Rajasekar* 305

The particle in a box problem in q-quantum mechanics ..... *G Vinod, K Babu Joseph and K M Valsamma* 311

Polarized light ..... *G Ramachandran, A R Usha Devi and N S Saandeep Kannadavardhana* 319

On the Dirac equation with anomalous magnetic moment term in a beam of electromagnetic wave ..... *N D Sen Gupta* 327

Fermilab top mass and modified Fritzsch mass matrices ..... *P S Gill and Manmohan Gupta* 333

Vacuum structure, chiral symmetry breaking and electric dipole moment of neutron ..... *A R Panda and K C Roy* 343

Controlling chaos: Stabilization of unstable orbits using exponential control for maps and flows ..... *Sangeeta D Gadre and V S Varma* 355

Macroscopic equation of motion in inhomogeneous media: A microscopic treatment ..... *A M Jayannavar and Mangal C Mahato* 369

Indexed in CURRENT CONTENTS ISSN 0304–4289

Edited and published by V K Gaur for the Indian Academy of Sciences, Bangalore 560 080. Typeset and printed at Thomson Press (I) Ltd., Faridabad 121 007.

PRAMANA

journal of physics

Vol. 45 No. 5
November 1995

DIAN ACADEMY OF SCIENCES
an National Science Academy
an Physics Association

Editor

R Nityananda
Raman Research Institute, Bangalore

Associate Editor

H R Krishnamurthy
Indian Institute of Science, Bangalore

Editorial Board

G S Agarwal, *Physical Research Laboratory, Ahmedabad*
V Balakrishnan, *Indian Institute of Technology, Madras*
M Barma, *Tata Institute of Fundamental Research, Bombay*
P Chaddah, *Centre for Advanced Technology, Indore*
B M Deb, *Panjab University, Chandigarh*
P K Kaw, *Institute for Plasma Research, Gandhinagar*
H S Mani, *Indian Institute of Technology, Kanpur*
N Mukunda, *Indian Institute of Science, Bangalore*
T Padmanabhan, *Inter-University Centre for Astronomy and Astrophysics, Pune*
J C Parikh, *Physical Research Laboratory, Ahmedabad*
G Rajasekaran, *Institute of Mathematical Sciences, Madras*
V S Ramamurthy, *Department of Science and Technology, New Delhi*
R Ramaswamy, *Jawaharlal Nehru University, New Delhi*
K R Rao, *Bhabha Atomic Research Centre, Bombay*
Probir Roy, *Tata Institute of Fundamental Research, Bombay*
A K Sood, *Indian Institute of Science, Bangalore*

Editor of Publications of the Academy

V K Gaur
C-MMACS, NAL, Bangalore

Subscription Rates
(1996)

All countries except India	1 year
(Price includes AIR MAIL charges)	US$ 200
India	1 year Rs. 200

Annual subscriptions for **individuals** for India and abroad are Rs. 75/- and $50 respectively.

All correspondence regarding subscription should be addressed to the **Circulation Department** of the Academy

---

Editorial Office

Indian Academy of Sciences, C V Raman Avenue,
P.B. No. 8005, Bangalore 560 080, India

Telephone: 334 2546
Telex: 845-2178 ACAD IN
Telefax: 91-80-334 6094

© 1995 by the Indian Academy of Sciences. All rights reserved.

"Information for contributors" is printed in the last issue of every volume.

physics
pp. 377–384

Nonlinear dynamics of a two-dimensional lattice

NABONITA D CHOWDHURY and SANKAR P SANYAL
Department of Physics, C V Raman Building, Barkatullah University, Bhopal 462026, India

MS received 23 December 1994; revised 1 August 1995

Abstract. The dynamics of the nonlinear excitations in a two-dimensional (2D) ϕ^4-diatomic lattice, with nonlinear on-site electron–phonon coupling at the polarizable ion site has been presented, without considering the self consistent phonon approximation. One of the major results obtained from our calculations is in the understanding of continuous structural phase transition, where we have obtained the minimum in soft mode frequency at a soft mode temperature $T_s (> T_c)$, not at critical temperature T_c. This occurs due to the anisotropy of such 2D systems.

Keywords. Lattice dynamics; phase transition; soft mode; nonlinear dynamics.

PACS No. 63·20

1. Introduction

During the last decade a great deal of interest has emerged to understand the dynamics of one-dimensional diatomic lattices with nonlinear ϕ^4-polarization potential at the anion site [1, 2]. The ϕ^4-polarizability model successfully describes the displacive type of phase transition in solids and its dynamics strongly resembles the structural phase transition in ferroelectrics and ferromagnetic materials. The phenomenology behind the structural phase transition (SPT) is that, the system goes from a stable high temperature phase to low temperature phase, at some critical temperature T_c at which, the frequency of a vibrational mode reduces to zero, a phenomenon well known as "mode softening" [3]. The motivation for studying the weakly coupled two-dimensional (2D) chains in the present paper is stronger than of academic interest.

Also the quasi one-dimensional materials e.g., polyacetylene toluene sulfonate [4] and low dimensional magnetic materials [5], which undergo mode softening and structural inhomogeneities near the transition have drawn considerable interest. Looking at the experimental successes in the identification and isolation of strongly nonlinear effects [4, 5], it is time to develop more theoretical understanding of the two-dimensional materials. Horovitz *et al* [6] for the first time investigated the solitary solutions in a two-dimensional lattice with inter-chain coupling. Static solitary excitations for the 2D lattice having strong anharmonic polarizability at the anion have been obtained by Behnke and Buttner [7]. This type of lattice serves as a model for certain ferroelectric materials. They found that the solitary finite energy excitations are stable against small perturbations. Apart from static solitary excitations, nonlinear periodic solutions are also obtained with harmonic first and second nearest neighbour interactions [7]. Kerr and Bishop [8] have investigated the central peak phenomena at

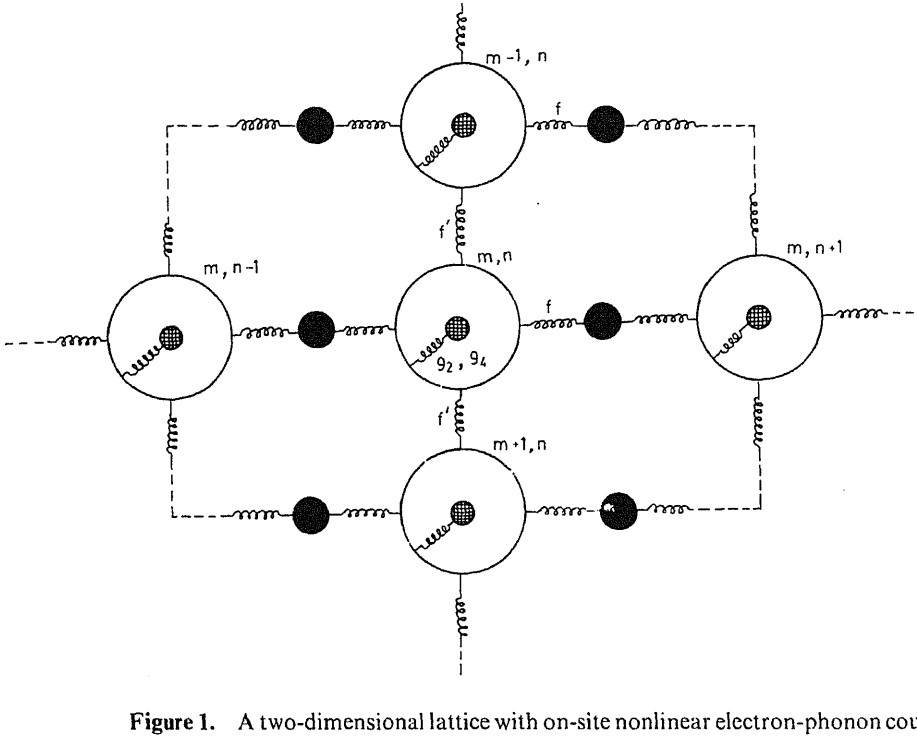

Figure 1. A two-dimensional lattice with on-site nonlinear electron-phonon cou ling at the polarizable ion.

SPT using computer simulation technique for a two-dimensional anharmonic latti They have used a model of displacive ϕ^4-monoatomic chain which is coupled weakly a 2D array with nonlinear interparticle coupling and predicted the incomplete mo softening at the transition temperature.

In the present paper we aim to investigate the dynamics of the nonlinear excitatio in two-dimensional displacive diatomic lattice with an on-site fourth order anharmo electron–phonon coupling at the polarizable ion site. Our analytical treatme differs from the previous workers [6–8], in the sense that we consider the nonlinear in the core-shell coordinate of the polarizable ion (i.e. on-site). We have also r considered the mean field approximation for obtaining the results as reported earl [6, 7]. We have calculated the frequency and energy of the 2D anharmonic oscillators a discussed the results in the light of the motion of domain walls in ferroelectric materi

2. Theory

The main features of the present 2D lattice with on-site nonlinear electron-phon interactions of fourth order at the polarizable ion site can be seen from figure 1. consists of m linear diatomic chains along x-axis of the lattice with a highly localiz fourth order core-shell coupling at the anion site and a rigid ion at the cation site. Th diatomic chains are coupled by a linear nearest neighbour shell-core force constant

weak anisotropy.

The displacement of the core of the anion at the nth position along the mth chain from its lattice site is denoted by $u_1^{m,n}$. Other displacements of the cation and shell of the anion are represented as $u_2^{m,n}$ and $v^{m,n}$ respectively (see figure 1). The polarization potential of the anions in 2D displacive array can be written as

$$\phi_P = \frac{1}{2}\sum_{m,n}\left[g_2(v^{m,n}-u_1^{m,n})^2 + \frac{1}{2}g_4(v^{m,n}-u_1^{m,n})^4\right] \tag{1}$$

where g_2 and g_4 are the on-site shell-core quartic (harmonic) and biquadratic (anharmonic) force constants. Here $g_2(<0)$ and g_4, f (both >0) are the parameters describing the double-well potential at (m,n)th site. This ϕ^4-potential has a minima at the displacements $w^{m,n} = \pm(-g_2/g_4)^{1/2}$ [1, 2]. The polarization potential for this displacement is obtained as $(-g_2^2/4g_4)$.

The Hamiltonian for the two-dimensional diatomic lattice can be written as

$$\begin{aligned} H = {} & \frac{1}{2}\sum_{m,n}[m_i(\dot{u}_i^{m,n})^2 + m_{ej}(\dot{v}_j^{m,n})^2] \\ & + \frac{1}{2}\sum_{m,n}[f(v^{m,n}-u_2^{m,n})^2 + f(v^{m,n}-u_2^{m,n-1})^2 \\ & + f'(v^{m+1,n}-v^{m,n})^2 + f'(v^{m-1,n}-v^{m,n})^2] + \phi_P \\ & i=1,2 \quad j=1. \end{aligned} \tag{2}$$

In order to obtain physical solutions for the 2D anisotropic lattice, the excitations are assumed to be propagating slowly in the x and y directions. Hence, it is appropriate to use the continuum limit, in which the relative shell-core displacement $w^{m,n}$ $(=v^{m,n}-u_1^{m,n})$ can be written as [7]

$$\begin{aligned} w^{m,n} &= w^m(x) = w(y,x) \\ w^{m\pm1,n} &= w^{m\pm1}(x) = w(y\pm a_2, x) \\ w^{m,n\pm1} &= w^{m\pm1}(x\pm a_1) = w(y, x\pm a_1) \end{aligned} \tag{3}$$

Similar solutions are also assumed for the displacements $u_1^{m,n}$ and $u_2^{m,n}$. Here a_1 and a_2 are the lattice spacings in x and y directions respectively. The relative displacements of the neighbouring two polarizable ions can be expanded for small lattice spacing a_1 and a_2 in Taylor's series as [7]

$$w(y, x\pm a_1) = w(y,x) \pm a_1 w_x(y,x) + \frac{a_1^2}{2}w_{xx}(y,x) \tag{4}$$

$$w(y\pm a_2, x) = w(y,x) \pm a_2 w_y(y,x) + \frac{a_2^2}{2}w_{yy}(y,x) \tag{5}$$

where $w_x(y,x) = (\mathrm{d}w(y,x))/\mathrm{d}x$ and $w_{xx}(y,x) = (\mathrm{d}^2 w(y,x))/\mathrm{d}x^2$ are the first and second derivatives with respect to x. Similar expressions can also be obtained for y direction.

Using the adiabatic approximation ($m_{ej} \sim 0$) and the method described in [2], we have obtained a coupled nonlinear equation of motion in terms of relative core-shell coordinate of the anion as

$$[2f + g_2 + 3g_4(w^{m,n})^2]\ddot{w}^{m,n} + [g_2 + 3g_4(w^{m+1,n})^2]\ddot{w}^{m+1,n} + [g_2 + 3g_4(w^{m-1,n})^2]\ddot{w}^{m-1,n} + 6g_4[(\dot{w}^{m+1,n})^2 w^{m+1,n} + (\dot{w}^{m-1,n})^2 w^{m-1,n} + (\dot{w}^{m,n})^2 w^{m,n}] + \frac{f}{\mu}[g_2 w^{m,n} + g_4(w^{m,n})^3] + \frac{f}{m_2}[g_2 w^{m+1,n} + g_4(w^{m+1,n})^3] + \frac{f}{m_2}[g_2 w^{m-1,n} + g_4(w^{m-1,n})^3] = 0 \quad (6)$$

with

$$\frac{1}{\mu} = \frac{1}{m_1} + \frac{1}{m_2}$$

and

$$f'(v^{m+1,n} + v^{m-1,n} - 2v^{m,n}) = g_2(w^{m+1,n} + w^{m-1,n}) + g_4[(w^{m+1,n})^3 + (w^{m-1,n})^3]. \quad (7)$$

In this paper we have considered the solutions for those nonlinear excitations which are uniformly varying along y direction i.e., $w_y(=\mathrm{d}w/\mathrm{d}y)$ is constant, and hence the second derivative w_{yy} $(=\mathrm{d}^2w/\mathrm{d}y^2)$ reduces to zero. In view of this fact, the relative core-shell displacement depends linearly along y direction (i.e., $w = cy$). By using (3), (4), (5) and the above assumptions, the second order differential equation of motion (eq (6)) reduces to

$$(\alpha + \beta' w^2 + \frac{2}{3}\beta' a_2^2 w^2)\ddot{w} + 2\beta' \dot{w}^2 w + \frac{f}{\mu}(g_2 w + g_4 w^3) + \frac{2}{9}\beta' g_4 a_2^3 w_y^3 + \frac{2}{3}\beta' \frac{g_2}{m_2} a_2^2 w_y^2 w = 0 \quad (8)$$

where

$$\alpha = 2f + g_2 \quad \text{and} \quad \beta' = 9g_4.$$

The method of solving such types of differential equation has been given in detail in [2]. The first integration of (8) using boundary conditions results into

$$\dot{w}^2 = \frac{f}{27\mu} \frac{F(w)}{\left(w^2 + \frac{\alpha}{\beta'} + \frac{2}{3}a_2^2 w_y^2\right)^2} \quad (9)$$

where

$$F(w) = w^6 + w^4\left[\frac{3}{2}\left(\frac{\alpha}{\beta'} + \frac{g_2}{g_4}\right) + a_2^2 w_y^2\left(1 + \frac{9\mu}{m_2}\right)\right] + \frac{6\mu}{m_2} a_2^3 w_y^3 w^3 + \left(3\frac{g_2}{g_4} + \frac{9\mu}{2m_2} a_2^2 w_y\right)\left(\frac{\alpha}{\beta'} + \frac{2}{3}a_2^2 w_y^2\right) w^2$$

$$+\frac{18\mu}{m_2}a_2^3 w_y^3\left(\frac{\alpha}{\beta'}+\frac{2}{3}a_2^2 w_y^2\right)-\lambda \tag{10}$$

C_0 and λ are the constants of integration and are defined in terms of initial root of the displacement w_0. The frequency is obtained from (9) by integrating it numerically and made temperature dependent by using the formula

$$T=\frac{\mu}{NK_B}\sum_n \dot{w}_{1,n}^2. \tag{11}$$

The energy of the system at the turning point ($w^{m,n}=\pm w_0$) can be obtained as

$$\begin{aligned}E=&\frac{1}{2f}[(u_2^{m,n}-v^{m,n})^2+(u_2^{m,n-1}-v^{m,n})^2]\\&+\frac{1}{2f'}[(v^{m+1,n}-v^{m,n})^2+(v^{m-1,n}-v^{m,n})^2]\\&+\frac{1}{2}g_2(w^{m,n})^2+\frac{1}{4}g_4(w^{m,n})^4.\end{aligned} \tag{12}$$

The energy expression is simplified by using (3), (4), (5) and (7). The energy is obtained as a sixth order polynomial in w_0, and gives an asymmetric double-well with respect to displacement with a central hump shifted towards the less equilibrium state, as discussed in the next section.

3. Results and discussion

The values of the parameters are chosen as $g_2/g_4=-0{\cdot}2$, $\alpha/\beta'=0{\cdot}2$, $\mu/m_2=0{\cdot}1$ and $a_2 w_y=0{\cdot}02$ in order to get a double-well structure of the potential, so that the scope of the present analysis includes simple ferroelectric systems. The force constants f, $g_2(<0)$ and f' are in the unit of 10^4 g/s^2 and $g_4(>0)$ is in the unit of 10^{22} g/(cm^2 s^2). The above values of the parameters are chosen, keeping in mind the conditions $|g_2|\ll g_4$ and $f<|g_2|$ to be obeyed for a double-well potential. The parameter μ/m_2 is a dimensionless quantity. The reduced mass μ is taken to be small as compared to the unpolarizable ion at (m,n)th site since the unpolarizable ion has been assumed to be heavier and has less displacement as compared to the polarizable ion. The parameter $a_2 w_y$ is in unit of lattice constant. The small value of the parameter $a_2 w_y$ is sufficient enough to visualize the dynamics of the anisotropic two-dimensional array.

The energy of the two-dimensional (2D) lattice as a function of initial displacement w_0 is shown in figure 2. An asymmetric double-well structure of the energy is obtained with a central hump shifted to one side and crosses the displacement axis at two different points. This fact decides the appearance of two characteristic temperatures, the critical temperature T_c and soft mode temperature T_s in an anisotropic two-dimensional lattice, similar to the one already shown by Bishop [8] who has carried out molecular dynamics of weakly coupled 2D lattice.

In figure 3 we have plotted the square of the soft mode frequency as a function of dimensionless temperature ($NK_B T/(g_2^2/g_4)$). From this figure, it is evident that the minimum in the soft mode frequency does not occur at the transition temperature T_c,

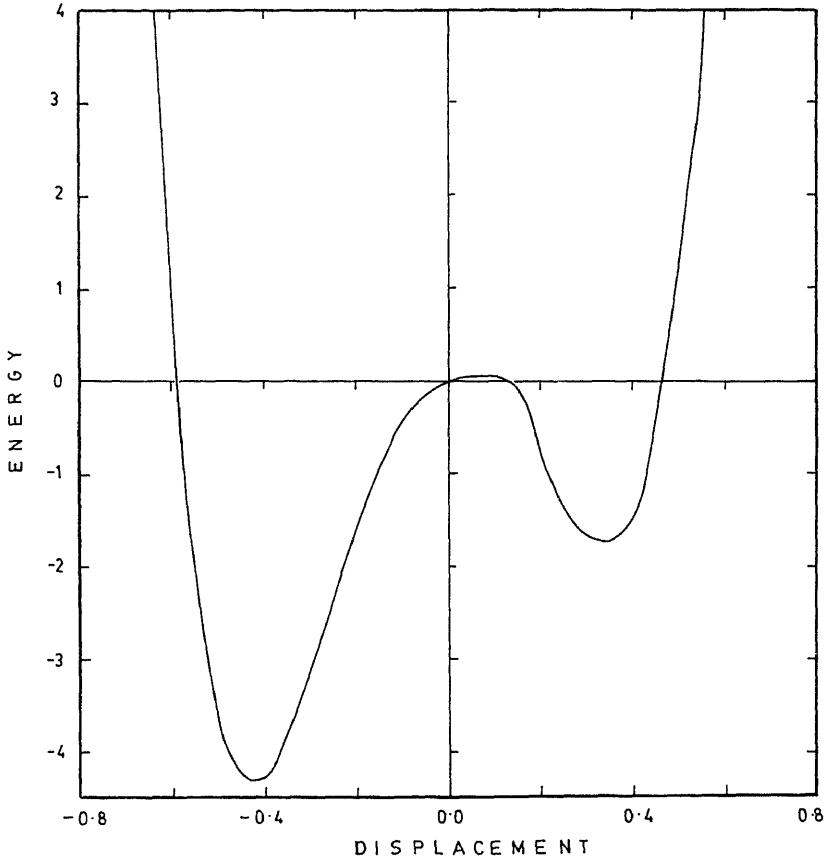

Figure 2. Energy of the two-dimensional lattice is plotted as a function of initial displacement w_0.

but at a temperature slightly greater than T_c, called soft mode temperature T_s. For temperatures much above T_s, the oscillations are completely across the asymmetric double-well resulting into an increase in frequency. In the temperature regime $T < T_s$, the particle can oscillate in either of the wells depending upon the equilibrium energy state (see figure 2). At very low temperature, the particle oscillates in either of the wells and remain localized leading to harmonic oscillation in this temperature regime ($0 < T < T_c$). Instability in the frequency at T_c is obtained because of the reduction of the domain wall separation between the para- and ferro-electric phases, which increase the electron-phonon interactions in the 2D system. Complete minimum does not occur at T_c as there remains some localized region in one of the equilibrium states. As a result, the soft mode frequency increases for a while with displacement and then reduces to its minimum at T_s. The reduction of frequency at T_s is very sharp which indicates that one will obtain a singularity in the physical properties at T_s (and not at T_c) for such a weakly coupled two-dimensional systems.

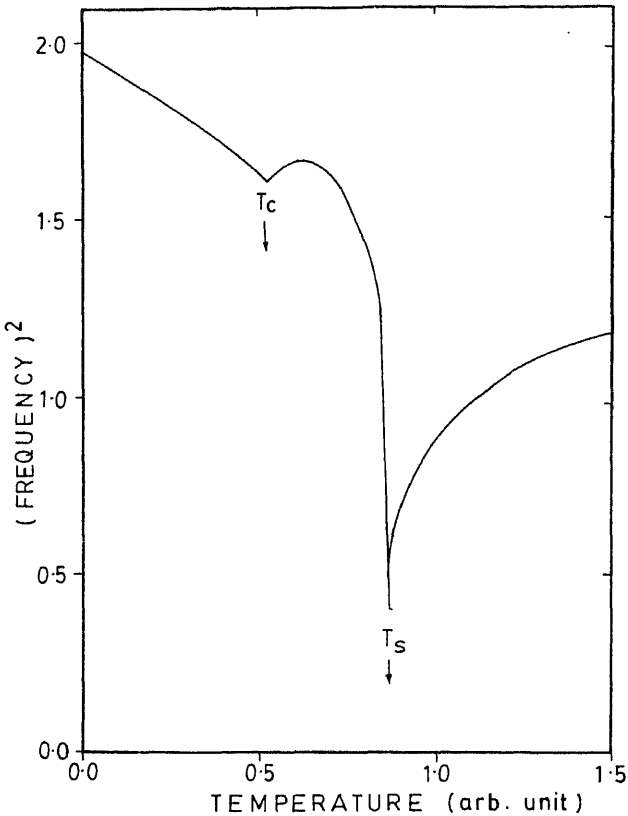

Figure 3. Square of the frequency of the 2D lattice versus dimensionless temperature ($NK_B T/(g_2^2/g_4)$).

Similar modelling of two-dimensional lattice with different types of ions at the alternate positions in the same column can be made, which leads to a somewhat simplified picture as the force constants between the shell of polarizable ion and core of cation along the chain and perpendicular to the chain will become nearly the same. This type of modelling of 2D lattice leads to only one transition temperature T_c, as the equation of motion is isotropic with respect to core-shell displacement of polarizable ion and hence no mode softening temperature T_s.

Our results have indicated that anisotropic 2D lattice (figure 1) shows interesting behaviour at the structural phase transition. These types of studies will help in the understanding of many recent experiments on the structural phase transition of hydrogen bonded macro-molecules [9] and quasi one-dimensional materials [10].

Acknowledgements

One of the authors (NDC) acknowledges the award of research associateship of CSIR. The computational facilities were provided by DST. SPS acknowledges the career award of UGC and financial assistance from UGC, CSIR and DST, New Delhi.

References

[1] S Aubry and R Pick, *Ferroelectrics* **8**, 471 (1974)
S Aubry, *J. Chem. Phys.* **62** 3217 (1975); **64**, 3392 (1976)
J A Krumhansl and J R Schrieffer, *Phys. Rev.* **B11**, 3535 (1975);
H Bilz, A Bussmann-Holder, G Benedek, H Buttner and D Strauch, *Ferroelectrics* **25**, 3 (1980)
[2] N D Chowdhury and S P Sanyal, *Pramana-J. Phys.* **37**, 115 (1991); **39**, 101 (1992)
[3] W C Kerr, *Phys. Rev.* **B19**, 5773 (1979)
T Schneider and E Stoll, *Phys. Rev.* **B13**, 1216 (1976)
W Cochran, *Adv. Phys.* **9**, 387 (1960)
[4] H Weiss and R Clarke, *Phys. Status Solidi* **A49**, 133 (1978)
M Dudley, J N Sherwood, D Bloor and D Ando, *J. Mater. Sci. Lett.* **1**, 479 (1982)
M Bertault, M Krauzman, M Le Postollec, R M Pick and M Scholt, *J. Phys.* (Paris) **43**, 7 (1982)
[5] M Steiner, K Kakurai and J K Kjems, *Z. Phys.* (Paris) **B53**, 117 (1983)
K Kakurai, R Pynn, B Dorner and M Steiner, *J. Phys.* **C17**, L123 (1984)
[6] B Horovitz, J A Krumhansl and E Domany, *Phys. Rev. Lett.* **38**, 778 (1977)
[7] G Behnke and H Buttner, *J. Phys.* **A14**, L113 (1981); **15**, 3869 (1982)
[8] W C Kerr and A R Bishop, *Phys. Rev.* **B34**, 6295 (1986)
[9] St. Pnevmatikos, *Phys. Rev. Lett.* **60**, 1534 (1988)
[10] A A Maradudin, A J Martin, H Bilz and R F Wallis, *J. Phys.* **C6**, 137 (1981)

journal of physics

November 1995
pp. 385–418

Microscopic theory of single particle and pair condensation of an attracting Bose gas as the basis for superfluidity and superconductivity

S DZHUMANOV[1]* and P K KHABIBULLAEV[2]
[1] International Center for Theoretical Physics, Trieste, Italy
* Permanent address: Institute of Nuclear Physics, Uzbek Academy of Sciences, Uzbekistan
[2] Department of Thermal Physics, Uzbek Academy of Sciences, Uzbekistan

MS received 11 February 1993; revised 5 August 1995

Abstract. A consistent and unified microscopic theory of superfluidity and superconductivity is developed on the basis of two-stage Fermi–Bose-liquid (FBL) (in particular case, one-stage Bose-liquid) scenarios. It is shown that these phase transition scenarios is accompanied, as a rule, by the formation of composite bosons (Cooper pair and bipolarons) with their subsequent single particle (SPC) and pair condensation (PC). A brief outline of the modified and generalized BCS-like pairing theory of fermions is presented. In an analogy to that, a detailed boson pairing theory is developed. The SPC and PC features of an attracting 3d- and 2d-BG as a function of the interboson coupling constant in the complete range $0 \leqslant T \leqslant T_B$ is studied in detail. It is argued that the coexistence of the order parameters of attracting fermions Δ_F and bosons Δ_B leads to the superfluidity (in ^{3}He) and superconductivity (in superconductors) by two FBL scenarios. One of these scenarios is realized in the so-called fermion superconductors (FSC) and the other in the boson superconductors (BSC) in which the gapless superconductivity is caused by the absence of the gap Δ_{SF} in the excitation spectrum of bosons and not by the presence of point or line nodes of the BCS-like gap Δ_F. The new adequate definitions for basic superconducting parameters of FSC and BSC are given. The theory proposed is consistent with the experimental data available.

Keywords. Microscopic theory of superfluidity and superconductivity; Fermi–Bose-liquid; composite bosons; single particle; pair condensation; fermion superconductors.

PACS No. 74·0

1. Introduction

At present, investigation of superfluidity and superconductivity takes much attention as this problem joins the broad class of phenomena observed in different condensed matters, such as, for example, ^{4}He, ^{3}He liquids, nuclears, low temperature (LTSC), heavy-fermion (HFSC), organic (OSC) and high-temperature (HTSC) superconductors and other systems [1–10]. For understanding these phenomena, numerous theoretical models [2–22] have been proposed. Nevertheless, the adequate theoretical scheme explaining the observations both in superfluid (SF) ^{4}He, ^{3}He and in superconducting (SC) materials has not been done as yet. For example, none of the existing theoretical models of superconductivity does not consider, complete scenarios of SC transition, starting from the Fermi-gas state, passing through the BCS-like ground state of Fermi-liquid and leading to the formation of unstable or stable presuperconducting (or precursor) state of Bose-gas (BG) and then to the true SC state of Bose-liquid. Usually,

main attention is given to one of the intermediate (but not SC) states, namely, to exp the electron pairing effect by means of phonon, exciton, plasmon, magnon, polaron other excitations exchange, as well as to use a conception of the Bose–Eins condensation (BEC) of ideal cooperons or bipolarons [6–9]. However, the pairin electrons is only necessary but not a sufficient condition for appearance of su conductivity (see also [8]). Therefore, many observed unusual properties of LT HFSC, OSC, HTSC and ^{3}He [3, 23–42] are difficult to be explained on the bas BCS-like pairing theory. Such inexplicable facts by BCS-like theory are: (i) non- density of states (DOS) is the inside of BCS-like gap and a peak of DOS is its ou [3, 23–28]; (ii) anomalous upward increasing of the lower critical magnetic field [29, 30], the critical current I_c [31], sound velocity [32] and the SC order param [33, 34] in HTSC and HFSC at $T \sim (0,6 \div 0,7)\, T_c$; (iii) the existence of the l pseudo-SC gap in HTSC not only below T_c, but also above T_c [24, 35–37]; (iv existence of the specific heat jumps, both below T_c and above T_c in HTSC and H [29, 38–40]; (v) gapless superconductivity [3–9]; (vi) sharp increasing of the cri current velocity and superfluid density and jump-like changes of other phy parameters at $T \sim (0,6 \div 0,7)\, T_c$ as well as the origin $A \rightarrow B$ transition and half-inte quantization of vorticity in ^{3}He [2, 41–44], etc. These experimental facts obse in HTSC cannot be explained on the basis of another highly attractive resona valence bond (RVB) models [6–9, 29, 45] and bipolaronic models [6–9, 32, 46]. RVB model based on the hypothetical spinon–holon phenomenology claims the normal state is not a Fermi-liquid and that the BCS-like approaches are applicable. These non-Fermi-liquid models are not as yet formulated in enough d to predict photoemission curve [6, 9, 26] as well as some above unusual properti HTSC. Indeed, recent experimental data [6, 9, 47] has confirmed the definite exist of a Fermi surface in HTSC. However, the RVB model represents indepen theoretical interest, from the standpoint gauge field theory and elaboration of l theory in low-dimensional systems is given much attention [6, 45, 48]. In the exis bipolaronic and bisolitonic models [6, 8, 32, 46] as well as in some variants of RVB mo (see [6, 8]), the SF state of bipolarons, bisolitons and holons is ident with the BEC state of an ideal BG which according to the Landau criterion is SF (see also [12]). So, the nature of the SF state of the electron liquid in all superconduc still remains unknown. While the existing theoretical models of a Bose-liquid superflu [12–19, 22], firstly, cannot explain a number of SF properties of ^{4}He and seco contradicts each other (see below), i.e. the theory of superfluidity is not suffici elaborated as yet. Further, separate consideration of related phenomena of superfluidity and superconductivity within the different approaches is quite unfou and does not allow to describe these phenomena from a unified position.

So, there are many reasons not to be locked on the existing BCS-like, bipolaro RVB-schemes and to consider the general case. In this respect, a novel two-s microscopic model of superfluidity and superconductivity proposed in [49–53] re sents one of the possible alternative. According to this model, the phase transition t state is realized by two possible Fermi–Bose-liquid (FBL) scenarios in contrast to above discussed one-stage Fermi-liquid and Bose-liquid or BG ones. In this, a r realistic model of superconductors, the composite bosons (e.g. Cooper pairs bipolarons) like non-composite ones (e.g. ^{4}He atoms and spinless holons [12–21])

have any values centre of mass impulse and undergo BEC of an ideal BG, single particle condensation (SPC) of a repulsive BG and SPC and pair condensation (PC) of an attracting BG. Existence of the SF or SC state of composite bosons, then, depends on two types of excitations, one of them characterizes the excitation of Fermi components of such bosons and another as a single whole. The first of these excitations may be considered within the BCS-like model of a Fermi-liquid and the second one on the basis of SPC and PC model of an attracting BG (or Bose-liquid) [52, 53]. Unlike the excitation spectrum of a Fermi-liquid with single BCS-like energy gap Δ_F in that of a Bose-liquid, there are two energy gaps Δ_B (order parameter bosons) and Δ_{SF} (energy gap in the excitation spectrum of an attractive BG). In the present paper, an attempt has been made to construct a consistent microscopic theory of a novel two-stage FBL scenarios of superfluidity and superconductivity as a combined theory of Fermi- and Bose-liquid. It will be shown that, the SPC and PC of an attracting composite bosons and not their formation by BCS-like pairing of fermions, plays a crucial role in the superfluidity and superconductivity in Fermi systems.

This paper is organized in the following manner. In § 2, we begin by short reviewing only the outline of the real-space pairing mechanisms of charge carriers leading to the formation of different bipolaronic states in various compounds (more detailed consideration will be reported elsewhere). In § 3, we consider the BCS-like pairing scenario of different interacting polarons in k-space leading to the formation coherent or ground state of Fermi-liquid. In § 4, at the beginning, we review the existing BG and Bose-liquid SF theories and then, we investigate in detail the ground state of a Bose-liquid on the basis of the concepts SPC and PC of an attracting two (2d)- and three (3d)-dimensional BG as the basis of their superfluidity. In particular, we determine the basic parameters characterizing these Bose-liquid. The calculation of the specific heat of 2d- and 3d-Bose-liquid on the basis of the proposed theory SPC and PC of an attracting BG is given in § 5. The discussion of the results and their validity and applicability degree for the adequate description of different experimental data in SF ^{4}He, ^{3}He and SC materials is the topic of § 6 and a summary is given in § 7. In the appendix, we give the basic calculations of the analytical expressions used in the text of the paper.

2. The real-space pairing mechanism of charge carriers

As is generally known, the ground state of electrons, holes and excitons in solids is their self-trapped (S) state that are discovered in many classes of substances, such as, alkali halides, rare-gas solids, oxides, organic molecular crystals and semiconductors [54, 55]. In [56] we have shown the existence (coexistence) possibility of four type (i.e. delocalized (D) and three S (continuum, atomic and molecular)) states of these quasiparticles in solids. According to [55–57] the holes and electrons in ionic compounds (to that are related HTSC also) are polarons not only in S- but also in D-states, i.e. they are dressed by deformation-polarization cloud or polaron-bag forming at static lattice deformations. In metals and some nonmetallic solids there is no optical phonons. There holes and electrons are polarons only in S-states and in D-states (to be precise we call it free (F)) and they are dressed by phonon (or dynamical polarization) cloud or bag. Further, the formation of the D- and S-states of bipolarons is quite possible in nonsuperconducting and superconducting materials at the interaction of

the identical and different polarons by polaron and phonon-bag exchanges. example, the existence of the bipolarons localized on the neighbour lattice site observed in Ti_4O_7, $(Ti_{1-x}V_x)_4O_7$, $Na_xV_2O_5$ and other materials (see [32]), anomalous characteristics of a number of compounds, such as Nb_3Sn, V_3Ga, $PbMO_6S_8$ and $BaBi_xPb_{1-x}O_3$ is considered also as the indication to the existe some above-named polarons and bipolarons [32]. So, in HTSC, the charge carrie most probably D- and different S-bipolarons (two of them, atomic and mole bipolarons, forming in oxygen sublattice). Indeed, the experimental data [58 indicate that two holes in HTSC are localized on ligands (i.e. on oxygen ions) and for example, atomic bipolarons of $O_N^{(2N-2)-}$ ($N = 4$ or 6) type or molecular bipol of charged dimer O_2^{2-} type [60]. The formation possibility of the D- (or large pol (bipolarons) in the context [46]) and continuum S-polarons (bipolarons) ma considered in the framework of the continuum model [56,57] and atomic molecular S-polarons (bipolarons), in the framework of a quasi-molecular model First of these approach is suitable for the quantitative determination of the bi energies of D- and S-bipolarons by the difference

$$|U_{Cn}| = |E_B - 2E_P|$$

where E_P and E_B is the polaron and bipolaron energy, respectively. Us $|U_{Cn}| \sim 0,01 \div 0,30$ and $\sim 0,1 \div 1$ eV for D- and S-bipolarons, respectively. real-space pairing scenario describes the attractive interaction of two sepa polarons. It corresponds to low polaron concentration or the narrow polaronic In this case 'bandlike' motion of polarons at the low temperature is unlikely and can form separated bipolarons which are immobile also (these real-space bipol may be considered as an ideal BG). So the real-space pairing scenario is not appli to study the collective (or coherent) properties of the interaction polarons bipolarons. However, with increasing of polarons concentration (or with decreas the distance between polarons) their deformation field begins to strongly overlap is accompanied by the decreasing of the lattice deformation degree, $|U_{Cn}|$ an broadening of the polaronic band. In such situations, due to the modulation of the parameters of polarons (caused by their collective effects) the real-space approxim [32,46] is not suitable for the description of their pairing. Then the BCS-like k- attractive pairing between polarons in extended spatial states is more suitable f study of the formation of both large D- and small S-bipolarons (e.g. Schafroth (see also [9,32]). In the present case, the D- and different S-bipolarons doe qualitatively differ from the Cooper pairs. These bipolarons and Cooper pairs (t dynamic bipolarons) can be regarded as interacting composite bosons (othe cussions are given in §6·4). So, in superconductors (including ^{3}He) existence (co ence) of the different types of unpaired and paired Fermi particle is quite possible multicomponent FBL [49–53]. For simplicity, we neglect interband fermion-l interaction in such mixed FBL assuming that the important mechanism responsi superconductivity is the intraband fermion-fermion and boson-boson attractive action. Indeed, fermion-composite boson interaction due to exclusion principle probably leads again to the formation of a Fermi and composite Bose particle. Th have dealings with two independent subsystems, where both fermionic N_F and bo N_B numbers are separately conserved.

The Hamiltonian of the multi-component Fermi-gas system with the pair interaction between particles has the form [43, 52]

$$H = \sum_{nk\sigma} [\varepsilon(k) - \mu_{Fn}] a^{\dagger}_{nk\sigma} a_{nk\sigma} + \frac{1}{2\Omega} \sum_{nk,lk'} V^{F}_{nl}(k, k') a^{\dagger}_{nk\uparrow} a^{\dagger}_{n-k\downarrow} a_{l-k'\downarrow} a_{lk'\uparrow} \quad (3.1)$$

where $\varepsilon(k) = \hbar^2 k^2 / 2m_{Fn}$, m_{Fn} and μ_{Fn} is the mass and chemical potential of the nth type of polarons, respectively, $a^{\dagger}_{nk\sigma}(a_{nk\sigma})$ is the creation (annihilation) operators of these polarons in state $|nk\sigma\rangle$, k and σ their wave vector and spin indices, respectively, $V^{F}_{nl}(k, k')$ is the pair interaction potential (which has both an attractive and a repulsive part) between nth and lth type polarons, Ω is the volume of the system, n, $l = \{1, 2, \ldots, \nu\}, \nu \leqslant 4$. The Hamiltonian (3.1) is diagonalized by the standard Bogolubov transformation of Fermi operators. Then in the excitation spectrum

$$\omega_{Fn}(k) = \sqrt{\tilde{\varepsilon}^2_{Fn}(k) + \Delta^2_{Fn}(k)}$$

there are n energy gaps determined from

$$\Delta_{Fn}(k) = -\frac{1}{\Omega} \sum_{k',l} V^{F}_{nl}(k, k') \frac{\Delta_{Fl}(k')}{E_{Fl}(k')} \operatorname{th} \frac{E_{Fl}(k')}{2T} \quad (3.2)$$

where $\tilde{\varepsilon}_{Fn}(k)$ is the energy of nth type polarons measured relative to μ_{Fn} and a repulsive Hartree–Fock potential (which can be incorporated and denoted as $\tilde{\mu}_{Fn}$) (see also [61]). For simplicity, we consider the case $V^{F}_{nn}(k, k') \neq 0$ and $V^{F}_{nl}(k, k') = 0$ $(n \neq l)$. Further, we use usual BCS-like approximation for $V^{F}_{nn}(k, k')$ [12, 62]

$$V^{F}_{nn}(k, k') = \begin{cases} V^{F}_{Rn} - V^{F}_{An} & \text{if } \varepsilon(k), \quad \varepsilon(k') < E_{An} = |U_{Cn}| + \hbar\omega_D \\ V^{F}_{Rn} & \text{if } E_{An} < \varepsilon(k), \quad \varepsilon(k') < E_{Rn} \\ 0 & \text{if } \varepsilon(k) \quad \text{or} \quad \varepsilon(k') > E_{Rn} \end{cases} \quad (3.3)$$

where E_{An} and E_{Rn} is the cutoff parameters for hybrid attractive V^{F}_{An} (which has both the phonon- and polaron-bag attracting part) and a repulsive V^{F}_{Rn} part of the potential $V^{F}_{nn}(k, k')$, respectively, in nth polaronic band, $E_{An} \ll E_{Rn}$. Then we determine the disappearance temperature of nth type bound polaron pairs T_{Fn} and the ratio $g_{Fn} = 2\Delta_{Fn}/T_{Fn}$ as

$$T_{Fn} \simeq 1,14(|U_{Cn}| + \hbar\omega_D) \exp(-1/\tilde{V}_{Fn} D_{Fn}) \quad (3.4)$$

and

$$g_{Fn} = 3,52 \quad (3.5)$$

when $\tilde{V}_{Fn} = V_{An} - V^{*}_{Rn}$, $V^{*}_{Rn} = V_{Rn}/[1 + D_{Fn} V_{Rn} \ln(E_{Rn}/E_{An})]$ and D_{Fn} is the effective interaction potential and density of states in the nth polaronic band, respectively, $\hbar\omega_D$ is the Debye energy. Here the combined polaron- and phonon-bag mediated processes are taken into account like it is done in case of the combined electronic (lochon)- and phonon-mediated ones in [63, 64]. While the expression of the cutoff energy obtained within the spin- and correlation-bag approaches [65, 66] are also similar to the results [63, 64]. So our and above-named approaches are modified variants of the basic BCS theory. In the absence of the static lattice deformation (that takes place in many LTSC) $|U_{Cn}| = 0$ and we have dealings with pure BCS picture. In general, pure BCS pairing is

[67]), the cutoff energy in (3.3) would be replaced by E_{Fn} (see [68]) or width o polaronic band [9]. In case $0 \leqslant V^*_{Rn} \leqslant V_{An}$ takes place, $0 \leqslant \tilde{V}_{Fn} D_{Fn} \leqslant 1$ and the a modified BCS-like pairing theory of polarons is quite applicable.

4. Ground state of Bose-liquid

Now we consider the SF state of a Bose-liquid that represents interaction of composite bosons (e.g. Cooper pairs and bipolarons) and non-composite ones su ^{4}He atoms (or hypothetical holons in RVB models). A brief survey of the ex theories of SF Bose systems is made. The BEC of an ideal BG cannot serve as a n for a study of SF properties of ^{4}He (see also [12]) and SC properties of electronic li in superconductors. Another most often discussed model of superfluidity is bas the SPC of a repulsive BG, theory of which was developed by Bogolubov However, the validity of such theory of superfluidity is not less controversial [14 As the theory of a repulsive BG superfluidity (or c-number of condensate theory based on the concept of SPC of bosons cannot explain a number of SF propert ^{4}He, such as, the observed half-integral values of circulation (see [15]), the obs ^{4}He specific heat departure from the phonon-like dependence (see [16]) an depletion of the zero-momentum state (some internal inconsistencies of the rep BG theory was discussed in [14, 69]). In this respect, a more consistent approach attractive BG model of superfluidity proposed in [14]. The theory of superfl developed within such model in [17, 18] is based only on the concept of PC attracting BG. The SPC and PC possibility of a 3d-BG in case of $T = 0$ and boson-boson attraction was studied in [19]. Recently, the attractive BG model ad to 2d-boson-like holon gas have been discussed in [20, 21], where however, only assumed of such exotic bosons and their SPC possibility at $T = 0$ remains unst At present, the situation is very much controversial and confusing for attractive systems, which increase the number of unsettled problems. So the basic propert a SF Bose-liquid is still not established as a function of the interboson intera coupling constant in the complete temperature range of $0 \leqslant T \leqslant T_B$ (where T_B attracting BG condensation temperature). For example, such unstated propert a SF Bose-liquid are: (i) specific features of the SPC and PC of an attracting B nature of the order parameter Δ_B and gap Δ_{SF}; (iii) depletion of the zero-mome state of condensed bosons (i.e. Bose–Einstein-like single particle condensate i context and not unphysical Bose–Einstein-like pair condensate considered by *et al* [14, 17, 22] and others [18]) and complete depletion of this state on temperature interval below $T_B (= T_\lambda$ for ^{4}He); (iv) specific heat pecularity in t state (e.g. at $T^*_B < T_B (= T_\lambda$ in ^{4}He and $= T_c$ in ^{3}He, HFSC and HTSC)), etc. F there are highly conflicting opinions about existence (absence) of a gap in the exci spectrum of a nonideal BG. For example, according to [14, 17, 18] there is no gap excitation spectrum of an attracting BG. On the contrary, some Bogolubo c-number condensate theory [18] (see also [16]) predicts the existence of a gap excitation spectrum of a repulsive BG in the zero-momentum state, while such

was not evidently observed. On the other hand, in several schemes of this theory, the excitation spectrum of a repulsive BG is gapless. The existence of a finite gap in the excitations spectrum of an attracting BG in its pair condensate state was predicted in [19] for $T = 0$. From the above-stated, it follows that the nature and structure of the SF state of a Bose-liquids is still far from being elucidated and the existing theoretical schemes is insufficient for understanding all SF properties of ^{4}He (to say nothing of ^{3}He for the description of that in the BCS model is not quite adequate). So, up to now, there is no consistent and adequate microscopic theory of SF Bose-liquid describing the available experimental data in ^{4}He (including ^{3}He and superconductors) from a unified position.

4.1 *The Hamiltonian model*

The Hamiltonian of the multi-component BG system with the pair interaction (which has both an attractive and repulsive part) between particles has the form (3.1) only by the absence of spin indices. The linearized part of this Hamiltonian (i.e. Hamiltonian model) for one component of BG may be written in the form (see also [13])

$$H = \sum_k \left[\tilde{\varepsilon}_B(k) c_k^\dagger c_k + \frac{1}{2}\Delta_B(k)(c_{-k}^\dagger c_k^\dagger + c_k c_{-k}) \right] \tag{4.1}$$

where $\tilde{\varepsilon}(k) = \varepsilon(k) - \mu_B + V_B(0)\rho_B + \chi_B(k)$, $\varepsilon(k) = \hbar^2 k^2/2m_B$ (here and further, for convenience, we omit the index in $\varepsilon(k)$), $\Delta_B(k) = (1/\Omega)\Sigma_{k'} V_B(k-k')\langle c_{-k'} c_{k'}\rangle$, $\chi_B(k) = (1/\Omega)\Sigma_{k'} V_B(k-k') n_B(k')$, $n_B(k) = \langle a_k^\dagger a_k\rangle$, $\rho_B = (1/\Omega)\Sigma_k n_B(k)$, m_B – the mass of Bose particles, μ_B – the chemical potential of BG, $c_k^\dagger(c_k)$ – the creation (annihilation) operators of bosons with the wave vector k, $V_B(k-k')$ – the interboson interaction potential. The Hamiltonian (4.1) is diagonalized by the Bogolubov transformations of Bose operators and the excitation spectrum of bosons has the form

$$E_B(k) = \sqrt{\tilde{\varepsilon}_B^2(k) - \Delta_B^2(k)}, \tag{4.2}$$

where the values of $\Delta_B(k)$, μ_B and $\chi_B(k)$ are determined from simultaneous equations

$$\begin{aligned}
\Delta_B(k) &= -\frac{1}{\Omega}\sum_{k'} V_B(k-k')\frac{\Delta_B(k')}{2E_B(k')}\operatorname{cth}\frac{E_B(k')}{2T} \\
N_B &= \sum_k n_B(k) = \sum_{k'}\left[\frac{\tilde{\varepsilon}_B(k)}{2E_B(k)}\operatorname{cth}\frac{E_B(k)}{2T} - \frac{1}{2}\right] \\
\chi_B(k) &= \frac{1}{\Omega}\sum_{k'} V_B(k-k')\left[\frac{\tilde{\varepsilon}_B(k')}{2E_B(k')}\operatorname{cth}\frac{E_B(k')}{2T} - \frac{1}{2}\right]
\end{aligned} \tag{4.3}$$

by means of their self-consistent solution.

At $E_B(0) = 0$ or $\mu_\beta + V_B(0)\rho_B + \chi_B(0) = |\tilde{\mu}_B| = |\Delta_B(0)|$ the terms of the sum (4.3) with $k, k' = 0$ should be considered separately according to the procedure proposed in [14]. Now, in order to find the solution of (4.3) the interboson interaction potential may be approximated in the simple separable form as is done in the theory of

superconductivity [12]

$$V_B(k-k') = \begin{cases} V_{BR} - V_{BA} & \text{if } 0 \leqslant \varepsilon(k), \quad \varepsilon(k') < \xi_{BA} \\ V_{BR} & \text{if } \xi_{BA} \leqslant \varepsilon(k) \quad \text{or} \quad \varepsilon(k') < \xi_{BR} \\ 0 & \text{if } \varepsilon(k), \quad \varepsilon(k') > \xi_{BR} \end{cases}$$

where ξ_{BA} and ξ_{BR} are the cutoff energies for attractive and repulsive parts of t $(k-k')$, respectively. This approximation allows us to carry out the calcul thoroughly and so it gives us a new insight to the problem of condensation (i.e. o possible properties of a SF Bose-liquid).

Further we assume $\varepsilon_{BA} \gg |\tilde{\mu}_B| \sim \Delta_B \sim T_B$, where T_B is the temperature of the parameter Δ_B disappearance. Then the main contribution to the $\Delta_B(k)$, N_B, $\chi_B(k)$ c from small values of $k < k_A$ whereas the large values of $k > k_A$ gives small correc that may be neglected. In the case of only two Bose particles interaction, the bi energy E_b of these particles is determined from the equation

$$\tilde{V}_B \sum_k \frac{1}{2\varepsilon(k) - E_b} = 1$$

where $\tilde{V}_B = V_{BA} - V_{BR}[1 + V_{BR} I_R]^{-1}$.

At $\xi_{BA} \gg E_b$ from (4.5) for 2d- and 3d-BG, correspondingly, it fo $I_R = \frac{1}{2} D_B \ln(\xi_{BR}/\xi_{BA})$, $D_B = m_B/2\pi\hbar^2$ and $I_R = D_B[\sqrt{\xi_{BR}} - \sqrt{\xi_{BA}}]$, $D_B = \sqrt{2} m_B^{3/2}/2$

4.2 *Three-dimensional Bose-liquid*

At first we consider the case $T = 0$. Going in (4.3) from summation to integrati ε and by making elementary transformation the following equations may be obt for determination of critical values of the ρ_B and $|\tilde{\mu}_B|$ at which SPC of bosons b with the vanishing of the gap $\Delta_{SF} = \sqrt{\tilde{\mu}_B^2 - \Delta_B^2}$ in $E_B(k)$ (Appendix 1)

$$\rho_B = \frac{D_B \xi_{BA}^{3/2}}{48} \left(\frac{\gamma_B^2 - 1}{\gamma_B} \right)^3$$

$$|\tilde{\mu}_B| = \frac{\xi_{BA}}{2} \left(\frac{\gamma_B^2 - 1}{2\gamma_B} \right)^2,$$

where $\gamma_B = \tilde{V}_B D_B \sqrt{\xi_{BA}}$ is a coupling constant of the interboson interaction as ξ_{BA} acterizes the thickness of the condensation layer including almost all Bose parti

From (4.5) the following equation is obtained for determination of E_b

$$y \operatorname{arctg}(1/y) = \frac{\gamma_B - 1}{\gamma_B}$$

where $y = \sqrt{|E_b|/2\xi_{BA}}$.

As it is obvious from (4.7), formation of the bound state of two isolated boson p possible only at $\gamma_B > \gamma_B^* = 1$ that coincides with the value of γ_B^* determined from (4. dilute BG ($\rho_B \to 0$, $\Delta_B = 0$). So in the case of dilute BG, $E_b = 2|\tilde{\mu}_B|$. However, othe $E_b = 2\Delta_{SF} < 2|\tilde{\mu}_B|$, i.e. the binding energy of the boson pairs in their intera collective is decreased. Hence at $\gamma_B = \gamma_B^* > 1$ the phase transition SPC⇔PC occ

a nonideal BG. The value of $|\tilde{\mu}_B|$ at $\gamma_B = \gamma_B^*$ is equal to [70] (Appendix 1).

$$|\tilde{\mu}_B| = |\Delta_B| = 2{,}88\, T_{BEC} \tag{4.9}$$

where T_{BEC} is the BEC temperature. For $\gamma_B < \gamma_B^*$ the fraction of condensed bosons in the zero-momentum state $n_{B0} = \rho_{B0}/\rho_B$ is determined as a function of γ_B from the simultaneous equations system [70] (Appendix 1):

$$3(\rho_B - \rho_{B0}) = \sqrt{2}\,|\tilde{\mu}_B|^{3/2} D_B \tag{4.10}$$

$$\rho_{B0} = \frac{D_B |\tilde{\mu}_B| \sqrt{\xi_{BA}}}{\gamma_B}\left[1 - \gamma_B\left(\sqrt{1 + 2|\tilde{\mu}_B|/\xi_{BA}} - \sqrt{2|\tilde{\mu}_B|/\xi_{BA}}\right)\right] \tag{4.11}$$

where $\rho_{B0} = N_{B0}/\Omega$, N_{B0} is the number of Bose particles with $k = 0$.

The $n_{B0}(\gamma_B)$ dependence is shown in figure 1. Now we consider the case $T \neq 0$. The numerical solution of (4.3) at $T < T_B$ taking into account (4.4) shows that the gap Δ_{SF} in $E_B(k)$ vanishes at $T = T_B^* \ll T_B$ [70]. In limit cases such solution may also be obtained analytically. So, at $\gamma_B < \gamma_B^*$ and $T \leqslant T_B^* \ll T_B$ assuming $|\tilde{\mu}_B| = \Delta_B$ from (4.3) it follows [70, 71] (Appendix 2):

$$3(\rho_B - \rho_{B0}) \simeq D_B\left[\sqrt{2}\,|\tilde{\mu}_B|^{3/2} + \frac{(\pi T)^2}{2\sqrt{2|\tilde{\mu}_B|}}\right] \tag{4.12}$$

$$-\rho_{B0} \simeq \left[\sqrt{\xi_{BA} + 2|\tilde{\mu}_B|} - \sqrt{2|\tilde{\mu}_B|} + \frac{(\pi T)^2}{6\sqrt{2}\,|\tilde{\mu}_B|^{3/2}} - \frac{\sqrt{\xi_{BA}}}{\gamma_B}\right]. \tag{4.13}$$

From these equations the values of $T_B^*(\gamma_B)$ and $n_{B0}(T)$ may be found. At $T < T_B^* \ll T_B$ one obtains [70] $n_{B0}(T)$ as

$$n_{B0}(T) = n_{B0}(0)[1 - gT^2] \tag{4.14}$$

where $g = m_B/12\rho_{B0}\hbar^3 v_C$, $v_C = \sqrt{|\tilde{\mu}_B|/m_B}$ is the sound velocity. Analogous relation for $n_{B0}(T)$ was also obtained in the framework of the phenomenological approach (see

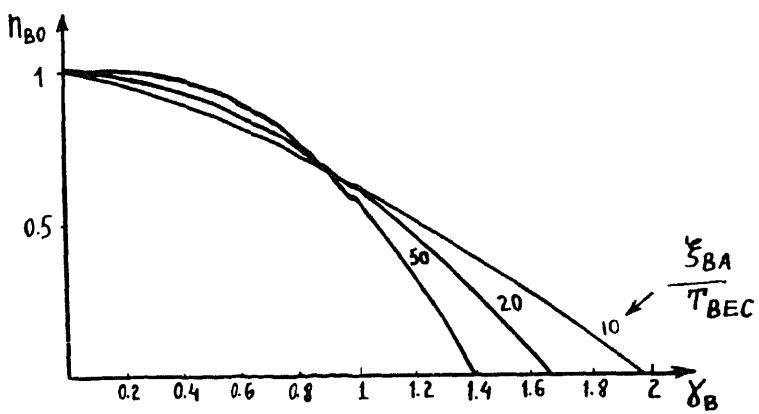

Figure 1. The dependence of n_{B0} on γ_B for 3d-BG.

[72]), where, however, instead of $\rho_{B0}(0)$ figures ρ_B that correspond to the BEC of an ideal BG. Near T_B^* approximately $n_{B0}(T) \sim (T_B^* - T)$ take place. In the case of $T \to T_B$, $\Delta_B \ll T_B$, $|\tilde{\mu}_B| \ll T_B$ solution of (4.3) may be found analytically and we have (Appendix II):

$$2{,}612\sqrt{\pi}T_{BEC}^{3/2} \simeq \sqrt{\pi}T^{3/2}\left[2{,}612 - 2\sqrt{\pi|\tilde{\mu}_B|/T}\left(1 - \frac{\Delta_B^2}{8|\tilde{\mu}_B|^2}\right)\right] \tag{4.15}$$

$$\frac{1}{\gamma_B} \simeq \frac{\pi T}{2\sqrt{|\tilde{\mu}_B|\xi_{BA}}}\left(1 + \frac{\Delta_B^2}{8|\mu_B|^2}\right) \tag{4.16}$$

from which at $T = T_B$ and $\Delta_B = 0$ it follows that for $\gamma_B < 1$ or $\gamma_B \ll \gamma_B^*$ (just in this case most probably the conditions $|\tilde{\mu}_B| \ll T_B$ is well satisfied)

$$T_B \simeq \frac{T_{BEC}}{[1 - 2{,}13\gamma_B\sqrt{T_B/\xi_{BA}}]^{2/3}} \tag{4.17}$$

and for a small $\gamma_B \ll 1$

$$T_B \simeq T_{BEC}[1 + c\gamma_B\sqrt{T_{BEC}/\xi_{BA}}], \tag{4.18}$$

where $c = \pi^{3/2}/3{,}912$.

From (4.15) and (4.16) it also follows that the $\Delta_B(T)$ and $\tilde{\mu}_B(T)$ near T_B is determined as [70] (Appendix 2).

$$|\tilde{\mu}_B(T)| \simeq |\tilde{\mu}_B(T_B)|\left[1 + a\left(\frac{T_B - T}{T_B}\right)^{0,5}\right] \tag{4.19}$$

$$\Delta_B \simeq 2|\tilde{\mu}_B(T_B)|\sqrt{a}\left(\frac{T_B - T}{T_B}\right)^{0,25} \tag{4.20}$$

where $a = 2(c\gamma_B)^{-0,5}(\xi_{BA}/T_{BEC})^{0,25}$.

In the case $T \to T_B^*$ and $|\tilde{\mu}_B(T_B^*| \ll T_B^* \leqslant T_B$ a solution of (4.3) is determined analogous to the case $T \to T_B$. Then the temperature dependence of $\tilde{\mu}_B$ (or Δ_B) and n_{B0} near $T = T_B^* < T_B$ accordingly has the form [70] (Appendix 2)

$$|\tilde{\mu}_B(T)| \simeq |\tilde{\mu}_B(T_B^*)|\left[1 + b\left(\frac{T_B^* - T}{T_B^*}\right)^{0,5}\right] \tag{4.21}$$

and

$$n_{B0}(T) \simeq \frac{b\gamma_B D_B(\pi T_B^*)^2}{2\rho_B\sqrt{2\xi_{BA}}}\left(\frac{T_B^* - T}{T_B^*}\right)^{0,5} \tag{4.22}$$

where $b = (c\gamma_B)^{-0,5}(\xi_{BA}/T_B^*)^{0,25}$.

From (4.16) (at $\Delta_B = 0$) and the l.h.s. of (A2.14) in Appendix, it follows that in case $1 \leqslant (|\tilde{\mu}_B(T_B^*)|/|\tilde{\mu}_B(T_B)|) \leqslant 2$, it must be $T/\sqrt{2} \leqslant T_B^* \leqslant T_B$, whereas from the l.h.s. of (A2.13) (that roughly is equal to 2,612 $T_{BEC}^{3/2}$ at $T = T_B^*$) in Appendix $-$ $T_B^* > T_{BEC}$.

In the case $T < T_B^* \ll T_B$ that corresponds to the case $\gamma_B < \gamma_B^*$, $|\tilde{\mu}_B| = \Delta_B \simeq$ const takes place. The phase diagram of states of the attracting BG is indicated in figure 2 and the temperature dependence of Δ_B, $\tilde{\mu}_B$ and n_{B0} are shown in figures 3 and 4, respectively.

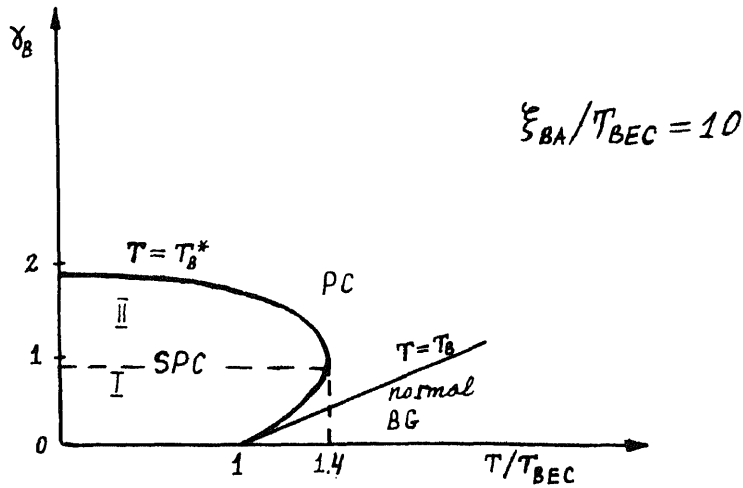

Figure 2. The phase states of an attracting 3d-BG for $\xi_{BA}/T_{BEC} = 10$ (in case $\gamma_B \sim 1$ is assumed $|\tilde{\mu}_B(T_B^*)| \sim |\tilde{\mu}_B(T_B)|$).

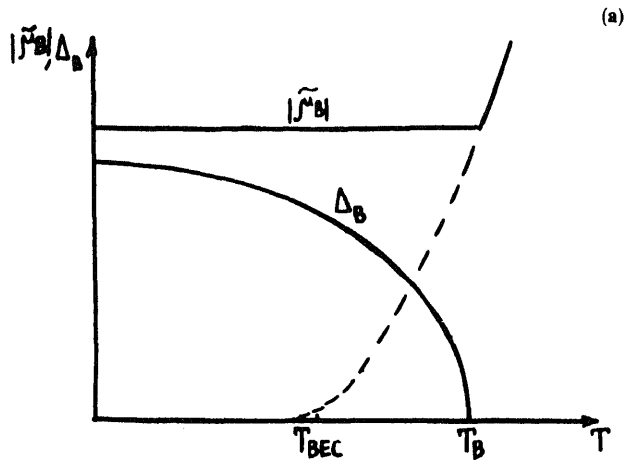

Figure 3. a.

4.3 *Two-dimensional Bose-liquid*

The case of $T = 0$. In (4.3) going from summation to integration on ε, it is easy to find the value of $\gamma_B = D_B \tilde{V}_B$ at which the gap Δ_{SF} is vanishing and this value of γ_B is determined from [20]

$$\gamma_B^* = \frac{1}{\mathrm{Arsh}\sqrt{[\xi_{BA}/4T_0]}} \tag{4.23}$$

that corresponds to the value of $|\tilde{\mu}_B| = 2T_0$, where $T_0 = 2\pi\hbar^2\rho_B/m_B$.

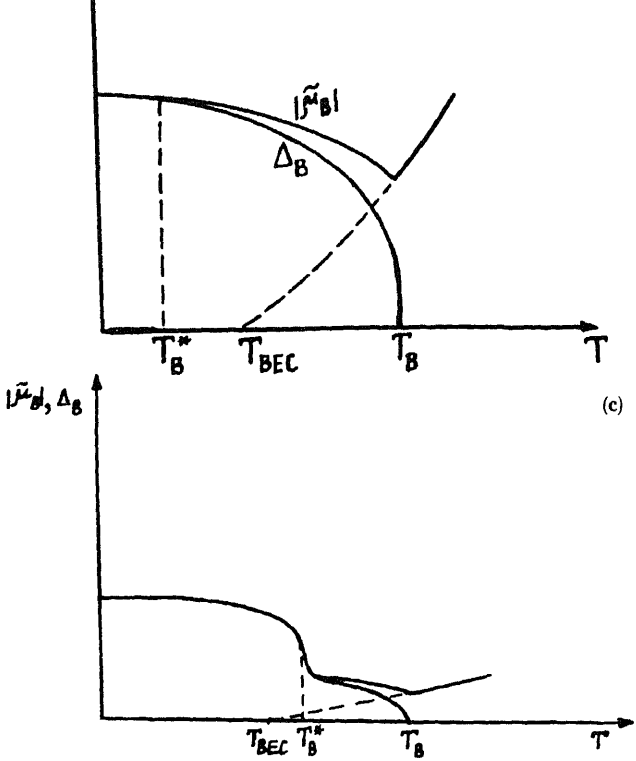

Figure 3. Schematic dependence of the $\tilde{\mu}_B$ and Δ_B vs. temperature a) at $\gamma_B > \gamma_B^*$; b) at $\gamma_B < \gamma_B^*$ and c) $\gamma_B \ll \gamma_B^*$.

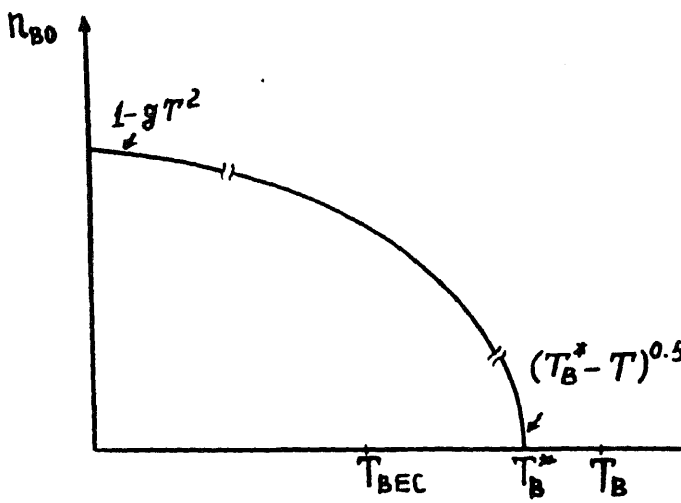

Figure 4. Schematic dependence of the n_{B0} vs. temperature T for 3

Unlike the 3d-BG, in 2d-BG the binding energy of isolated boson pairs is determined from (4.5) analogous to the binding energy of isolated fermion pairs in the BCS theory and bound state is formed even under weak interaction with $\gamma_B > 0$. In the case of dilute 2d-BG ($\Delta_B = 0$) analogous as in the case of 3d-BG, $E_B = 2|\tilde{\mu}_B|$ or $E_B = 2\Delta_{SF} < 2|\tilde{\mu}_B|$ takes place. The value of ρ_{B0} is determined from the simultaneous equations [70] (Appendix 1)

$$2(\rho_B - \rho_{B0}) \simeq D_B|\tilde{\mu}_B| \tag{4.24}$$

$$\rho_{B0} = \frac{D_B|\tilde{\mu}_B|}{\gamma_B}\left[1 - \gamma_B \ln\left(\frac{\sqrt{\xi_{BA}^2 + 2|\tilde{\mu}_B|\xi_{BA}} + 2(\xi_{BA} + |\tilde{\mu}_B|)}{2|\tilde{\mu}_B|}\right)\right] \tag{4.25}$$

The dependence of $\rho_B(\gamma_B^*)$, Δ_B on $|\tilde{\mu}_B|$ (at different values of γ_B and ρ_B) and $n_{B0}(\gamma_B)$ are presented in figures 5, 6, and 7, respectively.

The case of $T \neq 0$. In this case the gap

$$\Delta_{SF} = -2T\ln[\sqrt{4 + \eta^2} - \eta)/2] \tag{4.26}$$

always exists in $E_B(k)$ [20], where $\eta = \exp[(|\tilde{\mu}_B| - 2T_0)/2T]$. The temperature dependence of Δ_B at low temperatures has the form [49] (Appendix 2)

$$\Delta_B(T) \simeq -\frac{Z}{2}T + \sqrt{\Delta_B^2(0) + \frac{Z-4}{4Z}(ZT)^2} \tag{4.27}$$

where $Z = \exp(4/\gamma_B)/[1 + (\exp(2/\gamma_B)/2)^2]$, $\Delta_B(0) \simeq (\xi_{BA} + |\tilde{\mu}_B|)/\sqrt{1 + (\exp(2/\gamma_B)/2)^2}$.

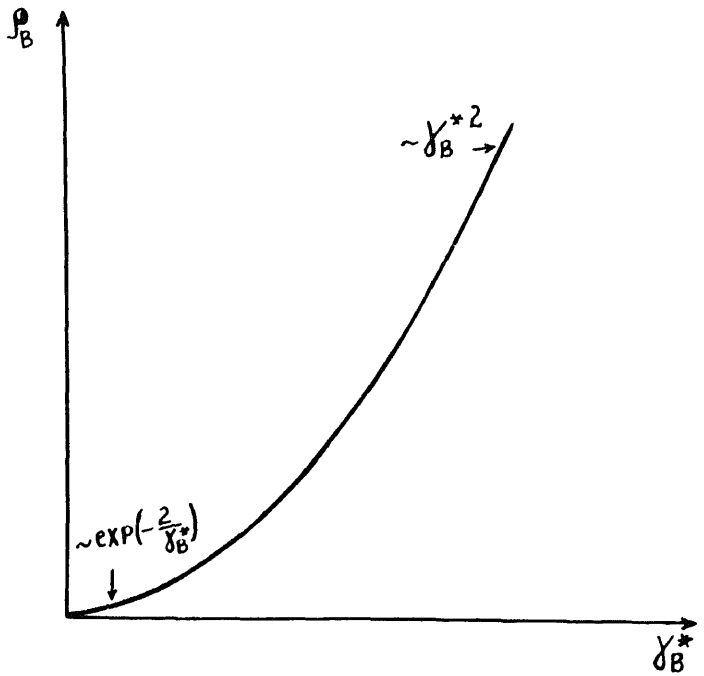

Figure 5 Schematic dependence of the ρ_B vs. γ^* for 2d-BG

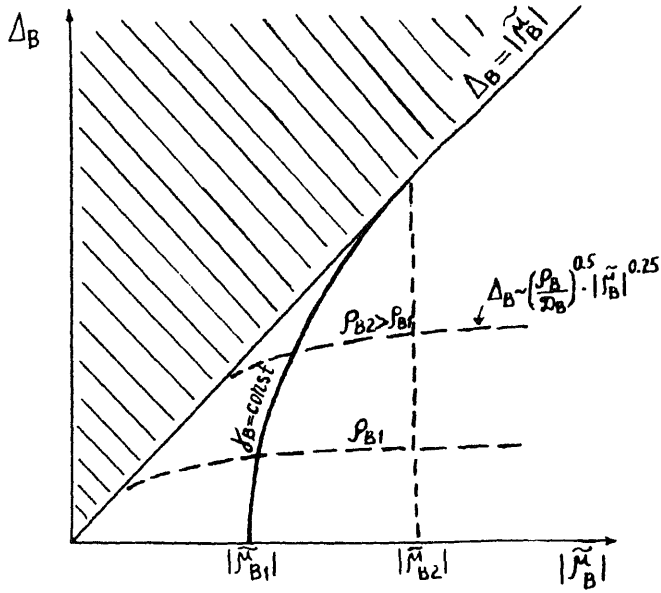

Figure 6. Schematic dependence of the Δ_B vs. $\tilde{\mu}_B$ for 2d-BG.

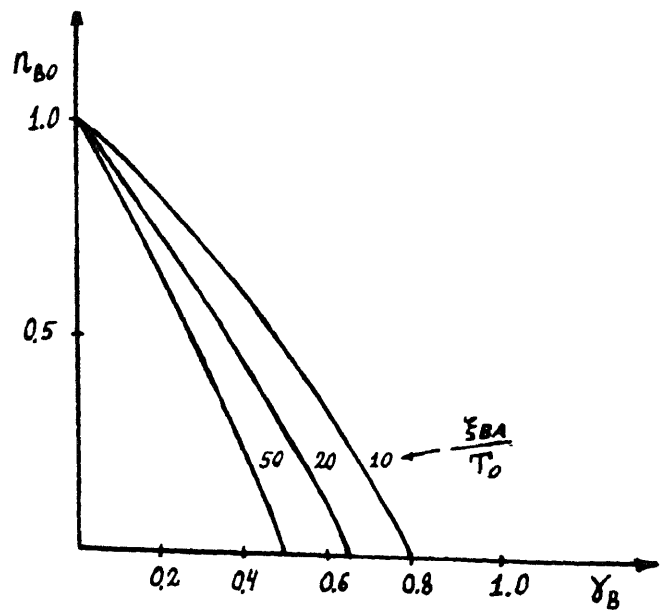

Figure 7. The dependence of n_{B0} on γ_B for 2d-BG.

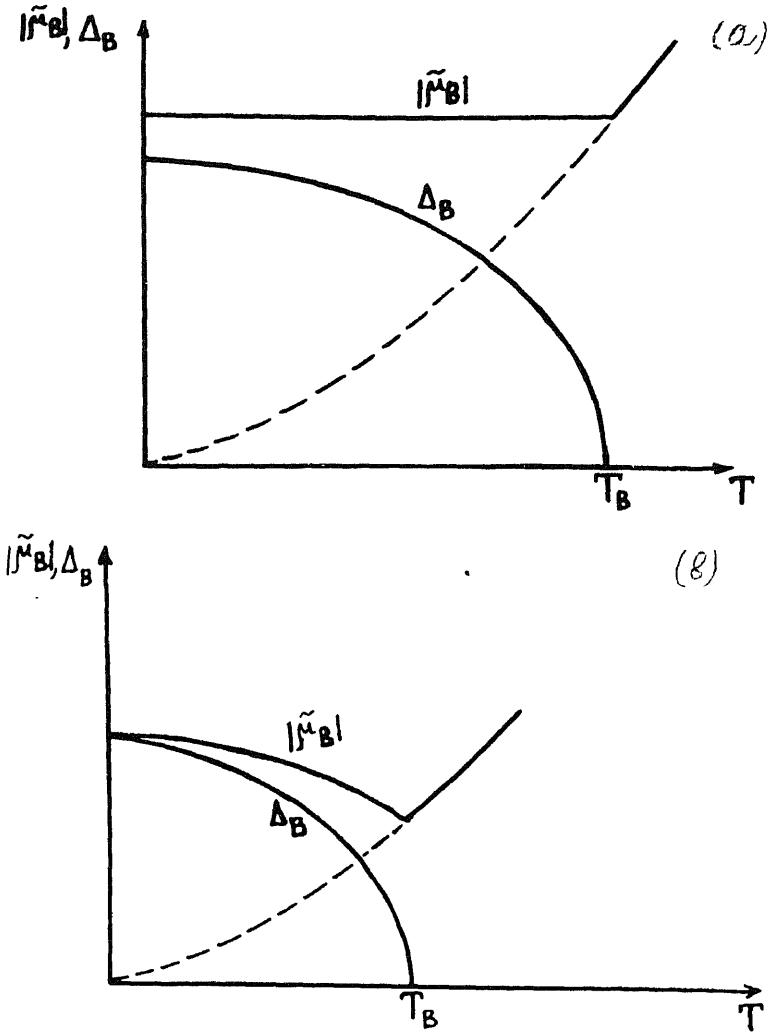

Figure 8. Schematic dependence of the $\tilde{\mu}_B$ and Δ_B vs. temperature T for 2d-BG: a) at $\gamma_B > \gamma_B^*$ and b) at $\gamma_B < \gamma_B^*$.

As it is clear from (4.27), Δ_B decreases with increasing of temperature and at $T \to T_B$, temperature-dependence of Δ_B and $\tilde{\mu}_B$ have forms [49] (Appendix 2)

$$\Delta_B(T) = (2+\gamma_B)\, T_B \left[\left(\frac{T}{T_B} \right)^{2-q} - \frac{T}{T_B} \right] \tag{4.28}$$

and

$$|\tilde{\mu}_B(T)| = \sqrt{\Delta_B^2(T) + (2T_B)^2 \left(\frac{\gamma_B}{2+\gamma_B} \right)^2 \left(\frac{T}{T_B} \right)^{2q}} \tag{4.29}$$

by means of the self-consistent solution of (4.26), (4.28) and (4.29). The tempera dependence of Δ_B and $|\tilde{\mu}_B|$ are shown in figure 8.

5. Specific heat of the Bose-liquid

The specific heat of the Bose-liquid is determined from [73]

$$c_v(T) = \frac{2}{T^2} \sum_k n_B(k)[1 + n_B(k)] \left\{ E_B^2(k) - T\left[\varepsilon \frac{\partial |\tilde{\mu}_B|}{\partial T} + \frac{1}{2} \frac{\partial}{\partial T} \Delta_{SF}^2 \right] \right\}.$$

At low temperature for 3d-Bose-liquid

$$c_v(T) \simeq \frac{\Omega D_B}{2T^2} \int_0^\infty \sqrt{\varepsilon} \frac{d\varepsilon}{\mathrm{sh}^2[E_B(\varepsilon)/2T]} E_B^2(\varepsilon).$$

In (5.2) at $\gamma_B > \gamma_B^*$, $|\tilde{\mu}_B| \gg T$, $\Delta_B \gg T$ and $\Delta_{SF} > 2T$ the $\mathrm{sh}[E_B(\varepsilon)/2T]$ may be rep by $\frac{1}{2}\exp[E_B(\varepsilon)/2T]$ and $E_B(\varepsilon)$ by $\sqrt{2|\tilde{\mu}_B|\varepsilon + \Delta_{SF}^2}$.

Then taking into account that an essential contribution to the integral comes a small ε and using in the exponent expansion $\sqrt{2|\tilde{\mu}_B|\varepsilon + \Delta_{SF}^2} \approx \Delta_{SF} + |\tilde{\mu}_B|\varepsilon/\Delta_{SF}$, w

$$c_v(T) \simeq \frac{3\Omega D_B \Delta_B^{5/2}}{|\tilde{\mu}_B|^{3/2}} \sqrt{\pi T} \left[1 + \frac{4}{3} \sqrt{2/\pi} \frac{\Delta_{SF}}{T} \right] \exp\left(-\frac{\Delta_{SF}}{T} \right).$$

However, at $\gamma_B < \gamma_B^*$, $T \leqslant T_B^*$ and at a small k the excitation spectrum of bos phonon-like $E_B(k) \sim \sqrt{|\tilde{\mu}_B|/m_B}\hbar k$ and $c_v(T) \sim T^3$. In the case of $\Delta_B, |\tilde{\mu}_B| \ll T_B^*$ T_B^* according to (4.21) $c_v(T) \sim \mathrm{const}/(T_B^* - T)^{0.5}$. Whereas according to (4.19

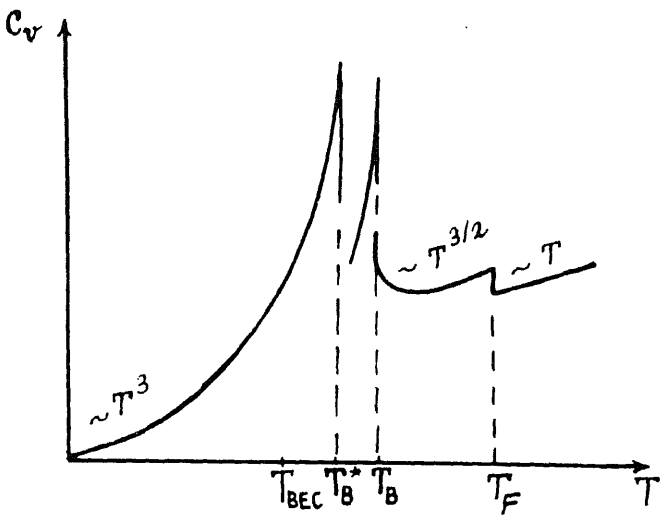

Figure 9. Schematic dependence of the specific heat of an attracting 3d-B temperature at $\gamma_B \ll \gamma_B^*$.

(4.20) near T_B the law $c_v(T) \sim \text{const}/(T_B - T)^{0.5}$ takes place. The $c_v(T)$ dependence at $\gamma_B \ll \gamma_B^*$ and $\Delta_B, |\tilde{\mu}_B| \ll T_B^*$ has the form shown in figure 9, where for $T > T_B$, $c_v(T) \sim T^{3/2}$ [36]. For 2d-Bose-liquid, the quantity of $c_v(T)$ at low temperature in the case of $\Delta_{SF} > 2T$ can be estimated analogous to that evaluated from the integral (5.2). Then

$$c_v(T) \simeq \frac{4\Omega D_B \Delta_{SF}}{|\tilde{\mu}_B|}\left[1 + \frac{\Delta_{SF}}{2T}\right]\exp\left(-\frac{\Delta_{SF}}{T}\right) \tag{5.4}$$

while for $\Delta_{SF} < 2T$ one obtains (Appendix II)

$$c_v(T) \simeq \frac{4\Omega D_B T^2}{\Delta_B}[1 - y_1^2 + 19\exp(-2)] \tag{5.5}$$

Thus, at small Δ_{SF} the dependence $c_v(T)$ is very close to phonon-like one.

6. Discussions of the results and their experimental evidences

In this section we discuss the experimental data available in ^{4}He, ^{3}He and existing classes of superconductors as details possible in the context of two-stage FBL model of superfluidity and superconductivity which can be realized by two possible FBL scenarios in the so-called fermion superconductors (FSC) and boson superconductors (BSC) [49, 52].

6.1 *^{4}He superfluidity*

It follows from the above relation (4.6) that the excitation spectrum $E_B(k)$ of a 3d-Bose-liquid at $\gamma_B < \gamma_B^*$ becomes gapless in the temperature interval $0 \leqslant T \leqslant T_B^*$ and at small k, is phonon-like. At $T > T_B^*$ in $E_B(k)$ the gap Δ_{SF} appears being responsible for half-integral values of the circulation (see [15]) and the $c_v(T)$ departure from the phonon-like T^3 dependence observed in ^{4}He (see [16]). Depletion of the zero-momentum state (or often named as condensate) of a 3d-BG at $T = 0$ and $0 < T \leqslant T_B^*$ as a function of γ_B (figure 1) and temperature (figure 4) as well as its complete absence in the interval $T_B^* < T \leqslant T_B = T_\lambda$ (where T_λ is the temperature of λ-transition in ^{4}He) is in good agreement also with the experimental data available for ^{4}He [69, 72].

The experimental dependence $n_{B0}(T)$ has a feature such as a noticeable increasing n_{B0} below ~ 1 K [72]. The above features of the velocity circulation quantum, $c_v(T)$ and $n_{B0}(T)$ indicate on appearance of the gap Δ_{SF} in $E_B(k)$ at $T \geqslant 1,1$ K in ^{4}He (i.e. $T_B^* \sim 1,1$ K). Further the experimental values of $n_{B0} = 0,10 \div 0,14$ (at $T = 0$) in ^{4}He [72] correspond to the values of $\gamma_B \simeq 1,5 \div 1,6$ for $T_{BEC}/\xi_{BA} = 0,05$, i.e. to the region II at figure 2. It means that the interaction is strong in ^{4}He. The existence of the pair condensate in the $k = 0$ state considered in [14, 17] is unphysical (that was noted also in [19]) and complete absence of such condensate (that in fact must be single particle condensate) in the complete range $0 \leqslant T \leqslant T_\lambda$ in ^{4}He is not consistent with the experimental data. At $\gamma_B < \gamma_B^*$ and $\gamma_B < 1$ (i.e. in the region II and I in figure 2) we obtain the relation $n_{B0}(T) \sim (T_B^* - T)^{(2-\beta)/3}$ (that have been derived earlier in the framework of a phenomenological approach [68, 72] for ^{4}He with $\beta \geqslant 0$ and T_λ instead of T_B^* corresponding to the case BEC of an ideal BG) with $\beta \geqslant -1$ and $\beta \geqslant 0,5$,

respectively. Therefore, near $T_B^* < T_\lambda$ jump of $c_v(T)$ may be expected at weak ($\gamma_B \ll 1$) and probably intermediate ($\gamma_B \leqslant 1$) coupling. While at strong coupling ($\gamma_B > 1$) in $c_v(T)$ instead of such jump only pecularity may be displayed as it was observed, for example, in ^{4}He (see [16]).

6.2 *^{3}He superfluidity*

Many experimental results speak well for the triplet pairing in ^{3}He with angular momentum $l = 1$ [74, 75]. Such pairing of ^{3}He atoms leading to the formation of composite bosons may be described also by the BCS-like pairing theory [74, 75]. Further in ^{3}He just as in ^{4}He the real SF state most probably is described by the order parameter Δ_B of the attracting composite bosons (i.e. paired atoms ^{3}He), whereas the BCS-like order parameter Δ_F of the attracting fermion pairs characterizes only presuperfluid (or precursor) state. As the BCS-like theory cannot explain the number of features of SF ^{3}He and HTSC (including also LTSC, HFSC and OSC) observed below the critical temperature T_c. It is reasonable to assume that the interboson (i.e. intercooperon) interaction in ^{3}He probably is much weaker ($\gamma_B < 1$ or even $\gamma_B \ll \gamma_B^* \leqslant 2$ (for $\xi_{BA}/T_{BEC} \geqslant 10$)) than such interaction in ^{4}He. Therefore the condensate fraction in ^{3}He must be larger than in ^{4}He. It is supposed that in ^{3}He just as in LTSC only small fraction of fermions may take part in pairing and $\rho_B/\rho_F \ll 1$ (where ρ_F is the density of Fermi particles in unit volume). Then at $\rho_F \sim 10^{23}\,\mathrm{cm}^{-3}$ and $\rho_B/\rho_F \sim 10^{-5}$ (just as in LTSC) we obtain $T_{BEC} \simeq 2,52 \cdot 10^{-3}$ K that is very close to the observed value of T_c in ^{3}He, where in all probability $T_c = T_F = T_B$ (see below). So, the gap Δ_{SF} in $E_B(k)$ most probably vanishes at $T = T_B^* \simeq 0,7 T_c$ and there some features of ^{3}He physical properties must be displayed. Indeed, such features are observed in the SF phase of ^{3}He as jump-like increasing of the critical current velocity v_c three times under pressure and such change of the SF density just at $T \simeq (0,6 \div 0,7)\, T_c$ [2, 41–44]. This jump-like increasing of the v_c and SF density is caused by the sharp increasing of Δ_B (or $v_c = \sqrt{\Delta_B/m_B}$) at T_B^* when $\gamma_B \ll \gamma_B^*$ (figure 3c). Further, it may be assumed that under pressure or rotation increasing of an interaction strength between composite bosons occur and it is accompanied by appearance of the gap Δ_{SF} in $E_B(k)$ at a more low temperature. Then the splitting of the B-phase into two phases B1 and B2 as well as the transition between them observed for $T \sim 0,6 T_c$ [41, 43, 44] most probably is caused by these circumstances. Hence, the origin of the A- and B-phases as well as transition between them in ^{3}He at $T \sim 0,7 T_c$ [2] (cf. with the above value of $T_B^* \geqslant 0,7 T_c$) is naturally caused by the phase transition SPC $\Leftrightarrow$ PC of composite bosons. The observed sharp increasing of the SF density in ^{3}He [2] just at the phase transition A $\rightarrow$ B speak in favour of this assumption. While the observed power law dependence $c_v(T) \sim T^3$ [2] is caused by the absence of the gap Δ_{SF} in $E_B(k)$ at $T \leqslant T_B^*$ and by $\Delta_{SF} \ll T$ and not by the presence of point or line nodes of the BCS-like energy gap Δ_F. Step-like jump of $c_v(T)$ at T_c in ^{3}He means that $T_c = T_F = T_B$ (as in this case near T_c, $\Delta_F \sim \Delta_B \ll \Delta_{SF}$ takes place). Finally the circulation quantum $\Phi_0 = h/2m_3$ and $= h/4m_3$ (where m_3 is the mass of ^{3}He atoms) observation is possible in B- and A-phase, respectively, i.e. the gap Δ_{SF} vanishes and appears in $E_B(k)$ at $T \leqslant T_B^*$ and $T > T_B^*$ the half-integral values of the circulation may observe when the gap Δ_{SF} appears in $E_B(k)$ at $T > T_B^*$. Apparently such situation is realized at the transition from B- to A-phase in ^{3}He (see [41, 42]).

6.3 *Superconductivity of charged bosons in superconductors*

To establish the mechanism of superconductivity in LTSC, HFSC, OSC and HTSC first of all it should elucidate a question about the physical essence of the order parameter Δ_F and Δ_B as well as the energy gap Δ_{SF} in different cases. As the relation between them undoubtedly plays an important role in determining a possible superconductivity scenarios and main SC properties of superconductors.

6.3.1 *Gap features of superconductors*: We consider the new scenarios according to that superconductivity (superfluidity) in the Fermi systems appears under the coexistence of two order parameter: one of them Δ_F characterizes the bond strength of bound fermion pairs and the other Δ_B, the bond strength of all condensed bosons (i.e. existence of a SF state). While the gap Δ_{SF} characterizes, as stated above, the binding energy of a single bound boson pairs or the structure of the SF state. In other words, the phase transition to the SC state is accompanied as a rule by the formation of bound fermion pairs (i.e. composite bosons) with their subsequent transition to the SF state by SPC and PC [70]. Here it should be distinguished as two possible cases: a) disappearance of bound fermion pairs (or Δ_F) at $T = T_F$ is simultaneously accompanied by vanishing their SF condensate (or Δ_B) and b) disappearance of a SF condensate (or Δ_B) of such composite bosons at $T = T_B$ does not lead as yet to the break-up of bound fermion

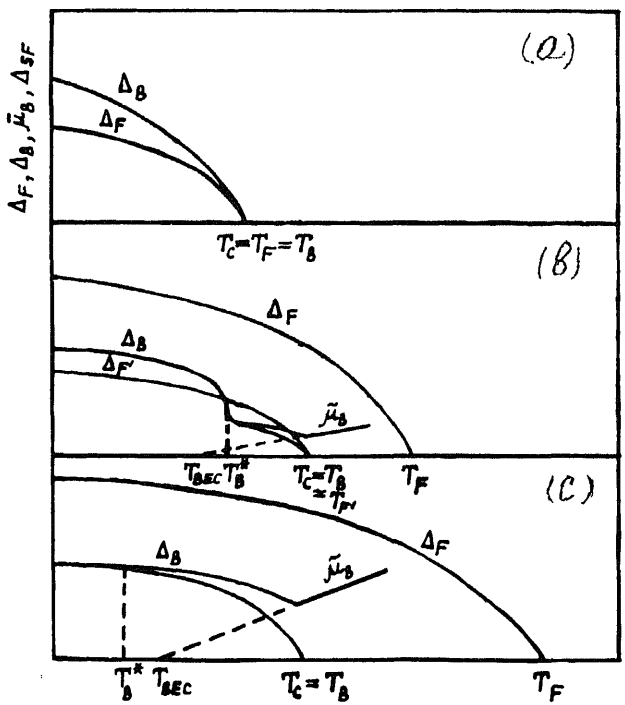

Figure 10. Schematic dependence of the Δ_F, Δ_B, $\tilde{\mu}_B$ and Δ_{SF} vs. temperature, for 3d-FSC: (a) and (b); for 3d-BSC: (b) and (c).

pairs which are dissociated at more higher temperatures (i.e. at $T = T_F > T_B$). Sc can exist two types of superconductors in which, may be realized, two FBL scena superconductivity [49–53]. These type superconductors are called fermion sup ductors (FSC) (with $\Delta_F < \Delta_B$ and $\Delta_F > \Delta_B$, $\Delta_{SC} = \Delta_F$, $T_c = T_F = T_B$) and boson conductors (BSC) (with $\Delta_F > \Delta_B$, $\Delta_{SC} = \Delta_B$, $T_c = T_B < T_F$), respectively (figure 10 FBL scenarios of superconductivity realizing in these FSC and BSC may be des by combined Fermi- and SF Bose-liquid theories which are given above. Then o a quasiparticle spectrum with a finite coexisting gaps Δ_F and Δ_B inside which wi collective soundlike modes (at $\gamma_B < \gamma_B^*$) caused by the closing of the gap Δ_{SF}. He FSC at $\Delta_F < \Delta_B$ some gap-like features associated with Δ_B and Δ_{SF} at $\Delta_F < \Delta_B$ appear outside the BCS-like gap $\Delta_{SC} = \Delta_F$ and inside it, respectively. Indee observed in LTSC non-zero DOS inside Δ_{SC} and a peak precursor its outsi nature of those remains unknown [3, 24], speak well for our predicts. While, i both the above gap-like feature Δ_B and Δ_{SF} will appear only inside the gap Δ_F w

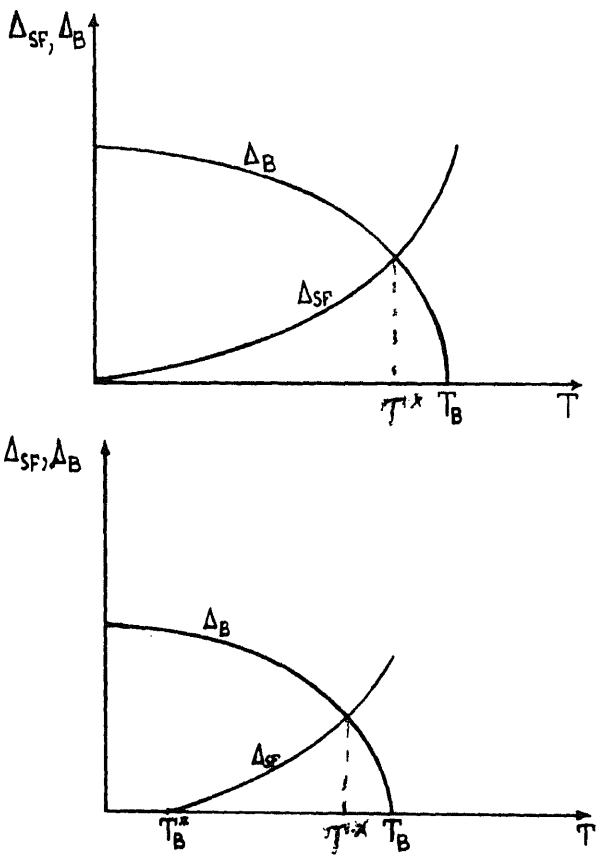

Figure 11. Schematic dependence of the Δ_{SF} and Δ_B vs. temperature in 3d-BSC for $\gamma_B = \gamma_B^*$ (a) and in 3d-BSC for $\gamma_B < \gamma_B^*$ (b).

a sharp maximum DOS. Further at $\gamma_B < \gamma_B^*$ and $T \leqslant T_B^*$ the non-zero DOS must exist also near the bottom of the gap Δ_F (that is displayed as a sharp maximum DOS not only in the SC but also in the normal state). Such pictures are observed in HTSC [23–28]. The observed large gap (or often called as pseudo-gap) in HTSC unknown nature is most probably the gap Δ_F and it bears no relation to real SC order parameter Δ_{SC}, as this gap exists also in the normal state [23, 35–37]. In BSC, at $T = T_F > T_B$ the phase transition in electronic subsystem having an effect on the lattice state must also occur. In all probability, the nature of the phase transitions unknown origin observed in $YBa_2Cu_3O_{7-x}$ at ~ 150 K and ~ 230 K [38, 76] are the same and are caused by the destroying of two type bipolarons at $T > T_c$. Further in BSC, identification of the gap Δ_{SC} and Δ_F must lead to an essential deviation of the temperature-dependence of such Δ_{SC} from its assumed BSC-dependence as T_c now does not correspond to T_F, i.e. at $T_F \geqslant 2T_B$ the pseudo-gap Δ_F almost does not depend on the temperature up to $T_c = T_B$. Such gap anomalies are observed also in HTSC [26, 35, 36]. Moreover, in BSC curves of the temperature-dependence of Δ_B and Δ_{SF} (figure 11) with the raising of the temperature it must shift to meeting each other and cross at $T = T^* < T_c = T_B$. These gap-like features were observed also in HTSC [28, 77]. Further, the gapless superconductivity in LTSC, HFSC, OSC and HTSC as well as such superfluidity in ^{3}He is caused by the vanishing of the gap Δ_{SF} at $T \leqslant T_B^*$ for $\gamma_B < \gamma_B^*$ and not by the point or line nodes of the gap Δ_F [52, 53]. Indeed, the experimental results show that often assumed point or line nodes of the BCS-like gap Δ_F responsible for gapless superconductivity is absent in fact [23, 25]. Therefore, the presence of the DOS near the bottom of the Δ_{SC} may be considered as one of the direct confirmation gapless superconductivity existence. Present theory (see also [52, 53, 70]) predicts that the gapless superconductivity can exist only in the temperature interval $0 < T < T_B^*$ (which can be observed experimentally).

6.3.2 *Ratio* $2\Delta_{SC}/T_c$: From the above-stated it follows that the ratio $g_{SC} = 2\Delta_{SC}/T_c$ and T_c in case of FSC may be determined from the BCS-like relation (3.4) and (3.3), respectively. However, in case of BSC such definition of Δ_{SC} is not applicable. In the present case, the ratio g_{SC} should be determined as $g_{SC} = 2\Delta_{SC}(=\Delta_B)/T_c(=T_B)$ and not as $g_{SC} = 2\Delta_{SC}(=\Delta_F)/T_c(=T_F)$ that leads to non-real large values of g_{SC} in comparison with its BCS-values (as the experimental value of T_c now is not corresponding to T_F). The observed values of $g_{SC} \geqslant 5$ and $\geqslant 8$ in HTSC [23–27] most probably is caused by these circumstances. So, according to (4.9) in the case of 3d-BSC at $\gamma_B \leqslant \gamma_B^*$, the quantity of g_{SC} is equal to [71]

$$g_{SC} = 2\Delta_{SC}(=\Delta_B)/T_c(=T_B) \leqslant 5,76 T_{BEC}/T_c \tag{6.1}$$

and in the case of 2d-BSC this ratio at $\gamma_B < \gamma_B^*$ is determined as [49, 50] (Appendix 2)

$$g_{SC} = 8\exp(-2/\gamma_B) \tag{6.2}$$

The numerical self-consistent solution of (4.3) after going to the integration and taking into account (4.4) at $\gamma_B = \gamma_B^*$ in case $T = T_B$ for 3d-BSC give $T_B/T_{BEC} \simeq 3$ and $g_{SC} \simeq 1,9$. Such solution of this equation at $0 < \gamma_B < \gamma_B^*$ gives $0 < g_{SC} \leqslant 1,7$ (figure 12). These values of g_{SC} agrees well with its observed values in HTSC [24, 25, 27]. While the observed values of $g_{SC} \geqslant 3,5 \div 8$ [24, 25, 27] have been determined according to

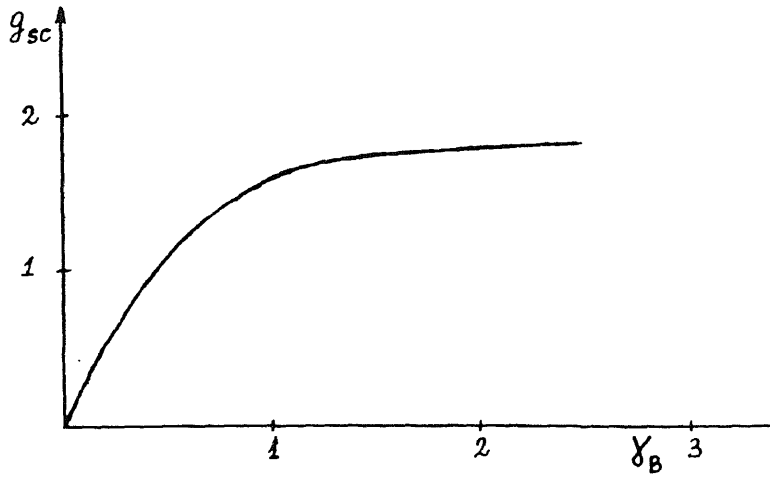

Figure 12. The dependence of g_{SC} on γ_B for 3d-BSC.

irrelevant BCS scheme as $g_{SC} = 2\Delta_{SC}(=\Delta_F)/T_c(=T_F)$. Since the temperature-dep ences of the gaps $g_{SC} \geqslant 5$ and $\geqslant 8$ is deviated strongly down and up from their assu BCS dependences, respectively [26, 78]. Moreover, the large gap $g_{SC} \simeq 8$ exists not below T_c but also above T_c [24, 35–37]. A novel two-stage FBL scenario superconductivity [49, 52] predicts disappearance of the BCS-like gap Δ_F in BS $T = T_F > T_c$ or even $T = T_F \gg T_c$. Indeed, at $\tilde{V}_{Fn} D_{Fn} \sim 0,5$ and $|U_{Cn}| + \hbar\omega_D \sim 0,$ from (3.3) it follows $T_{Fn} \sim 530$ K.

6.4 *Size and flux quantization effect for fermion and boson pairs*

The above observed in LTSC anomalies of gap-like features indicate [3] that Cooper pairs are real composite bosons obeying Bose–Einstein statistics and kee its identity. In fact, the real size of the Cooper pairs $a_F \sim \pi\hbar/\sqrt{4m_B\Delta_F}$ (at $m_B \sim 2m_e$ $\Delta_F \geqslant 10^{-4}$ eV, where m_e is the mass of a free electron) and the mean distance betv them is of the same order quantity, i.e. $a_F \geqslant 10^{-6}$ cm. So they are not strong overla spite of the prediction of BCS theory based on the estimation of $a_F \sim 10^{-4}$ cm th too overestimated. As in BCS-theory, the coherence length is usually estim according to incorrect assumption $\varepsilon(k) = E_F$ (i.e. $k = k_F$) that contradicts with its b supposition $\varepsilon(k) < \hbar\omega_D$. While the binding energy of boson pairs in their interac collective decreases and is equal to zero at $\gamma_B \leqslant \gamma_B^*$ (when boson pairs begins overl ing and bosons exchange from one pair to another becomes dominant). Therefore of identity or strong overlap are peculiar to the attracting boson pairs, and nc fermion pairs. These distinctive features of fermion and boson pairs are visu displayed in the flux quantization effects in ^{4}He and ^{3}He, LTSC, respectively. example, in ^{4}He are observed both $\Phi = h/m_4$ and $h/2m_4$ (where m_4 is the mass of atoms) flux quantum [1, 15], whereas in LTSC and ^{3}He only flux quantum $h/2e$ $h/2m_3$ (where m_3 is the mass of ^{3}He) is observed, respectively, and not h/e and h

Some experimental facts in ^{3}He (see [42]) indicate about the existence of quartets with flux quantum $\Phi = h/4m_3$ also. This corresponds to the case $\Delta_{SC} \neq 0$. The quartets with flux quantum $\Phi = h/4e$ may be formed also in superconductors (e.g. in HTSC) at $T > T_B^*$, i.e. in the temperature interval $T_B^* < T < T_c$.

6.5 *Specific heat*

The temperature-dependences of Δ_B and $|\tilde{\mu}_B|$ near T_B^* at $1 < \gamma_B \leqslant \gamma_B^*$ and $0 < \gamma_B < 1$ is weak and strong, respectively. In this connection the $c_v(T)$ curve near T_B^* for Δ_B, $|\tilde{\mu}_B| \ll T_B^*$ (or $\gamma_B \ll \gamma_B^*$) (the region I on figure 2) just as near T_B (where the condition Δ_B, $|\tilde{\mu}_B| \ll T_B$ and $\beta \geqslant 0,5$ may be well-satisfied even for $\gamma_B \sim 1$) may undergo λ-like jump and at $1 < \gamma_B \leqslant \gamma_B^*$ (the region II on figure 2) probably displayed only peculiarity. In all probability, the first of them takes place in HTSC and HFSC [39,40], and the second in ^{4}He (see [16]). As in HTSC and HFSC, λ-like jump of $c_v(T)$ are observed not only at T_c [38,79] but also at $T < T_c$ [39,40]. While in $YBa_2Cu_3O_{7-x}$ a small step-like jump of $c_v(T)$ at $T \geqslant 2,5T_c$ [76] is caused by destruction of bipolarons, i.e. the phase transition normal Bose-liquid$\Leftrightarrow$Fermi-liquid (figure 9) in electronic (and not lattice) subsystem [49–53] as stated above. In [76], on the basis of the experimental data, analogous assertion have also been made. This indicates that the HTSC are BSC. The HFSC and OSC are related also to this class so far they are characterized by $c_v(T) \sim T^3$ at low temperature [8,80] and at $T = T_c$, undergoes λ-like jump [5,79]. Such gapless superconductivity is most probably realized also in LTSC as there $c_v(T) \sim T^3$ is observed up to T_c [3]. Indeed, both in BSC and in FSC at $\Delta_{SF} < \Delta_{SC}$ and especially at $\Delta_{SF} \ll \Delta_{SC}$ (or $\Delta_{SF} = 0$) the main contribution to $c_v(T)$ comes from the excitation of the composite bosons (e.g. Cooper pairs in LTSC) as a whole and not from excitation of their Fermi components. The number of such bosons in LTSC is much smaller ($\rho_B \sim 10^{17} \div 10^{18}\,\mathrm{cm}^{-3}$) than their number in HTSC ($\rho_B \sim 10^{21}\,\mathrm{cm}^{-3}$). Unlike the BSC (where $\rho_B \simeq$ const up to T_B or even above T_B), in FSC at comparatively low temperatures ρ_B (or T_B) $\simeq$ const but at $T \to T_F$ fast decreation of ρ_B (or T_B) up to BG concentration for which $T_B \to T_F$ occurs. For inconstant ρ_B (at $T > T_F/2$ and especially at $T \to T_F$) the determination of the quantitative trend of $\tilde{\mu}_B(T)$ and $\Delta_B(T)$ changes is a very difficult problem as it requires a combined self-consistent solution of the equations for $\tilde{\mu}_F(T)$, $\Delta_F(T)$, $\tilde{\mu}_B(T)$ and $\Delta_B(T)$ under the conservation of the total particle number $N = N_F + 2N_B$. In this case we have to limit ourselves to predict the qualitative trend of $\tilde{\mu}_B(T)$ and $\Delta_B(T)$ changes which, however, may be found close enough to the real situation. So the value of T_B (including T_B^* and T_{BEC}) determined for $\rho_B \simeq$ const and expected above T_F becomes unphysical. Probably in FSC with a weak coupling the gap Δ_{SF} in $E_B(k)$ may be absent up to $T = T_c = T_F$ or appear near T_F, where $\Delta_{SF} > \Delta_F$. Then near T_c the $c_v(T)$ undergoes step-like (or BCS-like) jump that is observed in LTSC. Apparently in ^{3}He interaction between composite bosons is several times stronger than in LTSC and the gap opening in $E_B(k)$ occurs at $T \simeq 0,7T_c$. Then near T_c the situation $\Delta_{SF} \gg \Delta_F$ takes place and the jump of $c_v(T)$ at $T = T_c = T_F$ determined by BCS-theory has step-like also. So LTSC and ^{3}He are related to the FSC. Further in BSC, for T_B^* that is close to T_B, the $c_v(T)$ undergoes two jumps near $T_c = T_B$ separated by a small temperature interval. Indeed, such jumps of $c_v(T)$ are observed in HTSC [81] and HFSC [82]. Other explanation is given below.

all superconductors the dependence of $\lambda_L(T)$ must be determined on the basis Bose-liquid models [71] (in case of 2d-holon superconductors this questic considered in [20]) from

$$\frac{\lambda_L(T)}{\lambda_L(0)} = \left[1 - \frac{\rho_{Bn}}{\rho_B}\right]^{-1/2},$$

where $\lambda_L(0) = (m_B c^2/4\pi\rho_B e^2)^{1/2}$, c, is the light velocity; $\rho_B = \rho_{Bs} + \rho_{Bn}$; ρ_{Bs} and ρ_B density of the so-called 'SF' (nonexcited) and 'normal' (excited) Bose-liqui a 3d-Bose-liquid at $\Delta_{SF}(T \leqslant T_B^* < T_c) = 0$, $\rho_{Bn} \sim T^4$ and from (6.3) it follows [7

$$\frac{\lambda_L(T)}{\lambda_L(0)} = \left[1 - \left(\frac{T}{T_c}\right)^4\right]^{-1/2}$$

that has been only empirically obtained earlier. For, a 2d-Bose-liquid at Δ_s approximately takes place at $\rho_{Bn} \sim T^3$ and

$$\frac{\lambda_L(T)}{\lambda_L(0)} = \left[1 - \left(\frac{T}{T_c}\right)^3\right]^{-1/2}$$

and at $\Delta_{SF} > 2T$ one obtains

$$\frac{\lambda_L(T)}{\lambda_L(0)} = \left[1 - \left(\frac{T}{T_c}\right)\exp\left(-\frac{\Delta_{SF}}{T}\left(1 - \frac{T}{T_c}\right)\right)\right]^{-1/2}$$

Many experimental data both in LTSC [3], HFSC [83] and in HTSC [7, 84 agreement with (6.4) and do not, with exponential dependence of the BCS Further in HTSC, OSC are observed the power law dependence of $\lambda_L(T$ [7, 80, 85, 86] and that it follows from a 3d-Bose-liquid model also (this resul reported separately). In recently discovered high temperature OSC of the type the dependence $\lambda_L(T)/\lambda_L(0)$ is observed very close to the dependence (6.5), i.e. the of $(T/T_c)^\nu$ in $\lambda_L(T)/\lambda_L(0)$ is equal to $\nu = 3, 2$ (see [87]). Some experiments als $\nu = 1, 3 \div 3, 2$ in accordance with our results.

6.7 *Critical magnetic field and Meissner effect*

As is generally known, the critical magnetic field H_c for each type of SF car determined from the difference of the free energies of normal and SC states. difference for Bose-liquid is smaller than for Fermi-liquid, then the H_c sho determined from the difference of the free energies of normal and SF Bose Otherwise H_c is determined from the difference of the free energies of Fermi-li normal and SC states according to BCS theory. These cases is most probably r in BSC and FSC, respectively. Then for BSC one obtains [70]

$$H_c(T) \simeq \sqrt{4\pi D_B \xi_{BA}^{1/2} \Omega}\,\Delta_B(T)$$

The observed anomalies of the lower critical magnetic field H_{c1} in YBa_2Cu_3O

HFSC (see [29, 30]) is naturally explained by this relation as $H_c \sim H_{c1}$, i.e. unusual upturn of the low temperature part of $H_{c1}(T)$ curve is caused by the sharp increasing of the $\Delta_B(T)$ at $T \leqslant T_B^*$ when $\gamma_B < 1$ and especially when $\gamma_B \ll 1$ (figure 3).

The Meissner effect both in FSC and in BSC is determined by superfluidity of the Bose-liquid and not that of Fermi-liquid. It is not difficult to show the absence of the paramagnetic part of current for SF Bose-liquid analogous to that being done for 'such' Fermi-liquid in BCS theory (this result is reported separately).

6.8 *Existence of several types of superfluid carriers*

Many experimental data on the gap features, specific heat, London penetration depth, critical magnetic fields and fractional Meissner effect is indicative of the existence (coexistence) of several types of SF carriers in HTSC, HFSC and type II LTSC. For example, they speak well for the existence of at least two types of carriers with the different fermion and boson order parameters [4, 7, 38–40, 76], such as Δ_{F1}, Δ_{F2}, and Δ_{B1}, Δ_{B2} respectively, as well as Fermi-liquid [6, 9] and normal Bose-liquid [88, 89] in HTSC and HFSC. It is not excluded that some of the observed maxima of $c_v(T)$ in HTSC (including HFSC) below T_c are caused by the second SC transition at $T = T_{c2} < T_{c1} = T_c$.

Further, in BSC at $T_{F2} < T_{c1}$ and $T_{c1} < T_{F1}$ the temperature dependence of the Δ_{SC} determined as $\Delta_{SC}^{(1)}(T) = \Delta_{F1}(T)$ and $\Delta_{SC}^{(2)}(T) = \Delta_{F2}(T)$ should deviate down and up, respectively, from their assumed non-real BCS-dependence (i.e. when $T_c = T_{c1} < T_{F1}$ is assumed). Indeed, such deviation in the temperature-dependence of the gap-like features from their BCS-dependence are observed in HTSC [26, 35, 36, 78]. The observed two different temperature dependence $\lambda_L(T) \sim T^4$ and $\sim T^2$ (in HFSC and HTSC [7, 80, 83, 85]) or $\lambda_L(T) \sim T^3$ and $\sim T^2$ (in OSC [80, 86, 87]), as well as jump-like features of $c_v(T)$ at $T > T_c$ [38] and fractional Meissner effect or type III superconductivity [90] in HTSC may be explained also by the presence of several types of carriers. At different ρ_B, m_B or γ_B the crossing of the different order parameters $\Delta_B(T)$ and the formation of a new mixed state in the temperature interval $T_{c2} < T < T_{c1}$ as well as positive curvature near T_c is possible. Apparently, such situation is realized in HFSC and HTSC, where two jumps are observed near T_c separated by the temperature interval $60 \div 70$ mK [81] and $\sim 3, 5$ K [82], respectively. Also, a new mixed state in the comparatively wide temperature interval may be formed without the crossing of two $\Delta_B(T)$.

6.9 *Other confirmations*

The following are the experimental facts: (i) the small value of the entropy (or the large single particle condensate fraction in our context) observed in HTSC at $T < T_c$ (see [91]) in comparison with its values expected for an ideal 3d-BG; (ii) the SF density change $n_S \sim [1 - (T/T_c)^4]$ for HTSC [83] and HFSC [92]; (iii) the unusual upturn of the low temperature part of critical current $J_c(T)$ and sound velocity dependences [31, 32] (these features probably is caused also by the sharp increasing of the $\Delta_B(T)$ at $T \leqslant T_B^*$ for $\gamma_B < 1$). These observations once again confirm the validity of the above microscopic theory of SPC and PC of an attracting BG as the basis for superfluidity

7. Conclusion

It follows from the above-stated conceptions and arguments that the SC (SF) phase transition in Fermi and Bose system is two- and one-stage, respectively, where the SPC and PC of an attracting BG (as distinct from the often discussed SPC of a repulsive BG and BCS-like condensation of the Cooper pairs reminiscent of the BEC of an ideal BG) are responsible for superfluidity both of charged and uncharged Bose-liquids in superconductors, ^{3}He and ^{4}He. Further, two possible FBL scenarios, such as, Fermi-liquid $\rightarrow$ SF Bose-liquid and Fermi-liquid $\rightarrow$ normal Bose-liquid $\rightarrow$ SF Bose-liquid is realized in FSC and BSC, respectively.

In all probability, the SF and SC properties of ^{3}He and LTSC, being related to the type of FSC with weak coupling ($\gamma_B < 1$ or even probably $\gamma_B \ll 1$) have determined both the Fermi-liquid behaviour (e.g., $T_c, \Delta_{SC}(T)$ (or g_{SC}) and H_c) described within the BCS-like theory and Bose-liquid one (e.g., $c_v(T), \lambda_L(T)$, and gapless superfluidity (superconductivity)) described within the above theory of SPC and PC of an attracting BG [49–53]. While the properties of ^{4}He, HTSC, HFSC and OSC which, most probably are related to the BSC with weak ($\gamma_B < 1$) and possibly intermediate ($\gamma_B \sim 1$) or even strong ($\gamma_B > 1$ in case ^{4}He) coupling are determined almost entirely by Bose-liquid behaviour described within the above theory of SPC and PC of an attracting BG. In these superconductors the behaviour of the BCS-like Fermi-liquid will be displayed as the pseudo gap $\Delta_F > \Delta_{SC}$ and $\Delta_F \neq 0$ in SC and normal states, respectively and as the electronic phase transition at $T = T_F > T_c$. Many experimental data available both in SF ^{4}He, ^{3}He, different classes of superconductors simultaneously confirm the applicability and validity of the above proposed microscopic theory of two-stage FBL scenarios for description of superfluidity and superconductivity phenomena from a unified position. Thus, SPC and PC of an attracting BG serve as a key to superfluidity and superconductivity of both the composite bosons (e.g. Cooper pairs and bipolarons) and noncomposite ones (e.g. ^{4}He atoms).

Note added for the revised version

After submission of the first version of the present paper we have learnt about the work [93–95]. In accordance with our results, in [93] and [94] a half magnetic flux quantum $\Phi_0 = h/4e$ and a T^2 term in c_v has been observed, respectively. While the results of the work [95] obtained on the basis of a phenomenological approach and its predictions about the heat-flow induced anomalies in SF ^{4}He near T_λ, namely, a sizeable enhancement of the $c_v(Q)$ and a weak depression of the SF density $\rho_s(Q)$ (where Q is a stationary heat current) has any qualitative likeness with our microscopic ones. In our opinion, all these results once again demonstrates that the above proposed microscopic theory are adequate and valid for description of superfluidity and superconductivity.

Acknowledgement

One of the authors (SD) wishes to acknowledge with thanks the financial support allocated by the I.C.T.P. (Trieste, Italy).

Appendix 1

Calculating the basic parameters of an attracting BG for $T = 0$.

Using the BCS-like approximation (4.4) in (4.3) we have

$$\begin{cases} \Delta_{B1} = -(V_{BR} - V_{BA})\Delta_{B1} I_A - V_{BR}\Delta_{B2} I_R \\ \Delta_{B2} = -V_{BR}\Delta_{B1} I_A - V_{BR}\Delta_{B2} I_R \end{cases} \tag{A1.1}$$

$$\chi_B = \rho_{B1}(V_{BR} - V_{BA}) + V_{BR}\rho_{B2} \tag{A1.2}$$

where

$$\rho_{B1} = \frac{1}{\Omega}\sum_{k=0}^{k_A} n_B(k), \quad \rho_{B2} = \frac{1}{\Omega}\sum_{k=K_A}^{k_R} n_B(k), \quad n_B(k) = [\exp(E_B(k)/T - 1]^{-1},$$

$$\varepsilon(k_A) = \xi_{BA}, \quad \varepsilon(k_R) = \xi_{BR}, \quad I_A = \frac{1}{\Omega}\sum_{k'=0}^{k_A} \frac{(1 + 2n_B(k'))}{2E_B(k')},$$

$$I_B = \frac{1}{\Omega}\sum_{k'=k_A}^{k_R} \frac{(1 + 2n_B(k'))}{2E_B(k')}$$

From (A1.1) we obtain

$$\Delta_{B2} = [1 - V_{BA} I_A], \quad I_A = \frac{1}{\tilde{V}_B} \tag{A1.3}$$

As almost all Bose particles have energies smaller than ξ_{BA}, then going in (A1.1) and (A1.2) from summation to integration on ε we have

$$2\rho_B \simeq D_B \int_0^{\xi_{BA}} \sqrt{\varepsilon}\left[\frac{\varepsilon + |\tilde{\mu}_B|}{\sqrt{(\varepsilon + |\tilde{\mu}_B|)^2 - \Delta_{B1}^2}} \operatorname{cth}\frac{\sqrt{(\varepsilon + |\tilde{\mu}_B|)^2 - \Delta_{B1}^2}}{2T} - 1\right] d\varepsilon \tag{A1.4}$$

$$I_A = D_B \int_0^{\xi_{BA}} \sqrt{\varepsilon}\frac{\operatorname{cth}[\sqrt{(\varepsilon + |\tilde{\mu}_B|)^2 - \Delta_{B1}^2}/2T]}{2\sqrt{(\varepsilon + |\tilde{\mu}_B|)^2 - \Delta_{B1}^2}} d\varepsilon \tag{A1.5}$$

$$I_R = D_B \int_{\xi_{BA}}^{\xi_{BR}} \sqrt{\varepsilon}\frac{\operatorname{cth}[\sqrt{(\varepsilon + |\tilde{\mu}_B|)^2 - \Delta_{B2}^2}/2T]}{2\sqrt{(\varepsilon + |\tilde{\mu}_B|)^2 - \Delta_{B2}^2}} d\varepsilon \tag{A1.6}$$

For $\xi_{BA} \gg |\tilde{\mu}_B|, \Delta_{B1}, \Delta_{B2}, T$ one gets for 3d-BG and 2d-BG

$$I_R \simeq D_B \int_{\xi_{BA}}^{\xi_{BR}} \sqrt{\varepsilon}\frac{d\varepsilon}{\varepsilon} = D_B[\sqrt{\xi_{BR}} - \sqrt{\xi_{BA}}] \quad \text{and} \quad I_R \simeq \frac{D_B}{2}\ln\frac{\xi_{BR}}{\xi_{BA}}, \tag{A1.7}$$

respectively. Further at $V_{BR} I_R \gg 1$ from (A1.1) it follows

$$\tilde{V}_B I_A = [V_{BA} - V_{BR}(1 + V_{BR} I_R)^{-1}] I_A = 1 \tag{A1.8}$$

that at $\rho_{B2} \ll \rho_{B1}$ together with the (A1.4) determines the value of $|\tilde{\mu}_B| = -\mu_B + 2\rho_B$ $(V_{BR} - V_{BA})$ and $\Delta_B = \Delta_{B1}$. So the BCS-like case approximation (4.4) becomes equivalent to the following simple BCS-like one

$$\begin{cases} V_B(k - k') = -\tilde{V}_B, & \text{if } \varepsilon(k),\ \varepsilon(k') < \xi_{BA} \\ 0, & \text{otherwise} \end{cases} \tag{A1.9}$$

In the case $T=0$ and $|\tilde{\mu}_B|=\Delta_B$ from (A1.4) and (A1.8) at large ξ_{BA} for a 3d-BG one obtains

$$\frac{3\rho_B}{D_B}=\lim_{\xi_{BA}\to\infty}[\sqrt{\xi_{BA}+2|\tilde{\mu}_B|}(\xi_{BA}-|\tilde{\mu}_B|)+|\tilde{\mu}_B|\sqrt{2|\tilde{\mu}_B|}-\xi_{BA}^{3/2}]\simeq|\tilde{\mu}_B|\sqrt{2|\tilde{\mu}_B|} \tag{A1.10}$$

$$\frac{1}{D_B\tilde{V}_B}=\sqrt{\xi_{BA}+2|\tilde{\mu}_B|}-\sqrt{2|\tilde{\mu}_B|} \tag{A1.11}$$

From (A1.11) it follows (4.7) and its substitution into (A1.10) gives (4.6). Further from (A1.10) it follows (4.9). Now separating the term with $k=0$ in the summation (4.3) according to procedure [14] we have

$$\Delta_B(k)=-V_B(k)\rho_{B0}-\frac{1}{\Omega}\sum_{k'\neq 0}V_B(k-k')\frac{\Delta_B(k')}{2E_B(k')}(1+2n_B(k')),$$

$$\rho_B=\rho_{B0}+\frac{1}{\Omega}\sum_{k\neq 0}n_B(k),\quad \chi_B(k)=V_B(k)\rho_{B0}+\frac{1}{\Omega}\sum_{k'\neq 0}V_B(k-k')n_B(k') \tag{A1.12}$$

Now going in (A1.12) from summation to integration on ε taking into account (A1.9) we obtain

$$2(\rho_B-\rho_{B0})=D_B\int_0^{\xi_{BA}}\sqrt{\varepsilon}\left[\frac{\varepsilon+|\tilde{\mu}_B|}{\sqrt{\varepsilon^2+2|\tilde{\mu}_B|}}-1\right]d\varepsilon \tag{A1.13}$$

$$\tilde{V}_B\rho_{B0}=|\tilde{\mu}_B|\left[1-\tilde{V}_BD_B\int_0^{\xi_{BA}}\sqrt{\varepsilon}\frac{d\varepsilon}{\sqrt{\varepsilon^2+2|\tilde{\mu}_B|\varepsilon}}\right] \tag{A1.14}$$

From (A1.13) and (A1.14) one obtains (4.10) and (4.11), respectively. For a 2d-BG in (A1.13) and (A1.14) the multiplier $\sqrt{\varepsilon}$ under the integral is absent.

Appendix 2

Calculating the basic parameters of an attracting Bose-gas for $T\neq 0$.

For $T\neq 0$, (A1.4) and (A1.5) may be written as

$$\frac{2}{D_B\tilde{V}_B}=\int_0^{\xi_{BA}}\sqrt{\varepsilon}\frac{d\varepsilon}{\sqrt{(\varepsilon+\tilde{\mu}_B)^2-\Delta_B^2}}+2\int_0^{\xi_{BA}}\sqrt{\varepsilon}\frac{d\varepsilon}{\sqrt{(\varepsilon+\tilde{\mu}_B)^2-\Delta_B^2}[\exp(\sqrt{(\varepsilon+\tilde{\mu}_B)^2-\Delta_B^2}/T)-1]} \tag{A2.1}$$

$$\frac{2\rho_B}{D_B}=\int_0^{\infty}\sqrt{\varepsilon}\left[\frac{\varepsilon+\tilde{\mu}_B}{\sqrt{(\varepsilon+\tilde{\mu}_B)^2-\Delta_B^2}}-1\right]d\varepsilon+2\int_0^{\infty}\sqrt{\varepsilon}\frac{(\varepsilon+\tilde{\mu}_B)d\varepsilon}{\sqrt{(\varepsilon+\tilde{\mu}_B)^2-\Delta_B^2}[\exp(\sqrt{(\varepsilon+\tilde{\mu}_B)^2-\Delta_B^2}/T)-1]} \tag{A2.2}$$

For $T \ll T_B$ and $\tilde{\mu}_B = \Delta_B$ the second integral in (A2.1) and (A2.2) at a small ε is nearly equal to $(\pi T)^2/3\sqrt{2\tilde{\mu}_B^{3/2}}$ and $(\pi T)^2/3\sqrt{2\tilde{\mu}_B}$. Further, according to (A1.12) in (A2.1) and (A2.2), terms $2\rho_{B0}/\tilde{\mu}_B D_B$ and $\rho_{B0}/\tilde{\mu}_B D_B$, must be tolerated respectively. Then, taking into account (A1.10) and (A1.11), it is easy to obtain (4.12) and (4.13). In case of $\Delta_{SF} \neq 0$ (or $\rho_{B0} = 0$) the first integral in (A2.1), and (A2.2) can be evaluated approximately using the expansion

$$\frac{1}{\sqrt{(\varepsilon + |\tilde{\mu}_B|)^2 - \Delta_B}} \simeq \frac{1}{\varepsilon + |\tilde{\mu}_B|}\left[1 + \frac{\Delta_B^2}{2(\varepsilon + |\tilde{\mu}_B|)^2}\right] \tag{A2.3}$$

and after integration also using the expansion

$$\operatorname{arctg}\sqrt{\xi_{BA}/\tilde{\mu}_B} \simeq \frac{\pi}{2} - \sqrt{\frac{\tilde{\mu}_B}{\xi_{BA}}} + \frac{1}{3}(\tilde{\mu}_B/\xi_{BA})^{3/2} - \cdots$$

for these integrals we have

$$2\xi_{BA}\left[1 + \frac{3\pi}{32}\left(\frac{\Delta_B}{\tilde{\mu}_B}\right)^2\sqrt{\frac{\tilde{\mu}_B}{\xi_{BA}}}\right] \quad \text{and} \quad \frac{\pi\Delta_B^2}{4\sqrt{\tilde{\mu}_B}}, \tag{A2.4}$$

respectively. While the second integral in (A2.1) and (A2.2) is calculated by substitution $t = \sqrt{(\varepsilon/|\tilde{\mu}_B|)^2 + 2\varepsilon/|\tilde{\mu}_B|}$, $a_1^2 t^2 + a_2^2 = [(\varepsilon + |\tilde{\mu}_B|)^2 - \Delta_B^2]/T^2$ and using the method [96], where $a_1 = |\tilde{\mu}_B|/T$, $a_2 = \sqrt{|\tilde{\mu}_B|^2 - \Delta_B^2}/T$.

Then the second integral in (A2.2) has the form

$$I_2 = 2\tilde{\mu}_B \int_0^\infty \frac{\sqrt{(t^2+1)^2 - 1}\, t\, dt}{\sqrt{t^2 + (a_2/a_1)^2}\,[\exp(a_1\sqrt{t^2 + (a_2/a_1)^2}) - 1]} \tag{A2.5}$$

It is reasonable to assume that near T_B takes place $a_1 \ll 1$ and $a_2 \ll 1$ as well as $\Delta_B \ll \tilde{\mu}_B$. For such a_1 and a_2 the integral (A2.5) may be calculated by using the method [96]. Here we give the final results which has the form

$$I_2 = \sqrt{\pi}T^{3/2}\left[2,612 - \sqrt{2\pi}\sqrt{\frac{|\tilde{\mu}_B|}{T} + \frac{\Delta_{SF}}{T}} + 1,46\frac{|\tilde{\mu}_B|}{T} - \cdots\right]$$

$$\simeq \sqrt{\pi}T^{3/2}\left[2,612 - \sqrt{2\pi}\sqrt{\frac{\tilde{\mu}_B}{T} + \frac{\tilde{\mu}_B}{T}\left(1 - \frac{\Delta_B^2}{2\tilde{\mu}_B^2}\right)} + 1,46\frac{\tilde{\mu}_B}{T}\right] \tag{A2.6}$$

for (A2.2)

$$I_2' = \frac{\pi T}{\sqrt{2|\tilde{\mu}_B|}}\left[\sqrt{\frac{|\tilde{\mu}_B|}{|\tilde{\mu}_B| + \Delta_{SF}}} - 1,46\sqrt{\frac{2|\tilde{\mu}_B|}{\pi T}} + \cdots\right]$$

$$\simeq \frac{\pi T}{2\sqrt{\tilde{\mu}_B}}\left[\sqrt{\frac{1}{1 - \Delta_B^2/4\tilde{\mu}_B^2}} - 1,46\sqrt{2}\sqrt{\frac{2\tilde{\mu}_B}{\pi T}}\right] \tag{A2.7}$$

for (A2.1).

After expansion, the expressions

$$\sqrt{1 - \Delta_B^2/4\tilde{\mu}_B^2} \quad \text{and} \quad \sqrt{\frac{1}{1 - \Delta_B^2/4\tilde{\mu}_B^2}}$$

by the degrees of $\Delta_B/\tilde{\mu}_B$ and assuming $1,46\sqrt{2} \simeq 2$ from (A2.1), (A2.2), (A2.3), (A2.7) we obtain (with an accuracy to $\sim \tilde{\mu}_B(T)$)

$$\frac{1}{D_B \tilde{V}_B} \simeq \sqrt{\xi_{BA}}\left[1+\frac{3\pi}{32}\left(\frac{\Delta_B}{\tilde{\mu}_B}\right)^2\sqrt{\frac{\tilde{\mu}_B}{\xi_{BA}}}\right]+\frac{\pi T}{2\sqrt{\tilde{\mu}_B}}\left[\left(1+\frac{\Delta_B^2}{8\tilde{\mu}_B^2}\right)-2\sqrt{\frac{2}{\pi}}\right.$$

$$\frac{2\rho_B}{D_B} \simeq \frac{\pi\Delta_B^2}{4\sqrt{\tilde{\mu}_B}}+\sqrt{\pi}T^{3/2}\left[2,612-2\sqrt{\pi\tilde{\mu}_B/T}\left(1-\frac{\Delta_B^2}{8\tilde{\mu}_B^2}\right)\right]$$

From (A2.8) for $T/\xi_{BA} > \tilde{\mu}_B/T$ and $T/\xi_{BA} \leqslant 1/2\pi$ it follows (4.16). While in (A2.9 into account $2\rho_B/\Delta_B = 2,612\sqrt{\pi}T_{BEC}^{3/2}$ and making some transformation we ha

$$2,612\sqrt{\pi}T_{BEC}^{3/2} = \sqrt{\pi}T^{3/2}\left[\frac{\sqrt{\pi}}{4}\left(\frac{\Delta_B}{\tilde{\mu}_B}\right)^2\left(\frac{\tilde{\mu}_B}{T}\right)^{3/2}+2,612-2\sqrt{\frac{\pi\tilde{\mu}_B}{T}}\left(1-\right.\right.$$

from which it follows (4.15). Now the quantity of the $\tilde{\mu}_B(T)$ and $\Delta_B(T)$ near T_B found by elimination of $\Delta_B^2/8\tilde{\mu}_B^2$ in (4.15) and (4.16). After some algebra we ha

$$-\frac{2,612}{2\sqrt{\pi\tilde{\mu}_B(T)}}\left(\frac{T_B^{3/2}-T^{3/2}}{T}\right)+\sqrt{\frac{\tilde{\mu}_B(T_B)}{\tilde{\mu}_B(T)}}\frac{T_B}{T} = 1-\frac{\Delta_B^2}{8\tilde{\mu}_B^2}$$

$$\sqrt{\frac{\tilde{\mu}_B(T)}{\tilde{\mu}_B(T_B)}}\frac{T_B}{T} = 1+\frac{\Delta_B^2}{8\tilde{\mu}_B^2}$$

from which (at $T \sim T_B$) it follows

$$\sqrt{\frac{\tilde{\mu}_B(T)}{\tilde{\mu}_B(T_B)}}+\sqrt{\frac{\tilde{\mu}_B(T_B)}{\tilde{\mu}_B(T)}}\left[1-\frac{1,306}{\sqrt{\pi\tilde{\mu}_B(T_B)}}\left(\frac{T_B^{3/2}-T^{3/2}}{T_B}\right)\right]-2\frac{T}{T_B} = 0$$

The solution of this equation has the form

$$\sqrt{\frac{\tilde{\mu}_B(T)}{\tilde{\mu}_B(T_B)}} = \frac{T}{T_B}+\sqrt{\left(\frac{T}{T_B}\right)^2-1+\frac{1,306}{\sqrt{\pi\tilde{\mu}_B(T_B)}}\left(\frac{T_B^{3/2}-T^{3/2}}{T_B}\right)}$$

Further taking into account

$$\frac{T_B^{3/2}-T^{3/2}}{T_B} \simeq \frac{T_B^3-T^3}{2T_B^{5/2}} = \frac{(T_B-T)(T_B^2+T_B T+T^2)}{2T_B^{5/2}} \simeq \frac{3T_B^2(T_B-}{2T_B^{5/2}}$$

we have

$$\sqrt{\frac{\tilde{\mu}_B(T)}{\tilde{\mu}_B(T_B)}} = \frac{T}{T_B}+\sqrt{\left[\frac{3,918}{2\sqrt{\pi}}\sqrt{\frac{T_B}{\tilde{\mu}_B}}-2\right]\frac{(T_B-T)}{T_B}}$$

from which at $T_B/\tilde{\mu}_B \gg 1$ after the determination of $\tilde{\mu}_B(T_B)$ from (4.16) approxin follows (4.19). Near T_B, (4.16) may be written as

$$\frac{\pi T_B}{2\sqrt{\tilde{\mu}_B(T)\xi_{BA}}} \simeq \frac{\pi T}{2\sqrt{\tilde{\mu}_B(T)\,\xi_{BA}}}\left(1+\frac{\Delta_B^2(T)}{8\tilde{\mu}_B^2(T)}\right)$$

From (A2.12) and (4.19) it follows (4.20). Now we determine the $\tilde{\mu}_B(T)$ (or $\Delta_B(T)$) and $n_{B0}(T)$ near $T = T_B^* < T_B$ assuming $\tilde{\mu}_B(T)/T_B^* \ll 1$. Then for $T < T_B^*$ going in (A1.12) from summation to integration on ε and for T_B^* taking into account (4.15) and (4.16) the equations determining the $\tilde{\mu}_B(T)$ and $\rho_{B0}(T)$ (or $n_{B0}(T)$) may be written as

$$2,612\sqrt{\pi}(T_B^*)^{3/2} - \pi T_B^* \sqrt{2|\tilde{\mu}_B(T_B^*)|} = \frac{2\rho_{B0}(T)}{D_B}$$

$$+ 2,612\sqrt{\pi}T^{3/2} - \pi T\sqrt{2|\tilde{\mu}_B(T)|} \tag{A2.13}$$

$$\frac{\pi T_B^*}{\sqrt{2|\tilde{\mu}_B(T_B^*)|\xi_{BA}}} = \frac{\rho_{B0}(T)}{D_B|\tilde{\mu}_B(T)|\sqrt{\xi_{BA}}} + \frac{\pi T}{\sqrt{2|\tilde{\mu}_B(T)|\xi_{BA}}} \tag{A2.14}$$

from which after their combined solution and some algebra it follows the equation for $|\tilde{\mu}_B(T)|$ analogous as (A2.11) and the solution this equation near T_B^* has the form (4.21). Further substituting $|\tilde{\mu}_B(T)|/|\tilde{\mu}_B(T_B^*)|$ from (4.21) in (A2.13) gives (4.22). In the case of 2d-BG the first equation in (4.3) after going to the integration and substitution $x = \sqrt{(\varepsilon + |\tilde{\mu}_B|)^2 - \Delta_B^2}/2T$ has the form [49]

$$\frac{2}{\gamma_B} = \int_{x_1}^{x_2} \frac{\mathrm{cth} y \, \mathrm{d}y}{\sqrt{y2 + (\Delta_B^*)^2}} \tag{A2.15}$$

where $x_1 = \Delta_{SF}/2T$, $x_2 = \sqrt{(\xi_{BA} + |\tilde{\mu}_B|)^2 - \Delta_B^2}/2T$, $\Delta_B^* = \Delta_B/2T$. In the interval $x_1 < y < 1$ and $1 < y < x_2$ assuming $\mathrm{cth} y \sim 1/x$ and ~ 1, respectively, from (A2.15) we get

$$\frac{2}{\gamma_B} \simeq \ln\left\{\left[\frac{y_1(\Delta_B^* + \sqrt{1 + (\Delta_B^*)^2})}{\Delta_B^* + \sqrt{y_1^2 + (\Delta_B^*)^2}}\right]^{-(1/\Delta_B^*)}\left[\frac{y_2 + \sqrt{y_2^2 + (\Delta_B^*)^2}}{1 + \sqrt{1 + (\Delta_B^*)^2}}\right]\right\} \tag{A2.16}$$

At low temperature $\Delta_B^* \gg 1$, $y_2 \gg \Delta_B^*$ and $\Delta_B^* \gg y_1$. Then $\ln y_1$ is small and it can be neglected. In this case from (A2.15) approximately it follows

$$\frac{2}{\gamma_B} \simeq \ln\frac{2y_2}{1 + \Delta_B^*} \tag{A2.17}$$

from which after some algebra we obtain (4.27). While near T_B, $\Delta_B^* \ll 1$ and from (A2.16) we have (with an accuracy to $\sim(\Delta_B^*)^2$)

$$\frac{2}{\gamma_B} \simeq -\frac{1}{\Delta_B^*}\ln\left|\frac{y_1(1 + \Delta_B^*)}{y_1 + \Delta_B^*}\right| + \ln y_2 \tag{A2.18}$$

Further, assuming $y_2^{\Delta_B^*} \simeq 1$ and $\Delta_B^*/\gamma_B \ll 1$ from (A2.18) it follows

$$\frac{1 + \Delta_B^*/y_1}{1 + \Delta_B^*} \simeq \exp[2\Delta_B^*/\gamma_B) \simeq 1 + \frac{2\Delta_B^*}{\gamma_B} + \cdots$$

from which it follows

$$\Delta_B(T) = \gamma_B T\left[\frac{2T}{\Delta_{SF}(T)} - \frac{\gamma_B + 2}{\gamma_B}\right] \tag{2.19}$$

It is reasonable to assume that the $\Delta_{SF}(T)$ near T_B is changed as $\sim\alpha(2T)^q$ (whe determined at $T = T_B$ from the condition $\Delta_B(T_B) = 0$) with the variation param Then the $\Delta_B(T)$ and $|\tilde{\mu}_B(T)|$ is determined by (4.28) and (4.29).

Now we estimate the integrals (5.2) for $\Delta_{SF} < 2T$. After substitution $x = E_1$ assuming sh$t$ approximately to be equal to x and $1/2\exp(x)$ accordingly at $x <$ $x > 1$ one may obtain from (5.2)

$$c_v(T) \simeq 4\Omega D_B T\left\{\int_{y_1}^{1} \frac{x\mathrm{d}x}{\sqrt{x^2+(\Delta_B^*)^2}} + 4\int_1^{\infty} \frac{x^3\exp(-2x)\mathrm{d}x}{\sqrt{x^2+(\Delta_B^*)^2}}\right\} \quad (5.3)$$

We have done approximate estimations of the second integral ass $\sqrt{x^2+(\Delta_B^*)^2} \simeq \Delta_B^*$ (at low temperature) as the main contribution comes from a near lower limit of the integral, where $x \ll \Delta_B^*$. As a result one obtains (5.5). Fin $T = 0$ and $\Delta_{SF} = 0$ the integral (A2.15) is equal to

$$\frac{2}{\gamma_B} \simeq \ln\frac{2(\varepsilon+|\tilde{\mu}_B|)}{\Delta_B(0)} \quad (6.1)$$

While at $T = T_B$ the approximate estimation of the integral (A2.15) according above scheme gives

$$\frac{2}{\gamma_B} \simeq \int_{b_1}^{1}\frac{\mathrm{d}y}{y^2} + \int_1^{b_2}\frac{\mathrm{d}y}{y} = \frac{2T_B}{\tilde{\mu}_B(T_B)} - 1 + \ln\frac{\xi_{BA}}{2T_B} \quad (6.2)$$

where $b_1 = \tilde{\mu}_B/2T$, $b_2 = (\xi_{BA}+\tilde{\mu})/2T$. According to (4.29) at $T = T_B$, $\tilde{\mu}_B(T_B) = 2$ $(2+\gamma_B)$. Then, from (A2.21) and (A2.22) it follows (6.2).

References

[1] D R Tilley and J Tilley, *Superfluidity and superconductivity* (Mir, Moscow, 1977)
[2] J C Wheatley, *Physica* **C69**, 218 (1973)
[3] E A Lynton, *Superconductivity* (Mir, Moscow, 1971)
[4] D Rainer, *Phys. Scr.* **T23**, 103 (1988)
[5] D Jerome and H J Schulz, *Adv. Phys.* **32**, 299 (1982)
[6] B K Chakraverty, M Avignon and D Feinberg, *J. Less-Common Metals* **11**, 150 (1
[7] G Deutscher, *Phys. Scr.* **T29**, 9 (1989)
[8] A S Davidov, *Phys. Rep.* **190**, 193 (1990)
[9] D K Ray, *Indian J. Phys.* **A64**, 89 (1990)
[10] N F Mott, *Contemp. Phys.* **31**, 373 (1990)
[11] M L Cohen, *Int. J. Mod. Phys.* **B5**, 1495 (1991)
[12] N N Bogolubov, V V Tolmachev and D V Shirkov, *A new method in the th superconductivity* (Izd. Akad. Nauk SSSR, Moscow, 1958)
[13] J C Valatin and D Butler, *Nuovo Cimento* **10**, 37 (1958)
[14] W A B Evans and Y Imry, *Nuovo Cimento* **B63**, 155 (1969)
[15] A Coniglio, F Mancini and M Mturi, *Nuovo Cimento* **B63**, 227 (1969)
[16] R Hasting and J W Halley, *Phys. Rev.* **B12**, 267 (1975)
[17] W A B Evans and C G Harris, *J. Phys. Colloq. (Paris)* **C6, 39**, 237 (1978)
[18] P Dörre, H Haug and D B Tran Thoai, *J. Low Temp. Phys.* **35**, 465 (1979)
[19] P Noziers and D Saint Lames, *J. Phys. (Paris)* **42**, 1133 (1982)
[20] M J Rice and Y R Wang, *Phys. Rev.* **B37**, 5893 (1988)
[21] J M Wheatley, T C Hsu and P W Anderson, *Phys. Rev.* **B37**, 5897 (1988)
[22] W A B Evans, *Physica* **B165–166**, 513 (1990)

[23] D M Ginsberg (ed.), *Physical properties of high temperature superconductors I*, (World Scientific: Singapore, 1989) ch. 1
[24] Th Timusk and D B Tanner, *Physical properties of high temperature superconductors I*, edited by D M Ginsberg (World Scientific: Singapore, 1989) ch. 7
[25] Ch Thomsen and M Cardona, *Physical properties of high temperature superconductors I*, edited by D M Ginsberg (World Scientific: Singapore, 1989) ch. 8
[26] G M Eliashberg, *Physical properties of high temperature superconductors I*, edited by D M Ginsberg (World Scientific: Singapore, 1989) ch. 9
[27] N V Zavaritskii, *Usp. Fiz. Nauk* **160**, 177 (1990)
[28] E A Pashitsky, A E Pashitsky and A V Semenov, *Pis'ma v ZhETF*, **54**, 36 (1991)
[29] H Adrian, W Assmus and A Höhr *et al*, *Physica* **C162–164**, 329 (1988)
[30] D S Hirashima and T Matsuura, *J. Phys. Soc. Jpn.* **59**, 24 (1990)
[31] G Oya, M Aoyama, S Kishida and H Tokutaka, *Physica* **C185–189**, 2453 (1991)
[32] A S Alexandrov and A B Krebs, *Usp. Fiz. Nauk* **162**, 1 (1992)
[33] N Tsuda, D Ssimada and N Miyakawa, *Physica* **C185–189**, 1903 (1991)
[34] A A Bush, L I Leonyuk and T E Oskina *et al*, *Prog. in HTSC* **32**, 270 (1992)
[35] B N J Persson and J E Demuth, *Phys. Rev.* **B42**, 8057 (1990)
[36] M Boekholt, M Hoffmann and G Güntherodt, *Physica* **C175**, 127 (1991)
[37] S L Cooper, G A Tomas and J Orenstein *et al*, *Phys. Rev.* **B40**, 11358 (1989)
[38] J Fossheim, O M Nes and T Laegried *et al*, *Int. J. Mod. Phys.* **B1**, 1171 (1988)
[39] V B Lazarev, K S Gavrichev and V E Gorbunov *et al*, *Zh. Neor. Chem.* **35**, 3 (1990)
[40] H R Ott, H Rudigier, Z Fisk and J L Smith, *Phys. Rev.* **B31**, 1651 (1985)
[41] P Hakonen and O V Lounasmaa, *Physics Today*, February 70 (1987)
[42] G E Volovik, *Pis'ma v Zh. Exsp. Teor. Fiz.* **52** 972 (1990)
[43] P J Hakonen, M Krusins, M M Salomaa and J T Simola, *Phys. Rev. Lett.* **54**, 245 (1985)
[44] H Fukuyama, H I Shimoto, T Tazaki and S Ogawa, *Phys. Rev.* **B36**, 8921 (1987)
[45] Yu A Izyumov, N M Plakida and Yu N Skryabin, *Usp. Fiz. Nauk*, **159**, 621 (1989)
[46] D Emin and N S Hillery, *Phys. Rev.* **B39**, 6575 (1989)
[47] E G Maksimov and S Yu Savrasov, *Usp. Fiz. Nauk* **160**, 155 (1990)
[48] G Baskaran, E Tosatti and Y Lu, *Int. J. Mod. Phys.* **B2**, 255 (1988)
[49] S Dzhumanov and P K Khabibullaev, *Izv. Akad. Nauk Uzb. SSR, Ser. Fiz. Mat. Nauk*, **1**, 47 (1990); **2**, 53 (1990)
[50] S Dzhumanov, In *Abs. Int. Conf. on high temperature superconductivity and localization phenomena* (Moscow, USSR, 1991) p. T22
[51] S Dzhumanov, P J Baimatov and N I Rahmatov, In *Abs. 2nd Liquid Matter Conference* (Firenze, Italy, 1993) p. 117
[52] S Dzhumanov, *Physica* **C235–240**, 2269 (1994)
[53] S Dzhumanov, P J Baimatov, A A Baratov and N I Rahmatov, *Physica* **C235–240**, 2339 (1994)
[54] Ch B Lushchik and A Ch Lushchik, *Decay of electronic excitations with defect formation in solids* (Nauka, Moscow, 1989)
[55] E I Rashba, Excitons edited by E I Rashba and M D Sturge (North-Holland, Amsterdam, 1982) p. 543
[56] S Dzhumanov and P K Khabibullaev, *Phys. Status. Solidi.* **B152**, 395 (1989)
[57] Toyozawa, *Physica* **B116**, 7 (1983)
[58] D D Sarma and C N R Rao, *Synth. Metals* **33**, 131 (1989)
[59] B K Chakraverty, D D Sarma and C N R Rao, *Physica* **C156**, 413 (1988)
[60] V Vijayakrishnan, G U Kulkarni and C N R Rao, *Mod. Phys. Lett.* **B4**, 1451 (1990)
[61] A Martin-Rodero and F Flores, *Phys. Rev.* **B45**, 13008 (1992-II)
[62] M L Cohen, G Gladstone, M A Jensen and J R Schieffer, *Superconductivity in semiconductors and transition metals* (Mir, Moskow, 1972)
[63] M Singh and K P Sinha, *Solid State Commun.* **70**, 149 (1989)
[64] K P Sinha and M Singh, *Phys. Status. Solidi.* **B159**, 787 (1990)
[65] J R Schrieffer, X G Wen and S C Zhang, *Phys. Rev.* **B39**, 11663 (1989)
[66] J B Goodenough and J Zhou, *Phys. Rev.* **B42**, 4276 (1990)

[67] Yu P Monarkha and S S Sokolov, *Fiz. Nisk. Temp.* **16**, 164 (1990)
[68] E M Lifshitz and L P Pitaevskii, *Statistical physics* (Nauka, Moscow, 1978)
[69] R A Cowley and A D B Woods, *Can. J. Phys.* **49**, 177 (1971)
[70] S Dzhumanov, P J Baimatov and P K Khabibullaev, *Uzb. Zh. Phys.* **6**, 24 (1992)
[71] S Dzhumanov and P J Baimatov, Preprint (1991)
[72] I V Bogoyavlensky, L V Karnatsevich, G A Kozlov and A V Puchkov, *Fiz. Nisk. Temp.* **16**, 139 (1990)
[73] S Dzhumanov and P J Baimatov, *Uzb. Zh. Phys.* **4**, 28 (1991)
[74] P N Brusov and V N Popov, *Superfluidity and collective properties of quantum liquids* (Nauka, Moskow, 1988)
[75] J F Annett, *Adv. Phys.* **39**, 83 (1990)
[76] V N Morgun, N N Chebotarev and A V Bondarchenko, *Fiz. Nisk. Temp.* **16**, 264 (1990)
[77] M Lee, M Naito, A Kapitulnik and M R Beasley, *Solid State Commun.* **70**, 449 (1989)
[78] R Escudero, F Morales, F Estrada and R Barrio, *Mod. Phys. Lett.* **B3**, 73 (1989)
[79] M B Maple, *Physics Today March* 72 (1986)
[80] K Kanoda, K Akiba, K Suzuki and T Takahashi, *Phys. Rev. Lett.* **65**, 1271 (1990)
[81] H R Ott, *Physica* **C162–164**, 1669 (1989)
[82] S E Inderhees, M B Salamon and N Goldenfeld, *Phys. Rev. Lett.* **60**, 1178 (1988)
[83] A Cold, *Physica* **C190**, 483 (1992)
[84] B Pümpin, H Keller and W Kündig *et al*, *Phys. Rev.* **B42**, 8019 (1990)
[85] J Annett, N Goldenfeld and S R Renn, *Phys. Rev.* **B43**, 2778 (1991)
[86] I I Mazin, O V Dolgov, A Golubov and S V Shulga, *Phys. Rev.* **B47**, 538 (1993-I)
[87] A I Sokolov, *Superconductivity: Physica, Chemistry, Technika* **5**, 1794 (1992)
[88] R C Yu, M J Naughton and X Yan *et al*, *Phys. Rev.* **B37**, 7963 (1988)
[89] D Mihailovich, C M Foster, K Voss and A J Heeger, *Phys. Rev.* **B42**, 7989 (1990)
[90] J F Phillips, *Physics of high-T_c superconductors* (Academic Press, San Diego, 1989)
[91] N F Mott, *Physica* **C205**, 191 (1993)
[92] A Kallio, V Apaja and X Xiong, *Physica* **C191**, 23 (1992)
[93] C C Tsuei, J R Kirtley and C C Chi *et al*, *Phys. Rev. Lett.* **73**, 593 (1994)
[94] K A Moler, D J Boar, J S Urbach *et al*, *Phys. Rev. Lett.* **73**, 2744 (1994)
[95] R Haussman and V Dohn, *Phys. Rev. Lett.* **72**, 3060 (1994)
[96] M Luban, *Phys. Rev.* **128**, 965 (1962)

physics

November 1995
pp. 419-430

emperature dependence electron spin resonance spectra of a agnetic fluid

V UPADHYAY, D SRINIVAS +, R V MEHTA and P M TRIVEDI
epartment of Physics, Bhavnagar University, Bhavnagar 364 002, India
Central Salt and Marine Chemical Research Institute, Bhavnagar 364 002, India

S received 27 February 1995; revised 3 August 1995

stract. ESR spectra of a laboratory synthesized kerosene base magnetic fluid containing rafine magnetic particles (average diameter of 100 A) of $Zn_{0.1}Fe_{0.9}Fe_2O_4$ are recorded at fferent temperatures. A narrow signal was observed above the melting point of the carrier uid (200 K) which can be attributed to a very small volume fraction of superparamagnetic rticles in the system. The peak-to-peak line width for both low and high field cooled nfigurations show an increase with decreasing temperature. This observed behaviour has been plained by considering various energy terms which contribute to the line width.

ywords. Magnetic fluid; ESR; temperature dependence.

ACS Nos 76·50; 75·50; 75·60; 75·30

Introduction

erically stabilized colloidal dispersions of ultra-fine single domain ferro- or ferri-agnetic particles resemble superparamagnetic materials at room temperature. These lloids called magnetic fluids or ferrofluids do not exhibit hysteresis behaviour or ercivity [1]. Under the action of externally applied gradient magnetic fields such fluid can develop structural order similar to those in crystalline solids [2] or dipolar asses [3] and hence it can serve as a model system to study characterization of ndensed materials. Magnetic and Mössbauer measurements have been extensively ed to study the superparamagnetic behavior of particles dispersed in liquid carriers –8]. It has been demonstrated that electron spin resonance (ESR) is a complimentary ol for the investigation of ultra-fine colloidally dispersed magnetic particles [8–11]. sually, ESR spectra of magnetic fluids are recorded at room temperature and eak-to-peak linewidth (ΔH_{pp}) and the resonance field (H_r) are also reported for perparamagnetic particles dispersed in solidified kerosene [12]. A magnetic fluid hibits both superparamagnetism at one temperature (above the melting point of the rrier liquid, T_m) and may exhibit magnetic anisotropy at lower temperatures epending upon the particle size [1]. Hence it will be of interest to investigate the mperature dependence of ΔH_{pp} from room temperature to well below the melting oint of the carrier.

In this paper we report the results of our investigation of ESR spectra of a laboratory nthesized magnetic fluid, $Zn_{0.1}Fe_{0.9}Fe_2O_4$ for different temperatures.

2. Experimental

There are a number of preparation methods available for the synthesis of fine particles [13–17]. In the present case we have used the co-precipitation techni prepare ultra-fine particles of $Zn_{0\cdot1}Fe_{0\cdot9}Fe_2O_4$. Analytical reagent $FeCl_3 6H_2O$, $ZnCl_2$ and $FeSO_4 7H_2O$ were used to obtain Fe^{3+}, Zn^{2+} and Fe^{2} in the aqueous solution. An aqueous solution containing these ions in the appr molar proportions ($Fe^{3+}:Fe^{2+}:Zn^{2+} = 2:0{\cdot}9:0{\cdot}1$) was added to 8M NH_4OH s at room temperature under constant stirring. The pH was adjusted to 10·5. A hour, aliquot of the reaction mixture was collected for X-ray and EDAX studies acid was added to the mixture and the fluid was again stirred for one hour, which time the pH was kept at 10·5. The fluid was then heated to 90°C for 5 m cooled to room temperature (2°C/min). The sample was washed a number of tim distilled water and finally washed with acetone. This acetone wet slurry was dis in kerosene and heated to 65°C, in order to remove acetone. The sample wa below 200 K and liquid above this temperature.

The percentage substitution of Zn was verified by EDAX and found $9{\cdot}8 \pm 0{\cdot}3\%$. To characterize the formation of single phase spinel structure, diffraction pattern was recorded using Philips X-ray diffractometer with CuK ation. The structure was found to be single phase fcc spinel structure with a parameter of 8·36 A (figure 1). The average particle size was calculated using Sch formula, using the full width at half maximum intensity of the plane (3 1 1) pattern. The value thus obtained (after accounting for the instrumental line br ing) was 100 A. The specimen was also examined under AEI Cornith Transm Electron Microscope (TEM). The particles were found to be almost spherica

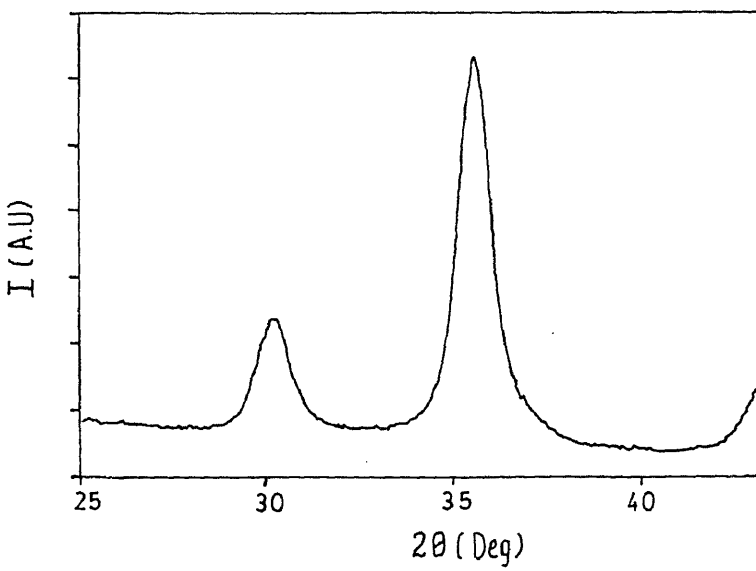

Figure 1. X-ray diffractogram of Zn-substituted ferrite sample (ZFO).

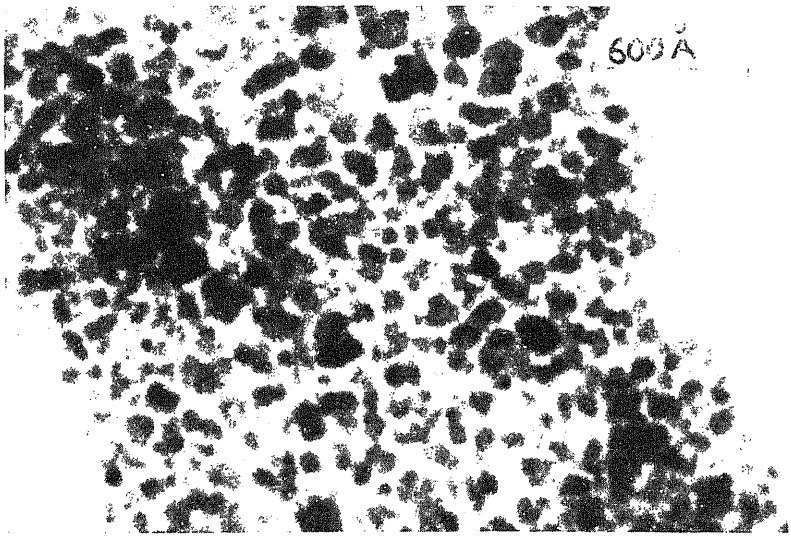

Figure 2a. Electron micrograph of ZFO sample.

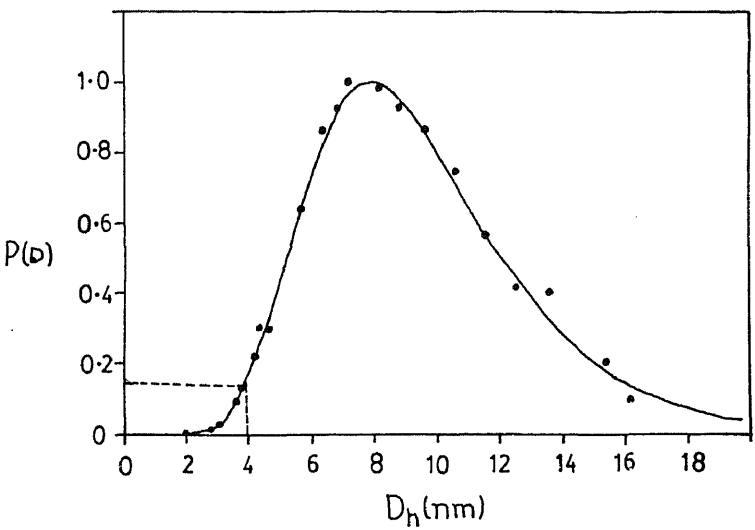

Figure 2b. Particle size distribution for ZFO sample. ● Expt. points. —Log-normal distribution.

average median diameter (Dm) of 90 A and standard deviation (σ) 0·36. Figure 2b shows the particle size distribution pattern using these values.

Room temperature magnetization measurements were carried out using search coil method [18]. Figure 3 shows the reduced magnetization (M/M_s) versus applied field (H) for the $Zn_{0.1}Fe_{0.9}Fe_2O_4$ magnetic fluid (ZFO) at room temperature. To describe

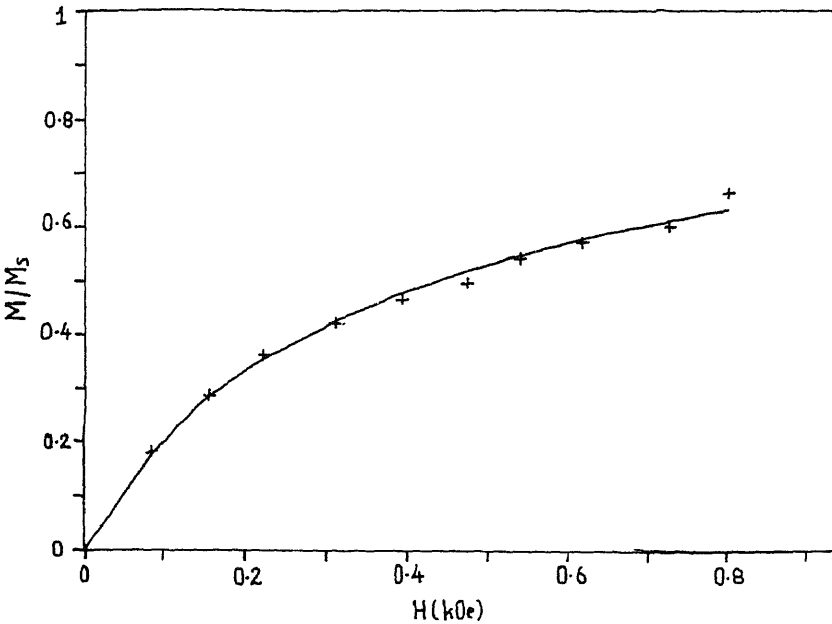

Figure 3. Room temperature M/M_s vs H. Line through the data point is a th cal fit using $Dm = 98$ Å and $\sigma = 0{\cdot}38$ [19].

the magnetization of the magnetic fluids several theoretical models are being use but the simplest one is Langevin's model. Using this model and our earlier m [20,21] M/M_s was calculated for each value of H. Fit to the data points in fi yielded the values of median diameter, standard deviation, and M_s (saturation ma ization of the fluid) as 98 A, 0·38 and 150 G, respectively.

ESR spectra were recorded using an X-band Bruker ESP-200 spectrometer. temperature cryogenic system attached with Bruker ER 4111 temperature con model was used to vary the temperature from 100 K to room temperature (300 K original fluid of 150 G was diluted 10 times in kerosene and two sets of data recorded. In one set the sample was cooled to 77 K in the residual field of 100 Oe while, in the second set the fluid was cooled in 1·1 kOe from room temperature to In both cases, the spectra were recorded during the heating cycle. Finally, ESR s of coated particles were recorded at 300 K and 77 K.

3. Results and discussion

3.1 *Lineshape analysis*

The conventional approach in analyzing the width and lineshape of a reso absorption curve is to use either the Lorenzian or Gaussian lineshape. The difference between these two is, Lorenzian lineshape is slightly sharper in the cent decreases much more slowly in the wings beyond the half amplitude or first deri

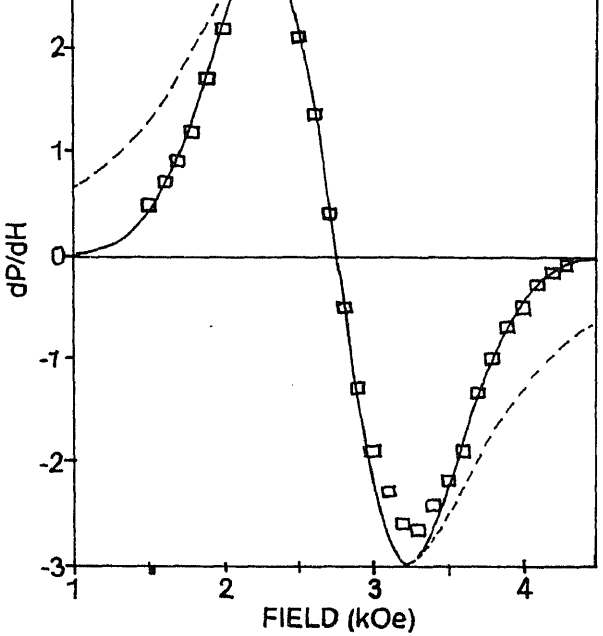

Figure 4. ESR curve of 125 K. – – – Lorentzian fit. ——Gaussian fit. □ expt. points.

points. This can be confirmed by using the value of peak amplitude, A_p, ΔH_{pp} and H_r deduced from experimental resonance curve. Figure 4 shows a resonance curve at 125 K with two different lineshapes. It is evident from the figure that the Gaussian lineshape given by [14],

$$dP/dH = A_p X \exp[-1/2(X^2 - 1)] \tag{1}$$

agrees well with the experimental points, where $X = (H - H_r)/(1/2\Delta H_{pp})$ and H = applied field. Throughout this work we have deduced values of H_r, ΔH_{pp} and A_p from the best fit to the data.

3.2 *Resonance spectra* $T > T_m$

Resonance spectra of the coated powder show an asymmetric line broadening (figure 5) both at 77 K and 300 K. The observed line broadening in the sample may arise due to random orientation of the easy axes, the interparticle dipolar interactions and to unresolved magnetostatics modes. But the spectrum becomes less asymmetric when the same particles are dispersed in liquid carrier like kerosene. This indicates that the deviation of easy axes from the applied field direction are reduced (this is because of Brownian motion of the particles). It was also observed that the line width decreases with dilution (varies from 857 Oe for the most concentrated fluid to 650 Oe for ten times

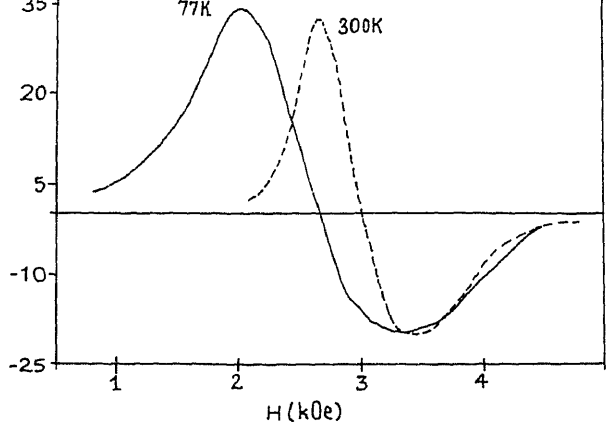

Figure 5. Resonance spectra of coated powder at 300 K and 77 K.

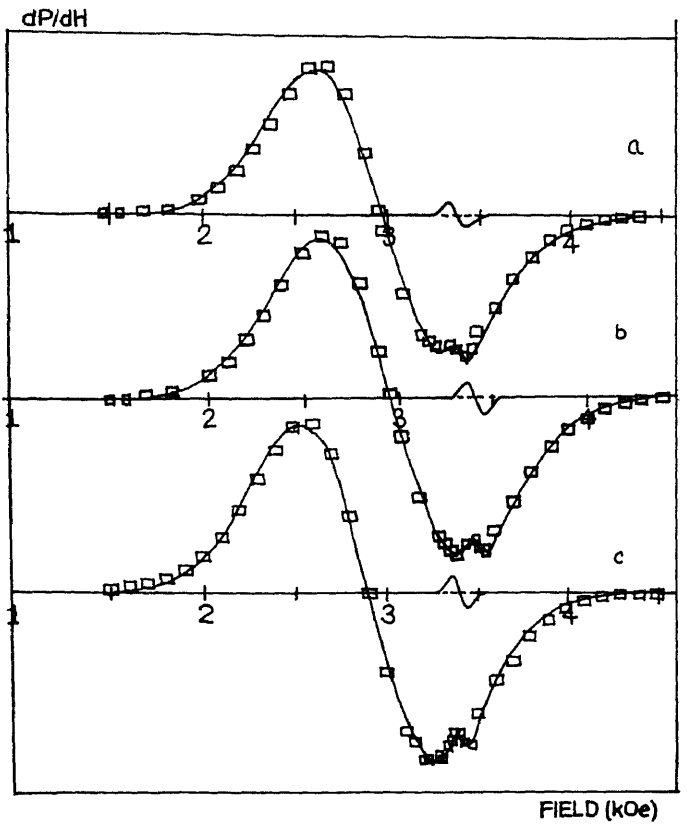

Figure 6. Typical ESR spectra for low field cooled sample ($T > T_m$). —— theoretical points using eq. (1). □ is expt. points (a) 214 K, (b) 235 K, (c) 245 K.

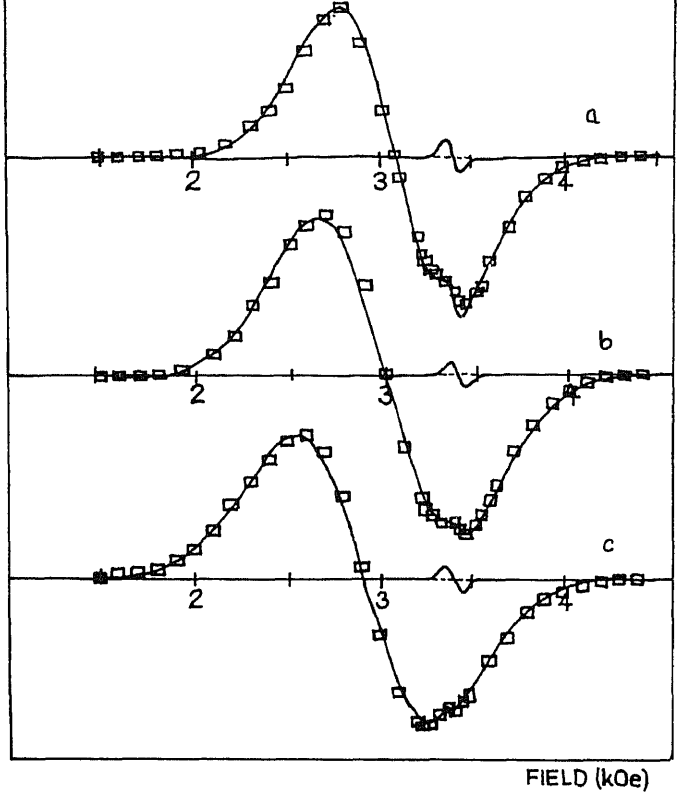

Figure 7. Typical ESR spectra for high field cooled sample ($T > T_m$) (a) 235 K, (b) 265 K, (c) 297 K.

diluted fluid). This decrease in line width may be due to decrease in interparticle dipolar field. Similar behaviour was also observed by Sharma and Waldner [9]. Figures 6 and 7 show some typical ESR spectra for LFC and HFC samples, respectively, for $T > T_m$. In both the cases, an additional narrow line was observed in the vicinity of the minimum. A notable feature in the above spectra is a systematic shift of the kink from left to right of the minima. This kink disappeared below the melting point of the carrier (figures 8 and 9).

Sharma and Waldner [9] observed a narrow line for Fe_3O_4 ferrofluid in a non-aqueous medium. They found [9] that the width of this narrow line is dilution-sensitive. The reason for this observed dilution sensitive width is due to the reduction in interparticle dipolar interaction upon dilution. From the present spectra (figures 6 and 7) it is very difficult to say whether the width of the narrow line is temperature sensitive or not. There are two possible sources which can give a narrow line in ESR spectra; (i) presence of free radicals either in the coating liquid or paramagnetic impurities in carrier liquid and (ii) superparamagnetic resonance because of the presence of very fine

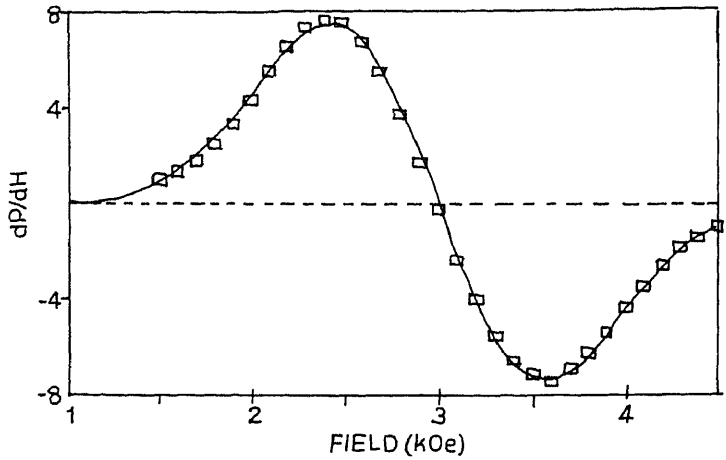

Figure 8. ESR spectra of LFC sample ($T < T_m$) $T = 121$ K.

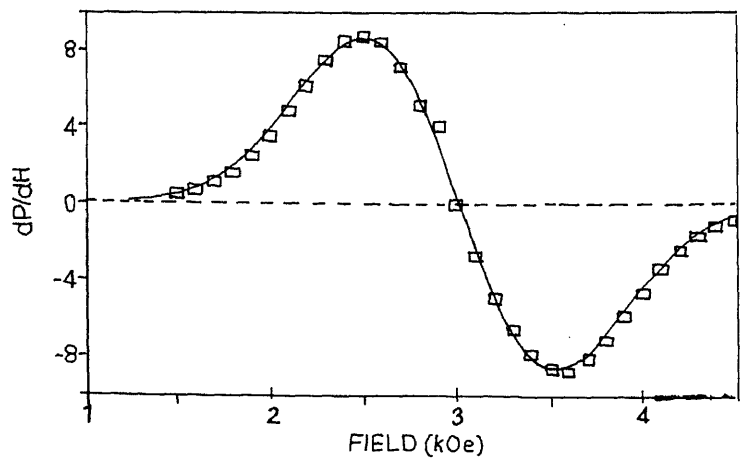

Figure 9. ESR spectra of HFC sample ($T < T_m$) $T = 155$ K.

particles in the system. The ESR spectra of surfactant and carrier show the absence of a narrow line which supports that this line is not due to free radicals or any paramagnetic impurities. Therefore, the only possible reason for this narrow line will be due to very small fraction of very fine particles, which gives superparamagnetic resonance effect at a given temperature and field.

In a magnetic fluid two relaxation mechanisms can occur (i) Brownian rotational diffusion characterized by relaxation time [22],

$$t_B = (3V_h\eta)/kT \tag{2}$$

and (ii) by Neel relaxation with relaxation time [23–24],

$$t_N = t_0(KV/kT)^{1/2}\exp(KV/kT) \quad \text{for} \quad KV/kT > 2 \tag{3}$$

$$= t_0(KV/kT) \quad \text{for} \quad KV/kT \ll 1. \tag{4}$$

where, V_h and V are the effective hydrodynamic and magnetic volumes of the particles, respectively. η is the viscosity of the fluid, K is the anisotropy constant, k is the Boltzmann constant and the pre-exponent factor t_0 has a value of approximately 10^{-9} s. Therefore, the dominant mode of magnetization process of the particle will be that which has the shortest relaxation time. In fact, large particles relax via Brownian rotation while, small particles through Neel rotation [1]. As ferrofluids contain a distribution of particle sizes both mechanism will, in general, contribute to the magnetization for $T > T_m$ with an effective relaxation time [25]

$$t_{eff} = t_N t_B/(t_N + t_B) \tag{5}$$

and superparamagnetic (SP) behavior will be exhibited by those for which t_N is much less than the characteristic Larmor precession time. Aharoni [26] has considered the effect of external magnetic field on SP relaxation time, because the field polarizes the large particles and reduces the size for SP behavior. However, the extremely small particles cannot be quenched unless a very large magnetic field is applied. Therefore, one expects a narrow magnetic resonance signal if a sample contains extremely small particles which are SP state in an applied field, H. Of course the width of the line may further reduce depending upon the viscosity of the fluid (equations 3 and 4).

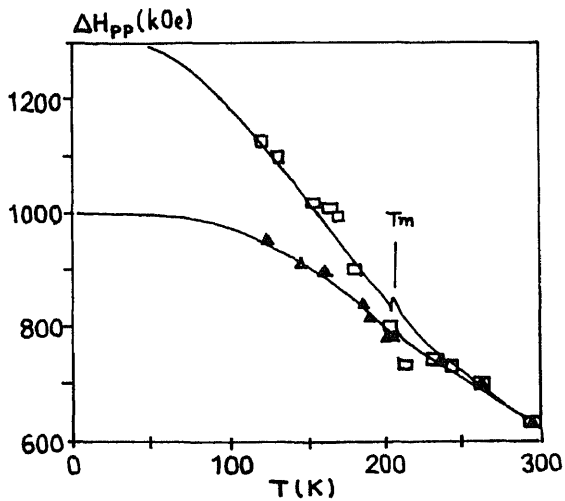

Figure 10. Variation of peak-to-peak line width for LFC (□) and HFC (Δ) samples, Line is fit to the eq. (14). The values used are i) L(LFC) = 1·45 kOe, L(HFC) = 1·0 kOe. ii) $B' = 5 \times 10^{-19}$ erg. iii) $F' = 0{\cdot}5$ K. iv) $KV = 3{\cdot}9 \times 10^{-14}$ erg. v) $Ed = 1{\cdot}4 \times 10^{-18}$ erg. vi) JmH (LFC) = $5{\cdot}2 \times 10^{-17}$ erg. JmH (HFC) = $2{\cdot}62 \times 10^{-14}$ erg [27].

In the case of very small particles, anisotropy energy (KV, where K is an anisotropy constant and V is the volume of the particle) is much smaller than the thermal energy (kT). Therefore the response time of the magnetic moments to random thermal force will be [23]

$$t_{sp} = M_s V/gkT \tag{6}$$

where, M_s is the saturation magnetization, g = gyromagnetic ratio. If this fluctuation is faster than Larmor precession time t_L, effects of magnetocrystalline anisotropy are motionally averaged out roughly by a narrowing factor, $f = t_{sp}/t_L$ which is equal to [9]

$$f = (M_s V H_r)/(2\pi kT). \tag{7}$$

From (7), it is clear that line width of SP resonance would be proportional to the volume of the particles. This is confirmed by Aharoni and Litt [27]. Adopting the procedure of Sharma and Waldner [9] in the present case, the particle size corresponding to the observed line width will be 41 A (neglecting the interparticle dipolar fields) for coated particles which is around 1·2% volume fraction of the particles in the system (this is obtained from particle size distribution curve for the present sample, figure 2b). This agrees with the observed 1% magnitude of SP-phase in comparison with the broad signal. All the above observations are consistent with the presence of small fraction of very fine magnetic particles in the system.

3.3 *Line width analysis*

Experimental points of peak-to-peak line width (ΔH_{pp}) for LFC and HFC configurations are shown in figure 10. The line width increases with decrease in temperature. The observed variation can be explained as follows.

Let us first consider a model of regularly spaced magnetic centres dispersed in a non-magnetic matrix and they are SP particles, i.e. net spin $\Delta nS \gg 0$, where Δn is the net population of spin aligned along the easy axis of magnetization and S is the effective spin of the magnetic centres. Assuming the presence of two level system, one can write the ESR line width as [19]

$$\Delta H_{pp} = L \tanh[\Delta E/2kT] \tag{8}$$

and

$$L = 5g\beta Sn/R^3, \tag{9}$$

where $g = g$-factor, β = Bohr magneton, n = total number of magnetic centres, R = distance between the adjacent particles and E is the energy barrier. Therefore the line width depends upon R and ΔE, which in turn depends on the particular system under study. In the present investigation, we are studying the effect of temperature on the system. Therefore, R remains unchanged and the main contribution to line width will be ΔE term. This makes us to consider the effect of various terms which contributes to ΔE.

As the system is in liquid state above the melting point of the carrier ($T_m \approx 200$ K), one can write ΔE as

$$\Delta E = E_v + E_a + E_m + E_d. \tag{10}$$

The first term in (10) is the energy of Brownian-orientational motion i.e. viscosity energy (E_v), which can be written as

$$E_v = 3\theta\eta V_h, \tag{11}$$

where θ is a coupling constant. As T approaches T_m, the magnetic particles can relax via Brownian rotation in addition to Neel which makes viscosity of the liquid an important parameter. The viscosity study of this fluid (ZFO) indicates that fluid is Newtonian and the change in viscosity with temperature can be described by the Andrade's equation

$$\eta = B\exp[F/\{R_g(T - T_m)\}]. \tag{12}$$

Here, B is a constant. F and R_g are apparent activation energy for the flow and universal gas constant, respectively. Substituting (12) into (11), the viscosity energy is

$$E_v = B'\exp[F'/(T - T_m)], \tag{13}$$

where $B' = 3\theta V_h B$ and $F' = F/R_g$.

The second term, E_a, is simply KV while E_m is JmH, where J is a coupling constant and m is the magnetic moment. Substituting all these values in (10), we can write (8) as,

$$\Delta H_{pp} = L\tanh[(1/2kT)\{B'\exp(F'/(T - T_m)) + KV + JmH + Ed\}]. \tag{14}$$

The line through the data points in figure 10 is the best fit to (12). It was found that KV remains constant for LFC and HFC samples, but JmH changes dramatically (nearly 500 times). This is due to the fact that as the system is frozen in the field of 1·1 kOe, the large number of particles is oriented in the direction of applied field and hence large value of JmH. The decrease in the value of ΔH_{pp} also supports this concept, because for more ordered state the thermal energy required to create a disorder is large. Therefore the line width will remain constant for larger temperature region. This is true for multidomain structure, where the ΔH_{pp} remains nearly constant till the Curie temperature is reached [24]. The observed discontinuity in the curve indicates the effect of viscosity on the line width. A remarkable feature in figure 10 is that above the melting point of the carrier, the variation of line width is the same for LFC and HFC samples which shows the validity of eq. (5).

4. Conclusion

The present study reveals that (i) A narrow line observed in room temperature and above melting point of the carrier is attributed to a very small volume fraction of particles present in the system. (ii) The percentage of very small particle volume fraction agrees well with particle size obtained from electron micrograph. (iii) Line width increases with decreasing temperature for both low and high field cooled samples.

Acknowledgements

Authors are thankful to Dr S W Charles, Department of Chemistry, UCNW, Bangor UK for providing experimental facilities. They are also thankful to UGC and British Council for ALIS programme and DST for financial assistance.

References

[1] S W Charles and J Popplewell, in *Ferromagnetic materials*, Edited by E P Wohlfarth Holland, Amsterdam, 1980) **2**, 509
[2] S D Bhagat and R V Mehta, *Indian J. Pure Appl. Phys.* **30**, 84 (1992)
[3] K O'Grady, J Popplewell and S W Charles, *J. Magn. Magn. Mater.* **39**, 56 (1983)
[4] A E Berkowitz, J A Lahut and C E Van Buren, *IEEE Trans. Magn.* **16**, 184 (1980)
[5] A Tari, J Popplewell and S W Charles, *J. Magn. Magn. Mater.* **15–18**, 1125 (1980)
[6] M El-Hilo, K O'Grady and R W Chantrell, *J. Magn. Magn. Mater.* **114**, 295, 307
[7] A E Berkowitz, J A Lahut, I S Jacobs and L M Levinson, *Phys. Rev. Lett.* **34**, 594
[8] J Tajada, X X Zhang and L Balcells, *J. Appl. Phys.* **73**, 6709 (199.)
[9] V K Sharma and F Waldner, *J. Appl. Phys.* **48**, 4298 (1977)
[10] S P Vaidya, R V Mehta and J M Patel, *Physics of magnetic materials*, Edi M Takahashi *et al* (World Scientific, 1987) 350
[11] A L Tronconi, P C Moraris, F Pelegrini and F A Tourinho, *J. Magn. Magn. Mater.* (1992)
[12] K Nagata and A Ishihara, *J. Magn. Magn. Mater.* **104–105**, 1571 (1992)
[13] G M Sutaria, R V Upadhyay and R V Mehta, *J. Colloidal Interface Sci.* **155**, 152
[14] T Miahara and K Wawakauri, *IEEE Trans. Magn.* **MAG-23**, 2877 (1987)
[15] G Xiao and C L Chien, *J. Appl. Phys.* **61**, 3308 (1987)
[16] C Hayashi, *J. Vac. Sci. Technol.* **A5**, 1375 (1987)
[17] V Pillai, P Kumar and D O Shah, *J. Magn. Magn. Mater.* **116**, L299 (1992)
[18] M I Shliomis, A F Pshenichnikov, K I Morozov and I Yu Shurubor, *J. Magn. Mater.* **85**, 40 (1990)
[19] R V Upadhyay and R V Mehta, *Pramana – J. Phys.* **41**, 429 (1993)
[20] W F Brown, *J. Appl. Phys.* **34**, 1319 (1963)
[21] W F Brown, *Phys. Rev.* **130**, 1677 (1963)
[22] L Neel, *Ann. Geophys.* **5**, 99 (1949)
[23] M I Shliomis, *Sov. Phys. USP* **17**, 53 (1974)
[24] A Ahroni, *Phys. Rev.* **177**, 793 (1969)
[25] S M Ahroni and M H Litt, *J. Appl. Phys.* **42**, 352 (1971)
[26] P C Moris, M C L Lara and K S Neto, *Philos. Mag. Lett.* **55**, 181 (1987)
[27] These values are in good agreement with the reported values of K and F using diameter of 90 Å. The value of K was found to be $1{\cdot}0 \times 10^5$ erg/cc and the value o 4 kCal/Mole [13]

— Journal of physics

November 1995
pp. 431–438

Dielectric properties of nano-particles of zinc sulphide

BINNY THOMAS and M ABDULKHADAR
School of Pure and Applied Physics, Mahatma Gandhi University, Priyadarsini Hills P O, Kottayam 686 560, India

MS received 9 November 1994; revised 2 August 1995

Abstract. The dielectric properties of nano-particles of ZnS have been studied over a temperature range from 300 to 525 K. The dielectric constant, dielectric loss and ac conductivity of the samples are larger than those of bulk ZnS crystals. Dielectric properties of composites consisting of nano-particles of Ag of different concentrations dispersed in nano-particles of ZnS have also been studied.

Keywords. Nano-particles; quantum size effect; semiconductors.

PACS Nos 82·70; 73·20; 72·20

1. Introduction

The synthesis and characterization of small particles of materials is currently an area of intense theoretical and experimental research. The revelation that physical properties of such systems are bound to be appreciably different from those of the bulk crystals excited much interest in the study of micro-materials termed nano-particles, small particles, clusters, microclusters or microcrystals [1–3]. Quantum size effect of confinement of electron in small particles has been theoretically predicted. It is expected that quantum size effect on electronic properties will be pronounced in mesoscopically small crystals and that electrical conductivity of small particles may be affected by a three dimensional quantum size effect [4–6]. Experimental studies on the electrical properties of nano-particles are limited [7]. The present paper reports the dielectric properties of nano-particles of ZnS and those of composites of nano-particles of Ag of different concentration dispersed in the former, over a temperature range of 300 to 525 K.

2. Experimental

Nano-particles of ZnS were prepared by chemical method taking into advantage its very small solubility in water. All the chemicals used were of analytical grade and were used without further purification. Freshly prepared aqueous solutions of chemicals were used for synthesis. Nano-particles of ZnS were prepared at room temperature by dropping simultaneously 10 ml of 1 M solution of zinc sulphate and 10 ml of 1 M solution of sodium sulphide into 80 ml of distilled water containing 10 ml 0·1 M solution of ethylene diamine tetraacetic acid (EDTA) which was kept stirred vigorously using a magnetic stirrer. The high insolubility of ZnS formed out of the chemical reaction caused the formation of a number of new nuclei while preventing the growth of

Table 1. Composition of pellets mixed with nano-particles of Ag.

Sample	Wt% of Ag	Sample code
ZnS	0	ZnS-0
	5	ZnS-1
	15	ZnS-2
	20	ZnS-3

already existing ones, thus limiting the particle size. The role of EDTA was to stabilize the particles against aggregation which may lead to an increase in the particle size. Nano-particles of silver were prepared according to Lee and Meisel's [8] method.

Composite samples were prepared by dispersing in distilled water by ultrasonication different weight percentages (wt%) of nano-particles of Ag and ZnS. The suspensions were concentrated by evaporating off the liquid phase. The particles were washed repeatedly using distilled water with the help of an ultrasonic disintegrator to remove any adsorbed ions. The particles were finally dried at about 100°C. Pellets of nano-particles of ZnS, and composite pellets with nano-particles of Ag dispersed in ZnS, of diameter 13 mm and thickness 1–2 mm were made by applying a pressure of 4 tonnes/cm^2 in a hand operated hydraulic press. Both the faces of pellets were then coated with silver electrodes for electrical measurements. For the purpose of reference, sample codes were assigned to the pellets as in table 1.

The crystal structure of particles was determined by X-ray powder diffraction using a Shimadzu XD 610 powder diffractometer. The average size of the particles was determined from the broadening of the diffraction lines and making use of Scherrer equation [9]. The diffraction pattern of ZnS nano-particles displayed three intense lines, corresponding to the wurtzite (8H) structure, confirming the crystallinity of the particles [10]. The X-ray diffraction pattern of the silver particles revealed three strong characteristic peaks of Ag. The average sizes of the particles determined from X-ray line broadening were 8 and 12 nm respectively for ZnS and Ag nano-particles. The diffraction peaks of the nano-particles were found to be shifted to slightly larger angles than expected for the corresponding bulk crystals, suggesting a possible lattice contraction [11].

Dielectric constant ε, dielectric loss (tan δ), and ac conductivity σ_{ac}, of the samples were determined using a Hewlett Packard Model 4192A LF impedance analyzer. Dielectric constant, dielectric loss and ac conductivity measurements at different frequencies from 10 kHz to 13 MHz were carried out over a temperature range of 300 to 525 K.

3. Results

The variations of dielectric constant ε, dielectric loss (tan δ) and ac conductivity σ_{ac} of the samples as a function of frequency and temperature are shown in figures 1 to 3. The numerical values of dielectric constant of the samples at different temperatures and frequencies are given in table 2. It is seen that ε of ZnS-0 is almost independent of frequency at low temperatures (figure 1a), showing a very slow decrease with frequency

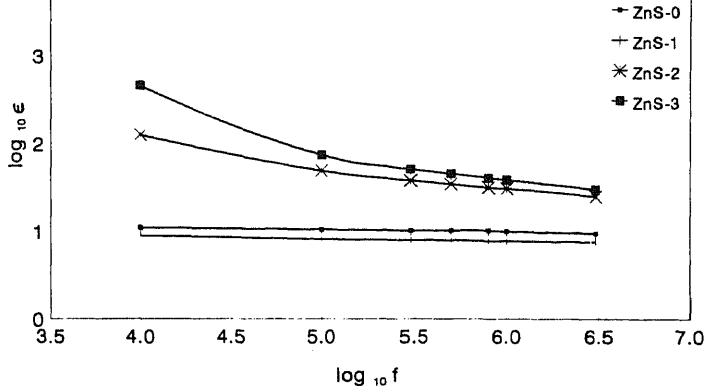

Figure 1a. Variation of dielectric constant at 343 K with frequency of nano-particles of ZnS and composites with different wt% of nano-particles of Ag.

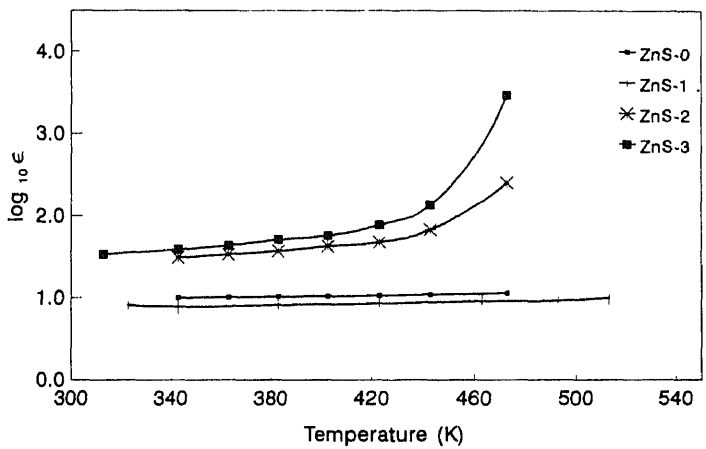

Figure 1b. Variation of dielectric constant at 1 MHz with temperature of nano-particles of ZnS and composites with different wt% of nano-particles of Ag.

from 10·9 at 10 kHz to 9·54 at 3 MHz. The general trend in the log ε vs frequency graph at higher temperature is similar but the rate of decrease in the value of ε with frequency is larger at high temperatures. ε of ZnS-1 is slightly lesser than that of ZnS-0, but increases with increase in the wt% of Ag. At a frequency of 10 kHz, ε of ZnS-2 was as high as about 127 and 7220 respectively at 343 and 473 K, the values for ZnS-3 being 459 and 12400 respectively. ε of all the samples, at low as well as high frequencies, increased with temperature, the rate of increase being strongly temperature dependent for ZnS-2 and ZnS-3 samples (figure 1b). The numerical value of ε of ZnS-0 at 1 MHz increased at a low rate from 10·1 at 343 to 11·4 at 473 K. The large values of ε for ZnS-2 and ZnS-3, although appear to be anomalous at first glance, may be considered to be

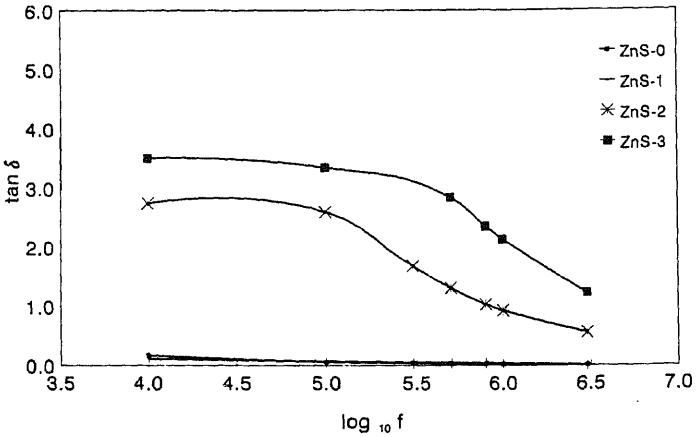

Figure 2a. Variation of dielectric loss factor at 423 K with frequency of nano-particles of ZnS and composites with different wt% of nano-particles of Ag.

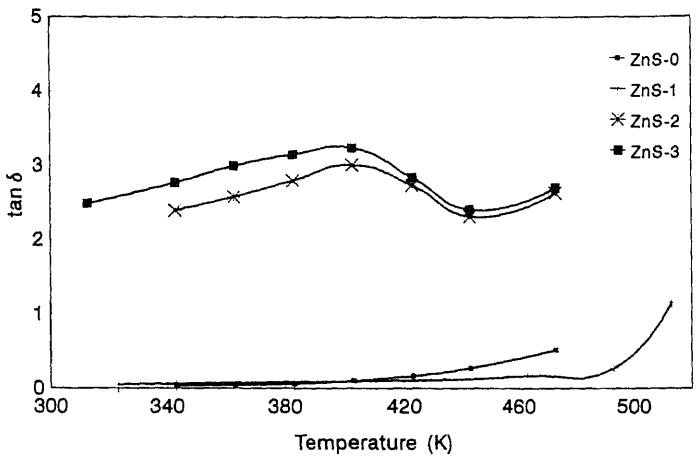

Figure 2b. Variation of dielectric loss factor at 10 kHz with temperature of nano-particles of ZnS and composites with different wt% of nano-particles of Ag.

representing the actual behaviour of the samples from the fact that they vary regularly with frequency and temperature.

The value of tan δ decreased with frequency (figure 2a), the rate of decrease being larger at larger frequencies. Tan δ of ZnS-0 and ZnS-1 had low numerical values but increased with wt% of Ag in the samples, attaining a value of about 2 to 3 at lower frequencies. Tan δ increased only slightly with temperature for ZnS-0 and ZnS-1, but for ZnS-2 and ZnS-3 it was strongly frequency- and temperature-dependent. At lower frequencies, it increased with temperature slowly from a large value of about 2, attaining a maximum value of about 3, then decreased and again showed a tendency to increase (figure 2b).

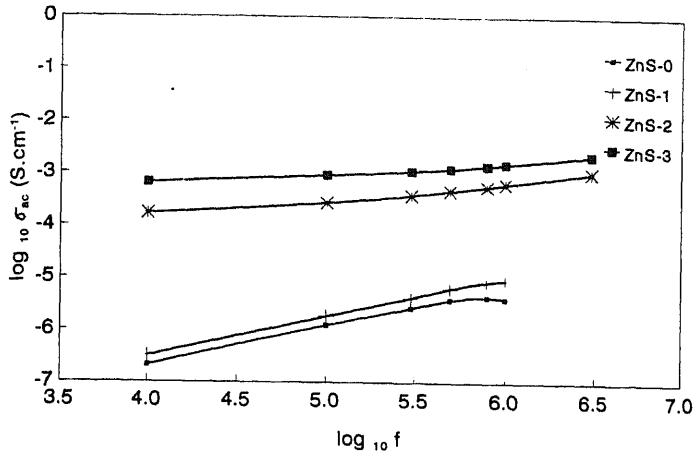

Figure 3a. Variation of ac conductivity at 343 K with frequency of nano-particles of ZnS and composites with different wt% of nano-particles of Ag.

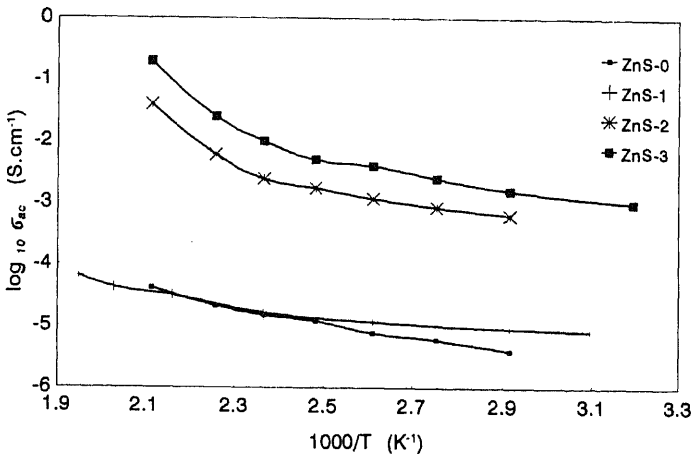

Figure 3b. Variation of ac conductivity at 1 MHz with temperature of nano-particles of ZnS and composites with different wt% of nano-particles of Ag.

The ac conductivity (σ_{ac}) increased with both frequency and temperature (figures 3a and 3b). σ_{ac} of ZnS-1 was slightly larger than that of ZnS-0, but its rate of increase with frequency was the same for both ZnS-0 and ZnS-1. σ_{ac} of ZnS-2 and ZnS-3 increased almost linearly with frequency. As regards variation with temperature, σ_{ac} of ZnS-0 increased at a low rate up to about 415 K and thereafter the increase was rapid. The numerical value of σ_{ac} at 1 MHz increased from about 4×10^{-6} S·cm^{-1} at 343 K to $4{\cdot}2 \times 10^{-5}$ S·cm^{-1} at 473 K. At a constant frequency, σ_{ac} increased with temperature at

Table 2. Dielectric constant of nano-particles of ZnS and composites with different wt% of nano-particles of Ag.

Sample	T(K)	10 kHz	100 kHz	500 kHz	1 MHz	3 MHz
ZnS-0	343	10·9	10·4	10·2	10·1	9·5
	383	11·5	10·8	10·6	10·4	9·8
	423	12·8	11·3	10·9	10·7	10·0
	473	17·2	13·0	11·8	11·4	10·5
ZnS-1	343	8·9	8·2	7·9	7·8	7·5
	383	9·6	8·7	8·4	8·2	8·0
	423	10·5	9·2	8·7	8·5	8·2
	473	13·0	10·5	9·6	9·2	8·6
ZnS-2	343	350·0	48·9	34·6	30·7	25·2
	383	959·0	69·0	43·4	37·3	29·7
	423	2892·0	117·0	59·2	48·2	36·5
	473	6044·0	2030·0	500·0	251·0	114·0
ZnS-3	343	459·0	74·7	45·4	38·8	30·4
	383	1620·0	136·0	62·3	50·8	38·5
	423	4590·0	379·0	106·0	76·8	52·8
	473	12400·0	7760·0	4630·0	2930·0	1160·0

temperature from about 313 to 473 K at a frequency of 1 MHz. σ_{ac} increased greatly with increase in wt% of Ag. σ_{ac} of ZnS-2 and ZnS-3 is more than 4 orders of magnitude larger than that of ZnS-0 and ZnS-1.

4. Discussion

The dielectric constant of single crystals of cubic ZnS at 25°C was reported to be 8·3 by Berlincourt *et al* [12]. The low frequency dielectric constant of polycrystalline ZnS [13] over a temperature range of 300 to 500 K was reported to increase only by a small amount from a value of 8·21 to 8·58. Also, in the case of thin films of thickness 2500 Å, the dielectric constant undergoes a very small decrease from 8·3 to 8·2 with frequency in the range from 10^2–10^5 Hz [14]. Samara [15] has reported that ε for cubic ZnS is strongly frequency dependent in the temperature range of 75·7 to 300 K, dielectric response was linear, ε having a value 8·1 at 75·6 K and 8·3 at 300 K. He also observed that at room temperature and at 100 kHz, tan δ is approximately 0·15.

In the present study, for pellets of ZnS nano-particles, ε at constant temperature (figure 1a) decreased at a slow rate with increase in frequency. Similarly, ε increased with temperature (figure 1b) both at low as well as high frequencies, the magnitude of increase in ε over a given temperature range being larger at low frequencies. ε of pellets of ZnS nano-particles is larger by about 25% than that of the bulk ZnS crystals [12, 13]. Tan δ for ZnS has a low numerical value which decreased with frequency (figure 2a). At constant frequency, tan δ increased rapidly with temperature (figure 2b). Tan δ of pellets of nano-particles of ZnS is larger than that of the corresponding values of bulk crystals reported in the literature [15]. Also, σ_{ac} of pellets of nano-particles of ZnS is many orders of magnitude larger than that of the bulk crystals [16, 17].

Unlike the ionic crystals where the effective field,

$$E_{\text{eff}} = E + 4/3\,\pi P,$$

for semiconductors E_{eff} should be essentially equal to the macroscopic field E, i.e.,

$$E_{\text{eff}} = E$$

This leads to an expression for ε of the form

$$\varepsilon - 1 = 4\pi(\alpha/V),$$

where V is the volume. The large value of ε of pellets of nano-particles of ZnS compared to the corresponding bulk value may be attributed to the small value of V in the above expression. The large values of ε, $\tan\delta$ and σ_{ac} of nano-particles of ZnS compared to the corresponding bulk values may be due to the small volume of the particles [15] and the disorder in their structure due to excess surface stress [18]. But the large increase in the values of ε, $\tan\delta$ and σ_{ac} when the nano-particles of ZnS are mixed with nano-particles of Ag must be expected to be caused by some other factor which causes a large increase in the electronic polarizability. The static dielectric constant ε of heteropolar semiconductors like CdS and ZnS can be written [15] as

$$\varepsilon = \varepsilon_\alpha + \varepsilon_1,$$

where ε_α is the high frequency or electronic contribution to the dielectric constant (dielectric constant in the absence of lattice vibrations) and ε_1 is the lattice contribution to the dielectric constant. Samara [15] has shown that for compound semiconductors, ε is dominated by the electronic contribution ε_α and the lattice contribution ε_1 is considerably smaller. The large value of ε in the case of ZnS, on the addition of nano-particles of Ag must be attributed to the large increase in ε_α, and the enhanced magnitude of $\tan\delta$ must be due to the disorder in the structure of the particles [18].

5. Conclusion

The dielectric properties of nano-particles of ZnS and composites with nano-particles of Ag of different concentrations dispersed in ZnS have been studied over a temperature range of 300 to 525 K. The large values of dielectric constant, dielectric loss and ac conductivity of nano-particles of ZnS compared to the corresponding values of bulk single crystals may be due to the small volume of the particles and the disorder in their structure.

References

[1] S Sugano, Y Nishina and S Ohnishi (eds) *Microclusters*, Springer series Materials Science (Springer, Berlin, 1987)
[2] T Halicioglu and C W Jr Bauschlicher, *Rep. Prog. Phys.* **51**, 883 (1988)
[3] R W Siegel, *Physics Today*, October 64 (1993)
[4] A I Ekimov, A I L Efos and A A Onuschchenko, *Solid State Commun.* **56**, 921 (1985)
[5] L Brus, *J. Phys. Chem.* **90**, 2555 (1986)
[6] W P Halperin, *Rev. Mod. Phys.* **58**, 533 (1986)
[7] P Marquardt, L Borngen, G Nimtz, R Sonnberger, H Gleiter and J Zhu, *Phys. Lett.* **A114**, 39 (1986)

[8] P C Lee and D Meisel, *J. Phys. Chem.* **86**, 3391 (1982)
[9] A Taylor, *X-ray metallography* (Wiley, New York, 1961) p. 674
[10] B Thomas and M Abdulkhadar, *XVI Int. Union of Crystallography*, Beijing, China (1993)
[11] M Ya Gamarnik and Yu Yu Sidorin, *Phys. Status. Solidi.* **B156**, K1 (1989)
[12] D Berlincourt, H Jaffe and L R Shiozawa, *Phys. Rev.* **129**, 1009 (1963)
[13] J S Browder, M E McCurry and S S Ballard, *Appl. Opt.* **23**, 537 (1984)
[14] A Goswami and A P Goswami, *Thin Solid Films* **16**, 175 (1973)
[15] G A Samara, *Phys. Rev.* **B27**, 3494 (1983)
[16] C Elbaum, *Phys. Rev. Lett.* **32**, 376 (1974)
[17] P Merchant and C Elbaum, *Solid State Commun.* **26**, 73 (1978)
[18] C Solliard and M Flueli, *Surf. Sci.* **156**, 487 (1985)

physics
pp. 439–451

Generation of picosecond optical pulses from single heterostructure GaAs diode laser and their emission characteristics

V N RAI, M SHUKLA and H C PANT
Laser Plasma Group, Centre for Advanced Technology, Indore 452 013, India

MS received 12 June 1995; revised 6 October 1995

Abstract. Emission characteristics of a single heterostructure GaAs diode laser are reported using a simple driver circuit. It provides a single picosecond time duration optical pulse, a pulse train or a broad optical pulse depending on the amplitude and time duration of the electrical pump pulse. Results show that relaxation oscillation frequency depends on the amplitude of pumping current pulse as well as on some inherent property of diode laser, which seems to be the level of impurity in lasing medium. Variation of relaxation oscillation frequency with amplitude of current pulse shows only the qualitative agreement with the reported theoretical predictions.

Keywords. Optical pulses; emission characteristics; oscillation frequency.

PACS Nos 04·30; 04·80

1. Introduction

Diode lasers are a low cost, compact and efficient optical source which can provide optical pulses of picosecond time duration at high repetition rate. These devices play an important role in the studies of ultrafast processes, optical communication as well as the testing of temporal behaviour of fast opto-electronic devices. It is therefore important to study in detail the emission characteristics of these lasers.

Picosecond pulse generation by semiconductor lasers has been investigated by several authors [1–13]. Various methods have been used to obtain these ultra short pulses, such as mode locking using external optical resonator [2] or by simpler gain switching methods. Two methods of gain switching have been demonstrated as injection of a short current pulse [1, 4, 11] or a sinusoidal RF wave in the presence of DC bias [5–10, 12]. Many types of diode lasers emitting in visible [13] as well as in infrared [1–12] wavelength regions have been used for this purpose. A large number of investigations related to picosecond optical pulse generation have been performed by RF current modulation technique or with an ultra short (picosecond) time duration electrical pulses [9] in the presence of a DC bias voltage. Paulus *et al* [9] have reported that the optical pulse width from laser diode first decreases and then remains constant at a certain minimum with an increase in the amplitude of the pumping current pulse. However, the pulse width (optical) first decreases up to a certain value and then increases with an increase in the DC bias current. These observations have been supported by numerical analysis. On the basis of theoretical calculations, MacFarlane [10] has reported that the time duration of the optical pulse first decreases and then attains a constant value, when time duration of electrical pulse was decreased.

However, the nature of variation remains same with a new value of optical time duration when the DC bias current was changed. According to Baker [11] the optical pulse generation combining the relaxation oscillation phenomenon of laser diode with large current pulse capacity of avalanche transistors could lead to optical pulses of < 100 ps pulse width. It has been reported that if the current impulse of the avalanche transistor returns to zero before the occurrence of the second oscillation of the laser diode, an optical impulse will be generated and if a current step is applied to the laser diode a train of pulses with decreasing optical amplitude will be generated. In another investigation Yariv [8] and Lau *et al* [7] have presented an analysis about the relaxation oscillation frequency observed in the laser diode, which was found dependent on the amplitude of the pumping electrical pulse as well as on the power emitted from the laser diode respectively. The latter relation fits better with the experimentally observed data.

The aim of this study is to verify the results of Paulus *et al* [9], Baker [11], Yariv [8] and Lau *et al* [7] when the laser diode is operated using a pumping pulse of subnanosecond (~ 800 ps) to 15 ns time duration. For this purpose, a single heterostructure GaAs laser diode was used to investigate the detailed emission characteristics of the laser diode with the amplitude and pulse width of the pumping electrical pulse.

2. Experimental details

Short duration optical pulses were generated [14, 15] by a single heterostructure GaAs laser diode (LD-62) obtained from Laser Diode Incorporated, USA. Laser diode was

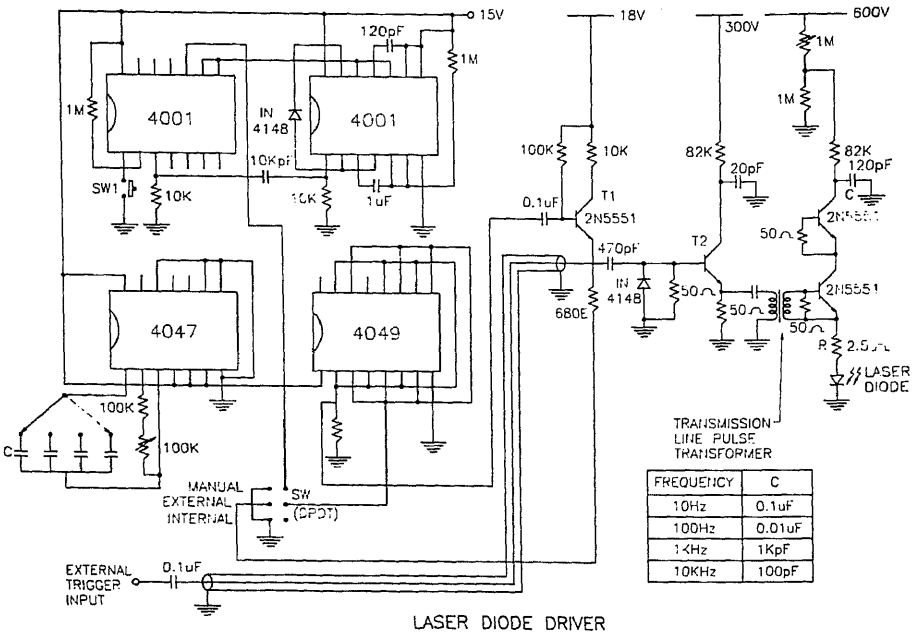

FREQUENCY	C
10Hz	0.1uF
100Hz	0.01uF
1KHz	1KpF
10KHz	100pF

Figure 1. Circuit diagram of diode laser driver.

driven by a simple driver (figure 1) where current pulse was generated by discharging a capacitor C (charged up to ~ 600 V) by switching the stack of two transistors (2N5551) connected in series. Two transistors were used to increase the amplitude of the current pulse. These transistors act as a switching element when operated in avalanche mode and were selected carefully such that they had same rise time ($\sim 1{\cdot}5$ ns) and breakdown voltage (~ 300 V). It was also noticed that the best transistors [16] were those having h_{FE} value ~ 120. However, the correlation of transistor parameter h_{FE} with the avalanche mode breakdown was not known. The actual peak current passing through the laser diode was adjusted by changing the charging voltage or the value of the capacitor C. This follows from the fact that the injection current to the diode is decided by the product of C and the charging voltage V, whereas the duration of the current pulse is decided by the product of C and the resistance in the discharging path. The rise time of the pulse is decided by the inductance of the circuit which was minimized in this case using a specially designed PCB. The laser diode was mounted on an aluminium plate which acts as a heat sink for the laser diode. The above circuit could be triggered by a pulse of ~ 5 V amplitude, but we used ~ 24 V amplitude trigger for a reliable triggering with a reduced time jitter. The trigger pulse was applied through a fast transmission line pulse transformer to the base of one of the transistors in the stack. The pulse transformer was made by wrapping four turns of co-axial cable of 50 Ω impedance where the outer shield acts as primary and the central wire as secondary of the transformer. It was operated either in manual single shot mode or at ~ 10 Hz repetition rate. The output emission from laser diode was detected using MRD 510 photodiode in combination with 100 MHz digital storage oscilloscope L and T Gould model 4074 (400 MS/S sampling rate) and a newly developed picosecond optical streak camera [17] having $S1$ photocathode. This streak camera provides a streak speed of ~ 15 mm/ns with a time resolution $\leqslant 17$ ps. The schematic diagram of the experimental set up to record the optical pulses from laser diode using streak camera is shown in figure 2. The image from the intensifier screen was captured using a CCD camera where

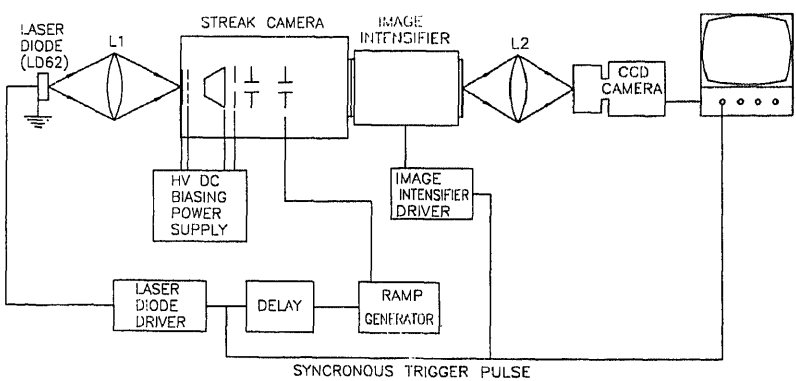

Figure 2. Schematic diagram of experimental set up.

an intensity profile was obtained on a PC monitor screen with the help of 'PROMISE' (Profile Measurement of Image Size and Edge Location) software programme [18].

3. Results and discussion

3.1 *Electrical properties of diode laser driver*

A simple fast rising current pulse is used to pump the diode laser to get a short duration optical pulse. These fast electrical pulses were obtained by the circuit given in figure 1 as described in previous section. However, before the study of emission characteristics of diode laser, study of electrical pulse is necessary. Two combinations of avalanche transistors were used as a switching element to drive the diode laser. In the first combination only two transistors connected in series acts as the switching element for discharging the capacitor C. Actual shape of current pulse was obtained by recording the shape of voltage pulse across 1·5 Ω resistance connected as a dummy in place of diode laser. Electrical pulses were recorded by a digital storage oscilloscope L and T Gould model 7074 (400 MS/S) which has low temporal resolution ~ 3·5 ns. Figure 3 shows the shape of electrical pulse obtained across 1·5 Ω when $C = 120$ pF capacitor charged to 600 V was discharged by triggering one of the transistors in the stack. This provides an electrical pulse of ~ 10 ns time duration along with some of the oscillating pulses having decreasing amplitude. An increase in the value of C as 60, 100 and 270 pF shows corresponding increase in time duration of the electrical pulse as ~ 6, 8 and 15 ns which is expected. It was also noted that any change in the charging voltage does not show any effect on the FWHM of the electrical pulse. Minimum rise time of ~ 1 ns and pulse duration ~ 3 ns were measured for the capacitors of value ⩽ 20 pF. However, 20 pF capacitor in two transistor circuit did not provide detectable intensity from diode laser.

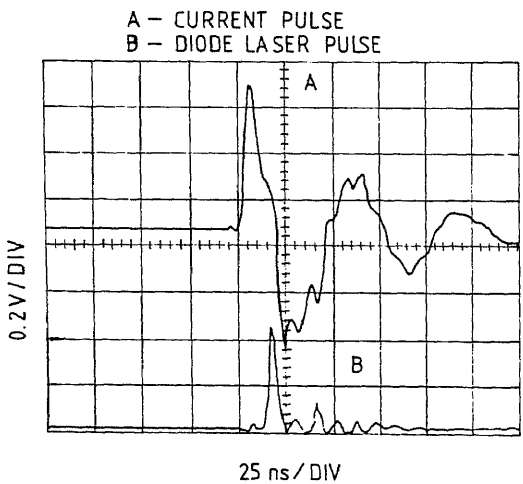

Figure 3. Oscillogram of the electrical pump pulse when series stack of two transistors (2N5551/2N5550) were used as switching element and the optical pulse obtained from diode laser.

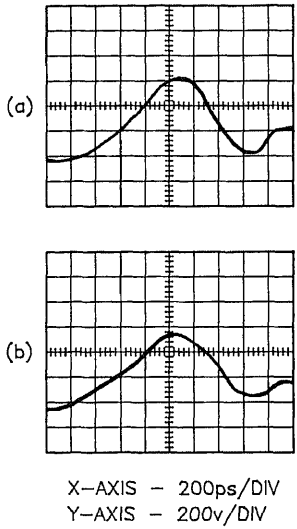

Figure 4. Oscillogram of the pump pulse when series stack of nine transistors (2N5551/2N5550) were used as switching element in the driver circuit. Capacitor was charged up to (a) 2·7 kV, (b) 2·5 kV.

It was observed that for low value of capacitor higher charging voltage is required which is possible only by increasing the number of transistors in the stack.

In order to improve the rise time and time duration of the pump electrical pulse another combination of switching element was used which has a series stack of nine transistors (2N5551/2N5550). This circuit uses 20 pF capacitor charged up to 2·7 kV. Electrical pulses obtained from this circuit for the charging voltage of 2·7 kV (figure 4a) and 2·5 kV (figure 4b) were recorded by Tektronix model 7104 oscilloscope. Figure 4a has a rise time and time duration of the pulse as ~ 600 ps (10%–90%) and ~ 800 ps respectively whereas figure 4b shows the rise time as ~ 800 ps and time duration as ~ 900 ps. These results indicate that rise time and duration of the pulse get improved by increasing the number of transistors in the switching stack. A small decrease in charging voltage increases the rise time and the pulse duration whereas no variation was observed in the rise time and pulse duration of the electrical pulse in the case of two transistors stack. However, similar variations are expected in both the cases but the small variation in two transistor case may not be observable. This improvement in the time duration of the pulse in the case of increased number of transistors in the stack seems to be due to change in the value of capacitance as a result of series connection of charging capacitor and junction capacitances of the switching transistors. However, rise time of the electrical pulse got improved due to the combined effect of decrease in effective junction capacitance of the switching transistors and decrease in the inductance of discharging path in the circuit.

3.2 *Emission characteristics of LD-62 diode laser*

The emission characteristics of the diode laser was investigated to understand the relationship between the driving current pulse at high amplitude and the shape of the

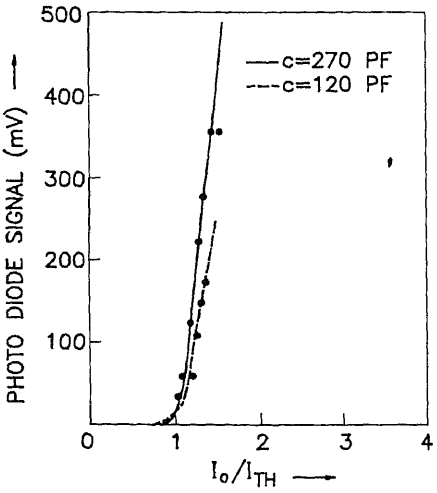

Figure 5. Variation of optical intensity emitted from laser diode with pumping current pulse (I_0/I_{Th}).

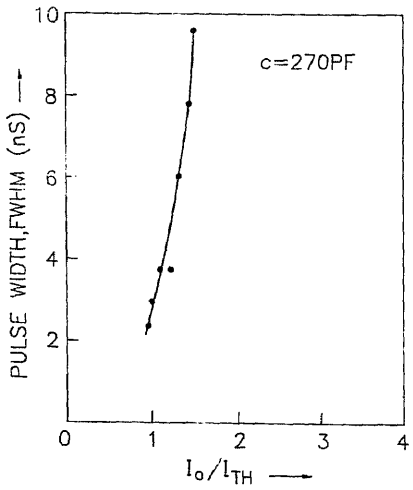

Figure 6. Variation of optical pulse width with the amplitude of the pump current (I_0/I_{Th}).

light pulse. Figure 3 shows the shape of the current pulse obtained after discharging a capacitor of ~ 120 pF and the optical pulse detected using photodiode MRD 510. Time duration of the electrical and optical pulse was measured as ~ 10 ns and ~ 5 ns, respectively. Here one can notice that the oscillations observed in the electrical current pulse did not generate corresponding optical pulses. However, at a higher current value, the amplitude of oscillations in current pulse crosses the lasing threshold and

provides corresponding optical pulses. Figure 5 shows the variation of the optical pulse amplitude with an increase in the ratio of injection current and the threshold lasing current I_0/I_{Th} for discharging capacitor of value $\sim$ 120 and 270 pF. When charging voltage on the capacitor decreases, then, as a result of decrease in the current pulse amplitude, the pulse width (figure 6) as well as intensity of the optical pulse decreases (figure 5). It was found (figure 5) that for getting a similar photodiode signal with both the charging capacitors, required current (charging voltage) is more in the case of smaller value of charging capacitor ($\sim$ 120 pF). Even the threshold for lasing is also high in the case of lower value of capacitor. An increase in the duration of the optical emission with large amplitude and ns time duration pumping current pulse (figure 6) may be due to two reasons: firstly, due to an increase in the temperature as a result of large current passing through the diode which is in agreement with the earlier reported results [1, 4], and secondly, due to the occurrence of multiple pulsation or relaxation oscillations [3, 7–13] which will be discussed in detail afterwards. The observation of figure 6 is contrary to the experimental and numerical results reported by Paulus *et al* [9] where picosecond pulses were used for pumping the laser diode. It seems that the small time duration pumping pulses are not producing multiple pulsation or producing it at very large amplitude of exciting current pulse. However, first decreasing (transition from spontaneous to stimulated emission) and then increasing (due to multiple pulsation) nature in optical pulse duration has been reported with an increase in the DC bias voltages [9] in the presence of a picosecond pump pulse. We are getting only increasing nature in optical pulse width with an increase in the amplitude of the current pulse. However, a small increase in optical pulse width at lower amplitude of the current pulse is possible near the threshold of lasing (near breakdown voltage of transistor stack) in our case also. Because a decrease in charging voltage, below breakdown voltage of transistor stack (to decrease the current) increases the rise time and pulse duration of the current pulse (figure 4) and consequently the time duration of the optical pulse. However, this change may not be observable due to the band-width

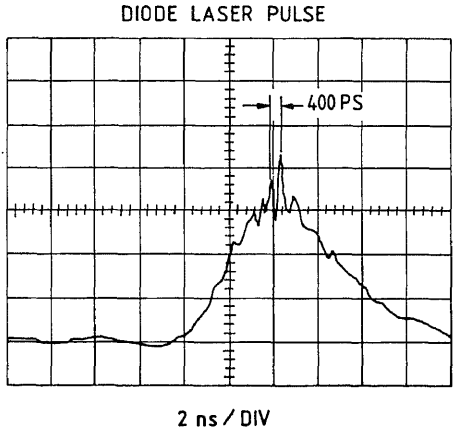

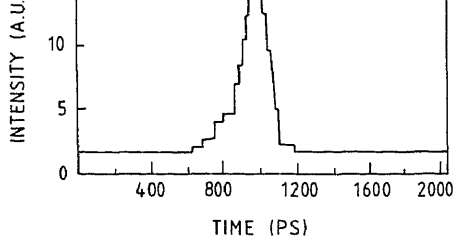

Figure 8. Single optical pulse from laser diode recorded using streak camera.

limitation of the recording oscilloscope. A comparison of our results with those of the Paulus *et al* [9] indicates that the large amplitude of the pumping pulse combined with its large time duration, has similar effect as the DC bias has in the presence of picosecond time duration electrical pulses. Figure 7 shows the photodiode signal recorded in equivalent time sampling mode at an injection current ratio $I_0/I_{Th} \sim 1{\cdot}32$ which provides a broad optical pulse along with a modulation of intensity at the top of the pulse. The small time duration pulsation occurs at nearly equal time intervals which is ~ 400 ps in the present case. Further increase (decrease) in the current pulse amplitude shows corresponding decrease (increase) in the time interval between the pulsations. A single optical pulse (figure 8) of ~ 180 ps duration was observed using a streak camera when laser diode was operated just above the threshold current value. However, smallest optical pulse duration of ~ 120 ps was recorded by discharging a 20 pF capacitor through diode laser (figure 4). At $I_0/I_{Th} \sim 1{\cdot}32$ a pulse train having pulses of duration ~ 180 ps was observed on the streak camera separated with the time interval of ~ 400 ps (figure 9a). Here again we note that the time period between the pulses decreases with an increase in I_0/I_{Th}. It was observed that at large injection current the optical pulse gets broadened (pulses merge together) in such a way that the train of the pulses got converted into a single large time duration pulse with intensity modulation at the top. The broad optical pulse has a similar shape as that of the current pulse. These observations indicate that emission of a short duration single pulse, a pulse train or a broad pulse with intensity modulation are the function of ratio I_0/I_{Th}. The difference in the shape of pulses at $I_0/I_{Th} \sim 1{\cdot}32$ in figures 7 and 9a is due to the difference in the temporal resolution of the recording systems. Experiments were repeated many times and results were found reproducible. The time duration of these optical pulses were changed using different values of the capacitors. Figures 9a and 9b show the intensity profile of two similar laser diodes connected in parallel and operated with the same current pulse in single shot operation by pumping the diodes simultaneously. A slight change was noticed in the intensity, time period of pulsation and time duration in the case of single pulse or in the pulse train when different laser diodes of the same specifications were tested using the same current pulse. In order to see the effect of improvement in the rise time and shortening the time duration of the pumping electrical pulse on the emitted optical pulse, we used a short time duration electrical

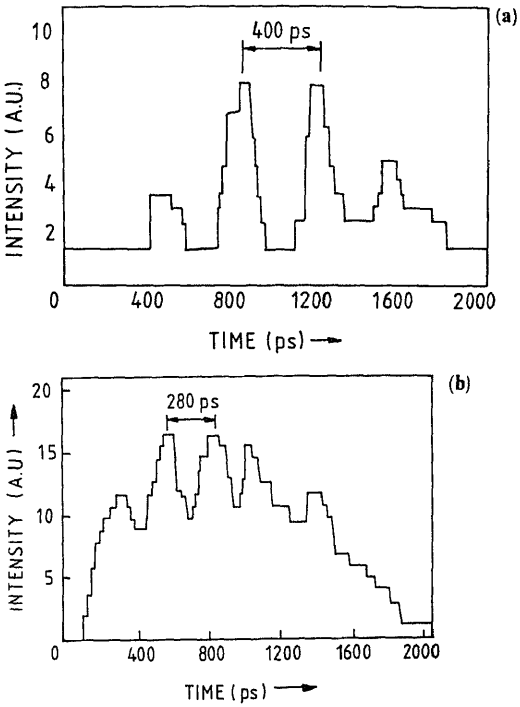

Figure 9. Multiple pulsation emitted from laser diode (for $I_0/I_{Th} \sim 1{\cdot}32$) and recorded using streak camera. (a) Laser diode I; (b) Laser diode II.

SCALE - 15 mm = 1 ns

Figure 10. Contact photograph of multiple pulsation when diode laser was pumped by discharging a 20 pF capacitor charged at 2·7 kV using a series stack of nine transistors (2N5551/2N5550) as a switch.

pulse (figure 4) for pumping the diode laser. Figure 10 shows the contact photograph of the laser diode emission taken using a streak camera on the polaroid film, which has

and rise time. Here again we observed that duration of optical pulses increases when charging voltage was decreased from 2·7 kV to 2·5 kV. This behaviour is similar to what has been observed in the two-transistor case. It was however noted during these experiments that multiple optical pulses of picosecond time duration were obtained always whenever the laser diode was driven by a large amplitude current pulse obtained by switching the transistors in the avalanche mode (figure 9) whereas it provided a single optical pulse of picosecond time duration with a slowly rising intensity at the leading edge of the pulse (figure 8), when transistors were operated below avalanche breakdown voltage whether a two-transistor or nine-transistor stack was used. The slow rise in the intensity at the beginning of the optical pulse may be due to spontaneous emission, which occurs as a result of an increase in the rise time and decrease in the amplitude of the electrical pulse.

3.3 *Comparison with theoretical results*

It is generally accepted that the modulation band-width of the semiconductor laser is equal to ν_{rel}, the relaxation oscillation frequency [7, 8] which varies from laser to laser. However, this frequency limits the useful band-width of the diode laser below relaxation oscillation frequency. Figure 11 shows the variation of relaxation oscillation frequency with the pumping current for some of the typical parameters of the diode laser. Frequencies have been calculated using a widely accepted formula [8].

$$2\pi\nu_{rel} = \left[\frac{\Gamma n_{tr} A\tau_p + 1}{\tau_s \tau_p}\left(\frac{I_0}{I_{Th}} - 1\right)\right]^{1/2} \tag{1}$$

and

$$\tau_p = \frac{1}{v}\left(\alpha + \frac{1}{L}\ln\frac{1}{R}\right)^{-1}$$

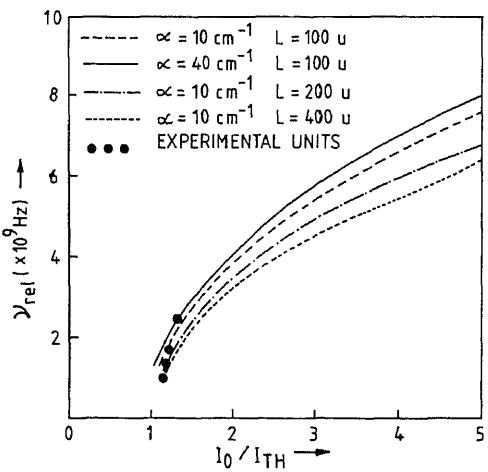

Figure 11. Variation of measured and calculated relaxation oscillation frequencies with pump current (I_0/I_{Th}).

where I_0 and I_{Th} are the pumping and threshold current for the occurrence of laser, τ_s and τ_p are the spontaneous carrier and photon life time respectively, Γ is the optical confinement factor, A is the optical gain co-efficient and n_{tr} is the carrier density at which the material becomes transparent. v is the group velocity of the light, α is the distributed loss, L is the length of the cavity and R is the mirror reflectivity.

The numerical values for these parameters have been obtained from references 7 and 8. The experimentally measured relaxation frequency data with pumping current has also been plotted on the same graph for comparison purpose. It was found that experimentally as well as theoretically obtained data are in qualitative agreement, that is, frequency increases with an increase in the pumping current. But experimental data do not fit correctly with any of the theoretically obtained curve. Figure 12 shows the variation of experimentally observed relaxation oscillation frequencies with the square root of the emitted light intensity, which is proportional to the photo diode signal. A linear variation of data points indicates better agreement with the relation given by Lau *et al* [7] for relaxation oscillation frequency as

$$\nu_{rel} = \left(\frac{1}{2\pi}\right)\left(\frac{AP_0}{\tau_p}\right)^{1/2}, \tag{2}$$

where P_0 is the steady state photon density in the active region. However a small deviation can be seen at the higher value of current in this experiment. The experimental observations, reported by Lau *et al* [7] for a burried heterostructure GaAs laser operated by current modulation at 0·1–8·5 GHz show a close agreement with (2). The data obtained from other laser diode (figure 9b) also show similar variation but provide entirely different frequencies for similar pumping current. The observed pulsation behaviour in both the diode lasers (figures 9a and 9b) were compared with the theoretical simulation results reported by Chik *et al* [3] who have taken into account the presence of defects (saturable absorber) in the cavity. Emission in figure 9b has a broad profile with intensity modulation on the top whereas figure 9a shows a higher order of modulation depth in intensity which seems to be due to the presence of large density of defects in figure 9a. The relaxation oscillation frequency obtained in

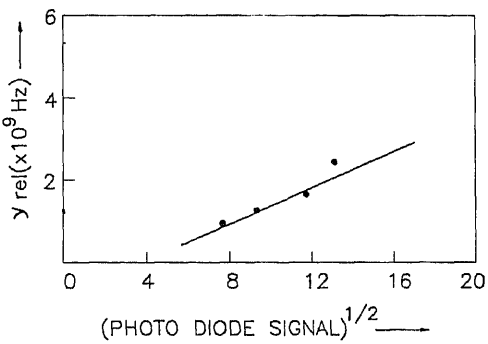

Figure 12. Variation of measured relaxation oscillation frequency with the square root of intensity emitted from diode laser.

of defects in the laser cavity plays an important role in providing self-sustained pulsation behaviour in the semiconductor diode laser.

4. Conclusion

In summary, a short picosecond time duration pulse was obtained from a single heterojunction GaAs laser diode by injection of a current pulse of time duration ranging from subnanosecond to 15 ns obtained from a simple circuit. However time duration of the single optical pulse depends on the time duration of the pumping electrical pulse. The shortest optical pulse obtained was of $\leqslant 120$ ps. One can obtain a single pulse, pulse train or a broad pulse with intensity modulation on the top depending on the amplitude of the current pulse which is independent of the electrical pulse duration. However, threshold of lasing is dependent on pump pulse time duration (value of capacitor, C). It was found that occurrence of relaxation oscillation or self-sustained pulsation does not depend only on the duration of electrical pump pulse as is reported by Baker [11]. It has been shown that the high amplitude of electrical pump pulse with large pulse duration in these experiments and the electrical pulse of ultrashort time duration with a DC bias in the case of Paulus *et al* [9] provide similar results, that is, an increase in optical time duration. Variation in optical pulse duration with electrical pulse duration was found in agreement with the results of MacFarlane [10]. Experimental observations further indicate the need for modification in the theory (consideration of impurity factor) to explain the observed variations in relaxation oscillation frequencies with the amplitude of pumping electrical pulse. However, the study of laser diode (GaAs) emission with a better time resolution may provide more important information.

Acknowledgements

The authors are thankful to D D Bhawalkar for many suggestions and helpful discussions during the experiment. Authors are also grateful to R K Khardekar for providing CCD camera and H S Vora for providing the image processing software PROMISE.

References

[1] J R Andrews, *Rev. Sci. Instrum.* **45**, 22 (1974)
[2] P T Ho, L A Glasser, E P Ippen and H A Haus, *Appl. Phys. Lett.* **33**, 241 (1978)
[3] K D Chik, J C Dyment and B A Richardson, *J. Appl. Phys.* **51**, 4029 (1980)
[4] Y Tsuchiya, A Takeshima and M Hosoda, *Rev. Sci. Instrum.* **52**, 579 (1981)
[5] Thomas L Paoli, *Appl. Phys. Lett.* **39**, 522 (1981)
[6] R A Elliot, H Dexill, R K Defreez, J M Hunt and P G Rickman, *Appl. Phys. Lett.* **42**, 1012 (1983)
[7] K Y Lau, N Bar-chaim, I Ury, Ch Harder and A Yariv, *Appl. Phys. Lett.* **43**, 1 (1983)
[8] A Yariv, *Optical electronics* (Holt, Rinehart and Winston, New York 1985) pp. 188–193

[9] P Paulus, R Langenhorst and D Jager, *IEEE J. Quant. Elect.* **QE24**, 1519 (1988)
[10] D L MacFarlane, *J. Appl. Phys.* **68**, 3013 (1990)
[11] R J Baker, *Rev. Sci. Instrum.* **62**, 1031 (1991)
[12] D L MacFarlane and J A Tatum, *IEEE J. Quant. Elect.* **28**, 1320 (1992) and references therein
[13] J A Tatum, J W Jennings and D L MacFarlane, *Rev. Sci. Instrum.* **63**, 2950 (1992)
[14] M Shukla, V N Rai and H C Pant, *Proceedings of National Laser Symposium* CAT, Indore, 1994, p. 92
[15] V N Rai, M Shukla, R K Khardekar and H C Pant, *Rev. Sci. Instrum.* **66**, 3125 (1995)
[16] V N Rai and M Shukla, *Rev. Sci. Instrum.* **65**, 2134 (1994)
[17] V N Rai, M Shukla, H C Pant and D D Bhawalkar, *Proceedings of National Laser Symposium*, Indore, 1994, p. 254 and Research Report No. CAT/95-11
[18] H S Vora, S V Nakhe, K K Sharangpani, P Saxena, R Bhatnagar and N D Shirke, *Proceedings of National Laser Symposium*, Indore, 1994, p. 260

PRAMANA
— journal of
physics

© Printed in India

Vol. 45, No. 5,
November 1995
pp. 453–462

Ion cyclotron instabilities in a mildly relativistic hydrogen-deuterium fusion plasma

CHANDU VENUGOPAL, P J KURIAN and G RENUKA*
School of Pure and Applied Physics, Mahatma Gandhi University, Priyadarshini Hills, Kottayam 686 560, India
*Department of Physics, University of Kerala, Trivandrum, India

MS received 1 February 1995; revised 14 August 1995

Abstract. A dispersion relation for the perpendicular propagation of the electromagnetic ion cyclotron wave around the second harmonic of the deuterium ion gyrofrequency in a mildly relativistic, anisotropic Maxwellian plasma with hydrogen as the majority species and deuterium as the minority component has been derived. The work has been carried out in the frame of reference of the majority hydrogen ions; to these ions the waves at $2\Omega_D$ would be at its own gyrofrequency.

Using a small quantity ε to order all relevant parameters of the plasma, it was possible to derive the dispersion relations in a simple form. To the lowest order the relativistic factors do not enter the dispersion relation. The plasma can now support two modes—one above and the other below the hydrogen gyrofrequency in agreement with the assumptions. This was also verified numerically using a standard root solver thereby justifying the correctness of the ordering scheme.

In the next higher order, the dispersion relation is a quartic equation and is sensitively dependent on the relativistic factors. The plasma can now support four modes, both above and below the hydrogen gyrofrequency and consistent with the ordering scheme used. However the modes can now coalesce resulting in complex conjugate roots to the dispersion relation thereby indicating an instability.

The advantage of such a scheme is that two dispersion relations – one of which is independent of the relativistic factors and the other which is sensitively dependent on them can be separated out.

Keywords. Ion cyclotron waves; two-ion relativistic plasma; dispersion relation.

PACS No. 52·40

1. Introduction

Ohmic heating alone is not sufficient to bring a plasma to its ignition conditions. Among the many options available, supplementary heating by waves in the ion cyclotron range of frequencies (ICRF) is probably the most common scheme at present and is being used in a large number of tokamaks and mirror machines. These heating experiments have concentrated on the use of RF waves at frequencies ω both above and below the ion gyrofrequency Ω_i. The method is inherently simple, technologically attractive and has proved to be quite successful in raising plasma temperatures.

In this method heating is accomplished by IC damping where the wave energy is absorbed and converted to particle energy and is therefore a hot plasma effect. In a pure hydrogen plasma for waves around the first harmonic of Ω_i, the lowest order thermal corrections to the cold plasma terms cancel and consequently wave absorption

rise to additional absorption processes. In fact, in early low power experiments, the physics of wave damping at $\omega \approx 2\Omega_D$ in a deuterium plasma was found to be dominated by the presence of a small amount of hydrogen ions (to which this wave is at its fundamental gyrofrequency). These ions played a dominant role in the propagation and absorption of wave energy. Starting with modest powers ICRF heating is at present an important scheme with which impressive powers of a few tens of MW have been achieved [2]. With larger and larger power inputs leading to higher and higher energies, relativistic effects can be expected to play an important role in ICRF heating experiments in future.

As mentioned above, fusion plasmas generally have various types of ions in differing concentrations. Of the many scenarios possible, we consider a mildly relativistic plasma containing hydrogen (H) as the majority species and deuterium (D) as the minority constituent and study IC propagation at the second harmonic of deuterium ion gyrofrequency in it (that is $\omega \approx 2\Omega_D$). Since we propose to work in the frame of the majority hydrogen ions this wave at $\omega \approx 2\Omega_D$ would be at its own gyrofrequency Ω_H.

Past analyses of dispersion relations for IC propagation in multi-ion component plasmas have been essentially numerical probably because of the complexity involved in an analytic calculation. Unfortunately, a fully numeric solution has the drawback that the cold plasma terms dominate the relativistic terms of the dielectric tensor thus masking many interesting features of wave propagation in relativistic plasmas. Guided by the experimental parameters of an early mirror experiment and the numerical solutions of the dispersion relations we have, by means of an ordering parameter ε derived two dispersion relations. To the lowest order we arrive at a quadratic equation which is independent of the relativistic terms. This relation supports two modes, one above and the other below the hydrogen gyrofrequency Ω_H. The next higher order dispersion relation is a fourth order equation which is sensitively dependent on the relativistic terms. This relation yields four modes on either side of Ω_H which can coalesce to make the plasma unstable.

The advantage of such an analytic scheme is that we have been able to separate out two dispersion relations, one of which is independent of the relativistic factors while the other is sensitively dependent on them. Such a separation is not possible in a fully numerical calculation.

2. The dielectric tensor elements

We are interested in the perpendicular propagation of IC waves around the second harmonic of the deuterium ion gyrofrequency ($\omega \approx 2\Omega_D$), in a mildly relativistic plasma with hydrogen as the majority species and deuterium as a minority constituent. The electrons form a neutralising background. The expressions for the relevant dielectric tensor elements have been derived earlier for a single ion plasma [3]; we extend these to a two-ion plasma. We too choose f_0 to be a bi-Maxwellian which is given by [3]

$$f_0 = f_\perp f_\parallel = \frac{1}{\pi^{3/2}\bar{v}_\perp^2 \bar{v}_\parallel} \exp\left(-\frac{v_\perp^2}{\bar{v}_\perp^2} - \frac{v_\parallel^2}{\bar{v}_\parallel^2}\right). \tag{1}$$

The thermal energies $\bar{v}_\perp^2$ and $\bar{v}_\parallel^2$ are related to the temperatures $T_\perp$ and $T_\parallel$, perpendicular and parallel to the magnetic field B_0 respectively by

$$\bar{v}_\perp^2 = \frac{2T_\perp}{M} \text{ and } \bar{v}_\parallel^2 = \frac{2T_\parallel}{M}, \tag{2}$$

where M is the rest mass.

On substituting (1) into the expressions for the dielectric tensor elements and carrying out the various integrations we get the following expressions for K_{xx}, K_{xy} and K_{yy}. A detailed derivation of these elements has been given earlier [3]; we, however, give only the final expressions to facilitate our discussions.

The relevant expressions are,

$$K_{xx} - 1 = \sum_{\text{H,D,e}} \bar{\omega}_p^2 \sum_{n=1}^{\infty} n^2 \left\{ \frac{T_0}{n^2 - Z^2} + \left[\frac{\bar{v}_\perp^2}{c^2} T_1 + \frac{1}{4}\frac{\bar{v}_\parallel^2}{c^2} T_0 \right] \frac{n^2 + Z^2}{(n^2 - Z^2)^2} + \left[\frac{3}{2}\left(\frac{\bar{v}_\perp^2}{c^2}\right)^2 T_2 + \frac{1}{2}\left(\frac{\bar{v}_\perp^2}{c^2}\right)\left(\frac{\bar{v}_\parallel^2}{c^2}\right) T_1 + \frac{3}{16}\left(\frac{\bar{v}_\parallel^2}{c^2}\right)^2 T_0 \right] \frac{Z^2(3n^2 + Z^2)}{(n^2 - Z^2)^3} \right\}. \tag{3a}$$

$$\frac{K_{xy}}{i} = \sum_{\text{H,D,e}} \frac{\bar{\omega}_p^2}{Z} \sum_{n=1}^{\infty} n^2 \left\{ \frac{T_0'}{n^2 - Z^2} + \left[\frac{\bar{v}_\perp^2}{c^2} T_1' + \frac{1}{4}\frac{\bar{v}_\parallel^2}{c^2} T_0' \right] \frac{2Z^2}{(n^2 - Z^2)^2} + \left[\frac{3}{2}\left(\frac{\bar{v}_\perp^2}{c^2}\right)^2 T_2' + \frac{1}{2}\left(\frac{\bar{v}_\perp^2}{c^2}\right)\left(\frac{\bar{v}_\parallel^2}{c^2}\right) T_1' + \frac{3}{16}\left(\frac{\bar{v}_\parallel^2}{c^2}\right)^2 T_0' \right] \frac{Z^2(n^2 + 3Z^2)}{(n^2 - Z^2)^3} \right\}. \tag{3b}$$

and

$$K_{yy} - 1 = \sum_{\text{H,D,e}} \bar{\omega}_p^2 \sum_{n=0}^{\infty} \left\{ \frac{T_0''}{n^2 - Z^2} + \left[\frac{\bar{v}_\perp^2}{c^2} T_1'' + \frac{1}{4}\frac{\bar{v}_\parallel^2}{c^2} T_0'' \right] \frac{n^2 + Z^2}{(n^2 - Z^2)^2} + \left[\frac{3}{2}\left(\frac{\bar{v}_\perp^2}{c^2}\right)^2 T_2'' + \frac{1}{2}\left(\frac{\bar{v}_\perp^2}{c^2}\right)\left(\frac{\bar{v}_\parallel^2}{c^2}\right) T_1'' + \frac{3}{16}\left(\frac{\bar{v}_\parallel^2}{c^2}\right)^2 T_0'' \right] \frac{Z^2(3n^2 + Z^2)}{(n^2 - Z^2)^3} \right\}. \tag{3c}$$

In the above the first summation is over the species (H indicating hydrogen, D deuterium and e electrons).

The definitions of the other parameters are

$$\omega_p^2 = \frac{4\pi N e^2}{M}, \quad \Omega_0 = \frac{eB_0}{Mc} = \gamma\Omega,$$

$$\bar{\omega}_p^2 = \frac{\omega_p^2}{\Omega_0^2} \quad \text{and} \quad Z = \frac{\omega}{\Omega_0} \tag{4}$$

where c is the velocity of light, N, the plasma density and γ the relativistic factor.

The Ts arise from the $dv_\perp$ integrations and are, in general, functions of the modified Bessel function $I_n(l_\perp)$ [3]. The argument $l_\perp$ of I_n is defined by

$$l_\perp = \frac{k_\perp^2 T_\perp}{\Omega_0^2 M}. \tag{5}$$

The explicit functional forms of the Ts are given in [3]. Also the prime on the summation in K_{yy} indicates that the $n = 0$ contribution has to be divided by 2.

3. The ordering procedure

We are interested in the perpendicular propagation of IC waves around $\omega \approx 2\Omega_D$ in a hydrogen-deuterium plasma. As mentioned, to the hydrogen ions these waves at $\omega \approx 2\Omega_D$ would be at its own gyrofrequency Ω_H. We shall thus work in the frame of the hydrogen ions.

The tensor elements (3a) to (3c) are all infinite summations and hence if used as such, the dispersion relation would become very complicated. Therefore, to arrive at a dispersion relation in a simple form, the dielectric tensor elements K_{ij} must contain only a finite number of terms to begin with. Such a truncation is possible only if the individual members of the tensor elements become progressively lesser than 1. We, therefore, define a small parameter ε to scale all the relevant parameters in the individual tensor elements and the final dispersion relation.

A quantity which is small and therefore convenient for the definition of ε is the ratio of the rest mass of the electron to that of the proton; thus $\varepsilon \approx (M_e/M_H)^{1/2}$. Having defined ε we next characterize the wave in terms of this small parameter, conforming with experiments over a wide range of parameters. Theoretically, for a resonance, the frequency ω must be equal to Ω_H; experimentally, however, the waves usually have a small range of frequencies around Ω_H. It is this deviation from the exact value of Ω_H that we scale by ε.

In the presently available ICRF heating experiments the parameter (5) is much less than unity [4] and hence we shall scale this factor also in terms of ε; that is $l_{\perp D} \approx \varepsilon$. Such an ordering, while agreeing with experiment, also has the advantage that the exponential and modified Bessel functions that occur in (3a) to (3c) can be expanded as a power series. We also make the simplifying assumption that the two ionic species are approximately in temperature equilibrium while the electrons are relatively colder than the ions. Thus $T_{\perp H}/T_{\perp D} \approx 1$ (so that $l_{\perp H} \approx \varepsilon$) while $T_{\perp e}/T_{\perp H} \approx \varepsilon$. However the electrons in spite of being colder will, because of their smaller mass, be more energetic and thus we shall assume that $\frac{\bar{v}_{\perp H}^2}{c^2} \approx \frac{\bar{v}_{\perp D}^2}{c^2} \approx \varepsilon^2$ while $\frac{\bar{v}_{\perp e}^2}{c^2} = \varepsilon$. And finally in many typical fusion experiments the ion plasma frequency is much larger than the ion gyrofrequency so that $(1/\bar{\omega}_{pH}^2) \approx \varepsilon$. Summarising, we have

$$M_e/M_H \approx \varepsilon^2, \quad \Gamma = 1 - Z_H^2 \approx \varepsilon, \quad T_{\perp H}/T_{\perp D} \approx 1, \quad T_{\perp e}/T_{\perp H} \approx \varepsilon,$$

$$\frac{\bar{v}_{\perp H}^2}{c^2} \approx \frac{\bar{v}_{\perp D}^2}{c^2} \approx \varepsilon^2, \quad \frac{\bar{v}_{\perp e}^2}{c^2} \approx \varepsilon, \quad l_{\perp H} \approx l_{\perp D} \approx \varepsilon \quad \text{and} \quad \frac{1}{\bar{\omega}_{PH}^2} \approx \varepsilon \tag{6}$$

We shall use this ordering scheme in the derivation of our dispersion relations.

4. The tensor elements and the dispersion relation

The expressions for the dielectric tensor elements K_{xx}, K_{xy} and K_{yy} can be derived using the ordering scheme of (6) and the relevant expressions from (3a) to (3c). In fact they are

lengthy and hence we shall not give them here; however, their derivation is straight forward.

Substituting the tensor elements into the formula for dispersion relation (equation (21) of [3]) and simplifying we arrive at our dispersion relation which we shall, for the moment, write as

$$D(\omega, k_\perp) = D_1(\omega, k_\perp; \approx \varepsilon^2) + D_2(\omega, k_\perp; \approx \varepsilon^4) = 0. \tag{7}$$

Relation (7) indicates that our dispersion relation has to be written as a sum of two parts—the first one, namely D_1, containing terms of order ε^2 and D_2 terms of order ε^4. Obviously the two have to be separately equated to zero and solutions obtained.

The dispersion relation, to order ε^2, has the form

$$\begin{aligned} D_1(\omega, k_\perp; \approx \varepsilon^2) = \Gamma^2 \Bigg\{ & - N_{DH}\left[\frac{1}{3}N_{DH} + \frac{4}{9} - \frac{2}{3}N_{eH} + \frac{2}{3}\frac{l_{\perp H}}{\beta_{\perp H}}\right] + N_{eH}^2 \Bigg\} \\ & + \Gamma\left\{\frac{l_{\perp H}}{\beta_{\perp H}} - 1 - \frac{4}{3}N_{DH} - \delta\right\} - \frac{1}{2}l_{\perp H}^2 \\ & + \left[\frac{4\bar{v}_{\perp H}^2 + \bar{v}_{\parallel H}^2}{c^2}\right]\left[\frac{l_{\perp H}}{\beta_{\perp H}} - 1 - \frac{4}{3}N_{DH}\right] = 0 \end{aligned} \tag{8}$$

where $N_{eH} = N_e/N_H$ etc, and

$$\begin{aligned} \delta = \Bigg\{ & \frac{2}{\bar{\omega}_{pH}^2} - l_{\perp D}\left[\frac{1}{2}N_{DH}\frac{l_{\perp H}}{\beta_{\perp H}} + \frac{1}{3}N_{DH}^2 + \frac{2}{3}N_{DH} - N_{eH}N_{DH}\right] \\ & + l_{\perp H}\left[\frac{1}{3} - 2N_{eH} + \frac{2}{3}N_{DH}\right] - l_{\perp H}\left[1 - \frac{l_{\perp H}}{\beta_\perp} + \frac{4}{3}N_{DH}\right]\Bigg\} \end{aligned}$$

and

$$\beta_{\perp H} = \frac{4\pi N_H T_{\perp H}}{B_0^2} \quad \text{with} \quad \frac{l_{\perp H}}{\beta_{\perp H}} \approx 1 + N_{DH}$$

As a check on (8) we note that for $N_D = 0$, it reduces to the dispersion relation in [3]; the small differences being due to our slightly different ordering. Inspecting (8), we find that for the first three terms to be of order ε^2 we need to set [6]

$$\left[1 - \frac{l_{\perp H}}{\beta_{\perp H}} + \frac{4}{3}N_{DH}\right] \approx \varepsilon. \tag{9}$$

With this the last term and a factor similar to (9) in δ in (8) is of the order ε^3 and hence drops out of it.

The dispersion relation, to order ε^2, is thus given by

$$D_1(\omega, k_\perp; \approx \varepsilon^2) = \Gamma^2\left\{N_{eH}^2 - N_{DH}\left[\frac{1}{3}N_{DH} + \frac{4}{9} - \frac{2}{3}N_{eH} + \frac{2}{3}\frac{l_{\perp H}}{\beta_{\perp H}}\right]\right\}$$

$$-\Gamma\left\{1-\frac{l_{\perp H}}{\beta_{\perp H}}+\frac{4}{3}N_{DH}+\delta\right\}-\frac{1}{2}l_{\perp H}^2=0 \tag{10}$$

where

$$\delta=\left\{\frac{2}{\omega_{pH}^2}-l_{\perp D}\left[\frac{1}{2}N_{DH}\frac{l_{\perp H}}{\beta_{\perp H}}+\frac{1}{3}N_{DH}^2+\frac{2}{3}N_{DH}-N_{eH}N_{DH}\right]\right.$$
$$\left.+l_{\perp H}\left[\frac{1}{3}-2N_{eH}+\frac{2}{3}N_{DH}\right]\right\}$$

Adding the higher order terms in (8) and in δ to $D_2(\omega, k_\perp: \approx \varepsilon^4)$ the dispersion relation, to order ε^4, is given by

$$a_4\Gamma^4+a_3\Gamma^3+a_2\Gamma^2+a_1\Gamma+a_0=0. \tag{11}$$

The expressions for the coefficients in (11) are lengthy and are therefore given in an appendix, namely Appendix A. As a check on these expressions we note that for $N_{DH}=0$ they reduce to the corresponding expressions for a single ion plasma [5]. Here too a term

$$\left[\frac{24(\bar{v}_{\perp H}^2)^2+8\bar{v}_{\perp H}^2\bar{v}_{\parallel H}^2+3(\bar{v}_{\parallel H}^2)^2}{4c^4}\right]\left(1+\frac{4}{3}N_{DH}-\frac{l_{\perp H}}{\beta_{\perp H}}\right)$$

drops out of (11) as it is now of order ε^5.

5. Discussion

In the derivation of our dispersion relations (10) and (11), the scaling adopted was that of $l_{\perp H}\approx l_{\perp D}\approx\varepsilon$ as the two ionic species were assumed to be in temperature equilibrium. It would, however, be interesting to also consider the case where the two ionic species have appreciably different temperatures and the consequent changes in our dispersion relation. Such a situation, though algebraically tedious, can easily be studied by changing the ordering of $l_{\perp H}$ and $l_{\perp D}$. We discuss below the cases where the majority hydrogen ions are much colder than deuterium and vice versa.

We first consider $T_{\perp H}\to 0$ so that $l_{\perp H}\approx\varepsilon^2$ and $\bar{v}_{\perp H}^2/c^2\approx\varepsilon^3$. However, $l_{\perp H}/\beta_{\perp H}$ is finite as it is independent of temperature. The quadratic equation (10) now has one solution at $Z_H(=\omega/\Omega_H)=1{\cdot}0$. This can be anticipated physically as the majority species hydrogen is now effectively cold. The other solution is still dependent on the finite temperature effects introduced by the second species deuterium. On the other hand the quartic equation (11) reduces to a cubic equation, the characteristics of which now depend on the deuterium density and temperature. A solution of this dispersion relation, for the parameters given below, gives one real root and a pair of complex conjugate roots around $Z_H=1{\cdot}0$. No major changes in the form of these equations were introduced when $T_{\parallel H}\to 0$.

No major changes in (10) and (11) were found for the other limiting case of $T_{\perp D}\to 0$ ($l_{\perp D}\approx\varepsilon^2$, $\bar{v}_{\perp D}^2/c^2\approx\varepsilon^3$).

6. Results

The dispersion relations have been plotted for conditions of a typical mirror experiment [7].

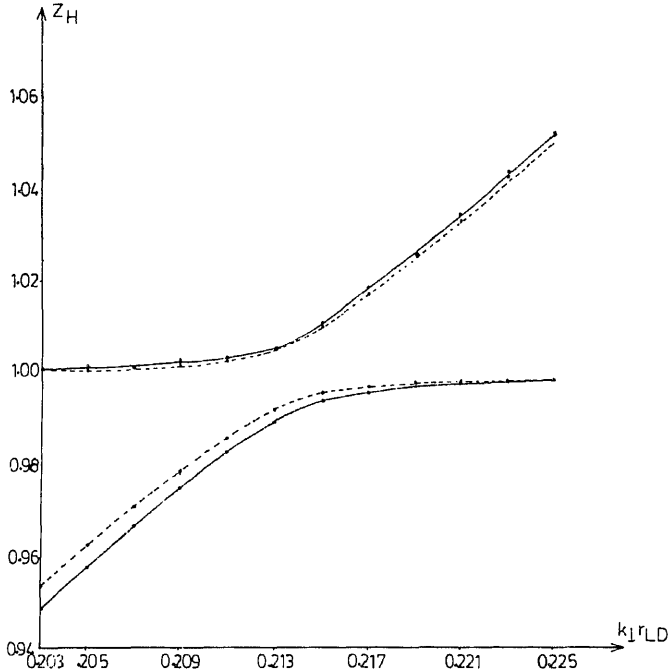

Figure 1. A plot of Z_H versus $k_\perp r_{LD}$ for $T_{\perp e}/T_{\perp H} = 0{\cdot}023$ and $T_{\perp D}/T_{\perp H} = 0{\cdot}5$ and $T_{\perp H} = 50$ keV. The dotted lines are the solutions of (10) for $N_H = 2{\cdot}67 * 10^{13}$ cm^{-3} and a deuterium density 30% of that of hydrogen. The solid lines are for a single ion plasma ($N_H = 3{\cdot}76318 * 10^{13}$ cm^{-3} and $N_D = 0{\cdot}0$). The dots on the curves are the solutions obtained numerically.

The ions in the experiment had a temperature $T_{\perp H} = 50$ keV and to conform to our ordering scheme we assume a slightly lower electron temperature of $T_{\perp e} = 1{\cdot}15$ keV compared to the observed value of 9 keV. Since the electron contributions to (10) and (11) are only minimal this assumption does not greatly alter our results. The other relevant parameter is $B_0 = 4 * 10^4$ G.

Figure 1 is a plot of Z_H versus $k_\perp r_{LD}$(r_{LD} is deuterium ion Larmour radius) for $T_{\perp e}/T_{\perp H} = 0{\cdot}023$ and $T_{\perp D}/T_{\perp H} = 0{\cdot}5$. Since $l_\perp \approx \varepsilon (= 0{\cdot}023)$, we are restricted to a small range of $k_\perp r_{LD}$ from 0·205 to 0·225. Corresponding to the midpoint of this interval, $\beta_{\perp H}$ was calculated using (9) and finally N_H from the definition of $\beta_{\perp H}$. The dotted lines are the solutions of (10) for $N_H = 2{\cdot}67 * 10^{13}$ cm^{-3} and a deuterium density of 30% of that of hydrogen. We find that there are two modes on either side of the hydrogen ion gyrofrequency Ω_H in agreement with our assumptions. The lower frequency (LF) mode approaches Ω_H while the other high frequency (HF) mode deviates away from it for increasing $k_\perp r_{LD}$. For a comparative study we also plot these modes for a single ion plasma ($N_H = 3{\cdot}76318 * 10^{13}$ cm^{-3} and N_D is 0·0) and these are depicted as the pair of solid lines. We find that the curves are similar; however the point of their closest approach decreases with increasing deuterium density.

Extensive numerical calculations were also performed to confirm the above results. The routines for the calculation of the modified Bessel functions in the tensor elements (3a) to (3c) were obtained from the well known text numerical recipes [8]. The returned values of $e^{-l_\perp} I_n(l_\perp)$ were then rechecked for their accuracy against their values available in literature [9]. The dispersion relations were then set up using (3a) to (3c) with the relativistic terms equal to zero ((10) is a non-relativistic dispersion relation) and solved iteratively using the standard root solver ZANLYT. The dots on the curves in figure 1 are the solutions obtained numerically. We find the agreement to be good especially for the LF mode where they are almost identical with the analytic solutions. Very slight variations occur for the HF mode. However, on the whole the numerical solutions confirm the soundness of our ordering scheme and the correctness of relation (10).

Figure 2 is a plot of our quartic relation (11) for $N_H = 2{\cdot}9563 * 10^{13}\,\mathrm{cm}^{-3}$ (with a deuterium density 20% of this value and depicted by solid lines) and $2{\cdot}67 * 10^{13}\,\mathrm{cm}^{-3}$ (deuterium density is equal to 30% of this value; depicted by dotted lines), the temperature $T_{\perp H}$ being $= 50\,\mathrm{keV}$ and $T_{\perp D}/T_{\perp H} = 0{\cdot}5$. As can be seen, the plasma can now support four modes on either side of Ω_H. However there is only a small region of wavelength where there are four distinct modes. The LF and HF modes then coalesce

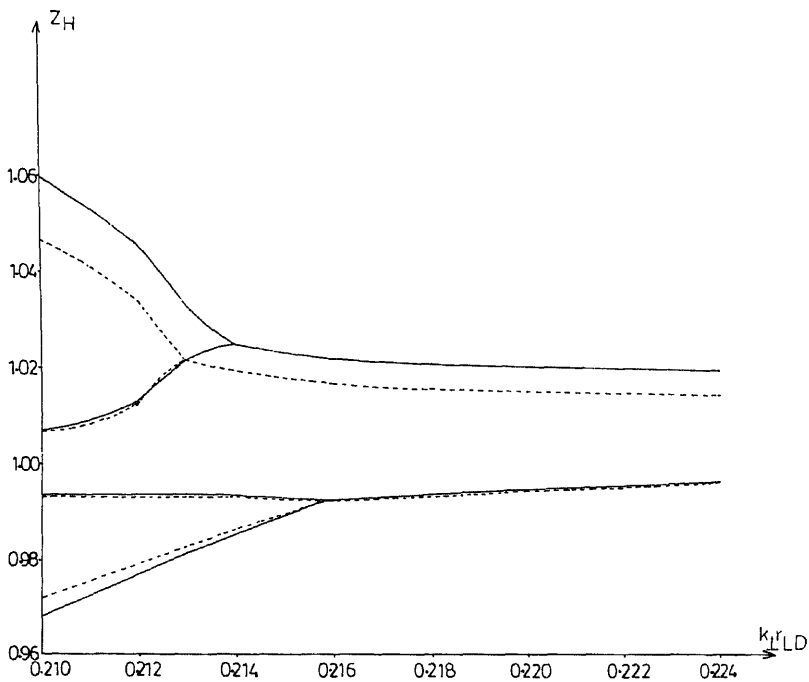

Figure 2. A plot of quartic equation (11). The solid lines are for $N_H = 2{\cdot}9563 * 10^{13}\,\mathrm{cm}^{-3}$ and a deuterium density 20% of that of hydrogen. The dotted lines are for $N_H = 2{\cdot}6700 * 10^{13}\,\mathrm{cm}^{-3}$ and a deuterium density 30% of that of hydrogen. The other parameters are the same as in figure 1.

instability for the HF mode for the latter case. Unfortunately we are not able to demonstrate any numerical confirmation of figure 2, due to the reasons mentioned in § 1. The non-relativistic terms "interfere" with and even dominate the relativistic terms in a fully numeric calculation; whereas analytically we have been successful in isolating the relativistic from the non-relativistic dispersion relation.

We now briefly compare these results with that obtained for a single ion plasma [5]. A weakly relativistic single ion plasma can support three modes—a pair of LF modes which coalesce to produce an instability and a HF mode. However, for a two ion plasma we find that in addition to the three modes, the second ion component introduces another HF mode.

7. Conclusions

We have in this paper studied the propagation and stability of IC modes in weakly relativistic two-ion component plasma with hydrogen as the majority species and deuterium as the minority species. We have, by means of an ordering parameter, been able to separate out two dispersion relations – one of which is independent of the relativistic factors (and having stable roots) and the other which depends on the relativistic terms. The non-relativistic relation has two solutions—a HF mode and a LF mode, with frequencies respectively higher and lower than the ion gyrofrequency. The latter dispersion relation supports four modes—a pair of HF and LF modes which can coalesce to make the plasma unstable. The relativistic terms are responsible for the instability. The results for the non-relativistic case have also been verified numerically using a standard root solver.

Acknowledgement

The authors thank the referee for his very useful comments which have greatly improved the contents of this paper.

Appendix A

$$a_4 = N_{DH}\left[\frac{8}{9}\frac{l_{\perp H}}{\beta_{\perp H}} + \frac{16}{27} + \frac{4}{9}N_{DH} - \frac{8}{9}N_{eH}\right]$$

$$a_3 = l_{\perp H}\left[-\frac{1}{3}\frac{l_{\perp H}}{\beta_{\perp H}} - \frac{4}{9} + \frac{4}{9}N_{DH} + \frac{4}{3}N_{eH}\right]$$

$$+ l_{\perp D}N_{DH}\left[\frac{4}{3}N_{eH} - \frac{2l_{\perp H}}{3\beta_{\perp H}} - \frac{8}{9} - \frac{4}{9}N_{DH}\right]$$

$$- \frac{1}{\bar{\omega}_{pH}^2}\left[\frac{l_{\perp H}}{\beta_{\perp H}} + 2 + \frac{4}{3}N_{DH}\right]$$

$$a_2 = -l_{\perp H}\left[\frac{5}{8}\frac{l_{\perp H}}{\beta_{\perp H}}l_{\perp H} + \frac{53}{48}l_{\perp H} + \frac{4}{\bar{\omega}_{pH}^2} + \frac{9}{4}l_{\perp H}N_{DH} + 2\frac{T_{\perp e}}{T_{\perp H}}N_{eH}\right.$$

$$-\frac{15}{4}l_{\perp H}N_{eH}\Bigg] + N_{DH}l_{\perp D}\Bigg[\frac{1}{2}\frac{l_{\perp H}}{\beta_{\perp H}}l_{\perp D} + \frac{3}{5}l_{\perp D} + \frac{1}{3}l_{\perp H} + \frac{1}{\bar{\omega}_{pH}^2}$$

$$+\frac{5}{12}l_{\perp D}N_{DH} - \frac{3}{2}l_{\perp D}N_{eH}\Bigg] + \Bigg[\frac{4\bar{v}_{\perp H}^2 + \bar{v}_{\parallel H}^2}{2c^2}\Bigg]\Bigg[\frac{l_{\perp H}}{2\beta_{\perp H}} + 1{\cdot}0\Bigg] + 2\frac{M_e}{M_H}N_{eH}$$

$$+\frac{2}{9}N_{DH}\Bigg[\frac{4\bar{v}_{\perp D}^2 + \bar{v}_{\parallel D}^2}{2c^2}\Bigg] + \Bigg[\frac{4\bar{v}_{\perp H}^2 + \bar{v}_{\parallel H}^2}{2c^2}\Bigg]\Bigg[\frac{4}{9}N_{DH} - 2N_{eH}\Bigg]$$

$$-l_{\perp H}\Bigg[1 + \frac{4}{3}N_{DH} - \frac{l_{\perp H}}{\beta_{\perp H}}\Bigg]$$

$$a_1 = \Bigg[\frac{4\bar{v}_{\perp H}^2 + \bar{v}_{\parallel H}^2}{2c^2}\Bigg]\Bigg[1 + \frac{4}{3}N_{DH} - \frac{l_{\perp H}}{\beta_{\perp H}}\Bigg] + l_{\perp H}\Bigg\{\frac{l_{\perp H}}{\beta_{\perp H}}\Bigg[\frac{6\bar{v}_{\perp H}^2 + \bar{v}_{\parallel H}^2}{2c^2}\Bigg] - l_{\perp H}^2$$

$$+\frac{4}{3}\Bigg[\frac{7\bar{v}_{\perp H}^2 + \bar{v}_{\parallel H}^2}{2c^2}\Bigg] + \Bigg[\frac{24\bar{v}_{\perp H}^2 + 4\bar{v}_{\parallel H}^2}{6c^2}\Bigg]N_{DH} - 4\Bigg[\frac{6\bar{v}_{\perp H}^2 + \bar{v}_{\parallel H}^2}{2c^2}\Bigg]N_{eH}\Bigg\}$$

$$+N_{DH}l_{\perp D}\Bigg\{-\frac{1}{2}\frac{l_{\perp H}}{\beta_{\perp H}}\Bigg[\frac{6\bar{v}_{\perp D}^2 + \bar{v}_{\parallel D}^2}{2c^2}\Bigg] + \frac{1}{6}l_{\perp D}^2 - \Bigg[\frac{6\bar{v}_{\perp D}^2 + \bar{v}_{\parallel D}^2}{4c^2}\Bigg] - \frac{1}{2}l_{\perp H}l_{\perp D}$$

$$-\frac{1}{6}\Bigg[\frac{4\bar{v}_{\perp H}^2 + \bar{v}_{\parallel H}^2}{2c^2}\Bigg] + \frac{3}{4}l_{\perp H}^2 - \frac{1}{3}\Bigg[\frac{6\bar{v}_{\perp D}^2 + \bar{v}_{\parallel D}^2}{2c^2}\Bigg]N_{DH}$$

$$+\Bigg[\frac{6\bar{v}_{\perp D}^2 + \bar{v}_{\parallel D}^2}{2c^2}\Bigg]N_{eH}\Bigg\} + \frac{2}{\bar{\omega}_{pH}^2}\Bigg[\frac{4\bar{v}_{\perp H}^2 + \bar{v}_{\parallel H}^2}{2c^2}\Bigg]$$

and

$$a_0 = l_{\perp H}^2\Bigg[\frac{6\bar{v}_{\perp H}^2 + \bar{v}_{\parallel H}^2}{2c^2}\Bigg].$$

References

[1] R A Cairns, *Radio frequency heating of plasmas* (Adam Hilger, England, 1991)
[2] A Kaye, T Brown, V Bhatnagar, P Crawley, J Jacquinot, R Lobel, J. Plancoulaine, P-H Rebut, T Wade and C Walker, *Fusion Eng. Des.* **24**, 1 (1994)
[3] R W Landau and S Cuperman, *J. Plasma Phys.* **4**, 495 (1970)
[4] V Fuchs and A Bers, *Phys. Fluids* **31**, 3702 (1988)
[5] Chandu Venugopal, P J Kurian and G Renuka, *J. Plasma Phys.* **51**, 371 (1994)
[6] R W Landau and S Cuperman, *J. Plasma Phys.* **6**, 495 (1971)
[7] G R Smith, W M Nevins and W M Sharp, *Phys. Fluids* **27**, 2120 (1984)
[8] W H Press, B P Flannery, S A Teukolsky and W T Vetterling, *Numerical recipes: The art of scientific computing* (Cambridge, University Press, 1986)
[9] M Abromowitz and I A Stegun, *Handbook of Mathematical Functions* (Dover Publications, New York, 1970)

journal of physics

pp. L463-L470

Estimation of parameters of gravitational waves from coalescing binaries

R BALASUBRAMANIAN, B S SATHYAPRAKASH and S V DHURANDHAR
Inter-University Centre for Astronomy and Astrophysics, Post Bag 4, Ganeshkhind, Pune 411 007, India

MS received 21 August 1995; revised 24 October 1995

Abstract. In this paper we deal with the measurement of parameters of the gravitational wave signal emitted by a coalescing binary system of compact stars. We present the results of Monte Carlo simulations carried out for initial LIGO, incorporating the first post-Newtonian corrections to the waveform. Using the parameters so determined, we estimate the direction to the source. We stress the use of the time-of-coalescence rather than the time-of-arrival of the signal to determine the direction of the source. We show that this can considerably reduce the errors in the determination of the direction of the source.

Keywords. Gravitational waves; coalescing binaries; data analysis.

PACS Nos 04·30; 04·80

1. Introduction and summary

A major source for the planned interferometric gravitational wave detectors like LIGO [1] and VIRGO [2] is the radiation emitted by a binary system of compact stars, e.g. neutron stars or black holes, during the last few minutes of its evolution just before the two stars coalesce. The interferometers are expected to have high enough sensitivity to detect sources at cosmological distances. Since the waveform emitted during a binary coalescence, often called the chirp, can be modeled fairly accurately it is possible to enhance the visibility or the 'signal-to-noise' ratio henceforth denoted as SNR, (defined later in the text in (eq. 9)) of the signal in noisy data by employing powerful data analysis techniques such as Weiner or matched filtering [3,4]. A filter, in the Fourier domain, is a copy of the expected signal weighted by the noise power spectral density. The process of filtering involves obtaining correlations of the detector output with a set of templates which together span the relevant range of the parameters of the waveform. On filtering the detector output for signal of known shape one enhances the raw SNR by comparing the signal energy with that of the noise as opposed to the case of a burst signal where one has to contend with the signal power vis-a-vis noise power [4]. The fact that the signal waveform can be predicted very well also implies that the parameters of the waveform can be estimated to a high accuracy. For instance, by tracking the radiation emitted by a neutron star-neutron star (In this paper a neutron star is considered to have a mass of 1·4 $M_\odot$, and a black hole will be considered to have a mass of 10 $M_\odot$.) (NS–NS) binary starting from 10 Hz to say 1 kHz, the masses can be determined to an accuracy better than a few per cent [5–9]. Observation of several

coalescence events could be potentially used to determine the Hubble parameter to an accuracy of $\sim 10\%$ [10]. Once in a while, when an event produces a very high SNR (≥ 40) it would be possible to infer the presence of such non-linear effects as tails of gravitational waves in the signal waveform and test general relativity in the strongly non-linear regime [11, 12].

When a signal is present in the detector output, amongst all filters the filter matched to that particular signal will, on the average, obtain the largest possible correlation with the detector output, thus enabling the detection as well as the estimation of parameters. The parameters of the template that obtains the maximum correlation are unbiased estimates of the actual signal parameters. Of course, the detector output also contains noise which can affect the correlation thereby giving rise to spurious maxima even when the parameters of the template and those of the signal are mismatched. Thus, the measured parameters are in error. These errors reduce with increasing SNR. In the limit of high SNR the covariance matrix gives errors in the estimation of parameters and the covariances among them. Based on the computation of the covariance matrix (for the advanced LIGO), it is now generally agreed that the chirp mass, which is a combination of the masses of the binary stars (see below for its definition), can be determined at a relative accuracy $\sim 0.1\% - 1\%$ at a SNR of 10. The reduced mass, as it turns out, will have a much larger error (few $- 50\%$) especially if the spins of the bodies are large [6]. The Cramer–Rao theorem asserts that the covariance matrix is only a lower bound on the errors in the estimation of parameters [13]. Consequently, a more rigorous or a different method of computing the variances and covariances is in order. Alternatively one can determine the errors through the Monte Carlo simulation method. The basic idea here is to mimic the actual detection problem on a computer by adding numerous realizations of the noise to the signal and then passing the resultant time series through a bank of filters each matched to a gravitational wave signal from a coalescing binary system with a particular set of parameters. The errors involved in the measurement can be computed by using the ensemble of measured values of the signal parameters. Such a method is robust in the sense that it does not make any assumptions about the SNR and is therefore much closer to the actual detection problem. It also squarely addresses the difficulties faced in a realistic data analysis exercise such as the finite sampling rate, the discreteness of the set of filters, etc. For details on the Monte Carlo method see Balasubramanian *et al* [14].

In this communication we summarize the outcome of the first in a series of Monte Carlo simulations which suggests that the covariance matrix grossly underestimates the errors in the estimation of the parameters by over a factor of 3 at an SNR of 10. The standard method to deduce the direction to the source of the gravitational radiation has been to use the differences in the times-of-arrival in a network of three or more detectors. We point out that since the instant of coalescence of a binary system can be measured to a much greater accuracy than the time-of-arrival, the former can be employed to infer the direction of the source at a much lower uncertainty than has been so far thought.

2. Basic equations and formalism

In the point mass approximation the restricted first-order post-Newtonian gravitational radiation emitted by a binary system of stars induces a strain in the detector

which can be written as

$$h(t) = A[\pi f(t)]^{2/3} \cos(\varphi(t)], \tag{1}$$

where $f(t)$ is the instantaneous gravitational wave frequency, which at this level of approximation is equal to twice the orbital frequency and is implicitly given by

$$t - t_a = \tau_0 \left[1 - \left(\frac{f}{f_a}\right)^{-8/3}\right] + \tau_1 \left[1 - \left(\frac{f}{f_a}\right)^{-2}\right] \tag{2}$$

and $\varphi(t)$ is the phase of the signal given by

$$\varphi(t) = \frac{16\pi f_a \tau_0}{5}\left[1 - \left(\frac{f}{f_a}\right)^{-5/3}\right] + 4\pi f_a \tau_1 \left[1 - \left(\frac{f}{f_a}\right)^{-1}\right] + \Phi \tag{3}$$

where t_a, the time-of-arrival, is the time at which the signal reaches a frequency f_a; and Φ is the phase of the signal at t_a a constant depending on the relative orientations of the binary orbit and the arms of the interferometer; τ_0 and τ_1 are constants, having dimensions of time, depending on the masses m_1 and m_2 of the binary system. They are referred to as Newtonian and post-Newtonian chirp time, respectively, and are given by,

$$\tau_0 = \frac{5}{256} \mathcal{M}^{-5/3} (\pi f_a)^{-8/3}, \quad \tau_1 = \frac{5}{192\mu(\pi f_a)^2}\left(\frac{743}{336} + \frac{11}{4}\frac{\mu}{M}\right). \tag{4}$$

Here μ is the reduced mass, M is the total mass, and $\mathcal{M} = \mu^{3/5} M^{2/5}$ is the chirp mass. In this level of approximation the post-Newtonian waveform is characterized by a set of five parameters: The amplitude parameter A, the time-of-arrival t_a, the phase at the time of arrival Φ, and the two masses m_1 and m_2. We shall find below a more convenient parametrization of the waveform.

The Fourier transform of the waveform in the stationary phase approximation for positive frequencies is given by

$$\tilde{h}(f) = \mathcal{A} f^{-7/6} \exp\left[i \sum_{\mu=1}^{4} \psi_\mu(f) \lambda^\mu - i\frac{\pi}{4}\right] \tag{5}$$

where $\mathcal{A}$ is a normalization constant and is fixed by specifying the SNR, and $\psi_\mu(f)$ are functions only of frequency given by

$$\psi_1 = 2\pi f, \quad \psi_2 = -1, \quad \psi_3 = \frac{6\pi f_a}{5}\left(\frac{f}{f_a}\right)^{-5/3}, \quad \psi_4 = 2\pi f_a \left(\frac{f}{f_a}\right)^{-1}. \tag{6}$$

Here λ^μ are related to the set of parameters introduced earlier: $\lambda^\mu = \{t_C, \Phi_C, \tau_0, \tau_1\}$, where

$$t_C = t_a + \tau_0 + \tau_1, \quad \Phi_C = \Phi - 2\pi f_a t_a + \frac{16\pi f_a \tau_0}{5} + 4\pi f_a \tau_1. \tag{7}$$

For $f < 0$, the Fourier transform can be obtained by the relation $\tilde{h}(-f) = \tilde{h}^*(f)$, obeyed by real functions $h(t)$.

Central to the computation of the covariance matrix of the parameters is the scalar product defined over the space of the signal waveforms. Given waveforms $h(t; \lambda)$ and

$h(t;\lambda')$ their scalar product is defined by,

$$\langle h,g\rangle = \int_{f_a}^{\infty} \frac{\tilde{h}(f;\lambda^\mu)\tilde{h}^*(f;\lambda'^\mu)}{S_n(f)}\mathrm{d}f + \text{c.c.} \tag{8}$$

where $S_n(f)$ is the two-sided detector noise power spectral density. The scalar product defines a norm on the vector space. The SNR obtained for a signal $h(t;\lambda)$ when it is passed through the matched filter is the norm of the signal [4]

$$\rho = \langle h,h\rangle^{1/2}. \tag{9}$$

The covariance matrix $C_{\mu\nu}$ is the inverse of the Fisher information matrix $\Gamma_{\mu\nu}$ [13] given by,

$$\Gamma_{\mu\nu} = \left\langle \frac{\partial h}{\partial\lambda^\mu}, \frac{\partial h}{\partial\lambda^\nu}\right\rangle; \quad C_{\mu\nu} = [\Gamma^{-1}]_{\mu\nu}. \tag{10}$$

The diagonal elements of the covariance matrix provide us an estimate of the variances to be expected in the measured values of the parameters in a given experiment. In figure 1 we have shown as a solid line the behaviour of the computed 1σ uncertainties (square root of the variances) in the estimation of parameters t_a, τ_0, τ_1 and τ_C, as a function of the SNR. As is well-known the covariance matrix predicts that the errors fall off in inverse proportion to the SNR.

3. Simulations

In the actual detection problem the detector output $x(t)$ is filtered through a host of search templates corresponding to test parameters, ${}_t\lambda$ and the template that obtains the maximum correlation with the output gives us the measured values ${}_m\lambda$ of the signal. These measured values will in general differ from the actual signal parameters. With the aid of a large number of detectors one obtains an ensemble of measured values ${}_m\lambda$. Such an ensemble provides us with an estimate ${}_e\lambda$, the errors σ_λ and correlation coefficients $\Sigma_{\mu\nu}$.

$$ {}_e\lambda = \overline{{}_m\lambda}, \quad \sigma_\lambda^2 = \overline{({}_m\lambda - \overline{{}_m\lambda})^2}, \quad \Sigma^{\mu\nu} = \frac{\overline{m\lambda^\mu\, m\lambda^\nu}}{\sigma_\mu\sigma_\nu}, \tag{11}$$

where the overbar denotes the average over an ensemble. In reality we will have only a few detectors and hence a numerical simulation needs to be carried out to deduce the errors in the estimation of parameters. We have carried out such a numerical simulation by using in excess of 5000 realizations of detector noise. Thus, the results of our simulations are statistically significant and the errors in the estimation of various statistical quantities, such as the mean and the variance (cf. figure 1), are negligible. In figure 1 the dotted line corresponds to the behaviour of the errors in the estimation of various parameters computed at several values of the SNR. At low values of the SNR ($\rho \sim 10$) there is a significant departure of the observed errors from those predicted by the covariance matrix. However at an SNR of ~ 30 the two curves merge together indicating the validity of the covariance matrix at high enough SNRs. Since most of the events which the interferometric detectors will observe are expected to have an SNR

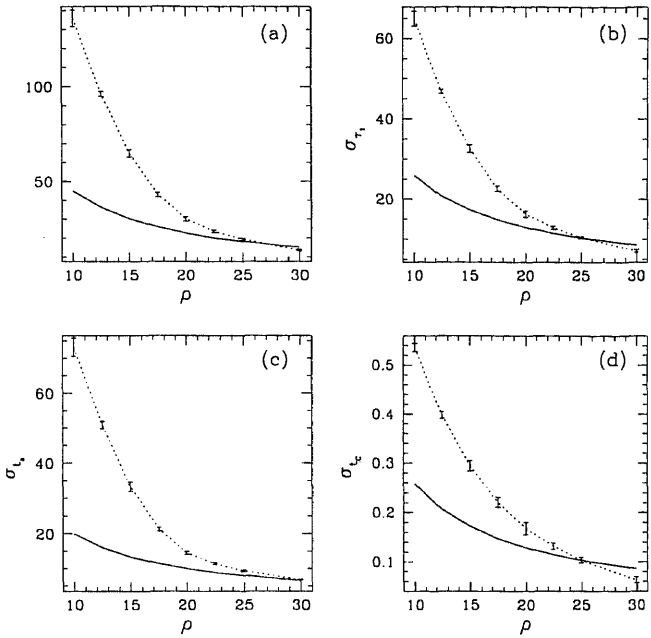

Figure 1. Dependence of the errors in the estimation of parameters of the post-Newtonian waveform i.e. $\{\sigma_{\tau_0}, \sigma_{\tau_1}, \sigma_{t_a}, \sigma_{t_c}\}$ as a function of SNR. The solid line represents the theoretically computed errors whereas the dotted line represents the errors obtained through Monte Carlo simulations. The simulations have been carried out for $10\,M_\odot - 1{\cdot}4\,M_\odot$ binary system. The errors in the parameters are expressed in ms.

less than 10, we conclude that the accuracy in the determination of the parameters is not as high as was thought to be. Detailed analysis suggests that this discrepancy is larger when higher post-Newtonian corrections are taken into account. Consequently, a more exhaustive analysis has been reported here or elsewhere [14] which is in order. At SNRs > 30 numerically estimated errors are somewhat lower than the covariance matrix, especially in the case of t_C, as opposed to what is expected from the Cramar-Rao bound. The reason for this discrepancy is that we do not have a high enough resolution (in particular, in the case of t_C) to determine the errors when the SNR is high. This is indicated by the increase in the error bars after the two curves cross over in figure 1. Moreover, the covariance matrix is computed using the stationary phase approximation to the Fourier transform of the signal while numerical estimation uses Fast Fourier Transforms.

With reference to figure 1 we point out that the instant of coalescence t_C can be determined to an accuracy much better than the time-of-arrival t_a. Typically σ_{t_c} is a factor of 50 less than σ_{t_a}. Consequently, with the aid of t_C we can fix the direction to the source at a much higher accuracy than with t_a. Since the parameters τ_0, τ_1 and t_a have negative covariances their sum, t_C, is more accurately determined. A possible physical interpretation of this result is that at the time-of-arrival the frequency is lower and

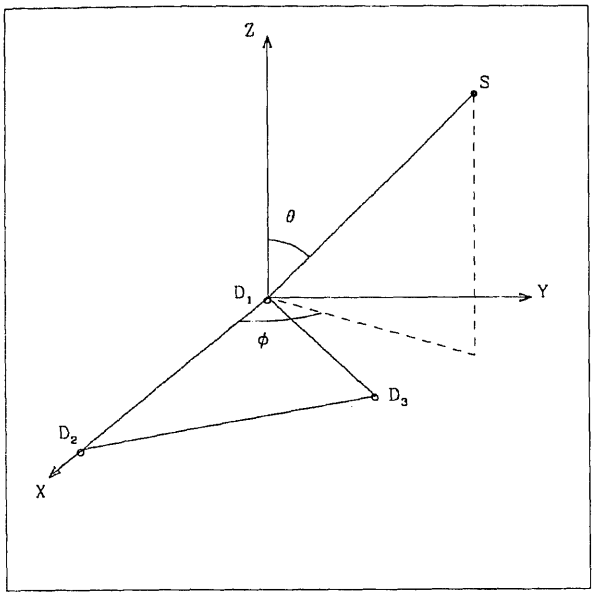

Figure 2. This figure illustrates the network of three identical detectors and the coordinate system employed. The detectors lie on the X–Y plane and θ and ϕ represent the angles determining the direction of the source (S).

hence allows for a larger variation in t_a without incurring a substantial error in the phase of the template relative to that of the signal. While close to coalescence the signal has a greater frequency and hence even a slight mismatch in t_C's of the signal and the template leads to a greater error in the phase. It is to be noted, however, that as of now we do not know the orbit of the binary accurately enough, to predict the exact instant of the coalescence. In fact the frequency cut off imposed by the onset of the plunge orbit will make it difficult to calculate t_C. In addition, for a realistic detector the noise increases with the frequency beyond about 150 Hz and the frequency which will be of more interest to us is the one where the power spectrum of the signal divided by that of the noise reaches a maximum. This, of course, assumes that the detectors, used in the measurement of the direction of the source, are all identical.

4. Determining source direction

Let t denote a convenient time parameter which, if measured at three detectors, gives the direction to the source. For our purpose we take this parameter to be either t_C or t_a. We assume a simple configuration of three identical detectors placed at the vertices of an equilateral triangle on the equatorial plane of the earth. We take the separation between any two detectors as L. Thus, the maximum delay in arrival times of the signal at the detectors is $\Delta = L/c$, where c is the speed of light. Figure 2 illustrates such a detector network and the coordinate system used. Given t_1, t_2 and t_3 as the measured values of t in the three detectors, respectively, we can deduce the direction to the source

$$\phi = \tan^{-1}\left[\frac{\quad}{\sqrt{3}\gamma}\right], \tag{12}$$

$$\theta = \sin^{-1}\left[\frac{2\gamma\sqrt{\gamma^2+\delta^2-\gamma\delta}}{\Delta(2\delta-\gamma)}\right]. \tag{13}$$

assumption of identical detectors means that the errors in t in different detectors l the same. As the noises in different detectors are uncorrelated, the fluctuations in neasurements of t_1, t_2 and t_3 are uncorrelated; however, γ and δ have non-zero riances. Thus,

$$\sigma_{t_1} = \sigma_{t_2} = \sigma_{t_3} = \sigma; \quad \sigma_\gamma = \sigma_\delta = \sqrt{2}\sigma. \tag{14}$$

errors in the measurement of time parameter will induce errors, σ_ϕ and σ_θ, in the urement of angles. Assuming the errors in time parameter to be small we can write,

$$\sigma_\phi = \frac{\sigma}{\Delta} g_\phi(\theta,\phi) \quad \text{and} \quad \sigma_\theta = \frac{\sigma}{\Delta} g_\theta(\theta,\phi), \tag{15}$$

e,

$$g_\phi(\theta,\phi) = \frac{1}{\sin\theta} \quad \text{and}$$

$$g_\theta(\theta,\phi) = \left(\frac{\cos^4\phi - \cos^2\phi - 1}{-1 + 3\cos^2\phi - 2\cos^4\phi - \cos^2\phi\cos^2\theta\sin^2\theta}\right)^{1/2} \tag{16}$$

factors $g_\phi(\theta,\phi)$ and $g_\theta(\theta,\phi)$ are typically of order unity for most directions. For based detectors the value of Δ is ≈ 15 ms. This certainly rules out the use of t_a to mine the direction as the error in this parameter, even for high SNRs ~ 15, is much than Δ. Though for the initial LIGO we can use t_C, the errors at an SNR of 10 will ound two degrees which is too large to make an optical identification of the source. der to determine the direction to arcsecond resolution one needs the sensitivity of dvanced LIGO or the VIRGO.

owledgements

authors would like to thank Biplab Bhawal and S D Mohanty for useful ssions. One of the authors (RB) would like to acknowledge CSIR, India for cial support through the senior research fellowship.

ences

A Abramovici *et al*, *Science* **256**, 325 (1992)

C Bradaschia *et al*, *Nucl. Instrum. Methods*, **A289**, 518 (1990)

K S Thorne, in *300 Years of gravitation*, edited by S W Hawking and W Israel (Cambridge Univ. Press, 1987)

B F Schutz, in *The detection of gravitational radiation*, edited by D Blair (Cambridge Univ. Press, Cambridge, 1989) pp 406–427

[5] L S Finn and D F Chernoff, *Phys. Rev.* **D47**, 2198 (1993)
[6] C Cutler and E Flanagan, *Phys. Rev.* **D49**, 2658 (1994)
[7] E Poisson and C M Will, *Phys. Rev.* **D52**, 848 (1995)
[8] A Krolak, K D Kokkotas and G Schäfer, *Phys. Rev.* **D52**, 2089 (1995)
[9] P Jaranowski, K D Kokkotas, A Krolak and G Tsegas, report (unpublished)
[10] D Marković, *Phys. Rev.* **D48**, 4738 (1993) and references therein
[11] L Blanchet and B S Sathyaprakash, *Class. Quantum Gravit.*, **11**, 2807 (1994)
[12] L Blanchet and B S Sathyaprakash, *Phys. Rev. Lett.* **74**, 1067 (1995)
[13] C W Helstrom, *Statistical theory of signal detection*, (Pergamon, Cambridge, 196(edition
[14] R Balasubramanian, B S Sathyaprakash and S V Dhurandhar, *Gravitational wa coalescing binaries: detection strategies and Monte Carlo estimation of parameters* ted for publication (1995)
[15] P Jaranowski and A Krolak, *Phys. Rev.* **D49** 1723 (1994)

Regd. No. KRN-A 64

Pramana journal of physics Vol. 45 (No. 5), November 1995

Contents

Nonlinear dynamics of a two-dimensional lattice.....
.....*Nabonita D Chowdhury and Sankar P Sanyal* 377

Microscopic theory of single particle and pair condensation of an attracting Bose-gas as the basis for superfluidity and superconductivity.....
.....*S Dzhumanov and P K Khabibullaev* 385

Temperature dependence electron spin resonance spectra of a magnetic fluid
.....*R V Upadhyay, D Srinivas, R V Mehta and P M Trivedi* 419

Dielectric properties of nano-particles of zinc sulphide.....
.....*Binny Thomas and M Abdulkhadar* 431

Generation of picosecond optical pulses from single heterostructure GaAs diode laser and study of their emission characteristics.....
.....*V N Rai, M Shukla and H C Pant* 439

Ion cyclotron instabilities in a mildly relativistic hydrogen-deuterium fusion plasma.....*Chandu Venugopal, P J Kurian and G Renuka* 453

Rapid Communication

Estimation of parameters of gravitational waves from coalescing binaries
.....*R Balasubramanian, B S Sathyaprakash and S V Dhurandhar* L463

Indexed in CURRENT CONTENTS ISSN 0304–4289

Edited and published by V K Gaur for the Indian Academy of Sciences, Bangalore 560 080. Typeset and printed at Thomson Press (I) Ltd., Faridabad 121 007.

PRAMANA

journal of physics

Vol. 45 No. 6
December 1995

INDIAN ACADEMY OF SCIENCES
ndian National Science Academy
ndiąn Physics Association

Editor

R Nityananda
Raman Research Institute, Bangalore

Associate Editor

H R Krishnamurthy
Indian Institute of Science, Bangalore

Editorial Board

G S Agarwal, *Physical Research Laboratory, Ahmedabad*
V Balakrishnan, *Indian Institute of Technology, Madras*
M Barma, *Tata Institute of Fundamental Research, Bombay*
P Chaddah, *Centre for Advanced Technology, Indore*
B M Deb, *Panjab University, Chandigarh*
P K Kaw, *Institute for Plasma Research, Gandhinagar*
H S Mani, *Indian Institute of Technology, Kanpur*
N Mukunda, *Indian Institute of Science, Bangalore*
T Padmanabhan, *Inter-University Centre for Astronomy and Astrophysics, Pune*
J C Parikh, *Physical Research Laboratory, Ahmedabad*
G Rajasekaran, *Institute of Mathematical Sciences, Madras*
V S Ramamurthy, *Department of Science and Technology, New Delhi*
R Ramaswamy, *Jawaharlal Nehru University, New Delhi*
K R Rao, *Bhabha Atomic Research Centre, Bombay*
Probir Roy, *Tata Institute of Fundamental Research, Bombay*
A K Sood, *Indian Institute of Science, Bangalore*

Editor of Publications of the Academy

V K Gaur
C-MMACS, NAL, Bangalore

Subscription Rates
(1996)

All countries except India	1 year
(Price includes AIR MAIL charges)	US$ 200
India	1 year Rs. 200

Annual subscriptions for **individuals** for India and abroad are Rs. 75/- and $50 respectively.

All correspondence regarding subscription should be addressed to the **Circulation Department** of the Academy

Editorial Office

Indian Academy of Sciences, C V Raman Avenue,
P.B. No. 8005, Bangalore 560 080, India

Telephone: 334 2546
Telex: 845-2178 ACAD IN
Telefax: 91-80-334 6094

© 1995 by the Indian Academy of Sciences. All rights reserved.

"Information for contributors" is printed in the last issue of every volume.

PRAMANA
— journal of
physics

© Printed in India

Vol. 45, No. 6,
December 1995
pp. 471–497

The real symplectic groups in quantum mechanics and optics

ARVIND, B DUTTA[1], N MUKUNDA[1,2] and R SIMON[3]
Department of Physics, Indian Institute of Science, Bangalore 560 012, India
[1]Jawaharlal Nehru Centre for Advanced Scientific Research, Jakkur, Bangalore 560 064, India
[2]Centre for Theoretical Studies and Department of Physics, Indian Institute of Science, Bangalore 560 012, India
[3]Institute of Mathematical Sciences, C. I. T. Campus, Madras 600 113, India

MS received 13 June 1995

Abstract. We present a utilitarian review of the family of matrix groups $Sp(2n, \mathscr{R})$, in a form suited to various applications both in optics and quantum mechanics. We contrast these groups and their geometry with the much more familiar Euclidean and unitary geometries. Both the properties of finite group elements and of the Lie algebra are studied, and special attention is paid to the so-called unitary metaplectic representation of $Sp(2n, \mathscr{R})$. Global decomposition theorems, interesting subgroups and their generators are described. Turning to n-mode quantum systems, we define and study their variance matrices in general states, the implications of the Heisenberg uncertainty principles, and develop a $U(n)$-invariant squeezing criterion. The particular properties of Wigner distributions and Gaussian pure state wavefunctions under $Sp(2n, \mathscr{R})$ action are delineated.

Keywords. Symplectic groups; symplectic geometry; Huyghens kernel; uncertainty principle; multimode squeezing; Gaussian states.

PACS Nos 3·65; 42·50

1. Introduction

The symplectic groups form one of the three major families of classical semisimple Lie groups, the other two being the real orthogonal family and the complex unitary family [1]. Apart from the groups describing nonrelativistic and relativistic space-time geometries, namely the Galilei, Lorentz and Poincare groups, most of the Lie groups encountered in physical problems, for example as symmetry groups, belong to either the real orthogonal or the unitary families [2]. These are multidimensional as well as complex generalisations of the rotation group of Euclidean geometry characterising physical three-dimensional space. As a result, the intuitive geometrical ideas that go with real orthogonal or complex unitary geometries are quite familiar to most physicists.

It has been realised recently, however, that in several problems both in quantum mechanics and in optics, the real symplectic groups play an important role [3]. In the latter context, this is so in both classical and quantum theories. More generally, these groups come in very naturally through the canonical formalism of classical dynamics, and its counterpart in quantum mechanics.

Symplectic geometry, on the other hand, differs profoundly from the real or complex Euclidean variety [4]. Here the intuitively familiar concepts of length, angle,

perpendicularity and the Pythagoras Theorem are all absent. In their place we have typically new concepts characteristic of canonical mechanics.

The purpose of this informal and utilitarian survey is to introduce methods based on the real symplectic groups to those who are otherwise familiar with the structures of quantum mechanics and/or the theory of partial coherence in optics. The intention is to "inform rather than astonish", and to describe the main features of the symplectic point of view, Our account will not contain complete proofs of all statements presented, but a motivated reader should easily be able to supply additional detail and proceed to make practical use of these methods.

The material of this article is organised as follows. Section 2 introduces the group $Sp(2n, \mathscr{R})$ as the group of linear transformations preserving the classical Poisson Brackets as well as the quantum commutation relations among n pairs of canonical variables. In the quantum case, the Stone-von Neumann theorem allows us to infer that these transformations are unitarily implementable. Section 3 develops some ideas related to real symplectic linear vector spaces, specially the concepts of symplectic complement and symplectic rank of a subspace, in order to contrast symplectic geometry with real Euclidean and complex unitary geometries. Some useful properties of the matrices occurring in the defining representation of $Sp(2n, \mathscr{R})$, and their complex form, are then explained in §4. Here we also list several useful subgroups of $Sp(2n, \mathscr{R})$, and describe four global decomposition theorems – the polar, Euler, pre-Iwasawa and Iwasawa decompositions. Section 5 studies the Lie algebra $\underline{Sp(2n, \mathscr{R})}$, first in the defining representation and then in a general, possibly unitary, representation. Convenient ways of breaking up the generators into subsets, and generators of various subgroups, are described. In §6 we set up and study the special unitary metaplectic representation of $Sp(2n, \mathscr{R})$ and relate it to the generalised Huyghens kernel in any number of dimensions. The characteristic differences between the compact and the noncompact generators of $Sp(2n, \mathscr{R})$ are seen in their dependences on mode annihilation and creation operators. The former (latter) conserve (do not conserve) the total number operator. Section 7 studies the relationship between the metaplectic unitary representation of $Sp(2n, \mathscr{R})$, and two often used descriptions of quantum mechanical operators, namely the Wigner function representation and the diagonal coherent state representation. While the former is covariant, i.e., transforms simply, under the full group $Sp(2n, \mathscr{R})$, the latter is covariant only under the maximal compact subgroup $K(n) = U(n)$ of $Sp(2n, \mathscr{R})$. Section 8 takes up the questions of defining the noise or variance matrix for any state of an n-mode quantum system, both in real and complex forms, and their behaviours under $Sp(2n, \mathscr{R})$. In §9 we carry this analysis further to show that the Heisenberg uncertainty principles for any number of modes can be given in explicitly $Sp(2n, \mathscr{R})$ covariant forms; a key role here is played by Williamson's Theorem relating to normal forms of quadratic Hamiltonians. This study leads in §10 to the setting up of an $U(n)$-invariant squeezing criterion for n-mode systems. This is the maximal physically reasonable invariance one could ask for in these systems, and it can be stated very elegantly in terms of the general variance matrix set up in §8. Section 11 describes and motivates some interesting classes of variance matrices with distinctive group theoretic properties, and §12 is devoted to a study of general centred and normalized pure Gaussian wavefunctions for n-mode systems. The transitive action of $Sp(2n, \mathscr{R})$ on these wavefunctions, via the metaplectic representation, and the emergence of a matrix form of the Mobius transformation, are described. Section 13 contains some concluding remarks.

2. The real symplectic groups Sp($2n, \mathscr{R}$)

We consider a classical or quantum canonical system with n degrees of freedom, that is, n pairs of mutually conjugate canonical variables. In the classical case these are numerical variables written as $q_r, p_r, r = 1, 2, \ldots, n$. In quantum mechanics we have an irreducible set of hermitian operators $\hat{q}_r, \hat{p}_r$ acting on a suitable Hilbert space $\mathscr{H}$. The basic kinematic structure is given by Poisson brackets (PB) in one case and by the Heisenberg commutation relations (CR) in the other. To express them both compactly and elegantly, we introduce the following notation. We assemble the q's and p's into $2n$-component vectors $\xi, \hat{\xi}$

$$\xi = (\xi_a) = (q_1 \cdots q_n p_1 \cdots p_n)^T,$$
$$\hat{\xi} = (\hat{\xi}_a) = (\hat{q}_1 \cdots \hat{q}_n \hat{p}_1 \cdots \hat{p}_n)^T, \quad a = 1, 2, \ldots, 2n. \tag{2.1}$$

Then the classical PB's and the quantum CR's are, respectively

$$\{\xi_a, \xi_b\} = \beta_{ab},$$
$$[\hat{\xi}_a, \hat{\xi}_b] = i\hbar\beta_{ab},$$
$$\beta = (\beta_{ab}) = \begin{pmatrix} 0_{n\times n} & 1_{n\times n} \\ -1_{n\times n} & 0_{n\times n} \end{pmatrix}. \tag{2.2}$$

The usual relations stated separately in terms of q's and p's are all contained here; and the even-dimensional real antisymmetric matrix β will play an important role.

We assume always that all the ξ_a, $\hat{\xi}_a$ are of the Cartesian type: the natural range (spectrum) for each of them is the entire real line $\mathscr{R}$.

Changes of $\xi, \hat{\xi}$ to new quantities $\xi', \hat{\xi}'$ given as functions of the old ones such that the basic kinematic relations are preserved may be called canonical transformations in both situations

$$\xi' = \text{numerical functions of } \xi : \{\xi'_a, \xi'_b\} = \beta_{ab};$$
$$\hat{\xi}' = \text{operator functions of } \hat{\xi} : [\hat{\xi}'_a, \hat{\xi}'_b] = i\hbar\beta_{ab}. \tag{2.3}$$

Apart from C-number translations (shift of origin) the simplest such transformations are the linear homogeneous ones. Each such transformation may be specified by a real $2n$-dimensional matrix S, the actions being

$$S = (S_{ab}) : \xi'_a = S_{ab}\xi_b.$$
$$\hat{\xi}'_a = S_{ab}\hat{\xi}_b. \tag{2.4}$$

In either case, the requirements (2.3) lead to a matrix condition on S [1]

$$S\beta S^T = \beta. \tag{2.5}$$

This is the defining condition for the real symplectic group in $2n$ dimensions

$$\text{Sp}(2n, \mathscr{R}) = \{S = \text{real } 2n \times 2n \text{ matrix} \mid S\beta S^T = \beta\}. \tag{2.6}$$

The matrix β is real, even-dimensional, antisymmetric and nonsingular. It is a "symplectic metric matrix". As we see explicitly later, Sp($2n, \mathscr{R}$) transformations preserve symplectic scalar products and the symplectic metric.

In quantum mechanics the Hilbert space $\mathscr{H}$ on which the ξ_a act irreducibly can described in many ways. The most familiar is the Schrödinger description using w functions on $\mathscr{R}^n$, that is, elements of $L^2(\mathscr{R}^n)$. The $\hat{q}_r$ act multiplicatively while the $\hat{p}_r$ differential operators

$$\mathscr{H} = \{\psi(\mathbf{q}) | \int_{\mathscr{R}^n} d^n q |\psi(\mathbf{q})|^2 < \infty\};$$

$$(\hat{q}_r \psi)(\mathbf{q}) = q_r \psi(\mathbf{q})$$

$$(\hat{p}_r \psi)(\mathbf{q}) = -i\hbar \frac{\partial}{\partial q_r} \psi(\mathbf{q}),$$

$$\mathbf{q} = (q_1, \ldots, q_n) \in \mathscr{R}^n. \qquad (3$$

Since the $\hat{\xi}_a$ are hermitian and irreducible, and since for any $S \in \mathrm{Sp}(2n, \mathscr{R})$ the tra formed $\hat{\xi}'_a$ are also hermitian and irreducible and obey the same CR's, by the Stone-Neumann theorem [5] the change $\hat{\xi} \to \hat{\xi}'$ is unitarily implementable. Thus for e $S \in \mathrm{Sp}(2n, \mathscr{R})$ it is definitely possible to construct a unitary operator $\mathscr{U}(S)$ acting $\mathscr{H}$ such that

$$\hat{\xi}'_a = S_{ab} \hat{\xi}_b = \mathscr{U}(S)^{-1} \hat{\xi}_a \mathscr{U}(S),$$

$$\mathscr{U}(S)^\dagger \mathscr{U}(S) = 1 \text{ on } \mathscr{H}. \qquad (3$$

This $\mathscr{U}(S)$ is arbitrary up to an S-dependent phase factor. The general composition that follows from the irreducibility of the $\hat{\xi}_a$ is

$$S', S \in \mathrm{Sp}(2n, \mathscr{R}): \mathscr{U}(S')\mathscr{U}(S) = (\text{phase factor dependent on } S', S)\mathscr{U}(S'S). \quad (3$$

We shall discuss in § 6 the maximum simplification that can be achieved in this ph factor by exploiting the phase freedom in each $\mathscr{U}(S)$.

3. Aspects of symplectic geometry

In this Section we develop a few basic concepts related to symplectic vector spaces that the contrast with Euclidean and unitary geometries can be clearly seen [4].

Let V be a real $2n$-dimensional vector space, with vectors $x, y, \ldots$. Suppose a n degenerate bilinear antisymmetric form $(\cdot, \cdot)$ – a "scalar product" – is given on V. T for any vectors $x, y \in V$, (x, y) is a real number separately linear in x and y; and in addit the following hold:

$$\text{antisymmetry: } (x, y) = -(y, x),$$

$$\text{nondegeneracy: } (x, y) = 0 \quad \text{for all} \quad y \Leftrightarrow x = 0. \qquad (3$$

Then V is a symplectic vector space, and $(.;.)$ is a symplectic scalar product.

We have stated the properties of the bilinear form in a basis independent way. It be shown that if in a general basis we express (x, y) in terms of components of x and the form

$$(x, y) = x^T \eta y, \qquad (3$$

involving an antisymmetric nonsingular matrix η, we can always change to more convenient bases in which η takes on particularly simple canonical, or normal, forms. Two such forms are worth mentioning. In one, η becomes the matrix β of (2.2)

$$\eta = \beta: \quad (x, y) = x_1 y_{n+1} + x_2 y_{n+2} + \cdots + x_n y_{2n} - x_{n+1} y_1 - x_{n+2} y_2 - \cdots - x_{2n} y_n. \tag{3.3}$$

Here the first and $(n+1)$th components belong to one canonical pair; the second and $(n+2)$th to the second pair; and so on. Another normal form disposes the canonical pairs one at a time

$$\eta = \text{block-diag}(i\sigma_2, i\sigma_2, \ldots, i\sigma_2):$$
$$(x, y) = x_1 y_2 - x_2 y_1 + x_3 y_4 - x_4 y_3 + \cdots \tag{3.4}$$

With the normal form (3.3) the meaning of the defining condition (2.5) for symplectic matrices becomes geometrically clear

$$S \in \text{Sp}(2n, \mathscr{R}),\ x' = Sx, \quad y' = Sy \Rightarrow (x', y') = (x, y). \tag{3.5}$$

In this sense the symplectic scalar product is preserved. Of course this means that we could have replaced the condition (2.5) by another entirely equivalent one, using in place of β the matrix in (3.4).

Now let us look at linear subspaces $V_1 \subseteq V$. In both Euclidean and unitary geometries, it is well known that all subspaces of the same dimension are basically similar, and cannot be distinguished from each other in any intrinsic sense. With symplectic geometry there is a difference, as a new concept comes in. Given a subspace V_1, we consider the bilinear form (x, y) defined over V, restrict both arguments to V_1, and regard the result as a bilinear form on V_1. Now the nondegeneracy property may well fail! Thus, there may exist a vector $x \in V_1$ such that $(x, y) = 0$ for all $y \in V_1$. So we define the rank of this restricted form as the symplectic rank of V_1

$$\text{Symp. rk.} \quad V_1 = \text{rank}\,(x, y), \quad x \text{ and } y \in V_1. \tag{3.6}$$

Thus, if x_r, $r = 1, \ldots, k$ is a basis for V_1, where k is the dimension of V_1, then Symp. rk. V_1 is the rank of the $k \times k$ antisymmetric matrix $((x_r, x_s))$. The symplectic rank is necessarily an even integer. We have the obvious limits

$$0 \leqslant \text{symp. rk.} \quad V_1 \leqslant k. \tag{3.7}$$

But nondegeneracy of $(.,.)$ over V leads to another nontrivial lower bound, which is effective if $k > n$

$$(0, 2(k-n))_> \leqslant \text{symp. rk.} \quad V_1 \leqslant k. \tag{3.8}$$

Basically we can say that the symplectic rank of a subspace V_1 is twice the number of complete canonical pairs contained in V_1. Clearly this concept is symplectic invariant. In particular two subspaces V_1 and V_1' of the same dimension cannot be mapped on to one another by any $\text{Sp}(2n, \mathscr{R})$ element if they have unequal symplectic ranks.

As in the Euclidean case, we can pass from V_1 to its complement written for convenience as $V_1^{\perp}$. But the geometrical significance is quite different. We call $V_1^{\perp}$ the

symplectic complement of V_1 and define it as a subspace of V by

$$V_1^{\perp} = \{x \in V | (x, y) = 0 \quad \text{for all} \quad y \in V_1\}.$$

Taking the complement twice gives back V_1

$$(V_1^{\perp})^{\perp} = V_1.$$

This is as in the Euclidean case. Even the dimensions follow the same rule

$$\text{Dim } V_1^{\perp} = 2n - k.$$

This can be shown by using the nondegeneracy of (.,.). But there the similarity en can well happen that V_1 and $V_1^{\perp}$ have nontrivial intersection, and to that extent sum does not give back all of V. In general,

$$V_1 \cap V_1^{\perp} \neq 0,$$
$$V \neq V_1 \oplus V_1^{\perp}.$$

The two symplectic ranks can be related:

$$\text{Symp. rk. } V_1^{\perp} = 2(n-k) + \text{symp. rk. } V_1.$$

The extreme case of (3.12), which is very nonintuitive on the basis of Eucl geometric notions, is when symp. rk. V_1 vanishes. For this case we give a special and find

$$\text{Symp. rk. } V_1 = 0 \Leftrightarrow V_1 \text{ is an isotropic subspace of } V \Leftrightarrow (x, y) = 0 \text{ for all } x, y \in V_1 \Leftrightarrow V_1 \subseteq V_1^{\perp} \Rightarrow k \leqslant n.$$

So in this case V_1 is contained in $V_1^{\perp}$. The opposite can also happen and then w V_1 a co-isotropic subspace

$$V_1 \text{ is a co-isotropic subspace of } V \Leftrightarrow V_1^{\perp} \text{ is isotropic} \Leftrightarrow V_1 \supseteq V_1^{\perp} \Rightarrow k \geqslant$$

So if one of the pair V_1, $V_1^{\perp}$ is isotropic, the other is co-isotropic.

An isotropic subspace has dimension $k \leqslant n$, while a co-isotropic one has dime $k \geqslant n$. When they coincide, we have a special situation and name. A n-dimens subspace V_1 of V which has vanishing symplectic rank is both isotropic an isotropic, and coincides with $V_1^{\perp}$. It is called a Lagrangian subspace. This noti important in Hamilton-Jacobi theory in classical dynamics; it is also relevant i choice of complete commuting sets of operators in quantum mechanics.

These properties and notions give a feeling for symplectic geometry, and for the in which it differs from orthogonal and unitary geometries. In particular the notic length, angle and perpendicularity are no longer available.

4. Properties of $Sp(2n, \mathscr{R})$ matrices, complex form, subgroups, decompositions

The matrices in the defining representation of $Sp(2n, \mathscr{R})$ obey (2.5). From here useful consequences follow, and we list them:

(i) $Sp(2n, \mathscr{R})$ is of dimension $n(2n+1)$.
(ii) $\beta \in Sp(2n, \mathscr{R})$.

(iv) $\det S = +1$.

(v) $S \in \mathrm{Sp}(2n, \mathscr{R}) \Rightarrow$ eigenvalue spectrum of S is invariant under reflection about the real axis, and through unit circle ($re^{i\theta} \to \frac{1}{r}e^{i\theta}$); eigenvalues ± 1 have even multiplicities. (4.1)

Property (i) can be seen from the number of conditions contained in (2.5), and will be confirmed at the Lie algebra level. While properties (ii) and (iii) are easily checked, (iv) is rather subtle; an indication will be given later to obtain it. Property (v) is a consequence of S and $(S^{-1})^T$ being real and related by a similarity transformation.

Sometimes it is convenient to write S in $n \times n$ block form, and then (2.5) becomes a set of conditions on the blocks

$$S = \begin{pmatrix} A & B \\ C & D \end{pmatrix} \in \mathrm{Sp}(2n, \mathscr{R}):$$

$$S\beta S^T = \beta \Leftrightarrow AB^T, CD^T \quad \text{symmetric}, \quad AD^T - BC^T = 1_{n\times n}$$

$$S^T\beta S = \beta \Leftrightarrow A^TC, B^TD \quad \text{symmetric}, \quad A^TD - C^TB = 1_{n\times n}. \tag{4.2}$$

While it is easy to check (as mentioned above) that $S \in \mathrm{Sp}(2n, \mathscr{R})$ implies $S^T \in \mathrm{Sp}(2n, \mathscr{R})$ as well, it is not so easy to pass directly from the first set of conditions above to the second set, aside from reconstituting A, B, C, D into S and then passing to S^T!

Complex form of $\mathrm{Sp}(2n, \mathscr{R})$

The β matrix reflects the precise way in which the real q's and p's have been put together in (2.1) to form the $2n$ component object ξ with real entries. Sometimes it is convenient, for instance in dealing with modes of the radiation field, to work with complex combinations of the $\hat{q}$'s and $\hat{p}$'s-mode annihilation and creation operators defined in this way

$$\hat{a}_j = \frac{1}{\sqrt{2}}(\hat{q}_j + i\hat{p}_j), \quad \hat{a}_j^\dagger = \frac{1}{\sqrt{2}}(\hat{q}_j - i\hat{p}_j), \quad j = 1, \ldots, n. \tag{4.3}$$

It is useful to arrange these into a new column vector $\hat{\xi}^{(c)}$ with non-hermitian entries,

$$\hat{\xi}^{(c)} = (\hat{\xi}_a^{(c)}) = (\hat{a}_1, \ldots, \hat{a}_n \quad \hat{a}_1^\dagger, \ldots, \hat{a}_n^\dagger)^T = \Omega\hat{\xi},$$

$$\hat{\xi} = \Omega^\dagger \hat{\xi}^{(c)},$$

$$\Omega = \frac{1}{\sqrt{2}}\begin{pmatrix} 1 & i1 \\ 1 & -i1 \end{pmatrix}, \quad \Omega^{-1} = \Omega^\dagger = \frac{1}{\sqrt{2}}\begin{pmatrix} 1 & 1 \\ -i1 & i1 \end{pmatrix}. \tag{4.4}$$

Then the basic commutation relations in (2.2) can be written in two equivalent ways

$$[\hat{\xi}_a^{(c)}, \hat{\xi}_b^{(c)}] = \beta_{ab}.$$

$$[\hat{\xi}_a^{(c)}, \hat{\xi}_b^{(c)\dagger}] = (\Sigma_3)_{ab},$$

$$\Sigma_3 = \begin{pmatrix} 1 & 0 \\ 0 & -1 \end{pmatrix}. \tag{4.5}$$

Now when we subject ξ to the real transformation $S \in \mathrm{Sp}(2n, \mathscr{R})$, $\xi^{(c)}$ experienc
equivalent complex transformation

$$\hat{\xi}' = S\hat{\xi} \Leftrightarrow \hat{\xi}'^{(c)} = S^{(c)}\hat{\xi}^{(c)},$$

$$S^{(c)} = \Omega S \Omega^{-1}$$

$$= \frac{1}{2}\begin{pmatrix} A + D + i(C - B) & A - D + i(B + C) \\ A - D - i(B + C) & A + D + i(B - C) \end{pmatrix}.$$

Thus $S^{(c)}$ is just a convenient complex form of the real transformation S, much lik
passage from Cartesian to spherical components of spherical tensors.

Some subgroups of $\mathrm{Sp}(2n, \mathscr{R})$

We shall describe here some useful subgroups of $\mathrm{Sp}(2n, \mathscr{R})$. Their dimensions w
given, and where it is useful their complex forms exhibited.

(a) $\mathrm{GL}(n, \mathscr{R})$: This is the n^2-dimensional general real linear group; in terms of the
matrices A, B, C, D it is given thus

$$A \in \mathrm{GL}(n, \mathscr{R}), \quad B = C = 0, \quad D = (A^{-1})^T.$$

Here the $\hat{q}$'s are subject to a general real linear nonsingular transformation a
themselves, and then the $\hat{p}$'s change in a compensating contragradient mann

(b) $\mathrm{O}(n, \mathscr{R})$: This is the orthogonal subgroup of $\mathrm{GL}(n, \mathscr{R})$, of dimension $\frac{1}{2}n(n-1$
that part of $\mathrm{GL}(n, \mathscr{R})$ under which the $\hat{q}$'s and the $\hat{p}$'s change in the same wa

$$A = D \in \mathrm{O}(n, \mathscr{R}), \quad B = C = 0.$$

If we impose the condition $\det A = +1$, we get the subgroup $\mathrm{SO}(n, \mathscr{R})$ of p
orthogonal transformations.

(c) $\mathrm{U}(n)$: Now we come to the n-dimensional unitary group, of dimension n^2, a
mal compact subgroup within the noncompact $\mathrm{Sp}(2n, \mathscr{R})$. We shall sometimes
$\mathrm{K}(n)$, or simply K, for it. The corresponding symplectic matrices S are identif
follows. If we split any $\mathrm{U} \in \mathrm{U}(n)$ into real and imaginary parts we find the prop

$$\mathrm{U} = X - iY \in \mathrm{U}(n), \quad \mathrm{U}^\dagger \mathrm{U} = \mathrm{U}\mathrm{U}^\dagger = 1 \Leftrightarrow X^T X + Y^T Y = XX^T + YY^T$$

$$X^T Y, XY^T \text{ symmetric.}$$

We can then produce a solution to the matrix condition (4.2). We find

$$A = D = X, \quad B = -C = Y$$

$$S(X, Y) = \begin{pmatrix} X & Y \\ -Y & X \end{pmatrix} \in \mathrm{Sp}(2n, \mathscr{R}).$$

It is an interesting and easy exercise to check the following: If a $2n \times 2n$ real n
is both orthogonal and symplectic, then it is unimodular as well and has to ha
form $S(X, Y)$ for some $\mathrm{U} = X - iY \in \mathrm{U}(n)$

$$\mathrm{O}(2n, \mathscr{R}) \cap \mathrm{Sp}(2n, \mathscr{R}) = \mathrm{SO}(2n, \mathscr{R}) \cap \mathrm{Sp}(2n, \mathscr{R}) = \mathrm{K}(n)$$

$$= \{S(X, Y) \mid X - iY \in \mathrm{U}(n)\}.$$

The complex form of these matrices is very revealing

$$S^{(c)}(X, Y) = \Omega S(X, Y)\Omega^{-1}$$
$$= S^{(c)}(U)$$
$$= \begin{pmatrix} U & 0 \\ 0 & U^* \end{pmatrix}. \tag{4.12}$$

So the $\hat{a}$'s and the $\hat{a}^\dagger$'s undergo separate unitary rotations, not mixing with one another

$$U \in U(n): \quad \hat{a} \to U\hat{a}, \quad \hat{a}^\dagger \to U^*\hat{a}^\dagger. \tag{4.13}$$

Indeed, $K(n)$ is the maximal subgroup of $Sp(2n, \mathscr{R})$ such that $\hat{a}$'s and $\hat{a}^\dagger$'s transform independently. We also have the expected relation between the subgroups $O(n, \mathscr{R})$, $GL(n, \mathscr{R})$, and $U(n)$ exhibited above

$$O(n, \mathscr{R}) = GL(n, \mathscr{R}) \cap U(n). \tag{4.14}$$

Finally we turn to some Abelian subgroups [6].

(d) T^f: This is a subgroup of dimension $\frac{1}{2}n(n+1)$ and may be called the "free propagation" subgroup

$$A = D = 1, \quad B = B^T, \quad C = 0. \tag{4.15}$$

The name comes from the actions on $\hat{q}$ and on $\hat{p}$

$$\hat{q}' = \hat{q} + B\hat{p}, \quad \hat{p}' = \hat{p}. \tag{4.16}$$

Group composition corresponds to adding the B matrices, which explains the Abelian nature.

(e) $T^{(l)}$: This is the result of conjugating elements of $T^{(f)}$ by β. We call it the "lens" subgroup, on account of the action on $\hat{q}$'s and $\hat{p}$'s

$$A = D = 1, \quad B = 0, \quad C = C^T;$$
$$\hat{q}' = \hat{q}, \quad \hat{p}' = \hat{p} + C\hat{q}. \tag{4.17}$$

The dimension is again $\frac{1}{2}n(n+1)$, and group composition amounts to adding the C matrices.

Some other subgroups of $Sp(2n, \mathscr{R})$ will appear in connection with global decomposition theorems.

Global decomposition theorems

Now we describe four useful ways of expressing any $S \in Sp(2n, \mathscr{R})$ as a product of specially chosen factors, either two or three in number.

(a) *Polar decomposition* [7]: This says that any $S \in Sp(2n, \mathscr{R})$ can be written uniquely as the product of two factors, one belonging to the maximal compact subgroup $K(n)$, the other to an important subset $\Pi(n)$ in $Sp(2n, \mathscr{R})$. This subset is defined by

$$\Pi(n) = \{S \in Sp(2n, \mathscr{R}) | S^T = S, S \text{ positive definite}\} \subset Sp(2n, \mathscr{R}). \tag{4.18}$$

$S(X, Y) \in K(n)$, $P \in \Pi(n)$.

Of course by conjugating P with $S(X, Y)$ one could have written the two fact the opposite sequence. The important points here are the global nature result, and the uniqueness of the factors. From this decomposition one can se of the two possibilities $\det S = \pm 1$ allowed by (2.5), the choice $\det S = +1$ only one allowed.

(b) *Euler decomposition*: Next we turn to a decomposition which involves factors, each drawn from a subgroup of $Sp(2n, \mathscr{R})$, but which is nonunique. T the factors are from $K(n)$, the third from those elements of $\Pi(n)$ which are dia and do form a subgroup

$$S \in Sp(2n, \mathscr{R}) \quad S = S(X_1, Y_1)\, D(\boldsymbol{\kappa})\, S(X_2, Y_2),$$

$$S(X_1, Y_1), S(X_2, Y_2) \in K(n),$$

$$D(\boldsymbol{\kappa}) = \mathrm{diag}(\kappa_1, \ldots, \kappa_n, \kappa_1^{-1}, \ldots, \kappa_n^{-1}) \in \Pi(n),$$

$$\kappa_r > 0, \quad r = 1, \ldots, n.$$

If one adds the number of free parameters in the three factors, one gets th $n(2n+1)$ which is just the dimension of $Sp(2n, \mathscr{R})$. Thus the nonuniqueness decomposition is of a discrete, not a continuous, nature. It stems essentially the freedom to order the first n diagonal elements of $D(\boldsymbol{\kappa})$ in any way we lik

(c) *Pre-Iwasawa decomposition*: Here we have a three-factor unique decompo which one encounters on the way to establishing the (next) Iwasawa decompo but the factors do not all belong to subgroups of $Sp(2n, \mathscr{R})$. The present decor tion results from attempting to reduce the off diagonal block B in a g $S \in Sp(2n, \mathscr{R})$ to zero, by using an element of $K(n)$ on the right. The result re

$$S = \begin{pmatrix} A & B \\ C & D \end{pmatrix} = \begin{pmatrix} 1 & 0 \\ C_0 A_0^{-1} & 1 \end{pmatrix} \begin{pmatrix} A_0 & 0 \\ 0 & A_0^{-1} \end{pmatrix} \begin{pmatrix} X & Y \\ -Y & X \end{pmatrix},$$

$$A_0 = (AA^T + BB^T)^{1/2},$$

$$X - iY = A_0^{-1}(A - iB),$$

$$C_0 = (CA^T + DB^T)A_0^{-1}.$$

Here the matrix A_0 is to be chosen symmetric positive definite, and all facto unique. The symmetry of $C_0 A_0^{-1}$ can be checked, so the first factor lies lens subgroup T^l of (4.17). The middle factor belongs to the inters $GL(n, \mathscr{R}) \cap \Pi(n)$, which is not a subgroup. And the third factor is from $K(n)$ particular decomposition is of importance in obtaining the generalised Huy kernel, which we describe in § 6.

(d) *Iwasawa decomposition* [8]: The polar and pre-Iwasawa decomposition similar since they involve unique factors, but each factor is not taken a subgroup. The Euler decomposition solves the latter problem, but in the p uniqueness is lost. The fourth and last Iwasawa decomposition retains both v

it is global, has unique factors, and each is taken from a characteristic subgroup of $\mathrm{Sp}(2n,\mathscr{R})$. It is a result of fundamental group theoretical significance, valid for all simple non-compact Lie groups. The three subgroups involved are the maximal compact $\mathrm{K}(n)$, a certain maximal Abelian subgroup $\mathscr{A}$, and a certain nilpotent subgroup $\mathscr{N}$. Therefore this decomposition is often called the $\mathscr{K}\mathscr{A}\mathscr{N}$ decomposition. We first display it for $\mathrm{Sp}(2,\mathscr{R})$

$$S=\begin{pmatrix} a & b \\ c & d \end{pmatrix}\in \mathrm{Sp}(2,\mathscr{R}), \quad ad-bc=1:$$

$$S=\begin{pmatrix} 1 & 0 \\ \xi & 1 \end{pmatrix}\begin{pmatrix} e^{\eta/2} & 0 \\ 0 & e^{-\eta/2} \end{pmatrix}\begin{pmatrix} \cos\varphi/2 & -\sin\varphi/2 \\ \sin\varphi/2 & \cos\varphi/2 \end{pmatrix},$$

$$\xi=(ac+bd)/(a^2+b^2)\in(-\infty,\infty),$$

$$\eta=\ln(a^2+b^2)\in(-\infty,\infty),$$

$$\varphi=2\arg(a-ib)\in(-2\pi,2\pi]. \tag{4.22}$$

Here the first $-\xi-$ factor belongs to the subgroup $\mathscr{N}$, coinciding for $n=1$ with the lens subgroup T^1; the second $-\eta-$ factor belongs to the subgroup $\mathscr{A}$; and the third $-\varphi-$ factor is from $\mathrm{K}(1)=\mathrm{SO}(2)$.

For general $\mathrm{Sp}(2n,\mathscr{R})$, the situation is more involved. The subgroups $\mathscr{A}$ and $\mathscr{N}$ are

$$\mathscr{A}=\{D(\boldsymbol{\kappa})=\mathrm{diag}(\kappa_1,\ldots,\kappa_n,\kappa_1^{-1},\ldots,\kappa_n^{-1})\,|\,\kappa_r>0\}\subset\Pi(n);$$

$$\mathscr{N}=\left\{\begin{pmatrix} A & 0 \\ C & (A^{-1})^T \end{pmatrix}\middle|\, A=\begin{pmatrix} 1 & \cdots & 0 \\ \vdots & 1 & \\ & & 1 \end{pmatrix},\ A^TC \text{ symmetric}\right\}\subset \mathrm{Sp}(2n,\mathscr{R}). \tag{4.23}$$

The abelian subgroup $\mathscr{A}$ consists of just the elements $D(\boldsymbol{\kappa})$ that were used in the Euler decomposition (4.20). The Iwasawa decomposition for $\mathrm{Sp}(2n,\mathscr{R})$ then states that any $S\in\mathrm{Sp}(2n,\mathscr{R})$ can be uniquely expressed as the product of three factors,

$$S=\begin{pmatrix} A & 0 \\ C & (A^{-1})^T \end{pmatrix}D(\boldsymbol{\kappa})\,S(X,Y). \tag{4.24}$$

taken respectively from $\mathscr{N}$, $\mathscr{A}$ and $\mathrm{K}(n)$. The dimensionalities of these subgroups, respectively n^2, n and n^2, add up correctly to $n(2n+1)$.

5. The Lie algebra of $\mathrm{Sp}(2n,\mathscr{R})$

We first study the Lie algebra $\underline{\mathrm{Sp}(2n,\mathscr{R})}$ in the defining representation, and then generalise to any other representation. In keeping with quantum mechanical convention, we shall retain a factor of i in the definition, even though this might seem unnecessary in dealing with a group of real matrices.

We examine the form of matrices $S\in\mathrm{Sp}(2n,\mathscr{R})$ close to the identity

$$S=\exp(-i\varepsilon J)\simeq 1-i\varepsilon J. \quad |\varepsilon|\ll 1:$$

other words in the defining representation we get all possible J's by pre- or multiplying all possible pure imaginary symmetric $2n \times 2n$ matrices by β. Takir former alternative and choosing the simplest possible basis for symmetric $2r$ matrices, we obtain the following basis for $\underline{\mathrm{Sp}(2n, \mathscr{R})}$:

$$X^{(0)}_{ab} = X^{(0)}_{ba}, \quad a, b = 1, \ldots, 2n;$$

$$(X^{(0)}_{ab})_{cd} = i(\delta_{ad}\beta_{cb} + \delta_{bd}\beta_{ca}).$$

These matrices can be easily seen to obey the commutation relations

$$[X^{(0)}_{ab}, X^{(0)}_{cd}] = i(\beta_{ac}X^{(0)}_{bd} + \beta_{bc}X^{(0)}_{ad} + \beta_{ad}X^{(0)}_{cb} + \beta_{bd}X^{(0)}_{ca}).$$

The structure of $\underline{\mathrm{Sp}(2n, \mathscr{R})}$ is determined by these relations. In a general represent of $\mathrm{Sp}(2n, \mathscr{R})$ we have generators $X_{ab} = X_{ba}$ obeying

$$[X_{ab}, X_{cd}] = i(\beta_{ac}X_{bd} + \beta_{bc}X_{ad} + \beta_{ad}X_{cb} + \beta_{bd}X_{ca}).$$

Finite dimensional representations of $\mathrm{Sp}(2n, \mathscr{R})$ are necessarily nonunitary, her them the X_{ab} cannot all be hermitian. This is because of the noncompactn $\mathrm{Sp}(2n, \mathscr{R})$. On the other hand, in a unitary representation which is necessarily ir dimensional, we have $X^{\dagger}_{ab} = X_{ab}$.

To help identify the subsets of generators for various subgroups it is useful to us index notation. We use $r, s, \ldots = 1, \ldots, n$ to label the various canonical pairs $\alpha, \beta, \ldots = 1, 2$ to pick out the q and the p in each pair

$$a, b, \ldots = 1, \ldots, 2n: \quad a \to r\alpha, \quad b \to s\beta;$$

$$\beta_{ab} = \beta_{r\alpha, s\beta} = \delta_{rs}\varepsilon_{\alpha\beta},$$

$$\varepsilon = \begin{pmatrix} 0 & 1 \\ -1 & 0 \end{pmatrix}.$$

Then the various components of $X_{ab} = X_{r\alpha, s\beta}$ are handled thus:

$$X_{r1,s1} = V_{rs} = V_{sr};$$

$$X_{r1,s2} = W_{rs},$$

$$X_{r2,s2} = Z_{rs} = Z_{sr}.$$

There are $\frac{1}{2}n(n+1)$ V's, a similar number of Z's, and n^2 W's; in a unitary represent each of them is hermitian. In this split form the commutation relations (5.4) rea

$$[W_{rs}, W_{uv}] = i(\delta_{rv}W_{us} - \delta_{us}W_{rv}).$$

$$[W_{rs}, V_{uv}] = -i(\delta_{us}V_{rv} + \delta_{vs}V_{ru}).$$

$$[W_{rs}, Z_{uv}] = i(\delta_{ru}Z_{sv} + \delta_{rv}Z_{su}).$$

$$[V_{rs}, Z_{uv}] = i(\delta_{ru} W_{sv} + \delta_{su} W_{rv} + \delta_{rv} W_{su} + \delta_{sv} W_{ru}).$$
$$[V, V] = [Z, Z] = 0. \tag{5.7}$$

Now one can pick out the subsets of generators for various subgroups of $\mathrm{Sp}(2n, \mathscr{R})$; we give the results in the form of a table.

Subgroup	Generators
$\mathrm{GL}(n, \mathscr{R})$	W_{rs}
$\mathrm{SO}(n, \mathscr{R})$	$J_{rs} = W_{sr} - W_{rs}$
$\mathrm{U}(n) = \mathrm{K}(n)$	$J_{rs}, Q_{rs} = V_{rs} + Z_{rs}$
	$A_{rs} = \frac{1}{2}(Q_{rs} - iJ_{rs})$
$T^{(J)}$	Z_{rs}
$T^{(I)}$	V_{rs}
$\mathscr{A}$	$W_{rr}, r = 1, \ldots, n$
$\mathscr{N}$	W_{rs} for $r < s$, and all V_{rs}.

We have mentioned that any nontrivial finite dimensional representation of $\mathrm{Sp}(2n, \mathscr{R})$ is necessarily nonunitary. It turns out that, with no loss of generality, we may assume that the "compact" generators of $\mathrm{K}(n)$ are hermitian, while a balance of "noncompact" generators are antihermitian. That is, in any finite dimensional representation we can assume the following

$$\text{Generators of } \mathrm{K}(n) = \text{compact generators}$$
$$= W_{rs} - W_{sr}, V_{rs} + Z_{rs} = \text{hermitian:}$$
$$\text{Balance of generators} = \text{noncompact generators}$$
$$= W_{rs} + W_{sr}, V_{rs} - Z_{rs} = \text{antihermitian.} \tag{5.8}$$

The noncompact generators can be arranged into complex combinations with definite tensor behaviour under $\mathrm{U}(n)$. These combinations are

$$T_{rs} = T_{sr} = V_{rs} - Z_{rs} - i(W_{rs} + W_{sr}).$$
$$\bar{T}_{rs} = \bar{T}_{sr} = V_{rs} - Z_{rs} + i(W_{rs} + W_{sr}). \tag{5.9}$$

Then the complete set of $\mathrm{Sp}(2n, \mathscr{R})$ commutation relations (5.4) appears in a $\mathrm{U}(n)$ adapted form [9]

$$[A_{rs}, A_{uv}] = \delta_{su} A_{rv} - \delta_{rv} A_{us};$$
$$[A_{rs}, T_{uv}] = \delta_{su} T_{rv} + \delta_{sv} T_{ru};$$
$$[A_{rs}, \bar{T}_{uv}] = -\delta_{ru} \bar{T}_{sv} - \delta_{rv} \bar{T}_{su};$$
$$[T_{rs}, \bar{T}_{uv}] = -4(\delta_{ru} A_{sv} + \delta_{rv} A_{su} + \delta_{su} A_{rv} + \delta_{sv} A_{ru});$$
$$[T, T] = [\bar{T}, \bar{T}] = 0. \tag{5.10}$$

We see that T_{rs} and $\bar{T}_{rs}$ are second rank symmetric tensors under $\mathrm{U}(n)$, of contravariant

the composition law (2.9) of the $\mathscr{U}$'s as simple as possible. The answer is that this can be done, and upon maximum simplification we can achieve

$$S_1, S_2 \in \mathrm{Sp}(2n, \mathscr{R}) \quad \mathscr{U}(S_1)\mathscr{U}(S_2) = \pm \mathscr{U}(S_1 S_2). \tag{6.1}$$

This sign ambiguity cannot be eliminated. So we say that we have here a two-valued unitary representation of $\mathrm{Sp}(2n, \mathscr{R})$. A more correct or useful statement is that the operators involved provide a faithful unitary representation of the metaplectic group $\mathrm{Mp}(2n)$, which is a two-fold covering of $\mathrm{Sp}(2n, \mathscr{R})$ [10]. Strictly speaking this means that the argument of $\mathscr{U}(\cdot)$ should be an element of $\mathrm{Mp}(2n)$, not $S \in \mathrm{Sp}(2n, \mathscr{R})$. However, having made this point, we shall continue to write $\mathscr{U}(S)$ as in (2.8), (2.9) and (6.1).

The generators of this metaplectic representation of $\mathrm{Sp}(2n, \mathscr{R})$ are all hermitian; in terms of $\hat{q}$'s and $\hat{p}$'s they are the quadratic expressions [11]

$$\hat{W}_{rs} = \tfrac{1}{2}\{\hat{q}_r, \hat{p}_s\},$$
$$\hat{V}_{rs} = \hat{q}_r \hat{q}_s, \; \hat{Z}_{rs} = \hat{p}_r \hat{p}_s. \tag{6.2}$$

The characteristic differences between the compact and the noncompact combinations become clear when expressed in terms of $\hat{a}$'s and $\hat{a}^\dagger$'s

$$\text{Compact generators: } \hat{W}_{rs} - \hat{W}_{sr} = i(\hat{a}_s^\dagger \hat{a}_r - \hat{a}_r^\dagger \hat{a}_s),$$
$$\hat{V}_{rs} + \hat{Z}_{rs} = (\hat{a}_r^\dagger \hat{a}_s + \hat{a}_s^\dagger \hat{a}_r + \delta_{rs}), \tag{6.3a}$$
$$\text{Non compact generators: } \hat{W}_{rs} + \hat{W}_{sr} = i(\hat{a}_r^\dagger \hat{a}_s^\dagger - \hat{a}_r \hat{a}_s),$$
$$\hat{V}_{rs} - \hat{Z}_{rs} = \hat{a}_r^\dagger \hat{a}_s^\dagger + \hat{a}_r \hat{a}_s. \tag{6.3b}$$

We see that the compact generators of $\mathrm{U}(n)$ conserve "total photon number", thus this subgroup of $\mathrm{Sp}(2n, \mathscr{R})$ consists of "passive" transformations. The noncompact generators on the other hand do not conserve "photon number", so we may call them "active" generators. These properties are expressed thus

$$\hat{N} = \hat{a}_r^\dagger \hat{a}_r:$$
$$[\hat{W}_{rs} - \hat{W}_{sr} \quad \text{or} \quad \hat{V}_{rs} + \hat{Z}_{rs}, \hat{N}] = 0,$$
$$[\hat{W}_{rs} + \hat{W}_{sr} \quad \text{or} \quad \hat{V}_{rs} - \hat{Z}_{rs}, \hat{N}] \neq 0. \tag{6.4}$$

In fact, single exponentials of i times real linear combinations of the compact generators give us operators of the form $\mathscr{U}(S(X, Y))$; while single exponentials of i times real linear combinations of the noncompact generators give us operators of the form $\mathscr{U}(P)$, $P \in \Pi(n)$. For this reason the latter may be called "squeezing transformations" [12], [13]; and the polar decomposition (4.19) may be read as stating that any metaplectic unitary transformation is uniquely the product of a compact passive factor and a noncompact active squeeze factor. The definition and production of squeezed states are taken up in more detail in § 10.

The Schrödinger description of the Hilbert space $\mathscr{H}$ on which the metaplectic representation acts has been given in (2.7). In this description, the eigenvectors $|\mathbf{q}\rangle$ of the commuting position operators $\hat{q}_r$ appear as a basis

$$
\begin{aligned}
&|\psi\rangle \in \mathscr{H}: \quad \psi(\mathbf{q}) = \langle \mathbf{q}|\psi\rangle, \\
&\hat{q}_r|\mathbf{q}\rangle = q_r|\mathbf{q}\rangle, \\
&\langle \mathbf{q}'|\mathbf{q}\rangle = \delta^{(n)}(\mathbf{q}' - \mathbf{q}), \\
&\langle \mathbf{q}|\hat{p}_r = -i\hbar \frac{\partial}{\partial q_r}\langle \mathbf{q}|. \qquad (6.5)
\end{aligned}
$$

It is useful to know that certain operators $\mathscr{U}(S)$ have very simple actions on these basis vectors. We list them below

$$
\begin{aligned}
&S(A) = \begin{pmatrix} A & 0 \\ 0 & (A^{-1})^T \end{pmatrix}, \quad A \in \mathrm{GL}(n, \mathscr{R}): \\
&\mathscr{U}(S(A))|\mathbf{q}\rangle = |\det A|^{1/2}|A\mathbf{q}\rangle. \\
&\langle \mathbf{q}|\mathscr{U}(S(A)) = |\det A|^{-1/2}\langle A^{-1}\mathbf{q}|; \qquad (6.6a) \\
&D(\boldsymbol{\kappa}) = \mathrm{diag}(\kappa_1, \ldots, \kappa_n, \kappa_1^{-1}, \ldots, \kappa_n^{-1}), \ \kappa_r > 0: \\
&\mathscr{U}(D(\boldsymbol{\kappa})) = \exp\left(-i \sum_{r=1}^{n} \ln(\kappa_r) \hat{W}_{rr} \right), \\
&\mathscr{U}(D(\boldsymbol{\kappa}))|\mathbf{q}\rangle = \left(\prod_{r=1}^{n} \kappa_r \right)^{1/2}, \quad |\kappa_1 q_1, \ldots, \kappa_n q_n\rangle, \\
&\langle \mathbf{q}|\mathscr{U}(D(\boldsymbol{\kappa})) = \left(\prod_{r=1}^{n} \kappa_r \right)^{-1/2} \langle \kappa_1^{-1} q_1, \ldots, \kappa_n^{-1} q_n|; \qquad (6.6b) \\
&L(g) = \begin{pmatrix} 1 & 0 \\ -g & 1 \end{pmatrix} \in T^{(1)}, \quad g^T = g: \\
&\mathscr{U}(L(g)) = \exp\left(-\frac{i}{2} g_{rs} \hat{V}_{rs} \right), \\
&\mathscr{U}(L(g))|\mathbf{q}\rangle = \exp\left(-\frac{i}{2} q^T g q \right)|\mathbf{q}\rangle. \qquad (6.6c)
\end{aligned}
$$

With the help of these results, and the pre-Iwasawa decomposition for elements of $\mathrm{Sp}(2n, \mathscr{R})$ described in §4, it turns out to be possible to calculate the generalized Huyghen's kernel in n-dimensions without too much effort. This kernel is the configuration space matrix element $\langle \mathbf{q}|\mathscr{U}(S)|\mathbf{q}'\rangle$ of the metaplectic unitary operator $\mathscr{U}(S)$. We recall that in the case of one degree of freedom, this kernel has the following form [11]

$$
S = \begin{pmatrix} a & b \\ c & d \end{pmatrix} \in \mathrm{Sp}(2, \mathscr{R})
$$

$$\langle q|\mathscr{U}(S)|q'\rangle = \begin{cases} \dfrac{e^{-i\pi/4}}{\sqrt{h|b|}}\exp[i(dq^2 - 2qq' + aq'^2)/2\hbar b], & b \neq 0; \\ \exp(icq^2/2a)\delta\left(\dfrac{q}{a} - q'\right)\Big/|a|^{1/2}, & b = 0. \end{cases}$$

(These results are, strictly speaking, valid only if S is sufficiently close to the ident point being that $\mathscr{U}(\cdot)$ is actually a representation of Mp(2) and so carries as argum element of this group. Therefore the generalised Huyghens kernel is not expr totally in terms of $S \in \mathrm{Sp}(2, \mathscr{R})$.) We may regard the case $b \neq 0$ as generic generalizes nicely to any number of dimensions and we find

$$S = \begin{pmatrix} A & B \\ C & D \end{pmatrix} \in \mathrm{Sp}(2n, \mathscr{R}), \quad \det B \neq 0:$$

$$\langle \mathbf{q}|\mathscr{U}(S)|\mathbf{q}'\rangle = \frac{e^{-in\pi/4}}{h^{n/2}} \cdot \frac{1}{\sqrt{|\det B|}} \times \exp\left[\frac{i}{2\hbar}\{q^T DB^{-1}q - 2q'^T B^{-1}q + q'^T B^{-1}Aq'\}\right].$$

The nongeneric case when $\det B = 0$ has to be handled carefully – then the collapses to a lower dimensional expression with a certain number of delta fu factors. However, having given an indication of the structure involved, we will into any further details.

7. Sp($2n, \mathscr{R}$) actions on Wigner and diagonal coherent state representations

Let $\hat{\Gamma}$ be any quantum mechanical operator, specified in the Schrödinger repre tion by its configuration space kernel $\langle \mathbf{q}|\hat{\Gamma}|\mathbf{q}'\rangle$. We can see that if $\hat{\Gamma}$ is conjuga $\mathscr{U}(S)$ for general $S \in \mathrm{Sp}(2n, \mathscr{R})$, the change in the kernel involves an integral tran ation in which the generalised Huygens kernel (6.8) and its complex conjugat appear. We can ask whether there is any other way of specifying or describing that this change takes a simpler form, not requiring any integrations at all. Indee is, and it is given by the use of the techniques due to Weyl, Wigner and Moyal (V [14]. We describe this aspect, and then go on to another practically important describing operators, namely via the diagonal coherent state representation, behaviour under Sp($2n, \mathscr{R}$).

Let us hereafter set $\hbar = 1$. From the configuration space kernel $\langle \mathbf{q}|\hat{\Gamma}|\mathbf{q}'\rangle$ o obtain its Wigner distribution or WWM representative by a partial Fourier tran ation

$$\hat{\Gamma} \to W(\xi) = (2\pi)^{-n} \int d^n q' \langle \mathbf{q} - \tfrac{1}{2}\mathbf{q}'|\hat{\Gamma}|\mathbf{q} + \tfrac{1}{2}\mathbf{q}'\rangle \exp(i\mathbf{q}' \cdot \mathbf{p}),$$

$$\langle \mathbf{q}|\hat{\Gamma}|\mathbf{q}'\rangle = \int d^n p\, W(\tfrac{1}{2}(\mathbf{q} + \mathbf{q}'), \mathbf{p}) \exp(-i\mathbf{p} \cdot (\mathbf{q} - \mathbf{q}')).$$

Here $W(\xi)$ is a function on the classical phase space corresponding to the qu system, with arguments which are $2n$ classical c-number q's and p's. As seen abo

can recover the operator $\hat{\Gamma}$ from its WWM representative $W(\xi)$ unambiguously. Then one finds that under conjugation by the metaplectic operators $\mathscr{U}(S)$, the changes in $\hat{\Gamma}$ are very simply expressed in terms of $W(\xi)$ [15]

$$\hat{\Gamma}' = \mathscr{U}(S)^{-1}\hat{\Gamma}\mathscr{U}(S) \Leftrightarrow W'(\xi) = W(S\xi). \tag{7.2}$$

This behaviour of $W(\xi)$ may in fact be regarded as the key or characteristic property of the WWM method in quantum mechanics; we may say that this description of operators is covariant under the full symplectic group $\mathrm{Sp}(2n, \mathscr{R})$.

Next we turn to the diagonal coherent state description of operators $\hat{\Gamma}$ [16]. For n degrees of freedom the coherent states are defined as usual by

$$|\mathbf{z}\rangle = \exp\left\{-\frac{1}{2}\sum_{r=1}^{n}|z_r|^2 + \sum_{r=1}^{n} z_r \hat{a}_r^\dagger\right\}|0\rangle,$$

$$\hat{a}_r|0\rangle = 0,$$

$$\hat{a}_r|\mathbf{z}\rangle = z_r|\mathbf{z}\rangle, \quad z_r \in C, \quad \mathbf{z} = (z_1, \ldots, z_n). \tag{7.3}$$

These are normalised states, no two being orthogonal, and can be written also as the result of phase space displacement operators acting on the ground state $|0\rangle$:

$$|\mathbf{z}\rangle = \exp\left\{\sum_{r=1}^{n}(z_r\hat{a}_r^\dagger - z_r^*\hat{a}_r)\right\}|0\rangle.$$

$$\langle \mathbf{z}'|\mathbf{z}\rangle = \exp\{-\tfrac{1}{2}z'^\dagger z' - \tfrac{1}{2}z^\dagger z + z'^\dagger z\}. \tag{7.4}$$

The coherent states form an (over) complete set; the resolution of the identity

$$1 = \int \prod_{r=1}^{n} \frac{\mathrm{d}^2 z_r}{\pi} |\mathbf{z}\rangle\langle\mathbf{z}| \tag{7.5}$$

shows that any vector $|\psi\rangle$ can certainly be expanded using them

$$|\psi\rangle = \int \prod_{r=1}^{n} \frac{\mathrm{d}^2 z_r}{\pi} \psi(\mathbf{z}^*)|\mathbf{z}\rangle,$$

$$\psi(\mathbf{z}) = \langle \mathbf{z}^*|\psi\rangle = \exp(-\tfrac{1}{2}z^\dagger z) \text{ (entire analytic function of } \mathbf{z}). \tag{7.6}$$

Moreover the overcompleteness allows expansion of any operator $\hat{\Gamma}$ in the form of an integral over projections to these states

$$\hat{\Gamma} = \int \prod_{r=1}^{n} \frac{\mathrm{d}^2 z_r}{\pi} \phi(\mathbf{z})|\mathbf{z}\rangle\langle\mathbf{z}|. \tag{7.7}$$

For given $\hat{\Gamma}$, this expansion and the weight function $\phi(\mathbf{z})$ are unique, however the latter could in general be a distribution of quite a singular kind.

Now we look at the behaviour under $\mathrm{Sp}(2n, \mathscr{R})$. It turns out that the states $|\mathbf{z}\rangle$ have a simple behaviour only under the "passive" maximal compact subgroup $\mathrm{K}(n) \subset \mathrm{Sp}(2n, \mathscr{R})$

$$U = X - iY \in \mathrm{U}(n): \mathscr{U}(S(X, Y))|\mathbf{z}\rangle = |U\mathbf{z}\rangle. \tag{7.8}$$

This can be traced to the fact that the generators of $\mathrm{K}(n)$ involve only terms of the form $\hat{a}^\dagger\hat{a}$, as we see in (6.3a). On the other hand, the effect of $\mathscr{U}(P)$, for any $P \in \Pi(n)$, on $|\mathbf{z}\rangle$

involves an integration using a suitable kernel, namely the generalised Hu kernel expressed in the coherent state language [17], which for the $Sp(2,\mathscr{R})$ cas written in a simple form in terms of complex $SU(1,1)$ parameters $\lambda\mu$

$$\mathscr{K}(z,z';S^c)=\langle z'|\mathscr{U}(S)|z\rangle$$

$$=\zeta(\varphi/2)^*\exp\left\{-\frac{z^2}{2}-\frac{z'^{*2}}{2}-|z'|^2\right\}$$

$$\times\begin{cases}\dfrac{1}{(2|\mathrm{Im}(\mu-\lambda)|)^{1/2}}\left(1-\dfrac{\lambda+\mu^*}{\lambda^*+\mu}\right)^{1/2}\left(1+\dfrac{\mu}{\lambda^*}\right)^{1/2} \\ \times\exp\left[\dfrac{1}{2\lambda^*}\{(\lambda^*+\mu)z^2+zz'^*+(\lambda^*-\mu^*)z'^{*2}\}\right] \\ \mathrm{Im}(\mu-\lambda)\neq 0, \quad \text{i.e.,} \quad \varphi\neq 2n\pi; \\ \left(\dfrac{2|\mathrm{Re}(\lambda+\mu)|}{1+(\lambda+\mu)\mathrm{Re}(\lambda+\mu)}\right)^{1/2}\exp\left[\dfrac{(z\,\mathrm{Re}(\lambda+\mu)+z}{1+(\lambda+\mu)\mathrm{Re}(\lambda}\right. \\ \mathrm{Im}(\mu-\lambda)=0, \quad \text{i.e.,} \quad \varphi=2n\pi, \quad n=-1,0,1,\end{cases}$$

$$S=\begin{pmatrix}a & b\\ c & d\end{pmatrix}\in Sp(2,\mathscr{R}), \quad S^c=\begin{pmatrix}\lambda & \mu\\ \mu^* & \lambda^*\end{pmatrix}, \quad \lambda=\tfrac{1}{2}(a+d+ic$$

$$\mu=\tfrac{1}{2}(a-d+ib$$

(Here each individual square root is defined to have a positive real part.)

In contrast to the WWM result (7.2), we now have covariance under $K(n)$ a

$$\hat{\Gamma}'=\mathscr{U}(S(X,Y))^{-1}\hat{\Gamma}\mathscr{U}(S(X,Y))\Leftrightarrow\phi'(\mathbf{z})=\phi(\mathrm{U}\mathbf{z})$$

Active elements of $Sp(2n,\mathscr{R})$ change ϕ in a manner involving a nontrivial transformation.

8. Quantum noise matrices and their $Sp(2n,\mathscr{R})$ behaviour

Let $\hat{\rho}$ be the density operator of any (pure or mixed) quantum state. For simplici let us assume that the means of $\hat{\xi}_a$ vanish

$$\langle\hat{\xi}_a\rangle=\mathrm{Tr}(\hat{\rho}\hat{\xi}_a)=0.$$

Nonzero values for these means can always be reinstated by a suitable phas displacement. The variance or noise or second order moment matrix of the s then defined as follows [12]

$$V=(V_{ab})=\begin{pmatrix}V_1 & V_2\\ V_2^T & V_3\end{pmatrix}.$$

$$V_{ab}=V_{ba}=\tfrac{1}{2}\langle\{\hat{\xi}_a,\hat{\xi}_b\}\rangle$$

$$(V_1)_{rs} = \langle \hat{q}_r \hat{q}_s \rangle.$$

$$(V_2)_{rs} = \tfrac{1}{2} \langle \{\hat{q}_r, \hat{p}_s\} \rangle.$$

$$(V_3)_{rs} = \langle \hat{p}_r \hat{p}_s \rangle. \tag{8.2}$$

This is a real symmetric $2n \times 2n$ positive definite matrix subject to further matrix inequalities which express the uncertainty principles (see below).

We must note the compact way in which we are able to express V_{ab} as a phase space integral involving the WWM representative $W(\xi)$ of the density operator $\hat{\rho}$. This is a consequence of the general rule [14]

$$\mathrm{Tr}(\hat{\rho} \exp\{i\xi_0^T \beta \hat{\xi}\}) = \int d^{2n}\xi \quad W(\xi) \exp\{i\xi_0^T \beta \xi\} \tag{8.3}$$

valid for any numerical ξ_0. Indeed, one can regard this property of $W(\xi)$ as being as basic as the symplectic transformation rule (7.2). A particular case of (8.3), when $\xi_0 = 0$, shows that $W(\xi)$ is normalised, because $\mathrm{Tr}\,\hat{\rho} = 1$; its phase space integral is unity. But we must remember that though for hermitian $\hat{\rho}$ the function $W(\xi)$ is real, it may not be non-negative everywhere.

The change in the noise matrix V when $\hat{\rho}$ is changed by a symplectic transformation is now easily obtained by exploiting (7.2) along with the above expression for V_{ab} in terms of $W(\xi)$. We have the extremely simple law, for any $S \in \mathrm{Sp}(2n, \mathscr{R})$

$$\hat{\rho}' = \mathscr{U}(S) \hat{\rho} \mathscr{U}(S)^{-1} \Rightarrow V' = SVS^T. \tag{8.4}$$

(Note that in comparison to the change $\hat{\Gamma} \to \hat{\Gamma}'$ in (7.2), S has been replaced by S^{-1} here). We may say that V undergoes a symmetric symplectic transformation, which preserves its symmetry and positive definiteness.

The information contained in V can also be given in complex form using second order moments of $\hat{a}$'s and $\hat{a}^\dagger$'s

$$V^{(c)} = (V^{(c)}_{ab}) = \begin{pmatrix} \mathscr{A} & \mathscr{B} \\ \mathscr{B}^* & \mathscr{A}^* \end{pmatrix},$$

$$V^{(c)}_{ab} = V^{(c)*}_{ba} = \tfrac{1}{2} \langle \{\hat{\xi}^{(c)}_a, \hat{\xi}^{(c)\dagger}_b\} \rangle;$$

$$\mathscr{A}_{rs} = \mathscr{A}^*_{sr} = \tfrac{1}{2} \langle \{\hat{a}_r, \hat{a}^\dagger_s\} \rangle,$$

$$\mathscr{B}_{rs} = \mathscr{B}_{sr} = \langle \hat{a}_r \hat{a}_s \rangle. \tag{8.5}$$

Thus $V^{(c)}$ is a hermitian $2n \times 2n$ positive definite matrix subject to further uncertainty inequalities given below.

The relations connecting these two forms of the noise matrix are

$$V^{(c)} = \Omega V \Omega^\dagger:$$

$$\mathscr{A} = \tfrac{1}{2}\{V_1 + V_3 + i(V_2^T - V_2)\},$$

$$\mathscr{B} = \tfrac{1}{2}\{V_1 - V_3 + i(V_2^T + V_2)\};$$

$$V_1 = \tfrac{1}{2}\{\mathscr{A} + \mathscr{A}^* + \mathscr{B} + \mathscr{B}^*\},$$

$$V_2 = \frac{i}{2}\{\mathscr{A} - \mathscr{A}^* - \mathscr{B} + \mathscr{B}^*\},$$

$$V_3 = \tfrac{1}{2}\{\mathscr{A} + \mathscr{A}^* - \mathscr{B} - \mathscr{B}^*\}.$$

Here the matrix Ω is as given in (4.4). And in place of (8.4) we have the equ transformation law

$$\hat{\rho}' = \mathscr{U}(S)\hat{\rho}\mathscr{U}(S)^{-1} \Leftrightarrow V^{(c)\prime} = S^{(c)}V^{(c)}S^{(c)\dagger}.$$

9. Williamson's theorem and uncertainty principles

For general $S \in \mathrm{Sp}(2n, \mathscr{R})$ the transformation law (8.4) for the noise matri a similarity transformation, it is a similarity only if $S = S(X, Y) \in \mathrm{K}(n)$. Norm expect that the diagonalization of V will require a matrix belonging to the $\mathrm{SO}(2n, \mathscr{R})$. However, the fundamental Theorem of Williamson comes to our [18]. This theorem is a complete answer to the question: Given a real sy $2n \times 2n$ matrix V, what is the maximum simplification we can achieve in the $V' = SVS^T$ by allowing S to vary all over $\mathrm{Sp}(2n, \mathscr{R})$? For general V, the no canonical form of V' is not a diagonal form; however the theorem shows that in positive (or negative) definite to begin with, then we can certainly choose an S s is diagonal. By suitable further rescaling and ordering of elements we can then the following

V real symmetric positive definite:

$$SVS^T = \mathrm{diag}(\kappa_1, \ldots, \kappa_n, \kappa_1, \ldots, \kappa_n),$$

$$\kappa_1 \leqslant \kappa_2 \leqslant \cdots \leqslant \kappa_n,$$

suitable $S \in \mathrm{Sp}(2n, \mathscr{R})$.

We shall call this the *Williamson normal form of V*. In general, the κ_r are eigenvalues of V at all. Also note that when V is in this form, then we have $V^{(c}$

In the Williamson normal form we see that for each canonical pair $\hat{q}_r, \hat{p}_r$ we ha uncertainties: $\Delta q_r = \Delta p_r = \kappa_r^{1/2}$. Also *all* the off-diagonal variances vanish. There complete statement of the uncertainty principles for all degrees of freedom wou

$$\kappa_r \geqslant 1/2, \quad r = 1, \ldots, n.$$

A given $2n \times 2n$ real symmetric positive definite matrix V is quantum mech realizable as the noise matrix of some state $\hat{\rho}$ if and only if in its Williamson form (9.1) every diagonal entry is greater than or equal to one-half. This is an S invariant statement. It is naturally useful to express these uncertainty pr directly in terms of V without actually passing to its Williamson normal for There are several ways of doing this and for illustration we quote just one, ex both in terms of V and $V^{(c)}$

$$V + \frac{i}{2}\beta = \text{hermitian positive semidefinite.}$$

$$V^{(c)} + \tfrac{1}{2}\Sigma_3 = \text{hermitian positive semidefinite.}$$

We emphasize that any $V, V^{(c)}$ obeying these conditions are quantum mechanically realizable – they are necessary and sufficient.

There is a subtle distinction between the matrix V being brought to diagonal form, and the matrix $V^{(c)}$ being diagonal. From the relations (8.6) among the two sets of submatrices we can see easily

$$\begin{aligned} V \text{ diagonal} &\Leftrightarrow V_1, V_3 \text{ diagonal, } V_2 = 0, \\ &\Leftrightarrow \mathscr{A}, \mathscr{B} \text{ real diagonal} \\ &\not\Rightarrow V^{(c)} \text{ diagonal:} \end{aligned} \tag{9.4a}$$

$$\begin{aligned} V^{(c)} \text{ diagonal} &\Leftrightarrow \mathscr{A} \text{ real diagonal, } \mathscr{B} = 0 \\ &\Rightarrow V_1, V_3 \text{ diagonal, } V_2 = 0 \\ &\Leftrightarrow V \text{ diagonal.} \end{aligned} \tag{9.4b}$$

This means that the set of states which have diagonal $V^{(c)}$ is a subset of the set of states having diagonal V: the former is a more restrictive condition, so fewer states obey it. In the particular situation when V is in Williamson normal form, it is not only diagonal but in addition $V_1 = V_3$; thus, in spite of the general statement (9.4a), we do find $V^{(c)}$ also diagonal in that case. In complex form, the relevant consequence of Williamson's Theorem for $V^{(c)}$ is that with the transformation law (8.7), $V^{(c)}$ can be "diagonalized".

10. A U(n)-invariant multimode squeezing criterion

The noise matrix V for any state of a single mode system is two dimensional and has the form

$$V = \begin{pmatrix} (\Delta q)^2 & \Delta(q,p) \\ \Delta(q,p) & (\Delta p)^2 \end{pmatrix} \tag{10.1}$$

with obvious meanings for the various matrix elements. The usual Heisenberg uncertainty relation (with $\hbar = 1$) which reads [19]

$$\Delta q \Delta p \geqslant \tfrac{1}{2} \tag{10.2}$$

can, as is well known, be strengthened to the statement [20]

$$\det V \equiv (\Delta q)^2 (\Delta p)^2 - (\Delta(q,p))^2 \geqslant \tfrac{1}{4}. \tag{10.3}$$

This is in fact the content of the conditions (9.3) in this case, and this is $\mathrm{Sp}(2, \mathscr{R})$ invariant.

The state $\hat{\rho}$ with variance matrix V is usually said to be a squeezed state if either one of the two diagonal elements of V (but of course not both) is less than one half. However this definition possesses no useful or interesting continuous invariance at all. A definition of squeezing possessing invariance under the maximal compact U(1) or SO(2) subgroup of $\mathrm{Sp}(2, \mathscr{R})$ is this: the state $\hat{\rho}$ is squeezed if and only if the lesser of the two eigenvalues of V is less than one half. A state squeezed in the former sense is squeezed also in the latter sense but not conversely, so the former is more restrictive

$$\Delta q \text{ or } \Delta p < \frac{1}{\sqrt{2}} \Rightarrow \text{lesser eigenvalue of } V < \tfrac{1}{2}. \tag{10.4}$$

The U(1)-invariant squeezing criterion has been used in several studies. It is of clear that we cannot ask for any more invariance in the squeezing criterion, for e it would be meaningless to think of an Sp(2, $\mathscr{R}$) invariant squeezing criterion.

Motivated by the above, we now describe a criterion for squeezing for st n mode systems [12]. Suppose that for a given state $\hat{\rho}$ the noise matrix V alre some diagonal element less than one half. Then we say that the state is ma squeezed. However it may happen that every diagonal element V_{aa} of V exc equals one half, yet squeezing is buried and not manifest. We have divided elem Sp(2n, $\mathscr{R}$) into passive U(n) elements and active $\Pi(n)$ elements. We would like a definition of squeezing invariant under passive U(n) transformations. Such a tion is the following

$$\hat{\rho} \text{ is a squeezed state} \Leftrightarrow (S(X, Y)\, V S(X, Y)^T)_{aa} < \tfrac{1}{2},$$
$$\text{some } X - iY \in \mathrm{U}(n),$$
$$\text{some } a = 1, 2, \ldots, 2n.$$

Thus, $\hat{\rho}$ is squeezed if V shows it to be manifestly so, or if this happens after a s passive transformation.

We know that in general V cannot be diagonalized by similarity transfor within K(n) – we expect to have to use matrices from the much larger group SO which may be noncanonical. Nevertheless it is remarkable that the abov invariant squeezing criterion can be expressed in terms of the eigenvalue spectr

$$\hat{\rho} \text{ is a squeezed state} \Leftrightarrow$$
$$l(V) = \text{minimum eigenvalue of } V < \tfrac{1}{2}.$$

This is precisely equivalent to the definition (10.5).

Obviously the squeezed or nonsqueezed nature of a state $\hat{\rho}$ is unchanged by elements of Sp(2n, $\mathscr{R}$) lying within K(n), since then V undergoes a similarity tra ation which leaves $l(V)$ unaltered. To change $l(V)$, and so the status of a state, i direction, we *must* use active noncompact elements lying in $\Pi(n)$, if we wish t within the framework of Sp(2n, $\mathscr{R}$) transformations. Thus justifies our using th "squeezing transformation" for the metaplectic unitary operator $\mathscr{U}(P)$ for el $P \in \Pi(n)$.

11. Some interesting families of variance matrices

Let us denote by s the set of all allowed noise matrices V, i.e., all physically rea ones obeying the uncertainty principles

$$s = \left\{ V = 2n \times 2n \text{ real symmetric positive definite} \,|\, V + \frac{i}{2}\beta \right.$$
$$\left. \text{positive semidefinite} \right\}.$$

This is an $n(2n+1)$ parameter family. We have seen that a general $V \in s$ diagonalizable by elements within K(n). We ask: can we characterize the subse consisting of all noise matrices which *are* diagonalizable using elements of K(

$$V \in s_K \Rightarrow S(X, Y)\, V S(X, Y)^T = \text{diagonal}$$

$$\text{some } \mathrm{U} = X - iY \in \mathrm{U}(n). \tag{11.2}$$

The subset s_K is an $n(n+2)$ parameter family.

There are two further subsets of s_K which are interesting [12]. We call them the "hermitian" family s_H and the "Gaussian" family s_G – they are of dimensions n^2 and $n(n+1)$ respectively. The definition of s_H is motivated by the fact that the general transformation rule (8.7) for $V^{(c)}$ becomes very simple if we have a $\mathrm{K}(n)$ element

$$\mathrm{U} \in \mathrm{U}(n):\ V^{(c)} \to S^{(c)}(\mathrm{U})\, V^{(c)} S^{(c)}(\mathrm{U})^\dagger.$$

$$\mathscr{A} \to \mathrm{U}\mathscr{A}\mathrm{U}^{-1}.$$

$$\mathscr{B} \to \mathrm{U}\mathscr{B}\mathrm{U}^T. \tag{11.3}$$

So if $\mathscr{B} = 0$ to begin with, it remains zero; and $\mathscr{A}$ being hermitian can be diagonalized by some U. This would then result in both $V^{(c)}$ and V becoming diagonal. Thus, including the uncertainty conditions (9.3), the definition of s_H is

$$s_H = \{ V \in s_K | \mathscr{B} = 0,\ \mathscr{A} - \tfrac{1}{2} \cdot 1 \text{ positive semidefinite} \} \subset s_K \subset s. \tag{11.4}$$

One can verify that *no* member of this family s_H is squeezed.

Next to the family s_G. Here the definition involves the "noncompact" subset $\Pi(n)$ of $\mathrm{Sp}(2n, \mathscr{R})$

$$s_G = \{ V \in s_K | 2V \in \Pi(n) \subset \mathrm{Sp}(2n, \mathscr{R}) \} \subset s_K \subset s. \tag{11.5}$$

It is a fact that such noise matrices are physically realizable, i.e., they obey the uncertainty conditions, and are diagonalizable within $\mathrm{K}(n)$. Further, except for $V = \frac{1}{2} \cdot 1$, *every other* $V \in s_G$ *is squeezed.* So we see incidentally that this is the only common element in s_H and s_G. All in all, we have

$$s_H, s_G \subset s_K \subset s$$

$$s_H \cap s_G = \{ \tfrac{1}{2} \cdot 1 \}. \tag{11.6}$$

12. Gaussian pure states, Gaussian Wigner distributions

The generators of the metaplectic unitary representation of $\mathrm{Sp}(2n, \mathscr{R})$ are quadratics in $\hat{q}$'s and $\hat{p}$'s. The most general centred n-mode Gaussian wave function involves a quadratic in the q's in the exponent. It turns out that the former act in very nice and compact ways on the latter [21]. We describe the main features briefly in this Section.

A general centred and normalized n-mode Gaussian pure state can be parameterized by two real symmetric $n \times n$ matrices u and v, of which the former is positive definite

$$\psi_{(u,v)}(\mathbf{q}) = \pi^{-n/4} (\det u)^{1/4} \exp\{ -\tfrac{1}{2} q^T (u + iv) q \}.$$

$$\int d^n q\, |\psi_{(u,v)}(\mathbf{q})|^2 = 1. \tag{12.1}$$

For $(u,v)=(1,0)$ we get the ground state

$$\psi_{(1.0)}(\mathbf{q}) = \pi^{-n/4}\exp(-\tfrac{1}{2}q^T q),$$

$$\hat{a}_r\psi_{(1,0)} = 0.$$

The calculation of the WWM representative for $\psi_{(u,v)}(\mathbf{q})$, and of the noise matr easy since only Gaussian integrals and moments are involved. The results are

$$W_{(u,v)}(\xi) = (2\pi)^{-n}\int d^n q'\psi_{(u,v)}(\mathbf{q}-\tfrac{1}{2}\mathbf{q}')\psi_{(u,v)}(\mathbf{q}+\tfrac{1}{2}\mathbf{q}')^*\exp(i\mathbf{q}'\cdot\mathbf{p})$$

$$= \pi^{-n}\exp\{-\xi^T G(u,v)\xi\}.$$

$$G(u,v) = \begin{pmatrix} u+vu^{-1}v & vu^{-1} \\ u^{-1}v & u^{-1} \end{pmatrix}$$

$$= (S(u,v)^{-1})^T S(u,v)^{-1}$$

$$S(u,v) = \begin{pmatrix} u^{-1/2} & 0 \\ -vu^{-1/2} & u^{1/2} \end{pmatrix} \in \mathrm{Sp}(2n,\mathscr{R});$$

$$V(u,v) = \tfrac{1}{2}G(u,v)^{-1} = \tfrac{1}{2}S(u,v)S(u,v)^T \in s_G.$$

While the calculations leading to these results are elementary, it is worth attention to the structures involved. The WWM representative $W_{(u,v)}(\xi)$ is expe be a Gaussian, with a positive definite matrix $G(u,v)$ in the exponent. W interesting is the factorization of this matrix in terms of an $\mathrm{Sp}(2n,\mathscr{R})$-matrix $S(u$ added feature is that this $S(u,v)$ is an example of the product of the first two fac the general pre-Iwasawa decomposition (4.21) for any $S\in\mathrm{Sp}(2n,\mathscr{R})$! That the matrix $V(u,v)$ should be essentially the inverse of $G(u,v)$ is clear from (8.2); it is th product structure for $G(u,v)$ that results in $V(u,v)$ being an element of the s_G defined in the previous Section. Incidentally we also see that $\Pi(n)\subset$ Sp defined in (4.18) and used in defining the family s_G in (11.4) can be describe explicitly using $S(u,v)$

$$\Pi(n) = \{S(u,v)S(u,v)^T \mid S(u,v)\in\mathrm{Sp}(2n,\mathscr{R})$$

u and v real symmetric $n\times n$ matrices, u positive definite$\}$.

We can argue further along similar lines, concerning the form to be expected action of an operator $\mathscr{U}(S)$ on any $\psi_{(u,v)}(\mathbf{q})$. From (7.2) it is clear that $W_{(u,v)}(\xi)$ m mapped onto another Gaussian; the fact that it arises from a pure state wave fu must also be retained; and the transformation rule (8.4) plus the explicit form of in (12.3) means that any $\psi_{(u,v)}(\mathbf{q})$ can be mapped onto $\psi_{(1,0)}(\mathbf{q})$ by a suitable $\mathscr{U}(S)$. is indeed true. We find that

$$\psi_{(u,v)} = (\text{phase factor})\mathscr{U}(S(u,v))\psi_{(1,0)},$$

$$V(u,v) = S(u,v)\,V(1,0)S(u,v)^T.$$

$$V(1,0) = \tfrac{1}{2}\cdot 1.$$

So $\mathrm{Sp}(2n,\mathscr{R})$ acts *transitively* on the set of Gaussian pure states. The subgroup of $\mathrm{Sp}(2n,\mathscr{R})$ leaving the particular state $\psi_{(1,0)}$ invariant (apart from phases) is just $\mathrm{K}(n)$ – $\hat{a}_r$ annihilates $\psi_{(1,0)}$, and the generators of $\mathrm{K}(n)$ in the metaplectic representation are of the form $\hat{a}_r^\dagger \hat{a}_s$. More precisely, the situation may be described as follows. One can easily establish that the behavior of $\psi_{(1,0)}$ under $\mathrm{K}(n)$ is given by

$$\mathrm{U} = X - iY \in \mathrm{U}(n):$$

$$\mathscr{U}(S(X, Y))\psi_{(1,0)} = \sqrt{\det \mathrm{U}}\,\psi_{(1,0)}. \tag{12.6}$$

The sign ambiguity here explains the appearance of the metaplectic group $\mathrm{Mp}(2n)$. The stability group of $\psi_{(1,0)}$ – the subgroup of $\mathrm{Sp}(2n,\mathscr{R})$ leaving this vector strictly invariant is thus the $n^2 - 1$ parameter subgroup $\mathrm{SU}(n) \in U(n)$. Correspondingly the orbit of $\psi_{(1,0)}$ under $\mathrm{Sp}(2n,\mathscr{R})$, made up of the vectors $\mathscr{U}(S)\psi_{(1,0)}$ for all $S \in \mathrm{Sp}(2n,\mathscr{R})$, is an $(n(n+1)+1)$ parameter family. It consists of the vectors $e^{i\alpha}\psi_{(u,v)}$ for $0 \leqslant \alpha < 2\pi$ and all allowed (u, v). This orbit is essentially the coset space $\mathrm{Sp}(2n,\mathscr{R})/\mathrm{SU}(n)$; there is a one-to-one correspondence between vectors $e^{i\alpha}\psi_{(u,v)}$ and points in this space. Suppressing the phase we can next say that the set of density matrices $\psi_{(u,v)}\psi_{(u,v)}^\dagger$, or equally well the set of representative vectors $\psi_{(u,v)}$, is essentially the coset space $\mathrm{Sp}(2n,\mathscr{R})/\mathrm{U}(n)$.

Turning next to the effect of $\mathscr{U}(S)$ on $\psi_{(u,v)}$, we see that apart from a phase factor it has to result in $\psi_{(u',v')}$ for suitable u' and v'. The formula for this change is a beautiful one

$$\begin{aligned}\mathscr{U}(S)\psi_{(u,v)} &= (\text{phase factor})\psi_{(u',v')};\\ \wedge &= (iu - v)^{-1} \to \wedge' = (iu' - v')^{-1}\\ &= (A\wedge + B)(C\wedge + D)^{-1}.\end{aligned} \tag{12.7}$$

The Gaussian WWM function in (12.3) arose from a pure state. Suppose now we consider a general centred normalized Gaussian phase space distribution with a general parameter matrix G

$$W_G(\xi) = \pi^{-n}(\det G)^{1/2}\exp(-\xi^T G\xi),$$

$$G = \text{real symmetric } 2n \times 2n \text{ positive definite matrix.} \tag{12.8}$$

The question is: When is this a WWM function corresponding to some pure or mixed quantum state? Thanks to Williamson's theorem, the answer is elementary [15]. The noise matrix would clearly be

$$V = \tfrac{1}{2}G^{-1}. \tag{12.9}$$

So we start from the given Gaussian $W_G(\xi)$, pass to its V, then go to the Williamson normal form (9.1) of V

$$V \to \mathrm{diag}(\kappa_1, \ldots, \kappa_n, \kappa_1, \ldots, \kappa_n). \tag{12.10}$$

and then demand that each κ_r be greater than or equal to one half. This is a complete necessary and sufficient condition for $W_G(\xi)$ to be a bonafide WWM phase space distribution; as we have seen, however, this condition can be stated directly without

going to the normal form

$$W_G(\xi) \text{ is a WWM distribution} \Leftrightarrow G^{-1} + i\beta = \text{hermitian positive sem}$$

13. Concluding remarks

In this review we have tried to convey the main features of the family of real sy groups $Sp(2n, \mathscr{R})$, and have outlined some problems in optics and quantum m where they are useful. Our account has been descriptive and suggestive, detailed proofs of various statements made. We believe that any intereste wishing to apply symplectic techniques to any concrete problem would equipped for the purpose, and able to supply necessary details.

Some general remarks – partly to counter apparently common misconce may be useful at this stage. The group $Sp(2n, \mathscr{R})$ comes in when we defir canonical transformations on given canonical variables. It is the fact that the co tion relations and hermiticity are maintained that is responsible for the exis unitary operators $\mathscr{U}(S)$ implementing these transformations. In particular, unitary whether $S \in K(n)$, when S itself is unitary, or $S \notin K(n)$, for example S which case S is hermitian rather than unitary. Correspondingly, the "Hamil generating these unitary operators $\mathscr{U}(S)$ are hermitian quadratics in the $\hat{q}$'s and the case of the most general unitary evolution via a general hermitian Hamilto action on $\hat{q}$'s and $\hat{p}$'s (equivalently on $\hat{a}$'s and $\hat{a}^\dagger$'s) definitely preserves the c commutation relations and hermiticity properties, but the transformed operat not be linear combinations of the original ones.

The maximal compact subgroup $U(n)$ of $Sp(2n, \mathscr{R})$ has naturally played ar tant role in our considerations. The n-mode squeezing criterion described in a built-in $U(n)$ invariance. As a result. for a state with a given variance m squeezing if present may be manifest (one of the diagonal elements of V is less t or may be hidden (this happens only after a suitable $U(n)$ transformation). This clear that our squeezing criterion is weaker than the usual one stated directly in the diagonal elements of V, since these would rule out the hidden case. Corresp there are more states which are squeezed by our criterion than by the usual on in any case has much less invariance built in.

The metaplectic group is essential to describe properly the structure of the operators implementing linear canonical transformations on the canonical v (in this respect the notation $\mathscr{U}(S)$ with $S \in Sp(2n, \mathscr{R})$ is inadequate – the argu $\mathscr{U}(S)$ should be an element of $Mp(2n)$). The importance of this group is see example, the calculation of geometric phases for cyclic evolution of squeezed st interpretation of the Guoy phase, etc [22]. It has also been shown elsewhere metaplectic group is relevant in setting up operator Mobius transformations degree of freedom [17].

Work on extending $U(n)$ invariant notions beyond quadrature squeezi progress and will be reported elsewhere. Thus, for two-mode systems, one can squeezing transformations into $U(2)$ invariant equivalence classes, study bunch antibunching with such invariance, etc. [13]. These notions can be genera n mode systems as well.

G Racah, *Ergeb. Exakt. Naturwiss.* **37**, 28 (1965)
B G Wybourne, *Classical Groups for Physicists* (Wiley, New York, 1974)
R Gilmore, *Lie Groups, Lie Algebras and some of their applications* (John Wiley and Sons, New York, USA, 1974)
F J Dyson, *Symmetry groups in nuclear and particle physics* (Benjamin, New York, 1966)
V Guillemin and S Sternberg, *Symplectic techniques in physics* (Cambridge University Press, 1984)
V I Arnold, *Mathematical methods of classical mechanics* (Springer, Berlin, 1978)
C L Siegel, *Am. J. Math.* **LXV**, 1 (1943), reprinted as C L Siegel, *Symplectic Geometry* (Academic Press, New York, 1964)
G Marmo, G Morandi and N Mukunda, *La Rivista del Nuovo Cimento* **13**, No. 8, 1990
R Abraham and J E Marsden, *Foundations of Mechanics* (Benjamin-Cummings, Reading, Mass., 1978)
T F Jordan, *Linear operators for quantum mechanics* (John Wiley, New York, 1974)
G Lion and M Vergne, *The Weil representation, Maslov Index, and Theta series* (Birkhauser, Basel, 1980)
These are generalizations to n dimensions of definitions familiar from first order optics for $n = 1, 2$. See for instance O N Stavroudis, *The Optics of Rays. Wave Fronts and Caustics,* (Academic Press, New York, 1972)
M Nazarathy and J Shamir, *J. Opt. Soc. Am.* **B72**, 356 (1982)
See for instance R Gilmore ref. [1] above
S Helgason, *Differential geometry and symmetric spaces,* (Academic Press, New York, 1962)
See for instance G. Racah in ref. [1] above
A Weil, *Acta Mathematica* **111**, 143 (1964)
R Ranga Rao, *The Maslov Index on the simply-connected covering group and the metaplectic representation, The metaplectic representation in the Fock model* (Preprints, Dept. of Mathematics, Univ. of Illinois, Urbana, Illinois 61801) (1992)
R Simon and N Mukunda, *The two-dimensional symplectic and metaplectic groups and their universal cover* in *Symmetries in Science VI: From the rotation group to quantum algebras,* edited by B Gruber, (Plenum Press, New York, 1993) p. 659–689
For the case of $Sp(2, \mathscr{R})$ these are discussed in K B Wolf, *Integral transforms in science and engineering* (Plenum Press, New York, 1979)
R Simon, N Mukunda and B Dutta, *Phys. Rev.* **A49**, 1567 (1994)
Arvind, B Dutta, N Mukunda and R Simon, *Phys. Rev.* **A52**, 1609 (1995)
H Weyl, *The theory of groups and quantum mechanics* (Dover, New York, 1931)
E P Wigner, *Phys. Rev.* **40**, 749 (1932); J E Moyal, *Proc. Camb. Philos. Soc.* **45**, 99 (1949)
R Simon, E C G Sudarshan and N Mukunda, *Phys. Rev.* **A36**, 3868 (1987)
N Mukunda, R Simon, and E C G Sudarshan, *Phys. Lett.* **A124**, 223 (1987)
J R Klauder and E C G Sudarshan, *Fundamentals of quantum optics* (Benjamin, New York, 1968)
Arvind, B Dutta, C L Mehta and N Mukunda, *Phys. Rev.* **A50**, 39 (1994)
J Williamson, *Am. J. Math.* **58**, 141 (1936)
D F Walls, *Nature (London)* **306**, 141 (1983)
W Schleich and J A Wheeler, *J. Opt. Soc. Am.* **B4**, 1715 (1987)
B Dutta, N Mukunda, R Simon and A Subramaniam, *J. Opt. Soc. Am.* **B10**, 253 (1993)
R Simon, E C G Sudarshan and N Mukunda, *Phys. Rev.* **A37**, 3028 (1988)
Bialynicki-Birula, in *Coherence Cooperation and Fluctuations,* edited by F Haake, L M Narducci and D F Walls (Cambridge University Press, London, 1984)
R Simon, and N Mukunda, *Phys. Rev. Lett.* **70**, 880 (1993)

physics

December 1995
pp. 499–509

Optical theorem and Aharonov–Bohm scattering

M M PANJA, P K BERA and B TALUKDAR
Department of Physics, Visva-Bharati University, Santiniketan 731 235, India

MS received 1 September 1995

Abstract. A rigorous derivation of the optical theorem (OT) from the conservation of probability flux (CPF) is presented for scattering on an arbitrary spherically symmetric potential in N-spatial dimensions (ND). The constructed expression for the OT is found to yield the corresponding well-known results for two- and three-dimensional cases in a rather natural way. The Aharonov-Bohm (AB) effect is considered as a scattering event of an electron by a magnetic field confined in an infinitely long shielded solenoid and a similar derivation is attempted for an appropriate optical theorem. Our current understanding of the scattering theory is found to be inadequate for the purpose. The reason for this is discussed in some detail.

Keywords. Optical theorem; AB scattering.

PACS No. 03·30

1. Introduction

In the three dimensional (3D) quantum mechanical scattering the optical theorem (OT) expresses the total cross section in terms of imaginary part of the forward scattering amplitude, $f(\theta = 0)$. In two spatial dimensions the theorem does not look exactly like that found in the 3D case. However, it can be made to appear so by not absorbing a phase factor [1] into the definition of scattering amplitude. Being related to the unitarity of S matrix or t matrix on the energy shell, the OT provides a mathematical statement for the conservation of probability flux [2] (CPF). Therefore, extraction of the OT from CPF should not involve assumptions or approximations that vary with the dimensionality of space for the scattering event. But studies in existing literature [3, 4] indicate that this is not the case with 2D scattering. The derivation of 2DOT does really involve mathematical approximations which are not demanded in a similar logical progression for the 3DOT. More specifically, the 2DOT is constructed by assuming $f(\theta) \simeq f(0)$ or by making explicit use of the stationary phase approximation [5]. The situation thus calls for a more detailed investigation into the causal connection between the OT and CPF. To that end we derive the optical theorem in N-spatial dimensions by using an equivalent mathematical procedure as is followed to deal with the 3DOT. Further, we examine the OT in the context of Aharonov-Bohm (AB) scattering [6, 7]. This is expected to be quite instructive because the AB effect is characterized by a non-trivial geometry [8] that does not fit into the framework of formal scattering theory. Also, regarded as a scattering event the process is characterized by kinetic momentum ($m\mathbf{r} = \mathbf{p} - (e/c)\mathbf{A}$) rather than the canonical momentum ($\mathbf{p}$).

In §2, we address the proposed generalization of OT for the time-indep Schrödinger equation in an arbitrary number (N) of spatial dimension. As a emphasized, our analysis will be based on the CPF rather than mere identificatior NDOT from partial wave expressions [9]. We shall pay special attention to the sul that arise in the course of our derivation. The optical theorem for the AB e considered in §3. We have chosen to work with two types of scattering states of system modelled by simply and non-simply connected spaces and found that nei the representations permits one to derive the theorem rigorously. However, our a of the difficulties encountered followed by appropriate attempts to deal with s them will be quite illuminating for future researchers in this area of investigatio example, in view of the apprehension that the AB scattering cross section is st beamsize dependent, it may be worthwhile to see if an accurate statement of OT co made by limiting the spatial extent of the incident beam. Finally, in §4, we sum our outlook on the present work and make some concluding remarks.

2. OT in many dimensions

The N dimensional Schrödinger equation for a hypercentral potential $V(r)$ at an e $E = k^2 > 0$ is given by [10]

$$\left(\frac{1}{2}\nabla_N^2 - V(r) + k^2\right)\psi(\mathbf{r}) = 0$$

with the hyperradius r written as

$$r = \left(\sum_{i=1}^{N} x_i x^i\right)^{1/2}, \quad x_i = r\sin\theta_1 \sin\theta_2 \cdots \sin\theta_{i-1}\cos\theta_i.$$

The angular variables θ's satisfy the relation

$$0 \leqslant \theta_i \leqslant \pi, \quad i = 1, 2, \ldots, N-2; \quad 0 \leqslant \theta_{N-1} \leqslant 2\pi \text{ and } \theta_N = 0.$$

The Laplacian ∇_N^2 is

$$\nabla_N^2 = \frac{1}{r^{N-1}}\frac{\partial}{\partial r}\left(r^{N-1}\frac{\partial}{\partial r}\right) + \frac{L^2(\Omega)}{r^2}.$$

Here $L^2(\Omega)$ stands for the grand orbital operator at the hyperangle $\Omega(=(\theta_1, \theta_{N-1}))$ on the hypersphere S^{N-1}. From (1) and (4) we have

$$\left(\frac{\partial^2}{\partial r^2} + \frac{N-1}{r}\frac{\partial}{\partial r} + \frac{L^2(\Omega)}{r^2} - V(r) + k^2\right)\psi(r, \Omega) = 0.$$

Separation of the angular and radial part of (5) yields the radial equation

$$\left(\frac{\mathrm{d}^2}{\mathrm{d}r^2} + \frac{N-1}{r}\frac{\mathrm{d}}{\mathrm{d}r} - \frac{L(L+N-2)}{r^2} - V(r) + k^2\right)R_L(r) = 0.$$

The conservation of probability flux for the ND scattering is expressed as

$$\lim_{r\to\infty} r^{N-1}\int j_r(r, \Omega)\mathrm{d}\Omega = 0$$

$$j_r(r,\Omega) = \mathrm{Re}\left(\psi^* \frac{\hbar}{im}\frac{\partial}{\partial r}\psi\right). \tag{8}$$

On the unit sphere S^{N-1} the surface element

$$\mathrm{d}\Omega = \prod_{j-1}^{N-1} \sin^{N-j-1}\theta_j \mathrm{d}\theta_j. \tag{9}$$

The physical or outgoing wave solution of (5) behaves asymptotically as [11]

$$\psi(r,\Omega) \sim e^{ikr\cos\theta} + f(\Omega)\frac{e^{ikr}}{r^{(N-1)/2}}. \tag{10}$$

Clearly, θ is the angle between the wave vector **k** and **r**. In terms of the L-th partial wave scattering phase shift δ_L and the Gegenbauer polynomial $C_n^{(\beta)}(x)$, the amplitude $f(\Omega)$ is given by

$$f(\Omega) = -\left(\frac{2}{i}\right)^{(N-5)/2} \frac{\Gamma\left(\frac{N}{2}-1\right)}{\sqrt{\pi}} \frac{1}{k^{(N-1)/2}}$$

$$\sum_{L=0}^{\infty} (2L+N-2)(e^{2i\delta_L}-1) C_L^{((N/2)-1)}(\cos\theta). \tag{11}$$

Substituting (10) in (8), we get

$$j_r(r,\Omega) = \frac{\hbar k}{m}\left[\cos\theta + \frac{1}{r^{N-1}}|f(\Omega)|^2 + \frac{1}{r^{(N-1)/2}}(1+\cos\theta)\,\mathrm{Re}\{f(\Omega)e^{ikr(1-\cos\theta)}\}\right]$$

$$+ \frac{\hbar}{m}\frac{N-1}{2}\frac{1}{r^{((N-1)/2)+1}}\,\mathrm{Im}\{f(\Omega)e^{ikr(1-\cos\theta)}\}. \tag{12}$$

If we take the incident wave along the x_1-axis, (7), (11) and (12) supplemented by the definition

$$\sigma_{\mathrm{tot}} = \int |f(\Omega)|^2 \mathrm{d}\Omega \tag{13}$$

give

$$\sigma_{\mathrm{tot}} = -\lim_{r\to\infty} r^{(N-1)/2}\mathrm{Re}\left[-\left(\frac{2}{i}\right)^{(N-5)/2}\frac{\Gamma((N/2)-1)}{\sqrt{\pi}}\frac{1}{k^{(N-1)/2}}e^{ikr}\right.$$

$$\left.\times \sum_{L=0}^{\infty}(2L+N-2)(e^{2i\delta_L}-1)\left\{I_L^{(N)} - i\frac{N-1}{2}\frac{1}{kr}\tilde{I}_L^{(N)}\right\}\right] \tag{14a}$$

with

$$I_L^{(N)} = \int_0^{2\pi}\int_0^{\pi}\cdots\int_0^{\pi}[1+\cos\theta_1]e^{-ikr\cos\theta_1}C_L^{((N/2)-1)}(\cos\theta_1)$$

$$\times \prod_{j=1}^{N-1}\sin^{N-j-1}\theta_j \mathrm{d}\theta_j. \tag{14b}$$

The integral $\tilde{I}_L^{(N)}$ is obtained from $I_L^{(N)}$ by replacing the quantity in the square by unity. The expression for $I_L^{(N)}$ is found as

$$I_L^{(N)} = \frac{(2\pi)^{N/2}\Gamma(L+N-2)}{i^L\Gamma(N-2)\Gamma(L+1)(kr)^{((N-2)/2)}}\left[J_{L+((N-2)/2)}(kr) + iJ'_{L+((N-2)/2)}(kr)\right]$$

Here the prime denotes differentiation with respect to the argument. The d of this result is given in appendix A. Using the asymptotic form of the its derivative in (15) the resulting expression can be used in (14a) to reca the form

$$\sigma_{\text{tot}} = \frac{4\pi^{(N-1)/2)}}{\Gamma\left(\frac{N-1}{2}\right)}\frac{1}{k^{N-1}}\sum_{L=0}^{\infty}(2L+N-2)\frac{\Gamma(L+N-2)}{\Gamma(L+1)}\sin^2\delta_L.$$

In the asymptotic limit the contribution of $\tilde{I}_L^{(N)}$ to the scattering cross section di because of the factor $(kr)^{-1}$ in front of it. From (11) and (16), we get the OT,

$$\sigma_{\text{tot}} = 2\left(\frac{2\pi}{k}\right)^{(N-1)/2}\text{Im}\left\{i^{(N-3)/2}f(\Omega_{\mathbf{k}})\right\}$$

for the ND scattering. Clearly $f(\Omega_{\mathbf{k}})$ is the scattering amplitude in the direction plane wave.

In three dimensional problems with *rotational-reflectional symmetry*, $f(\Omega_{\mathbf{k}}$ a function of θ_1 only and by our choice $\theta_1 = 0$. Therefore, for $N = 3$ we recover known optical theorem [2]

$$\sigma_{\text{tot}} = \frac{4\pi}{k}\text{Im}\, f(0).$$

Similarly for 2D scattering we have [3]

$$\sigma_{\text{tot}} = 2\sqrt{\frac{\pi}{k}}\left[\text{Im}\, f(0) - \text{Re}\, f(0)\right].$$

We have seen that for all spatial dimensions the optical theorem is a direct cons of CPF and our derivation for the NDOT does not involve any approxi However, from (15) it is clear that use of the asymptotic values for J_ν and J'_ν through $I_L^{(N)}$ requires $\delta_L(k)$ to vanish for large L. This observation will play a cru in the discussion of OT for the AB effect. In wave language, the OT follows from that the total cross section represents the removal of flux from the incident be such a removal can only occur as a result of destructive interference betw incident wave and the elastically scattered wave in the forward direction. Th point is followed to visualize the 3D optical theorem in terms of *shadow scatteri* Specific examples are often used to make the situation more transparent. Cons the hard-sphere scattering [13] we have

$$\sigma_{\text{tot}} = \frac{4\pi}{k}\text{Im}[f_{\text{hard sphere}}(0)]$$

where

$$f_{\text{shadow}}(\theta) = \frac{i}{2k} \sum_{l=0}^{kR} (2l+1) P_l(\cos\theta) \tag{21}$$

with R, the radius of the sphere. The equivalence of (18) and (20) for the present instance can be established by using the fact that $\text{Im}[f_{\text{reflection}}(0)]$ averages to zero due to oscillating phase. Interestingly, by exploiting the orthogonality properties of Gegenbauer polynomials we can also arrive at a similar conclusion for the N-dimensional scattering.

3. OT in AB scattering

The AB effect is a typical quantum mechanical phenomenon which results from the scattering of electrons by a magnetic field confined in an infinite solenoid [6]. It thus constitutes the observable consequence of a hidden field **B**. Here the vector potential **A** plays a crucial role. For example, despite $\mathbf{B} = 0$, the space region outside the solenoid is characterized by a non-vanishing gauge potential together with concentrated singularity along the negative x-axis. The essential singularity in **A** along the line is called Dirac string which, from geometer's point of view, manifest itself in giving rise to a multi-connected space [8]. The AB effect exists for those representations in which the electron wave function is either (i) discontinuous in a simply connected space $\mathscr{R}^2$ or (ii) continuous over a non-simply connected space $(\mathscr{R}^2/\{X_1 \leqslant 0,\ X_2 = 0\})$. Also the long-range behaviour of the vector potential does not permit clear separation of the complete wave function into the incoming and scattered part. In the course of our study we shall see that these features of the AB effect pose problems to write an optical theorem for the process.

Consider the Schrödinger equation

$$\left[\left(\nabla - \frac{ie}{c\hbar}\mathbf{A}\right)^2 + k^2\right]\psi(\mathbf{r}) = 0 \tag{22}$$

for scattering of a charged particle by an impenetrable infinitely long thin cylindrical solenoid of radius R. The vector potential $\mathbf{A} = (0, \Phi/2\pi r)$ outside the solenoid containing the magnetic flux Φ lies on a plane perpendicular to the axis of the cylinder. As already noted, there can be two types of scattering solutions for (22). In the following we use them, one by one to look for an appropriate optical theorem for the AB scattering.

3.1 *Wave function in the simply-connected space*

This wave function has been obtained by making use of the two-potential formula of Gellman and Goldbarger [14]. Asymptotically, $\psi(\mathbf{r})$ behaves as

$$\psi \sim \psi_{\text{AB}} + \psi_C. \tag{23}$$

Here

$$\psi_{\text{AB}} \sim e^{i\alpha(\phi-\pi)+ikr\cos\phi} + \frac{i\sin(\pi\alpha)e^{i(\phi/2)}e^{ikr}}{\sqrt{1-2ikr\sin^2\phi/2}} \tag{24}$$

represents the asymptotic wave function for the non-shielded solenoid [15]. The effect

of shielding is taken care of by the second term in (23) and we have

$$\psi_C \sim f_s(\phi)\frac{e^{ikr}}{\sqrt{r}}$$

with

$$f_s(\phi) = \sqrt{\frac{2}{\pi ik}}\sum_m \frac{J_{|m+\alpha|}(kR)}{H_{|m+\alpha|}(kR)} e^{i\pi(|m|-|m+\alpha|)} e^{im\phi}.$$

The marked difference in the structure of (24) from the standard scattering form shown in (10) may be attributed to the inextricable mixing between the r angular variables in the scattered part. However, if we restrict to $kr\sin^2\phi/2 \gg$ recast it in the form of (10) to get the scattering amplitude

$$f_{AB}(\phi) = \sqrt{\frac{1}{2\pi ik}}\sin(\pi\alpha)\frac{e^{i(\phi/2)}}{\sin(\phi/2)}$$

as obtained by Aharonov and Bohm [16]. It is crucial to observe that the mation sought here precludes the value $\phi = 0$. This forbids to write an optical for the AB effect by using the wave function in a simply connected space.

3.2 *Wave function in the non-simply connected space*

The wave function in this case is constructed by considering (22) in the cylindri coordinates (r, ϕ) and assuming a general solution in the form

$$\psi(\mathbf{r}) \equiv \psi(r,\phi) = \sum_{m=-\infty}^{\infty} A_m f_m(r)\Phi_m(\phi).$$

This leads us to the differential equations

$$\left[\frac{d^2}{dr^2} + \frac{1}{r}\frac{d}{dr} + k^2 - \frac{(m+\alpha)^2}{r^2}\right] f_m(r) = 0$$

and

$$\left[\frac{d^2}{d\phi^2} + m^2\right]\Phi_m(\phi) = 0$$

for the radial and angular parts of (28). Using the Dirichlet and periodic b conditions, solutions of (29) and (30) can be obtained to read

$$f_m(r) = A_m[J_{|m+\alpha|}(kr)\, Y_{|m+\alpha|}(kR) - J_{|m+\alpha|}(kR)\, Y_{|m+\alpha|}(kr)]$$

and

$$\Phi_m(\phi) = e^{im\phi}, \quad m \in I.$$

In analogy with (10), we choose the asymptotic form of $\psi(r, \phi)$ as

$$\psi(r,\phi) \sim e^{ikr\cos\phi} + f(\phi)\frac{e^{ikr}}{\sqrt{r}}.$$

From (28), (31) and (33) we get

$$f(\phi) = \frac{1}{\sqrt{2\pi k}} e^{-i(\pi/4)} \sum_{m=-\infty}^{\infty} [e^{2i(\Delta_m + \delta_m(\alpha))} - 1] e^{im\phi}$$

$$A_m = \frac{i^{-|m+\alpha|}}{|H^{(1)}_{|m+\alpha|}(kR)|}. \tag{35}$$

he quantities $\delta_m(\alpha)$ and Δ_m given by

$$\delta_m(\alpha) = (|m| - |m+\alpha|)\frac{\pi}{2} \tag{36}$$

$$e^{2i\Delta_m} = 1 - \frac{2J_{|m+\alpha|}(kR)}{H^{(1)}_{|m+\alpha|}(kR)} \tag{37}$$

for the phases induced by the vector potential **A** and the impenetrable cylinder, tively.

ıations (7), (12), (13) and (34) can be combined to write

$$\sigma^{AB}_{tot} = -\lim_{r\to\infty}\sqrt{r}\frac{1}{\sqrt{2\pi k}}\mathrm{Re}\left[e^{-i(\pi/4)+ikr}\sum_{m=-\infty}^{\infty}(e^{2i(\Delta_m+\delta_m(\alpha))}-1)I^{(2)}_m\right]. \tag{38}$$

esult for $I^{(2)}_m$ can be obtained from (14b) and we have

$$I^{(2)}_m = \frac{2\pi}{i^m}\left[J_m(kr) + iJ'_m(kr)\right]. \tag{39}$$

ears that (34), (35) and (39) together with the asymptotic forms

$$J_m(kr) \sim \sqrt{\frac{2}{\pi kr}}\cos\left(kr - \frac{m\pi}{2} - \frac{\pi}{4}\right) + o\left(\frac{1}{kr}\right) \tag{40a}$$

$$J'_m(kr) \sim \sqrt{\frac{2}{\pi kr}}\sin\left(kr - \frac{m\pi}{2} - \frac{\pi}{4}\right) + o\left(\frac{1}{kr}\right) \tag{40b}$$

o the optical theorem for AB scattering. Unfortunately, such a derivation involves ous logical flaw. This can be seen as follows.

e asymptotic forms in (40) are valid only for $m \ll kr$. This inequality is violated for tely many of the terms in a Bessel function expansion. Since $\Delta_m + \delta_m(\alpha)$ takes stant value as $|m| \to \infty$, use of (40) in (38) gives rise to a divergent σ^{AB}_{tot}. This does appen for the ordinary scattering on short range interactions as discussed in most e text books. With Henneberger [17] one may attempt to resolve the difficulty iated with the AB effect by controlling of the incident beam ψ_{inc} and study its cation for the optical theorem.

e partial wave expansion for $\psi_{inc} = e^{ikr\cos\phi}$ is taken in the form

$$\psi_{inc} = \sum_m i^{|m|}e^{-|m|\varepsilon}J_{|m|}(kr)e^{im\phi}, \tag{41}$$

e the small positive quantity ε satisfies $\varepsilon \gg 1/kd$ and d is the distance from the erer to the detector. In this case one obtains the scattering amplitude and cross on as

$$f_\varepsilon(\phi) = \frac{1}{\sqrt{2\pi k}}e^{-i(\pi/4)}\sum_{m=-\infty}^{\infty}e^{-|m|\varepsilon}[e^{2i(\Delta_m+\delta_m(\alpha))}-1]e^{im\phi} \tag{42}$$

and

$$\sigma_{\text{tot}}^{\varepsilon} = -\lim_{r\to\infty}\sqrt{r}\frac{1}{\sqrt{2\pi k}}\text{Re}\left[e^{-i(\pi/4)+ikr}\sum_{m=-\infty}^{\infty}\frac{e^{-|m|\varepsilon}}{i^m}(e^{2i(\Delta_m+\delta_m(\alpha))}-1\right.$$

$$\left.\times\{J_m(k\rho)+iJ'_m(k\rho)\}\right]$$

The damping exponential $e^{-|m|\varepsilon}$ tends to remove the awkward divergence resulting from the use of (40) and thus, in principle, one could write an optical for the process. But we can see that this claim will also be based on in mathematical treatment of the problem.

For pure AB scattering ($\Delta_m = 0$), (37) and (42) can be combined to write [

$$f_\varepsilon(\phi) = \frac{1}{\sqrt{2\pi ik}}\left[e^{-i\pi\alpha} + 2\text{Re}\sum_{1}^{\infty}e^{-i\pi\alpha}e^{im\phi}e^{-m\varepsilon} - \sum_{-\infty}^{\infty}e^{-im\phi}e^{-|m|\varepsilon}\right].$$

Interestingly, (44) can be reduced to the standard AB scattering ampli provided one agrees to drop the third term which vanishes for angles deviating forward direction by an amount $\gg \varepsilon$. This is in agreement with the obser Corinaldesi and Rafeli [18]. However, suppression of this term amoun violation of unitarity for the S matrix. Thus, it is not possible to make a statem OT by using (42) and yet keep the well known AB scattering amplitude unch this context another significant point to note is the following.

The two wave functions, one described in the simply-connected space and the non-simply connected space, are locally gauge equivalent. Since the gau formation does not change the physics of the problem, the claimed validity of (will contradict the conclusion drawn by working with the local gauge e multiple valued representation. A more instructive step to dispense with the constructing OT in the present instance is now in order. For example, use of (4 and (19) leads to

$$\sigma_{\text{tot}}^{\varepsilon} = \frac{4}{k}\sum_{m=-\infty}^{\infty}e^{-2|m|\varepsilon}\sin^2(\delta_m(\alpha)+\Delta_m)$$

and

$$\sigma_{\text{tot}}^{\varepsilon} = \frac{4}{k}\sum_{m=-\infty}^{\infty}e^{-|m|\varepsilon}\sin^2(\delta_m(\alpha)+\Delta_m).$$

Since $\delta_m(\alpha)$ does not go to zero as $|m|\to\infty$, the results in (45) and (46) do not ag disagreement prohibits use of (13) in the derivation of OT from the CPF. Thus possible to provide a definitive statement for the OT even by working wi valued wave function in our unified approach.

4. Concluding remarks

The optical theorem is embedded in the partial-wave expressions for the s quantities. But it is widely believed that to appreciate the physical significar theorem, the OT should be derived directly from CPF. We have followed point to construct an expression for the OT for N-dimensional potential s

without using any approximation like that of Boya and Murray [21]. Being mathematically rigorous, the present derivation exhibits the causal connection between the OT and CPF in a more general context. As special instances of our general expression, we have obtained the well-known results for three- and two-dimensional optical theorem. The 3D optical theorem is often physically visualized in terms of shadow scattering. The same is found true for the ND scattering.

We have attempted to provide a statement of the optical theorem for the Aharonov-Bohm scattering. Being related to the observable effects of a hidden field, it is very difficult to treat this process by the methods of formal scattering theory. Despite that, we worked with two types of wave functions in looking for an appropriate OT for the AB process. The scattering amplitude for the wave function in the simply-connected space is not defined in the forward direction and is thus unsuitable for deriving the optical theorem. This is reminiscent of the so-called Coulomb scattering. For the Coulomb problem, divergence in cross section and/or scattering amplitude arises from the long-range nature of the interaction. The speciality of the AB process is that there is no long-range force to cause divergence. However, the long-range vector potential can lead to divergent scattering cross section for an incident beam of infinite extent.

Our next choice of the wave function was that in the non-simply connected space. Here the vector potential is gauged everywhere except on a ray, viz., the negative real axis such that the present wave function is related to that in the simply connected space by unitary transformation. Here we have also chosen to work with an incident beam of finite extent. Even with all these modifications a rigorous derivation of the optical theorem was not possible, presumably because the reflection symmetry of the scattering interaction is broken by the presence of the noted branch-cut. We, therefore, conclude by noting that one requires a thorough modification of the scattering theory to deal with the AB process, but this seems to be far from clear.

Acknowledgement

This work forms a part of the research project, "Quantum phases from generalized classical theory" supported by the Department of Science and Technology, Government of India.

Appendix A

The integral $I_L^{(N)}$ in (14b) can be written as

$$I_L^{(N)} = A(I_L'^{(N)} + I_L''^{(N)}), \tag{A1}$$

where

$$I_L'^{(N)} = \int_0^{\pi} e^{-ikr\cos\theta_1} C_L^{((N/2)-1)}(\cos\theta_1)\sin^{N-2}\theta_1 \mathrm{d}\theta_1, \tag{A2}$$

$$I_L''^{(N)} = \int_0^{\pi} e^{-ikr\cos\theta_1} C_L^{((N/2)-1)}(\cos\theta_1)\sin^{N-2}\theta_1 \cos\theta_1 \mathrm{d}\theta_1 \tag{A3}$$

and

$$A = \int_0^{2\pi} \mathrm{d}\phi \int_0^{\pi} \sin^{N-3}\theta_2 \mathrm{d}\theta_2 \int_0^{\pi} \sin^{N-4}\theta_3 \mathrm{d}\theta_3 \cdots \int_0^{\pi} \sin\theta_{N-2} \mathrm{d}\theta_{N-2}. \tag{A4}$$

Using the formulae [19]

$$\int_0^\pi e^{iz\cos\theta}\sin^{2\nu}\theta\, C_n^{(\nu)}(\theta)\mathrm{d}\theta = \frac{\Gamma\left(\nu+\frac{1}{2}\right)\Gamma(2\nu+n)\sqrt{\pi}2^\nu}{(-i)^n\Gamma(2\nu)\Gamma(n+1)z^\nu} J_{\nu+n}($$

and

$$J_\nu(e^{i\pi}z) = e^{i\nu\pi}J_\nu(z)$$

in (A2) one obtains

$$I_L'^{(N)} = \frac{\Gamma\left(\frac{N-2}{2}+\frac{1}{2}\right)\Gamma(L+N-2)\sqrt{\pi}2^{(N-2)/2}}{i^L\Gamma(N-2)\Gamma(L+1)(kr)^{(N-2)/2}} J_{L+((N-2)/2)}$$

Differentiation of (A2) under the sign of integration with respect to kr

$$I_L''^{(N)} = i\frac{\mathrm{d}I_L'^{(N)}}{\mathrm{d}(kr)}.$$

The results in (A5) and (A6) give

$$I_L''^{(N)} = \frac{\Gamma\left(\frac{N-2}{2}+\frac{1}{2}\right)\Gamma(L+N-2)\sqrt{\pi}2^{(N-2)/2}}{i^L\Gamma(N-2)\Gamma(L+1)(kr)^{(N-2)/2}}$$

$$\times i\left[J'_{L+((N-2)/2)}(kr) - \left(\frac{N-2}{2}\right)\frac{J_{L+((N-2)/2)}(kr)}{kr}\right].$$

Furthermore [20],

$$\frac{1}{kr}J_{L+((N-2)/2)}(kr) = \frac{1}{(2L+N-2)}[J_{L+(N/2)}(kr) + J_{L+(N/2)-2}($$

$$\sim \frac{1}{(2L+N-2)}\sqrt{\frac{2}{\pi kr}}\left[\cos\left\{kr-\left(L+\frac{N}{2}\right.\right.\right.$$

$$+\cos\left\{kr-\left(L+\frac{N}{2}-\frac{3}{2}\right)\frac{\pi}{2}\right\}\Bigg]$$

$$= \frac{2}{(2L+N-2)}\sqrt{\frac{2}{\pi kr}}\cos\left\{kr-\left(L+\frac{N-1}{2}\right.\right.$$

$$= 0.$$

Thus, (A7) becomes

$$I_L''^{(N)} = \frac{\Gamma\left(\frac{N-2}{2}+\frac{1}{2}\right)\Gamma(L+N-2)\sqrt{\pi}2^{(N-2)/2}}{i^L\Gamma(N-2)\Gamma(L+1)(kr)^{(N-2)/2}} iJ'_{L+((N-2)/2)}($$

To evaluate the integrals in (A4), we use the formula

$$\int_0^{\pi/2} \sin^p\theta \cos^q\theta \, d\theta = \frac{\Gamma\left(\frac{p+1}{2}\right)\Gamma\left(\frac{q+1}{2}\right)}{2\Gamma\left(\frac{p+q+2}{2}\right)}$$

and find

$$A = \frac{2\pi^{((N-1)/2)}}{\Gamma\left(\frac{N-1}{2}\right)}. \tag{A9}$$

From (A1), (A5), (A8) and (A9), one obtains the desired expression for $I_L^{(N)}$ given in (15).

References

[1] S K Adhikari, *Am. J. Phys.* **54**, 362 (1986)
[2] R G Newton, *Scattering theory of waves and particles* (Springer Verlag, New York, 1982)
[3] P A Maurone and T K Lim, *Am. J. Phys.* **51**, 856 (1983)
[4] Z Y Gu and S W Qian, *Phys. Lett.* **A136**, 6 (1989)
[5] H Jeffreys and B S Jeffreys, *Methods of mathematical physics* (Cambridge University Press, Cambridge, U.K. 1956)
[6] M Peshkin and A Tonomura, *The Aharonov-Bohm Effect* (Springer-Verlag, Berlin, 1989)
[7] Y Aharonov, C K Au, E C Lerner and J Q Liang, *Phys. Rev.* **D29**, 2396 (1984)
[8] B Felsager, *Geometry, particles and fields* (Odense University Press, Copenhagen, 1987)
[9] I Adawi, *J. Math. Phys.* **12**, 358 (1971)
[10] M Fabre de la Ripelle, *Ann. Phys.* **147**, 281 (1983)
[11] M Fabre de la Ripelle, *Few-Body systems* **14**, 1 (1993)
[12] L S Rodberg and R M Thalar, *Introduction to quantum theory of scattering* (Academic, New York, 1967)
[13] J J Sakurai, *Modern quantum mechanics* (Addison Wesley Publishing Co. Inc., California, 1985)
[14] M Gell-Mann and M L Goldberger, *Phys. Rev.* **91**, 358 (1953)
[15] G N Afnasiev and V M Shilov, *J. Phys.* **A22**, 5195 (1989); **23**, 5185 (1990)
[16] Y Aharonov and D Bohm, *Phys. Rev.* **115**, 485 (1959)
[17] W-C Henneberger, *Phys. Rev.* **A22**, 1383 (1980); *J. Math. Phys.* **22**, 116 (1981)
[18] E Corinaldesi and F Rafeli, *Am. J. Phys.* **46**, 1187 (1978)
[19] G N Watson, *A treatise on the theory of Bessel functions* (Cambridge University Press, Cambridge, 1958)
[20] M Abromowitz and I A Stegun, *Handbook of Mathematical Functions* (Dover Publications Inc., New York, 1972)
[21] L J Boya and R Murray, *Phys. Rev.* **A50**, 4397 (1994)

Journal of physics

December 1995
pp. 511–517

BD–FRW models in the framework of Israel–Stewart–Hiscock theory

KALYANI DESIKAN
Department of Mathematics, Indian Institute of Technology, Madras 600 036, India

MS received 3 July 1995

Abstract. BD–FRW universe filled with imperfect fluid having bulk viscosity is investigated under the framework of Israel–Stewart–Hiscock causal theory. The field equations have been solved by using the relation $\phi = KR^{\alpha}$ where K and α are constants, between the Brans–Dicke scalar field φ and the scale factor R. This relation, in fact, leads to a constant deceleration parameter q. It is shown that the constancy of the deceleration parameter permits only two possibilities i.e. either $H =$ constant with $m = 1$ or $m = (1 + b - \alpha)/(2(1 + b) - \alpha)$, irrespective of the value of ε.

Keywords. Cosmology; Brans–Dicke theory; Israel–Stewart–Hiscock causal thermodynamics.

PACS No. 98·80

1. Introduction

The evolution of the universe includes a number of dissipative processes. The role of dissipative effects on the evolution of the universe has been investigated by many authors [1]. These investigations are based on the conventional thermodynamic theory of irreversible processes due to Eckart [2]. Hiscock and Lindblom [3] showed that Eckart's theory is non-causal (since it admits dissipative signals with super-luminal velocities) and all its equilibrium states are unstable. These problems arise due to the first order nature of the theory i.e. it considers only first-order deviations from equilibrium. The neglected second-order terms are in fact necessary to prevent non-causal and unstable behaviour. Alternatively, second-order theories [4–6] have been proposed to remedy this drawback. Particularly successful is the so-called 'extended irreversible thermodynamics' (EIT) theory [4, 6]. However, Hiscock and co-workers [7, 8] have shown that most versions of the causal second-order theories, including EIT, omit certain divergence terms. Hence, the resulting "truncated" evolution equations give rise to very different behaviour than the full equations. Therefore, the best currently available theory for analysing dissipative processes in the universe is the full Israel–Stewart–Hiscock causal thermodynamics.

In this paper we wish to investigate the Brans–Dicke [BD]-FRW universe filled with imperfect fluid having bulk viscosity under the frame-work of the full Israel–Stewart–Hiscock causal theory. Most of the well known BD-FRW models of the universe with curvature parameter $k = 0$ are models with constant deceleration parameter. Hence, in this paper the field equations have been solved by considering the relation $\phi = KR^{\alpha}$ between the scalar field ϕ and the scale factor R. This relation leads to the constancy of the deceleration parameter.

2. Field equations

The field equations of BD theory (with $c = 1$) are

$$G_{ab} = -\frac{8\pi}{\phi} T_{ab} - \frac{\omega}{\phi^2}\left[\phi_{;a}\phi_{;b} - \frac{1}{2} g_{ab}\phi_{;c}\phi^{;c}\right]$$

$$-\frac{1}{\phi}[\phi_{;a;b} - g_{ab}\Box^2\phi]$$

and

$$\Box^2\phi = \frac{8\pi}{3+2\omega} T^a_{\ .a}$$

where ϕ is the scalar field and ω the BD coupling parameter; T_{ab}, the momentum tensor for a bulk viscous fluid, is given by

$$T_{ab} = [\rho + p + \Pi]u_a u_b + [p + \Pi]g_{ab}$$

where ρ is the energy density, p the thermodynamic pressure, Π the bulk pressure and u_a the four velocity satisfying the condition $u_a u^a = 1$.

Considering the FRW metric, with $k = 0$

$$ds^2 = dt^2 - R^2(t)[dr^2 + r^2(d\theta^2 + \sin^2\theta\, d\phi^2)]$$

and an equation of state

$$p = \gamma\rho, \quad 0 \leqslant \gamma \leqslant 1$$

the field eqs (1) and (2) reduce to

$$3\left[\frac{\dot{R}}{R}\right]^2 + 3\frac{\dot{\phi}}{\phi}\frac{\dot{R}}{R} - \frac{\omega}{2}\left[\frac{\dot{\phi}}{\phi}\right]^2 = \frac{8\pi\rho}{\phi}$$

$$2\frac{\ddot{R}}{R} + \left[\frac{\dot{R}}{R}\right]^2 + 2\frac{\dot{\phi}}{\phi}\frac{\dot{R}}{R} + \frac{\omega}{2}\left[\frac{\dot{\phi}}{\phi}\right]^2 + \frac{\ddot{\phi}}{\phi} = -\frac{8\pi\gamma\rho}{\phi} - \frac{8\pi\Pi}{\phi}$$

$$\ddot{\phi} + 3\frac{\dot{R}}{R}\dot{\phi} = \frac{8\pi}{3+2\omega}[(1-3\gamma)\rho - 3\Pi]$$

while the continuity equation $T^{ab}_{\ ;b} = 0$ gives

$$\dot{\rho} + 3(1+\gamma)H\rho = -3\Pi H$$

where $H \equiv \dot{R}/R$ is the Hubble's constant.

The causal evolution equation for the bulk viscous pressure is given by

$$\Pi + \tau\dot{\Pi} = -3\xi H - \frac{\varepsilon}{2}\tau H\left(3H + \frac{\dot{\tau}}{\tau} - \frac{\dot{\xi}}{\xi} - \frac{\dot{T}}{T}\right)$$

where T is the temperature, ξ the bulk viscosity co-efficient and τ the relaxat
For $\tau = 0$, (10) reduces to the non-causal equation. In (10), $\varepsilon = 0$ gives the t
theory (extended irreversible thermodynamics [EIT]), while $\varepsilon = 1$ gives the fu
Stewart–Hiscock theory.

ew of the complex non-linear character of the BD field equations, to solve these tions we assume a functional relation between ϕ and R to be of the form

$$\phi = KR^{\alpha} \tag{11}$$

e K and α are constants. With the choice (11), (6) to (8) reduce to

$$\frac{8\pi\rho}{\phi} = \left[3 + 3\alpha - \frac{\omega\alpha^2}{2}\right] H^2 \tag{12}$$

$$-\frac{8\pi\gamma\rho}{\phi} - \frac{8\pi\Pi}{\phi} = (2+\alpha)\dot{H} + \left[3 + \frac{\omega\alpha^2}{2} + 2\alpha + \alpha^2\right] H^2 \tag{13}$$

$$\frac{8\pi}{\phi}[(1-3\gamma)\rho - 3\Pi] = (3+2\omega)[\alpha(\alpha+3)H^2 + \alpha\dot{H}]. \tag{14}$$

inating ρ and Π from the above equations, we have

$$\dot{H} = -(1+b)H^2 \tag{15}$$

$$\frac{\ddot{R}}{R} + b\left[\frac{\dot{R}}{R}\right]^2 = 0 \tag{16}$$

e

$$b = \frac{\omega\alpha^2 + 4\omega\alpha - 6}{2(\omega\alpha - 3)}; \quad \omega\alpha - 3 \neq 0. \tag{17}$$

ation (15) shows that these models have a constant deceleration parameter b. lentally, most of the well-known perfect fluid models in general relativity and BD ry belong to this category.

quations (12–14), (9) and (10) imply the dynamical equation for the Hubble meter

$$\frac{\tau}{8\pi}[(2+\alpha)\dot{H}\phi + [6(1+\gamma) + \omega\alpha^2(1-\gamma) + 2\alpha(2+3\gamma) + 2\alpha^2]H\dot{H}\phi] \tag{18}$$

$$= 3\xi H + \frac{\varepsilon}{2}\tau\Pi\left(3H + \frac{\dot{\tau}}{\tau} - \frac{\dot{\xi}}{\xi} - \frac{\dot{T}}{T}\right) + \Pi.$$

n integration, (16) gives the exact solution

$$R(t) = \begin{cases} [D + Ct]^{1/(1+b)} & b \neq -1 \\ R_0 e^{\chi t} & b = -1 \end{cases} \tag{19}$$

e C, D and χ are constants of integration.

(i): $b \neq -1$

is case it can be seen that the Hubble parameter can be written in terms of the scale or as

$$H = \frac{C}{(1+b)} R^{-(1+b)}. \tag{20}$$

$$\Pi = \frac{-\phi}{8\pi}\left[(2+\alpha)\dot{H} + \left[3(1+\gamma)+(2+3\gamma)\alpha+(1-\gamma)\frac{\omega\alpha^2}{2}+\alpha^2\right]H^2\right.$$

Now using (21) and (22) in (18) yields

$$\frac{\phi_0}{8\pi}\left[\tau(2+\alpha)\ddot{H}H^{-\alpha/(1+b)} + 2\left[3(1+\gamma)+(2+3\gamma)\alpha+(1-\gamma)\frac{\omega\alpha^2}{2}+\alpha^2\right.\right.$$
$$\times \tau\dot{H}H^{1-(\alpha/(1+b))} + (2+\alpha)\dot{H}H^{-\alpha/(1+b)}$$
$$\left.\left.+\left[3(1+\gamma)+(2+3\gamma)\alpha+(1-\gamma)\frac{\omega\alpha^2}{2}+\alpha^2\right]H^{2-(\alpha/(1+b))}\right]\right.$$
$$= 3\xi H - \frac{\varepsilon}{2}\frac{\tau}{8\pi}\phi_0 H^{-(\alpha/(1+b))}\left[(2+\alpha)\dot{H}+\left[3(1+\gamma)+(2+3\gamma)\alpha+(1-\right.\right.$$
$$\left.\left.\times\frac{\omega\alpha^2}{2}+\alpha^2\right]H^2\right]\quad\left(3H+\frac{\dot{\tau}}{\tau}-\frac{\dot{\xi}}{\xi}-\frac{\dot{T}}{T}\right.$$

Further, if we assume

$$\xi = \alpha'\rho^m, \quad \tau = \frac{\xi}{\rho} = \alpha'\rho^{m-1}, \quad T = \beta\rho^r$$

where $\alpha'(\geqslant 0)$, $m(\geqslant 0)$, $\beta(\geqslant 0)$ and $r(\geqslant 0)$ are constants, then we have

$$\frac{\dot{\tau}}{\tau}-\frac{\dot{\xi}}{\xi}-\frac{\dot{T}}{T} = -\left[2-\frac{\alpha}{1+b}\right](1+r)\frac{\dot{H}}{H}.$$

Using (25) in (23) leads to

$$\frac{\phi_0}{8\pi}\left[\tau(2+\alpha)\ddot{H}H^{1-(\alpha/(1+b))} + 2\left[3(1+\gamma)+(2+3\gamma)\alpha+(1-\gamma)\frac{\omega\alpha^2}{2}+\alpha\right.\right.$$
$$\times \tau\dot{H}H^{2-(\alpha/(1+b))} + (2+\alpha)\dot{H}H^{1-(\alpha/(1+b))}$$
$$\left.+\left[3(1+\gamma)+(2+3\gamma)\alpha+(1-\gamma)\frac{\omega\alpha^2}{2}+\alpha^2\right]H^{3-(\alpha/(1+b))}\right.$$
$$+\frac{\varepsilon}{2}\tau H^{-(\alpha/(1+b))}\left[(2+\alpha)\dot{H}+\left[3(1+\gamma)+(2+3\gamma)\alpha+(1-\gamma)\right.\right.$$
$$\left.\left.\left.\times\frac{\omega\alpha^2}{2}+\alpha^2\right]H^2\right]\left(3H^2-\left[2-\frac{\alpha}{1+b}\right](1+r)\dot{H}\right)\right]-3\xi H$$

Now using (24) together with (12) and (15) in (26) we have

$$\frac{\phi_0}{8\pi}\Bigg[\Bigg[2(2+\alpha)(1+b)^2B-2B(1+b)\Bigg[3(1+\gamma)+(2+3\gamma)\alpha+(1-\gamma)\frac{\omega\alpha^2}{2}+\alpha^2\Bigg]$$
$$-\frac{3\varepsilon}{2}(2+\alpha)(1+b)B-3A\Bigg]H^{(2(1+b)+m(2(1+b)-\alpha))/(1+b)}$$
$$+\Bigg[\Bigg[3(1+\gamma)+(2+3\gamma)\alpha+(1-\gamma)\frac{\omega\alpha^2}{2}+\alpha^2\Bigg]-(1+b)(2+\alpha)\Bigg]$$
$$\times H^{3-(\alpha/1+b)}+B\Bigg[\frac{\varepsilon}{2}\left(2-\frac{\alpha}{1+b}\right)(1+r)(2+\alpha)(1+b)^2$$
$$-\frac{3\varepsilon}{2}\Bigg[3(1+\gamma)+(2+3\gamma)\alpha+(1-\gamma)\frac{\omega\alpha^2}{2}+\alpha^2\Bigg]$$
$$-\frac{\varepsilon}{2}\left(2-\frac{\alpha}{1+b}\right)(1+r)(2+\alpha)(1+b)\Bigg[3(1+\gamma)+(2+3\gamma)\alpha+(1-\gamma)$$
$$\times\frac{\omega\alpha^2}{2}+\alpha^2\Bigg]\Bigg]\Bigg]H^{(2(1+b)+m(2(1+b)-\alpha)/(1+b)}\Bigg]=0 \tag{27}$$

where $A=\alpha'\left[\dfrac{3+3\alpha-(\omega\alpha^2/2)}{8\pi}\right]^m\phi_0^m$ and $B=\alpha'\left[\dfrac{3+3\alpha-(\omega\alpha^2/2)}{8\pi}\right]^{m-1}\phi_0^{m-1}$.

From (27) it can be seen that m can only take the value

$$m=\frac{1+b-\alpha}{2(1+b)-\alpha} \tag{28}$$

Now (28) can be rewritten as

$$1+b=\frac{(m-1)\alpha}{(2m-1)}. \tag{29}$$

For models of the expanding universe with ϕ increasing we require $\alpha>0$ and $1+\beta>0$; this constrains m not to lie in the range $\frac{1}{2}\leqslant m\leqslant 1$.

For singular models, since $R(0)=0$, (19) leads to

$$R=R_0t^{1/(1+b)}. \tag{30}$$

From (30) and (11) we have

$$\phi=\phi_0t^{\alpha/(1+b)}. \tag{31}$$

Using (30) and (31) in (12) yields

$$\rho=\frac{\phi_0}{8\pi}\left[3+3\alpha-\frac{\omega\alpha^2}{2}\right]t^{(\alpha/1+b)-2}. \tag{32}$$

From (32) it can be seen that ρ would increase or decrease with time according as

$$\Pi = -\frac{\phi_0}{8\pi}\left[3(1+\gamma)+(2+3\gamma)\alpha+(1-\gamma)\frac{}{2}+\alpha^2-(2+\alpha)(1+b)\right]t^{(\alpha-(1+b))/(1+b)}. \tag{33}$$

From (24) and (32) with $m=(1+b-\alpha)/(2(1+b)-\alpha)$ we get

$$\xi = At^{(\alpha-(1+b))/(1+b)} \tag{34}$$

$$\tau = Bt. \tag{35}$$

From (34) it can be seen that ξ would increase or decrease according as

$$\alpha > (1+b) \quad \text{or} \quad \alpha < (1+b).$$

From (35) it can be seen that the behaviour of the relaxation time τ is independent of the scalar-field ϕ (i.e., the power-index α) and it increases with time.

Case (ii): $b = -1$

In this case H is a constant (as can be seen from (15)) given by

$$H = \chi = \text{constant}. \tag{36}$$

From (11) and (19) we have

$$\phi = \phi_0 \exp(\alpha\chi t). \tag{37}$$

Using (36) and (37) in (12) leads to

$$\rho = \frac{\phi_0}{8\pi}\left[3+3\alpha-\frac{\omega\alpha^2}{2}\right]\chi^2\exp(\alpha\chi t). \tag{38}$$

Now using (36), (37) and (38) in (13) yields

$$\Pi = -\frac{\phi_0}{8\pi}\left[3(1+\gamma)+(2+3\gamma)\alpha+(1-\gamma)\frac{\omega\alpha^2}{2}+\alpha^2-(2+\alpha)(1+b)\right]\chi^2\exp(\alpha\chi t). \tag{39}$$

Equation (18) now reduces to

$$3\xi\chi+\frac{\varepsilon}{2}\tau\Pi\left(3H+\frac{\dot{\tau}}{\tau}-\frac{\dot{\xi}}{\xi}-\frac{\dot{T}}{T}\right)+\Pi=0. \tag{40}$$

Using (38) in (24) we have

$$\xi = A'\exp(\alpha m\chi t) \tag{41}$$

$$\tau = B'\exp(\alpha(m-1)\chi t) \tag{42}$$

where

$$A' = \alpha'\left[\frac{3+3\alpha-(\omega\alpha^2/2)}{8\pi}\right]^m \phi_0^m \chi^{2m}$$

$$B' = \alpha'\left[\frac{3+3\alpha-(\omega\alpha^2/2)}{8\pi}\right]^{m-1} \phi_0^{m-1} \chi^{2(m-1)}.$$

From (24) we have

$$\frac{\dot{\tau}}{\tau}-\frac{\dot{\xi}}{\xi}-\frac{\dot{T}}{T}=-(1+r)\frac{\dot{\rho}}{\rho}. \tag{43}$$

Using (38) in (43) leads to

$$\frac{\dot{\tau}}{\tau}-\frac{\dot{\xi}}{\xi}-\frac{\dot{T}}{T}=-(1+r)\alpha\chi. \tag{44}$$

Using (44) in (40) yields

$$3\xi\chi+\frac{\varepsilon}{2}\tau\Pi\chi(3-(1+r)\alpha)+\Pi=0. \tag{45}$$

From (39), (41), (42) and (45) we see that m can only take the value 1.

4. Conclusion

Constancy of the deceleration parameter permits only two possibilities i.e., either $H=$ constant with $m=1$ or $m=(1+b-\alpha)/(2(1+b)-\alpha)$, irrespective of the value of ε. Incidentally, most of the well known perfect fluid models in general relativity and BD theory are models with constant deceleration parameter. It is interesting to note that in the presence of bulk viscous pressure there could be exponential expansion in BD theory.

References

[1] H F M Goenner and F Kowalewski, *Gen. Relativ. Gravit.* **21**, 467 (1989)
[2] C Eckart, *Phys. Rev.* **58**, 919 (1940)
[3] W A Hiscock and L Lindblom, *Phys. Rev.* **D31**, 725 (1985); *Phys. Rev.* **D35**, 3723 (1987)
[4] W Israel, *Ann. Phys. (NY)* **100**, 310 (1976)
[5] W Israel and J M Stewart, *Phys. Lett.* **A58**, 213 (1976)
[6] D Pavon, D Jou and J Casa-Vazquez, *Ann. Inst. H Poincare* **A36**, 79 (1982)
[7] W A Hiscock and L Lindblom, *Ann. Phys. (NY)* **151**, 466 (1989)
[8] W A Hiscock and J Salmonson, *Phys. Rev.* **D43**, 3249 (1991)

— journal of
physics

December 1995
pp. 519–531

Fission fragment angular distribution in alpha-particle-induced fission of actinide elements

R K JAIN, S K BOSE and J RAMA RAO
Department of Physics, Banaras Hindu University, Varanasi 221 005, India

MS received 12 December 1994; revised 15 November 1995

Abstract. Using Lexan polycarbonate plastic as the fission fragment track detectors, the fragment angular distributions have been measured in the cases of fission of ^{232}Th and ^{238}U induced by alpha particles of various energies ranging from 40 to 70 MeV obtained from the 88″ variable energy cyclotron at Calcutta. The center-of-mass angular distributions have been calculated and fitted by a series of Legendre polynomials. The $W(10^{\circ})/W(90^{\circ})$ ratios (defined as anisotropy) were measured at several energies for both the targets. These data are utilized in calculation of the energy dependence of K_0^2, the standard deviation of the distribution in the angular momentum projection on the nuclear symmetry axis at the saddle point. Values of Γ_f/Γ_n, i.e. the ratio of the fission width to neutron emission width have been determined for ^{232}Th and ^{238}U nuclei. The integral cross-section for alpha induced fission in each target was determined by numerical integration of the respective center-of-mass angular differential cross-sections. The results were compared with similar data available in the literature which served to resolve some of the discrepancies observed in earlier measurements. The results were also compared with theoretical cross-sections.

Keywords. Angular distribution; angular momentum; fission cross-section; alpha particle; fission width; neutron emission width; nuclear track detectors.

PACS No. 25·85

1. Introduction

The present investigations on fission fragment angular distributions are undertaken to study the saddle point configuration and the competition between fission and neutron evaporation. Several measurements on the fission cross-section and fragment angular distribution in the fission of a number of nuclei induced by a variety of projectiles have been reported, a few of them using SSNTDs (Solid State Nuclear Track Detectors) [1–7]. The interpretation of the observed angular distributions and the important inferences drawn from them, are all primarily based on the model proposed by Bohr [8]. The underlying idea of the model is that the stretched fission nucleus, in passing over the saddle point, exhibits quantum states similar to those observed in the permanently deformed nuclei, except that the states of the saddle point nucleus are expected to be quasi-stationary since the nucleus only stays a while at the saddle point. Then the angular distribution of the fragments depends on the available quantum states characterized by I, M and K, where I is the total angular momentum of the nucleus, M is the projection of I on a space fixed axis (taken as the incident beam direction) and K is the projection of I on the symmetry axis of

M is usually zero for particle induced fission [9].

Another interesting information, the angular distribution study can yield, is about the dissipation of the large angular momentum brought in by the incident particle into the fissioning system. The simple classical model of Coffin and Halpern [3], is useful for letting one see qualitatively what sort of insight can be obtained. In three dimensions one would observe the number of fragments per unit solid angle to be $dN/\sin\theta\, d\theta$, which would consequently be proportional to $(\sin\theta)^{-1}$. The angular distribution peaks very sharply in the forward and backward directions (figure 3). Thus if a major fraction of the 'input' angular momentum were to feed into the orbital momentum between the fragments, then one would observe a very large anisotropy. However the experimental observations point out to a much less anisotropy. It is expected that there would be a general increase of the anisotropy in the angular distribution of the fission fragments with increasing bombarding energy and hence with the excitation energy for a particular fissioning species [10]. The simplest way to extract the relative orbital angular momentum of the fission fragments is to fit the angular distribution pattern in terms of a series of Legendre polynomials

$$\frac{W(\theta^\circ)}{W(90^\circ)} = 1 + \sum_{l=2,\text{even}} A_l P_l(\cos\theta) - A_l P_l(0).$$

A weighted least squares fitting is usually done taking into account the experimental uncertainties. The l-value corresponding to the highest angular momentum component with a non-zero coefficient gives an idea of the number of units of angular momentum carried by the fission fragment.

From the angular distribution measurements, the value of K_0^2 is evaluated for each compound nucleus as a function of excitation energy in excess of the fission barrier. The general features of the variation of anisotropy with projectile bombarding energy can be worked out by the theory advanced by Bohr [8] and amplified by Strutinsky [11], Halpern and Strutinsky [12], Griffin [13] and others. According to this theory, the angular distribution $W(\theta)$ of fission fragments emitted per unit solid angle for a single fissioning species is described by the relation

$$W(\theta) \sim \int dI \int dK\, f(K, I) \left[\sin^2\theta - \frac{K^2}{I^2}\right]^{-1/2} \tag{1}$$

where θ is the direction of the fission fragment with respect to the beam direction, I is the angular momentum of the compound state and K is the component of angular momentum along the symmetry axis.

With the assumptions (1) that $f(K, I)$ is a product of functions $f_K(K)$ and $f_I(I)$, (2) that $f_K(K) \sim \exp(-K^2/2K_0^2)$ and (3) that $f_I(I) \sim I$ up to some limiting value I_{max}, the integration of (1) results in an expression dependent upon K_0 and I_{max}. Both $W(\theta)$ and the ratio $W(\theta^\circ)/W(90^\circ)$ can be characterized by a parameter $p = (I_{max}/2K_0)^2$ [1] in

$$\frac{W(\theta)}{W(90^\circ)} = \frac{\int_0 \qquad \operatorname{erf}(\sqrt{2x})}{\int_0^p dx \frac{x^{1/2}\exp(-x)J_0(ix)}{\operatorname{erf}(\sqrt{2x})}} \tag{2}$$

where J_0 is the zero-order Bessel function. Calculations based on this expression are shown in figure 3. From statistical considerations, coupled with Fermi gas model, K_0^2 is given by

$$K_0^2 = J_{\text{eff}}\, T/\hbar^2 \tag{3}$$

where T is the nuclear temperature at the saddle point and J_{eff} is the effective moment of inertia, defined as

$$J_{\text{eff}} = \frac{J_\perp J_\parallel}{(J_\perp - J_\parallel)}$$

where $J_\perp$ is the moment of inertia perpendicular to symmetry axis and $J_\parallel$ is the moment of inertia parallel to the symmetry axis. Further, T on the basis of Fermi gas model, is given by

$$T = \left[\frac{E_x^s}{a_f}\right]^{1/2} \tag{4}$$

where E_x^s and a_f are the excitation energy and nuclear level density parameter, both corresponding to the saddle point configuration of the fissioning nucleus.

Thus K_0^2 turns out to be proportional to the square root of the excitation energy E_x^s at the saddle point. I_{max}^2 taken to be equal to $2\langle I^2\rangle_{\text{av}}$ exhibits a nearly linear dependence upon the bombarding energy of the projectile. Consequently, because the parameter $p = I_{\text{max}}^2/4K_0^2$ controls the angular anisotropy $W(\theta^\circ)/W(90^\circ)$, it is expected that there would be a general increase of the anisotropy in the angular distribution of the fission fragments with increasing bombarding energy, and hence with the excitation energy for a particular fissioning species.

2. Experimental details

2.1 *General*

The energetic alpha particles were obtained from the variable energy cyclotron (VEC) at Calcutta, India. The collimating system restricts the diameter of the beam at the target to < 2 mm. The beam current on the target was of the order of 50 nA. The total number of alpha particles striking the target was measured by a Faraday cup (FC) equipped with a secondary electron suppression device. The connections of FC were brought out and fed to an integrator. The details of experimental procedure and detector assembly can be found in our earlier paper [4].

2.2 *Target preparation*

The thorium target was prepared by electrodeposition having thickness $= 200\ \mu g/cm^2$ of the fissionable material (ThO_2) onto a $3\ mg/cm^2$ nickel backing foil. The uranium

target was prepared by vacuum evaporation of $^{238}UO_2$ onto a 2 mg/cm^2 Ni-backing foil. These targets were obtained from the VEC Target Lab., Calcutta.

2.3 *Experimental observation*

The fission fragment track densities were measured for thorium and uranium targets for angles between 10° and 80° in the laboratory system. Data collected for fissioning nucleus were converted to center-of-mass coordinates assuming (1) full momentum transfer of the incident charged particle to the compound nucleus, (2) equal kinetic energy for all fission fragments and (3) symmetric fragment mass distribution. These three conditions are more or less generally satisfied in charged particle induced fission of actinide elements at medium energies as those employed in the present investigation. The kinetic energy release in the center-of-mass system was estimated from the relation [14]

$$E_K = 0{\cdot}1189\frac{Z^2}{A^{1/3}} + 7{\cdot}3\,\text{MeV}$$

where E_K represents the average total kinetic energy of the fission fragments before neutron emission and Z and A are the atomic and mass numbers, respectively, of the compound nucleus.

3. Results and discussion

The analysis of the data essentially consists of the following parts:

(1) least square fitting of the center-of-mass angular distributions by a series of Legendre polynomials, to draw inferences about the relative orbital angular momentum of the fission fragments.
(2) a comparison of the asymmetry of the angular distribution for different targets as a function Z^2/A, to assess the competition between fission and neutron evaporation.
(3) determination of K_0^2 values from (5) and (6) as given below [1, 15, 4a]:

$$p = \frac{I_{\max}^2}{4K_0^2} \tag{5}$$

$$\frac{W(0°)}{W(90°)} = 1 + \frac{I_{\max}^2}{8K_0^2} = 1 + \frac{p}{2} \tag{6}$$

(4) measurement of the total fission cross-section by integrating the measured differential cross-sections and comparing the results with theory and previous data to resolve discrepancies and
(5) calculation of Γ_f/Γ_n from σ_f/σ_R where σ_R is the total reaction cross-section taken from the calculations of Igo and Huizenga [16, 17].

The difficulty in obtaining angular distributions to the desired accuracy is connection with a background of small tracks in the plastic track detector, which was observed in the forward hemisphere. Although the cause of such a background is not yet well understood, normally this is consistent with the expectation that in addition to fission

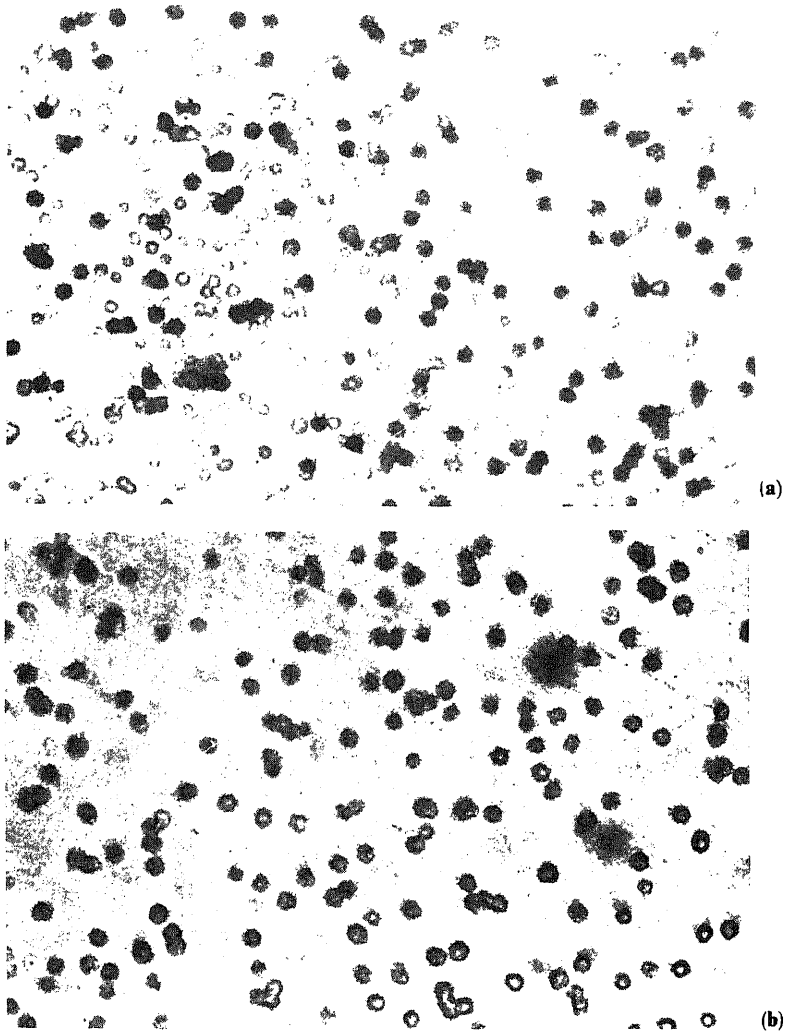

Figure 1. Photomicrographs of the fission fragment tracks in Lexan from 60 MeV He-ion induced fission of ^{232}Th **(a)** without covering the plastic with scotch tape, **(b)** after covering the plastic with scotch-tape.

fragments these would appear in the forward hemisphere due to some radioactive recoils from nuclear reactions [3]. However, these background tracks caused no difficulty in counting the fission tracks. In one particular instance where this background did become serious, the simple device of covering the plastic detector with scotch-tape dramatically reduced the background without appreciably affecting the fission tracks. Presumably the soft gum on the tape fills in the shallow "pits" on the surface. The fission tracks, being formed much deeper into the surface, were not very

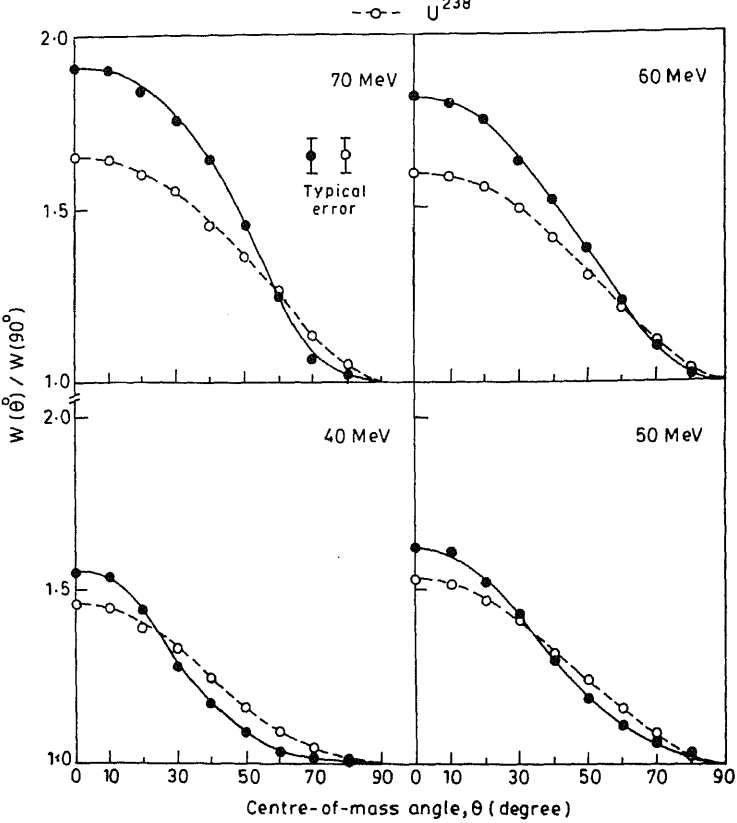

Figure 2. Angular distributions of fission fragments from the helium–ion-induced fission of ^{232}Th and ^{238}U at different incident energies of helium ion.

plastic detector with scotch-tape and (b) corresponds to after covering the plastic detector with scotch tape.

The measured track densities in the laboratory frame $W_L(\theta)$ are converted into laboratory differential cross-section $(d\sigma/d\Omega)_L$ using the formula

$$\left(\frac{d\sigma}{d\Omega}\right)_L = \frac{W_L(\theta)}{\Omega_L \phi N} \tag{7}$$

where Ω_L is the laboratory solid angle subtended by the unit area of the detector over which the track density $W_L(\theta)$ is measured, ϕ is the incident alpha particle flux and N is the number of target nuclei per unit area. The laboratory differential cross-sections are then converted into center-of-mass differential cross-sections $d\sigma/d\Omega$, using the relevant transformation equations described in our earlier paper [4]. The relative differential fission cross-section $(d\sigma(\theta^\circ)/d\Omega)/(d\sigma(90^\circ)/d\Omega)$ or angular anisotropies $W(\theta^\circ)/W(90^\circ)$ as

Table 1. Anisotropy, Z^2/A and coefficients of Legendre polynomial terms resulting from least square fit of center-of-mass angular distributions from ^{232}Th and ^{238}U.

Target	Energy (Lab) MeV	$\frac{W(10°)}{W(90°)}$	Z^2/A	A_0	A_2	A_4	A_6
^{232}Th	40	1·54 ± 0·06	35·86	1·1076 ± 0·0240	0·3023 ± 0·0136	0·136 ± 0·0155	0·0240 ± 0·0203
	50	1·61 ± 0·06	35·86	1·2369 ± 0·0260	0·3900 ± 0·0145	− 0·0942 ± 0·0162	0·0211 ± 0·0213
	60	1·80 ± 0·07	35·86	1·2928 ± 0·0320	0·5643 ± 0·0164	− 0·0315 ± 0·0183	− 0·0036 ± 0·0237
	70	1·91 ± 0·07	35·86	1·3320 ± 0·0360	0·6786 ± 0·0170	− 0·0369 ± 0·0187	− 0·0674 ± 0·0242
^{238}U	40	1·45 ± 0·05	36·51	1·1388 ± 0·0312	0·3006 ± 0·0135	0·0268 ± 0·0154	− 0·0045 ± 0·0201
	50	1·52 ± 0·05	36·51	1·1939 ± 0·0300	0·3391 ± 0·0135	− 0·0281 ± 0·0158	0·044 ± 0·0201
	60	1·59 ± 0·06	36·51	1·2400 ± 0·0300	0·4168 ± 0·0144	− 0·0660 ± 0·0163	0·018 ± 0·0213
	70	1·64 ± 0·06	36·51	1·2700 ± 0·0600	0·4496 ± 0·0146	− 0·0967 ± 0·0165	0·0324 ± 0·0215

a function of angle θ were deduced for thorium and uranium targets and shown in figure 2 for different energies.

The solid and dashed lines in figure 2 for ^{232}Th and ^{238}U respectively are the best fit to the experimental data obtained using Legendre polynomials with terms up to $P_6(\cos\theta)$ with coefficients as tabulated in table 1. Coefficients higher than A_6 were found to be statistically not significant and hence not included in the table.

The dashed line in figure 3 indicates $(\sin\theta)^{-1}$ variation of the anisotropy as expected from a classical model in which all the angular momentum brought in by the incident particle is delivered to the fission fragments and appears as their relative orbital angular momentum. Mathematically in terms of Legendre polynomials the variation of the anisotropy is expressed as [3]

$$\frac{W(\theta^\circ)}{W(90^\circ)} = \frac{1}{\sin\theta} = 1 + 1{\cdot}25\,P_2 + 1{\cdot}27\,P_4 + 1{\cdot}27\,P_6 \tag{8}$$

Comparing these coefficients with the experimentally observed coefficients listed in table 1, one can see that higher angular momentum components in the experimentally observed distributions drop off rapidly as compared to those in $(\sin\theta)^{-1}$. This is an indication that the observed relative orbital angular momentum of the fission fragments is much smaller than the actual angular momentum brought in by the incident particle.

In an approximate way, one may expect the average orbital angular momentum of the fission fragments to be given by the 1 value of the highest angular momentum term (with statistically significant coefficient) in the Legendre polynomial expansion. On this

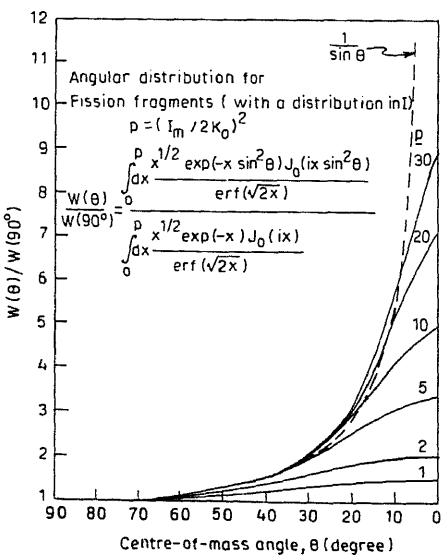

Figure 3. Calculated angular distributions for fission fragments obtained by summing over a classical sharp cut-off distribution of I (from 0 to I_{max}) (Vaz and Alexander [1]).

basis and looking at table 1, one can conclude that in the presently studied alpha induced fission of ^{232}Th and ^{238}U, the orbital momentum of the fission fragments generally does not exceed $3\hbar$ while the average incident angular momentum is about $20\hbar$. The difference between the two values is dissipated into the formation of high spin states of the fission fragments as well as into collective rotational degrees of freedom such as rolling friction in some cases.

The experimental anisotropy may be conveniently defined as $W(10°)/W(90°)$ and is listed in table 1 as a function of the parameter Z^2/A for the two fissioning nuclei at different energies. It can be seen from table 1 that the anisotropy $W(10°)/W(90°)$ increases with increase of incident particle energy; on the other hand $W(10°)/W(90°)$ decreases with increasing value of Z^2/A of the target nucleus. This trend is generally observed experimentally, but the correlation between anisotropy and Z^2/A cannot be described from the theoretical stand point as fundamental to the fission process. On the other hand, it is mostly likely to arise from fortuitous effects connected with neutron evaporation before fission.

To check the systematics of the present experiment, we deduced the value of K_0^2 which is the standard deviation of the angular momentum projection on the nuclear symmetry axis in the saddle point configuration, which sensitively controls the fission fragment angular distribution. For this purpose we used (5) and (6). The value of K_0^2 from (5) matches well with the value of K_0^2 derived from (6). For calculation the value of K_0^2 and parameter p has been taken from the figure 3 corresponding to the experimental anisotropy, which has been measured in the present experimental work. The value of p has been interpolated from figure 3 corresponding to our experimental anisotropy $W(10°)/W(90°)$. For example, in case of alpha induced fission of ^{232}Th at 40 MeV, we have taken the value of $p \simeq 1{\cdot}11$ (from figure 3) corresponding to the value of experimental anisotropy $\simeq 1{\cdot}54$. Values of I_{max} are estimated from the fusion cross-section code FRANPIE Vaz [18] which utilises empirical fusion barriers from Vaz *et al* [19] and (for high energies) the critical radius approach of Galin *et al* [20]. Values of I_{max}, p and K_0^2 are shown in table 2 corresponding to incident particle

Table 2. Values of I_{max} angular momentum, p-parameter corresponding to anisotropy ($W(10°)/W(90°)$) and K_0^2 obtained by the eqs (5) and (6) for the various energies of alpha particles.

Target	Energy (MeV)	Value of I_{max} ($\hbar$)	Value of p-parameter taken from figure 3 (corresponds to anisotropy)	Value of K_0^2 $\frac{W(0°)}{W(90°)} = 1 + \frac{I_{max}^2}{8K_0^2}$(eq (6))	$p = \frac{I_{max}^2}{4K_0^2}$(eq. (5))
^{232}Th	40	19	1·11	82	81
	50	23	1·26	107	105
	60	26	1·65	103	102
	70	28	1·80	106	109
^{238}U	40	19	0·92	98	98
	50	23	1·00	125	132
	60	26	1·20	141	141
	70	28	1·30	151	151

energies. From table 2, it can be noted that the value of K_0^2 increases with increa particle energy and the value of K_0^2 in the fission of $(\alpha + {}^{238}\mathrm{U})$ system is greater that of $(\alpha + {}^{232}\mathrm{Th})$ system.

The integral cross-section for fission at a given energy of the projectile σ_f ca determined by integration, over the solid angle, as follows [5],

$$\sigma_f = \frac{2\pi W(90^\circ)}{\phi N \Omega} \int_0^\pi \frac{W(\theta)}{W(90^\circ)} \sin\theta \, d\theta$$

where ϕ is the flux of bombarding particles, N is the number of target nuclei per $W(90^\circ)$ is the number of tracks detected at 90° in the center-of-mass coordin system, Ω is the solid angle subtended by the detector, $W(\theta)/W(90^\circ)$ is the cente mass angular distribution for the particular energy of the charged particle involved the integration is made over 2π steradians.

The experimentally measured cross-sections are listed in table 3 for ${}^{232}\mathrm{Th}$ and targets. The errors associated with the (α, f) cross-sections are estimated to be n 5% for thorium as well as uranium target. The measurements of some of these fis cross-sections have been made by different methods by different authors. The resu those measurements are shown in figure 4 for comparison with the present data. I be seen that there are wide discrepancies in the fission cross-section measure different authors with different detectors. In case of $(\alpha + {}^{232}\mathrm{Th})$ system, Junger Hicks *et al* [21, 22] and Ford and Leachman [23] measured the fission cross-sectio to only 42 MeV. Ralarosy *et al* [24] measured the fission cross-sections at diff energies. If we interpolate the data of Ralarosy *et al* [24] then our present results to confirm the experimental results of Ralarosy *et al* [24] for ${}^{238}\mathrm{U}(\alpha, f)$ as well a ${}^{232}\mathrm{Th}(\alpha, f)$. However, in the case of ${}^{238}\mathrm{U}(\alpha, f)$, the measured fission cross-section found to be less than that measured by Kapoor *et al* [2]. But at 40 MeV, our r matches well with the results of Kapoor *et al* [2], Jungerman [21], Colby *et al* Viola and Sikkeland [26] and Wing *et al* [27]. In both cases, ${}^{232}\mathrm{Th}$ and ${}^{238}\mathrm{U}$ measured fission cross-sections are found to be very close to the total optical m reaction cross-section due to Blatt and Weisskopf [28]. This shows the predomin of the fission process in actinide elements even at high bombarding energies.

The fission cross-sections presented in figure 4 and listed in table 3 can be us deduce quantitative information on the ratio of the partial widths for fission neutron emission. The steep excitation functions (see figure 4) suggest that the n ured fission cross-sections are mostly due to first chance fission. Therefore the fi with Γ_f is very nearly equal to the fission cross-section σ_f. Charged particle emi can be ignored at these moderate energies and therefore the neutron emission wid can be approximated with the total reaction cross-section σ_R. Thus

$$\Gamma_f/\Gamma_n \approx \sigma_f/\sigma_R.$$

The experimental values of Γ_f/Γ_n as a function of incident particle energy for ${}^{232}\mathrm{Th}$ ${}^{238}\mathrm{U}$ are listed in table 3. The total reaction cross sections were calculated as discu earlier. From table 3 one can notice that all the values of Γ_f/Γ_n are nearly equal to

Table 3. Experimental fission and calculated reaction cross-sections for alpha particle induced fission of ^{232}Th and ^{238}U.

Target	Energy (MeV)	Fission cross-section σ_f (cm^2)	Calculated reaction cross-section σ_R (cm^2)	$\Gamma_f/\Gamma_n \approx \sigma_f/\sigma_R$	Blatt and Weisskopf [28] σ_R(cm^2)
^{232}Th	40	$(1{\cdot}15 \pm 0{\cdot}06) \times 10^{-24}$	$1{\cdot}50 \times 10^{-24}$	0·76	$1{\cdot}2 \times 10^{-24}$
	50	$(1{\cdot}25 \pm 0{\cdot}06) \times 10^{-24}$	$2{\cdot}00 \times 10^{-24}$	0·62	$1{\cdot}6 \times 10^{-24}$
	60	$(1{\cdot}52 \pm 0{\cdot}07) \times 10^{-24}$	$2{\cdot}20 \times 10^{-24}$	0·69	$1{\cdot}8 \times 10^{-24}$
	70	$(1{\cdot}65 \pm 0{\cdot}08) \times 10^{-24}$	$2{\cdot}35 \times 10^{-24}$	0·70	$2{\cdot}0 \times 10^{-24}$
^{238}U	40	$(1{\cdot}46 \pm 0{\cdot}07) \times 10^{-24}$	$1{\cdot}70 \times 10^{-24}$	0·86	$1{\cdot}5 \times 10^{-24}$
	50	$(1{\cdot}65 \pm 0{\cdot}08) \times 10^{-24}$	$2{\cdot}15 \times 10^{-24}$	0·76	$1{\cdot}8 \times 10^{-24}$
	60	$(1{\cdot}98 \pm 0{\cdot}10) \times 10^{-24}$	$2{\cdot}33 \times 10^{-24}$	0·85	$2{\cdot}0 \times 10^{-24}$
	70	$(2{\cdot}10 \pm 0{\cdot}10) \times 10^{-24}$	$2{\cdot}62 \times 10^{-24}$	0·80	$2{\cdot}3 \times 10^{-24}$

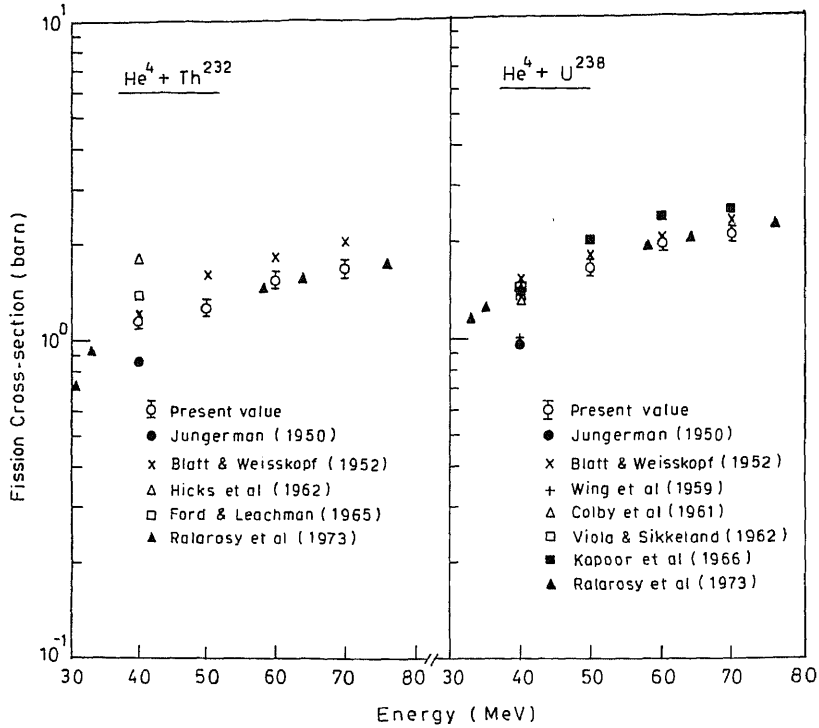
$He^4 + Th^{232}$
$He^4 + U^{238}$
Fission Cross-section (barn)
Energy (MeV)
Present value
Jungerman (1950)
Blatt & Weisskopf (1952)
Hicks et al (1962)
Ford & Leachman (1965)
Ralarosy et al (1973)
Present value
Jungerman (1950)
Blatt & Weisskopf (1952)
Wing et al (1959)
Colby et al (1961)
Viola & Sikkeland (1962)
Kapoor et al (1966)
Ralarosy et al (1973)

Figure 4. Measured fission cross-section at different alpha bombarding energies for the case of alpha induced fission of ^{232}Th and ^{238}U and other author's values for the same energies.

Acknowledgements

The authors are indebted and thankful to Dr V J Menon for many helpful discussions. The authors are also thankful to Secretary, VEC Users Committee for the excellent research facilities made available for us at Variable Energy Cyclotron Centre. One of the authors (RKJ) is thankful to CSIR for providing him with a Research Associateship.

References

[1] L C Vaz and J M Alexander, *Phys. Rep.* **97**, 1 (1983)
[2] S S Kapoor, H Baba and S G Thompson, *Phys. Rev.* **149**, 965 (1966)
[3] C T Coffin and I Halpern, *Phys. Rev.* **112**, 536 (1958)
[4] R K Jain, J Rama Rao and S K Bose, *Pramana – J. Phys.* **39**, 85 (1992)
[4a] R K Jain, Ch V Sastry, J Rama Rao and S K Bose, *DAE Symp. on Nucl. Phys.* **B35**, 290 (1992)
[5] R K Jain, J Rama Rao and S K Bose, *Indian J. Phys.* **A67**, 149 (1993)
[6] R Vandenbosch, H Warharek and J R Huizengs, *Phys. Rev.* **124**, 846 (1961)
[7] R H Iyer, A K Pandey, P C Kalsi and R C Sharma, *Phys. Rev.* **C44**, 2644 (1991)
[8] A Bohr, *Proc. Int. Conf. Peaceful uses of atomic energy*, Geneva Paper P/911, (1955)
[9] R Vandenbosch and J R Huizenga, *Nuclear Fission* (New York, Academic, 1973)
[10] S S Kapoor and V S Ramamurthy, *Pramana – J. Phys.* **33**, 161 (1989)

[11] V M Strutinski, *Eksptl. i Teoret. Fiz.* **30**, 606 (1957); *Atomnaya Energi* **2**, 508; *Sov. J. Atomic Energy* **2**, 621 (1957)
[12] I Halpern and V M Strutinsky, *Proc. Int. Conf. Peaceful uses of Atomic Energy*, Geneva (1958) **15**, p. 408
[13] J J Griffin, *Phys. Rev.* **116**, 107 (1959)
[14] V E Viola, K Kwiatkowski and M Walker, *Phys. Rev.* **C31**, 1550 (1985)
[15] R H Iyer, A K Pandey, P C Kalsi and R C Sharma, *DAE Symp. on Nucl. Phys.* **B33**, 111 (1990)
[16] G Igo, *Phys. Rev.* **115**, 1665 (1959)
[17] J R Huizenga and G Igo, *Nucl. Phys.* **29**, 462 (1962)
[18] L C Vaz, *Computer Phys. Commun.* **22**, 451 (1981)
[19] L C Vaz, J M Alexander and G R Satchler, *Phys. Rep.* **69**, 373 (1981)
[20] J Galin, D Guerreau, M Lefort and X Tarrago, *Phys. Rev.* **C9**, 1018 (1974)
[21] J Jungerman, *Phys. Rev.* **79**, 632 (1950)
[22] H G Hicks, H B Levy, W E Nervik, P C Stevenson, J B Niday and J C Amstrong, *Phys. Rev.* **128**, 700 (1962)
[23] G P Ford and R B Leachman, *Phys. Rev.* **B137**, 826 (1965)
[24] J Ralarosy, M Debeauvais, G Remy, J Tripier, R Stein and D Huss, *Phys. Rev.* **C8**, 2372 (1973)
[25] L J Colby, M Lasalle Shoaf and J N Cobble, *Phys. Rev.* **121**, 1415 (1961)
[26] V E Viola and T Sikkeland, *Phys. Rev.* **128**, 767 (1962)
[27] J Wing, W J Ramler, A L Harkness, J R Huizenga, *Phys. Rev.* **114**, 163 (1959)
[28] J M Blatt and V F Weisskopf, *Theoretical nuclear physics* (New York, Wiley, 1952)

Relativistic correction to the dipole polarizability of a hydrogenic ion

K L BALUJA
Department of Physics and Astrophysics, University of Delhi, Delhi 110 007, India

MS received 5 July 1995

Abstract. The first relativistic correction of order α^2 to the dipole polarizability of a hydrogenic ion has been investigated by using mean excitation energy of the ion within the second-order perturbation theory. The density-dependent mean excitation energy is estimated via Bethe theory for the stopping cross section for a moving point charge interacting with the hydrogenic ion. In this approach only the unperturbed Dirac wavefunctions are required to evaluate the appropriate matrix elements. The first relativistic correction turns out to be $-(13/12)(\alpha Z)^2$. This has the correct sign and is within 5% of the exact result which is $-(28/27)(\alpha Z)^2$.

Keywords. Dipole polarizability; mean excitation energy; completeness relation; stopping cross section; unperturbed Dirac wave function.

PACS Nos 31·30; 35·10

1. Introduction

The electric dipole polarizability α_d of an atom represents the simplest linear response of the electronic charge cloud to an electric field. It determines the most important term in the asymptotic behaviour of electron–atom interaction in the low energy collisions [1]. In electrostatics, it is closely related to dielectric constant [2] and it is also a measure of the Stark shift of energy levels. In optics, it is useful in the analysis of refraction and scattering of light, and of the electrical birefringence [3]. It is of interest to know the relativistic correction due to Dirac nature of the electron cloud. This can improve the accuracy of the coefficient in the intermolecular potentials [4, 5].

The dipole polarizability is given by [6]

$$\alpha_d = 2\left(\psi_1^{(1)}, \sum_{i=1}^{N} r_i P_1(\cos\theta_i)\psi_0\right) \tag{1}$$

where ψ_0 is the unperturbed ground state wave function, $\psi_1^{(1)}$ is the first-order perturbed wave function, N is the number of electrons in the system. For one-electron systems, $\psi_1^{(1)}$ can be calculated exactly by the method of Dalgarno and Lewis [7] in which the perturbed wave function satisfies an inhomogeneous differential equation. For H atom, the non-relativistic value of $\alpha_d = 4{\cdot}5$. When the perturbation theory is applied for the relativistic calculation of α_d, the calculation is quite complicated even for H atom. For atoms other than H, or for a Coulomb potential perturbed by other central potentials, the calculation becomes severely complicated.

There are several calculations of relativistic corrections to α_d for H atom. A general theory [8] of electromagnetic polarizabilities of composite system described by

infinite-component wave equation has been developed and applied to the relativistic H atom which is described completely by an O(4, 2) infinite-component wave equation. The method of Dalgarno and Lewis [7] has been used [9] to obtain the relativistic α_d for an H atom. Several calculations using the method of Coulomb's Green function [10, 11] have been performed for the relativistic calculation of α_d for H atom. In one calculation [12], only the Darwin Hamiltonian was taken into account which produced wrong results. Kaneko [13] showed that the explicit solution of the perturbed Dirac equation is not necessary to calculate the exact values of the corrections.

2. Theory

By expressing $\psi_1^{(1)}$ over a complete set of unperturbed eigenstates, we get

$$\alpha_d = 2 \sum_{n \neq 0} \frac{|(\psi_n \Sigma_{i=1}^{N} r_i P_1(\cos\theta_i)\psi_0)|^2}{E_n - E_0}. \tag{2}$$

The summation is over all intermediate states including the continuum. Equation (2) requires a complete knowledge of the spectrum of the atomic system. A useful approach is to replace $E_n - E_0$ by a mean excitation energy Δ, and making use of the completeness relation

$$\sum_{n=0} |\psi_n\rangle\langle\psi_n| = 1, \tag{3}$$

we now get

$$\alpha_d = \frac{2}{\Delta}\left[\left(\psi_0, \sum_{i=1}^{N} r_i^2 P_1^2(\cos\theta_i)\psi_0\right) - \left(\psi_0, \sum_{i=1}^{N} r_i P_1(\cos\theta_i)\psi_0\right)^2\right]. \tag{4}$$

If Δ is taken to be equal to the ionization potential then α_d comes out to be correct within an order of magnitude [6].

In the present work, we show that Δ can be connected to the electron density $\rho(r)$. The stopping cross section S for a high-speed point charge penetrating through a homogeneous electron gas is given by [14, 15]

$$S = K \frac{\ln E}{E} \ln \Delta \tag{5}$$

where K is a constant, E is the energy of the penetrating charge and

$$\ln \Delta = \int d^3 r \rho(r) \ln \omega_p(r) \tag{6}$$

with $\omega_p(r)$ being the plasma frequency of the medium which is given by

$$\omega_p(r) = (4\pi\rho(r)z)^{1/2} \tag{7}$$

where $z = Z - N + 1$, is the residual charge of the electron gas which has nuclear charge Z and N electrons.

We now apply (4) with the definition of Δ given by (6) to calculate α_d for a hydrogenic ion in the ground state.

We can now write

$$\alpha_d = \frac{2}{3\Delta}\langle r^2 \rangle. \tag{8}$$

The relativistic charge density of a hydrogenic ion is [16]

$$\rho(r) = \frac{(2Z)^3(1+\gamma_1)e^{-2Zr}(2Zr)^{(2\gamma_1-2)}}{4\pi(1+\varepsilon_1)\Gamma(2\gamma_1+1)} \tag{9}$$

where

$$\gamma_1 = (1-\alpha^2 Z^2)^{1/2}$$

and

$$\varepsilon_1 = \left[1+\left(\frac{\alpha Z}{\gamma_1}\right)^2\right]^{-1/2}. \tag{10}$$

α is the fine-structure constant.

With $\rho(r)$ given by (9), we obtained all the relevant integrals analytically [17] and got the following expressions for $\langle r^2 \rangle$ and $\ln \Delta$

$$\langle r^2 \rangle = \frac{(1+\gamma_1)\Gamma(2\gamma_1+3)}{4Z^2(1+\varepsilon_1)\Gamma(2\gamma_1+1)} \tag{11}$$

$$2\ln\Delta = \ln(4\pi Z) + \frac{(1+\gamma_1)}{(1+\varepsilon_1)}\left[\ln\frac{(2Z)^3(1+\gamma_1)}{4\pi(1+\varepsilon_1)\Gamma(2\gamma_1+1)} - (2\gamma_1+1) + (2\gamma_1-2)\psi(2\gamma_1+1)\right] \tag{12}$$

where

$$\psi(2\gamma_1+1) = -C + \sum_{n=0}^{\infty}\left(\frac{1}{n+1} - \frac{1}{2\gamma_1+1+n}\right) \tag{13}$$

with $C = 0{\cdot}577215\cdots$ as the Euler's constant.

Now we expand γ_1, ε_1 and their functions up to terms of order $(\alpha Z)^2$, after some algebra, we obtain

$$\langle r^2 \rangle = \frac{3}{Z^2}\left[1 - \frac{7}{12}(\alpha Z)^2\right] \tag{14}$$

and

$$\Delta = 2Z^2 \exp\left(-\frac{3}{2} + \frac{1}{2}\alpha^2 Z^2\right). \tag{15}$$

We finally obtain α_d correct to order $(\alpha Z)^2$.

$$\alpha_d = \frac{e^{3/2}}{Z^4}\left[1 - \frac{13}{12}(\alpha Z)^2\right]. \tag{16}$$

3. Results

The first term in (16) yields the non-relativistic value with the correct Z dependence. Our non-relativistic value of H atom is 4·4817 against the exact value of 4·50. The

second term gives the first-order relativistic correction. Our coefficient 13/12 is within five per cent of the exact value 28/27 given by Kaneko [13], who did a perturbation calculation by use of the Dirac equation. The negative sign indicates relativistic contraction of the mean radius of the electron orbit. Feiock and Johnson [12] obtained a positive sign for their first-order relativistic correction because they employed incorrect first-order perturbed wave function.

Though our calculations presented here are much simpler than other calculations present in the literature, yet they yield quite accurate results. The same formalism, which requires only the unperturbed density, can be applied to Coulomb potentials perturbed by more complex potentials.

References

[1] L O'Malley, L Spruch and L Rosenberg, *J. Math. Phys.* **2**, 491 (1961)
[2] C J F Bottcher, *Theory of electric polarization* (Elsevier, Amsterdam, 1952)
[3] D E Logan and P A Madden, *Mol. Phys.* **46**, 715 (1982)
[4] H B G Casimir and D Polder, *Phys. Rev.* **73**, 360 (1948)
[5] J O Hirschfelder and W J Meath, *Adv. Chem. Phys.* **12**, 3 (1967)
[6] A Dalgarno, *Adv. Phys.* **11**, 281 (1962)
[7] A Dalgarno and J T Lewis, *Proc. R. Soc. (London)* **A233**, 70 (1955)
[8] A O Barut and J Nagel, *Phys. Rev.* **D13**, 2075 (1976)
[9] M L Bartlett and E A Power, *J. Phys.* **A2**, 419 (1969)
[10] N L Marakov, L P Rappoport and S A Zapryagaev, *J. Phys.* **B7**, 1076 (1974)
[11] Le Anh Thu, Le Van Hoang, L I Komarov and T S Romanova, *J. Phys.* **B27**, 4083 (1994)
[12] F D Feiock and W R Johnson, *Phys. Rev.* **187**, 39 (1969)
[13] S Kaneko, *J. Phys.* **B10**, 3347 (1977)
[14] J Lindhard, *Mat. Fys. Medd. Dan Vid. Selsk* **28**, 1 (1954)
[15] J Lindhard and A Winther, *Mat. Fys. Medd. Dan Vid. Selsk* **34**, 1 (1964)
[16] H A Bethe and E E Salpeter, *Quantum mechanics of one- and two-electron atoms* (Berlin: Springer-Verlag, 1957)
[17] I S Gradshteyn and I M Ryzhik, *Tables of integrals, series and products* (Academic Press: New York, London, 1980)

— journal of
physics

December 1995
pp. 537–543

Systematic trends in the line strengths and radial matrix elements of E1 transitions in the Be isoelectronic sequence

ANAND BHARADVAJA and K L BALUJA
Department of Physics and Astrophysics, University of Delhi, Delhi 110007, India

MS received 26 June 1995; revised 22 September 1995

Abstract. Line strength S and radial matrix element σ for the dipole allowed transitions within $n=2$ complex of ions in the Be isoelectronic sequence have been fitted in the forms $Z^2S = A + B/(Z-C)$ and $Z\sigma = A' + B'/(Z-C')$. The constants A, B, C and A', B', C' have been calculated by employing a non-linear least square method. The relevant data for S and σ have been taken from calculations which includes correlation effects. It is shown that the fitted values of A and A' are in excellent accord with their hydrogenic values ($Z \to \alpha$) provided that we express the zeroth-order wavefunction of the ground state $1s^2 2s^2\,{}^1S$ as a quantum-mechanical admixture of the Hartree-Fock (HF) state $1s^2 2s^2\,{}^1S$ and the near-degenerate state $1s^2 2p^2\,{}^1S$.

Keywords. Radial matrix elements; line strength; oscillator strength; Hartree–Fock; near-degeneracy; hydrogenic limit.

PACS No. 32·70

1. Introduction

The optical oscillator strength between the two bound states of an atomic system is an important atomic quantity. This is related to the transition probability, refractive index, the dipole polarizability and the diamagnetic susceptibility. The optical oscillator strength can be used to test the accuracy of the generalized oscillator strength [1]. Its knowledge is useful in fields like astrophysics [2] to compute the opacity of the stellar envelopes [3]. It also finds application in fusion research [4].

Experimentally, the oscillator strength can be extracted from the measurements of transition probabilities by beam-foil [5] and beam-laser [6, 7] techniques. Various theoretical methods [8–11] which take into account the correlation effects can be employed for its calculations. The amount of correlation depends upon the size and nature of the basis function included in the calculation. If the values of oscillator strengths for few ions in an isoelectronic sequence of an atomic system are known, then an interpolation curve based on perturbation theory may be used to extract the information about other ions in the sequence. The perturbation theory is based upon $1/Z$ expansion of oscillator strength, where Z is the nuclear charge of an ion. This method is valid only when there are no plunging configurations involved for an ion in an isoelectronic sequence. An interpolation curve based on the expansion of Z^2S is more suitable as it does not involve the transition energy. In the limit of $Z \to \infty$, the value of Z^2S approaches a finite hydrogenic value which can be trivially calculated. However, this limit is appropriate only when the near-degenerate effects [12], if

correlation effect. This effect is present in the ground state configuration of Be, B, C, N and O isoelectronic sequences within the $n=2$ complex. The Z^2S expansion has been studied for carbon [13] and oxygen [14] isoelectronic sequences which included the effects of near-degeneracy. The effect of 2s–2p near-degeneracy was studied for these sequences and it was then shown that the correct value of Z^2S was obtained in the limit of infinite nuclear charge. In the present work, we have extended the Z^2S expansion for Be isoelectronic sequence. We have shown that the correct value of Z^2S is obtained in the limit $Z \to \infty$ if we augment the HF ground state $1s^2 2s^2\,{}^1S$ with its near-degenerate state $1s^2 2p^2\,{}^1S$. We have also expanded the dipole radial matrix elements based upon the perturbation expansion method for the dipole allowed transitions in the Be sequence.

2. Theory

The length form of line strength S between an initial bound state ϕ and a final bound state ϕ' is given by [15]

$$S = |\langle \phi(LS\pi)| \sum_{i=1}^{N} \mathbf{r}_i | \phi'(L'S'\pi') \rangle|^2 \tag{1}$$

where summation is taken over all the electrons of an atom, $\mathbf{r}_i$ is the dipole operator for the ith electron, $LS\pi(L'S'\pi')$ refer to the total angular momentum, spin angular momentum and parity of the initial (final) states. Because of the odd parity of the dipole operator, only states of opposite parity are connected by the dipole operator.

According to the perturbation theory the expansion for S is

$$Z^2S = \sum_{i=0}^{\infty} S_i/Z^i. \tag{2}$$

In terms of the radial matrix elements, the perturbation expansion becomes

$$Z\sigma = \sum_{i=0}^{\infty} R_i/Z^i \tag{3}$$

where

$$S = \Lambda\sigma^2 \tag{4}$$

with Λ being an angular factor and σ is the dipole radial matrix element between an initial and the final bound states. The infinite series expansion of (2) and (3) can be written in a more compact fashion as

$$Z^2S = A + \frac{B}{(Z-C)} \tag{5}$$

$$Z\sigma = A' + \frac{B'}{(Z-C')}. \tag{6}$$

It is trivial to note that $S_0 = A, S_1 = B, S_j = B(C^{j-1})$ with $j \geq 2$. In other words, we have replaced the summation in (2) with a two-term expansion. The constant C may loosely be interpreted as a screening constant and B accounts for the residual correlation left over and above the HF correlation and the internal correlation. The same interpretation can

be given to the constants B' and C'. Equation (5) was originally suggested by Edlen [16]. The constants A, B, C or A', B', C' were obtained by fitting the assumed forms given by (5) or (6) to the known values of Z^2S or $Z\sigma$ by employing a non-linear least square method. The details of this procedure have already been given in [14]. In this reference there is a slight misprint in (8). There should be a minus sign in the denominator in front of the square brackets. Here we have studied the transitions $1s^2 2s^2\,{}^1S^e \rightarrow 1s^2 2s2p\,{}^1P^0$, $1s^2 2s2p\,{}^3P^0 \rightarrow 1s^2 2p^2\,{}^3P$ and $1s^2 2p^2\,{}^1S \rightarrow 1s^2 2s2p\,{}^1P^0$ in the Be isoelectronic sequence for ions in the range $Z = 6$ to 10, for which data for atomic opacity calculations was available [17]. These calculations involve correlation effects within and outside the $n = 2$ complex. We have also used the data of Cheng *et al* [18] for the resonant transition $1s^2 2s^2\,{}^1S \rightarrow 1s^2 2s2p\,{}^1P^0$ for ions up to $Z = 26$ which includes only the internal correlations. These calculations were done in j–j coupling scheme by employing multi-configuration Dirac-Fock (MCDF) technique [18]. The MCDF wavefunctions are combinations of Slater determinants constructed from $1s_{1/2}, 2s_{1/2}, 2p_{1/2}, 2p_{3/2}$ orbitals to form eigenfunctions of total angular momentum J and parity π. We truncated the data at $Z = 26$ because for heavier ions relativistic effects begin to become appreciable.

The values of constants for the transitions studied here are presented in tables 1–3. We have also calculated the ab-initio values A_0 and A'_0, which correspond to the values of Z^2S and $Z\sigma$ respectively in the limit $Z \rightarrow \infty$. In this limit the nuclear term dominates over electron–electron repulsion term and the HF orbitals assume their hydrogenic character. For the $1s^2 2s^2\,{}^1S$ ground state, near degenerate effects are present due to the promotion of two '2s' electrons into the two '2p' electrons giving rise to the near-degenerate state $1s^2 2p^2\,{}^1S$ which strongly interacts with the HF state $1s^2 2s^2\,{}^1S$. In the limit $Z \rightarrow \infty$ we can write the ground state wavefunction as a quantum mechanical admixture of the HF state ϕ_1 and the near-degenerate state ϕ_2 i.e.

$$\phi(1s^2 2s^2\,{}^1S) = c_1\phi_1(1s^2 2s^2\,{}^1S) + c_2\phi_2(1s^2 2p^2\,{}^1S). \tag{7}$$

The expansion coefficients c_1, c_2 can be calculated trivially by diagonalizing the

Table 1a. The values of parameters of eq. (5). A_0 is the ab-initio value of Z^2S with $Z \rightarrow \infty$.

Transition	A_0	A	B	C	χ^2
$1s^2 2s^2\,{}^1S \rightarrow$ $1s^2 2s2p\,{}^1P^0$	38·495	38·714	145·418	2·353	1·0E–03

Table 1b. The values of parameters of eq. (6). A'_0 is the ab-initio value of $Z\sigma$ with $Z \rightarrow \infty$.

Transition	A'_0	A'	B'	C'	χ^2
$1s^2 2s^2\,{}^1S \rightarrow$ $1s^2 2s2p\,{}^1P^0$	−4·242	−4·271	−7·561	1·788	2·2E–05

Table 2a. The values of parameters of eq. (5). A_0 is the ab-initio value of Z^2S with $Z \to \infty$.

Transition	A_0	A	B	C	χ^2
$1s^2 2s^2\,{}^1S \to$ $1s^2 2s2p\,{}^1P^0$	38·495	39·250	134·461	3·296	5·4E−15
$1s^2 2p^2\,{}^1S \to$ $1s^2 2s2p\,{}^1P^0$	33·504	34·194	102·529	3·318	1·7E−15

Table 2b. The values of parameters of eq. (6). A'_0 is the ab-initio value of $Z\sigma$ with $Z \to \infty$.

Transition	A'_0	A'	B'	C'	χ^2
$1s^2 2s^2\,{}^1S \to$ $1s^2 2s2p\,{}^1P^0$	−4·242	−4·308	−6·929	2·765	1·0E−16
$1s^2 2p^2\,{}^1S \to$ $1s^2 2s2p\,{}^1P^0$	−4·242	−4·304	−6·127	2·836	4·7E−17

Table 3a. The values of parameters of eq. (5). A_0 is the ab-initio value of Z^2S with $Z \to \infty$.

Transition	A_0	A	B	C	χ^2
$1s^2 2s2p\,{}^3P \to$ $1s^2 2p^2\,{}^3P$	162·0	156·657	691·283	2·407	6·7E−15

Table 3b. The values of parameters of eq. (6). A'_0 is the ab-initio value of $Z\sigma$ with $Z \to \infty$.

Transition	A'_0	A'	B'	C'	χ^2
$1s^2 2s2p\,{}^3P^0 \to$ $1s^2 2p^2\,{}^3P$	−5·196	−5·143	−10·597	1·733	2·53E−16

Hamiltonian in this two-basis set. We solve the secular equation

$$\sum_{i=1}^{2} c_i(H_{ji} - E\delta_{ji}) = 0, \quad j = 1,2 \tag{8}$$

where H_{ij} is a typical Hamiltonian matrix element; and

$$\frac{c_1}{c_2} = \frac{-2H_{12}}{(H_{11} - H_{22}) \pm \{(H_{11} - H_{22})^2 + 4H_{12}H_{21}\}^{1/2}} \tag{9}$$

with the normalization condition

$$c_1^2 + c_2^2 = 1. \tag{10}$$

Using Slater's approach [17], we can write down

$$H_{11} - H_{22} = 2I(2s, 2s) + 4F^0(1s, 2s) - 2G^0(1s, 2s) + F^0(2s, 2s) - 2I(2p, 2p) - 4F^0(1s, 2p) - F^0(2p, 2p) - 0{\cdot}4F^2(2p, 2p) + 0{\cdot}66666667G^1(1s, 2p)$$

$$H_{12} = H_{21} = (3)^{-1/2} G^1(2s, 2p).$$

The $I(\mathrm{nl}, \mathrm{nl})$, $F^k(\mathrm{nl}, \mathrm{n'l'})$ and $G^k(\mathrm{nl}, \mathrm{n'l'})$ are the one- and two-electron Slater integrals [13]. Using the hydrogenic values of these integrals we get

$$\phi(1s^2 2s^2\,{}^1S) = -0{\cdot}974321\phi_1(1s^2 2s^2\,{}^1S) + 0{\cdot}225165\phi_2(1s^2 2p^2\,{}^1S) \tag{11}$$

and

$$\phi(1s^2 2p^2\,{}^1S) = 0{\cdot}974321\phi_1(1s^2 2p^2\,{}^1S) + 0{\cdot}225165\phi_2(1s^2 2s^2\,{}^1S). \tag{12}$$

It is now possible to write the line-strength S as

$$S_0(LS \rightarrow L'S') = c_1^2 S_1 + c_2^2 S_2 + 2c_1 c_2 \sqrt{S_1 S_2} \tag{13}$$

where

$$S_1 = |\langle \phi_1(1s^2 2s^2\,{}^1S)|\mathbf{r}|\phi_3(1s^2 2s2p\,{}^1P^0)\rangle|^2 \tag{14}$$

$$S_2 = |\langle \phi_2(1s^2 2p^2\,{}^1S)|\mathbf{r}|\phi_3(1s^2 2s2p\,{}^1P^0)\rangle|^2. \tag{15}$$

The angular factor Λ for each transition is calculated using the standard Racah algebra [19]. The angular factors for various transitions are

$$\Lambda(1s^2 2s^2\,{}^1S \rightarrow 1s^2 2s2p\,{}^1P^0) = 2$$

$$\Lambda(1s^2 2p^2\,{}^1S \rightarrow 1s^2 2s2p\,{}^1P^0) = 2/3$$

$$\Lambda(1s^2 2s2p\,{}^3P^0 \rightarrow 1s^2 2p^2\,{}^3P) = 6.$$

For the mixed state

$$\Lambda(c_1\{1s^2 2s^2\,{}^1S\} + c_2\{1s^2 2p^2\,{}^1S\} \rightarrow 1s^2 2s2p\,{}^1P^0) = 2{\cdot}138636414$$

$$\Lambda(c_1\{1s^2 2p^2\,{}^1S\} + c_2\{1s^2 2s^2\,{}^1S\} \rightarrow 1s^2 2s2p\,{}^1P^0) = 1{\cdot}861363589.$$

The radial matrix elements are given by

$$Z\sigma(2s \rightarrow 2p) = \int_0^\infty P_{2S}(r) P_{2P}(r) r\,\mathrm{d}r = -\sqrt{27}. \tag{16}$$

The zeroth order multiplet strengths for various transitions in the hydrogenic limit are

$$Z^2 S_1(1s^2 2s^2\,{}^1S \rightarrow 1s^2 2s2p\,{}^1P^0) = 54$$

$$Z^2 S_2(1s^2 2p^2\,{}^1S \rightarrow 1s^2 2s2p\,{}^1P^0) = 18$$

$$Z^2 S_0(1s^2 2s2p\,{}^3P^0 \rightarrow 1s^2 2p^2\,{}^3P) = 162{\cdot}0.$$

We finally get

$$Z^2 S_0(1s^2 2s^2\,{}^1S \rightarrow 1s^2 2s2p\,{}^1P^0) = 38{\cdot}485$$

$$Z^2 S_0(1s^2 2p^2\,{}^1S \rightarrow 1s^2 2s2p\,{}^1P^0) = 33{\cdot}504.$$

3. Results and discussion

We obtained excellent fits for Z^2S and $Z\sigma$ data of Cheng *et al* [18] from their assumed forms given by (5) and (6) for the values of Z up to 26. From tables 1a and 1b, we notice that for the transition $1s^2 2s^2\,{}^1S \rightarrow 1s^2 2s2p\,{}^1P^0$ the fitted value $A(=38{\cdot}7146)$ is in excellent accord with the corresponding ab-initio value $A_0(=38{\cdot}495)$. However, if the near-degeneracy effect is omitted, then the HF value $(=54{\cdot}0)$ for this transition becomes higher than the ab-initio value by about 40%. The value of A' which refers to the value of $Z\sigma$ in the limit of $Z \rightarrow \infty$ for this transition is $-4{\cdot}271$ which is again in excellent accord with the ab-initio value $-4{\cdot}242$. Its corresponding HF value is $-5{\cdot}196$ which is higher than the ab-initio value by about 22%.

In table 2a, we have displayed the values of fitted and ab-initio constants for the resonant transition and the transition $1s^2 2p^2\,{}^1S \rightarrow 1s^2 2s2p\,{}^1P^0$ where we have used the opacity data [17] which is given only up to $Z = 10$. For the resonant transition our fitted value is once again in good agreement with the ab-initio value. For the transition $1s^2 2p^2\,{}^1S \rightarrow 1s^2 2s2p\,{}^1P^0$, our fitted value of 34·194 differs from the ab-initio value of 33·504 by about 2%. These values (ab-initio and fitted) are almost twice the HF value which is 18. From table 2b, we notice that the agreement between A'_0 and A' with their respective ab-initio values persist for both the transitions. These ab-initio values differ from their corresponding HF values of $-5{\cdot}196$ by 22%.

We have also carried out calculations for the transition $1s^2 2s2p\,{}^3P^0 \rightarrow 1s^2 2p^2\,{}^3P$ using the opacity data [17]. In this transition there is no near-degeneracy effect present and so it is expected that the fitted value of A and A' would be in good agreement with the single-configuration value. From table 3a we notice that the fitted value of A is 156·657 which is in good agreement with the HF value of 162·0. Similarly, in table 3b the value of A' is $-5{\cdot}143$ which differs from its ab-initio value of $-5{\cdot}196$ by about 1%.

We conclude from our present study that both the fitted forms of Z^2S and $Z\sigma$ give a good description of trends in S and σ along an isoelectronic sequence if the near-degenerate effects are included in the interpretation of A or A' values.

Acknowledgement

One of the authors (AB) is grateful to the Council of Scientific and Industrial Research, New Delhi, India for its financial support.

References

[1] M Inokuti, *Rev. Mod. Phys.* **43**, 297 (1971)
[2] D E Osterbrock, *Astrophysics of gaseous nebulae* (San Francisco, Freeman, 1974)
[3] M J Seaton, *J. Phys.* **B20**, 6363 (1987)
[4] E Hinnov and S Suckewer, *Phys. Lett.* **A79**, 298 (1980)
[5] G Astner, L J Curtis, L Liljeby, S Mannervik and I Martinson, *Z. Phys.* **A279**, 1 (1976)
[6] S Kandela and H Schmoranzer, *Phys. Lett.* **A86**, 101 (1981)
[7] A Gauppe, P Kuske and H J Andra, *Phys. Rev.* **A26**, 3351 (1982)
[8] A Hibbert, *Rep. Prog. Phys.* **38**, 1217 (1975)
[9] C F Fischer, *Comput. Phys. Commun.* **14**, 145 (1978)
[10] C F Fischer, *J. Phys.* **B16**, 157 (1983)
[11] O Sinanoglu, *Beam-foil spectroscopy* edited by S Bashkin (Heidelberg, Springer, 1976)

[12] D Layzer, *Ann. Phys.* (*NY*) **8**, 271 (1959)
[13] K L Baluja and A Agrawal, *Z. Phys.* **D33**, 11 (1995)
[14] A Agrawal and K L Baluja, *Pramana – J. Phys.* **43**, 477 (1994)
[15] C F Fischer, *The Hartree-Fock method for atoms* (Wiley, New York, 1977)
[16] B Edlen, *Phys. Scr.* **17**, 565 (1978)
[17] M J Seaton, *J. Phys.* **B21**, 3033 (1988)
[18] K T Cheng, Y K Kim and J P Desclaux, *At. Data Nucl. Data Tables* **24**, 111 (1979)
[19] I I Sobelman, *Atomic spectra and radiative transitions* (Springer, Berlin 1979)

physics

December 1995
pp. 545–560

Propagation of a wavepacket on a model fractal lattice

P K CHATTARAJ* and S NATH†
Department of Chemistry, Indian Institute of Technology, Kharagpur 721 302, India
†Present address: Department of Physical Chemistry, Indian Association for the Cultivation of Science, Calcutta 700 032, India
*Author for correspondence

MS received 23 January 1995; revised 22 June 1995

Abstract. Dynamics of a wavepacket on a model fractal surface has been studied by solving the pertinent time dependent Schrödinger equation. Spatial and temporal behaviour of charge and current densities and a local chemical potential for two different fractal lattices have been considered. Important insight into the dynamics has been obtained through time dependence of various quantities like macroscopic kinetic energy, global current, Shanon entropy, density correlation and global chemical potential. This study would be helpful in simulating adsorption and catalysis.

Keywords. Fractal surface; spatio temporal variations.

PACS Nos 05·45; 47·53; 34·10; 82·65

1. Introduction

One of the commonly used methods of studying dynamical problems is to follow the time evolution of a wavepacket through numerical integration of the pertinent time dependent Schrödinger equation (TDSE). Different variants of this method successfully accounted for various time dependent processes like chemical reactions [1, 2], collision induced dissociation [3, 4], gas-surface scattering [5], photodissociation [6], photoabsorption and emission [7], Raman scattering [8], atom diffraction by surfaces [9], etc. An excellent review [10] on this subject has also been published. In recent years wavepacket dynamics has been extensively used [11–16] in understanding quantum domain behaviour of a classically chaotic system. Since any chaotic system is geometrically characterized [17] by its scale invariance property a detailed knowledge of the corresponding fractal [18] behaviour is important. This study is supposed to provide [19–22] a connection between structural and dynamical information. As has been pointed out [23] the relevance of fractal behaviour is likely to be manifested in heterogeneous reaction dynamics which has been explicitly demonstrated [24] in a study of catalytic properties of solid surfaces. Another way is to simulate a catalyst or any disordered surface in general as a fractal surface, e.g. the diffusion-limited aggregate [25–27], devil's staircase [28] or a Cantor set [28] like structure. In this article we have solved the pertinent TDSE to study the dynamics of a wavepacket on a model fractal lattice. While methodology is discussed in § 2, a brief outline of the numerical solution is given in § 3. In § 4 the results and discussion are presented. Finally, § 5 contains some concluding remarks.

2. Methodology

The time dependent Schrödinger equation for a single particle moving under some external potential can be written as (in a.u.)

$$\left[-\frac{1}{2}\nabla^2 + v(r,t)\right]\psi(r,t) = i\frac{\partial\psi(r,t)}{\partial t}. \tag{1}$$

Dynamics of a single particle, simulated by a wavepacket, on a model fractal lattice can be studied by solving (1). The external potential $v(r,t)$ arising from a fractal lattice of embedding Euclidean dimension two has been formulated as,

$$v(x,y) = -\sum_i \sum_j \frac{1}{[(x-a_i)^2 + (y-b_j)^2]^{1/2}} \tag{2}$$

where (a_i, b_j) denote the Cartesian coordinates of a point on the fractal lattice which acts as an attractive Coulomb source of unit charge. The points $\{(a_i, b_j)\}$ are obtained as follows. Start with a conventional Cantor set-like fractal lattice of dimension $\log 2/\log 3$. Take the interval (0, 1), divide it into three equal segments and delete the central one (1/3, 2/3). The process is continued until the third generation lattice with 16 lattice points is obtained. A two-dimensional extension to this lattice has been generated by replacing each point of this horizontal Cantor lattice by a similar vertical Cantor lattice with an overall fractal dimension [18] $2\log 2/\log 3$. Finally these points are normalized to have the lattice points. We term this lattice as lattice I. For comparison, another lattice of dimension $2\log 3/\log 5$ has been constructed in its second generation with 18 lattice points. This lattice is termed as lattice II. It may be noted that external potential given in (5) does not contain any time. For a real system explicit time dependence may come from the relative motion between the target and the projectile and/or the oscillation of the lattice. Thus, the dynamics in the present study has only implicit time dependence arising from the temporal evolution of the wavepacket.

3. Numerical solution

The numerical solution is launched with the following initial and boundary conditions

$$\psi(x,y,0) = \frac{1}{\sqrt{\pi}}\exp\left[-\frac{1}{2}(x^2+y^2)\right]$$

$$\psi(\pm\infty, y, t) = 0 \quad \forall y, t$$

$$\psi(x, \pm\infty, t) = 0 \quad \forall x, t. \tag{3}$$

The TDSE (1) is solved using an alternating direction implicit (ADI) finite difference algorithm [29] with the above initial and boundary conditions. Spatial and temporal mesh sizes adopted here are $\Delta x = \Delta y = 0{\cdot}097$ and $\Delta t = 0{\cdot}01$. Spatial grid has been chosen in such a way that it avoids singularity associated with the Coulomb potential in (2). Each ADI cycle comprises two steps, i) substitute all x derivatives by Cranck-Nicolson analogues and y derivatives by explicit scheme. Therefore the finite difference

analogue (FDA) of (1) at a mesh point (x_l, y_m) becomes

$$c_l \psi_{l-1,m}^{n+1} + a_l \psi_{l,m}^{n+1} + b_l \psi_{l+1,m}^{n+1} = d_l \tag{4}$$

where,

$$c_l = b_l = \frac{i}{4(\Delta x)^2},$$

$$a_l = -\left(\frac{i}{2(\Delta x)^2} + \frac{i v_{l,m}}{2} + \frac{1}{\Delta t}\right)$$

and

$$d_l = \psi_{l,m}^n \left(\frac{i v_{l,m}}{2} - \frac{1}{\Delta t}\right) - \frac{i}{4}\frac{\partial^2 \psi}{\partial x^2} - \frac{i}{2}\frac{\partial^2 \psi}{\partial y^2}.$$

Explicit FDA of derivatives in d_l of (4) are used; (ii) in the next step Cranck-Nicolson explicit sequence is reversed and the corresponding FDA of (1) becomes

$$c_m \psi_{l,m-1}^{n+2} + a_m \psi_{l,m}^{n+2} + b_m \psi_{l,m+1}^{n+2} = d_m \tag{5}$$

where

$$c_m = b_m = \frac{i}{4(\Delta y)^2},$$

$$a_m = -\left(\frac{i}{2(\Delta y)^2} + \frac{i v_{l,m}}{2} + \frac{1}{\Delta t}\right)$$

and

$$d_m = \psi_{l,m}^{n+1} \left(\frac{i v_{l,m}}{2} - \frac{1}{\Delta t}\right) - \frac{i}{4}\frac{\partial^2 \psi}{\partial y^2} - \frac{i}{2}\frac{\partial^2 \psi}{\partial x^2}.$$

In order to follow the dynamics we have also calculated the following quantities:

a) charge density given by

$$\rho(r, t) = |\psi(r, t)|^2,$$

b) current density given by

$$j(r, t) = \psi_{re} \nabla \psi_{im} - \psi_{im} \nabla \psi_{re'},$$

c) global current defined as

$$j = \int |j(r, t)| \rho(r, t) \mathrm{d}r,$$

d) Shanon entropy as

$$S = -k \int \rho(r, t) \ln \rho(r, t) \mathrm{d}r,$$

k being the Boltzmann constant,

e) density correlation as

$$C = 2\pi \int \rho(r, 0)\, \rho(r, t) \mathrm{d}r,$$

$$2\int \rho$$

g) local chemical potential defined as [30]

$$\mu(r,t) = \frac{\delta E(t)}{\delta \rho} = \frac{1}{8}\left[\left(\frac{\nabla\rho}{\rho}\right)^2 - \frac{2\nabla^2\rho}{\rho}\right] + \frac{1}{2}\left(\frac{j}{\rho}\right)^2 + v$$

and

h) chemical potential as,

$$\mu(t) = \int \mu(r,t)\,\rho(r,t)\mathrm{d}r.$$

4. Results and discussion

Figures 1a and 1b depict the spatial behaviour of external potentials associated with two different fractal lattices (I and II). Local extrema in these plots are different both in magnitude and in position.

Time evolution of charge density profile is presented in figures 2a to 2e. Initial density profile (figure 2a) gets decomposed and dispersed in course of time over lattice I (figures 2b and 2c, at $t = 0{\cdot}16$ and 1 respectively) and lattice II (figures 2d and 2e, at $t = 0{\cdot}16$ and 1 respectively). Although the initial decomposition patterns (figures 2b and 2d) are different in two lattices, the long time behaviour (figures 2c and 2e) is similar but

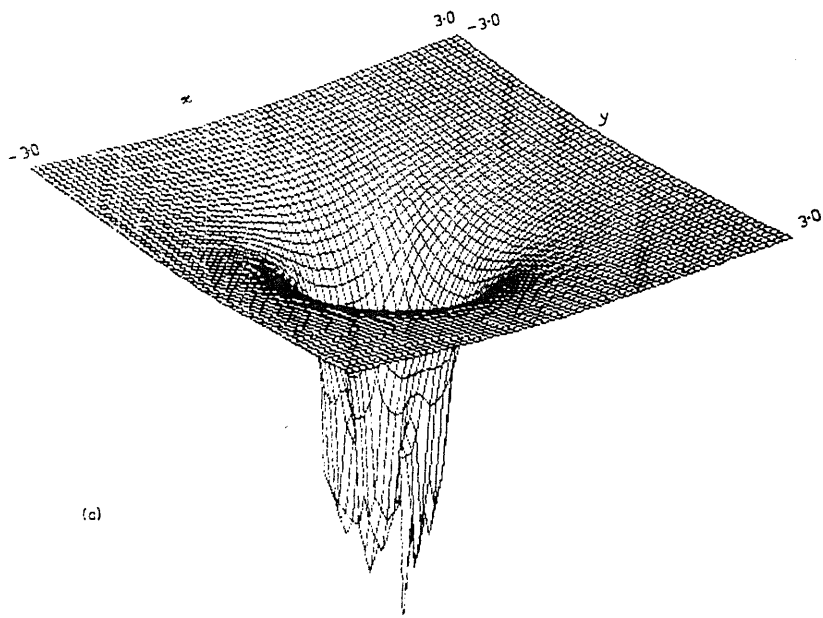

Figure 1a.

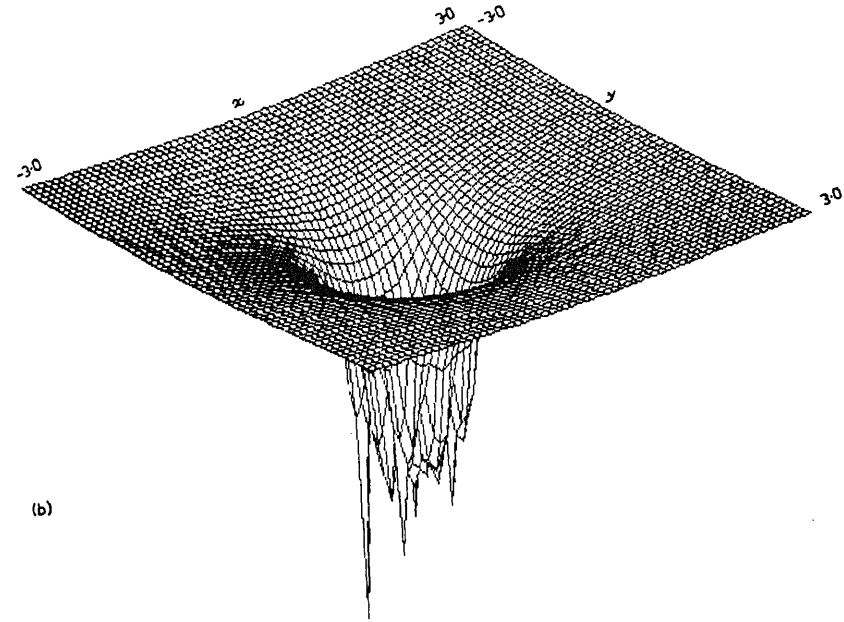

Figure 1. Spatial profile of external potential for propagation of a wavepacket on model fractal lattices. The basal square mesh designates $-3 \leqslant x \leqslant 3$ and $-3 \leqslant y \leqslant 3$ (**a**) Lattice I; (**b**) Lattice II.

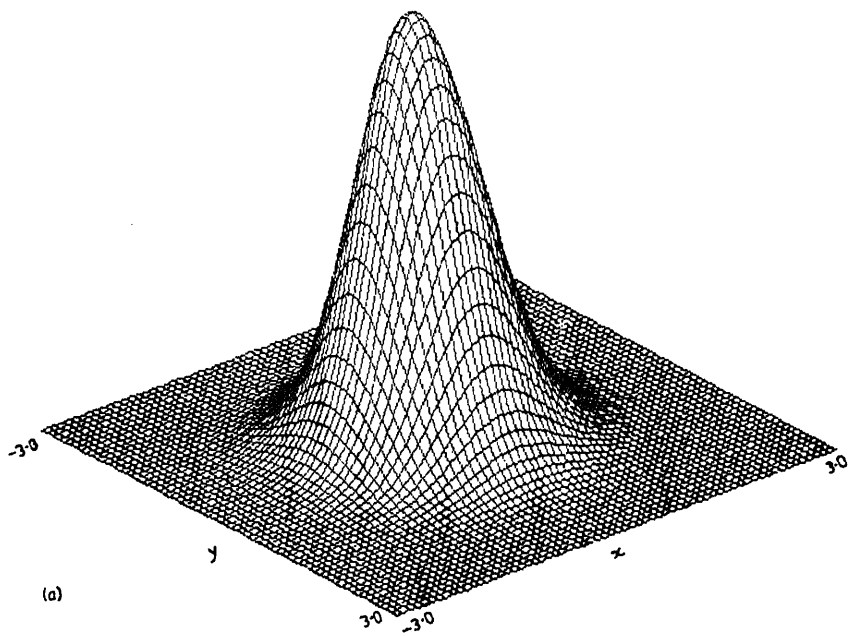

Figure 2a.

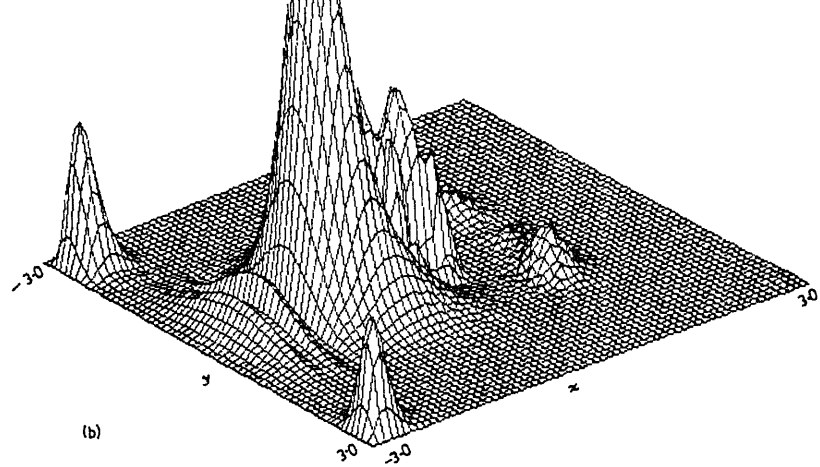

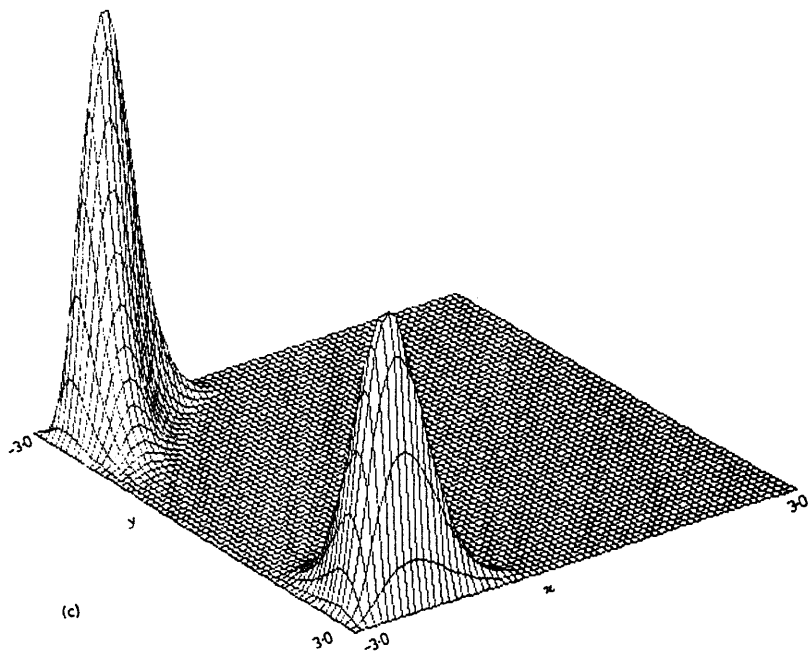

Figure 2b–c.

for different peak heights. While kinetic energy operator tries to move the wavepacket the attractive coulomb operator likes it to be localized in the fractal lattice points. Overall dynamics of the wavepacket is governed by an interplay of these kinetic and

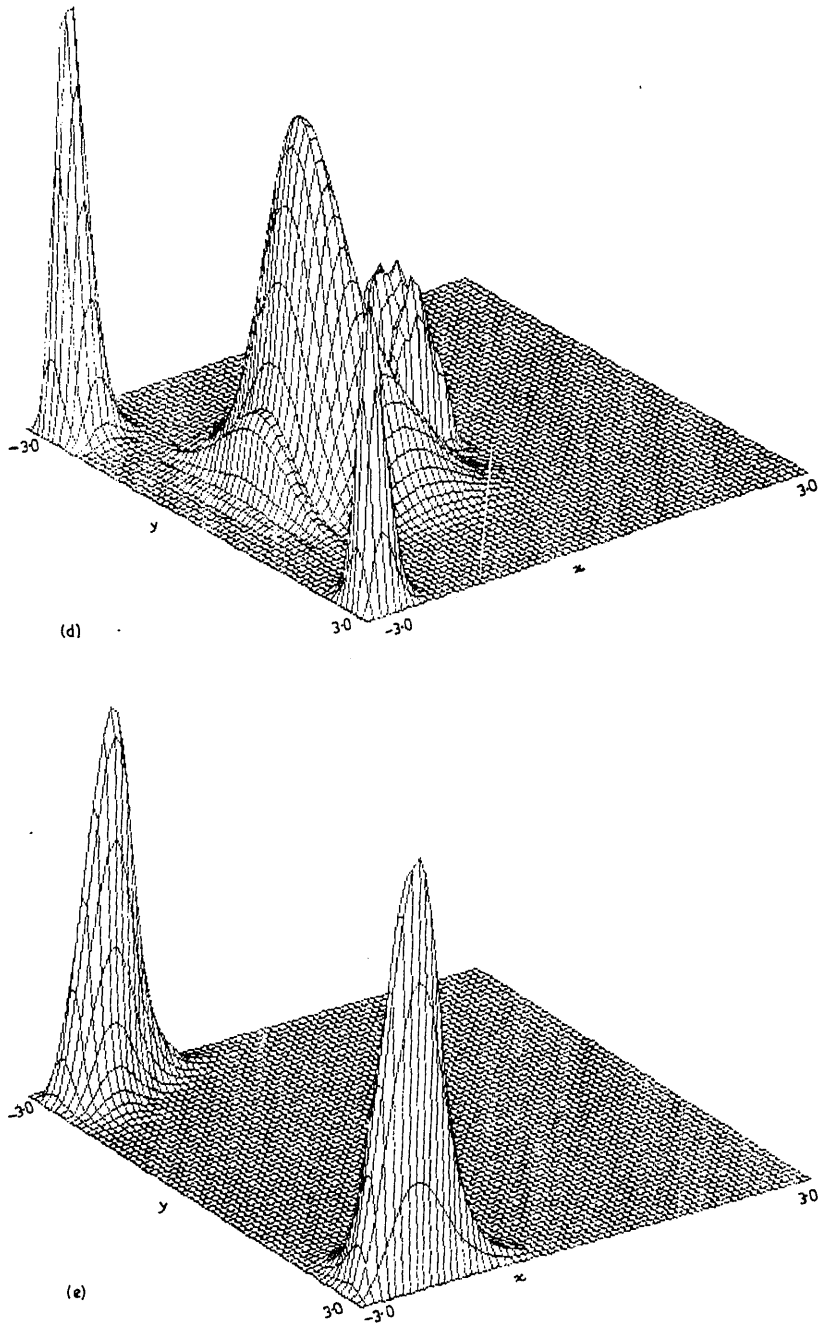

Figure 2. Spatial profile of density (**a**) $t = 0$; (**b**), (**c**) lattice I, $t = 0{\cdot}16$, 1 and (**d**), (**e**) lattice II, $t = 0{\cdot}16$, 1. See caption of figure 1 for details.

potential effects. Potential effect is dominant at the beginning and the wavepacket is mostly localized around coulomb attractors. As time progresses the kinetic effect takes over and the probability of getting the particle maximizes (albeit unequal) in two zones near the edges of the mesh and away from coulomb centres.

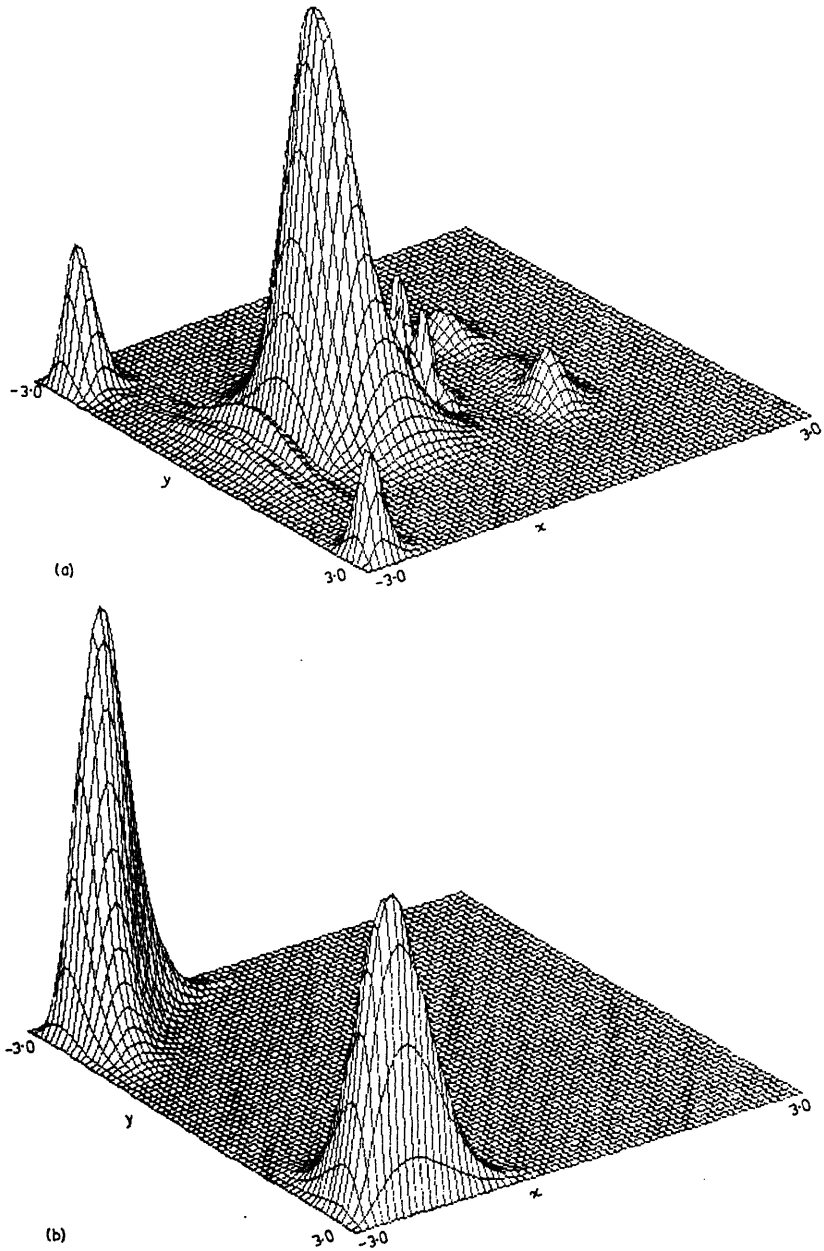

Figure 3a–b.

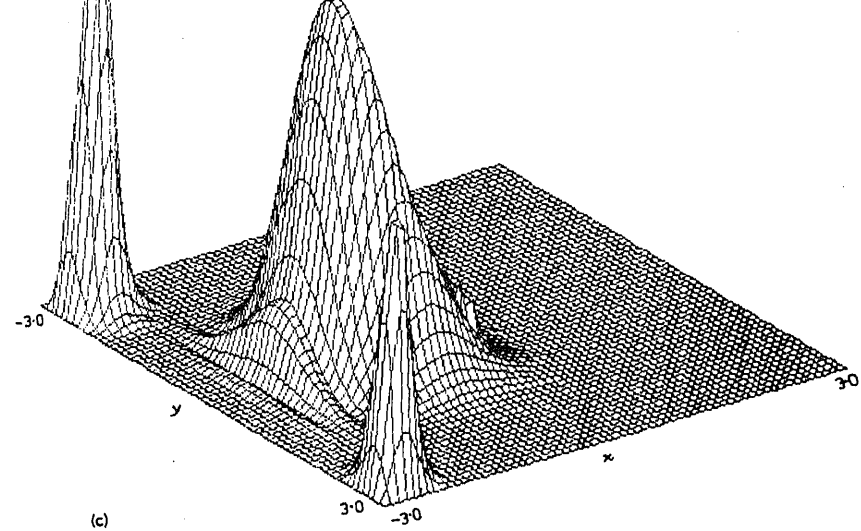

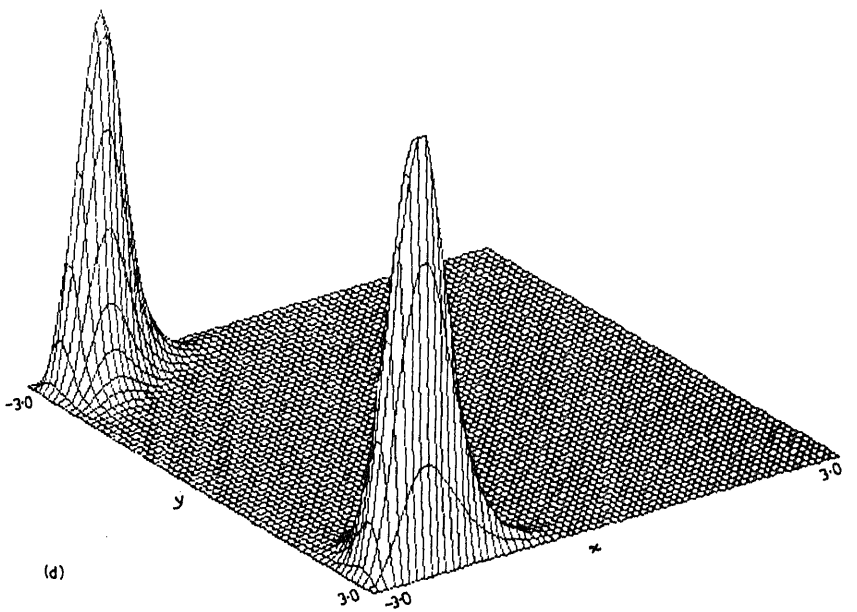

Figure 3. Spatial profile of current density (**a**), (**b**) lattice I, $t = 0{\cdot}16$, 1 and (**c**), (**d**) lattice II, $t = 0{\cdot}16$, 1. See caption of figure 1 for details.

difference is reduced as time progresses. Out of the two accessible zones the probability of getting the particle is more where the current density is higher.

The most intricate dynamical behaviour is revealed through the plots of local chemical potential (figures 4a to 4e). It starts from a cot-like structure at $t = 0$. Since in

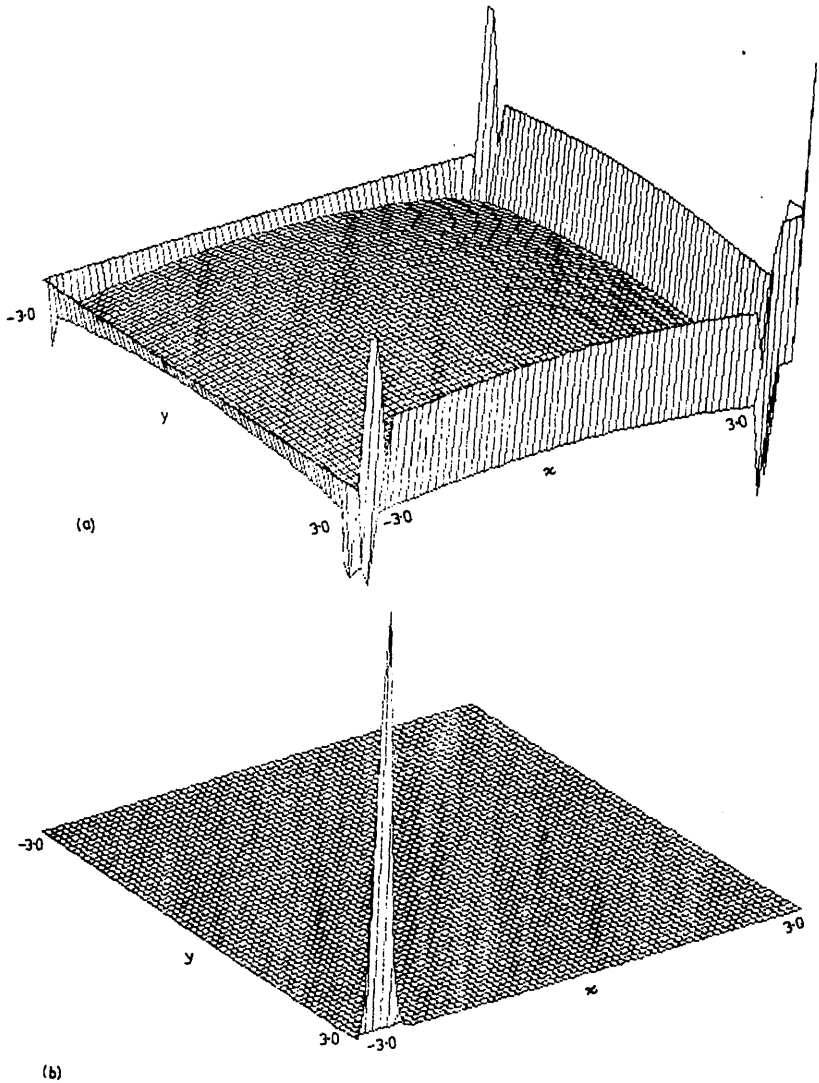

Figure 4a–b.

the present problem v does not vary with time local chemical potential is plotted relative to v in figure 3. Local chemical potential gets concentrated at a specific site and its base broadens in course of time. This site is around one of the two zones discussed above. High positive values of μ here reveal that energy of the system increases on charge accumulation and hence the lower current/probability zone does not like further charge transfer towards it.

Figures 5–9 depict respectively the time variations of global current, Shanon entropy, density correlation, macroscopic kinetic energy and chemical potential. In each figure two different curves refer to lattices I and II respectively. As expected, although the numerical values differ the overall behaviour of a given quantity remains same in two lattices in all figures. Global current increases to a maximum value around

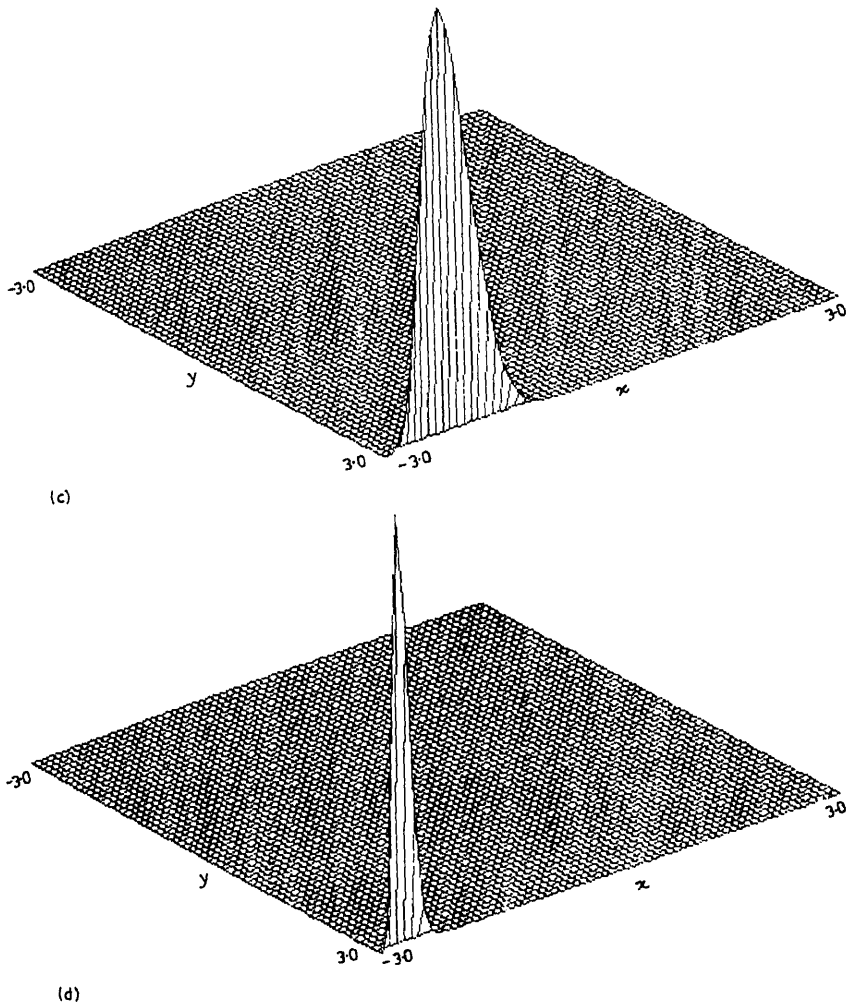

Figure 4c–d.

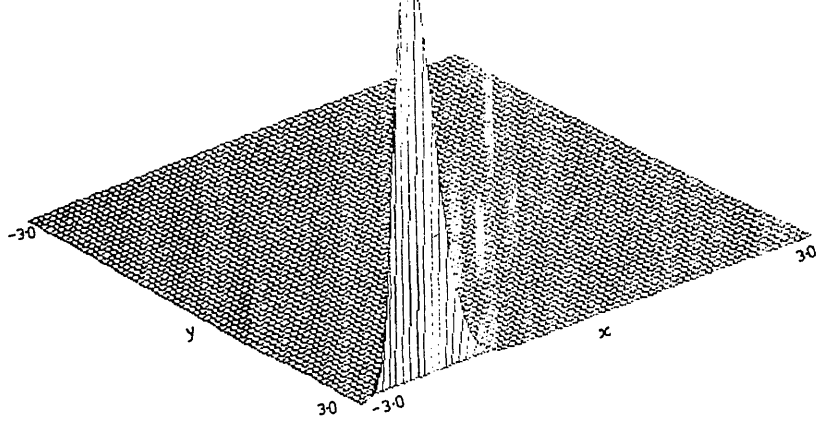

(e)

Figure 4. Spatial profile of local chemical potential (**a**) $t = 0$; (**b**), (**c**) lattice I, $t = 0{\cdot}16$, 1 and (**d**), (**e**) lattice II, $t = 0{\cdot}16$, 1. See caption of figure 1 for details.

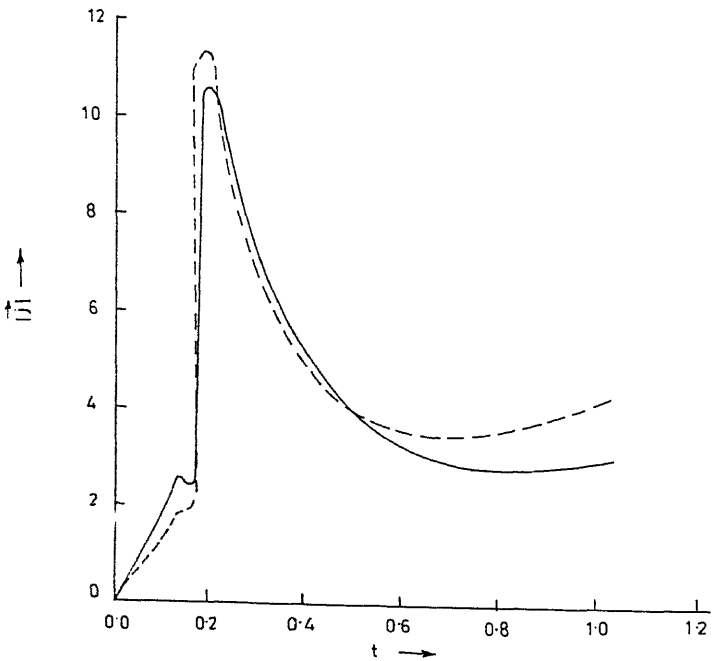

Figure 5. Temporal evolution of global current (a) (———) lattice I, (b) (– – –) lattice II. See caption of figure 1 for details.

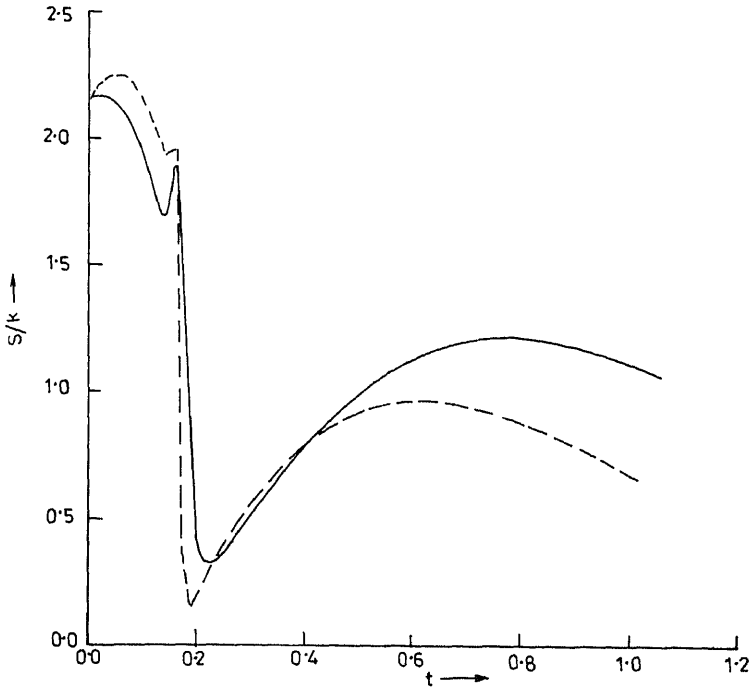

Figure 6. Temporal evolution of Shanon entropy (a) (———) lattice I, (b) (– – –) lattice II. See caption of figure 1 for details.

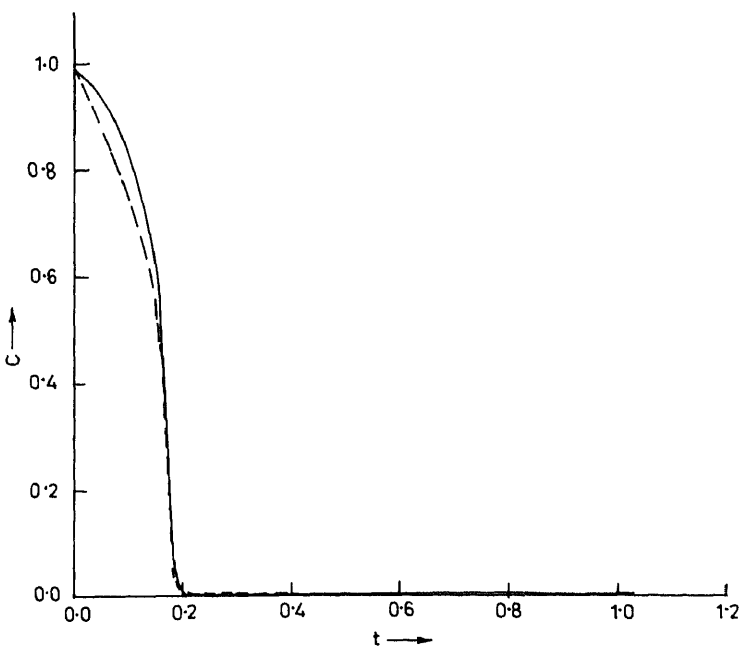

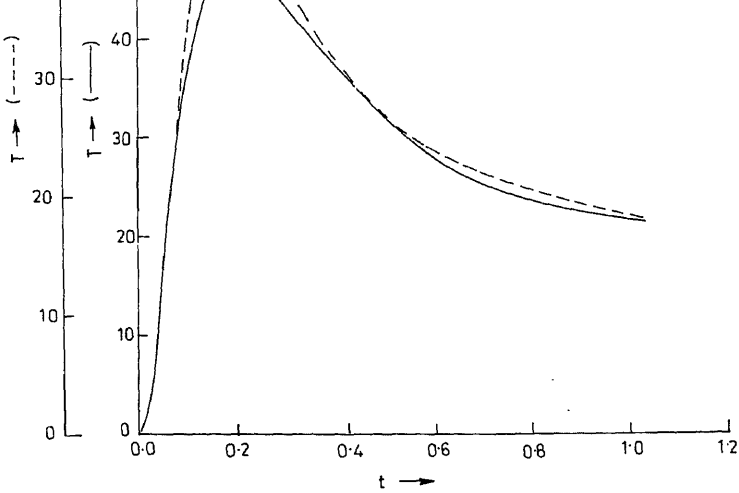

Figure 8. Temporal evolution of macroscopic kinetic energy (a) (———) lattice I, (b) (– – –) lattice II. See caption of figure 1 for details.

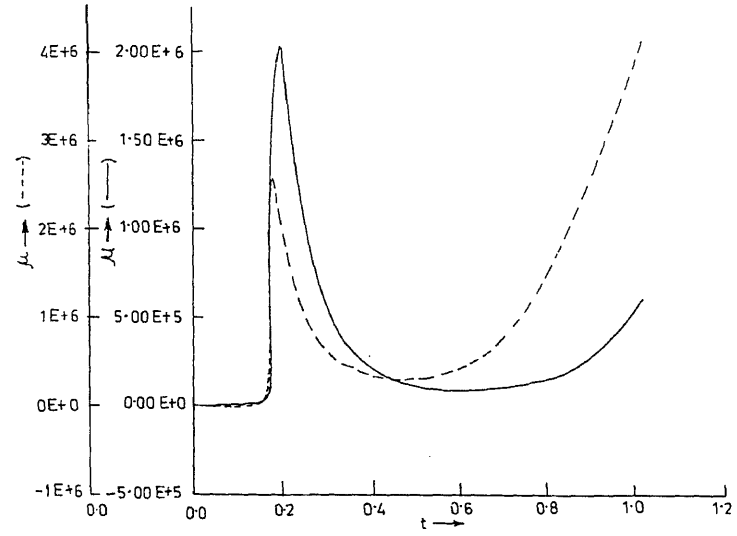

Figure 9. Temporal evolution of chemical potential (a) (———) lattice I, (b) (– – –) lattice II. See caption of figure 1 for details.

= 0·2 where kinetic energy also becomes maximum. Density correlation starts ecreasing from an initial value unity. At around $t = 0{\cdot}2$ it goes to zero and system loses correlation with its initial state. At $t = 0$, Shanon entropy has the value $k(1 + \ln \pi)$, being the Boltzmann constant. It starts oscillating with time and a local maximum in tropy (a measure of disorderliness) slightly before $t = 0{\cdot}2$ goes along with maxima in obal current and KE and zero value of correlation. However, the minimum in tropy around $t = 0{\cdot}2$ is apparently not in conformity with extremal behaviour of her quantities at that time step. Entropy then starts increasing and a broad maximum it, zero value of correlation and very small values for current and KE are internally nsistent. Global chemical potential starts from a negative value ($-360{\cdot}28$ and $466{\cdot}43$ for lattices I and II respectively at $t = 0$ which are not conspicuous in the gures) and increases rapidly to a maximum positive value around $t = 0{\cdot}2$. Then it arts decreasing and passes through a broad minimum. Since its extremal characteris- as a function of time resembles that of current density it can be treated as a useful dex for studying dynamical problems. This quantity contains information of the rrect time of charge transfer such that the change in the energy of the system stabilizes the most.

Concluding remarks

portant insight into the dynamics of a wavepacket on a model fractal lattice has been tained through spatial and temporal variations of several quantities which depend time dependent charge and current densities. Interplay of kinetic and potential fects governs the overall dynamics. Initially the wavepacket remains confined around ulomb centres of the fractal lattice. In course of time there result two accessible zones ound the edges, away from the coulomb sources. Local chemical potential exhibits triguing spatio-temporal behaviour. Different time dependent quantities extremize in ne in a consistent manner. After certain time most of these quantities do not change preciably. Chemical potential seems to contain valuable dynamical information and serves closer scrutiny. As expected the qualitative behaviour of various dynamical antities in two lattices is similar although they differ quantitatively. At this stage the act connection between structure of the surface and the resulting dynamical informa- n is not clear. However, the dependence of the dynamical observables on the fractal haviour of the lattice is conspicuous.

cknowledgement

ne authors would like to thank the referee for constructive criticism and one of them N) would like to thank CSIR, New Delhi for financial assistance.

eferences

1] J Mazur and R J Rubin, *J. Chem. Phys.* **31**, 1395 (1959)
2] E A McCullough Jr and R E Wyatt, *J. Chem. Phys.* **51**, 1253 (1969)
3] K C Kulander, *J. Chem. Phys.* **69**, 5064 (1978)
4] C Leforestier, *Chem. Phys.* **87**, 241 (1984)

[5] R B Gerber, R Kosloff and M Berman, *Comput. Phys. Rep.* **5**, 59 (1986)
[6] E J Heller, *J. Chem. Phys.* **68**, 2066 (1978)
[7] E J Heller, *Acc. Chem. Res.* **14**, 368 (1981)
[8] D J Tannor and E J Heller, *J. Chem. Phys.* **77**, 202 (1982)
[9] G Drolshagen and E J Heller, *J. Chem. Phys.* **79**, 2072 (1983)
[0] V Mohan and N Sathyamurthy, *Comput. Phys. Rep.* **7**, 213 (1988)
[1] P Brumer and M Shapiro, *Chem. Phys. Lett.* **72**, 528 (1980)
[2] M J Davis, E B Stechel and E J Heller, *Chem. Phys. Lett.* **76**, 21 (1980)
[3] J S Hutchinson and R E Wyatt, *Phys. Rev.* **A23**, 1567 (1981)
[4] M Bixon and J Jortner, *J. Chem. Phys.* **77**, 4175 (1982)
[5] M D Feit and J A Fleck Jr, *J. Chem. Phys.* **80**, 2578 (1984)
[6] P K Chattaraj and S Sengupta, *Phys. Lett.* **A181**, 225 (1993)
P K Chattaraj, *Indian J. Pure Appl. Phys.* **32**, 101 (1994)
[7] Hao Bai-Lin, *Chaos* (Singapore: World Scientific, 1984)
[8] B B Mandelbrot, *The fractal geometry of nature* (New York: Freeman, 1982)
[9] H Singh and P K Chattaraj, *Proc. Indian Acad. Sci. (Chem. Sci.)* **99**, 47 (1987)
[20] H Singh and P K Chattaraj, *Phys. Lett.* **A128**, 355 (1988)
[21] P K Chattaraj, *Chem. Phys. Lett.* **175**, 613 (1990)
[22] P K Chattaraj, *Symmetries and singularity structures: Integrability and chaos in nonlinear dynamical systems*, edited by M Lakshmanan and M Daniel (Berlin: Springer, 1990) pp 172–182
[23] P Pfeifer and D Avnir, *J. Chem. Phys.* **79**, 3558 (1983)
[24] P Meakin, *Chem. Phys. Lett.* **123**, 428 (1986)
[25] T A Witten Jr and L M Sander, *Phys. Chem. Rev.* **47**, 1400 (1981)
[26] T A Witten Jr and L M Sander, *Phys. Rev.* **B27**, 5686 (1983)
[27] S S Tambe, P Badola and B D Kulkarni, *Chem. Phys. Lett.* **173**, 67 (1990)
[28] R Gutfraind, M Sheintuch and D Avnir, *Chem. Phys. Lett.* **174**, 8 (1990)
[29] W F Ames, *Numerical methods for partial differential equations* (Academic: New York, 1977)
[30] P K Chattaraj and S Nath, *Int. J. Quantum Chem.* **49**, 705 (1994)
S Nath and P K Chattaraj, *Pramana – J. Phys.* **45**, 65 (1995)

Kinetic description of ion acoustic waves in a dusty plasma

B P PANDEY and SUSHEEL KUMAR
Indian Institute of Geomagnetism, Dr Nanabhai Moos Marg, Colaba, Bombay 400 005, India

MS received 29 May 1995; revised 20 October 1995

Abstract. A self-consistent model for the description of the ion sound wave in a dusty plasma is given. We show that proper consideration of the ion attachment to the grains gives rise to the dissipation of the ion acoustic wave in a dusty plasma medium. Dissipation rate is proportional to the sum of the electron and twice the ion attachment frequencies.

Keywords. Ion acoustic wave; dusty plasma; charge fluctuations.

PACS Nos 52·25; 52·35

1. Introduction

Investigations of the dusty plasma in recent times have acquired considerable momentum. Major reason for the spurt in the interest is due to its numerous applications to the industrial (e.g. semiconductor industry, plasma etching, etc.) as well as cosmic plasmas (e.g. planetary rings, cometary tails, etc.). Periodicity of the subject being reviewed at present is 1·5 years [1–4]. Recent interest in the investigation of the dielectric response of the dusty plasma medium focusses around charge fluctuating grains. A consistent formulation of the dynamics of the dusty plasma (with constant mass and radius of the grain) is given by Bhatt and Pandey [5] and Vladmirov [6]. Mass of the grain may also vary e.g. due to coagulation of the grains [7] and thus, grain radius and mass in general, may also become dynamical quantities. Set of equations considering mass as a dynamical variable have been given elsewhere [8]. For the present however, we shall assume that the grain is spherical and of fixed radius and mass and that the grain charging is solely due to the attachment of electrons and ions. Grains will be assumed massive compared to the electrons and ions and therefore, immobile. Dynamical response time of the grain is slowest in comparison with the response time of the plasma particles so that the assumption about their immobileness is justified.

We shall study the ion acoustic waves in a dusty plasma. Ion acoustic mode has been studied, in the past by several authors e.g. Tsytovich and Havnes [9], D'Angelo [10], Bhatt and Pandey [5] and Ma and Yu [11]. Tsytovich and Havnes [9] describe the ion acoustic mode by assuming that the plasma fluctuations maintain their quasineutrality. They demonstrate that the mode is damped by the charge fluctuation and that the charge fluctuation induced damping could be larger than the collisionless Landau damping. In the kinetic description of Ma and Yu [11], ion acoustic mode is described by assuming that the perturbations in the plasma may cause space charge field and that the mode may damp or grow depending upon how strong the deviation of plasma is from quasineutrality. D'Angelo [10] gives a fluid description of the ion acoustic mode

and shows that the mode damps at the frequency at which ions are injected in the plasma. He calls it 'creation damping' as fresh ions injected in the plasma counters the loss caused by the sticking of the ion to the grain surface. His description assumes that the plasma always maintains quasineutrality. Bhatt and Pandey [5] investigate the ion-acoustic streaming instability and show that the charge fluctuation narrows the parameter space of instability. Scope of the present work includes the consistent formulation of the kinetic problem for the ion acoustic mode in the spirit of Vladmirov [9] and explore, whether conclusions arrived by previous investigation in general and Ma and Yu [11] in particular, are valid. To that end, we shall investigate the ion acoustic wave in the dusty plasma.

Since we are interested in the low frequency ion acoustic mode, electrons can be assumed to follow Boltzmann distribution i.e. they are in thermodynamic equilibrium. Furthermore, charging time scale is comparable with the attachment time scale of the ions which in turn is comparable with the acoustic time scale leading to appreciable dissipation of the acoustic mode.

This paper is organized in the following fashion. Section 2 describes the basic equations. In § 3 we discuss the perturbed equations and derive the dispersion relation. In § 4 discussion of the result and comparison with the previous work are given.

2. Basic equation

It is assumed that the grains are spherical conductors and charging of the grains are due to the potential difference between plasma (electrons and ions) and grain surface. Equilibrium currents are given by [12]

$$I_{eo} = -\pi a^2 e \sqrt{\frac{8T_e}{\pi m_e}} n_{eo} \exp\left[\frac{e(\phi_g - \phi)}{T_e}\right] \tag{1}$$

$$I_{io} = -\pi a^2 e \sqrt{\frac{8T_i}{\pi m_i}} n_{io} \left[1 - \frac{e(\phi_g - \phi)}{T_i}\right] \tag{2}$$

where subscript o denotes the equilibrium quantities; m_α, T_α and $n_{\alpha o}$ are the mass, temperature and equilibrium density of the αth particle; a and ϕ_g are the grain radius and potential respectively; ϕ is the plasma potential and e is the electronic charge. Charge on the grain is a dynamical quantity and its dynamics is described by the following equation

$$\frac{dQ}{dt} = I_e + I_i \tag{3}$$

where Q is the average grain charge i.e.

$$Q = \frac{1}{n_d} \int f_d \, dq \tag{4}$$

and charge q is an additional independent variable and f_d is the grain distribution function. In equilibrium $I_{eo} + I_{io} = 0$ and Q_0 charge is carried by the grains. Equilibrium grain distribution is given by

$$f_{do} = n_d \delta(q + Q_0). \tag{5}$$

namics of the ion is described by kinetic Boltzmann equation

$$\frac{\partial f_i}{\partial t}+\mathbf{v}\cdot\frac{\partial f_i}{\partial \mathbf{r}}+\frac{e}{m_i}\mathbf{E}\cdot\frac{\partial f_i}{\partial \mathbf{v}}=-\int \sigma_i v(f_d f_i - f_{do} f_{io})\mathrm{d}q \tag{6}$$

ere,

$$\sigma_i=\begin{cases}\pi a^2\left(1-\dfrac{2eq}{am_i v^2}\right) & \dfrac{2eq}{am_i v^2}<1\\ 0 & \dfrac{2eq}{am_i v^2}\geqslant 1\end{cases} \tag{7}$$

he effective collision cross section of the ions with the grains. Moment of eq (5) is scribed by Bhatt and Pandey [5]. We shall assume that in the equilibrium state, loss ion is compensated by the external source and the ion distribution function f_{io} is axwellian. We should add that assumption of ion following Maxwellian distribution in general not valid in the vicinity of the grains. Ion will respond to the electric field of highly charged grains and therefore in general should be described by the Maxwell ltzmann distribution.

Electron follows Boltzmann distribution

$$n_e=n_{eo}\exp\left[\frac{e\phi}{T_e}\right]. \tag{8}$$

Localized charge build-up is described by Poisson's equation

$$\nabla^2\phi=4\pi[en_e-n_d Q]-4\pi e\int f_i \mathrm{d}\mathbf{v}. \tag{9}$$

uations (1)–(9) will adequately describe the ion dynamics in a dusty plasma.

Dispersion relation

xt, we introduce small perturbation in the distribution function

$$f_d=f_{do}+\hat{f}_d;\quad f_i=f_{io}+\hat{f}_i,\quad \text{with}\quad |\hat{f}_d|\ll f_{do}, |\hat{f}_i|\ll f_{io}.$$

arge fluctuation equation can be written as

$$\frac{\partial \hat{Q}}{\partial t}+\nu_d^o\hat{Q}=-\frac{e|I_{eo}|}{n_{eo}}\hat{n}_e+e\int_0^{\infty}\hat{f}_i v\sigma(v,Q_0)\mathrm{d}\mathbf{v} \tag{10}$$

ere $\hat{n}_e$ is the perturbed electron density. Last term in the above equation is from the turbed ion currents. The charge dissipation is described by the charging frequency which for Maxwellian particle distribution is given by

$$\nu_d^o=\left.\frac{\partial I(q)}{\partial q}\right|_{q=-Q_0}=\frac{1}{\sqrt{2\pi}}\frac{\omega_{pi}^2 a}{v_{Ti}}(1+\tau+z) \tag{11}$$

h $\tau\equiv T_i/T_e$, $z\equiv eQ_0/aT_e$. Fluctuation in the grain distribution is described by

For the ion distribution, one has

$$\frac{\partial \hat{f}_i}{\partial t} + \mathbf{v}\cdot\frac{\partial \hat{f}_i}{\partial \mathbf{r}} + \frac{e}{m_i}\mathbf{E}\cdot\frac{\partial f_{io}}{\partial \mathbf{v}} = -\nu_{id}^{o}(v)\hat{f}_i - \hat{\nu}_{id}(v)f_{io} \tag{13}$$

where attachment frequencies $\nu_{id}^{o}(v)$ and $\hat{\nu}_{id}(v)$ are given by

$$\nu_{id}^{o}(v) = \int \sigma_i v f_{do}\,\mathrm{d}q \tag{14}$$

$$\hat{\nu}_{id}(v) = \int \sigma_i v \hat{f}_d\,\mathrm{d}q. \tag{15}$$

Assuming that the fluctuations can be represented as the normal mode $\sim \exp i(\omega t - \mathbf{kx})$, ion distribution function is given by

$$\hat{f}_i = \frac{1}{\omega - \mathbf{k}\cdot\mathbf{v} - i\nu_{id}^{o}(v)}\left[-\left(\frac{ek\hat{\phi}}{m_i}\right)\frac{\partial f_o}{\partial \mathbf{v}} + i\hat{\nu}_{id}(v)f_{io}\right] \tag{16}$$

and the charge fluctuation $\hat{Q}$ is given by

$$\hat{Q} = \frac{ie|I_{eo}|\hat{\phi}}{(\omega - i\nu_d^o)\,T_i} + \frac{i}{\omega - i\nu_d^o}\left[\frac{e^2k\hat{\phi}}{m_i}\int \frac{(\partial f_{io}/\partial \mathbf{v})v\sigma_i\,\mathrm{d}\mathbf{v}}{\omega - \mathbf{k}\cdot\mathbf{v} - i\nu_{id}^{o}(v)} + e\int \frac{\hat{\nu}_{id}(v)f_{io}}{\omega - \mathbf{k}\cdot\mathbf{v} - i\nu_{id}^{o}(v)} v\sigma_i\,\mathrm{d}\mathbf{v}\right]. \tag{17}$$

Last term in the above expression is $O(\nu_{id}^{o}\nu_d^o/\omega)$ and thus can be ignored. Then taking note of the fact that for $\omega \sim \omega_{pi} \gg \max(kv_{Ti}, \nu_d^o, \nu_{id}^o)$, where $\omega_{pi} = \sqrt{4\pi n_{io}e^2/m_i}$, we can approximate the following integral as

$$ie\int \frac{\hat{\nu}_{id}(v)f_{io}}{\omega - \mathbf{k}\cdot\mathbf{v} - i\nu_{id}^{o}(v)}\,\mathrm{d}\mathbf{v} \approx n_{io}\left(\frac{i\nu_d^o}{\omega}\right)\hat{Q}. \tag{18}$$

Then plugging back (16) and (17) in the Poisson's equation (9) and taking note of (18), one gets the following dispersion relation (DR)

$$\frac{1 + k^2\lambda_e^2}{k^2\lambda_e^2} + \chi_i - \frac{i\left(1 + \frac{i\nu_{id}^o}{\omega}\frac{n_{io}}{n_{do}}\right)}{(\omega - i\nu_d^o)}\left[\frac{\alpha}{k^2\lambda_e^2} - \beta\frac{\omega_p i^2}{\omega^2}\right] = 0 \tag{19}$$

where $\lambda_e^2 = T_e/4\pi n_{eo}e^2$, $\alpha = |I_{eo}|n_{do}/en_{eo}$. We note that α is the electron attachment frequency, as have been shown by Bhatt and Pandey [5]. One may calculate ν_{ed}^o for a Maxwellian electron

$$\nu_{ed}^{o} = \frac{n_{do}}{n_{eo}}\int \sigma_e v f_{eo}\,\mathrm{d}\mathbf{v} = \frac{n_{do}|I_{eo}|}{en_{io}}. \tag{20}$$

Similarly ion attachment frequency is given by

$$\nu_{id}^{o} = \frac{n_{do}}{n_{io}}\int \sigma_i v f_{io}\,\mathrm{d}\mathbf{v} = \frac{n_{do}I_{io}}{en_{io}}. \tag{21}$$

Thus, we see that using the constraint $I_{eo} + I_{io} = 0$, one can write $\nu_{id}^o = \nu_{ed}^o(1 + (n_{eo}/n_{io}))$. This result is in agreement with the result derived on the intuitive ground by Bhatt and Pandey [5]

$$\beta = -\left(\frac{\omega^2}{k^2}\right)\frac{n_{do}}{n_{io}}\int_0^\infty \frac{(\partial f_{io}/\partial \mathbf{v})v\sigma(v, Q_0)}{\omega - \mathbf{k}\cdot\mathbf{v} - i\nu_{id}^o(v)}\mathrm{d}\mathbf{v} \tag{22}$$

$$\chi_i = -\frac{\omega_{p_i}^2}{\omega^2}\frac{1}{n_{io}}\int \frac{(\partial f_{io}/\partial \mathbf{v})}{\omega - \mathbf{k}\cdot\mathbf{v} - i\nu_{id}^o(v)}\mathrm{d}\mathbf{v}. \tag{23}$$

Without loss of generality, assuming $\mathbf{k} \| \hat{\mathbf{x}}$ and going to spherical polar coordinate to evaluate (19) with $\omega \sim \omega_{pi} \gg (kv_{Ti}, \nu_d^o, \nu_{id}^o)$, one gets

$$\beta = \frac{4}{3}\pi a^2\sqrt{\frac{8T_i}{\pi m_i}}n_{do}\left(1 - \frac{eQ_0}{2CT_i}\right) = \frac{2}{3}\frac{I_{io}}{e}\frac{n_{do}}{n_{io}}A \tag{24}$$

where $A = 1 + (1 - (eQ_0/CT_i))^{-1}$. Ion susceptibility χ_i becomes

$$\chi_i \approx -\frac{\omega_{pi}^2}{\omega^2}\left(1 + \frac{2i\nu_{id}^o}{\omega}\right). \tag{25}$$

The above expression has been derived by assuming $\nu_{id}^o(v) \approx \nu_{id}$ which tantamounts to assuming that $Z_d e^2/am_i v^2 \ll 1$ i.e. ratio of the dust potential to the kinetic energy is much less than 1. In the other limit, one cannot take ν_{id}^o out of integral and the result will renormalize the ion acoustic speed.

While evaluating (23) we have not considered the resonant contribution to the ion susceptibility. For $\omega \ll P\nu_d^o$, where $P = (n_d/n_e)(aT_e/e^2)$ is the ratio of dust space change to the electron space change (Havnes *et al* [13]) resonant denominator is evaluated by the usual Landau rule. It has been demonstrated by Tsytovich and Havnes [9], that the change fluctuation induced damping rate may exceed the Landau damping.

Thus, DR can be written as

$$(\omega^2 - k^2C_s^2)(\omega - i\nu_d^{o'}) - i(\varepsilon + 2\nu_{id}^o)k^2C_s^2 = 0 \tag{26}$$

where $\nu_d^{o'} \equiv \nu_d^o + \alpha/(1 + k^2\lambda_e^2)$, $C_s = \lambda_e\omega_{pi}/(\sqrt{1 + k^2\lambda_e^2})$, $\varepsilon = \alpha(1 - (2n_{eo}A/3n_{io}))$. In writing DR (26) we have ignored terms $O(\nu_d^o\alpha, \nu_d^o\beta, \nu_{id}^o\nu_d^o)$. We see that DR (26) reduces to DR of [11] in $\nu_{id}^o \to 0$ limit. As $\varepsilon \approx \nu_{id}^o$, we see that the proper consideration of ion attachment causes the mode to damp faster than have been reported [11].

4. Discussion

DR (26) can be solved analytically. However, since $\omega \gg (\nu_{id}^o \sim \varepsilon)$, it is instructive to solve the above equation perturbatively. Then the roots are

$$\omega_{1,2} = kc_s \pm i\varepsilon\left(\frac{1}{2} + \frac{\nu_{id}^o}{\varepsilon}\right)$$

$$\omega_3 \approx i\varepsilon\left(\frac{1}{2} + \frac{\nu_{id}^o}{\varepsilon}\right). \tag{27}$$

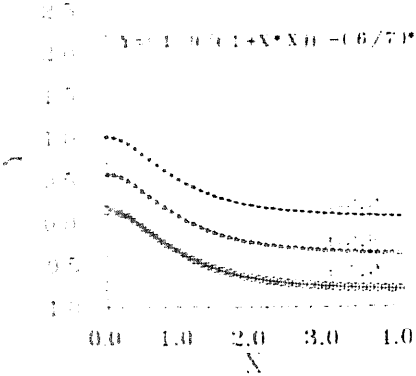

Figure 1. This figure shows variation of $y = (2\omega_i)/\alpha$ against $x = k\lambda_e$ for differ values of $d = (n_{e_0}, n_{i_0})$ and $(eQ_d, CT_i) = -2{\cdot}5$ when $\nu_{id}^o = 0$. It is evident from figure that for certain values of x, mode becomes unstable.

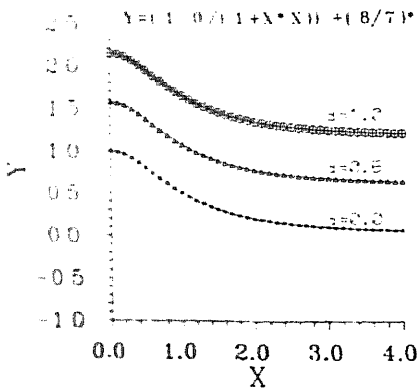

Figure 2. This figure shows the same when $\nu_{id}^o \neq 0$. It is clear from figure 2 that all wavelengths, charge fluctuation will cause the damping of ion acoustic mod

Thus, we see that the ion acoustic mode acquires a damping rate proportional $\sim \varepsilon/2 + \nu_{id}^o \approx \nu_{id}^o$. The above result modifies the damping rate predicted by Ma and [11]. Energy transfer between ion acoustic wave and dust charge fluctuation leads this damping. Our result is broadly in agreement with the conclusions drawn Tsytovich and Havnes [9] and D'Angelo [10]. It must be mentioned however, that dissipation derived by D'Angelo [10] is caused primarily by the injection of the i and thus is proportional to the injection frequency of the ion in the plasma whereas the present analysis dissipation is due to the attachment of ions to the grains.

It is interesting to note that without the ion attachment frequency ν_{id}^o ion acou mode may become unstable [11], if $\varepsilon < 0$, i.e. $\lambda_e^2 k^2 > 3/2(n_{io}/n_{eo})A$. However, consistent treatment of the charge fluctuation shows that even when $\varepsilon < 0$, there is instability unless additional condition $(\nu_{id}^o - \varepsilon/2) < 0$ is satisfied. As is evident from

nd (21) and the discussion therein $\nu_{id}^{o}/\varepsilon \approx d = n_{eo}/n_{io}$. The number density ratio d may ave different values, e.g. for diffuse cloud in the interstellar media $\delta \approx 0$ [10] whereas in e planetary rings and cometary tails $d \leqslant 1$ [1–4]. Thus we see that the charge ıctuation will invariably cause the damping of ion acoustic response of the plasma. ne instability suggested in ref. [11] is, thus highly unlikely in a dusty plasma. Figure 1 epicts the plot of $y = (2\omega_i/\alpha)$ vs. $x = k\lambda_e$ for $d = 0, 0{\cdot}5, 1$ and $(eQ_0/CT_i) = -2{\cdot}5$ when n attachment frequency has been ignored. We see that for $d = 0{\cdot}5$ and 1, mode ecomes unstable for some critical wavelength. Figure 2 depicts the same for non-zero n attachment frequency. We see from figure 2 that there is no instability, and ion oustic mode can only damp in a dusty plasma.

We conclude that the self-consistent treatment of charge dynamics leads to the mping of the acoustic wave. Further, Landau damping will also cause the mode to ssipate [9] and thus, there is no window whatsoever contrary to the claim mode in ref. 1] where the mode may become unstable. The parameter regime in which the oustic mode becomes unstable is highly unlikely. Our analysis demonstrates that the le of ion attachment in the charge dynamics of a dusty plasma is crucial. It is through is attachment that the ion loses its energy to the grains and causes the damping.

cknowledgements

ne of the authors [BP] thanks Prof. S Vladmirov for discussion during the prepara- on of the manuscript. We thank the referee for bringing to our notice the work of D'Angelo [10].

eferences

1] C K Goertz, *Rev. Geophys.* **27**, 271 (1989)
2] U de Angelis, *Phys. Scr.* **45**, 465 (1992)
3] T W Hartquist, O Havnes and G E Morfill, *Fund. of Cosmic Plasma* **15**, 167 (1992)
4] D A Mendis and M Rosenberg, *Ann. Rev. Astron. Astrophys.* **32**, 419 (1994)
5] J R Bhatt and B P Pandey, *Phys. Rev.* **E50**, 3980 (1994)
6] S V Vladmirov, *Phys. Plasmas* **1**, 2762 (1994); *Phys. Rev.* **E50**, 1422 (1994)
7] M Horayani and C K Goertz, *Astrophys. J.* **361**, 155 (1990)
8] B P Pandey and C B Dwivedi, *Pramana – J. Phys.* (in Press) (1995)
9] V Tsytovich and O Havnes, *Comm. Plasma Phys. Controlled Fusion* **15**, 267 (1993)
0] N D'Angelo, *Planet Space Sci.* **42**, 507 (1994)
1] Ma Jin-Xiu and M Y Yu, *Phys. Plasmas* **1**, 3520 (1994)
2] L Spitzer, in *Physical processes in the interstellar medium* (John Wiley, New York, 1978)
3] O Havnes, G Morfill and C Goertz, *J. Geophys. Res.* **89**, 10999 (1984)

PRAMANA
— journal of
physics

© Printed in India

Vol. 45, No. 6,
December 1995
pp. 569–582

A comparative study of two learning rules for associative memory

G ATHITHAN
Advanced Numerical Research and Analysis Group, P.O. Kanchanbagh, Hyderabad 500 258, India

MS received 22 May 1995; revised 20 October 1995

Abstract. This paper addresses itself to a practical problem encountered in using iterative learning rules for associative memory models. The performance of a learning rule based on linear programming which overcomes this problem is compared with that of a representative iterative rule by numerical simulation. Results indicate superior performance by the linear programming rule. An algorithm for computing radii of maximal hyperspheres around patterns in the state space of a model is presented. Fractional volumes of basins of attractions are computed for the representative iterative rule as well as the linear programming rule. With the radii of maximal hyperspheres as weight factors for corresponding patterns to be stored, the linear programming rule gives rise to the maximal utilisation of the state space.

Keywords. Associative memory; learning rule; linear programming.

PACS Nos 87·10; 89·10; 89·80

1. Introduction

There has been much interest recently in the McCulloch–Pitts [1] neural networks as models of associative memories. In the Hopfield [2] version of such a network, the main task of a designer is to compute the neural interaction strengths as a function of the patterns to be stored and recalled associatively. Algorithms to compute interaction strengths are generally known as learning rules. The simplest of them is based on an hypothesis by Hebb [3]. Though biologically meaningful, the Hebb rule cannot be used to store more than $0{\cdot}14N$ random uncorrelated patterns where N is the number of neurons in the network [4]. The pseudo-inverse rule [5] can store N linearly independent patterns. Earlier, Willshaw *et al* [6] have proposed a rule for highly correlated patterns which stores patterns of the order of $N^2/(\log N)^2$. In these and other rules [7] the sizes of basins of attraction around the patterns in the state space are not controlled explicitly. Using a number of rules proposed subsequently [8–14], it is not only possible to ensure that patterns are stored in the network but also to provide around each one a basin of attraction whose measure is specified by the designer. Conditions for stability in terms of measures of the sizes of basins of attraction, the patterns and the interaction strengths are formulated first. Beginning with arbitrary values for the interaction strengths, these rules help the designer to move towards the correct values iteratively till these conditions are satisfied. Convergence to the correct values are ensured, provided a solution satisfying the initial conditions exists in the space of interaction strengths. However, in practical situations it will be difficult to know if a solution exists a priori. Therefore, one would have to assume conservative values for

the sizes of basins of attraction. Consequently the basins of attraction may not pack the state space of the network as tightly as possible.

A learning rule based on linear programming [11] overcomes the above mentioned drawback of iterative rules. The linearity of conditions of stability combined with linear normalization of interaction strengths enables one to employ the linear programming approach. Unlike the case of iterative rules where measures of the sizes of basins attraction are expected as external inputs, in the linear programming approach, maximal values for these measures are computed automatically. The interaction strengths are computed as a byproduct. Though this rule was first formulated by Krauth and Mezard, its distinct advantages are not argued or brought out clearly in their paper. Moreover, they do not report extensive numerical studies of this rule's performance in recalling stored patterns. This paper proposes to complement their work and fill out the above mentioned gaps.

While employing the linear programming approach, it is possible to specify different relative weights for different patterns. If these weights are selected in accordance with the inter-pattern distances, then maximal utilization of the state space of the model can be achieved as a result. An algorithm to compute the radii of maximal geometric hyperspheres around each pattern is presented. Use of these radii as relative weights for patterns results in maximal fractional volume of basins of attraction as shown by Monte-Carlo simulations.

The paper is organized as follows. The terms and notations are introduced in § 2 by way of briefly reviewing the iterative learning rules. It is followed by § 3, which describes the rule based on linear programming. Section 4 discusses numerical simulations for comparing the performances of a representative iterative and linear programming rules. The next section presents an algorithm to compute the radii of maximal geometric hyperspheres around each pattern. It also describes a Monte-Carlo method to compute the fractional volume of basins of attraction and presents the results. Discussions and conclusions make up the last section.

2. Iterative learning rules

The standard Hopfield network consists of N Ising spins $\sigma_i = \pm 1$ for $i = 1, \ldots, N$. The interaction strength from spin j to spin i is denoted by J_{ij}. All self-interactions, J_{ii}, are assumed to be zero throughout this paper and the $\{J_{ij}\}$ need not be symmetric. The local field, $h_i(t)$, at site i and at time t is computed by

$$h_i(t) = \sum_{j=1}^{N} J_{ij}\sigma_j(t) \tag{1}$$

where $\sigma_j(t)$ is the Ising spin at site j and at time t. The spins, or equivalently neurons, are updated according to the rule

$$\sigma_i(t + \delta t) = \text{sign}(h_i(t)). \tag{2}$$

A configuration, or equivalently a pattern, $\{\xi_i : i = 1, \ldots, N\}$ is stored, i.e., becomes a fixed point of dynamics (2), if

$$c_i = \xi_i h_i(\{\xi_i\}) \tag{3}$$

is positive for all i. In fact, c_i is a measure of the size of basin of attraction for the pattern $\{\xi_i\}$. Therefore, for effective associative recall, c_i must be greater than a positive constant, say, k. For storing p patterns, biased or random, $\{\xi_i^\mu : i = 1, \ldots, N; \mu = 1, \ldots, p\}$, the fixed point conditions

$$\xi_i^\mu h_i(\{\xi_i^\mu\}) > k \tag{4}$$

must be satisfied at each site i for each pattern μ. The positive constant could be pattern dependent, if required. Without some sort of normalization or bounds for the J_{ij}'s, the inequalities (4) would be devoid of meaning. Two types of normalizations are used in the iterative rules proposed in the literature. In the first type the J_{ij}'s are expected to obey

$$\sum_{j=1}^{N} J_{ij}^2 = N, \tag{5}$$

for each i (in some cases N is replaced by 1). In the second, the bound

$$|J_{ij}| < J_{\max} \tag{6}$$

is imposed on all J_{ij}'s.

In Gardner's version of the iterative approach, the interaction strengths $\{J_{ij}\}$ are computed as follows. The $\{J_{ij}\}$ are assigned any set of values to begin with. A mask ε_i^μ is defined at each site i and for each pattern μ as follows.

$$\varepsilon_i^\mu = \theta\left[k\left(\sum_{j=1}^{N} J_{ij}^2\right)^{1/2} - \sum_{j=1}^{N} J_{ij}\xi_i^\mu \xi_j^\mu\right] \tag{7}$$

where $\theta(x)$ is the Heaviside step function. The iterative corrections for $\{J_{ij}\}$ are computed as

$$\Delta J_{ij} = \varepsilon_i^\mu \xi_i^\mu \xi_j^\mu \tag{8}$$

to update the $\{J_{ij}\}$ till ε_i^μ become zero for all i and μ. The normalization condition (5) is made use of implicitly in computing ε_i^μ using (7). This local, Hebb rule like, algorithm is guaranteed to converge provided a solution of $\{J_{ij}\}$ satisfying the conditions (4) exists in the space of interactions [15]. Existence of a solution is, of course, dependent on the number and nature of patterns and also on the constant k. Larger the value of p and k, the less probable it is for a solution to exist. Gardner's deep analytical results are useful in knowing about the existence of such solutions when one deals with an abstract category of patterns drawn from a known probability distribution. However, in practical situations where one needs to store a specific set of p patterns there is no way of knowing if a solution exists or not. There are no guidelines either for choosing an optimal value for k. Both these problems are easily overcome by adopting the linear programming approach to compute the interaction strengths.

Two other iterative rules [10, 11] make use of the fact that the inequality conditions (4) can be decoupled into N independent sets. The latter rule, called minimum-overlap rule, is a minor variant of the former. Starting with some a priori value of k, the rules iteratively try to satisfy these N sets of conditions independently. Once again, convergence is ensured only if a solution for $\{J_{ij}\}$ exists. Therefore both these rules are subject

to the critical observations made against Gardner's iterative rule. In fact, unless the computation of $\{J_{ij}\}$ is posed as a problem of optimizing k, the problem of finding out a priori if a solution of $\{J_{ij}\}$ exists or not cannot be avoided whatever be the iterative formulation. Griniasty and Gutfreund [16] do point out that learning can be viewed as an optimization problem. However they do not discuss the application of linear programming for learning patterns.

Krauth and Mezard [11] present the linear programming approach in the same paper where they discuss the minimum-overlap rule and compare the two. They compute measures of stabilities or equivalent sizes of basins attraction in case of both the rules. When the normalization condition (6) is used, these measures turn out to be larger for the linear programming rule, as one would expect. If one uses (5) for normalization, then the problem of computing $\{J_{ij}\}$ can no longer be posed as a linear programming problem. However, in their paper a comparison between the two rules with normalization based on (5) is presented which shows the linear programming approach in poor light. It is not clear how they used the simplex algorithm to maximise k subject to conditions (4) and (5) as the latter are quadratic. The point argued here is that when all the conditions involved in the problem are linear the best approach is one based on linear programming. Besides finding out if a suitable solution of $\{J_{ij}\}$ exists or not, this approach provides unique and maximal possible stabilities or sizes of basins attraction for the patterns to be stored.

3. Linear programming rule

Linear programming is concerned with finding optimum values of linear objective functions subject to a set of equality or inequality constraints. The constraints have to be linear and the standard method for solving a linear programming problem (LPP) is known as the simplex algorithm. Starting with a feasible solution which satisfies the given constraints, the algorithm improves the solution from one step to another till the optimum is reached. In case no feasible solution exists, the algorithm is capable of detecting that as well as the possibility of unboundedness of the optimal value. In the canonical formulation of an LPP one has a linear objective function which is to be maximised and a number of linear constraints. The variables are normally assumed to take only positive values.

The problem of computing $\{J_{ij}\}$ can be formulated as an LPP in the following manner. Let the objective function c be specified by

$$c = k. \tag{9}$$

One set of constraints are

$$\xi_i^\mu \sum_{j=1}^{N} J_{ij}\xi_j^\mu - k > 0. \tag{10}$$

The other set of constraints are the normalization bounds specified by (6). The problem is to maximise c subject to (10) and (6) which are a set of $pN + N(N-1)$ linear constraints.

The $\{J_{ij}\}$ can be positive or negative, whereas in the canonical formulation of LPP, negative values for the variables are not permissible. Therefore a new variable

J'_{ij} is defined as

$$J'_{ij} = J_{ij} + J_{\max}. \tag{11}$$

Substituting for J_{ij} in (10) and (6) from (11) one obtains

$$\xi_i^\mu \sum_{j=1}^{N} J'_{ij}\xi_j^\mu - k > \xi_i^\mu \left[\sum_{j \neq i} \xi_j^\mu \right] J_{\max} \tag{12}$$

and

$$J'_{ij} > 0 \tag{13}$$

$$J'_{ij} < 2J_{\max} \tag{14}$$

for all i, j and μ. The diagonal J'_{ii} are presumed to be 0. The standard requirement that the variables must have positive values is met by (13) while (14) provides positive bounds on $\{J'_{ij}\}$. These bounds eliminate the possibility of an unbounded optimum. The final formulation is then, maximise $c = k$ subject to (12) and (14). This formulation is only marginally different from that of Krauth and Mezard [11].

4. Numerical simulation

The principal aim of the numerical simulation reported here is to compare the performances of Gardner's version of iterative rule and the linear programming rule. Throughout the simulations N is assumed to be 100. The performance of a learning rule is evaluated as follows. Firstly a value of p is chosen between 1 and N, and that many unbiased patterns are generated. The interaction strengths are computed next using the learning rule to be evaluated. One of the stored patterns, say $\{\xi_i^\nu : i = 1, \ldots, N\}$, is selected as a test pattern and is persisted with throughout the evaluation. The test pattern is corrupted by selecting IN (denotes Input Noise) sites randomly and inverting the spin values there. Using the result as the input key, the network is used to recall the original test pattern. For a given value of IN, a total of ten recall experiments are carried out. In each case the overlap, m, of the recalled state, $\{\sigma_i\}$, with the original test pattern is computed using

$$m = \frac{1}{N} \sum_{i=1}^{N} \sigma_i \xi_i^\nu,$$

and the average of these ten overlaps is evaluated. By varying $\alpha = p/N$ from $5/N$ to 1 and IN from 0 to 50, a surface of overlaps over the phase plane $\alpha \times$ IN is obtained. The shape of the surface by itself is an indicator of the efficacy of the learning rule being evaluated. Let an overlap value greater than or equal to 0·99 in a recall experiment be termed a success. By sectioning the overlap surface with a $m = 0{\cdot}99$ plane parallel to the phase plane, a contour line of IN as a function of α is obtained. It is easy to see that the value of IN on this line at a given α is an experimental measure of the radius of the basin of attraction, r, around the test pattern. This line separates the phase plane into two regions in one of which the network functions as useful associative memory. Thus, the shape and location of this line on the phase plane is a good index of performance of the

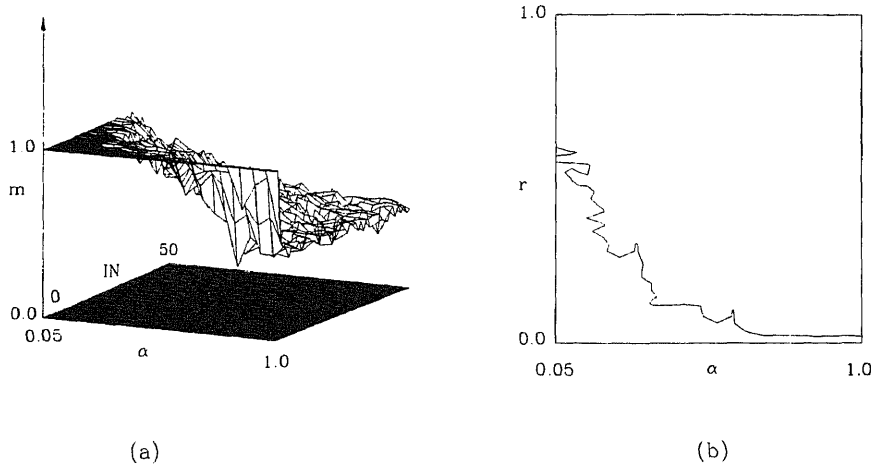

Figure 1. The surface of overlaps (m) between recalled patterns and the original test pattern is shown in (**a**) for the iterative learning rule. The number of bits selected randomly and reversed in the test pattern to generate the input key for recall experiments is represented by IN. The variable α denotes the storage capacity p/N. The contour line on the surface of overlaps at a value of $m = 0{\cdot}99$ is shown in (**b**). This contour line represents the radius of the basin of attraction of the test pattern as a function of α. The value of the parameter k is 10.

The evaluation of Gardner's version of iterative rule has been done taking the value of k to be 10. Also, to make the comparison with the linear programming rule meaningful, instead of using (5), eq. (6) is used for the normalization of $\{J'_{ij}\}$. That is, the mask ε_i^μ is defined as

$$\varepsilon_i^\mu = \theta\left[k - \sum_{j=1}^{N} J_{ij}\xi_i^\mu \xi_j^\mu\right]. \tag{15}$$

While updating $\{J_{ij}\}$, condition (6) is enforced by clipping those values of $|J_{ij}|$ which exceed J_{max}. A value 10 is assumed for J_{max}. With constant magnitude of the correction term ΔJ_{ij} in (8), convergence has been found to be slow and sometimes impossible. Attenuating the correction term progressively as the iterations proceed has helped to speed up the convergence. Assuming a maximum permissible number of iterations, the correction term was linearly attenuated from a maximum value of 1 to a minimum value of 0. The resulting overlap surface and the $m = 0{\cdot}99$ contour line for the iterative rule are shown in figure 1.

Evaluation of the linear programming rule, however, runs into implementational problems as a direct employment of the simplex algorithm would require a huge amount of computer memory. With $N = 100$, the size of the co-efficient matrix representing constraints (12) and (14) would be of the order of 10^8. Such a size cannot be accommodated within the memories of standard workstations which usually have memories of the order of 10^6 to 10^7. Therefore a subdivision of the LPP becomes necessary. In this context it may be noted that the constraints (12) decouple into N independent sets of constraints one set for each i. Optimization of k for each set using

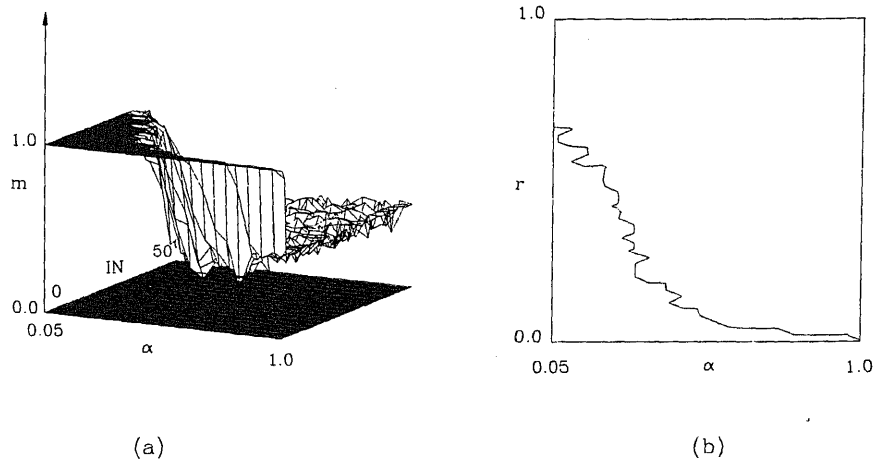

Figure 2. The surface of overlaps (m) and the $m = 0{\cdot}99$ contour line in the case of the linear programming rule. The meaning of the variables and parameters is the same as given for figure 1. The value of J_{max} is 10.

the simplex algorithm will result in the computations of $\{J'_{ij}: j = 1, \ldots, N\}$ for the corresponding i. The entire set of $\{J'_{ij}\}$ can be computed by employing the simplex method for $i = 1, \ldots, N$, individually. This scheme requires memory of the order of 10^4 which is manageable. Keeping the co-efficient matrix small also helps in limiting the numerical round-off and truncation errors. However, a side effect of this scheme of computing $\{J_{ij}\}$ is the dependence of optimal k on i. In the actual simulation, k as a function of i has been found to vary only slightly. In fact, the standard deviation of k's for various i's turns out to be less than 5%. For J_{max} a value of 10 is assumed, as in the case of the iterative rule. The simplex implementation due to Press *et al* [17] has been used in the computations. The overlap surface and the corresponding $m = 0{\cdot}99$ contour-line for the linear programming rule are shown in figure 2.

Qualitatively the linear programming rule appears to perform better than the iterative one. The overlap surface bounded between the contour line and the origin is flat with fewer undulations compared to that of the iterative rule implying error-free recall in that region of the phase plane. For a close visual comparison the $m = 0{\cdot}99$ contour lines of both the rules are shown together in figure 3. In view of the fact that only ten recall experiments are carried out at each point to determine the overlap, the error margins on these contour lines are likely to be high. Nevertheless from the general trend of these lines, linear programming rule appears to perform better than the iterative one, though towards the $\alpha = 1{\cdot}0$ limit the contour lines tend to coincide. This is expected, because the optimal values of k around $\alpha = 1{\cdot}0$ as found by the linear programming rule turn out to be close to 10. The optimal values of k as a function of α decrease with increasing α which is again expected. Fewer patterns mean larger basins of attraction for each one of them and vice versa. For a visual comparison of the performances of linear programming and iterative rules with that of Hebb rule, the interested reader may refer to figure 4.

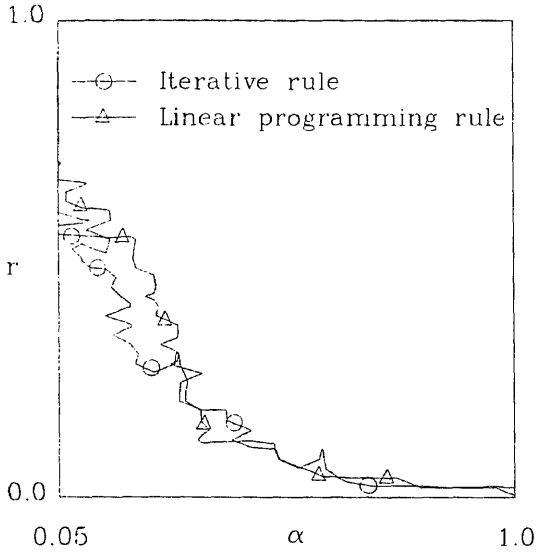

Figure 3. For a close comparison, $m = 0{\cdot}99$ contour lines in figures 1 and 2 are shown together here. The line with circles corresponds to the iterative rule while that with triangles corresponds to the linear programming rule. For a substantial part of the α axis, the linear programming rule has a larger radius of basin of attraction compared to the iterative rule.

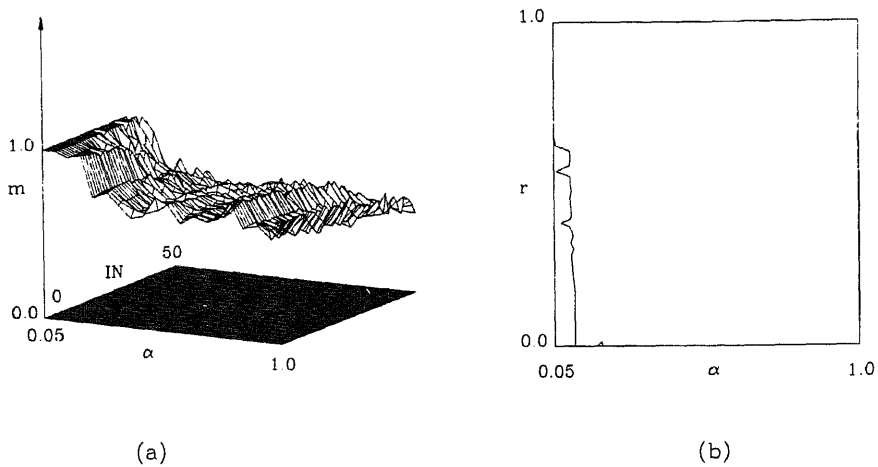

Figure 4. The surface of overlaps (m) and the $m = 0{\cdot}99$ contour line are shown here for the Hebb learning rule. The meaning of the variables and parameters is the same as given for figure 1.

As mentioned earlier, the near perfect flatness on the overlap surface corresponding to the linear programming rule suggests perfect recall in that region of the phase plane. To confirm that, recall experiments are carried out on either side of the $m = 0{\cdot}99$

Table 1. A comparison of the transition from perfect recall performance to no proper recall for two learning rules is presented in this table. In the first column α denotes the storage capacity p/N. While n_u denotes the maximal number of bit changes which ensures perfect recall, n_l denotes the minimal number of bit changes which results in no proper recall. In each case a hundred recall experiments have been carried out for determining these numbers.

	Iterative rule		Linear programming rule	
α	n_u	n_l	n_u	n_l
0·1	18	47	30	48
0·2	1	38	21	42
0·3	1	29	13	32
0·4	1	24	9	21
0·5	1	21	3	10

contour line along the IN axis. A total of 100 experiments are carried out at some discrete intervals of α and at various values of IN. For a given α, a threshold value of IN, n_l, above the contour line is found beyond which none of the 100 experiments results in a perfect recall. Similarly a threshold value of IN, n_u, below the contour line is found so that everyone of the experiments results in a perfect recall. The values of n_u and n_l are presented in table 1 for five different values of α, for both the iterative and the linear programming rules. These data confirm the perfect performance of the linear programming rule over a much larger region of the phase plane compared to the iterative rule. Also the transition from perfect performance to total failure is narrower in the case of the linear programming rule.

5. Maximal basins of attraction

In the evaluation of the linear programming rule, it is presumed that the weights for patterns are equal. As a result the basins of attraction around each one of the patterns are likely to be approximately of the same size. Given a set of patterns, the inter-pattern distances in the state space of the network are bound to have a spread. Therefore some patterns can afford to have larger basins of attraction compared to others so that the state space is more optimally utilised. However, with equal weights for all patterns such an eventuality may not be explicitly realized. Ideally, the basins of attraction for various patterns should close out any gap between them and be tangential to each other. Such an ideal situation may be obtained as follows.

Let the p patterns be conceived as p points in the state space. Then the task is to find maximal hyperspheres centred around each point such that these hyperspheres do not intersect each other but are just mutually tangential. The radii of these hyperspheres can be characterized as follows. Let hyperspheres with zero initial radii around each one of the p points expand at a uniform rate. Once two or more hyperspheres come in contact, they shall stop expanding and their radii reach their final

values. Once all expansion stops, the radii of the frozen hyperspheres become the maximal radii associated with the corresponding points. The assumption of uniform rate of expansion ensures equal rights for all patterns to the space around them. The following procedure which is a heuristic one finds close approximations to these radii using suitable metric.

Firstly, for each point, its nearest neighbour is found. The initial approximation to the radius of the maximal hypersphere at that point is assigned as half the distance to its nearest neighbour. After this step, all the points are sorted with respect to their initial radii in ascending order. For each point i, beginning with the first point in the sorted array, it is checked whether that point and its nearest neighbour are mutual nearest neighbours. If yes, then the initial approximate radii are taken as the final radii for both. If not, maximum permissible radius for the point i is computed as the distance to its neighbour minus the current radius associated with the neighbour. This maximum permissible radius is checked against the current radii of all other points to see if corresponding hyperspheres intersect. During this check, the maximum permissible radius is updated if necessary. At the end of this check, the final value of maximum permissible radius is assigned as the radius of the maximal hypersphere at point i. Once all the points are assigned their radii, the procedure stops. More details of this procedure are given in appendix-1.

To verify the above procedure, maximal circles for several sets of 50 points within a square have been computed. A sample output of the algorithm is illustrated in figure 5. The radii of these maximal circles can, of course, be computed by brute force simulation of the problem scenario assuming a small though finite incremental step for expanding the radii. In practice it has been found that the above heuristic algorithm could compute about 95% of the radii correctly; also, the error in the remaining 5% cases was found to be within 20% of the correct values.

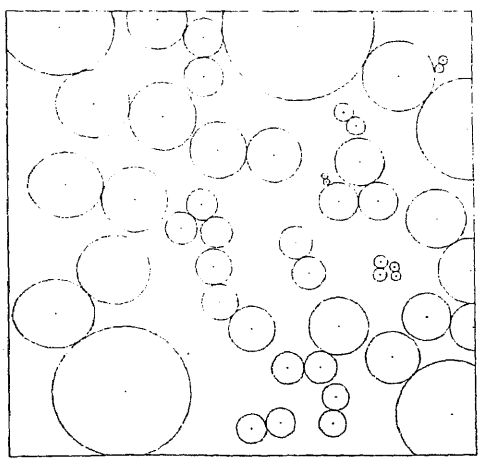

Figure 5. A sample set of fifty random points inside a square on a plane with maximal circles around each one of them. The radii of these circles are computed by an algorithm described in text.

Let the radii for maximal hyperspheres around patterns be denoted by γ^μ. Using these γ^μ's as weight factors for the patterns, condition (10) may be written as

$$\xi_i^\mu \sum_{j=1}^{N} J_{ij}\xi_j^\mu - k\gamma^\mu > 0. \tag{16}$$

The linear programming rule may be employed to maximise k subject to (16) and (6). The outcome is bound to be the maximum possible utilization of the state space to carve out the various basins of attraction. To verify this assertion, the Monte-Carlo method has been employed to compute the fractional volume of basins of attraction. A total of 10000 recall experiments are carried out starting from random input patterns. Each time the recalled state is compared with all the stored patterns and the maximum overlap is computed. If the overlap is above or equal to a preselected threshold the random input pattern is deemed to be inside the basin of attraction; else outside. The fractional volume of basins attraction is then computed as the ratio of the random input patterns that are found to be inside the basins to the total number of experiments.

Employing this method the fractional volumes of basins of attraction have been computed for three cases; firstly for the linear programming rule with radii of maximal hyperspheres around patterns as their weights; secondly for the linear programming rule with equal weights for the patterns; thirdly for the iterative rule. Hamming metric is used while computing the radii of maximal hyperspheres. The fractional volumes are computed as a function of α from $\alpha = 0{\cdot}05$ to $\alpha = 0{\cdot}5$. The value of α is increased by

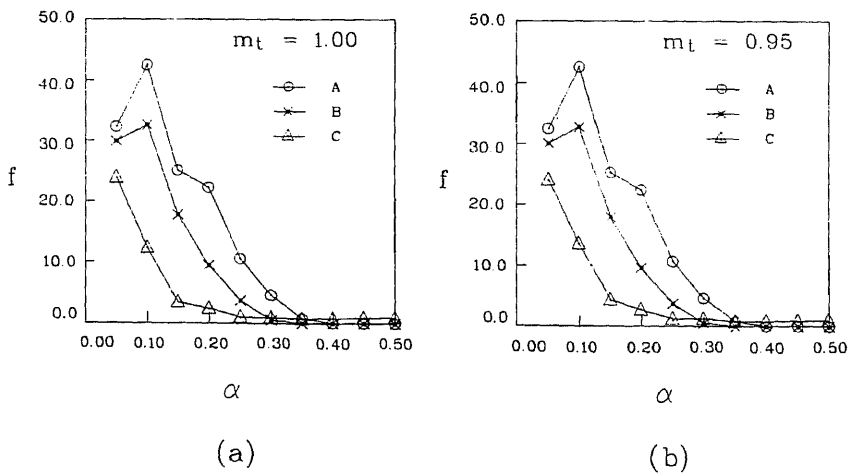

Figure 6. Fractional volume, f, of basins of attraction for stored patterns as a function of storage capacity α is shown here. Line A corresponds to the case of linear programming rule with radii of maximal hyperspheres around stored patterns as weights for these patterns. Line B corresponds to the case of the same rule with equal weights for the patterns. Line C corresponds to the iterative rule. Figure 6a represents the case of basins whose minima have 100% overlap with stored patterns. Figure 6b represents the case of basins with one or more local minima whose overlaps with stored patterns are greater than or equal to 95%.

adding the required number of additional patterns to the set of already existing ones. The results of the Monte-Carlo experiments are presented in figure 6. Figure 6a corresponds to the overlap threshold of value 1·0 while figure 6b corresponds to a value of 0·95. As remarked earlier, the first case utilizes the state space most optimally. Also, the difference between the second and first cases is quite pronounced, implying that the use of maximal radii as weights for the patterns further improves the sizes of the basins of attraction wherever possible.

6. Discussions and conclusions

A striking feature of the LP rule is the sharp transition exhibited by its overlap surface. In contrast, the overlap surface corresponding to the iterative rule shows a gradual downward trend as IN and α increase. Though a steady degradation in performance is desirable, a sharp fall in the recalling ability has its advantage. If an input key does not match with any of the stored patterns then the linear programming rule is capable of reporting a clear failure. Such an ability may be valuable in cognitive modelling. Another important aspect of the linear programming rule is the associated linear normalizing bounds on the $\{J_{ij}\}$. This aspect will be useful in designing VLSI neural chips with finite precision synaptic strengths. Limiting the magnitude of interaction strengths is also biologically meaningful as biological synapses cannot represent strengths of arbitrary precision.

Results of the computer simulations suggest that the basins of attraction in case of linear programming rule have smooth shapes converging to unique local minima. Thus, when an input key falls within a specific basin of attraction it leads to the recalling of the corresponding pattern without any error. Both the flatness on the overlap surface in figure 2 and the high values of n_u in table 1 corroborate this fact. Further evidence is available from data presented in figure 6. The dependence of f on α in cases A and B as shown in the figure has been observed to be invariant with respect to the two values of threshold overlaps implying the presence of unique local minima. With the iterative rule, however, f as a function of α has been found to depend on threshold overlaps.

The radius of the maximal hypersphere around a pattern as defined in the previous section gives an estimate of noise which the pattern can tolerate without losing its uniqueness. In that sense these radii could be useful in the study of associative memory and pattern recognition models. The procedure outlined earlier for computing radii of the maximal hyperspheres requires computing time of the order of $O(p^2)$ where p is the number of patterns. It is not an exact algorithm, though its solutions in hundreds of test cases in two-dimensions have proved to be satisfactory. Developing an exact algorithm based on either an 'incremental' or 'divide and conquer' approach may prove to be a worthwhile exercise.

Maximal possible utilization of the state space of the network is demonstrated employing linear programming rule with differentiated weight factors for the patterns. A trivial approach to find the closest match is, of course, to compute distances between the input and all the patterns to be stored and then select one of the latter that is least distant from the input. It is instructive to know that the basins of attractions in such an approach are nothing but Voronoi polytopes which cover the state space completely. This is a most ideal situation, which may not be achieved by the Hopfield network.

As pointed out earlier, the computational approach adopted here for implementing the linear programming rule makes the sizes of the basins of attraction depend on the neuronal index i. During computer simulations, however, this dependence was found to be small. As the standard Hopfield network is homogeneous, it is necessary that its performance parameters are independent of neuronal indices. In its extensions where homogeneity may not be desirable, making the sizes of basins of attraction depend on neuronal indices may be functionally necessary. The human brain, it may be noted, is highly differentiated even in regions dedicated to specialized tasks and any attempt in understanding it should consider heterogeneous networks sooner or later.

Acknowledgements

The author thanks Prof. Dipan K Ghosh and Dr G Venkataraman for their help and guidance at various stages of the work reported here.

Appendix 1

```
Procedure FindRadiiMaxHyperspheres (p)
    p:Number of points
{
    For each point i
    {
      RadiiAssignedFlags [i] = − 1;
      For each point j ≠ i
        Compute Distance [i,j];
      Compute its nearest neighbour, k;
      NearNeighbour [i] = k;
      Set the initial approximation to the radius of hypersphere at i as
      Radii [i] = Distance [i, k]*0·5;
    }
    Sort the points with their associated radii in ascending order;
    Initialize a pointcounter to 1;
Step L:  Pickup the current point, i, from the sorted points array
    If RadiiAssignedFlags [i] = − 1) then{
      Neighbour = NearNeighbour [i];
      If (i = NearNeighbour [Neighbour]) Then
      {
        RadiiAssignedFlags [i] = 1;
        RadiiAssignedFlags [Neighbour] = 1;
      }
      Else
      {
        MaxRadius = Distance [i, Neighbour] − Radii [Neighbour];
        For each point j ≠ i
          If  (Distance [i,j] < MaxRadius + Radii [j])
              MaxRadius = Distance [i,j] − Radii [j];
```

```
            Radii [i] = MaxRadius;
            RadiiAssignedFlags [i] = 1;
          }
        }
      }
      Increment pointcounter by 1;
      If (pointcounter < = p) Go To Step L;
      Else
        STOP;
}
```

References

[1] W S McCulloch and W A Pitts, *Bull. Math. Biophys.* **5**, 115 (1943)
[2] J J Hopfield, *Proc. Natl. Acad. Sci. USA* **79**, 2554 (1982)
[3] D O Hebb, *Organisation of behaviour* (New York: Wiley, 1949)
[4] D J Amit, H Gutfreund and H Sompolinsky, *Ann. Phys. NY* **173**, 30 (1987)
[5] L Personnaz, L Guyon and G Dreyfus, *J. Phys. Lett.* **46**, L359 (1985)
[6] D J Willshaw, O P Buneman and H C Languet-Higgins, *Nature* (*London*) **222**, 960
[7] E Domany, J L van Hemmen and K Shulten (eds), *Models of neural networks* (
Heidelberg: Springer Verlag, 1991)
[8] E Gardner, *Europhys. Lett.* **4**, 481 (1987)
[9] G Poeppel and U Krey, *Europhys. Lett.* **4**, 979 (1988)
[10] S Diederich and M Opper, *Phys. Rev. Lett.* **58**, 949 (1987)
[11] W Krauth and M Mezard, *J. Phys.* **A20**, L745 (1987)
[12] B Forrest, *J. Phys.* **A21**, 245 (1988)
[13] L F Abbott and T B Kepler, *J. Phys.* **A22**, L711 (1989)
[14] J K Anlauf and M Biehl, *Europhys. Lett.* **10**, 687 (1989)
[15] E Gardner, *J. Phys.* **A21**, 257 (1988)
[16] M Griniasty and H Gutfreund, *J. Phys.* **A24**, 715 (1991)
[17] W H Press, S A Teukolsky, W T Vellerling and B P Flannery, *Numerical rec*
C (Cambridge University Press, 1992)

SUBJECT INDEX

General and Mathematical Physics

Generalized Fock spaces, new forms of quantum statistics and their algebras — *A K Mishra and G Rajasekaran* — 91–139

Time dependent canonical perturbation theory I: General theory — *B R Sitaram and Mitaxi P Mehta* — 141–148

Time dependent canonical perturbation theory II: Application to the Henon–Heiles system — *Mitaxi P Mehta and B R Sitaram* — 149–164

The Coulomb Green's function revisited — *S S Vasan and M Seetharaman* — 165–174

Painlevé analysis and integrability of the damped anharmonic oscillator equation — *S Paul Raj and S Rajasekar* — 305–309

The particle in a box problem in q-quantum mechanics — *G Vinod, K Babu Joseph and K M Valsamma* — 311–317

Polarized light — *G Ramachandran, A R Usha Devi and N S Saandeep Kannadavardhana* — 319–326

On the Dirac equation with anomalous magnetic moment term in a beam of electromagnetic wave — *N D Sen Gupta* — 327–331

Controlling chaos: Stabilization of unstable orbits using exponential control for maps and flows — *Sangeeta D Gadre and V S Varma* — 355–368

The real symplectic groups in quantum mechanics and optics — *Arvind, B Dutta, N Mukunda and R Simon* — 471–497

Optical theorem and Aharonov-Bohm scattering — *M M Panja, P K Bera and B Talukdar* — 499–509

Relativity and Gravitation

Gravitational and electromagnetic fields of a charged tachyon — *K S Virbhadra* — 175–179

A radiating dyon solution — *A Chamorro and K S Virbhadra* — 181–187

Static models of cosmic strings in general relativity — *G P Singh* — 189–193

BD-FRW models in the framework of Israel–Stewart–Hiscock theory — *Kalyani Desikan* — 511–517

Statistical Physics

Macroscopic equation of motion in inhomogeneous media: A microscopic treatment — *A M Jayannavar and Mangal C Mahato* — 369–376

A comparative study of two learning rules for associative memory — *G Athithan* — 569–582

Particle Physics

Neutrino emissivity of quark matter at finite temperatures — *V K Gupta, A Wadhwa and J D Anand* — 195–208

Search for the χ_c' charmonium states as solution to the CDF ψ' puzzle — *S F Tuan* — 209–214

Fermilab top mass and modified Fritzsch mass matrices — *P S Gill and Manmohan Gupta* — 333–342

Vacuum structure, chiral symmetry breaking and electric dipole moment of neutron — *A R Panda and K C Roy* — 343–353

Nuclear Physics

Fission fragment angular distribution in alpha-particle-induced fission of actinide elements — *R K Jain, S K Bose and J Rama Rao* — 519–531

Atomic and Molecular Physics

Triple differential cross sections for ionization of hydrogen atoms by positrons in a Schwinger variational calculation — *J N Das, A Dey and K Chakrabarti* — 41–46

Bound state population and dissociation dynamics of a Morse oscillator with oscillating well-depth and driven by intense radiation: Perturbative and numerical studies — *Pranab Sarkar and S P Bhattacharyya* — 47–63

Electronegativity and hardness profiles of a chemical process: Comparison between quantum fluid density functional theory and *ab initio* SCF method — *S Nath and P K Chattaraj* — 65–73

The inversion potential for NH_3 and its isotopic species
A N Aquino, A Palma, J L López and M A Rosales 75–80

Relativistic correction to the dipole polarizability of a hydrogenic ion
K L Baluja 533–536

Systematic trends in the line strengths and radial matrix elements of E1 transitions in the Be isoelectronic sequence
Anand Bharadvaja and K L Baluja 537–543

Propagation of a wave packet on a model fractal lattice
P K Chattaraj and S Nath 545–560

Lasers, Optics and Spectroscopy

Two photon absorption spectrum of *p*-dichlorobenzene
I B Singh, S B Rai and D K Rai 271–278

Picosecond time-resolved laser emission of coumarin 102: Solvent relaxation
S R Inamdar, K Chandrasekhar, D C Patil, N N Math and M I Savadatti 279–290

Generation of picosecond optical pulses from single heterostructure GaAs diode laser and study of their emission characteristics
V N Rai, M Shukla and H C Pant 439–451

Plasma Physics

Streaming instability of a dusty plasma in the presence of mass and charge variation *B P Pandey and C B Dwivedi* 255–260

Ion cyclotron instabilities in a mildly relativistic hydrogen-deuterium fusion plasma *Chandu Venugopal, P J Kurian and G Renuka* 453–462

Kinetic description of ion acoustic waves in a dusty plasma
B P Pandey and Susheel Kumar 561–567

Condensed Matter Physics

Diffusing wave spectroscopy of dense colloids: Liquid, crystal and glassy states *Subrata Sanyal and Ajay K Sood* 1–17

A comparative dielectric relaxation study between hydrogen- and non-hydrogen-bonded liquids: Nitriles vs alcohols
S N Helambe, M P Lokhande, A C Kumbharkhane and S C Mehrotra 19–24

Phonon dispersion in quasiperiodic semiconductor superlattices
Sujata Rath, P K Jha and S P Sanyal 25–32

Effect of crystal field on the spin density at the copper nucleus in copper complexes *V Gomathy, U S Ghosh and C Basu* 33–39

Theoretical calculation of acoustic non-linearity parameter B/A of binary mixtures *J Jugan, Roshan Abraham and M Abdulkhadar* 221–226

Gyrotropic and piezoelectric coefficients and attenuation of elastic waves in $BaTiO_3$ *B Subramanyam* 227–234

Heat capacity and phonons in poly(L-leucine) *Seema Srivastava, Poonam Tandon, V D Gupta, Shantanu Rastogi, S B Katti and L Burman* 235–254

Geometry effect on the nonlinear magnetic response of $YBa_2Cu_3O_{7-y}$ *Parshant Batham, S B Roy, Shailendra Kumar, A K Pradhan, A K Grover, P Chaddah, Ram Prasad and N C Soni* 261–269

Microscopic theory of single particle and pair condensation of an attracting Bose gas as the basis for superfluidity and superconductivity *S Dzhumanov and P K Khabibullaev* 385–418

Nonlinear dynamics of a two-dimensional lattice *Nabonita D Chowdhury and Sankar P Sanyal* 377–384

Temperature dependence electron spin resonance spectra of a magnetic fluid *R V Upadhyay, D Srinivas, R V Mehta and P M Trivedi* 419–430

Dielectric properties of nano-particles of zinc sulphide *Binny Thomas and M Abdulkhadar* 431–438

Experimental Techniques and Instrumentation

A low cost PC based card for heat-capacity measurements at low temperatures *R S Sannabhadti, S Ramakrishnan, K Ghosh, Arun Patade and Girish Chandra* 81–89

Development of an experimental facility for studying atomic-field, bremsstrahlung from keV electrons interacting with atoms and molecules *S K Goel, M J Singh and R Shanker* 291–304

Brief Report

Energy and momentum of cylindrical gravitational waves-II *K S Virbhadra* 215–219

Rapid Communication

Estimation of parameters of gravitational waves from coalescing binaries
R Balasubramanian, B S Sathyaprakash and S V Dhurandhar L463–L470

AUTHOR INDEX

Abdulkhadar M
see Jugan J 221
Abraham Roshan
see Jugan J 221
Anand J D
see Gupta V K 195
Aquino A N
The inversion potential for NH_3 and its isotopic species 75
Arvind
The real symplectic groups in quantum mechanics and optics 471
Athithan G
A comparative study of two learning rules for associative memory 569

Babu Joseph K
see Vinod G 311
Balasubramanian R
Estimation of parameters of gravitational waves from coalescing binaries L463
Baluja K L
Relativistic correction to the dipole polarizability of a hydrogenic ion 533
see Bharadvaja Anand 537
Basu C
see Gomathy V 33
Batham Parshant
Geometry effect on the nonlinear magnetic response of $YBa_2Cu_3O_{7-y}$ 261
Bera P K
see Panja M M 499
Bharadvaja Anand
Systematic trends in the line strengths and radial matrix elements of E1 transitions in the Be isoelectronic sequence 537
Bhattacharyya S P
see Sarkar Pranab 47
Bose S K
see Jain R K 519
Burman L
see Srivastava Seema 235

Chaddah P
see Batham Parshant 261
Chakrabarti K
see Das J N 41
Chamorro A
A radiating dyon solution 181
Chandra Girish
see Sannabhadti R S 81
Chandrasekhar K
see Inamdar S R 279
Chattaraj P K
see Nath S 65
Propagation of a wave packet on a model fractal lattice 545
Chowdhury Nabonita D
Nonlinear dynamics of a two-dimensional lattice 377

Das J N
Triple differential cross sections for ionization of hydrogen atoms by positrons in a Schwinger variational calculation 41
Desikan Kalyani
BD-FRW models in the framework of Israel–Stewart–Hiscock theory 511
Dey A
see Das J N 41
Dhurandhar S V
see Balasubramanian R L463
Dutta B
see Arvind 471
Dwivedi C B
see Pandey B P 255
Dzhumanov S
Microscopic theory of single particle and pair condensation of an attracting Bose gas as the basis for superfluidity and superconductivity 385

Gadre Sangeeta D
Controlling chaos: Stabilization of unstable orbits using exponential control for maps and flows 355
Ghosh K
see Sannabhadti R S 81
Ghosh U S
see Gomathy V 33
Gill P S
Fermilab top mass and modified Fritzsch mass matrices 333
Goel S K
Development of an experimental facility for studying atomic-field, bremsstrahlung from keV electrons interacting with atoms and molecules 291
Gomathy V
Effect of crystal field on the spin density at the copper nucleus in copper complexes 33

Grover A K
see Batham Parshant 261
Gupta Manmohan
see Gill P S 333
Gupta V D
see Srivastava Seema 235
Gupta V K
Neutrino emissivity of quark matter at finite temperatures 195

Helambe S N
A comparative dielectric relaxation study between hydrogen- and non-hydrogen-bonded liquids: Nitriles vs alcohols 19

Inamdar S R
Picosecond time-resolved laser emission of coumarin 102: Solvent relaxation 279

Jain R K
Fission fragment angular distribution in alpha-particle-induced fission of actinide elements 519
Jayannavar A M
Macroscopic equation of motion in inhomogeneous media: A microscopic treatment 369
Jha P K
see Rath Sujata 25
Jugan J
Theoretical calculation of acoustic nonlinearity parameter B/A of binary mixtures 221

Katti S B
see Srivastava Seema 235
Khabibullaev P K
see Dzhumanov S 385
Khadar M Abdul
see Thomas Binny 431
Kumar Shailendra
see Batham Parshant 261
Kumar Susheel
see Pandey B P 561
Kumbharkhane A C
see Helambe S N 19
Kurian P J
see Venugopal Chandu 453

Lokhande M P
see Helambe S N 19
López J L
see Aquino A N 75

Mahato Mangal C
see Jayannavar A M 369
Math N N
see Inamdar S R 279
Mehrotra S C
see Helambe S N 19
Mehta Mitaxi P
see Sitaram B R 141
Time dependent canonical perturbation theory II: Application to the Henon–Heiles system 149
Mehta R V
see Upadhyay R V 419
Mishra A K
Generalized Fock spaces, new forms of quantum statistics and their algebras 91
Mukunda N
see Arvind 471

Nath S
Electronegativity and hardness profiles of a chemical process: Comparison between quantum fluid density functional theory and *ab initio* SCF method 65
see Chattaraj P K 545

Palma A
see Aquino A N 75
Panda A R
Vacuum structure, chiral symmetry breaking and electric dipole moment of neutron 343
Pandey B P
Streaming instability of a dusty plasma in the presence of mass and charge variation 255
Kinetic description of ion acoustic waves in a dusty plasma 561
Panja M M
Optical theorem and Aharonov–Bohm scattering 499
Pant H C
see Rai V N 439
Patade Arun
see Sannabhadti R S 81
Patil D C
see Inamdar S R 279
Paul Raj S
Painlevé analysis and integrability of the damped anharmonic oscillator equation 305
Pradhan A K
see Batham Parshant 261
Prasad Ram
see Batham Parshant 261

Rai D K
see Singh I B 271
Rai S B
see Singh I B 271

Rai V N
Generation of picosecond optical pulses from single heterostructure GaAs diode laser and study of their emission characteristics 439
Rajasekar S
see Paul Raj S 305
Rajasekaran G
see Mishra A K 91
Ramachandran G
Polarized light 319
Ramakrishnan S
see Sannabhadti R S 81
Rama Rao J
see Jain R K 519
Rastogi Shantanu
see Srivastava Seema 235
Rath Sujata
Phonon dispersion in quasiperiodic semiconductor superlattices 25
Renuka G
see Venugopal Chandu 453
Rosales M A
see Aquino A N 75
Roy K C
see Panda A R 343
Roy S B
see Batham Parshant 261

Saandeep Kannadavardhana N S
see Ramachandran G 319
Sannabhadti R S
A low cost PC based card for heat-capacity measurements at low temperatures 81
Sanyal S P
see Rath Sujata 25
Sanyal Sankar P
see Chowdhury Nabonita D 439
Sanyal Subrata
Diffusing wave spectroscopy of dense colloids: Liquid, crystal and glassy states 1
Sarkar Pranab
Bound state population and dissociation dynamics of a Morse oscillator with oscillating well-depth and driven by intense radiation: Perturbative and numerical studies 47
Sathyaprakash B S
see Balasubramanian R L463
Savadatti M I
see Inamdar S R 279
Seetharaman M
see Vasan S S 165
Sen Gupta N D
On the Dirac equation with anomalous magnetic moment term in a beam of electromagnetic wave 327
Shanker R
see Goel S K 291
Shukla M
see Rai V N 439
Simon R
see Arvind 471
Singh G P
Static models of cosmic strings in general relativity 189
Singh I B
Two photon absorption spectrum of *p*-dichlorobenzene 271
Singh M J
see Goel S K 291
Sitaram B R
Time dependent canonical perturbation theory I: General theory 141
see Mehta Mitaxi P 149
Soni N C
see Batham Parshant 261
Sood Ajay K
see Sanyal Subrata 1
Srinivas D
see Upadhyay R V 419
Srivastava Seema
Heat capacity and phonons in poly(L-leucine) 235
Subramanyam B
Gyrotropic and piezoelectric coefficients and attenuation of elastic waves in $BaTiO_3$ 227

Talukdar B
see Panja M M 499
Tandon Poonam
see Srivastava Seema 235
Thomas Binny
Dielectric properties of nanoparticles of zinc sulphide 431
Trivedi P M
see Upadhyay R V 419
Tuan S F
Search for the χ_c charmonium states as solution to the CDF ψ' puzzle 209

Upadhyay R V
Temperature dependence electron spin resonance spectra of a magnetic fluid 419
Usha Devi A R
see Ramachandran G 319

Valsamma K M
see Vinod G 311
Varma V S
see Gadre Sangeeta D 355
Vasan S S
The Coulomb Green's function revisited 165
Venugopal Chandu
Ion cyclotron instabilities in a mildly relativistic hydrogen-deuterium fusion plasma 453

Vinod G
The particle in a box problem in q-quantum mechanics 311
Virbhadra K S
Gravitational and electromagnetic fields of a charged tachyon 175
see Chamorro A 181
Energy and momentum of cylindrical gravitational waves-II 215

Wadhwa A
see Gupta V K 195

Pramana – journal of physics

Volume 45
1995

Published by The Indian Academy of Sciences
Bangalore 560 080

Editor

R Nityananda
Raman Research Institute, Bangalore

Associate Editor

H R Krishnamurthy
Indian Institute of Science, Bangalore

Editorial Board

G S Agarwal, *Physical Research Laboratory, Ahmedabad*
V Balakrishnan, *Indian Institute of Technology, Madras*
M Barma, *Tata Institute of Fundamental Research, Bombay*
P Chaddah, *Centre for Advanced Technology, Indore*
B M Deb, *Panjab University, Chandigarh*
P K Kaw, *Institute for Plasma Research, Gandhinagar*
H S Mani, *Indian Institute of Technology, Kanpur*
N Mukunda, *Indian Institute of Science, Bangalore*
T Padmanabhan, *Inter-University Centre for Astronomy and Astrophysics, Pune*
J C Parikh, *Physical Research Laboratory, Ahmedabad*
G Rajasekaran, *Institute of Mathematical Sciences, Madras*
V S Ramamurthy, *Department of Science and Technology, New Delhi*
R Ramaswamy, *Jawaharlal Nehru University, New Delhi*
K R Rao, *Bhabha Atomic Research Centre, Bombay*
Probir Roy, *Tata Institute of Fundamental Research, Bombay*
A K Sood, *Indian Institute of Science, Bangalore*

Editor of Publications of the Academy

V K Gaur
C-MMACS, NAL, Bangalore

Subscription Rates
(1996)

All countries except India	1 year
(Price includes AIR MAIL charges)	US$ 200
India	1 year Rs. 200

Annual subscriptions for **individuals** for India and abroad are Rs. 75/- and $50 respectively.

All correspondence regarding subscription should be addressed to the **Circulation Department** of the Academy

Editorial Office

Indian Academy of Sciences, C V Raman Avenue,
P.B. No. 8005, Bangalore 560 080, India

Telephone: 334 2546
Telex: 845-2178 ACAD IN
Telefax: 91-80-334 6094

© 1995 by the Indian Academy of Sciences. All rights reserved.

CONTENTS – VOLUME 45

(July–December 1995)

Number 1

Diffusing wave spectroscopy of dense colloids: Liquid, crystal and glassy states ..... *Subrata Sanyal and Ajay K Sood* 1

A comparative dielectric relaxation study between hydrogen- and non-hydrogen-bonded liquids: Nitriles vs alcohols ..... *S N Helambe, M P Lokhande, A C Kumbharkhane and S C Mehrotra* 19

Phonon dispersion in quasiperiodic semiconductor superlattices ..... *Sujata Rath, P K Jha and S P Sanyal* 25

Effect of crystal field on the spin density at the copper nucleus in copper complexes ..... *V Gomathy, U S Ghosh and C Basu* 33

Triple differential cross sections for ionization of hydrogen atoms by positrons in a Schwinger variational calculation ..... *J N Das, A Dey and K Chakrabarti* 41

Bound state population and dissociation dynamics of a Morse oscillator with oscillating well-depth and driven by intense radiation: Perturbative and numerical studies ..... *Pranab Sarkar and S P Bhattacharyya* 47

Electronegativity and hardness profiles of a chemical process: Comparison between quantum fluid density functional theory and *ab initio* SCF method ..... *S Nath and P K Chattaraj* 65

The inversion potential for NH_3 and its isotopic species ..... *A N Aquino, A Palma, J L López and M A Rosales* 75

A low cost PC based card for heat-capacity measurements at low temperatures ..... *R S Sannabhadti, S Ramakrishnan, K Ghosh, Arun Patade and Girish Chandra* 81

Number 2

Generalized Fock spaces, new forms of quantum statistics and their algebras ..... *A K Mishra and G Rajasekaran* 91

Time dependent canonical perturbation theory I: General theory ..... *B R Sitaram and Mitaxi P Mehta* 141

Time dependent canonical perturbation theory II: Application to the Henon–Heiles system ..... *Mitaxi P Mehta and B R Sitaram* 149

The Coulomb Green's function revisited.....
.....*S S Vasan and M Seetharaman* 165

Gravitational and electromagnetic fields of a charged tachyon.....
.....*K S Virbhadra* 175

A radiating dyon solution.....*A Chamorro and K S Virbhadra* 181

Static models of cosmic strings in general relativity.....*G P Singh* 189

Neutrino emissivity of quark matter at finite temperatures.....
.....*V K Gupta, A Wadhwa and J D Anand* 195

Search for the χ_c' charmonium states as solution to the CDF ψ' puzzle.....
.....*S F Tuan* 209

Brief Report

Energy and momentum of cylindrical gravitational waves-II.....
.....*K S Virbhadra* 215

Number 3

Theoretical calculation of acoustic non-linearity parameter B/A of binary mixtures.....*J Jugan, Roshan Abraham and M Abdulkhadar* 221

Gyrotropic and piezoelectric coefficients and attenuation of elastic waves in $BaTiO_3$.....*B Subramanyam* 227

Heat capacity and phonons in poly (L-leucine).....
.....*Seema Srivastava, Poonam Tandon, V D Gupta, Shantanu Rastogi, S B Katti and L Burman* 235

Streaming instability of a dusty plasma in the presence of mass and charge variation.....*B P Pandey and C B Dwivedi* 255

Geometry effect on the nonlinear magnetic response of $YBa_2Cu_3O_{7-y}$.....
.....*Parshant Batham, S B Roy, Shailendra Kumar, A K Pradhan, A K Grover, P Chaddah, Ram Prasad and N C Soni* 261

Two photon absorption spectrum of *p*-dichlorobenzene.....
.....*I B Singh, S B Rai and D K Rai* 271

Picosecond time-resolved laser emission of coumarin 102: Solvent relaxation
.....*S R Inamdar, K Chandrasekhar, D C Patil, N N Math and M I Savadatti* 279

Development of an experimental facility for studying atomic-field, bremsstrahlung from keV electrons interacting with atoms and molecules
.....*S K Goel, M J Singh and R Shanker* 291

The particle in a box problem in q-quantum mechanics.....
.....*G Vinod, K Babu Joseph and K M Valsamma* 311

Polarized light.....*G Ramachandran, A R Usha Devi and N S Saandeep Kannadavardhana* 319

On the Dirac equation with anomalous magnetic moment term in a beam of electromagnetic wave.....*N D Sen Gupta* 327

Fermilab top mass and modified Fritzsch mass matrices.....
.....*P S Gill and Manmohan Gupta* 333

Vacuum structure, chiral symmetry breaking and electric dipole moment of neutron.....*A R Panda and K C Roy* 343

Controlling chaos: Stabilization of unstable orbits using exponential control for maps and flows.....*Sangeeta D Gadre and V S Varma* 355

Macroscopic equation of motion in inhomogeneous media: A microscopic treatment.....*A M Jayannavar and Mangal C Mahato* 369

Number 5

Nonlinear dynamics of a two-dimensional lattice.....
.....*Nabonita D Chowdhury and Sankar P Sanyal* 377

Microscopic theory of single particle and pair condensation of an attracting Bose gas as the basis for superfluidity and superconductivity.....
.....*S Dzhumanov and P K Khabibullaev* 385

Temperature dependence electron spin resonance spectra of a magnetic fluid
.....*R V Upadhyay, D Srinivas, R V Mehta and P M Trivedi* 419

Dielectric properties of nano-particles of zinc sulphide.....
.....*Binny Thomas and M Abdulkhadar* 431

Generation of picosecond optical pulses from single heterostructure GaAs diode laser and study of their emission characteristics.....
.....*V N Rai, M Shukla and H C Pant* 439

Ion cyclotron instabilities in a mildly relativistic hydrogen-deuterium fusion plasma.....*Chandu Venugopal, P J Kurian and G Renuka* 453

Rapid Communication

Estimation of parameters of gravitational waves from coalescing binaries
.....*R Balasubramanian, B S Sathyaprakash and S V Dhurandhar* L463

Number 6

Review

The real symplectic groups in quantum mechanics and optics..... *Arvind, B Dutta, N Mukunda and R Simon* 471

Research articles

Optical theorem and Aharonov–Bohm scattering..... *M M Panja, P K Bera and B Talukdar* 499

BD-FRW models in the framework of Israel–Stewart–Hiscock theory..... *Kalyani Desikan* 511

Fission fragment angular distribution in alpha-particle-induced fission of actinide elements..... *R K Jain, S K Bose and J Rama Rao* 519

Relativistic correction to the dipole polarizability of a hydrogenic ion..... *K L Baluja* 533

Systematic trends in the line strengths and radial matrix elements of E1 transitions in the Be isoelectronic sequence..... *Anand Bharadvaja and K L Baluja* 537

Propagation of a wave packet on a model fractal lattice..... *P K Chattaraj and S Nath* 545

Kinetic description of ion acoustic waves in a dusty plasma..... *B P Pandey and Susheel Kumar* 561

A comparative study of two learning rules for associative memory..... *G Athithan* 569

Subject Index..... 583

Author Index..... 588

Volume Contents

Information for Contributors

Pramana – journal of physics

Information for contributors

Pramana – journal of physics welcomes articles communicating current research work in physics, which will be published subject to acceptability after referee and editorial assessment. Articles may be submitted under any of the following categories:

(1) **Research papers:** Normal full length papers which describe significant and substantial original work. These should not normally exceed 8000 words or equivalent in length.

(2) **Rapid Communications:** This will be processed faster by the journal. A need for urgent publication, as judged by our referees and editors, will be an important additional criterion in the acceptance of such contributions. The paper should describe the work concisely, being not longer than 2500 words or equivalent. A longer article, containing full details of the same work, can be separately entertained under category (1) above – (research papers).

(3) **Comments:** Comments on papers which have already appeared in Pramana, or **addenda** and **errata** to such papers by the authors themselves. These could be as short as a paragraph, but not ordinarily longer than 1000 words or equivalent.

(4) **Brief reports:** These should be short articles (less than 2500 words or equivalent) making specific technical points of interest to others in the area, even though the content may not be substantial enough to be considered under category 1.

Review articles: In addition to the different categories of papers mentioned above, Pramana now publishes review articles. These are by invitation and represent a scholarly review of an area of physics, with substantial references to the existing literature in the field. The invitations are generally initiated by the Editorial Board. However any author(s) with ideas for a potential review article are welcome to communicate to the Editors a synopsis and a detailed plan of the proposed review. This will be assessed and if found acceptable an invitation to contribute a review could result. All review articles are still refereed after their submittal.

Pramana also intends to publish topical reviews which are not necessarily comprehensive but represent a particularly interesting or important viewpoint (even if it is not universally accepted) since such articles can stimulate further work.

Authors wishing to have papers published in Pramana in any of the above categories should send them to the Editorial Office.

Three copies of the paper must be submitted.

The submission of a paper by a set of authors will be held to imply that it represents the results of their original research not previously published that

it is not under consideration for publication elsewhere; and that if accepted for Pramana it will not be published elsewhere.

Typescript: Papers must be written clearly and concisely in English, the preferred spelling being that of the Concise Oxford Dictionary. They must be typed double spaced with ample margin on all sides on white bond paper, 292 × 210 mm. This also applies to the abstract, tables, figure captions and the list of references each of which are to be typed on separate sheets.

Title Page: The first page must bear **a**) title of the paper **b**) the initials and the names of the authors **c**) names and addresses of the institutions where the work was carried out **d**) the permanent or present addresses of the authors, if different from c) and **e**) the Physics and Astronomy Classification Scheme Number for the manuscript. A copy of the scheme can be obtained from the Editorial Office. Authors should suggest an abbreviated running title of not more than 50 characters including spaces. The title must be specific and should contain words useful for indexing.

Abstract: All papers must have an abstract of not more than 200 words. The abstract should indicate the general scope of the paper, the important findings and the conclusions drawn.

Keywords: Between 3 and 6 keywords must be provided for indexing and information retrieval services.

List of Symbols: In cases where the number of symbols used is large, the authors should attach to the manuscript a separate complete list of symbols identified typographically, not mathematically. This list will not appear in print but is essential in order to avoid costly corrections at the proof stage. In other cases, a clear typographical identification of each symbol, made in the margin in quotes (e.g. "epsilon") the first time it appears in the text should be adequate.

Text: The paper must be divided into sections starting preferably with "Introduction" and ending with "Conclusions". The main sections should be numbered 1, 2, 3 etc and subsections 2.1, 2.2 etc.

Tables: All tables must be numbered consecutively in Arabic numerals (not Roman) (e.g. Table 3) in the order of appearance in the text. The tables should be self-contained and have a descriptive title. Column headings of tables should be brief. Extensive tables will be reproduced photographically and should therefore be typed carefully and in the exact format desired. Footnotes to the tables, if any, should be identified by superscript symbols and placed at the bottom of the page containing the table.

Footnotes: Footnotes to the text should be avoided if possible. When necessary they should be numbered along with the references (numbers in square brackets) sequentially in the main text. The matter of each footnote should appear after the appropriate number in the list of references.

Appendices: Appendices should be labelled as A, B, etc. and the equations appearing in them be labelled as A1, A2, B1, B2, etc.

Proofs: Normally two sets of page-proofs are sent to authors for correction along with a reprint order form. One set of corrected proofs should be posted back to the Editorial Office within two days of receipt. If the corrected proofs are not received within a reasonable time, it will be presumed that the authors have no corrections to make.

The articles are typeset by computer photocomposition and printed by the offset process. While this process is neat, it makes corrections at the proof stage very difficult and expensive. Addition or deletion of a letter or a word or a sentence in the proof means resetting the whole line or para and sometimes even a few pages. Authors are therefore requested to indicate only typographical or composing errors. Fresh corrections which are absolutely essential and unavoidable can be indicated on the proof but will be charged to the authors at actuals.

Reprints. Fifty reprints of each article will be supplied free of charge. If additional reprints are desired these can be ordered at the proof stage at the cost indicated in the reprint order form.

The authors' attention is specially drawn to the instructions on items below. If these are not followed strictly, both the quality of reproduction and the technical accuracy would be jeopardised. Therefore in such cases the manuscripts may have to be returned to the authors for improvement causing delays in their publication.

References: References should be numbered in order of appearance in the text of the paper, the number being enclosed in square brackets in the same line. Eg. "It has been shown [1, 2] that..." or "Ramachandran and Raman [14] developed a formalism in 1955 which made it possible..."

The second example is meant to show that while names of authors and dates are not essential, they can be included even in this format. At the end of the manuscript, references to articles in journals should be listed by number, again in square brackets, followed by authors names (preceded by initials), abbreviated journal title, volume, first page number and year in brackets, e.g.

[4] P W Anderson, *Phys. Rev.* **109**, 1492 (1958)

References to books should include: name(s) of author(s) (preceded by initials), title of the book, edition if not the first, initials and name(s) of editor(s) if any, preceded by "edited by" and publisher, place of publication, year within brackets and chapter or pages referred to, e.g.

[12] J de Boer and J Eichler, in *Advances in nuclear physics* edited by M Baranger and E Vogt (Plenum, New York, 1968) Vol. 1, p. 1.

References to theses must include the title of the thesis, the degree for which submitted, the University and year.

Mathematical Material: Equations must be clearly written, each on its own line, well away from the text. All equations must be numbered consecutively in Arabic numerals with the number in parentheses near the right hand margin. If desired, equations can be numbered consecutively in each section preceded by a point and the section number e.g. (3.14) for the 14th equation in section 3. Indices, subscripts, superscripts and exponents must be clearly indicated in pencil in one copy of the manuscript, for example like a_{N} b_{i}, b^{a}, b_{x+1}... etc. 'Oh' and 'zero', K, k and Kappa, 'ell' and 'one', etc. must be clearly distinguished. Authors must indicate wherever special characters (Greek, Gothic, script, scalar, vector, tensor, matrix, etc) are required. All other letters will be set in italic type. Vectors must be underlined by a wavy line and tensors and matrices by two wavy lines. The SI system of units and symbols is recommended.

Figure: All figures, including photographs (which must be glossy prints) should be numbered consecutively in Arabic numerals in the order of occurrence in the text. Figure captions must be typed on a separate sheet.

Line drawings must be in Indian ink on good quality tracing paper. Curves should be drawn sufficiently thick to permit reduction to one half or even one third of the original size. The axes and letterings must be about 0·3 mm thick and curves 0·6 mm thick. Whenever computer outputs are directly submitted as figures, they should conform to the same specifications given earlier for drawings.

Regd. No. KRN-A 64

Pramana journal of physics Vol. 45 (No. 6), December 1995

Contents

Review

The real symplectic groups in quantum mechanics and optics..... *Arvind, B Dutta, N Mukunda and R Simon* 471

Research Articles

Optical theorem and Aharonov–Bohm scattering..... *M M Panja, P K Bera and B Talukdar* 499

BD–FRW models in the framework of Israel–Stewart–Hiscock theory..... *Kalyani Desikan* 511

Fission fragment angular distribution in alpha-particle-induced fission of actinide elements..... *R K Jain, S K Bose and J Rama Rao* 519

Relativistic correction to the dipole polarizability of a hydrogenic ion..... *K L Baluja* 533

Systematic trends in the line strengths and radial matrix elements of E1 transitions in the Be isoelectronic sequence..... *Anand Bharadvaja and K L Baluja* 537

Propagation of a wavepacket on a model fractal lattice..... *P K Chattaraj and S Nath* 545

Kinetic description of ion acoustic waves in a dusty plasma..... *B P Pandey and Susheel Kumar* 561

A comparative study of two learning rules for associative memory..... *G Athithan* 569

Subject Index..... 583

Author Index..... 588

Volume Contents

Information for Contributors

PRAMANA

journal of physics

Proceedings of the Third
Workshop on High Energy Particle Physics
Madras, January 1994

Supplement to
Vol. 45, October 1995

DIAN ACADEMY OF SCIENCES
ian National Science Academy
ian Physics Association

Editor

R Nityananda

Raman Research Institute, Bangalore

Associate Editor

H R Krishnamurthy

Indian Institute of Science, Bangalore

Editorial Board

G S Agarwal, *Physical Research Laboratory, Ahmedabad*
V Balakrishnan, *Indian Institute of Technology, Madras*
M Barma, *Tata Institute of Fundamental Research, Bombay*
P Chaddah, *Centre for Advanced Technology, Indore*
B M Deb, *Panjab University, Chandigarh*
P K Kaw, *Institute for Plasma Research, Gandhinagar*
H S Mani, *Indian Institute of Technology, Kanpur*
N Mukunda, *Indian Institute of Science, Bangalore*
T Padmanabhan, *Inter-University Centre for Astronomy and Astrophysics, Pune*
J C Parikh, *Physical Research Laboratory, Ahmedabad*
G Rajasekaran, *Institute of Mathematical Sciences, Madras*
V S Ramamurthy, *Department of Science and Technology, New Delhi*
R Ramaswamy, *Jawaharlal Nehru University, New Delhi*
K R Rao, *Bhabha Atomic Research Centre, Bombay*
Probir Roy, *Tata Institute of Fundamental Research, Bombay*
A K Sood, *Indian Institute of Science, Bangalore*

Editor of Publications of the Academy

V K Gaur

C-MMACS, NAL, Bangalore

Subscription Rates
(Effective from 1989)

All countries except India	1 year	3 years	5 years
(Price includes AIR MAIL charges)	US$ 175	$ 470	$ 700
India	1 year	10 years (1989-1998 only)	
	Rs. 100	Rs. 500	

All correspondence regarding subscription should be addressed to the **Circulation Department** of the Academy

---

Editorial Office

Indian Academy of Sciences, C V Raman Avenue,
P.B. No. 8005, Bangalore 560 080, India

Telephone: 80-334 2546
Telex: 845-2178 ACAD IN
Telefax: 91-80-334 6094

© 1995 by the Indian Academy of Sciences. All rights reserved.

"Information for contributors" is printed in the last issue of every volume.

THIRD WORKSHOP ON HIGH ENERGY PARTICLE PHYSICS

Editor
S Uma Sankar

PREFACE

The Third Workshop on High Energy Particle Physics (WHEPP-3) was held at the Institute of Mathematical Sciences, Madras during January 10-22, 1994. This is the third in the series of workshops; the first one was held at T. I. F. R., Bombay (January 1989) and the second one was held by S. N. Bose Centre, Calcutta (January 1991). About 100 particle physicists have attended the workshop.

As in the previous two workshops, four broad topics were chosen for the formation of working groups. These are

1. Collider physics and structure functions (coordinated by Amitava Datta and Rohini Godbole)
2. Beyond standard model (coordinated by Anjan Joshipura and Probir Roy)
3. Heavy ion physics (coordinated by Sourendu Gupta and J. C. Parikh)
4. Heavy flavour physics (coordinated by S. Uma Sankar)

The first week was devoted to review talks on various topics of current interest and to the formation of working groups. The second week was devoted to talks by participants on their work and the discussion of the problems that were raised in working group sessions. The group coordinators presented the results of the discussions on the last day of the workshop.

These proceedings contain the written version of the review talks given during the first week. In addition to the contributions included here, the following talks were also presented:

1. Top quark search at tevatron ... *N. K. Mondal*
2. Searches for new physics at LEP200 ... *Sudhakar Katta*
3. Neutrino Masses and Mixing Angles ... *K. S. Babu*
4. Lepton Number Violation ... *J. W. F. Valle*

Most of the support for the workshop has come from S. N. Bose National Centre for Basic Sciences, Calcutta. Additional support was also given by the Department of Science and Technology, Government of India, New Delhi, The Institute of Mathematical Sciences, Madras and the International Center for Theoretical Physics (ICTP), Trieste.

I thank Prof. R. Ramachandran, Director, Institute of Mathematical Sciences, for the enthusiasm with which he agreed to host the workshop and for providing constant support. I also thank Prof. G. Rajasekaran, Dr. M. V. N. Murthy and Dr. Rahul Sinha for offering their help without any hesitation at all times. My sincere thanks to all the office, the library and the guest house staff

of the Institute of Mathematical Sciences, who worked untiringly to take care of the workshop participants and made the workshop a success. Finally I would like to thank my colleagues at T. I. F. R., particularly Dr. Sourendu Gupta and Dr. Suresh Govindarajan of the Theory Group and Dr. Kajari Mazumdar of the E. H. E. P. Group, for their help in preparing the proceedings.

S. Uma Sankar

B physics at LEP

TARIQ AZIZ
Tata Institute of Fundamental Research, Bombay 400005, India

Abstract. The Z factory at LEP is like a mini B factory. About 20% of the time a Z decays to a pair of b flavoured hadrons. As a result, this has provided a major boost to B physics studies. The four sophisticated LEP detectors, with millions of Z events, have provided a variety of interesting results. Only a snapshot of the major developments can be covered in one review. We have considered the results related to $Z \rightarrow b\bar{b}$ coupling, in particular, the measurements of $R_b = \Gamma_b/\Gamma_{had}$ and the forward backward charge asymmetry. The b hadron properties, like inclusive and exclusive lifetime measurements are summarised briefly. Measurements of B°-$\bar{B}^\circ$ oscillation parameter as well as the evidence for time dependent evolution have been discussed. Studies of interesting decay modes have been mentioned.

1 Introduction

The Z factory at LEP is a copious source of b flavoured hadron production via $Z \rightarrow b\bar{b}$. About 20% of the visible Z decay to this channel. As a consequence B physics at LEP has become one of the most interesting issues being persued vigorously. A glimps of various interesting topics is shown in figure 1. An attempt is made to cover significant part of this exciting area with a minimum, but unavoidable, sacrifice to the rest. As a broad line of separation, there are two specific areas, the one which has to do with $Z \rightarrow b\bar{b}$ coupling, like partial width and asymmetry. The second one has to do with the b flavoured hadron properties, like lifetime of hadrons, neutral meson mixing and branching ratios. Another issue that deals with the strong interaction feature of b quark, like fragmentation parameter and strong coupling constant, α_s, are not touched at all.

2 Measurement of $R_b = \Gamma_b/\Gamma_{had}$

Within the SM framework $Z \rightarrow b\bar{b}$ partial width is an important measurement, both at the tree level and beyond. A precise measurement is essential for understanding top mass dependent weak radiative correction in $Z \rightarrow b\bar{b}$ vertex. The virtual effects of fermions and bosons lead to the following weak corrections [1].

- The propagator/oblique correction, called $\Delta\rho$, where relevant contribution comes from top quark and Higgs boson. All partial widths and asymmetries increase with increasing top mass while due to Higgs boson the effect is opposite.

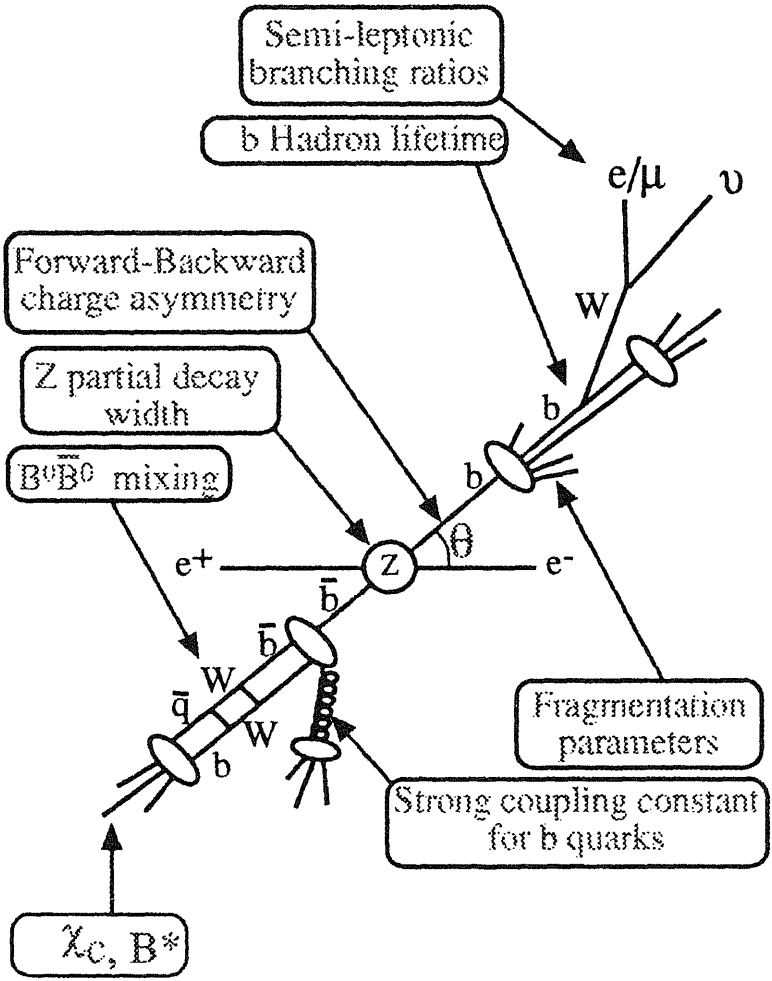

Figure 1: Different topics at LEP

- The vertex correction where the relevant effect is in $Z \rightarrow b\bar{b}$ vertex due to massive top quark, called δ_{vtb}. Due to this effect the $Z \rightarrow b\bar{b}$ partial width decreases with inceasing top mass. The b quark asymmetry however remains unaffected [2].

As a result of the above two corrections, the ratio $R_b = \Gamma_b/\Gamma_{had}$, where Γ_b is the $Z \rightarrow b\bar{b}$ partial width and Γ_{had}, the partial width due to all five quark flavours (u,d,s,c,b), depends only upon the top quark mass. All common corrections in the propagator get cancelled, making R_b a clean top mass indicator, free from Higgs and QCD effects [3]. Specifically,

$$R_b \simeq R_{bo}(1 + \delta_{vtb}(1 - R_{bo})),$$

where $R_{bo} = 0.2197 \pm 0.0001$ is estimated switching off the vertex correction, δ_{vtb}. For top mass above 100 GeV [4],

$$\delta_{vtb} \simeq -\frac{20}{13}\frac{\alpha}{\pi}\left(\frac{m_t^2}{m_Z^2} + \frac{13}{6}\ln\frac{m_t^2}{m_Z^2}\right)$$

Due to this clean dependence on top quark mass, any possible deviation from this trend will also be a clean indication for physics beyond SM (see figure 2). Thus an

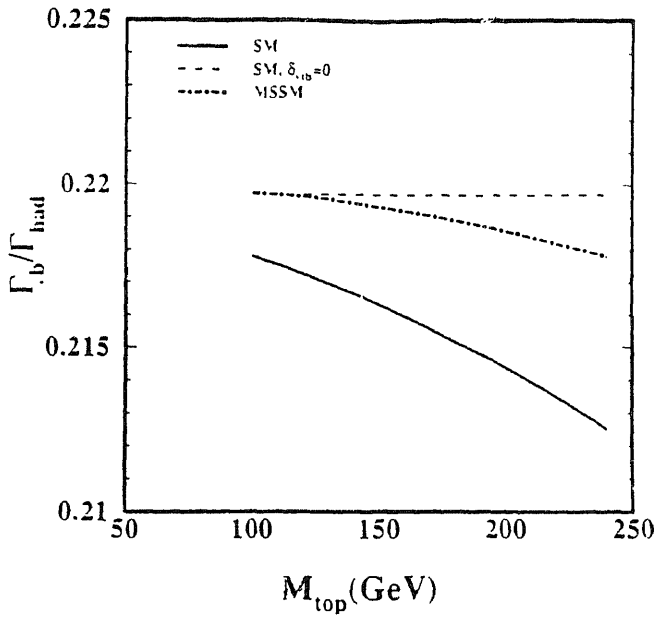

Figure 2: R_b as a function of top mass. The MSSM (Minimal Supersymmetric Standard Model) calculations are performed with a choice of parameters to show the maximal effect [5].

accurate measurement of R_b at LEP is one of the topmost priorities, exploiting all possibilities of tagging b quark.
Three different techniques have been used to isolate the signal.

- Using large momentum, p, large transverse momentum, p_T, leptons from SL decays. Where p_T is with respect to the nearest candidate jet axis.
- Exploiting the multidimensional event shape in a sophisticated neural network analysis.
- Exploiting lifetime and hence displaced decay vertex of b flavoured hadron in a sophisticated Silicon Microvertex Detectors (SMD).

2.1 R_b from Lepton tag

The massive ($\sim$ 5 GeV) b flavoured hadron leads to large P_T of the charged lepton in a semileptonic decay. Due to the hard b quark fragmentation (suppressed gluon emission) the b falvoured hadron is energetic. About 70% of b quark/beam energy is carried by the b hadron. This leads to the large momentum lepton. Thus restricting to large p, p_T leptons it is possible to select high purity b sample. By applying a typical cut on $p > 3$ GeV/c and $p_T > 1$ GeV/c a sample purity of 80% for b quark can be achieved. The relevant backgrounds to the signal come from charm semileptonic decays and the fake leptons. The fake μ are the punch-throughs pointing to the vertex, whereas fake electrons are the the charged hadrons matched wrongly to an electromagnetic shower. Thus the important systematics come partly from the knowledge of SL branching ratios and partly from MC modelling of the event in the detector. A substantial control to these systematics is achieved by tagging both the b quarks using two high p, p_T charged leptons, called the double tag. The double tag to single tag ratio is used to minimise the MC dependence. However this is achieved at the cost of losing statistics. The results from the four LEP experiments, ALEPH [6], DELPHI [7], L3 [8] and OPAL [9] based on this technique are summarised in table 1.

2.2 R_b from Eventshape Anaylsis

The $Z \rightarrow b\bar{b}$ event is identified using general properties of the event as a whole. A sophisticated neural network technique is used to exploite the multidimensional correlations in several eventshape variables. This method has the advantage of being least sensitive to the semileptonic branching ratio. Even though heavy b quark radiates less energy as gluons, the resulting b flavoured hadron being short lived decays to several particles. The energy sharing among the secondaries is, thus, more even compared to the case of light quark where the resulting leading light hadron being stable can be fairly energetic. The mass effect of b quark manifests itself in the jet boost($\gamma\beta = p/m$) which tends to be small. With these features a set of variables are defined which are used as input to neural network. ALEPH [10], DELPHI [11] and L3 [12] have performed such analysis. An example of such an analysis is considered from the L3 experiment. A set of five variables for each of the two most energetic jets of the event are defined:

Table 1: Γ_{bb}/Γ_{had} from Lepton Tagging

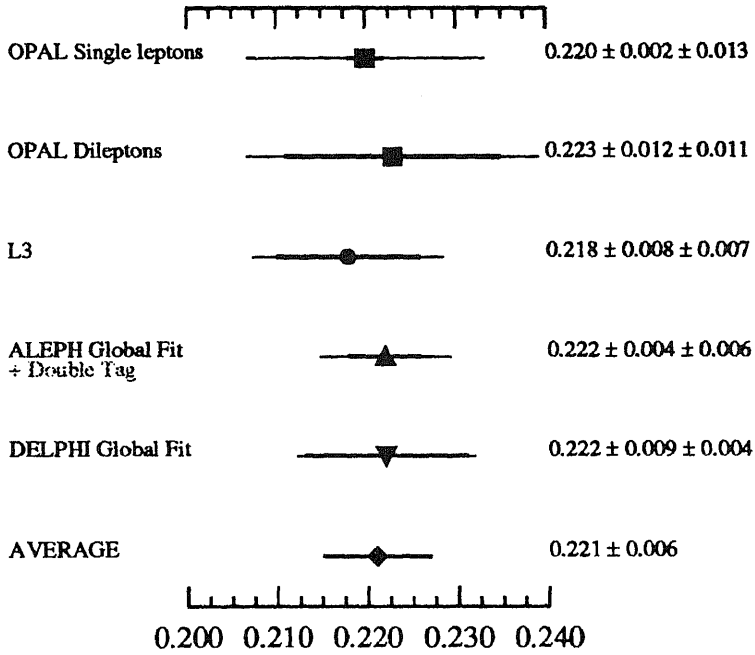

- The directed sphericity of the jet $S_{\rm dir} = \frac{\sum p_T^2}{\sum p^2}$, defined using clusters in the jet.

- The $\gamma\beta$ of the set of the four leading clusters in the jet

- The energy gap between first and fourth leading cluster $E_{\rm gap} = \frac{E_1 - E_4}{E_{jet}}$

In addition there is one global variable $E_{\rm left}$ defined as the fraction of energy outside the two most energetic jets in the event
Using a functional expansion neural network developed by the L3 collaboration, they achieve a 35% b tagging efficiency with a sample purity of 60%. The discriminating strength of various variables is confirmed by using high p_T lepton tagged events in data and MC. The network response and the purity versus efficiency plot for b tagging are shown in figure 3. The network response is checked using lepton tagged events to confirm that the correlations are well simulated in the MC. Finally a fit to the data response using b and non-b from MC deduces the value of R_b. Figure 4 shows the network response for lepton tagged events and the overall distribution to determine R_b. A summary of all the measurements at LEP using neural network technique is given in table 2. The major systematics in this kind of analysis come from the understanding of the fragmentation behaviour and the

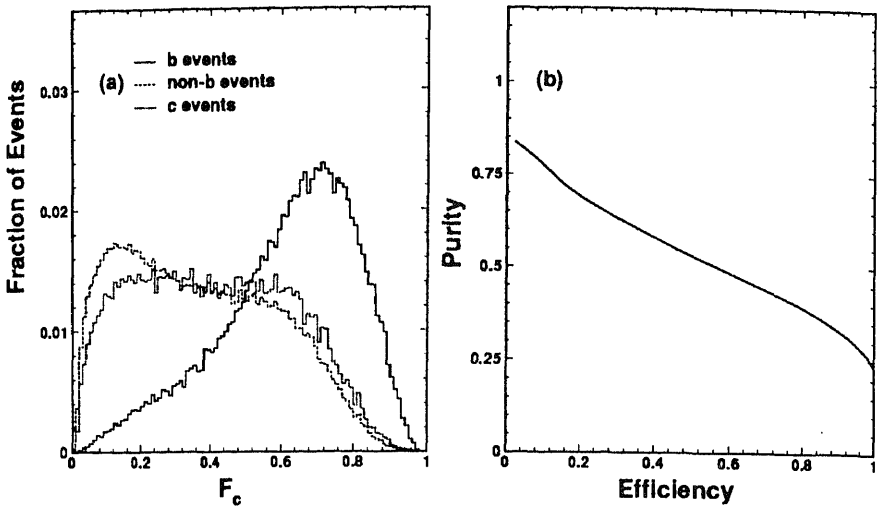

Figure 3: (a) The network response for b events and non-b events separately. (b) Purity and efficiency of the classifier function for b events.

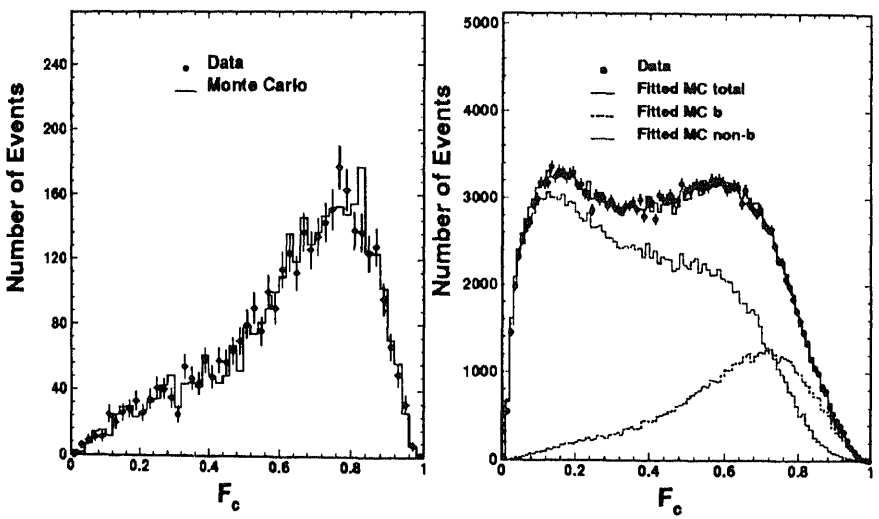

Figure 4: The network response for high p_T muon tagged events for which b purity is 80% (left). Fit of the network response to the data (right).

Table 2:

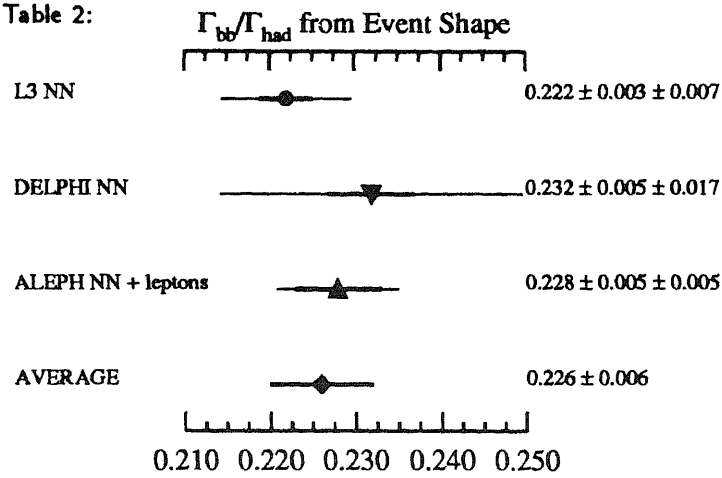

2.3 R_b from Lifetime Tag

The b hadron lifetime ($\tau_b \sim 1.5ps$) is exploited for impact parameter measurement or secondary vertex reconstruction using a high resolution vertex detector. ALEPH [13], DELPHI [14] and OPAL [15] have used this technique to measure R_b. ALEPH has used three dimensional (3D) signed impact parameter, δ, using silicon microvertex detector. (For illustration of impact parameter see later in lifetime section.) DELPHI has used 2D signed impact parameter alongwith p_T^2 of charged tracks with respect to jet axis as well as decay distance in a multidimensional analysis (MDA). OPAL has used 2D signed impact parameter to count the so called forward multiplicity (tracks originating from secondary vertex, forward to the primary vertex). Initially they used their conventional tracking chamber and added SMD later. The results being consistent. To reduce the MC dependence, the double tag technique is applied. The event is divided in to two hemispheres using the event thrust axis.

The relevant systematics here come from the knowledge of lifetime, mixtures of mesons, baryons and the decay braching ratios to charged particles as well as the ratios like D^+/D° etc. To give an example, we describe the ALEPH analysis. The typical features of ALEPH silicon micorovetex detector are the following. The vertical resolution is $\sim 10\ \mu m$; horizontal resolution is $\sim 20\ \mu m$, with an RMS for interaction region $\sim 110\ \mu m$. The significance for tracks originating from a secondary vertex is defined as $S = \delta/\sigma(\delta)$, where $\sigma(\delta)$ is the measurement uncertainty. For tracks originating from b hadron decay, $S \sim 4.5$. A further cut of $\delta < 2.5mm$ is applied to remove K_s° decay and γ conversion background. A joint probability P_H for a given hemisphere tracks is calculated using S values such that none of the tracks are from secondary vertex. A small value of P_H means larger signal probability. A cut on $P_H (< 10^{-4})$ is used to select good purity b sample ($\simeq 96\%$) with a good tagging efficiency ($\simeq 26\%$). Using the active detector acceptance, the net tagging efficiency ($\simeq 15\%$) is still signifcantly large. A plot of purity and efficiency as function of P_H is shown in figure 5. Using cut on P_H from the two hemispheres the single and double tag probabilities are defined. For single tag

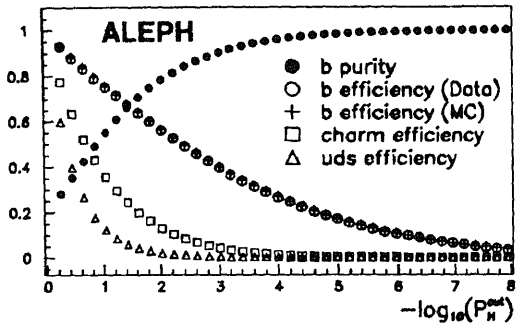

Figure 5: Hemisphere tag efficiency and signal purity as a function of P_H cut.

$$F1 = R_b\epsilon_b + (1 - R_b)\epsilon_x = R_b\epsilon_b + R_x\epsilon_x$$

and for double tag

$$F2 = R_b\epsilon_b^2 + (1 - R_b)\epsilon_x^2 + R_b\lambda_b(\epsilon_b - \epsilon_b^2)$$

Here λ_b is the correlation coefficient between the two hemisphere tag probabilities and it is determined using MC. ϵ_b and ϵ_x are tagging efficiencies for b and non-b. The two expressions are solved for R_b and ϵ_b iteratively whereas ϵ_x is determined using MC. The important sources of correlations are:
The detector dependent correlation where both jets are back to back; being both either in good or bad measurement regions due to detector symmetry.
The physics processes, for example energetic gluons making third jet and in that case the event thrust axis and the hemispheres are affected. The net systematic uncertainties from all sources are still the smallest in this measurement. A summary of all measurements using this technique is given in table 3.

2.4 Summary of R_b from different methods

The results from the three methods for all the experiments al LEP are summarised in table 4. The average $R_b = 0.2207 \pm 0.0027$ is somewhat large when compared with the SM prediction. To give some idea, for an optimistic top mass of $\sim$ 160 GeV the expected value of $R_b = 0.2162$. Since the errors are still large, it is premature to talk of any deviation from SM. On the other hand an interpretation in the framework of SM will indicate a top mas $<$ 185 GeV at 2σ level if no other information from LEP or Tevatron is used. An improved measuremnet of R_b with better understanding of systematics is likely to prove very exciting from the point of view of new physics, once top mass is known from Tevatron direct searches.

3 Forward-Backward Charge Asymmetry

The forward-backward charge asymmetry of b quark provides a sensitive measurement of weak mixing angle. For the process $Z \rightarrow f\bar{f}$ (f: fermion) ,where final

Table 3:

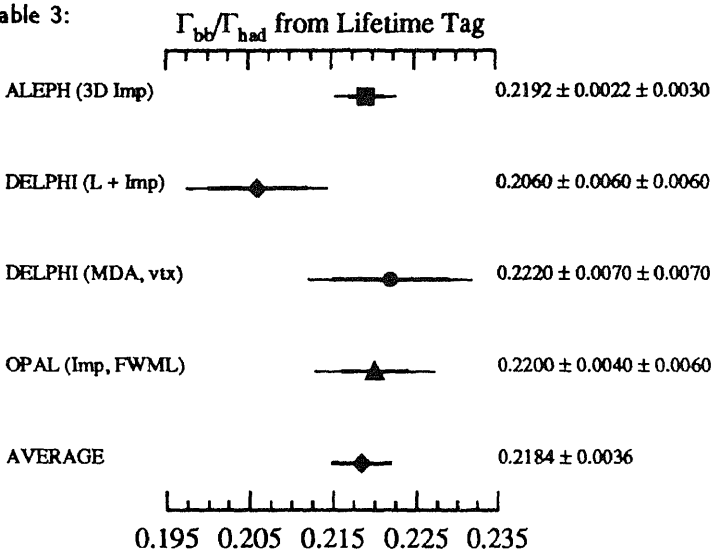

Table 4:

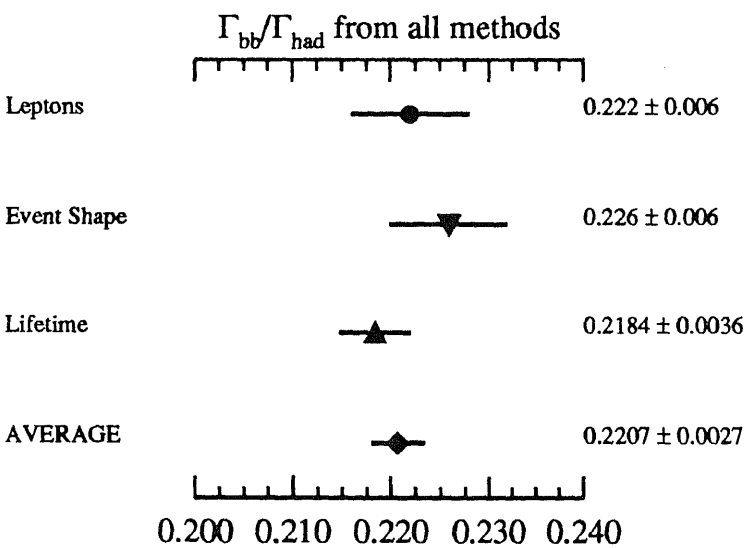

state fermion angle θ is measured with respect to the electron beam direction, the differential cross-section is given by

$$\frac{d\sigma}{d\cos\theta} = \frac{3}{8}(1+\cos^2\theta)(\sigma^{vv}+\sigma^{aa}) + \frac{3}{4}\cos\theta\sigma^{va}$$

where σ^{vv} and σ^{aa} are symmetric vector/axial vector coupling cotributions to the cross-section and σ^{va} is the interference term and it is asymmetric. The forward backward asymmetry is given by

$$A_{fb} = \frac{3}{4}\frac{\sigma^{va}}{\sigma_T} \; ; \; \sigma_T = \sigma^{vv}+\sigma^{aa}$$

On the Z peak

$$A_{fb} = 3\frac{v_e a_e v_f a_f}{(v_e^2+a_e^2)(v_f^2+a_f^2)}$$

For charge Q = 1/3 quark (b,s,d) v_f is large which leads to large A_{fb}. Furthermore, because of large v_f the above expression simply reduces to a convenient form

$$A_{fb} \simeq C\, v_e = C(1-4\sin^2\bar{\theta}_W)$$

where $v_e = (1-4\sin^2\bar{\theta}_W)$ is the vector coupling of electron and $\sin^2\bar{\theta}_W$ the effective weak mixing angle. An important consequence of this simplicity is that b quark asymmetry is independent of $Z \rightarrow b\bar{b}$ vertex corrections [2]. To an excellent approximation $C \simeq 1.395$. The QED and QCD effects tend to dilute the asymmetry. Taking these effects into account $C \simeq \frac{40}{31}$ to be compared with the measured asymmetry on the peak. A word of caution is in order. The QED effects are easier to understand, however QCD effects need better understanding keeping realistic limitations of the detectors and the fact that the event thrust axis is used to represent the b quark direction. Also the effect of missing neutrinos, which is more important for lepton tag analysis needs to be taken into account carefully. Any poor understanding of detector as well as physics process only dilutes the sensitivity of the angular distribution under consideration and hence asymmetry.
The apparently observed $b\bar{b}$ asymmetry as measured using charged lepton tag is further diluted due to B^0-$\bar{B}^0$ mixing as the sign of tagging charged lepton is flipped. Thus

$$A_{fb_{true}} = A_{fb_{observed}}/(1-2\chi_B)$$

where $\chi_B(=0.115)$ is measured B^0-$\bar{B}^0$ mixing at LEP.

3.1 Asymmetry measurement using lepton tag

This is the standard procedure. The b enriched sample is tagged by lepton and the b quark charge is assigned using lepton charge keeping decay sequence in mind. The event thrust axis is used to approximate the b quark direction and the hemisphere is assigned to be the lepton hemisphere. A plot of angular distribution for the tagged events is shown in figure 6. A summary of the measured b quark asymmetry from these experiments is given in table 5. The results are based on the data of ALEPH(90-92) [16], DELPHI(92) [17], L3(90-92) [18] and OPAL(90-91) [19]. In all these cases the background asymmetries are estimated using MC. The important systematics as reported by these experiments are based on b hadron decay models and $Br(b \rightarrow c \rightarrow \ell^+)$ and $Br(b \rightarrow \bar{c} \rightarrow \ell^-)$.

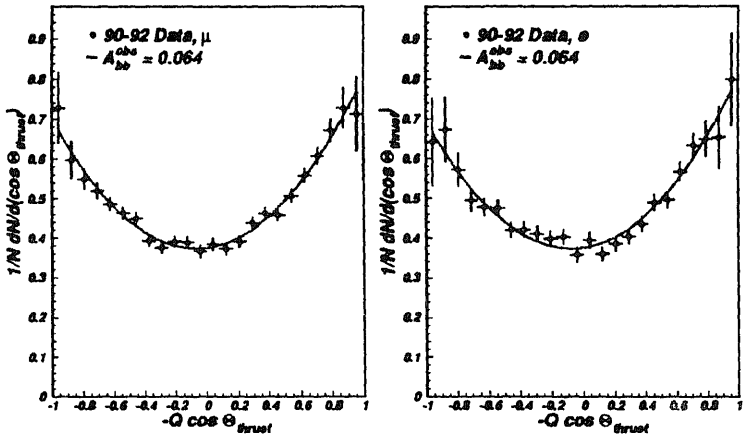

gure 6: The distribution of $-Q\cos\theta_{thrust}$ for prompt muon and electron tagged nts taken from L3. The curves are the result of the fit.

Table 5:

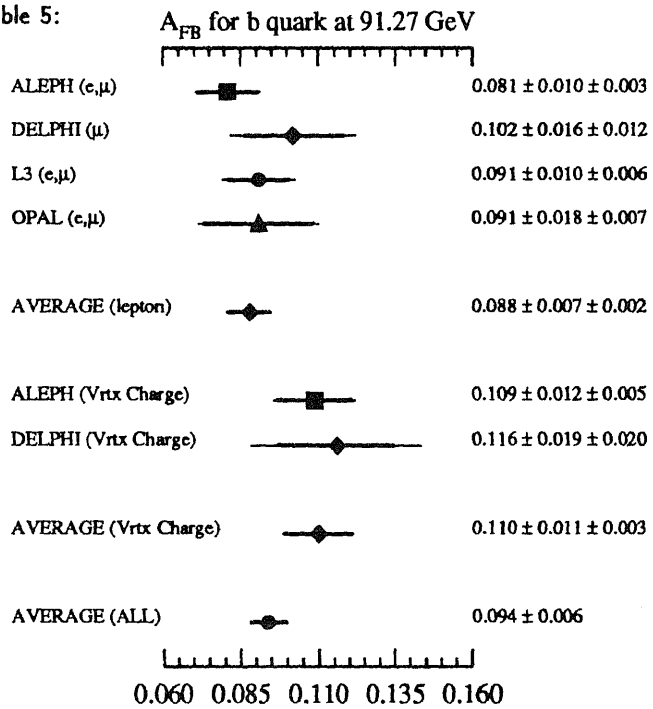

The secondary vertex/impact parameter is used to tag b hadron. The momentum weighted jet charge using all charged particles in the jet is used to assign the b quark charge. The relevant systematics here are due to fragmentation and decay models assumed to describe the data as well as meson/baryon composition. The results are however competitive to the lepton tag. Moreover the effect of missing neutrino is less relevant in this case.
ALEPH [20] and DELPHI [21] have used this technique and their results are shown in the table 5. Averages for lepton tag, vertex and jet charge tag as well as overall are shown in the same table. These results are already corrected for the mixing parameter. Since these measurements are performed slightly above the Z peak, a small correction is applied and the final measured peak asymmetry is

$$A_{fb}^{\circ} = 0.092 \pm 0.006$$

which leads to $\sin^2\overline{\theta}_W = 0.2322 \pm 0.0011$ to be compared with the LEP average $\sin^2\overline{\theta}_W = 0.2321 \pm 0.0006$ from all methods including this measurement. Conservatively one would expect true $\sin^2\overline{\theta}_W$ to be smaller, if all the effects mentioned above are taken fully into account.

4 b Hadron Lifetimes

The measurement of b hadrons lifetimes at LEP has the advantage of relatively larger boost making it a cleaner measurement without any mixing of the tracks from the two jets in $Z \rightarrow b\bar{b}$. Excellent measurements, both inclusive as well as exclusive, for b hadrons have been performed. Real justice can not be done in this kind of review. Only a gilmps of the overall situation is given. Being of fundamental importance, these measurements are relevant not only for the understanding of b hadron decay mechanisms and the Cabbibo-Kobayashi-Maskawa (CKM) matrix elements in cosequence, but also from the fact that b tagging using lifetime technique requires an accurate measurement to minimise the systematics, in particular for R_b. The most naive, yet simplest to connect the lifetime with CKM elements, is the so called spectator model. In this scheme, the light partner is ignored and the b quark is treated to decay analogous to a muon.
For muon decay

$$\Gamma(\mu \rightarrow e\bar{\nu}_e\nu_\mu) = \frac{G_F^2 m_\mu^5}{192\pi^3} f_\mu$$

where f_μ is the phase space factor, and G_F the Fermi coupling constant. In a similar way for b hadron decay

$$\Gamma(b \rightarrow \ell, X) = \frac{G_F^2 m_b^5}{192\pi^3}(f_c |V_{cb}|^2 + f_u |V_{ub}|^2)$$

$$= \frac{Br(b \rightarrow \ell, X)}{\tau_b}$$

where f_c and f_u are combined phase space and QCD correction factors corresponding to the relevant decay modes.

is obvious to see that in such a scheme the lifetimes for different mesons (charged, neutral, strange) and baryons should be the same. There are several relevant diagrams like W annihilation, W exchange and quark interference which need to be considered depending upon the quark content of the b hadron. Consequently one would expect

$$\tau_{B^+} > \tau_{B_s^0} \approx \tau_{B_d^0} > \tau_{\Lambda_b}$$

to be the more realistic case within 10-20% [22]. Exact predictions are still difficult as it requires to understand hadronic decay matrix (quark masses , QCD effects etc). The experimental measurements can help a great deal in this direction.

4.1 Inclusive lifetime measurements

The 4 LEP experiments ALEPH [23], DELPHI [24], L3 [25] and OPAL [26] have performed this measurement. The impact parameter of the lepton (μ and e) are used for this purpose. The method is illustrated in figure 7 . An example for

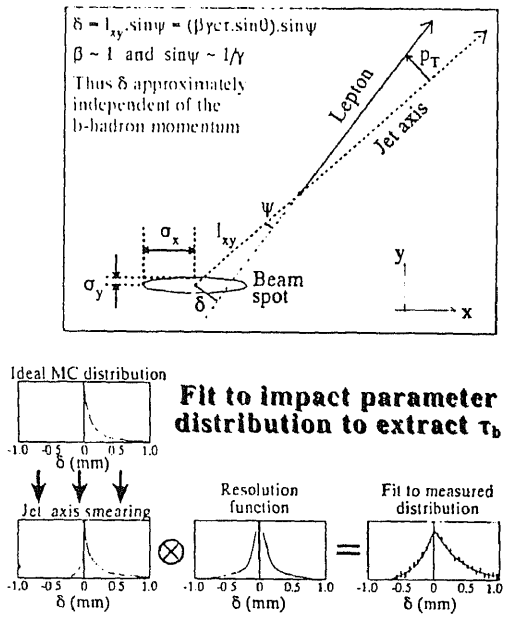

Figure 7: Definition of the transverse impact parameter and various resolution effects.

the actual fit to the data taken from the L3 experiment is shown in figure 8 . The important systematics for this measurement come from the understanding of semileptonic branching ratios, fragmentation parameters for heavy and light quarks and the measurement resolution function.

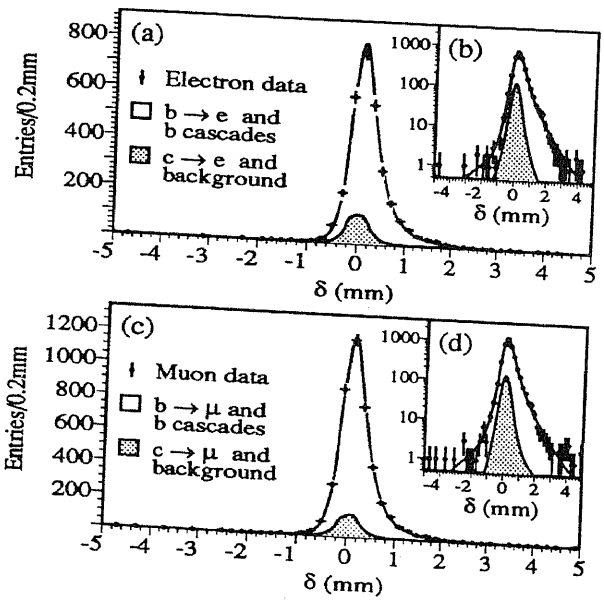

Figure 8: L3 lifetime analysis using electron and muon tagged events. The i
sets show the same impact parameter plots on log scale. Curves are the result
maximum likelihood fit.

detector to reconstruct the invaraint mass of the charged tracks in order to remove the non-b background using mass cut and also to calculate the boost for the b hadron. The secondary vertex is used for the decay length and thus the proper time is extracted.

ALEPH has also used charged tracks to reconstruct the two secondary vertices (dipoles) and the distance between them is exploited to infer lifetime.

A summary of the inclusive τ_b measurements from 4 LEP experiments is given in

Table 6:

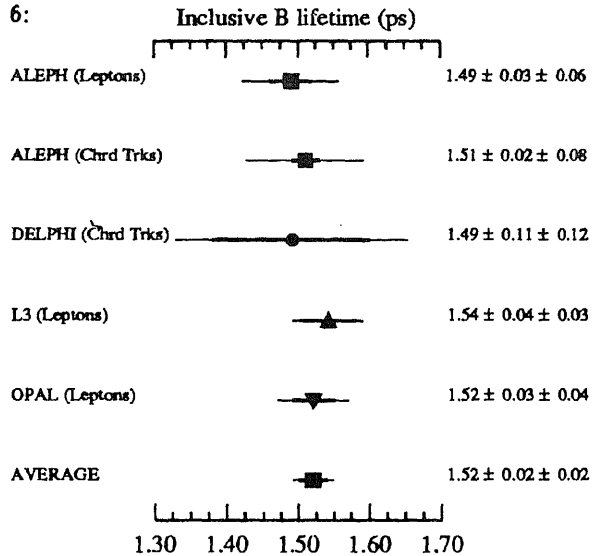

table 6. We have avoided those measurements which, in our opinion, are 'too preliminary'. A look at the average τ_b given here and the averages in PDG for the last few years will show that τ_b has been increasing with time. Whether it has reached to the asymptote is not very obvious.

4.2 Exclusive Lifetimes

The exclusive lifetimes for $B^{\pm}$, B°, B_s°, Λ_b are measured by looking for correlations like (D^*, ℓ), (D°, ℓ), (D_s, ℓ) and (Λ, ℓ) with the right sign combination for a desired state. In the following we describe one example each from the three experiments.

ALEPH anaylysis for B^- and B° life time: B^- is inferred from a (D°, ℓ^-) correlation whereas $\bar{B}^{\circ}$ is inferred from (D^{*+}, ℓ^-) correlation. A D^{*+} is unfavoured in B^- decay. It is idetified using the mass difference technique with the condition $\Delta M = M(D^{\circ}\pi) - M(D^{\circ}) \sim 145$ MeV where D° is reconstructed from $K\pi$ and $K3\pi$ mass combinations. The (D^0, ℓ) flight intersection is used to extract the decay length and the invariant mass of the combination is used to extract the b hadron boost. The effect of the missing neutrino is convoluted in the fit using MC modelling of the data. The important systematics are due to fake D^* or fake lepton or both apart from MC modelling for semileptonic decay as well as D^* and D^{**} relative contributions. A summary of all the measurements for $B^{\pm}$ and B^0 lifetimes

Table 7:

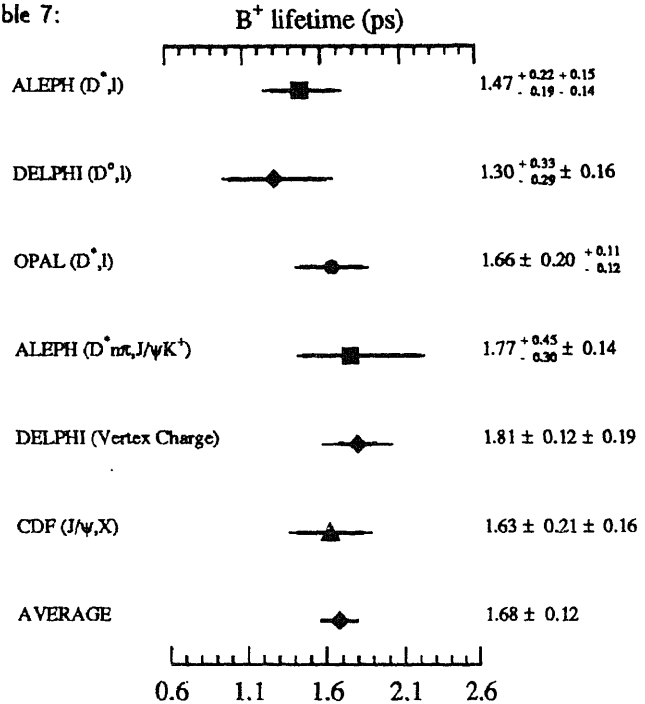

by ALEPH [27], DELPHI [28], OPAL [29] including result from CDF [30] is given in tables 7 and 8.

DELPHI B_s° **lifetime analysis:** In this case (D_s, ℓ) correlation is used. The D_s is reconstructed from $\phi\pi^-$ or $K^{*\circ}K^-$ combinations. The decay length is considered between primary vertex and D_s vertex. Again missing neutrino effect is convoluted using MC. The signal quality of this analysis for $\phi\pi^-$ channel is shown in figure 9. A summary of the measurements by ALEPH [31], DELPHI [32], and OPAL [33] is given in table 9.

OPAL Λ_b **lifetime analysis:** The analysis is based on their central tracking chamber. It is assumed that $\Lambda_b^\circ \rightarrow \Lambda_c \ell^- \bar{\nu} X$ and that $\Lambda_c \rightarrow \Lambda(p\pi^-)X$. The analysis ignores the production of Ξ_b. Here (Λ, ℓ) flight intersection is taken as the decay vertex. Again the effect of missing neutrino is convoluted using MC. The largest systematics to the lifetime estimate come from decay length estimate as the opening angle between (Λ, ℓ) is small. This is simply because of small reaction energy available in a baryonic decay. An example of the signal and the fit quality is shown in figure 10. A summary of all the measurements by ALEPH [34], DELPHI [35] and OPAL [36] is given in table 10. Some preliminary results from ALEPH and DELPHI using (Λ_c, ℓ) correlation exploiting their SMD are also included.

Finally a summary of average B hadron lifetimes based mainly on LEP is given in table 11. To conclude this table, exclusive lifetimes follow the trend:

$$\tau_{B^+} > \tau_{B_s^\circ} \approx \tau_{B_d^\circ} > \tau_{\Lambda_b}$$

and considering the extremes we can say that spectator model is not enough and other diagrams can not be ignored. Considering the situation a few years back, we

Table 8:

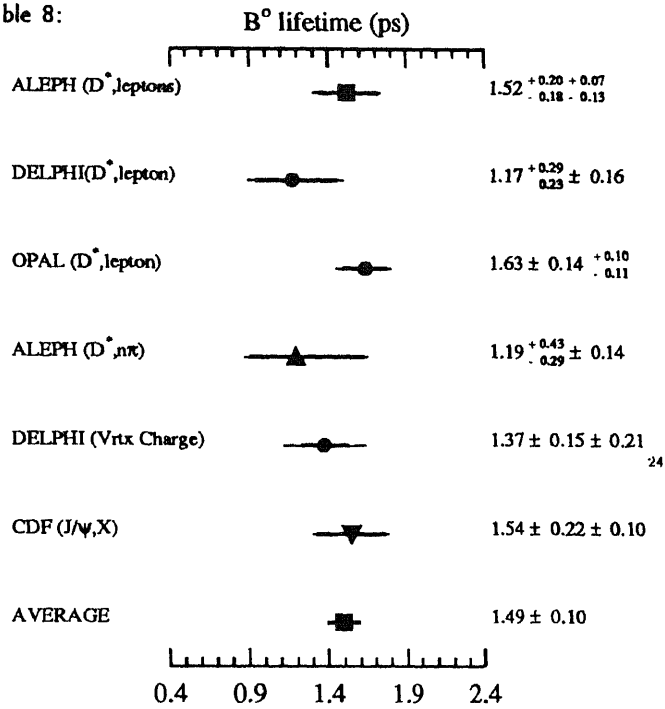

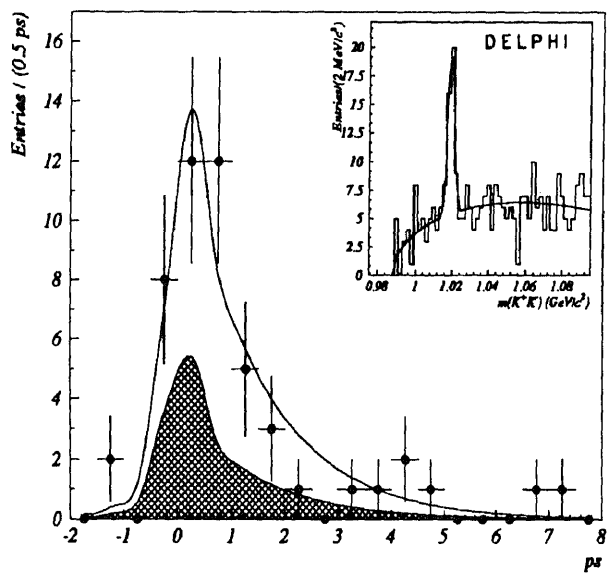

Figure 9: Proper time distribution for B_s candidates. The inset show the signal

Table 9:

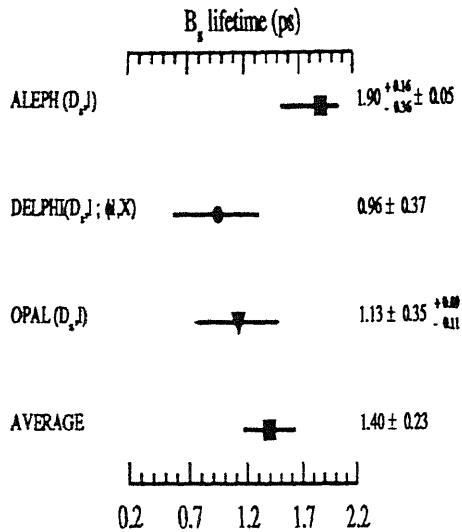

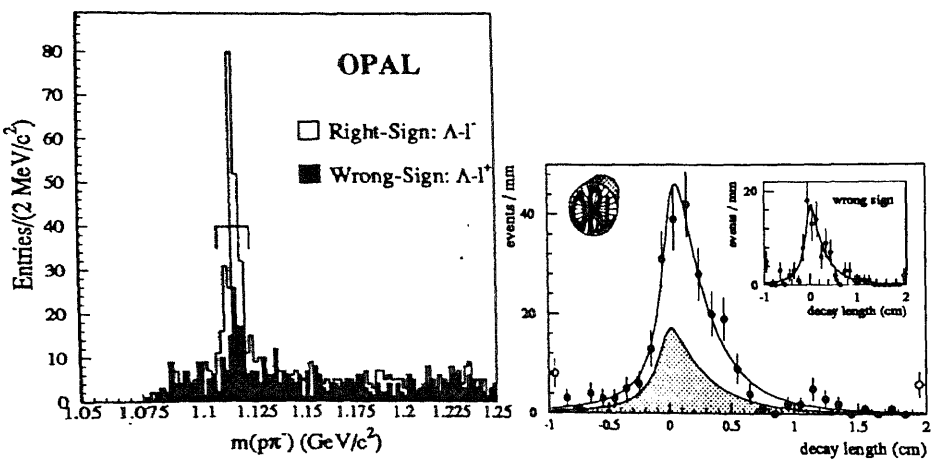

Figure 10: A signal for right sign (Λ, ℓ) combination (261 events) as well as the wrong sign (104 events) for the background (left). Fit to the decay length distribution to extract the Λ_b lifetime (right).

Table 10:

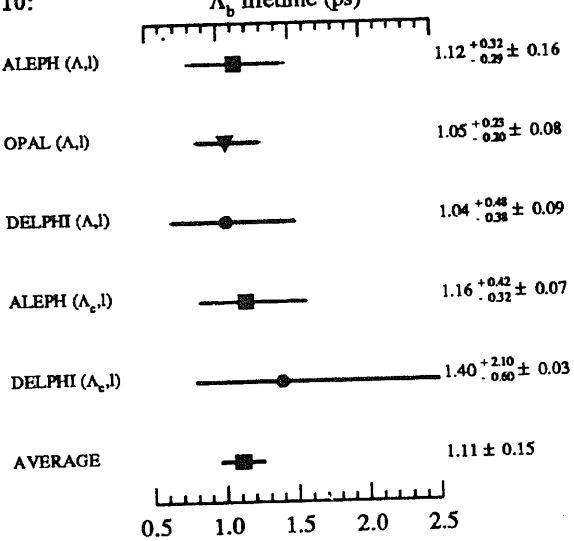

Table 11:

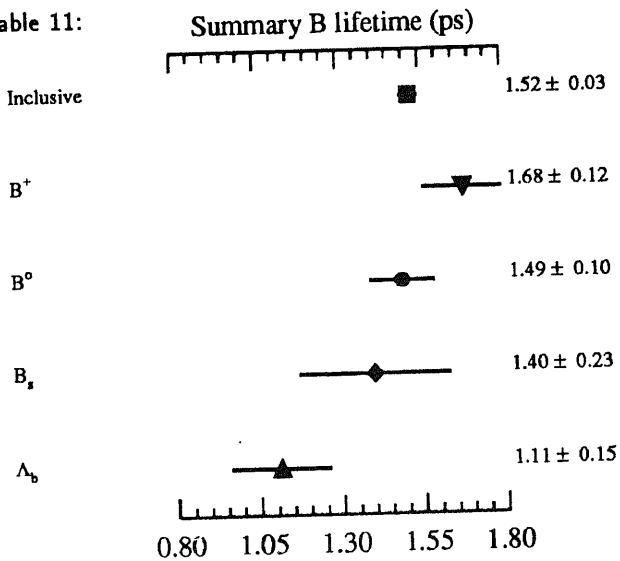

can say that major progress has been made in this sector, thanks mainly to LEP.

5 B^0-$\bar{B}^0$ Oscillation/Mixing

Like K^0, the B^0 weak eigenstates are not the same as the mass eigenstates, rather a linear combination of them. Thus,

$$| B^0 >= \frac{| B1 > + | B2 >}{\sqrt{2}} \quad \text{and} \quad | \bar{B}^0 >= \frac{| B1 > - | B2 >}{\sqrt{2}}$$

where the two states have mass difference $\Delta m = M1 - M2$ and similarly a lifetime difference which is considered to be small and neglected in this case. Thus a beam of pure B^0 studied as a function of time evolves into two components, a fraction of which is $\bar{B}^0$. This can be inferred from the final state decay products. This probability can be expressed as follows:

$$P(B^0 \rightarrow \bar{B}^0)_t = \frac{1}{2}\, e^{-t\Gamma/\hbar}(1 - \cos \Delta m t/\hbar)$$

$$P(B^0 \rightarrow B^0)_t = \frac{1}{2}\, e^{-t\Gamma/\hbar}(1 + \cos \Delta m t/\hbar)$$

Where $\Gamma = (\frac{\hbar}{\tau})$ is the decaywidth. For the detector resolution where only time integerated measurements are possible:

$$P(B^0 \rightarrow \bar{B}^0) = \chi = \frac{1}{2}\, \frac{(\frac{\Delta m}{\Gamma})^2}{1 + (\frac{\Delta m}{\Gamma})^2}$$

Where χ is called the mean mixing parameter and $\frac{\Delta m}{\Gamma} = x$, the oscillation frequency. For reasonably large oscillation frequency ($x > 5$), the time integerated measurement loses its sensitivity as $\chi \simeq 1/2$, the mixing is maximal.

Mixing measurements are relevant for several reasons. Within SM framework, second order weak transitions lead to e neutral meson oscillation (illustrated in figure 11). Considering the B^0-$\bar{B}^0$ oscillation, the strength of oscillation is related to mass difference;

$$\Delta m_q = \frac{G_F^2}{6\pi^2}\, m_b\, m_t^2\, F(\frac{m_t^2}{m_W^2})\, \eta_{QCD}\, \mathcal{B}\, f_B^2\, |\, V_{tb}^* V_{tq}\, |^2$$

where $V_{qq'}$ are CKM elements; F gives functional dependence on m_t; η_{QCD} is the QCD correction factor;$\mathcal{B}$ the bag factor and f_B the decay constant [37]. From this one would expects $\frac{\Delta m_s}{\Delta m_d} \approx |\, \frac{V_{ts}}{V_{td}}\, |^2$. Using unitarity arguments $|\, V_{ts}\, | \approx |\, V_{cb}\, |$ and $|\, \frac{V_{td}}{V_{cb}}\, | < \sin\theta_c + |\, \frac{V_{ub}}{V_{cb}}\, | < 0.35$(at 90% CL). This translates to $\frac{\Delta m_s}{\Delta m_d} > 8$(actually ~ 20), indicating large mixing for B_s system [38].

5.1 Measurements

Time Integerated

The simplest signature of B^0-$\bar{B}^0$ mixing is the presence of same sign dilepton events. In the normal course $B \rightarrow \ell^+ X$ and $\bar{B} \rightarrow \ell^- X$ and thus for no mixing in a B^0-$\bar{B}^0$ event one should expect only unlike sign dileptons. However, owing to mixing

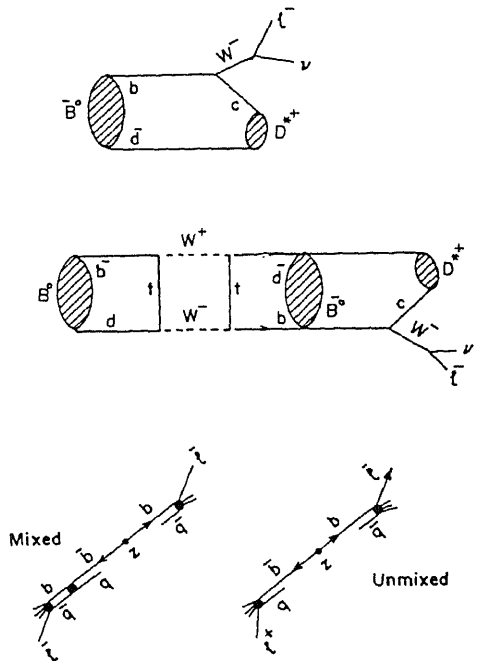

Figure 11: Mixing diagrams within the framework of SM. The simplest signatu
for B^0-$\bar{B}^0$ is the same sign dilepton event.

one can observe even the like sign dileptons. A counting of like sign dileptons, thus provides a measure of mixing;

$$R_{\ell\ell} = \frac{N_{like}}{N_T} = \frac{N^{++} + N^{--}}{N^{++} + N^{--} + N^{\pm}} = 2\chi(1-\chi)$$

Which gives $\chi = \frac{R_{\ell\ell}}{1+\sqrt{1-2R_{\ell\ell}}}$. For large enough P_T ($> 1GeV/c$) cut, the relevant background that fakes mixing is the cascade decay ($b \rightarrow c \rightarrow \ell$) since in this process also the sign of lepton is reversed. Thus, the true mixing is given by $\chi_{true} = \chi_{observed} - \chi_{cascade}$

At LEP, all kind of B hadrons are produced and hence one measures an average mixing for both d type and s type neutral B mesons;

$$\chi = f_d\chi_d + f_s\chi_s$$

Where, $f_d = P(b \rightarrow B_d)$ and $f_s = P(b \rightarrow B_s)$ are the probabilities to observe the two kind of mesons in an overall hadronic b sample. The four LEP experiments have measured the average mixing parameter χ in the follwoing way.

ALEPH [39]: They count dileptons after P_T cut and correct for backgrounds.

DELPHI [40], OPAL [41]: They perform two dimensional maximum likelihood fit using $P_{comb}(1,2)$ (defined later).

L3 [42]: Perform 4D ML fit using $P(1,2), P_T(1,2)$.

ALEPH and DELPHI have also tried another method where one jet charge is assigned by using the momentum weighted charge of the tracks in the jet, while the second is tagged by lepton. This improves the statistics, however at the cost of increased systematics. We have ingnored this measurement at the moment.

To illustrate the measurement of χ we have considered one example from OPAL experiment. A special variable :

$$P_{comb} = \sqrt{(P/10)^2 + P_T^2}$$

is defined to fit the dilepton spectrum. The example of plot for smaller of the two P_{comb} is shown in figure 12 alongwith the fits. The cases for mixing and no mixing are illustrated. The largest systematics are from $Br(b \rightarrow c)$ and $Br(b \rightarrow c \rightarrow \ell)$. A summary of all the results from the four experiments is shown in table 12. The LEP average $\chi = 0.115 \pm 0.011$ can be compared with the world average $\chi = 0.121 \pm 0.010$ that includes the CDF and D0 collaboration results. Using the value of $\chi_d = 0.155 \pm 0.026$ from ARGUS and CLEO and assuming $f_d = 0.39$ and $f_s = 0.12$, we get $\chi_s = 0.45 \pm 0.09$, a number consistent with maximal mixing [43].

Time Differential Measurement

The way to extract B_s mixing parameter is to separate the slow and fast components of the oscillation by studying the time dependent behaviour or use exclusively identified states. As a first step to this goal, ALEPH has demonstrated the measurement of B_d^0 frequency. This has been done by two methods. In one case (D^*, ℓ) correlation has been studied as a function of time [44]. In the other case (ℓ, ℓ) cor-

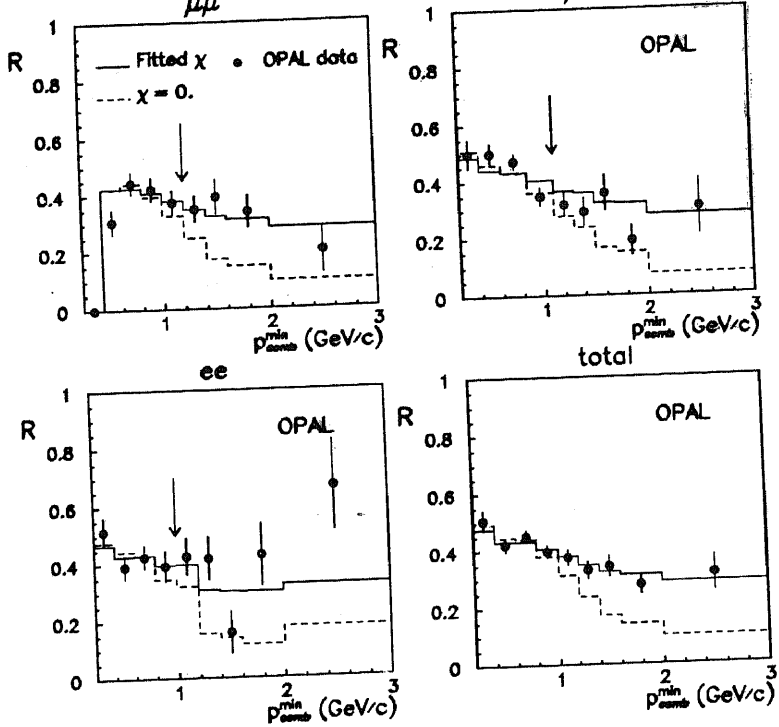

Figure 12: Determination of mixing parameter by OPAL in different channels.

Table 12: Mixing Parameter χ from dileptons

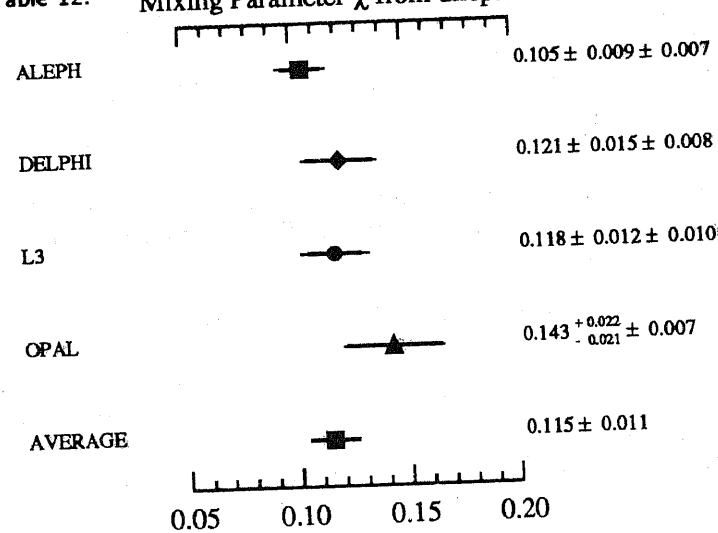

(D^*, ℓ) Analysis

One side of the event is tagged by lepton with $P_T > 0.75$ GeV/c. In this case, the D^* seen on the other side comes mainly from $\bar{B}^0 \rightarrow D^{*+}, X$. Since the reconstruction of D^* vertex is difficult, owing to low momentum of the pion and the small opening angle in $D^{*+} \rightarrow D^0\pi^+$, the D^0 vertex is used instead for decay length and time information. Thus the total decay length is the sum of B^0 and D^0 decay lengths. To determin B^0 boost, MC modeling is required. The unlike sign pair of (D^*, ℓ) signals mixing.

$$R_{\ell D}(t) = \frac{N^{like}(t) - N^{unlike}(t)}{N^{like}(t) + N^{unlike}(t)} = \frac{N^{unmixed}(t) - N^{mixed}(t)}{N^{unmixed}(t) + N^{mixed}(t)}$$

In an ideal situation

$$R_{\ell D}(t) \; \alpha \; \cos \Delta mt$$

However in the real situation oscillation amplitude is damped due to backgrounds and detector resolution effects. The various effects are illustrated in figure 13 where study is made as a function of decay length. The charge asymmetry is shown in figure 14. An unbinned maximum likelihood fit demonstrates that the time independent fit is excluded at 3.2σ level and leads to

$$\Delta m_d = (3.44^{+0.65+0.26}_{-0.70-0.20}) \times 10^{-4} \; eV.$$

Using their measured $\tau_{B_d} = 1.44 \pm 0.15$ ps they determine

$$x_d = \frac{\Delta m_d}{\Gamma} = 0.75^{+0.15+0.08}_{-0.14-0.05}$$

(ℓ, ℓ) Analysis

Both ALEPH and DELPHI have tried this analysis where the latter analysis is very preliminary. In case of ALEPH the event topology defines the secondary vertex and the lepton serves to tag the charge as well as the purity. The energy flow analysis is used to extract the boost for the secondary vertex and hence extract the proper time using the intersection of a bunch of tracks and the lepton. The like sign dilepton is studied as a function of time. In an ideal situation,

$$R_{\ell\ell}(t) \; \alpha \; (1 - \cos \Delta mt)$$

However, due to background and resolution effects, the amplitude is damped. The result of ALEPH analysis is shown in figure 15. The time independent fit is excluded at 99% CL. They extract

$$\Delta m_d = (3.5^{+0.5}_{-0.4} \pm 0.7) \times 10^{-4} eV$$

which leads to $x_d = 0.76 \pm 0.10 \pm 0.16$ consistent with the previous measurement, but with improved error. Further, these results are also consistent with the results from ARGUS ($x_d = 0.72 \pm 0.15$) [46] and CLEO ($x_d = 0.65 \pm 0.10$) [47]. It is hoped that this kind of study will be able to reveal the second component of the oscillation with increase in statistics and should provide the measurement of x_s for B_s.

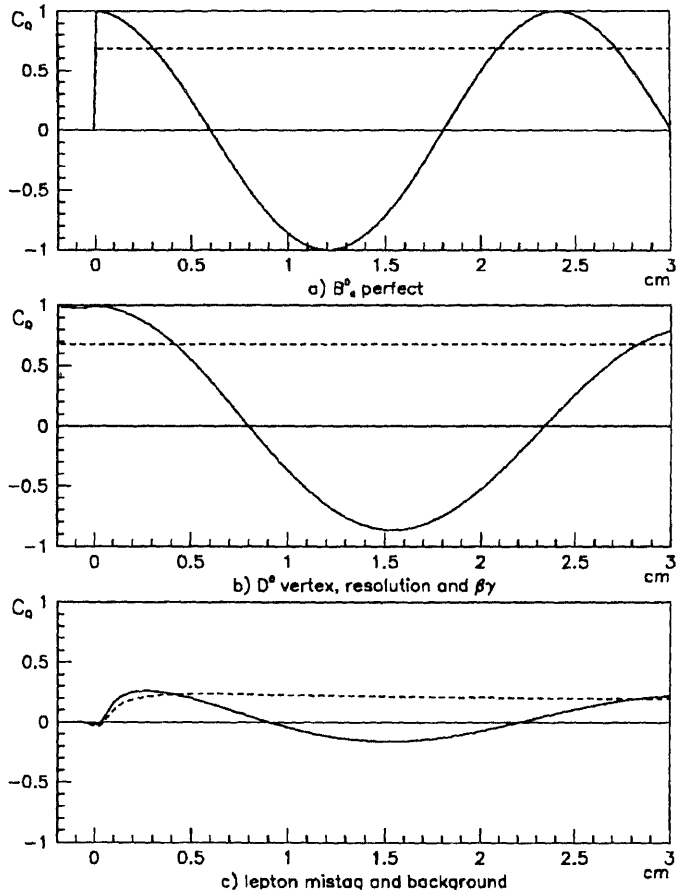

Figure 13: Detector resolution and background effects on the oscillation amplitude.

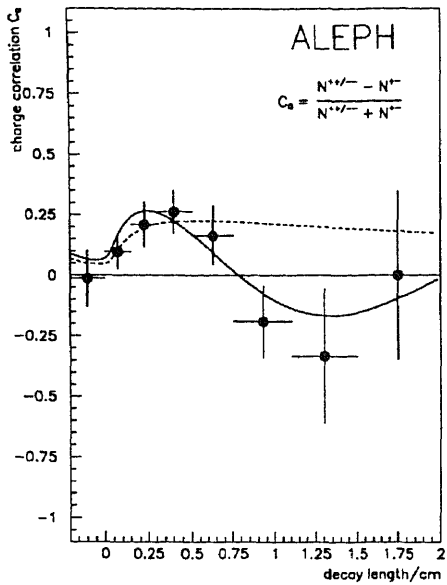

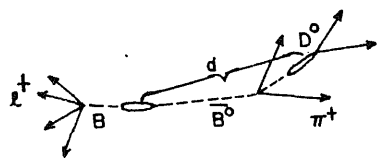

Figure 14: Determination of oscillation frequency, $x_d = \frac{\Delta m_d}{\Gamma}$ by ALEPH. The time independent alternative is shown by dashed line (left). Schematic illustration of the event topology for the study of time dependent mixing using (D^*, ℓ) events (right).

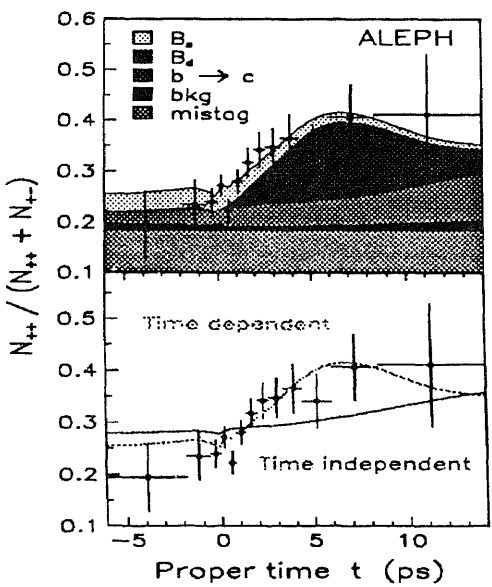

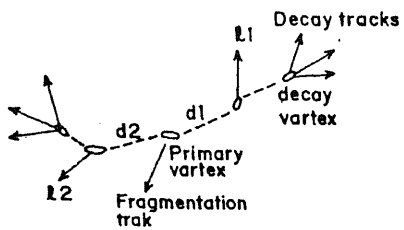

Figure 15: Determination of oscillation frequency (left). Schematic illustration of the event toplogy for the study of time dependent mixing using dilepton events (right).

Prospects for B_s Oscillation

The possibilities to see B_s oscillation in fully identified events are not very exciting. It is, however, expected that with increased statistics in (ℓ, ℓ) events, it should be possible to see the second fast component in the time dependent analysis in near future. In the meantime, to our satisfaction, ALEPH [31] has been lucky to see one fully reconstructed event, out of the two, that exhibits even oscillation. This event is shown in figure 16 with zoomed up view of the vertex region. This is a low

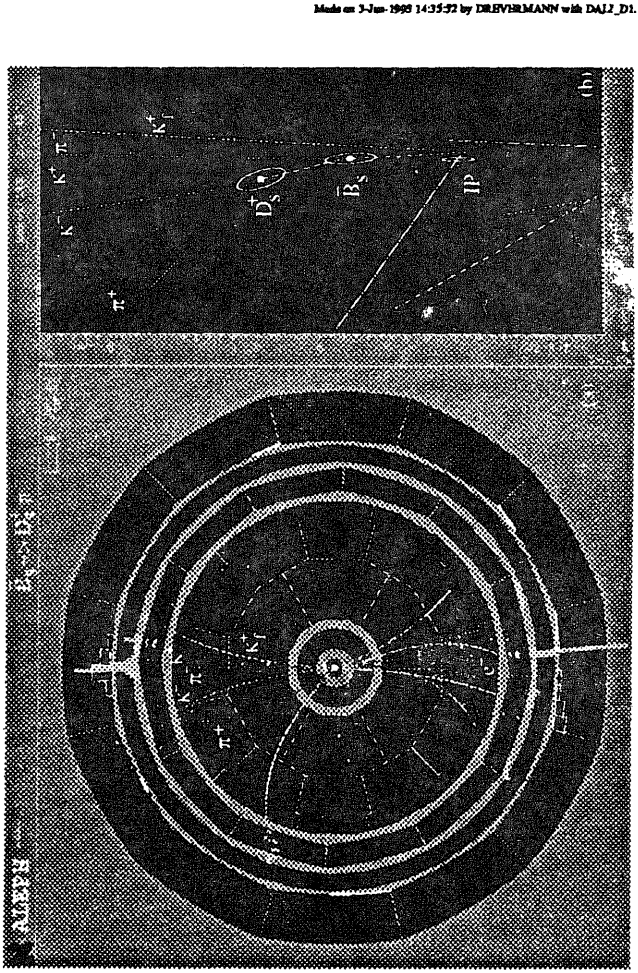

Figure 16: B_s oscillation event seen by ALEPH.

multiplicity event where a $K^+(u\bar{s})$ is seen from the primary vertex. The particle reconstructed at the secondary vertex using $(D_s^+(c\bar{s}), \pi^-)$ is $\bar{B}_s(b\bar{s})$. This is possible only if the $B_s(\bar{b}s)$ which was produced at primary vertex in association with K^+ has oscillated to $\bar{B}_s$ by the time it decays. Since there are no other tracks other than accounted for, any other explanation is unlikely.

6 Interesting B decays

B decay characteristics have been studied both at low energies as well as at LEP. Signifcant contributions, specially from LEP, are in the case of $Br(B \rightarrow \tau + X)$ and $Br(B \rightarrow \chi_c + X)$. We discuss here an example of χ_c mode. This decay mode is interesting to understand the colour suppression mechanism [48]. Moreover a knowledge of the branching ratio is important for optimising CP violation experiments.
For the first time at LEP, L3 [49] has exploited its high resolution photon detection to extract χ_c signal from its decay to $(J/\psi, \gamma)$ where J/ψ is reconstructed from dimuons. The mass difference
$\Delta M = M(J/\psi, \gamma) - M(J/\psi)$ is used to demonstrate the signal, shown in figure 17. Assuming all to be χ_{c1} as $\chi_{c0,2}$ are suppressed, they determine $Br(B \rightarrow \chi_{c1} + X)$

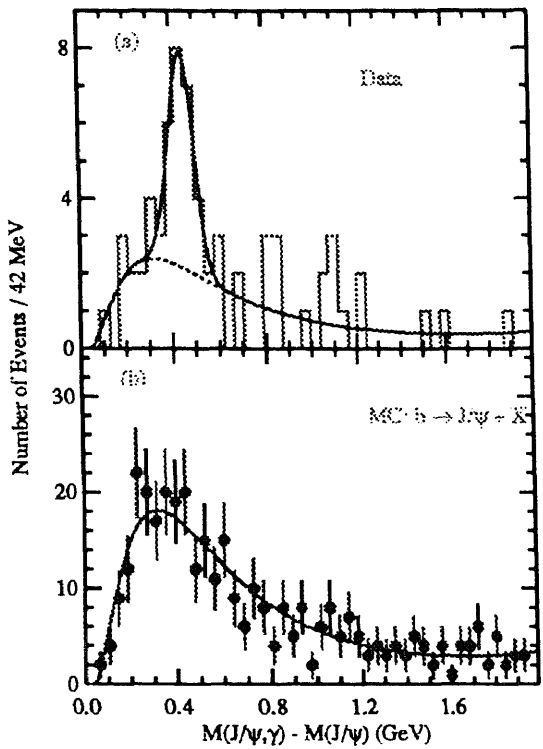

Figure 17: χ_c signal seen by the L3 detector. The background shape is estimated using MC.

$= (2.4 \pm 0.9 \pm 0.2) \times 10^{-2}$. The only other measurement for this mode comes from low energy experiment, ARGUS [50]. Their value being $Br(B \rightarrow \chi_{c1} + X)$
$= (1.23 \pm 0.41 \pm 0.29) \times 10^{-2}$. For any realistic use these numbers have to be improved. With more and more data being collected, LEP experiments are likely to improve this result considerably.
Studies of rare decays are being persued vigorously at LEP, however, the excite-

7 Conclusions

LEP has contributed in an impressive way to the B physics sector. Notable among the results are:

- Using three different techniques for b tagging, namely the lepton tag, the eventshape tag using neural networks, and the lifetime tag, $R_b = \Gamma_b/\Gamma_{had}$ has been measured. The average of the three methods is $R_b = 0.2207 \pm 0.0027$. Compared to this value the SM prediction for a top mass of 160 GeV is =0.2162. If the systematic effects from QCD considerations are understood and the overall errors could be brought down, this may well be an interesting result in near future for new physics.

- The Z peak forward backward charge asymmetry of b quark is measured to be

$$A_{fb}^{\circ} = 0.092 \pm 0.006.$$

  This leads to $\sin^2\bar{\theta}_W = 0.2322 \pm 0.0011$ after QED and QCD corrections are applied. We believe that QCD effects need to be better understood, in view of the fact that the event thrust axis is used to approximate the b quark direction. The sensitivity of the angular measurement depends upon the hadronisation effects, missing neutrino in case of leptonic tag, as well as detector energy and angular resolution where usually calorimetry plays a vital role.

- Impressive progress has been made in the lifetime measurements for b hadrons, both inclusive as well as exclusive. For the inclusive measurements

$$\tau_b = 1.53 \pm 0.03 \text{ ps}.$$

  The exclusive lifetimes follow the trend:

$$\tau_{B^+} > \tau_{B_s^\circ} \approx \tau_{B_d^\circ} > \tau_{\Lambda_b}.$$

  Some of the exclusive lifetimes have been measured at LEP for the first time.

- B°-$\bar{B}^\circ$ oscillation/mixing parameter has been measured with better precision. The LEP average $\chi_B = 0.115 \pm 0.011$ is essentially the world average. The time differential measurement of B°-$\bar{B}^\circ$ oscillation has been demonstrated only at LEP. Both (D°, ℓ) and (ℓ, ℓ) correlations have been used for time dependent analysis using silicon microvertex detector. The (ℓ, ℓ) analysis seems to be promising to extract the second oscillation frequency for B_s, apart from that observed for B_d currently.

- Several branching ratios have been measured, including $(B \rightarrow \tau, X)$ and $(B \rightarrow \chi_c, X)$.

In short LEP has produced plenty of exciting B physics and much more is expected in near future.

I am very much indebted to Maneesh Wadhwa for his untiring help during the preparation of this talk and many stimulating discussions and suggestions. I am also grateful to the organisers of the workshop for providing me local hospitality and partial travel support.

References

[1] M. Consoli, W. Hollik and F. Jegerlehner, Z Physics at LEP, CERN report: CERN 89-08, Vol 1., p 7. Eds: G. Altarelli etal.

[2] T. Aziz, Some interesting approximations of A_{FB} on the Z° peak, TIFR-EHEP 90/6, November 1990.
L3 Collaboration, Phys. Lett. **B252**, 713 (1990).

[3] T. Aziz, $R_b = \Gamma_b/\Gamma_{had}$ as a measure of $Z \to b\bar{b}$ vertex correction, TIFR-EHEP, 90/7, December, 1990.
T. Aziz, Heavy Flavour Physics Symposium, Montreal, July, 1993.

[4] F. Boudjema, A. Djouadi and C. Verzegnassi, Phys. Lett. **B238**, 423 (1990);
F. M. Renard and C. Verzegnassi, Phys. Lett. **260**, 225 (1991).

[5] M. Boulware and D. Finnel, Phys. Rev. **D44**, 2054 (1991).
Djouadi, G. Girardi, W. Hollik, F. M. Renard and C. Verzegnassi, High Luminosity at LEP, CERN Yellow report, CERN 91-02/91 1991, pp. 135. Eds: E. Blucher *et al.*

[6] ALEPH Collaboration, Contributed to EPS Conference, Marseille, July 1993.

[7] DELPHI Collaboration, Contributed to EPS Conference, Marseille, July 1993.

[8] L3 Collaboration, Contributed to EPS Conference, Marseille, July 1993.

[9] OPAL Collaboration, Contributed to EPS Conference, Marseille, July 1993; CERN, PPE/93-46, 193.

[10] ALEPH Colaboration, Phys. Lett. **B313** (1993) 549.

[11] DELPHI Collaboration, Phys. Lett. **B295** (1992) 383.

[12] L3 Collaboration, Phys. Lett. **B307** (1993) 237.

[13] ALEPH Collaboration, Phys. Lett. **B313** (1993) 535.

[14] DELPHI Collaboration, Contributed to EPS Conference, Marseille, July 1993.

[15] OPAL Collaboration, CERN, PPE/93-155 (1993).

[16] ALEPH Collaboration, Contributed to EPS Conference, Marseille, July 1993.

[17] DELPHI Collaboration, Contributed to EPS Conference, Marseille, July 1993.

[18] L3 Collaboration, Contributed to EPS Conference, Marseille, July 1993.

[19] OPAL Collaboration, CERN, PPE/93-78.

[20] ALEPH Collaboration, Contributed to EPS Conference, Marseille, July 1993.

[21] DELPHI Collaboration, Contributed to EPS Conference, Marseille, July 1993.

[22] D. Karlen, "B lifetimes" Heavy Physics Symposium, Montreal, July 1993.

[23] ALEPH Collaboration, Phys. Lett. **B295** (1992) 174
ALEPH Collaboration, CERN, PPE/93-116.

[24] DELPHI Collaboration, Contributed to LEPTON-PHOTON Symposium , Cornell, August 1993; CERN, PPE/93-80.

[25] L3 Collaboration, CERN, PPE/93-158.

[26] OPAL Collaboration, CERN, PPE/93-92.

[27] ALEPH Collaboration, CERN, PPE/93-42.
ALEPH Collaboration, Contributed to EPS Conference, Marseille, July 1993.

[28] DELPHI Collaboration, Contributed to LEPTON-PHOTON Symposium , Cornell, August 1993; Z. Phys. **C57** (1993) 81.

[29] OPAL Collaboration, Contributed to LEPTON-PHOTON Symposium , Cornell, August 1993.

[30] CDF Collaboration, Contributed to LEPTON-PHOTON Symposium , Cornell, August 1993.

[31] ALEPH Collaboration, CERN, PPE/93-214.

[32] DELPHI Collaboration, CERN, PPE/93-176.

[33] OPAL Collaboration, CERN, PPE/93-95.

[34] ALEPH Collaboration, Phys. Lett. **B297** (1992) 449.
ALEPH Collaboration, Contributed to EPS Conference, Marseille, July 1993.

[35] DELPHI Collaboration, Contributed to EPS Conference, Marseille, July 1993.

[36] OPAL Collaboration, CERN, PPE/93-132.

[37] K. V. L. Sarma, TIFR/TH/94-04; A. Ali and D. London, DESY-92-057 (1992) and A. Ali, DESY-92-152 (1992).

[38] R. Forty, CERN PPE/93-165.

[39] ALEPH Collaboration, Contributed to EPS Conference, Marseille, July 1993.

[40] DELPHI Collaboration, Contributed to EPS Conference, Marseille, July 1993.

[41] OPAL Collaboration, CERN, PPE/93-106.

[42] L3 Collaboration, Contributed to EPS Conference, Marseille, July 1993.

[43] W. Venus, Review Talk, LEPTON-PHOTON Symposium, Cornell, August 1993.

[44] ALEPH Collaboration, CERN, PPE/93-99.

[45] ALEPH Collaboration, CERN, PPE/93-105

[46] ARGUS Collaboration, Z. Phys. **C55** (1992) 363; EPS Conference, Marseille, July 1993.

[47] CLEO Collaboration, Heavy Flavour Physics Symposium, Montreal, July 1993.

[48] J. H. Kuhn and R. Ruckl, Phys. Lett. **B135** (1984) 477.
P. H. Cox et al. Phys. Rev. **D32** (1985) 1157.

[49] L3 Collaboration, Phys. Lett. **B317** (1993) 467; M. Wadhwa, Ph. D. Thesis, LAPP, Annecy (1993).

[50] ARGUS Collaboration, Phys. Lett. **B277** (1992) 209.

[51] "Rare B decays", Heavy Flavour Phsyics Symposium, Montreal, July 1993.

Limits on 3 boson vertex parameters from LEP200

S. BANERJEE
Tata Institute of Fundamental Research, Bombay 400 005

Abstract. LEP will be operating at cm energies above W pair threshold from 1996. The process $e^+e^- \rightarrow W^+W^-$ will provide a unique opportunity to test some important aspects of the Standard Model. The methodology of studying this process has been reviewed in this report. The study of the process will probe at the triple vector boson coupling. The sensitivity to anomalous coupling of W boson has been discussed in detail.

1. Introduction

One of the main motivations of LEP200 is a study of the process $e^+e^- \rightarrow W^+W^-$. The reaction $e^+e^- \rightarrow W^+W^-$ has contributions from ν exchange in the t-channel and γ, Z exchange in the s-channel. Of these, the ν exchange gives the largest contribution to the amplitude. In the Standard Model [1] large cancellation takes place between the various amplitudes and the resultant cross section is small and well behaved (see figure 1) at high energies. As a result, small deviation from the Standard Model will show up in this process and can be studied at LEP200. The physics possibilities and limitation have been studied in several earlier reviews [2, 3] and some of those results will be highlighted here.

The main importance of studying the process $e^+e^- \rightarrow W^+W^-$ lies in the γWW and ZWW couplings (see figure 2).
The interaction vertex is given by $ig_{WWV}\Gamma_V^{\alpha\beta\mu}(q, \bar{q}, p)$, where V is the vector boson γ or Z.

$$g_{WW\gamma} = -e; \qquad g_{WWZ} = -e\cot\theta_W$$

$\Gamma_V^{\alpha\beta\mu}$ involves 2×7 independent form factors f_i^γ and f_i^Z. The three form factors f_1^V, f_2^V, f_3^V are related to magnetic and electric dipole moments of W. One can write

$$\begin{aligned} f_1^V &= 1 + \frac{s}{2m_W{}^2} \\ f_2^V &= \lambda_V \\ f_3^V &= 1 + \kappa_V + \lambda_V \\ \mu_W &= \frac{e\,(1 + \kappa_\gamma + \lambda_\gamma)}{2m_W} \\ Q_W &= \frac{e\,(\kappa_\gamma - \lambda_\gamma)}{m_W{}^2} \end{aligned}$$

The other form factors are restricted by C, P and CP invariance

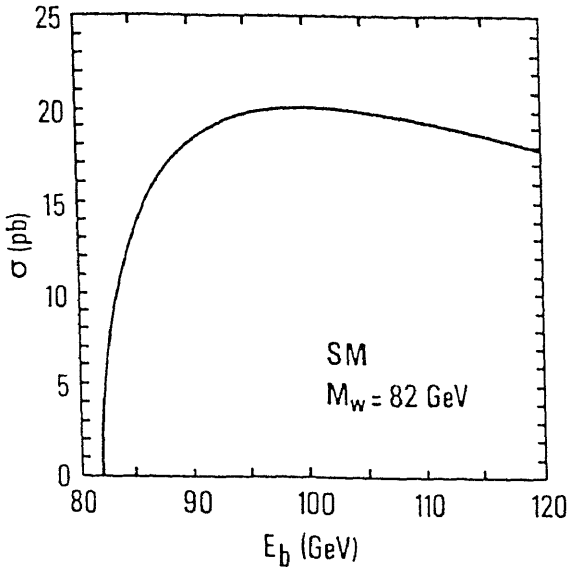

Figure 1. Total cross section for $e^+e^- \rightarrow W^+W^-$ in the Standard Model as a function of beam energy for $m_W = 82$ GeV

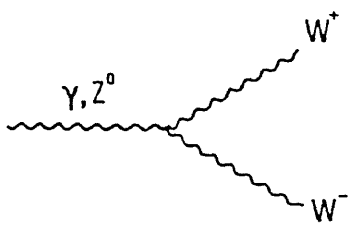

Figure 2. The three boson coupling $Z(\gamma)WW$

CP invaraince	$\Longrightarrow$	$f_4^V = f_6^V = f_7^V = 0$
C and P invariance	$\Longrightarrow$	$f_4^\gamma = f_5^\gamma = f_6^\gamma = f_7^\gamma = 0$

In the Standard Model, one has at the lowest order

$$\kappa_\gamma = \kappa_Z = 1$$
$$\lambda_\gamma = \lambda_Z = 0$$
$$f_{4,5,6,7}^{\gamma,Z} = 0$$

So to test the validity of the Standard Model, one needs to measure

κ_γ, κ_Z
λ_γ, λ_Z
gwwz
$f_{4,5,6,7}^Z$

In the various study groups [4], the following parameters have been studied : δg_{WWZ}, λ (with $\lambda_\gamma = \lambda_Z$), κ_γ and κ_Z.

2. Observables

Experimentally, one can make the following measurements :

- Total cross section
- Production angle of W^+ (W^-)
- Decay angular distribution of W^+ and W^-

As seen in figure 1, the W pair cross section is rather small ($\sim$ 20 pb) compared to typical LEP100 cross sections. It is approximately flat over the energy range of interest (at cm energies above 175 GeV). One can expect to observe about 4000 events per year in one experiment if the LEP luminosity reaches 2×10^{31} cm^{-2}sec^{-1}.

In the standard Model, the W couples universally to quarks and leptons. One can write down [2]

$$\Gamma_W = \Gamma(W \rightarrow \ell\nu)\left[3 + \left(2 + (1 + \frac{{m_t}^2}{2{m_W}^2})(1 - \frac{{m_t}^4}{{m_W}^4})^2\right)(1 + \frac{\alpha_s}{\pi})\right]$$

This leads to 8.9% of W's decaying to each of the leptonic channels ($e\nu$, $\mu\nu$ or $\tau\nu$) and the remaining 73.3% decaying to $q\bar{q}'$ system ($u\bar{d}$ or $c\bar{s}$). As a result, out of all the W^+W^- events, one will have the following final states

54%	4 jets (pure hadronic)
39%	$j_1 j_2 \ell\nu$ (semi leptonic)
7%	$\ell_1 \nu_1 \ell_2 \nu_2$ (pure leptonic)

For the semileptonic final state (j_1 j_2 ℓ ν), one can make the following observations

- j_1 j_2 will determine the folded direction of W

- ℓ determines the charge of W unambiguously. So one can study product angle of W^+ (W^-).

- One can study the complete decay angular distribution of the W which dec leptonically

- One can also study folded decay angular distribution of the W decay hadronically. If tagging of the jet charge is possible, a study of comp decay angular distribution from W decay can be done.

For pure hadronic final states (j_1 j_2 j_3 j_4), the jets determine W direct However, one needs some measure of jet charge to decide about the charge of W in principle, one can always study folded production angle of W^+ (W^-). Simil one can study the folded decay angular distribution of W's.

For pure leptonic final states (ℓ_1 ν_1 ℓ_2 ν_2), the momenta of the two ν's ca calculated within a twofold ambiguity if W width and photons from initial s radiation are ignored. It is nevertheless a very clean sample. But it is difficul obtain the production or decay angular distribution uniquely.

Production of transversely polarized W ($\lambda = \pm 1$) dominates over that of gitudinally polarized W ($\lambda = 0$) for all values of production angle. Howeve the backward region, the dominant $\Delta\lambda = -2$ amplitude from ν exchange vanis So this region is more sensitive in measuring the gauge couplings. Decay ang distribution of W depends on W polarization. So a study of the decay distribu helps in separating contributions from different W helicity components.

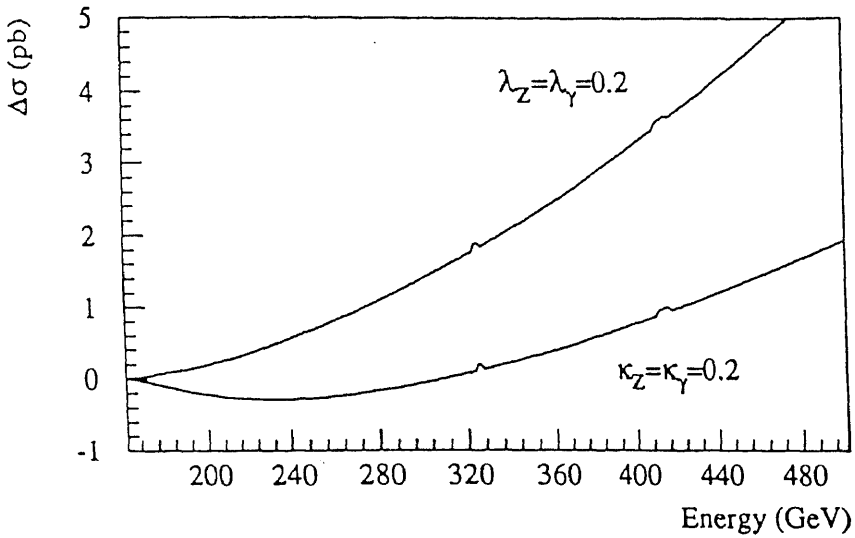

Figure 3. Difference between the SM and non-SM total cross section for $e^+e^- \rightarrow W$ as a function of cm energy [4]

Figure 3 shows a plot of deviation of total cross section of $e^+e^- \rightarrow W^+$ from Standard Model value as a function of cm energy for two sets of anom 3 boson coupling ($\kappa_\gamma = \kappa_Z = 0.2$ and $\lambda_\gamma = \lambda_Z = 0.2$). The figure clearly s that large deviation from the Standard Model is seen only at very high cm en

So LEP200 operating near the W^+W^- threshold will not be able to detect any significant deviation from the Standard Model from this measurement.

Figure 4 shows distribution of production angle of the W's as expected in the Standard Model and also for some non-standard couplings of the 3 boson system. One sees large deviation from the Standard Model only in the very backward directions. So to be sensitive to anomalous W couplings, the detectors should have a large angular acceptance and also high precision in the forward backward direction.

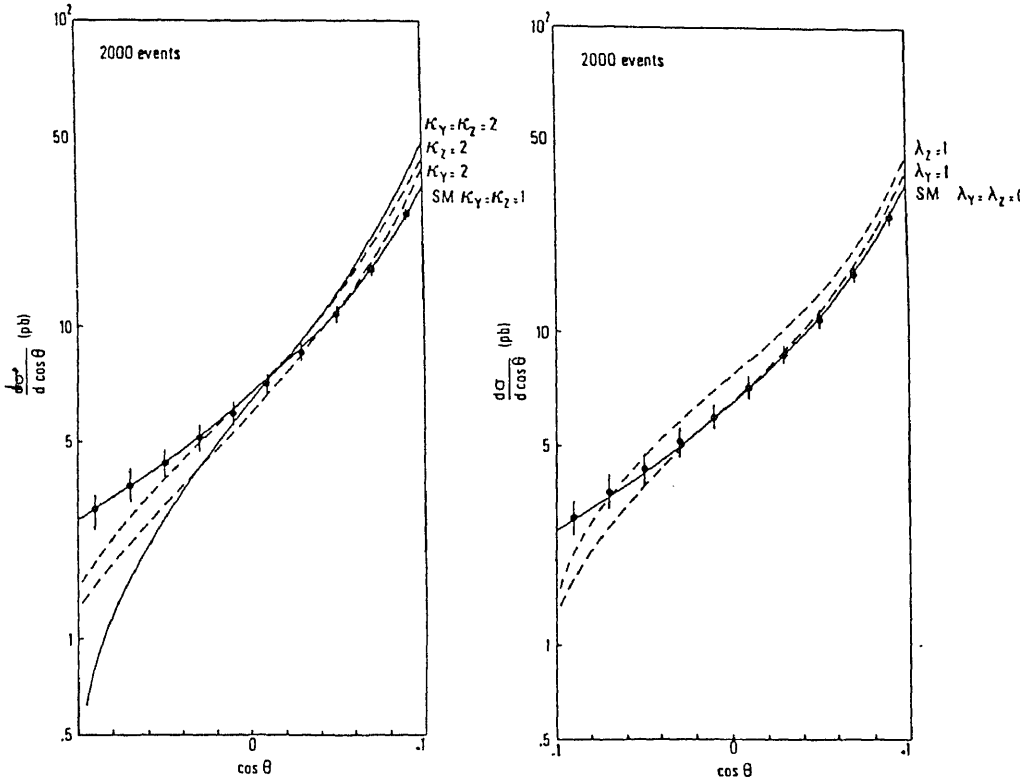

Figure 4. Effect of the angular distribution for W-production due to different values of the parameters κ_γ, κ_Z, λ_γ, λ_Z [3]

3. Event Classification and W Reconstruction

It is necessary to classify the W pair events into three different categories (1) four jet events ($j_1\ j_2\ j_3\ j_4$); (2) two jet plus two lepton events ($j_1\ j_2\ \ell\ \nu$) and (3) four lepton events ($\ell_1\ \nu_1\ \ell_2\ \nu_2$) from the general event characteristics and to select these events from a background of other physics events and noise. A first attempt in this direction has been carried out in [5] by looking into fully simulated and reconstructed events from W-pair generator GENTLE [6].

Leptonic decays of W give rise to events with low multiplicity and sizeable missing energy.On the other hand, hadronic decays of W lead to high multiplicity

events with small missing energy. So global event shape variables like visible energy, energy imbalance, total multiplicity would be useful variables for event classification alongwith particle identification capabilities.

Four jet events are classified by selecting events with high multiplicity ($N > 45$), large visible energy ($E_{vis}/\sqrt{s} > 0.72$), small energy imbalance in the transverse direction ($E_\perp/E_{vis} < 0.25$). Leptonic decays of W to $e\nu$ or $\mu\nu$ are removed by rejecting events with electron candidates with energy above 30 GeV or with muon candidates with momentum above 20 GeV. This set of criteria leads to an efficiency of (94±1)% with (98.9±0.5)% purity.

Four lepton events are classified by selecting events with low multiplicity ($N < 12$) and the presence of two high energy leptons (electrons or muons). High energy electrons are selected with energy above 25 GeV and muons with momentum above 20 GeV. The selection efficiency and purity for the three channels $e\nu e\nu$, $\mu\nu\mu\nu$, $e\nu\mu\nu$ as obtained in [5] are summarized in table 1.

Table 1. Selection efficiency and purity of the four lepton final state

	Efficiency	Purity
$e\nu e\nu$	(79±11)%	(92±8)%
$\mu\nu\mu\nu$	(95±5)%	(95±5)%
$e\nu\mu\nu$	(62±13)%	(83±15)%

For events with 2 jets and 2 leptons, one uses the following criteria : (1) moderate multiplicity ($12 < N < 60$), (2) large missing energy ($E_\perp/E_{vis} > 0.1$–0.15), (3) moderate visible energy ($E_{vis}/\sqrt{s} < 0.88$). In addition, separate selection criteria (on energy of identified particles) were applied to classify these into electron, muon or tau category. The resulting efficiency and purity of the samples are summarized in table 2.

Table 2. Selection efficiency and purity of $j_1\ j_2\ \ell\ \nu$ final state

	Efficiency	Purity
$j_1j_2e\nu$	(74±4)%	(87±3)%
$j_1j_2\mu\nu$	(69±4)%	(94±2)%
$j_1j_2\tau\nu$	(80±3)%	(60±3)%

The stable leptons/hadrons are detected in the detector. For W's decaying hadronically, one needs to reconstruct jets. For both W's decaying hadronically, the number of jets to be reconstructed is 4. For only one W decaying hadronically, the number of jets to be reconstructed is 2 (excluding the lepton when associated with e/μ) or 3 (including the lepton when associated with τ). Several jet reconstruction algorithms [7, 8] have been tried out [9]. In most of these algorithms

are combined into clusters until only four clusters are left. The difference in these algorithms lie in the choice of the closeness variable y_{ij} as summarized in table 3.

Table 3. Closeness variable y_{ij} for various jet algorithms

Algorithm	y_{ij}
JADE	$2E_iE_j(1-\cos\theta_{ij})/{E_{vis}}^2$
Durham	$2\mathrm{Min}(E_i^2,E_j^2)(1-\cos\theta_{ij})/{E_{vis}}^2$
Geneva	$8E_iE_j(1-\cos\theta_{ij})/9(E_i+E_j)^2$
Lund	$2\lvert\vec{p}_i\rvert\lvert\vec{p}_j\rvert\sin(\theta_{ij}/2)/\lvert\vec{p}_i+\vec{p}_j\rvert$

In generalized thrust approach [8], one defines the generalized thrust as

$$T_4 = \max_{\vec{n}_j}\left(\frac{\sum_i \max_j(\vec{p}_i\cdot\vec{n}_j)}{\sum_i|\vec{p}_i|}\right)$$

by dividing the set of particles into 4 groups. T_4 is maximized by regrouping particles and finding the four jet axes from the particle 4-momenta in each group. Technically this is achieved by

- Defining event plane according to the 2 largest eigenvectors of the momentum tensor
- Maximizing T_3 on the event plane by dividing the particles in zones of ϕ angle
- Removing the nicest of the three jets (one with the largest thrust)
- Boosting the rest of the particles in the reduced cm system
- Applying the same 3 jet algorithm to divide these particles to a set of 3 jets
- Checking if the particles in each of the jet has the largest $p_{\|}$ with respect to the jet. If not, reclassification is required.

Jet energies are recalculated using the jet angles as measured, assuming 0 parton mass and energy momentum conservation.

The energy and angular resolution of the jets, thus obtained, are summarized in table 4.

This study suggests that Durham or Lund algorithm is most suitable for jet reconstruction.

Further constraint can be put by imposing energy-momentum conservation in the W-pair production process. These conservation relations as well as the mass shell criteria for the W's can be written down as

$$(p_{j_1}+p_{j_2}+p_3+p_4\,(+p_\gamma))-\begin{pmatrix}\sqrt{s}\\0\\0\\0\end{pmatrix}=f_{1\cdots4}$$

Reconstruction method	σ_E (GeV)	σ_θ (rad)	σ_ϕi (rad)
JADE	6.13	0.113	0.121
Durham	5.96	0.110	0.118
Geneva	6.16	0.115	0.126
Lund	5.58	0.107	0.115
Generalized Thrust	8.50	0.143	0.145

$$(p_{j_1} + p_{j_2})^2 - m^2_{W_1} = f_5$$
$$(p_3 + p_4)^2 - m^2_{W_2} = f_6$$

$p_3 \equiv p_{j_3}$, $p_4 \equiv p_{j_4}$ for four jet final states and $p_3 \equiv p_\ell$, $p_4 \equiv p_\nu$ for $j_1 j_2 \ell\nu$ final state. For perfect measurements, one should have

$$f_j = 0$$

However, because of detector resolution and acceptance, the constraint relations are strictly speaking not satisfied. Energy and direction of the jets and the charged leptons are measured with precision determined by detector resolution and acceptance. After m_W, Γ_W measurement, m_{W_1}, m_{W_2} would be known with some precision. For $j_1\ j_2\ \ell\nu$ final state, $\vec{p}_\nu$ is unmeasured. All these are taken care of by using the method of Lagrangian multiplier. Here one minimizes χ^2 of deviation of measured quatities in an iterative way.

$$\chi^2 = \sum_i \frac{(x_i - x_i^f)^2}{\sigma_i^2} + \sum_j \xi_j f_j$$

The minimum χ^2 should occur for $f_j = 0$ so that the choice of multipliers ξ_j is arbitary. Convergence of the fits are decided by

- the maximum constraint value after fit (e.g. $|f_j| < 10$)
- χ^2 to be small after fit and change of χ^2 in iteration to be also small

The effect of the kinematic fit [10] is summarized in table 5 and figure 5 where one shows the resolutions in production and decay angles of the W's before and after the fit.
The fit improves resolution in all measured distributions.

DELPHI [4] has proposed to use momentum weighted charge of the decay products to measure the charge of the W.

$$C = \sum_i Q_i p_i^\alpha$$

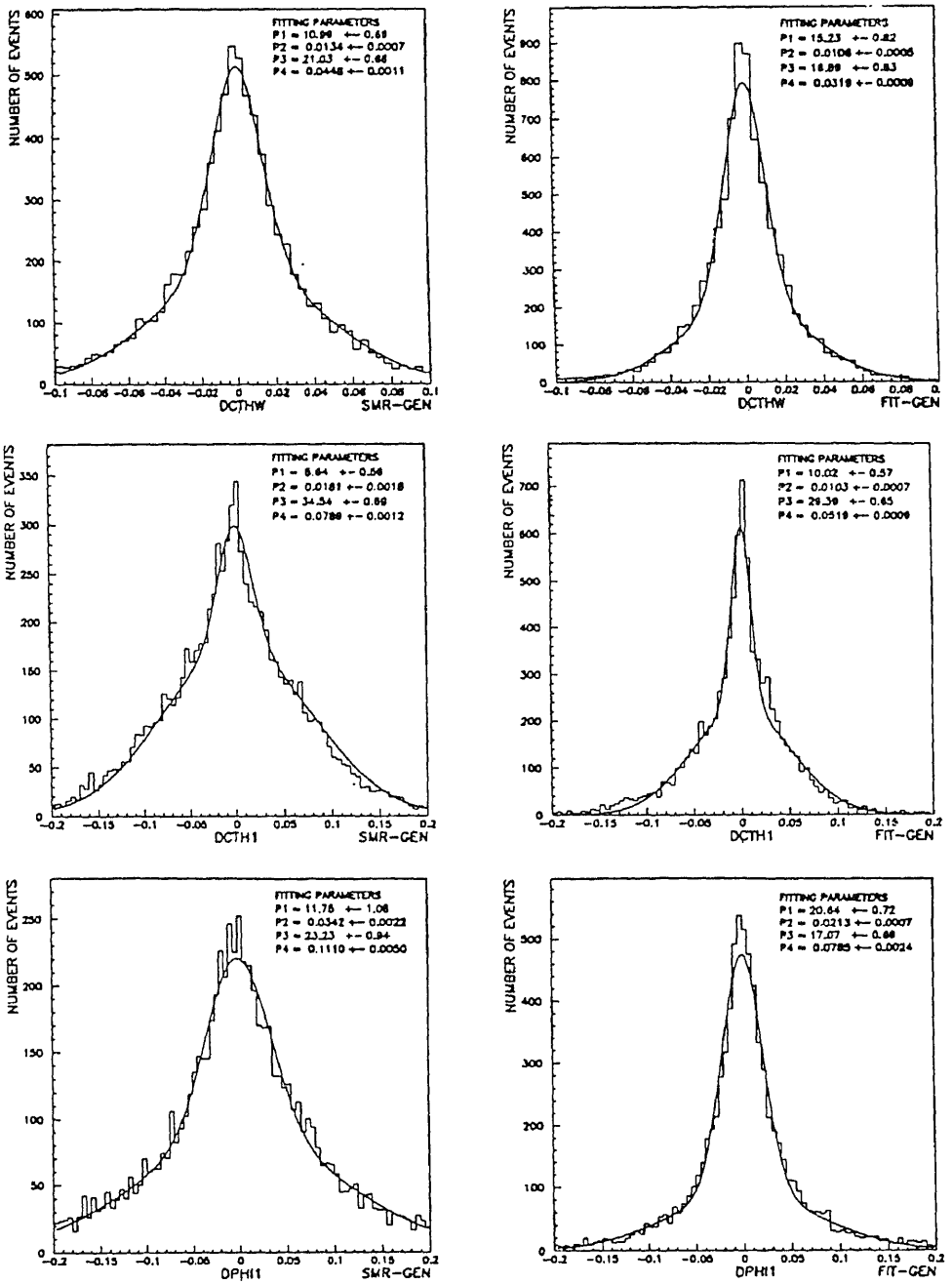

Figure 5. Production (a-b) and decay θ (c-d), ϕ (e-f) angular distribution of W before and after the kinematic fits

Table 5. Resolution in production and decay angular distribution of W before a the kinematic fit

	Before fit	After fit
$\cos\theta_W$	0.0134	0.0108
$\cos\theta_d$	0.0181	0.0103
ϕ_d (rad)	0.034	0.021

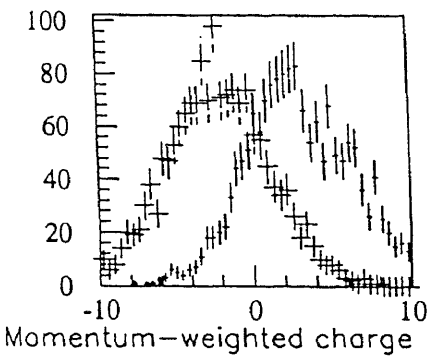

Figure 6. Distribution of momentum weighted charges C_- (the left one) and right one) for jets assigned to W^- and W^+ respectively

removes ~ 30% of the events.

4. Determination of the 3 Boson Couplings

DELPHI [4] has studied the limits which can be realistically set to the parameters of the 3 boson coupling by their detector. They have generated events with complete detector simulation. After the jet reconstruction and kinematic fitting, they correct the observed W production angular distribution from detector effects by deconvoluting the observed distribution with a binned smearing matrix $F(\cos\theta_W^{cor}, \cos\theta_W^{ob})$

$$\frac{d\sigma}{d\cos\theta_W^{cor}} = \int_{-1}^{1} \frac{d\sigma}{d\cos\theta_W^{ob}} \cdot F(\cos\theta_W^{cor}, \cos\theta_W^{ob}) \cdot \epsilon(\cos\theta_W^{ob}) \cdot d\cos\theta_W^{ob}$$

where $\epsilon(\cos\theta_W^{ob})$ represents the efficiency of the selection criteria for the appropriate final state. For 4 jet final states, they apply the jet charge tagging technique to distinguish between W^+ and W^-.

The corrected distribution is then fitted to the theory by varying each of the parameters (δg_{WWZ}, λ, κ_γ and κ_Z) in turn for 500 pb^{-1} data. The results obtained for two cm energies of 176 and 190 GeV are summarized in table 6.

Table 6. Precision in measuring anomalous 3 boson coupling constant for single parameter fit

	$\sqrt{s} = 176$ GeV	$\sqrt{s} = 190$ GeV
δg_{WWZ}	0.051 ± 0.151	-0.166 ± 0.085
λ	0.034 ± 0.095	-0.095 ± 0.048
κ_γ	1.07 ± 0.20	0.86 ± 0.09
κ_Z	1.05 ± 0.16	0.85 ± 0.08

Thus the anomalous coupling can be measured with a precision of 0.1–0.2 for LEP200 operating at a cm energy of 176 GeV. The precision is improved by a factor of 2 by going to a higher cm energy of 190 GeV.

Alternately, one can fit to several parameters simultaneously. This will give rise to contours at 95% confidence level. Figure 7 shows such contours for δg_{WWZ} vs λ for a two parameter fit to generated and reconstructed angular distributions from $j_1 j_2 \ell\nu$ events.

One can draw the following conclusions from these fits

- The constraint on λ is tight and is not too dependent on the values of other parameters

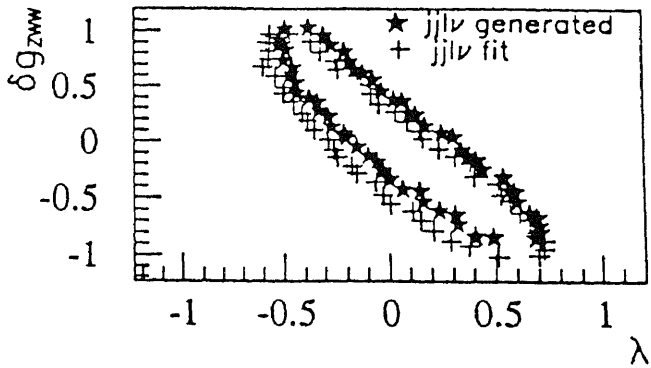

Figure 7. 95% Confidence level contour obtained for δg_{WWZ} and λ from generated and reconstructed production angular distributions using $j_1 j_2 \ell\nu$ events [4]

- The jet charge tagging improves the limits significantly
- One obtains better precision for the anomalous couplings by going to higher cm energies

As has been mentioned earlier, decay angles can be unambiguously determined for leptonic decay of W's in $j_1 j_2 \ell\nu$ event sample. For 4 jet final state, one can obtain folded distribution of decay angular distributions. The charge tagging technique does not work very well for individual jets. Following the suggestions of Hagiwara *et al.* [2], one can parametrize the triple differential cross section in terms of a complete set of known orthogonal functions L_i's, which are used to produce projections $F_i^{\pm}$ of the W^+ and W^- production cross sections respectively.

$$\frac{d\sigma(W^{\pm} \to \ell\nu)}{d\cos\theta_W d\cos\theta_d d\phi_d} = \sum_{i=1}^{9} F_i^{\pm}(\cos\theta_W) L_i(\theta_d, \phi_d)$$

One can now examine a set of linear combinations of F_i^+ and F_i^- to put limits to nonstandard 3 boson parameters. DELPHI [4] have examined the effect of including the decay angular distributions to the parameters (see figure 8).
It is obvious from the figure that the decay angular distributions improve the limit on δg_{WWZ} or κ substantially. The parameter space is more restricted at higher cm energies.

5. Summary

From the studies made so far, one can draw the follwing conclusions :

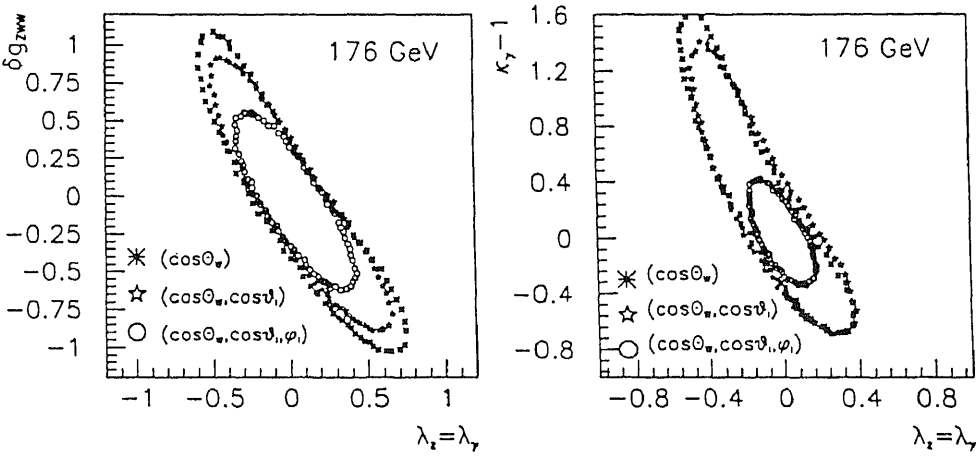

Figure 8. 95% Confidence level contours from the distributions of $\cos\theta_W$, ($\cos\theta_W$, $\cos\theta_d$) and ($\cos\theta_W$, $\cos\theta_d$, ϕ_d) using $j_1j_2\ell\nu$ events [4]

- Techniques have been developed to reconstruct W production and decay angular distributions from the $j_1j_2\ell\nu$ channel as well as the $j_1j_2j_3j_4$ channel. The use of 4 jet channel has the potential of increasing statistics and hence reducing statistical error.
- With 500 pb^{-1} integrated luminosity at LEP200, the 3 boson coupling parameters can be measured from W production angle with a precision of $\pm$0.1-0.2 at 176 GeV.
- Precision of the coupling paramter determination is significantly improved by utilizing the decay angular distribution of W.
- The precision is further improved by operating at a higher energy. Event selection efficiency as well as angular resolution improves with LEP energy.

References

[1] S.L. Glashow, Nucl. Phys. **22** (1961) 579;
S. Weinberg, Phys. Rev. Lett. **19** (1967) 1264;
A. Salam, "Elementary Particle Theory", Ed. N. Svartholm, Stockholm, "Almquist and Wiksell" (1968), 367.

[2] G. Barbiellini *et al.*, in Physics at LEP, ed. J. Ellis and R. Pecci, CERN 86-02, Vol. 2, 1;
K. Hagiwara *et al.*, Nucl. Phys. **B282** (1987) 253.

[3] A. Blondel *et al.*, in ECFA Workshop on LEP200, ed. A. Böhm and W. Hoogland, CERN 87-08, Vol. 1, 120.

[4] S. Katsanevas *et al.*, DELPHI 92-166 Phys 250 (1992).

[5] F. Cavallari and M. Grünewald, L3 Note 1498 (1993).

[6] D. Bardin *et al.*, Phys. Lett. **B308** (1993) 403.

[7] JADE Collaboration, W.Bartel et al., Z. Phys. **C33** (1986) 23;
Y. Dokshizer, J. Phys. **G17** (1991) 1441;
S. Bethke *et al.*, Nucl. Phys. **B370** (1992) 310;
T. Sjostrand, Comp. Phys. Comm. **28** (1983) 227.

[8] S.L. Wu, Z. Phys. **C9** (1981) 329.

[9] T. Aziz *et al.*, L3 Note 1474 (1993).

[10] B.N. Jin and M. Pohl, L3 Note 1479 (1993).

The effective use of precision electroweak measurements

C. P. BURGESS

Institut de Physique, Université de Neuchâtel
1 Rue A.L. Breguet, CH-2000 Neuchâtel, Switzerland.
and
Physics Department, McGill University
3600 University St., Montréal, Québec, Canada, H3A 2T8.

Abstract. Several reasonably model-independent formulations of the implications of new physics for precision electroweak measurements have been developed over the past years, most notably by Peskin and Takeuchi, and by Altarelli *et al.* These formulations work by identifying a small, but useful, set of parameters through which new physics often enters into well-measured physical observables. For the theories to which such an analysis applies, this approach greatly streamlines the confrontation with the data. Since the experimentally-allowed range for these parameters has been determined from global fits to the data, theorists need only compute their predictions for these parameters to constrain their models. We summarize these methods here, together with several recent generalizations which permit applications to wider classes of new physics, and which include the original approaches as special cases.

1. Introduction

The attainment of high precision in measurements of Z-boson properties has been perhaps the most significant experimental result in high-energy physics over the last decade. Besides testing the Standard Model (SM) to high precision, experiments at LEP and at SLC [1] are providing the first experimental winnowing of the bumper crop of theories that hope to describe the physics at energies well above 100 GeV.

Indeed, the data on the Z resonance is now so good that model builders ignore it at their peril. There is a very real benefit in confronting the various models of current theoretical interest with the constantly improving experimental results. One way to proceed is to simply compute the relevant observables explicitly on a model-by-model basis, and to fit the results to the data in order to constrain the model's parameter space. Unfortunately, this is a time-consuming procedure and so one is limited in the number of models which can be treated in this way. For well-motivated theories, such as the minimal supersymmetric generalizations to the standard model (MSSM) for instance, such detailed calculations may be worth the effort they require, although even here it is impractical to explore the model's entire parameter space.

Happily, there is another way to proceed which can substantially reduce the labour that is required to confront a model with the implications of the data. This alternative is based on the realization that many models often only contribute to deviations from the SM — for the well-measured observables of interest — in a limited number of ways. For instance, this could happen if all of the new particles only couple to the presently-observed ones in a restricted manner, such as through the exchange of electroweak gauge bosons. Or all of the new particles could be extremely heavy. In either case it is typically true that only a small number of independent combinations of the model's coupling constants ever appear in — and so are well constrained by — the observables that are measured. In these cases it is useful to confront the data in two steps. First, one can parameterize the well-measured observables in terms of a few independent variables which can then be constrained, once and for all, by comparing with the experiments. Next, constraints on any given model may be obtained by comparing the bounds on these parameters with the model's predictions for them as functions of its underlying couplings.

Such a two-step procedure has the advantage of separating the statistical fit to the data from model-dependent calculations. Since the data can be fit, once and for all, to a general set of parameters, it is not necessary to repeat this analysis separately for every model. Although, in principle, the permitted parameter space that is obtained for a particular theory in this way can differ somewhat from what would be obtained by a direct fit to the model, in practice the two procedures turn out to give constraints which are essentially equivalent. Furthermore, the comparative model-independence of the fit to the data in the two-step approach permits an efficient comparison of many models, and so gives a reasonably broad picture of the kinds of new physics which can produce deviations in different observables.

There are a number of similar, but not completely equivalent, examples of this type of reasoning which have become widely used in the literature [2, 3, 4, 5, 6]. The most widely used of these are based on the parameterizations of Peskin *et.al.* [2], and of Altarelli *et.al.* [5]. Both of these formalisms are very useful for describing the implications for precision electroweak measurements of a wide class of new physics. Neither of these parameterizations of the observables can encompass all models, however, and so it is important to bear in mind the limits to their applicability when attempting to use their results for comparing with any particular theory. Some well-motivated models and observables cannot be analysed completely within the framework of either approach, motivating their extension to more general situations [7, 8]. The purpose of this review is to describe those extensions which I have helped to develop, and to relate these extensions to earlier approaches. Some applications of the resulting techniques are also described.

This article is organized as follows. There are two main categories of new physics that have been considered to date: those which dominantly contribute to observables through 'oblique' corrections, and those for which the new physics is heavy. The next two sections are devoted to describing how each of these kinds of corrections can contribute to electroweak observables. In the next section the case of 'oblique' corrections is considered, while heavy, non-oblique, new physics is considered in section 3. Section 4 briefly describes a number of the applications of

Almost all of the observables that are presently amenable to accurate measurement can be phrased in terms of the two-particle scattering of light fermions. This is because these experiments either involve the scattering of two quarks or leptons, or the decay of an initial fermion into three lighter ones. There are three ways in which new physics can affect such experiments, given that the new particles are not themselves directly produced. It can: (*a*) change the propagation of the gauge bosons that can be exchanged by the fermions; (*b*) alter the three-point fermion – boson couplings; and (*c*) modify the four-point direct fermion – fermion interactions (*i.e.*: 'box'-diagram corrections).

An important class of new-physics models contribute dominantly to precision measurements through process (*a*): changes to the vacuum polarizations of the electroweak bosons. Such corrections are called 'oblique' [9], and when they dominate they imply *universal* modifications to light-particle scattering, in the sense that the changes depend only on the electroweak quantum numbers of the light fermion involved. Oblique corrections can be the most important when the direct couplings between the observed light fermions and any new particles are either forbidden or highly suppressed.

2.1 General oblique corrections

The effects of oblique corrections on fermion scattering can be determined by examining how the gauge boson vacuum polarizations

$$\Pi^{\mu\nu}_{ab}(q) = \Pi_{ab}(q^2)\,\eta^{\mu\nu} + (q^\mu q^\nu \text{ terms}), \tag{1}$$

(with $a, b = \gamma, W, Z$) appear in the observables of interest [9, 10]. The contribution to these due to new physics we denote as $\delta\Pi_{ab}(q^2)$, so the full vacuum polarization is given by: $\Pi_{ab}(q^2) = \Pi^{SM}_{ab}(q^2) + \delta\Pi_{ab}(q^2)$.

In general, each of the $\delta\Pi_{ab}(q^2)$ can be arbitrary functions of q^2, and so the vacuum polarizations in principle contain several unknown functions, each of which can potentially enter into all physical observables. Any attempt to extract general information by fitting these functions to the data might therefore seem to be doomed because of the large number of unknown quantities in comparison to the amount of data that is available. This turns out to be too pessimistic a view, however, because currently accurate measurements are performed either at very low energies, or on the Z resonance: *i.e.* only for $q^2 = m_z^2$ and $q^2 \approx 0$. ($q^2 = m_w^2$ should also be considered to the extent that the mass and width of the W boson are thought to be sufficiently well measured.) As a result, the unknown functions, $\delta\Pi_{ab}(q^2)$, are presently only accurately sampled at these few values of four-momentum transfer.

This restriction — that precision observables only probe $q^2 \approx 0$ and $q^2 = m_z^2$ and m_W^2 — implies that all oblique corrections to electroweak observables can be expressed in terms of six independent combinations of the various $\delta\Pi$'s [7]. The counting proceeds as follows.

1. Inspection of the graphs with vacuum polarization insertions shows that, *a priori*, there are ten quantities to consider. For neutral-current processes at $q^2 = 0$ and $q^2 = m_z^2$ these are: $\delta\Pi_{\gamma\gamma}(q^2)/q^2$, $\delta\Pi_{z\gamma}(q^2)/q^2$ and $\delta\Pi_{zz}(q^2)$. (Notice that electromagnetic gauge invariance ensures that both $\delta\Pi_{\gamma\gamma}(q^2)/q^2$

denoting differentiation with respect to q^2, also contributes at $q^2 = m_z^2$. Finally, charged-current observables, or those involving physical W particles, involve $\delta\Pi_{ww}(q^2)$ at $q^2 = 0$ and m_w^2, as well as $\delta\Pi'_{ww}(m_w^2)$.

2. Of these ten possible parameters, three combinations can never lead to observable deviations from the SM, since they can be absorbed into SM renormalizations. For instance, they can be absorbed into renormalizations for the electroweak gauge potentials, W_μ^a, B_μ, and of the Higgs *vev*, $\langle\phi\rangle$. This reduces the total number of possible oblique parameters to seven.

3. Finally, at the present levels of accuracy, new-physics contributions to $\delta\Pi_{\gamma\gamma}(m_z^2)$ are not detectable. This is because this term contributes purely through photon exchange, which is not resonantly enhanced when $q^2 = m_z^2$. As a result, the influence of $\delta\Pi_{\gamma\gamma}(m_z^2)$ is suppressed by $O(\Gamma_z/m_z) \sim 0.03$ in comparison to the effects of the Z-mediated terms $\delta\Pi_{z\gamma}(m_z^2)$ and $\delta\Pi_{zz}(m_z^2)$. We are therefore left with six measurable oblique parameters.

There is obviously a great deal of freedom in how to parameterize this six-dimensional parameter space. A convenient way to define the six oblique parameters is:

$$
\begin{aligned}
\frac{\alpha S}{4 s_w^2 c_w^2} &= \left[\frac{\delta\Pi_{zz}(m_z^2) - \delta\Pi_{zz}(0)}{m_z^2}\right] - \frac{(c_w^2 - s_w^2)}{s_w c_w}\,\delta\widehat{\Pi}_{z\gamma}(0) - \delta\widehat{\Pi}_{\gamma\gamma}(0), \\
\alpha T &= \frac{\delta\Pi_{ww}(0)}{m_w^2} - \frac{\delta\Pi_{zz}(0)}{m_z^2}, \\
\frac{\alpha U}{4 s_w^2} &= \left[\frac{\delta\Pi_{ww}(m_w^2) - \delta\Pi_{ww}(0)}{m_w^2}\right] - c_w^2\left[\frac{\delta\Pi_{zz}(m_z^2) - \delta\Pi_{zz}(0)}{m_z^2}\right] \\
&\qquad - s_w^2\,\delta\widehat{\Pi}_{\gamma\gamma}(0) - 2 s_w c_w\,\delta\widehat{\Pi}_{z\gamma}(0) \qquad (2) \\
\alpha V &= \delta\Pi'_{zz}(m_z^2) - \left[\frac{\delta\Pi_{zz}(m_z^2) - \delta\Pi_{zz}(0)}{m_z^2}\right], \\
\alpha W &= \delta\Pi'_{ww}(m_w^2) - \left[\frac{\delta\Pi_{ww}(m_w^2) - \delta\Pi_{ww}(0)}{m_w^2}\right], \\
\alpha X &= -s_w c_w\left[\delta\widehat{\Pi}_{z\gamma}(m_z^2) - \delta\widehat{\Pi}_{z\gamma}(0)\right],
\end{aligned}
$$

where s_w and c_w denote the sin and cosine of the weak mixing angle, θ_w, and α represents the electromagnetic fine-structure constant. For numerical purposes we later use $\alpha(m_z^2) = 1/128$ and $s_w^2 = 0.23$. The quantity $\delta\widehat{\Pi}_{ab}(q^2)$ denotes the ratio $\delta\Pi_{ab}(q^2)/q^2$. These definitions are chosen so that (*i*) the first three agree with the definitions of S, T and U that are used in Ref. [3], (*ii*) the remaining three quantities, V, W and X, vanish if $\delta\Pi_{ab}(q^2)$ should be simply a linear function of q^2, and (*iii*) each parameter contributes to a particular kind of observable (see below).

A straightforward calculation gives expressions for the corrections to the various electroweak observables in terms of the parameters S through X. One complication arises because these corrections must be referred to the corresponding (radiatively corrected) SM prediction. Because of the necessity for performing radiative corrections, the expressions for the SM predictions, in turn, depend on (*i*) which three

observables are used to infer the experimental values for the SM couplings, and (*ii*) unknown quantities, such as the masses, m_t, m_H, of the t quark and Higgs boson.

We follow the universal practice of using the three best-measured observables — α from low-energy electron properties, G_F from muon decay, and m_Z from LEP — as inputs for fixing the values of the SM couplings from experiment. How the parameters, S through X, appear in the final expressions depends in detail upon this choice, since new physics also affects these input observables, and so shifts the inferred values for the SM couplings. With these inputs, and with the definitions of S through X given above, U and W only enter into 'charged-current' quantities like the mass and width of the W boson, and of these W appears only in the W-boson width. Purely neutral-current data depend only on S, T, V and X, and of these only S and T appear in observables at low energies (for which $q^2 \approx 0$). V and X arise only in observables defined at the Z resonance. Of these two, X enters as a correction to the effective weak mixing angle, and so contributes to asymmetries such as A_{LR} or A_{FB}. V, on the other hand, drops out of these asymmetries, but instead changes the Z partial widths, since it alters the normalization of the Z-fermion couplings. The numerical expressions for these observables as functions of S through X are summarized in Table 1.

Table 1. Oblique Contributions to Observables
The dependence of some electroweak observables on S, T, U, V, W and X. The numerical values $\alpha(m_Z^2) = 1/128$ and $s_w^2 = 0.23$ are used in preparing this table. The precise definitions of the observables can be found in Refs. [7].

$$\Gamma_Z = (\Gamma_Z)_{SM} - 0.00961S + 0.0263T + 0.0194V - 0.0207X \text{ (GeV)}$$
$$\Gamma_{b\bar{b}} = (\Gamma_{b\bar{b}})_{SM} - 0.00171S + 0.00416T + 0.00295V - 0.00369X \text{ (GeV)}$$
$$\Gamma_{l^+l^-} = (\Gamma_{l^+l^-})_{SM} - 0.000192S + 0.000790T + 0.000653V - 0.000416X \text{ (GeV)}$$
$$\Gamma_{had} = (\Gamma_{had})_{SM} - 0.00901S + 0.0200T + 0.0136V - 0.0195X \text{ (GeV)}$$
$$A_{FB}(\mu) = (A_{FB}(\mu))_{SM} - 0.00677S + 0.00479T - 0.0146X$$
$$A_{pol}(\tau) = (A_{pol}(\tau))_{SM} - 0.0284S + 0.0201T - 0.0613X$$
$$A_e(P_\tau) = (A_e(P_\tau))_{SM} - 0.0284S + 0.0201T - 0.0613X$$
$$A_{FB}(b) = (A_{FB}(b))_{SM} - 0.0188S + 0.0131T - 0.0406X$$
$$A_{FB}(c) = (A_{FB}(c))_{SM} - 0.0147S + 0.0104T - 0.03175X$$
$$A_{LR} = (A_{LR})_{SM} - 0.0284S + 0.0201T - 0.0613X$$
$$m_W^2 = (m_W^2)_{SM}(1 - 0.00723S + 0.0111T + 0.00849U)$$
$$\Gamma_W = (\Gamma_W)_{SM}(1 - 0.00723S + 0.0111T + 0.00849U + 0.00781W)$$
$$g_L^2 = (g_L^2)_{SM} - 0.00269S + 0.00663T$$
$$g_R^2 = (g_R^2)_{SM} + 0.000937S - 0.000192T$$
$$g_V^e(\nu e \to \nu e) = (g_V^e)_{SM} + 0.00723S - 0.00541T$$
$$g_A^e(\nu e \to \nu e) = (g_A^e)_{SM} - 0.00395T$$
$$Q_W(^{133}_{55}Cs) = Q_W(Cs)_{SM} - 0.795S - 0.0116T$$

The expressions from Table 1 can now be compared with the data to obtain bounds on the phenomenologically allowed range for the parameters S through X. In making this comparison we use the values $m_t = 150$ GeV and $m_H = 300$ GeV for

addressed in section 4. The one-σ allowed ranges for the oblique parameters which result from the fit to the data of Ref. [7] are then given by:

$$S = -0.93 \pm 1.7; \qquad T = -0.67 \pm 0.92; \qquad U = -0.6 \pm 1.1;$$
$$V = 0.47 \pm 1.0; \qquad W = 1.2 \pm 7.0; \qquad X = 0.10 \pm 0.58. \tag{3}$$

Notice that since the parameter W only appears in the width of the W boson, it is the most poorly constrained.

2.2 When the new physics is heavy

There is an important special case for which the above oblique analysis simplifies considerably. This is when the lightest mass, M, for all of the new particles is much larger than m_z. Since the scale over which q^2 varies appreciably in $\delta\Pi_{ab}(q^2)$ is set by M, in this case these functions may be well approximated by the first terms in their Taylor expansion in powers of q^2/M^2. Since current measurements are restricted to the regime $q^2 \lesssim m_z^2$, this approximation is controlled by powers of the small parameter m_z^2/M^2.

The leading contributions in this limit — *i.e.* those which are not suppressed by inverse powers of M^2 — are simply linear functions [2, 3, 4]. of q^2:

$$\delta\Pi_{ab}(q^2) \approx A_{ab} + B_{ab}\, q^2. \tag{4}$$

(Higher-order terms have also been considered in the literature. [11]) With this assumption three of the oblique parameters, V, W and X, vanish identically and so all new physics effects are described by the three parameters S, T and U. The expressions for observables in terms of these three parameters may therefore be obtained simply by setting $V = W = X = 0$ in Table 1. A fit to the data, [7] with V, W and X constrained to vanish, then gives the following one-σ allowed ranges for S, T and U:

$$S = -0.48 \pm 0.40; \qquad T = -0.32 \pm 0.40; \qquad U = -0.12 \pm 0.69. \tag{5}$$

Not surprisingly, the allowed range for S and T in this two-parameter fit is smaller than was permitted in the six-parameter fit whose results are given above.

Since the neutral-current data are completely controlled by the two parameters S and T, it has become conventional to display the results of fits to this data by plotting the ellipses of constant confidence interval in the two-dimensional S-T plane. Figure 1 displays the results of the two fits described above. Notice that, since m_W can depend on the parameter U as well as on S and T, m_W should only be included in such a plot if there are *a priori* reasons for believing U to be negligibly small.

2.3 Using only the Z resonance

In recent years the electroweak data on the Z resonance has become more accurate than are the older low-energy measurements. As a result it is now possible [5] to usefully constrain new physics using *only* the data at $q^2 = m_z^2$. As is clear from the earlier counting of parameters, such a restriction to only one value of four-momentum transfer permits a description of the data in terms of fewer oblique parameters than the six that were required when $q^2 \approx 0$ was also considered. This

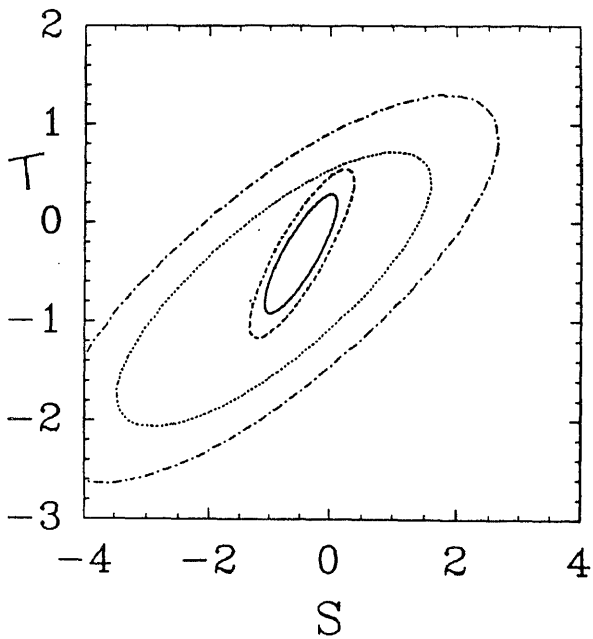

Figure 1. Constraints on S and T from a fit to both high- and low-energy electroweak measurements. The solid line represents the 68% C.L. setting VWX to zero, the dashed line represents the 90% C.L. Setting VWX to zero, the dotted line represents the 68% C.L. allowing VWX to vary, and the dot-dashed line represents the 90% C.L. allowing VWX to vary.

As is easily verified by repeating the counting argument given earlier, only three parameters are required to describe the general oblique corrections in this case. A convenient choice for these three parameters is: [12]

$$\begin{aligned} S' &= S + 4s_w^2 c_w^2\, V + 4(c_w^2 - s_w^2)\, X, \\ T' &= T + V, \\ U' &= U - 4s_w^2 c_w^2 V + 8 s_w^2 X. \end{aligned} \tag{6}$$

With this choice, the parameters S', T' and U' reduce to S, T and U in the limit where $V = W = X = 0$. This ensures that the dependence of all Z-pole observables on S', T' and U' can be simply read off from Table 1 by replacing $(S, T, U, V, W, X) \to (S', T', U', 0, 0, 0)$.

As before, since the data on the Z resonance only depends on two parameters S' and T', it is convenient to display the result of a fit of these two parameters to the data as a plot in the S'-T' plane. The result of such a fit, including the more recent 1994 data, [13] is displayed in Figure 2.

It is noteworthy that the constraints on S' and T' from Figure 2 are comparable to those on S and T using the larger data set, including also the $q^2 \approx 0$ observables, that are used for Figure 1. This illustrates the high quality of the data that has been obtained over recent years at the Z resonance. The conceptual difference between Figures 1 and 2 remains crucial, however. Whereas a two-parameter, $S' - T'$, description of the Z-pole data relies only on the assumption that oblique corrections dominate, the extension of such a description to include also neutral-current measurements at $q^2 \approx 0$ relies on the additional assumption that all of the new physics is sufficiently massive to permit the neglect of V and X.

2.4 A cultural aside

Treating the Z-pole data by itself is very much in the spirit of the approach of Ref. [5]. The formalism of these authors differs from that described so far in the following two ways, however.

1. These authors introduce three parameters, ϵ_1, ϵ_2, and ϵ_3, which broadly correspond to the three parameters S', T' and U'. Their definitions, however, are made directly in terms of the observables, and do not separate the new-physics contributions from those due to SM radiative corrections. As a result only the deviation, $\delta\epsilon_i = \epsilon_i - \epsilon_{SM}$, from the SM predictions — using the fiducial choices for m_t and m_H — are directly related to S', T' and U'. The connection between the two sets of parameters is [5, 14, 15]:

$$\delta\epsilon_1 = \alpha T', \qquad \delta\epsilon_2 = -\frac{\alpha U'}{4s_w^2}, \qquad \delta\epsilon_3 = \frac{\alpha S'}{4s_w^2}. \tag{7}$$

2. A second important difference in the approach of Altarelli *et.al.* is to permit one non-oblique correction, parameterized by ϵ_b, to the Zbb vertex. The inclusion of this correction is motivated by the large m_t-dependent contributions it receives from SM radiative corrections, and potentially from other kinds of new physics. We return to this type of term in the next section.

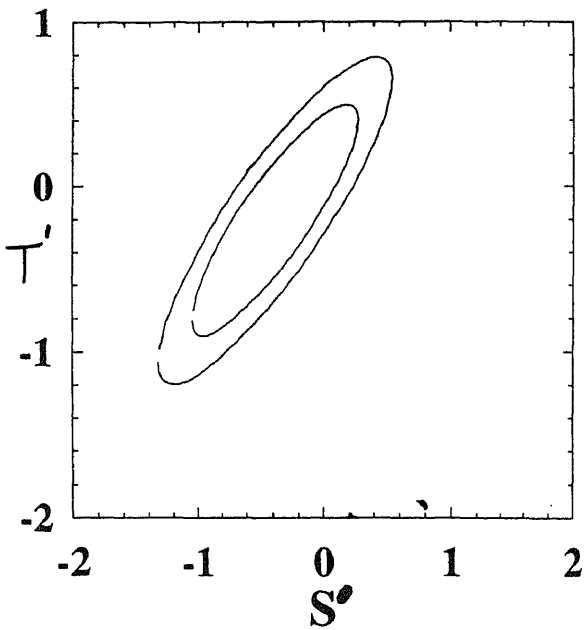

Figure 2. Constaints on S' and T' from a global fit of precison electroweak measurements at the Z resonance only. The two lines represent the 68% C.L. and 90% C.L. ellipses.

3. Nonoblique new physics

Although many kinds of new physics dominantly produce oblique corrections to electroweak observables, this is certainly not true for all kinds. Examples include any new physics which preferentially couples to, say, the heavy generations. Another worthwhile generalization of the previous formalism is therefore to extend it to include nonoblique corrections. In order to be practical, however, such a generalization cannot be permitted to introduce too many new parameters, or else the utility of the confrontation with the data will be lost. Some criterion is necessary to limit and organize the number of independent interactions that need be considered.

A very natural way to provide the required organization is to assume that all of the new physics is much heavier than the electroweak scale, m_z. In this case the implication of such new physics for current experiments can be parameterized in terms of a low-energy effective lagrangian [16] such as would be obtained by integrating out all of the presently-undiscovered heavy particles. In this section the results of such an analysis [8] are summarized.

The limit of large masses, M, for all hypothetical new particles allows their low-energy interactions to be organized according to dimension, with operators having a higher mass dimension being more suppressed by inverse powers of M. Simple dimension counting need not be the whole story, of course, as low-energy selection rules and symmetries can also help to determine the relative size of the various effective interactions. For a more complete discussion of the issues involved see Ref. [8].

3.1 The effective interactions

Consider, therefore, the most general effective interactions that are consistent with the particle and symmetry content that is appropriate for applications to processes having energies $\lesssim 100$ GeV. Since our intention is to study current experiments in this energy range, we take our particle content to include only those which already have been detected. This includes most of the SM particles, including precisely three left-handed neutrinos, but does *not* include the Higgs boson and the top quark, which we take to have been integrated out (if they indeed exist [17]). Due to the absence of these particles, the electroweak gauge group must be nonlinearly realized on the given fields, and so in practice it can be completely ignored [18] (apart from the unbroken electromagnetic subgroup) in what follows. The price for choosing this particle content is that the resulting effective lagrangian has to violate unitarity at energies at or below the TeV range.

Typically, any such lagrangian contains a great many effective interactions. Fortunately, there is a great deal of latitude in how the interactions can be written, since there is considerable freedom to redefine fields to simplify terms in the lagrangian. We choose to work with fields for which the kinetic and mass terms take their standard diagonal forms. The nonstandard interactions which arise in the most general effective lagrangian up to mass dimension five can then be written in the following way.[8]

1. Fermion Masses: The only possible effective interactions having dimension two or three are an arbitrary set of masses for the W and Z bosons and for each of the low-energy fermions. The fermion mass terms so obtained are indistinguishable

A neutrino mass matrix would have two effects. It would (*i*) give the neutrino mass eigenstates nonzero masses, and (*ii*) it would introduce unitary Cabbibo-Kobayashi-Maskawa (CKM) style mixing matrices, $\tilde{V}_\ell^{ij}$ into the various charged-current neutrino couplings. (Flavour off-diagonal neutrino kinetic terms, such as can arise when sterile neutrinos are integrated out, can also introduce off-diagonal neutral-current interactions, and can make the charged-current mixing matrices nonunitary.) Notice that, unlike most other new-physics corrections, these mixing angles need not be small, even if the neutrino masses are.

2. Electromagnetic Couplings: The total electromagnetic couplings of fermions are straightforward to write down:

$$\mathcal{L}_{\rm em} = -e\left[\overline{f}_i\gamma^\mu Q_i\, f_i\, A_\mu + \overline{f}_i\sigma^{\mu\nu}(d_L^{ij}\gamma_L + d_R^{ij}\gamma_R)\, f_j\, F_{\mu\nu}\right], \tag{8}$$

where the indices i and j are to be summed over all possible flavours of light fermions, f_i. Q_i represents the electric charge of f_i, in units of the proton charge. γ_L and γ_R denote the usual projection matrices onto left- and right-handed spinors. Linear combinations of the effective coupling matrices, d_L^{ij} and d_R^{ij}, represent non-standard magnetic- and electric-dipole moment interactions.

3. Charged-Current Interactions: The fermion charged-current interactions become:

$$\begin{aligned}\mathcal{L}_{\rm cc} &= -\frac{e}{\sqrt{2}s_w}\left[\overline{f}_i\gamma^\mu(h_L^{ij}\gamma_L + h_R^{ij}\gamma_R)\, f_j\, W_\mu^*\right.\\ &\qquad \left.+\overline{f}_i\sigma^{\mu\nu}(c_L^{ij}\gamma_L + c_R^{ij}\gamma_R)\, f_j\, W_{\mu\nu}^*\right] + {\rm cc},\end{aligned} \tag{9}$$

where $W_{\mu\nu} = D_\mu W_\nu - D_\nu W_\mu$ is the W field strength using electromagnetic covariant derivatives, D_μ. For leptons,

$$\begin{aligned}h_L^{\nu_i\ell_j} &= \delta\tilde{h}_L^{\nu_i\ell_j}\\ &\quad +\tilde{V}_\ell^{ij}\left(1 - \frac{\alpha S}{4(c_w^2 - s_w^2)} + \frac{c_w^2\,\alpha T}{2(c_w^2 - s_w^2)} + \frac{\alpha U}{8s_w^2} - \frac{c_w^2\,(\Delta_e + \Delta_\mu)}{2(c_w^2 - s_w^2)}\right),\\ h_R^{\nu_i\ell_j} &= \delta\tilde{h}_R^{\nu_i\ell_j},\end{aligned} \tag{10}$$

while for quarks:

$$\begin{aligned}h_L^{u_id_j} &= \delta\tilde{h}_L^{u_id_j}\\ &\quad +\tilde{V}_q^{ij}\left(1 - \frac{\alpha S}{4(c_w^2 - s_w^2)} + \frac{c_w^2\,\alpha T}{2(c_w^2 - s_w^2)} + \frac{\alpha U}{8s_w^2} - \frac{c_w^2\,(\Delta_e + \Delta_\mu)}{2(c_w^2 - s_w^2)}\right),\\ h_R^{u_id_j} &= \delta\tilde{h}_R^{u_id_j}.\end{aligned} \tag{11}$$

Here $\tilde{V}_\ell^{ij}$ and $\tilde{V}_q^{ij}$ respectively denote the unitary CKM matrices for the left-handed charged current interactions of the leptons and quarks. The coefficients $\delta\tilde{h}_{L(R)}^{u_id_j}$ and $c_{L(R)}^{ij}$ represent a set of arbitrary nonstandard fermion-W couplings, and S, T and U are defined in terms of the vacuum polarizations as in the previous section. Finally, Δ_f (with $f = e$, μ or τ) denotes the following quantity: $\Delta_f \equiv \sqrt{\sum_i \left|h_L^{\nu_i f}\right|^2} - 1$.

4. The W Mass: Although the SM contains gauge boson mass terms, these arise only in a particular linear combination, leading to a calculable mass relation for m_W in terms of the three inputs, m_z, G_F and α: $m_W = m_W^{SM} \equiv m_z c_w$+(radiative corrections). This relation is ruined by the generic effective gauge-boson mass terms, leading to the following nonstandard contribution to the W mass: [8]

$$m_W^2 = (m_W^{SM})^2 \left[1 - \frac{\alpha S}{2(c_w^2 - s_w^2)} + \frac{c_w^2\, \alpha T}{c_w^2 - s_w^2} + \frac{\alpha U}{4 s_w^2} - \frac{s_w^2(\Delta_e + \Delta_\mu)}{c_w^2 - s_w^2}\right] \tag{12}$$

5. Neutral-Current Couplings: The general interactions between the light fermions and the Z boson can be written as follows:

$$\mathcal{L}_{\rm nc} = -\frac{e}{s_w c_w}\left[\overline{f}_i \gamma^\mu (g_L^{ij}\gamma_L + g_R^{ij}\gamma_R) f_j\, Z_\mu + \overline{f}_i \sigma^{\mu\nu}(n_L^{ij}\gamma_L + n_R^{ij}\gamma_R) f_j\, Z_{\mu\nu}\right], \tag{13}$$

where

$$\begin{aligned}
\left(g_L^{ij}\right)_{SM} &= \left(T_{3i} - Q_i\, s_w^2\right)\delta^{ij} \\
\left(g_R^{ij}\right)_{SM} &= \left(-Q_i\, s_w^2\right)\delta^{ij} \\
g_{L(R)}^{ij} &= \left(g_{L,R}^{ij}\right)_{SM}\left[1 + \frac{1}{2}(\alpha T - \Delta_e - \Delta_\mu)\right] \qquad (14) \\
&\quad -Q_i\,\delta^{ij}\left(\frac{\alpha S}{4(c_w^2 - s_w^2)} - \frac{c_w^2 s_w^2\, \alpha T}{c_w^2 - s_w^2} + \frac{c_w^2 s_w^2(\Delta_e + \Delta_\mu)}{c_w^2 - s_w^2}\right) \\
&\quad +\delta\tilde{g}_{L(R)}^{ij}. \qquad (15)
\end{aligned}$$

As before, Q_i represents here the electric charge of fermion f_i, and T_{3i} is its eigenvalue for the third component of weak isospin. $Z_{\mu\nu}$ denotes the abelian curl: $\partial_\mu Z_\nu - \partial_\nu Z_\mu$. The effective coupling matrices $\delta\tilde{g}_{L(R)}^{ij}$ and $n_{L(R)}^{ij}$ represent arbitrary sets of nonstandard couplings between the fermions and the Z boson.

These expressions may now be used to compute electroweak observables. Working to linear order in the effective couplings permits the neglect of all interactions which cannot interfere with the corresponding SM contribution. This eliminates a good many of the effective vertices that are listed above, including most flavour-changing interactions. (Ref. [8] gives a more general discussion which also includes the strongly bounded flavour-changing couplings.) The results for a number of low-energy observables (those for which $q^2 \approx 0$) are listed in Table 2, and those for observables at the weak scale in Table 3.

The parameters which appear in Tables 2 and 3 can be fit to the precision electroweak data, just as was done for the oblique parameters S through X. The results of such a fit [8] are quoted in Tables 4, 5 and 6. In these tables the results of two types of fits are presented. In one of these (the 'Individual Fit') the parameter in question has been considered in isolation, with all of the other parameters set to zero by hand. This kind of fit is not realistic, but has often been considered in the literature. The second fit (the 'Global Fit') allows all of the parameters to be varied in fitting the data. Perhaps surprisingly, the resulting bounds on the various parameters are nevertheless quite good.

Table 2. Low-Energy Observables

The contributions to low-energy ($q^2 \approx 0$) electroweak observables that are generated by the various interactions of the general non-oblique effective lagrangian. The precise definitions of the observables can be found in Ref. [8].

$$R_\pi \equiv \Gamma(\pi \to e\nu)/\Gamma(\pi \to \mu\nu) = R_\pi^{SM}\,(1 + 2\Delta_e - 2\Delta_\mu)$$
$$R_\tau \equiv \Gamma(\tau \to e\nu\bar{\nu})/\Gamma(\mu \to e\nu\bar{\nu}) = R_\tau^{SM}\,(1 + 2\Delta_\tau - 2\Delta_\mu)$$
$$R_{\mu\tau} \equiv \Gamma(\tau \to \mu\nu\bar{\nu})/\Gamma(\mu \to e\nu\bar{\nu}) = R_{\mu\tau}^{SM}\,(1 + 2\Delta_\tau - 2\Delta_e)$$
$$\rho = 1 + \alpha T$$
$$\sigma(\nu N \to \mu^- X) = \sigma^{SM}(\nu N \to \mu^- X)\left[1 + 2\Delta_\mu - 2\Delta_e - 2\,(\mathrm{Re}\,(\delta\tilde{h}_R^{ud})/|V_{ud}|)\right]$$
$$\begin{aligned}(g_L^2) = (g_L^2)_{SM} &- 0.00269\,S + 0.00663\,T - 1.452\Delta_\mu - 0.244\Delta_e \\ &+0.620\,\mathrm{Re}\,(\delta\tilde{h}_R^{ud}) - 0.856\,\delta\tilde{g}_L^{dd} + 0.689\,\delta\tilde{g}_L^{uu} + 1.208\,\delta\tilde{g}_L^{\nu_\mu\nu_\mu}\end{aligned}$$
$$\begin{aligned}(g_R^2) = (g_R^2)_{SM} &+ 0.000937\,S - 0.000192\,T + 0.085\Delta_e - 0.0359\Delta_\mu \\ &+0.0620\,\mathrm{Re}\,(\delta\tilde{h}_R^{ud}) + 0.156\,\delta\tilde{g}_R^{dd} - 0.311\,\delta\tilde{g}_R^{uu} + 0.121\,\delta\tilde{g}_L^{\nu_\mu\nu_\mu}\end{aligned}$$
$$\begin{aligned}g_{eV} = (g_{eV})_{SM} &+ 0.00723\,S - 0.00541\,T + 0.656\Delta_e + 0.730\Delta_\mu \\ &+\delta\tilde{g}_L^{ee} + \delta\tilde{g}_R^{ee} - 0.074\,\delta\tilde{g}_L^{\nu_\mu\nu_\mu} - 0.037\,\mathrm{Re}\,(\delta\tilde{h}_R^{ud})\end{aligned}$$
$$\begin{aligned}g_{eA} = (g_{eA})_{SM} &- 0.00395\,T + 1.012\Delta_\mu + \delta\tilde{g}_L^{ee} - \delta\tilde{g}_R^{ee} - 1.012\,\delta\tilde{g}_L^{\nu_\mu\nu_\mu} - \\ &0.0506\,\mathrm{Re}\,(\delta\tilde{h}_R^{ud})\end{aligned}$$
$$\begin{aligned}C_{1u} = C_{1u}^{SM} &+ 0.00482\,S - 0.00493\,T + 0.631(\Delta_e + \Delta_\mu) \\ &+0.387\,\delta\tilde{g}_L^{ee} - \delta\tilde{g}_L^{uu} - 0.387\,\delta\tilde{g}_R^{ee} - \delta\tilde{g}_R^{uu}\end{aligned}$$
$$\begin{aligned}C_{1d} = C_{1d}^{SM} &- 0.00241\,S + 0.00442\,T - 0.565(\Delta_e + \Delta_\mu) \\ &-0.693\,\delta\tilde{g}_L^{ee} - \delta\tilde{g}_L^{dd} + 0.693\,\delta\tilde{g}_R^{ee} - \delta\tilde{g}_R^{dd}\end{aligned}$$
$$\begin{aligned}C_{2u} = C_{2u}^{SM} &+ 0.00723\,S - 0.00544\,T + 0.696(\Delta_e + \Delta_\mu) \\ &+\delta\tilde{g}_L^{ee} - 0.08\,\delta\tilde{g}_L^{uu} + \delta\tilde{g}_R^{ee} + 0.08\,\delta\tilde{g}_R^{uu}\end{aligned}$$
$$\begin{aligned}C_{2d} = C_{2d}^{SM} &- 0.00723\,S + 0.00544\,T - 0.696(\Delta_e + \Delta_\mu) \\ &-\delta\tilde{g}_L^{ee} - 0.08\,\delta\tilde{g}_L^{dd} - \delta\tilde{g}_R^{ee} + 0.08\,\delta\tilde{g}_R^{dd}\end{aligned}$$
$$\begin{aligned}Q_W(^{133}_{55}Cs) = \left[Q_W(^{133}_{55}Cs)\right]_{SM} &- 0.796\,S - 0.0113\,T + 1.45(\Delta_e + \Delta_\mu) \\ &+147\,(\delta\tilde{g}_L^{ee} - \delta\tilde{g}_R^{ee}) + 422\,(\delta\tilde{g}_L^{dd} + \delta\tilde{g}_R^{dd}) + 376\,(\delta\tilde{g}_L^{uu} + \delta\tilde{g}_R^{uu})\end{aligned}$$

Table 3. Weak-Scale Observables
The contributions to weak-scale ($q^2 = m_Z^2$ or m_W^2) electroweak observables that a
generated by the various interactions of the general non-oblique effective lagrangia
The precise definitions of the observables can be found in Ref. [8].

$$
\begin{aligned}
m_W^2 &= (m_W^2)_{SM}[1 - 0.00723\,S + 0.0111\,T + 0.00849\,U - 0.426(\Delta_e + \Delta_\mu)] \\
\Gamma_{\ell^+\ell^-} &= (\Gamma_{\ell^+\ell^-})_{SM}\Big[1 - 0.00230\,S + 0.00944T - 1.209(\Delta_e + \Delta_\mu) \\
&\qquad -4.29\,\delta\tilde{g}_L^{\ell\ell} + 3.66\,\delta\tilde{g}_R^{\ell\ell}\Big] \\
\Gamma_{u\bar{u}} &= (\Gamma_{u\bar{u}})_{SM}\Big[1 - 0.00649\,S + 0.0124T - 1.59(\Delta_e + \Delta_\mu) \\
&\qquad +4.82\,\delta\tilde{g}_L^{uu} - 2.13\,\delta\tilde{g}_R^{uu}\Big] \\
\Gamma_{d\bar{d}} &= (\Gamma_{d\bar{d}})_{SM}\Big[1 - 0.00452\,S + 0.0110T - 1.41(\Delta_e + \Delta_\mu) \\
&\qquad -4.57\,\delta\tilde{g}_L^{dd} + 0.828\,\delta\tilde{g}_R^{dd}\Big] \\
\Gamma_{b\bar{b}} &= (\Gamma_{b\bar{b}})_{SM}\Big[1 - 0.00452\,S + 0.0110T - 1.41(\Delta_e + \Delta_\mu) \\
&\qquad -4.57\,\delta\tilde{g}_L^{bb} + 0.828\,\delta\tilde{g}_R^{bb}\Big] \\
\Gamma_{\rm had} &= (\Gamma_{\rm had})_{SM}\Big[1 - 0.00518\,S + 0.0114T - 1.469(\Delta_e + \Delta_\mu) \\
&\qquad -1.01\Big(\delta\tilde{g}_L^{dd} + \delta\tilde{g}_L^{ss} + \delta\tilde{g}_L^{bb}\Big) + 0.183\Big(\delta\tilde{g}_R^{dd} + \delta\tilde{g}_R^{ss} + \delta\tilde{g}_R^{bb}\Big) \\
&\qquad +0.822\Big(\delta\tilde{g}_L^{uu} + \delta\tilde{g}_L^{cc}\Big) - 0.363\Big(\delta\tilde{g}_R^{uu} + \delta\tilde{g}_R^{cc}\Big)\Big] \\
\Gamma_{\nu_i\bar{\nu}_i} &= (\Gamma_{\nu_i\bar{\nu}_i})_{SM}\Big[1 + 0.00781T - (\Delta_e + \Delta_\mu) + 4\,\delta\tilde{g}_L^{\nu_i\nu_i}\Big] \\
\Gamma_Z &= (\Gamma_Z)_{SM}\Big[1 - 0.00385\,S + 0.0105\,T - 1.35(\Delta_e + \Delta_\mu) + 0.574\,(\delta\tilde{g}_L^{uu} + \delta\tilde{g}_L^{cc}) \\
&\qquad -0.254\,(\delta\tilde{g}_R^{uu} + \delta\tilde{g}_R^{cc}) + 0.268\,(\delta\tilde{g}_L^{\nu_e\nu_e} + \delta\tilde{g}_L^{\nu_\mu\nu_\mu} + \delta\tilde{g}_L^{\nu_\tau\nu_\tau}) \\
&\qquad -0.144\,(\delta\tilde{g}_L^{ee} + \delta\tilde{g}_L^{\mu\mu} + OBB\delta\tilde{g}_L^{\tau\tau}) + 0.123\,(\delta\tilde{g}_R^{ee} + \delta\tilde{g}_R^{\mu\mu} + \delta\tilde{g}_R^{\tau\tau}) \\
&\qquad -0.707\,(\delta\tilde{g}_L^{dd} + \delta\tilde{g}_L^{ss} + \delta\tilde{g}_L^{bb}) + 0.128\,(\delta\tilde{g}_R^{dd} + \delta\tilde{g}_R^{ss} + \delta\tilde{g}_R^{bb})\Big] \\
A_{LR} &= A_{LR}^{SM} - 0.0284\,S + 0.0201\,T - 2.574(\Delta_e + \Delta_\mu) - 3.61\,\delta\tilde{g}_L^{ee} - 4.238\,\delta\tilde{g}_R^{ee} \\
A_{FB}^{\ell^+\ell^-} &= (A_{FB})_{SM} - 0.00677\,S + 0.00480\,T - 0.614(\Delta_e + \Delta_\mu) \\
&\qquad -0.430\,(\delta\tilde{g}_L^{ee} + \delta\tilde{g}_L^{\ell\ell}) - 0.505\,(\delta\tilde{g}_R^{ee} + \delta\tilde{g}_R^{\ell\ell}) \\
A_{FB}(b\bar{b}) &= (A_{FB}(b\bar{b}))_{SM} - 0.0188\,S + 0.0133\,T - 1.70(\Delta_e + \Delta_\mu) \\
&\qquad -2.36\,\delta\tilde{g}_L^{ee} - 2.77\,\delta\tilde{g}_R^{ee} - 0.0322\,\delta\tilde{g}_L^{bb} - 0.178\,\delta\tilde{g}_R^{bb} \\
A_{FB}(c\bar{c}) &= (A_{FB}(c\bar{c}))_{SM} - 0.0147\,S + 0.0104\,T - 1.333(\Delta_e + \Delta_\mu) \\
&\qquad -1.69\,\delta\tilde{g}_L^{ee} - 1.99\,\delta\tilde{g}_R^{ee} + 0.175\,\delta\tilde{g}_L^{cc} + 0.396\,\delta\tilde{g}_R^{cc}
\end{aligned}
$$

Table 4. Oblique Parameters

Results for the oblique parameters S, T and U obtained from the fit of the new-physics parameters to the data. The second column gives the result for the (unrealistic) case where all other parameters are constrained to vanish. Column three gives the result of a global fit in which all of the parameters of the effective lagrangian are varied.

Parameter	Individual Fit	Global Fit
S	-0.10 ± 0.16	-0.2 ± 1.0
T	$+0.01 \pm 0.17$	-0.02 ± 0.89
U	-0.14 ± 0.63	$+0.3 \pm 1.2$

3.2 The Zbb vertex

An important special case of the above analysis is to simply add a nonstandard dimension-four coupling between the Z boson and the b quark, in addition to the oblique corrections S, T and U. This corresponds to the approach of Ref. [5], with the parameters ϵ_1, ϵ_2 and ϵ_3 given as in the previous section, and ϵ_b given by:

$$\delta\epsilon_b \equiv \epsilon_b - \epsilon_b^{SM} = -2\,\delta\tilde{g}_L^{bb}. \tag{16}$$

Notice that, like all of the flavour-diagonal neutral-current couplings, the reality of the lagrangian implies that $\delta\tilde{g}_L^{bb}$ must be real. In this case, the formulae of Tables 2 and 3 simplify considerably.

4. Applications

With the above results in place for the experimental limits on the various effective parameters, the next step is to compute the values of these parameters in terms of the couplings and masses of various underlying models. We therefore now turn to a brief summary of some of the applications to which the above formalism has been made.

4.1 m_t dependence

The starting point for the comparison with experiment is the choice of a set of fiducial values, $\hat{m}_t$ and $\hat{m}_H$, for the unknown masses, m_t and m_H, which appear in the SM contributions to various observables. We have chosen $\hat{m}_t \equiv 150$ GeV and $\hat{m}_H \equiv 300$ GeV in performing the fits, but it is natural to wonder how the SM predictions change as these masses vary.

Perhaps the simplest, and most useful, application of the techniques described in earlier sections is to approximately determine this m_t and m_H dependence. To do so, imagine both the top quark and the Higgs boson to be much heavier than m_Z. In this case, all of the implications for lower-energy observables due to these heavy particles can be phrased in terms of the effective lagrangian obtained by integrating them out of the SM. It can therefore be mimicked by choosing an appropriate m_t and m_H dependence for some of the effective couplings of section 3.

Table 5. Charged-Current Parameters

More results of the fits of the new-physics parameters to the data. The quantities Σ_1 and Σ_2 arise in tests for the unitarity of the CKM matrix, and are defined as: $\Sigma_1 \equiv \mathrm{Re}\,(\delta\tilde{h}_L^{us}) + \left[\mathrm{Re}\,(V_{ub})\mathrm{Re}\,(\delta\tilde{h}_L^{ub}) + \mathrm{Im}\,(V_{ub})\mathrm{Im}\,(\delta\tilde{h}_L^{ub})\right]/|V_{us}|$ and $\Sigma_2 \equiv \mathrm{Re}\,(\delta\tilde{h}_L^{cd}) + |V_{cs}|\mathrm{Re}\,(\delta\tilde{h}_L^{cs} + \delta\tilde{h}_R^{cs})/|V_{cd}| + |V_{cb}|\mathrm{Re}\,(\delta\tilde{h}_L^{cb})/|V_{cd}|$. Blanks indicate where the corresponding fit would be inappropriate, such as for when a parameter always appears in a particular combination with others, and so cannot be individually fit.

Parameter	Individual Fit	Global Fit
Δ_e	$-0.0008 \pm .0010$	$-0.0011 \pm .0041$
Δ_μ	$+0.00047 \pm .00056$	$+0.0005 \pm .0039$
Δ_τ	-0.018 ± 0.008	$-0.018 \pm .009$
$\mathrm{Re}\,(\delta\tilde{h}_L^{ud})$	$-0.00041 \pm .00072$	$+0.0001 \pm .0060$
$\mathrm{Re}\,(\delta\tilde{h}_R^{ud})$	$-0.00055 \pm .00066$	$+0.0003 \pm .0073$
$\mathrm{Im}\,(\delta\tilde{h}_R^{ud})$	0 ± 0.0036	$-0.0036 \pm .0080$
$\mathrm{Re}\,(\delta\tilde{h}_L^{us})$	$-0.0018 \pm .0032$	—
$\mathrm{Re}\,(\delta\tilde{h}_R^{us})$	$-0.00088 \pm .00079$	$+0.0007 \pm .0016$
$\mathrm{Im}\,(\delta\tilde{h}_R^{us})$	0 ± 0.0008	$-0.0004 \pm .0016$
$\mathrm{Re}\,(\delta\tilde{h}_L^{ub})$,$\mathrm{Im}\,(\delta\tilde{h}_L^{ub})$	$-0.09 \pm .16$	—
Σ_1	—	$+0.005 \pm .027$
$\mathrm{Re}\,(\delta\tilde{h}_R^{ub})$	—	—
$\mathrm{Re}\,(\delta\tilde{h}_L^{cd})$	$+0.11 \pm .98$	—
$\mathrm{Re}\,(\delta\tilde{h}_R^{cd})$	—	—
$\mathrm{Re}\,(\delta\tilde{h}_L^{cs})$	$+0.022 \pm .20$	—
$\mathrm{Re}\,(\delta\tilde{h}_R^{cs})$	$+0.022 \pm .20$	—
$\mathrm{Re}\,(\delta\tilde{h}_L^{cb})$	$+0.5 \pm 4.6$	—
Σ_2	—	$+0.11 \pm 0.98$
$\mathrm{Re}\,(\delta\tilde{h}_R^{cb})$	—	—

Table 6. Neutral-Current Parameters

Still more results of the fits of the new-physics parameters to the data. As before, blanks indicate where the corresponding fit would be inappropriate, such as for when a parameter always appears in a particular combination with others, and so cannot be individually fit.

Parameter	Individual Fit	Global Fit
$\delta\tilde{g}_L^{dd}$	$+0.0016 \pm .0015$	$+0.003 \pm .012$
$\delta\tilde{g}_R^{dd}$	$+0.0037 \pm .0038$	$+0.007 \pm .015$
$\delta\tilde{g}_L^{uu}$	$-0.0003 \pm .0018$	-0.002 ± 0.014
$\delta\tilde{g}_R^{uu}$	$+0.0032 \pm .0032$	$-0.003 \pm .010$
$\delta\tilde{g}_L^{ss}$	$-0.0009 \pm .0017$	$-0.003 \pm .015$
$\delta\tilde{g}_R^{ss}$	$-0.0052 \pm .00095$	$+0.002 \pm .085$
$\delta\tilde{g}_L^{cc}$	$-0.0011 \pm .0021$	$+0.001 \pm .018$
$\delta\tilde{g}_R^{cc}$	$+0.0028 \pm .0047$	$+0.009 \pm .029$
$\delta\tilde{g}_L^{bb}$	$-0.0005 \pm .0016$	$-0.0015 \pm .0094$
$\delta\tilde{g}_R^{bb}$	$+0.0019 \pm .0083$	$0.013 \pm .054$
$\delta\tilde{g}_L^{\nu_e\nu_e}$	$-0.0048 \pm .0052$	—
$\delta\tilde{g}_L^{\nu_\mu\nu_\mu}$	$-0.0021 \pm .0027$	$+0.0023 \pm .0097$
$\delta\tilde{g}_L^{\nu_\tau\nu_\tau}$	$-0.0048 \pm .0052$	—
$\delta\tilde{g}_L^{\nu_e\nu_e} + \delta\tilde{g}_L^{\nu_\tau\nu_\tau}$	—	$-0.004 \pm .033$
$\delta\tilde{g}_L^{ee}$	$-0.00029 \pm .00043$	$-0.0001 \pm .0032$
$\delta\tilde{g}_R^{ee}$	$-0.00014 \pm .00050$	$+0.0001 \pm .0030$
$\delta\tilde{g}_L^{\mu\mu}$	$+0.0040 \pm .0051$	$+0.005 \pm .032$
$\delta\tilde{g}_R^{\mu\mu}$	$-0.0003 \pm .0047$	$+0.001 \pm .028$
$\delta\tilde{g}_L^{\tau\tau}$	$-0.0021 \pm .0032$	$0.000 \pm .022$
$\delta\tilde{g}_R^{\tau\tau}$	$-0.0034 \pm .0028$	$-0.0015 \pm .019$

Evaluating the one-loop vacuum polarization graphs [2, 3, 4, 5] containing top and Higgs loops gives the following large-mass dependence for the oblique parameters:

$$\begin{aligned}
\delta S_{SM} &\simeq -\frac{1}{3\pi}\ln\left(\frac{m_t}{\hat{m}_t}\right)+\frac{1}{6\pi}\ln\left(\frac{m_H}{\hat{m}_H}\right)\\
\delta T_{SM} &\simeq \frac{3}{16\pi s_w^2 c_w^2}\left(\frac{m_t^2-\hat{m}_t^2}{m_z^2}\right)+\frac{3}{8\pi c_w^2}\left[\ln\left(\frac{m_t}{\hat{m}_t}\right)-\ln\left(\frac{m_H}{\hat{m}_H}\right)\right]\\
\delta U_{SM} &\simeq -\frac{1}{\pi}\ln\left(\frac{m_t}{\hat{m}_t}\right)
\end{aligned} \tag{17}$$

Similarly, the Zbb vertex-correction graph involving a virtual top quark gives [5, 19]

$$\left(\delta\bar{g}_L^{bb}\right)_{SM} \simeq \frac{\alpha}{8\pi s_w^2 c_w^2}\left(\frac{m_t^2-\hat{m}_t^2}{m_z^2}\right) \tag{18}$$

These are the *only* virtual contributions which can both (*i*) depend strongly, at one loop, on m_t, and (*ii*) contribute appreciably to electroweak observables.

4.2 Exotic fermions

One application to which the above formalism has been applied [8] is the determination of the constraints on the masses and couplings that are possible for hypothetical exotic fermions which can mix with the ordinary ones. For the present purposes we take 'exotic' to mean new fermions which transform under the $SU_L(2)$ gauge group as either left-handed singlets and/or right-handed doublets. Because of their mixing with ordinary fermions, exotic fermions of this sort can change the couplings of the ordinary fermions to the W and Z. Constraints on these mixings can be inferred from present precision measurements of these couplings.

One motivation for doing this analysis, is that it also has been performed [20] by fitting these models directly to the data. By comparing the bounds obtained here with those of the direct fit to the model we can learn how closely they agree with one another. One would expect the present approach to give bounds that are marginally weaker than those of a direct fit to the model, since there are typically more parameters in the general effective lagrangian than there are couplings in a particular underlying theory. In this sense our results can be considered the most conservative bounds possible. The interesting point is that the limits we obtain are not very much weaker at all, and so very little information is lost by using the simpler effective-lagrangian fit. For simplicity of presentation we restrict ourselves here to charged quarks, although neutrino mixing can be handled in much the same way [8].

In general, mixing between the known fermions and exotic ones induces flavour-changing processes into the neutral current interactions of ordinary fermions (FCNC's). For simplicity we ignore these types of induced couplings here, although they can be treated in a similar manner. FCNC's are avoided if every known electroweak multiplet of fermions mixes separately with its own exotic partner, in which case the mixing can be characterized in terms of a mixing angle, $\theta^i_{L(R)}$, $i = e, \mu, \tau, u, d, s, \ldots$.

To make contact with our general formalism, simply integrate out all of the undiscovered exotic particles to produce the low-energy effective theory. Sufficient

accuracy is obtained by working at tree level, and so it is easy to integrate out the heavy fermions: one transforms to a basis of mass eigenstates, and sets all heavy fields equal to zero. As a result we find $S{=}T{=}U{=}0$, and the nonstandard neutral current and charged-current couplings of the ordinary fermions become modified by [8]:

$$\delta\tilde{g}_L^{ii} = -T_{3i}\left(s_L^i\right)^2 \ , \qquad \delta\tilde{g}_R^{ii} = +T_{3i}\left(s_R^i\right)^2 \ , \tag{19}$$

and

$$\delta\tilde{h}_L^{u_i d_j} = -\frac{1}{2}\,\tilde{V}_q^{ij}\left[(s_L^{u_i})^2 + (s_L^{d_j})^2\right] \ , \qquad \delta\tilde{h}_R^{u_i d_j} = s_R^{u_i} s_R^{d_j}\,\tilde{U}_R^{ij} \ , \tag{20}$$

in which $\left(s^i_{L(R)}\right)^2 \equiv 1 - \left(c^i_{L(R)}\right)^2 \equiv \sin^2\theta^i_{L(R)}$, and $\tilde{U}_R^{ij}$ is a unitary CKM-type matrix for the right-handed charged-current couplings. Similar expressions also hold for leptons [8].

It is now a simple matter to bound the mixing angles using these expressions together with the constraints of Tables 5 and 6. We find the following limits at 90% c.l. (defined as 1.64σ):

$$\begin{aligned}
\Delta_{e,\mu}: &\quad (s_L^e)^2, (s_L^{\nu_e})^2 < 0.016; \qquad (s_L^\mu)^2, \left(s_L^{\nu_\mu}\right)^2 < 0.012 \\
\delta\tilde{h}_L^{ud}: &\quad (s_L^u)^2, \left(s_L^d\right)^2 < 0.02 \\
\delta g^{ii}_{L,R}: &\quad (s_R^e)^2 < 0.01; \quad (s_R^\mu)^2 < 0.09; \quad (s_R^u)^2 < 0.03; \\
&\quad \left(s_R^d\right)^2 < 0.05; \quad (s_L^s)^2 < 0.05; \quad \left(s_L^b\right)^2 < 0.03,
\end{aligned} \tag{21}$$

A comparison of the above numbers with those in the literature [20] confirms that they are very similar to, but marginally weaker than, those found by fitting directly to the mixing angles themselves.

4.3 Light exotic particles

Another application that has been examined with this formalism [12, 14, 21] is the case of new exotic particles whose quantum numbers preclude their mixing with ordinary fermions [22]. Such particles arise in a great many types of theories for new physics, including supersymmetric models, theories with additional generations, and technicolour models. In these examples the new particles need *not* be much heavier than the weak scale, and so we do not make this assumption here.

Unlike for the previous example, in this case the absence of tree-level mixing implies that the dominant effects of the new physics arise through its one-loop contributions to well-measured observables. This is in most cases dominated by the contributions to gauge boson vacuum polarizations, and so we consider here only oblique corrections.

Formulae for the one-loop contributions to the six oblique parameters, $S - X$, by scalars and fermions in general representations of the electroweak gauge group have been given in the literature [7, 23, 24]. For example, the one-loop vacuum polarization due to a fermion with left- and right-handed coupling constants, $k^a_{L(R)}$, to gauge boson 'a' (with $a = \gamma, W, Z$) is:

$$\delta\Pi_{ab}(q^2) = \frac{1}{2\pi^2}\sum_{ij}\int_0^1 dx\; f_{ab}(q^2,x)\;\ln\left[\frac{m_{ij}^2(x) - q^2x(1-x)}{\mu^2}\right] . \tag{22}$$

Here $m_{ij}^2(x) \equiv m_i^2(1-x) + m_j^2 x$, where m_i and m_j are the masses of the two fermions which appear within the loop, and

$$f_{ab}(q^2, x) = \frac{k_L^a k_L^{b*} + k_R^a k_R^{b*}}{2} \left[x(1-x)\, q^2 - \frac{m_{ij}^2(x)}{2} \right] + \frac{k_L^a k_R^{b*} + k_R^a k_L^{b*}}{2} \left(\frac{m_i m_j}{2} \right) \tag{23}$$

For example, a standard-model doublet would have $k_L^\gamma = k_R^\gamma = eQ_i$, $k_L^z = (e/s_w c_w)[T_{3i} - Q_i s_w^2]$, $k_R^z = (e/s_w c_w)[-Q_i s_w^2]$, $k_L^W = e/\sqrt{2}s_w$ and $k_R^W = 0$. μ^2 denotes the renormalization point, where we have renormalized using dimensional regularization and $\overline{\rm MS}$.

Expressions such as these permit a survey of the couplings and masses that are permitted for exotic particles transforming in a variety of electroweak gauge representations [12]. For the purposes of illustration, Figure 3 displays the range of values for S' and T' that are produced by an additional generation of quarks and leptons. Notice that this region does *not* necessarily include the origin ($S' = T' = 0$) in the limit that the members of this additional generation become very heavy. This is because heavy fermions like these need not decouple from S' and T' in this limit. This makes the oblique parameters especially sensitive i probes for these types of new particles.

4.4 Is technicolour dead?

The above observation, that some heavy particles need not decouple from oblique parameters like S and T as their masses get very large, has been used to argue that technicolour-like models for dynamical electroweak symmetry breaking are ruled out by the current electroweak data [2, 3, 4, 5]. Various estimates for the oblique parameters in these theories predict $S' \gtrsim O(+1)$, and the two-parameter $S - T$ fit to the Z-pole data excludes these values at roughly the three-σ level. (A similar conclusion has been reached by considering the anomalous Zbb coupling as well [25].)

This conclusion would be inescapable provided that these parameters could be reliably computed to be $O(+1)$ in technicolour models. Unfortunately, since these are strongly coupled theories, the robustness of the various estimates is not clear [26]. For example, a potential loophole may exist when light particles are present in the technispectrum — such as often happens in these theories due to the appearance of pseudogoldtone bosons. In this case the analysis requires the additional parameters V through X, and the contributions of the light particles *can* be made to contribute negatively to S' and T' [24, 12], for some choices for their masses and mixings.

These loopholes are difficult to completely close due to the difficulty in computing with these theories. In the meantime, it must be conceded that the case against these theories remains persuasive, albeit circumstantial.

4.5 TGV's

As a final application we consider how the oblique analysis of section 2 can be used to bound [27] the potential existence of nonstandard self-couplings for the elec-

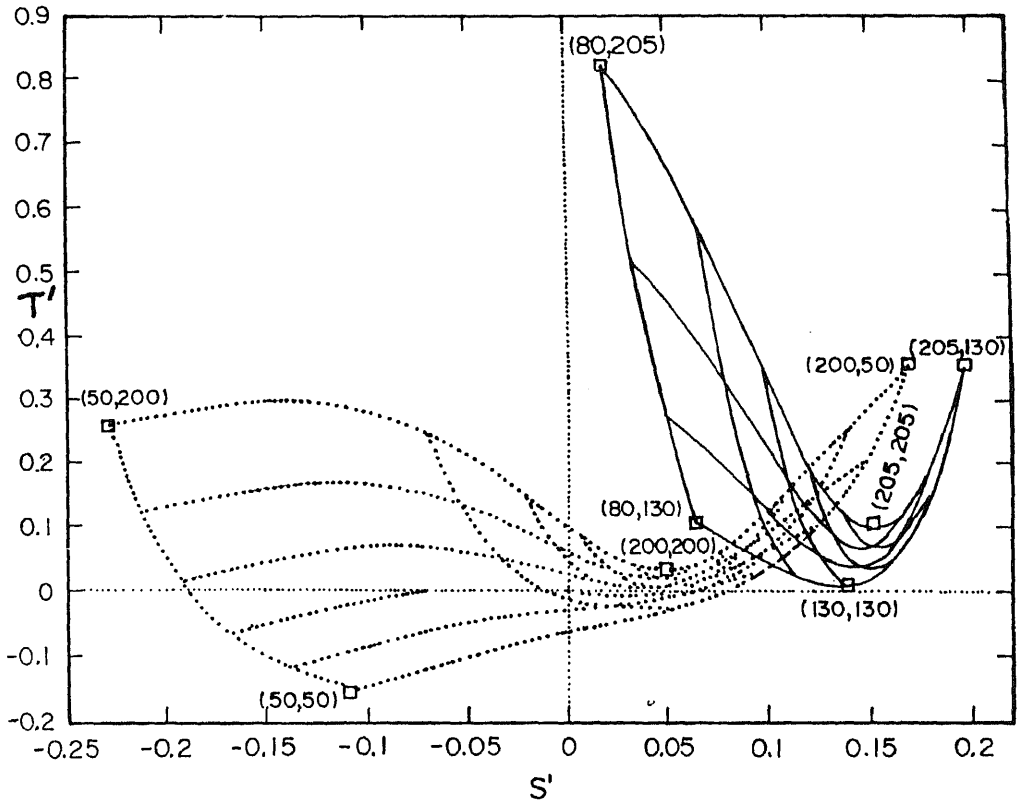

Figure 3. The contribution of an extra SM family to the oblique parameters S' and T'. Solid line: a colour-triplet, $Y = \frac{1}{6}$ quark doublet with masses $(m_{b'}, m_{t'})$ as indicated in brackets. Dotted line: a colour-singlet, $Y = \frac{1}{2}$ lepton doublet with masses $(m_{\nu'}, m_{l'})$. The grid spacing represents steps of 25 (resp. 30) GeV for the solid (resp. dotted) plots.

included.

The starting assumption is that the lightest mass, M, of any undiscovered particle is high in comparison with the weak scale, m_z. Integrating out this heavy physics gives an effective lagrangian, defined at the scale M, which we assume to include the five CP-conserving TGV's, whose coefficients are, in a standard [28] notation: $\Delta\kappa_\gamma$, $\Delta\kappa_z$, Δg_{1z}, λ_z, and λ_γ. The goal is to constrain the coefficients of these effective interactions using precision electroweak measurements at lower energies, $E \lesssim m_z$.

In order to do so we imagine running the effective lagrangian defined at the scale M, down to the scale m_z where current measurements are made. Since anomalous TGV's are not directly probed at these energies, the bounds come from the other effective interactions which are generated by the TGV's during the running down from M to m_z. We therefore compute all of the effective interactions at the weak scale that get generated (at one loop) by loops containing TGV's.

There are two kinds of effective interactions that are produced by TGV's in this way: (*i*) oblique parameters, and (*ii*) nonstandard fermion/gauge-boson vertices. The fermion/gauge-boson vertices themselves come in two types: (*a*) those which are universal, in that they are independent of the masses of the SM fermions, and (*b*) those which depend strongly on the top-quark mass, m_t. Interestingly, we find that all of the vertex corrections of type (*a*) that are generated by TGV's can be rewritten as oblique corrections by performing a suitable field redefinition [27]. The entire analysis can therefore be done using the oblique parameters, together with a small number of m_t-dependent terms.

The TGV-generated oblique parameters that are produced by this analysis are displayed in Table 7, where the numerical values $\alpha(m_z^2) = 1/128$ and $s_w^2 = 0.23$ are used. We also take $M = 1$ TeV and the effective couplings are evaluated at the low-energy scale $\mu = 100$ GeV. The quantities $\hat{V}$ and $\hat{X}$ incorporate the nonuniversal, m_t-dependent, contributions, and are to be used instead of V and X in the expressions for any observables which are based on the process $Z \to b\bar{b}$.

The expressions from Table 7 can then be used in Table 1, for the electroweak observables in terms of the oblique parameters. When all five TGV coefficients are left free in the resulting fit to the data, no useful bound is obtained, beyond the ever-present ones like perturbative unitarity. This shows that the data is not yet sufficiently accurate to constrain these quantities. A common procedure in the literature is to instead bound each TGV separately, with all of the others constrained to vanish. This type of analysis gives, in our case, the following one-σ allowed ranges [27]:

$$\begin{aligned} \Delta g_{1z} &= -0.033 \pm 0.031; \\ \Delta\kappa_\gamma = 0.056 \pm 0.056; &\qquad \Delta\kappa_z = -0.0019 \pm 0.044; \\ \lambda_\gamma = -0.036 \pm 0.034; &\qquad \lambda_z = 0.049 \pm 0.045. \end{aligned} \tag{24}$$

Although the bounds obtained in this way are more restrictive, they are also not

Table 7. TGV Contributions to Oblique Parameters
One-loop results for the induced parameters S, T, U, V, W and X, defined at $\mu = 100$ GeV, in terms of the various TGV couplings defined at $M = 1$ TeV. As usual, $\alpha(m_Z^2) = 1/128$ and $s_w^2 = 0.23$.

Parameter	One-Loop Result
S	$2.63\Delta g_{1z} - 2.98\Delta\kappa_\gamma + 2.38\Delta\kappa_z + 5.97\lambda_\gamma - 4.50\lambda_z$
T	$-1.82\Delta g_{1z} + 0.550\Delta\kappa_\gamma + 5.83\Delta\kappa_z$
U	$2.42\Delta g_{1z} - 0.908\Delta\kappa_\gamma - 1.91\Delta\kappa_z + 2.04\lambda_\gamma - 2.04\lambda_z$
V	$0.183\Delta\kappa_z$
W	$0.202\Delta g_{1z}$
X	$-0.0213\Delta\kappa_\gamma - 0.0611\Delta\kappa_z$
$\hat{V}$	$0.183\Delta\kappa_z - (3.68\Delta g_{1z} + 0.797\Delta\kappa_z)(m_t^2/m_w^2)$
$\hat{X}$	$-0.0213\Delta\kappa_\gamma - 0.0611\Delta\kappa_z + (0.423\Delta g_{1z} + 0.0916\Delta\kappa_z)(m_t^2/m_w^2)$

realistic for any underlying theory, for which all couplings would be expected to be generated together.

5. Conclusions

This article reviews two approaches to parameterizing the effects of new physics for precision electroweak measurements. The two approaches are based on one of the following two assumptions. Either: (*i*) the new physics is assumed to be very heavy in comparison with the weak scale, m_z, or: (*ii*) it is *not* assumed to be heavy, but it is assumed to dominantly contribute to observables through oblique corrections. These two approaches contain the popular formalisms of Peskin *et.al.*, and of Altarelli *et.al.*, as important special cases.

The advantage of parameterizing the data in this way is the efficiency with which it permits the comparison of specific models to the data. Rather than having to perform a detailed fit to the data of every proposed theory, it is possible to fit the data once and for all to the proposed parameters. To constrain any particular model it is then simply necessary to compute these parameters in terms of the couplings of the underlying theory. A conservative estimate of the allowed range for these couplings can be found by simply using the appropriate confidence intervals for the basic parameterization. The bounds that are obtained in this way turn out to be remarkably similar to those which are obtained from model-by-model fits.

A number of phenomenological analyses have been performed using this procedure, some of which have been briefly summarized here. These calculations illustrate the potential applications of the method, and the simplicity with which it may be carried out.

I would like to thank the organizers of the workshop for their warm hospitality, and for their kind invitation to speak. The research described here was the result of fabulous collaborations with Peter Bamert, Steve Godfrey, Heinz Konig, David London and Ivan Maksymyk, and has been supported by the Swiss National Foundation, N.S.E.R.C. of Canada and les Fonds F.C.A.R. du Québec.

References

[1] D. Schaile, *Precision Tests of the Electroweak Interactions*, in the proceedings of the XXVII International Conference on High Energy Physics, Glasgow, July 1994.

[2] M.E. Peskin and T. Takeuchi, *Phys. Rev. Lett.* **65** (1990) 964; *Phys. Rev.* **D46** (1992) 381.

[3] W.J. Marciano and J.L. Rosner, *Phys. Rev. Lett.* **65** (1990) 2963.

[4] D.C. Kennedy and P. Langacker, *Phys. Rev. Lett.* **65** (1990) 2967.

[5] G. Altarelli and R. Barbieri, *Phys. Lett.* **B253** (1991) 161; G. Altarelli, R. Barbieri and S. Jadach, *Nuc. Phys.* **B369** (1992) 3, (erratum) *ibid.* **B376** (1992) 444; G. Altarelli, R. Barbieri and F. Caravaglios, *Nuc. Phys.* **B405** (1993) 3.

[6] K. Hagiwara, S. Matsumoto, D. Haidt, C.S. Kim, preprint KEK-TH-375, (hep-ph/9409380).

[7] I. Maksymyk, C.P. Burgess and D. London, *Phys. Rev.* **D50** (1994) 529; C.P Burgess, S. Godfrey, H. Kõnig, D. London and I. Maksymyk, *Phys. Lett.* **B326** (1994) 276.

[8] C.P. Burgess, S. Godfrey, H. Konig, D. London and I. Maksymyk, *Phys. Rev.* **D49** (1994) 6115.

[9] B. Lynn, M. Peskin, R. Stuart, in *Physics at LEP*, CERN Report 86-02.

[10] D. Kennedy, B.W. Lynn, *Nuc. Phys.* **B322** (1989) 1.

[11] B. Grinstein and M.B. Wise, *Phys. Lett.* **B265** (1991) 326.

[12] P. Bamert and C.P. Burgess, *Zeit. Phys. C* (to appear), (hep-ph/9407203).

[13] S. Godfrey, (private communication) August 1994.

[14] N. Evans, Swansea preprint SWAT/40, (hep-ph/9408308).

[15] I. Maksymyk, (private communication).

[16] S. Weinberg, *Physica* **96A** (1979) 327; C.P. Burgess and J.A. Robinson, in *BNL Summer Study on CP Violation* S. Dawson and A. Soni editors, (World Scientific, Singapore, 1991); J. Polchinski, preprint NSF-ITP-92-132, UTTG-92-20, (hep-th/9210046), H. Georgi, *Ann. Rev. Nucl. Part. Sci.* **43** (1994) 209.

[17] At this writing some evidence for the existence of a t quark having a mass of roughly 170 GeV has been reported by: F. Abe *et.al.* , *Phys. Rev. Lett.* **73** (1994) 225; *Phys. Rev.* **D50** (1994) 2966.

[18] J.M. Cornwall, D.N. Levin and G. Tiktopoulos, *Phys. Rev.* **D10** (1974) 1145; M.S. Chanowitz, M. Golden and H. Georgi, *Phys. Rev.* **D36** (1987) 1490; C.P. Burgess and D. London, *Phys. Rev. Lett.* **69** (1992) 3428; *Phys. Rev.* **D48** (1993) 4337.

[19] A.A. Akundov *et.al.* , *Nuc. Phys.* **B276** (1988) 1; W. Beenakker and H. Hollik, *Zeit. Phys.* **C40** (1988) 569; B.W. Lynn and R.G. Stuart, *Phys. Lett.* **B252** (1990) 676; J. Bernabeu, A. Pich and A. Santamaria, *Phys. Lett.* **B200** (1988) 569; *Nuc. Phys.* **B363** (1991) 326; S. Peris, preprint CERN-TH-7446-94, (hep-ph/9409340).

[20] P. Langacker and D. London, *Phys. Rev.* **D38** (1988) 886; E. Nardi, E. Roulet and D. Tommasini, *Nuc. Phys.* **B386** (1992) 239; preprint CERN-TH-7443-94, (hep-ph/9409310).

[21] G. Bhattacharyya, S. Banerjee and P. Roy, *Phys. Rev.* **D45** (1992) R729.

[22] Mixings with new gauge bosons have also been considered by T.G. Rizzo, *Phys. Rev.* **D50** (1994) 2256; and F. Caravaglios, G.G. Ross, preprint (hep-ph/9410322).

[23] L. Lavoura and L.F. Li, *Phys. Rev.* **D49** (1994) 1409.

[24] N. Evans, *Phys. Rev.* **D49** (1994) 4785.

[25] R. Sekhar Chivukula, B. Selipsky, E.H. Simmons, *Phys. Rev. Lett.* **69** (1992) 575.

[26] H. Georgi, *Nuc. Phys.* **B363** (1991) 301; E. Gates and J. Terning, *Phys. Rev. Lett.* **67** (1991) 1840; E. Ma and P. Roy, *Phys. Rev. Lett.* **68** (1992) 2879; M. Luty and R. Sundrum, *Phys. Rev. Lett.* **70** (1993) 529; L. Lavoura, L.-F. Li, *Phys. Rev.* **D48** (1993) 234; M.J. Dugan and L. Randall, *Phys. Lett.* **B264** (1991) 154.

[27] C.P. Burgess, S. Godfrey, H. König, D. London and I. Maksymyk, *Phys. Rev.* **D** (1994) (in press), (hep-ph/9307223).

[28] K. Hagiwara, R.D. Peccei, D. Zeppenfeld and K. Hikasa, *Nuc. Phys.* **B282** (1987) 253.

PRAMANA
journal of
physics

© Printed in India

Supplement to Vol. 45
October 1995
pp. 73-83

CP violation in a multi higgs doublet model

N. G. DESHPANDE AND XIAO-GANG HE
Institute of Theoretical Science, University of Oregon, Eugene, OR 97403-5203, USA

Abstract.

We study CP violation in a multi-Higgs doublet model based on a $S_3 \times Z_3$ horizontal symmetry. We consider two mechanisms for CP violation in this model: a) CP violation due to complex Yukawa couplings; and b) CP violation due to scalar-pseudoscalar mixings. We find that the predictions for ϵ'/ϵ, CP violation in B decays and the electric dipole moments of neutron and electron are different between these two mechanisms. These predictions are also dramatically different from the minimal Standard Model predictions.

1. Introduction

The origin of CP violation, is one of the outstanding problems of particle physics today. So far CP violation has only been observed in the neutral Kaon system. The observed CP violation can be explained in many models. It is therefore important to study other CP violating experimental observables and compare the results with different model predictions. Such study may reveal the real origin of CP violation.

In the minimal $SU(3)_C \times SU(2)_L \times U(1)_Y$ Standard Model (MSM), there is only one Higgs doublet. When the Higgs develops valcuum expectation value (VEV) v, all fermion receive masses. In the mass eigenstate basis, the Higgs coupling to fermions is diagonal, it does not mediate CP violating interaction. However, the coupling of the charged current to the W-boson becomes complex. It is given by

$$L_C = \frac{g}{\sqrt{2}} \bar{u}_i V_{ij} \gamma^\mu \frac{1-\gamma_5}{2} d_j W_\mu^+ + H.C., \tag{1}$$

where the matrix V_{ij} is the CKM matrix V_{KM}[1]. For three generations of quarks, there is a non-removable phase in the matrix. This is the source of CP violation in the MSM. This matrix is conveniently parametrized as, following Wolfenstein [2]

$$V_{KM} = \begin{pmatrix} 1-\lambda^2/2 & \lambda & A\lambda^3(\rho - i\eta) \\ -\lambda & 1-\lambda^2/2 - iA^2\lambda^4\eta & A\lambda^2 \\ A\lambda^3(1-\rho-i\eta) & -A\lambda^2 & 1 \end{pmatrix}, \tag{2}$$

where $\lambda = V_{us} = 0.221$. If $\eta \neq 0$, CP is violated. Unitarity constraints on the matrix elements provide very powerful and interesting realtions. The most interesting one is the triangle defined by

in the

$$V_{ub} + V_{td}^* \approx V_{ub} V_{cb} \,.$$

This defines the triangle shown in Figure 1 with three angles α, β and γ. The of the triangle is given by $A^2\lambda^6\eta/2$. CP violation in the neutral Kaon system be explained by the "box" interaction[3]. If CP violation due to the phase i CKM matrix is the only source for CP violation, experiments at B factories w able to determine all the three angles[4].

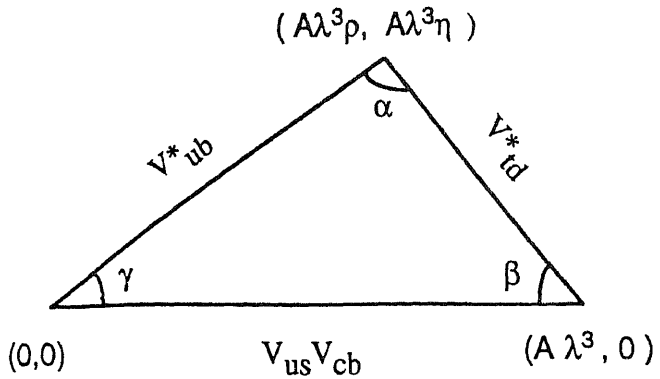

Figure 1. The unitary triangle

Another class of model for CP violation is the multi-Higgs doublet mod there are more than one Higgs doublets, the neutral scalar couplings to the q are not necessarily diagonal, and therefore provide new sources for CP violati CP violation can arise in three places in this type of models: 1) Non-trivial ph the V_{KM} matrix; 2)Non-trivial phases in the Yukawa couplings; and 3) Mixi scalar and pseudoscalar Higgs bosons. In cases 2) and 3), CP violation can o at the tree level by exchanging neutral Higgs bosons. In this talk we will pr some studies of CP violation in multi-Higgs models with flavour changing ne currents at the trre level which has CP violation predominantly throug mecha 2) and 3).

A most general study suffers from too many free parameters. To have a de idea, we carry out the study in a $S_3 \times Z_3$ model proposed by Ma[7]. This mod some very interesting predictions for fermion masses and their mixings. It als interesting predictions for CP violation[8, 9, 10]. We study the predictions fo ϵ'/ϵ; (ii) CP violation in the neutral B system; and (iii) the neutron and ele electric dipole moments (EDM). We compare these predictions with those i MSM.

2. Yukawa couplings in the $S_3 \times Z_3$ model

In the $S_3 \times Z_3$ model, there are four Higgs doublets, $\phi_{1,2,3,4}$. The quark

where $\omega \neq 1, \omega^3 = 1$ is the Z_3 element. The Yukawa couplings consistent with the $S_3 \times Z_3$ symmetry are given by

$$\begin{aligned} L_Y &= -f_1(\bar{q}_{1L}\tilde{\phi}_3 u_R + \bar{q}_{2L}\tilde{\phi}_4 c_R) - f_2\bar{q}_{3L}\tilde{\phi}_1 t_R - f_3(\bar{q}_{1L}\phi_2 s_R + \bar{q}_{2L}\phi_2 d_R) \\ &- f_4(\bar{q}_{1L}\phi_3 b_R + \bar{q}_{2L}\phi_4 b_R) - f_5(\bar{q}_{3L}\phi_3 d_R + \bar{q}_{3L}\phi_4 s_R) - f_6\bar{q}_{3L}\phi_1 b_R + H(c) \end{aligned}$$

where $\tilde{\phi}_i = (\phi_i^{0*}, -\phi_i^-)^T$. Without loss of generality we work in a basis where all VEVs are real. The up-quark mass matrix is diagonal : $\hat{M}^u = Diag(f_1 v_3, f_1 v_4, f_2 v_1)$, and the down-quark mass matrix can be written as, with a suitable choice of quark phases,

$$M^d = \begin{pmatrix} 0 & a & \xi b \\ a & 0 & b \\ \xi c & c & d \end{pmatrix} , \tag{7}$$

with a, b, c, d real and $\xi = |\xi| e^{i\sigma}$ complex. M^d can be diagonalized by a bi-unitary transformation $M^d = V_L \hat{M}^d V_R^\dagger$. Here $\hat{M}^d$ is the diagonalized down quark mass matrix. V_L and V_R are unitary matrices. Because the up quark mass matrix is already diagonalized, V_L is the CKM matrix V_{KM}.

It is convenient to work in a basis of the Higgs bosons in which the Goldstone bosons are removed. To this end we define the following[9]

$$\begin{pmatrix} \phi_1 \\ \phi_2 \\ \phi_3 \\ \phi_4 \end{pmatrix} = \begin{pmatrix} v_1/v & v_2/v_{12} & v_1 v_4/v_{12} v_{124} & -v_1 v_3/v v_{124} \\ v_2/v & -v_1/v_{12} & v_2 v_4/v_{12} v_{124} & -v_2 v_3/v v_{124} \\ v_3/v & 0 & 0 & v_{124}/v \\ v_4/v & 0 & -v_{12}/v_{124} & -v_3 v_4/v v_{124} \end{pmatrix} \begin{pmatrix} G \\ H_1 \\ H_2 \\ H_3 \end{pmatrix} , \tag{8}$$

where $v_{12}^2 = v_1^2 + v_2^2$, $v_{124}^2 = v_1^2 + v_2^2 + v_4^2$, and $v^2 = v_1^2 + v_2^2 + v_3^2 + v_4^2$. The transformation is the same for both the neutral and charged Higgs bosons. For the neutral Higgs bosons, $G = h^0 + iG_Z$, where G_Z is the Goldstone boson 'eaten' by Z, and h^0 is a physical field whose couplings are the same as the Higgs boson in the MSM. For the charged Higgs bosons G is the Goldstone boson 'eaten' by W. In this basis, we have

$$\begin{aligned} L_Y &= -(\bar{D}_L \hat{M}^d D_R + \bar{U}_L \hat{M}^u U_R)(1 + \frac{Re h^0}{v\sqrt{2}}) \\ &- \bar{D}_L \tilde{Y}_i^d D_R \frac{h_i^0}{\sqrt{2}} - \bar{U}_L \tilde{Y}_i^u U_R \frac{h_i^{0*}}{\sqrt{2}} \\ &- \bar{U}_L V_{KM} \tilde{Y}_i^d D_R h_i^+ + \bar{D}_L V_{KM}^\dagger \tilde{Y}_i^u U_R h_i^- + H.C. , \end{aligned} \tag{9}$$

where h_i are the component fields of H_i with $H_i = (h_i^+, h_i^0/\sqrt{2})$. $U_{L,R} = (u, c, t)_{L,R}^T$, and $D_{L,R} = (d, s, b)_{L,R}^T$. The couplings $\tilde{Y}_i$ can be easily expressed in term of quark masses, $V_{L,R}$, and VEVs.

$$\begin{pmatrix} Reh_k^0 \\ Imh_k^0 \end{pmatrix} = \begin{pmatrix} \alpha_{k0} & \alpha_{ki} & \beta'_{kj} \\ \alpha'_{k0} & \alpha'_{ki} & \beta_{kj} \end{pmatrix} \begin{pmatrix} R_0 \\ R_i \\ I_j \end{pmatrix} ,$$

$$h_i^+ = (\gamma_{ij})\eta_j^+ , \tag{10}$$

where R_i, I_i and η_i are the mass eigenstates, the matrix $(\alpha\beta)$ is a 7×7 othogonal matrix, and (γ) is a 3×3 unitary matrix.

The specific values for the mixings depend on the details of the Higgs potential. Unfortunately they are not determined. To simplify the problem, we will discuss two cases: a) CP violation only comes from complex Yukawa couplings; and b) CP violation only comes from the mixings of real and imaginary h_i^0[10]. Case a) can be realised by constraining certain soft symmetry breaking terms in the potential[9]. We further assume, for simplicity, that Reh_i^0 are the mass eigenstate R_i and consider their effects. The same analysis can be easily carried out for Imh_i^0 in the same way. The source for CP violation is the non-zero value for σ which is a free parameter. We will present our results for $\sigma = 80^0$, which is close to the maximum of the allowed phase. Case b) can be realised by requiring spontaneous CP violation. The value of σ will be zero and CP violation arises due to scalar-pesudoscalar Higgs boson mixing. For illustration, we consider the effects of a neutral mixed state

$$R = cos\theta Reh_2^0 + sin\theta Imh_3^0 , \tag{11}$$

and for the charged Higgs boson we consider mixing

$$\eta^+ = \gamma_{22}h_2^+ + \gamma_{23}h_3^+ , \tag{12}$$

where γ_{ij} are complex numbers, and $|\gamma_{22}|^2 + |\gamma_{23}|^2 = 1$.

The parameters a, b, c, and d are constrained from the down quark masses and the CKM mixings. We take as input parameters $a = 0.04GeV$, $b = 0.25GeV$, $c = 2.66GeV$, $d = 4GeV$. The mass eigenvalues for the down quarks are quite insensitive to the phase σ. For both cases, we have $m_b = 4.8GeV$, $m_s = 149MeV$ and $m_d = 9.5MeV$. These values are well within the allowed regions[11]. The CKM matrix for case a) is

$$V_{KM} = \begin{pmatrix} 0.975 & -0.222 & 0.00476 \\ 0.221 + i0.0033 & 0.974 + i0.014 & 0.043 - i0.0015 \\ -0.014 + i1.2 \times 10^{-5} & -0.041 - i6.8 \times 10^{-4} & 0.998 - i0.034 \end{pmatrix} ,$$

and for case b)

$$V_{KM} = \begin{pmatrix} 0.975 & 0.22 & 0.0048 \\ -0.219 & 0.975 & -0.0436 \\ -0.014 & 0.0415 & 0.999 \end{pmatrix} \tag{14}$$

The values for the VEV's are not fixed, we only know $v_3/v_4 = m_u/m_c$. We will use the values: $v_1 = v_2 = 44GeV$, $v_3 = 0.9$ GeV and $v_4 = 238GeV$ for illustration. We shall comment on effects of changing these values later.

3. Constraints on the Higgs masses from the neutral K and B mesons

The $S_3 \times Z_3$ model has very restrictive allowed values for the non-trivial CP violating phase in the CKM matrix. The CP violating measure J[12] is less than 2.5×10^{-6} which is too small to explain CP violation in the neutral Kaon sysytem. Therefore in this model CP violation due to Higgs boson exchange has to be considered.

The CP violating parameter $\bar{\epsilon}$ is given by

$$\bar{\epsilon} = \frac{ImM_{12}^K}{\sqrt{2}\Delta m_K} e^{i\pi/4}\,, \tag{15}$$

where M_{12}^K is the matrix element which mixes K^0 with $\bar{K}^0$, and Δm_K is the mass difference between m_{K_L} and m_{K_S}. Experimental value for $\bar{\epsilon}$ is $2.3 \times 10^{-3} e^{i\pi/4}$. The $\Delta S = 2$ Hamiltonian, responsible for M_{12}^K, generated by exchanging neutral Higgs bosons R_i is given by

$$H_{eff} = -\frac{1}{2M_{R_i}^2}\left(\bar{d}[(\alpha_{ki} + i\alpha'_{ki})\tilde{Y}^d_{k,12}\frac{1+\gamma_5}{2} + (\alpha_{ki} - i\alpha'_{ki})\tilde{Y}^{d*}_{k,21}\frac{1-\gamma_5}{2}]s\right)^2 . \tag{16}$$

We obtain

$$\begin{aligned} M_{12}^K &= < K^0|H_{eff}|\bar{K}^0 > \\ &= -\frac{f_k^2 m_K}{2M_{R_i}^2}(-\frac{5}{24}\frac{m_K^2}{(m_s+m_d)^2}[(\alpha_{ki} + i\alpha'_{ki})\tilde{Y}^d_{k,12})^2 + (\alpha_{ki} - i\alpha'_{ki})\tilde{Y}^{d*}_{k,21})^2] \\ &+ (\alpha_{ki} + i\alpha'_{ki})\tilde{Y}^d_{k,12}(\alpha_{k'i} - i\alpha'_{k'i})\tilde{Y}^{d*}_{k',21}(\frac{1}{12} + \frac{1}{2}\frac{m_K^2}{(m_s+m_d)^2})) . \end{aligned} \tag{17}$$

Here we have used the vaccum saturation and factorization approximation results for the matrix elements[13]. The contribution to the mass difference Δm_K is given by $2ReM_{12}$. Similar formula holds for the neutral B system.

To constrain the Higgs boson masses, we require that the neutral Higgs boson contributions to the mass differences in the neutral K and B systems to be less than the experimental values: $\Delta m_K/m_K = 7 \times 10^{-15}$, and $\Delta m_B/m_B = 8 \times 10^{-14}$. We find that for case a) the tightest constraints on the masses of $Reh^0_{1,2}$ are from the mass difference ΔM_B of the neutral B mesons which gives $M_{h_1} > 2.9TeV$ and $M_{h_2} > 3.1TeV$. With these masses, $Reh^0_{1,2}$ can not produce large enough $\bar{\epsilon}$. Similar consideration yields $M_{h3} > 3.5TeV$, and we find the experimental value of $\bar{\epsilon}$ can now be produced if the mass is about $5.6TeV$. The mass difference ΔM_K of the neutral K mesons gives weaker bounds in all cases. For case b), the experimental value of ΔM_B constrains $M_R > 3TeV$. From the experimental value of $\bar{\epsilon}$, we obtain $sin\theta cos\theta/M_R^2 = 1.1 \times 10^{-8}\,\mathrm{GeV}^{-2}$ which implies $M_R < 7TeV$.

4. Predictions for ϵ'/ϵ.

In this section we study the direct CP violation in $K_{L,S} \to 2\pi$ decays. CP violation in these processes is characterized by the value of ϵ'/ϵ. ϵ'/ϵ is defined as

$$\frac{\epsilon'}{\epsilon} = \frac{\omega\xi - ImA_2/ReA_0}{\xi + ImM_{12}/\Delta M_K}\,, \tag{18}$$

In the MSM, the contribution to ϵ'/ϵ is donminantly from the gluon penguin. However, for large top quark mass of order 200 GeV, the electroweak penguin also contribute significantly and may even cancel the gluon penguin contribution. There are large uncertainties from hadronic matrix evaluation, $\Lambda_4^{(QCD)}$ dependce and errors in the CKM matrix. The range for ϵ'/ϵ is predicted to be between 10^{-4} to 10^{-3} for $\Lambda_4^{(QCD)} = 300$ MeV[14]. This is consisten with the experimental constraints from Fermilab, $(7.4 \pm 6.0) \times 10^{-4}$ and CERN, $(23 \pm 6.5) \times 10^{-4}$[15].

In the $S_3 \times Z_3$ model there are several contributions to ϵ'/ϵ. Due to large neutral Higgs masses, the neutral Higgs boson contributions to ϵ'/ϵ are very small. However there may be large contributions from the charged Higgs bosons. The dominant contribution is from the charged Higgs boson mediated gluon penguin. The relevant $\Delta S = 1$ effective Larangian is given by

$$L_{\Delta S=1} = i\bar{d}\sigma^{\mu\nu}(\tilde{f}_1 \frac{1+\gamma_5}{2} + \tilde{f}_2 \frac{1-\gamma_5}{2})\lambda^a s G^a_{\mu\nu} \,, \tag{19}$$

where $G^a_{\mu\nu}$ is the gluon field strength, λ^a are the $SU(3)_C$ generators, and

$$\begin{aligned}
\tilde{f}_1 &= \frac{g_s(\mu)}{32\pi^2}\frac{m_l}{M^2_{h_j^+}}(\frac{3}{2} - ln\frac{m_l^2}{M^2_{h_j^+}}) Im\{(V_{KM}\tilde{Y}_i^d\gamma_{ij})_{l1}(\tilde{Y}_k^{u\dagger}V_{KM}\gamma_{kj})^*_{l2}\}\zeta_f \,, \\
\tilde{f}_2 &= \frac{g_s(\mu)}{32\pi^2}\frac{m_l}{M^2_{h_j^+}}(\frac{3}{2} - ln\frac{m_l^2}{M^2_{h_j^+}}) Im\{(V_{KM}\tilde{Y}_i^d\gamma_{ij})^*_{l2}(\tilde{Y}_k^{u\dagger}V_{KM}\gamma_{kj})_{l1}\}\zeta_f \,,
\end{aligned} \tag{20}$$

where $\zeta_f = (\alpha_s(m_h)/\alpha_s(\mu))^{14/23} \approx 0.17$ is the QCD correction factor, and l is summed over u, c and t. We will use $\alpha_s(\mu) \approx 4\pi/6$ for $\mu = 1GeV$. The above effective Lagrangian will generate a non-zero value for ImA_0[16]. $L_{\Delta S=1}$ also generates a non-zero value $\bar{\epsilon}_{LD}$ for CP violation in $K^0 - \bar{K}^0$ mixing due to long distance interactions through K^0 and π, η, η' mixings[17]. One obtains[17, 18]

$$\begin{aligned}
\frac{\xi}{\bar{\epsilon}_{LD}} &\approx -0.196D \,, \\
2m_K Im M^K_{12,LD} &\approx 0.8 \times 10^{-7}(\tilde{f}_1 + \tilde{f}_2)(GeV^3) \,,
\end{aligned} \tag{21}$$

where D is a supression factor of order $O(m_K^2, m_\pi^2)/\Lambda^2$. $\xi/\bar{\epsilon}_{LD}$ is of order -0.014 to -0.1.

We find that in both a) and b) cases, the donimant contributions are from the top quark in the loop arising from mixing in the charged Higgs boson couplings. For case a), we have

$$\bar{\epsilon}_{LD}(h_i^+) \approx a_i \frac{GeV^2}{m^2_{h_i^+}} \frac{m_t}{150GeV} ln\frac{m_t^2}{m^2_{h_i^+}} \,, \tag{22}$$

with $a_1 = 18$, $a_2 = 25$ and $a_3 = -7$.

And for case b), we have

$$\bar{\epsilon}_{LD} \approx -7.35 \times 10^3 Im(\gamma_{22}\gamma^*_{23}) \frac{GeV^2}{m^2_{\eta^+}} \frac{m_t}{150GeV} ln\frac{m_t^2}{m^2_{\eta^+}} \,. \tag{23}$$

The contributions to $\bar{\epsilon}$ can be significant in both cases depending on the Higgs boson masses and the CP violating parameter $Im(\gamma_{22}\gamma_{23}^*)$. We will study constraints on these parameters in Sec.VI. When these constraints are taken into account, $\bar{\epsilon}_{LD}$ is generally constrained to be less than 3×10^{-5} for case a) and ϵ'/ϵ to be less than 3×10^{-5}. However, for case b), $\bar{\epsilon}_{LD}$ can still be as large as 10^{-3} and ϵ'/ϵ can be 10^{-3}.

5. CP violation in the neutral B system.

There are many processes which can test CP violation in the neutral B system. Some particularly interesting ones are[4]

$$B_d \to J/\psi K_S \ , \ B_d \to \pi^+\pi^- \ , \ B_s \to \rho K_S \ . \tag{24}$$

The differences of time variation of decay rates for the above processes and their CP tranformed states are given by

$$\begin{aligned} a_{fCP} &= \frac{\Gamma(B^0(t) \to f_{CP}) - \Gamma(\bar{B}^0(t) \to f_{CP})}{\Gamma(B^0(t) \to f_{CP}) + \Gamma(\bar{B}^0(t) \to f_{CP})} \\ &= \frac{(1-|\lambda|^2)cos(\Delta M_B t) - 2Im\lambda sin(\Delta M_B t)}{1+|\lambda|^2} \ , \end{aligned} \tag{25}$$

where f_{CP} indicates the final states. λ is defined as

$$\lambda = \left(\frac{q}{p}\right)_B \frac{\bar{A}}{A} S \ , \tag{26}$$

where $(q/p)_B = \sqrt{M_{12}^{B*}/M_{12}^B}$, A and $\bar{A}$ are the decay amplitudes. If the final state contains K_S, $S = (q/p)_K$ which has a phase of order 10^{-3}. For other cases S is equal to one.

Non-zero asymmetry a_{fCP} signals CP violation. If $|\lambda|$ is not equal to one, it indicates that CP is violated in the decay amplitudes. In the MSM $|\lambda|$ is equal to one to a very good approximation for the above three processes. The asymmetries are proportional to $Im\lambda$. In the MSM, the processes in Eq.(24) measure the three angles α,β and γ,

$$\begin{aligned} Im\lambda(B_d \to J/\psi K_S) &= -sin2\beta \ , \\ Im\lambda(B_d \to \pi^+\pi^-) &= sin2\alpha \ , \\ Im\lambda(B_s \to \rho K_S) &= -sin2\gamma \ , \end{aligned} \tag{27}$$

In the $S_3 \times Z_3$ model, the situation is very different. Although the CP violating decay amplitudes A and $\bar{A}$ are small, the phase of $\sqrt{M_{12}^{B*}/M_{12}^B}$ in the $B-\bar{B}$ mixing due to neutral Higgs boson exchange can be large. In case a), there is CP violation arising from the phase in Yukawa coupling of Higgs bosons, as well as CKM matrix, but the former is much larger. The three meaurements in Eq.(24) do not measure the angles α, β and γ anymore. The first two processes will mostly measure the phases in $M_{12}^{B_d}$. We have

$$\begin{aligned} Im\lambda(B_d \to \pi^+\pi^-) &\approx Im\lambda(B_d \to J/\psi K_S) \leq 0.42 \ , \ from \ Reh_1^0, \\ Im\lambda(B_d \to \pi^+\pi^-) &\approx Im\lambda(B_d \to J/\psi K_S) \leq 0.19 \ , \ from \ Reh_2^0 \ , \\ Im\lambda(B_d \to \pi^+\pi^-) &\approx Im\lambda(B_d \to J/\psi K_S) \approx 0.19 \ , \ form \ Reh_3^0 \ . \end{aligned} \tag{28}$$

$$Im\lambda(B_d \to \pi^+\pi^-) \approx Im\lambda(B_d \to J/\psi K_S) \approx -0.25\ . \qquad (29)$$

$Im\lambda$ for $B_s \to \rho K_S$ is different for a) and b). For case a), the neutral Higgs boson contributions to the asymmetry are small. However $Im\lambda(B_s \to \rho K_S)$ due to CP violation in the KM-matrix can be about 0.1. For case b), $Im\lambda(B_s \to \rho K_S)$ from neutral Higgs boson exchange is only about 0.02.

If interpreted as in Eq.(27), we find for case a), $sin2\alpha = -sin2\beta$, $sin\gamma = 0.05$, and $\alpha + \beta + \gamma \neq 180^0$. For case b), we have, $sin2\alpha = -sin2\beta$, $sin\gamma = 0.01$. We again find, $\alpha + \beta + \gamma \neq 180^0$.

6. The neutron and electron electric dipole moments.

The EDMs of neutron and electron in the MSM model are extremely small. The neutron EDM D_n can only be generated at three loop level. It is predicted to be less than 10^{-31} ecm[19]. The electron EDM is even smaller ($< 10^{-36}$ ecm)[20]. The experimental upper bound on the neutron EDM is 1.2×10^{-25} ecm[21]. For the electron the bound is about 10^{-26} ecm[22]. If future measurement will obtain an EDM larger than the MSM model prediction, it will be an indication for new physics beyond the MSM.

The prediction for the EDMs in the $S_3 \times Z_3$ are very different from the MSM. They may reach the experimental bounds.

At the one loop level, the neutral Higgs contributions to the neutron EDM are small. For case a) we find that $D_n < 2 \times 10^{-28}$ ecm For case b), we have $D_n(d) \approx 2 \times 10^{-29} ecm$. The u quark EDM is zero at the one loop level.

There may be large contributions to the neutron EDM at the two loop level from the Weinberg operator[23] $D_n(W)$ and from the color dipole moment of gluon due to Bar-Zee type of diagrams[24, 25] $D_n(BZ)$. In our model, we have

$$\begin{aligned} D_n(W) &\approx e\zeta_W \Lambda \frac{1}{64\pi^2} ImZ^i_{tt} \frac{m_t^2}{m^2_{h^0_i}} ln \frac{m_t^2}{m^2_{h^0_i}}\ , \\ D_n(BZ,q) &\approx \frac{m_q}{64\pi^3}\frac{c_q}{9}\alpha_s(\mu)\zeta_{bz}\frac{m_t^2}{m^2_{h^0_i}}\left(ln\frac{m_t^2}{m^2_{h^0_i}}\right)^2 ImZ^i_{iq}\ , \end{aligned} \qquad (30)$$

where $\zeta_W \approx 6 \times 10^{-6}$, and $\zeta_{bz} \approx 10^{-2}$ are the QCD correction factors, $c_u = 2$ and $c_d = 4$, and $\Lambda \approx 1 GeV$ is the chiral symmetry breaking scale. The parameters ImZ are given by

$$\begin{aligned} ImZ^i_{tt} &= \frac{1}{m_t^2} Re(\tilde{Y}^u_{k,33}(\alpha_{ki} - i\alpha'_{ki}))Im(\tilde{Y}^u_{k',33}(\alpha_{k'i} - i\alpha'_{k'i}))\ , \\ ImZ^i_{tu} &= \frac{1}{m_u m_t} Im(\tilde{Y}^u_{k,33}(\alpha_{ki} - i\alpha'_{ki})\tilde{Y}^u_{k',11}(\alpha_{k'i} - i\alpha'_{k'i})) \\ ImZ^i_{td} &= \frac{1}{m_d m_t} Im(\tilde{Y}^u_{k,33}(\alpha_{ki} - i\alpha'_{ki})\tilde{Y}^d_{k',11}(\alpha_{k'i} + i\alpha'_{k'i}))\ . \end{aligned} \qquad (31)$$

For case a), because there is no CP violation in the up quark sector only down quark loops contribute, $D_n(W)$ from the Weinberg operator at the two loop level

is small. There are non-zero $D_n(BZ)$ from d-quark due to Bar-Zee mechanism. We find that the contributions from $Reh^0_{1,2}$ is also small ($< 4 \times 10^{-28} ecm$). Reh^0_3 contribution is even smaller.

For case b), the two loop contributions to the EDM are significantly larger because in this case there is CP violation in the top quark interaction. We have

$$D_n(BZ,u) \approx (2 \sim 8) \times 10^{-26} ecm \,,$$
$$D_n(BZ,d) \approx (2 \sim 8) \times 10^{-27} ecm \,, \tag{32}$$

for m_t between 100 GeV to 200 GeV. The contribution from the Weinberg operator is small, $D_n(W) \leq 10^{-30} ecm$.

The charged Higgs bosons can also contribute to the neutron EDM. At the one loop level, the u and d quark EDM are given by

$$d_u = -\frac{1}{48\pi^2}\frac{m_l}{m^2_{h^+_i}} ln \frac{m^2_l}{m^2_{h^+_i}} Im[\gamma_{ji}\gamma^*_{ki}(V_{KM}\tilde{Y}^d_j)_{1l}(V^\dagger_{KM}\tilde{Y}^u_k)_{l1}] \,,$$
$$d_d = \frac{1}{24\pi^2}\frac{m_l}{m^2_{h^+_i}} ln \frac{m^2_l}{m^2_{h^+_i}} Im[\gamma_{ji}\gamma^*_{ki}(V_{KM}\tilde{Y}^d_j)_{l1}(V^\dagger_{KM}\tilde{Y}^u_k)_{1l}] \,. \tag{33}$$

For d_u, l is summed over d, s, and b; and for d_d, l is summed over u, c, and t. At the two loop level, there is a large contribution from the Weinberg operator,

$$D_n(W) \approx e\zeta'_W \Lambda \frac{1}{32\pi^2} ImZ'^{li}_{tt} \frac{m^2_t}{m^2_{h^+_i}} ln \frac{m^2_t}{m^2_{h^+_i}} \,, \tag{34}$$

where $\zeta'_W = 3 \times 10^{-4}$ is the QCD correction factor, and

$$ImZ'^{li}_{tt} = \frac{1}{m_b m_t} Im[\gamma_{ji}\gamma^*_{ki}(V_{KM}\tilde{Y}^d_j)_{33}(V_{KM}\tilde{Y}^u_k)_{33}] \,. \tag{35}$$

We find that in case a) the dominant contributions are from the two loop Weinberg operator. We have

$$D_n(W) \approx b_i \times 10^{-19} \frac{GeV^2}{m^2_{h^+_i}} ln \frac{m^2_t}{m^2_{h^+_i}} \frac{m^2_t}{(150GeV)^2} ecm \,, \tag{36}$$

where $b_1 = 1.6$, $b_2 = 1.4$ and $b_3 = 1.2 \times 10^{-6}$.

Requiring the contributions to be less than the experimental value, we find the masses of $h^+_{1,2}$ have to be larger than $2.5 TeV$. There is no constraint on h^+_3 mass. Combining this information with those from Eqs.(22) and (23), we find the charged Higgs boson contributions to $\bar{\epsilon}_{LD}$ is less than 3×10^{-5}, and ϵ'/ϵ is less than 3×10^{-5}.

For case b), we find the dominant contribution is from the one loop d quark EDM. We have

$$D_n(d) \approx 5.4 \times 10^{-19} Im(\gamma_{22}\gamma^*_{23}) \frac{GeV^2}{m^2_{\eta^+}} ln \frac{m^2_t}{m^2_{\eta^+}} \frac{m_t}{150GeV} ecm \,. \tag{37}$$

Requiring $D_n(d)$ to be less than the experimental value, $\bar{\epsilon}_{LD}$ is constrained to be less than 10^{-3}, and ϵ'/ϵ can still be of order 10^{-3}. Assuming maximum mixing, the mass of η^+ is constrained to be larger than $5 TeV$.

lepton sector. We assume the same $S_3 \times Z_3$ assignments for the left handed and the charged right handed leptons as their quark partnenrs[7]. The mass matrix and Yukawa couplings for the charged leptons are similar to the down quarks. One simply changes the parameters (a, b, c, d , and ξ) for quarks to (a_l , b_l , c_l , d_l , and $\xi_l = |\xi| e^{i\sigma'}$) for leptons. We use[8]: $a_l = 0.106 GeV$, $b_l = 0$, $c_l = 1.781 GeV$, $d_l = 8.6 \times 10^{-3} GeV$. For this set of parameters, we have $m_e = 0.511 MeV$, $m_\mu = 106 MeV$ and $m_\tau = 1784 MeV$ which are in good agreement with experimental data.

The calculation for the electron EDM is similar to the neutron EDM. For case a) we find that the one loop contributions are small ($< 10^{29} ecm$) with $\sigma' = 80^0$. However the two loop contribution due to Bar-Zee mechanism[24, 26] can be as large as 10^{-27} ecm, for $m_t < 200 GeV$. For case b), we find that the one loop and two loop contributions are small ($< 10^{-33} ecm$).

7. Conclusions

We have studied in detail some effects due to two different CP violating mechanisms in the $S_3 \times Z_3$ model. Both mechanisms discussed in this paper can explain the observed CP violation in the neutral K system. CP violation in the neutral K system and the mass difference in the neutral B system constrain the neutral Higgs boson masses to be in the multi TeV region. In the previous discussions we have chosen a particular set of parameters. The detailed predictions will depend on all the parameters, but the general features will remain to be the same. We have checked the predictions using another set of parameters, we find the changes are not significant except that the electron EDM for case b) can reach 10^{-28} ecm. The predictions presented here represent the typical values for the observables. We summarize our results for ϵ'/ϵ, CP violation in B decays and the neutron and electron EDMs in the table below. It is clear from the table, that the predictions for the observables considered are very different in the MSM and in multi-Higgs doublet models. Future experiments will be able to rule out some models.

Observable	MSM	Case a)	Case b)
$\bar{\epsilon}$	Input	Input	Input
ϵ'/ϵ	$10^{-4} \sim 10^{-3}$	$\sim 10^{-5}$	$\sim 10^{-3}$
B Decay Asymmetry	$\alpha+\beta+\gamma = 180^0$	$\alpha+\beta+\gamma \neq 180^0$ $sin2\gamma \approx -sin2\beta \approx$ $0.2 \sim 0.4$ $sin\gamma < 0.1$	$\alpha+\beta+\gamma \neq 180^0$ $sin2\gamma \approx -sin2\beta \approx$ 0.25 $sin\gamma \approx 0$
D_n(ecm)	$10^{-31} \sim 10^{-33}$	can reach 10^{-25}	can reach 10^{-25}
D_e(ecm)	$< 10^{-36}$	$< 10^{-27}$	$< 10^{-28}$

This research was supported by the Department of Energy Grant No. DE-FG06-85ER40224. One of the authors (NGD) would like to acknowledge the local hospitality at the Institute of Mathematical Sciences.

References

[1] M. Kobayashi and K. Maskawa, Prog. Theor. Phys. **49**, 652(1973).

[2] L. Wolfenstein, Phys. Rev. Lett. **51**, 1945(1983).

[3] T. Inami and C.S. Lim, Prog. Theor. Phys. **65**, 297(1981).

[4] For a recent review, see, e.g., Y. Nir and H.R. Quinn in B Decays, edited by S. Stone (Worl Scientific, Singapore, 1992), P. 362; I. Dunietz, ibid, P. 393.

[5] Y. Yamanaka, H. Sugawara and S. Pakvasa, Phys. Rev. **D25**, 1895(1982); T. Brown, N.G. Deshpande, S. Pakvasa and H. Sugawara, Phys. Lett. **B144**, 95(1984);J. Liu and L. Wolfenstein, Nucl. Phys. **B289**, 1(1987); L. Hall and S. Weinberg, Phys. Rev. **D48**, R979(1993).

[6] S. Weinberg, Phys. Rev. Lett. **37**, 657(1976).

[7] E. Ma, Phys. Rev. **D43**, 2761(1991); ibid **D44**, 587(1991).

[8] N.G. Deshpande, M. Gupta and P. B. Pal. Phys. Rev. **D45**, 953(1992).

[9] L. Lavoura, Phys. Rev. **D46**, 4101(1992).

[10] N.G. Deshpande and Xiao-Gang He, Phys. Rev. **D49**, 4812 (1994).

[11] J. Gasser and H. Leutwyler, Nulc. Phys. **B250**, 465(1985).

[12] C. Jarlskog, Phys. Rev. Lett. **55**, 1039(1985); O.W. Greenberg, Phys. Rev. **D32**, 1941(1985); D.-D. Wu, Phys. Rev. **D33**, 860(1986).

[13] J. Trampetic, Phys. Rev. **D27**, 1565(1983).

[14] A. Buras, M. Jamin and M. Lautenbacher,Nucl. Phys. **B408**, 209(1993).

[15] A. Wagner, talk presented at the European Physics Symposium on High Energy Physics, Marseille, July (1993); L.K. Gibbons et al., Phys. Rev. Lett. **70**, 203(1993).

[16] N.G. Deshpande, Phys. Rev. **D23**, 2654(1981); A. Sanda, ibid, **23**, 2647(1981).

[17] J. Donoghue and B. Holstein, Phys. Rev. **D32**, 1152(1985).

[18] H.-Y. Cheng, Int. J. Mod. Phys. **A7**, 1059(1992).

[19] B. McKellar, S. Choudhury, X.-G. He, and S. Pakvasa, Phys. Lett. **B197**, 556(1987); X.-G. He, B. McKellar and S. Pakvasa, Int. J. Mod. Phys. **A4**, 5011(1989).

[20] M.E. Pospelov and I.B. Khriplovich, Sov. J. Nucl. Phys. **53**, 638(1991).

[21] K. Smith et al., Phys. Lett. **B234**, 234(1990); I.S. Altarev et al., Phys. Lett. **B276**, 242(1992).

[22] K. Abdullah et al., Phys. Rev. Lett. **65**, 2347(1990).

[23] S. Weinberg, Phys. Rev. lett. **63**, 2333(1989).

[24] S.M. Barr and A. Zee, Phys. Rev. Lett. **65**, 21(1990).

[25] J. Gunion and D. Wyler, Phys. Lett. **B248**, 170(1990); D. Chang, W.-Y. Keung and T.C. Yuan, Phys. Lett. **B251**, 608(1990).

[26] D. Chang, W.-Y. Keung and T.C. Yuan, Phys. Rev. **D43**, R14(1991); R.G. Leigh, S. Paban and R.M. Xu, Nucl. Phys. **B352**, 45 (1991).

PRAMANA
journal of
physics

© Printed in India

Supplement to Vol. 45
October 1995
pp. 85-108

Phenomenology of the minimal supergravity $SU(5)$ model

MANUEL DREES

Physics Department, University of Wisconsin, Madison, WI 53706, USA

Abstract. The minimal grand unified supergravity model is discussed. Requiring radiative breaking of the electroweak gauge symmetry, the unification of b and τ Yukawa couplings, a sufficiently stable nucleon, and not too large a relic density of neutralinos produced in the Big Bang constrains the parameter space significantly. In particular, the soft breaking parameter $m_{1/2}$ has to be less than about 130 GeV, and the top quark Yukawa coupling has to be near its (quasi) fixed point. The former condition implies $m_{\tilde{g}} \leq 400$ GeV and hence very large production rates for gluino pairs at the LHC, while the latter constraint implies that the lighter stop and sbottom eigenstates are significantly lighter than the other squarks, leading to characteristic signatures for gluino pair events.

1. Introduction

Supersymmetry (SUSY) [1] now seems to be the most popular extension of the Standard Model (SM). There are several reasons for this. First of all, SUSY solves the (technical) hierarchy problem [2] (also known as finetuning or naturalness problem), i.e. stabilizes the weak scale against radiative corrections that otherwise tend to pull it up towards the GUT or Planck scale. This is also true for SUSY's main competitor, technicolor (TC) [3], although through a completely different mechanism. However, it seems increasingly difficult to find realisations of the TC idea that are not ruled out, or at least strongly disfavoured, by LEP measurements, in particular of the so-called S parameter [4] and of the $Z \to b\bar{b}$ partial width [5]. In contrast, sparticles decouple quickly, i.e. do not affect predictions for LEP observables noticably if sparticle masses exceed 100 GeV or so, so that LEP measurements can only rule out SUSY if they also exclude the SM (with a light Higgs boson) at the same time. Moreover, if sparticles are light, agreement between LEP measurements and predictions is often (slightly) improved compared to the non-supersymmetric SM [6].

Another strong motivation for SUSY is that the minimal supersymmetric standard model (MSSM) allows for a predictive grand unification of all gauge interactions, in contrast to the SM [7], [8]. Actually GUTs were in better agreement with data [9] with than without SUSY already before LEP was turned on, but the higher precision achieved by LEP experiments has made this argument much more convincing.

All these arguments are independent of the way SUSY is broken, provided only

TeV; if either of these conditions were violated, the naturalness problem would r
appear. Unfortunately no completely convincing dynamical mechanism of SUS
breaking has yet been suggested. For example, the one thing we know for sure abo
SUSY breaking in superstring theories is that it does not happen at any order
perturbation theory [11], i.e. SUSY breaking is an intrinsically nonperturbati
problem and thus not easily treatable [12]. At present we are therefore forced
use a phenomenological approach to SUSY breaking.

In many analyses of SUSY signals at colliders [1, 13] or elsewhere, it has be
assumed that the sparticle spectrum has a high degree of degeneracy at the *we*
energy scale, $\mathcal{O}(100)$ GeV, where present and near-future experiments operat
Specifically, it has often been assumed that all squarks (with the possible exceptic
of stops) are exactly degenerate in mass with each other as well as with all slepton
On the other hand, in these same analyses the parameters of the Higgs sector ha
usually been chosen "by hand", *independently* of the sparticle spectrum. Bot
these assumptions are, in my view at least, rather unnatural. First of all, we kno
experimentally that within the MSSM the running gauge couplings meet (unify)
$M_X \simeq 2 \cdot 10^{16}$ GeV. In other words, starting from a seemingly complicated situatic
(described by three "independent" gauge couplings) at low energies we are led t
a much simpler scenario with only a single gauge coupling at very high energie
On the other hand, if we similarly run the soft breaking parameters from the wea
to the GUT scale, starting from a degenerate spectrum at the weak scale leads t
a complicated, highly non-degenerate spectrum at the GUT scale. This violate
what can be called the "unification dogma", which stipulates that nature shoul
become simpler, i.e. more symmetric, at higher energies. Secondly, the main beaut
of SUSY is that it naturally includes (elementary) scalar particles, which seem t
be required for the breaking of the electroweak symmetry in accordance with LE
data. Some of this beauty is lost if we treat matter (sfermion) and Higgs scalar
differently.

It thus seems much more natural to me to assume a highly degenerate (s)particl
spectrum at the GUT (or even Planck) scale, and to extend this degeneracy t
include the Higgs bosons. This is called the minimal supergravity (mSUGRA
scenario [14], the idea being that local supersymmetry or supergravity is sponta
neously broken in a "hidden sector", and that this is communicated to the visi
ble (gauge/Higgs/matter) sector only through flavour-blind gravitational-strengt
interactions. One very attractive feature of this scenario is that it (almost) *au*
tomatically leads to the correct symmetry breaking pattern; that is, even though
all scalars get the same nonsupersymmetric (positive) mass term at scale M_X, a
the weak scale the Higgs fields (and *only* the Higgs fields) acquire nonvanishing
vacuum expectation values (vevs), provided only that the top quark is not much
lighter than the W boson, which we now know to be true [15]. This "miracle"
occurs since radiative corrections involving Yukawa interactions reduce the squared
masses of the Higgs bosons, eventually driving a combination of these masses to
negative values [14, 16], at which point the electroweak gauge symmetry is broken.
Notice that this mechanism of radiative gauge symmetry breaking "explains" both
the existence of the gauge hierarchy and the large mass of the top quark, in the
sense that it only works if $\log(M_X/M_Z) \gg 1$ and the top Yukawa $h_t \sim \mathcal{O}(1)$.

Of course, this approach to SUSY breaking is most naturally combined with

group, $SU(5)$. Moreover, only the minimal necessary number of fields will be assumed to exist at the GUT scale as well as at lower energies. As discussed in more detail in sec. 2, this leads to a fairly predictive (constrained) scenario [17], although some freedom in the choice of parameters, and of the resulting phenomenology, still exists. It should be emphasized that it is not at all trivial that this simplest of all SUSY GUTs is still experimentally viable [18].

The remainder of this contribution is organized as follows. Sec. 2 contains a description of the model as well as a discussion of the constraints that have been imposed. In sec. 3 the resulting (s)particle spectrum will be discussed in some detail; this section contains the only material that cannot be found in our publication [19]. In sec. 4 signals for sparticle production at the LHC are treated for a few characteristic spectra; the emphasis will be on methods to distinguish these spectra from each other as well as from the kind of spectrum that has been studied previously. Finally, sec. 5 is devoted to summary and conclusions.

2. The model

As explained in the Introduction, I will assume a simple form for the sparticle and Higgs spectrum at very high energy scales. In fact, one ultimately hopes to describe all of SUSY breaking by a single parameter, the equivalent of the electroweak symmetry breaking scale $(\sqrt{2}G_F)^{-1/2} = 246$ GeV. At present we are still far from this ambitious goal, so it is prudent to allow at least a few free parameters to describe the spectrum. Here I will follow the standard assumptions [14] and introduce four independent SUSY breaking parameters: m_0^2, which contributes to the squared masses of all scalar bosons; a common gaugino mass $m_{1/2}$; and common nonsupersymmetric trilinear and bilinear scalar interaction strengths A and B, respectively [20]. In addition one has to introduce a supersymmetric Higgs(ino) mass μ in order to avoid the existence of a (visible) axion and to give masses to both up- and down-type quarks. Altogether the masses of the two $SU(2)$ doublets of Higgs bosons needed in any realistic SUSY model are then

$$m_H^2(M_X) = m_{\bar{H}}^2(M_X) = m_0^2 + \mu^2(M_X). \tag{1}$$

One can show quite easily that spontaneous $SU(2) \times U(1)_Y$ breaking is not possible as long as $m_H^2 = m_{\bar{H}}^2$. Fortunately this degeneracy is lifted by radiative corrections. The reason is that $\bar{H}$ only has Yukawa couplings to up-type quarks, while H only couples to down-type quarks and leptons. Of course, the t quark belongs to the former category, and has by far the largest Yukawa coupling of all SM fermions (unless $\tan\beta \gg 1$; see below). This implies that radiative corrections from Yukawa interactions will be much larger for $m_{\bar{H}}^2$ than for m_H^2. The crucial point is that these corrections *reduce* the (running) squared mass when going to lower energy scales, eventually leading to nonzero vevs for H and $\bar{H}$. As already emphasized in the Introduction, this mechanism will only work if $\log M_X/M_Z \gg 1$ and the top Yukawa coupling h_t is large [21].

The running of the soft SUSY breaking parameters as well the of the gauge and Yukawa couplings is described by a set of renormalization group equations (RGE) [22]. As a consequence of the assumption of minimal particle content the

therefore allow to uniquely determine the values of parameters at the weak scale from the input parameters at M_X. Of course, at the weak scale certain equalities have to be satisfied. First of all, we know that

$$\frac{g^2+g'^2}{2}\left(\langle H^0\rangle^2+\langle \bar{H}^0\rangle^2\right)=M_Z^2. \tag{2}$$

It is often convenient to introduce the weak scale parameter $\tan\beta \equiv \langle \bar{H}^0\rangle/\langle H^0\rangle$. With the help of this parameter, eq.(2) can be solved for μ^2 at the weak scale Q_0:[23]

$$\mu^2(Q_0)=\frac{m_1^2(Q_0)-m_2^2(Q_0)}{\tan^2\beta-1}-\frac{1}{2}M_Z^2, \tag{3}$$

where m_1^2, m_2^2 are the nonsupersymmetric contributions to the squared Higgs masses, i.e. $m_H^2=m_1^2+\mu^2$, $m_{\bar{H}}^2=m_2^2+\mu^2$. For heavy top, $m_2^2(Q_0)$ is negative, giving a positive (and usually quite large) contribution to μ^2. A similar equation determines $B\cdot\mu$ at scale Q_0 in terms of m_1^2, m_2^2 and $\tan\beta$.

Having fixed M_Z, we are left with the parameters $m_0, m_{1/2}$ and A (at the GUT scale) as well as $\tan\beta$ (at the weak scale). In addition the mass m_t of the top quark is an important parameter, since the top Yukawa coupling plays a vital role in radiative gauge symmetry breaking. At this point the assumption of a minimal $SU(5)$ GUT helps to further reduce the number of free parameters. The reason is that minimal $SU(5)$ implies the equality of b and τ Yukawa couplings at scale M_X. As has been shown by several groups [26], this can only be brought into agreement with the experimentally measured ratio m_b/m_τ if either h_t is close to its upper bound or if $h_b \simeq h_t$, which implies $\tan\beta \simeq m_t/m_b$ [27]. The second choice not only necessitates some finetuning in this minimal scenario [28], it also makes it more difficult to satisfy proton decay constraints (see below). I therefore only consider the first solution here. Within the precision of a 1-loop calculation it can simply be implemented by taking

$$h_t(M_X)=2. \tag{4}$$

This ensures that at low energies h_t is very close to its infrared quasi fixed point [26], which implies

$$m_t(m_t)\simeq 190\ \text{GeV}\cdot\sin\beta, \tag{5}$$

where $m_t(m_t)$ is the running ($\overline{\text{MS}}$) top mass at scale m_t; the on-shell (physical) top mass is about 5% larger. Eq.(5) reduces the number of free parameters from five to four in this scenario. Assuming $m_t(\text{pole})\leq$ 185 GeV, as indicated by LEP data [29] if the Higgs is light, then implies

$$\tan\beta \leq 2.5. \tag{6}$$

In addition to the relations discussed so far a number of conditions has to be satisfied. These can all be expressed in terms of inequalities, i.e. they define allowed ranges of parameter values rather than determining them uniquely. One important constraint emerges from the requirement that nucleons should be sufficiently long-lived. In minimal SUSY $SU(5)$ the main contribution to nucleon decay comes

from the exchange of the fermionic superpartners of the $SU(5)$ partners of the elw. Higgs bosons, i.e. from higgsino triplet exchange [30]. The reason is that the corresponding diagrams are only suppressed by one power of a mass $\mathcal{O}(M_X)$, as compared to two such powers for $SU(5)$ gauge boson exchange. However, while higgsino exchange suffices to violate both baryon and lepton number, it leads to two sfermions, rather than two fermions, in the final state. These sfermions have to be transformed into a lepton and an anti–quark by gaugino (mostly chargino) exchange, i.e. the decay only occurs at 1–loop level. The matrix element therefore contains a so–called dressing loop function, which scales like $m_{1/2}/m_0^2$ for $m_0 \geq m_{1/2}$. Altogether one thus has [30]

$$\mathcal{M}(p \to K\nu) \propto \frac{\tan\beta}{m_{\tilde{H}_3}} \frac{m_{1/2}}{m_0^2}, \tag{7}$$

where $m_{\tilde{H}_3}$ is the mass of the Higgsino triplet, and the factor $\tan\beta$ appears since Yukawa couplings to d and s quarks grow $\propto \tan\beta$. The experimental lower bound on the proton lifetime τ_p gives an upper bound on the matrix element (7); assuming conservatively that $m_{\tilde{H}_3}$ could be as much as ten times larger than the scale M_X where the gauge couplings meet, and taking into account that we are only interested in rather small values of $\tan\beta$, eq.(6), a conservative interpretation of the constraint imposed by the bound on τ_p is[8] [30] [31]

$$m_0 \geq \min(300 \text{ GeV}, \ 3m_{1/2}). \tag{8}$$

Another important constraint can be derived from the requirement that relic LSPs produced in the Big Bang do not overclose the universe, in which case it would never have reached its present age of at least 10^{10} years. In minimal SUGRA the lightest supersymmetric particle (LSP) is always the lightest of the four neutralino states. Moreover, the large value of h_t, eq.(4), and small $\tan\beta$ (6) imply that $|\mu(Q_0)|$ is quite large, see eq.(3). The LSP is therefore always a gaugino (mostly bino) with small higgsino component. The LSP relic density is essentially inversely proportional to its annihilation cross section, summed over all accessible channels. Gaugino–like LSPs mostly annihilate into $f\bar{f}$ final states [32], where f stands for any SM fermion with mass below that of the LSP. This final state is accessible via $\tilde{f}$ exchange in the t or u channel, as well as via the exchange of the Z boson or one of the neutral Higgs bosons in the s channel. However, the constraint (8) implies that the $\tilde{f}$ exchange contribution is strongly suppressed, due to the large sfermion masses. (Recall that all sfermions get a contribution $+m_0^2$ to their squared masses at scale M_X.) Moreover, since both m_0 and $|\mu|$ are large, most Higgs bosons are very heavy. Finally, the LSP–LSP–Z coupling needs two factors of the small higgsino component of the LSP, while the LSP–LSP–Higgs couplings only need one such factor. Therefore the only potentially large contribution to LSP annihilation comes from the exchange of the light neutral Higgs boson h^0. Fortunately it has recently been shown [33] that this contribution suffices to reduce the LSP relic density to acceptable values for a substantial range of LSP masses, *provided* it is below $m_h/2$. The upper bound (6) on $\tan\beta$ implies that $m_h \leq 110$ GeV even after radiative corrections [34, 25] are included, while Higgs searches at LEP imply [35] $m_h \geq 63$ GeV. (The couplings of h^0 are very similar to that of the SM Higgs boson

this implies

$$60 \text{ GeV} \leq m_{1/2} \leq 130 \text{ GeV}. \tag{9}$$

It should be emphasized that such a strong upper bound on $m_{1/2}$ only holds in this specific scenario. If we give up on the unification of b and τ Yukawa couplings, we can allow smaller h_t and/or larger $\tan\beta$, leading to smaller values of $|\mu(Q_0)|$, and hence a larger higgsino component of the LSP and stronger annihilation into final states containing Higgs and/or gauge bosons. If we allow for a sufficiently non-minimal GUT Higgs sector the bound on the proton lifetime can be satisfied even if the constraint (8) is violated, allowing for efficient LSP annihilation through $\tilde{f}$ exchange. Finally, if we allow new, R-parity violating interactions, relic LSPs could have decayed a long time ago, and no constraint on LSP annihilation could be given.

Eqs.(4), (6), (8) and (9) describe the basic allowed parameter space of the model, except for the A parameter. The bounds on this parameter are intimately linked to to the details of the (s)particle spectrum, which is the topic of the next section.

3. The spectrum

In this section I discuss the sparticle and Higgs spectrum of the model defined in the previous section, with emphasis on features that are relevant for "new physics" searches at colliders; see also refs.[36, 37] for recent discussions of the spectrum in mSUGRA models with top Yukawa coupling close to its fixed point.

A general feature of all mSUGRA models is that the Higgs(ino) mass parameter μ is *not* an independent variable, but can be computed from the SUSY breaking parameters, m_t and $\tan\beta$ (as well as M_Z, of course), as described by eq.(3). In general, the r.h.s. of that equation is a complicated function of all input parameters, which has to be computed by solving the relevant RGE [22] numerically. However, the following analytical expression are often sufficient for practical purposes:

$$m_1^2(Q_0) \simeq m_0^2 + 0.5 m_{1/2}^2; \tag{10a}$$

$$m_2^2(Q_0) \simeq m_1^2(Q_0) - \frac{X_2}{\sin^2\beta}, \quad \text{where} \tag{10b}$$

$$X_2 = \left(\frac{m_t}{150 \text{ GeV}}\right)^2 \left\{0.9 m_0^2 + 2.1 m_{1/2}^2 + \left[1 - \left(\frac{m_t}{190 \text{ GeV } \sin\beta}\right)^3\right] (0.24 A^2 + A \cdot m_{1/2})\right\} \tag{10c}$$

Eqs.(10) reproduce the exact numerical results to 10% or better if Q_0 is around 350 GeV (which corresponds [25] to squark masses around 600 GeV), and if $h_b \ll 1$, which is always true here due to the upper bound (6) on $\tan\beta$. Note that m_t in eqs.(10) is the running top mass $m_t(m_t)$. The expression in square brackets in eq.(10c) will therefore always be small if h_t is close to its fixed point, see eq.(5). The resulting very weak dependence of X_2 on A has also been observed in ref.[36] [38].

certainly true in the given scenario. Specifically, if h_t is close to the fixed point one has

$$\mu^2(Q_0) > m_0^2 \frac{1 + 0.44 \tan^2\beta}{\tan^2\beta - 1} > 0.72 m_0^2, \tag{11}$$

where I have used (6) in the second inequality; the lower bound (8) on m_0 then implies that the LSP is indeed always a very pure gaugino, as stated in the previous section. It also means that the two heavier neutralinos and the heavier chargino, whose masses are all very close to $|\mu(Q_0)|$, will be very difficult to detect: Their production cross section at the LHC is much too small to yield a viable signal, while they are too heavy to be produced at all at a linear e^+e^- collider with $\sqrt{s} \simeq 500$ GeV, which is likely to be the next high–energy e^+e^- collider.

Another useful identity is [25]

$$m_P^2 = \frac{m_{\tilde{\nu}}^2 + \mu^2(Q_0)}{\sin^2\beta}, \tag{12}$$

where

$$m_{\tilde{\nu}}^2 \simeq m_0^2 + 0.5 m_{1/2}^2 + 0.5 M_Z^2 \cos 2\beta \tag{13}$$

is the squared sneutrino mass and m_P is the mass of the pseudoscalar Higgs boson, which is almost degenerate with the charged and heavy neutral scalar Higgs bosons if $M_P^2 \gg M_Z^2$ [39]. Note that eq.(12) is *exact*, unlike eqs.(10), up to corrections of order h_b^2. In our fixed point scenario eq.(12) and the bounds (8) and (11) imply that m_P can easily exceed 1 TeV even for quite modest values of m_0; such heavy SUSY Higgses are very difficult to detect (or even produce) experimentally. On the other hand, this also implies that the couplings of the light neutral scalar Higgs boson h^0 to SM fermions and gauge bosons are practically identical to those of the SM Higgs [39], so that h^0 will be produced copiously at the LHC, at future e^+e^- linacs, and perhaps even at the second stage of LEP [40]

Since we have $m_0^2 \gg m_{1/2}^2$ in our model, all sleptons have very similar masses; eqs.(13) and (8) then imply that they are most likely too heavy to be detectable at the LHC [41], while they cannot be produced at all at a 500 GeV e^+e^- collider.

Clearly the best chance for a decisive test of the model is given by the upper bound (9) on $m_{1/2}$. Since $|\mu(Q_0)|$ is so large the masses of the lighter chargino and the next–to–lightest neutralino lie within a few GeV of the low–energy $SU(2)$ gaugino mass $M_2 \simeq 0.82 m_{1/2}$. In particular, the lighter chargino always lies below 105 GeV [17], offering a good chance for its discovery at LEP, especially if the machine energy can be boosted beyond the currently foreseen value of 176 GeV.

The situation is slightly more complicated for the gluino. The bound (9) implies a rather low upper bound for the running ($\overline{MS}$ or $\overline{DR}$) gluino mass, $m_{\tilde{g}}(m_{\tilde{g}}) \simeq 2.5 m_{1/2} \leq 330$ GeV. However, it has recently been pointed out [42] that the on–shell gluino mass can be substantially larger than this, especially if squarks are heavy:

$$m_{\tilde{g}}(\text{pole}) \simeq m_{\tilde{g}}(m_{\tilde{g}}) \left[1 + \frac{\alpha_s(m_{\tilde{g}})}{\pi} \left(3 + \frac{1}{4} \sum_{\tilde{q}} \log \frac{m_{\tilde{q}}}{m_{\tilde{g}}} \right) \right], \tag{14}$$

where I have only included the leading logarithmic correction from squark–quark loops. Requiring somewhat arbitrarily

$$m_0 \leq 1 \text{ TeV} \tag{15}$$

in order to avoid excessive finetuning in eq.(3), we see that the "threshold correction" (14) can change the gluino mass by about 30% if $m_{1/2}$ is close to its lower bound and m_0 is at its upper bound. This can change both the cross section and the signal for gluino pair production quite significantly. Including the correction (14), the bound (8) implies $m_{\tilde{g}}(\text{pole}) \leq 400$ GeV if (15) is imposed.

The lower bound (8) on m_0 also implies that the squarks of the first two generations are significantly heavier than the gluinos; they will thus dominantly decay into $\tilde{g} + q$, although the left-handed ($SU(2)$ doublet) squarks also have $\mathcal{O}(10\%)$ branching ratios into an elw. gaugino and a quark. The masses of the first two generations of squarks lie between about 330 GeV and a little above 1 TeV in this model, where the upper bound merely reflects the somewhat arbitrary constraint (15).

So far the spectrum resembles a special case of the type of models whose signatures were discussed in the existing literature [1, 13], with heavy squarks and sleptons, large $|\mu|$ and m_P, but rather light gluino and elw. gauginos. This is not surprising, since in these ealiers studies μ and m_P were considered to be free parameters; they could thus be chosen to be large, whereas the present model *requires* them to be large. However, as already remarked in the Introduction, in these papers all squarks were also assumed to have the same mass at the weak scale. It is here that the present model makes specific predictions which cannot be mimicked by these earlier treatments, in spite of the larger number of free parameters.

The reason is that the same kind of radiative corrections that reduce the Higgs mass parameter m_2^2 to negative values also reduce the masses of the stop and left–handed sbottom squarks, as compared to the masses of first generation squarks. Specifically, one finds

$$m^2_{\tilde{b}_L} = m^2_{\tilde{t}_L} \simeq m^2_{\tilde{q}} - \frac{X_2}{3\sin^2\beta}; \tag{16a}$$

$$m^2_{\tilde{t}_R} \simeq m^2_{\tilde{q}} - \frac{2X_2}{3\sin^2\beta}, \tag{16b}$$

where

$$m^2_{\tilde{q}} \simeq m_0^2 + 6m_{1/2}^2 \tag{17}$$

is a typical first generation squark mass (at scale $Q = m_{\tilde{q}}$), and X_2 has been given in eq.(10c).

Since for the small values of $\tan\beta$ of interest here $\tilde{b}_L - \tilde{b}_R$ mixing is almost negligible, $\tilde{b}_L$ is to good approximation the mass eigenstate $\tilde{b}_1$, with mass given by eq.(16a). The ratio $m_{\tilde{b}_1}/m_{\tilde{u}_L}$ (including small mixing effects and D–terms) is shown in fig. 1 as a function of $A_0 \equiv A/m_0$, for various values of m_0 and $m_{1/2}$ and $\mu < 0$ [44]. We observe that the dependence on A is indeed quite weak here, as claimed earlier. The allowed range for A_0 is determined by various constraints: The squared mass of the lightest stop eigenstate (see below) must be larger than $+(45 \text{ GeV})^2$; the scalar potential at the weak scale should not have minima [45]

in the directions $\langle\tilde{\tau}_R\rangle = \langle\tilde{\tau}_L\rangle = \langle H^0\rangle$ or $\langle\tilde{t}_R\rangle = \langle\tilde{t}_L\rangle = \langle\bar{H}^0\rangle$ that are deeper than the desired minimum where only $\langle H^0\rangle$ and $\langle\bar{H}^0\rangle$ are nonzero; and the potential must be bounded from below at the GUT scale, which requires $m_0^2 + \mu^2(M_X) \geq 2|B(M_X)\mu(M_X)|$.

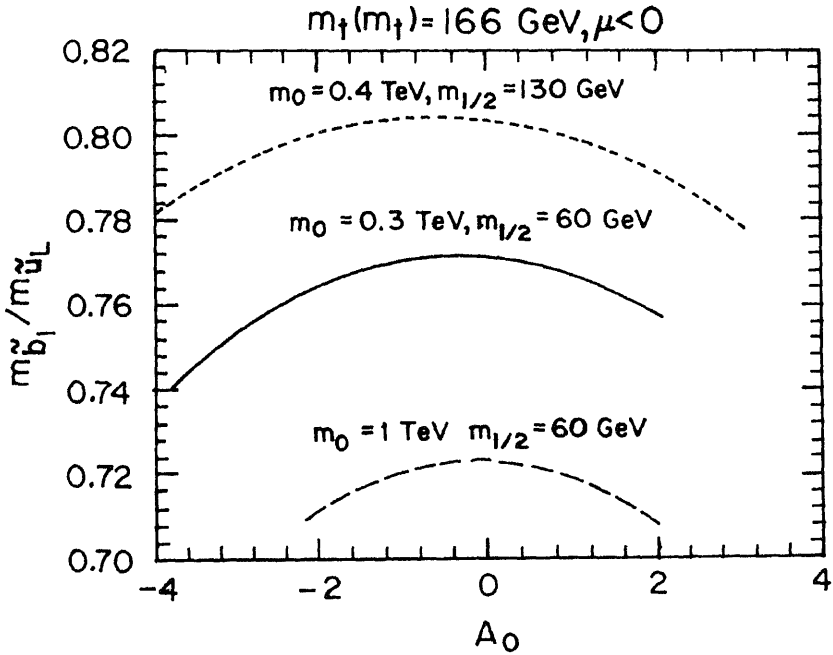

Figure 1. The ratio $m_{\tilde{b}_1}/m_{\tilde{u}_L}$ as a function of the GUT scale parameter $A_0 \equiv A/m_0$.

The ratio $m_{\tilde{b}_1}/m_{\tilde{u}_L}$ does depend somewhat on the ratio $m_{1/2}/m_0$, however, being maximal where $m_{1/2}/m_0$ is minimal (and vice versa). We see that in our fixed-point scenario $m_{\tilde{b}_1}$ is reduced by typically 20 to 30% compared to first generation squark masses. This can be quite significant, since partial widths for three-body decays of gluinos or elw. gauginos that involve squark exchange scale approximately like the inverse fourth power of the squark mass. A reduction of the squark mass by 20% (30%) therefore leads to an increase of the corresponding partial width or branching ratio by a factor of 2.1 (2.9). This leads to b-rich final states, as will be discussed in more detail in sec. 4.

Eq.(16b) implies that the mass of the $\tilde{t}_R$ current state is reduced even more than $m_{\tilde{b}_L}$. Moreover, $\tilde{t}_L - \tilde{t}_R$ mixing is not negligible; it reduces the mass $m_{\tilde{t}_1}$ of the lighter $\tilde{t}$ mass eigenstate even further. In the convention of ref.[43] the $\tilde{t}$ mass matrix is given by [46]:

$$\mathcal{M}_{\tilde{t}}^2 = \begin{pmatrix} m_{\tilde{t}_L}^2 + m_t^2 + 0.35 M_Z^2 \cos 2\beta & -m_t(A_t + \mu\cot\beta) \\ -m_t(A_t + \mu\cot\beta) & m_{\tilde{t}_R}^2 + m_t^2 + 0.16 M_Z^2 \cos 2\beta \end{pmatrix} \tag{18}$$

At scale M_X, $A_t = A$, but it is subject to radiative corrections due to both gauge

and Yukawa interactions. For small $\tan\beta$, one has approximately:

$$A_t(Q_0) \simeq A\left[1-\left(\frac{m_t}{190\ \mathrm{GeV}\ \sin\beta}\right)^2\right]+m_{1/2}\left[3.5-1.9\left(\frac{m_t}{190\ \mathrm{GeV}\ \sin\beta}\right)^2\right], \quad (19)$$

where I have again assumed $Q_0 \simeq 350$ GeV. Right at the fixed point of h_t, where eq.(5) becomes exact, the weak–scale value of A_t is again independent of A [36]. However, even for values of $h_t(M_X)$ as large as 2, $m_{\tilde{t}_1}$ can still show substantial A–dependence. The reason is that in the expression for $m_{\tilde{t}_1}$ strong cancellations occur between the contributions from diagonal and off–diagonal entries of the stop mass matrix; relatively small changes of these elements, of the size shown in fig. 1, can therefore have sizable effects on $m_{\tilde{t}_1}$. This is especially true for $\mu > 0$, since there all effects go in the same direction: Increasing A increases X_2, which simultaneously reduces $m^2_{\tilde{t}_L}$ and $m^2_{\tilde{t}_R}$ in the diagonal entries, eq.(16), and increases the off–diagonal elements by increasing μ, see eqs.(3) and (10); note that A_t and μ have the same sign in this case.

$m_{\tilde{t}_1}$ also depends quite strongly on m_t in the fixed–point scenario. The reason is that a larger m_t implies larger $\tan\beta$, see eq.(5), and hence smaller $|\mu|$, eq.(3); in addition, the off–diagonal term in the stop mass matrix (18) is reduced, due to the explicit $\cot\beta$ factor. Therefore larger m_t also imply larger $m_{\tilde{t}_1}$ here. (This is not generally true if h_t is significantly below its fixed point [43].)

In all of parameter space allowed in our model one finds that $m_{\tilde{t}_1}$ is close to or even well below the gluino mass. This is partly due to the correction (14) [47]. Not surprisingly, this statement remains true [36, 37] if the constraint (8) from the proton lifetime is not imposed, i.e. if larger ratios $m_{1/2}/m_0$ are allowed, as long as h_t is close to its fixed point. Light stops are hence a quite generic prediction of SUGRA models with large h_t. Their phenomenology depends on whether or not they can be produced in gluino decays (i.e., whether $m_{\tilde{g}} > m_t + m_{\tilde{t}_1}$), and also whether the decay $\tilde{t}_1 \to b + \widetilde{W}_1$ is allowed, where $\widetilde{W}_1$ is the lighter chargino; if (and only if) this decay is forbidden, $\tilde{t}_1 \to c + \tilde{Z}_1$ via loop diagrams [49].

The ordering of $m_{\tilde{g}}$, $m_{\tilde{t}_1}$, m_t and $m_{\widetilde{W}_1}$ depends quite strongly on A, $m_{1/2}$ and m_t, as well as on the sign of μ. This is demonstrated by figs. 2 a–d, which show regions in the $(A_0, m_{1/2})$ plane for $m_0 = 500$ GeV; results for other values of m_0 allowed by (8) are quite similar. Figs. 2a,b are for $m_t(m_t) = 160$ GeV, corresponding to $m_t(\mathrm{pole}) = 168$ GeV, while c,d are for $m_t(m_t) = 175$ GeV or $m_t(\mathrm{pole}) = 183$ GeV; μ has been chosen positive in a,c and negative in b,d. In all these figures the regions outside the dotted lines are excluded by the constraints described in the discussion of fig. 1. Along the solid line one has $m_{\tilde{g}} = m_{\tilde{t}_1} + m_t$, i.e. on one side of this line $\tilde{g} \to \tilde{t}_1 + t$ decays are allowed; since all other squarks are considerably heavier, this is the only possible two–body decay mode of the gluino and will hence have a branching ratio of nearly 100% if allowed at all. Similarly, the long dashed lines separate regions where $\tilde{t}_1 \to \widetilde{W}_1 + b$ is open, in which case it has a branching ratio very close to 100%, from those where $\tilde{t}_1 \to \tilde{Z}_1 + c$. The decay $\tilde{t}_1 \to t + \tilde{Z}_1$ is almost never allowed here (it opens up if both $m_{1/2}$ and m_0 are near their upper bounds); instead, the short dashed lines are contours of constant $m_{\tilde{t}_1} = m_t$. In all cases $m_{\tilde{t}_1}$ increases with increasing $m_{1/2}$, and it generally also increases with decreasing $|A_0|$, although the maximum (for given $m_{1/2}$) is not exactly at $A_0 = 0$.

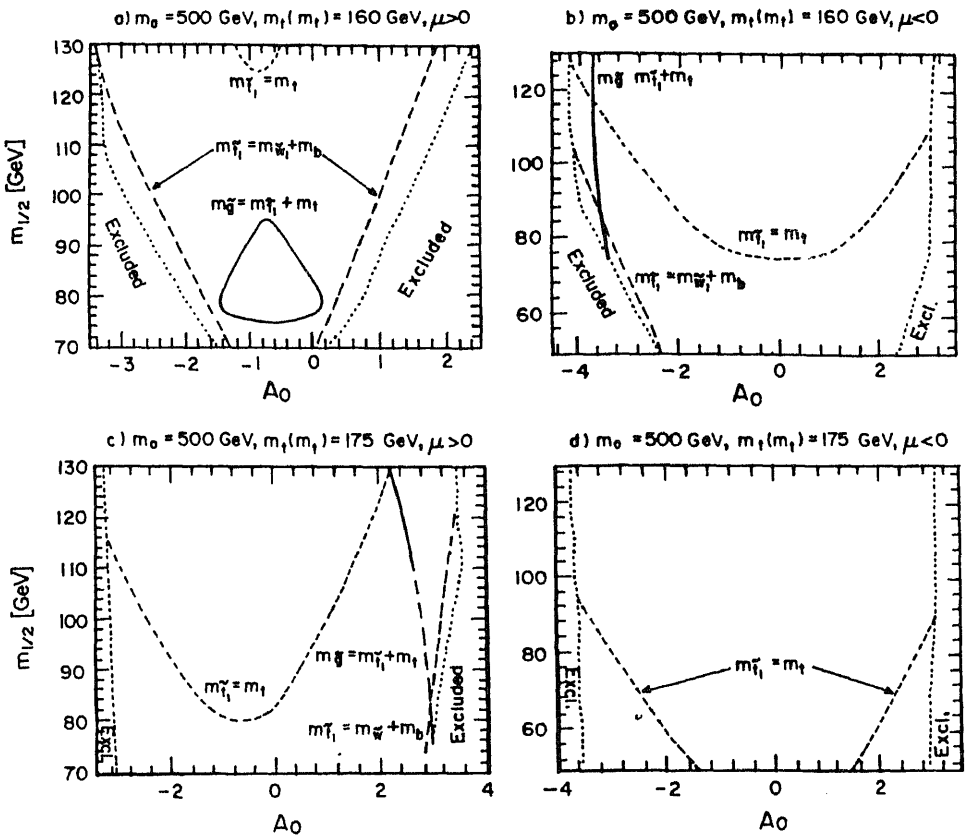

Figure 2. Regions in the $(A_0, m_{1/2})$ plane leading to different gluino and stop decays.

In fig. 2a, $\tilde{g} \to \tilde{t}_1 + t$ decays are allowed everywhere except within the small triangular region delineated by the solid line. There are also substantial regions where $\tilde{t}_1 \to \widetilde{W}_1 + b$ is not possible, and $m_{\tilde{t}_1} < m_t$ almost everywhere except for the small region enclosed by the the short dashed curve. Changing the sign of μ (fig. 2b) or increasing $m_t(m_t)$ to 175 GeV (fig. 2c) changes the situation quite drastically, however. The region where $\tilde{g} \to \tilde{t}_1 + t$ is allowed is now confined to the narrow strips between the solid and dotted lines, and $m_{\tilde{t}_1} < m_{\widetilde{W}_1} + m_b$ only in the even narrower strips between the long dashed and dotted lines. In contrast, the region where $m_{\tilde{t}_1} > m_t$ (above the short dashed lines) is now quite large. Finally, if m_t is close to its upper bound and $\mu < 0$, fig. 2d, the gluino can never decay into $\tilde{t}_1 + t$, and $\tilde{t}_1$ always decays into $\widetilde{W}_1 + b$; moreover, now $m_{\tilde{t}_1} > m_t$ over most of the allowd part of the $(A_0, m_{1/2})$ plane.

Since $\tilde{t}_1$ and the gluino are by far the lightest strongly interacting sparticles in our model, SUSY signals at the LHC (or other hadron colliders) will obviously depend quite sensitively on which of the regions depicted in figs. 2 is picked. This is the subject of the next section, where these signals are discussed in more detail.

4. Signals at the LHC

In this section I discuss the specific signatures produced by the kind of spectrum described in the previous section. The signatures at e^+e^- colliders are rather straightforward: A light chargino (below 105 GeV), a rather light neutral scalar Higgs boson (below 110 GeV), and a light $\tilde{t}_1$ (below ~ 300 GeV), all of which can be detected in a straightforward way [50]. Due to numerous backgrounds the situation at hadron colliders is much more complicated. Moreover, at these machines the largest signals come from the production of strongly interacting sparticles. Since these are usually heavier than many other sparticles they tend to decay via lengthy cascades [13]. While this makes signals more difficult to analyze, it also offers the opportunity to determine various branching ratios, which greatly helps to distinguish between different SUSY scenarios.

Here I summarize the results of ref.[19], where a full Monte Carlo study of signals and backgrounds was performed, using the latest version of ISAJET which contains the ISASUSY program package to compute sparticle masses and decay branching ratios. The program includes initial and final state showering, fragmentation, and crude detector modelling, where we took present designs of LHC detectors as guidelines; see ref.[51] for more details on this program package.

A simulation of this type consumes a substantial amount of CPU time [52]. We therefore limited ourselves to the study of six spectra that can occur within SUGRA $SU(5)$, see table 1. We saw already in the previous section that over a substantial region of parameter space the gluino can decay into $t + \tilde{t}_1$. The two 'A' spectra were picked from that region, with A1 being an example where $\tilde{t}_1 \to \widetilde{W}_1 + b$ while in case A2 the light stop decays into charm plus LSP. In the remaining four 'B' cases the gluino has no two–body decay modes; here we picked points where m_0 and $m_{1/2}$ are minimal or maximal: $(m_0,\ m_{1/2}) = (0.3$ TeV, 60 GeV) (B1); (1 TeV, 70 GeV) (B2); (0.4 TeV, 130 GeV) (B3); and (1 TeV, 130 GeV) (B4). These six spectra show all the features discussed earlier: Light $\tilde{Z}_1$, $\tilde{Z}_2$, $\widetilde{W}_1$, h^0 and $\tilde{g}$; quite heavy squarks and sleptons, except for $\tilde{t}_1$, with $\tilde{b}_1$ significantly below first

Table 1. Parameters and masses for six SUGRA cases A1, A2 and B1–B4.

parameter	A1	A2	B1	B2	B3	B4
m_0	500	500	300	1000	400	1000
$m_{1/2}$	120	130	60	70	130	130
A_0/m_0	0.6	3.75	0.1	0.0	0.0	0.0
$\tan\beta$	1.49	2.2	1.94	1.32	2.22	2.11
μ	697.1	580	-313.3	-1571.7	430	964.7
m_t	160	175	170	155	175	175
$m_{\tilde{g}}$	346	371	185	231	364	400
$m_{\tilde{q}}$	568	578	328	1011	496	1039
$m_{\tilde{t}_1}$	131	83.6	198	121	225	288
$m_{\tilde{t}_2}$	521	500	304	781	470	799
$m_{\tilde{b}_L}$	437	426	250	732	396	765
$m_{\tilde{l}}$	508	501	305	1001	412	1005
$m_{\widetilde{Z}_1}$	43.6	48.0	27.1	28.8	46.1	50.7
$m_{\widetilde{Z}_2}$	85.1	93.5	63.5	59.8	89.3	99.9
$m_{\widetilde{Z}_3}$	698	582	316	1572	432	966
$m_{\widetilde{Z}_4}$	710	595	333	1577	450	973
$m_{\widetilde{W}_1}$	84.5	92.9	62.2	59.7	87.9	99.6
$m_{\widetilde{W}_2}$	707	593	331	1576	448	972
m_{h^0}	85.2	99.7	61.6	86.0	91.3	101
m_{H^0}	1038	841	492	2339	652	1543
m_P	1038	842	487	2342	649	1542
$m_{H^\pm}$	1040	845	492	2343	653	1544

generation squarks; heavy $\tilde{Z}_3$, $\tilde{Z}_4$ and $\widetilde{W}_2$; and very heavy Higgs bosons P, H^0 and $H^{\pm}$.

In order to see how mSUGRA signals differ from the signals of "conventional SUSY" models of the type considered in ref.[13], we also studied four cases (labelled BTW1 through BTW4) where all squarks and sleptons are assumed to be degenerate. In all 'BTW' cases we took $m_{\tilde{g}} = 300$ GeV, and picked $(m_{\tilde{q}}, \mu) = (320$ GeV, −150 GeV) (BTW1); (600 GeV, −150 GeV) (BTW2); (320 GeV, −500 GeV) (BTW3); and (600 GeV, −500 GeV) (BTW4) [53].

In table 2 SUSY event fractions as well as important sparticle decay branching ratios are listed. In the 'A' cases with very light $\tilde{t}_1$, more than half of all SUSY events are $\tilde{t}_1\tilde{t}_1^*$ pairs, while in the four 'B' cases, gluino pairs constitute the most copiously produced supersymmetric final state. Pairs of electroweak gauginos are produced only in a few percent or even few permille of all SUSY events; their detection therefore necessitates a dedicated search [54], as opposed to the "generic SUSY search" presented here.

Many of the branching ratios shown in table 2 can be understood directly from the sparticle masses listed in table 1, keeping in mind that two–body final states will always overwhelm three–body final states if both are accessible at tree level. A few features are worth pointing out, however. For example, in cases B1, B2 the $\tilde{Z}_1 b\bar{b}_L$ coupling is "accidentally" suppressed. The branching ratio for $\tilde{g} \to \tilde{Z}_1 b\bar{b}$ is therefore dominated by $\tilde{b}_R$ exchange, whose mass is not reduced compared to first generation squark masses; therefore $\tilde{g} \to \tilde{Z}_1 b\bar{b}$ is not enhanced significantly over $\tilde{g} \to \tilde{Z}_1 d\bar{d}$ in these cases. Nevertheless $\tilde{Z}_2 \to \tilde{Z}_1 b\bar{b}$ is enhanced considerably over $\tilde{Z}_2 d\bar{d}$. The reason is that virtual h^0 exchange diagrams, which contribute much more strongly to $b\bar{b}$ final states, are not negligible here. This can be understood from the observation that h^0 exchange is only suppressed [39] by one power of the small higgsino component of $\tilde{Z}_2$ or $\tilde{Z}_1$, while Z exchange needs [1] two such powers, and $\tilde{f}$ exchange is suppressed by the large sfermion masses.

h^0 exchange contributes negligibly to $\tilde{Z}_2 \to \tilde{Z}_1 e^+ e^-$ decays, so it reduces the corresponding branching ratio [55]. The leptonic branching ratio of $\tilde{Z}_2$ can nevertheless exceed considerably that of the Z boson, even if (most) squarks and sleptons have almost the same mass, as is the case here; this is largely due to interference between Z and sfermion exchange diagrams, which can however also result in very small leptonic branching ratios for $\tilde{Z}_2$, see cases B3 and B4. In contrast, the branching ratios of the light chargino very closely track that of the W bosons, since the $\widetilde{W}_1 \tilde{Z}_1 W$ couplings get contributions from both the higgsino and $SU(2)$ gaugino components of $\widetilde{W}_1$ and $\tilde{Z}_1$, and are therefore much less suppressed than the $\tilde{Z}_2 \tilde{Z}_1 Z$ coupling. The only exception occurs in case A2, where the two–body decay $\widetilde{W}_1 \to \tilde{t}_1 + b$ is allowed and hence completely dominates all $\widetilde{W}_1$ decays.

It is by now quite well known that, in addition to the "classical" missing E_T+jets signature, sparticle production at hadron colliders can also give rise to final states containing hard leptons [13, 56]. In the present study a hard lepton is defined as an electron or muon with $p_T > 20$ GeV, pseudorapidity $|\eta| < 2.5$, and visible (hadronic or electromagnetic) activity in a cone $\Delta R = 0.3$ around the lepton less than 5 GeV. Hadronic clusters with $E_T > 50$ GeV in a cone $\Delta R = 0.7$ are labelled as jets. We can then define various mutually exclusive event classes:

- "Missing E_T" events have no hard leptons, $n_j \geq 4$ jets, missing $E_T > 150$

Table 2. (a) Fractions of SUSY particle pairs produced in pp collisions at the LHC; and (b) branching fractions of selected decay modes, for six SUGRA cases A1, A2 and B1–B4, where $\tilde{q}$ stands for all squarks except stops, and $\widetilde{\chi}\widetilde{\chi}$ stands for all possible chargino and neutralino pairs.

SUSY particles\ Case	A1	A2	B1	B2	B3	B4
(a) Sparticle Pairs Produced						
$\tilde{g}\tilde{g}$	0.30	0.093	0.72	0.74	0.44	0.73
$\tilde{t}_1\tilde{t}_1*$	0.51	0.84	0.011	0.21	0.10	0.083
$\tilde{g}\tilde{q}$	0.13	0.050	0.23	0.013	0.33	0.081
$\tilde{q}\tilde{q}$	0.018	0.007	0.029	3×10^{-4}	0.067	0.005
$\widetilde{W}_1^{\pm}\widetilde{Z}_2$	0.018	0.006	0.004	0.019	0.027	0.066
$\widetilde{\chi}\widetilde{\chi}$	0.026	0.009	0.007	0.027	0.042	0.088
(b) Important Decay Modes						
$\tilde{g} \to \tilde{t}_1\bar{t}, \bar{\tilde{t}}_1 t$	1.0	1.0	-	-	-	-
$\tilde{g} \to \widetilde{W}_1^- t\bar{b}, \widetilde{W}_1^+ b\bar{t}$	1.6×10^{-4}	1.4×10^{-4}	-	0.091	0.12	0.25
$\tilde{g} \to \widetilde{W}_1^- u\bar{d}, \widetilde{W}_1^+ d\bar{u}$	4.6×10^{-4}	2.9×10^{-4}	0.21	0.10	0.19	0.16
$\tilde{g} \to \widetilde{Z}_1 d\bar{d}$	3.1×10^{-5}	1.9×10^{-5}	0.012	0.005	0.014	0.01
$\tilde{g} \to \widetilde{Z}_1 b\bar{b}$	6.8×10^{-5}	5.4×10^{-5}	0.012	0.006	0.035	0.018
$\tilde{g} \to \widetilde{Z}_2 b\bar{b}$	4.3×10^{-4}	3.9×10^{-4}	0.21	0.10	0.18	0.15
$\tilde{t}_1 \to \widetilde{W}_1^+ b$	1.0	-	0.95	1.0	0.93	0.29
$\tilde{t}_1 \to \widetilde{Z}_1 t$	-	-	0.05	-	0.07	0.64
$\tilde{t}_1 \to \widetilde{Z}_2 t$	-	-	-	-	-	0.07
$\tilde{t}_1 \to \widetilde{Z}_1 c$	-	1.0	-	-	-	-
$\widetilde{Z}_2 \to \widetilde{Z}_1 d\bar{d}$	0.11	0.18	0.024	0.028	0.21	0.17
$\widetilde{Z}_2 \to \widetilde{Z}_1 b\bar{b}$	0.37	0.39	0.057	0.22	0.38	0.42
$\widetilde{Z}_2 \to \widetilde{Z}_1 e^+e^-$	0.047	0.018	0.14	0.12	0.007	0.012
$\widetilde{W}_1^+ \to \widetilde{Z}_1 e^+\nu_e$	0.11	6.9×10^{-5}	0.11	0.11	0.11	0.11

GeV. If $n = 1$, we in addition required the scalar E_T to exceed 700 GeV, and demanded that the transverse mass computed from the missing p_T and the leptonic p_T does *not* fall in the interval between 60 and 100 GeV, where the background from real W decay has a Jacobian peak. For $n = 2$ we distinguish opposite sign (OS) and same sign (SS) events, and required total $E_T > 700$ GeV in the OS sample in order to suppress $t\bar{t}$ backgrounds.

Cross sections after cuts for these final states are listed in table 3, for the six mSUGRA cases, 4 'BTW' cases and leading sources of background, i.e. $t\bar{t}$, W+jets and Z+jets events. (We checked that backgrounds from W^+W^-, $c\bar{c}$ and $b\bar{b}$ production are always very small.) The table extends out to $n = 4$ leptons, but the results for $n = 4$ already suffer from substantial statistical errors (we generated 50,000 events for each SUSY spectrum, and several hundred thousand background events). We observe that the missing E_T, SS and (except in case A2) $3l$ signals are all well above background; the $1l$ and OS signals are also always larger than, or at least similar to, backgrounds [57].

The size of the missing E_T cross section is mostly determined by the gluino mass; direct $\tilde{t}_1\tilde{t}_1^*$ production contributes little to the signal after cuts even in case A2, mostly because we demand at least 4 jets here. However, due to the potentially sizable contribution from $\tilde{g}\tilde{q}$ production shown in table 2, the masses of first generation squarks also play a role. Moreover, even this relatively robust signal can change by a factor of more than 2 depending on gluino branching ratios: Even though case A2 has a slightly heavier gluino than case A1, and hence an almost 50% smaller gluino pair cross section, it produces a two times stronger missing E_T signal than case A1 does. The reason is that $\tilde{t}_1 \to \tilde{Z}_1 + c$ decays give much harder LSPs than $\tilde{t}_1 \to \widetilde{W}_1 + b \to \tilde{Z}_1 + q\bar{q}' + b$ decays do. Similarly, the missing E_T signal in case B2 is almost as strong as in case B1, inspite of the more than three times smaller sum of $\tilde{g}\tilde{g}$ and $\tilde{g}\tilde{q}$ cross sections. This is mostly due to a large (22%) branching ratio for $\tilde{g} \to \tilde{Z}_1 + g$ loop decays. ($\tilde{g} \to \tilde{Z}_2 + g$ decays also have a branching ratio of about 22%, and about 20% of all $\tilde{Z}_2$ decay invisbly into $\tilde{Z}_1\nu\bar{\nu}$ in this case.) These $\tilde{Z}_1$ produced in $\tilde{g}$ two–body decays are very energetic, much more so than the LSPs produced at the end of a cascade. The branching ratios for these loop decays of the gluino are enhanced in case B2 because ordinary squarks are very heavy, while $\tilde{t}_1$ (which contributes to loops) is quite light.

The size of the $1l$ signal is generally roughly comparable to that of the missing E_T signal, but backgrounds are about three times larger here. Real top quarks are very efficient in producing hard leptons (and missing E_T, needed to pass the cut $\not{E}_T > 100$ GeV); in case A1 the $1l$ signal is therefore actually larger than the missing E_T signal. Notice also that the effect of increasing m_0 to 1 TeV is now about the same for cases B1/B2 and B3/B4, reducing the signal by approximately a factor of two. Many "1l" events in cases B1, B2 actually come from $\tilde{Z}_2 \to \tilde{Z}_1 l^+ l^-$ decays where one of the leptons failed to pass the cuts. The large leptonic branching ratio of $\tilde{Z}_2$ in these cases also leads to quite large OS $2l$ signals, large OS/SS ratios, and sizable $3l$ signals. Case A1 also has substantial OS and $3l$ signals, but the OS/SS

Table 3. Cross sections in *pb* for various event topologies after cuts described in the text, for pp collisions at $\sqrt{s} = 14$ TeV. The various SUGRA cases are listed in the first column. The OS/SS ratio is computed with the OS dilepton sample *before* the scalar E_T cut.

case	$\not{E}_T$	$1\,\ell$	OS	SS	OS/SS	$3\,\ell$	$4\,\ell$
A1	24.6	36.2	5.4	3.7	2.0	1.2	0.017
A2	48.0	31.4	1.5	2.1	1.2	< 0.02	< 0.02
B1	79.1	76.8	11.9	3.4	6.9	1.7	0.17
B2	67.7	37.5	9.0	2.4	7.7	0.8	0.1
B3	51.8	21.2	1.4	0.6	3.3	0.09	< 0.01
B4	20.1	10.1	1.1	0.4	3.5	0.1	< 0.004
BTW1	105	39.8	2.8	1.4	3.1	0.21	0.03
BTW2	57.3	22.5	2.2	0.85	3.6	0.14	< 0.02
BTW3	96	58	10.9	2.9	6.7	1.5	0.06
BTW4	52.3	23.9	2.3	0.9	3.7	0.2	< 0.02
$t\bar{t}(160)$	2.9	8.0	1.1	0.01	640	< 0.004	< 0.004
$W + jet$	0.6	3.8	0.29	–		–	–
$Z + jet$	0.6	0.2	0.02	–		–	–
total BG	4.3	12.02	1.411	0.01		< 0.004	< 0.004

ratio is much smaller here, since $\tilde{g}\tilde{g}$ events produce tt and $\bar{t}\bar{t}$ final states with equal abundance as $t\bar{t}$ final states. Case A2 has very few $n \geq 3$ lepton events, since basically all gluinos decay into $t + \bar{c} + \tilde{Z}_1$ (or the charge conjugate thereof) here, giving at most one hard lepton per gluino. Cases B3 and B4 give smaller leptonic signals, due to the larger gluino mass; they differ from each other by a factor of two in the missing E_T and (marginal) $1l$ signals, but become more similar to each other as more leptons are required, mostly due to the sizable $\tilde{g} \to \widetilde{W}_1 tb$ branching ratio in case B4.

Finally, the "conventional" BTW cases can produce even larger missing E_T signals than our mSUGRA cases, since we allowed squarks to lie just above gluinos here, leading to large $\tilde{g}\tilde{q}$ production rates. Case BTW3 also has a large leptonic branching ratio of $\tilde{Z}_2$ (12.5% per generation), and hence large cross sections for the n lepton final states; for the other BTW cases the leptonic branching ratio of $\tilde{Z}_2$ is close to that of the Z boson.

This discussion shows that the counting rates in the six or seven independent signal channels listed in table 3 already go a long way towards distinguishing the various mSUGRA cases from each other as well as from the 'BTW' cases. Some ambiguities remain, however; for example, cases B1 and BTW3 are are very similar at this level (except perhaps in the $4l$ signal, but statistics is poor here). The remaining ambiguity can be resolved by looking at the events within one signal class in more detail. An example is shown in table 4, where event fractions for the missing E_T sample are shown, together with the average total scalar E_T and average missing E_T per event.

The most useful discriminators appear to be the fractions of events with at least

Table 4. Cross sections and event fractions for missing energy plus jets events for various SUSY cases at the LHC.

case	$\sigma(pb)$	$n_j = 4-5$	$6-7$	≥ 8	$n_b \geq 1$	$n_b \geq 2$	$\langle \Sigma E_T \rangle$	$\langle \not{E}_T \rangle$
A1	24.6	0.54	0.35	0.10	0.65	0.28	1160	212
A2	48.0	0.55	0.35	0.10	0.47	0.09	1112	221
B1	79.1	0.73	0.25	0.02	0.21	0.04	964	195
B2	67.7	0.77	0.20	0.03	0.23	0.05	999	211
B3	51.8	0.57	0.35	0.08	0.36	0.12	1118	215
B4	20.1	0.54	0.36	0.10	0.44	0.15	1204	217
BTW1	105	0.69	0.26	0.04	0.17	0.04	1006	214
BTW2	57.3	0.61	0.33	0.05	0.18	0.04	1091	211
BTW3	96	0.69	0.27	0.04	0.15	0.03	1011	217
BTW4	52.3	0.60	0.33	0.06	0.18	0.04	1109	208
$t\bar{t}(160)$	2.9	0.81	0.17	0.01	0.56	0.12	895	201
$Z + jets$	0.63	0.89	0.11	0.0	0.11	0.02	905	281

one or two tagged b quarks. Here we have assumed a b tagging efficiency of 40% if the b–flavoured hadron has $p_T > 20$ GeV and pseudorapidity $|\eta| < 2$, and zero efficiency otherwise; we have ignored the possibility of false tags. The spectra where $\tilde{g} \to \tilde{t}_1 + t$ is allowed clearly lead to the largest b content; the difference between $\tilde{t}_1 \to \widetilde{W}_1 + b$ (A1) and $\tilde{t}_1 \to \tilde{Z}_1 + c$ (A2) decays is also evident, especially in the fraction of events with at least two tagged b's. Cases B3 and B4 still have fairly large b content, partly due to $\tilde{g} \to \widetilde{W}_1 tb$ decays which can produce up to four b quarks in a gluino pair event; enhanced $\tilde{g} \to \tilde{Z}_2 + b\bar{b}$ and $\tilde{Z}_2 \to \tilde{Z}_1 + b\bar{b}$ branching ratios also play a role, see table 2. Finally, in the light gluino scenarios B1, B2 the b–fraction is considerably smaller than in the cases where gluinos can decay into top quarks; the enhanced branching ratios into final states containing $b\bar{b}$ still lead to b–fractions that exceed those of the BTW cases, however.

The presence of t quarks in gluino decays also leads to large average jet multiplicities: 10% of all events in cases A1, A2 and B4 have at least 8 reconstructed jets in them (recall that we require each jet of have $p_T > 50$ GeV). Moreover, the comparison of BTW2,4 with BTW1,3 shows that the presence of first generation squarks significantly, but not infinitely, heavier than the gluino increases the average number of jets and the average scalar E_T per event; this is due to $\tilde{g}\tilde{q}$ production, of course. This effect is less pronounced when comparing B4 to B3, or B2 to B1, since in cases B4 and B2 first generation squarks are so heavy that they contribute little to the total SUSY signal; see table 2. The average missing E_T seems to be a less useful discriminator, clustering around 210 to 220 GeV in almost all cases. The only exception is case B1, which has a very light gluino; in case B2, where the gluino is also light, the missing E_T is enhanced by the large branching ratios for loop–induced $\tilde{g} \to \tilde{Z}_{1,2} + g$ decays discussed earlier.

Similar tables can be shown for the other samples of signal events [19]; for reasons of space I here merely summarize the most important points. The results

jet multiplicities are very similar for all samples, except that a larger number of tons implies an overall reduction of the number of jets [58]. The b–content of nts in the $1l$ sample are similar to those in the missing E_T sample, with a slight ıancement in case B1 and slight reductions in the BTW cases which increases differences between these scenarios.

In the mSUGRA cases B1–B4 the b fraction is considerably larger in the OS nple than in the missing E_T or $1l$ samples. This effect is especially pronounced cases B3 and B4, where $\tilde{g} \to \widetilde{W}_1 tb$ decays are good sources of both hard leptons d b quarks; indeed, in these two cases the b fraction exceeds that in case A2 in the dilepton sample. The correlation between the number of b's and the number of tons in cases B1 and B2 is due to the fact that here most leptons come from $\tilde{Z}_2$ ays, and $\tilde{g} \to \tilde{Z}_2$ decays frequently lead to a $b\bar{b}$ final state; the enhancement of final states is much weaker in $\tilde{g} \to \tilde{Z}_1$ decays, as shown in table 1, while $\tilde{g} \to \widetilde{W}_1$ ays cannot contain b quarks in these cases.

The contribution from $\tilde{Z}_2 \to \tilde{Z}_1 l^+ l^-$ decays to the OS signal can also be tested looking at the flavour of the produced leptons: $\tilde{Z}_2$ decays always produce e^+e^- or μ^- pairs, while OS events that originate from (semi–)leptonic decays of charginos t quarks are equally likely to contain an $e\mu$ pair. Indeed, one finds a strong ponderance of like–flavour pairs in cases B1 and B2 as well as in all BTW cases, ile all combinations of lepton flavours occur with equal frequency in cases A1 and where $\tilde{Z}_2$ is hardly ever produced; in cases B3 and B4 there is a smaller but still nificant preference for like–flavour lepton pairs. The invariant mass distribution the two charged leptons in like–flavour opposite–charge dilepton events should ow to determine the $\tilde{Z}_2 - \tilde{Z}_1$ mass difference, which in our mSUGRA scenario is proximately given by $0.4m_{1/2}$. Unfortunately, other (combinations of) sparticle sses are much more difficult to determine at hadron colliders.

Summary and conclusions

this contribution I have described the phenomenology of the minimal SUGRA (5) model. The underlying theme of this model is unification. First of all, the y existence of a GUT sector implies that the Higgs sector of the SM is ill–behaved the quantum level unless SUSY exists at an energy scale not much above the ak scale. Moreover, we now know that the particle content of the SM by itself es not allow for unification of all gauge interactions; new degrees of freedom are eded, and minimal SUSY just fits the bill.

Secondly, in this model one can also successfully unify the b and τ Yukawa ıplings, provided that the top Yukawa coupling is large, i.e. close to its IR ıasi) fixed point. The idea of unification can even be extended into the SUSY eaking sector by assuming a single gaugino mass as well as a single scalar mass. is leads to the very elegant mechanism of radiative breaking of the electroweak ıge symmetry, which hints towards explanations for the large mass of the top ark and the large hierarchy between M_X and M_Z.

In this scenario constraints from proton decay, and from the relic density of Ps produced in the Big Bang, imply that gauginos must be quite light, while ost sfermions and Higgs bosons are heavy. Light charginos, and the light scalar ggs boson predicted by this model, are quite easily detectable at e^+e^- colliders

below $\sim$ 105 GeV or no gluino with mass below $\sim$ 400 GeV is found mSUGRA $SU(5)$ has to be discarded, but their discovery can hardly be considered proof of this model. However, it also predicts that left–handed $\tilde{b}$ squarks and, much more dramatically, the lighter $\tilde{t}$ eigenstate lie well below the other squarks. Indeed, $\tilde{t}_1$ might even be produced in $\tilde{g}$ decays, giving events with several b–quarks. Even if this decay is not possible the reduced masses of $\tilde{t}_1$ and $\tilde{b}_L$ give enhanced branching ratios for $\tilde{g} \to \widetilde{W}_1 tb$ and $\tilde{g} \to \tilde{Z}_{1,2} b\bar{b}$ three–body decays and hence again an enhaced b–quark content of SUSY events at the LHC; in this case the enhancement is usually less, and increases with the number of hard leptons in the event. Notice that the event rates are so large that a "low" luminosity of a few times 10^{32} cm^{-2}sec^{-1} is quite sufficient, which should allow for b–tagging at least in principle. Further clues to the nature of the spectrum can come, e.g., from the average jet mulitplicity per event and from the flavour composition of opposite–sign dilepton events.

It should be emphasized that in this model a SUSY signal should be seen at the LHC in at least three, and possibly as many as seven independent channels, where only the number and charge of hard leptons has been used to classify events. This clearly offers great opportunities for the LHC. Nevertheless the LHC by itself will not suffice to find all the new particles predicted by this model: The heavy Higgs bosons, higgsinos and sleptons are in my opinion impossible to detect at the LHC. Finding first generation squarks on top of the "background" of light gluinos will also be difficult, especially if they are close to the TeV scale in mass. More surprisingly, even the direct pair production of light $\tilde{t}_1$ squarks seems difficult to detect. If we are lucky light stops might be detected at the tevatron [59]. However, if this model is correct the completion of the sparticle and Higgs spectrum will most likely have to await the construction of a TeV scale e^+e^- collider. Finally, one would eventually want to see direct evidence for the existence of GUT particles, the best hope probably being proton decay experiments. The model presented here would therefore keep particle physicists busy for some decades to come.

Acknowledgements

I thank my collaborators Howie Baer, Chung Kao, Mihoko Nojiri and Xerxes Tata, who did all the work while I got to swim in the Indian ocean. I also thank the workshop organizers for their kind invitation, which helped me to complete some biochemical research as well. This work was supported in part by the U.S. Department of Energy under contract No. DE-AC02-76ER00881, by the Wisconsin Research Committee with funds granted by the Wisconsin Alumni Research Foundation, as well as by a grant from the Deutsche Forschungsgemeinschaft under the Heisenberg program.

References

[1] For reviews of SUSY, see e.g. H.E. Haber and G.L. Kane, Phys Rep. **117**, 75 (1985); X. Tata, in *The Standard Model and Beyond*, p.304, ed. J.E. Kim (World Scientific, Singapore, 1991).

[2] E. Witten, Nucl. Phys. **B188**, 513 (1981).

[3] For a review of TC, see E. Farhi and L. Susskind, Phys. Rep. **74**, 277 (1981).

D46, 381 (1992); G. Bhattacharyya, S. Banerjee and P. Roy, Phys. Rev. **D45**, 729 (1992); erratum: **D46**, 3215 (1992).

] For example, R.S. Chivukula, E. Gates, E.H. Simmons and J. Terning, Phys. Lett. **B311**, 157 (1993).

] For example, R. Barbieri, M. Frigeni and F. Caravaglios, Phys. Lett. **B279**, 169 (1992); M. Boulware and D. Finell, Phys. Rev. **D44**, 2054 (1991).

] U. Amaldi, W. de Boer and H. Fürstenau, Phys. Lett. **260B**, 447 (1991); J. Ellis, S. Kelley and D.V. Nanopoulos, Phys. Lett. **B260**, 447 (1991); P. Langacker and M. Luo, Phys. Rev. **D44**, 817 (1991).

] "Predictive" here means that grand unification can be achieved for experimentally acceptable values of the gauge coupling constants *without* having to resort to the ad–hoc introduction of new fields with masses anywhere between the weak and the GUT scale. Of course, SUSY does predict the existence of many new (s)particles, but this is an inescapable consequence of the assumed symmetry.

] For example, U. Amaldi et al., Phys. Rev. **D36**, 1385 (1987).

] L. Girardello and M.T. Grisaru, Nucl. Phys. **B194**, 65 (1982).

] M. Green, J. Schwarz and E. Witten, *Superstrings* (Oxford Univ. Press, 1987).

] That should not be held against SUSY per se. Remember that another prominent nonperturbative problem of modern field theory, the confinement problem of QCD, has still not been solved, even though it only involves fields with known mass and known interactions, and even though a wealth of experimental data exists.

] H.A. Baer, X.R. Tata and J. Woodside, Phys. Rev. **D45**, 142 (1992).

] For reviews, see H.P. Nilles, Phys. Rep. 110, 1 (1984); P. Nath, R. Arnowitt and A. Chamseddine, *Applied N=1 Supergravity*, ITCP Series in Theoretical Physics (World Scientific, Singapore, 1984), Vol. 1.

] D0 collab., S. Abachi et al., FERMILAB–PUB–94–004–E; CDF collab., F. Abe et al., FERMILAB–PUB–94–097–E, and FERMILAB–PUB–94–116–E.

] L.E. Ibàñez and G.G. Ross, in *Perspectives on Higgs Physics*, p. 229, G.L. Kane, editor; W. de Boer, Univ. Karlsruhe preprint IEKP–KA–93–8 (hep–ph 9402266), and references therein.

] Some aspects of this model have recently been discussed in R. Arnowitt and P. Nath, Phys. Lett. **B299**, 58 (1993) and erratum, **B307**, 403 (1993); Phys. Rev. **D49**, 1479 (1994); J.L. Lopez, D.V. Nanopoulos and A. Zichichi, CERN–TH–7136–94. These papers also contain references to earlier work.

] For example, the simplest TC model has been ruled out many times.

] H.A. Baer, M. Drees, C. Kao, M.M. Nojiri and X.R. Tata, Madison preprint MAD/PH/825 (1994), to appear in Phys. Rev. **D**.

] From supergravity or superstring theories one might expect such a spectrum to emerge from an effective theory at scales below the Planck scale ($M_P = 2.4 \cdot 10^{18}$ GeV) or perhaps the string compactification scale ($M_c \simeq 5 \cdot 10^{17}$ GeV). Here I will assume that this ansatz is still valid at the GUT scale $M_X \simeq 2 \cdot 10^{16}$ GeV; in the scenario presented here the running of parameters from M_P or M_c down to M_X is not expected to play a major role.

] Strictly speaking, any nonzero h_t will give a finite region of input parameter space where radiative gauge symmetry breaking can be achieved. However, this region would have been small, i.e. some fine–tuning would have been needed, if h_t were much smaller than the gauge couplings. Radiative symmetry breaking is therefore more natural for heavy top.

(1982) and **71**, 413 (1984).

[23] Eq.(3) is valid if the tree–level Higgs potential is used with running parameters to include radiative correctios $\propto \log(M_X/Q_0)$. However, it is always possible to chose the scale Q_0 where the RG running is terminated such that corrections to eq.(3) are small even when the full 1–loop Higgs potential is used [24, 25], which is almost independent of Q_0. The same choice of Q_0 also minimizes corrections to the mass of the pseudoscalar Higgs boson.

[24] G. Gamberini, G. Ridolfi and F. Zwirner, Nucl. Phys. **B331**, 331 (1990).

[25] M. Drees and M.M. Nojiri, Phys. Rev. **D45**, 2482 (1992).

[26] V. Barger, M.S. Berger, P. Ohmann and R.J.N. Phillips, Phys. Lett. **B314**, 351 (1993); M. Carena, S. Pokorski and C. Wagner, Nucl. Phys. **B406**, 59 (1993); P. Langacker and N. Polonsky, Phys. Rev. **D49**, 1454 (1994).

[27] This conclusion remains valid if h_b/h_τ is allowed to vary by $\sim 10\%$ from unity due to threshold effects or "Planck slop".

[28] A.E. Nelson and L. Randall, Phys. Lett. **B316**, 516 (1993).

[29] B. Pietrzyk for the LEP collaborations, talk presented at the *XXIX Rencontres de Morion*, Meribel, Savoie, France, March 1994.

[30] R. Arnowitt and P. Nath, Phys. Rev. Lett. **69**, 725 (1992); J. Hisano, H. Murayama and T. Yanagida, Nucl. Phys. **B402**, 46 (1993); and references therein.

[31] Strictly speaking the Higgs sector of minimal $SU(5)$ is not realistic, since it leads to wrong predictions for the masses of SM fermions of the first two generations. Adding new Higgs fields and/or non–renormalizable interactions to solve this problem can in general also change predictions for τ_p. However, refs.[30] already use the physical quark masses as input. Furthermore, the constraint (8) is really rather lenient; it can therefore be expected to hold even in slightly extended models.

[32] For example, K. Griest, M. Kamionkowski and M. Turner, Phys. Rev. **D41**, 3565 (1990); K. Olive and M. Srednicki, Nucl. Phys. **B355**, 208 (1991); L. Roszkowski, Phys. Lett. **B278**, 147 (1992); M. Drees and M.M. Nojiri, Phys. Rev. **D47**, 376 (1993).

[33] P. Nath and R. Arnowitt, Phys. Rev. Lett. **70**, 3696 (1993); J.L. Lopez, D.V. Nanopoulos and K. Yuan, Phys. Rev. **D48**, 2766 (1993).

[34] Y. Okada, M. Yamaguchi and T. Yanagida, Phys. Lett. **B262**, 54 (1991), and Prog. Theor. Phys. **85**, 1 (1991); H.E. Haber and R. Hempfling, Phys. Rev. Lett. **66**, 1815 (1991); J. Ellis, G. Ridolfi and F. Zwirner, Phys. Lett. **B257**, 83 (1991), and **B262**, 477 (1991).

[35] ALEPH collab., D. Buskulic et al., Phys. Lett. **B313**, 312 (1993).

[36] M. Carena, M. Olechowski, S. Pokorski and C.E.M. Wagner, Nucl. Phys. **B419**, 213 (1994).

[37] V. Barger, M.S. Berger and P. Ohmann, Phys. Rev. **D49**, 4908 (1994).

[38] Eqs.(10) are valid also away from the IR fixed point of h_t. They differ from the analytical expressions given in ref.[36] partly because in that paper $Q_0 = M_Z$ has been assumed, which is not appropriate [24, 25] for the heavy scalar spectrum implied by the condition (8). (All numerical results in ref.[36] use the 1–loop corrected potential, and hence do not depend significantly on the choice of Q_0.) Since most parameters run much more quickly just above Q_0 than just below M_X changing Q_0 by a factor 4 is not completely irrelevant. Notice also that ref.[36] uses the opposite sign convention for A.

[39] J.F. Gunion and H.E. Haber, Nucl. Phys. **B272**, 1 (1986).

[40] While by construction the invisible decay of h^0 into two LSPs is always allowed in this model, the corresponding branching ratio is very small, being proportional to the square of the small higgsino component of the LSP.

[41] F. del Aguila and L. Ametller, Phys. Lett. **B261**, 326 (1991); H.A. Baer, C.-H. Chen, F. Paige and X.R. Tata, Phys. Rev. **D49**, 3283 (1994).

[42] S.P. Martin and M.T. Vaughn, Phys. Lett. **B318**, 331 (1993); Y. Yamada, Phys. Rev. Lett. **72**, 25 (1994).

[43] M. Drees and M.M. Nojiri, Nucl. Phys. **B369**, 54 (1992).

[44] Note that eq.(5) only determines the absolute value of μ. In this paper I assume $m_{1/2} > 0$, $\tan\beta > 0$ without loss of generality; however, A, B and μ must then in general all be allowed to have either sign. The sign conventions for μ and $m_{1/2}$ used here are the same as in refs.[39, 43].

[45] J.M. Frère, D.R.T. Jones and S. Raby, Nucl. Phys. **B222**, 11 (1983); M. Claudson, L. Hall and I. Hinchliffe, Nucl. Phys. **B228**, 501 (1983).

[46] J. Ellis and S. Rudaz, Phys. Lett. **128B**, 248 (1983).

[47] The difference between running and on-shell masses is much smaller [48] for squarks than for gluinos, since squarks are color triplets (rather than octets) and no sum over flavours occurs, unlike in eq.(14).

[48] S.P. Martin, private communication.

[49] K. Hikasa and M. Kobayashi, Phys. Rev. **D36**, 724 (1987).

[50] The only possible problem could occur if $\tilde{t}_1$ is very close in mass to the LSP, which is in principle possible. The model also predicts the existence of a light $\tilde{Z}_2$, with mass very close to $m_{\widetilde{W}_1}$, but its production cross section at e^+e^- colliders is small, since it is a rather pure gaugino, so that Z exchange is suppressed by small couplings, while selectron exchange is suppressed by the large selectron mass.

[51] H.A. Baer, F. Paige, S. Protopopescu and X.R. Tata, in the *Proceedings of the Workshop at Current Accelerators and the Supercollider*, ed. J. Hewett, A. White and D. Zeppenfeld, Argonne preprint ANL-HEP-CP-93-02.

[52] A typical gluino pair event has $\mathcal{O}(1000)$ hadrons and photons in the final state.

[53] Recall that μ is assumed to be a free parameter in this "conventional" treatment. The *calculated* values of μ in the six mSUGRA cases are listed in table 1.

[54] H.A. Baer, C.-H. Chen, F. Paige and X.R. Tata, preprint FSU-HEP-940310, to appear in Phys. Rev. **D**.

[55] Note that, at least in the limit $m_b \ll m_{\tilde{Z}_2}$, h^0 exchange does not interfere with sfermion or Z exchange; it therefore always contributes positively.

[56] R.M. Barnett, J.F. Gunion and H.E. Haber, Phys. Lett. **B315**, 349 (1993), and references therein.

[57] A warning: All cross sections in table 3 are not only subject to unknown NLO QCD corrections, but also depend sensitively on the resolution and coverage of the calorimeters, since both signal and background are backed up against the missing E_T cut. Notice that the predicted missing E_T also depends on, for example, the amount of initial state radiation that is being generated. One will therefore have to understand both the detector and "ordinary" QCD events in some detail before quantitative studies of absolute rates can be undertaken with some confidence. However, the *ratios* of various cross sections, including signal/background, will hopefully be rather robust against future refinements.

[58] Recall that our definition of leptonic events does not require a minimal number of jets; this also reduces the average jet multiplicity compared to the missing E_T sample, of course.

[59] H.A. Baer, J. Sender and X.R. Tata, preprint FSU-HEP-940430, hep-ph/9404342.

PRAMANA
journal of
physics

© Printed in India

Supplement to Vol. 45
October 1995
pp. 109-111

Spontaneous CP violation and neutral B meson decays

PAUL H FRAMPTON

Institute of Field Physics, Department of Physics and Astronomy,
University of North Carolina, Chapel Hill, NC, 27599-3255, USA

Abstract. A model in which CP is spontaneously broken is described; it solves the strong CP problem and provides an additional mechanism for weak CP violation. This is the aspon model. Application to B decays leads to predictions for CP asymmetries much smaller than expected from the KM mechanism of explicit CP breaking.

In this presentation I shall cover the three topics all of which pertain to the aspon model:

1)The motivation, arising from the strong CP problem.

2)The phenomenology of CP violation, giving upper bounds on the masses.

3)Estimation of CP asymmetries in B meson decays.

Topic (3), done in collaboration with Ackley, Kayser and Leung, is the most recent work in the model so I shall emphasize it.

(1) Solution of Strong CP Problem.

In solving the strong CP problem there are three alternatives:

1) Axion

2) $m_u = 0$

3) Spontaneous (or soft) CP violation

(1) is looking less and less plausible experimentally since the allowed window is $10^{-5}eV \leq m_a \leq 10^{-3}eV$.

(2) is at odds with pseudoscalar meson masses and spontaneous chiral symmetry breaking.

The *aspon model* is an economical (minimal) version of (3).

The strong CP problem is due to the term $\Theta_{QCD}G_{\mu\nu}\tilde{G}^{\mu\nu}$ in the QCD lagrangian. The physical quantity $\bar{\Theta} = (\Theta_{QCD} + \Theta_{QFD}) \leq 2\times 10^{-10}$ for $d_n \leq 10^{-25}e.cm.$ where $\Theta_{QFD} = -argdetM$, M being the quark mass matrix.

With a CP invariant lagrangian $\Theta_{QCD} = 0$ so we must arrange that $\Theta_{QFD} \leq 2 \times 10^{-10}$.

To do this we introduce $U(1)_{new}$ which will be local (gauged). Thus the model has gauge group $SU(3)_C \times SU(2)_L \times U(1)_Y \times U(1)_{new}$. All the particles in the three family standard model are neutral under this $U(1)_{new}$. In the simplest version of the aspon model we add one doublet of vector-like quarks which carry the new charge

them.

The new quarks have gauge-invariant (heavy) Dirac masses and Yukawa couplings to the light quarks:

$$h_i^\alpha U_L^C u_L^i \chi_{alpha}; \qquad h_i^\alpha D_L^C d_L^i \chi_{alpha}. \tag{1}$$

Here $\alpha = 1, 2$ and i = 1,2,3. The superscript C implies charge conjugate. There are *no* Yukawa couplings to U_L or to D_L because of the $U(1)_{new}$ gauge invariance.

The gauge invariance under $U(1)_{new}$ forces the 4×4 quark mass matrices (both *up* and *down* sectors) to have a texture such that the determinant is real. The diagonal blocks are real because of CP conservation; let the heavy quarks have mass M. The off-diagonal terms are of the form:

$$F_i = \sum_\alpha h_i^\alpha < \chi_\alpha > \tag{2}$$

and arise from the off-diagonal Yukawa couplings listed earlier. Only one of the two off-diagonal blocks has this form, the other being zero; this is how the determinant is real.

(2) The Phenomenology of CP Violation, Giving Upper Bounds on the Masses

The Yukawa couplings h_α^i are restricted to be $<< 1$ by the limit on $\bar{\Theta}$ which is generated by one-loop corrections. In diagonalization of the quark mass matrix the relevant expansion parameter is $x_i = F_i/M$ ($i = 1, 2, 3$ for the three families). In the aspon model these satisfy $x_i << 1$.

Since $U(1)_{new}$ is clearly anomaly free, it can be gauged and its gauge boson, the *aspon* become massive by the Higgs mechanism. Combining the upper limit on $\bar{\Theta}$ and the values of ϵ and ϵ' from K^0 decay it is possible to show that both the aspon and the vector-like quarks have masses $\leq 600 GeV$. The analysis also bounds the values of $|x_i|$ to be $\leq 10^{-2}, 10^{-3}, 10^{-4}$ for i = 1,2,3 respectively.

I shall not go through the details here. In the treatment of CP violation, there is a parallel to the recent paper of Deshpande and He (OITS-529 12/93) which uses a $S_3 \times Z_3$ family symmetry introdued in 1991 by Ernest Ma. Their case (a) has hard explicit CP violation, but their case (b) has spontaneous violation and has too small a KM phase to account for the effect in the K system which is instead explained by charged Higgs exchange [the analog of aspon exchange].

In the MSSM new CP phases occur and must be suppressed to avoid too large a value of d_n. Babu and Barr (1993) suggest spontaneous CP violation at a high scale to solve this by providing phases only in gaugino mass terms.

These are two examples of other recent work suggesting spontaneous CP violation. They both differ from the aspon model as can be seen by the fact that they both require an axion to solve strong CP.

(3) Estimation of CP Asymmetries in B Decays

In B decays, using the KM mechanism it has been estimated that with 10^8 samples one could see CP asymmetries and begin to check the unitarity relations required for the (complex) CKM matrix elements.

As shown in [1], the details are different in the aspon model because aspon exchange can compete with the usual box diagrams for the decay amplitudes. In the K system, the mixing is dominated by aspon exchange and that led to the upper limits on the masses mentioned above. The large phase there compensated for the small phase in the $K \to \pi\pi$ amplitude from W exchange.

For the B system, the mixing acquires a sizeable contribution from the W^+W^- box graph and the compensation is incomplete for the small phase occurring in the decay amplitude. The reason that the aspon exchange is relatively less important in the mixing can be traced to two large suppression factors: (1) $(m_c/m_t)^2 \simeq 10^{-4}$ and (2) $|x_3/x_2|^2 \simeq 10^{-2}$.

As a result, in a sample of 10^8 B decays one would *not* see the CP asymmetry if the aspon model were correct. This is good in that it will refute the standard model if one defines the KM mechanism as a part thereof (this may be unfair to the standard model). It is bad because there would still be no example of CP violation seen outside of the neutral K system.

To confirm the aspon model, the most convincing would be the production of the aspon particle in a collider.

In conclusion, if CP asymmetries are undetectably tiny in B decay, spontaneous CP violation is an alternative to the KM mechanism.

This work was supported in part by the US Department of Energy under Grant No. DE-FG05-85ER-40219.

References

[1] A. W. Ackley, P. H. Frampton, B. Kayser and C. N. Leung, Phys. Rev. **D** (1994, in press) and references cited therein.

PRAMANA
journal of
physics

© Printed in India

Supplement to Vol. 45
October 1995
pp. 113-116

Family symmetry

PAUL H. FRAMPTON
Institute of Field Physics, Department of Physics and Astronomy,
University of North Carolina, Chapel Hill, NC 27599-3255, USA

Abstract. In this presentation, I discuss an extension of the standard model which is motivated by the desire to allow non-trivial accommodation of three families and is testable by the production of new particles (especially dileptons).

The present talk includes (1) a description of the model (331 model); (2) the cubic see-saw for neutrino masses; (3) brief comments on phenomenology of the 331 model for hadronic and leptonic colliders.

(1) Desciption of the Model

Family symmetry is usually taken to mean a horizontal symmetry, either global or gauged, under which the three families transform under some nontrivial representation. The family symmetry is *broken* in order to avoid unobserved mass degeneracies. In this meaning of family symmetry, there is no explanation of *why* there are three families which is an input. Rather the hope is that the postulated family symmetry may explain the observed hierarchies of the fermion masses and the quark flavor mixing angles.

In the present model, the aim is indeed to attempt to address such unexplained hierarchies *and* to explain why there are three families. This may be a necessary first step to understanding the hierarchies themselves.

To introduce the 331 model the following are motivating factors:

(1) Consistency (unitarity, renormalizability) of a gauge theory requires that chiral anomalies be cancelled. This requirement alone is able to fix all electric charges in the standard model, and to explain charge quantization, e.g. the electric neutrality of the hydrogen atom, without the necessity for grand unification.

(2) This does not explain why there are three families but is sufficiently impressive to suggest that $N_g = 3$ may be explicable by anomaly cancellation in an extension of the standard model. This requires *both* that each extended family have a non-vanishing anomaly *and* that the three families are not all treated similarly.

(3) A striking feature of the mass spectrum of the standard model is the top quark mass suggesting that the third family be treated differently from the first two and that the anomaly cancellation be proportional to the combination $+1+1-2=0$ for the three families.

(4) There is a factor -2 (suggested by (3) above) already occurring in the theory.

bosons. The adjoint of $SU(3)$ breaks down to $3+(2+2)+1$. The 1 is a Z and the two doublets are readily identified as dileptonic gauge bosons of the type first encountered in $SU(15)$ grand unification.

Several interesting contributions to $SU(15)$ have been made since 1991 (the WHEPP2 meeting in Calcutta) by B. Brahmachari of the Physical Research Laboratory in Ahmedabad. These include (with Mann, Steele and Sarker) the influence of Higgs on unification for different patterns of symmetry breaking - published in Phys. Rev. D in 1991; (with Sarkar) the increase in the GUT scake for supersymmetrized SU(15) - published in Phys. Lett. B in 1992; and the extension to SU(16), including a right-handed neutrino, and the symmetry breaking patterns and phenomenology - published in Phys. Rev. D in 1993. There have also been significant contributions to $SU(15)$ by Deshpande, Lavowa, and others.

The two principal shortcomings of $SU(15)$ grand unification are (1) The group is so large that the ratio of unknown particles to known ones is unacceptably high; and (2) the anomaly cancellation is inelegant, being accomplished by mirror fermions.

One feature of $SU(15)$ which survives in the 331 model is the presence of an $SU(3)$ electroweak gauge group. But it is not a subgroup of $SU(15)$ as can be seen by the fact that the dileptonic gauge bosons do not couple to the quarks in $SU(15)$ wheras they do in the 331 model.

Now we are ready to describe the structure of the model. The gauge group is extended to $SU(3)_C \times SU(3)_L \times U(1)_X$. The triplets of $SU(3)_L$ have electric charges (X-1,X,X+1) while antitriplets have charges (X+1,X,X-1). In either case the X value is the electric charge of the middle component.

For the leptons we assign (e^-, ν_e, e^+) to an antitriplet and similarly for the μ and τ families. The left handed quarks are assigned to triplets for the first two families and to an antitriplet for the third family. The right-handed quarks are taken to be singlets as in the standard model. No new leptons have been introduced but there is a new quark per family: D , S (Q=-4/3) in the first and second, and T (Q=+5/3) in the third.

Anomaly cancellation occurs in a nontrivial manner *between* the families. One can check in turn all the relevant gauge anomalies: $(3_C)^3, (3_L)^3, (3_C)^2X, (3_L)^2X$, $X^3, X(T_{\mu\nu})^2$. Each extended family has non-vanishing anomaly for the 2nd,4th and 5th of these, while the three families taken together cancel with anomalies proportional to $+1+1-2$ as expected. The 1st, 3rd and 6th anomalies *do* cancel family by family.

In the Higgs sector there is a triplet Φ with X = +1 whose VEV breaks the 331 gauge group to the 321 gauge group of the standard model. This also allows D,S,T quarks as well as the Z_2 and (Y^{--}, Y^-), (Y^{++}, Y^+) gauge bosons to acquire mass. The electroweak breaking involves three $SU(2)$ doublets embedded in two triplets $\phi(X=0)$ and $\phi'(X=-1)$ and a sextet $H^{\alpha\beta}(X=0)$. The sextet is necessary to give a symmetric (in family space) contribution to the charged fermion masses. Note that ϕ gives masses to d,s,t (and an antisymmetric contribution to the charged lepton masses) while ϕ' gives masses to u,c and b. Let the scale of breaking of 331 to 321, the VEV of Φ, be denoted by U. What can the scale U be? There is a lower bound coming from precision electroweak data: what makes the 331 model more interesting is that there is also an upper bound.

The lower bound comes from the limits on $Z - Z'$ mixing and from the absence of flavor-changing neutral currents. The latter requires that it is the third family which is treated asymmetrically rather than the first or second. A lower bound on the Y mass comes from data on polarized muon decay. The Y would give a component (V+A) compared to the W which is (V-A). The strong limits on the parameter ξ defined as the coefficient of (-A), namely $1 \geq \xi \geq 0.997$ imply that the mass of the dilepton must exceed 300 GeV. More accurate measurements of muon decay, and of muonium-antimuonium conversion will put better limit on the dilepton mass. Incidentally, it is fascinating that these low energy experiments rather than, say, LEP data place the most stringent limits on this new physics.

The upper limit on U arises because the electroweak mixing angle must be less than 0.25 in order that the 321 standard model can be embedded in 331. It is easy to see that if $SU(2) \times U(1)$ is embedded just in $SU(3)$ then the value of $sin^2\theta$ is exactly 1/4, and if this value is exceeded then the X coupling constant becomes imaginary. Since the value is already close to one quarter at the Z mass and it increases with energy the consequence is that the scale U cannot be more than a few TeV. Requiring that α_X not exceed 2π then enforces that $M(Z_2) \leq 2.2$ TeV.

(2) Cubic See-Saw for Neutrino Masses

In the minimal 331 model neutrinos are massless since $\Delta L = 0$ and there are no right-handed neutrino fields. We have examined (with P. Krastev and J.T.Liu) the effects of soft breaking of L on the neutrino masses.

Spontaneous breaking of L would lead to a massless Majoron. Therefore we employ explicit breaking by terms:

$$m_1 H^{\alpha_1\beta_1} H^{\alpha_2\beta_2} H^{\alpha_3\beta_3} \epsilon_{\alpha_1\alpha_2\alpha_3} \epsilon_{\beta_1\beta_2\beta_3} + m_2 (H^{\alpha\beta} \bar{\phi}_\alpha \bar{\phi}_\beta + h.c.) \quad (1)$$

The Yukawa couplings to the leptons are given by:

$$h_1^{ij} L_\alpha^i L_\beta^j H^{\alpha\beta} + h_2^{ij} (L_\alpha^i L_\beta^j \bar{\phi}_\gamma \epsilon^{\alpha\beta\gamma} + h.c.) \quad (2)$$

The couplings h_1,h_2 are symmetric, antisymmetric respectively in family space.

At one loop level there are diagrams where the soft breaking of L through the parameters m_1, m_2 gives rise to neutrino masses. What is unique to the 331 model is the presence of contributions of the general form:

$$M(\nu_i) = CM(l_i)^3/M_W^2 \quad (3)$$

This is the cubic see-saw. $M(l_i)$ is the mass ofthe corresponding charged lepton.It arises because all the Yukawa couplings are related by $SU(3)$.

If we take, merely as an example, Dennis Sciama's favorite value for the tau neutrino mass of 29.3 eV, then the mu neutrino mass is 6.2meV (that is, 0.062 eV), and the electron neutrino mass is 690 peV. This last tiny mass gives rise to a contribution to neutrinoless double beta decay but it is many orders of magnitude below present experimental limits.

As is usual with this type of formula, one can fit any two out of Cold Dark

Our formula is called a cubic see-saw but really it is not a see-saw at all because there is no right-handed neutrino involved.

(3) Phenomenology of the 331 Model for Hadronic and Leptonic Colliders

In hadronic colliders, for example pp at 10 TeV center of mass, dileptons can be both pair produced and associatedly produced in conjunction with new quarks (which themselves carry lepton number). Explicit calculations show that such events have a healthy detectable rate for any luminosity sufficiently high to be otherwise interesting in looking for Higgs bosons or low-energy supersymmetry.

In an e^-e^- collider at 300-1000 GeV center of mass energy the Y^{--} could appear as a striking narrow direct channel resonance. One would best look at the channel $e^-e^- \to \mu^-\mu^-$ for which the standard model background is zero.

This work was supported in part by the US Department of Energy under Grant No. DE-FG05-85ER-40219.

Journal of physics
October 1995
pp. 117-140

Determination of mass and width of W at LEP200

S. N. GANGULI
Tata Institute of Fundamental Research, Bombay 400 005.

1. Introduction

Large Electron Positron collider (LEP) at CERN, Geneva, is in operation since September 1989. There are four mammoth detectors - ALEPH, DELPHI, L3 and OPAL- which are collecting data at LEP. The purpose of LEP is to study the Z^0 during LEP100 Phase (1989-1995) at $\sqrt{s} \simeq 90$GeV. By the end 1993 each of the four detectors collected a total number of Z^0 events $\simeq 2 \times 10^6$. Some of the results from these studies are [1]:

(a) **Mass of Z^0** is measured to a precision of $\frac{\Delta m}{m} = 10^{-4}$.
(b) **Number of light ν** is measured as $N_\nu = 3.00 \pm 0.03$.
(c) Effective value of the electroweak mixing angle is measured to be $\sin^2\theta_{\rm eff} = 0.2321 \pm 0.0006$.
(d) **Running of α_s** is established at LEP.
(e) **Top mass** is estimated to be $166^{+17}_{-19} \pm 20$ GeV
(f) **Lower limit** on Higgs boson mass is 63.5 GeV
(g) **Standard Model** of EW interactions is tested at LEP to a precision better than 0.5 %.

LEP200: The second phase of LEP, sometimes called LEP200 phase, is to achieve centre of mass energy for e^+e^- collision above the W production threshold so as to observe and study for the first time the reaction

$$e^+e^- \rightarrow W^+W^- \qquad (1)$$

It may be recalled that one of the main reasons for the need of Z^0 is to regularise the production cross section of W^+W^-; without the Z^0 the energy dependence of the cross section violates unitarity bound, fig 1.

Beam Energy: The upgradation of the LEP beam energy from $\simeq 45$ GeV to above the W mass threshold will be achieved by adding 192 superconducting RF cavities in the LEP ring. This will lead to $E_{\rm beam} = 88$ GeV yielding centre of mass energy for collision as $\sqrt{s} = 176$ GeV.

Luminosity: The expected luminosity is $4 \times 10^{31}{\rm cm}^{-2}{\rm sec}^{-1}$. With the running period of $\simeq$ 6 months a year for LEP, the integrated luminosity in a year will be $\simeq 240{\rm pb}^{-1}$. Total approved luminosity at LEP200 is expected to be $500\ {\rm pb}^{-1}$. With $\sigma\ (e^+e^- \rightarrow W^+W^-) \simeq 16$pb, the number of expected W pairs per experiment will be $\simeq 8000$.

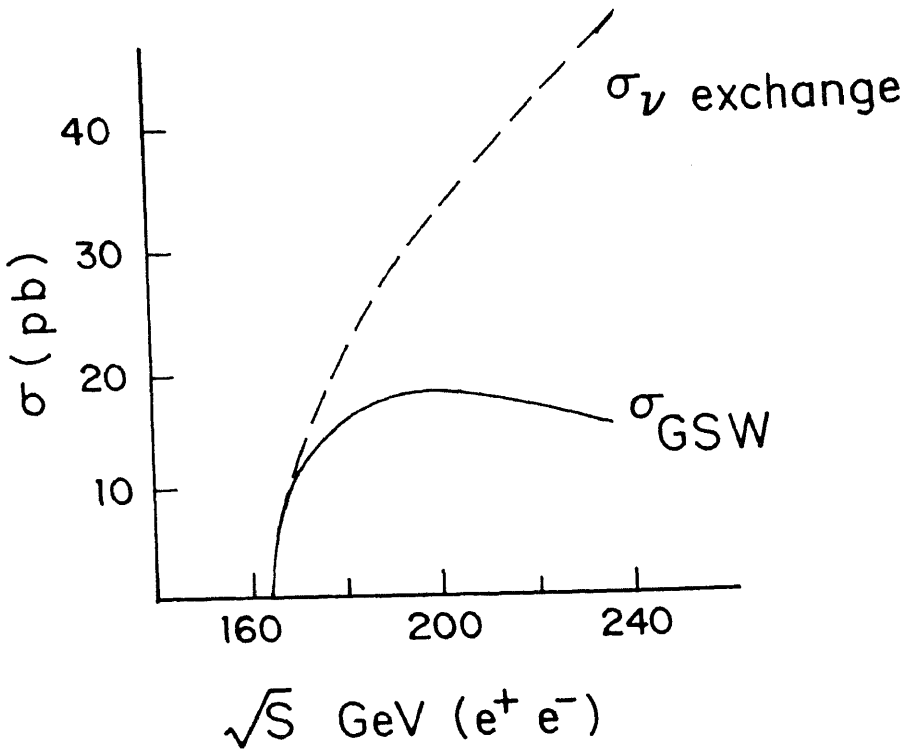

Figure 1. Production cross section of $e^+e^- \rightarrow W^+W^-$ as a function of $\sqrt{s}$. Dotted line is for only ν exchange while the solid line is from the Standard Model.

Aims of LEP200: The physics capabilities of LEP200 have been extensively studied [2, 3]. There are however three main topics: (a) Precision measurement of M_W and Γ_W; (b) Determination of Triple Gauge Boson couplings, and (c) Search of New Particles. In this talk we will restrict ourselves to the first topic.

2. Prsent knowledge of M_W and Γ_W

Present knowledge of M_W: Mass of W has been measured in two ways:

(i) Direct Measurements

Experiments at $\bar{p}p$ colliders, UA2 and CDF, made direct measurements [4] of the W mass from $W \rightarrow l\nu$ events. Their results are summarised below.

$$M_W/M_Z = 0.8813 \pm 0.0036 \pm 0.0019 \text{ GeV (UA2)}$$
$$M_W = 79.91 \pm 0.39 \text{ GeV (CDF)}$$

The combined result is: $\boxed{M_W = 80.22 \pm 0.26 \text{ GeV}}$

(ii) Indirect Estimation

The LEP data consisting of energy dependence of various cross sections ($e^+e^- \rightarrow Z^0$ and $Z^0 \rightarrow$ hadrons, e^+e^-, $\mu^+\mu^-$ and $\tau^+\tau^-$) and asymmetries when fitted in the framework of the Standard Model leads to the mass of W and this value is [1]:

$$M_W = 80.25 \pm 0.10 \pm 0.03 \text{ GeV (LEP)}$$

[Second error due to variation of Higgs between 60-1000 GeV]

Present knowledge of Γ_W: The W width as quoted by UA2, UA1 and CDF experiments [4] **are not direct measurements**; the width is **'extracted'** from the measurement of R

$$R = \sigma(W \rightarrow e\nu)/\sigma(Z \rightarrow e^+e^-) \quad (2)$$

$$(3)$$

$$= \frac{\sigma(\bar{p}p \rightarrow W + X)}{\sigma(\bar{p}p \rightarrow Z + X)} \cdot \frac{\Gamma(W \rightarrow e\nu)}{\Gamma(Z \rightarrow e^+e^-)} \cdot \frac{\Gamma_Z}{\Gamma_W} \quad (4)$$

The quantities $\sigma(\bar{p}p \rightarrow W + X)/\sigma(\bar{p}p \rightarrow Z + X)$ and $\Gamma(W \rightarrow e\nu)/\Gamma(Z \rightarrow e^+e^-)$ are calculated from theory, and Γ_Z is taken from LEP measurements.

Values from the three collider experiments are summarised below:

$$\Gamma_W = 2.10 \pm 0.14 \pm 0.09 \text{ GeV (UA2)} \quad (5)$$
$$\Gamma_W = 2.18 \pm 0.26 \pm 0.04 \text{ GeV (UA1)} \quad (6)$$
$$\Gamma_W = 2.12 \pm 0.20 \text{ GeV (CDF)} \quad (7)$$

The combined result is: $\boxed{\Gamma_W = 2.12 \pm 0.11 \text{ GeV}}$

W is a vector gauge boson and therefore the knowledge of its mass is very important. Some of the other reasons are:

[A] It may be recalled that the top quark and the Higgs boson are the two unknowns in the Standard Model. Precision measurement of M_W will give further constraints on the mass of the Higgs if the top quark mass is known, fig. 2, [5].

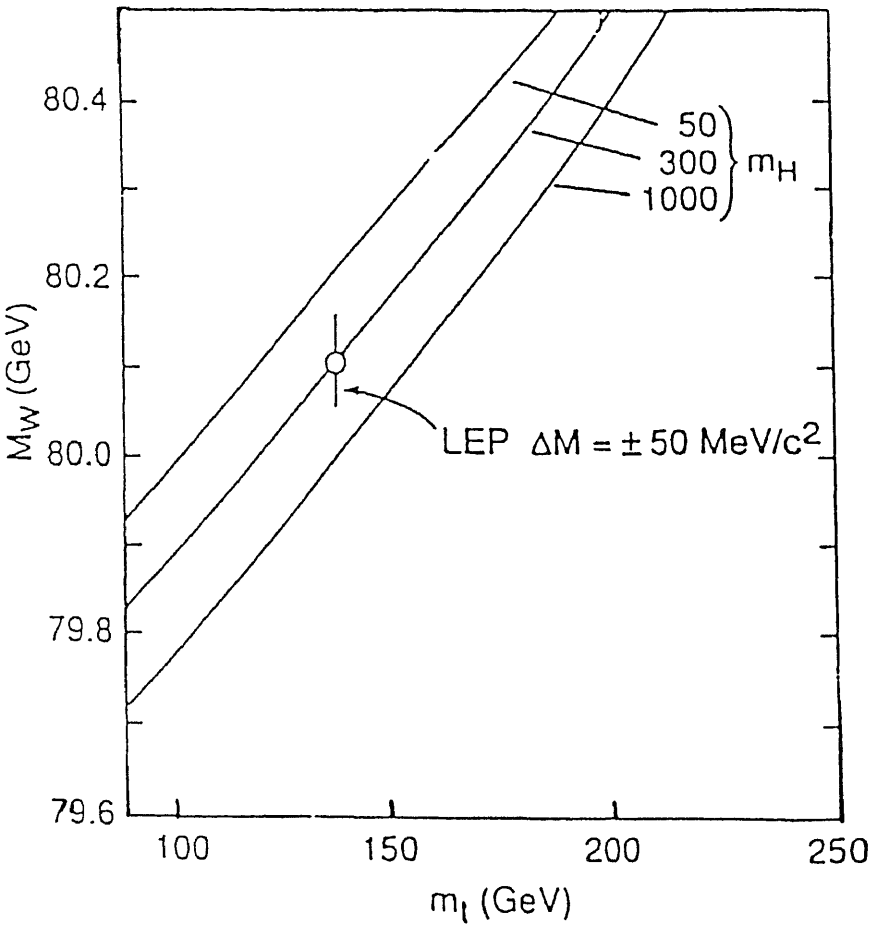

Figure 2. M_W vs M_{top} curves in the framework of the Standard Model for three different values of Higgs mass.

For example if Top mass is known from hadron collider experiments at Fermilab (a) with a precision of $\Delta M_{top} = 10$ GeV, then 50 MeV error on W mass measurement will lead to $\Delta M_{Higgs} = ^{+340}_{-170}$ GeV, and (b) precision in $\Delta M_{top} = 2$ GeV and 50 MeV in M_W will yield $\Delta M_{Higgs} = ^{+176}_{-118}$ GeV.

[B] Testing radiative corrections

Radiative corrections come from self energies , formfactors, box diagrams etc. The mass of the W and Z are related by,

$$M_W^2 = \frac{\pi\alpha}{\sqrt{2}G_F(1 - M_W^2/M_Z^2)} \cdot \frac{1}{1 - \Delta r} \tag{8}$$

The error in the radiative correction Δr arises mainly from the error in M_W as the value of M_Z is known to a very high precision ($\Delta M_Z = 6$ MeV). The error of 50 MeV in M_W will lead to error on Δr as 0.003.

It may be noted that the radiative correction Δr depends on M_{top} andM_{Higgs} and hence can be determined independent of M_W. The L3 experiment [6] at LEP has determined the value of $\Delta r = 0.045 \pm 0.013$.

Two ways of determining radiative corrections as mentioned above can thus be compared.

4. *W* production mechanism

Leading order diagrams are due to Z, γ and ν exchanges and their interferences.

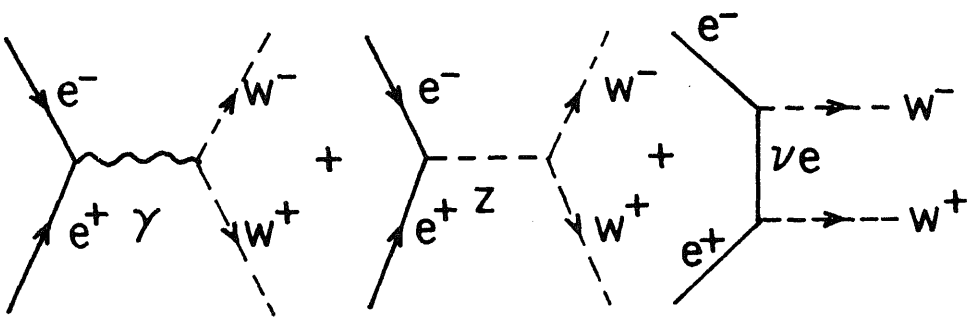

Initial state helicities are LR or RL for the Z and γ exchanges, while only the LR diagram is allowed for the ν exchange (since ν is left handed). It may be noted that the ν diagram is the dominant one and as a result W^+ and W^- are peaked along the $\vec{p}_{e+}$ and $\vec{p}_{e-}$ directions respectively, fig.3.

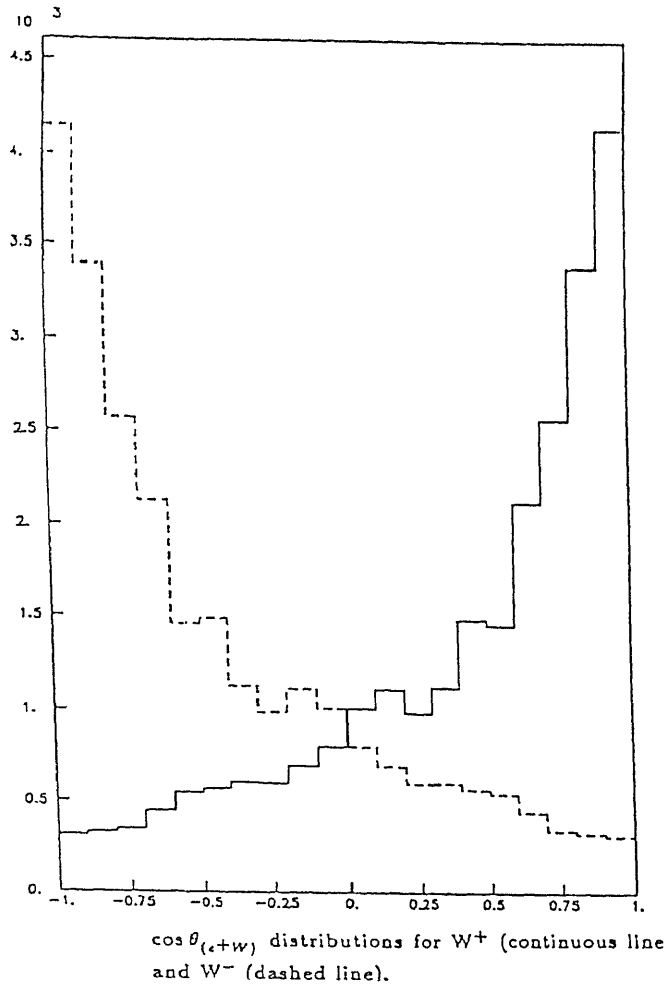

Figure 3. Angular distribution of W^+ and W^- with respect to the direction of e^+ beam.

For the forward-backward production the longitudinal component of the W helicity ($\lambda = 0$) is equally important as the transverse states ($\lambda = +1$ *or* -1).

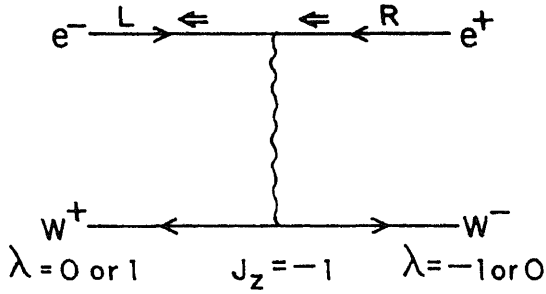

5. *W* decay modes

Final states from $e^+e^- \rightarrow W^+W^-$ are classified into three classes depending on W decay modes

Pure Leptonic :	$WW \rightarrow l\nu l\nu$:	7.5 %
Semi Leptonic :	$WW \rightarrow l\nu q\bar{q}$:	40 %
Pure Quark :	$WW \rightarrow q\bar{q}q\bar{q}$:	52.5 %

A quark from W decay will undergo fragmentation/hadronization leading to a formation of jet in the final state.

Topology of WW events

(i) Since the W^+ and W^- are peaked along $\vec{p}_{e^+}$ and $\vec{p}_{e^-}$ respectively and hence the charged leptons from W decay will reflect the parents angular distributions.

(ii) Pure Leptonic Mode: Two visible leptons or a thin jet from the hadronic decay of τ will be seen in the final state.

(iii) Semi-leptonic decay : Two jets and one isolated lepton or, two jets and one thin jet in the final state.

(iv) Pure Quark decay : Four jets or more in the final state.

Production cross-section of W^+W^- process is $\simeq$ 16pb. In this section we discuss briefly several sources of some of the background and they are:

(i) $e^+e^- \rightarrow Z\,Z \rightarrow f\bar{f}$:

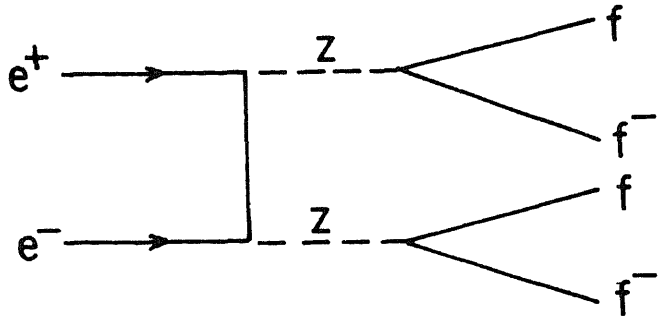

Total yield of this reaction is only a few % of the WW signal.

(ii) $e^+e^- \rightarrow f\,\bar{f}$:

The cross-section is 10 pb for f = lepton and leads to nearly back to back leptons which can be removed by an appropriate cut. The cross-section is 26 pb for f = quark, but then this reaction is dominated by 2 and 3 jets, while WW signal leads to 4 or more jets.

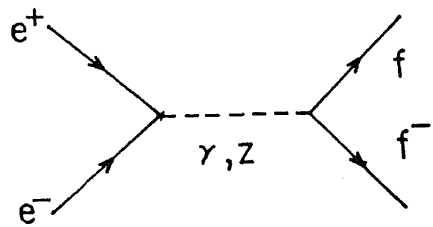

(iii) $e^+e^- \rightarrow f\,f\,\gamma$

This reaction is due to on-mass shell Z^0 exchange with monochromatic γ of $\simeq$ 70 GeV. Cross section for this reaction is 80 pb for f = quark & 20 pb for f = lepton; Major fraction of these events can be rejected from large missing momentum.

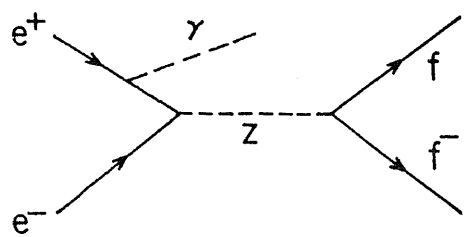

This reaction will have two leading electrons which are lost in the beam pipe. Missing p_T and acoplanarity will remove most of this background.

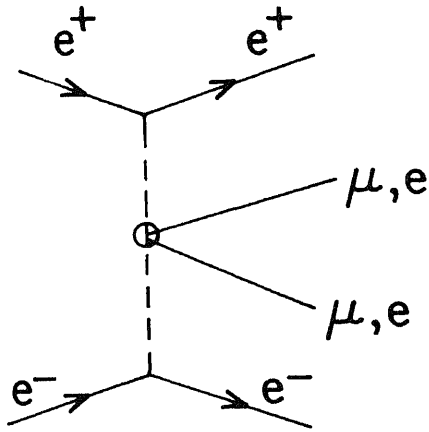

7. Experimental methods to measure M_W

Three methods have been discussed in the literature and they are:

[A] Direct Reconstruction:

W's are reconstructed using either hadronic events, where both W decay into jets, or hadronic-leptonic events, where one W decays hadronically while the other into leptonic mode.

Note that the masses of the two W's produced will have different masses due to finite width of W. Some of the groups have assumed equal masses for reconstructing W's [5]. In L3 we have assumed unequal masses for reconstructing W's.

[B] **Shape of the Excitation Curve**:

From the measured shape of the production cross section one deduces the value of M_W.

[C] Lepton end point energy:

The value of M_W is obtained from the lepton spectrum of leptonic decays of W's

8. W pair generators

To carry out simulation studies we need Monte Carlo programs that generate $e^+e^- \rightarrow W^+W^-$ events. There are several generators available and they are summarised in Table 1. Some of the important ingredients used in a generator like inclusion of W width, proper implementation of CKM matrix elements, incorporation of the initial state radiation, flexibility in triple gauge boson coupling, and hadronization scheme are also indicated in Table 1.

Table 1.

Generator	Herwig	Pythia	LEPWW	GENTLE	WWgamma
Γ_W	Y	Y	Y	Y	Y
V_{CKM}	Y	Y	N	Y	Y
ISR	N	Y	Y	Y	hard photon
General ZWW, γWW	N	N	Y	N	N
Hadronization	Cluster	LUND	LUND	LUND	LUND
Author	Webber	Sjostrand	Kleiss	Bardin	KEK-LAPP

REMARKS: GENTLE [7] makes a detailed implementation of ISR taking into account t-channel exchange diagrams properly.

9. Jet reconstruction algorithms

When both the Ws decay by hadronic mode, one recombines the hadrons to make four jets; each jet representing a parent quark. Since the W's are slow ($\beta \simeq 0.5$), the hadrons of a given jet are not well separated from those of other jets. Therefore a reconstructed jet may have particles of another jet. When one W decays hadronically and the other via leptonic mode then the number of jets is reduced and the mismatch is much less.

There are several different algorithms for the reconstruction of jets. Below we discuss six different algorithms.

(i) Generator History:

In this procedure one recombines the hadrons, belonging to a given quark, to form a jet. Therefore no mismatch of particles between different jets. This is possible because we are dealing with generated events.

(ii) Jade algorithm [8] :

$$y_{ij} = \frac{2E_i E_j(1-\cos\theta_{ij})}{E_{vis}^2} \tag{9}$$

The quantity y_{ij} is based on invariant mass squared of 'jets' i and j (to start with one uses small resolvable cluster as a jet). E_i and E_j are energies of jets with θ_{ij} and E_{vis} as opening angle and total visible energy respectively. The pair of jets with the smallest y_{ij} are combined into a new jet and all y'_{ij}s are recalculated; this procedure is repeated iteratively until we are left with four jets. The exact definition of y_{ij} is different in (iii), (iv) and (v) below.

(iii) Durham algorithm [9]:

$$y_{ij} = \frac{2Min(E_i^2, E_j^2)(1-\cos\theta_{ij})}{E_{vis}^2} \tag{10}$$

(iv) Geneva algorithm [10]:

$$y_{ij} = \frac{8E_i E_j(1-\cos\theta_{ij})}{9(E_i+E_j)^2} \tag{11}$$

(v) Lund algorithm [11]:

$$y_{ij} = \frac{2|\vec{p_i}||\vec{p_j}|\sin\frac{\theta}{2}}{|\vec{p_i}+\vec{p_j}|} \tag{12}$$

(vi) Generalised thrust approach [12] : Thia approach has been used at PETRA to study 4 jet events. The aim is to find four jet axes as the unit vectors $\hat{n_j}$ so that a generalised form of the standard thrust

$$T_4 = Max\left(\frac{\sum_i \max_i(\vec{p_i}\cdot\hat{n_j})}{\sum_i|\vec{p_i}|}\right) \tag{13}$$

is maximised.

10. M_W from direct measurement

There are three types of events:
(i) **Pure Quark or** 'HadronicDecay : $W^+ W^- \rightarrow q_1\,\bar{q}_2\,q_3\,\bar{q}_4$

(ii) **Semi Leptonic Decay** : (a) $W^+ W^- \rightarrow q_1\,\bar{q}_2\,e\,\nu_e$, (b) $W^+ W^- \rightarrow q_1\,\bar{q}_2\,\mu\,\nu_\mu$
(c) $W^+ W^- \rightarrow q_1\,\bar{q}_2\,\tau\,\nu_\tau$

(iii) **Pure Leptonic Decay** : $W^+ W^- \rightarrow l\,\nu_l\,l'\,\nu_{l'}$

Energy and momentum conservation of the reaction can be made if we are able

(a) ν momentum as it is not detected, this decreases the number of constraint by three, and (b) energy of τ as its decay involves ν corresponding to a decrease of one constraint.

Keeping in mind the above points we will not presently use (iic) and (iii) for our kinematic fits.

10.1 Details of Kinematic Fitting :

As mentioned earlier one carries out kinematic fits to impose energy momentum conservation. Constraint equations are described in detail below.

(i) $WW \rightarrow (j_1 j_2)(j_3 j_4)$

Constraint equations are $\Longrightarrow$

$$
\begin{aligned}
&(1)\ E_{j1} + E_{j2} + E_{j3} + E_{j4} - \sqrt{s} = 0 \\
&(2)\ p^x_{j1} + p^x_{j2} + p^x_{j3} + p^x_{j4} = 0 \\
&(3)\ p^y_{j1} + p^y_{j2} + p^y_{j3} + p^y_{j4} = 0 \\
&(4)\ p^z_{j1} + p^z_{j2} + p^z_{j3} + p^z_{j4} = 0
\end{aligned}
$$

Besides the above 4 constraints, two more constraints can be used if one assumes equal masses for the two W's

$$
\begin{aligned}
&(5)\ (E_{j1} + E_{j2})^2 - (\vec{p}_{j1} + \vec{p}_{j2})^2 - M_W^2 = 0 \\
&(6)\ (E_{j3} + E_{j4})^2 - (\vec{p}_{j3} + \vec{p}_{j4})^2 - M_W^2 = 0
\end{aligned}
$$

With unknown as M_W one ends up with 5C fit.

(ii) $WW \rightarrow (j_1 j_2)(l\nu)$

Repeating the procedure as described in (i) yields 2C fit for this reaction.

Remark: Allowing the two W masses to be unequal one ends up with 4C and 1C fits respectively

10.2 Effect of initial state radiation

Initial state radiation (ISR) is a common feature in e^+e^- interactions i.e., the e^- emits a photon in the presence of the Coulomb field of the e^+ or vice versa. The distribution in the photon energy from ISR is shown in fig.4 from the GENTLE generator and its mean value is: $< E_{rad} >= 1.211\text{GeV}$ at $\sqrt{s} = 176$ GeV.

The effect of ISR in the cross section for $e^+e^- \rightarrow W^+W^-$ is incorporated as follows:

Without ISR the cross-section is given by [13]:

$$\sigma(s) = \int_0^s dm_1^2 \cdot \rho(m_1) \int_0^{(\sqrt{s}-m_1)^2} dm_2^2 \cdot \rho(m_2) \cdot \sigma_0(s; m_1, m_2) \qquad (14)$$

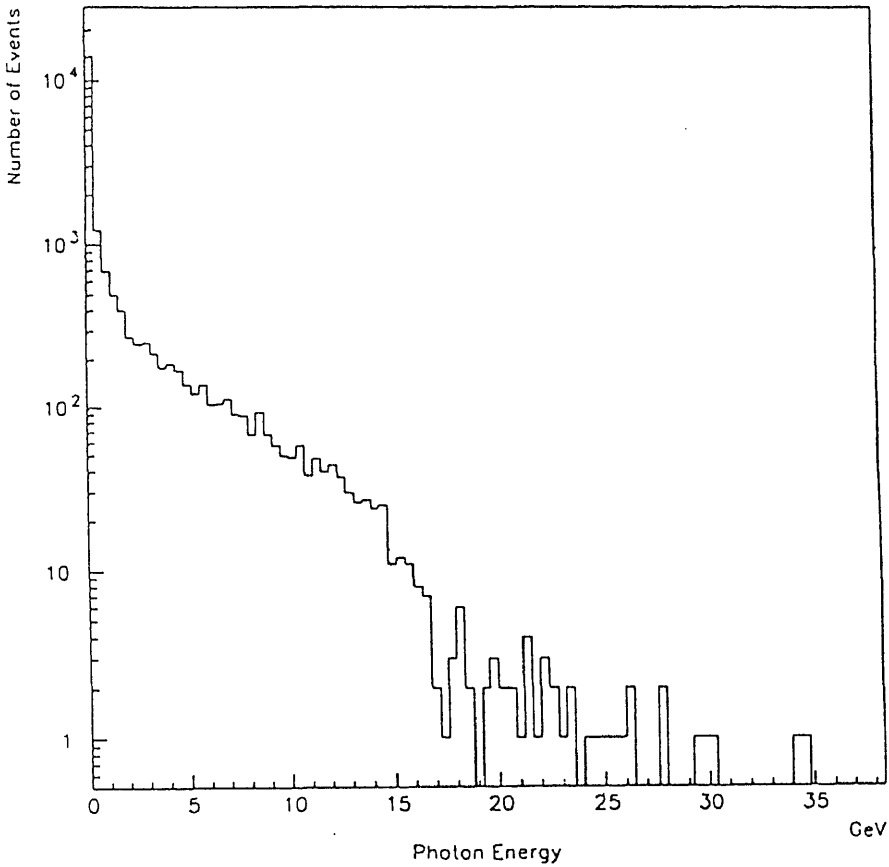

Figure 4. Energy distribution of ISR photons.

$$\rho(m) = \frac{1}{\pi M_W} \cdot \frac{m^2 \Gamma_W}{(m^2 - M_W^2)^2 + m^2 \Gamma_W^2} \quad (15)$$

M_W and Γ_W are the mass and width of W; m_1 and m_2 are the two produced W masses and $\rho(m)$ is the Breit-Wigner (BW) distribution. $\sigma_0(s; m_1, m_2)$ is the Born cross section [13] at the centre of mass energy of $\sqrt{s}$.

With ISR the cross-section is given by [7]:

$$\sigma(s) = \int_0^s dm_1^2 \cdot \rho(m_1) \int_0^{(\sqrt{s}-m_1)^2} dm_2^2 \cdot \rho(m_2) \cdot \overline{\sigma}(s, s') \quad (16)$$

$$\overline{\sigma}(s, s') = \int_0^{1-(m_1+m_2)^2/s} dx \cdot \sigma_0(s(1-x)) \cdot H(x, s) \quad (17)$$

$$H(x, s) = \beta \cdot x^{(\beta-1)} \cdot (1 + \overline{S}) + \overline{H} \quad (18)$$

$$\overline{S} = \frac{\alpha}{\pi}[\frac{\pi^2}{3} - \frac{1}{2}] + \frac{3}{4}\beta + \mathcal{O}(\alpha^2) \quad (19)$$

$$\overline{H} = -\beta(1 - x/2) + \mathcal{O}(\alpha^2) \quad (20)$$

$$\beta = \frac{2\alpha}{\pi}[\log(s/m_e^2) - 1] \quad (21)$$

H(x,s) is the radiator function [14] and x is a fractional momentum carried by the photon.

From the two distributions, eqs.(14) and (16), we calculated the average value of mass, $< (m_1 + m_2)/2 >$ and the mass difference $|m_1 - m_2|$ and they are listed below.

Parameters	Q_0 Without ISR (GeV)	Q_1 With ISR (GeV)	Q_0 - Q_1 (MeV)
Mass	80.046 (3.19)	79.972 (3.20)	74.0
$< (m_1 + m_2)/2 >$	79.835 (2.85)	79.732 (2.93)	103.0
$\|m_1 - m_2\|$	3.292 (4.61)	3.341 (4.77)	-49.0

The effect of ISR [15]: Finally we may conclude the following effect due to ISR on our distributions:

(a) To lower the mean values of mass and $< (m_1 + m_2)/2 >$ by 74 and 103 MeV respectively,

(b) To increase the dispersion by nearly 0.2%,

(c) To decrease the total cross section by $\simeq 2$ pb.

They have generated ≈ 3500 events of $W^+W^- \rightarrow$ 4jet and ≈ 1300 events of (2jet + $l\nu$) corresponding to $\approx 400 pb^{-1}$. Events were simulated through DELPHI detector. Jet reconstructions were carried out using generalised thrust algorithm.

Kinematic fit was carried out with the constraint that the two W masses are equal [5C & 2C fit for 4-jet & 2-jet+eν_e respectively]. To extract M_W from the data : fit was made with a BW of fixed width folded with a Gaussian (detector resolution function) plus a constant background.

RESULTS: Fitted mass distributions of W are shown in figs.5(a)-5(c) for three types of events: 4 jets, 2 jets + $\mu\nu$ and 2 jets + eν. They find a systematic positive offset of the fitted value of the mass with respect to true W mass used in the generator. This is summarised below:

$$\boxed{(\text{Fitted } M_W - M_W^{true}) = 422 \pm 79 \text{ MeV}, \quad (4\text{-jet})}$$
$$(\text{Fitted } M_W - M_W^{true}) = 819 \pm 160 \text{ MeV}, \quad (2 \text{ jet} + e)$$
$$(\text{Fitted } M_W - M_W^{true}) = 432 \pm 116 \text{ MeV}, \quad (2 \text{ jet} + \mu)$$

Results from L3 study [15]

L3 collaboration has also carried out similar study but **without the detector simulation.** They have used events generated by GENTLE and quarks were allowed to undergo hadronization. Jets were then reconstructed **ignoring ISR photons.** Kinematic fits were carried out by ignoring the ISR photons.

Figs.6(a) and (b) show the distributions of (Fitted - Generated) mass for two cases: (i) for all events and (ii) for events with ISR photon energy $E_\gamma < 20$ MeV.
Mean values of the two distributions are:

$$\boxed{(\text{Fitted } M_W - M_W^{true}) = 477 \pm 16 \text{ MeV}, \quad (\text{all events})}$$
$$(\text{Fitted } M_W - M_W^{true}) = -11 \pm 7 \text{ MeV}, \quad (\text{events with } E_\gamma < 20 \text{ MeV.})$$

From the above results it is clear that (i) when there is no ISR photons (which is same as selecting events with $E_\gamma < 20$MeV) the value of (Fitted $M_W - M_W^{true}$) is consistent with zero, and (ii) when all events are used (and not using ISR photons in kinematic fits) one sees the positive offset as seen by DELPHI.

Understanding the positive offset in M_W

The emmision of ISR actually reduces the effective centre of mass energy to $\sqrt{s'}$, which is lower than the nominal energy $\sqrt{s} = 2 \times E_{beam}$. If x is the fractional beam energy carried by the initial state photon then $\sqrt{s'} = s(1-x)$.

But kinematic fits as discussed earlier assume nominal cm energy $\sqrt{s}$. This results in higher Fitted Mass and the positive offset can be written down as: $\Delta m = + <$

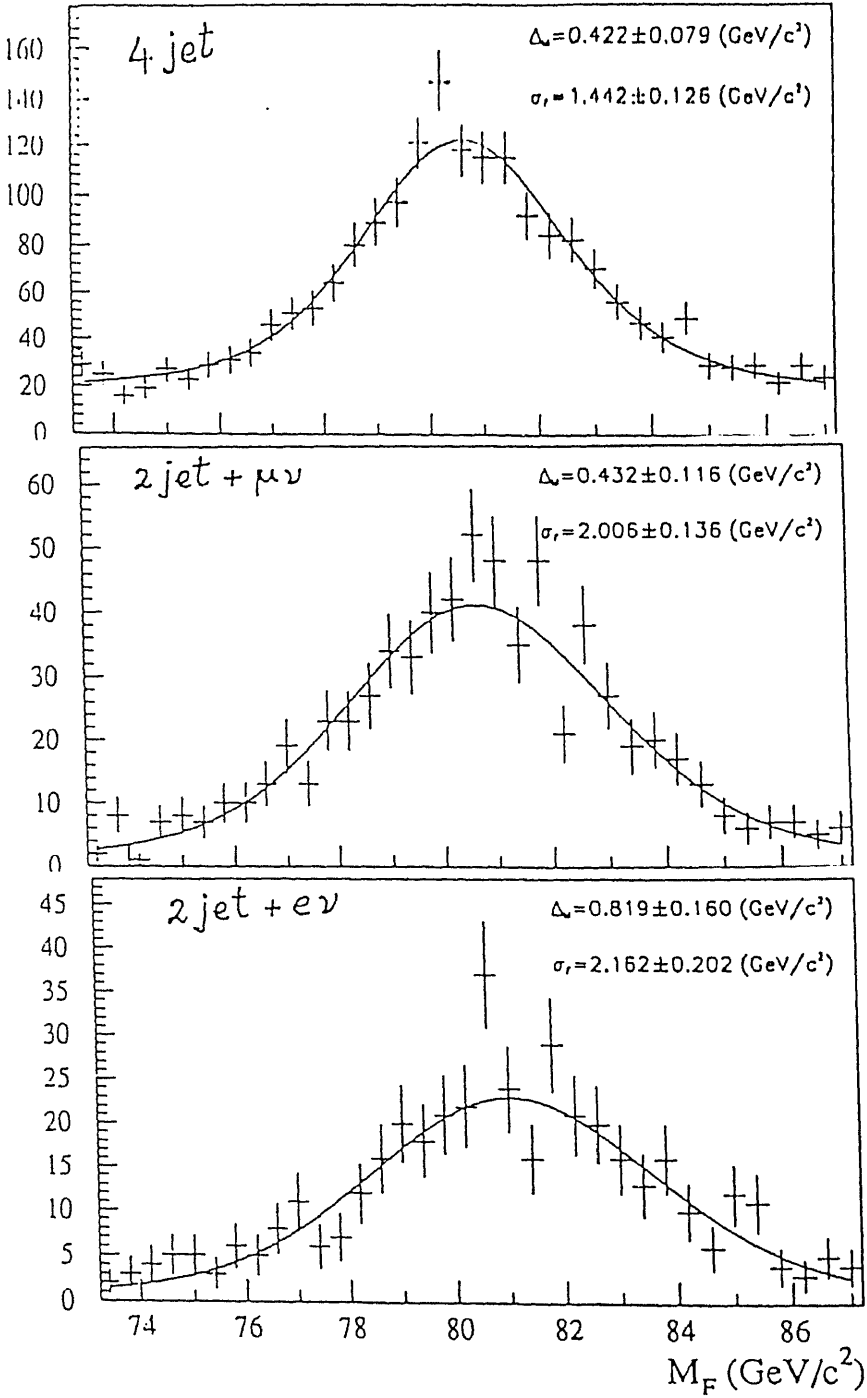

Figure 5. Fitted mass distributions of W for three types of events (a) 4 jets, (b) 2 jets + $\mu\nu$ and (c) 2 jets + eν.

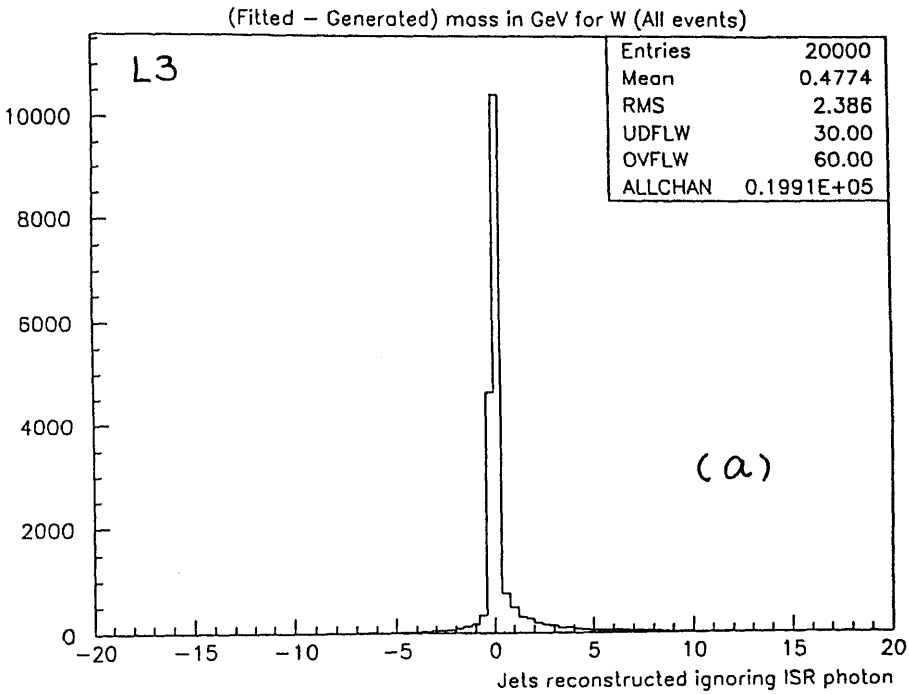

Figure 6a. (Fitted - generated) mass distribution for all events

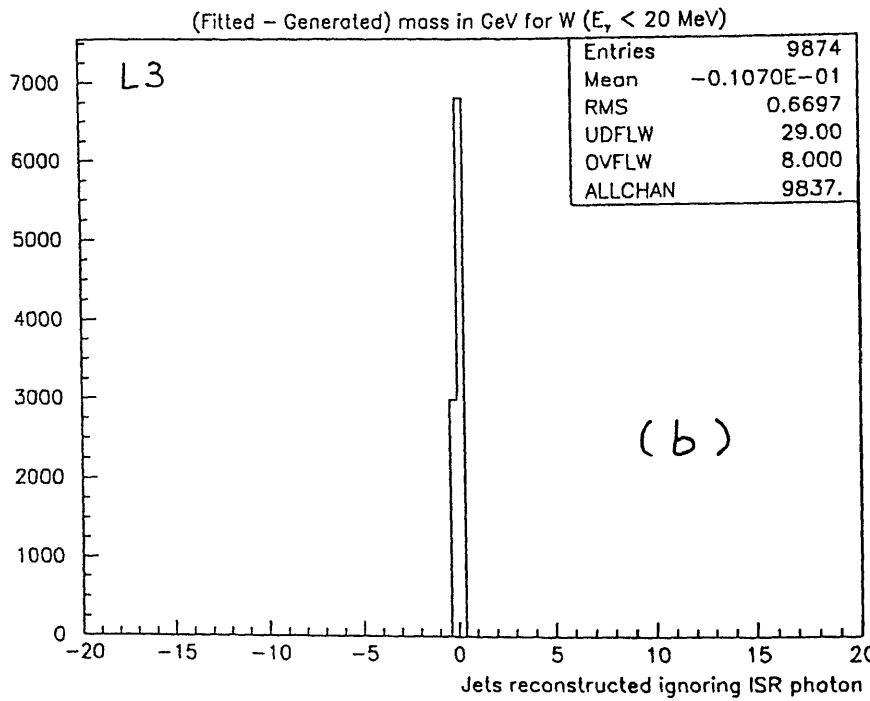

Figure 6b. (Fitted - generated) mass distribution for events with ISR photon en $E_\gamma < 20$ MeV.

$E_{rad} > \cdot \frac{}{\sqrt{s}}$.

For $\sqrt{s} = 176$ GeV and the value of $< E_{rad} >= 1.2$ GeV yield $\Delta m = 500$ MeV.

Shift in M_W due to Reconstruction algorithm

DELPHI collaboration repeated their fit analysis without ISR in the Monte Carlo and obtained (Fitted $M_W - M_W^{true}$) $= -130$ MeV. This is due to reconstruction algorithm and this needs to be done by other groups.

Expected precision in M_W

Projecting the Fit Analysis to $500 pb^{-1}$ DELPHI estimated the expected precision in M_W to be 55 MeV. Similar value for the precision has also been estimated by L3 [16], ALEPH & OPAL.

11. Simultaneous determination of M_W and Γ_W (L3) [17]

The analysis mentioned above was based on fitting equal mass to both the W, which is not technically right and also there is no straight way to determine the Γ_W.

L3 collaboration has proposed a strategy to determine simultaneously the mass and width of the W. They have used proper expression for the cross section involving convolution of two Breit-Wigner distributions weighted by tree level cross-section:

$$\sigma(s) = \int_0^s dm_1^2 \cdot \rho(m_1) \int_0^{(\sqrt{s}-m_1)^2} dm_2^2 \cdot \rho(m_2) \cdot \sigma_0(s; m_1, m_2) \tag{22}$$

$$\rho(m) = \frac{1}{\pi M_W} \cdot \frac{m^2 \Gamma_W}{(m^2 - M_W^2)^2 + m^2 \Gamma_W^2} \tag{23}$$

Distributions of mass, mass difference and mean mass are then given by

$$d\sigma/dm_1 = 4m_1\rho(m_1) \cdot \int_0^{(\sqrt{s}-m_1)} dm_2[m_2\rho(m_2)\sigma_0(s; m_1, m_2)] \tag{24}$$

$$d\sigma/d\Delta m = 8 \cdot \int_{0.5\Delta m}^{0.5\sqrt{s}} d < m > [m_1 m_2 \rho(m_1)\rho(m_2)\overline{\sigma}(s, s') \tag{25}$$

$$d\sigma/d < m > = 8 \cdot \int_0^{2<m>} d\Delta m[m_1 m_2 \rho(m_1)\rho(m_2)\overline{\sigma}(s, s') \tag{26}$$

Where $\Delta m = |m_1 - m_2|$, and $< m >= (m_1 + m_2)/2$

It is proposed to use either the variables m_1 and m_2 or Δm and $< m >$. ISR has been incorporated in these expressions, see sect. 10.2.

RESULTS: Results are presented here at the generator level i.e., without simulating through the detector. Total event sample used was 10,000 events without

using maximum likelihood method [15], and (ii) Δm & $< m >$ using χ^2 minimisation method. Fits from (ii) are shown in fig.7. Values of our fits are shown in the Table 2.

Table 2.

Fitted quantities	M_W (GeV)	Γ_W (GeV)
$\Delta m, < m >$	80.231 ± 0.014	2.038 ± 0.022
m_1, m_2	80.194 ± 0.012	2.041 ± 0.027

At the generator level the errors on mass and width from 10,000 events are 14 and 27 MeV respectively. Estimated errors on mass and width with detector resolution are $\simeq 50$ MeV and $\simeq 100$ MeV respectively.

12. M_W from the excitation curve

This approach utilises the energy dependence of the production cross section of (W^+W^-). But it is difficult to disentangle the effect due to M_{top}, M_{Higgs}, possible new physics etc. on the cross section. Sensitivity of cross section on M_W is shown [5] in the fig.8. Fractional change in cross section for change in mass by 100 and 200 Mev are shown. It is seen that the fractional change is less than 1% even for change in mass by 200 MeV for $\sqrt{s} > 172$ GeV. This method as it stands at present does not seem to be very useful.

13. M_W from the lepton end-point energy

The lepton energy, E_l, from the decay of W is limited by M_W

$$E_l < E_+ = \tfrac{1}{2}E_b + \tfrac{1}{2}\sqrt{E_b^2 - M_W^2}$$

Here E_b is the beam energy. The error on M_W due to error ΔE_+ on the end point is given by,

$$\Delta M_W = \frac{\sqrt{E_b^2 - M_W^2}}{M_W} \Delta E_+$$

Several studies, see e.g. [5], have been made from the distribution of the generated

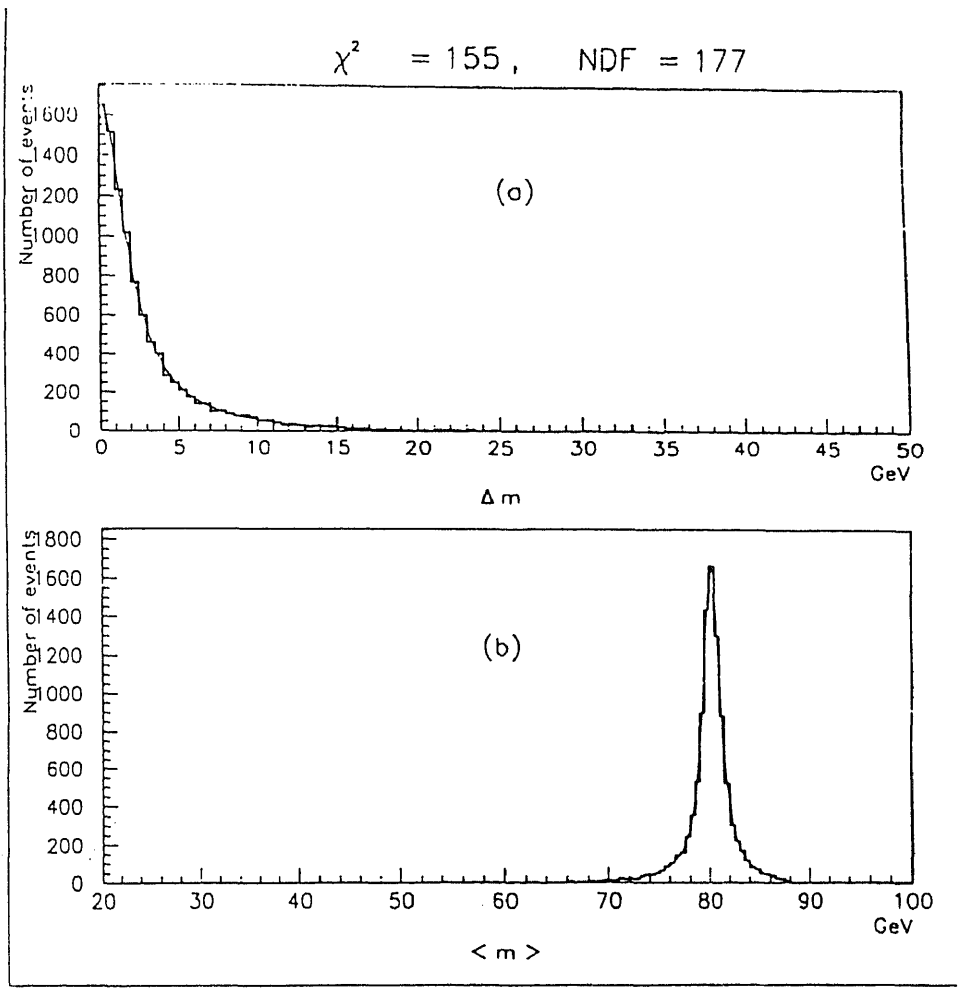

Figure 7. Δm and $< m >$ distributions. Solid lines are simultaneous fits to the two distributions.

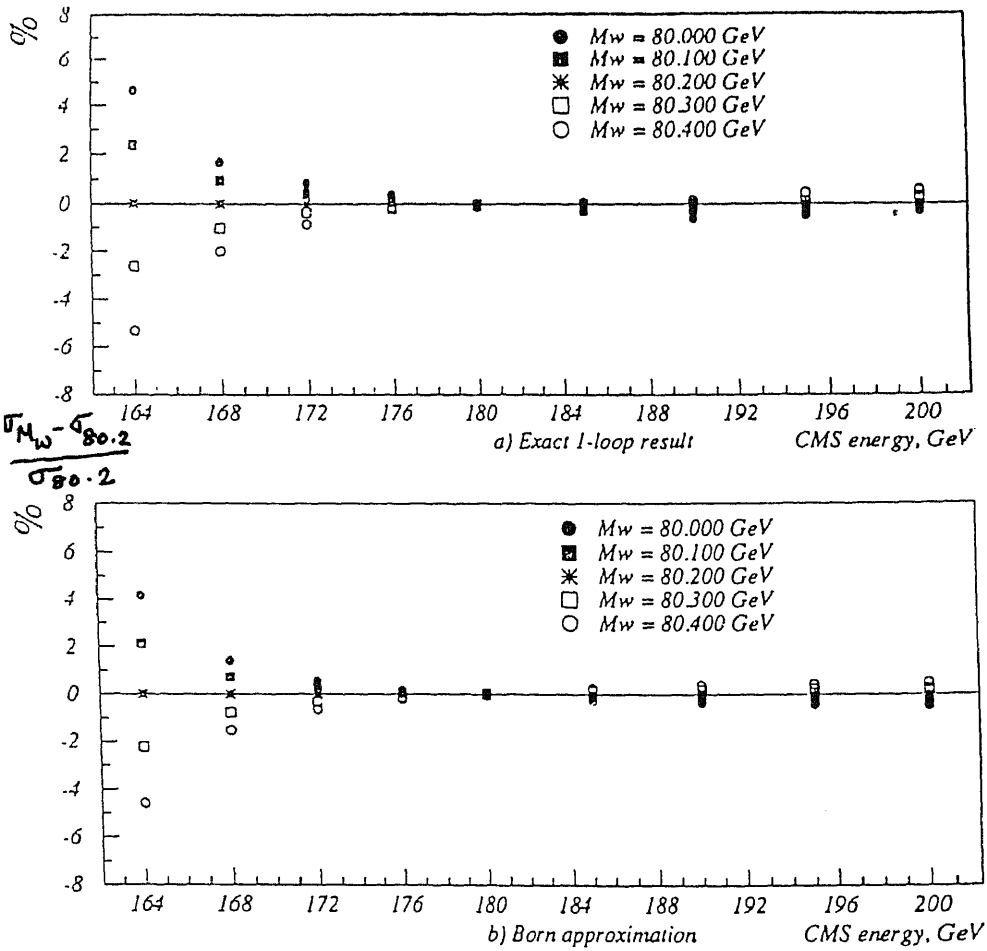

Figure 8. Fractional change in cross section as a function of $\sqrt{s}$. (a) Exact one loop result, and (b) Born approximation.

lepton energy and it is estimated, see fig.9, that the error on M_W from this metho
is expected to be,

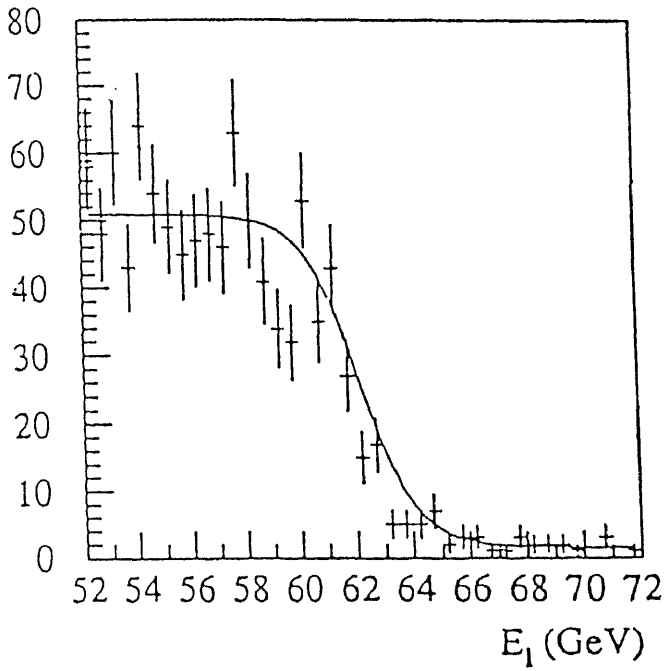

Figure 9. Lepton energy distribution from W$\rightarrow l\nu$.

$$\Delta M_W \approx 270\text{MeV}\sqrt{\frac{500\text{pb}^{-1}}{\epsilon\mathcal{L}}}$$

i.e., the error expected is more than 200 MeV.

14. Summary

- After a very useful run of physics at the Z^0 peak the reaction $e^+e^- \rightarrow W^+W^-$ will be studied at LEP200 starting from 1996.
- Longitudinal polarization of W will become available besides the transverse one
- The approved integrated luminosity is 500 pb^{-1} corresponding to $\simeq$ 8000 events
- **Aims of LEP200**
  - (a) Precision measurement of M_W and Γ_W
  - (b) Determination of Triple Gauge Boson couplings
  - (c) Search of New Particles
- Three methods have been studied regarding the measurement of M_W and Γ_W

[B] **Shape of the Excitation Curve**
[C] **Lepton end point energy**

Last two methods are not very useful.

- Precision expected for M_W is $\simeq 50$ MeV.
- Precision expected for Γ_W is $\simeq 100$ MeV.

References

[1] The LEP Collaborations: 'Updated parameters of the Z^0 resonance from combine preliminary data of the LEP experiments: CERN/PPE/93-157, 26 August 1993.

[2] Proceedings of the ECFA Workshop on LEP200, CERN 87-08: D.H.Perkins, pag 1; P.Roudeau et al., page 49; M.Davier et al., page 120.

[3] D.Treille, The LEP200 Programme: CERN-PPE 93-54, 26 March 1993.
L.Camilleri et al.: presentation at 1992 LEP200 Workshop, 2-4 November, 1992.

[4] Alitti et al.: CERN-PPE/91-208; CERN-PPE/91-162.
Abe et al.: Phys.Rev. D44(1991)29; Phys.Rev.Lett. 64(1990)152.
Albajar et al.: Phys.Lett. B253(1991)503.

[5] DELPHI Collaboration, D.Bardin et al.: DELPHI 92-166 PHYS 250(1992).

[6] L3 Collaboration, M.Acciarri et al.: CERN-PPE/94-45 March 1994.

[7] D.Bardin et al.: Phys.Lett. B308(1993)403.

[8] JADE Collaboration, W.Bartel et al.: Z.Phys. C33(1986)23.

[9] Y.Dokshizer: J.Phys. G17(1991)1441.

[10] S.Bethke et al.: Nucl.Phys. B370(1992)310.

[11] T.Sjostrand: Comp.Phys.Comm. 28(1983)227.

[12] S.L.Wu: Z.Phys. C9(1981)329.

[13] T.Muta et al.: Mod.Phys.Lett. A1(1986)203.

[14] O.Nicrosini and L.Trentadue: Phys.Lett. B196(1987)551.

[15] S.Banerjee, S.N.Ganguli, A.Gurtu and K.Sudhakar: TIFR/EHEP 94-4, April 199

[16] T.Aziz et al.: L3 Note #1474, August 28, 1993.

[17] S.N.Ganguli and K.Sudhakar: L3 Note #1496, September 17, 1993.

PRAMANA
journal of
physics

© Printed in India

Supplement to Vol. 45
October 1995
pp. 141-154

How good is the quenched approximation of QCD?

MAARTEN F. L. GOLTERMAN
Department of Physics, Washington University, St. Louis, MO 63130, U S A

Abstract. The quenched approximation for QCD is, at present and in the foreseeable future, unavoidable in lattice calculations with realistic choices of the lattice spacing, volume and quark masses. In this talk, I review an analytic study of the effects of quenching based on chiral perturbation theory. Quenched chiral perturbation theory leads to quantitative insight on the difference between quenched and unquenched QCD, and reveals clearly some of the diseases which are expected to plague quenched QCD.

1. Introduction

The lattice formulation of QCD has proven to be a powerful tool for computing QCD quantities of direct phenomenological interest, such as hadron masses, decay constants, weak matrix elements, the strong coupling constant, *etc.* (For reviews see for instance refs. [1, 2], or the proceedings of Lattice 93 [3].)

In order to perform such computations numerically, one obviously needs to consider a system with a finite number of degrees of freedom, which is accomplished by putting lattice QCD in a finite box. This box is then hopefully large enough to accomodate the physics one is interested in without serious finite size effects. This leads to the requirement that the Compton wavelength of the particles of interest is sufficiently smaller than the linear dimension of the box, *i.e.* the mass has to be large enough for the particles to fit in the box.

In order to have a small enough lattice spacing, small enough masses (in particular for the pion) and a large enough box size, one needs a large number of degrees of freedom in a numerical computation. It turns out that for QCD with realistic choices of the lattice spacing a, volume V and the quark masses (in particular the light quark masses), the presently available computational power is not adequate. The most severe problem comes from the fermion determinant, the logarithm of which is a very nonlocal part of the gluon effective action (specially for light quark masses). This nonlocality slows down the Monte Carlo algorithms dramatically.

In order to circumvent this problem, most numerical computations in lattice QCD have been done in the quenched approximation, in which one simply sets the fermion determinant equal to one [4]. This amounts to ignoring all fermion loops which occur in QCD correlation functions (except those put in by hand through the choice of operators on the external lines). While some handwaving arguments exist as to why this might not be unreasonable, the quenched approximation does

roughly inversely proportional to its mass, this error is expected to be particularly severe for quantities involving light quarks. It appears therefore that chiral perturbation theory ChPT maybe a useful tool for investigating the difference between quenched and unquenched ("full") QCD.

In this talk, I will review a systematic approach to the study of the quenched approximation through ChPT [5, 6, 7, 8]. There are two reasons why ChPT is useful in this context:

- It turns out that ChPT can be systematically adapted to describe the low energy sector of quenched QCD [6]. It will therefore give us nontrivial, quantitative information on the difference between quenched and full QCD.
- ChPT describes the approach to the chiral limit, and can be used for extrapolation of numerical results to small masses and large volumes. If these results come from quenched computations, one will of course need a quenched version of ChPT. (For finite volume ChPT, see refs. [9]. For quenched finite volume results, see refs. [6, 7].)

In this review, I will concentrate on the first point. I will first show how ChPT is developed for the quenched approximation, and then use it for a quantitative comparison between full and quenched QCD. The quantities that I will discuss are f_K/f_π [6, 8] and the octet baryon masses [10].

I will then address a number of theoretical problems that arise as a consequence of quenching. That such problems arise is no surprise, as quenching QCD mutilates the theory quite severely. It is however quite instructive to see what the detailed consequences are.

2. Systematic ChPT for quenched QCD

In this section I will outline the construction of a chiral effective action for the Goldstone boson sector of quenched QCD [6]. I will first introduce the formalism, and then show how it works in some examples. For early ideas on quenched ChPT, see ref. [11, 5].

We will start from a lagrangian definition of euclidean quenched QCD. (We will restrict ourselves entirely to the euclidean theory which can be defined by a pathintegral. Hamiltonian quenched QCD presumably does not exist.) To the usual QCD lagrangian with three flavors of quarks q_a, $a = u, d, s$, we add three ghost quarks $\tilde{q}_a$ with exactly the same quantum numbers and masses m_a, but with opposite, bosonic, statistics [11]:

$$\mathcal{L}_{\text{quarks}} = \sum_a \overline{q}_a(\not{D} + m_a)q_a + \sum_a \overline{\tilde{q}}_a(\not{D} + m_a)\tilde{q}_a, \tag{1}$$

where $\not{D}$ is the covariant derivative coupling the quark and ghost quarks to the gluon field. The gluon effective action produced by integrating over the quark- and ghost quarkfields vanishes, since the fermion determinant of the quark sector is exactly cancelled by that of the ghost sector. Note that the ghost quarks violate the spin-statistics theorem.

We will now assume that mesons are formed as (ghost) quark - (ghost) antiquark

breaking. The Goldstone particle spectrum of quenched QCD will then contain not only $q\bar{q}$, but also $\tilde{q}\bar{\tilde{q}}$, $q\bar{\tilde{q}}$ and $\tilde{q}\bar{q}$ bound states. We will denote this 36-plet by

$$\Phi \equiv \begin{pmatrix} \phi & \chi^\dagger \\ \chi & \tilde{\phi} \end{pmatrix} \sim \begin{pmatrix} q\bar{q} & q\bar{\tilde{q}} \\ \tilde{q}\bar{q} & \tilde{q}\bar{\tilde{q}} \end{pmatrix}. \tag{2}$$

Note that the fields χ and $\chi^\dagger$ describe Goldstone fermions.

The quenched QCD lagrangian (1) for vanishing quark masses has a much larger symmetry group than the usual $U(3)_L \times U(3)_R$ flavor group; it is invariant under the graded group $U(3|3)_L \times U(3|3)_R$ [6], where $U(3|3)$ is a graded version of $U(6)$ since it mixes the fermion and boson fields q and $\tilde{q}$. Writing an element U of $U(3|3)$ in block form as

$$U = \begin{pmatrix} A & C \\ D & B \end{pmatrix}, \tag{3}$$

the 3×3 matrices A and B consist of commuting numbers, while the 3×3 matrices C and D consist of anticommuting numbers.

We can now construct a low energy effective action for the Goldstone modes along the usual lines. We introduce the unitary field

$$\Sigma = exp(2i\Phi/f), \tag{4}$$

which transforms as $\Sigma \to U_L \Sigma U_R^\dagger$ with U_L and U_R elements of $U(3|3)$. Because we are dealing here with a graded group, in order to build invariants, we need to use the supertrace *str* and the superdeterminant *sdet* instead of the normal trace and determinant, with [12]

$$\begin{aligned} str(U) &= tr(A) - tr(B), \\ sdet(U) &= exp(str \log(U)) = det(A - CB^{-1}D)/det(B). \quad (strsdet) \end{aligned} \tag{5}$$

To lowest order in the derivative expansion, and to lowest order in the quark masses, the chiral effective lagrangian consistent with our graded symmetry group is

$$\mathcal{L}_0 = \frac{f^2}{8} str(\partial_\mu \Sigma \partial_\mu \Sigma^\dagger) - v\ str(\mathcal{M}\Sigma + \mathcal{M}\Sigma^\dagger), \tag{6}$$

where $\mathcal{M}$ is the quark mass matrix

$$\mathcal{M} = \begin{pmatrix} M & 0 \\ 0 & M \end{pmatrix}, \qquad M = \begin{pmatrix} m_u & 0 & 0 \\ 0 & m_d & 0 \\ 0 & 0 & m_s \end{pmatrix}. \tag{7}$$

f and v are bare coupling constants which are not yet determined at this stage.

The symmetry group is broken by the anomaly to the smaller group $[SU(3|3)_L \times SU(3|3)_R] \circledS U(1)$ (the semidirect product arises as a consequence of the graded nature of the groups involved; the details are irrelevant for this talk). $SU(3|3)$ consists of all elements $U \in U(3|3)$ with $sdet(U) = 1$. The anomalous field is $\Phi_0 = (\eta' - \tilde{\eta}')/\sqrt{2}$, where the relative minus sign comes from the fact that in order to get a nonvanishing triangle diagram, one needs to choose opposite explicit signs for the quark and ghost quark loops, due to the different statistics of these fields. η' is the field describing the normal η' particle, while $\tilde{\eta}'$ is the ghost η' consisting of ghost quarks and ghost antiquarks. We will call the field Φ_0 the super-η' field. The

and we should include arbitrary functions of this field in our effective lagrangian. Following ref. [13], the correct chiral effective lagrangian is

$$\begin{aligned}\mathcal{L} = \; & V_1(\Phi_0) str(\partial_\mu \Sigma \partial_\mu \Sigma^\dagger) - V_2(\Phi_0) str(\mathcal{M}\Sigma + \mathcal{M}\Sigma^\dagger) \\ & + V_0(\Phi_0) + V_5(\Phi_0)(\partial_\mu \Phi_0)^2, \end{aligned} \tag{8}$$

where the function multiplying $i\ str(\mathcal{M}\Sigma - \mathcal{M}\Sigma^\dagger)$ can be chosen equal to zero after a field redefinition. This lagrangian describes quenched ChPT systematically, as we will show now with a few examples.

For our first example, let us isolate just the quadratic terms for the fields η' and $\tilde{\eta}'$, choosing degenerate quark masses for simplicity. We expand

$$\begin{aligned} V_1(\Phi_0) &= \tfrac{f^2}{8} + \ldots, \\ V_2(\Phi_0) &= v + \ldots, \\ V_0(\Phi_0) &= \text{constant} + \mu^2 \Phi_0^2 + \ldots, \\ V_5(\Phi_0) &= \alpha + \ldots, \end{aligned} \tag{9}$$

and obtain

$$\begin{aligned}\mathcal{L}(\eta', \tilde{\eta}') = \; & \tfrac{1}{2}(\partial_\mu \eta')^2 - \tfrac{1}{2}(\partial_\mu \tilde{\eta}')^2 + \tfrac{1}{2}\alpha(\partial_\mu \eta' - \partial_\mu \tilde{\eta}')^2 \\ & + \tfrac{1}{2} m_\pi^2 (\eta')^2 - \tfrac{1}{2} m_\pi^2 (\tilde{\eta}')^2 + \tfrac{1}{2}\mu^2 (\eta' - \tilde{\eta}')^2 + \ldots, \end{aligned} \tag{10}$$

where $m_\pi^2 = 8mv/f^2$. The relative minus signs between the η' and $\tilde{\eta}'$ terms in (10) come from the supertraces in (8), and are related to the graded nature of the chiral symmetry group of quenched QCD.

The inverse propagator in momentum space,

$$(p^2 + m_\pi^2) \begin{pmatrix} 1 & 0 \\ 0 & -1 \end{pmatrix} + (\mu^2 + \alpha p^2) \begin{pmatrix} 1 & -1 \\ -1 & 1 \end{pmatrix}, \tag{11}$$

clearly cannot be diagonalized in a p independent way, which is quite different from what one would expect from a normal field theory! Treating the $\mu^2 + \alpha p^2$ term as a twopoint vertex, one can easily show that the repetition of this vertex on one meson line vanishes, due to the fact that the propagator matrix $\begin{pmatrix} 1 & 0 \\ 0 & -1 \end{pmatrix}$ multiplied on both sides by the vertex matrix $\begin{pmatrix} 1 & -1 \\ -1 & 1 \end{pmatrix}$ gives zero. This result coincides exactly with what one would expect from the quark flow picture for η' propagation, as depicted in fig. 1. The straight-through and double hairpin contributions do not contain any virtual quark loops, and are therefore present in the quenched approximation. All other contributions should vanish because they do contain virtual quark loops, and this is exactly what happens as a consequence of the (admittedly strange) Feynman rules for the propagator in the η'-$\tilde{\eta}'$ sector! This propagator is given by the inverse of (11) and reads

$$\frac{1}{p^2 + m_\pi^2} \begin{pmatrix} 1 & 0 \\ 0 & -1 \end{pmatrix} - \frac{\mu^2 + \alpha p^2}{(p^2 + m_\pi^2)^2} \begin{pmatrix} 1 & 1 \\ 1 & 1 \end{pmatrix}, \tag{12}$$

in which the two terms correspond to the two first diagrams in fig. 1.

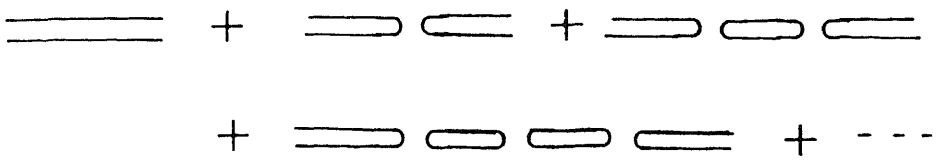

Figure 1. Quark flow diagrams for the η' propagator in full QCD

From (12) we learn several things. First, because μ^2, which in full ChPT would correspond to the singlet part of the η' mass, appears in the numerator, we need to keep the η' (and its ghost partner) in quenched ChPT: it cannot be decoupled by taking μ^2 large. Second, this "propagator" is definitely sick, due to the double pole term. It should be stressed here that this double pole term is an unescapable consequence of quenched QCD, and does not result from our way of setting up chiral perturbation theory. In the case of nondegenerate quark masses, this double pole also shows up in the π^0 and η propagators, due to mixing with the η'. I will return to these strange properties of quenched QCD in section 4.

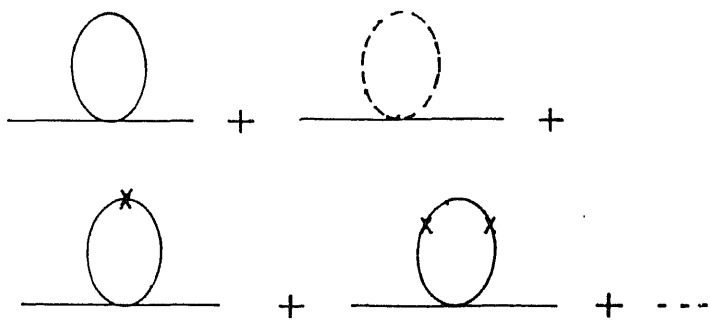

Figure 2. One loop pion selfenergy in quenched ChPT.

As a second example, we will consider the (charged) pion selfenergy at one loop, again with degenerate quark masses. I will set $\alpha = 0$ for simplicity. At one loop, the pion selfenergy only contains tadpoles, with either ϕ or χ lines (*cf.* (2)) on the loop. Also, on the ϕ loop, one can have an arbitrary number of insertions of the vertex μ^2 if the internal ϕ line is an $SU(3)$ singlet. These various contributions are drawn in fig. 2, where a solid line denotes a ϕ line, a dashed line denotes a χ line, and a cross denotes a μ^2 vertex. One finds that the diagrams with the ϕ and χ lines on the loop without any crosses cancel, and then, of course, that the diagrams with more than one cross vanish, using our earlier result for the η'–$\tilde{\eta}'$ propagator. We are left with only one term, and the result is

$$\Sigma_\pi(p) = \frac{2m_\pi^2}{3f^2}\mu^2 \int \frac{d^4k}{(2\pi)^4}\frac{1}{(k^2+m_\pi^2)^2}. \tag{13}$$

The pion selfenergy is logarithmically divergent, but the origin of this divergence is completely different from those that arise in the unquenched theory, as it is proportional to μ^2. One can easily convince oneself that the diagrams in fig. 2 which

aspect of the chiral expansion in quenched ChPT. The chiral expansion is basically an expansion in the pion mass (see *e.g.* ref. [14]). However, as we have argued above, in quenched ChPT there is unavoidably another mass scale, namely the singlet part of the η' mass, μ^2. For our expansion to be systematic as an expansion in the pion mass, we would have to sum up all orders in μ^2, at a fixed order in the pion mass. This is clearly a formidable task. In order to avoid this complication in a systematic way, we can think of $\mu^2/3$ (which turns out to be the natural parameter as it appears in the chiral expansion) as an independent small parameter. To check whether this makes any sense, one may note that from the experimental value of the η' mass one obtains a value $\mu^2/3 \approx (500\ MeV)^2$, which is roughly equal to the kaon mass squared, m_K^2. Of course, for quenched QCD the parameter μ^2 need not have the same value, after all quenched QCD is a different theory. A lattice computation of this parameter [15] gives $\mu^2_{\rm quenched}/\mu^2_{\rm full} \approx 0.75$. ($\alpha$ can be estimated from η–η' mixing, and is very small.) Finally, one may also note that both μ^2 and α are of order $1/N_c$, where N_c is the number of colors [16]. I will return to this point in section 4.

3. Quantitative comparison of quenched and full ChPT

Let us first consider the quenched result for the ratio of the kaon and pion decay constants f_K and f_π [6, 8]. I will set $\alpha = 0$ and take $m_u = m_d \equiv m$:

$$\left(\frac{f_K}{f_\pi}\right)^{\rm 1-loop}_{\rm quenched} = 1 + \frac{\mu^2/3}{16\pi^2 f_\pi^2}\left[\frac{m_K^2}{2(m_K^2 - m_\pi^2)}\log\left(\frac{2m_K^2}{m_\pi^2} - 1\right) - 1\right] + (m_s - m)L. \quad (14)$$

L is a certain combination of "low energy constants" [13]. Since this constant is a bare parameter of the quenched chiral lagrangian, the result (14) is not directly comparable to the equivalent result for the full theory. In other words, in order to compare quenched and full QCD, we have to consider quantities which are independent of the bare parameters of the effective action. (Alternatively, we would need to extract the values of the bare parameters from some independent measurement or lattice computation, in this case, we would need independent determinations of L in both quenched and full QCD.) In the full theory, $(f_\eta f_\pi^{1/3})/f_K^{4/3}$ is such a quantity [13], but in the quenched theory this quantity is not well defined, due to the double poles which occur in the propagators of neutral mesons.

We will therefore choose to consider a slightly different theory, in which sufficiently many decay constants referring only to charged (*i.e.* off-diagonal) mesons are present [8]. This theory is a theory with two light quarks $m_u = m_d = m$ and two heavy quarks $m_s = m_{s'} = m'$. This theory contains a $u\bar{d}$ pion π, an $s'\bar{s}$ pion π' and a $u\bar{s}$ kaon K, with mass relation

$$m_K^2 = \frac{1}{2}(m_\pi^2 + m_{\pi'}^2). \quad (15)$$

One can show that the ratio $f_K/\sqrt{f_\pi f_{\pi'}}$ is independent of the low energy constants L. For the quenched theory we find

$$\left(\frac{f_K}{\sqrt{f_\pi f_{\pi'}}}\right)^{1-\text{loop}}_{\text{quenched}} = 1 + \frac{\mu^2/3}{16\pi^2 f_\pi^2}\left[\frac{m_\pi^2 + m_{\pi'}^2}{2(m_{\pi'}^2 - m_\pi^2)}\log\left(\frac{m_{\pi'}^2}{m_\pi^2}\right) - 1\right], \tag{16}$$

whereas in the full theory

$$\left(\frac{f_K}{\sqrt{f_\pi f_{\pi'}}}\right)^{1-\text{loop}}_{\text{full}} = 1 - \frac{1}{64\pi^2 f_\pi^2}\left[m_\pi^2 \log\left(\frac{m_K^2}{m_\pi^2}\right) + m_{\pi'}^2 \log\left(\frac{m_K^2}{m_{\pi'}^2}\right)\right]. \tag{17}$$

Note again that the logarithms in the quenched and unquenched expressions are completely different in origin.

We may now compare these two expressions using "real world" data, where we'll determine the value of the π' mass from the mass relation (15). With $m_\pi = 140\ MeV$, $m_K = 494\ MeV$ and $\mu^2/3 = 0.75 \times (500\ MeV)^2$ we find

$$\begin{aligned}\left(\frac{f_K}{\sqrt{f_\pi f_{\pi'}}}\right)^{1-\text{loop}}_{\text{quenched}} &= 1.049,\\ \left(\frac{f_K}{\sqrt{f_\pi f_{\pi'}}}\right)^{1-\text{loop}}_{\text{full}} &= 1.023,\end{aligned} \tag{18}$$

a difference of 3%. If we choose $\mu^2/3 = (500\ MeV)^2$, we find a difference of about 4%. This difference is small. Note however, that this is due to the fact that for this particular ratio, ChPT seems to work very well, both for the full and the quenched theories. If one only considers the size of the one loop corrections (the numbers behind the decimal point), the quenched and full results are very different. It is also possible, and in fact not unlikely, that part of the difference between the full and quenched theory gets "washed out" by the fact that we are considering a "ratio of ratios". It follows that the relative difference is a lower bound on the difference between the quenched and full values of the decay constants. For another quantity for which the difference between quenched and full ChPT has been calculated, see ref. [8].

Next, I will review some very recent work on baryons in quenched ChPT by Labrenz and Sharpe [10]. They calculated the one loop corrections to the octet baryon mass coming from the cloud of Goldstone mesons. They employed an effective lagrangian for quenched heavy baryon ChPT, constructed using the same techniques as described in section 2. In the case of degenerate quark masses, the result for the nucleon mass is

$$\begin{aligned} m_N = \quad & \overline{m} - \tfrac{3\pi}{2}(D-3F)^2 \tfrac{\mu^2/3}{8\pi^2 f_\pi^2} m_\pi + 2(b_D - 3b_F)m_\pi^2 \\ & + \left[\tfrac{2}{3}(D-3F)(2D+3\gamma) + \tfrac{5}{6}\alpha(D-3F)^2\right] \tfrac{m_\pi^3}{8\pi f_\pi^2}. \end{aligned} \tag{19}$$

In this equation, $\overline{m}$, D, F, b_D, b_F and γ are bare parameters which occur in the baryon effective action. $\overline{m}$ is the bare "average" octet mass, D and F are the well known baryon-meson couplings, b_D and b_F are low energy constant which arise

a cross on the ϕ internal line, *i.e.* an insertion of the μ^2 twopoint vertex. Note that in this case there are also one loop corrections not involving μ^2 which survive the quenched approximation, in contrast to the pion selfenergy, (13), or f_K/f_π, (14). The authors of ref. [10] then calculated the coefficients using full QCD values for the various parameters (from ref. [19]). With $\alpha = 0$ and $\gamma = 0$ ($\gamma = 0$ is consistent with available information, which however is limited [17]), they obtained

$$m_N = 0.97 - 0.5\frac{\delta}{0.2}m_\pi + 3.4m_\pi^2 - 1.5m_\pi^3, \tag{20}$$

with $\delta \equiv \mu^2/(24\pi^2 f_\pi^2)$ and $\delta \approx 0.2$ for the full theory.

In ref. [10], (19) was also compared to recent numerical results from ref. [20]. These data are presented in fig. 3, where the scale $a^{-1} = 1.63\ GeV$ is set by f_π [10]. If one calculates the coefficients in (19) by "fitting" the four data points, one finds

$$m_N = 0.96 - 1.0m_\pi + 3.6m_\pi^2 - 2.0m_\pi^3. \tag{21}$$

This is only four data points for four parameters, and the "fit" is quite sensitive to for instance an additional m_π^4 term. From the agreement between (20) and (21) it appears that it is reasonable to apply ChPT to the results of ref. [20]. Note that the individual terms in (20) are quite large for the two higher pion masses in fig. 3 (this is not unlike the case of unquenched ChPT). From fig. 3 it is also clear that $(\overline{m}/f_\pi)_{\text{quenched}} \neq (\overline{m}/f_\pi)_{\text{full}}$ because of the term linear in (19), which is absent in full ChPT.

Labrenz and Sharpe then went on to consider octet mass splittings. In order to remove effects which can be accomodated by a change of scale, they calculated the ratios

$$R_{ij} = \frac{m_i}{m_j}, \quad i,j = N, \Lambda, \Sigma, \Xi \tag{22}$$

in quenched ChPT, and compared these with similar ratios obtained from ref. [19]. They assumed that all bare parameters in the equations for the octet masses (for explicit expressions, see their paper) are equal in the full and quenched theory, and then calculated the ratios

$$r_{ij} = \frac{R_{ij}^{\text{quenched}}}{R_{ij}^{\text{full}}}. \tag{23}$$

With the assumption that the bare parameters of the quenched and full theories are equal, b_D and b_F drop out of the ratios, and with $\gamma = 0$, $\alpha = 0$ and D and F equal to their full QCD values, they obtain

$$\begin{aligned} r_{\Sigma N} &= 1 + 0.19(\delta/0.2) + 0.13 = 1.31[1.27] \text{ for } \delta = 0.2[0.15], \\ r_{\Xi N} &= 1 - 0.46(\delta/0.2) + 0.43 = 0.97[1.09] \text{ for } \delta = 0.2[0.15], \\ r_{\Lambda N} &= 1 - 0.39(\delta/0.2) + 0.26 = 0.87[0.97] \text{ for } \delta = 0.2[0.15]. \end{aligned} \tag{24}$$

(The choice $\delta = 0.15$ corresponds to the value reported in ref. [15].)

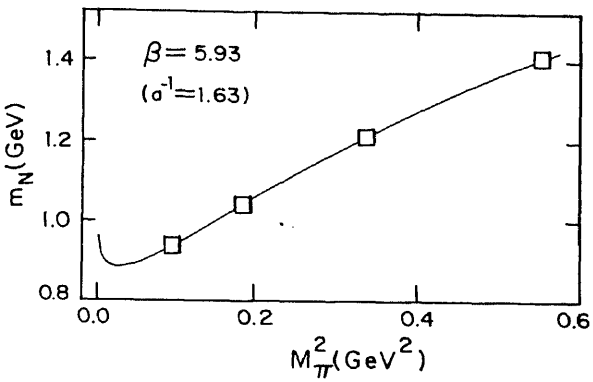

Figure 3. The nucleon mass from the lattice [20] (copied from ref. [10]). The curve is from a fit to the form $m_N = \overline{m} + am_\pi + bm_\pi^2 + cm_\pi^3$.

From this, one would conclude that one can expect errors from quenching of at least 20% in the octet splittings. These differences between the quenched and full theories cannot be compensated for by a change in scale between quenched and full QCD.

At this point I would like to comment on the above mentioned assumption that was used in order to obtain (24). Let us consider in particular the parameters b_D and b_F. They correspond to higher derivative terms in the baryon-meson effective action, and are needed in order to absorb the UV divergences which arise at one loop in ChPT. Since the size of these divergences is in principle different between the full and quenched theories, one expects that $b_{D,\text{quenched}}$ and $b_{F,\text{quenched}}$ can be different from $b_{D,\text{full}}$ and $b_{F,\text{full}}$. If we want to proceed without assuming that the quenched and full b's are equal, we have to consider ratios of quantities independent of the parameters b_D and b_F. The situation is essentially the same as in the case of f_K/f_π. From the available results [10], only one ratio independent of b_D and b_F can be formed:

$$X = \frac{m_\Sigma m_\Lambda^3}{m_N^2 m_\Xi^2}. \tag{25}$$

deviation from the Gell-Mann–Okubo formula (*cf.* ref. [19] for the full theory).

Setting $m_\pi = 0$ keeping only m_K as in ref. [10], one finds

$$X_{\text{quenched}} = 1 - 1.1046\frac{m_K^3}{8\pi\overline{m}f_\pi^2}\left(D^2-3F^2\right) + 1.3333\delta\frac{\pi m_K}{\sqrt{2}\overline{m}}\left(D^2-3F^2\right),$$
$$X_{\text{full}} = 1 - 0.4125\frac{m_K^3}{8\pi\overline{m}f_\pi^2}\left(D^2-3F^2\right). \tag{26}$$

(The parameter γ drops out of this particular combination and we again take $\alpha = 0$.) These quantities still depend on the other bare parameters, D, F and $\overline{m}$. Again, they could be different in the quenched and full theories, and I will leave the quenched values as free parameters. Substituting $m_K = 495\ MeV$, $f_\pi = 132\ MeV$, $D_{\text{full}} = 0.75$, $F_{\text{full}} = 0.5$ and $\overline{m}_{\text{full}} = 1\ GeV$ [19] finally gives

$$\frac{X_{\text{quenched}}}{X_{\text{full}}} = 1 - 0.0214 + \left[0.293\frac{\delta}{0.2} - 0.306\right]\frac{\left(D^2-3F^2\right)_{\text{quenched}}}{\overline{m}_{\text{quenched}}/1\ GeV}. \tag{27}$$

For any reasonable values of $\overline{m}$ and δ, and for $\left(D^2-3F^2\right)_{\text{quenched}}$ not too far from its full theory value of -0.1875, the difference between the quenched and full theories as measured by the ratio $X_{\text{quenched}}/X_{\text{full}}$ is not more than a few percent. Of course the same comment that applied in the case of f_K/f_π applies here, that part of the difference may have been washed out by taking "ratios of ratios". Summarizing, the conclusion of this analysis seems to be that the error from quenching for octet baryon masses is at least a few percent, and could be as much as 20%.

4. A sickness of quenched QCD

Let us again consider the quenched result for f_K/f_π, (14), as a function of the quark masses (using treelevel relations between meson masses and quark masses),

$$\left(\frac{f_K}{f_\pi}\right)^{1-\text{loop}}_{\text{quenched}} = 1 + \frac{\mu^3/3}{16\pi^2 f_\pi^2}\left[\frac{m_u+m_s}{2(m_s-m_u)}\log\frac{m_s}{m_u} - 1\right] + (\text{L}-\text{terms}).$$

From this expression it is clear that we cannot take $m_u \to 0$ keeping m_s fixed, or, to put it differently, that if we take both m_u and m_s to zero keeping the ratio fixed, the limit depends on this ratio, and is not equal to one! This is quite unlike the case of full ChPT, where one can take any quark mass to zero uniformly, and deviations from $SU(3)$ symmetry due to this quark mass vanish in this limit. Technically, the reason for this strange behavior is that there is another mass μ, which, as we argued before, cannot be avoided in quenched ChPT. This mass is related to the singlet part of the η' mass, and is not a free parameter of the theory. Even if we do not consider any Green's functions with η' external lines, this mass shows up through the double pole term in 12 on internal lines. Because of the double pole, such contributions can lead to new infrared divergences in the $m_\pi \to 0$ limit. This problem with the chiral limit of quenched ChPT shows up in other quantities, such as meson masses and $\langle\bar{\psi}\psi\rangle$ [6, 7, 21].

A question one might ask is whether this problem is an artifact of one loop quenched ChPT [8]. For instance, if we would sum all contributions to the η'

improving the infrared behavior of diagrams in which the double pole terms appear. Let us address this question in the chiral limit, $m_a = 0$, where the problem is most severe. In the full theory, we can write the fully dressed η' propagator as

$$\frac{Z(p)}{p^2 + \Sigma(p)}, \tag{28}$$

and define $\mu_F^2(p) = \Sigma(p)$, which onshell is the η' mass in the chiral limit. Likewise, in the quenched theory we can write the dressed η', $\tilde{\eta}'$ propagator as

$$Z_Q(p)\left[\frac{1}{p^2}\begin{pmatrix}1 & 0\\ 0 & -1\end{pmatrix} - \frac{\mu_Q^2(p)}{(p^2)^2}\begin{pmatrix}1 & 1\\ 1 & 1\end{pmatrix}\right], \tag{29}$$

which defines $\mu_Q^2(p)$. To leading order in $1/N_c$, these two definitions of $\mu^2(p)$ should lead to the same result:

$$\mu_Q^2(p) = \mu_F^2(p)\left(1 + O\left(\frac{1}{N_c}\right)\right). \tag{30}$$

We also believe that $\mu_F^2(p=0)$ is not equal to zero, since we expect the η' to remain a well-behaved, massive particle in the chiral limit. This implies, in sofar as we can rely on the large N_c expansion, that $\mu_Q^2(0) \neq 0$, and that the double pole in (12) is a true feature of the theory.

While this argument is not very rigorous, I believe that the foregoing discussion implies that the chiral limit of quenched QCD really does not exist. This believe is futhermore supported by the following remarks:

- Sharpe [7] has summed a class of diagrams in the case of degenerate quark masses for a very simple quantity (the pion mass), and found a result that is actually more divergent than the one loop result.
- With nondegenerate quark masses there are many more diagrams that are infrared divergent in the chiral limit, and it is even less probable that resummation will improve the situation.
- Any mechanism improving the infrared behavior would have to work for each divergent quantity. One expects that such a mechanism would be related to the double pole term in the η' propagator, which created the problem in the first place. But this seems unlikely in view of the arguments given above.
- The bare quark mass parameter appearing in the chiral effective action is not the same as that appearing in the (unrenormalized) QCD lagrangian. But one can argue that the two bare quark masses should be analytically related, and the infrared problem is not just a problem of quenched ChPT, but of quenched QCD.

5. Conclusion

The quenched approximation leads to an unknown systematic error in all lattice calculations that employ this approximation. It would of course be very nice to have a parameter that interpolates between full and quenched QCD, and in principle the quark masses could play such a role, since one expects that quenched QCD corresponds to full QCD with very heavy quarks. One would have to distinguish

Quenched QCD can be defined from a euclidean pathintegral as rigorously as full QCD. In this talk I have explained that euclidean quenched ChPT can be used as a tool for a systematic investigation of quenched QCD. Quenched ChPT does not quite accomplish a task equivalent to that of an interpolating parameter. Since the bare parameters appearing in the quenched and full chiral effective actions are not the same (as explained in section 3) one cannot directly compare quantities calculated in full and in quenched ChPT. However, one can calculate combinations of physical quantities which do not depend on the bare parameters, and in that case a direct comparison between quenched and full QCD is possible, as we demonstrated with an example involving meson decay constants. This makes it possible to estimate lower bounds on the differences which come from quenching; these estimates are dependent on the values of the meson masses, which can be taken to be the (known) independent parameters of the theory. For realistic values of these masses, such differences turn out to be of the order of a few percent for ratios of decay constants and for baryon octet splittings.

The disadvantage of this more conservative approach is that part of the difference maybe hidden, because these specific combinations of physical quantities maybe less sensitive to the effects of quenching than other quantities of interest. This is particularly clear in the example of baryon octet masses. In this case, a comparison based on the assumption that the bare parameters of the full and quenched effective theories are the same, lead to differences of up to 20% and more. Of course, it is not known to what extend this assumption is valid.

The differences between the quenched and full theories become markedly larger for decreasing quark masses. This is due to the fact that new infrared divergences occur in quenched QCD, which do not have a counterpart in full QCD. These divergences lead to the nonexistence of the chiral limit for quenched ChPT (as discussed in section 4). The origin of this phenomenon can be traced to the special role of the η' in the quenched approximation. In the quenched approximation, the η' is a Goldstone boson (it develops massless poles in the chiral limit), but an additional double pole term arises in its propagator, rendering it a "sick" particle. For nondegenerate quark masses this problem is also inherited by the π^0 and the η. In section 4 I argued that the nonexistence of the chiral limit is a fundamental feature of quenched QCD.

In principle therefore, the chiral expansion breaks down for quenched QCD. For very small quark masses, at fixed values of the singlet part of the η' mass μ^2, the expansion becomes unreliable. In order to make progress, one may take the expansion to be an expansion in $\mu^2/3$ (which was shown to be roughly equal to m_K^2 phenomenologically), with coefficients which are functions of the quark mass. These functions then can be expanded in terms of the quark masses, sometimes leading to divergent behavior of the leading term (*e.g.* the one loop correction to f_K/f_π). If such divergences occur, the expansion is only valid for a range of quark masses which are neither too small, nor too large. It would be interesting to see whether this point of view can be made solid.

It is in principle interesting to study any quantity which is being computed in

(meson masses, decay constants, condensates and the kaon B parameter have been calculated [6, 5, 8]). As discussed, this includes not only Goldstone meson physics *per se*, but also chiral corrections to baryon masses [10], and for the same reason, to mesons containing heavy quarks.

Recently, also attempts have been made to compute pion and nucleon scattering lengths [23, 24] from quenched lattice QCD. If one tries to calculate the $I = 0$ pion scattering amplitude in quenched ChPT, one actually finds that the imaginary part is divergent at threshold, even for nonvanishing pion mass [25]! Again, this can be related to double pole terms in the η' propagator. An additional reason is that apparently euclidean quenched correlation functions in general cannot be analytically continued to Minkowski space-time. (The euclidean four pion correlation functions are well defined.) Further work is needed on pion scattering lengths.

Acknowledgements

First, I would like to thank Claude Bernard for a pleasant collaboration, and for very many discussions. I also thank Steve Sharpe, Jim Labrenz, Akira Ukawa, Hari Dass, Julius Kuti and Don Weingarten for discussions. I am grateful for the opportunity to present this talk given to me by the organizers of WHEPP III, Madras, India, 1994. Finally, I thank the Institute of Mathematical Sciences in Madras, and in particular Hari Dass, for hospitality. This work is supported in part by the Department of Energy under contract #DOE-2FG02-91ER40628.

References

[1] S.R. Sharpe, in *The Fermilab Meeting*, 7th meeting of the DPF, eds. C.H. Albright, P.H. Kasper, R. Raja and J. Yoh, World Scientific, 1993.

[2] P.B. Mackenzie, preprint FERMILAB-CONF-93-343-T, to be published in the proceedings of the 16th International Symposium on Lepton and Photon Interactions, 1993, hep-ph/9311242; A.S. Kronfeld and P.B. Mackenzie, Ann. Rev. Nucl. Part. Phys. **43** (1993) 793.

[3] Lattice'93, proceedings of the International Symposium on Lattice Field Theory, Dallas, Texas, 1993.

[4] H. Hamber and G. Parisi, Phys. Rev. Lett. **47** (1981) 1792; E. Marinari, G. Parisi and C. Rebbi, Phys. Rev. Lett. **47** (1981) 1795; D.H. Weingarten, Phys. Lett. **109B** (1982) 57.

[5] S.R. Sharpe, Phys. Rev. **D41** (1990) 3233; Nucl. Phys. **B** (Proc.Suppl.) **17** (1990) 146; G. Kilcup *et al.*, Phys. Rev. Lett. **64** (1990) 25; S.R. Sharpe, DOE/ER/40614-5, to be published in *Standard Model, Hadron Phenomenology and Weak Decays on the Lattice*, ed. G. Martinelli, World Scientific.

[6] C.W. Bernard and M.F.L. Golterman, Phys. Rev. **D46** (1992) 853; Nucl. Phys. **B** (Proc.Suppl.) **26** (1992) 360.

[7] S.R. Sharpe, Phys. Rev. **D46** (1992) 3146; Nucl. Phys. **B**(Proc.Suppl.) **30** (1993) 213.

[8] C.W. Bernard and M.F.L. Golterman, Nucl. Phys. **B**(Proc.Suppl.) **30** (1993) 217.

[9] J. Gasser and H. Leutwyler, Phys. Lett. **184B** (1987) 83,Phys. Lett. **188B** (1987) 477, and Nucl. Phys. **B307** (1988) 763; H. Leutwyler, Nucl. Phys. **B** (Proc.Suppl.) **4** (1988) 248 and Phys. Lett. **189B** (1987) 197; H. Neuberger, Nucl. Phys. **B300** (1988) 180; P. Hasenfratz and H. Leutwyler, Nucl. Phys. **B343** (1990) 241.

[12] For a description of the properties of graded groups, see for example, B. DeWitt, *Supermanifolds*, Cambridge, 1984.

[13] J. Gasser and H. Leutwyler, Nucl. Phys. **B250** (1985) 465.

[14] S. Weinberg, Physica **96A** (1979) 327.

[15] Y. Kuramashi, M. Fukugita, H. Mino, M. Okawa and A. Ukawa, preprint KEK-CP-13, 1994; preprint KEK-CP-010, to be published in the proceedings of the International Symposium on Lattice Field Theory, Dallas, Texas, 1993, hep-lat/9312016.

[16] E. Witten, Nucl. Phys. **B156** (1979) 269; G. Veneziano, Nucl. Phys. **B159** (1979) 213.

[17] T. Hatsuda, Nucl. Phys. **B329** (1990) 376; S.R. Sharpe, private communication.

[18] E. Jenkins and A. Manohar, Phys. Lett. **255B** (1991) 558; E. Jenkins, Nucl. Phys. **B368** (1992) 190.

[19] V. Bernard, N. Kaiser and U. Meissner, Z. Phys. **C60** (1993) 111.

[20] F. Butler, H. Chen, J. Sexton, A. Vaccarino and D. Weingarten, Phys. Rev. Lett. **70** (1993) 2849; Nucl. Phys. **B** (Proc.Suppl) **30** (1993) 377.

[21] M.F.L. Golterman and N.D. Hari Dass, in preparation.

[22] C.W. Bernard and M.F.L. Golterman, Phys. Rev. **D49** (1994) 486; preprint WASH-U-HEP-93-61, to be published in the proceedings of the International Symposium on Lattice Field Theory, Dallas, Texas, 1993, hep-lat/9311070.

[23] R. Gupta, A. Patel and S.R. Sharpe, Phys. Rev. **D48** (1993) 388.

[24] Y. Kuramashi, M. Fukugita, H. Mino, M. Okawa and A. Ukawa, Phys. Rev. Lett. **71** (1993) 2387.

[25] C.W. Bernard, M.F.L. Golterman, J.N. Labrenz, S.R. Sharpe and A. Ukawa, preprint Wash. U. HEP/93-62, to be published in the proceedings of the International Symposium on Lattice Field Theory, Dallas, Texas, 1993.

physics

pp. 155-171

Polarised structure functions

D. INDUMATHI

Physical Research Laboratory, Navrangpura, Ahmedabad 380 009.

Abstract. This talk discusses the current understanding in some aspects of polarised lepton–nucleon deep inelastic scattering. The first section focuses on the non-singlet part of available spin dependent structure function data. The results, though consistent with theoretical predictions in this sector, are extremely sensitive to extrapolation of the data to the $x \rightarrow 1$ region and seem to indicate that the quarks *do* carry a very small fraction of the nucleon spin. We then review the formalism of DIS processes with emphasis on the gluon sector.

In this talk we focus on some aspects of polarisation phenomena in deep inelastic scattering (DIS) of high energy leptons (e, μ) off a nucleon target through virtual photon exchange. The energy involved in the process is such that the target completely breaks up. The debris remains unobserved; only the lepton is detected after the collision (its energy and angle of scattering). If both the initial particles are polarised (here, longitudinally, along the beam axis), then the lepton probes the internal spin structure of the nucleon. Hence such experiments can shed light on the distribution of the nucleon spin in terms of that of its component partons (quarks and gluons).

Section 1 discusses the current data and the phenomenology of polarised DIS with emphasis on the nonsinglet sector. While the data turn out to be consistent with theoretical expectations in this sector, the total contribution of quarks to the spin of the proton is small. There is thus a possibly significant gluon contribution to the proton spin. Section 2 therefore addresses the question of the gluonic contribution to the polarised DIS cross section. This section is basically a pedagogical review of the formalism of such processes. We establish that the gluon contribution to the spin of the proton is well defined, though it *cannot* be extracted from data in polarised DIS.

1. Polarised Deep Inelastic Scattering

1.1 The Formalism

The European Muon Collaboration (EMC) measured the asymmetry with respect to the polarised μp Deep Inelastic Scattering (DIS) cross sections when the muon and proton spins were parallel and antiparallel respectively. Theoretically, this asymmetry is given in terms of the spin dependent and spin independent proton

structure functions, g_1 and F_1, as,

$$A_1^p(x) = \frac{g_1^p(x)}{F_1^p(x)} \, .$$

Here, x, as usual, is the Bjorken scaling variable, $x = Q^2/(2p \cdot q)$, where $Q^2 = -q^2$, p and q are the 4-momenta of the virtual photon and the proton in the DIS process and $0 < x \leq 1$. The SMC and E142 measured the asymmetries,

$$A_1^D(x) = \frac{g_1^D(x)}{F_1^D(x)} \, , \qquad A_1^n(x) = \frac{g_1^n(x)}{F_1^n(x)} \, ,$$

where the quantities are correspondingly defined for the deuteron and neutron. The spin dependent structure functions are then extracted as the denominators are known. These structure functions are a measure of the distribution of the nucleon spin in terms of that of the partons.

There are other structure functions occurring not only in polarised DIS experiments but also in other processes such as Drell Yan in polarised pp collisions. These have recently been the subject of intense study. For want of adequate time, however, we do not discuss them here [1].

The structure functions of interest can be expressed in terms of parton densities (to leading order) as

$$F_1^p(x) \;=\; \frac{1}{2} \sum_f e_f^2 q(x) \qquad\qquad g_1^p(x) \;=\; \frac{1}{2} \sum_f e_f^2 \tilde{q}_f(x) \, ,$$

where the summation runs over both quark as well as antiquark flavours and q and $\tilde{q}$ are the spin summed and spin dependent quark densities. x is then interpreted as the fraction of nucleon momentum carried by that parton. The Bjorken sum rule relates the moments of the proton and neutron spin dependent structure functions. To $\mathcal{O}(\alpha_s)$, we have

$$\int_0^1 (g_1^p(x) - g_1^n(x)) \, \mathrm{d}x = \frac{g_A}{6} \left(1 - \frac{\alpha_s}{\pi}\right) \, .$$

Note that higher order (through $\mathcal{O}(\alpha_s)^3$) corrections have been calculated and are less than 2% at the scale of interest, $Q^2 = 5$ GeV^2.

1.2 The data

The five year old data on the spin dependent proton structure function [2] has recently been augmented by data from the Spin Muon Collaboration (SMC) [3] and the E142 Collaboration [4] on spin dependent deuteron and neutron structure functions respectively.

The new information gained from these experiments is in the non-singlet sector since these experiments probe three different combinations of the two (u and d) valence densities in a nucleon. In fact, the problem is over specified. Hence we can get stringent bounds not only on the Bjorken Sum Rule [5] (which involves moments of non-singlet densities) but also on the x-dependence of these non-singlet densities.

equations, i.e., the x-dependent unpolarised structure functions, F_1.

Recent data in the unpolarised sector from both NMC [6] and HERA [7] have radically changed our understanding of the small-x behaviour of spin independent structure functions [8]. This will affect the extraction of the spin dependent functions from the asymmetry data. The EMC used the old EMC F_2 data and obtained F_1 by setting the ratio, R (of longitudinal to transverse photoproduction cross sections), to zero while the E142 collaboration used their older F_2 and R data. (Specifically, $F_1 = F_2/(2x(1+R))$.) The NMC have used their own current F_2 data as well as corrected for non-zero R. Furthermore, all the experiments are at different average Q^2 values. Table 1 shows the results as announced by the various groups, in comparison with theoretical predictions.

Table 1. The results of various polarised DIS experiments: the moment of g_1 vs the Ellis Jaffe [9] prediction and the total quark contribution ($2\Delta\Sigma \equiv \Delta u + \Delta d + \Delta s$) to the proton spin are listed. Also shown are the Bjorken Sum Rule [5] computations using two data sets at a time.

Collab. & Target(Q^2)	$\int g_1 dx$ measured/EJSR	$2\,\Delta\Sigma$
EMC p(10GeV^2)	$0.126 \pm 0.01 \pm 0.015$/ 0.189 ± 0.005	$0.12 \pm 0.09 \pm 0.13$
SMC D(5GeV^2)	$0.023 \pm 0.02 \pm 0.015$/ 0.094 ± 0.005	$0.06 \pm 0.2 \pm 0.15$
E142 n(2GeV^2)	-0.022 ± 0.011/ -0.021 ± 0.018	0.57 ± 0.11
B.S.R. (Measured/Predicted)		
EMC + SMC pD(5GeV^2)	$0.20 \pm 0.05 \pm 0.04/0.189 \pm 0.005$	
SMC + E142 Dn(2GeV^2)	$0.146 \pm 0.021/0.183 \pm 0.007$	

While the combined EMC/SMC data are essentially in agreement with the Bjorken sum rule, the EMC/E142 data were found to differ by nearly two standard deviations. Various reanalyses have been done, taking into consideration the fact that these data are at different Q^2 values and cannot be combined per se and also by including higher twist effects. Recently, the SMC [10] has done a combined analysis

of all these data. They claim that there is no conflict between the data; furthermore, that the Bjorken Sum Rule is confirmed to within 17% uncertainty using these data. Their procedure involved a reanalysis of the *neutron* spin dependent structure function data, using the EMC/SMC data, which have smaller errors, to determine the neutron spin dependent structure function, $g_1^n(x)$, at small-x values. Hence, there exist widely differing viewpoints [11], [12], [13] on whether the Bjorken sum rule is violated or not.

1.3 The phenomenology

In what follows, we shall study, in depth, the behaviour of *both* the asymmetries and the structure functions at small- and large-x respectively and the impact on the moments and Bjorken sum rule of extrapolation to these experimentally inaccessible kinematic regimes.

Before we begin the actual analysis, the following comments are in order:

1. The spin independent as well as spin dependent densities can be constructed from the helicity densities, $q_f^{\uparrow}(x)$ and $q_f^{\downarrow}(x)$, of f-flavour quarks with momentum fraction x and spins parallel and opposed to that of the nucleon. Specifically, $\widetilde{q} = q^{\uparrow} - q^{\downarrow}$ and $q = q^{\uparrow} + q^{\downarrow}$. For a large-x behaviour, $q^{\uparrow,\downarrow} \sim (1-x)^{\alpha_{\uparrow},\alpha_{\downarrow}}$, *both* $\widetilde{q}$ and q have a behaviour given by $q, \widetilde{q} \sim (1-x)^{\alpha}$, where α is the smaller of $(\alpha_{\uparrow}, \alpha_{\downarrow})$. Hence, they vanish at large-x at the same rate.

2. $q^{\uparrow}$, $q^{\downarrow}$ are positive definite densities; hence, $|\widetilde{q}| \leq |q|$ for all x. Hence the partonic asymmetries, $A_q \equiv \widetilde{q}/q$, are bounded by ± 1 . In fact, unless $\alpha_{\uparrow} = \alpha_{\downarrow}$ (which is unlikely), $A_q \rightarrow \pm 1$ as $x \rightarrow 1$. Furthermore, it is experimentally established that the unpolarised u-quark density dominates over the d and s at large-x; hence, the proton, neutron and deuteron asymmetries **must** approach each other as $x \rightarrow 1$.

Our observations now follow automatically. We use the parametrisation of $F_2^{p,d}$ as given by the NMC [6] (with $F_2^n = 2F_2^D - F_2^p$) and use $R = \sigma_L/\sigma_T$ as given by the SLAC group [14]. This way, there is no need to specify the individual parton densities. We assume all the A_1 to be Q^2 independent, as observed, and analyse all data at $Q^2 = 5$ GeV^2 .

1.4 The unconstrained fits

The corresponding g_1 from the three experiments are shown in fig. 1; the solid curve is the best fit to the data for a parametrisation, $g_1(x) = Nx^{\alpha}(1+bx)(1-x)^{\beta}$, with $b = 0$ for the proton case and a large-x dependence, $(1-x^2)^{\beta}$, specially for the neutron case due to the very fast fall-off of g_1^n at large-x. (The errors in the deuteron data preclude us from specifying the exact crossing point, x_0 $(= -1/b)$, where the structure function (or asymmetry) changes sign; the two curves shown indicate the maximum extent of variation of b). These fits to the structure functions result in fits to the asymmetry shown by the dotted lines in fig. 2. It is observed that the intermediate-x asymmetry is distinctly different from zero only for the proton.

The corresponding moments are shown in table 2. We assume our errors to be the same as the experimentally quoted ones as the errors due to the fit are negligible in all but the deuteron case. The range of variation in the deuteron case due to

the allowed range, $0.04 \leq x_0 \leq 0.06$, may be considered as an error in the moment coming from the fit. The moments are not all in agreement (to within 1σ) with the predictions of the Bjorken sum rule. Of course, the proton and deuteron data are also not in accordance with the Ellis Jaffe prediction [9], although we do not discuss this further.

Table 2. The nonsinglet moments, $\int (g_1^p - g_1^n)\mathrm{d}x$, $\int 2(g_1^p - g_1^d)\mathrm{d}x$ and $\int 2(g_1^d - g_1^n)\mathrm{d}x$ are shown for $Q^2 = 5$ GeV^2.

Target	$\int g_1\, \mathrm{d}x\ (Q^2)$ (expt)	(fit to g_1)	$\int g_1 \mathrm{d}x$ (5 GeV^2) from fit to A_1.
p	$0.126 \pm 0.01 \pm 0.015(10)$	0.125(10) 0.124(5)	0.131
n	-0.022 ± 0.011 (2)	$-0.030(2)$ $-0.036(5)$	-0.035
d	$0.023 \pm 0.02 \pm 0.015(5)$	0.0176(5)	0.052
d′	"	0.0135(5)	0.042

We now move on to the x dependence of these structure functions, which is really the focus of the talk. We first express every quark density as a sum of valence and sea parts, i.e.,

$$q^f(x) = q_V^f(x) + q_s^f(x)\ ; \qquad \overline{q}^f(x) = q_s^f(x).$$

We ignore (small) corrections due to deviations from the Gottfried sum rule, i.e., we assume $\overline{u} = \overline{d}$. The three measurements that we have in the spin dependent sector are *not* sufficient to extract any of the unknown densities individually; we can only extract the non-singlet combination $(\widetilde{u}(x) - \widetilde{d}(x))$. This is because all the experiments measure quantities whose singlet parts are identical. Then the combinations, $(g_1^p - g_1^n)$, $2(g_1^p - g_1^d)$ and $2(g_1^d - g_1^n)$ all give information on the non-singlet quantity, $(\widetilde{u} - \widetilde{d})$. We use the parametrised fits to the various structure functions at $Q^2 = 5$ GeV^2 to plot these differences which we denote as pn, pd and dn, as functions of x in fig. 3. We have chosen the deuteron parametrisation, d, corresponding to $x_0 = 0.06$. Similar results are obtained on using the d', i.e., the $x_0 = 0.04$ fit. The non-singlet moments of all combinations are shown in table 3. The dn combination is seen to deviate substantially from the Bjorken sum rule prediction.

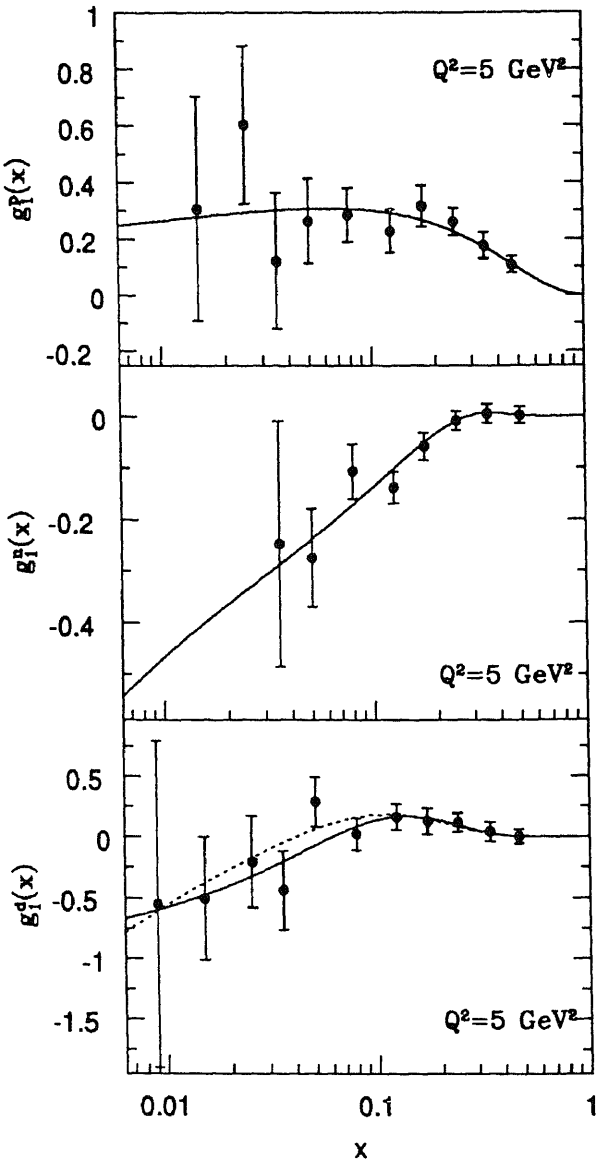

Figure 1. The structure function data for the proton, neutron and deuteron are sho as a function of x. The solid curves are our fits to the data.

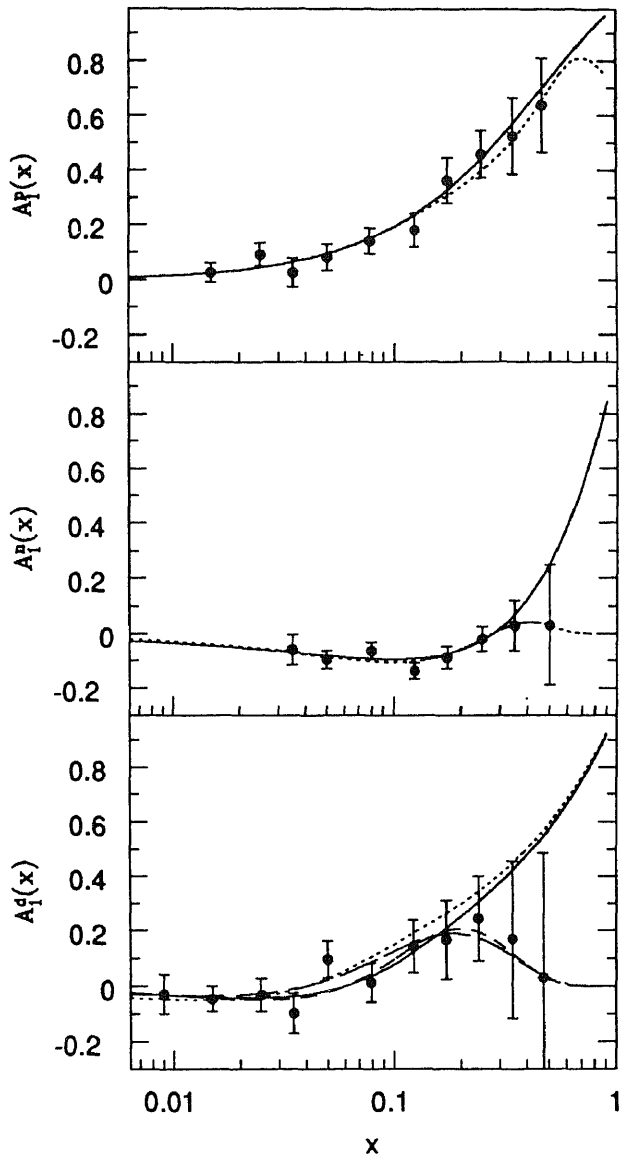

Figure 2. The proton, neutron and deuteron asymmetry data are shown as a function of x. The solid curves are our constrained fits to the data ($A_1(1) = 1$), while the dotted

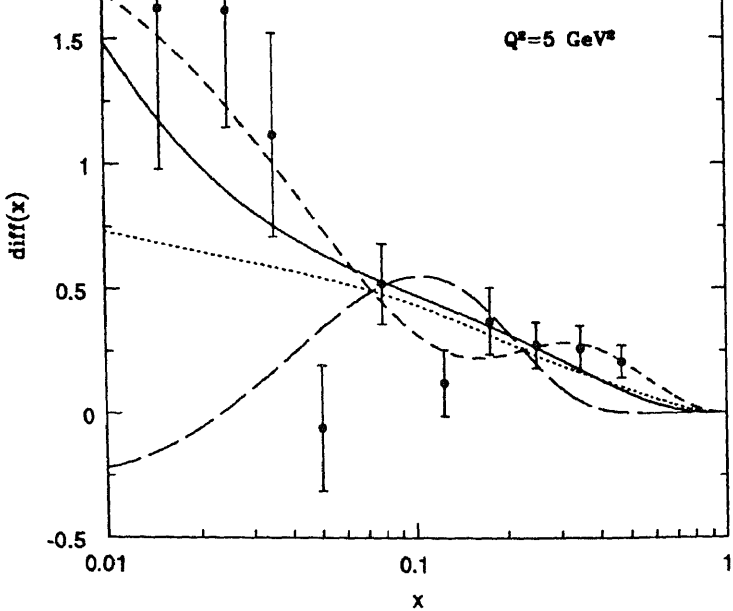

Figure 3. The non-singlet combinations, $(g_1^p - g_1^n)$ (dotted curves), $2(g_1^p - g_1^d)$ (dashe curves) and $2(g_1^d - g_1^n)$ (long dashed curves) are plotted as a function of x. The solid li corresponds to a prediction in agreement with the Bjorken sum rule.

Table 3. The nonsinglet moments, $\int (g_1^p - g_1^n)\mathrm{d}x$, $\int 2(g_1^p - g_1^d)\mathrm{d}x$ and $\int 2(g_1^d - g_1^n)\mathrm{d}x$ a shown for $Q^2 = 5$ GeV^2.

Set	Moments of non-singlet structure functions from fits to	
	$g_1(x)$	$A_1(x)$
$p-n$	0.161 ± 0.015	0.166 ± 0.015
$2(p-d)$	$(0.215\text{–}0.223) \pm 0.032$	$(0.160\text{–}0.179) \pm 0.032$
$2(d-n)$	$(0.099\text{–}0.107) \pm 0.033$	$(0.154\text{–}0.173) \pm 0.033$
Average value:		0.166 ± 0.013
Bjorken Sum Rule prediction:		0.189 ± 0.005

To proceed further, we need some more input. For this, we parametrise the *spin dependent* valence densities [15] using the Carlitz Kaur model [16]. Specifically, we have

$$\begin{aligned} \widetilde{u_V}(x) &= \left(u_V(x) - \tfrac{2}{3}\, d_V(x)\right) \cos 2\phi(x) \,, \\ \widetilde{d_V}(x) &= -\tfrac{1}{3}\, d_V(x) \cos 2\phi(x) \,, \end{aligned}$$

where $\cos 2\phi(x) = 1/(1+\gamma\sqrt{1-x}/x^{0.1})$ is a one-parameter spin dilution function. We use the GRV parametrisations [17] for the spin independent densities, though results are *not* sensitive to choice of parametrisation. Since u_V and d_V are known, γ fixes $\widetilde{u_V}$ and $\widetilde{d_V}$ individually.

The input that we use is the Bjorken sum rule prediction itself! We *choose* γ so that the combination, $(\widetilde{u_V}(x) - \widetilde{d_V}(x))/6$ integrates to g_A, so the Bjorken sum rule is satisfied. The resulting $\mathcal{O}(\alpha_s)$ corrected non-singlet combination, [18] $(\widetilde{u_V}(x) - \widetilde{d_V}(x))(1-\alpha_s/\pi)/6$, is plotted as the solid curve in fig. 3, for comparison with the data differences. We see that the *pd* and *pn* combinations are quite close to the Carlitz-Kaur fit while *dn* deviates severely from it, especially at small-x. Furthermore, at large-x ($x \geq 0.2$), the combination *dn* underestimates the fit while *pd* overestimates it. We have also plotted the actual data points for the *pd* combination (made possible as EMC and SMC have data in the same x-bins) to give an idea of the errors involved.

Therefore, deviations from the expected behaviour (where by 'expected' we mean an x-dependence of the non-singlet density compatible with the Bjorken sum rule) occur at both large as well as small values of x. Hence deviations in the moments of these differences also arise from both these kinematically distinct regions. Is there any way to explain these deviations?

1.5 The constrained fits

Note that the errors on the data, especially at $x \geq 0.2$, are fairly large. Also recall the phenomenological bias that *all* the asymmetries should approach each other at large-x. Furthermore, the parton model expects this value to be ± 1 at $x = 1$. We now *reparametrise* the data with this bias or constraint. Our motivation for such a procedure is that the proton asymmetry is *clearly distinct from zero* at large-x values. Hence, the deuteron and neutron asymmetries (which are not so clear, due to large errors at large-x, as can be seen seen from fig. 2) *must* also follow this trend. So we fit the asymmetries to the form, $A_1^{p,d,n}(x) = N x^{\alpha} \{1 - \exp[a(x - x_0)]\}$, where the constraint $A_1(1) = 1$ determines N from $N\{1 - \exp[a(1-x_0)]\} = 1$, and $x_0 = 0$ for the proton. These fits are shown as solid lines in fig. 2. The differences between the two fits are strongly marked at larger x values for the neutron and deuteron. Surprisingly, the χ^2 values are not very different for these new fits as compared to the case when the data were fitted without any theoretical bias (see table 4). This is obvious for the proton case as the data are clearly compatible with the assumption that $A_1^p \to 1$ as $x \to 1$. For the deuteron and neutron data,

Table 4. The χ^2 values of the fits (at $Q^2 = 5$ GeV^2) to the data in figs. 1 and 2 are shown. d (d') is the deuteron fit corresponding to $x_0 = 0.06$ (0.04).

Target	No. of data points	No. of parameters in fit	χ^2/d.o.f from fits to $g_1(x)$	$A_1(x)$
p	10	3	4/7	4/8
n	8	4	4/4	5/5
d	11	4	5/7	6/8
d'	11	4	5/7	8/8

These new fits to the asymmetry yield corresponding spin dependent structure functions as shown in fig. 4.
While the small-x fits are good, the large-x data are systematically overestimated (while remaining within 1σ) for the neutron and deuteron. The next logical step is to find the moments of *these* fits; these are shown in the last column of table 2. The moments of the proton and neutron do not change much, as expected; however, the deuteron moment goes up remarkably. The deuteron result is very sensitive to the value of x_0. Earlier, the (negative) integral in the small-x region was being more or less cancelled by the positive contribution from the remaining interval. By increasing the large-x contribution, the moment is now clearly positive.

We show the x-dependence of these new (theoretically constrained) non-singlet combinations, pn, pd and dn, as defined earlier, in fig. 5. The small-x fits do not change much; what is dramatic, however, is the behaviour of **all** the combinations at large-x, which now precisely satisfy the theoretical requirements. The agreement of *all* the three combinations with the predicted non-singlet density is visible from $x = 0.2$ onwards. (Recall that the earlier parametrisations had yielded fits which either overestimated or underestimated the non-singlet density in this region). Furthermore, the corresponding moments of all these non-singlet distributions are now very much in accordance with the prediction of the Bjorken sum rule, as seen from table 3. The errors are those from the data; errors in the fit are only accounted for in the deuteron case, leading to corresponding range of values for the pd and dn moments. We emphasise that these fits, though tailored to theoretical considerations, are definitely consistent with the data.

To sum up, while the results are sensitive to large-x extrapolation, the non-singlet data from all the experiments are compatible, within errors (1σ), with theoretical expectations in the large-x region and the Bjorken sum rule. The small-x non-singlet data still deviate considerably from the naïve parton model picture. This sector is already controversial and poorly understood. There has been a great deal of literature on the subject; we do not comment on it further.

Since we do not have three independent measurements, we cannot specify the individual quark contributions (Δu, Δd and Δs) without a further assumption We choose this to be the constraint coming from the non-singlet SU(3) symmetric combination:

$$\Delta u + \Delta d - 2\Delta s = g_8 \ ,$$

where $g_8 = 0.584 \pm 0.018$ based on nucleon and Σ^- decay data.

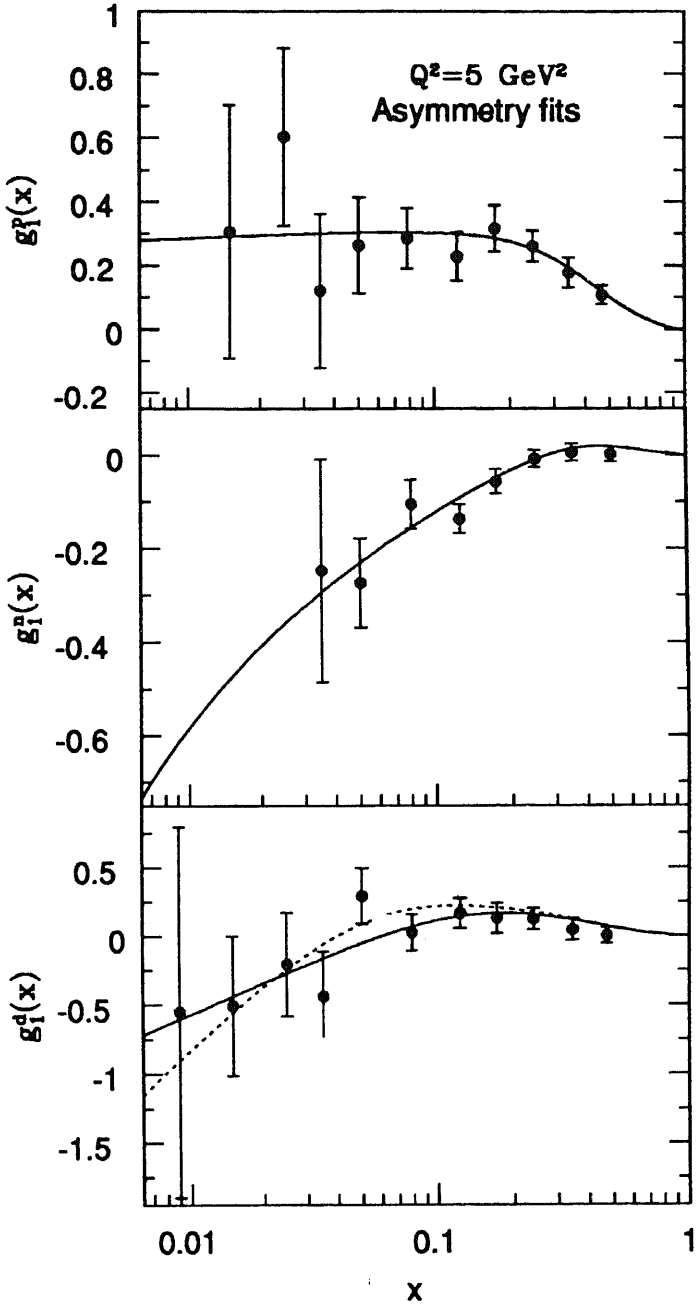

Figure 4. The same as fig. 1, but with the solid curves corresponding to constrained fits to the asymmetry data.

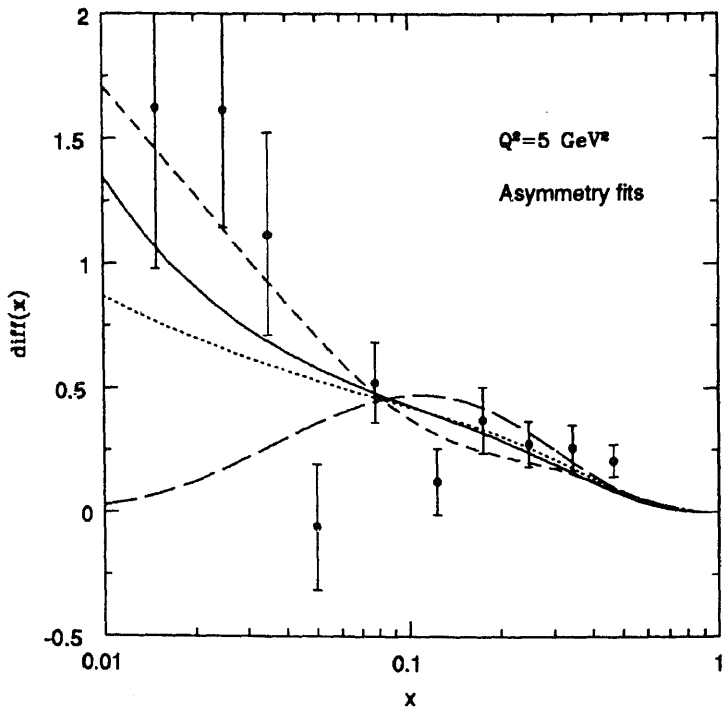

Figure 5. The same as fig. 3, with the structure functions evaluated from constrained fits to the asymmetry data.

We then use the moment of the proton g_1 structure function and $(\Delta u - \Delta d) = 1.097 \pm 0.083$ obtained from tables 2 and 3 respectively to get

$$\Delta u = 0.701 \pm 0.037, \quad \Delta d = -0.396 \pm 0.091, \quad \Delta s = -0.140 \pm 0.050 ,$$

so that

$$\Sigma \equiv \frac{1}{2}(\Delta u + \Delta d + \Delta s) = 0.083 \pm 0.055 .$$

This is still small, just as the nearly zero result first obtained by the EMC (though with large errors). In some sense then, the new data not only indicate that the Bjorken sum rule is valid, but also that the original controversy on the nature of the nucleon spin and the smallness of the quark contribution remains.

We emphasise the need for more data, particularly in the intermediate and large-x region. Only when the data improve to a point where the large-x p, d and n asymmetries clearly differ from each other can we say that the old proton "singlet spin puzzle" has been joined by a new "non-singlet spin puzzle!" In short, we believe that current data are not in conflict with the Bjorken sum rule.

We briefly comment on possible higher twist effects. These affect the large-x data. The aymmetries are seen to be largely Q^2 independent. So all the Q^2 dependence of $g_1^{p,d,n}$ *must* come from that of F_2 and R. This has already been accounted for. In fact, the NMC parametrisation of F_2 includes both logarithmic and higher twist corrections. Hence, it is unlikely that higher twist terms play any major role in the process of lining up the data with the Bjorken sum rule. Certainly we have shown that agreement can be brought about without the use of such extra terms.

Finally, it seems that non-singlet densities are interesting and deserve to be studied in their own right. In this context, we recall a proposal [19] for studying spin dependent valence densities through semi-inclusive hadroproduction in polarised DIS, which can be immediately performed without difficulty. In particular, the asymmetry for K meson production, (defined to be the usual spin asymmetry, but for the difference in production of K^+ and K^- mesons) is

$$A^K(x) \equiv \frac{d\sigma^{K^+}(\uparrow\downarrow - \uparrow\uparrow) - d\sigma^{K^-}(\uparrow\downarrow - \uparrow\uparrow)}{d\sigma^{K^+}(\uparrow\downarrow + \uparrow\uparrow) - d\sigma^{K^-}(\uparrow\downarrow + \uparrow\uparrow)} = \frac{\widetilde{u_V}(x)}{u_V(x)} ,$$

i.e., it measures $\widetilde{u_V}$. The asymmetry for π production involves both $\widetilde{u_V}$ and $\widetilde{d_V}$ although it uses the currently controversial [20] assumption of isospin invariance (the former does not). Certainly these two asymmetries should well be able to supplement results from inclusive DIS as both are expected to be large and positive over all x.

2. The spin dependent gluon densities

Finally, we briefly address the question of extraction of the spin dependent gluon densities. Since the nucleon spin is not saturated by the quark contribution, the gluons are likely to contribute substantially, although they occur at $\mathcal{O}(\alpha_s)$ in the expression for the spin dependent structure function. This has been the subject of a

great deal of controversy; in fact, it was even argued that the magnitude of the gluonic contribution to the spin of the proton may well turn out to be renormalisation scheme dependent! We outline why this is not the case, and pinpoint the source of ambiguity in this sector. To do this, we go back to the parton interpretation of $g_1(x)$. This section is mainly a review of already existent formalism [21, 22, 23, 24] addressing the question, "Is there a sizable singlet quark/gluon contribution to the first moment of g_1?"

Look at the leading Q^2 dependence of the moments of the parton densities (or spin contributions to that of the nucleon):

$$\begin{aligned} \frac{\mathrm{d}}{\mathrm{d}t}\left(\alpha_s(Q^2)\Delta g(Q^2)\right) &= 0 \\ \frac{\mathrm{d}}{\mathrm{d}t}\left(\Delta\Sigma(Q^2)\right) &= 0\,, \end{aligned}$$

where $t = \ln(Q^2/\mu^2)$ and μ is the renormalisation scale.

Since α_s vanishes logarithmically as $Q^2 \to \infty$, Δg *grows* with Q^2 at the same rate. Hence Δg may be large even at finite Q^2. Since quarks and gluons (as also their relative orbital angular momentum) contribute to the nucleon spin, there is *apriori* no reason to leave this contribution out of the g_1 calculation. This means we need to go beyond the leading order. (Contrast this with the spin independent case where the momentum, $xg(x) \to 0$ as $\alpha_s \to 0$).

2.1 The parton model calculation

Parton densities are not uniquely defined beyond the leading order. Furthermore, the gluon contribution to g_1 suffers from both infrared and collinear divergences. In other words, the result depends on the mode of regularisation of the contributing box diagram (Fig 6).

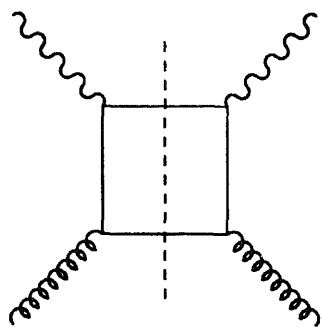

Figure 6. The gluon contribution to the g_1 structure function in the parton model.

2.2 The factorisation approach

Here, there is a clean separation of the 'hard' and 'soft' components of the total

cross section. The structure function symbolically evaluates to

$$g_1^{\gamma^* N} = \hat{g}_1^q \otimes f_{\frac{\Delta q + \Delta \overline{q}}{N}} + \hat{g}_1^g \otimes f_{\frac{\Delta g}{N}} \cdot \tag{1}$$

The two terms represent the quark and gluon contributions to the structure function, respectively. $f_{p+/N}(x)$ ($f_{p-/N}(x)$) is the probability of locating a parton ($p = q, \overline{q}, g$) in a nucleon, N, with spin parallel (antiparallel) to that of the parent nucleon and $f_{\Delta p/N}$ is the difference of these two probabilities and was denoted as $\tilde{p}$ in the previous section for simplicity. The symbol $\otimes$ stands for the convolution,

$$a(x) \otimes b(x) \equiv \int_x^1 \frac{\mathrm{d}y}{y} a(x/y) b(y) \ .$$

Each term is therefore a convolution of the soft (nonperturbative, and therefore incomputable) parton densities and the hard (perturbative and computable) scattering coefficients. These hard scattering coefficients, $\hat{g}_1^{q,g}$ are target independent. The simplest way to calculate them is to replace the nucleon target N by a known (point) target, say, gluon. $f_{\Delta q/g}$ and $f_{\Delta g/g}$ are now computable. So is $g_1^{\gamma^* g}$. Hence the only unknowns in eq. (1) are the hard scattering coefficients. However, since $f_{\Delta q/g}$ is of order $\mathcal{O}(\alpha_s)$ we need to compute $\hat{g}_1^q$ only to leading order, $\mathcal{O}(1)$. This is already known ($= \delta(1-x)/2$). This leaves $\hat{g}_1^g$ as the only unknown which can thus be found.

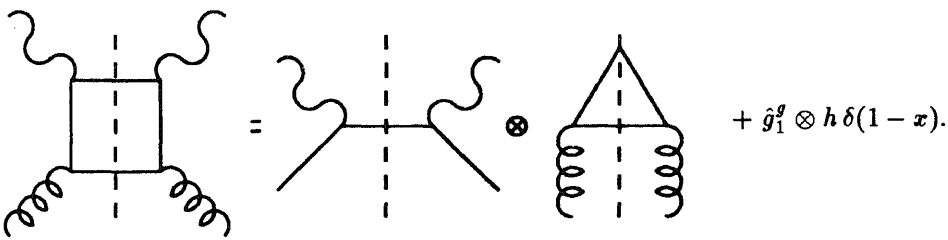

Figure 7. The gluon–virtual photon scattering cross section in the factorisation approach. The LHS corresponds to fig. 6. The terms in the RHS are the quark and gluon contributions respectively.

Specifically, with gluon replacing the nucleon target in eq. (1), the equation can be diagrammatically represented as shown in fig. 7. The LHS of fig. 7 is known (it is the parton model result) and has both IR and collinear divergences. However, these are exactly cancelled by corresponding divergences on the RHS. However, the RHS is renormalisation scheme dependent, while the LHS is not. The result is that $\hat{g}_1^g$ is hard, prescription independent, and scheme dependent. Due to this, the gluonic contribution to the first moment of the nucleon structure function ($\int g_1(x)\mathrm{d}x$) vanishes or does not (equals $-\alpha_s/2\pi$) depending on whether the computation is performed in the $\overline{\mathrm{MS}}$ or MOM scheme.

This means that meaningful results can be obtained only if all quantities (F_2, g_1, etc) are defined upto next-to-leading order in the same scheme. Then only will

the experimentally measurable cross sections be scheme invariant. However, we emphasise that the spin dependent gluon density and its moment Δg are well defined always and therefore can be unambiguously measured. In fact, the advantage of the factorisation approach is that it yields [25] an *operator definition* of the densities (both spin independent and spin dependent). It is the coefficient of the Δg term in the cross section that is scheme dependent.

A simple way of seeing this is to write the spin dependent DIS cross section for a nucleon target of mass, M:

$$\sigma_N(x,Q^2,M) = \hat{\sigma}_q(x,Q^2,\mu) \otimes \tilde{q}(x,M,\mu) + \hat{\sigma}_g(x,Q^2,\mu) \otimes \tilde{g}(x,M,\mu) \ , \qquad (2)$$

where $\tilde{q} = f_{\Delta q/N}$ and $\tilde{g} = f_{\Delta g/N}$ as before. Replacing N by a gluon target, factorisation yields

$$\begin{aligned} \sigma_g(x,Q^2,M) &= \hat{\sigma}_q(x,Q^2,\mu) \otimes f_{\Delta q/g}(x,M,\mu) \\ &\quad + \hat{\sigma}_g(x,Q^2,\mu) \otimes f_{\Delta g/g}(x,M,\mu) \ . \end{aligned} \qquad (3)$$

Here $\hat{\sigma}_{q,g}$ are target independent while $f_{\Delta g/g} \sim \delta(1-x)$. Substituting for $\hat{\sigma}_g$ from eq. (3) in eq. (2), we have

$$\sigma_N = \hat{\sigma}_q \otimes \tilde{q} + \sigma_g \otimes \tilde{g} - \hat{\sigma}_q \otimes f_{\Delta q/g} \otimes \tilde{g} \ .$$

The last term can be thought of as either a correction to $\tilde{q}$ or a correction to σ_g. Hence we are free to redefine

$$\begin{aligned} \tilde{q}' &= \tilde{q} - \delta f_{\Delta q/g} \otimes \tilde{g} \\ \text{OR} \quad \hat{\sigma}_{g'} &= \sigma_g - \hat{\sigma}_q \otimes \delta f_{\Delta q/g} \ . \end{aligned}$$

That is, there is ambiguity in q and/or $\hat{\sigma}_g$ to order $\mathcal{O}(\alpha_s)$, *but none in* $\tilde{g}$ or in $g_1(x)$. Hence, although g_1 itself may not be able to distinguish between models with large and small Δg, it will be possible (say, in direct photon production in polarised pp collisions) to establish the gluonic contribution to the spin of the nucleon.

3. Conclusions

We have established that current polarised DIS data on spin dependent nucleon structure functions are consistent with predictions in the nonsinglet sector (Bjorken Sum Rule). The quark contribution to the spin of the proton remains small (about 17%). It is therefore likely that gluons may contribute substantially. In view of this, and other controversies in the field, we have reviewed the formalism of DIS and the contribution of the gluonic term to the structure functions, in the factorisation approach. We emphasise that, although DIS cannot measure the gluon contribution to the proton spin, such a quantity is well-defined and can be measured elsewhere. In fact, several new structure functions [25] have recently been defined, occurring in both DIS and pp collision processes in longitudinal as well as transversely polarised collisions, that may throw more light on the issue of the proton spin.

References

[1] Two informal lectures were later given on them by V. Ravindran and I in the group sessions.

[2] J. Ashman et al., EMC, Nucl. Phys. **B328** (1989) 1

[3] B. Adeva et al., SMC, Phys. Lett. **B302** (1993) 533

[4] P.L. Anthony et al., E142 Collaboration, Phys. Rev. Lett. **71** (1993) 959; E. Hughes, private communication

[5] J.D. Bjorken, Phys. Rev. **148** (1966) 1467; Phys. Rev. **D1** (1970) 1376

[6] P. Amaudruz et al., NMC, Phys. Lett. **B295** (1992) 159

[7] M. Derrick, et al., ZEUS Collaboration, Phys. Lett. **B316** (1993) 412; I. Abt, et al., H1 Collaboration, Nucl. Phys. **B407** (1993) 515

[8] We do not comment on possible effects of Gottfried sum rule violation here.

[9] J. Ellis and R.L. Jaffe, Phys. Rev. **D9** (1974) 1444; E: **D10** (1974) 1669

[10] B. Adeva et al., SMC, Phys. Lett. **B320** (1994) 400

[11] F.E. Close and R.G. Roberts, Phys. Lett. **B316** (1993) 165

[12] J. Ellis and M. Karliner, Phys. Lett. **B313** (1993) 131

[13] G. Altarelli, P. Nason and G. Ridolfi, Phys. Lett. **B320** (1994) 152

[14] L.W. Whitlow, Phys. Lett. **B250** (1990) 193

[15] D. Indumathi, M.V.N. Murthy, V. Ravindran, Z. Phys. **C56** (1992) 427

[16] R. Carlitz and J. Kaur, Phys. Rev. Lett. **38** (1977) 673; J. Kaur, Nucl. Phys. **B128** (1977) 219

[17] M. Glück, E. Reya, A. Vogt, Z. Phys. **C53** (1992) 127

[18] Since we are working at $Q^2 = 5$ GeV^2, higher order corrections to this sum rule are negligible.

[19] S. Gupta, D. Indumathi, M.V.N. Murthy, Z. Phys. **C47** (1990) 227

[20] P. Amaudruz et al., NMC, Phys. Rev. Lett. **66** (1991) 2712

[21] Ahmed and G.G. Ross, Phys. Lett. **B56** (1975) 385; G. Altarelli and G.G. Ross, Phys. Lett. **B212** (1988) 391

[22] A. Manohar, Phys. Rev. Lett. **66** (1991) 289

[23] P. Mathews and V. Ravindran, Phys. Lett. **B278** (1992) 175

[24] U. Ellwanger, Phys. Lett. **B259** (1991) 469

[25] R.L. Jaffe and X.-Ji, Nucl. Phys. **B375** (1992) 527; X. Ji, Phys. Lett. **B284** (1992) 137

Oscillating neutrinos: theory vs experiment

ANJAN S. JOSHIPURA

Theory Group, Physical Research Lab., Ahmedabad, India.

Abstract. Possible hints on neutrino masses are reviewed. They come from the deficits in the solar as well as atmospheric neutrinos and from need of a significant amount of hot component in the dark matter of the universe. The role of three generation mixing in simultaneously solving the solar and atmospheric neutrino problem is discussed. All the three hints can be reconciled if three neutrinos are almost degenerate. Models for neutrino masses and mixing implied by the above hints are briefly discussed.

1. Introduction

We discuss in this talk the implications of present experiments on the properties - masses and mixing - of the known neutrinos. So far, one does not have any conclusive evidence from laboratory in favour of neutrino masses. But there exist a number of hints which strongly point to non-vanishing neutrino masses. More importantly, when taken in totality, these hints imply a definite pattern for the neutrino masses. We shall review [1] these hints and try to present general conclusions about the structure of neutrino masses following from them. Then we shall briefly review theoretical schemes which can lead to the desired pattern for neutrino masses and mixing.

2. Hints on neutrino masses

The hints on neutrino masses come at least from three different sources: (1) Solar neutrino deficit (2) Atmospheric neutrino deficit and (3) need for a significant hot component in the dark matter of the universe. Many reviews [2, 3, 4] exist which summarize these hints. We briefly mention salient features of each of these topics.

2.1 Solar neutrino deficit

Four different experiments looking for the electron neutrino of the solar origin have found depletion in the solar ν_e flux compared to theoretical expectations based on

the standard solar model (SSM). The recent results are [3]

$$\begin{aligned} R_{sol} = \frac{\text{Observedflux}}{\text{SSMflux}} &= 0.318 \pm 0.051 \quad \text{(Homestake)} \\ &= 0.51 \pm 0.04 \pm 0.06 \quad \text{(Kamioka II + III)} \\ &= 0.58 \pm 0.07 \quad \text{(GALLEX + SAGE)} \end{aligned} \tag{1}$$

- The SSM rates are calculated using the flux of Bachall's group.
- Different experiments observed different amount of depletion. Since these experiments are sensitive to different parts of the neutrino energy spectrum, the above results can be understood in terms of some underlying mechanism which can cause the energy dependent suppression. This would occur if the Mikhyev Smirnov Wolfenstein (MSW) [5] conversion or the long wave length vacuum [6] oscillations cause the depletion in the ν_e flux. In contrast, the vacuum oscillations with a wavelength much shorter than the Sun-Earth distance cannot explain the observed energy dependence of depletion.
- It has been argued [7] that various experimental results are indicative of some new physics rather than of uncertainty in our knowledge of the Sun.
- If one assumes neutrino oscillations to be responsible for the depletion of ν_e then the relevant parameter space is restricted to the following in case of the two generation mixing. For the vacuum solution, one has

$$\delta m^2 \sim (0.55 - 1.1) \times 10^{-10}\text{eV}^2 \quad \sin^2 2\theta \sim 0.75 - 1 \tag{2}$$

while for the MSW solution, one has

$$\begin{aligned} \delta m^2 \sim 6 \times 10^{-6}\text{eV}^2 \quad \sin^2 2\theta \sim 0.007 \quad \text{(Non} - \text{Adiabatic)} \\ \delta m^2 \sim 9 \times 10^{-6} \quad (\text{eV}^2)\ ; \quad \sin^2 2\theta \sim 0.6 \text{(Adiabatic)} \end{aligned} \tag{3}$$

2.2 Atmospheric neutrino deficit

The atmospheric neutrinos are produced in decays of pions, kaons and muons originating from interactions of cosmic rays with the atmosphere. Observations of these neutrinos seem to indicate the depletion in the muon to electron neutrino flux ratio compared to the theoretical expectations. Experimental findings of various groups are as follows [3]:

$$\begin{aligned} R &= \frac{(\mu/e)_{OBS}}{(\mu/e)_{MC}} = 0.60^{+0.06}_{-0.05} \pm 0.05 \quad \text{(KAM Sub GeV)} \\ &= 0.57^{+0.08}_{-0.07} \quad \text{(KAM Multi GeV)} \\ &= 0.54 \pm 0.05 \pm 0.12, \quad \text{(IMB} - 3\text{)} \\ &= 0.69 \pm 0.19 \pm 0.09, \quad \text{(SOUDAN)} \\ &= 0.87 \pm 0.16 \pm 0.08. \quad \text{(FREJUS)} \end{aligned}$$

where $(\mu/e)_{MC}$ is the ratio generated through the monte carlo simulation using the theoretically calculated fluxes.

The following remarks are in order:

- The absolute flux of ν_e and ν_μ have about 30% uncertainty but their ratio is much less uncertain ($\sim$ 5%). Thus the experimental indication in the depletion in R can be pointing to genuine effects like oscillations.
- The deficit is seen [8] by Kamioka in two sets of data. One corresponding to the contained events with energy $\leq \mathcal{O}$(GeV) approximately. The other set consists of contained and partially contained events in the multi GeV range.
- IMB group has also looked for the upward going muons. Their numbers in this case are consistent with no oscillation hypothesis.
- The Kamioka group finds [8] strong dependence on the zenith angle in the multi GeV data. The down coming neutrinos do not show much depletion compared to the upgoing ones which are depleted by about 50%. Since, the latter travels much larger distance compared to the down going neutrinos, this zenith angle dependence is strongly suggestive of the oscillation phenomena with typical wavelength of order few tens of km. In fact, the best fit values of parameters quoted by Kamioka assuming the oscillations to be the cause of depletion are

$$\Delta m^2 \simeq 1.6 \times 10^{-2}\ eV^2\ ,\ \sin^2 2\theta \simeq 1\ . \tag{5}$$

2.3 Dark matter

Combinations of experimental evidences and strong theoretical arguments lead one to believe that our universe is mostly made up of non baryonic dark matter [9, 10].

Neutrinos are the only known particles among various candidates for the dark matter that have been proposed. But it is likely that neutrinos by themselves may not be responsible for all the non baryonic dark matter. This follows from the arguments based on the structure formation [10] in the early universe. Because of relatively small masses, neutrinos are relativistic till quite late in the evolution of the universe. Free streaming of these neutrinos cannot allow for the growth of small structures which could have evolved to the galactic sizes at present. The structures at smaller scales arise more naturally if the dark matter is cold, for example, heavy weakly interacting particle like the lightest supersymmetric state. But this by itself is not successful in explaining the large scale structure. This has given rise [11] to suggestion of the mixed dark matter scenario with simultaneous presence of the hot and cold component in the dark matter. Assuming the hot component to be in the form of neutrinos one finds that roughly 30% contribution by them in addition to cold matter simultaneously fit the COBE and IRAS observations. Taken at the face value this suggests that the sum of the neutrino masses [11] should be

$$\Sigma m_{\nu_i} \sim 7\text{eV} \tag{6}$$

It is likely that neutrino masses may not be responsible for one or more of the phenomena discussed in the last section or that the experimental findings themselves may need some revision. But if one takes all these hints seriously than one could draw strong theoretical conclusions about the pattern of neutrino masses. First, we discuss the possible pattern of neutrino masses and mixing necessary in order to simultaneously solve the solar and atmospheric neutrino problems. If one also wants neutrinos to provide the hot component in the dark matter then the structure of neutrino masses get further constrained. We discuss this in the subsequent subsection.

3.1 Solar and atmospheric neutrino deficits

The restrictions imposed by the solar and atmospheric neutrino deficits on masses and mixing have already been displayed in eqs.(2,3) and eq. (5). One can draw the following obvious conclusions from these equations:

(*i*) At least two of the three masses and mixing angles among neutrinos must be non-zero.

(*ii*) At least one of the mixing angles must be large and

(*iii*) two independent $(\text{mass})^2$ differences between neutrinos must be hierarchical. Such hierarchy can result if the non-zero masses themselves are hierarchical or if two are nearly degenerate with the common $(\text{mass})^2$ around 10^{-2} $(\text{eV})^2$ and $(\text{mass})^2$ splitting around $10^{-5} - 10^{-6}$ $(\text{eV})^2$.

The (*i*) above imply that all three neutrinos would be involved in the oscillations and conventional analysis of the neutrino oscillations in terms of two generations may be inadequate in general. More importantly, in many cases the observed atmospheric neutrino deficit can influence the region of parameter space allowed by the solar neutrino experiments and vice versa.

A priori, the analysis of neutrino experiments in terms of three neutrino generations seems complicated since in general two independent $(\text{mass})^2$ differences and three mixing angles are involved. But the fact that $(\text{mass})^2$ differences are hierarchical greatly simplifies the analysis of oscillations both in vacuum as well as in the presence of the matter. Thus it becomes possible to simultaneously analyze the combined implications of the solar and atmospheric neutrino data.

Consider first the vacuum oscillations and the simplest mass hierarchy $m_{\nu_1} \ll m_{\nu_2} \ll m_{\nu_3}$ with $\Delta_{32} \sim 10^{-2}$ $(\text{eV})^2$, $\Delta_{12} \sim 10^{-5}$ $(\text{eV})^2$. The length scale associated with Δ_{12} is $\sim 10^5(\frac{E}{100\,MeV})$ km. The effects of such oscillations cannot be felt in the laboratory or in the atmospheric neutrino experiments. Hence, one can take $m_1 = m_2$ in analyzing these phenomena and all relevant conversion probabilities

[12] depend only on Δ_{32}.

$$\begin{aligned} P_{\nu_e\,\nu_e} &= 1-4s_{13}^2c_{13}^2\mathcal{S}; & P_{\nu_e\,\nu_\mu} &= s_{13}^2c_{13}^2s_{23}^2\mathcal{S} \\ P_{\nu_\mu\,\nu_\mu} &= 1-4s_{23}^2c_{13}^2(1-c_{13}^2s_{23}^2)\mathcal{S}; & P_{\nu_e\,\nu_\tau} &= 4s_{13}^2c_{13}^2s_{23}^2\mathcal{S} \\ P_{\nu_\tau\,\nu_\tau} &= 1-c_{23}^2c_{13}^2(1-c_{13}^2c_{23}^2)\mathcal{S}; & P_{\nu_\mu\,\nu_\tau} &= 4s_{23}^2c_{13}^4c_{23}^2\mathcal{S} \end{aligned} \tag{7}$$

where $\mathcal{S}=\sin^2\frac{\Delta_{23}L}{4E}$. Note that only two of the three mixing angles appear in all the probabilities. Thus one has effectively one more parameter compared to the conventional analysis in terms of only two generations. The detailed restrictions on the angles θ_{13} , θ_{23} and on Δ_{23} following from the laboratory search of the oscillations can be found for example in ref.[12].

Consider now the matter effects inside the Sun. The matter can enhance the conversion of ν_e if the latter go through the MSW resonance inside the Sun. As is well known, this requires the relevant (mass)^2 differences around 10^{-5} (eV)^2. The oscillations characterized by $\Delta_{32}\sim 10^{-2}$ (eV)^2 do not go through a resonance and the matter effects also get simplified in spite of the presence of three generations [12, 13, 14]. More specifically, the effective matter dependent (mass)^2 matrix can be expressed as

$$M_A^2=\begin{pmatrix} s_{12}^2\Delta_{21}+Ac_{13}^2 & s_{12}c_{12}\Delta_{21} & 0 \\ s_{12}c_{12}\Delta_{21} & c_{12}^2\Delta_{21} & 0 \\ 0 & 0 & \Delta_{31} \end{pmatrix}+O(\frac{\sin 2\theta_{13}A}{2\Delta_{32}}) \tag{8}$$

where $A=2\sqrt{2}G_Fn_eE$. The above equation is formally the same as in case of two generations. There are two important differences however. The resonance condition following from eq.(8) now becomes

$$\Delta_{21}\cos 2\theta_{12}=c_{13}^2A \tag{9}$$

Secondly, the survival probability for the electron neutrino now takes the form

$$P_{\nu_e\,\nu_e}=c_{13}^4P_2(\theta_{12},\Delta_{12})+s_{13}^4 \tag{10}$$

where $P_2(\theta_{12},\Delta_{12})$ is the standard survival probability in case of the two generations. Both eqs (9) and (10) differ from the corresponding two genration case because of the presence of one more mixing angle namely, θ_{13}.

One could distinguish between two physically different possibilities:

(b) Alternatively, the solar neutrino problem can be solved by the ν_e ν_τ oscillations and atmospheric neutrino by the ν_e ν_μ [14]. The survival probability is given in this case by

$$P_{\nu_e\,\nu_e} = c_{12}^4 P_2(\theta_{13}, \Delta_{13}) + s_{12}^4 \tag{11}$$

Note that in case (b), the additional angle entering the survival probabilities for the solar ν_e is required to be large from the atmospheric neutrino anomaly in contrast to the case (a) where the angle θ_{13} could be small. Thus, in case (b), one *cannot* treat the solar neutrino deficitė as purely two generation problem and the allowed region in parameter space changes. The region allowed by the solar neutrino data including the energy distribution observed by the Kamioka is determined for the case (b) in [14]. The allowed region is considerably larger in comparision to the two generation scenario.

Note that the cases (b) above requires a mass hierarchy different from the conventional one namely $m_{\nu_e} \ll m_{\nu_\mu} \ll m_{\nu_\tau}$. But such inverted hierarchies are not uncommon and occur for example in one of the most popular models for the neutrino masses namely, the Zee model [15]. The detailed mixing pattern predicted in this model is however not favoured [16] by the data in case of scenario (b).

3.2 Combined solution

While it is possible to solve the atmospheric and solar neutrino problems in variety of ways, combined solution of all three problems imply stringent constraints on the neutrino mass spectrum. The requirement that neutrinos provide the hot component in the dark matter demands that at least one of the neutrino mass should be in the eV range. But if there are only three neutrinos then one cannot generate two (mass)^2 differences both of which are much smaller then O(eV) unless all the neutrinos are degenerate to a high degree. Alternatively, one needs to introduce additional light sterile [4] neutrino. We shall consider the minimal scenario without any light sterile neutrinos in the following.

4. Models for neutrino masses

The mass terms for three light neutrinos can be written in general as follows:

$$-\mathcal{L}_{mass} = \frac{1}{2}\nu_L^T\, m_{eff}\, \nu_L \tag{12}$$

where m_{eff} is a matrix in generation space transforming under $SU(2)_L$ as a triplet. m_{eff} breaks the lepton number but it can preserve some linear combinations of the family lepton numbers. m_{eff} can be generated in one of the following ways [4]:

- Add an $SU(2)$ triplet scalar field T and assign non-zero vacuum expectation value (vev) to its neutral component. This way of generating mass term gives

width of Z.

- Generate an effective triplet term by radiative corrections. A proto-type of this way of mass generation is provided by the Zee model [15].

- Couple the ν_L to one or more heavy neutrinos. This results in the effective couplings of the above type. The prime example of this is the well known seesaw mechanism which is characterized by the following mass matrix between ν_L and ν_R

$$\mathcal{M}_\nu = \begin{pmatrix} 0 & m_D \\ m_D^T & M_R \end{pmatrix} \tag{13}$$

leading to the effective mass matrix

$$m_{eff} = -m_D M_R^{-1} m_D^T \tag{14}$$

Any one or more of above can be used to generate masses for the known left-handed neutrinos.

The seesaw models naturally arise in grand unified theories like $SO(10)$. The simplest of such theory also relates the neutrino Dirac masses to the mass matrix for the charged 2/3 quarks. As a result, the neutrino masses display strong generation dependence as long as M_R is generation blind. Typically,

$$m_{\nu_e} \sim \frac{m_u^2}{M_R} \; ; m_{\nu_\mu} \sim \frac{m_c^2}{M_R} \; ; m_{\nu_\tau} \sim \frac{m_t^2}{M_R} \tag{15}$$

The above equations imply

$$\frac{\Delta_{32}}{\Delta_{21}} \approx (\frac{m_t}{m_c})^4 \sim 10^8 \tag{16}$$

Hence it is not possible to solve both the atmospheric and solar neutrino problems simultaneously in the seesaw model based on the simplest $SO(10)$. It should however be remembered that the above results, many times taken as predictions of the seesaw scheme, are strongly model dependent. If M_R shows some generation dependence then the predictions could change drastically. For example, it is possible [17] to construct models where all the three neutrinos have masses in the eV range and two of them have mass splitting which could account for the solar neutrino deficit through the MSW mechanism. Moreover, such structure follows from natural assumptions namely m_D coinciding with the up quark masses and all the nonzero elements of M_R having the same order of magnitudes. Such models are interesting from the point of view that they display completely different pattern compared to the standard seesaw prediction. But, one cannot still obtain almost

discussed above.

A possible mechanism to obtain (almost) degenerate spectrum and the required departures from degeneracy was proposed in ref.[18, 19]. The mechanism presented there is quite natural in the context of the left right symmetric theories with manifest parity invariance. The majorana masses for the right handed neutrinos come from the $SU(2)_R$ triplet. But then the manifest left right symmetry requires the presence of a left handed triplet field with non-zero vev resulting in the following structure instead of eq.(13)

$$\mathcal{M}_\nu = \begin{pmatrix} m_L & m_D \\ m_D^T & M_R \end{pmatrix} \tag{17}$$

where m_L is the majorana mass for the left handed neutrinos. This generates the following effective mass

$$m_{eff} = m_L - m_D M_R^{-1} m_D^T \tag{18}$$

If there exists some horizontal symmetry [22] which makes the majorana mass matrices m_L,M_R proportional to identity matrix then the following pattern emerges for the masses

$$m_{\nu_e} \sim m_0 - \frac{m_u^2}{M_R} \tag{19}$$

$$m_{\nu_\mu} \sim m_0 - \frac{m_c^2}{M_R} \tag{20}$$

$$m_{\nu_\tau} \sim m_0 - \frac{m_t^2}{M_R} \tag{21}$$

$$\tag{22}$$

This leads to the following prediction [19]

$$\frac{\Delta_{32}}{\Delta_{12}} \sim (\frac{m_t}{m_c})^2 \sim 10^4 \tag{23}$$

Thus the hierarchy needed to solve the solar and atmospheric problems simultaneously is automatically reproduced in this picture. Moreover, the common degenerate mass m_0 can be writen as

$$m_0 \sim (2.5eV) \left(\frac{\Delta_{21}}{10^{-6}eV^2}\right) \left(\frac{M_R}{10^{16}\ GeV}\right) \tag{24}$$

Hence if the Δ_{12} is in the range appropriate for a solution to the solar neutrino problem through the MSW mechanism and M_R around the GUT scale then the degenerate mass m_0 is automatically fixed in the eV range needed to provide the hot component in the dark matter.

One possible problem in the above scheme is difficulty in generating a large mixing needed to solve the atmospheric neutrino problem. The mixing in the lepton sector is correlated to mixing in the quark sector in $SO(10)$ type models. In case of the ordinary seesaw model, one could destroy this correlation by making the M_R [23] to be generation dependent. This does not happen in the present case since m_L and hence M_R is required to be proportional to the identity matrix. This can be avoided if one introduce extra singlet [20] fermions or makes the Higgs structure complex enough to destroy the interesting relations between femion masses existing in the simple $SO(10)$ scenario.

The above scheme predicts a non-zero effective mass of the O(2 eV) for the neutrinoless double beta decay amplitude. This is to be contrasted with the latest [24] limit of about 0.68 eV. Thus even after allowing for a factor of two uncertainty in the nuclear matrix elements, the simplest model seems to be ruled out. This however does not exclude the theoretically interesting possibility of degenerate neutrino spectrum since in principal, there could be cancellations among different neutrino contributions. Constructing a realistic model displaying this cancellation is however quite challanging.

5. Conclusions

We have reviewed the hints on neutrino masses following from present experiments and have discussed their implications. All the hints can be simultaneously satisfied within the minimal scenario only if all the three neutrinos are almost degenerate. This seemingly different pattern compared to other fermion masses can be naturally understood in the seesaw picture with additional discrete symmetry. The present models for degenerate masses do not seem to be favoured by the neutrinoless double beta decay results if the degenerate mass is to provide the hot dark matter. This may be a pointer to the existence of more than three light neutrinos.

References

[1] We have up dated here some of the material presented at the workshop in the light of new results on the solar and atmospheric neutrino problems.

[2] For a review see A. Yu. Smirnov, invited talk at Lepton Photon Conference, Cornell, 1993, ICTP preprint IC/93/388.

[3] K.V.L. Sarma, Tata Inst. of Fundamental Research, Bombay preprint, TIFR/TH/84-13, HEP-PH 9408277

[4] J. W. F. Valle, *Gauge Theories and the Physics of Neutrino Mass*, *Prog. Part. Nucl. Phys.* **26** (1991) 91-171.

[5] M. Mikheyev, A. Smirnov, *Sov. J. Nucl. Phys.* **42** (1986) 913; L. Wolfenstein, *Phys. Rev.* **D17** (1978) 2369; *ibid.* **D20** (1979) 2634.

[6] S. Glashow, L. Krauss, *Phys. Lett.* **B190** (1987) 199; V. Barger, R. Phillips, *Phys. Rev. Lett.* **69** (1992) 3135 and references therein P. Krastev and S. T. Petcov, *Phys. Rev. Lett.* **72** (1994) 1960; V. Barger, et al *Phys. Rev.* **D43** (1991) 1759

[7] A. Yu. Smirnov,Talk given at the Int. Workshop on Solar neutrino problem: Astrophysics or oscillations, Gran Sasso, 1994, ed. V. Berezinsky and V. Fiorini,p4 (1994)

[8] Y. Fukuda *et al* *Phys. Lett.* **B335** (1994) 237

[9] E. Kolb, M. Turner, *The Early Universe*, Addison Wesley, 1990

[10] For a review, see talks by C. Frenk and J. Primack, proceedings of the *International School on Cosmological Dark Matter*, Valencia Oct.1993, (World Scientific, 1994), p. 7-18, edited by J. W. F. Valle and A. Perez, pages 65 and 81.

[11] A.N. Taylor and M. Rowan-Robinson, Nature **359** (1992) 396; M. Davis, F. J. Summers and D. Schlegel, Nature, **359** (1992) 393.

[12] G.L.Fogli,E.Lisi and D. Montanino, *Phys. Rev.* **D494** (1994) 3626.

[13] T.K. Kuo and J. Pantaleone, *Rev. Mod. Phys.* **61** (1989) 937

[14] A.S.Joshipura and P. Krastev, *Phys. Rev.* **D50** (1994) 3484

[15] A. Zee, *Phys. Lett.* **B93** (1980) 389

[16] A. Yu. Smirnov and Z. Tao, *Nucl. Phys.* **B 426** (1994) 415

[17] G. Datta and A.S. Joshipura, preprint PRL-TH/94/13.

[18] D.O. Caldwell and R.N. Mohapatra, *Phys. Rev.* **D48** (1993) 3259

[19] A. S. Joshipura, *Zeit. fur Physik* **C** (19) , to appear.

[20] A. S. Joshipura, preprint PRL-TH/94/08,to appear in *Phys. Rev.* **D** (1995)

[21] S. T. Petcov, A. Smirnov, preprint SISSA 113/93/EP A. Ioannissyan, J.W.F. Valle, *Phys. Lett.* **B332** (1994) 93-99; D.O. Caldwell and R.N. Mohapatra, preprint UCSB-HEP-94-03, February 1994; B. Bamert, C.P. Burgess, preprint McGill-94/07, February 1994; D. Caldwell and R. N. Mohapatra, Maryland report, UMD-PP-94-90 (1994); D. G. Lee and R. N. Mohapatra, Maryland Report, UMD-PP-94-95 (1994).

[22] Many models for the degenerate neutrinos were proposed [20, 21] after the workshop. Some of these were by the participants in the workshop.

[23] A. Yu Smirnov, *Phys. Rev.* **D48** (1993) 3264

[24] A. Balysh et al, talk presented by K. Zuber at the XXVII confenrence on High Energy physics, Glasgow (1994).

Topics in chiral perturbation theory

ULF-G. MEIßNER

Centre de Recherches Nucléaires et Uiniversité Louis Pasteur de Strasbourg, Physique Théorique, BP 20Cr, 67037 Strasbourg Cedex 2, France

Abstract. I consider some selected topics in chiral perturbation theory (CHPT). For the meson sector, emphasis is put on processes involving pions in the isospin zero S-wave which require multi-loop calculations. The advantages and shortcomings of heavy baryon CHPT are discussed. Some recent results on the structure of the baryons are also presented.

1. Introduction

This talk will be concerned with certain aspects of the standard model in the long-distance regime. I will argue that there exists a rigorous calculational scheme and that plenty of interesting and *fundamental* problems await a solution. I hope this will trigger further detailed studies of these topics (and others which can only be mentioned en passant).

Our starting point is the observation that in the three flavor sector, the QCD Hamiltonian can be written as

$$\begin{aligned} H_{\rm QCD} &= H^0_{\rm QCD} + H^I_{\rm QCD} \\ H^I_{\rm QCD} &= \int d^3x \{ m_u \bar{u}u + m_d \bar{d}d + m_s \bar{s}s \} \end{aligned} \tag{1}$$

with $H^0_{\rm QCD}$ symmetric under chiral SU(3)$_L\times$ SU(3)$_R$. On a typical hadronic scale, say $M_\rho = 770$ MeV, the current quark masses $m_q = m_u, m_d, m_s$ can be considered as perturbations. The chiral symmetry of the Hamiltonian is spontaneously broken down to its vectorial subgroup SU(3)$_V$ with the occurence of eight (almost) massless pseudoscalar mesons, the Goldstone bosons ($\varphi = \pi^+, \pi^0, \pi^-, K^+, K^-, K^0, \bar{K}^0, \eta$)

$$M^2_\varphi = m_q\, B + \mathcal{O}(m_q^2) \tag{2}$$

with $B = -<0|\bar{q}q|0>/F_\pi^2$ and F_π the pion decay constant. In the confinement (long-distance) regime, the properties of the standard model related to this symmetry can be unambigously worked out in terms of an effective Lagrangian,

$$\mathcal{L}_{\rm QCD} = \mathcal{L}_{\rm eff}[U, \partial_\mu U, \ldots, \mathcal{M}] \tag{3}$$

with $\mathcal{M} = {\rm diag}(m_u, m_d, m_s)$ the quark mass matrix and the Goldstone bosons are collected in the matrix-valued field $U(x) = \exp\{i\sum_{a=1}^8 \varphi_a(x)\lambda^a/F_\pi\}$. Of course,

there is an infinity of possibilities of representing the non-linearly realized chiral symmetry. While the QCD Lagrangian is formulated in terms of quark and gluon fields and the rapid rise of the strong coupling constant $a_S(Q^2)$ with decreasing Q^2 forbids a systematic perturbative expansion, matters are different for the effective field theory (EFT) based on the effective Lagrangian (3). It can be written as a string of terms with increasing dimension,

$$\mathcal{L}_{\rm eff} = \mathcal{L}_{\rm eff}^{(2)} + \mathcal{L}_{\rm eff}^{(4)} + \mathcal{L}_{\rm eff}^{(6)} + \ldots \tag{4}$$

if one counts the quark masses as energy squared. To lowest order, the effective Lagrangian contains two parameters, F_π and B. It is worth to stress that B never appears alone but only in combination with the quark mass matrix, alas the pseudoscalar meson masses. Consequently, any matrix–element $< ME >$ for the interactions between the pseudoscalars can be written as

$$< ME >= c_0 \left(\frac{E}{\Lambda}\right)^2 + \left[\sum_{i=1}^{n}(c_{1i}) + ({\rm non-local})\right]\left(\frac{E}{\Lambda}\right)^4 + \mathcal{O}\left(\frac{E}{\Lambda}\right)^6 \tag{5}$$

This is obviously an energy expansion or, more precisely, a simultaneous expansion in small external momenta *and* quark masses. The first term on the r.h.s. of (5) leads to nothing but the well–known current algebra results, the pertinent coefficient c_0 can be entirely expressed in terms of F_π, the Goldstone masses and some numerical constants. As one of the most famous examples I quote Weinberg's result for the S-wave, isospin zero scattering length [1],

$$a_0^0 = \frac{7M_\pi^2}{32\pi F_\pi^2} \tag{6}$$

which is such an interesting observable because it vanishes in the chiral limit $M_\pi \to 0$. At next-to-leading order, life is somewhat more complicated. As first shown by Weinberg [2] and discussed in detail by Gasser and Leutwyler [3], one has to account for meson loops which are naturally generated by the interactions. These lead to what I called "non–local" in (5). In fact, it can be shown straightforwardly that any N–loop contribution is suppressed with respect to the leading order result by $(E/\Lambda)^{2N}$. At $\mathcal{O}(E^4)$, the loop contributions do not introduce any new parameters. However, one also has to account for the contact terms of dimension four which are accompanied by a priori unknown coupling constants (the c_{1i} in (5)). These so–called low–energy constants serve to renormalize the infinities related to the pion loops. Their finite pieces are then fixed from some experimental input. In the case of flavor SU(2), one has $n = 7$. Two of these constants are related to interactions between the pseudoscalars, three to quark mass insertions and the remaining two have to be determined from current matrix elements. The inclusion of gauge boson couplings to the Goldstone bosons is most simply and economically done in the framework of external background sources. Notice also that at order E^4 the chiral anomaly can be unambigously included in the EFT. At order E^6, one has to consider loop diagrams with insertions from $\mathcal{L}_{\rm eff}^{(2)}$ and $\mathcal{L}_{\rm eff}^{(4)}$ as well as contact terms from $\mathcal{L}_{\rm eff}^{(6)}$ which introduces new couplings. Once the low–energy constants are fixed, the aspects of the dynamics of the standard model related to the chiral symmetry

more cumbersome (but can't always be avoided as will be discussed below). This is the basic framework of CHPT in a nutshell. For more details, I refer to refs.[2,3], my review [4] and the extensive list of references given therein. It is worth pointing out that Leutwyler has recently given a more sound foundation of the effective Lagrangian approach by relating it directly to the pertinent Ward–Identities [5].

2. Meson-meson scattering and the mode of quark condensation

Pion–pion and pion–kaon scattering are the purest reactions between the pseudoscalar Goldstone bosons. The Goldstone theorem mandates that as the energy goes to zero, the interaction between the pseudoscalars vanishes. Consequently, $\pi\pi$ and πK scattering are the optimal testing grounds for CHPT.

Let me first consider the chiral expansion of the isospin zero S–wave in $\pi\pi$ scattering. In the standard formulation of CHPT, Gasser and Leutwyler have derived a low–energy theorem generalizing Weinberg's result (6) [6],

$$a_0^0 = 0.20 \pm 0.01 \tag{7}$$

which is compatible with the data, $a_0^0 = 0.23 \pm 0.08$ [7]. The theoretical value (7) rests on the assumption that B is large, i.e. of the order of 1 GeV (from current values of the scalar quark condensates). However, if B happens to be small, say of the order of F_π, one has to generalize the CHPT framework as proposed by Stern et al.[8]. In that case, the quark mass expansion of the Goldstone bosons takes the form

$$M_\varphi^2 = m_q\, B + m_q^2\, A + \mathcal{O}(m_q^3) \tag{8}$$

with the second term of comparable size to the first one. In ref.[9], this framework is discussed in more detail and a novel representation of the $\pi\pi$ amplitude which is exact including order E^6 and allows to represent the *whole* $\pi\pi$ scattering amplitude in terms of the S– and P–waves and six subtraction constants is given. The presently available data are not sufficiently accurate to disentangle these two possibilities. More light might be shed on this when the ϕ–factory DAΦNE will be in operation (via precise measurements of $K_{\ell 4}$–decays) or if the proposed experiment to measure the lifetime of pionic molecules [10] will be done. It should also be pointed out that recent lattice QCD results seem to be at variance with the expansion (8), but this can only be considered as indicative [11]. Also, the experimentally well–fulfilled GMO relation for the pseudoscalar meson masses arises naturally in the conventional CHPT framework but requires parameter fine–tuning in case of a small value of $B \sim 100$ MeV. Novel high precision experiments at *low energies* are called for. This is an important question concerning our understanding of the standard model and it definitively should deserve more attention. For more details, I refer to sections 4.1 and 4.2 of ref.[4] as well as ref.[9].

In fig.1, I show the phase–shift δ_0^0 from threshold (280 MeV) to approximately 600 MeV [12]. One notices the rapid rise of the phase shift, and at 600 MeV it is already as large as 55 degrees and passes through 90 degrees at about 850 MeV. At energies below 600 MeV, the other partial waves do not exceed 15 degrees (in magnitude). This behaviour of δ_0^0 is attributed to the so–called strong pionic final

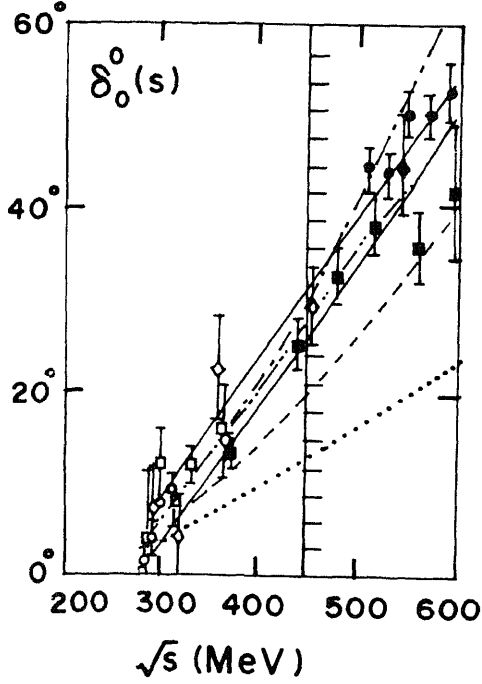

Figure 1. $\pi\pi$ scattering phase shift $\delta_0^0(s)$. The dashed line gives the tree result and the dashed–dotted the one–loop prediction. Also shown is the Roy equation band. The data can be traced back from ref.[12]. The double–dashed line corresponds to the one–loop result based on another definition of the phase–shift which differs at order E^6 from the one leading to the dashed–dotted line (and thus gives a measure of higher order corrections). On the right side of the hatched area, the one–loop corrections exceed 50 per cent of the tree result.

phase of the CP–violation parameter ϵ'[12],

$$\Phi(\epsilon') = \frac{\pi}{2} - (\delta_0^0 - \delta_0^2)\Big|_{s=M_{K^0}^2} = (45 \pm 6)^\circ \tag{9}$$

This is due to the fact that the corrections to δ_0^2 are of the same sign as the ones to δ_0^0 and thus cancel. At tree level, $\Phi(\epsilon') = 37^\circ$. The accuracy of the theoretical prediction is as good as the resent empirical one, $\Phi(\epsilon')_{\rm exp} = (43 \pm 8)^\circ$ [7]. Notice that it is much more difficult to get a precise number on $\Phi(\epsilon')$ from $K \to 2\pi$ decays because of the variety of isospin breaking effects one has to account for (this theme is touched upon in ref.[12]).

I briefly turn to the case of πK scattering. Here, the empirical situation is even worse, which is very unfortunate. In the framework of conventional CHPT, the threshold behaviour of the low partial waves can be unambigously predicted [13] since all low–energy constants in SU(3) are fixed. Furthermore, since the mass of the strange quark is of the order of the QCD scale–parameter, it is less obvious that the chiral expansion at next–to–leading order will be sufficiently accurate. Much improved empirical information of these threshold parameters might therefore lead to a better understanding of the three flavor CHPT. Another possibility is that the threshold of πK scattering at 635 MeV is alreday so high that one has to connect CHPT constraints with dispersion theory. This concept has investigated in detail by Dobado and Pelaez [14] and certainly improves the prediction in the P–wave drastically. Another way of extending the EFT through the implicit inclusion of resonance degrees of freedom is discussed in ref.[62]. On the experimental side, a measurement of πK molecule decays would certainly help to clarify the situation [11].

3. Two loops and beyond

The simplest object to study in detail the strong pionic final state interactions in the isospin zero S–wave is a three–point function, namely the so–called scalar form factor (ff) of the pion,

$$< \pi^a(p')\pi^b(p)|\hat{m}(\bar{u}u + \bar{d}d)|0 >= \delta^{ab}\,\Gamma_\pi(s) M_\pi^2 \tag{10}$$

with $s = (p'+p)^2$. To one loop order, the scalar ff $\Gamma_{\pi,2}(s)$ has been given in ref.[3]. As shown in fig.2, closely about the two–pion cut, the real as well as the imaginary part of the one loop representation are at variance with the empirical information obtained from a dispersion–theoretical analysis [15]. However, unitarity allows one to write down a two–loop representation [16],

$$\Gamma_\pi(s) = d_0 + d_1\, s + d_2\, s^2 + \frac{s^3}{\pi}\int_{4M_\pi^2}^{\infty} \frac{ds'}{s'^3}\frac{\sigma(s')}{s'-s}\left\{T_{0,2}^0(1 + {\rm Re}\Gamma_{\pi,2}) + T_{0,4}^0\right\} \tag{11}$$

where $T_{0,2}^0$ and $T_{0,4}^0$ are the tree and one loop representations of the $\pi\pi$ S–wave, isospin zero scattering matrix. Notice that the imaginary part of $\Gamma_\pi(s)$ to two

loops is entirely given in terms of known one loop amplitudes. The three subtraction constants appearing in (11) can be fixed from the empirical knowledge of the normalization, the slope and the curvature of the scalar ff at the origin. In the chiral expansion, these numbers are combinations of two low–energy constants from $\mathcal{L}_{\rm eff}^{(4)}$ and two from $\mathcal{L}_{\rm eff}^{(6)}$.

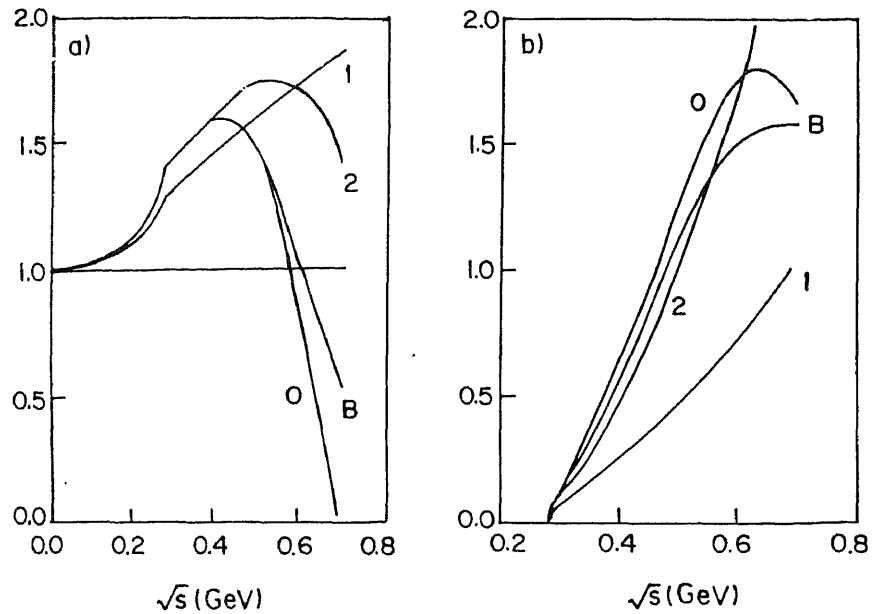

Figure 2. Scalar form factor of the pion. The curves labelled '1', '2', 'O' and 'B' correspond to the chiral prediction to one–loop, to two–loops, the modified Omnès representation and the result of the dispersive analysis, respectively. The real part is shown in (a) and the imaginary part in (b).

The turnover of the scalar ff at around 550 MeV can be understood if one rewrites (11) in an exponential form,

$$\mathrm{Re}\Gamma_\pi(s) = P(s)\exp[\mathrm{Re}\Delta_0(s)]\cos\delta_0^0 + \mathcal{O}(E^6) \tag{12}$$

with $\mathrm{Im}\ \Delta_0(s) = \delta_0^0 + \mathcal{O}(E^6)$ fulfilling the final–state theorem at next–to–leading order. Although this representation is not unique, it allows to understand the vanishing of $\mathrm{Re}\Gamma_\pi(s)$ at 680 MeV since the phase (in the loop approximation) passes through 90° at this energy thus forcing the turnover. Expanding $\cos\delta_0^0 = 1-(\delta_0^0)^2+\ldots = 1+\mathcal{O}(s^2/F_\pi^4)$ it becomes clear why this behaviour can only show up at two loop order (and higher). One can do even better and sum up all leading and next–to–leading logarithms by means of an Omnes representation [16]. This leads to

a further improvement in $\mathrm{Re}\Gamma_\pi(s)$ and allows to understand that the very accurate two loop result for $\mathrm{Im}\Gamma_\pi(s)$ is not spoiled by higher orders, these can be estimated from the improved chiral expansion of the scalar ff and are found to be small below 550 MeV. The physics behind all this is that the two–loop corrections lead to the two–pion cut with proper strength which dominates the scalar ff below 600 MeV. To go further one would have to include inelasticities (which start at order E^8), in particular the strong coupling to the $\bar{K}K$ channel. It is also worth pointing out that the scalar ff can only be represented by a polynomial below $s = 4M_\pi^2$. Notice that in this energy range the normalized scalar ff varies from 1 to 1.4, signaling a large scalar radius of the pion. For comparison, the vector ff changes from 1 to 1.15 for $0 \leq s \leq 4M_\pi^2$. In this way, unitarity allows to extend the range of CHPT, however, one has to be able to fix the pertinent subtraction constants (which is the equivalent to determining the corresponding low–energy constants).

Another reaction which has attracted much attention recently is $\gamma\gamma \to \pi^0\pi^0$ in the threshold region. It belongs to the rare class of processes which are vanishing at tree level (since the photon can only couple to charged pions, one needs at least one loop) and do not involve any of the low–energy couplings from $\mathcal{L}_{\rm eff}^{(4)}$ at one loop order. Some years ago, Bijnens and Cornet [17] and Donoghue, Holstein and Lin [18] calculated the one–loop cross section and found that it is at variance with the Crystal ball data [19] even close to threshold (see fig.3).

This is another case where one has to account for the strong pionic final state interactions. At 400 MeV, one has

$$\left(\frac{\sigma^{\rm exp}}{\sigma^{1-\rm loop}}\right)^{1/2} = 1.3 \tag{13}$$

which is a typical correction in this channel (see discussion above on a_0^0 and the scalar ff). In fact, dispersion theoretical calculations supplemented with current algebra constraints by Pennington [20] tend to give the trend of the data (see the shaded area in fig.3). An improved combination of chiral machinery and dispersion theory has been given by Donoghue and Holstein [21]. Even better, Bellucci, Gasser and Sainio [22] have performed a full two loop calculation. It involves some massive algebra and three new low–energy constants have been estimated from resonance exchange (the main contribution comes form the ω). These couplings play, however, no role below 400 MeV. The solid line in fig.3 shows the two–loop result for the central values of the coupling constants. One finds a good agreement with the data up to $E_{\pi\pi} = 700$ MeV. This resolves the long–standing discrepancy between the chiral prediction and the data in the threshold region. For a more detailed discussion of these topics and the related neutral pion polarizabilities, I refer to ref.[22].

The last topic I briefly want to mention is the radiative kaon decay $K_L \to \pi^0\gamma\gamma$ which has no tree–level contribution and is given by a finite one–loop calculation at order E^4 [23]. The predicted two–photon invariant mass spectrum turned out to be in amazing agreement with the later measurements [24]. However, the branching

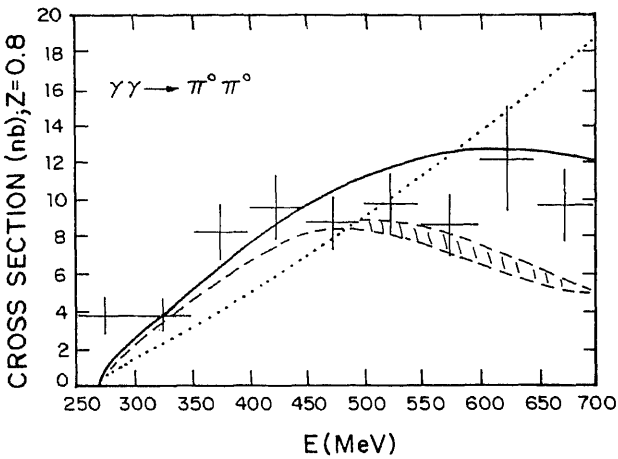

Figure 3. Cross section for $\gamma\gamma \to \pi^0\pi^0$. The chiral one and two loop predictions are given by the dotted and the solid line, in order. The hatched area is a dispersion–theoretical fit. The Crystal ball data are also shown. From [22].

4. Inclusion of baryons

While the chiral Lagrangian is particularly suited to investigate the properties of the pseudoscalar mesons, it can also be used to gain insight into the structure of the low-lying baryons. I will be brief on the formal aspects but rather refer to the reviews [4,27] and the extensive papers by Gasser, Sainio and Švarc [28] and Krause [29].

Let me first restrict myself to the two flavor sector, the pion-nucleon system. To lowest order $\mathcal{O}(E)$, the effective Lagrangian takes the form

$$\mathcal{L}_{\pi N} = \bar{\Psi}\big(i\gamma_\mu D^\mu - m + \frac{1}{2} g_A \gamma_\mu \gamma_5 u^\mu\big)\Psi \tag{14}$$

with D_μ the covariant derivative, m the nucleon mass (in the chiral limit), g_A the axial-vector coupling constant (in the chiral limit) and $u_\mu = iu^\dagger \nabla_\mu U u^\dagger$, $u = \sqrt{U}$ and Ψ embodies the proton and neutron fields. The physics becomes most transparent if one expands the various terms in powers of the pion and external fields (like e.g. the photon). The vectorial coupling includes e.g. the photon-nucleon vertex and the two-pion seagull ("Weinberg term") whereas the axial-vector term in (14) leads to the pseudovector πN coupling and the famous Kroll-Rudermann vertex (among others). The presence of the nucleon mass term, which is of comparable size to the chiral symmetry breaking scale, does not allow the nucleon four-momentum to be treated as small. This spoils the one-to-one correspondence between the loop and the energy expansion (for more details see refs.[27,28]). As pointed out in particular by Jenkins and Manohar [30], heavy quark EFT methods help to overcome this problem. Consider the nucleon as a very heavy, static source, i.e. non-relativistically. In that case, one can write its four-momentum as

$$p_\mu = m v_\mu + l_\mu \tag{15}$$

with v_μ the four-velocity ($v^2 = 1$) and l_μ a small off-shell momemtum, $v \cdot l \ll m$. One can therefore write the nucleon wave function in terms of velocity eigenstates,

$$\Psi = \exp\{-imv \cdot x\}(H + h) \tag{16}$$

with $\not{v} H = H$ and $\not{v} h = -h$ (notice that I have interchanged the H and the h in comparison to the standard (funny) notation). If one now eliminates h by use of its equation of motion (or by a Foldy-Wouthuysen transformation), one finds (for details, see e.g. ref.[31])

$$\mathcal{L}_{\pi N} = \bar{H}\big(iv \cdot D + g_A u \cdot S\big)H + \mathcal{O}(1/m) \tag{17}$$

with S_μ the covariant spin-operator, $S_\mu = i\gamma_5 \sigma_{\mu\nu} v^\nu/2$, known to our anchestors also as the Pauli-Lubanski vector. The cumbersome baryon mass term has disappeared and thus a consistent power counting emerges (this is discussed very nicely

in Ecker's lectures [32]). One also notices that all Dirac bilinears can be expressed in terms of v_μ and S_μ thus faciliating the algebra enormeously. The one loop graphs contribute at order E^3. As will be discussed below, it is however mandatory to include the terms of order E^4 in the effective Lagrangian for accurate one–loop calculations, i.e.

$$\mathcal{L}_{\pi N} = \mathcal{L}^{(1)}_{\pi N} + \mathcal{L}^{(2)}_{\pi N} + \mathcal{L}^{(3)}_{\pi N} + \mathcal{L}^{(4)}_{\pi N} \tag{18}$$

where I have not exhibited the meson Lagrangian discussed before. The coefficients accompanying $\mathcal{L}^{(2)}_{\pi N}$ are all finite since the loops start to contribute at order E^3. A complete analysis of the divergence structure at order E^3 will soon be available [33]. A systematic analysis of nucleon properties to order E^3 can be found in [31] and some E^4 calculations have recently been performed. I will discuss one particular case in some more detail below. I will also elaborate on two yet unsolved problems in the heavy mass approach, one is related to the analytical structure of S–matrix elements (which does not appear in the relativistic formulation, see section 8) and the other is the extension to flavor SU(3) and the inclusion of decuplet fields (see sections 6 and 7).

5. Baryon compton scattering

Compton scattering off the nucleon at low energies offers important information about the structure of these particles in the non-perturbative regime of QCD. The spin–averaged forward scattering amplitude for real photons in the nucleon rest frame can be expanded as a power series in the photon energy ω,

$$T(\omega) = f_1(\omega^2)\, \vec{\epsilon}^{\,*}_f \cdot \vec{\epsilon}_i, \quad f_1(\omega^2) = a_0 + a_1\, \omega^2 + a_2\, \omega^4 + \ldots \tag{19}$$

where $\vec{\epsilon}_{i,f}$ are the polarization vectors of the initial and final photon, respectively, and due to crossing symmetry only even powers of ω occur. The Taylor coefficients a_i encode the information about the nucleon structure. The first term in eq.(19), $a_0 = -e^2 Z^2/4\pi m$, dominates as the photon energy approaches zero, it is only sensitive to the charge Z and the mass m of the particle the photon scatters off (the Thomson limit). The term quadratic in the energy is equal to the sum of the so-called electric ($\bar{\alpha}$) and magnetic ($\bar{\beta}$) Compton polarizabilities, $a_1 = \bar{\alpha} + \bar{\beta}$. Corrections of higher order in ω start out with the term proportional to a_2. Over the last years, high precision measurements at Mainz, Illinois, Oak Ridge and Saskatoon [34] have lead to the following empirical values: $\bar{\alpha}_p = (10.4 \pm 0.6) \cdot 10^{-4}\mathrm{fm}^3$, $\bar{\beta}_p = (3.8 \mp 0.6) \cdot 10^{-4}\mathrm{fm}^3$, $\bar{\alpha}_n = (12.3 \pm 1.3) \cdot 10^{-4}\mathrm{fm}^3$, $\bar{\beta}_n = (3.5 \mp 1.3) \cdot 10^{-4}\mathrm{fm}^3$ making use of the dispersion sum rules [35] $(\bar{\alpha}+\bar{\beta})_p = (14.2 \pm 0.3) \cdot 10^{-4}\ \mathrm{fm}^3$ and $(\bar{\alpha}+\bar{\beta})_n = (15.8 \pm 0.5) \cdot 10^{-4}\ \mathrm{fm}^3$. The two outstanding features of these numbers are the fact that $(\bar{\alpha} + \bar{\beta})_p \simeq (\bar{\alpha} + \bar{\beta})_n$ and that the proton as well as the neutron behave essentially as (induced) electric dipoles.

In CHPT, it was found that to leading order in the chiral expansion the nucleon em polarizabilities are given by a few one loop diagrams (whose sum is finite) [36] with no counter term contributions (much like the reactions $K_L \to \pi^0\gamma\gamma$ and $\gamma\gamma \to \pi^0\pi^0$ discussed before). This calculation was later redone in the heavy mass approach [31]. The pertinent diagrams are shown in fig.4.

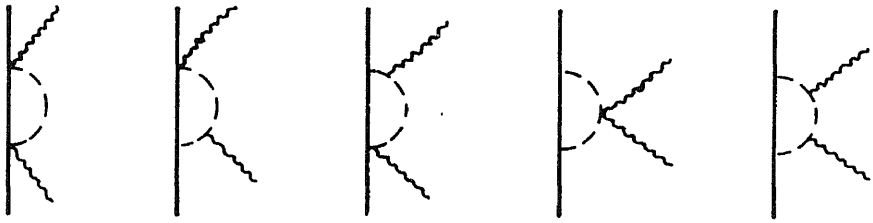

Figure 4. One–loop diagrams which lead to the nucleon em polarizabilities (20).

By isospin arguments, one finds that they will lead to the same polarizabilities for the proton and the neutron. The resulting expressions for $\bar{\alpha}_{p,n}$ and $\bar{\beta}_{p,n}$ contain therefore only parameters from the lowest order effective Lagrangian $\mathcal{L}_{\pi N}^{(1)} + \mathcal{L}_{\pi\pi}^{(2)}$ [31,36],

$$\bar{\alpha}_p = \bar{\alpha}_n = \frac{5e^2 g_A^2}{384\pi^2 F_\pi^2} \frac{1}{M_\pi} = 12.2 \cdot 10^{-4}\text{fm}^3, \quad \bar{\beta}_p = \bar{\beta}_n = \frac{\bar{\alpha}_p}{10} = 1.2 \cdot 10^{-4}\text{fm}^3 \quad (20)$$

In the chiral limit, the em polarizabilities diverge. This is expected since the Yukawa suppression for massive pions turns into a long–range power–law fall–off as $M_\pi \to 0$. Clearly, the leading order CHPT results (20) explain the trends of the data. However, one might argue that the result for the magnetic polarizabilities is not very meaningful since one has not accounted for the strong $N\Delta$ M1 transition. In fact, this starts to contribute at order E^4 (and higher) in agreement with the decoupling theorem [37]. In ref.[38], a *complete* calculation of the em polarizabilities to $\mathcal{O}(E^4)$ was given. At this order, contact terms from $\mathcal{L}_{\pi N}^{(2,3,4)}$ enter. Some of them can be directly related to empirical information (viz πN scattering [39]), others are estimated from resonance exchange, and this is where the $\Delta(1232)$ comes in. It should be stressed that the resonance saturation hypothesis to understand the values of the low–energy constants has only strictly been tested in the meson sector [40]. In the absence of sufficiently many accurate low–energy data, it serves as a working hypothesis in the baryon sector (this situation will be improved when more data will become available). The em polarizabilities to order E^4 take the form

$$(\bar{\alpha}, \bar{\beta})_{p,n} = \frac{C_1}{M_\pi} + C_2 \ln M_\pi + C_3 \quad (21)$$

with $C_1 = 5e^2 g_A^2 / 384\pi^2 F_\pi^2$. The coefficient C_2 contains some low–energy constants from $\mathcal{L}_{\pi N}^{(2)}$ and C_3 four novel ones from $\mathcal{L}_{\pi N}^{(4)}$. The second and the third term in (21) are the new E^4 contributions. The $\Delta(1232)$ strongly dominates the constant C_3. The non–analytic loop contribution $\sim \ln M_\pi$ is potentially large. Indeed, in the case of $\bar{\beta}_p$ the ln contribution is negative with a large coefficient and cancels most of the large positive one related to the $\Delta(1232)$ exchange. In ref.[41], a thorough study of the theoretical uncertainties entering the E^4 calculation was performed and the following results emerged

$$\bar{\alpha}_p = 10.5 \pm 2.0\,, \bar{\beta}_p = 3.5 \pm 3.6\,, \bar{\alpha}_n = 13.4 \pm 1.5\,, \bar{\beta}_n = 7.8 \pm 3.6\,, \quad (22)$$

In fig.5, I show the real part of the proton forward Compton scattering amplitude $A_p(\omega) = -4\pi f_1(\omega^2)$ in comparison to the data which follow from the total photonucleon absorption cross section via

$$\mathrm{Re}\, A_p(\omega) = \frac{e^2 Z^2}{m} - \frac{2\omega^2}{\pi} \mathcal{P} \int_{\omega_0}^{\infty} d\omega' \frac{\sigma_{\mathrm{tot}}(\omega')}{\omega'^2 - \omega^2} \tag{23}$$

The amplitude has a branch point related to the threshold energy for single pion photoproduction at

$$\omega_0 = M_\pi (1 + \frac{M_\pi}{2m}) \tag{24}$$

Notice that to order E^3 the chiral representation [31] has a cut starting at $\omega_0 = M_\pi$ and only at $\mathcal{O}(E^4)$ one recovers the recoil correction $\sim 1/m$ in (24). This problem is inherent to the heavy mass formulation of baryon CHPT. In the relativistic formulation, the corresponding analytic structures (location of cut singularities) are always given correctly and do not depend on the order of the chiral expansion. I will pick up this theme in section 8. Fig.5 also shows that the E^4 result for $A_p(\omega)$ reproduces the cusp at ω_0. However, above that energy, the chiral prediction is at variance with the data. This can be traced back to the fact that the imaginary part changes sign at $\omega \simeq 180$ MeV. One would have to go to two loops to get an improved prediction for the imaginary part as alreday stressed in section 3.

It is fairly straightforward to extend the lowest order E^3 calculation to the three flavor sector. This allows to predict the hyperon polarizabilities which eventually will be measured at Fermilab and CERN via the Primakoff effect. In SU(3), one has two axial couplings and thus the lowest order effective meson–baryon Lagrangian reads

$$\mathcal{L}^{(1)}_{MB} = \mathrm{Tr}(\bar{B}\, iv\cdot\mathcal{D}\, B) + D\, \mathrm{Tr}(\bar{B} S^\mu \{u_\mu, B\}) + F\, \mathrm{Tr}(\bar{B} S^\mu [u_\mu, B]) \tag{25}$$

where $U(x)$ now contains the eight pseudoscalar fields (π, K, η) and B is a 3×3 matrix containing the low–lying baryon octet,

$$B = \begin{pmatrix} \frac{1}{\sqrt{2}}\Sigma^0 + \frac{1}{\sqrt{6}}\Lambda & \Sigma^+ & p \\ \Sigma^- & -\frac{1}{\sqrt{2}}\Sigma^0 + \frac{1}{\sqrt{6}}\Lambda & n \\ \Xi^- & \Xi^0 & -\frac{2}{\sqrt{6}}\Lambda \end{pmatrix} \tag{26}$$

The numerical values for the two axial couplings D and F are $D \simeq 3/4$ and $F \simeq 1/2$ subject to the constraint $D + F = g_A = 1.26$. The hyperon polarizabilities can be calculated from the diagrams in fig.4 with π and K loops and one finds e.g. [42]

$$\bar{\alpha}_{\Sigma^-} = 6, \quad \bar{\alpha}_{\Sigma^+} = 9, \tag{27}$$

(in canonical units), i.e. the Σ^+ is expected to have a larger electric polarizability then the Σ^- due to the kaon loop contributions. Quark model estimates give a

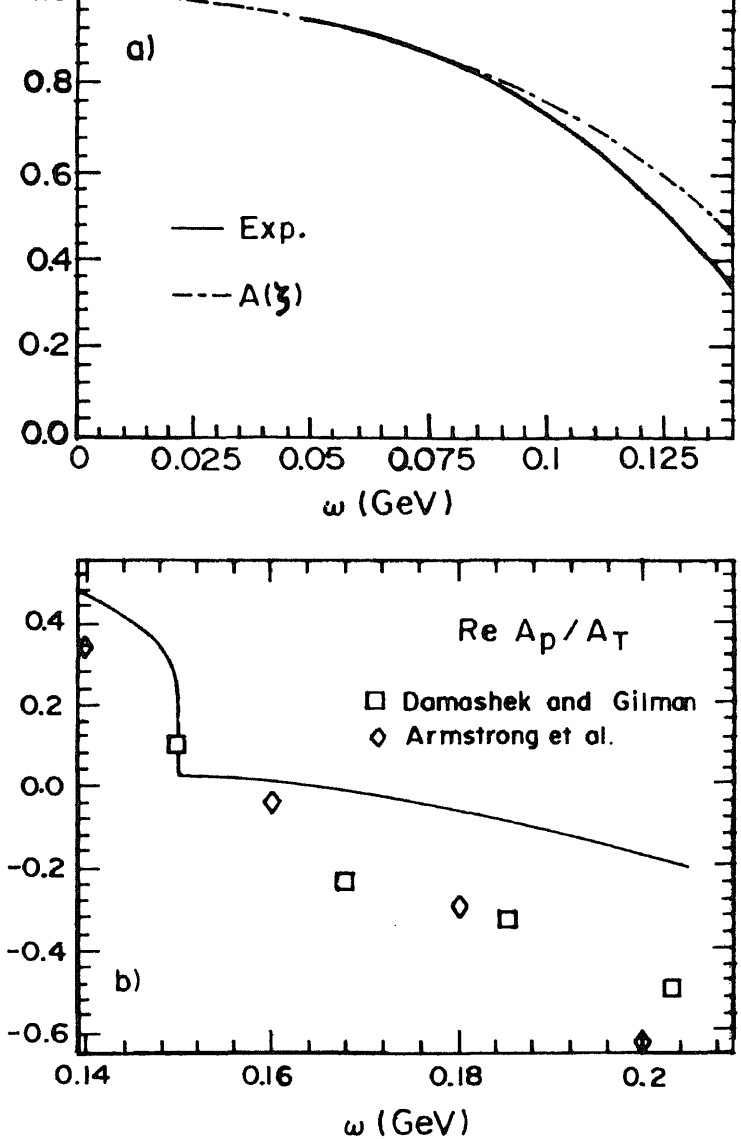

igure 5. Forward spin–averaged Compton amplitude for the proton in comparison to ıe data. (a) $0 \leq \omega \leq 140$ MeV and (b) $140 \leq \omega \leq 210$ MeV.

similar pattern [43]. The Σ^+ is made of u and s quarks (which have opposite charges) and this allows for internal electric dipole excitations. In contrast, the charge–like d and s quarks in the Σ^- tend to hinder such excitations leading to a small electric polarizability. The numbers given in (27) should be considered as first estimates since a complete E^4 calculation in SU(3) has yet to be performed. I will now take a critical look at the status of three flavor baryon CHPT.

6. Baryon masses and σ-terms

The simplest observbles to investigate in flavor SU(3) are the baryon masses m_N, m_Λ, m_Σ, m_Ξ and the three proton σ–terms defined via

$$\begin{aligned}
\sigma_{\pi N}(t) &= \hat{m} < p'|\bar{u}u + \bar{d}d|p > \\
\sigma^{(1)}_{KN}(t) &= \frac{1}{2}(\hat{m} + m_s) < p'|\bar{u}u + \bar{s}s|p > \\
\sigma^{(2)}_{KN}(t) &= \frac{1}{2}(\hat{m} + m_s) < p'| - \bar{u}u + 2\bar{d}d + \bar{s}s|p >
\end{aligned} \tag{28}$$

with $t = (p' - p)^2$ the invariant momentum transfer squared and $\hat{m} = (m_u + m_d)/2$ the average light quark mass. At zero momentum transfer, the strange quark contribution to the proton mass is given by [44]

$$m_s < p|\bar{s}s|p >= \left(\frac{1}{2} - \frac{M_\pi^2}{4M_K^2}\right)\left[3\sigma^{(1)}_{KN}(0) + \sigma^{(2)}_{KN}(0)\right] + \left(\frac{1}{2} - \frac{M_K^2}{M_\pi^2}\right)\sigma_{\pi N}(0) \tag{29}$$

making use of the leading order meson mass formulae $M_\pi^2 = 2\hat{m}B$ and $M_K^2 = (\hat{m} + m_s)B$. This defines the scalar sector of baryon CHPT. To calculate the mass spectrum to order E^3, we need the symmetry breaking terms from

$$\mathcal{L}^{(2)}_{MB} = b_D\ \mathrm{Tr}\,(\bar{B}\{\chi_+, B\}) + b_F\ \mathrm{Tr}\,(\bar{B}[\chi_+, B]) + b_0\ \mathrm{Tr}\,(\bar{B}B)\,\mathrm{Tr}\,(\chi_+) \tag{30}$$

with $\chi_+ = u^\dagger\chi u^\dagger + u\chi^\dagger u$ and $\chi = 2B(\mathcal{M} + \mathcal{S})$ where $\mathcal{S}$ denotes the nonet of external scalar sources. The constants b_D, b_F and b_0 can be fixed from the knowledge of the baryon masses and the πN σ-term (or one of the KN σ-terms). The constant b_0 can not be determined from the baryon mass spectrum alone since it contributes to all octet members in the same way. To this order in the chiral expansion, any baryon mass takes the form [44,45]

$$m_B = m_0 - \frac{1}{24\pi F_\pi^2}\left[\alpha_B^\pi M_\pi^3 + \alpha_B^K M_K^3 + \alpha_B^\eta M_\eta^3\right] + \gamma_B^D b_D + \gamma_B^F b_F - 2b_0(M_\pi^2 + 2M_K^2) \tag{31}$$

The first term on the right hand side of (31) is the average octet mass in the chiral limit, the second one comprises the Goldstone boson loop contributions and the third term stems from the counter terms in (30) ("resonance physics"). Notice that the loop contribution is ultraviolet finite and non-analytic in the quark masses since $M_\phi^3 \sim m_q^{3/2}$. The constants b_D, b_F and b_0 are therefore finite. A typical result at $\mathcal{O}(E^3)$ from a least–square fit to m_N, m_Λ, m_Σ, m_Ξ and $\sigma_{\pi N}(0) = 45$ Mev [46] is [44]

$$\begin{aligned}
m_N &= (0.965 - 0.018 - 0.264 + 0.248)\,\mathrm{GeV} = 0.936\,\mathrm{GeV} \\
m_\Lambda &= (0.965 - 0.006 - 0.588 + 0.743)\,\mathrm{GeV} = 1.141\,\mathrm{GeV}
\end{aligned} \tag{32}$$

terms. To have a more well-behaved chiral expansion, one might want to include the low-lying decuplet baryons as will be discussed below. At this order and within the accuracy of the E^3 calculation, the KN σ-terms turn out to be

$$\sigma_{KN}^{(1)}(0) \simeq 200 \pm 50\,\mathrm{MeV}, \quad \sigma_{KN}^{(2)}(0) \simeq 140 \pm 40\,\mathrm{MeV} \tag{33}$$

which is comparable to the first order perturbation theory analysis having no strange quarks, $\sigma_{KN}^{(1)}(0) = 205$ MeV and $\sigma_{KN}^{(2)}(0) = 63$ MeV [47]. At present, the KN σ-terms are not well determined. Since most of the phase shift data stem from kaon-nucleus scattering, it is of advantage to define them in terms of nuclear isospin, $\sigma'_{KN} = (3\sigma_{KN}^{(2)} + \sigma_{KN}^{(1)})/4$ and $\sigma''_{KN} = (\sigma_{KN}^{(2)} - \sigma_{KN}^{(1)})/2$. The best determinations available gives $\sigma'_{KN}(0) = 599 \pm 377$ MeV and $\sigma''_{KN}(0) = 87 \pm 66$ MeV [48]. This translates into $\sigma_{KN}^{(1)}(0) = 469 \pm 390$ MeV and $\sigma_{KN}^{(2)}(0) = 643 \pm 378$ MeV. Let me finish this section with a remark on the calculation of m_N in a recent lattice simulation in quenched baryon CHPT [49] (which is discussed in some detail by Golterman in these proceedings),

$$\begin{aligned} m_N^{\mathrm{CHPT}} &= (0.97 - 0.5M_\pi + 3.4M_\pi^2 - 1.5M_\pi^3)\,\mathrm{GeV} \\ m_N^{\mathrm{LFIT}} &= (0.96 - 1.0M_\pi + 3.6M_\pi^2 - 2.0M_\pi^3)\,\mathrm{GeV} \end{aligned} \tag{34}$$

where LFIT denotes the fit to the lattice data. It is most significant that the negative curvature due to the M_π^3 term from quenched CHPT and from the lattice fit are of the same magnitude. There is, however, a problem at small M_π. The lattice data give a too large pion mass so that one has to plot m_N versus M_π and interpolate to the physical pion mass. On finds a hook at the lower end of this curve which sheds some doubts on the accuracy of the recently reported results by Butler et al. [63]. For more details on this, see Golterman [64].

7. Inclusion of the decouplet in the EFT

The low-lying decuplet is only separated by $\Delta = 231$ MeV from the octet baryons, which is just $(5/2)F_\pi$ (notice that I have not used the conventional argument $\Delta = (5/3)M_\pi$ since the splitting stays finite in the chiral limit much like F_π and not at all like M_π) and considerably smaller than the kaon or eta mass. One therefore expects the excitations of these resonances to play an important role even at low energies. This is also backed by phenomenological models of the nucleon in which the $\Delta(1232)$ excitations play an important role. In addition, there are large N_C arguments [50] which, however, have to be taken *cum grano salis* since the chiral and infinite number of colors limites do not commute. In the meson sector, the first resonances are the vector mesons ρ and ω at about 800 MeV, *i.e.* they are considerably heavier than the Goldstone bosons. However, it is not only the small octet-decuplet splitting which plays a role. One should also notice that the $\Delta(1232)$ coupling to the πN system is very large, $g_{\pi\Delta N} \simeq 2g_{\pi NN}$ with $g_{\pi NN} = 13.5$. Similarly, the $\gamma\Delta N$ coupling is very strong. Would the $\Delta(1232)$ (or the decuplet) be weakly coupled to the nucleon (octet), its role would be very different. It was therefore argued by Jenkins and Manohar [51] to include the spin-3/2 decuplet in the

mass formulation satisfying $v \cdot l = 0$. The effective Lagrangian of the spin 3/2 at lowest order reads

$$\mathcal{L}_{MBT} = -i\bar{T}^\mu v \cdot \mathcal{D} T_\mu + \Delta \bar{T}^\mu T_\mu + \frac{C}{2}(\bar{T}^\mu u_\mu B + \bar{B} u_\mu T^\mu) .$$

where we have suppressed the flavor SU(3) indices. For an explicit expressi ref.[65]. Notic that there is a remaining mass dependence which comes fr average decuplet-octet splitting Δ which does not vanish in the chiral limi constant C is fixed from the decay $\Delta \to N\pi$ or the average of some strong de decays, $|C| = 1.5 \ldots 1.9$. The decuplet propagator carries the information the mass splitting Δ and reads

$$\frac{iP_{\mu\nu}}{v \cdot l - \Delta + i\epsilon}$$

with $P_{\mu\nu}$ a projector (for a review, see ref.[52]). The appearance of the mas ting Δ spoils the exact one–to–one correspondence between the loop and low- expansion. The two scales F_π and Δ which are both non-vanishing in the limit enter the loop calculations and they can combine in the form (Δ/F_π) breakdown of the consistent chiral counting in the presence of the decuplet in the loop contribution to the baryon mass. The loop diagrams with inte ate decuplets states which naively count as order E^4 renormalize the averag baryon mass even in the chiral limit by an infinite amount. Therefore one add a counter term of chiral power E^0 to keep the value m_0 fixed

$$\begin{aligned}
\delta\mathcal{L}^{(0)}_{MB} &= -\delta m_0 \, \mathrm{Tr}\,(\bar{B}B) \\
\delta m_0 &= \frac{10}{3}\frac{C^2\Delta^3}{F_\pi^2}\left[L + \frac{1}{16\pi^2}\left(\ln\frac{2\Delta}{\lambda} - \frac{5}{6}\right)\right] \\
L &= \frac{\lambda^{d-4}}{16\pi^2}\left[\frac{1}{d-4} + \frac{1}{2}(\gamma_E - \ln 4\pi - 1)\right]
\end{aligned}$$

with λ the scale introduced in dimensional regularization and γ_E the Mascheroni constant. This mass shift is similar to the one in the relativistic of pion-nucleon CHPT, where the non-vanishing nucleon mass in the chira leads to the same kind of complications [28]. The inclusion of the decuple has three effects on the mass formulae (31). First there is an infinite loop bution with decuplet intermediate states and, second, an infinite renormal of the order E^2 of the low-energy constants b_D, b_F and b_0 plus a finite contri which starts out at $\mathcal{O}(E^4)$. The constants b_D, b_F and b_0 have to be renorm as follows:

$$\begin{aligned}
b_D &= b_D^r(\lambda) - \frac{\Delta C^2}{2F_p^2}L, \\
b_F &= b_F^r(\lambda) + \frac{5\Delta C^2}{12F_p^2}L, \\
b_0 &= b_0^r(\lambda) + \frac{7\Delta C^2}{6F_p^2}L,
\end{aligned}$$

where the finite pieces $b^r_{D,F,0}(\lambda)$ are then determined by the fitting procedur explicit form of the decuplet contributions to the octet masses can be fo

tadpole diagrams with insertions from $\mathcal{L}^{(2)}_{MB}$ have also been included but that does not alter these conclusions). As already stressed a couple of times, a *complete* E^4 calculation should be performed. For doing that, it might be easier to use the decuplet to estimate some low–energy constants rather than taking it as dynamical dof's in the EFT. The role of the decuplet contributions has also been critically examined by Luty and White [53].

Table 1. Results of the calculation including the full decuplet intermediate states. The values of D, F, Δ and C are input. All dimensionful numbers are in MeV. Empirically, $\Delta\sigma_{\pi N} = 15$ MeV and $\Sigma^p_s = m_s < p|\bar{s}s|p >= 130$ MeV [46].

D	F	Δ	C	$\sigma^{(1)}_{KN}(0)$	$\sigma^{(2)}_{KN}(0)$	$\Delta\sigma_{\pi N}$	Σ^p_s
0.75	0.50	293	1.8	38	-23	14.3	513
0.75	0.50	293	1.5	86	28	12.3	419
0.75	0.50	231	1.8	67	10	15.1	455
0.75	0.50	231	1.5	106	51	12.8	379
0.56	$2D/3$	293	$2D$	244	150	6.8	132
0.56	$2D/3$	231	$2D$	255	163	7.1	110

8. Spectral distribution of the nucleon form factors

When discussing the forward Compton amplitude, I mentioned that the corresponding branch point related to the one–pion threshold has itself a $1/m$ expansion in the heavy mass formulation which disturbs the analytical structure of the amplitude. To take a closer look at this problem, let us consider the chiral expansion of the so–called (isovector) Pauli form factor $F_2^V(t)$. It is defined by the matrix–element of the isovector–vector quark current,

$$< p'|\bar{q}\gamma_\mu \frac{\tau^a}{2} q|p >= \bar{u}(p')\left[\gamma_\mu F_1^V(t) + \frac{i\sigma_{\mu\nu}k^\nu}{2m} F_2^V(t)\right]\frac{\tau^a}{2}u(p) \qquad (39)$$

with $k = p' - p$ and $t = k^2$. As first observed by Frazer and Fulco [54] and discussed in detail by Höhler and Pietarinen [55] the imaginary part of $F_2^V(t)$ exhibits a strong enhancement very close to threshold ($t = 4M_\pi^2$) as shown in fig.6a. The imaginary part of the isovector nucleon form factors inherit the singularity on the second sheet

due to the projection of the Born term (at $t_0 = 4M_\pi^2(1 - M_\pi^2/4m^2) = 3.98M_\pi^2$) in πN scattering (from diagrams of the type $\gamma \to \pi\pi \to \bar{N}N$).

Let us first consider the chiral expansion of Im $F_2^V(t)$ in the relativistic formulation of baryon CHPT. Following Gasser et al. [28], one has

$$\mathrm{Im}F_2^V(t) = \frac{8g_A^2}{F_\pi^2} m^4 \left[4\,\mathrm{Im}\,\gamma_4(t) + \mathrm{Im}\,\Gamma_4(t) \right] \tag{40}$$

where the loop functions and their imaginary parts γ_4 and Γ_4 are given in ref.[28]. For our purpose, we only need Im $\gamma_4(t)$ since its threshold is the two–pion cut whereas Im $\Gamma_4(t)$ only starts to contribute at $t = 4m^2$. The resulting imaginary part for Im $F_2^V(t)/t^2$ is shown in fig.6b (solid line). One sees that the strong increase at threshold is reproduced (see also the remarks in ref.[28]) since the chiral representation of Im $\gamma_4(t)$ indeed has the proper analytical structure, i.e. the singularity on the second sheet at t_0. The chiral representation of Im $F_2^V(t)/t^2$ does not stay constant on the left shoulder of the ρ–resonance but rather drops. This is due to the fact that in the one loop approximation, one is only sensitive to the first term in the chiral expansion of the pion charge form factor $F_\pi^V(t)$. In fig.6a I also show calculations with $F_\pi^V(t) = 1$ (dashed line) and $F_\pi^V(t) = 1 + < r_\pi^2 > t/6$ (dash–dotted line). These curves resemble very much the chiral expansion. To reiterate, this particular example shows that in the relativistic version of baryon CHPT the pertinent analytical structures of current and S–matrix elements are given correctly.

Let us now consider the heavy mass approach. The corresponding imaginary part follows from ref.[31],

$$\mathrm{Im}F_2^V(t) = \frac{g_A^2 m}{8F_\pi^2} \left(\frac{1}{4} - \frac{M_\pi^2}{t} \right) \sqrt{t}\, \Theta(t - 4M_\pi^2) \tag{41}$$

Here, the imaginary part comes form a $\ln(2M_\pi - \sqrt{t})$ which has a branch point at $t = 4M_\pi^2$ (chiefly because to lowest order in the $1/m$ expansion the threshold energy of πN scattering is $\omega_0 = M_\pi$ [39] and the corresponding left–handed cut starts there). This also leads to an enhancement of the imaginary part of $F_2^V(t)$ as shown by the dashed line in fig.6b. The enhancement is stronger than in the relativistic case. Stated differently, to this order in the chiral expansion the analytic structure is not given correctly much like in the case of the forward Compton scattering amplitude discussed before. One should therefore perform an order E^5 calculation in the heavy mass approach to have a sufficently accurate and *correct* representation of the isovector nucleon form factors. A two loop calculation will also answer the yet unresolved question whether or not in the isoscalar channel there is an enhancement around $t = 9M_\pi^2$. State of the art dispersion theoretical analysis of the nucleon form factors assume only a set of poles in the corresponding spectral distributions [56]. Finally, I wish to stress that in this context the matching formalism discussed in ref.[31] starts to play a role (which allows to relate matrix–elements in the heavy mass and relativistic formulation of CHPT).

9. Aspects of electroweak pion production

In this section, I will discuss some physics aspects related to threshold pion produc-

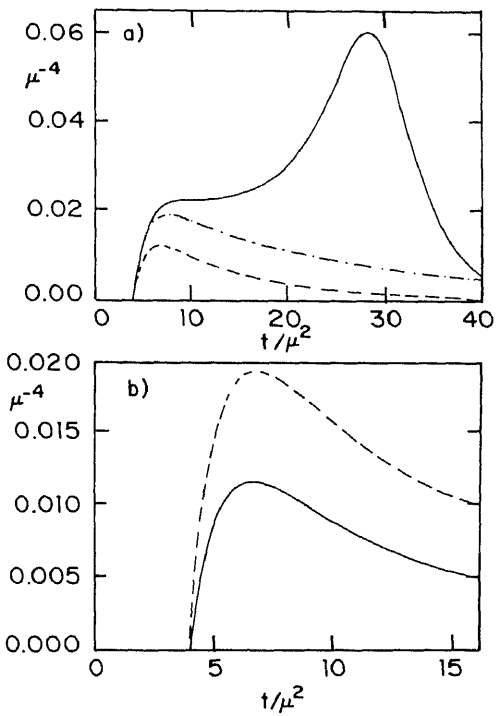

ure 6. (a) Dispersion–theoretical result for Im $F_2^V(t)/t^2$ (t in units of the pion mass, oted μ here). As D-function, the inverse pion form factor is used, $D(t) = 1/F_\pi^V(t)$. dash–dotted and dashed lines are explained in the text. (b) Chiral representation he relativistic formulation of baryon CHPT [28] (solid line) and in the heavy mass roach (dashed line) [31].

Let me first consider the production of one single pion by the isovector axial current. As particularly stressed by Adler [57], a unified treatment of em and weak pion production allows to relate information from neutrino–nucleon and electron–nucleon scattering experiments. Obviously, by using PCAC, the coupling of the weak axial current to the nucleon in the initial state and a nucleon plus a pion in the final state is closely related to πN scattering. Consider now a reaction of the type $\nu(k_1) + N(p_1) \to l(k_2) + N(p_2) + \pi^a(q)$ and define $k = k_1 - k_2$. The threshold energy squared is $s = (p_1 + k)^2 = (m + M_\pi)^2$. At threshold and in the πN cms frame, one can express the pertinent matrix–element in terms of six S–wave multipoles,

$$T^{(\pm)} \cdot \epsilon = 4\pi(1+\mu)\chi_2^\dagger [\epsilon_0 L_{0+}^{(\pm)} + \epsilon \cdot k H_{0+}^{(\pm)} + i\vec{\sigma} \cdot (\hat{k} \times \vec{\epsilon}) M_{0+}^{(\pm)}] \chi_1 \tag{42}$$

with $\chi_{1,2}$ two–component Pauli spinors, $\mu = M_\pi/m$ the ratio of the pion and nucleon mass and $\epsilon_\mu \sim \bar{u}_l \gamma_5 \gamma_\mu u_\nu$ the axial polarization vector. The superscript '$\pm$' refers to the isospin even/odd part of the amplitude. In ref.[58], we derived the chiral expansions of these threshold multipoles to order E^3. Of particular interest is the multipole $L_{0+}^{(+)}$ since it is directly proportional to the so–called scalar form factor of the nucleon, $\sigma_{\pi N}(t) \sim < p'|\hat{m}(\bar{u}u + \bar{d}d)|p >$ [58],

$$\begin{aligned} L_{0+}^{(+)} &= \frac{1}{3\pi M_\pi F_\pi} \left\{ \sigma_{\pi N}(k^2 - M_\pi^2) - \frac{1}{4}\sigma_{\pi N}(0) \right\} \\ &\quad - \frac{a^+ F_\pi}{M_\pi} - \frac{g_A^2 M_\pi}{16\pi m F_\pi} + C_L^{(+)} M_\pi^2 + \mathcal{O}(q^3) \end{aligned} \tag{43}$$

The constant $C_L^{(+)}$ subsumes numerous k^2–independent kinematical, loop and counter term contributions. If one assumes $C_L^{(+)}$ to be of the order of 1 GeV^{-3}, the term proportional to the scalar form factor dominates the amplitude (43) in the threshold region. This might offer another determination of this much discussed quantity. However, an analysis including also higher order effects has to be performed to find out how cleanly this multipole can be separated in neutrino–induced pion production and how large the corresponding cross section is. It is furthermore interesting to note that although $L_{0+}^{(+)}$ vanishes at the photon point $k^2 = 0$ in the chiral limit, its slope nevertheless stays finite - this is a particular effect due to chiral loops.

Another reaction of interest is the photoproduction of two pions in the threshold region. It gives complimentary information to the extensive studies of single pion photo– and electroproduction performed over the last few years. Dahm and Drechsel [59] were the first to systematically study the process $\gamma N \to \pi\pi N$ in a chiral field theory. To be specific, they considered Weinberg's pion–nucleon Lagrangian [60] coupling in the photon via minimal substitution. At threshold, the transition current takes the form

$$T \cdot \epsilon\big|_{\rm thr} = i\vec{\sigma} \cdot (\vec{\epsilon} \times \vec{k}) [M_1 \delta_{ab} + M_2 \delta_{ab} \tau_3 + M_3(\tau_a \delta_{b3} + \tau_b \delta_{a3})] \tag{44}$$

where 'a,b' are the pion isospin indices and the τ's act on the nucleon. The explicit form of the corresponding five–fold differential cross section is given in [59]. Here,

their expansion in powers of M_π. In general, the reaction $\gamma N \to \pi\pi N$ involves five independent Mandelstam variables. At threshold, the kinematics is simplified since the pion four–momenta are equal, $q_1 = q_2 = (M_\pi, 0, 0, 0)$. In heavy fermion CHPT the calculation furthermore simplifies if one works in the Coulomb gauge $\epsilon \cdot v = 0$ and realizes that $S \cdot q_1 = S \cdot q_2 = 0$ [61]. The lowest order result stems from tree diagrams with one insertion from $\mathcal{L}_{\pi N}^{(2)}$ as shown in fig.7.

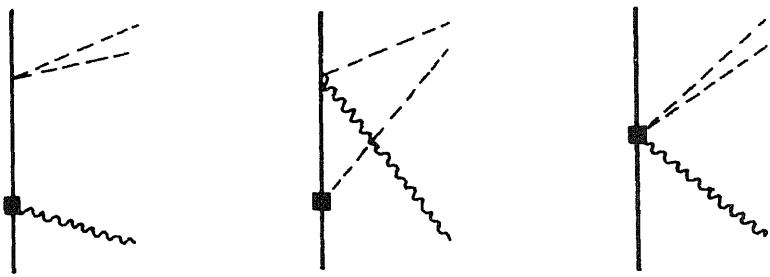

Figure 7. Tree diagrams which lead to eq.(45). The box denotes an insertion from $\mathcal{L}_{\pi N}^{(2)}$. Solid, dashed and wiggly lines denote nucleons, pions and photons, respectively.

One finds

$$M_1 = \mathcal{O}(M_\pi),\ M_2 = \frac{e}{4mF_\pi^2}(2g_A^2 - 1 - \kappa_V) + \mathcal{O}(M_\pi),\ M_3 = -\frac{M_2}{2}\ . \tag{45}$$

These differ from the results in [59] by the terms proportional to κ_V and are a factor two smaller in magnitude. The reason is that gauging the Weinberg Lagrangian can not generate the anomalous couplings of the photon. Of course, simply calculating these tree diagrams is not sufficient, one has to at least work out the $\mathcal{O}(M_\pi)$ corrections. These are (i) kinematical corrections of the type M_π/m, (ii) contributions from one–loop diagrams, (iii) further insertions from $\mathcal{L}_{\pi N}^{(2,3)}$ and (iv) contributions from tree diagrams with intermediate $\Delta(1232)$ states. As a preliminary result, let me consider the corrections of the first two types (a more thorough discussion can be found in ref.[61]). Although the $\Delta(1232)$ is very close to the two pion production threshold (the energy difference being 17 MeV), the potentially large diagrams with small energy denominators of the type $m_\Delta - (m_N + 2M_\pi)$ are suppressed by corresponding numerators. The corrections of type (i) and (ii) lead to [61]

$$\begin{aligned} M_1 &= \frac{eg_A^2 M_\pi}{4m^2 F_\pi^2} = 0.019\,\mathrm{fm}^3 \\ M_2 &= \frac{eM_\pi}{4m^2 F_\pi^2}(g_A^2 - \kappa_V) + \frac{eg_A^2 M_\pi}{64\pi F_\pi^4}\left[\frac{3\pi}{2} + i(2\sqrt{3} - \ln(2+\sqrt{3}))\right] \end{aligned}$$

$$
\begin{aligned}
&= (0.159 + i\,0.082)\,\mathrm{fm}^3 \\
M_3 &= \frac{eM_\pi \kappa_V}{8m^2F_\pi^2} + \frac{eg_A^2 M_\pi}{256\pi F_\pi^4}\left[6 - \frac{3\pi}{2} + i(2\sqrt{3} - \ln(2+\sqrt{3}))\right] \\
&= (0.032 + i\,0.020)\,\mathrm{fm}^3 \qquad (46)
\end{aligned}
$$

For M_1, the loops do not contribute to order M_π where as for $M_{2,3}$ they lead to a complex correction. This due to some loop diagrams involving two or three pion propagators which acquire an imaginary part for $\omega > M_\pi$ (here, $\omega = 2M_\pi$). The first term on the r.h.s. of (46) stems from the kinematical corrections. Comparing the numbers in (46) to the lowest order results $M_1 = 0$, $M_2 = -2M_3 = 0.084$ fm^3, one sees that the M_π corrections are large. One might therefore question the whole approach, but it is conceivable that once the type (iv) corrections from the Δ are included, the dominant physics will be under control and subsequent higher order corrections play a minor role. This topic is under investigation [61]. To get an idea about the role of the loop and kinematical corrections, let us consider the specific final states like in $\gamma p \to \pi^0\pi^0 p$. In that case, the cross section is proportional to the quantity $|\mathcal{M}_{00}| = [(M_1 + M_2 + 2M_3)(M_1 + M_2 + 2M_3)^*]^{1/2}$ and similarly for the other channels. In table 2, I show $|\mathcal{M}_{ij}|$ in fm^3 for the lowest order (45) and with the M_π corrections (46). The most prominent result is that the double π^0 channels, which are vanishing to lowest order, are in fact dominant after the inclusion of the $\mathcal{O}(M_\pi)$ corrections.

Table 2. Contribution of the threshold multipoles to two pion production channels in fm^3 (no phase space factors are accounted for).

process	$\mathcal{O}(1)$	$\mathcal{O}(1) + \mathcal{O}(M_\pi)$
$\gamma p \to \pi^+\pi^- p$	0.084	0.125
$\gamma p \to \pi^+\pi^0 n$	0.059	0.108
$\gamma p \to \pi^0\pi^0 p$	0.000	0.271
$\gamma n \to \pi^+\pi^- n$	0.084	0.099
$\gamma n \to \pi^-\pi^0 p$	0.059	0.108
$\gamma n \to \pi^0\pi^0 n$	0.000	0.238

This is completely different from the single photoproduction case in which the final states including a charged pion have the largest cross sections. An experimental verification of this pattern would be of utmost interest. It also persists when one

$$\sigma_{\rm tot}^{\gamma N\to\pi\pi N}(E_\gamma)=\frac{M_\pi^2(1+\mu)}{32\pi^2(1+2\mu)^{11/2}}(E_\gamma-E_\gamma^{\rm thr})^2|\eta_1M_1+\eta_2M_2+\eta_3M_3|^2\xi \quad (47)$$

with E_γ the photon energy in the lab frame, $\eta_{1,2,3}$ isospin factors (like e.g. $\eta_1=\eta_2=1,\eta_3=2$ for the $p\pi^0\pi^0$ final state) and ξ is a Bose factor ($=1/2$ in case of equal particles in the final state, one otherwise). The threshold energy is $E_\gamma^{\rm thr}=2M_\pi(1+\mu)=320.7$ MeV with $\mu=M_\pi/m$. The formula (47) is only valid close to threshold assuming that the amplitude in the threshold region can be approximated by the threshold amplitude. Furthermore, the three–body phase space has been approximated by an analytical expression which is good within a few percent. For $E_\gamma=330$ MeV, i.e. 10 MeV above threshold, the total cross section is 0.35, 0.15 and 0.11 nbarn for $\gamma p\to p\pi^0\pi^0, p\pi^+\pi^-$ and $n\pi^+\pi^0$, in order. Of course, these numbers should only be taken as a first approximation due to the assumptions going into their calculation. It is therefore a tough experimental task to measure these reactions close to threshold and verify the effects of the chiral loops.

10. Brief outlook

In this lecture I could only give a glimpse of the many facets of chiral perturbation theory. The role of effective Lagrangian methods in the parametrization of physics beyond the standard model and in the context of longitudinal vector boson scattering to test the Higgs sector of the electroweak symmetry breaking has been discussed here by Burgess [66] and Phillips [67]. Another widely discussed topic is the combined application of chiral symmetry and heavy quark effective field theory methods (some references can be traced back from [4]). Furthermore, these methods allow also to make precise statements for finite temperature and volume effects and much more. There remain many open theoretical problems and challenging experimental tasks to further tighten our understanding of the strong interactions at momentum scales were they are really *strong*.

I would like to thank the organizers, in particular Dr. Uma Sankar, for the warm hospitality extended to me and an efficient organization. I also thank the Saha Institute for Nuclear Physics, in particular Prof. S. Mallik, for providing a stimulating atmosphere and support to perform part of this work.

References

[1] S. Weinberg, *Phys. Rev. Lett.* **17** (1966) 616.

[2] S. Weinberg, *Physica* **96A** (1979) 327.

[3] J. Gasser and H. Leutwyler, *Ann. Phys.* (N.Y.) **158** (1984) 142; *Nucl. Phys.* **B250** (1985) 465.

[4] Ulf-G. Meißner, *Rep. Prog. Phys.* **56** (1993) 903.

[5] H. Leutwyler, Bern University preprint BUTP-93/24, 1993.

[6] J. Gasser and H. Leutwyler, *Phys. Lett.* **125B** (1983) 325.

[7] W. Ochs, Max–Planck–Institute preprint MPI–Ph/Ph 91–35, 1991.

[9] N. H. Fuchs, H. Szadijan and J. Stern, *Phys. Rev.* **D47** (1993) 3814.

[10] L. L. Nemenov, *Yad. Fiz.* **41** (1985) 980;
J. Uretsky and J. Palfrey, *Phys. Rev.* **121** (1961) 1798;
G. Czapek et al., letter of intent CERN/SPSLC 92–44, 1992.

[11] R. Altmeyer et al., Jülich preprint HLRZ 92–17, 1992.

[12] J. Gasser and Ulf-G. Meißner, *Phys. Lett.* **B258** (1991) 219.

[13] V. Bernard, N. Kaiser and Ulf-G. Meißner, *Nucl. Phys.* **B357** (1991) 129; *Phys. Rev.* **D43** (1991) R3557.

[14] A. Dobado and J. R. Pelaez, *Phys. Rev.* **D47** (1993) 4883.

[15] J. F. Donoghue, J. Gasser and H. Leutwyler, *Nucl. Phys.* **B343** (1990) 341.

[16] J. Gasser and Ulf-G. Meißner, *Nucl.Phys.* **B357** (1991) 90.

[17] J. Bijnens and F. Cornet, *Nucl. Phys.* **B296** (1988) 557.

[18] J. F. Donoghue, B. R. Holstein and Y. C. R. Lin, *Phys. Rev.* **D37** (1988) 2423.

[19] H. Marsiske et al., *Phys. Rev.* **D41** (1990) 3324.

[20] M.R. Pennington, in The DAΦNE Physics Handbook, eds. L. Maiani, G. Pancheri and N. Paver, Frascati, 1992.

[21] J. F. Donoghue and B. R. Holstein, *Phys. Rev.* **D48** (1993) 37.

[22] S. Belluci, J. Gasser and M.E. Sainio, Bern University preprint BUTP-93/18, 1993.

[23] G. Ecker, A. Pich and E. de Rafael, *Phys. Lett.* **B189** (1987) 363; *Nucl. Phys.* **B291** (1987) 692; *Nucl. Phys.* **B303** (1988) 665.

[24] G.D. Barr et al., *Phys. Lett.* **B242** (1990) 523; **B284** (1992) 440;
V. Papadimitriou et al., *Phys. Rev.* **D44** (1991) 573.

[25] A. Cohen, G. Ecker and A. Pich, *Phys. Lett.* **B304** (1993) 347.

[26] J. Kambor and B.R. Holstein, Amherst preprint UMHEP–397, 1993.

[27] Ulf-G. Meißner, *Int. J. Mod. Phys.* **E1** (1992) 561.

[28] J. Gasser, M.E. Sainio and A. Švarc, *Nucl. Phys.* **B307** (1988) 779.

[29] A. Krause, *Helv. Phys. Acta* **63** (1990) 3.

[30] E. Jenkins and A.V. Manohar, *Phys. Lett.* **B255** (1991) 558.

[31] V. Bernard, N. Kaiser, J. Kambor and Ulf-G. Meißner, *Nucl. Phys.* **B388** (1992) 315.

[32] G. Ecker, *Czech. J. Phys.*, in print.

[33] G. Ecker, private communication.

[34] M. Damashek and F. Gilman, *Phys. Rev.* **D1** (1970) 1319;
V.A. Petrunkin, *Sov. J. Nucl. Phys.* **12** (1981) 278;
T.A. Armstrong et al., *Phys. Rev.* **D5** (1970) 1640.

[35] A. Zieger *et al.*, *Phys. Lett.* **B278** (1992) 34;
F.J. Federspiel *et al.*, *Phys. Rev. Lett.* **67** (1991) 1511;
E.L. Hallin *et al.*, *Phys. Rev.* **C48** (1993) 1497.
K.W. Rose *et al.*, *Phys. Lett.* **B234** (1990) 460;
J. Schmiedmayer *et al.*, *Phys. Rev. Lett.* **66** (1991) 1015.

[36] V. Bernard, N. Kaiser and Ulf-G. Meißner, *Phys. Rev. Lett.* **67** (1991) 1515; *Nucl. Phys.* **B373** (1992) 364.

[37] J. Gasser and A. Zepeda, *Nucl. Phys.* **B174** (1980) 445.

[38] V. Bernard, N. Kaiser, A. Schmidt and Ulf-G. Meißner, *Phys. Lett.* **B319** (1993) 261.

[39] V. Bernard, N. Kaiser and Ulf-G. Meißner, *Phys. Lett.* **B309** (1993) 421.

[40] G. Ecker, J. Gasser, A. Pich and E. de Rafael, *Nucl. Phys.* **B321** (1989) 311.

[41] V. Bernard, N. Kaiser, A. Schmidt and Ulf-G. Meißner, preprint CRN-93/55, 1993.

[42] V. Bernard, N. Kaiser, J. Kambor and Ulf-G. Meißner, *Phys. Rev.* **D46** (1992) 2756.

[43] H.J. Lipkin and M. Moinester, *Phys. Lett.* **B287** (1992) 179.

[44] V. Bernard, N. Kaiser and Ulf-G. Meißner, *Z. Phys.* **C60** (1993) 111.

[45] E. Jenkins, *Nucl. Phys.* **B368** (1992) 190.

[46] J. Gasser, H. Leutwyler and M.E. Sainio, *Phys. Lett.* **253B** (1991) 252, 260.

[47] J.N. Labrenz and S.R. Sharpe, University of Washington preprint UW/PT-93-07, 1993.

[48] R.L. Jaffe and C. Korpa, *Comments Nucl. Part. Phys.* **17** (1987) 163.

[49] P. Gensini, *πN Newsletter* **6** (1992) 21.

[50] R. Dashen, E. Jenkins and A.V. Manohar, preprint UCSD/PTH 93-21, 1993.

[51] E. Jenkins and A.V. Manohar, *Phys. Lett.* **B259** (1991) 353.

[52] E. Jenkins and A.V. Manohar, in "Effective field theories of the standard model", ed. Ulf-G. Meißner, World Scientific, Singapore, 1992.

[53] M. Luty and A. White, *Phys. Lett.* **B319** (1993) 261.

[54] W.R. Frazer and J. Fulco, *Phys. Rev.* **117** (1960) 1603, 1609.

[55] G. Höhler and E. Pietarinen, *Phys. Lett.* **B53** (1975) 471.

[56] G. Höhler, in Landolt-Börnstein, vol.9 b2, ed. H. Schopper (Springer, Berlin, 1983).

[57] S.L. Adler, *Ann.Phys.* (N.Y.) **50** (1968) 189.

[58] V. Bernard, N. Kaiser and Ulf-G. Meißner, CRN preprint CRN-93/56, 1993.

[59] R. Dahm and D. Drechsel, in Proc. Seventh Amsterdam Mini-Conference, eds. H.P. Blok, J.H. Koch and H. De Vries, Amsterdam, 1991.

[60] S. Weinberg, *Phys. Rev.* **166** (1968) 1568.

[61] V. Bernard, N. Kaiser, Ulf-G. Meißner and A. Schmidt, in preparation.

[62] V. Bernard, N. Kaiser and Ulf-G. Meißner, *Nucl. Phys.* **B364** (1991) 283.

[63] F. Butler et al., *Phys. Rev. Lett.* **70** (1993) 2849.

[64] M. Golterman, these proceedings.

[65] V. Bernard, N. Kaiser and Ulf-G. Meißner, *Phys. Rev.* **D48** (1993) 3062.

[66] C. Burgess, these proceedings.

[67] R.J.N. Phillips, these proceedings.

Threshold effects in SUSY and non-SUSY GUTs

M. K. PARIDA
Physics Department, North-Easatern Hill University,
P. O. Box 21, Laitumkhrah, Shillong 793 003.

Abstract. We discuss recent contributions on threshold effects in grand unfiied theories including minimal SUSY SU(5), non-SUSY modifications of the grand desert in SU(5) and SO(10), and SO(10) with single intermediate symmetires. Consequences of theorems on vanishing GUT-scale corrections to $\sin^2\theta_W$ in SO(10) with $SU(2)_L$ $XSU(2)_R$ $XSU(4)_C$ ($g_{2L} = g_{2R}$) intermediate symmetry are discussed and vanishing corrections on the intermediate scale are explicitly demonstrated where predictions are more precise. Threshold and higher dimensional operator effects in SUSY SU(5) recently derived by a number of authors are presented.

1. Introduction

Experimental measurements at the CERN-LEP at the Z-peak and improved estimation of the finestructure constant have rpovided more precise values of $\sin^2\theta_W, \alpha_S$ and α^{-1},

$$\begin{aligned} \sin^2\theta_W &= 0.2324 \pm 0.0006 \\ \alpha_{s_{-1}} &= 0.12 \pm 0.01 \\ \alpha &= 127.9 \pm 0.2 \end{aligned} \tag{1}$$

leading to very accurate determination of the standard model gauge couplings,

$$\begin{aligned} \alpha_1 &= 0.016887 \pm 0.00004 \\ \alpha_2 &= 0.03322 \pm 0.000025 \\ \alpha_3 &= \alpha_S \end{aligned} \tag{2}$$

at the Z-mass. These have revived interests in grand unified theores [1] resulting in more precise predictions than before[2]. In addition to one- and two-loop contributions to the gauge-symmetry-breaking scales threshold [3] and higher dimensional operator effects [4] have been estimated and their impact on GUT-prediction on $\sin^2\theta_W$,α_S, proton lifetime, and neutrino masses have been calculated. It has also been found in a class of GUTs that in addition tot he vanishing of multiloop corrections at high mass scales, the unknown uncertainties on $\sin^2\theta_W$ and the intermediate scale due to threshold and higher dimensional operator effects are absent leading to more precise predictions[4-6]. The purpose of the present talk is to review these works and other corrections obtained in SUSY and nonSUSY GUTS. In addition we demonstrate explicitly the stability of the G_{224P}-breaking scale under threshold and higher dimensional operator effects leading to a more precise predictions of degenerate and see-saw contributions to neutrino masses in a class of GUTs.

The plan of the talk is organised in the following manner. In Sec.1 we obtain generalised formulas for mass scales and threshold effects. In Sec.2 we discuss in detail the threshold effects in modified grand desert models such as SU(5) and SO(10). In Sec.3 we derive threshold corrections in modified grand desert models [7,8]. In Sec.4 we estimate threshold effects in SO(10) with G_{224p} intermediate symmetry. Threshold effects in other single intermediate scale models of SO(10) are summarized in Sec.5. Section 6 is devoted to discussions on corrections in SUSY SU(5). We provide a brief summary and conclusions in Sec.7.

2. Generalized formulas for mass scales

Although minimal nonSUSY SU(5) is ruled out experimentally, the modified grand desert models based upon SU(5), SO(10) and others with light degrees of freedom are consistent with all the available data. Evidences on neutrino masses would rule out SU(5)-based modifications of the grand desert, but a number of other GUT would survive. In the absence of theoretical formulas for the mass scales or $\sin^2\theta_W$ it might be still possible to study the unification constraints by plotting the coupling constants numerically, but accurate estimations of the model predictions including experimental and theoretical uncertainties analytic formulas are essential. Such formulas can be obtained more easily for single step breaking of any GUT to the standard with or without SUSY[9,10]. We derive here generalised theoretical formulas for mass scales for modified grand desert models and two step breakings in GUTs. These formulas contain explicitly the loop contributions to each order although at present contributions upto two-loops only are calculated. More important is that the formulas have analytic expressions for different types of corrections arising at the intermediate or the GUT-scales[4.7,8,13].

At first we consider the following class of models,

$$(a) \qquad SO(10) \xrightarrow{M_U} G_{213} \xrightarrow{M_Z} G_{13}$$

where $G_{213}(= SU(2)_L XU(1)_Y XSU(3)_C)$ is the standard model (SM), $G_{13} = U(1)_{em} XSU(3)_{C'}$ and the presence of light degrees of freedom corresponding to additional Higgs scalars or fermions has been assumed. We also consider the following class of models based upon $SO(10)$,

$$(b) \qquad SO(10) \xrightarrow{M_U} G_I \xrightarrow{M_I} G_{213} \xrightarrow{M_W} G_{13}$$

where $G = SU(2)_L XU(1)_{I_{3R}} XSU(4)_C (= G_{214})$[12], $SU(2)_L XSU(2)_R XSU(4)_C$ $(= G_{224}, g_{2L} = g_{2R})$, $SU(2)_L XSU(2)_R XU(1)_{B-L} XSU(3)_C (= G_{2213}, g_{2L} = g_{2R})$[11], $G_{2213P} (= G_{2213} XP, P =$ Parity $=$ Left-right discrete symmetry, $g_{2L} = g_{2R})$, G_{224P} $(G_{224} XP, g_{2L} = g_{2R})$. It may be noted that SO(10) also permits the left-right discrete symmetry to be broken at a higher scale without breaking $SU(2)_R XU(1)_{B-L}$ or $SU(2)_R XSU(4)_C$ which can survive down to lower scales as in the cases of G_{2213} or G_{224}. In such a situation the parity and the $SU(2)_{2R}$-breakings are decoupled [11].

In models of the type (a) or (b) the renormalisation group equations (RGEs) for the gauge couplings of G_{213} or G_I can be written in the following manner in the two mass ranges,

$M_Z < \mu < M_I$

$$\frac{1}{\alpha_i(M_Z)} = \frac{1}{\alpha_i(M_I)} + \frac{a_i}{2\pi} ln \frac{M_I}{M_Z} + \frac{P_i^I}{4\pi} - \frac{L_i^I}{12\pi} \tag{3}$$

In model (a) M_I = degenerate mass of additional degrees of freedom in the desert.

$M_I < \mu < M_U$

$$\frac{1}{\alpha_i(M_I)} = \frac{1}{\alpha_G} + \frac{a_i'}{2\pi} ln \frac{M_U}{M_I} + \frac{P_i^U}{4\pi} - \frac{L_i^U}{12\pi} \tag{4}$$

where α_G is the GUT-coupling constant and the two-loop contributions are represented by terms containing P_i-functions,

$$\begin{aligned} p_i^I &= \textstyle\sum_j B_{ij} ln \frac{\alpha_j(M_I)}{\alpha_j(M_Z)} \quad , \quad B_{ij} = b_{ij}/a_j \\ p_i^U &= \textstyle\sum_j B'_{ij} ln \frac{\alpha_j(M_U)}{\alpha_j(M_I)} \quad , \quad B'_{ij} = b'_{ij}/a'_j \end{aligned} \tag{5}$$

In (3)-(5) $a_i(b_{ij})$ and $a_i'(b_{ij}')$ are the one(two)-loop coefficients of the β-function in the two mass ranges. The λ_i-functions in (3) and (4) represent threshold effects due to heavy or superheavy particles whose masses are of the order M_I or M_U. But as these masses are unknown theoretically, the threshold effects due to heavy or superheavy particles whose masses are of the order M_I or M_U. But as these masses are unknown theoretically, the threshold effects contribute to the uncertainties of the model predictions on the mass scales, $\sin^2\theta_W$, and α_S etc. For $\mu \approx M_I$ of M_U, the general expression for $\lambda_i(\mu)$ in nonSUSY theories is[14],

$$\begin{aligned} L_i(\mu) &= Tr(t_{iV}^2) + \lambda_i(\mu) \\ \lambda_i(\mu) &= -21 Tr(t_{iV}^2 ln \frac{M_i^V}{\mu}) + 8 Tr(t_{iF}^2 ln \frac{M_i^F}{\mu}) + Tr(t_{iS}^2 ln \frac{M_i^S}{\mu}) \end{aligned} \tag{6}$$

where t_{iV}, t_{iF}, and t_{iS} are the generators in the representations of the heavy or superheavy gauge bosons(V), fermions(F), and scalars(S), respectively. In our notation

$$\lambda_i^I = \lambda_i(\mu = M_I), \quad \lambda_i^U = \lambda_i(\mu = M_U) \tag{7}$$

Physically the first two terms are the vacuum polarisation contribution of the heavy gauge bosons(V) and the next two are similar contributions due to fermions(F) and Higgs scalars(S) in the theory. Using (3) and (4) and suitable linear combinations of the SM gauge couplings we derive and following generalised formulas for mass scales for models(a) and (b),

$$ln \frac{M_U}{M_Z} = [(L_S B_I - L_\theta A_I) + (J_2 B_I - K_2 A_I) + (K_\lambda A_I - J_\lambda B_I)]/D \tag{8}$$

$$ln \frac{M_I}{M_Z} = [(A_U L_\theta - B_U L_S) + (K_2 A_U - J_2 B_U) + (J_\lambda B_U - K_\lambda A_U)]/D \tag{9}$$

where

$$D = A_U B_I - A_I B_U \ . \ L_S = \frac{16\pi}{3}\left(\alpha_S^{-1} - \frac{3}{8}\alpha^{-1}\right)$$

In (8) and (9) the first, second, and the thrid terms represent the one-loop, two-loo
and the threshold contributions, respectively and the values A_i, B_i, J_i and K_i diff
from one model to the other,

MODEL (a)

$$
\begin{aligned}
A_I &= a_{2L} + \tfrac{5}{3}a_Y - \tfrac{8}{3}a_{3C} - \left(a'_{2L} + \tfrac{5}{3}a'_Y - \tfrac{8}{3}a'_{3C}\right) \\
B_I &= \tfrac{5}{3}(a_Y - a_{2L} - a'_Y + a'_{2L} \\
A_U &= a'_{2L} + \tfrac{5}{3}a'_Y - \tfrac{8}{3}a'_{3C} \\
B_U &= \tfrac{5}{3}(a'_Y - a'_{2L}) \\
J_2 &= \tfrac{1}{2}[(P^I_{2L} + \tfrac{5}{3}P^I_Y - \tfrac{8}{3}P^I_{3C}) + (P^U_{2L} + \tfrac{5}{3}P^U_Y - \tfrac{8}{3}P^U_{3C})] \\
K_2 &= \tfrac{5}{6}(P^I_Y - P^I_{2L}) + \tfrac{5}{6}(P^U_Y - P^U_{2L}) \\
J_\lambda &= \tfrac{1}{6}(L^U_{2L} + \tfrac{5}{3}L^U_Y - \tfrac{8}{3}L^U_{3C}) \\
K_\lambda &= \tfrac{5}{18}(L^U_Y - L^U_{2L})
\end{aligned}
\qquad (1
$$

MODEL (b)

(i) $G_I = G_{224}$ or G_{224P}

$$
\begin{aligned}
A_I &= \tfrac{8}{3}a_{3C} - a_{2L} - \tfrac{5}{3}a_Y - 2a'_{4C} + a'_{2L} + a'_{2R} \\
B_I &= \tfrac{5}{3}(a_{2L} - a_Y) + a'_{2R} + \tfrac{2}{3}a'_{4C} - \tfrac{5}{3}a'_{2L} \\
A_U &= 2a'_{4C} - a'_{2L} - a'_{2R} \\
B_U &= \tfrac{5}{3}a'_{2L} - a'_{2R} - \tfrac{2}{3}a'_{4C} \\
J_2 &= \tfrac{1}{2}(P^I_{2L} + \tfrac{5}{3}P^I_Y - \tfrac{8}{3}P^I_{3C}) + \tfrac{1}{2}(P^U_{2L} + P^U_{2R} - 2P^U_{4C}) \\
K_2 &= \tfrac{5}{6}(P^I_Y - P^I_{2L}) + \tfrac{1}{2}(P^U_{2R} + \tfrac{2}{3}P^U_{4C} - \tfrac{5}{3}P^U_{2L}) \\
J_\lambda &= \tfrac{1}{6}(L^U_{2L} + L^U_{2R} - 2L^U_{4C}) + \tfrac{1}{6}(L^I_{2L} + \tfrac{5}{3}L^I_Y - \tfrac{8}{3}L^I_{3C}) \\
K_\lambda &= \tfrac{1}{6}(L^U_{2R} + \tfrac{2}{3}L^U_{4C} - \tfrac{5}{3}L^U_{2L}) + \tfrac{5}{18}(L^I_Y - L^I_{2L})
\end{aligned}
\qquad (1
$$

(ii) $G_I = G_{2213}$ or G_{2213P}

Generalised formulas for mass scales are obtained from (11) of model (b) (i)

the replacements,

$$
\begin{aligned}
2a'_{4C} &\longrightarrow \tfrac{8}{3}a'_{3C} - \tfrac{2}{3}a'_{BL} \;,\; \tfrac{2}{3}a'_{4C} \longrightarrow \tfrac{2}{3}a'_{BL} \\
2L^U_{4C} &\longrightarrow \tfrac{8}{3}L^U_{3C} - \tfrac{2}{3}L^U_{BL} \;,\; \tfrac{2}{3}L^U_{4C} \longrightarrow \tfrac{2}{3}L^U_{BL} \\
2P^U_{4C} &\longrightarrow \tfrac{8}{3}P^U_{3C} - \tfrac{2}{3}P^U_{BL} \;,\; \tfrac{2}{3}P^U_{4C} \longrightarrow \tfrac{2}{3}P^U_{BL}
\end{aligned} \tag{12}
$$

(iii) $G_I = G_{214} = SU(2)_L XU(1)_{I_{3R}} XSU(4)_C$

Generalised formulas for mass scales are obtained from (7), (8) and (10) by replacing

$$
\begin{aligned}
a'_{2R} &\longrightarrow a'_{1R} = a'_{I_{3R}} \\
P^U_{2R} &\longrightarrow P^U_{1R} \;,\; L^U_{2R} \longrightarrow L^U_{1R}
\end{aligned} \tag{13}
$$

(iv) $G_I = G_{2113} = SU(2)_L XU(1)_{I_{3R}} XU(1)_{B-L} XSU(3)_C$

The generalised formulas in this case are obtained by combining (12) and (13).

Before closing this section it is worth pointing out that other corrections due to Yukawa couplings, top quark mass, higher dimensional operators etc. can be derived following the same procedure as threshold effects with appropriate replacements of the λ-functions.

3. Threshold effects in modified grand desert models

It has been found that the SU(5) model with additional light degrees of freedom corresponding to fermions or Higgs scalars is consistent with the CERN-LEP data and proton lifetime for the $p \longrightarrow e^+\pi^0$ mode [8,15-160,

$$
(\tau_p)_{expt.} \;>\; 3 \times 10^{32}\ yrs. \tag{14}
$$

The added presence of new degrees of freedom such as the Higgs scalars significantly below M_U needs additional finetuning of parameters which is not natural. In order to keep this unnatural act to a minimum we have successfully implemented new minimal modification of the grand desert which needs only one additional SM irreducible real scalar representation transforming as $\zeta(3,0,8)$ and needs only one additional finetuning of parameters [7]. Moreover the model has been implemented in SU(5) and the popular GUT like SO(10) thereby accounting for the CERN-LEP data, the proton lifetime and small neutrino masses necessary to explain the solar neutrino flux and the dark matter of the Universe in the latter case. The additional Higgs scalar $\zeta(3,0,8)$ C **75** of SU(5) and **210** of SO(10). Thus the implementation needs the Higgs representations **24**, **5** and **75** in SU(5) and **45**, **126**, **10** and **210** in SO(10). Thus keeping $M_Z < M_I = M_\zeta < M_U$ and evaluating the coefficients in (7)-(10) yields the following analytic expressions for the mass scales.

$$
\begin{aligned}
ln\tfrac{M_U}{M_Z} &= \tfrac{16\pi}{187\alpha}(\tfrac{7}{8} - \tfrac{10\alpha}{3\alpha_S} + \sin^2\theta_W) + \tfrac{5}{187}[\tfrac{8}{3}(P^U_3 + P^\zeta_3) \\
&- \tfrac{3}{2}(P^U_2 + P^\zeta_2) - \tfrac{7}{6}(P^U_1 + P^\zeta_1)] + \tfrac{5}{3366}(7\lambda_1 \\
&+ 9\lambda_2 - 16\lambda_3) + \tfrac{25}{561}
\end{aligned} \tag{15}
$$

$$ln\frac{M_\zeta}{M_Z} = \frac{4\pi}{187\alpha}(15-\frac{23\alpha}{\alpha_S}+63\sin^2\theta_W)+\frac{3}{187}[16(P_2^U+P_2^\zeta) - \frac{23}{3}(P_3^U+P_3^\zeta)-\frac{25}{3}(P_1^U+P_1^\zeta)]+\frac{1}{561}(25\lambda_1-48\lambda_2 + 23\lambda_3)+\frac{9}{187} \quad (16)$$

$$\frac{1}{\alpha_G} = \frac{3}{8\alpha}+\frac{1}{187\alpha}(\frac{347}{8}+\frac{466\alpha}{3\alpha_S}-271\sin^2\theta_W)-\frac{1}{4488\pi}[932(P_3^U+P_3^\zeta) - 945(P_2^U+P_2^\zeta)+1135(P_1^U+P_1^\zeta)]+\frac{1}{13464\pi}(1135\lambda_1-945\lambda_2 + 932\lambda_3)+\frac{196}{561\pi} \quad (17)$$

where the invrse of the GUT-coupling constant α_G^{-1} has been derived from the finestructure constant relation,

$$\frac{1}{\alpha(M_Z)} = \frac{5}{3\alpha_1(M_Z)}+\frac{1}{\alpha_2(M_Z)} \quad (18)$$

and the RGEs for the gauge couplings. Clearly the threshold effects are,

$$\Delta_U = \Delta ln\,\frac{M_U}{M_Z} = \frac{5}{3366}(7\lambda_1+9\lambda_2-16\lambda_3)$$

$$\Delta_\zeta = \Delta ln\,\frac{M_\zeta}{M_Z} = \frac{1}{561}(25\lambda_1-48\lambda_2-23\lambda_3) \quad (19)$$

$$\Delta_G = \Delta\alpha^{-1}G = \frac{1}{13464\pi}(1135\lambda_1-945\lambda_2-932\lambda_3)$$

where $\lambda_i = \lambda_i^U$ which are evaluated using the decomposition of the superheavy components of the Higgs representations under G_{213}.

3.1 The SU(5) model

$$\underline{24} \supset D_1(3,0,1)+D_2(1,0,8)$$

$$\underline{5} \supset C(1,-\tfrac{2}{3},3)$$

$$\underline{75} \supset E_1(1,\tfrac{10}{3},3)+E_2(2,\tfrac{5}{3},3)+E_3(1,-\tfrac{10}{3},\bar{3})+E_4(2,-\tfrac{5}{3},\bar{3}) + E_5(2,-\tfrac{5}{3},\bar{6})+E_6(2,\tfrac{5}{3},6)+E_7(1,0,8)$$

Defining $\eta_i = ln\frac{M_i}{M_U}$, extremisation of Δ_U requires

$$\eta_{D_1} = \eta_{E_1} = \eta_{E_2} = \eta_{E_3} = \eta_{E_4} = \eta^{(+)} = \pm\, ln\beta$$

$$\eta_C = \eta_{D_1} = \eta_{E_2} = \eta_{E_6} = \eta_{E_7} = \eta^{(-)} = \mp\, ln\beta$$

leading to

$$\Delta_U = \pm 0.38\, ln\beta\ ,\ \Delta_\zeta = \pm 1.0\, ln\beta\ ,\ \Delta_G = \pm\frac{3795}{6232\pi}ln\beta \quad (20)$$

Here the significance of β is that the superheavy scalar components can have a mass $\beta M_U(M_U/\beta), \beta = 1-10$ in analogy with the standard model Higgs boson. Without threshold effects the solutions are,

$$M_\zeta^0 = 10^{10.2\pm 0.6}\ ,\ M_U^0 = 10^{15\pm 0.2}GeV\ ,\ \alpha_G^{0^{-1}} = 39.05\pm 0.7 \quad (21)$$

$\alpha^{-1}i(\mu)$ are prevented to cross below the unification mass because of the presence of ζ at $M_I^0 = M_\zeta^0 = 10^{10.2\pm0.3} GeV$ which changes the slopes of $\alpha_{2L}^{-1}(\mu)$ and $\alpha_{3C}^{-1}(\mu)$ for $\mu > M_\zeta^0$. The unification mass has been increased by almost an order of magnitude increasing the proton lifetime consistent with the experimental limit. Inlcuding threshold effects the values of mass sclaes and coupling constants are given in Table 1. Clearly the model predictions with $\beta = 10$ saturates the Suprkamiokande limit for $p \longrightarrow e^+ + \pi^0$.

Table 1. Threshold effects on mass scales, GUT coupling and proton lifetime predictions in the degenerate(D) and nondegenerate(ND) cases of superheavy scalars in nonSUSY SU(5) with modified grand desert.

β	M_ζ/M_ζ^o	M_U/M_U^o	$\Delta\alpha_G^{-1}$	τ_p/τ_p^o
$10(D)$	$10^{+1.0}_{-1.0}$	$10^{-.02}_{+.08}$	$+2.9$ -1.9	$10^{-.08}_{+.30}$
$5(ND)$	$10^{+2.2}_{-1.7}$	$10^{\pm.29}$	$-.3$ $+.4$	$10^{\pm.92}$
$10(ND)$	$10^{+3.0}_{-2.6}$	$10^{\pm.38}$	$-.5$ $+.7$	$10^{\pm1.52}$

3.2 The SO(10) model

One important advantage of SO(10) over SU(5) is the generation of Majorana neutrino masses over a wide range of values. The real scalar $\zeta(3,0,8) \subset \mathbf{210}$ of SO(1). The implementation of the modified grand desert model in SO(10) requires the Higgs representation **10**, **45**, **126**, and **210** although the model also works by replacing **45** by another **210**. The superhevy components are identified in each representation. Then following the procedure explained for SU(5) we obtain[7],

$$\begin{aligned} \Delta_U &= [^{+.44}_{-.64}] ln\beta \\ \Delta_I &= [^{-2.37}_{+2.65}] ln\beta \end{aligned} \tag{22}$$

Numerical values on threshold effects on mass scales, GUT coupling contants and proton lifetimes are presented in Table 2 in the degenerate (D) and nondegenerate cases for $\beta = 5 - 10$ where $\beta = M_i/M_U . M_.$ being the superheavy Higgs scalar masses. It is clear that for superheavy masses differing by a factor $10(1/10)$ from M_U the increase in the proton lifetime could be as large as 50 times the uncorrected value and the model can not be rules out by the planned experiments in near future. The Majorna netrino masses in the jodel can arise in various ways. For example

$$m_{\nu_i} = \lambda h_i < \phi^0 <^2 < \Delta_R^0 > /M_{\Delta_L}^2 \ , \ i = e, \mu, \tau \tag{23}$$

with

$$\begin{aligned} m_{\nu_e} &= (2.5 \times 10^{-6} \ -- \ 2.5 \times 10^{-4}) eV \\ m_{\nu_\mu} &= (7.5 \times 10^{-4} \ -- \ 2.5 \times 10^{-2}) eV \\ m_{\nu_\tau} &= (7 \times 10^{-2} \ -- \ 7) eV \end{aligned} \tag{24}$$

where Δ_R^0 is the neutral comonent in $\Delta_R(1,3,\bar{10})$ carrying $B-L=2$ and $\Delta_L(3,1,10)$ is the corresponding left-handed triplet. Both are contained in **126** of SO(10). Here ϕ^0 is the netural comonent of the standard doublet $\subset$ **10** of SO(10) and $\lambda(h_i)$ is the Higgs quartic (Yukawa) coupling between **126** and **10**. Here we have used $h_i < \phi^0 >= m_{q_i}$. It is evident that while m_{ν_e} and m_{ni_μ} are compatible with the solar neutrino flux n_{ν_τ} value can be made to be consistent with the dard matter of the universe. The model can be also modified slightly to produce degenerate and see-saw contributions[17-18].

Table 2. Same as Table 1 but for nonSUSY SO(10).

β	M_ζ/M_ζ^o	M_U/M_U^o	$\Delta\alpha_G^{-1}$	τ_p/τ_p^o
$10(D)$	$10^{+.85}_{-.00}$	$10^{-.02}_{+.00}$	-12.0 $+0.0$	$10^{-.24}_{+.00}$
$5(ND)$	$10^{+2.4}_{-2.6}$	$10^{-.46}_{+.30}$	$+4.5$ -7.2	$10^{-1.7}_{+0.8}$
$10(ND)$	$10^{+3.6}_{-3.7}$	$10^{-6.8}$	$+6.8$ -10.0	$10^{-.57}_{+1.61}$

Although corrections to the intermediate mass M_ζ is quite significant that on M_U and hence on τ_p are small. Such results have been also obtained[8] in computing threshold effects in SU(5) with split multiplets[16]. We observe from these analyses that the presence of G_{213} below the GUT-scale reduces uncertainty on the proton lifetime prediction.

4. Threshold effects in SO(10) with intermediate scale and theorems on vanishing corrections

Here we discuss threshold effects in SO(10) with G_{224P} intermediate symmetry in detail and breifly mention the results with other intermediate symmetries.

(a) G_{224P} Intermediate Symmetry

With the choice of minimal Higgs representations **54**, **126**, and **10**, we have

$$a_i'^T = (11/3, 11/3, -14/3)\ ,\ A_U = -50/3\ ,\ B_U = 50/9$$

$$A_I = -17/3\ ,\ B_I = -53/3$$

$$B'_{ij} = \begin{bmatrix} 584/3 & 3 & 765/2 \\ 3 & 584/3 & 765/2 \\ 153/2 & 153/2 & 1759/6 \end{bmatrix} \tag{25}$$

Using these in (8)-(10) we obtain,

$$\begin{aligned} \Delta_U &= -\tfrac{3}{4400}(-9\lambda'^U_{2R} + \tfrac{88}{3}\lambda'^U_{4C} - \tfrac{61}{3}\lambda'^U_{2L} \\ &\qquad -15\lambda'^I_Y - \tfrac{61}{3}\lambda'^I_{2L} + \tfrac{106}{3}\lambda'^I_{3C}) \end{aligned} \tag{26}$$

$$\Delta_I = -\frac{1}{88}(\lambda'^U_{2L} - \lambda'^U_{2R} + \lambda'^I_{2L} + \frac{2}{3}\lambda'^I_{3C} - \frac{5}{3}\lambda'^I_Y) \tag{27}$$

It is important to note that the presence of L-R symmetry for $\mu > M_I$ demands $\lambda'^U_{2L} = \lambda'^U_{2R}$ which leads to vanishing GUT-threshold corrections on Δ_I or equivalently on M_I. This is a manifestation of theorems on vanishing corrections on $\sin^2\theta_W$ to be discussed a little later.

We make the simplifying assumption that all the superheavy components belinging to a single GUT representation have the same mass. Also we use $M_{L_i} = M_L$ and $M_{R_i} = M_R$ leading to $\eta_{L_i} = \eta_L, \eta_{R_i} = \eta_R$,

$$\begin{aligned} \Delta_U &= \tfrac{1}{1100}(11\eta_{54} - 88\eta_{126} - 44\eta_{10} + 11\eta_\phi - 131\eta_R + 189\eta_L) \\ \Delta_I &= \tfrac{1}{22}(9\eta_R - 10\eta_L) \end{aligned} \tag{28}$$

(a.1) Theorem on vanishing corrections on $\sin^2\theta_W$

It is important to note that the GUT threshold contributions such as η_{10}, η_{54} and η_{126} are absent in Δ_I. Also the contributions of two loop functions P^U_{2L}, P^U_{2R} and P^U_{4C} in Δ_I cancel out. These are due to theorems proved recently in SO(10) with G_{224P} intermediate symmetry occuring at the highest intermeidate scale[5,6].

Theorem 1 In all GUTs where the G_{224P} symmetry breaks at the highest intermediate scale (M_I), the GUT - threshold contribution to $\sin^2\theta_W$ vanishes[5].

Theorem 2 In all GUTs where the G_{224P} symmetry breaks at the highest intermediate scale (M_I), the gauge boson renormalization to every m - loop order ($m \geq 2$) in the mass range $M_I - M_U$ has vanishing contribution to $\sin^2\theta_W$.

(1.2) Vanishing corrections on $\Delta ln(M_I/M_Z)$ *and precise ptediction on neutrino masses*

In ref[5] it was shown that all perturbative and non-pertubative corrections including gravity-induced higher dimensional operator effects occuring at the GUT sclae also have vanishing contributions on $\sin^2\theta_W$ making the intermediate scale M_I quite stable. Here we provide a proof on the stability of M_I against all such uncertainities. Since left-right symmetry is restored in the presence of G_{224P}, we have

$$a'_{2L} = a'_{2R}\ ,\ \lambda'^U_{2L} = \lambda'^U_{2R}\ ,\ C^U_{2L} = C^U_{2R} \tag{29}$$

contributions due to higher-dimensional operators. The corrections to the coupling constants at $\mu = M_U$ can be written in the form

$$\frac{1}{\alpha_i(M_U)} = \frac{1}{\alpha_G} - \frac{(\lambda_i^U + C_i^U)}{12}\ ,\ i = 2L, 2R, 4C$$

Then all the formulas derived so far hold hold if we replace $\lambda_i'^U \longrightarrow \lambda_i'^U + C_i^U$. In eq.(9),

$$\begin{aligned}
A_U &= 2(a'_{4C} - a'_{2L})\,, \\
B_U &= \tfrac{2}{3}(a'_{2L} - a'_{4C})\,, \\
A_I &= \tfrac{8}{3}a_{3C} - a_{2L} - \tfrac{5}{3}a_Y - 2(a'_{4C} - a'_{2L})\,, \\
B_I &= \tfrac{5}{3}(a_{2L} - a_Y) - \tfrac{2}{3}(a'_{2L} - a'_{4C})\,, \\
J_\lambda^U &= \tfrac{1}{3}(\lambda_{2L}^U + C_{2L}^U - \lambda_{4C}^U - C_{4C}^U)\,, \\
K_\lambda^U &= \tfrac{1}{9}(\lambda_{4C}^U + C_{4C}^U - \lambda_{2L}^U - C_{2L}^U)\,.
\end{aligned} \tag{30}$$

which by virtue of (29) lead to

$$\Delta_I^U = 0 \tag{31}$$

This can also be verified through eqs.(17) and (29). It is to be noted that (31) holds irrespective of the nature of the correction arising at the GUT scale and it is indevendent of the presence or absence of supersymmetry. The cancellation occurs for any possible nonperturbative contributions also. Thus the G_{224P} -breaking scale is not affected due to any corrections emerging from the GUT-sclae although the GUT-scale itself is affected by the corrections. In the absence of threshold corrections we obtain

$$\begin{aligned}
M_U^0 &= 10^{15\pm 0.25} GeV \\
M_I^0 &= 10^{13.6\pm 0.2} GeV \\
\alpha_G^{-1} &= 40.6 \pm 0.2
\end{aligned} \tag{32}$$

where the uncertainties are due to those in the input parameters.

The threshold effects are computed by extremising Δ_U or Δ_I while taking into account the parity restoration constraint for $\mu \geq M_U$ with

$$\eta_L \leq 0\ ,\ \eta_R \leq 0\ ,\ \eta_\phi \leq 0\,.$$

Numerical values of corrections are given in Table 2 for $\beta = 5 - 10$. Predictions for proton lifetime for the $p \longrightarrow e^+\pi^0$ is amde using[21]

$$\tau_p^0 = \frac{5}{8}\left[\frac{\alpha_G^{SU(5)}}{\alpha_G^{SO(10)}}\right]^2 \times 4.5 \times 10^{29\pm.7}\left(\frac{M_U}{2\times 10^{14} GeV}\right)^4 Yrs. \tag{33}$$

For $\beta = 10$ the model predicts

$$\tau_p = 1.44 \times 10^{32.1\pm.7\pm 1.0\pm 1.9} Yrs. \tag{34}$$

where the first, second and third uncertainties are due to matrix element, input parametrs, and threshold effects. It is clear that the maximum value for τ_p exceeds the current Super-kamiokande limit by almost one order. Thus, as against the conclusions of ref[19], this model can not be ruled out by any improvement on proton-lifetime measurement.

Table 3. Threshold effects in SO(10) with G_{224P} intermediate symmetry.

β	M_I/M_I^o	M_U/M_U^o	$\Delta\alpha_G^{-1}$	τ_p/τ_p^o
$5(ND)$	$10^{+.26}_{-.20}$	$10^{+.27}_{-.30}$	$^{-1.4}_{+0.2}$	$10^{\mp 1.2}$
$10(ND)$	$10^{+.40}_{-.30}$	$10^{+.40}_{-.44}$	$^{-2.0}_{+0.2}$	$10^{\mp 1.7}$

Threshold effect on M_I shown in Table 3 is due to that at the intermediate-scale boundary only.

$$\log_{10}(M_I/M_I^0) \;=\; \pm 0.4$$

The higher-dimensional operators scaled by the Planck mass do not modify the intermediate scale. Also imposition of a horizontal symmetry does not change the scale unless additional light scalars are introduced below M_I. Even if the left-handed triplet is not given a VEV explicitly[28], it can be induced[29,30],

$$\begin{aligned} m_\nu &= \gamma\frac{M_Z^2}{M_I} = (2-200)\times 10^{\pm 0.2\pm 0.4} f\lambda eV \\ &= (0.5-800) f\lambda eV\,, \end{aligned} \tag{35}$$

where we have evaluated[30]

$$\gamma \approx 10 f\lambda/\beta^2\;,\; \beta = 0.1-1\,,$$

$f(\lambda)$ being a Yukawa(quartic) coupling. The see-saw contributions are,

$$\begin{aligned} m_{\nu_e} &= 5\times 10^{-10.6\pm.2\pm.4} eV\,, \\ m_{\nu_\mu} &= 1.6\times 10^{-3.6\pm.2\pm.4} eV\,, \\ m_{\nu_\tau} &= 0.5\times 10^{-.6\pm.2\pm.4} eV\,. \end{aligned} \tag{36}$$

These neutrino masses are capable of explaining the solar and the atmospheric neutrino oscullations while offering neutrinos as strong candidates for the dark matter of the Universe. In addition the degenerate neutrino mass for ν_e could be confirmed by the neutrinoless double-beta decay experiments.

Threshold effects in SO(10) with $G_I = G_{224}$ or G_{2213} without parity ($g_{2L} \neq g_{2R}$) have been extensively discussed in ref.[3]. Although larger undertainty was noted earlier[22] allowing for parity restoration and hence complete SO(10) symmetry at $\mu > (10-30)M_U$, it has been found in ref[3] that the imposition of the parity restoration constraint at the GUT-scale can reduce the uncertainties significantly. Among the two the models, the one with $G_I = G_{224}$ appear to be more favoured for explaining the solar neutrino puzzle.

For $G_I = G_{2213P'}$ the threshold effects have been computed in ref.[20] and for $G_I = G_{214}$ they have been computed in ref.[12]. The computations in all cases can be made following the methods outlined in Secs.2-4. We summarise the results without going into details in Table 4. The predictions on the proton lifetime in different cases with $\beta = 10$ are given below for extremised $\Delta_{U'}$

Table 4. Threshold effects in SO(10) with single intermediate symmetries: G_{224} (model A), G_{2213} (model B), G_{2213P} (model C), and G_{214} (model D) for $\beta = 10$ in the nondegenerate case.

	G_{224} (A)	G_{2213} (B)	G_{2213P} (C)	G_{214} (D)
M_I/M_I^o	$10^{+2.60}_{-0.07}$	$10^{+.3}_{-.1}$	$10^{\pm.1}$	$10^{-.15}_{+.45}$
M_U/M_U^o	$10^{+0.13}_{-1.24}$	$10^{+.2}_{-.5}$	$10^{\pm.43}$	$10^{+.66}_{-.20}$
τ_p/τ_p^o	$10^{+0.5}_{-5.0}$	$10^{+0.8}_{-2.0}$	$10^{\pm1.7}$	$10^{+2.6}_{-0.8}$

(A) $G_I = G_{224}$

$$\tau_p = 1.44 \times 10^{37.4\pm.7\pm1.0^{+0.5}_{-5.0}} Y_{rs}.$$

(B) $G_I = G_{2213}$

$$\tau_p = 1.44 \times 10^{37.7\pm.7\pm.9^{+0.7}_{-2.0}} Y_{rs}.$$

(C) $G_I = G_{2213P}$

$$\tau_p = 1.44 \times 10^{34.2\pm.7\pm.8\pm1.7} Y_{rs}.$$

(D) $G_I = G_{214}$

$$\tau_p = 1.44 \times 10^{29.8\pm.7\pm.8\pm^{2.6}_{0.8}} Y_{rs}.$$

Some comments and conclusions are in order. Including threshold effects we find that even if $\beta = 7$ the model (D) is consistent with the available experimental limit

(MSSM). In one approach the superpartner scale has been introduced at M_S which is expected not to exceed few TeVs. Below M_S global SUSY is assumed to have broken down but the effects of superpartner masses is taken into account by threshold correction at that scale,

(i) $SU(5) \times SUSY \xrightarrow{M_U} G_{213} \times SUSY \xrightarrow{M_S} G_{213} \xrightarrow{M_Z} G_{13}$ In the other case it is assumed that SUSY survives down to M_Z and the effects of superpartner masses are taken into account through threshold effects at M_Z.

(ii) $SU(5) \times SUSY \xrightarrow{M_U} G_{213} \times SUSY \xrightarrow{M_Z} G_{13}$

Threshold effects due to superheavy masses are estimated at M_U and the corrections due to the top quark is computed as in the SM at M_Z in both cases.

6.1 Threshold effects on M_S

With the chain(i) the generalized form of eqs.(3)-(5) and (8) - (9) apply with $M_I = M_S$ but different numerical values of the coefficients for $i, j = 1, 2, 3$

$$a_i' = \begin{vmatrix} 33/5 \\ 1 \\ -3 \end{vmatrix} \quad b_{ij}' = \begin{vmatrix} 7.96 & 5.4 & 17.6 \\ 1.8 & 25 & 24 \\ 2.2. & 9 & 14 \end{vmatrix}$$

and with

$$L_i^U/12\pi \longrightarrow \Delta_i^U \cdot L_i^I/12\pi \longrightarrow \Delta_i^S$$

where

$$\Delta_i^U = \Delta_i^{CNV} + \Delta_i^{SH} \tag{37}$$

The first term in the RHS of (37) represents conversion from DR to $\overline{MS}$ scheme and the second term includes the superheavy particle effects near M_U. In order to find the latter, it is noted that the scalar multiplets have the components,

$$\underline{24} = M_\sigma(1,0,8) + M_\sigma(3,0,1) + M_V(2,5/6,3) + M_V(2,-5/6.\bar{3}) + M_0(1,0,1),$$

$$\underline{5} = M_{H_C}(1,1/3,3) + M_{H^0}(2,1/2.1),$$

$$\underline{5} = M_{H_C}(1,-1/3,\bar{3}) + M_{H_2}(2.-1/2.1).$$

At first evaluating only the GUT-threshold corrections to the gauge couplings by using the superheavy-particle - one-loop β-functions yields

$$\alpha_3^{-1} = \alpha_G^{-1} + \tfrac{1}{2\pi}[-4ln\tfrac{M_S}{M_Z} + ln\tfrac{M_V}{M_Z} - 3ln\tfrac{M_\sigma}{M_Z} - ln\tfrac{M_{H_C}}{M_Z}] + \tfrac{1}{4\pi}[P_3 + P_3'] + \tfrac{1}{4\pi} - \Delta_3^S$$

$$\alpha_2^{-1} = \alpha_G^{-1} + \tfrac{1}{2\pi}[-\tfrac{25}{6}ln\tfrac{M_S}{M_Z} + 3ln\tfrac{M_V}{M_Z} - 2ln\tfrac{M_\sigma}{M_Z}] + \tfrac{1}{4\pi}[P_2 + P_2'] + \tfrac{1}{6\pi} - \Delta_3^S$$

$$\alpha_1^{-1} = \alpha_G^{-1} + \tfrac{1}{2\pi}[-\tfrac{5}{2}ln\tfrac{M_S}{M_Z} + 7ln\tfrac{M_V}{M_Z} - \tfrac{2}{5}ln\tfrac{M_{H_C}}{M_Z}] + \tfrac{1}{4\pi}[P_1 + P_1'] - \Delta_1^S$$

The superheavy-mass contributions to the corrections are given in Table 5. Using (38) and the standard procedure gives

$$\begin{aligned} ln\frac{M_U}{M_Z} &= \frac{\pi}{19\alpha}(\frac{1}{2}+7s^2-\frac{25}{\alpha_s})+\frac{5}{76}[\frac{1}{6}(P_1'+P_1)+\frac{3}{2}(P_2'+P_2) \\ &\quad -\frac{5}{3}(P_3'+P_3)]+\delta_U \\ ln\frac{M_S}{M_Z} &= \frac{12\pi}{19\alpha}(1-5s^2+\frac{7\alpha}{3\alpha_s})-\frac{1}{19}[5(P_1'+P_1)-12(P_2'+P_2) \\ &\quad +7(P_3'+P_3)]+\delta_S \\ \alpha_G^{-1} &= \frac{3}{8\alpha}+\frac{3}{76\alpha}(\frac{47}{2}+\frac{250\alpha}{\alpha_S}-146s^2)[45(P_1'+P_1) \\ &\quad -51(P_2'+P_2)]+25(P_3'+P_3)]+\delta_S \end{aligned} \tag{39}$$

Table 5. Threshold and 5-dim. operator contributions to the matching functions [9].

	Δ_i^{CNV}	Δ_i^L	Δ_i^{SH}	Δ_i^{5-dim}
Δ_1	0	$\frac{5}{4\pi}ln\frac{M_1}{M_Z}$	$-\frac{5}{\pi}ln\frac{M_V}{M_U}+\frac{1}{5\pi}ln\frac{M_{Hc}}{M_U}$	$-.015\eta$
Δ_2	$-\frac{1}{6\pi}$	$\frac{25}{12\pi}ln\frac{M_2}{M_Z}$	$-\frac{3}{\pi}ln\frac{M_V}{M_U}+\frac{1}{\pi}ln\frac{M_{Hc}}{M_U}$	$-.042\eta$
Δ_3	$-\frac{1}{4\pi}$	$\frac{2}{\pi}ln\frac{M_3}{M_Z}$	$-\frac{2}{\pi}ln\frac{M_V}{M_U}+\frac{3}{2\pi}ln\frac{M_\Sigma}{M_U}$	
			$+\frac{1}{2\pi}ln\frac{M_{Hc}}{M_U}$	$-.028\eta$

$$\begin{aligned} \delta_U &= \frac{5\pi}{19}[\frac{1}{6}(\Delta_1^U+\Delta_1^S)+\frac{3}{2}(\Delta_2^U+\Delta_2^S)-\frac{5}{3}(\Delta_3^U+\Delta_3^S)] \\ \delta_S &= \frac{4\pi}{19}[5(\Delta_1^U+\Delta_1^S)-12(\Delta_2^U+\Delta_2^S)+7(\Delta_3^U+\Delta_3^S)] \end{aligned} \tag{40}$$

$$\delta_G = \frac{1}{19}[45(\Delta_1^U+\Delta_1^S)-5(\Delta_2^U+\Delta_2^S)+25(\Delta_3^U+\Delta_3^S)] \tag{41}$$

Ignoring all threshold corrections except Δ_1^{CNV} and using the input parameters from eq.(1) in (38)-(40) gives

$$M_U^0 = 10^{16.1\pm.49}GeV,\ M_S^0 = 10^{2.44\pm1.85}GeV,\ \alpha_G^{-1} = 26.5\pm.3 \tag{42}$$

Two loop contributions which were ignored from M_S^0 estimation in [24] is found to be comparable to the one-loop contribution in $ln(M_S^0/M_Z)$,

$$ln(M_S^0/M_Z) = -2.53+3.66\pm4.26 \tag{43}$$

GUT-threshold corrections are

$$\begin{aligned}
\delta_U &= \tfrac{4}{19} ln \tfrac{M_{H_c}}{M_Z} - \tfrac{5}{19} ln \tfrac{M_\Sigma}{M_Z} \\
\delta_S &= \tfrac{18}{19} ln \tfrac{M_\Sigma}{M_U} - \tfrac{6}{19} ln \tfrac{M_\Sigma}{M_U} \\
\delta_G &= \tfrac{1}{48\pi} (43 ln \tfrac{M_{H_c}}{M_U} - 27 ln \tfrac{M_\Sigma}{M_U}
\end{aligned} \tag{44}$$

The GUT-threshold effects are estimated in Table 6 in the degenerate(D), and nondegenerate(ND) cases assuming the superheavy masses to vary between M_U/β and βM_U with $\beta = 5 - 10$ where, as per the conclusion of ref.[24], the uncertainty in M_S is of the order $10^{\pm 1.2}$ for $\beta = 10$.

Table 6. GUT-threshold effects on the unification mass and superpartner scale in MSSM in the degenerate(D) and nondegenerate(ND) cases.

β	M_U/M_U^o	M_S/M_S^o
$5(D)$	$10^{\mp .1}$	$10^{\pm .44}$
$10(D)$	$10^{\mp .14}$	$10^{\pm .66}$
$5(ND)$	$10^{\pm .33}$	$10^{\pm .66}$
$10(D)$	$10^{\pm .47}$	$10^{\pm 1.26}$

6.2 Constraint on superheavy masses from the CERN-LEP data

Hisano, Murayama and Yanagida [25] have observed that the combination $p/\alpha_1 + q/\alpha_2 + r/\alpha_3$ is dependent only on the Higgs colour-triplet mass(M_{H_C}) if $(p, q, r) = (-1, 3, -2)$. Similarly the other combination $(5, -3, -2)$ depends on M_V and M_Σ leading to,

$$\begin{aligned}
(-2\alpha_3^{-1} + 3\alpha_2^{-1} - \alpha_1^{-1}) &= \frac{1}{2\pi} \left[\frac{12}{5} ln(M_{H_c}/M_Z) - 2 ln \frac{M_S}{M_Z} \right] \\
(5\alpha_1^{-1} - 3\alpha_2^{-1} - 2\alpha_3^{-1}) &= \frac{1}{2\pi} \left[12 ln \frac{M_V^2 M_\Sigma}{M_Z^3} + 8 ln \frac{M_S}{M_Z} \right]
\end{aligned} \tag{45}$$

Incorporating Δ_i^S effects leads to the replacements of second terms in the RHS of (45) by the logarithmic functions of super partner and the second Higgs-doublet masses [25]. Restricting the model to the minimal supergravity SU(5), the particle spectrum and the CERN-LEP measurements impose the following constraints on

the colour triplet mass and the effective unification scale $(M_V^2 M_\Sigma)^{1/3}$,

$$\begin{aligned} 2.2 \times 10^{13} GeV &< M_{H_c} < 2.3 \times 10^{17} GeV \\ 0.95 \times 10^{16} GeV &< (M_V^2 M_\Sigma)^{1/3} < 3.3 \times 10^{16} GeV \end{aligned} \tag{46}$$

for the gluino mass 100 GeV - 1TeV.

6.3 Higher-dimensional operator effects

The effects of the 5-dim. operator,

$$-\frac{\eta}{2M_G} Tr[F_{\mu\nu} \Sigma_{(24)} F^{\mu\nu}] \tag{47}$$

on the MSSM predictions have been analysed by Langacker and Polonsky [9] and Hall and Sarid [26]. The analytic expressions for the strong interaction coupling and M_{H_c} are [26],

$$\begin{aligned} \alpha_s &= .132\{1 - .024\sigma - .02 ln[\mu^{4/5} M_{H_2}^{1/5}/M_Z] + .025 ln[\tfrac{M_{H_c}}{9 \times 10^{16} GeV}] \\ &\quad -.025\eta(1 - .1\alpha)(m_{1/2}/M_Z)^{-2/9\lambda_{24}-1/2}\} \\ M_{H_c} &= (3 \times 10^{16} GeV)\lambda_5(1 - .1\sigma)\lambda_{24}^{-1/3}(m_{1/2}/M_Z)^{-2/9} \end{aligned} \tag{48}$$

where $M_G = (8\pi G_N)^{-1/2} = 2.4 \times 10^{18} GeV$, M_{H2} = second Higgs doublet mass $m_{1/2}$ = universal gaugino mass, μ = two-doublets mixing parameter, $\sigma = (s^2 - .2326)/.008$, and λ_5 and λ_{24} are the trilinear couplings in the superpotential,

$$W = \lambda_5 \bar{H}_5 \Sigma H_5 + \frac{1}{3}\lambda_{24} tr(\Sigma^3) + \ldots$$

It is clear from (48) that α_S increases with logarithmic increment of the colour triplet mass when $\eta = 0$. Due to gravitational smearing (e.g., $\eta = -1$ to $+1$) the allowed region in the α_s vs. M_{Hc} plot is found to be enhanced and blurred.

6.4 Threshold effects through effective mass parameters

Using the symmetry breaking pattern(i) Langacker and Polonsky[9] have computed SUSY particle threshold effects near the boundary M_Z, in addition to the GUT-boundary corrections[9] by parametrising these corrections in terms two separate sets of effective masses. The RGEs for the three gauge couplings can be written as,

$$\frac{1}{\alpha_i(M_Z)} = \frac{1}{\alpha_G} + \frac{a_i}{2\pi} ln \frac{M_u}{M_z} + \frac{1}{4\pi} P_i' - \Delta_i \tag{49}$$

The correction term Δ_i includes several contributions,

$$\Delta_i = \Delta_i^U + \Delta_i^{ho} + \Delta_i^t + \Delta_i^Y + \Delta_i^L$$

where Δ_i^U is the same as (37), Δ_i^L is the anlogue of Δ_i^S but evaluated at the boundary M_Z, and the others are the Higgs(ho), the top quartk(t), and the Yukawa coupling(Y) contributions evaluated at the boundary M_Z. Using the RGEs and

lytic expressions which are independent of the GUT symmetry but only dependent upon the grand desert hypothesis. We furnish analytic expressions on threshold effects for one set of predictions,

$$
\begin{aligned}
ln\frac{M_U}{M_Z} &= 2\pi(3\alpha^{-1} - 8\alpha_S^{-1})/F - (5P_1' + 3P_2' - 8P_3')/(2F) + \delta_U \\
S^2(M_Z) &= \sin^2\theta_w(M_Z) = [3(a_1' - a_3') + (a_1' - a_2')\alpha/\alpha_s]/ - 5\alpha[(a_2' - a_3')P_1' \\
&\quad + (a_3' - a_1')P_2' + (a_1' - a_2')P_3']/(4\pi F) + \delta_{s^2} \\
\alpha_G^{-1} &= [-3a_3'\alpha^{-1} + (5a_1' + 3a_2')\alpha_s^{-1}]/F + [(5P_1' + 3P_s')a_3' \\
&\quad - (5a_1' + 3a_2')P_3']/(4\pi F) + \delta_G
\end{aligned}
\tag{50}
$$

The threshold corrections are given below which can be computed numerically from the Tables given in ref.[9],

$$
\begin{aligned}
\delta_U &= \Delta ln\frac{M_U}{M_Z} = 2\pi(5\Delta_1 + 3\Delta_2 + 8\Delta_3)/F \\
\delta_{s^2} &= \Delta\sin^2\theta_w(M_Z) = 5\alpha[(a_2' - a_3')\Delta_1 + (a_3' - a_1')\Delta_2 + (a_1' - a_2')\Delta_3]/F \\
\delta_G &= [(5a_1' + 3a_2')\Delta_3 - (5\Delta_1 + 3\Delta_2)a_3']/F \\
F &= 5a_1' + 3a_2' - 8a_3'
\end{aligned}
\tag{51}
$$

Using $\alpha^{-1}(M_Z) = 127.9, \alpha_s(M_Z) = 0.12$ gives

$$M_U = 10^{15.9} GeV, \alpha_G^{-1} = 23.5, \sin^2\theta_w = 0.2335\,.$$

Table 7. The top quark and the Yukawa coupling corrections. Here m_t is in GeV and h_t is the Higgs-top quark Yukawa coupling [9].

	Top quark corrections corrections	Yukawa coupling
Δ_1	$-.15 + .13ln(m_t/138) + .15(m_t/138)^2$	$.17h_t^2$
Δ_2	$-.25 + .065ln(m_t/138) + .025(m_t/138)^2$	$.20h_t^2$
Δ_3	$.04 + .105ln(m_t/138)$	$.13h_t^2$

The top quark and Yukawa coupling corrections which are the same as the Standard Model are given in Table 7[9]. The corrections at M_Z-boundary due to the SUSY particle masses have been parametrized in terms of three effective mass

$$\Sigma_\zeta \frac{a_i^\zeta}{2\pi} ln\left(\frac{M_\zeta}{M_z}\right) = \frac{a_i^{SUSY} - a_i^{SM}}{2\pi} ln\left(\frac{M_i}{M_z}\right) \; ; \; i = 1,2,3 \qquad (52)$$

where $a_i^{SUSY} = a_i', a_i^\zeta$ is the analogue of a_i but for particle ζ only, and M_ζ is the mass of ζ. Using the SUSY particle spectrum [27] the effective mass parameters have been evaluated : for example a possible solution is

$$m_t = 160Gev \; , \; M_1 = 261Gev \; , \; M_2 = 207Gev \; , \; M_3 = 352Gev$$

For evaluation of threshold effects at M_U a parametrisation similar to (52) has also been suggested,

$$\Sigma_\zeta \frac{a_i^\zeta}{2\pi} ln \frac{M_\zeta}{M_Z} = \frac{a_i^{matter}}{M_U} \; ; \; i = 1,2,3$$

where ζ stands for superheavy particles near the GUT-scale. The prediction for $\sin^2\theta_W(M_Z)$ turns out to be [9],

$$\sin^2\theta_W(M_Z) = 0.2334 \pm .0025 \pm .0014 \pm .0006 \; ^{+.0013}_{-.0005} \pm .0016 \qquad (53)$$

To predict (53) one starts with the input parameters $\alpha_S(M_Z)$ and $\alpha(M_Z)$. One can start with the parameters $\sin^2\theta_W(M_Z)$ and $\alpha(M_Z)$ to predict $\alpha_S(M_Z), M_U$ and α_G[9],

$$\alpha_S(M_Z) = .125 \pm .001 \pm .005 \pm .002 \; ^{+.005}_{-.002} \pm .006 \qquad (54)$$

The first number on the RHS of (53) or (54) is for $m_t = 138GeV$. The second entry in (53) ((54)) is due to the uncertainty in the input parameter $\alpha_S(\sin^2\theta_W)$. The third, fouth, fifth, and sixth entries are due to SUSY threshold. m_t and m_{ho}, GUT-threshold and 5-dimensional operator effects. Predicted values of M_U and α_G with uncertainties are given in ref.[9].

7. Summary and conclusions

We have discussed threshold effects in modified nonSUSY grand desert models with SU(5) and SO(10) GUTs, single intermediate scale models of SO(10), and in the minimal SUSY SU(5). We have also estimated neutrino masses predicted in nonSUSY SO(10) with G_{224P} intermediate symmetry where vanishing corrections on the intermediate scale has been explicitly demonstrated. We conlcude that

1. A minimal extension of the grand desert by the introduction of a single real scalar $\zeta(3,0,8)$ makes SU(5) consistent with the CERN-LEP data and the proton lifetime measurment. In addition SO(10) can account for small neutrino masses needed for solar neutrino oscillation and the dark matter of the Universe. Also the model has the potentiality to provide degenerate neutrino masses.

2. When the GUT symmetry breaks down to the SM gauge group in one step threshold uncertainty appears to be smaller on the proton lifetime prediction.

3. Certain models appearing to be ruled out by two-loop calculations could survive when threshold and 5-dim. operator effects are taken into account. It is essential to include such effects while questioning their survival against the CERN-LEP data and the proton lifetime.

4. Including threshold effects alone the SO(10) model with G_{214} intermediate symmetry is consistent with the CERN-LEP data, proton lifetime and small neutrino masses.

5. In a number of GUTs with G_{224P} intermediate symmetry we prove explicitly due to high-sclae-loop effects, GUT-threshold and higher dimensional operator effects with

$$M_I = 10^{13.6\pm0.2\pm0.4} GeV$$

leading to more precise values of degenerate and see-saw values of neutrino masses needed to explain the solar and atmospheric neutrino oscillations and the dark matter of the universe. The degenerate mass predictions, $m_{\nu_e} = 0(1)eV$, could be confirmed by the neutrinoless double beta-decay experiments. This prediction is universal to a large class of grand unified theories such as SO(10), SO(18), SU(16), $E_{6'}SU(8)_L \times SU(8)_R$ and all $SO(2N)$ with $N \geq 5$.

6. As shown by Hisano et.al. [25] the Higgs-colour-triplet mass and the effective unification mass in MSSM can be constrained by the CERN-LEP data.

7. There could be gravitational smearing effects in MSSM on α_s prediction due to 5-dim. operator effects[26].

8. There threshold uncertainties on MSSM predictions can also be parametrised in terms of effective mass parameters[9].

Acknowledgement

The author is thankful to Professors R.Ramachandran, G.Rajasekaran, Partha Ghose, and S.Uma Sankar for hospitality during the workshop and acknowledges support in the research project SP/S2/K-09/91 from the Department of Science and Technology, New Delhi.

References

[1] J.C.Pati and A.Salam, Phys. Rev. **D10** (1974) 275. For reviews see J.C.Pati, Proc. A.D.Shakarov Int. Conf. Moscow (1991) ; R.N.Mohapatra, Unification and Supersymmetry (Springer, New York, 1992) ; H.P.Niles, Phys. Rep. 110 (1984)1.

[2] U.Amaldi, W. de Boer, and H.Furstenau, Phys. Lett. **B260** (1991) 447 ; P.Langacker and M.Luo, Phys. Rev. **D44** (1991) 817.

[3] R.N.Mohapatra and M.K.Parida, Phys. Rev. **D47** (1993) 264.

[4] M.K.Parida, Proc. X DAE Symposium, Bombay (1992), ed. S.Banerjee and P.Roy, Pramana (J. Phys.) suppl. **41** (1993) 271.

[5] M.K.Parida and P.K.Patra, Phys. Rev. Lett. **66** (1991) 858.

[6] M.K.Parida and P.K.Patra, Phys. Rev. Lett. **68** (1992) 754.

[8] M.L.Kynshi and M.K.Parida, Phys. Rev. **D49** (1994).

[9] P.Langacker and N.Polonsky, Phys. Rev. **D47** (1993) 4028.

[10] W.J.Marciano, Proc. Eighth Workshop on Grand Unification, Syracuse, NY. ed. K.C.Wali (World Scientific, Singapore, 1988) ; in Field Theory and Elementary Particles, ed. A. Perlmutter (Plenum. N.Y.1982) ; Proc. Fourth Workshop on Grand Unification, Philadelphia, Pennsylvania (1983), ed. H.A.Weldon et.al (Birkhauser, Boston (1983)).

[11] D.Chang, R.N.Mohapatra, and M.K.Parida, Phys.Rev.Lett. **52** (1984) 1072 ; Phys. Rev. **D30** (1984) 1052.

[12] D.Chang, R.N.Mohapatra, J.Gipson, R.E.Marshak and M.K.Parida, Phys. Rev. **D31** (1985) 1718.

[13] M.Rani and M.K.Parida, Phys. Rev. **D48** (1994).

[14] S.Weinberg, Phys. Lett. **B91** (1980) 51 ; L.J.Hall, Nucl. Phys. **B178** (1981) 75 ; M.K.Parida, Phys. Lett. **B196** (1987) 163. For SUSY theories see M.B.Einhorn and D.R.T.Jones, Nucl. Phys. **B196** (1982) 475.

[15] H.Murayama and T.Yanagida, TU-370 (1991) ; T.G.Rizzo, Phys. Rev. **D45** (1992) 3903.

[16] U.Amaldi, W de Boer, H.Furstenau, P.H.Frampton and J.T.Liu, Phys. Lett. **B281** (1992) 374.

[17] D.Caldwell and R.N.Mohapatra, Phys. Rev. **D47** (1993) ; R.N.Mohapatra, Proc. ICNAPP, Bangalore (1994).

[18] A.S.Joshipura, these proceedings.

[19] N.G.Deshpande, E.Keith and P.Pal, Phys. Rev. **D46** (1992) 2261.

[20] D.G. Lee, R.N.Mohapatra, M.K.Parida and M.Rani, UMD-PP-94-117 (1994).

[21] P.Langacker, in Inner Space and Outer Space, ed. E.Kolb et. al. (Univ. of Chicago Press, 1986).

[22] M.K.Parida and C.C.Hazra, Phys. Rev. **D40** (1989) 3074.

[23] V.V.Dixit and M.Sher, Phys. Rev. **D49** (1989) 3765.

[24] R.Barbieri and L.J.Hall, Phys. Rev. Lett. **68** (1992) 752.

[25] J.Hisano, H.Murayama and T.Yanagida, Phys. Rev. Lett. **69** (1992) 1014 ; Nucl. Phys. **B402** (1993) 46.

[26] L.J.Hall and U.Sarid, Phys. Rev. Lett. **70** (1993) 2673.

[27] M.Drees and M.Nojiri, Nucl. Phys. **B369** (1992) 54.

[28] R.N.Mohapatra and G.Senjanovic, Phys. Rev. **D23** (1981) 165.

[29] D.Chang and R.N.Mohapatra, Phys. Rev. **D32** (1985) 1248 ; M.K.Parida, P.K.Patra and C.C.Hazra, Phys. Rev. **D43** (1991) 2351.

[30] M.K.Parida, In preparation.

[31] S.Bludman, D.Kennedy and P.Langacker, Phys. Rev. **D45** (1992) 1810.

PRAMANA
journal of
physics

© Printed in India

Supplement to Vol. 45
October 1995
pp. 229-254

Higgs searches and WW scattering

R. J. N. PHILLIPS
Rutherford Appleton Laboratory, Chilton, Didcot,
Oxon, OX11 0QX, England.

1. Introduction

This lecture is about aspects of Electroweak Symmetry Breaking (EWSB). There are sections on Higgs searches in the Standard Model (SM), on WW, WZ and ZZ scattering as probes of EWSB, and on Higgs phenomenology in the Minimal Supersymmetric Standard Model (MSSM).

The SM has one complex SU(2)-doublet of scalar fields,

$$\Phi = \begin{pmatrix} \phi^+ \\ \phi^0 \end{pmatrix} = \begin{pmatrix} -iw^+ \\ (-iz + H + v)/\sqrt{2} \end{pmatrix},$$

with vacuum expectation value v arising from the self-interaction

$$V(\Phi) = \lambda[|\Phi|^2 - v^2/2]^2.$$

In the resulting EWSB pattern, where W and Z fields acquire masses, the scalar field components $w^\pm$ and z become the new longitudinal components $W_L^\pm$ and Z_L while H survives as a real SU(2)-singlet scalar field - the Higgs boson - with mass $m_H = \sqrt{2\lambda}v$. To recover standard Fermi couplings we must have $v = (\sqrt{2}G_F)^{-1/2}$, but the quartic coupling λ is not determined *a priori*.

How can we probe the EWSB dynamics?
(i) Look for H^0 ; its mass measures λ; its couplings to W,Z and fermions are prescribed by v and the particle masses, and should be checked.
(ii) Study $W_L^\pm$ and Z_L scattering; they remember their origins as would-be Goldstone bosons $w^\pm$ and z, and their scattering via $V(\Phi)$ will be strong if λ is large.
These strategies, motivated here by the SM case, extend naturally to more general scenarios. We shall mostly illustrate the possibilities for the proposed Large Hadron Collider LHC at CERN, but for convenience shall also take some examples from studies for the comparable but cancelled SSC project.

2. SM HIggs searches at hadron colliders

Higgs hadroproduction goes mainly through the diagrams in Fig.1 [1]:
(a) $gg \to H$ via heavy quark loops usually gives the biggest rate;
(b) $qq(\bar{q}) \to H$ via WW (or ZZ) fusion is also big, and has taggable jets;

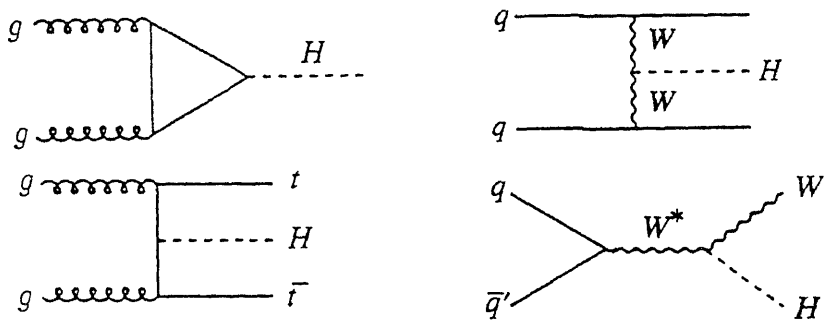

Figure 1. SM higgs hadroproduction subprocesses

tag the leptons from $W \to \ell\nu$ and $t \to bW \to b\ell\nu$.
Fig.2 shows the corresponding lowest-order LHC cross sections, for $m_t = 140$ GeV, and Fig.3 gives the principal decay branching fractions.

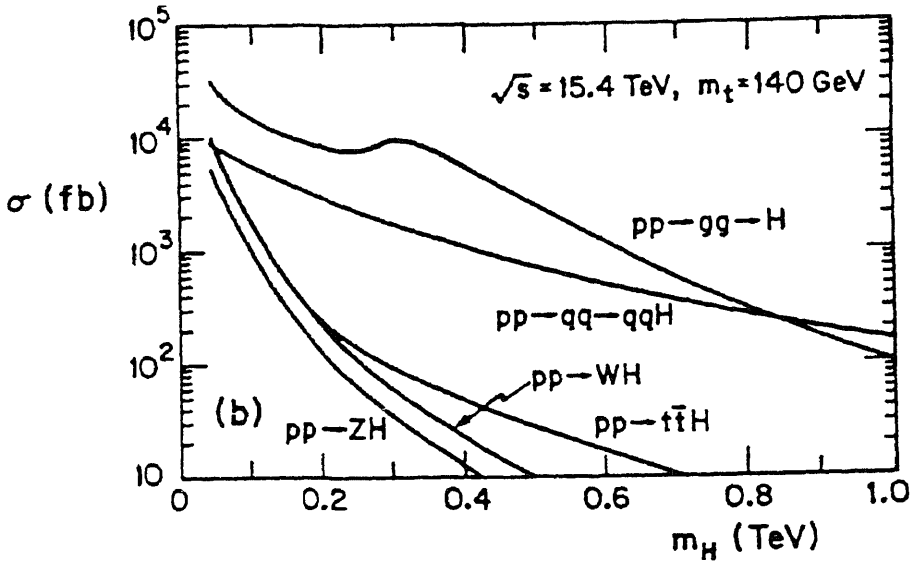

Figure 2. SM expectation for Higgs hadroproduction

2.1 Intermediate mass range.

Light Higgses ($m_H \lesssim M_Z$) should be detectable at LEP1 or LEP2, but the intermediate mass range $M_Z \lesssim m_H \lesssim 2M_Z$ needs higher energy. The dominant $H \to b\bar{b}$ mode was widely believed to be undetectable at hadron colliders, because of enormous $b\bar{b}$ backgrounds from QCD; the $\tau\bar{\tau}$ mode too is interesting but problematical. Until recently, most attention was therefore focussed on the more promising signals

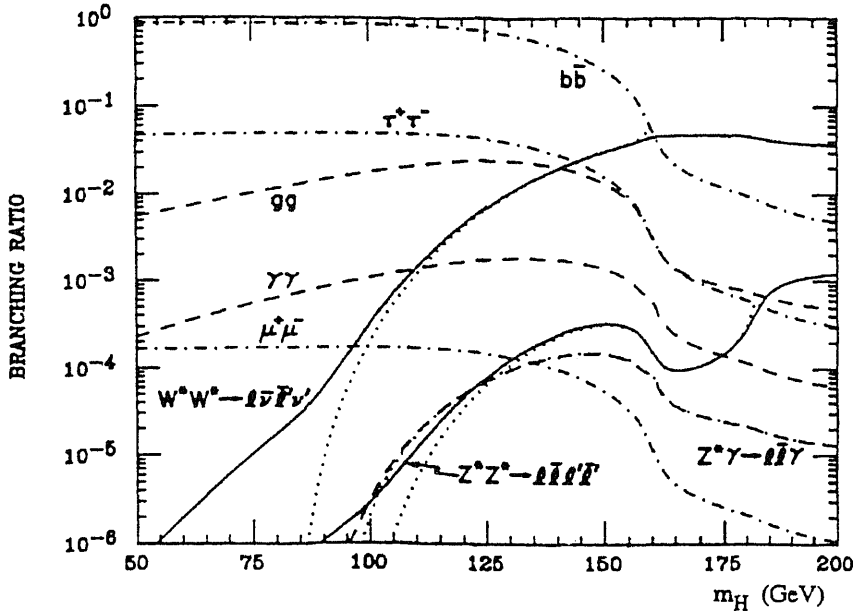

Figure 3. SM Higgs branching fractions

Inclusive $H \to \gamma\gamma$ signals are difficult to see above large backgrounds from $gg, q\bar{q} \to \gamma\gamma$ production and also from $jet + jet$ and $jet + \gamma$ states where $jet \to \pi^0$ fakes γ. To extract a signal requires excellent mass resolution $\delta M_{\gamma\gamma} < 1.5$ GeV and rejection factor $R(jet \to fake\,\gamma) < 10^{-4}$ (see GEM studies for SSC[2]). Fig.4 shows typical predicted $M_{\gamma\gamma}$ distributions, before and after background subtraction. Note the very low signal/background ratios here, requiring very high statistics.

Lepton-tagged $H \to \gamma\gamma$ signals, based on the $t\bar{t}H$ and WH production channels, are smaller but much cleaner since the lepton requirement strongly suppresses backgrounds, so less stringent mass resolution $\delta M_{\gamma\gamma} < 3$ GeV and rejection factor $R(jet \to fake\,\gamma) < 5 \times 10^{-4}$ may suffice (see SDC studies for SSC[3]). Fig.5 shows typical $M_{\gamma\gamma}$ signal and background distributions.

Four-lepton signals, based on $H \to ZZ^*$ decays with one Z off-shell, are also very clean and have a big enough branching fraction for $m_H > 120$ GeV - see Fig.3; the dip near $m_H = 2M_W = 160$ GeV is due to competition from the $H \to W^+W^-$ channel that opens here. After suitable p_T and isolation cuts on the leptons, the backgrounds from continuum ZZ^*, $Zb\bar{b}$, $Zt\bar{t}$ and $t\bar{t}$ production are small; Fig.6 shows typical signal and background curves for an SSC example[3].

Very recently it has been argued that $H \to b\bar{b}$ dijet signals may be detectable after all, with the backgrounds sufficiently suppressed by suitable tagging.
(a) Tag two leptonic W-decays in the $gg \to t\bar{t}H \to (bW^+)(\bar{b}W^-)(b\bar{b})$ channel; this gives a 2-lepton + 4-jet + missing-E_T signature, with a peak at m_H in the dijet invariant mass $m(jj)$ distribution[4]. There is a combinatorial background (from 'wrong' dijet pairings) and a much bigger background from $t\bar{t}jj$ production; a narrow peak from $t\bar{t}Z$ production also has to be calculated and subtracted; but the

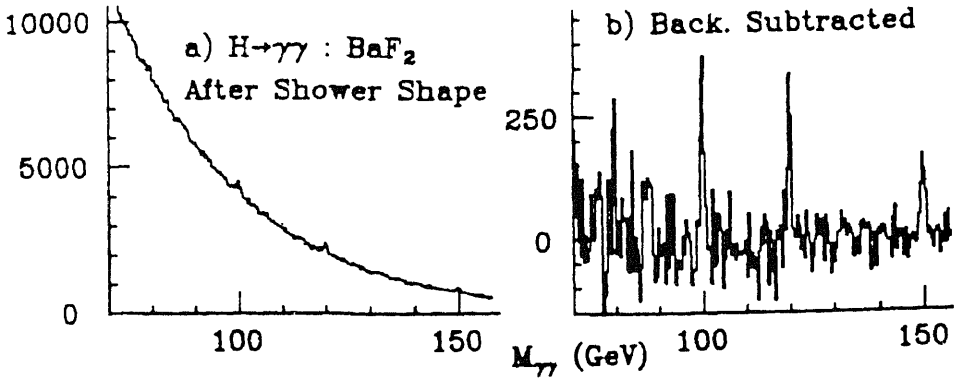

Figure 4. $H \rightarrow \gamma\gamma$ signals for $m_H = 80, 100, 120, 150$ GeV [2]. Plotted on y-axis: Events/0.4 GeV/SSC-year.

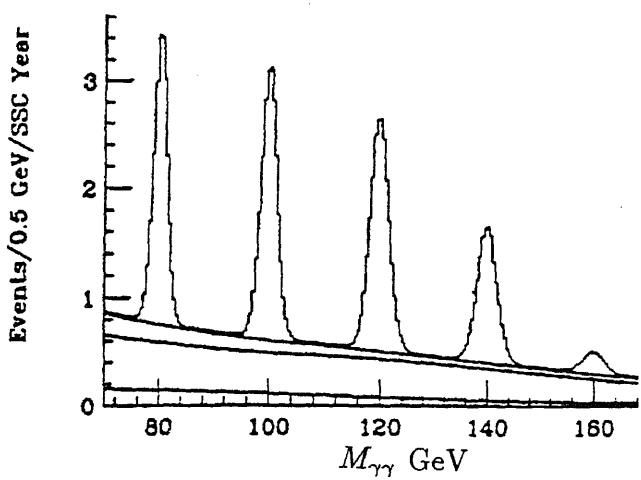

Figure 5. Lepton-tagged $H \rightarrow \gamma\gamma$ signals for $m_H = 80, 100, ...160$ GeV [3]

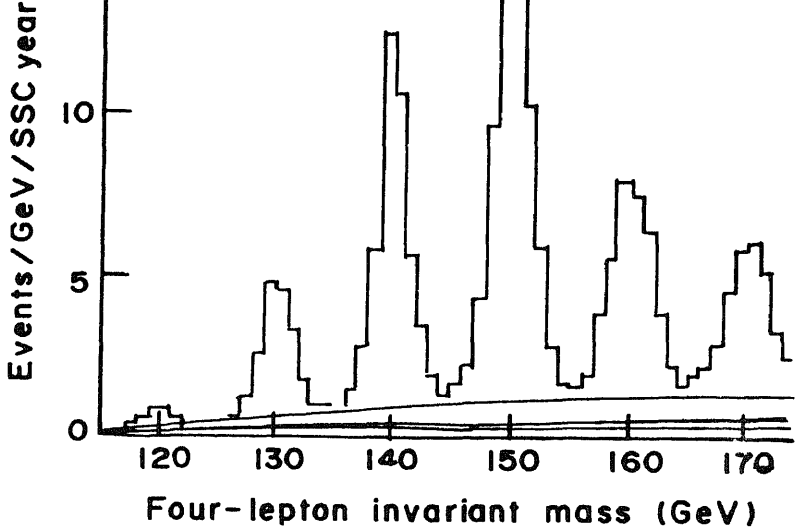

Figure 6. $H \to l\bar{l}l'\bar{l}'$ signals for $m_H = 120, 130, ...170$ GeV [3]

SSC illustration in Fig.7 suggests this approach could possibly work.

(b) Tag 3 or 4 b-jets in the $gg \to t\bar{t}H \to (bW^+)(\bar{b}W^-)(b\bar{b})$ channel, using a microvertex detector to pick out the displaced vertices from b-decays, and look for a peak in the $2b$ invariant mass spectrum[5]. With sufficiently high b-tag efficiency and purity, all background channels except $t\bar{t}Z$ (with $Z \to b\bar{b}$) and $t\bar{t}b\bar{b}$ are suppressed. Fig.8 shows an SSC illustration with 3-b-tagging; the upper curves assume tagging efficiencies $\epsilon_b = 0.4$ and $\epsilon_g = 0.005$ for b-jets and gluon-jets, respectively; the lower curves (displaced by 100 units) assume values 0.3 and 0.01 instead. Note once more the low signal/background ratios, requiring high statistics in this game ! For LHC, taking $m_H = 100$ GeV and $m_t = 140$ GeV and the less optimistic tagging efficiencies, we need integrated luminosity $L = 200\ fb^{-1}$ to get a signal $S = 600$ events over a background $B = 14000$ events with statistical significance $S/\sqrt{B} = 5$ standard deviations. But the situation improves if t is heavier; with $m_t = 180$ GeV, $L = 60\ fb^{-1}$ is enough to give $S = 210$, $B = 1800$, and $S/\sqrt{B} = 5$ again[5]. (c) Rapidity-gap tagging may also work[6]. The $qq \to qqH$ mechanism has no colour exchange and is therefore unlikely to radiate additional soft gluons or $q\bar{q}$ pairs in the central region, unlike the other H production processes or typical background channels. By requiring that there is no particle production (apart from an $H \to b\bar{b}$ dijet candidate) in a wide central interval of rapidity, it may be possible to suppress backgrounds enough to extract a $qq \to qqH, H \to b\bar{b}$ dijet signal. But such rapidity gaps can get filled in by soft interactions of spectator partons ('the underlying event'), or faked by statistical fluctuations. Detailed studies are needed[6]; the intermediate- mass Higgs case has received little attention so far[7].

We see that one or other of the popular $\gamma\gamma$ and 4-lepton signals should be

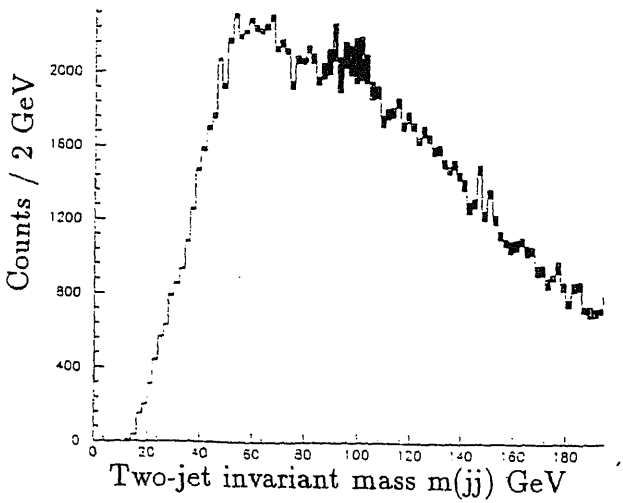

Figure 7. Double-lepton tagged $H \to b\bar{b}$ dijet signal and background for $m_H = 100$ GeV [4]. $t\bar{t}H$ and $t\bar{t}Z$ contributions are shaded.

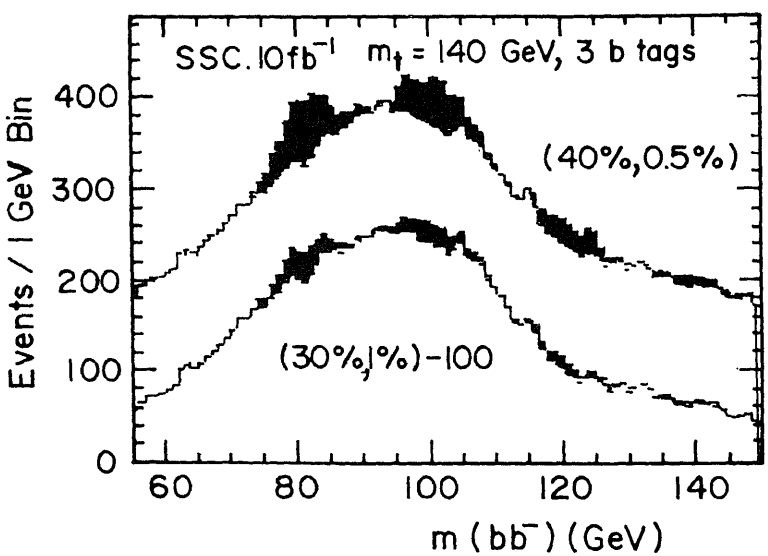

Figure 8. $H \to b\bar{b}$ dijet signals and background with $3 - b$–jet tagging for m_H = 80, 100, 120, 140 GeV [5]

For heavy Higgses ($m_H > 2M_Z$), the decay chain $H \to ZZ \to 4\ell$ offers a very clean 'gold-plated' signal with a nice peak in the invariant mass $m(\ell\ell\ell\ell)$ and relatively little background, mostly from continuum ZZ production. Fig.9 shows cross sections for this signal versus m_H; note that they are an order of magnitude smaller at LHC than at the late lamented SSC, requiring that much more luminosity. Fig.10 shows the mass peaks for $m_H = 600$ and 800 GeV at LHC after suitable cuts[8]. We see that the mass peak broadens and becomes harder to detect as m_H increases; in fact

$$\Gamma_H \simeq (0.5TeV)(m_H/1\,TeV)^3.$$

Thus the range $m_H < 0.6$ TeV is relatively easy; $m_H > 0.8$ TeV is hard.

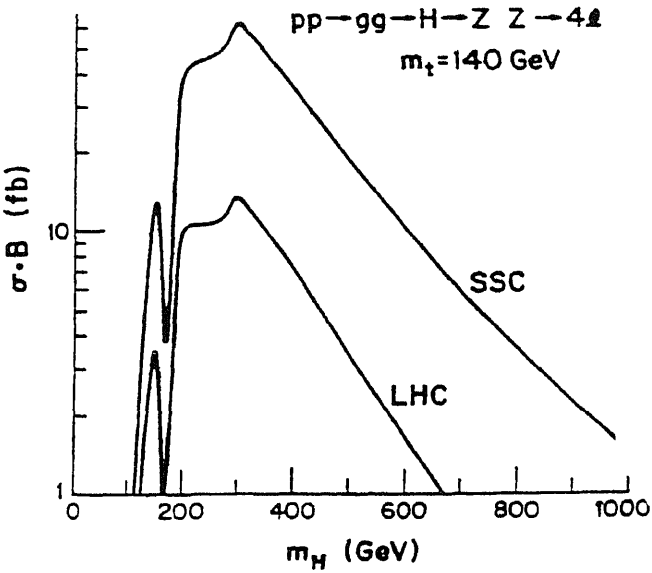

Figure 9. Cross sections for the $H \to l\bar{l}l'\bar{l}'$ gold-plated signals at SSC and LHC

An alternative 'silver-plated' $H \to ZZ \to (\ell^+\ell^-)(\nu\bar{\nu})$ signal is also promising. It has a somewhat less clean signature, namely one leptonic Z plus missing-E_T, but has six times bigger branching fraction than the gold-plated signal - which could be helpful at large m_H . The main backgrounds from $Z + jets$, $t\bar{t}$ and ZZ continuum production can be suppressed by suitable cuts, especially by requiring large missing-E_T, since the $H \to ZZ$ decay gives a Jacobian peak near $p_T(Z) = \frac{1}{2}\sqrt{m_H^2 - 4M_Z^2}$ that translates into a peak in missing-E_T; see Fig.11. The mass m_H can be estimated from the missing-E_T distribution, but a cleaner estimate (from a narrower peak) can be made using the 'transverse mass' variable $m_T(\ell\ell, \nu\nu)$[9]

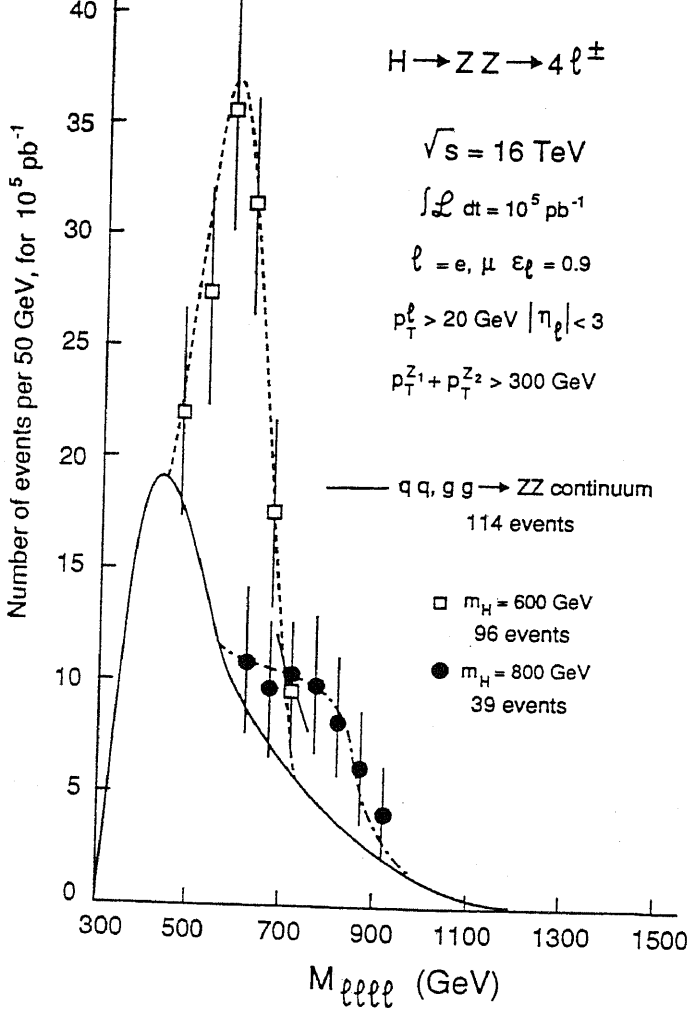

Figure 10. Gold-plated $H \rightarrow ZZ \rightarrow 4l$ mass peaks and background predicted at the CERN LHC for $m_H = 600, 800$ GeV [8]

$$m_T(\ell\ell,\nu\nu)^2 = [\sqrt{p_T(\ell\ell)^2 + M_Z^2} + \sqrt{p_T(\nu\nu)^2 + M_Z^2}]^2 - [\vec{p_T}(\ell\ell) + \vec{p_T}(\nu\nu)]^2$$

where $\vec{p_T}(\nu\nu) = \vec{E_T}$-missing. Both $p_T(\ell\ell)$ and $p_T(\nu\nu)$ have Jacobian peaks that are smeared by the transverse motion of H, but this smearing approximately cancels in the combination m_T.

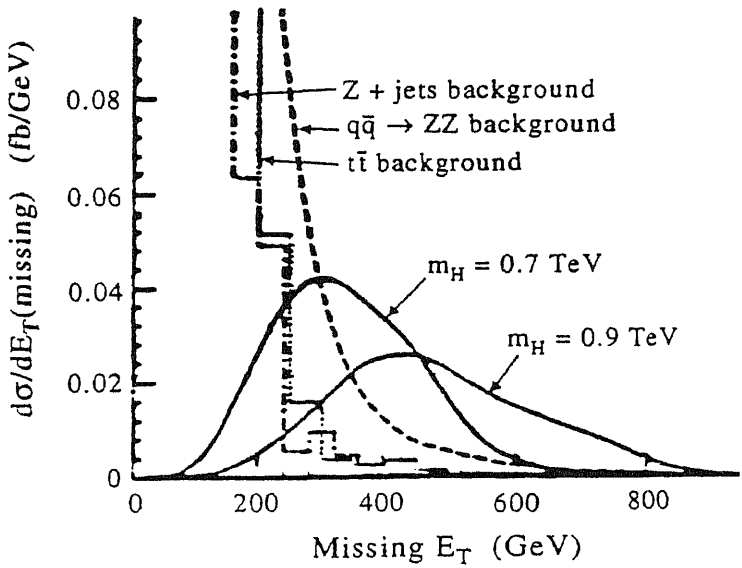

Figure 11. Silver-plated $H \to ZZ \to llll\nu\nu$ signals appearing as shoulders in the missing-E_T plot (an SSC example [3]).

The $H \to W^+W^- \to (\ell\nu)(\ell'\nu')$ signal has the biggest branching fraction of the all-leptonic modes; the signature is two isolated large-p_T leptons plus missing-E_T, but there is a horrendous background from $t\bar{t} \to bW^+\bar{b}W^-$. A strategy of jet-tagging and anti-tagging (vetoing) has been proposed to rescue this signal. Note first that the important $qq \to qqH$ production subprocess (see Figs.1 and 2) contains two jets with typically large pseudo-rapidity $|\eta| \sim 3-5$, but no central jets when $H \to \ell\nu\ell'\nu'$. In contrast, the QCD background process $gg, q\bar{q} \to t\bar{t} \to bW^+\bar{b}W^-$ contains typically no forward jets but has two central b-jets. Hence, by requiring at least one forward jet with $3 < |\eta| < 5$ and no central jet with $|\eta| < 3$, the background can be suppressed relative to the signal. [Jet tagging/vetoing can help to reduce backgrounds to the previous $H \to ZZ$ signals also]. It has been shown that the $H \to WW$ signal can be separated by these and other suitable cuts, at least for $0.6 \lesssim m_H \lesssim 1$ TeV[10]. The mass m_H can then be estimated from the dilepton invariant mass $m(\ell\ell')$ or another transverse mass $m(\ell\ell',\nu\nu')$ defined by[11]

$$m_T(\ell\ell',\nu\nu')^2 = [\sqrt{p_T(\ell\ell')^2 + m(\ell\ell')^2} + p_T(\nu\nu')]^2 - [\vec{p_T}(\ell\ell') + \vec{p_T}(\nu\nu')]^2$$

because we no longer have the constraints $m(\ell\ell) = m(\nu\nu) = M_Z$ and indeed $m(\nu\nu')$ cannot be measured. These variables peak at $m(\ell\ell') \simeq \frac{1}{2}m_H$ and $m_T(\ell\ell', \nu\nu') \simeq \frac{3}{4}m_H$, respectively.

Combining the coverage of $H \to ZZ \to 4\ell$, $H \to ZZ \to 2\ell 2\nu$ and $H \to WW \to 2\ell 2\nu$ signals, we see that heavy Higgses will be detectable for $m_H \lesssim 1$ TeV.

2.3. Studying higgs couplings separately.

In principle, the strengths of H couplings to WW, ZZ, tt, $b\bar{b}$ can be separated in various ways; examples follow. Note that the signal rate in each particular channel has the general form

$$\sigma(pp \to H \to channel) = \sigma(pp \to H) \times \Gamma(H \to channel)/\Gamma_H$$

(a) The dominant untagged or lepton-tagged $\gamma\gamma$ signals depend directly on the $Ht\bar{t}$ coupling, both at the H production vertex (t-quark loop or associated production with $t\bar{t}$) and at the H decay (via t-quark loop), but the total decay width in the denominator is dominated by $Hb\bar{b}$ at the relevant low-intermediate masses. Thus the rate determines $(Ht\bar{t})^4/(Hb\bar{b})^2$ approximately.
(b) If the WH and $t\bar{t}H$ lepton-tagged $\gamma\gamma$ signals can be separated via final-state criteria, their ratio will determine

$$(WH \to \gamma\gamma\ rate)/(t\bar{t}H \to \gamma\gamma\ rate) \sim (HWW)^2/(Ht\bar{t})^2$$

(c) The $t\bar{t}H \to t\bar{t}(b\bar{b})$ tagged dijet signals depend on the $Ht\bar{t}$ coupling for H production, with branching fraction $B(H \to b\bar{b}) \sim 1$ for decay. Thus the signal rate determines $(Ht\bar{t})^2$ approximately, and the ratio to $\gamma\gamma$ rates determines

$$(tagged\ bb\ dijet\ rate)/(\gamma\gamma\ rate) \sim (Hb\bar{b})^2/(Ht\bar{t})^2.$$

(d) For high-intermediate masses $m_H > 120$ GeV, the total width Γ_H depends non-trivially on $Hb\bar{b}$, HWW and HZZ couplings, so nothing simple can be said about the $H \to 4\ell$ signals here.
(e) For heavy Higgses, the ratio of WW/ZZ signals could determine the ratio of $(HWW)/(HZZ)$ couplings.
(f) The ratio of jet-tagged/untagged heavy Higgs signals could determine the ratio of $qq \to qqH$ and $gg \to H$ production mechanisms, that depends directly on the $(HVV)/(Ht\bar{t})$ coupling ratio, where $V = W, Z$ but W dominates.
(g) Γ_H for a heavy Higgs, directly measurable from the width of the mass peak, should be dominated by the HWW coupling with smaller contributions from HZZ and $Ht\bar{t}$.

3. WW, WZ and ZZ scattering

In the SM, the coupling strength of the scalar potential is

$$\lambda = \frac{m_H^2}{2v^2} = [\frac{m_H}{348GeV}]^2$$

which is large if H is heavy, implying strong scattering of the Goldstone bosons $w^{\pm}$ and z that become $W_L^{\pm}$ and Z_L. This can also happen more generally, outside the SM. Figure 12 shows a generic W_L, Z_L scattering process at LHC. Different final states are sensitive to different physics: $W_L^+W_L^-$ and Z_LZ_L states probe Higgs-like resonances; $W_L^+W_L^+$ and $W_L^-W_L^-$ states probe non-resonant scattering (except in some exotic models); W_LZ_L states probe techni-ρ-type resonances.

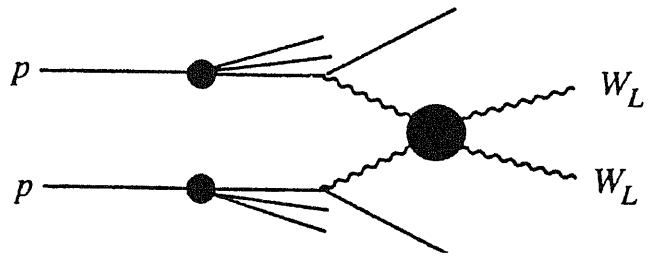

Figure 12. Longitudinal weak boson scattering at a pp collider

The idea is that enhanced WW, WZ, ZZ production may be attributed to strong W_L and Z_L scattering, since the transversely polarized states W_T and Z_T only have the weak $SU(2) \times U(1)$ gauge interactions. Details of the enhancement will shed light on EWSB. To discuss this scattering, we must first introduce a number of ideas, approximations and constraints.

3.1 The effective W approximation (EWA).

In analogy with the Weizsacker-Williams approximation for photons, the incident quark beams can be replaced by beams of approximately on-shell W and Z bosons. Writing $P^{\alpha}_{W/q}(x)$ as the known probability distribution (splitting function) for finding a W with polarization α and momentum fraction x in quark q, the subprocess cross section for $q_1q_2 \to q_3q_4W_3^{\gamma}W_4^{\delta}$ is

$$\sigma(q_1q_2 \to q_3q_4W_3^{\gamma}W_4^{\delta}) = \sum_{\alpha,\beta} \int dx_1dx_2 P^{\alpha}_{W1/q1}(x_1)P^{\beta}_{W2/q2}(x_2)\sigma(W_1^{\alpha}W_2^{\beta} \to W_3^{\gamma}W_4^{\delta})$$

The physical cross section for $pp \to q_3q_4W_3W_4X$ is found by further integrating over incident quark distributions and summing over final W spins. The splitting functions for W_L and Z_L are

$$P^L_{W+/u} = P^L_{W-/d} = P^L_{W+/\bar{d}} = P^L_{W-/\bar{u}} = \frac{g^2}{16\pi^2}\frac{(1-x)}{x},$$

$$P^L_{Z/q} = P^L_{Z/\bar{q}} = \frac{g^2}{32\pi^2}\frac{1-4x_W|Q|+8x_W^2Q^2}{1-x_W}\frac{(1-x)}{x},$$

where $x_W = \sin^2\theta_W = 0.23$, Q is the electric charge of quark q and $g^2 = 8M_W^2G_F/\sqrt{2}$ is the SU(2) gauge coupling squared. The EWA is the only known way to separate the contributions of W_L and Z_L scattering in a high energy process. The approxi-

3.2 The Goldstone boson equivalence theorem (GBET).

This theorem[12] relates any scattering amplitude for real W_L and Z_L to the amplitude for the corresponding Goldstone bosons w and z:

$$M[W_L(p_1), W_L(p_2), ...] = M[w(p_1), w(p_2), ...]_R + \mathcal{O}(M_W/E_W),$$

where R indicates a renormalizable R_ξ gauge. The p_i are momenta (masses are neglected here). The EWA provides essentially real incoming W_L and Z_L; the GBET allows us to compute their scattering from any given model of the Goldstone boson sector, up to corrections of order M_W/E_W.

3.3 Isospin, crossing and unitarity.

The various ww, wz and zz scattering amplitudes are all related by SU(2) isospin and crossing symmetries, just like $\pi\pi$ scattering. In terms of components w_i ($i = 1, 2, 3$; $w^\pm = (w_1 \mp w_2)/\sqrt{2}$, $z = w_3$), the general amplitude has the form

$$M(w_a w_b \to w_c w_d) = A(s,t,u)\delta_{ab}\delta_{cd} + A(t,s,u)\delta_{ac}\delta_{bd} + A(u,t,s)\delta_{ad}\delta_{bc},$$

where $s = (p_a + p_b)^2$, $t = (p_a - p_c)^2$, $u = (p_a - p_d)^2$ and A is symmetrical in its last two arguments: $A(s,t,u) = A(s,u,t)$. In terms of this single basic amplitude A, the various channel amplitudes are

$$\begin{aligned}
M(w^+w^- \to w^+w^-) &= A(s,t,u) + A(t,s,u), \\
M(w^+w^- \to zz) &= A(s,t,u), \\
M(zz \to zz) &= A(s,t,u) + A(t,s,u) + A(u,t,s), \\
M(w^\pm z \to w^\pm z) &= A(t,s,u), \\
M(w^+w^+ \to w^+w^+) &= A(t,s,u) + A(u,t,s).
\end{aligned}$$

The amplitudes for s-channel isospin $T = 0, 1, 2$ are

$$\begin{aligned}
M(T=0) &= 3A(s,t,u) + A(t,s,u) + A(u,t,s), \\
M(T=1) &= A(t,s,u) - A(u,t,s), \\
M(T=2) &= A(t,s,u) + A(u,t,s).
\end{aligned}$$

These pure-isospin channels diagonalize the S-matrix, so their s-channel partial wave amplitudes a_L^T defined by

$$M(T) = 32\pi \sum_L (2L+1)\, a_L^T\, P_L(\cos\theta)$$

should satisfy the unitarity condition $|2a_L^T - i| \leq 1$, i.e. lie within a circle in the complex plane.

3.4 Low energy theorem (LET).

In the low-energy limit, Goldstone boson scattering is expected to be controlled by the dynamics of EWSB. Since EWSB in the SM is essentially the non-linear sigma model with chiral $SU(2) \times SU(2)$ symmetry, it has been pointed out[13] that the low-energy theorems of $\pi\pi$ scattering[14] can be directly applied to the case of w and z scattering, simply replacing the pion decay constant $F_\pi = 94$ MeV by the

$$A(s,t,u) \simeq s/v^2.$$

Hence the low-energy partial wave amplitudes are

$$a_0^0 = \frac{s}{16\pi v^2},\ a_1^1 = \frac{s}{96\pi v^2},\ a_0^2 = -\frac{s}{32\pi v^2}.$$

This linear rise with s cannot be extrapolated indefinitely without violating unitarity. Strictly speaking, since these formulae give purely real a_L^T, any non-zero value lies outside the unitarity circle, but this could at first be cured by adding a small imaginary part. However, the real part of a_0^0 exceeds its unitarity limit $\Re a_L^T \leq \frac{1}{2}$ when $\sqrt{s} > \sqrt{8\pi}v = 1.2$ TeV, while the T=2 amplitude exceeds this limit for $\sqrt{s} > 1.7$ TeV. We see that unitarity is likely to be an important constraint in the TeV range.

3.5 Models for Goldstone boson scattering.

A wide variety of models have been proposed, to illustrate and parameterize the scattering of $w^{\pm}$ and z. We confine ourselves here to the models evaluated in a recent survey by Bagger et al[15] of possible strong WW, WZ, ZZ scattering at hadron colliders.

(i) Standard Model.

This gives the form

$$A(s,t,u) = \frac{-m_H^2}{v^2}(1 + \frac{m_H^2}{s - m_H^2 + im_H\Gamma_H\theta(s)}),$$

where m_H is the Higgs mass, $v = 246$ GeV is the usual vev, and a Breit-Wigner form has been imposed for the Higgs resonance. θ is the step-function: $\theta(s) = 1(0)$ for $s > 0 (s \leq 0)$. $A(t,s,u)$ and $A(u,t,s)$ are obtained by permuting s,t,u. For illustration we shall take $m_H = 1$ TeV[15].

(ii) O(2N) Model [16].

Motivated by the isomorphism between $SU(2)_L \times SU(2)_R$ and $O(4)$ symmetries, and using a large-N approximation, this model gives

$$A(s,t,u) = \frac{16\pi^2 s}{16\pi^2 v^2 - sN[2 + \ln(\Lambda^2/|s|) + i\pi\theta(s)]},$$

where $\theta(s)$ is the step-function as before. Following Ref.[15], we take the case $N = 2$ with physical cut-off $\Lambda = 3$ TeV.

(iii) Chirally-Coupled Scalar Model[15].

This model describes the low-energy behaviour of a technicolor-type model with a techni-sigma scalar resonance, through the amplitude

$$A(s,t,u) = \frac{s}{v^2} - (\frac{g^2 s^2}{v^2})\frac{1}{s - M_S^2 + iM_S\Gamma_S\theta(s)},$$

where M_S and Γ_S are the scalar resonance mass and its decay width into Goldstone fields, $\Gamma_S = 3g^2 M_S^3/(32\pi v^2)$. We choose $M_S = 1.0$ TeV and $\Gamma_S = 0.35$ TeV, following Ref.[15].

This model describes the low-energy behaviour of a technicolor-type model with a techni-rho vector resonance, through the amplitude

$$A(s,t,u) = \frac{s}{4v^2}(4-3a) + \frac{aM_V^2}{4v^2}[\frac{u-s}{t-M_V^2+iM_V\Gamma_V\theta(t)} + \frac{t-s}{u-M_V^2+iM_V\Gamma_V\theta(u)}],$$

where M_V and Γ_V are the vector resonance mass and width while $a = 192\pi v^2\Gamma_V/M_V^3$. We choose the two cases $M_V = 2.0$ TeV with $\Gamma_V = 0.7$ TeV and $M_V = 2.5$ TeV with $\Gamma_V = 1.3$ TeV, following Ref.[15].

(v) LET-CG Model[13]

This model simply extrapolates the low-energy amplitudes, prescribed by low-energy theorems (LET) in terms of the vev v:

$$A(s,t,u) = s/v^2.$$

These amplitudes eventually violate unitarity, as we saw above, so the partial wave amplitudes are held constant after they reach the bound $|a_L^T| \leq 1$ (less stringent than the bound $\Re a_L^T \leq \frac{1}{2}$ we mentioned earlier).

(vi) LET-K Model[18].

Here the LET amplitudes above are unitarized instead by the K-matrix prescription,

$$a_L^T \to a_L^T/(1-ia_L^T),$$

that enforces the elastic unitarity condition $|2a_L^T - i| = 1$.

(vii) Delay-K Model[15].

This is an example of non-resonant models, based on an effective Lagrangian method[19]. To order p^4 in the momentum expansion, all model amplitudes have the form

$$A(s,t,u) = \frac{s}{v^2} + \frac{1}{4\pi^2v^4}(2L_1(\mu)s^2 + L_2(\mu)(t^2+u^2))$$
$$+\frac{1}{16\pi^2v^4}[-\frac{t}{6}(s+2t)\ln(\frac{-t}{\mu^2}) - \frac{u}{6}(s+2u)\ln(\frac{-u}{\mu^2}) - \frac{s^2}{2}\ln(\frac{-s}{\mu^2})],$$

where μ is the renormalization scale and $L_i(\mu)$ are renormalized coefficients in the effective Lagrangian. The parameters $L_1(\mu)$, $L_2(\mu)$ and μ essentially cover all possible non-resonant physics in this approximation. Following Ref.[15] we choose the example $L_1(\mu) = -0.26$, $L_2(\mu) = 0.23$ with $\mu = 1.5$ TeV, for which unitarity breakdown is delayed until $\sqrt{s} = 2$ TeV. These amplitudes are complex; for simplicity, unitarity is imposed by the K-matrix prescription based on the real part of a_L^I, i.e. $a_L^I \to \Re a_L^I/(1-i\Re a_L^I)$.

3.6 Model results

At a hadron collider we can only hope to recognize $W \to \ell\nu$ and $Z \to \ell\ell$ leptonic final states in the face of QCD multijet backgrounds. Even so, there remain backgrounds from electroweak W and Z production, from Drell-Yan lepton pairs and from the semileptonic decays of heavy quarks. Selection cuts to enhance signal/background include lepton isolation, high lepton p_T, central leptons with $|\eta(\ell)| \lesssim 2$, high invariant mass $m(\ell\ell')$ for WW and $m(ZZ)$ for ZZ ; in WW cases

it also helps to require the two leptons to be back-to-back in azimuth and have high relative momentum. Finally, it can be helpful to tag one of the spectator jets and/or veto central jets with $|\eta(j)| < 3$ (as in Section 2.2 for heavy Higgs searches). The following table shows results from Ref.[15] for the LHC, with typical realistic cuts. The signals here are the total production of $W_L W_L \to \ell\nu\ell\nu$ (etc); the background column (Bkgd) includes SM production of $W_T W_T$, $W_T W_L$ (etc) calculated using small m_H.

Table 1. Events for luminosity $100 fb^{-1}$, assuming $m_t = 140$ GeV, $\sqrt{s} = 16$ TeV.

Case	*Bkgd*	*SM*	*Scalar*	*O(2N)*
ZZ	0.1	3.9	2.7	1.8
W^+W^-	15	32	21	16
W^+Z	0.3	0.3	0.4	0.3
W^+W^+	1.7	3.7	5.2	4.3

Case	*Vec2.0*	*Vec2.5*	*LETCG*	*LETK*	*DelayK*
ZZ	0.4	0.6	1.1	0.9	0.6
W^+W^-	7.4	6.1	8.3	6.3	5.5
W^+Z	3.3	1.8	1.6	1.4	1.7
W^+W^+	4.8	7.3	16	14	8.3

We see that every model predicts a signal in at least one channel, although more luminosity would be desirable, and that the different channels are helpfully complementary. There seem to be good prospects for probing EWSB via weak boson scattering.

Fig.13 illustrates some of the more promising signals versus invariant mass $m(ZZ)$ for ZZ, $m(\ell\ell')$ for WW and a suitable $\ell\ell\ell\nu$ transverse mass variable m_T for WZ cases [15]. These illustrations are for the defunct SSC, but something similar should hold for LHC.

4. SUSY higgs possibilities at LEP and LHC

The Higgs sector is the shakiest part of the SM, where something extra may well be added. Let us consider the new degrees of freedom coming from some possible extensions[1].

(a) SM has one complex scalar doublet ϕ with vev $\sqrt{2} < \phi^0 > = v = 246$ GeV. Its 4 degrees of freedom show up as W_L^+, W_L^-, Z_L and H^0. There is just 1 free parameter m_H in the scalar sector.

(b) MSSM (minimal SUSY SM) has two scalar doublets with $\sqrt{2} < \phi_1^0 >= v \cos\beta$ and $\sqrt{2} < \phi_2^0 >= v \sin\beta$. Their 8 degrees of freedom show up as W_L^+, W_L^-, Z_L plus five spin-0 Higgs bosons h^0, H^0, A^0, H^+, H^-. h^0 and H^0 have $CP = +1$ (by convention $m_h < m_H$) and A has $CP = -1$. There are now 2 free parameters, often taken to be m_A and $\tan\beta = v_2/v_1$.

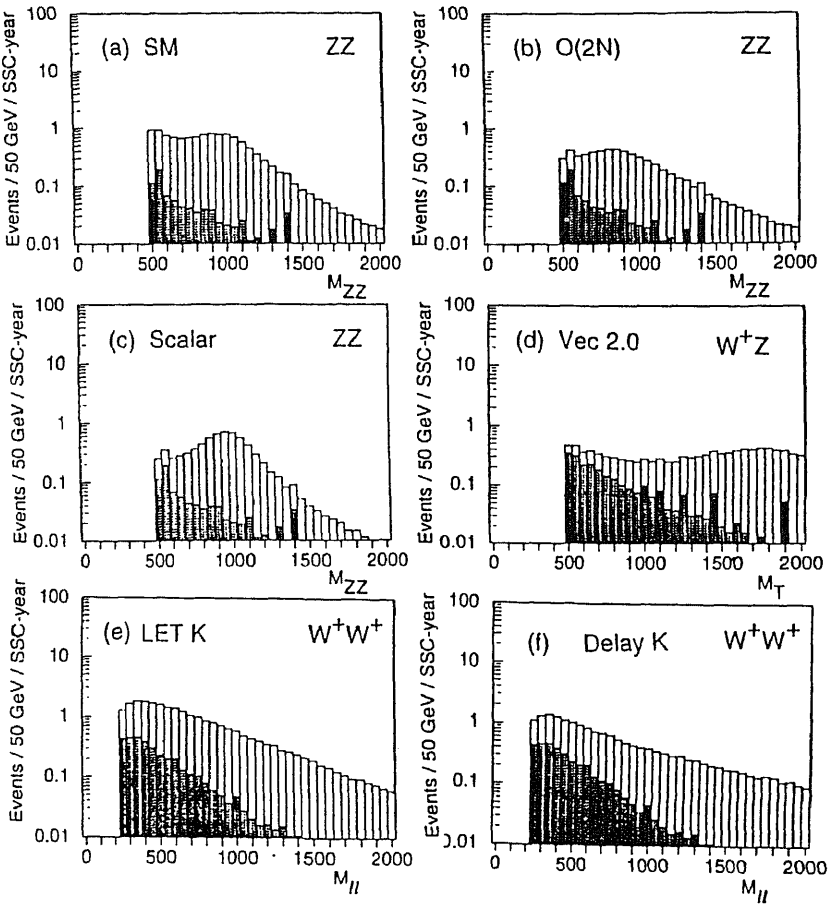

Figure 13. Typical weak boson scattering signals (unshaded) and backgrounds (shaded) [15]. Plotted on y-axis: Events/50 GeV/SSC-year.

n with vev $< n > = x$ non-zero but free. The 10 degrees of freedom show up as W_L^+, W_L^-, Z_L plus seven spin-0 Higgs bosons h^0, H_1^0, H_2^0, A_1^0, A_2^0, H^+ , H^- (where A_1 and A_2 have $CP = -1$). The number of free parameters now jumps to 6, however, because there are suddenly many more possible terms in the general scalar potential. This model has a richer spectrum and also looser limits.
For today we shall concentrate on the more constrained example of MSSM.

4.1 MSSM at tree level.

All MSSM Higgs masses and couplings, plus a mixing angle α that relates h and H to $\Re\phi_1$ and $\Re\phi_2$, are determined at tree level by m_A and $\tan\beta$:

$$\begin{aligned} \tan 2\alpha &= \tan 2\beta\,(m_A^2 + M_Z^2)/(m_A^2 - M_Z^2) \\ m_h^2, m_H^2 &= \frac{1}{2}[m_A^2 + M_Z^2 \mp \sqrt{(m_A^2 + M_Z^2)^2 - 4m_A^2 M_Z^2 \cos^2 2\beta}] \\ m_{H\pm}^2 &= m_A^2 + M_W^2 \end{aligned}$$

with $-\frac{\pi}{2} \leq \alpha \leq 0$. Hence at tree level

$$m_h \leq M_Z, m_A \; ; \; m_H \geq M_Z \; ; \; m_{H\pm} \geq M_W, m_A.$$

Thus there is always at least one Higgs boson h lighter than Z. However, in the limit $m_A \gg m_Z$, all the other bosons H, A and $H^\pm$ become very heavy and approximately degenerate while $m_h \simeq M_Z \cos 2\beta$, so it is conceivable that only this one light boson may be accessible.

4.2 MSSM with radiative corrections.

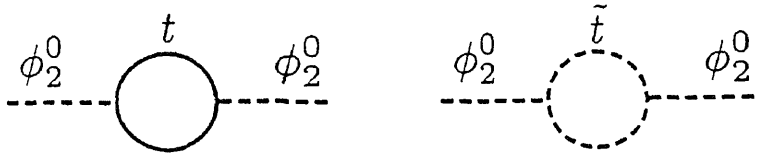

Figure 14. Typical t and $\tilde{t}$ one-loop graphs.

MSSM Higgs physics does not depend only on the scalar-sector parameters m_A and $\tan\beta$, but also has important loop corrections because the top quark is so heavy (Fig.14). These radiative corrections depend on m_t, $m_{\tilde{t}}$ (the mean t-squark mass), m_Q, m_U and m_D (soft SUSY-breaking squark masses), A_t and A_b (coefficients of trilinear $\tilde{t}_L\tilde{t}_R\phi_2$ and $\tilde{b}_L\tilde{b}_R\phi_1$ soft SUSY-breaking terms), and μ (coefficient of $\phi_1\phi_2$ mixing in the superpotential); see e.g. Ref.[20]. This dependence is mainly on m_t and (logarithmically) on $m_{\tilde{t}}$; neglecting the other parameters, the upper limit on m_h becomes

$$m_h^2 \leq M_Z^2 + \frac{3g^2 m_t^4}{4\pi^2 M_W^2} \ln(m_{\tilde{t}}/m_t),$$

in one-loop approximation.

In the following we shall estimate these radiative corrections by assuming that $m_t \simeq 150$ GeV, $m_{\tilde{t}} \simeq 1$ TeV, and that squark mixing is moderate (explicitly

$m_Q = m_U = m_D = 2A_t = 2A_b = 4\mu = 1$ TeV, following Ref.[21]). With this choice, the m_h upper limit is $m_h \lesssim 115$ GeV; the full dependence of m_h, m_H and $m_{H\pm}$ on the remaining parameters m_A and $\tan\beta$ is shown in Fig.15[21]. Searches for h at LEP1 (via $e^+e^- \to Zh, Ah$) have already covered the region $m_h \lesssim 50$ GeV, depending somewhat on $\tan\beta$; the higher energy $\sqrt{s} \sim 170 - 190$ GeV at LEP2 will arguably allow searches up to $m_h \sim 90$ GeV; but Fig.15 shows there is a large region of parameter space ($m_A \gtrsim 90$ GeV, $\tan\beta \gtrsim 2$) where h and all the heavier Higgses could be hiding undetected. This is LHC territory.

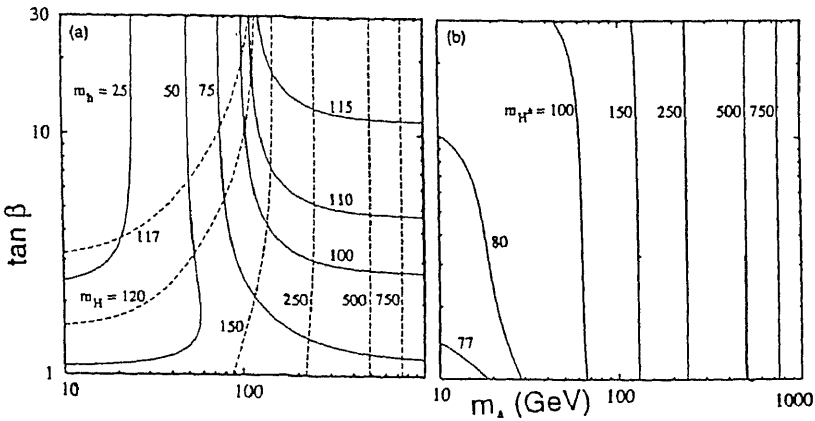

Figure 15. Behaviour of h, H and $H^\pm$ masses in the $(m_A, \tan\beta)$ plane including radiative corrections [21].

Compared to the SM Higgs coupling to fermions and gauge bosons, given by $L = -(m_i/v)\bar{f}_i f_i H + \frac{1}{2}g^2 vWWH + \frac{1}{4}(g^2 + g'^2)vZZH$, the MSSM neutral Higgs couplings have the following extra factors:

	h	H	A
$t\bar{t}$	$\cos\alpha/\sin\beta$	$\sin\alpha/\sin\beta$	$-i\gamma_5\cot\beta$
$b\bar{b}$, $\tau\bar{\tau}$	$-\sin\alpha/\cos\beta$	$\cos\alpha/\cos\beta$	$-i\gamma_5\tan\beta$
WW, ZZ	$\sin(\beta-\alpha)$	$\cos(\beta-\alpha)$	
ZA	$\cos(\beta-\alpha)$	$\sin(\beta-\alpha)$	

We see that h and H share their coupling strengths, that A does not couple directly to WW, ZZ or ZA, and that for large $\tan\beta$ (small $\cos\beta$) all the $b\bar{b}$ couplings are greatly enhanced. These coupling factors vary enormously as α varies across the

The charged scalars $H^{\pm}$ couple to typical fermions by

$$L = \frac{g}{2\sqrt{2}M_W} H^+ [m_t V_{tb} \cot\beta\, \bar{t}(1-\gamma_5)b + m_b V_{tb} \tan\beta\, \bar{t}(1+\gamma_5)b + m_c V_{cs} \cot\beta\, \bar{c}(1-\gamma_5)s + m_\tau \tan\beta\, \bar{\nu}(1+\gamma_5)\tau],$$

but have no tree-level coupling to WZ.

These new coupling factors and new kinds of coupling show that the production and decay of MSSM Higgses are not just trivial extensions of the SM situation, in general. There is however one particularly simple region, where m_A becomes large ($\gtrsim 300$ GeV); here A, H and $H^{\pm}$ become approximately degenerate, α approaches $\beta - \pi/2$, and all h couplings approach SM values. In this region, h fakes H_{SM} while the heavier Higgses are largely irrelevant; we essentially recover the SM but with the extra constraint $m_h \lesssim 130$ GeV (from MSSM with radiative corrections), whereas the SM alone has a much weaker bound $m_{HSM} \lesssim 600 - 1000$ GeV from triviality and perturbative-unitarity considerations.

4.3 Parameter constraints.

What are the constraints on the MSSM parameters $\tan\beta$ and m_A ?
(a) Requiring the charged-Higgs couplings to $t\bar{b}$ above to remain perturbative gives $m_t/500GeV \lesssim \tan\beta \lesssim 500GeV/m_b$ [22]; the precise limits are somewhat subjective. Essentially, values $\tan\beta << 1$ and $\tan\beta >> 30$ are disfavoured.
(b) Proton decay sets limits in SUSY-GUT models, typically $\tan\beta \lesssim 85$ [23].
(c) Since up-type (down-type) quarks get their masses via the vev v_2 (v_1), the empirical mass hierarchy $m_c >> m_s$ and $m_t >> m_b$ suggests a corresponding hierarchy of vevs $v_2 >> v_1$, i.e. $\tan\beta >> 1$[24].
(d) SUSY-GUT models generally find solutions with $1 \lesssim \tan\beta \lesssim m_t/m_b$. For example, Ref.[25] obtains solutions with $2 < \tan\beta < 40$ while Ref.[26] finds solutions in the range $0.6 < \tan\beta < 60$.
(e) SUSY-GUT models where electroweak symmetry is broken radiatively (a Higgs mass-square goes negative during evolution downward from the GUT scale) require $\tan\beta > 1$ (see e.g. Ref.[25]).
The consensus on $\tan\beta$ is therefore

$$0 \lesssim \tan\beta \lesssim 60.$$

What now about the other parameter, m_A ?
(f) Higgs boson searches at LEP1 give $20\ GeV \lesssim m_A$ (assuming $\tan\beta > 1$).
(g) In SUSY-GUT models, $m_A \lesssim M_{SUSY} \lesssim 1 - 2$ TeV.
(h) Global electroweak analysis in the MSSM finds a preferred value for m_A below 100 GeV or so, but much larger values are not excluded [27].
The consensus on m_A is therefore

$$20\ GeV \lesssim m_A \lesssim 1 - 2\ TeV.$$

Various other indirect constraints should also be mentioned.
(i) LEP1 searches for $e^+e^- \to H^+H^-$ exclude a parameter region with $\tan\beta < 0$ [28].
(j) Virtual $H^{\pm}$ can contribute to $B \to \tau\nu X$, but essentially not to $B \to e\nu X$, $\mu\nu X$,

limit on this contribution and hence a bound $\tan\beta < 0.54(m_H/1\,GeV)$ [29]. This is not very stringent, because the virtual $H^{\pm}$ and standard $W^{\pm}$ contributions add incoherently, i.e. a 10% amplitude gives only a 1% correction.

(k) Virtual $H^- t$ loop contributions to $b \to s\gamma$ decays apparently offer a much more stringent constraint; they add coherently to the SM $W^- t$ loop amplitudes. Neglecting possible additional SUSY loops, the present CLEO upper bound on $B(B \to \gamma X) \simeq B(b \to s\gamma)$ gives rather strong lower bounds on the charged-Higgs mass and hence on regions of the $(m_A, \tan\beta)$ plane [30]. However, in the present MSSM context we cannot ignore SUSY loops, especially chargino-stop loops, that can interfere strongly and destructively with the SM amplitude[31]. To apply this constraint we need more information about the sparticle spectrum, e.g. a complete SUSY-GUT model with all masses and mixings prescribed.

4.4 MSSM Higgs production and decay at LHC.

Production and decay of neutral Higgses can proceed by the SM processes, modulo the additional factors discussed above. However, there are new non-SM decay modes like $h \to AA$, $H \to AZ$, $H \to hh$, that tend to dominate when kinematically allowed, blotting out the familiar SM signals in various regions of parameter space; see Fig.16. Note that $H \to hh$ is allowed almost everywhere (except in the shaded region and along a dashed line where the Hhh coupling vanishes), making H usually hard to detect at LHC.

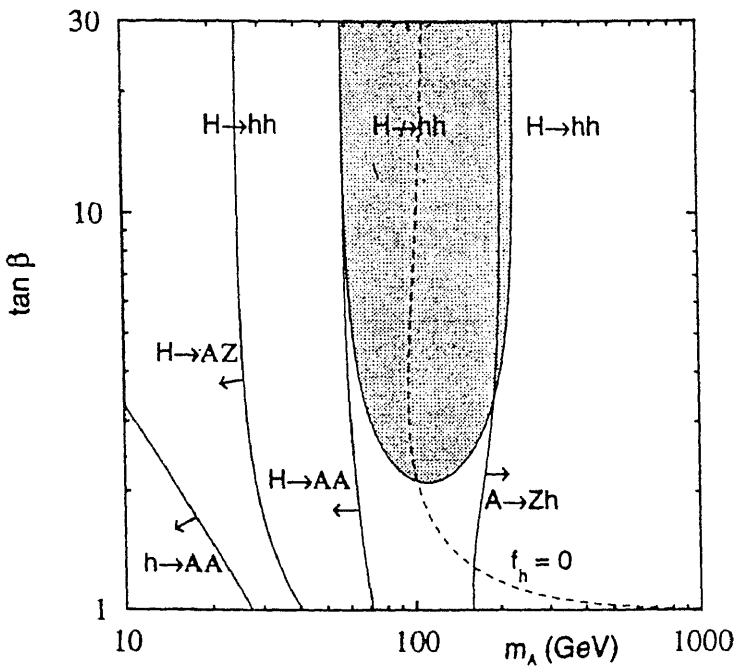

Figure 16. Regions wherenon-SM neutral Higgs decays compete [21].

$m_{H^\pm} > m_t$ there can still be signals from $gg \to t\bar{b}H^-$ production with $H^- \to \bar{b}t$ decay, leading to a $bb\bar{b}\bar{b}W^+W^-$ final state; multiple b-tagging is essential here[33].

There are regions of SUSY parameter space where SUSY decay modes like $h \to \chi_1^0\chi_1^0$ to lightest neutralino pairs are allowed; this is potentially dangerous since χ_1^0 is usually the lightest sparticle (LSP), stable, weakly interacting and essentially invisible. However, after LEP1 constraints there remains only a very small parameter range where this decay dominates; unless we are very unlucky, this may dilute the standard signals a bit but will not wash them out. Other decays like $A \to \chi_2^0\chi_2^0 \to (\ell^+\ell^-\chi_1^0)(\ell^+\ell^-\chi_1^0)$ might provide interesting new signals[34].

4.5 Expected MSSM Higgs signals.

For neutral Higgses, the strategy has been first to think about SM-like signals in conventional $\gamma\gamma$ and 4-lepton channels, and also in $b\bar{b}$ and $\tau\bar{\tau}$ channels; h, H and A can all in principle give such signals. For charged Higgses, the emphasis has been mostly on $t \to bH^+ \to b\tau\nu$ signals.

Four groups have made extensive calculations for LHC and SSC, covering the range $m_A > 20$ GeV and $0 < \tan\beta < 50$ [21, 35, 36, 37]. All get broadly similar results, including radiative corrections but mostly ignoring possible SUSY decay modes, and estimate in what regions of parameter space the various MSSM Higgs signals would be detectable. Typical results from Ref.[21] for $m_t = 150$ GeV are shown in Fig.17. Notice that H and A have only small detectability regions for these standard signals, and even the h regions are restricted, although the MSSM $\to$ SM limiting region ($m_A \to$ large) is covered as we would expect. In fact, the conventional $h, H, A \to \gamma\gamma$, ZZ^*, ZZ and $t \to H^+b$ searches do not cover the whole $(m_A, \tan\beta)$ parameter plane. Even when we include LEP1 and LEP2 search potential, there is an intermediate region, approximately $110 < m_A < 160$ GeV and $\tan\beta > 3$ (depending on your choice of m_t and authors), where none of the usual signals would be detectable.

There have been various responses to this inaccessible area (IA).

(a) Additional signals from $H \to \tau\tau$ and $A \to \tau\tau$ could possibly cover the large-$\tan\beta$ part of the IA[37], but identifying and measuring tau pairs is very difficult.

(b) Additional signals from $A \to Zh \to \ell\ell\tau\tau$ would not reduce the IA; neither would new $A \to \chi_2^0\chi_2^0 \to \ell\ell\ell\ell$+missing-$p_T$ signals[34].

(c) SUSY-GUT models have attractive solutions where the top Yukawa coupling λ_t approaches a fixed point (see e.g. Ref.[26]) and gives a constraint $m_t \simeq (200\ GeV)$ $\sin\beta$. With $m_t \simeq 150 - 170$ GeV, this defines a small-$\tan\beta$ region outside the IA, and incidentally predicts that h is light enough to be discovered at LEP2 [38]. However, even in this optimistic scenario, not all 5 Higgses can be simultaneously detectable.

(d) With efficient multiple-b-tagging, the signals from $t\bar{t}h(H,A) \to bbbbWW$ or $b\bar{b}h(H,A) \to bbbb$ could be visible at LHC. For $\tan\beta \gtrsim 5$, where the Higgs couplings to b are enhanced, Ref.[39] argues that it will be possible to detect either A and h, or A and H, and essentially remove the IA. Fig.18 shows discovery regions at the two-sigma level for luminosity 100 fb^{-1} = one LHC year (i.e. the two-sigma level after four years) with $m_t = 150$ GeV and $m_{\tilde{t}} = 1$ TeV; the boundary curves marked

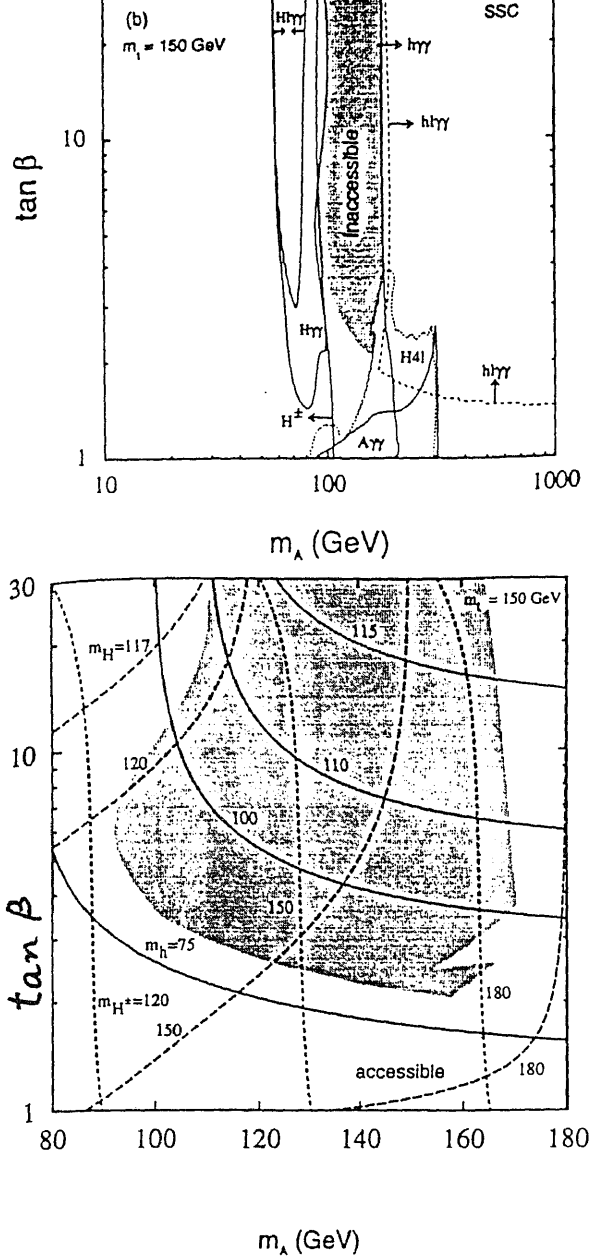

Figure 17. (a) Combined Potential discovery regions for at least one MSSM Higgs boson at SSC are shown as the unshaded area. (b) Expanded view of the region of no coverage shown as the shaded area. Contours of m_A (solid), m_H (dashed) and m_{H+} (dotted) are superimposed.

h, i, j, k, l, m correspond to ttH, tth, ttA, bbH, bbh, bbA signals respectively, and the label lies on the detectable side[39].

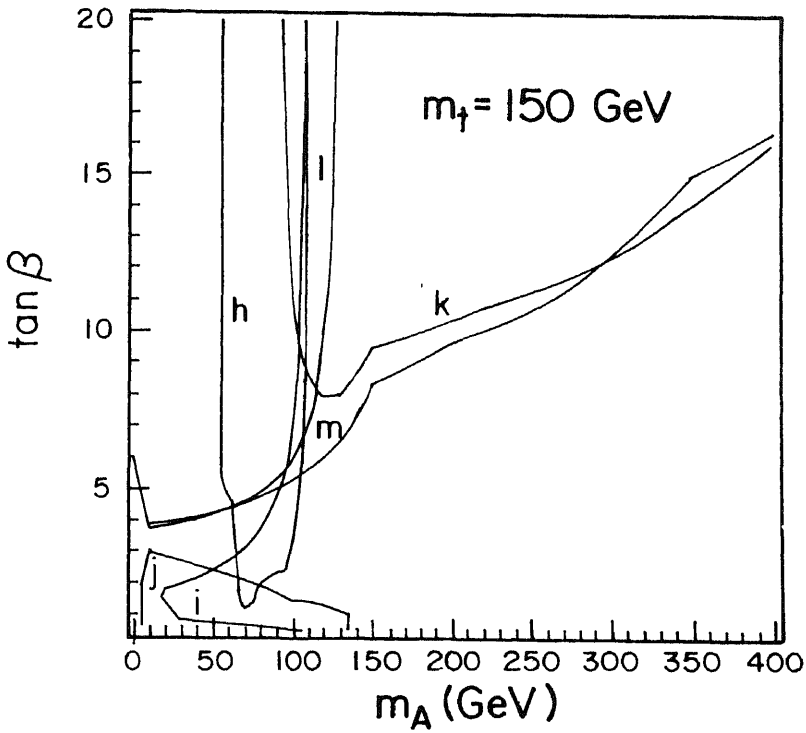

Figure 18. Expected LHC discovery regions for $tth(H, A)$ and $bbh(H, A)$ signals [38].

(e) Alternatively, e^+e^- colliders with energy above LEP2 (where $\sqrt{s} \simeq 170 - 190$ GeV at most is planned) would be able to find at least one of the neutral Higgses via $e^+e^- \to hZ, hA, HZ, HA$ searches, since there is an upper bound on m_h. Fig.19 shows the necessary conditions on $\sqrt{s}$ and luminosity $\mathcal{L}$ to cover the whole $(m_A, \tan\beta)$ half-plane with $\tan\beta > 1$, using $Zh \to \tau\tau jj, \ell\ell jj, \nu\nu jj$ and $jjjj$ final states with b-tagging [40]. The condition depends on m_t because of radiative corrections ($m_{\tilde{t}} = 1$ TeV is assumed here).

4.6 Summary.

(a) The five MSSM Higgses have a richer spectrum than the SM, but are in some ways more elusive.
(b) The lightest scalar mass is bounded much more stringently than in the SM.
(c) There will be evidence for physics beyond the SM if we find any neutral scalar with non-SM coupling, or more than one neutral scalar, or a charged scalar.
(d) The principal Higgs-sector parameters are m_A and $\tan\beta$, with radiative corrections controlled mostly by m_t and $m_{\tilde{t}}$. Masses, couplings, production and decay

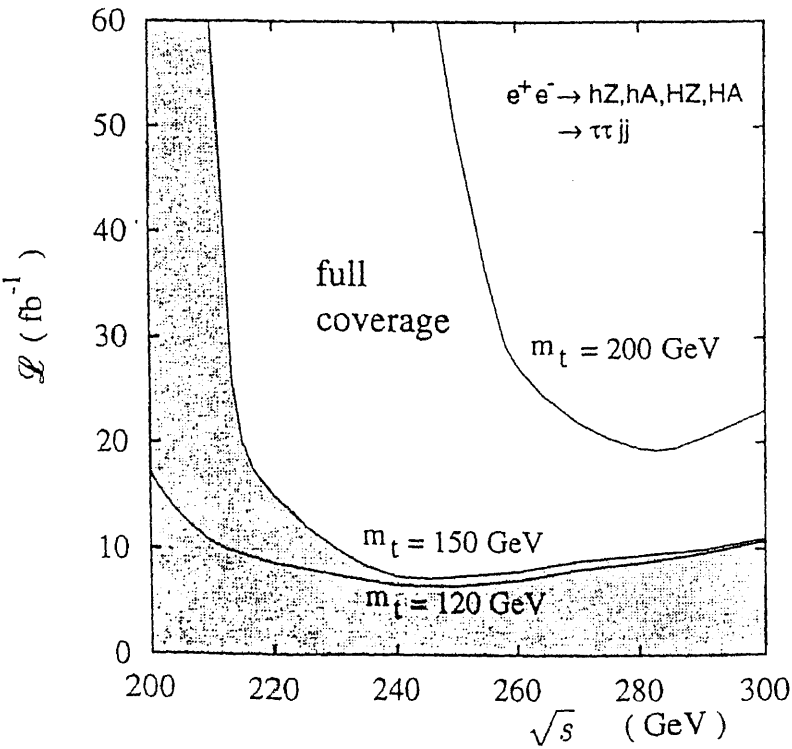

Figure 19. Conditions for covering the $(m_A, \tan\beta)$ parameter space with an e^+e^- collider [39].

and hence Higgs signals – vary strongly across the $(m_A, \tan\beta)$ plane.
(e) LEP1 plus LEP2 coverage in this plane is limited (approximately to the $m_h < 90$ GeV region in Fig.15(a).
(f) LHC coverage (earlier SSC studies are similar) of the remaining parameter space was thought to be incomplete; but recent studies of $tth(H,A) \to bbbbWW$ and $bbh(H,A) \to bbbb$ signals assuming efficient multiple-b-tagging remove this weakness.
(g) An e^+e^- collider with energy just a little way above LEP200 could also guarantee to see at least h.
(h) Future useful signals could include $A \to Zh \to \ell\ell\tau\tau$, $A \to \chi_2^0\chi_2^0 \to 4\ell$+missing-$p_T$, heavy $H^\pm \to tb$.
(i) Future theory constraints could come from SUSY-GUT refinements and $b \to s\gamma$.

References

[1] For a review of Higgs phenomenology, see J.F. Gunion, H.E. Haber, G.L. Kane, S. Dawson, "The Higgs- Hunter's Guide", Addison- Wesley (1990).

[2] GEM collaboration: Letter of Intent GEM TN-92-49 (Nov.1991).

[3] SDC collaboration: Technical Design Report SDC-92-201 (April 1992).

[4] T. Garavaglia, W. Kwong, D.-D. Wu, Phys. Rev. **48**, R1899 (1993).

[5] J. Dai, J.F. Gunion, R. Vega, Phys. Rev. Lett. **71**, 2699 (1993).

[6] Y.L. Dokshitzer, V. Khoze, T. Sjostrand, Phys. Lett. **B274**, 116 (1992); J.D. Bjorken, Phys.Rev. **D47**, 101 (1993); R.S. Fletcher, T. Stelzer, ibid. **D48**, 5162 (1993).

[7] T. Stelzer, Wisconsin PhD thesis (1993).

[8] D. Froidevaux, Proc. LHC Workshop, CERN 90-10, Vol.II, p.444.

[9] V.Barger, T.Han. R.J.N.Phillips, Phys.Lett.**B206**, 339 (1988).

[10] V.Barger et al, Phys.Rev. **D44**, 2701 (1991), **D48**, 5433, 5444(E) (1993).

[11] V.Barger, A.D.Martin, R.J.N.Phillips, Phys.Lett. **125B**,339 (1983); V.Barger, T.Han, J. Ohnemus, Phys.Rev. **D37**,1174 (1988).

[12] J.M.Cornwall, D.N.Levin, G.Tiktopoulos, Phys.Rev. **D10**,1145(1974); B.W. Lee, C. Quigg, H. Thacker, ibid. **D16**,1519(1977).

[13] M.S.Chanowitz, M.K.Gaillard, Nucl.Phys.**B261**, 379 (1985).

[14] S.Weinberg, Phys.Rev.Lett.**17**, 11 (1966).

[15] J. Bagger et al., Phys. Rev. **D49**, 1246 (1994).

[16] S. Nachulich and C.P. Yuan, Phys. Lett. **B293**, 395 (1992).

[17] R. Casalbuoni et al, Phys. Lett. **B249**,130; **B253**, 275 (1990).

[18] M. Golden in "Beyond the Standard Model" (eds. K. Whisnant, B.L. Young, World Scientific 1989).

[19] A. Dobado, M.J. Herrero and J. Terron, Z.Phys.**C50**, 205, 465 (1991).

[20] J.Ellis, G.Ridolfi, F.Zwirner, Phys.Lett.**B257**, 83, **B262**, 477 (1991); A. Brignole et al, ibid. **B271**, 123 (1991).

[21] V.Barger et al, Phys.Rev. **D45**, 4128, **D46**,4914 (1992).

[22] V.Barger, J.L.Hewett, R.J.N.Phillips, Phys.Rev.**D41**, 3421 (1990).

[24] M.Olechowski, S.Pokorski, Phys. Lett. **B214**, 393 (1988).

[25] G.Ross, R.G.Roberts, Nucl.Phys. **B377**, 571 (1992).

[26] V.Barger, M.S.Berger, P.Ohmann, Phys.Rev. **D47**, 1093 (1993).

[27] J.Ellis, G.L.Fogli, E.Lisi, Nucl.Phys. **B393**, 3 (1993).

[28] M.A.Diaz, H.E.Haber, Phys.Rev. **D45**, 4246 (1992).

[29] G.Isidori, Phys.Lett. **B298**, 409 (1993); J.L.Hewett, ANL-HEP-CP-92-125.

[30] J.L.Hewett, Phys.Rev.Lett.**70**,1045(1993); V. Barger, M.S. Berger, R.J.N. Phillips, ibid **70**, 1368 (1993).

[31] S.Bertolini et al, Nucl. Phys. **B353**, 591 (1991); R.Barbieri, G.F.Giudice, Phys. Lett. **B309**, 86 (1993).

[32] R.M. Godbole, D.P. Roy, Phys. Rev. **D43**, 3641 (1991).

[33] J.F. Gunion, Phys. Lett. **B322**, 125 (1994); V. Barger, D.P. Roy, R.J.N. Phillips, ibid **B324**, 236 (1994).

[34] H. Baer et al, Phys. Rev. **D47**, 1062 (1993).

[35] H.Baer et al, Phys. Rev. **D46**, 1067 (1992).

[36] J.F. Gunion et al, Phys. Rev. **D46**, 2040, 2052 (1992); R.M. Barnett et al, ibid **D47**, 1030 (1993).

[37] Z. Kunszt, F. Zwirner, Nucl. Phys. **B385**, 3 (1992).

[38] V.Barger et al, Phys. Lett. **B314**, 351 (1993).

[39] J. Dai, J.F. Gunion, R. Vega, Phys. Lett. **B315**, 355 (1993) and UCD-94-7.

[40] V.Barger, K.Cheung, R.J.N.Phillips, A.L.Stange, Phys.Rev. **D47**, 3041 (1993).

PRAMANA
journal of
physics

© Printed in India

Supplement to Vol. 45
October 1995
pp. 255-262

The inclusive semileptonic B decay lepton spectrum from $B \to Xe\overline{\nu}$

LISA RANDALL

Massachusetts Institute of Technology, Cambridge, MA 02139, U. S. A.

Abstract. In this talk, we review the QCD calculations of the lepton spectrum from inclusive semileptonic B decay. We compare this prediction to that of the ACCMM model. This latter work was done in collaboration with Csaba Csaki.

In this talk we discuss the calculation of the inclusive semileptonic decay lepton spectrum from $B \to Xe\overline{\nu}$. We first discuss the motivation for renewed interest in this calculation, and discuss the use of the OPE and HQET to determine this spectrum. We then compare this prediction to that of heavy quark models, in particular that of Altarelli, Cabbibo, Corbo, Maiani, and Martinelli [1] (hereafter referred to as ACCMM). I will concentrate on $B \to X_c e\overline{\nu}$ and not the detailed questions of the endpoint of the spectrum which are important for $B \to X_u e\overline{\nu}$.

There are several reasons for renewed interest in this prediction. First of all is the copious production of b quarks at LEP and CLEO. A good understanding of the decay spectrum is necessary for understanding fundamental b quark parameters, which are being precisely studied, such as the b width and the forward-backward asymmetry at LEP and those couplings relevant to the rare decays studied by CLEO. Furthermore, with a good understanding of the spectrum one can do detailed measurements of heavy quark fragmentation, which could give interesting tests of heavy quark theory and QCD predictions [2, 3]. Furthermore, in order to do high statistics measurements, one needs to do inclusive measurements. On the theoretical side, it is of interest to study the inclusive decays because they are under much better control theoretically than predictions for exclusive modes, where one needs to know hadronic matrix elements. An understanding of the lepton spectrum is therefore crucial to extracting fundamental parameters.

In the seminal paper of Chay, Georgi, and Grinstein [4] it was shown that one can treat the decay spectrum with the operator product expansion and heavy quark methods. They showed the leading Λ/m corrections to the free quark result vanish in the matrix elements. Subsequently, Bigi, Blok, Koryakh, Shifman, Uraltsev, and Vainshtein [5] studied $(\Lambda/m)^2$ corrections. They compared the results to a free quark, ACCMM model where they did not see the vanishing of the Λ/m corrections as manifest. Following, there were further calculations of $(\Lambda/m)^2$ suppressed effects by Falk, Luke, Savage [7] in the context of $b \to s\gamma$ and by Manohar and Wise [6] in the context of semileptonic decays. We will borrow heavily from these latter two papers in our review of the QCD calculation.

given by

$$\frac{d\Gamma(m_b,E)}{dx}=\frac{G_F^2m^5}{96\pi^3}\frac{x^2(x_m-x)^2}{(1-x)^3}\left[(1-x)(3-2x)+(1-x_m)(3-x)\right] \tag{1}$$

The idea is then to justify and improve on this free quark result. For the study of the inclusive decay, we sum over all final states with given quantum numbers. The spectrum and rate of the inclusive decay is then governed by short distance physics. Intuitively,the justification is that in the $m\rightarrow\infty$ limit, the decay time is much shorter than hadronization time scale. With the OPE and HQET, this can be made precise. The crucial observation is that there is a large range of mass scales in the final state $m_D^2\leq P_X^2\leq m_B^2$ so that the energy flowing through the hadron system scales with the mass of the decaying heavy quark. In the $m\rightarrow\infty$ limit, this is much larger than the QCD scale. Away from $P_X^2\approx m_D^2$, the internal quark is far from mass shell. In this case, we expect the OPE to be useful; it will prove valid except near the endpoint.

The general idea is to relate the square of the matrix element of interest to the imaginary part of the time ordered product of currents. One can then perturbatively compute the time ordered product with the operator product expansion (in the region of phase space where it is valid). However unlike a standard OPE it is useful to expand in the heavy quark mass rather than q^2 in order to apply HQET. The coefficients of the heavy quark operators are then obtained by evaluating the time ordered product between quark and gluon states. The time ordered product is evaluated in the end by taking matrix elements of the operators appearing in the OPE between meson states. One can use the HQET to learn about these matrix elements.

Semileptonic decay is determined from the weak hamiltonian density:

$$H_W=-V_{jb}\frac{4G_F}{\sqrt{2}}\,\overline{q}_j\gamma^\mu P_L b\,\overline{e}\gamma_\mu P_L\nu_e=-V_{jb}\frac{4G_F}{\sqrt{2}}\,J_j^\mu J_{\ell\mu}, \tag{2}$$

The inclusive differential decay rate for $H_b\rightarrow X_{u,c}e\overline{\nu_e}$ (here we will be restricting attention to meson decay) is governed by

$$W_j^{\mu\nu}=(2\pi)^3\sum_X\delta^4\left(p_{H_b}-q-p_X\right)\langle H_b(v,s)|J_j^{\mu\,\dagger}|X\rangle\langle X|J_j^\nu|H_b(v,s)\rangle \tag{3}$$

where

$$p_{H_b}=M_{H_b}v^\mu=m_bv^\mu+k^\mu \tag{4}$$

The $W^{\mu\nu}$ can be expanded in terms of five form factors

$$W^{\mu\nu}=-g^{\mu\nu}W_1+v^\mu v^\nu W_2-i\epsilon^{\mu\nu\alpha\beta}v_\alpha q_\beta W_3+q^\mu q^\nu W_4+(q^\mu v^\nu+q^\nu v^\mu)W_5, \tag{5}$$

One then relates this to a time ordered product via $\mathrm{Im}\,T^{\mu\nu}=-\pi W^{\mu\nu}$ where

$$\begin{aligned}T^{\mu\nu}&=-i\int d^4x\,e^{-iq\cdot x}\sum_s\langle H_b(v,s)|T\left(J^{\mu\,\dagger}(x)\,J^\nu(0)\right)|H_b(v,s)\rangle\\&=-g^{\mu\nu}T_1+v^\mu v^\nu T_2-i\epsilon^{\mu\nu\alpha\beta}v_\alpha q_\beta T_3+q^\mu q^\nu T_4+(q^\mu v^\nu+q^\nu v^\mu)T_5.\end{aligned}$$

Let us consider the analytic structure. There are cuts corresponding to the

As an example,we find the leading order result. This is done explicitly in [6]. The matrix element of the time Fourier transformed, time ordered product of currents

$$-i\int d^4x e^{-iq\cdot x}T(J^{\mu\dagger}J^{\nu}) \tag{6}$$

is

$$\frac{1}{(m_b v-q+k)^2-m_j^2+i\epsilon}\;\overline{u}\;\gamma^{\mu}\;P_L\;\left(m_b\not{v}-\not{q}+\not{k}+m_j\right)\;\gamma^{\nu}\;P_L\;u, \tag{7}$$

Using

$$\gamma^{\mu}\gamma^{\alpha}\gamma^{\nu}=g^{\mu\alpha}\gamma^{\nu}+g^{\nu\alpha}\gamma^{\mu}-g^{\mu\nu}\gamma^{\alpha}+i\epsilon^{\mu\nu\alpha\beta}\gamma_{\beta}\gamma_5. \tag{8}$$

one finds the order k^0 term is

$$\begin{aligned}\frac{1}{\Delta_0}\quad & \overline{u}\Big\{\;(m_b v-q)^{\mu}\,\gamma^{\nu}+(m_b v-q)^{\nu}\,\gamma^{\mu}-(m_b\not{v}-\not{q})\,g^{\mu\nu}\\ & -i\epsilon^{\mu\nu\alpha\beta}\,(m_b v-q)_{\alpha}\,\gamma_{\beta}\;\Big\}P_L\,u,\end{aligned} \tag{9}$$

where

$$\Delta_0=(m_b v-q)^2-m_j^2+i\epsilon \tag{10}$$

By replacing the matrix element with the b quark operator which yields this amplitude when evaluated between b quark states, one obtains

$$\begin{aligned}\frac{1}{\Delta_0}\quad & \Big\{(m_b v-q)^{\mu}\,g^{\nu\lambda}+(m_b v-q)^{\nu}\,g^{\mu\lambda}-(m_b v-q)^{\lambda}\,g^{\mu\nu}\\ & -i\epsilon^{\mu\nu\alpha\lambda}\,(m_b v-q)_{\alpha}\Big\}\,\overline{b}\,\gamma_{\lambda}P_L\,b.\end{aligned}$$

Because it is a current, one has

$$\langle H_b(v,s)|\,\overline{b}\,\gamma^{\lambda}\,b\,|H_b(v,s)\rangle=v^{\lambda}, \tag{11}$$

since b quark number is an exact symmetry.

So we can evaluate the leading order contribution *exactly*. By taking the matrix element of the OPE between H states, we get

$$\begin{aligned}T_1^0 &= \frac{1}{2\Delta_0}(m_b-q\cdot v)\\ T_2^0 &= \frac{1}{\Delta_0}m_b\\ T_3^0 &= \frac{1}{2\Delta_0}\end{aligned}$$

So to get the amplitude $W^{\mu\nu}$ which determines the spectrum, we need the imaginary part of $T^{\mu\nu}$. This is readily obtained from

$$\frac{1}{\Delta_0} = \delta((m_b v-q)^2-m^2) \tag{12}$$

$$\frac{1}{\Delta_0^2} = -\delta'((m_b v-q)^2-m^2) \tag{13}$$

$$\frac{1}{\Delta_0^3} = \frac{1}{2}\delta''((m_b v-q)^2-m^2) \tag{14}$$

The mass shell condition above when integrated over phase space leads to just the free quark decay distribution!

However, with these methods, one can also consider higher order corrections. The important result will be that Λ_{QCD}/m corrections vanish and only two matrix elements, one of which is known, are required to obtain $(\Lambda_{QCD}/m)^2$ corrections

We first introduce heavy quark fields and the heavy quark effective theory. Recall that in the heavy quark limit, the heavy quark mass and spin decouple from the soft degrees of freedom. The heavy quark state looks like a static point source of charge. The b quark is almost on mass shell $p = m_b v + k$.

Define the heavy quark field

$$b_v = \frac{(1+\not{v})}{2} e^{im_b v\cdot x} b + \ldots, \tag{15}$$

with leading order lagrangian

$$\mathcal{L} = \bar{b}_v (iv\cdot D) b_v + \ldots. \tag{16}$$

Now expand in terms of HQET operators. We follow [7] who give the leading term in terms of the standard quark field, but the mass suppressed operators in terms of heavy quark fields.

$$T\{\mathcal{O}^\dagger, \mathcal{O}\} \stackrel{\text{OPE}}{=} \frac{1}{m_b}\left[\mathcal{O}_0 + \frac{1}{2m_b}\mathcal{O}_1 + \frac{1}{4m_b^2}\mathcal{O}_2 + \ldots\right] \tag{17}$$

$$\begin{aligned}
\mathcal{O}_0 &= \bar{\mathrm{b}}\,\Gamma\,\mathrm{b}\,, \\
\mathcal{O}_1 &= \bar{b}_v\,\Gamma\,\mathrm{i}\mathrm{D}_\mu b_v\,, \\
\mathcal{O}_2 &= \bar{b}_v\,\Gamma\,\mathrm{i}\mathrm{D}_\mu \mathrm{i}\mathrm{D}_\nu b_v
\end{aligned}$$

As before, at leading order, we have

$$\langle B|\,\bar{\mathrm{b}}\gamma^\mu \mathrm{b}\,|B\rangle = 2P_B^\mu \tag{18}$$

Now consider the first order mass suppressed terms.

$$\langle M|\,\mathcal{O}_1\,|M\rangle = \langle M|\,\bar{h}\,\Gamma\,\mathrm{i}\mathrm{D}_\mu h\,|M\rangle = \langle M|\,\bar{h}\,\Gamma v_\mu v\cdot \mathrm{i}\mathrm{D} h\,|M\rangle \tag{19}$$

This vanishes by the equation of motion! Notice this critically depends on our phase choice in defining heavy quark field.

An arbitrary counterterm

$$\delta m \bar{b}_v b_v \tag{20}$$

was taken to vanish. With this choice of quark mass, all linear corrections to the free quark result vanish!

At higher order in $1/m$, one needs the two matrix elements

$$\begin{aligned}
K_b &\equiv -\langle H_b(v,s)|\,\bar{b}_v \frac{(iD)^2}{2m_b^2}\, b_v\,|H_b(v,s)\rangle \\
G_b &\equiv Z_b\,\langle H_b(v,s)|\,\bar{b}_v \frac{gG_{\alpha\beta}\sigma^{\alpha\beta}}{4m_b^2}\, b_v\,|H_b(v,s)\rangle\,,
\end{aligned} \tag{21}$$

The second matrix element is known because it is related to the known spin dependent mass splittings. The first is not known, and is a parameter to be determined.

So, to summarize, the leading order result for the rate and spectrum is the free quark result. The first order corrections vanish. At second order, there is one unknown coefficient and one which has been determined. This analysis has assumed we are far from endpoint, where the OPE is valid. Had we applied this near the endpoint, higher dimension operators would not be suppressed and it would be necessary to average the spectrum over a range of energies.

One can compare this result to the predictions of models. It is interesting to see how models reflect and differ from these general QCD predictions. Consider for example the ACCMM model. Here I review work of Csaba Csaki and myself [8], but other interesting references are that by Grant Baillie [9] and Ref. [10]. One finds that one can always *define* a quark mass so that $1/m$ corrections vanish. However, at $1/m^2$, the model would differ from the QCD result.

In the ACCMM model, one models a B meson decay as *disintegration*. There is a spectator quark with mass m_{sp} and momentum distribution $\phi(|p|)$.

$$\phi(|p|) = \frac{4}{\sqrt{\pi} p_f^3} \exp\left(-\frac{|p|^2}{p_f^2}\right) \tag{22}$$

The b quark momentum is determined by kinematic constraints. The lepton spectrum is determined from the decaying off shell b quark. Define

$$E_W = M_B - \sqrt{p^2 + m_{sp}^2} \tag{23}$$

The invariant mass of the b quark will then be

$$W^2 = m_B^2 + m_{sp}^2 - 2m_B\sqrt{p^2 + m_{sp}^2} \tag{24}$$

Define

$$\begin{aligned} x &= \frac{2E_e}{m} \\ \epsilon &= \frac{m_f^2}{m_b^2} \\ x_m &= 1 - \epsilon \end{aligned}$$

Recall the formula for free quark decay.

$$\frac{d\Gamma(m_b, E)}{dx} = \frac{G_F^2 m^5}{96\pi^3} \frac{x^2(x_m - x)^2}{(1-x)^3} [(1-x)(3-2x) + (1-x_m)(3-x)] \tag{25}$$

Then the lepton spectrum in the ACCMM model is

$$\begin{aligned} \frac{d\Gamma_B}{dE} &= \int_0^{p_{max}} dp p^2 \phi(|p|) \int \frac{1}{\gamma} \frac{d^2\Gamma(W, E')}{dE' d\cos\theta} dE' \times \\ & \quad d\cos\theta \int \frac{d\cos\theta_p}{2} \delta(E - \gamma E' - \gamma\beta E' \cos\theta_p) \end{aligned}$$

$$\frac{d\Gamma_B}{dE} = \int dp p^2 \phi(|p|) \frac{1}{2\beta\gamma^2} \int \frac{d^2\Gamma}{dE' d\cos\theta} d\cos\theta' \frac{dE'}{E'} \tag{26}$$

Using $\beta\gamma^2 = pE_W/W(p)^2$ yields

$$\frac{d\Gamma_B}{dE} = \int dp p^2 \phi(|p|) \frac{W^2}{2pE_W} \int_{E_-}^{E_{max}} \frac{dE'}{E'} \frac{d\Gamma(W,E')}{dE'} \tag{27}$$

where

$$E^{\mp} = \frac{EW}{E_W \pm p} \tag{28}$$

$$E_{max} = min\{E_+, \frac{W}{2}(1-x_m)\} \tag{29}$$

$$p_{max} = \frac{m_B}{2} - \frac{m_f^2}{m_B^2} \tag{30}$$

Now do a heavy meson mass expansion.

$$\frac{d\Gamma_B}{dE} = \int_0^{p_{max}} \phi(|p|) p^2 \frac{W^2}{2pE_W} \frac{G_F^2 W^4}{48\pi^3} \int_{E_-}^{E_+} \frac{dE'}{E'} \left(\frac{2E}{W}\right)^2 \left(3 - \frac{4E'}{W}\right) \tag{31}$$

We can explicitly evaluate the E' integral, to get

$$\frac{d\Gamma_B}{dE} = \frac{G_F^2 E^2}{24\pi^3} \int_0^{p_{max}} \frac{dp}{E_W} \left(6E_W W^2 - 8EE_W^2 - \frac{8}{3}p^2 E\right) p^2 \phi(|p|) \tag{32}$$

Take p_f small.

$$\frac{d\Gamma_B}{dE} = \frac{d\Gamma_B^0}{dE} + \frac{G_F^2 E^2 M_B^2}{12\pi^3\sqrt{\pi}} \left(8\frac{E}{m_B} - 12\right) \frac{p_f}{m_B} + P(\frac{p_F^2}{m_B})^2 \frac{d\Gamma_q}{dE} \tag{33}$$

It looks like there are nonvanishing linear corrections, but that is because we expanded in the meson mass m_B, rather than the quark mass m_b. To do a heavy quark expansion, one needs to *define* a quark mass. This can be done so that the linear correction vanishes.

$$\frac{d\Gamma_B}{dE} = \frac{G_F^2 E^2}{24\pi^3} \int_0^{p_{max}} \frac{dp}{E_W} \left(6E_W W^2 - 8EE_W^2 - \frac{8}{3}p^2 E\right) p^2 \phi(|p|) \tag{34}$$

If we define

$$m_b = \langle W(p) \rangle \tag{35}$$

Up to quadratic terms in p,we have

$$\langle W \rangle = \langle E_W \rangle = m_b = m_B - \langle p \rangle \tag{36}$$

$$\langle f(W, E_W) \rangle = f(m_B, m_B) - \langle p \rangle f'(m_B, m_B) + O(p^2) = f(m_b, m_b) + O(p^2) \tag{37}$$

We see that it was possible to define a b quark mass so that linear corrections vanished because the p dependence was all through E_W. So we can eliminate linear corrections through a proper choice of m_b. It is easy to extend this to nonzero spectator mass.

$$\langle E_W \rangle = m_B - \langle \sqrt{m_{sp}^2 + p^2} \rangle \tag{38}$$

Now consider the total rate and the full spectrum.

$$\int \frac{d\Gamma_B}{dE} = \int dp p^2 \int \frac{d\cos\theta_p}{2} \int dE' \frac{d\Gamma(W,E')}{E'} \delta(E - \gamma E' - \gamma\beta E' \cos\theta_p) \qquad (39)$$

However, the spectra themselves are very different near the endpoint.

$$\begin{aligned} \frac{d\Gamma_B}{dE} &= \int_0^{p_1} dp p^2 \phi(|p|) \frac{W}{2p} \int_{E_-}^{E_+} \frac{d\Gamma(W,E')}{E'} \\ &+ \int_{p_1}^{p_{max}} dp p^2 \phi(|p|) \frac{W}{2p} \int_{E_-}^{E_1} \frac{d\Gamma(W,E')}{E'} \end{aligned}$$

where $E_1 = W(1-\epsilon)/2$, $p_1 = m_B/2(1 - \frac{m_f^2}{m_B^2} - E$ for $m_{sp} = 0$. This spectrum extends up to $E_{max} = \frac{m_B - m_{sp}}{2}\left(1 - \frac{m_f^2}{(m_B - m_{sp})^2}\right)$

We see the ACCMM spectrum and the free quark spectrum deviate due to two effects near the endpoint. The first term is not integrated up to $p \approx \infty$ and the second term integrates over a rapidly falling spectrum so it is no longer a good approximation to replace $\langle f(W)\rangle$ by $f(\langle W\rangle)$. The spectrum extends beyond naive quark mass endpoint.

Since we have a specific model, we can also investigate the question of how large an energy interval must be averaged over to get good agreement between the model and the free quark prediction. In ref. [8] we used the averaging function

$$\frac{d\Gamma}{dE}(E_0) = \int \frac{1}{\sqrt{\pi}\Delta E} e^{-\left(\frac{(E-E_0)^2}{\Delta E^2}\right)} \frac{d\Gamma(E)}{dE}(E) \qquad (40)$$

We expect to require an average of approximately $2p_f$ to get $(p_f/m)^2$ agreement. This was appproximately correct. We also checked that the best fit quark mass is generally very close to the exact quark mass, so the deviation of the model from the free quark prediction is probably not very important for practical purposes.

At higher order, the predictions of this model will not agree with general QCD predictions. This is because gauge invariance is not incorporated. There are corrections to the free quark result due to the fact that terms proportional to $\langle p_0^2\rangle$ and $\langle \vec{p}^2\rangle$ both yield $1/m^2$ corrections. Recall that in the heavy quark theory the operator $\langle D_0^2\rangle$ contributions only at higher order in the heavy quark mass expansion by the equation of motion. In the ACCMM model, both contribute at the same order. Obviously, the ACCMM model also doesn't give you spin dependent gluon operator. We conclude that although the model is probably adequate in practice (as would be free quark decay) it does not properly incorporate QCD dynamics.

We conclude that there has been much advancement in our understanding of the lepton decay spectrum. It is unclear at what level this will be tested. Most of the large deviations from the free quark prediction are in the endpoint region, where one must smear to get reliable predictions. Furthermore, the higher order correction involves an unknown parameter and requires very accurate measurements. However, from a practical point of view, when using the spectrum to extract b quark couplings, we see that the free quark decay models b quark decay very well. It might be better to fit the spectrum to a free quark spectrum that that of a model, such as the ACCMM model. The vanishing of Λ_{QCD}/m corrections is very important to

Acknowledgements: I thank my collaborator C. Csaki. I also thank the Institute for Theoretical Physics in Santa Barbara where this writeup was completed.

References

[1] G. Altarelli, N. Cabibbo, G. Corbó, L. Maiani, and G. Martinelli, *Nucl. Phys.***B208** (1982) 365.

[2] L. Randall and N. Rius, hep-ph-9405217

[3] R. Jaffe and L. Randall, *Nucl. Phys.* **B412** (1994) 79.

[4] J. Chay, H.Georgi and B.Grinstein, *Phys. Lett.* **247B** (1990) 399.

[5] I. G. Bigi, M. Shifman, N. G. Uraltsev and A. I. Vainshtein, *Phys. Rev. Lett.* 71 (1993) 496; B. Blok, L. Koryakh, M. Shifman and A. I. Vainshtein *Phys. Rev.***D49** (1994) 3356.

[6] A. Manohar and M. B. Wise, *Phys. Rev.***D49**(1994)1310.

[7] A. Falk, M. Luke, M. Savage *Phys. Rev.* **D49** (1994) 555.

[8] C. Csáki and L. Randall, *Phys. Lett.***B324** (1994) 451.

[9] G. Baillie,*Phys. Lett.* **B324** (1994) 446.

[10] I. Bigi, M. Shifman, N. Uraltsev, and A. Vainshtein, hep-ph-9401298.

journal of physics

October 1995
pp. 263-276

CP violation at colliders

SAURABH D RINDANI
Theory Group, Physical Research Laboratory,
Navrangpura, Ahmedabad 380 009, INDIA

Abstract. The prospects of experimental detection of CP violation at e^+e^- and $pp/p\bar{p}$ colliders are reviewed. After a general discussion on the quantities which can measure CP violation and on the implications of the CPT theorem, various possibilities of measuring CP violation arising outside the standard model are taken up. CP violation in leptonic processes, especially polarization effects in $e^+e^- \to l^+l^-$ are discussed next. CP violation in $t\bar{t}$ and W^+W^- production and decay is also described.

1. Introduction

1.1 CP violation in the standard model

CP violation in the standard model (SM), as is well known, arises due to complex Yukawa couplings, and finally shows up through quark mixing in the Cabibbo-Kobayashi-Maskawa matrix as a single phase. The reparametrization invariant quantity

$$J = \sin^2\theta_1 \sin\theta_2 \sin\theta_3 \cos\theta_1 \cos\theta_2 \cos\theta_3 \sin\delta \tag{1}$$

is a measure of CP violation in SM, and though small, produces measurable effects in the K meson system, and hopefully the effects in the b-quark states will be measurable. The effects in other sectors (as for example the neutron electric dipole moment) and in high-energy processes is generally predicted to be too small to be observed.

In the leptonic sector of SM the prospects of CP violation being observable are worse, since there is no analogue of the CKM phase in the absence of neutrino masses. CP violation in leptonic systems has to feed in from the hadronic sector through loops. For example, electric dipole moments (EDM) of charged leptons are induced due to the W EDM, and are found to vanish up to three-loop order. The electron EDM is then estimated to be around 10^{-41} e cm. [1]

Thus, any new observable CP violation would be a signal of non-standard physics. It might be mentioned that perhaps there is already a hint towards non-standard CP violation in current ideas on electroweak baryogenesis.

1.2 Scenarios for CP violation beyond SM

CP violation beyond SM can arise due to almost any extra Yukawa couplings which can be complex, and possibly also due to new Higgs self-interactions and complex

scalar vacuum expectation values. Thus, introduction of extra fermions or scalars could give rise to new sources of CP violation.

Retaining the gauge group to be $SU(2)_L \times U(1)$, CP violation can arise due to extra fermion or Higgs doublets or singlets. Since the SM measure of CP violation J (eq.(1)) is small owing to the small mixing angles among quark generations as experimentally observed, larger CP violating effects would arise if there are extra generations of quarks, whose mixing angles may be less constrained. If there are new fermions (quarks or leptons) in exotic representations (left-handed singlets and/or right-handed doublets of $SU(2)_L$) there are further complex flavour-changing couplings to Z which violate CP.

Supersymmetry requires the addition of extra scalars and fermions, whose couplings violate CP. In left-right symmetric models, again, there further sources of CP violation.

1.3 Use of effective Lagrangians for model-independent analysis

There is a large variety of sources of CP violation beyond SM, and rather than discuss predictions of each model for each observable quantity, it is more economical to analyze CP-violating quantities in terms of the parameters of an effective Lagrangian. Examples of CP-violating terms in an effective Lagrangian with which we will be concerned here are given below:

$$\begin{aligned}\mathcal{L}_{eff} &= -\frac{i}{2}\sum_i d_{\psi_i}\overline{\psi}_i\sigma^{\mu\nu}\gamma_5\psi_i F_{\mu\nu} - \frac{i}{2}\sum_i \widetilde{d}_{\psi_i}\overline{\psi}_i\sigma^{\mu\nu}\gamma_5\psi_i(\partial_\mu Z_\nu - \partial_\nu Z_\mu) \\ &+ \sum_{V=A,Z} ig_V\left[\widetilde{\kappa}^V W_\mu^\dagger W_\nu \widetilde{V}^{\mu\nu} + \frac{\widetilde{\lambda}^V}{m_W^2} W_{\lambda\mu}^\dagger W_\nu^\mu \widetilde{V}^{\nu\lambda}\right. \\ &\left. + g_4^V W_\mu^\dagger W_\nu(\partial^\mu V^\nu + \partial^\nu V^\mu)\right]. \qquad (2)\end{aligned}$$

($\widetilde{V}^{\mu\nu} \equiv \frac{1}{2}\epsilon^{\mu\nu\alpha\beta}V_{\alpha\beta}$; $V_{\mu\nu} = \partial_\mu V_\nu - \partial_\nu V_\mu$; $W_{\mu\nu} = \partial_\mu W_\nu - \partial_\nu W_\mu$). These terms are of dimension ≤ 6. In eq.(2), ψ_i refers to various fermionic fields (quarks and leptons), whose electric and "weak" dipole moment is given by d_{ψ_i} and $\widetilde{d}_{\psi_i}$, respectively. It should be noted that all the parameters are in reality scale dependent "form factors", and can be complex.

2. Some general considerations

2.1 Observable quantities which measure CP violation

There are basically two types of observables which can be used to characterize CP violation: asymmetries and correlations.

An example of an asymmetry is the partial-width asymmetry for decay of particles i and $\overline{i}$ which are CP conjugates of each other:

$$A = \frac{\Gamma(i \to f) - \Gamma(\overline{i} \to \overline{f})}{\Gamma(i \to f) + \Gamma(\overline{i} \to \overline{f})}. \qquad (3)$$

If CP is a symmetry of the theory, $A = 0$. Non-vanishing A implies violation of CP. A is a convenient parameter because it is dimensionless and lies between -1

and 1. In particular, if i is an eigenstate of CP, $\bar{i} = i$, and A in (3) simplifies and measures the fractional difference in the decay rates of i to two CP-conjugate states f and $\bar{f}$. As we shall see later, the CPT theorem implies that A is zero even if CP is violated unless the amplitude has an absorptive part which can arise because of final-state interactions or loop effects in perturbation theory.

Another type of asymmetry is an asymmetry in a final-state variable like energy or angle. It is defined in general (for $i = \bar{i}$) as

$$A = \frac{\sum_{f\in S} d\sigma(i \to f) - \sum_{f\in \bar{S}} d\sigma(i \to f)}{\sum_{f\in S} d\sigma(i \to f) + \sum_{f\in \bar{S}} d\sigma(i \to f)}. \tag{4}$$

Here S and $\bar{S}$ are sets of states with CP-conjugate kinematic ranges, and f is a final state assumed to have particles conjugate to one another in pairs. An example is energy asymmetry between the energies E_+ and E_- of CP-conjugate particles in f:

$$A = \frac{\int_{E_+>E_-} d\sigma(i \to f) - \int_{E_+<E_-} d\sigma(i \to f)}{\int_{E_+,E_-} d\sigma(i \to f)}. \tag{5}$$

The other category of quantities consists of CP-odd correlations which are expectations values of CP-odd operators in a process with initial as well final states described by CP-even density matrices. Thus for an observable $\mathcal{O}(\{\mathbf{p}_{A_i}, \mathbf{s}_{A_i}\})$ which is a function of momenta $\mathbf{p}_{A_i}$ and spins $\mathbf{s}_{A_i}$ of particles A_i, and which transforms under CP as

$$\mathcal{O}(\{\mathbf{p}_{A_i}, \mathbf{s}_{A_i}\}) \to \mathcal{O}(\{-\mathbf{p}_{A_i}, \mathbf{s}_{A_i}\}) = -\mathcal{O}(\{\mathbf{p}_{A_i}, \mathbf{s}_{A_i}\}), \tag{6}$$

the CP-odd correlation is

$$\langle \mathcal{O} \rangle = \frac{\int d\sigma \mathcal{O}(\{\mathbf{p}_{A_i}, \mathbf{s}_{A_i}\})}{\int d\sigma}. \tag{7}$$

A non-zero value of such a correlation signals CP violation.

It may be noted that an asymmetry in the variable $\mathcal{O}$may be described as a special case of a correlation of $\epsilon(\mathcal{O})$, where ϵ is the antisymmetric step function:

$$\langle \epsilon(\mathcal{O}) \rangle = \frac{\int_{\mathcal{O}>0} d\sigma - \int_{\mathcal{O}<0} d\sigma}{\int_{\mathcal{O}} d\sigma}. \tag{8}$$

2.2 Statistical significance

Whether or not a measured asymmetry or correlation can really signal CP violation naturally depends on its statistical significance decided by the statistical fluctuation expected in the event sample.

For a rate asymmetry A, the number of asymmetric events ΔN is

$$\Delta N = AN, \tag{9}$$

where N is the total number of events in the channel considered. The statistical fluctuation in these N events is $\sqrt{N}$. Hence for discrimination of the signal, at the one standard deviation level, we require

$$\Delta N > \sqrt{N}, \tag{10}$$

Thus, it would be possible to measure an asymmetry if its predicted value is larger than $1/\sqrt{N}$. To put it differently, the number of events should be larger than $1/A^2$.

In the case of a CP-odd correlation $\langle\mathcal{O}\rangle$, CP-invariant interactions can give individual events with $\mathcal{O} \neq 0$, averaging out to zero. Thus the mean square deviation

$$\Delta\mathcal{O} = \sqrt{\langle\mathcal{O}^2\rangle - \langle\mathcal{O}\rangle^2} \tag{12}$$

is a measure of the background coming from CP-invariant interactions. For N events in the channel, the CP-even events give rise to a fluctuation $\Delta\mathcal{O}/\sqrt{N}$. The signal $\langle\mathcal{O}\rangle$ should be larger than this to be measurable at the one standard deviation level:

$$\langle\mathcal{O}\rangle > \frac{1}{\sqrt{N}}\sqrt{\langle\mathcal{O}^2\rangle - \langle\mathcal{O}\rangle^2}. \tag{13}$$

There is a further experimental requirement for measuring CP violation. All experimental cuts must respect CP invariance. If not, they would introduce artificial asymmetries, diluting or obliterating the genuine signal of CP violation.

2.3 CPT theorem and all that

Since a combined CPT transformation is a good symmetry according to the CPT theorem, CP invariance (or violation) implies T invariance (or violation), and *vice versa*. However, it should be borne in mind that observation of a T-odd asymmetry or correlation is not necessarily an indication of CP (or even T) violation. The reason for this is the anti-unitary nature of the time-reversal operator in quantum mechanics. As a consequence of this, a T operation not only reverses spin and three-momenta of all particles, but also interchanges initial and final states. This last interchange is difficult to meet with in practice, and one usually has a situation where only momenta and spins are reversed, with the initial and final states kept as such. In that case, non-zero T-odd observables do not necessarily signal genuine T violation.

There is, however, a case when T-odd observables imply T violation, and that is when final-state interactions and loop effects can be neglected. In that case the transition operator $\mathcal{T}$ obeys $\mathcal{T} = \mathcal{T}^\dagger$, since the right-hand side in the unitarity relation

$$\mathcal{T} - \mathcal{T}^\dagger = i\mathcal{T}^\dagger\mathcal{T} \tag{14}$$

can be neglected. Then

$$\langle f|\mathcal{T}|i\rangle \approx \langle f|\mathcal{T}^\dagger|i\rangle = \langle i|\mathcal{T}|f\rangle^*. \tag{15}$$

Now if T invariance holds, then

$$\langle f|\mathcal{T}|i\rangle = \langle i_T|\mathcal{T}|f_T\rangle, \tag{16}$$

where $|i_T\rangle$, $|f_T\rangle$ represent states with all momenta and spins inverted in sign. Combining eq.(16) with (15) for time-reversed states, we have

$$|\langle f|\mathcal{T}|i\rangle| = |\langle f_T|\mathcal{T}|i_T\rangle|. \tag{17}$$

In this case, if a T-odd observable is non-zero, it implies T violation. Thus, T invariance (and CP invariance through the CPT theorem) implies equality of amplitudes with all momenta and spins reversed if and only if final-state interaction (absorptive part for the amplitude) vanishes.

Put differently, this means that final-state interactions can mimic T violation, but not genuine CP violation. One should therefore use, as far as possible, CP-odd observables to test CP invariance, not T-odd observables (unless they are also CP odd).

For a genuine CP-odd quantity, there are two possibilities,
A. it is T odd, and therefore CPT even, or
B. it is T even, and therefore CPT odd.
In case B, there is no violation of the CPT theorem provided the amplitude has an absorptive part. (This is again due to the fact the CPT operator is antiunitary, and interchanges initial and final states). Thus non-vanishing of CPT-odd operators necessarily requires an absorptive part of the amplitude to exist.

The absorptive part of CP-odd CPT-odd quantities in perturbation theory usually comes from loop contributions where the intermediate state can be on shell. An interesting way of realizing this possibility in the case of an intermediate state of an unstable particle is through the Breit-Wigner form of its propagator. In this case the absorptive part is proportional to its width. This trick has been used in the case of the top, Z and Higgs propagators [2, 3, 4]. One must however be careful to subtract out the part of the width corresponding to decay into the initial or final state for consistency with the CPT theorem [5]. It has also been pointed out recently [6] that off-diagonal contributions to the self-energy of the virtual particles are also needed for consistency with the CPT theorem.

3. CP violation in the leptonic sector

3.1 Scenarios for leptonic CP violation

In the standard model, no right-handed neutrinos are introduced. As a result, there is no mass matrix to diagonalize for the neutrinos. Hence the CKM matrix is the unit matrix, and no CP-violating phases can arise. However, in extensions of the standard model, CP violation can arise either because of the presence of neutrino masses or because of extra leptons introduced (even though neutrinos may be massless), or both.

A. Massive neutrinos. Neutrinos can have Dirac or Majorana masses. CP violation in the Dirac case is exactly analogous to that in the quark sector of the standard model. In case of Majorana masses, the freedom of phase redefinition of the neutral lepton fields is reduced because Majorana mass terms are not invariant under phase transformations. As a result there are more CP-violating phases in the CKM matrix than the corresponding Dirac case. It is thus possible to have CP violation with even two generations of Majorana neutrinos.

B. Massless neutrinos with exotic leptons. It is possible to have CP violation because of either charged or neutral leptons in exotic representations of $SU(2) \times$

$U(1)$. The leptons then have flavour-violating couplings to Z or Higgses, which can be complex and hence CP violating.

We consider below some leptonic CP-violating processes at high-energy colliders which make use of the above mechanisms of CP violation. The importance of leptonic processes stems from the fact that they are relatively clean from the experimental point of view.

3.2 Leptonic flavour violating Z decays

Leptons can have flavour-violating couplings to Z giving rise to flavour violating Z decays into charged leptons either at tree level or at one-loop level:

$$Z \to l_i \overline{l_j} \quad (i \neq j). \tag{18}$$

The corresponding CP-violating asymmetry is

$$A = \frac{\Gamma(Z \to l_i \overline{l_j}) - \Gamma(Z \to \overline{l_i} l_j)}{\Gamma(Z \to l_i \overline{l_j}) + \Gamma(Z \to \overline{l_i} l_j)}. \tag{19}$$

This is T even and therefore CPT odd. It therefore needs an absorptive part to be present.

Flavour-violating tree-level couplings of charged leptons to Z arise in models with exotic charged leptons transforming as either left-handed singlets and/or right-handed doublets. In such a case the Glashow-Weinberg condition for flavour-diagonal couplings is not satisfied, and (18) occurs at tree level. For A of (19) to be non-zero, one-loop correction to (18) is also needed, and only the absorptive part of that amplitude contributes. The asymmetry is then $\mathcal{O}(\alpha)$[7].

On the other hand, models with exotic neutral leptons have flavour-violating couplings of neutral leptons at the tree-level giving rise to (18) at the loop level [8]. The absorptive part now comes from one of these loop diagrams. A is now $\mathcal{O}(1)$. However, unlike in the previous case, the rate of the flavour-violating process (18) is $\mathcal{O}(\alpha^3)$. Thus, the minimum total number N_Z of Z events for an observable asymmetry is in both cases $\mathcal{O}(1/\alpha^3)$. However, constraints on leptonic mixing angles and masses of exotic leptons make this process too rare to observe at LEP.

3.3 CP violation in $e^+e^- \to \gamma^*, Z^* \to l^+l^-$

In case of CP violation in $e^+e^- \to \gamma, Z \to l^+l^-$ there are two general results [9]: (i) No CP violation can be seen without measuring initial or final spins. This follows basically because no CP-odd observable can be constructed without spins. (ii) The only CP-violating couplings for the on-shell process are the dipole moment type couplings of e or l (electric or "weak" dipole moments). Since there are strong experimental limits on the electron and muon electric dipole moments ($d_e \lesssim 10^{-27} e$ cm, $d_\mu \lesssim 10^{-19} e$ cm), τ may be a good candidate for l. In fact, the weak moment of τ has been constrained using τ polarization in this reaction (see below).

Since it is clear from (i) that either initial or final spins have to be observed to detect CP violation, we consider below both these cases for $e^+e^- \to Z \to \tau^+\tau^-$.

3.3.1 CP tests using τ polarization in $e^+e^- \to \tau^+\tau^-$: This possibility has been discussed by several authors [2,10–12]. For the process

$$e^-(p_-) + e^+(p_+) \to \tau^-(k_-, s_-) + \tau^+(k_+, s_+), \tag{20}$$

possible CP-odd quantities that can be constructed out of the momenta and spins in the centre-of-mass (cm) frame are $(\mathbf{p}_- - \mathbf{p}_+)\cdot(\mathbf{s}_- - \mathbf{s}_+)$ and $(\mathbf{p}_- - \mathbf{p}_+)\cdot\mathbf{s}_- \times \mathbf{s}_+$.

To measure these quantities, one must, of course, be able to measure $\mathbf{s}_\pm$. This can be done by looking at decay distributions of $\tau_\pm$. In the rest frame of τ, the angular distribution of an observed decay particle is

$$\frac{d\Gamma}{d\Omega^*} = \frac{1}{4\pi}(1 + \alpha \mathbf{s}\cdot\hat{\mathbf{q}}^*), \tag{21}$$

where $\hat{\mathbf{q}}^*$ is the unit vector along the momentum of the observed particle, and α is a constant called the analyzing power of the channel. For example,

$$\begin{aligned} \alpha &= \mp 1 \quad \text{for} \quad \tau^\pm \to \pi^\pm \nu_\tau, \\ &= \pm 1/3 \quad \text{for} \quad \tau^\pm \to l^\pm \nu_l \nu_\tau, \end{aligned}$$

as deduced from the theory of weak τ decay. Using (21), spin correlations can be translated to momentum correlations.

In terms of the observed momenta, possible CP-odd variables are $\hat{\mathbf{p}}\cdot(\mathbf{q}_+ \times \mathbf{q}_-)$ $(CPT = +1)$, $\hat{\mathbf{p}}\cdot(\mathbf{q}_+ + \mathbf{q}_-)$ $(CPT = -1)$, $\hat{\mathbf{p}}\cdot(\mathbf{q}_+ \times \mathbf{q}_-)\hat{\mathbf{p}}\cdot(\mathbf{q}_+ - \mathbf{q}_-)$ $(CPT = +1)$, $\hat{\mathbf{p}}\cdot(\mathbf{q}_+ + \mathbf{q}_-)\hat{\mathbf{p}}\cdot(\mathbf{q}_+ - \mathbf{q}_-)$ $(CPT = -1)$. Expectation values of the last two were suggested by Bernreuther *et al.* [11, 12] for measuring respectively the real and imaginary parts of the τ weak dipole form factor $\tilde{d}_\tau(m_Z^2)$. The suggestion has been carried out at LEP for $\mathrm{Re}\,\tilde{d}_\tau(m_Z^2)$ by the OPAL [13] and ALEPH [14] groups. OPAL looked at inclusive leptonic and hadronic decays of τ, whereas ALEPH analyzed all channels exclusively. The results obtained are the 95% confidence-level upper limits $\mathrm{Re}\,\tilde{d}_\tau(m_Z^2) < 7.0 \times 10^{-17} e$ cm (OPAL [13]) and $\mathrm{Re}\,\tilde{d}_\tau(m_Z^2) < 3.7 \times 10^{-17} e$ cm (ALEPH [14]).

The theoretical prediction for the 1 s.d. limit obtainable in the measurement of $\mathrm{Im}\,\tilde{d}_\tau(m_Z^2)$ is 10^{-16} using the correlation $\langle \hat{\mathbf{p}}\cdot(\mathbf{q}_+ + \mathbf{q}_-)\hat{\mathbf{p}}\cdot(\mathbf{q}_+ - \mathbf{q}_-)\rangle$ and a sample of 10^7 Z's [12].

3.3.2 Longitudinal beam polarization: The Stanford Linear Collider (SLC), operating presently at the Z resonance, has an e^- polarization of about 62%, and is likely to reach 75% in the future. The present sample collected is of 50,000 Z's, and the hope is to reach 5×10^5, or even 10^6 Z's.

Can this longitudinal e^- polarization help in measuring the τ weak dipole moment? The answer is "yes" [15]. In fact, as we shall see, SLC can do better than LEP so far as $\mathrm{Im}\tilde{d}_\tau$ is concerned.

The essential point is that the vector polarization of Z gets enhanced in the presence of e^+e^- longitudinal polarization. For vanishing beam polarization, $P_{e^-} = P_{e^+} = 0$, the Z vector polarization is

$$P_Z^{(0)} = \frac{2 g_{Ve} g_{Ae}}{g_{Ae}^2 + g_{Ve}^2} \approx 0.16, \tag{22}$$

where g_{Ve}, g_{Ae} are vector and axial-vector couplings of e^+e^- to Z. For non-zero polarization,

$$P_Z = \frac{P_Z^{(0)} - P_{e^+e^-}}{1 - P_Z^{(0)} P_{e^+e^-}}, \tag{23}$$

$$P_{e^+e^-} = \frac{P_{e^-} - P_{e^+}}{1 - P_{e^-}P_{e^+}}. \tag{24}$$

Thus, $P_Z \approx 0.71$ for $P_{e^-} = -.62$ and $P_{e^+} = 0$, which is an enhancement by a factor of about 4.5.

It is therefore profitable to look for CP-odd observables involving the Z spin $\mathbf{s}_Z = P_Z\hat{\mathbf{p}}$, where $\hat{\mathbf{p}}$ is the unit vector along $\mathbf{p}_+ = -\mathbf{p}_-$ in the c.m. frame. Examples of such observables are $\hat{\mathbf{p}} \cdot (\mathbf{q}_+ \times \mathbf{q}_-)$ and $\hat{\mathbf{p}} \cdot (\mathbf{q}_+ + \mathbf{q}_-)$. While both are CP odd, the former is CPT even and the latter is CPT odd.

The above is not entirely correct in principle. CP-odd correlations give a measure of underlying CP violation only if the initial state is CP even. Otherwise there may be contributions to correlations which arise from CP-invariant interactions due to the CP-odd part of the initial state. In the case when only the electron beam is polarized, the initial state is not CP even. In practice, however, this CP-even background is small because for $m_e \to 0$, only the CP-even helicity combinations $e^-_L e^+_R$ and $e^-_R e^+_L$ survive, making the corrections proportional to $m_e/m_Z \approx 5 \times 10^{-6}$. If one includes order α collinear photon emission from the initial state, which could flip the helicity of the $e^\pm$, then like-helicity e^+e^- states could also survive for vanishing electron mass [16]. However, it turns out that this being a non-resonant effect, the corresponding cross section at the Z peak is small. It is therefore expected that the correlations coming from CP-invariant SM interactions in such a case will be negligible.

The correlations $\langle O_1 \rangle \sim \langle \hat{\mathbf{p}} \cdot (\mathbf{q}_+ \times \mathbf{q}_-) \rangle$ and $\langle O_2 \rangle \sim \langle \hat{\mathbf{p}} \cdot (\mathbf{q}_+ + \mathbf{q}_-) \rangle$ have been calculated analytically for the single-pion and ρ decay mode of each τ. Also calculated analytically are $\langle O_1^2 \rangle$ and $\langle O_2^2 \rangle$ needed for obtaining the 1 s.d. limit on the measurability of $\tilde{d}_\tau$ obtained using eq.(13) [15].

The results for only the single-pion channel are summarized in tables 1a and 1b, which give, respectively for O_1 and O_2 and for electron polarizations $P_{e^-} = 0, \pm 0.62$, the correlations in units of $\tilde{d}_\tau m_Z/e$, the square root of the variance, and the 1σ limit on $\mathrm{Re}\,\tilde{d}_\tau$ and $\mathrm{Im}\,\tilde{d}_\tau$ obtainable with 10^6 Z's. The enhancement of $\langle O_{1,2} \rangle$ and hence the sensitivity of $\tilde{d}_\tau$ measurement with polarization is evident from the tables.

Table 1a Correlation of O_1, the standard deviation from SM interactions, and the 1 s.d. limit on the real and imaginary parts of the weak dipole moment, for different polarizations P_e.

P_e	$\langle O_1 \rangle$ (GeV^2) for $\mathrm{Re}\,\tilde{d}_\tau = e/m_Z$	$\sqrt{\langle O_1^2 \rangle}$ (GeV^2)	1 s.d. limit on $\mathrm{Re}\,\tilde{d}_\tau$ for 10^6 Z's (in e cm)
0	0.90	12.86	1.5×10^{-16}
+0.62	−2.89	12.86	4.6×10^{-17}
−0.62	4.01	12.86	3.3×10^{-17}

Table 1b Quantities as in table 1a, but for O_2

P_e	$\langle O_2 \rangle$ (GeV) for $\mathrm{Im}\,\tilde{d}_\tau = e/m_Z$	$\sqrt{\langle O_2^2 \rangle}$ (GeV)	1 s.d. limit on $\mathrm{Im}\,d_\tau$ for 10^6 Z's (in e cm)
0	−0.16	9.57	6.2×10^{-16}
+0.62	0.51	9.57	1.9×10^{-16}
−0.62	−0.70	9.57	1.4×10^{-16}

The sensitivity can be further improved by looking at only the P_{e^-} dependent part of the cross section. This can be done by looking at a sample corresponding to the difference in the number of events for a polarization P_{e^-} and polarization $-P_{e^-}$. The correlations are evaluated with respect to $d\sigma(P_{e^-}) - d\sigma(-P_{e^-})$. This reduces the number of events. However, correlations are enhanced by a larger factor giving a net gain in the sensitivity. The result for $P_{e^-} = .62$ and 10^6 Z's is given in table 2.

Table 2 Quantities as in table 1a, but for a distribution asymmetrized between polarizations +0.62 and −0.62.

Observable	$\langle O \rangle$ for $\lvert\tilde{d}_\tau\rvert = e/m_Z$	$\sqrt{\langle O^2 \rangle}$	1 s.d. limit on $\lvert d_\tau \rvert$ for 10^6 Z's (in e cm)
O_1	35.55 GeV^2	12.86 GeV^2	1.2×10^{-17}
O_2	−6.22 GeV	9.57 GeV	5.0×10^{-17}

The 1 s.d. limit for $\mathrm{Im}\tilde{d}_\tau$ should be compared with the LEP expectation of 10^{-16} e cm for a larger sample of 10^7 Z's [12].

The use of correlations for measuring the τ edm at the proposed τ-charm factories employing longitudinal polarization of electron and positron beams has also been studied in detail in [17].

3.3.3 Transverse beam polarization: Use of transversely polarized e^+e^- beams for the study of CP violation has been studied by several people (see for example [2, 18]). For a reaction

$$e^-(p_-, s_-) + e^+(p_+, s_+) \to f(k_+) + \overline{f}(k_-) \tag{25}$$

in the c.m. frame, where f denotes a fermion, possible T-odd triple products are $\mathbf{s}_- \cdot (\mathbf{p} \times \mathbf{k})$, $\mathbf{s}_+ \cdot (\mathbf{p} \times \mathbf{k})$, $\mathbf{p} \cdot (\mathbf{s}_- \times \mathbf{s}_+)$, $\mathbf{k} \cdot (\mathbf{s}_- \times \mathbf{s}_+)$, where $\mathbf{p}_+ = -\mathbf{p}_- = \mathbf{p}$ and $\mathbf{k}_+ = -\mathbf{k}_- = \mathbf{k}$. Of these triple products, the last two are purely CP odd, whereas only the difference of the first two is CP odd. Burgess and Robinson [18] have done an analysis of $e^+e^- \to \tau^+\tau^-, c\bar{c}, b\bar{b}$ in terms of operators

$$\mathcal{L}_Y = \frac{i}{2}\lambda_Y \left[g_1 B_{\mu\nu} \left(\bar{L}\gamma^{\mu\nu} P_R E\right) \phi\right] + H.c. \tag{27}$$

Their results for $\lambda_W = (400\,\mathrm{GeV})^{-2}$ and $L = 4.8 \times 10^5\,\mathrm{pb}^{-1}$ at LEP are given in table 3, where A is the asymmetry for $\mathbf{s}_- \cdot (\mathbf{p} \times \mathbf{k})$ given by

$$\mathcal{A} = \left[\int d\sigma(\mathbf{p}_i, \mathbf{s}_i) - \int d\sigma(-\mathbf{p}_i, -\mathbf{s}_i)\right] \mathbf{s}_- \cdot (\mathbf{p} \times \mathbf{k}). \tag{28}$$

Though this is an interesting effect, a theoretical estimate for λ_W is needed before concluding whether the effect would be observable. Assuming a systematic error of 0.1%, the 2-σ limits possible on λ_W are estimated to be $(570\ \mathrm{GeV})^{-2}$ and $(660\ \mathrm{GeV})^{-2}$ respectively for up- and down-type quarks.

Table 3 The transverse polarization asymmetry $\mathcal{A}$ (defined in the text) compared with the standard model events for $e^+e^- \to \tau^+\tau^-, c\bar{c}, b\bar{b}$.

	$\tau^+\tau^-$	$c\bar{c}$	$b\bar{b}$
N (SM events)$\times 10^{-8}$	6.5	24	31
$\mathcal{A} \times 10^{-5}$	−6.1	97	−170
$\mathcal{A}/N \times 10^3$	0.9	4.0	5.5

4. CP violation in top pair production

Evidence for a top quark of mass of about 174 GeV at the Tevatron has been reported by the CDF collaboration [19]. Even though the data is not conclusive, it is generally believed that the top quark will eventually be found with a mass of a similar magnitude. Top-antitop pairs can then be produced at large rates at future colliders and used for various studies. In particular, since a heavy top ($m_t > 120$ GeV) decays before it hadronizes [20], information about its polarization is preserved in its decay products. Schmidt and Peskin [21] have suggested (elaborating on an old suggestion of Donoghue and Valencia [22]) looking for the asymmetry between $t_L\bar{t}_L$ and $t_R\bar{t}_R$ as a signal for CP violation (see also [23]). Note that this is possible only for a heavy particle like the top quark because for a light particle, the dominant helicity combination would be $t_L\bar{t}_R$ or $t_R\bar{t}_L$, each being self-conjugate.

The asymmetry $N(t_L\bar{t}_L) - N(t_R\bar{t}_R)$ can be probed through the energy spectra of prompt leptons from $t \to Wb$; $W \to l\nu$. This is understood as follows.

For a heavy top, the dominant W helicity in $t \to Wb$ is 0. Now, due to $V - A$ interaction, b is produced with left-handed helicity (neglecting the b mass). Hence in the t rest frame, W^+ momentum is dominantly along the t spin direction. It follows that l^+ in W^+ decay is produced preferentially in the direction of the t spin. In fact, the distribution is $1 + \cos\psi$, where ψ is the angle between the l^+ momentum direction and the t spin direction. In going to the laboratory frame, the t gets boosted. Thus l^+ from t_R is more energetic than l^+ from t_L, and l^- from $\bar{t}_L$

has more energy than l^- from $\bar{t}_R$. Therefore, in the decay of $t_L\bar{t}_L$, l^- from $\bar{t}_L$ has higher energy than l^+ from t_L, and the reverse is true for $t_R\bar{t}_R$. Thus the energy asymmetry of leptons measures $N(t_L\bar{t}_L) - N(t_R\bar{t}_R)$.

Schmidt and Peskin [21] looked at this asymmetry in hadron collisions in a CP-violating multi-Higgs model where the CP violation is described by the Lagrangian terms

$$\delta\mathcal{L} = -\frac{m_t}{v}\phi\bar{t}\,[AP_L + A^* P_R]\,t, \tag{29}$$

where only the effect of the dominant lightest Higgs field ϕ is kept. v is the SM Higgs vacuum expectation value, and A is a complex combination of mixing angles and phases.

Since $N(t_L\bar{t}_L) - N(t_R\bar{t}_R)$ is CP odd and T even, the CPT theorem requires the existence of an absorptive part for it to be non-zero. Looking at the tree and one-loop diagrams for $q\bar{q} \leftrightarrow t\bar{t}$, they conclude that

$$\mathcal{A} = \frac{N(t_L\bar{t}_L) - N(t_R\bar{t}_R)}{N(t_L\bar{t}_L) + N(t_R\bar{t}_R)} \approx 10^{-3} \tag{30}$$

for $m_t = 150$ GeV, $m_\phi = 100$–400 GeV and $\mathrm{Im}[A^2] = \sqrt{2}$. Thus the asymmetry $\mathcal{A}$ would be observable with 10^8 $t\bar{t}$ a year.

For pp collisions, since the pp state is not a CP eigenstate, there is also a CP-invariant contribution present, but this is shown to be small [21].

As in the case of pp or $p\bar{p}$ collisions, lepton energy asymmetry can be used to measure CP violation in $e^+e^- \to t\bar{t}$ [24]. The authors of ref.[24] also consider another asymmetry, viz., the up-down asymmetry of the charged leptons with respect to the $t\bar{t}$ production plane in the laboratory frame. It is also possible to construct a "left-right" asymmetry of leptons with respect to a plane perpendicular to the $t\bar{t}$ production plane, but containing the $t\bar{t}$ momentum direction [25]. Certain combinations of up-down and left-right symmetry with forward-backward asymmetry can also be considered. All these probe different combinations of CP-violating couplings [25].

The result of ref.[24] is that asymmetry is at the few per cent level for the top-quark electric and weak dipole moments $d_t, \tilde{d}_t \sim e/m_t$. For $\sqrt{s} = 300$ GeV and $m_t = 120$ GeV, $\sigma \approx 1400$ fb, which corresponds to 20,000 prompt leptons a year for a luminosity of 10^{33} cm^{-2}s^{-1}. In such a case, $d_t, \tilde{d}_t$ can be determined to a few percent level. This should be compared with the prediction of $10^{-2} - 10^{-3}$ from the Higgs model for CP violation.

Apart from the above asymmetries, CP-odd correlations could provide a measure of CP violation in $t\bar{t}$ production [26]. Certain correlations are more sensitive to CP violation in t decay, rather than production [26].

Another process which has been suggested is $e^+e^- \to t\bar{t}\nu\bar{\nu}$ through $W^+W^- \to t\bar{t}$ [4]. Two diagrams contribute to $W^+W^- \to t\bar{t}$, one corresponding to t-channel b exchange and the other with an s-channel heavy Higgs ϕ, which can be on shell for $m_\phi > 2m_t$. Then, the absorptive part needed for a CP-odd CPT-odd asymmetry is provided by the width of the Higgs. A sizable asymmetry can be obtained thus [4].

dipole moments independently [25, 27]

5. CP violation in other processes

The process $e^+e^- \to W^+W^-$, which will be studied in the near future at LEP200, will be the first one to be able to test the SM couplings of the electroweak gauge bosons. The process is expected to put bounds on non-standard γ and Z couplings to W^+W^-. The non-standard couplings could be CP violating ones, as in (2). These can be studied in a way similar to the one used for probing CP violation in $e^+e^- \to \tau^+\tau^-$ and $e^+e^- \to t\bar{t}$ considered earlier. As in the case of $e^+e^- \to t\bar{t}$ with leptonic $t, \bar{t}$ decays, energy or up-down asymmetry of leptons may be used [28, 29]. Whereas Chang *et al.* [28] consider asymmetries, Mani *et al* [29] gave estimated the energy correlation ratio

$$A = \frac{\langle E_- \rangle - \langle E_+ \rangle}{\langle E_- \rangle + \langle E_+ \rangle},$$

and suggest the angular correlation ratio

$$\delta = \frac{\langle \theta_- \rangle - \langle \theta_+ \rangle}{\langle \theta_- \rangle + \langle \theta_+ \rangle},$$

where $E_\pm$ are the energies of the leptons $l^\pm$ produced in the decay of $W^\pm$, and $\theta_\pm$ are the angles of $l^\pm$ momenta with respect to the e^+ beam direction. The general expectation is $A \approx 10^{-3}$ for $\tilde{\kappa}$ or $\tilde{\lambda} \approx 0.1$.

Some other processes considered in the literature are $t, \bar{t}$ decay asymmetries in $\phi \to t\bar{t}$, where ϕ is a heavy Higgs [30], decay lepton asymmetries in $e^+e^- \to \tilde{\chi}\tilde{\chi}$, where $\tilde{\chi}$ is a neutralino in the minimal supersymmetric standard model [31], decay correlations in $\gamma\gamma \to W^+W^-$ [32], and forward-backward asymmetry in $e^+e^- \to \gamma Z$ [33].

6. Conclusions

We have seen above the various points to be kept in mind when selecting processes and variables for detecting and measuring CP violation, a number of processes and scenarios of CP-violating signatures which could be looked for. The above discussion is mainly aimed at arriving at an idea of the sensitivities possible in different measurements. In general, the results in most popular models of CP violation beyond SM indicate that CP violation in the most optimistic theoretical scenario would be measurable only with some difficulty in the existing or presently envisaged experiments. Nevertheless, it would be good to keep one's eyes open to these possibilities.

References

[1] M.J. Booth, Chicago preprint EFI-93-1 (1993).

[2] F. Hoogeveen and L. Stodolsky, Phys. Lett. B **212**, 505 (1988).

[3] A. Pilaftsis, Z. Phys. C **47**, 95 (1990); M. Nowakowski and A. Pilaftsis, Mod. Phys. Lett. A **6**, 1933 (1991); A.S. Joshipura and S.D. Rindani, Pramana – J. Phys. **38**, 469 (1992), Phys. Rev. D **46**, 3008 (1992); G. Eilam, J.L. Hewett and A. Soni, Phys. Rev. Lett. **67**, 1979 (1991), **68**, 2103 (1992).

[4] A. Pilaftsis and M. Nowakowski, Int. J. Mod. Phys. A **9**, 1097 (1994).

[5] L. Wolfenstein, Phys. Rev. D **43**, 151 (1991); J.M. Soares, Phys. Rev. Lett. **68**, 2102 (1992).

[6] T. Arens and L.M. Sehgal, Aachen preprint PITHA 94/19 (1994).

[7] D. Choudhury, A.S. Joshipura and S.D. Rindani, Phys. Rev. Lett. **67**, 548 (1991).

[8] N. Rius and J.W.F. Valle, Phys. Lett. B **246**, 249 (1990).

[9] W. Bernreuther *et al.*, Z. Phys. C **43**, 117 (1989).

[10] S. Goozovat and C.A. Nelson, Phys. Lett. B **267**, 128 (1991); G. Couture, Phys. Lett. B **272**, 404 (1991); W. Bernreuther and O. Nachtmann, Phys. Rev. Lett. **63**, 2787 (1989).

[11] W. Bernreuther *et al.*, Z. Phys. C **52**, 567 (1991).

[12] W. Bernreuther, O. Nachtmann and P. Overmann, Phys. Rev. D **48**, 78 (1993).

[13] OPAL Collaboration, P.D. Acton *et al.*, Phys. Lett. B **281**, 405 (1992).

[14] ALEPH Collaboration, D. Buskulic *et al.*, Phys. Lett. B **297**, 459 (1992).

[15] B. Ananthanarayan and S.D. Rindani, Phys. Rev. Lett. **73**, 1215 (1994); Phys. Rev. D **50**, 4447 (1994).

[16] I thank Prof. L.M. Sehgal for drawing my attention to this fact.

[17] B. Ananthanarayan and S.D. Rindani, PRL preprint PRL-TH-94/32 (1994).

[18] C.P. Burgess and J.A. Robinson, Mod. Phys. Lett. A **6**, 2707 (1992)

[19] CDF Collaboration, F. Abe *et al.*, Phys. Rev. Lett. **73**, 225 (1994); Phys. Rev. D (to appear).

[20] I. Bigi and H. Krasemann, Z. Phys. C **7**, 127 (1981); J. Kühn, Acta Phys. Austr. Suppl. XXIV, 203 (1982); I. Bigi *et al.*, Phys. Lett. B **181**, 157 (1986).

[21] C.R. Schmidt and M.E. Peskin, Phys. Rev. Lett. **69**, 410 (1992).

[22] J.F. Donoghue and G. Valencia, Phys. Rev. Lett. **58**, 451 (1987).

[23] G.L. Kane, G.A. Ladinsky and C.-P. Yuan, Phys. Rev. D **45**, 124 (1991).

[24] D. Chang, W.-Y. Keung and I. Phillips, Nucl. Phys. B **408**, 208 (1993).

[25] P. Poulose and S.D. Rindani, PRL preprint PRL-TH-94/31 (1994).

[26] W. Bernreuther, T. Schröder and T.N. Pham, Phys. Lett. B **279**, 389 (1992); W. Bernreuther and P. Overmann, Nucl. Phys. B **388**, 53 (1992), Heidelberg preprint HD-THEP-93-11 (1993); W. Bernreuther and A. Brandenburg, Phys. Lett. B **314**, 104 (1993); J.P. Ma and A. Brandenburg, Z. Phys. C **56**, 97 (1992); A. Brandenburg and J.P. Ma, Phys. Lett. B **298**, 211 (1993).

[27] F. Cuypers and S.D. Rindani, MPI-PhT/94-54, PRL-TH-94/24 (to appear in Phys. Lett. B).

[28] D. Chang, W.-Y. Keung and I. Phillips, Phys. Rev. D , (1993).

[30] A. Soni and R.M. Xu, Phys. Rev. Lett. **69**, 33 (1992); D. Chang, W.-Y and I. Phillips, Phys. Rev. D **48**, 3225 (1993), Phys. Lett. B **305**, 261 (1 Ilakovac, B.A. Kniehl and A. Pilaftsis, Phys. Lett. B **317**, 609 (1993).

[31] Y. Kizukuri and N. Oshimo, preprint IFM 8/93, TKU-HEP 93/05 (1993).

[32] J.P. Ma and B.H.J. McKellar, Phys. Lett. B **319**, 533 (1993).

[33] D. Choudhury and S.D. Rindani, Phys. Lett. B **335**, 198 (1994).

Structure functions and parton distributions

R G ROBERTS
Rutherford Appleton Laboratory, Chilton,
Didcot OX11 0QX, England

Abstract. We review recent developments in the determination of parton densities from deep inelastic and related data. We show how the asymmetries observed in the $W^{\pm}$ rapidity distributions and in pp/pn Drell-Yan production further constrain the partons at moderate x.

1. Introduction

An idea of the rapid improvement in our knowledge of the structure function, $F_2(x,Q^2)$, of deep inelastic electron (or muon)-proton scattering can be glimpsed from the data shown in Fig. 1. In fact it should not be too long before we have precision measurements (perhaps as good as $\pm 5\%$) of F_2 at HERA almost down to $x \sim 10^{-4}$. The data show a dramatic rise of F_2 with decreasing x, which some optimists had anticipated might occur from the precocious onset of the leading $\alpha_s \log(1/x)$ resummation of soft gluon emissions.

The curves marked D'_- and D'_0 are simply two extrapolations obtained from parton fits to the fixed target data, which at the time it was thought might span the subsequent measurements of F_2 at HERA – one represents the upper limit expected for the precocious resummation behaviour, the other the lower limit of conventional (Regge-motivated) expectations. Such extrapolations are notoriously unreliable.

Section 2 is mainly devoted to recent developments in the determination of partons in the $x \gtrsim 10^{-2}$ region. For the purposes of illustration we mainly concentrate on the MRS analyses. In Section 3 we discuss the description of F_2^{ep} at small x and find that both GLAP-based extrapolations and BFKL-based predictions have sufficient freedom to describe the HERA data.

2. Recent developments in the determination of parton densities

There is a long history of determining parton distributions from deep inelastic scattering and related data. The increased precision in the experimental measurements over the last couple of years has led to a considerable improvement in our knowledge of the partons, at least for $x \gtrsim 0.01$. The recent experiments are listed in Table 1, together with the leading order partonic subprocess, which help us to see which partons are constrained by the various processes. In particular it is useful to note

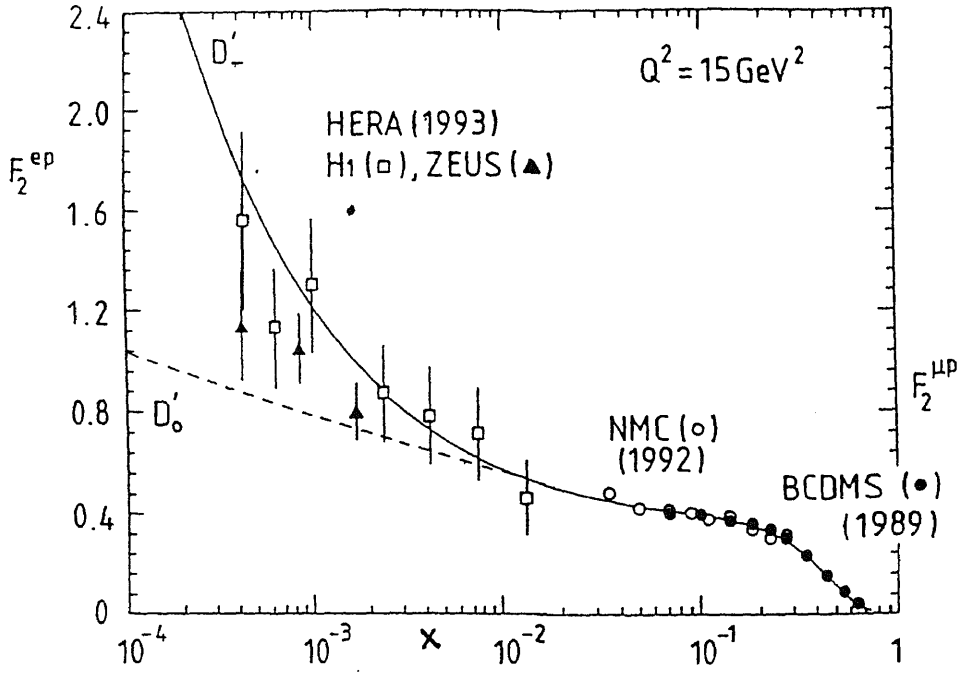

Figure 1. The x dependence of the structure function $F_2(x,Q^2)$ at $Q^2 = 15$ GeV^2. The data are from the BCDMS [1], NMC [2], H1 [3] and ZEUS [4] collaborations. The curves are calculated from the MRS(D'_0,D'_-) sets of partons [5].

that the four deep-inelastic structure functions can, to leading order, be expressed in terms of parton densities in the form

$$F_2^{\mu p} - F_2^{\mu n} = \tfrac{1}{3}x(u + \bar{u} - d - \bar{d}) \quad (1)$$

$$\tfrac{1}{2}(F_2^{\mu p} + F_2^{\mu n}) = \tfrac{5}{18}x(u + \bar{u} + d + \bar{d} + \tfrac{4}{5}s) \quad (2)$$

$$F_2^{\nu N} = F_2^{\bar{\nu} N} = x(u + \bar{u} + d + \bar{d} + 2s) \quad (3)$$

$$\tfrac{1}{2}x(F_3^{\nu N} + F_3^{\bar{\nu} N}) = x(u - \bar{u} + d - \bar{d}) \quad (4)$$

where N is an isoscalar nuclear target. We have included the s quark (and assumed [5] that $s = \bar{s}$), but neglected the small c quark contribution. These four observables, $F_i(x,Q^2)$, measured in the fixed-target ($\mu N \to \mu X$ and $\nu N \to \mu X$) deep-inelastic experiments, do not on their own determine the five distributions u, d, $\bar{u}$, $\bar{d}$ and s, but only four combinations, which we may take to be $u + \bar{u}$, $d + \bar{d}$, $\bar{u} + \bar{d}$ and s. The difference $\bar{d} - \bar{u}$ is not determined, and, moreover, at leading order it appears that the only constraint on the gluon is through the momentum sum rule. In practice the situation is worse. From (2) and (3) we see that the strange quark distribution is essentially determined by the structure function difference

$$xs(x) \simeq \tfrac{5}{6}F_2^{\nu N}(x) - 3F_2^{\mu D}(x) \quad (5)$$

which is sensitive to the relative normalization of the two data sets and to heavy target corrections to the neutrino measurements. However, we see from Table 1 that valuable independent information comes from other processes: (i) the gluon is constrained by prompt photon production, where $g(x)$ enters to leading order, (ii)

the strange sea is measured by neutrino-induced dimuon production (see Fig. 2), and (iii) there is a measurement of the difference $\bar{d} - \bar{u}$, which was released for the first time at this conference, from the observed asymmetry of Drell-Yan production in pp and pn collisions (see subsection (c)).

(a) MRS global analysis

Here we describe the MRS determination [6] of the parton densities, $f_i(x, Q^2)$, from a global analysis of the data, which was performed before the HERA measurements of F_2^{ep} became available. Only deep inelastic data with $Q^2 > 5$ GeV^2 (and $W^2 > 10$ GeV^2) were used. The input distributions at $Q_0^2 = 4$ GeV^2 were parametrized in the form

$$x f_i(x, Q_0^2) \;=\; A_i x^{-\lambda_i}(1-x)^{\beta_i}(1+\gamma_i x^{\frac{1}{2}} + \delta_i x) \tag{6}$$

for $i =$ the valence quarks u_v, d_v, the sea S, and the gluon g. Three of the four A_i's are determined by the momentum and flavour sum rules. Since, pre-HERA, there were no data for $x < 10^{-2}$, we imposed two different extrapolations of the gluon and sea quark distributions to small x (with the expectation that they should span the forthcoming HERA measurements). To be precise for the gluon and sea quarks we choose

$$\begin{aligned} \lambda_i &\equiv 0 \quad \text{for the } \mathrm{D}_0' \text{ set} \\ \lambda_i &\equiv 0.5 \quad \text{for the } \mathrm{D}_-' \text{ set} \end{aligned} \tag{7}$$

where, since $\sigma(\gamma^* p) \sim s^{\lambda_i}$, the first choice corresponds to conventional Pomeron exchange leading to constant total cross sections, and the second is motivated by the small x behaviour expected from the BFKL (Balitsky, Fadin, Kuraev, Lipatov) equation [7]. The β_i and the valence λ_i are left as free parameters although we have some idea what values will be physically reasonable. First, the small x behaviour anticipated from meson Regge exchanges for the valence quark distributions would correspond to $\lambda_v \sim -0.5$. Secondly, naive counting rule arguments imply that $x f_i \sim (1-x)^{2n-1}$ as $x \to 1$, where n is the minimum number of spectator quarks which accompany the struck parton. This rule would suggest $\beta_i \sim 5$, 3 and 7 for, respectively, the gluon, valence and sea quark distributions.

In the MRS analysis the flavour structure of the quark sea S at $Q_0^2 = 4$ GeV^2 is taken to be

$$\begin{aligned} 2\bar{u} &= 0.4S - \Delta \\ 2\bar{d} &= 0.4S + \Delta \\ 2\bar{s} &= 0.2S \\ x\Delta &\equiv x(\bar{d} - \bar{u}) = A_\Delta x^{-\lambda_\Delta}(1-x)^{\eta_S}. \end{aligned} \tag{8}$$

As mentioned before, the most reliable method to estimate the strength of the strange sea distribution $\bar{s}(x, Q^2)$ is to observe deep-inelastic dimuon production, $\nu N \to \mu^- \mu^+ X$, for which the dominant subprocess is $\nu s \to \mu^- + c(\to \mu^+)$. Early dimuon data were the motivation of the 50% suppression of the input strange sea

Table 1 The experimental data used to determine the MRS parton distributions. T last column gives an indication of the main type of constraint imposed by a part ular set of data.

Process/ Experiment	Leading order subprocess	Parton determination
DIS $(\mu N \to \mu X)$ BCDMS, NMC $F_2^{\mu p}, F_2^{\mu n}$	$\gamma^* q \to q$	Four structure functions → $u+\bar{u}$ $d+\bar{d}$ $\bar{u}+\bar{d}$
DIS $(\nu N \to \mu X)$ CCFR (CDHSW) $F_2^{\nu N}, xF_3^{\nu N}$	$W^* q \to q'$	s (assumed $= \bar{s}$), but only $\int xg(x)dx \simeq 0.5$ $[\bar{u} - \bar{d}$ is not determined]
$\nu N \to \mu^+\mu^- X$ CCFR	$\nu s \to \mu^- c$ $\hookrightarrow \mu^+$	$s \approx \frac{1}{2}\bar{u}$ (or $\frac{1}{2}\bar{d}$)
DIS (HERA) F_2^{ep} (H1,ZEUS)	$\gamma^* q \to q$	λ $(x\bar{q} \sim xg \sim x^{-\lambda}$, via $g \to q\bar{q})$
$pp \to \gamma X$ WA70 (UA6)	$qg \to \gamma q$	$g(x \approx 0.4)$
$pN \to \mu^+\mu^- X$ E605	$q\bar{q} \to \gamma^*$	$\bar{q} = ...(1-x)^{\eta s}$
$pp, pn \to \mu^+\mu^- X$ NA51	$u\bar{u}, d\bar{d} \to \gamma^*$ $u\bar{d}, d\bar{u} \to \gamma^*$	$(\bar{u} - \bar{d})$ at $x = 0.18$
$pp \to WX(ZX)$ UA2, CDF, D0	$ud \to W$	u, d at $x_1 x_2 s \simeq M_W^2 \to$ $x \approx 0.13$ CERN $x \approx 0.05$ FNAL
$\to W^{\pm}$ asym CDF		slope of u/d at $x \approx 0.05$

excellent agreement with their results (see Fig. 2) and moreover CCFR find that the ratio $\bar{s}/(\bar{u}+\bar{d})$ is essentially independent of x. It has been emphasized [9] that the strange sea as measured in neutrino scattering should be different from that in muon scattering on account of the different mass thresholds in $W^*g \to s\bar{c}$ versus $\gamma^*g \to s\bar{s}$. In practice the neutrino data have been corrected by CCFR to approximately take into account the $m_c \neq 0$ effects and allow for this difference.

The first evidence that $\bar{d} \neq \bar{u}$, and hence the need to introduce Δ in (8), came from the NMC study of the Gottfried sum rule [10]. We return to discuss this later. Finally, the heavy quark contributions are determined by assuming that

$$\bar{Q} = 0 \quad \text{for} \quad Q^2 \leq 4m_Q^2 \qquad \text{with} \quad Q = c, b, ..., \tag{9}$$

and by generating non-zero distributions at higher Q^2, via $g \to Q\bar{Q}$, using QCD evolution with $m_Q = 0$. Near threshold clearly this prescription is unreliable, but it has been shown to give reasonable results at higher Q^2 [11]. The charm quark distribution in the proton has attracted much attention but the phenomenological situation is far from clear.

The input distributions (6) and (8) are evolved up in Q^2 using next-to-leading order GLAP or Altarelli-Parisi equations [13] and fitted to deep-inelastic structure functions (with $Q^2 > 5$ GeV^2 and $W^2 > 10$ GeV^2) and related data. The distributions are defined in the $\overline{\text{MS}}$ renormalization and mass factorization scheme. The fitted value of the QCD scale parameter is $\Lambda_{\overline{\text{MS}}}(n_f = 4) = 230$ MeV (that is $\alpha_s(M_Z^2) = 0.112_5$), which is consistent with the values $\alpha_s = 0.113$ and 0.111 found by analyses of BCDMS [14] and CCFR [15] subsets of the overall data.

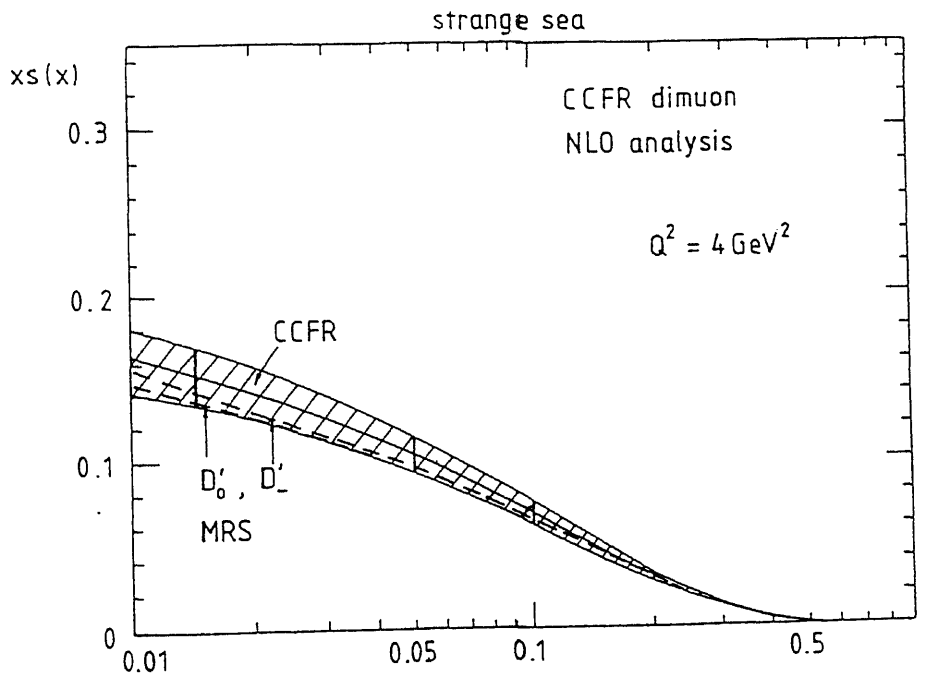

Figure 2. The shaded band shows the strange quark distribution extracted by CCFR from their dimuon data [7], together with the MRS distributions of ref. [5].

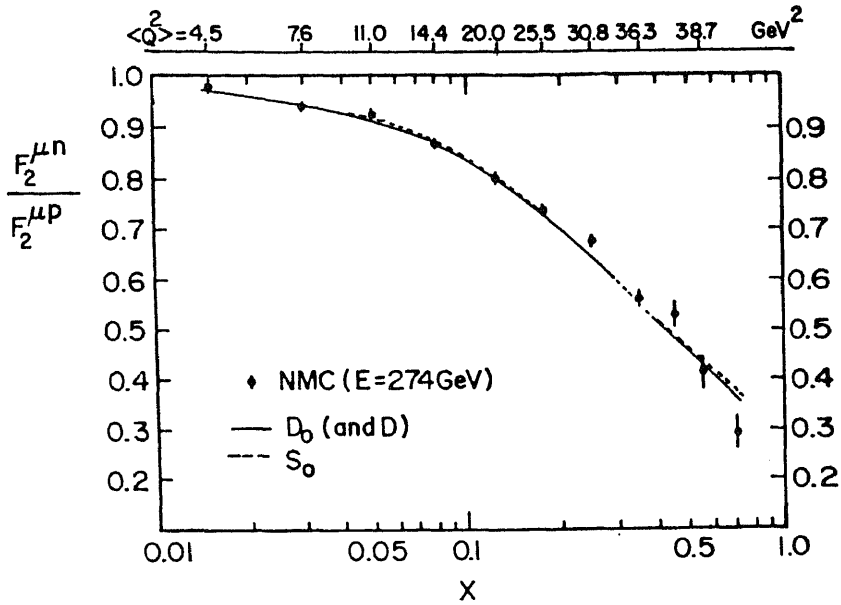

Figure 3. The description of the NMC data [2] for the structure function ratio $F_2^{\mu n}/F_2^{\mu p}$ given by the MRS partons of ref. [5].

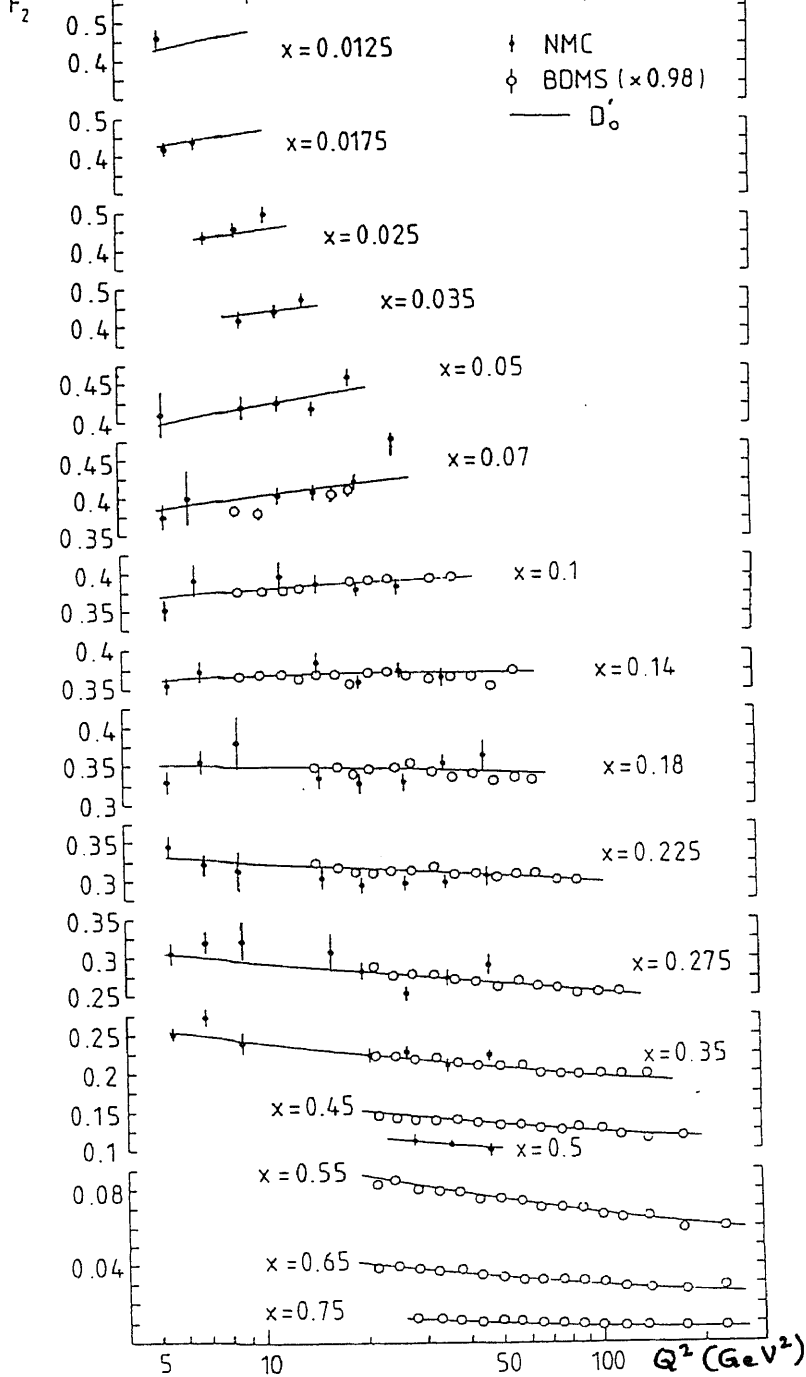

Figure 4. The BCDMS [1] and NMC [2] measurements of $F_2^{\mu p}$, together with the MRS fit [5].

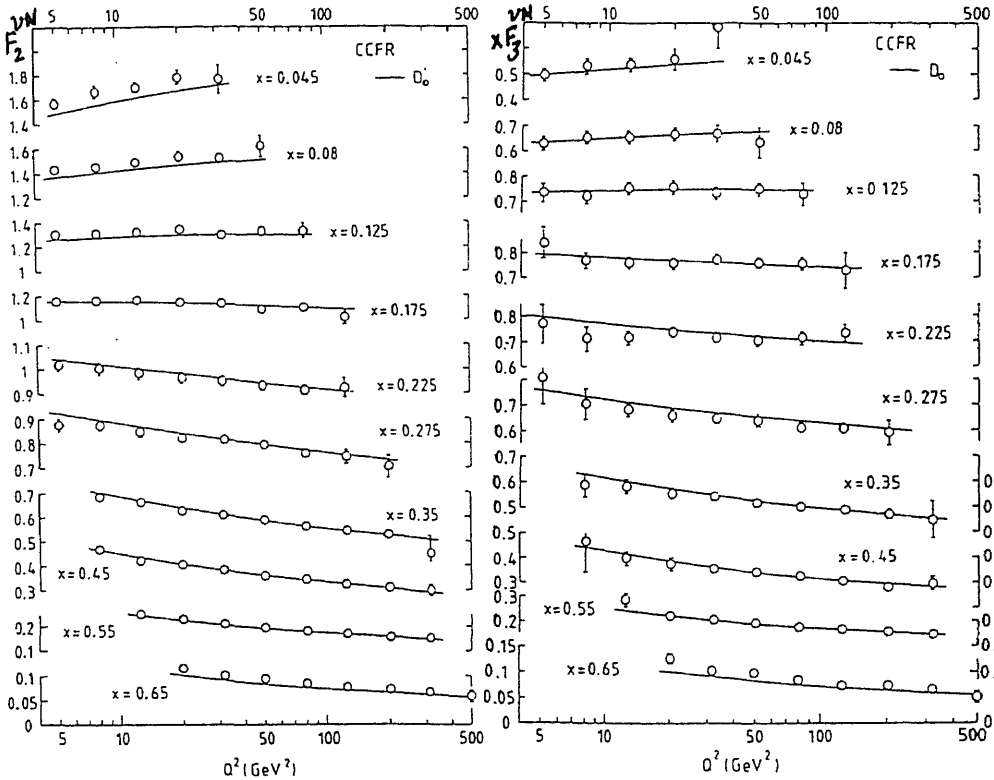

Figure 5. The continuous curves show the description of the CCFR [14] measurements of $F_2^{\nu N}(x, Q^2)$ and $xF_3^{\nu N}(x, Q^2)$ by the MRS(D_0') set of partons [5]. The data are shown after correction for the heavy target effects and after the overall renormalization of 0.95 required by the global fit.

Figs. 3-5 show the high precision of recent deep-inelastic structure function measurements, as well as the quality of the fit. Accurate data exist also for related processes and are equally well described. This should mean that the parton distributions are well determined, at least in the x range $0.02 \lesssim x \lesssim 0.7$ where data are available for a full range of different processes. At smaller x, $x \lesssim 10^{-3}$, the measurements of F_2^{ep} at HERA give information on the x behaviour of the quark sea. We will discuss the expectations of the small x behaviour in some detail later. For the moment we simply note that it is possible to 'tune' the exponent λ_i of the input sea and gluon distributions of (6) to obtain the best global fit to a data set which now includes the new HERA measurements of F_2 [3, 4]. The result, set MRS(H) of partons [16], has $\lambda_i = 0.3$.

Before turning to a theoretical discussion of the small x region, we must mention two recent measurements which impose valuable new constraints on the partons in the $x \gtrsim 0.02$ region. The first is the measurement of the rapidity asymmetry of $W^{\pm}$ bosons produced in $p\bar{p}$ collisions and the second is the Drell-Yan asymmetry observed in pp and pn collisions.

(b) $W^{\pm}$ rapidity asymmetry

$W^{\pm}$ bosons produced in $\bar{p}p$ collisions have different rapidity (y_W) distributions. A comparison of parton distributions shows that the u quark in the proton tends to go more forward than the d quark, so that the W^+ is produced preferentially in the direction of the incident proton, while the W^- tends to go in the direction of the antiproton. Thus we anticipate that the asymmetry

$$A_W(y_W) = \frac{\sigma(W^+) - \sigma(W^-)}{\sigma(W^+) + \sigma(W^-)} \tag{10}$$

will be positive and increase with the rapidity y_W of the produced $W^{\pm}$ bosons. It turns out that the asymmetry A_W is correlated with the slope of F_2^n/F_2^p in the $x \simeq M_W^2/\sqrt{s}$ region [17] – larger slopes tend to imply greater asymmetry. In practice it is the rapidity asymmetry of the $\ell^{\pm}$ decay leptons which is observed

$$A(y_\ell) = \frac{\sigma(\ell^+) - \sigma(\ell^-)}{\sigma(\ell^+) + \sigma(\ell^-)}. \tag{11}$$

Folding in the $W \to \ell\nu$ decay dilutes the asymmetry, but the measurements shown in Fig. 6 indicate that it is still sizeable. The present data favour the recent MRS rather than the CTEQ parton sets. As the experimental precision increases we see that there is a great potential for the asymmetry to further discriminate between parton sets – indeed these data should be included in future global analyses from the beginning.

(c) $\bar{d} - \bar{u}$ and the Drell-Yan asymmetry

Inspection of the leading order expressions (1)-(4) shows that measurement of the four independent deep-inelastic structure functions do not determine $\bar{d} - \bar{u}$ on a (x, Q^2) point-by-point basis. The difference $\bar{d} - \bar{u}$ is only constrained if the form of the x dependence of partons is assumed. Indeed prior to 1992 all global analyses set $\bar{u} = \bar{d}$. The first hint that $\bar{u} \neq \bar{d}$ came from an NMC study [21] of the Gottfried

sum rule. NMC found that their data gave

$$\int_{0.004}^{0.8} \frac{dx}{x}(F_2^{\mu p} - F_2^{\mu n}) \;=\; 0.227 \pm 0.007(\text{stat.}) \pm 0.014(\text{sys.})$$

at $Q^2 = 4\ \text{GeV}^2$, as compared to the Gottfried sum

$$I_{\text{GSR}} \;=\; \int_0^1 \frac{dx}{x}(F_2^{\mu p} - F_2^{\mu n}) \;=\; \tfrac{1}{3}\int_0^1 dx(u_v - d_v) + \tfrac{2}{3}\int_0^1 dx(\bar{u} - \bar{d})$$

$$= \tfrac{1}{3} \qquad \text{if} \quad \bar{u} = \bar{d}. \tag{12}$$

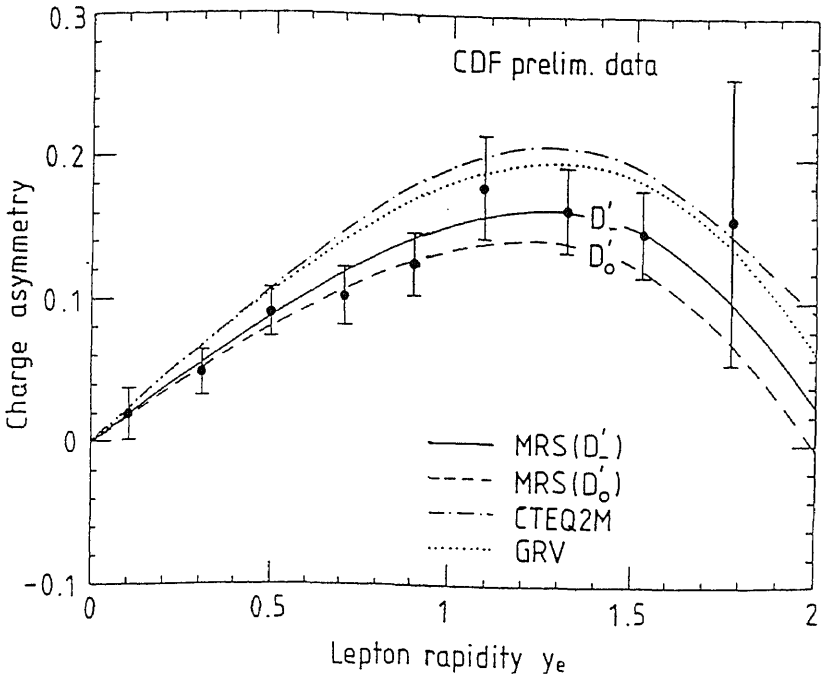

Figure 6. A plot of the CDF data for the lepton charge asymmetry, (11), compared to the predictions of various sets of partons [5, 18, 19]. The plot is taken from ref. [16]. These data were fitted in the MRS(A) analysis [20] which gives a description essentially equal to that of MRS(D'_).

Using their data to extrapolate over the unmeasured regions of x, NMC obtained $I_{\text{GSR}} = 0.240 \pm 0.016$ [21] [22]. The most plausible explanation of the difference between the NMC value and the Gottfried sum of $\frac{1}{3}$ is that $\bar{d} > \bar{u}$. In the MRS 'D' fits $\bar{d} - \bar{u}$ is parametrized according to (8) with the parameter A_Δ chosen to reproduce the measured value of I_{GSR}. It is interesting to note, however, that even including the NMC data, it is still possible to maintain $\bar{u} = \bar{d}$ and obtain an equally good global description of the data, but at the expense of a contrived small x behaviour of the valence distributions, as in set S_0' of ref. [6]. The comparison of the $(F_2^p - F_2^n)$ NMC data with S_0' and D_0' is shown in Fig. 7 – the area under the curves gives $I_{\text{GSR}} = 0.333$ and 0.256 respectively, the difference coming primarily from the unmeasured $x \lesssim 10^{-2}$ region. The most physical assumption is to allow

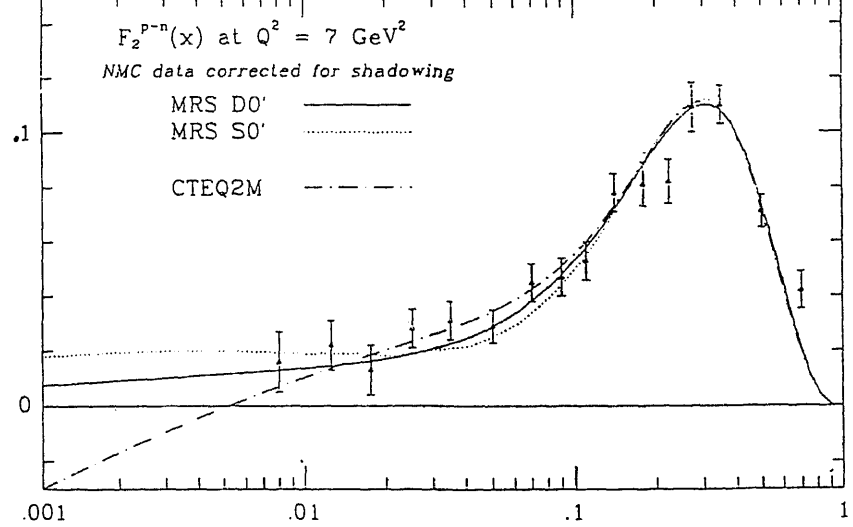

Figure 7. The structure function difference $F_2^{\mu p} - F_2^{\mu n}$ measured by NMC [22] compared with the description by partons from refs. [5, 18].

$\bar{u} \neq \bar{d}$, as in the 'D'-type fits. Nevertheless the conclusion is that the detailed structure of $\bar{d} - \bar{u}$ is not determined by the available deep-inelastic data.

As the $W^{\pm}$ rapidity asymmetry measurements improve they become increasingly sensitive to the behaviour of $\bar{u}$ and $\bar{d}$ in the region $x \simeq M_W^2/\sqrt{s}$. However a more direct method [24] to obtain information on $\bar{d} - \bar{u}$ is to compare (Drell-Yan) lepton-pair production in pp and pn collisions, via the asymmetry

$$A_{\rm DY} = \frac{\sigma_{pp} - \sigma_{pn}}{\sigma_{pp} + \sigma_{pn}}. \tag{13}$$

Because $u > d$ in the proton, the asymmetry $A_{\rm DY}$ is positive for parton sets with $\bar{d} - \bar{u}$ zero or small, but $A_{\rm DY}$ is reduced and can even be negative for parton sets with larger $\bar{d} - \bar{u}$ [25]. An asymmetry measurement by the NA51 collaboration [26],

$$A_{\rm DY} = -0.09 \pm 0.02 \pm 0.02 \tag{14}$$

at $x = 0.18$, was announced at this conference. This result, which implies $\bar{u}/\bar{d} \simeq 0.5$ at $x = 0.18$, corresponds to a breaking of flavour symmetry considerably beyond that associated with the MRS(D_0',D_-') partons and almost as large as that calculated using CTEQ2M partons, see Fig. 8.

We may conclude that, as far as the asymmetries are concerned, the MRS partons accurately reproduce the $W^{\pm}$ rapidity asymmetry (Fig. 6) but do not describe the new Drell-Yan asymmetry measurement. On the other hand the CTEQ partons describe the $W^{\pm}$ asymmetry rather poorly, but offer a much better description of the Drell-Yan asymmetry.

(d) Present status of parton distributions

We noticed that the high precision deep-inelastic data are well described by the parton distributions but that they do not pin down the $\bar{d} - \bar{u}$ combination. However

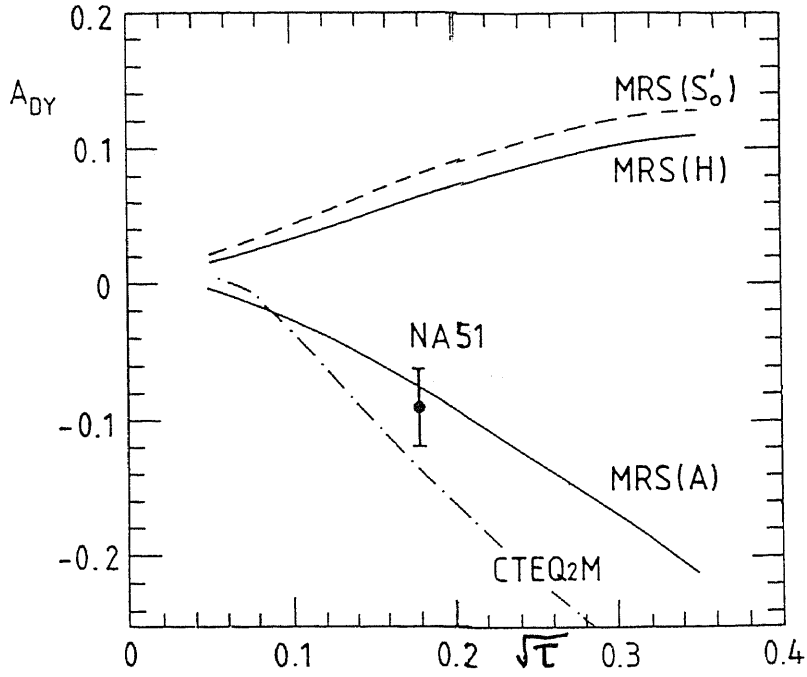

Figure 8. The *pp/pn* Drell-Yan asymmetry of (13) measured by NA51 [25] compared to values obtained by various sets of partons [5, 15, 20, 18]. The data point was included in the MRS(A) analysis [20].

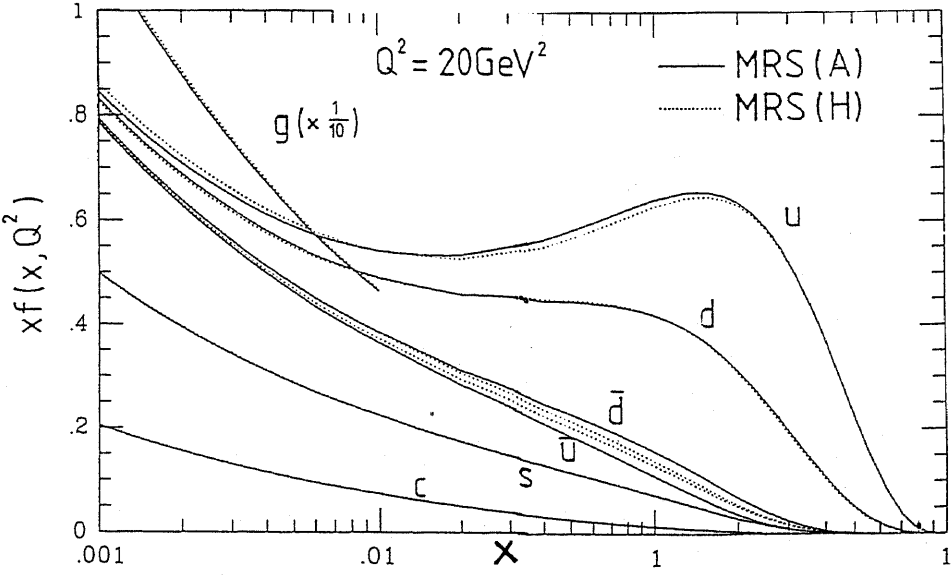

Figure 9. The MRS(A) [20] and MRS(H) [15] parton distributions at $Q^2 = 20$ GeV^2 shown by continuous and dotted curves respectively. Unlike MRS(H), MRS(A) incorpo-

other measurements give independent information on the partons. In particular the new asymmetry measurements probe fine details of the quark distributions.

Can we use the residual freedom of $\bar{d}-\bar{u}$ to modify the MRS(H) set of partons so as to describe the new Drell-Yan asymmetry measurement [26] while maintaining the quality of the global fit to the data? In particular can we maintain the quality of the description of the $W^{\pm}$ asymmetry (Fig. 6) and of the accurate NMC measurements of F_2^n/F_2^p? It turns out that such a fit is possible – we denote the new set of partons by MRS(A) [20]. The asymmetries resulting from this set of partons are shown in Figs. 6 and 8. We would expect the MRS(A) partons to be very similar to those of MRS(H), except that $\bar{d}-\bar{u}$ would be much larger while at the same time approximately conserving $\bar{u}+\bar{d}$, $d+\bar{d}$ and $u+\bar{u}$ (as required by (1)-(4)). Thus we anticipate an increase of $\bar{d}$ which is compensated by a corresponding decrease in $\bar{u}$ and d, which in turn requires a similar increase in u. The comparison of MRS(H) and MRS(A) parton sets is shown in Fig. 9, and displays these trends in the region $0.02 \lesssim x \lesssim 0.7$ where a full set of deep inelastic data exist.

Although the quark distributions are well-constrained by the data, the same is not so true for the gluon. Within the global analyses, we can identify three types of constraint on the gluon: (i) the momentum sum rule, (ii) the prompt photon production measurements and (iii) the observed overall pattern of scale violations, $\partial F_i/\partial \log Q^2$, for $x \lesssim 0.1$. The measurements of F_2^{ep} at HERA probe primarily the behaviour of the sea quark distributions at small x, although accurate measurements of $\partial F_2^{ep}/\partial \log Q^2$ will further constrain the gluon. If the observed steep rise of F_2 with decreasing x is attributed to the Lipatov or BFKL perturbative QCD mechanism via $g \to q\bar{q}$, then the same behaviour should be seen also in the gluon distribution. A direct measurement of the gluon in the $x \lesssim 10^{-2}$ region would be invaluable.

In addition to the potential constraints coming from accurate measurements of $\partial F_2/\partial \log Q^2$, there are several other possible ways of measuring the gluon at HERA, including F_L, J/ψ, $Q\bar{Q}$... production. In principle the observation of the longitudinal structure function is a gold-plated measurement, but in practice it will be difficult. To extract F_L as a function of x, Q^2, requires observation of the $y = Q^2/xs$ dependence of deep inelastic scattering, which means having electron-proton collisions at different c.m. energies $\sqrt{s}$.

There are also possibilities to obtain information on the gluon from hadron colliders, in particular the Fermilab $p\bar{p}$ collider. At $\sqrt{s} = 1.8$ TeV, x values comparable to those currently measured at HERA can be probed either by observing small mass systems produced centrally (e.g. $b\bar{b}$ or Drell-Yan production or by more massive final states at large rapidity y (e.g. same-side W+jet or dijet production). As an illustration Fig. 10 shows the ratio of same-side to opposite-side jet cross sections from uncorrected CDF data, as a function of the equal and opposite rapidities y. At large y the same-side cross section originates dominantly from subprocesses of $g(\text{small } x)q_{\text{val}}(\text{large } x)$ origin. The curves are the MRS(D'_-,D'_0,H) predictions evaluated at leading order with a renormalization/factorization scale chosen to mimic the next-to-leading order corrections. Further details of this analysis can be found in ref. [27]. We see that at large rapidity the ratio is sensitive to the small x behaviour of the gluon and that the preliminary CDF data favour the singular distributions. Dijet production from 'direct' photons at HERA offers similar possibilities of probing the gluon at small x via $\gamma g \to q\bar{q}$ [28].

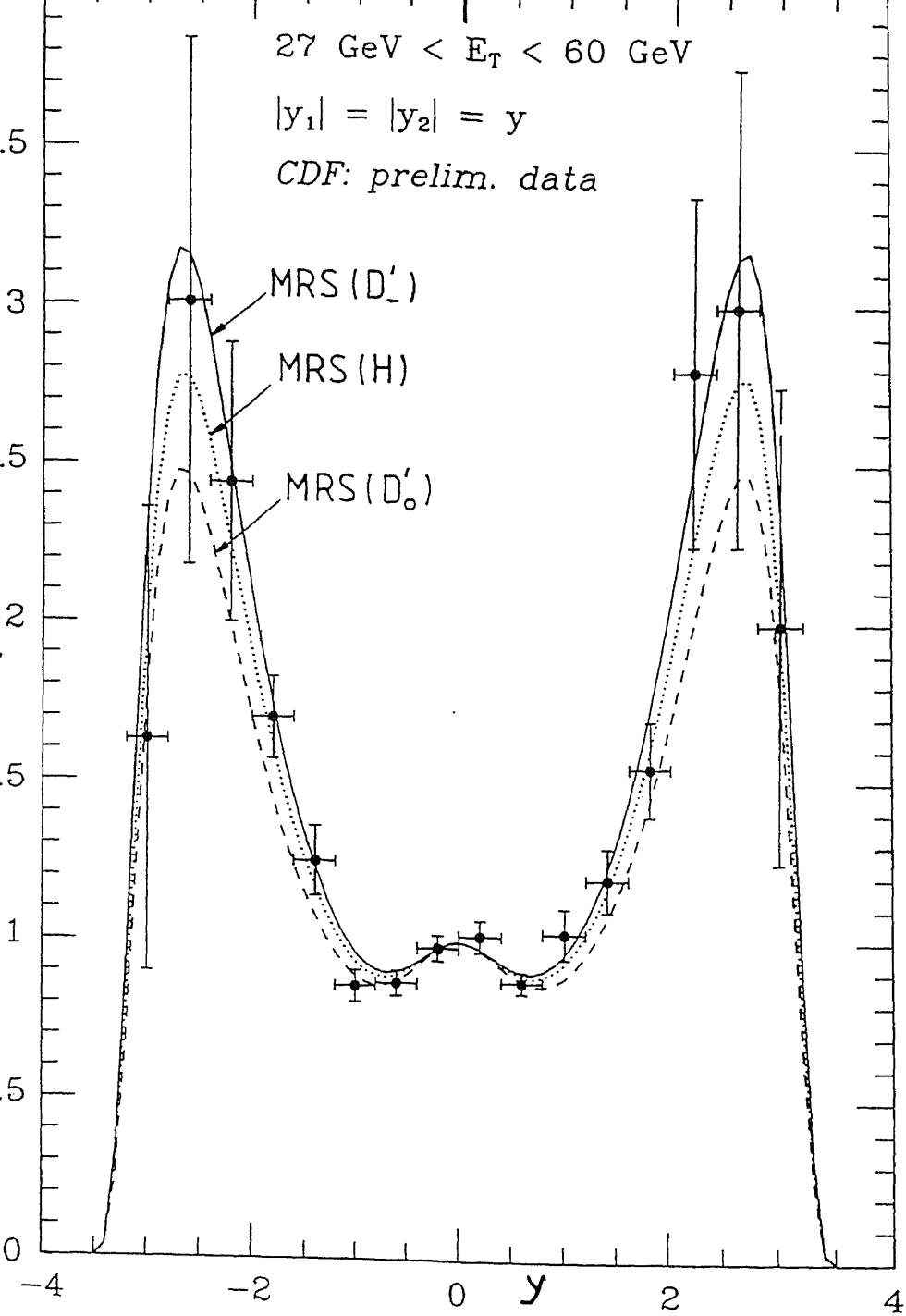

Figure 10. The same-side/opposite-side dijet ratio predicted by parton sets of refs. [5, 5] compared with preliminary, uncorrected CDF data.

3. Conclusions

The parton densities of the proton are well determined in the region $0.02 \lesssim x \lesssim 0.7$ where high precision data for a wide range of deep-inelastic and related processes are available. The one combination, $\bar{d} - \bar{u}$, that is not constrained by the deep-inelastic data, has for the first time been determined at $x = 0.18$ by a measurement of the Drell-Yan asymmetry in pp and pn collisions [26]. This measurement, together with the $W^{\pm}$ rapidity asymmetry measurements probe fine details of the quark densities. It is therefore not surprising that the existing MRS (and CTEQ) partons require minor modification. The result is a new set of partons [20] – MRS(A) – which is essentially identical to MRS(H) at small x; recall that the latter parton set [16] was obtained by incorporating the 1992 HERA measurements of F_2 [3, 4] into the analysis. It is found that MRS(A,H) also give an excellent description of the new preliminary 1993 higher statistics HERA data for F_2.

Acknowledgements

I thank Alan Martin and James Stirling with whom I collaborated on the MRS analysis presented here. I warmly thank Uma Sankar and DP Roy for inviting me to this excellent workshop.

References

[1] BCDMS collaboration: A.C. Benvenuti et al., Phys. Lett. **B223** (1989) 485

[2] NMC: P. Amaudruz et al., Phys. Lett. **B295** (1992) 159

[3] H1 collaboration: I. Abt et al., Nucl. Phys. **B407** (1993) 515

[4] ZEUS collaboration: M. Derrick et al., Phys. Lett. **B316** (1993) 412

[5] In principle s and $\bar{s}$ could be distinguished by accurate νN and $\bar{\nu} N$ data.

[6] A.D. Martin, R.G. Roberts and W.J. Stirling, Phys. Lett. **B306** (1993) 145

[7] E.A. Kuraev, L.N. Lipatov and V.S. Fadin, Sov. Phys. JETP **45** (1977) 199
Ya.Ya. Balitsky and L.N. Lipatov, Sov. J. Nucl. Phys. **28** (1978) 822

[8] CCFR collaboration: A. Bazarko et al., Columbia University preprint NEVIS-1492 (1993)

[9] V. Barone et al., Phys. Lett. **B268** (1991) 279

[10] NMC: P. Amaudruz et al., Phys. Rev. Lett. **66** (1991) 2712

[11] A.D. Martin, R.G. Roberts and W.J. Stirling, Phys. Lett. **B228** (1989) 149

[12] W.-K. Tung, these proceedings
S. Brodsky, contribution to this workshop

[13] V.N. Gribov and L.N. Lipatov, Sov. J. Nucl. Phys. **15** (1972) 438
G. Altarelli and G. Parisi, Nucl. Phys. **B126** (1977) 298
Yu.L. Dokshitzer, Sov. Phys. JETP **46** (1977) 641

[14] M. Virchaux and A. Milsztajn, Phys. Lett. **B272** (1992) 221

[15] CCFR collaboration: S.R. Mishra, Proc. of Lepton-Photon Symposium, Geneva (1991); P.Z. Quintas et al., Phys. Rev. Lett. **71** (1993) 1307

[16] A.D. Martin, R.G. Roberts and W.J. Stirling, Proc. Workshop on Quant
Theoretical Aspects of HE Physics, Kyffhäusser, Germany, eds. B. Geyer
Ilgenfritz, Leipzig (1993) p. 11

[17] A.D. Martin, R.G. Roberts and W.J. Stirling, Mod. Phys. Lett. A4 (198
E.L. Berger, F. Halzen, C.S. Kim and S. Willenbrock, Phys. Rev. D40
E3789

[18] CTEQ collaboration: J. Botts et al., Phys. Lett. B304 (1993) 159, now s
by CTEQ2.

[19] M. Glück, E. Reya and A. Vogt, Z. Phys. C53 (1992) 127; Phys. Lett. B3
391

[20] A.D. Martin, R.G. Roberts and W.J. Stirling, preprint RAL-94-055, DT
to appear in Phys. Rev.

[21] NMC: M. Arneodo et al., CERN preprint PPE/93-117 (1993)

[22] An updated analysis of the Gottfried sum by NMC [21] gives $I_{GSR} = 0.2$
(stat.) ± 0.015 (sys.) at $Q^2 = 4$ GeV^2. If $F_2^{\mu n}$ is corrected for deuteron
effects then I_{GSR} is reduced to $\simeq 0.23$.

[23] NMC: E.M. Kabuss, Nucl. Phys. B (Proc. Suppl.) 29A (1992) 1

[24] S.D. Ellis and W.J. Stirling, Phys. Lett. B256 (1991) 258

[25] A.D. Martin, R.G. Roberts and W.J. Stirling, Phys. Lett. B308 (1993) 3

[26] NA51 collaboration: A. Baldit et al., Phys. Lett. to be published.

[27] A.D. Martin, R.G. Roberts and W.J. Stirling, Phys. Lett. B318 (1993) 1

[28] J.R. Forshaw and R.G. Roberts, Phys. Lett. B319 (1993) 539; RAL prepr
(1994)

journal of physics

October 1995
pp. 293-312

Physics prospects at the hadron colliders

D. P. ROY

Theoretical Physics Group, Tata Institute of Fundamental Research
Homi Bhabha Road, Bombay - 400 005, India

Abstract. I start with a brief introduction to the elementary particles and their interactions, Higgs mechanism and supersymmetry. The major physics objectives of the Tevatron and LHC colliders are identified. The status and prospects of the top quark, charged Higgs boson and superparticle searches are discussed in detail, while those of the neutral Higgs boson(s) are covered in a parallel talk by R.J.N. Phillips at this workshop.

The hadron colliders are best suited to explore a new domain of energy for a wide variety of new physics signals because of their higher energy reach and greater versatility. With the loss of SSC, one looks forward to the Tevatron upgrade and especially the large hadron collider (LHC) to survey the energy range of 100 – 1000 GeV. I plan to give an overview of the main physics issues to be probed by these colliders. To put them in perspective, let me briefly recall our current understanding of the elementary particles and their interactions.

Basic Constituents of Matter and Their Interactions – As per the standard model, the basic constituents of matter are the 3 pairs of leptons and quarks shown below. Each pair represents 2 charge states differing by 1 unit – charge 0, -1 for the leptons and 2/3, -1/3 for the quarks – which is relevant for their weak interaction. Apart from this electric charge of course the quarks possess the so-called colour charge, which is relevant for their strong interaction.

Table 1. Basic constituents of matter

leptons	charge	quarks	charge
ν_e ν_μ ν_τ	0	u c t	2/3
e μ τ	-1	d s b	-1/3

Almost half of these elementary particles have been observed during the last two decades, thanks to the advent of the colliders. The discovery of the τ lepton and the charm quark and study of their detailed properties were the highlights of the SPEAR (e^+e^-) collider. Although the bottom quark was first discovered in a fixed target hadron machine (the Fermilab SPS), its detailed study could be made only at

the DORIS and CESR (e^+e^-) colliders. The first experimental evidence (though still indirect) of ν_τ has come from the observation of $W \rightarrow \tau\ \nu_\tau$ events at the CERN $\bar{p}p$ collider. These are the (in)famous monojet plus missing-p_T events of the UA1 experiment which were originally thought to signal supersymmetric particle production. As regards the top quark – the last and the most massive member of the above table – the CDF experiment has recently reported a tentative signal in the mass range of ~ 175 GeV [1, 2] from the Tevatron $\bar{p}p$ collider [3]. One expects a more definitive signal to emerge from the ongoing CDF and $D\!\!\!/$ experiments at the Tevatron collider. For there is sufficient indirect evidence for the existence of top quark in the above mass range, as we shall see below.

Next consider the interactions between these elementary particles. Apart from gravitation, which is too weak to be of interest to particle physics phenomenology, there are 3 basic interactions – strong, electromagnetic and weak. They are all gauge interactions, mediated by vector particles. The strong interaction (QCD) is mediated by the exchange of massless vector gluons with couplings proportional to the colour charge C (Fig. 1a). This is analogous to the electromagnetic interaction (QED), mediated by the massless vector photon with couplings proportional to the electric charge e (Fig. 1b). The gluon was detected at the PETRA (e^+e^-) collider via the three-jet events i coming from gluon radiation [4]

$$e^+e^- \rightarrow q\bar{q}g\ .$$

Unlike the photons which possess no electric charge the gluons possess colour charge and can therefore interact among themselves. The gluon self interaction, the most distinctive feature of strong interaction, has been observed at the CERN $\bar{p}p$ collider, via the two-jet events coming from [4]

$$gg \xrightarrow{g} gg.$$

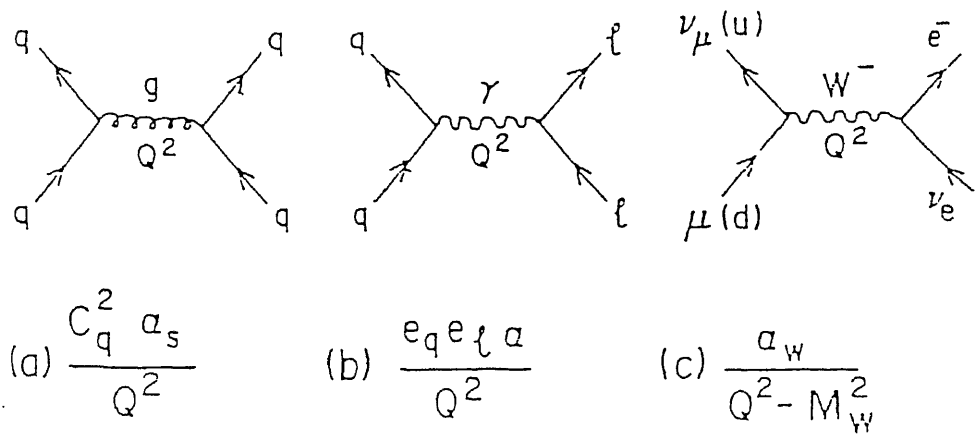

Figure 1. The basic amplitudes of (a) strong, (b) electromagnetic and (c) charged current weak interaction.

The weak interactions are mediated by the massive charged and neutral vector bosons $W^\pm$ and Z°. The charged W boson couples to each of the above pairs of

leptons and quarks with the same universal coupling (Fig. 1c), while the Z boson couplings are given by the standard $SU(2) \times U(1)$ electro-weak model of Glashow, Weinberg and Salam in terms of the mixing angle θ_W. It also relates the weak and electromagnetic couplings

$$\alpha_W = \alpha / \sin^2 \theta_W \ , \tag{1}$$

where $\sin^2 \theta_W$ is known from the neutrino scattering (and more recently the LEP data) [1], i.e.

$$\sin^2 \theta_W \simeq .23 \ . \tag{2}$$

Thus the W mass is predicted by estimating the Fermi coupling from μ decay (Fig. 1c); i.e

$$G_F = \frac{\pi}{\sqrt{2}} \frac{\alpha_W}{M_W^2} = \frac{\pi}{\sqrt{2}} \frac{\alpha}{\sin^2 \theta_W \cdot M_W^2} = 1.1663 \times 10^{-5} \ \text{GeV}^{-2} \ . \tag{3}$$

Substituting eq. (2) and the fine structure constant at the appropriate mass scale

$$\alpha(M_W^2) \simeq 1/128 \tag{4}$$

one gets

$$M_W \simeq 80 \ \text{GeV}, \ M_Z = M_W / \cos \theta_W \simeq 91 \ \text{GeV} \ . \tag{5}$$

The W and Z bosons were seen at these masses at the CERN $\bar{p}p$ collider and more recently at the Tevatron collider. Finally, it has been possible to produce millions of Z bosons and study its detailed properties at the large electron positron collider (LEP).

It would appear from the above discussion that all that remains to be seen at the future colliders is a definitive signal of the top quark! This is of course not the whole story, as we see below.

The Mass Problem (Higgs Mech.) – It arises from the fact that for massive vector bosons, the mass term in the Lagrangian breaks gauge invariance and hence the renormalisability of the theory. Let us consider the SU(2) gauge interaction, mediated by the Isotriplet of vector bosons

$$\vec{W}_\mu = W_\mu^{\pm,0},$$

in the presence of charged scalar particles represented by the complex field ϕ. We have

$$\begin{aligned} \mathcal{L} &= \left(\partial_\mu \phi + ig \frac{\vec{\tau}}{2} \cdot \vec{W}_\mu \phi\right)^+ \left(\partial_\mu \phi + ig \frac{\vec{\tau}}{2} \cdot \vec{W}_\mu \phi\right) \\ &\quad -(\mu^2 \phi^+ \phi + \lambda(\phi^+ \phi)^2) - \frac{1}{4} \vec{W}_{\mu\nu} \cdot \vec{W}_{\mu\nu}, \\ \vec{W}_{\mu\nu} &\equiv \partial_\mu \vec{W}_\nu - \partial_\nu \vec{W}_\mu - g \vec{W}_\mu \times \vec{W}_\nu \ . \end{aligned} \tag{6}$$

The three terms in the Lagrangian from right to left represent the vector boson

and the scalar kinetic energy and gauge-interaction term. Each of them is invariant under the gauge transformations

$$\phi \rightarrow e^{i\vec{\alpha}\cdot\frac{\vec{\tau}}{2}}\phi, \vec{W}_\mu \rightarrow \vec{W}_\mu - \frac{1}{g}\partial_\mu\vec{\alpha} - \vec{\alpha}\times\vec{W}_\mu \ . \tag{7}$$

But adding a mass term for the vector boson

$$M^2\vec{W}_\mu\cdot\vec{W}_\mu$$

will clearly break the gauge invariance [5]. In contrast, the scalar mass term is gauge invariant. This fact is used to give mass to the vector bosons through back-door. One starts with an Isodoublet of complex scalar field with imaginary mass,

$$\phi = \begin{pmatrix} \phi_3 & + & i\phi_4 \\ \phi_1 & + & i\phi_2 \end{pmatrix} \ , \quad \mu^2 < 0 \tag{8}$$

and turns on the Higgs mechanism [6]. Three of the scalar fields are absorbed as Goldstone bosons to give mass and hence longitudinal components to the 3 vector bosons, while the remaining one becomes a physical scalar particle (the famous Higgs particle) with real mass

$$M_{H^\circ} = M_W\left(\frac{2\sqrt{2\lambda}}{g}\right) . \tag{9}$$

Although the mass is related to the unknown scalar self-coupling λ, the validity of the perturbation theory implies

$$\lambda < 1 \Rightarrow M_{H^\circ} < 1TeV \ . \tag{10}$$

Finally, the Higgs coupling to the vector bosons as well as the quarks and leptons (not mentioned so far) are predicted to be

$$\begin{aligned} g_{HWW,HZZ} &= g\cdot M_{W,Z} \\ g_{Hq\bar{q},H\ell\bar{\ell}} &= \frac{1}{2}g\cdot\frac{M_{\ell,q}}{M_W} \ . \end{aligned} \tag{11}$$

Thus the Higgs particle has appreciable couplings only to the heavy particles like W, Z bosons or the t quark; and the best place to look for it is in the decay of Z or the toponium ($t\bar{t}$) state [7]. Even then the branching ratio is tiny, so that one needs copious production of Z as provided by the LEP (e^+e^-) collider. It has yeilded a lower mass bound of about 60 GeV [1] for Higgs particle which is close to its discovery limit. The search can be pushed up further to about 80 GeV at LEP-II. If we do not find a Higgs particle in this mass range, then the search must be extended over the hundreds of GeV range since the theoretical mass limit is 1 TeV. This is the main physics goal of LHC, which is proposed to be a 14 TeV pp collider. The reason for the pp option instead of $\bar{p}p$ is its high luminosity and hence a higher mass reach for the Higgs search.

Hierarchy Problem (SUSY Soln.) – Solving the mass problem by the Higgs scalars leads to the so-called hierarchy problem. The property that scalar particle mass is not protected by any gauge symmetry, which was in fact used to solve the mass

problem, implies that they are quadratically divergent under radiative correction (Fig. 2). Consequently the output Higgs mass would become as large as the cutoff scale of the electroweak theory, i.e.

$$M_H \to M_{GUT}(10^{16}\ \text{GeV}) \text{ or } M_{\text{Planck}}(10^{19}\ \text{GeV}).$$

How to restrict the Higgs mass to

$$M_H \sim M_W \sim 100\ \text{GeV}?$$

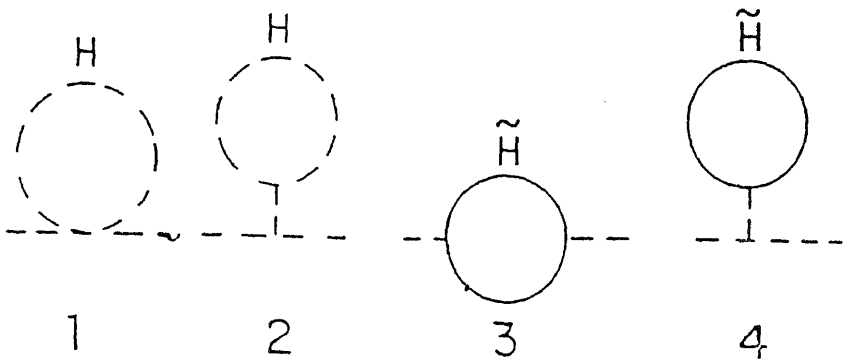

Figure 2. The quadratically divergent contributions to the Higgs mass from the radiative Higgs loops (1,2) and the cancelling SUSY contribution from the Higgsino loops (3,4).

By far the most attractive solution to this problem is provided by supersymmetry (SUSY) [8]. It provides canceling contributions from radiative loops with Higgsino, fermionic superpartner of the Higgs scalar (Fig. 2). For the cancellation to be exact up to a mass scale of $\sim$ 100 GeV, one requires

1) Exact supersymmetry in the couplings

2) A bound on supersymmetry breaking in masses

$$M_{\tilde{H}} - M_H = \Delta M \lesssim 100\ \text{GeV}.$$

Thus one expects to see superpartners of standard particles – scalar partners of quarks and leptons $(\tilde{q}, \tilde{\ell})$ and fermionic partners of gauge and Higgs bosons $(\tilde{g}, \tilde{\gamma}, \tilde{W}, \tilde{Z}, \tilde{H})$ – within the mass scale of several hundred GeV. Search for such particles is an important programme of present and proposed colliders. By far the strongest mass bound on superparticles comes from the CDF experiment [9] at the Tevatron $(\bar{p}p)$ collider, i.e.

$$M_{\tilde{q},\tilde{g}} > 140\ \text{GeV}. \tag{12}$$

The ongoing CDF and $D\oslash$ experiments at Tevatron are expected to extend this search up to a mass range of $\sim$ 250 GeV. The search can be extended to over 1 TeV at LHC.

It is clear from the above discussions that the searches for top quark, Higgs boson(s) and possible superparticles are the most important physics objectives of

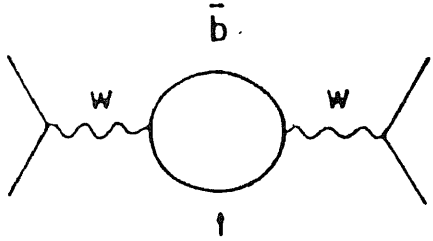

Figure 3. Radiative correction to the W boson mass arising from the $t\bar{b}$ loop.

the forthcoming high energy collider experiments. While it will take a 21st century machine like LHC to carry on the Higgs boson and superparticle searches upto their predicted mass bounds of ~ 1 TeV, there is a strong indirect evidence for the top quark to lie in the mass range of ~ 170 GeV. This comes from the radiative correction to eq. (3) coming from the $t\bar{b}$ loop contribution to W self energy (Fig. 3) and the analogous $t\bar{t}$ contribution to the Z self energy. Since these vector bosons acquire longitudinal components by swallowing Higgs scalars their fermionic couplings are propertional to the fermion mass (eq. 11), which can be sizeable for a large M_t. The resulting radiative correction is quadratic in M_t. More precisely eq. (3) has a radiative correction factor $(1 + \Delta r)$, where

$$\Delta r \simeq \frac{-3\sqrt{2}}{16\pi^2} G_F \cot^2\theta_W M_t^2 \tag{13}$$

for $M_t \gg M_W$. Thus for $M_t \geq 200$ GeV, one would get untenably low values of $\sin^2\theta_W$ or M_W (M_Z). Consistency with the precission measurements of these quantities (particularly at LEP) requires [1]

$$M_t \simeq 170 \pm 25 \text{ GeV}. \tag{14}$$

Therefore one expects a definitive top quark signal to emerge from the ongoing experiments at the Tevatron $\bar{p}p$ collider.

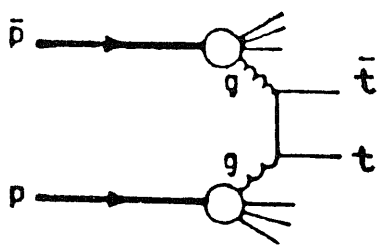

Figure 4. Top quark production in $\bar{p}p$ (pp) collision via gluon-gluon fusion.

Top Quark Search – The hadron colliders are the most promising machines for top quark search because of their high energy reach. But the signal is messy; and

one has to use special tricks to separate it from the background. The dominant mechanism for top quark production is the so-called flavour creation process via gluon-gluon fusion (Fig. 4) and quark-antiquark fusion (Fig. 1a), i.e.

$$gg(\bar{q}q) \to \bar{t}t. \tag{15}$$

One looks for a prompt charged lepton ℓ (i.e. e or μ) coming from its leptonic decay

$$t \to b\nu\ell \tag{16}$$

which eliminates the background from gluon and ordinary stable quarks (u, d, s). Of course the charged lepton could come from the unstable quarks b and c, i.e.

$$\begin{aligned} gg(\bar{q}q) &\to \bar{b}b, \bar{c}c; \\ b \to c\nu\ell,\ c &\to s\nu\ell. \end{aligned} \tag{17}$$

These background can be effectively suppressed by requiring the charged lepton to be isolated from the other particles. Because of the large energy release in the decay of the massive top quark, the decay products come wide apart. In contrast the energy release in the light b or c quark decay is small, so that the decay products come together in a narrow cone – i.e. the charged lepton appears as a part of the decay quark jet. The isolated lepton signature provides a simple but very powerful signature for top quark, first suggested in [10]. Using this signature the top quark search was carried out at the CERN $\bar{p}p$ collider and then at the Tevatron collider – the latter giving a mass limit of $M_t > 89$ GeV [11].

With the luminosity upgrade of the Tevatron collider it is possible now to extend the search to the mass range of $100 - 200$ GeV. A top quark in this mass range decays into a real W boson, so that one has a $2W$ final state, i.e.

$$\bar{t}t \to \bar{b}bWW \to \bar{b}b\bar{q}q\ell\nu. \tag{18}$$

The most serious background in this case is direct W production with additional QCD jets,

$$\bar{q}q \to ggW \to j_1 j_2 \ell\nu. \tag{19}$$

Since the QCD jets are largely soft and/or collinear, they can be suppressed to a large extent by transverse momentum and invariant mass cuts – e.g. $p_j^T > 60$ GeV, $M_{j_1 j_2} \sim 80$ GeV – without affecting the signal.

Fig. 5 shows an early prediction of the $\bar{t}t$ signal and the $W + 2$ jets background with these cuts for the Tevatron upgrade [12]; the right hand scale corresponds to a luminosity of 100 pb^{-1}. One sees firstly that for the relatively clean dilepton channel, corresponding to leptonic decay of both the W bosons in (18), one has a measurable signal upto $M_t \sim 150$ GeV. For the isolated lepton plus multijet channel the signal remains measurable right upto $M_t \sim 200$ GeV, although one has to contend with a formidable background. Here one hopes to be helped by the fact the signal is dominated by 3 jets accompanying the isolated lepton, for which the QCD background would be further suppressed by an order of magnitude [12, 13]. Finally the presence of a pair of b quark jets in the signal (18) would help to enhance the signal to background ratio further, if one has a reasonably efficient b identification.

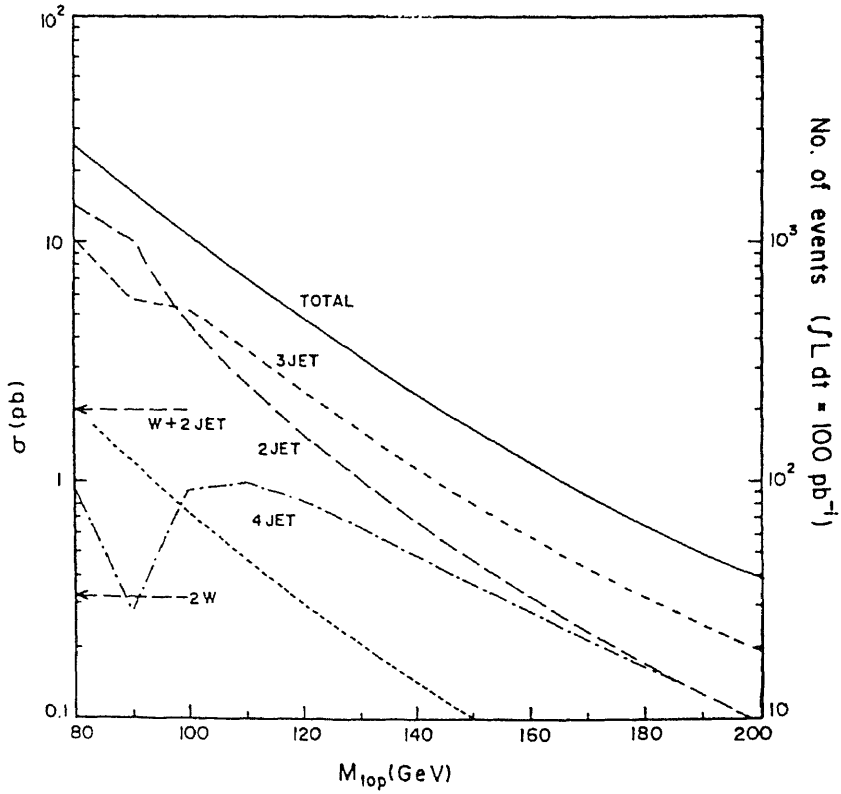

Figure 5. Top quark contribution to the isolated lepton plus n-jet events and also dilepton events (dotted line) shown for the typical energy (2 TeV) and luminosity (100 pb^{-1}) of the Tevatron upgrade. The background to the 2-jet events from W plus 2-jet and W pair production processes are also shown [12].

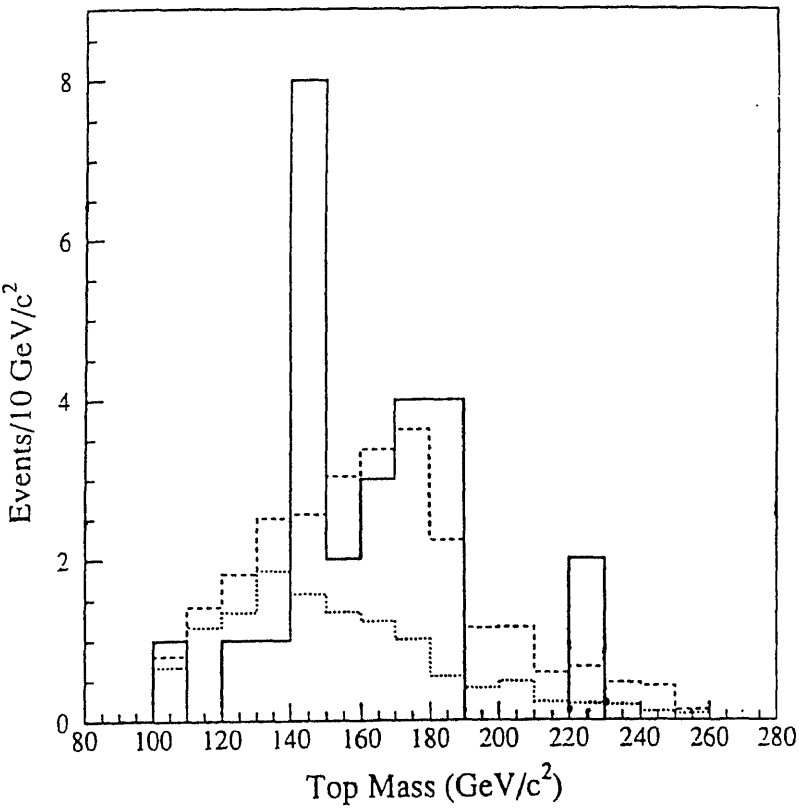

Figure 6. Top mass distribution for 26 events in the $W + 3$ or more jet sample (solid histogram) and the background of 13 events (dots) obtained from $W+$ multijets Monte Carlo simulation. The dashed histogram represnts the sum of 13 $t\bar{t}$ Monte Carlo events with $M_t = 175$ GeV plus the 13 background events [2].

of 26 events in the W $(\rightarrow \ell\nu) + 3$ or more jets channel against the expected background of $\sim$ 13 events from $W+$ QCD jets. The excess is consistent with a top quark signal of mass $\sim$ 175 GeV (Fig. 6). They also have a reasonable efficiency of b identification ($\sim$ 30%) by combining informations on its decay vertex in the microvertex detector and on the lepton coming from its semileptonic decay. Requiring at least one identified b jet leaves a sample 7 events against an expected background of 1.4 (Fig. 7). The excess of 5.6 events has been tentatively interpreted as a top quark signal of mass $\sim$ 175 GeV [2].

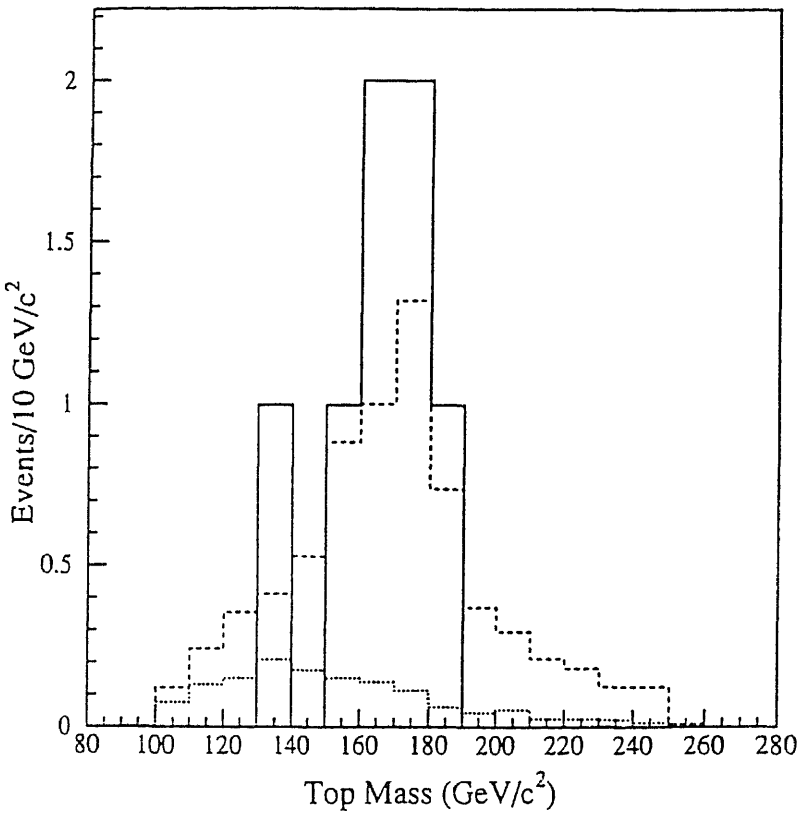

Figure 7. Top mass distribution for the data (solid histogram) and the background of 1.4 $W+$ multijets Monte Carlo events (dots) having a tagged b. The dashed histogram represents the sum of 5.6 $t\bar{t}$ Monte Carlo events with $M_t = 175$ GeV plus the 1.4 background events [2].

But of course the data sample is too small to draw any definitive conclusion. It may be noted here that this data sample was based on a luminosity of ~ 20 pb^{-1}, while the ongoing CDF and $D\oslash$ runs at the Tevatron are expected to accumulate a luminosity of $\sim$ 100 pb^{-1}. Therefore a more definitive picture is expected to emerge soon. Even then one would have of course no more than a dozen or two of

top candidate events. With an accumulated luminosity of ~ 1000 pb^{-1}, expected for the next phase of the Tevatron upgrade, one expects to see ~ 100 top quark events. This will be sufficient to establish a definitive top signal, but still inadequate to study its decay properties.

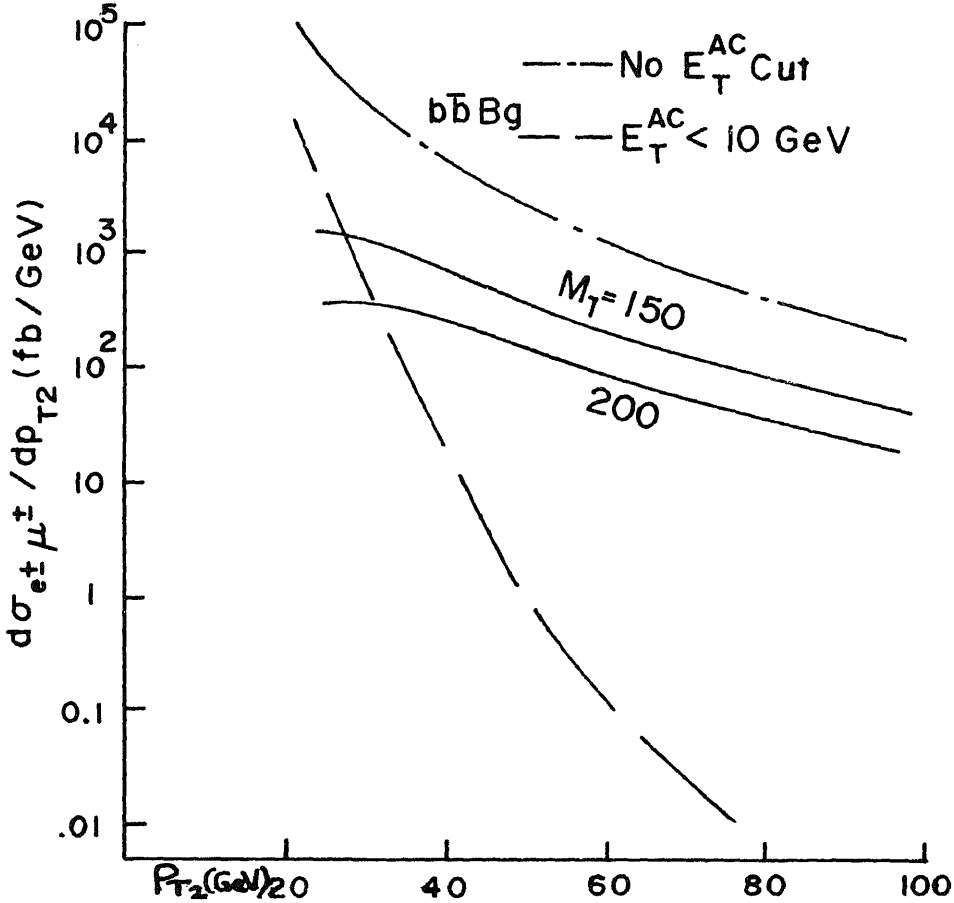

Figure 8. The expected $t\bar{t}$ signal at LHC in the cleanest ($e\mu$) channel shown against the p_T of the 2nd (softer) lepton. The $b\bar{b}$ background with and without the isolation cut are also shown [14].

In contrast one expects copious production of top at the LHC. In the cleanest ($e\mu$) channel, shown in Fig. 8 [14], one expects a top cross-section of $\sim 10^4$ fb. This corresponds to a cross-section of $\sim 10^5$ fb in the lepton + multijet channel (18) discussed above. Even with the low luminosity option of LHC (~ 10 fb^{-1}/year), this would imply an annual rate of ~ 1 million top quark events – i.e. similar to the rate of Z events at LEP. This will enable one to study its decay properties in detail and in particular to search for new particles in the decay of top. In particular there is a good deal of recent interest in the search of one such new particle in top quark decay, i.e. the charged Higgs boson $H^\pm$ of the supersymmetric standard model.

Charged Higgs Boson Search – The minimal supersymmetric standard model (MSSM) has two Higgs isospin doublets with opposite hypercharge $Y = \pm 1$ to ensure anomaly cancellation between their fermionic partners [6, 8]. The two doublets of complex scalar fields correspond to 8 independent scalars, 3 of which are absorbed as Goldstone bosons to give mass to the $W^{\pm}$ and Z. So there are 5 physical Higgs bosons – 3 neutral (h^0, H^0, A^0) and 2 charged ones ($H^{\pm}$). We have the following fermionic couplings of the charged Higgs boson in the diagonal KM matrix approximation,

$$\mathcal{L} = \frac{g}{\sqrt{2}M_W} H^+ \Big[\cot\beta M_t \bar{t} b_L \; + \; \tan\beta M_b \bar{t} b_R + \cot\beta M_c \bar{c} s_L + \tan\beta M_\tau \bar{\nu}\tau_R \Big] + hc, \tag{20}$$

where we have neglected the couplings propertional to the light quark and lepton masses. The subscript $L(R)$ stands for the left (right) handed spinor state and $\tan\beta$ represents the ratio of the two Higgs vacuum expectation values. In the supergravity models $1 < \tan\beta < M_t/M_b$.

As we see from (20), the t couplings to bH^+ and bW^+ are comparable over a large range of $\tan\beta$ and so are the H^+ couplings to $c\bar{s}$ and $\nu\tau^+$. Thus for $M_H < M_t$, one expects significant branching fractions for the decays

$$\begin{aligned} t &\to bH^+ \\ H^+ &\to \tau^+\nu. \end{aligned} \tag{21}$$

In contrast to the preferencial H^+ decay into τ, there is a universal branching fraction ($= 1/9$) for W boson decay into the 3 lepton species, i.e.

$$\begin{aligned} t &\to bW^+ \\ W^+ &\to e^+\nu, \mu^+\nu, \tau^+\nu. \end{aligned} \tag{22}$$

Thus an excess of top decay into τ vis a vis the e, μ channels

$$B_{t\to b\tau\nu} > B_{t\to be\nu, b\mu\nu} \tag{23}$$

constitutes a distinctive signature for charged Higgs boson [17].

A second signature for charged Higgs boson is provided by the τ polarisation – the τ leptons coming from the decay of a scalar ($H^{\pm}$) and vector ($W^{\pm}$) boson have exactly opposite polarisations [18]. Using the two signatures one can carry on the $H^{\pm}$ search close to the top quark mass at LHC over the whole range of $\tan\beta$ [19].

For $M_H > M_t$ one still expects a sizeable rate of $H^{\pm}$ production at LHC via the gluon $-b$ quark fusion

$$gb \to tH^- \to t\bar{t}b; \tag{24}$$

but the dominant decay mode into $\bar{t}b$ has an enormous QCD background. With a good b quark identification, however, one expects to have a viable signal if $\tan\beta \sim 1$ or very large ($\sim M_t/M_b$) [20, 21].

Fig. 9 shows the expected signal against the QCD background for $\tan\beta = 1$ and 50 assuming a b-identification efficiency of 30% [20]. Interestingly, these two regions

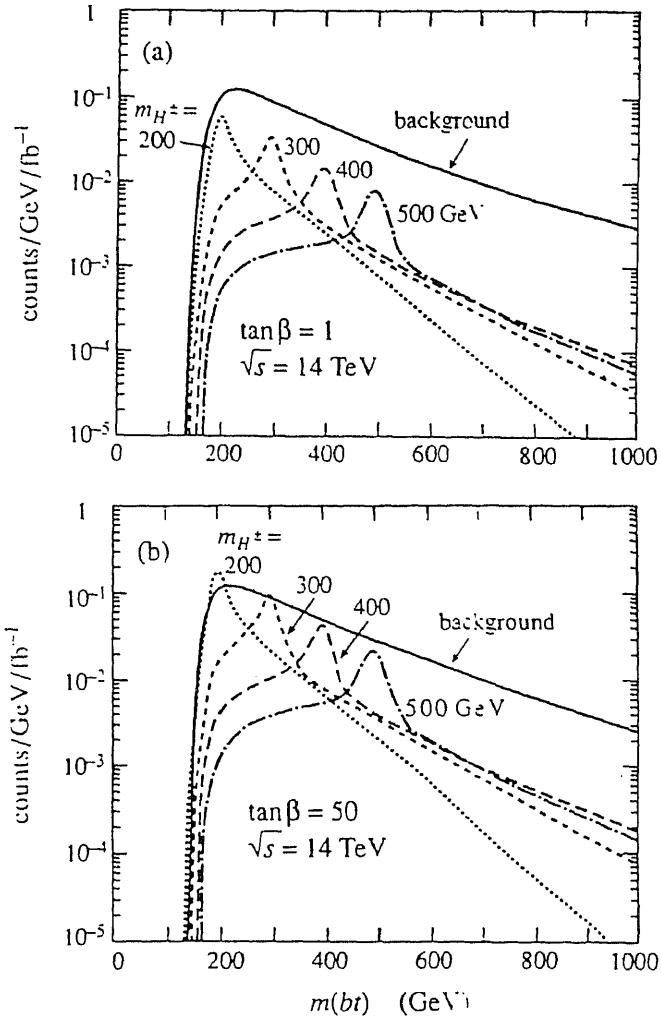

Figure 9. The expected charged Higgs signals at LHS shown against the reconstructed $H^\pm$ mass along with the background. The cases $M_{H\pm} = 200, 300, 400, 500$ GeV are shown for (a) $\tan\beta = 1$ and (b) $\tan\beta = 50$ [20].

couplings at the GUT scale [22]. The underlying reason for favouring these two regions of $\tan\beta$ is of course the same in both the cases – i.e. a large $Ht\bar{b}$ Yukawa coupling a la eq. (20).

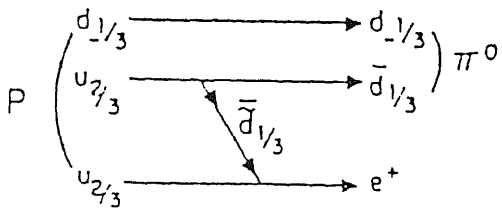

Figure 10. The proton decay process arising from squark exchange.

Search for Superparticles – Let me start with a brief discussion of R-parity, which underlies the canonical missing-p_T signature for superparticle search. The presence of scalar quarks and leptons $(\tilde{q}, \tilde{\ell})$ in SUSY imply baryon and lepton number violating interactions shown in Fig. 10. Moreover this diagram would imply proton decay with a typical time scale of weak interaction ($\tau_p \sim 10^{-8}$ sec!), since the mass of the exchanged particle $M_{\tilde{q}}$ is comparable to M_W. To forbid this catastrophic proton decay one assumes R-parity conservation, where

$$R = (-1)^{3B+L+2S} \tag{25}$$

so that it is $+1$ for all the standard particles and -1 for their superpartners differing by half a unit of spin(S). It automatically forbids single emission/absorption of a superparticle. It implies that (i) the superparticles are produced in pair; and (ii) the lightest superparticle (LSP) resulting from their decay is stable. The LSP is also expected to be colour and charge neutral for cosmological reasons; and in most SUSY models it turns out to be the photino $\tilde{\gamma}$. Finally the LSP is expected to interact very weakly with matter like the neutrino (Fig. 11); and hence escape the detector without a trace. The apparent imbalance of transverse momentum (missing-p_T) resulting from this serves as a signature for superparticle production [23].

The superparticles having the largest production rates at the hadron colliders are the strongly interacting ones, i.e. squark $\tilde{q}$ and gluino $\tilde{g}$. They are produced via gluon-gluon fusion (Fig. 12)

$$gg \rightarrow \tilde{g}\tilde{g} \text{ or } \tilde{q}\bar{\tilde{q}} \tag{26}$$

and decay via

$$\tilde{q} \rightarrow q\tilde{\gamma},\ \tilde{g} \rightarrow q\bar{q}\tilde{\gamma}. \tag{27}$$

The decay of one of the squarks (gluinos) into a leading photino carrying the bulk of its momentum results in a large missing-p_T event accompanied by one or more jets. This is illustrated in Fig. 13; the number of visible jets depend on the jet detection algorithm. The rate of such large missing-p_T events can be predicted as

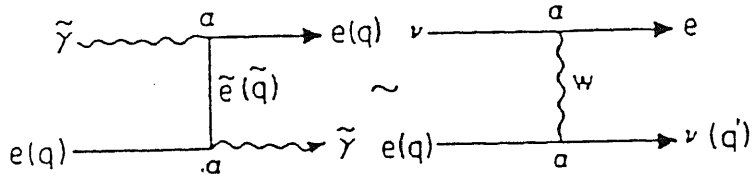

Figure 11. Comparison of the rates of LSP ($\tilde{\gamma}$) and ν interaction with ordinary matter (e, q).

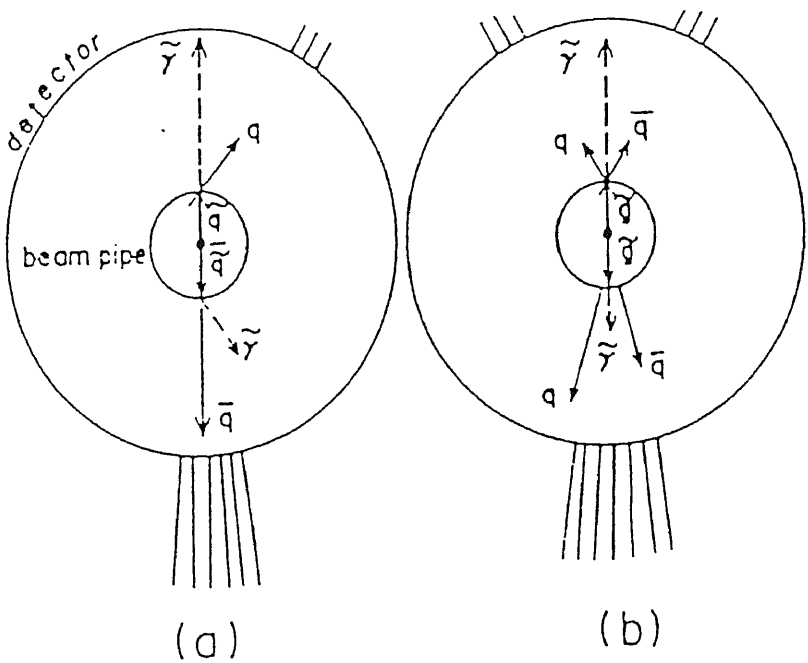

Figure 12. Event configuration in the transverse plane for a pair of (a) squark and (b) gluino production at a hadron collider.

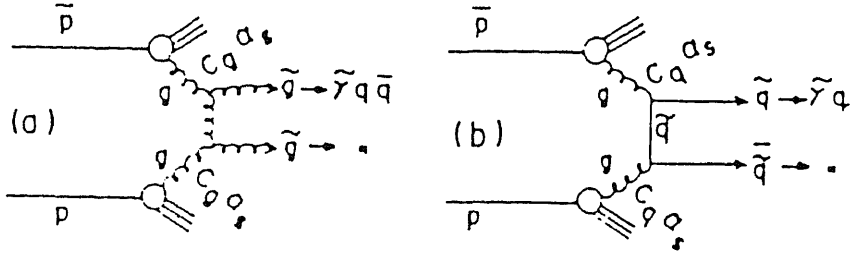

Figure 13. Pair production of (a) gluino and (b) squark via gluon-gluon fusion.

a function of $\tilde{q}$ or $\tilde{g}$ mass by convoluting their pair production cross-section with the probability of one of them decaying into a leading $\tilde{\gamma}$ [24].

The SM background for large missing-p_T events come from prompt neutrino production processes, notably $W \to \tau\nu$ ($Z \to \nu\bar{\nu}$) accompanied by QCD jets. The size of this background can be estimated from the observed rate of $W \to \ell\nu$ ($Z \to \ell\bar{\ell}$) accompanied by QCD jets. Observation of no clear excess over this background has led to lower mass limits of $\tilde{q}$ and $\tilde{g}$ from the CERN $\bar{p}p$ and Tevatron colliders. The strongest mass limit of (12) is based on the early Tevatron data with an integrated luminosity of ~ 4 pb^{-1} [9]. With luminosity upgradation it is possible to extend to search to ~ 250 GeV. Finally the search can be carried up to the theoretical mass bound of ~ 1 TeV at the LHC. Fig. 14 shows the expected gluino signal against the SM background at LHC [25].

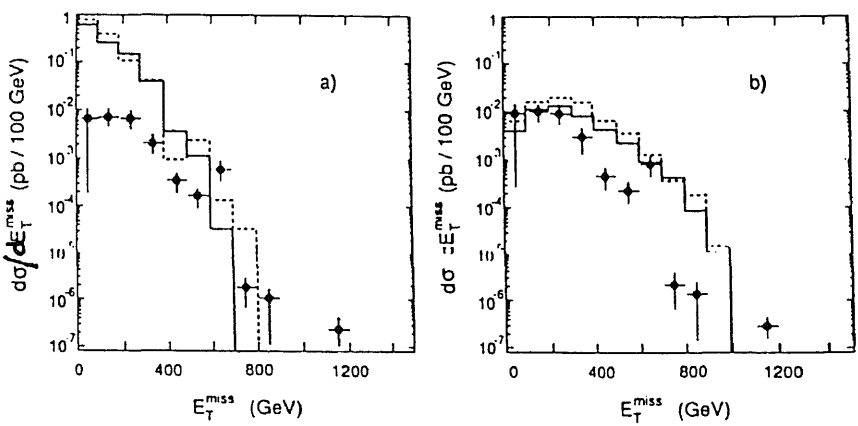

Figure 14. ISA JET Monte Carlo prediction for missing $-E_T$ distribution after selection cuts for (a) $M_{\tilde{g}} = 300$ GeV and (b) $m_{\tilde{g}} = 100$ GeV at LHC. The solid (dashed) line corresponds to the gluino signal for $\tan\beta = 2(10)$, while the points represent the total SM background [25].

There is a good deal of recent interest in a second type of superparticle signature – i.e. the multilepton and in particular the like sign dilepton signature. It arises from i) the leptonic decay of LSP in the R-parity violating SUSY model and ii) from

the cascade decay of $\tilde{g}$ or $\tilde{q}$ into LSP ($\tilde{\gamma}$) via W/Z, which holds for the R-conserving SUSY model as well.

i) It is clear from Fig. 10 that proton stability requires B or L conservation, but not necessarily both. Hence one can have two types of R-violating SUSY models, corresponding to B and L violation [25]. The former implies LSP decay into a multiquark channel which are hard to distinguish from the QCD background; but the latter implies a distinctive leptonic decay of LSP

$$\tilde{\gamma} \to \ell\bar{q}q' \text{ (or } \ell\bar{\ell}'\nu). \tag{28}$$

Eqs. 26-28 imply at least 2 leptons in the final state; and they are expected to have like sign half the time, thanks to the Majorana nature of $\tilde{\gamma}$. This results in a distinctive like sign dilepton (LSD) signature for superparticle production in the R-violating SUSY model, analogous to the missing-p_T signature for the R-conserving model. The CDF dilepton data from the Tevatron collider [11] has been analysed in [26] to give a mass limit of

$$M_{\tilde{q},\tilde{g}} > 100 \text{ GeV} \tag{29}$$

in the R-violating SUSY model. This is comparable to the corresponding mass limit (12) for the R-conserving model. Using the LSD signature one can extend the $\tilde{g}$ search in the R-violating SUSY model upto a mass range of ~ 1 TeV at the LHC [27]. Moreover the LSD signature is also relevant for $\tilde{g}$ search at LHC in the R-conserving SUSY model as we see below.

ii) In the mass range of a few hundred GeV, the gluino undergoes cascade decay into photino via $\tilde{W}$ and $\tilde{Z}$. In particular

$$\tilde{g} \xrightarrow{50\%} \bar{q}q'\tilde{W} \tag{30}$$

followed by

$$\tilde{W} \to W\tilde{\gamma} \xrightarrow{20\%} \ell\nu\tilde{\gamma}. \tag{31}$$

This means a leptonic branching fraction of $\sim 10\%$ for $\tilde{g}$ decay, i.e. a branching fraction of $\sim 1\%$ for a dilepton final state resulting from the $\tilde{g}\tilde{g}$ pair. Finally the Majorana nature of $\tilde{g}$ implies a LSD final state half the time. Despite its small branching fraction ($\sim 1/2\%$) the LSD channel provides a viable gluino signature upto $M_{\tilde{g}} \sim 1$ TeV at LHC because of the small SM background.

Fig. 15 shows the expected gluino signal along with the background in the LSD channel as functions of the accompanying missing-p_T [27]. It may be mentioned here that the neutral and charged gauginos ($\tilde{\gamma}, \tilde{Z}$ and $\tilde{W}$) mix with their Higgsino counterparts; and one has to diagonalise the resulting neutralino and chargino mass matrices for a quantitative estimate of the gluino signal [27]. Nonetheless the simplified description of the signal outlined above is valid to a good accuracy.

Conclusion – In summary, the searches for top quark, Higgs boson(s) and possible superparticles are the three main physics objectives of Tevatron and the LHC. There is good reason to expect a definitive top quark signal in the mass range of ~ 175 GeV to emerge from the forthcoming Tevatron data. But one needs the LHC to carry the Higgs and superparticle searches over the predicted mass range going upto

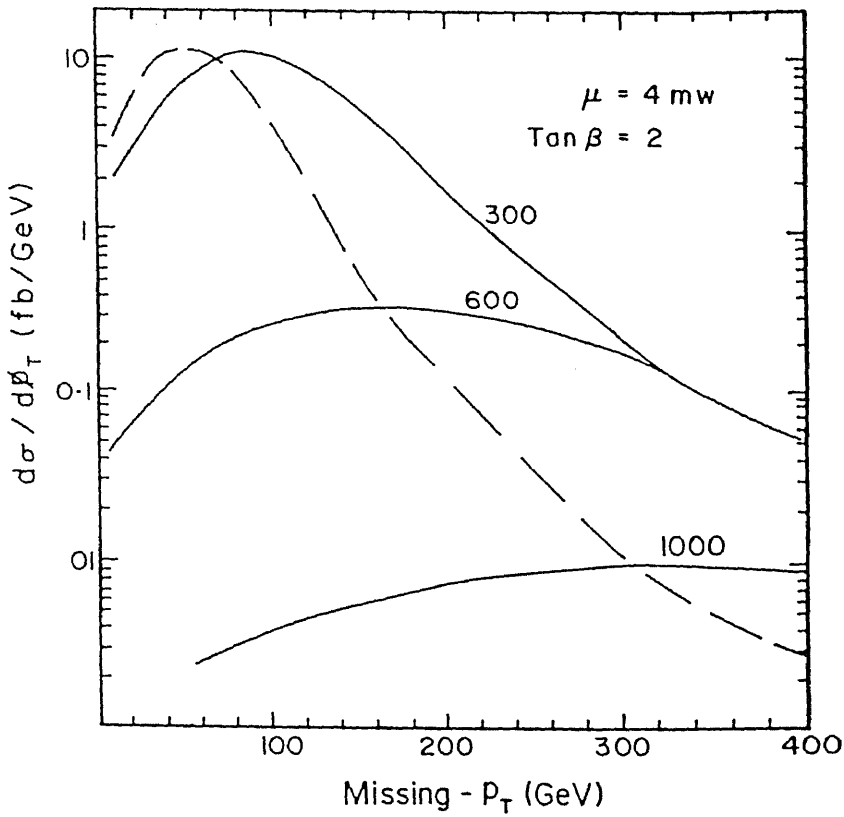

Figure 15. The expected LSD signals for different gluino masses (300,600,1000 GeV) shown against the accompanying missing-p_T along with the dominant background (dashed line) at LHC. The signal curves are for the R-conserving SUSY model with $\tan\beta = 2$ and the Higgsino mass parameter $\mu = 4M_W$ [27].

~ 1 TeV. It should be noted here that the Higgs and supersymmetric particles are the minimal set of missing pieces which will complete the picture of elementary particles and their interactions. But of course this is not the only set. It may very well be that the nature has chosen an alternative way of completing this picture with a different (and larger) set of missing pieces. In that case one expects to see experimental signals of this new physics alternative in lieu of the Higgs and superparticles, but still in the energy range of $\lesssim 1$ TeV. Thus one hopes that the LHC data will help to complete the picture of elementary particle physics along the lines outlined above (i.e. the MSSM), or else provide crucial experimental clue pointing to the alternative route.

References

[1] Review of Particle Properties, Phys. Rev. D50, 1173-1826 (1994).

[2] CDF Collaboration: F. Abe et al., Phys. Rev. Lett. 73, 225 (1994); Fermilab-Pub-94/097-E (submitted to Phys. Rev. D).

[3] These top quark candidate events of the CDF experiment were reported [2] after the WHEPP-3; but a brief discussion of these events shall be included for the sake of completeness.

[4] See e.g. V. Barger and R.J.N. Phillips, "Collider Physics", Addison-Wesley (1987).

[5] All these are very similar to the QED case.

[6] See e.g. J. Gunion, H. Haber, G. Kane and S. Dawson "The Higgs Hunters Guide", Addison-Wesley (1990).

[7] Unfortunately the high top quark mass makes it too unstable to form toponium states.

[8] See e.g. H. Haber and G. Kane, Phys. Rep. 117C, 75 (1985).

[9] CDF collaboration: F. Abe et al., Phys. Rev. Lett. 69, 3439 (1992).

[10] R.M. Godbole, S. Pakvasa and D.P. Roy, Phys. Rev. Lett. 50, 1539 (1983); see also V. Barger, A.D. Martin and R.J.N. Phillips, Phys. Rev. D28, 145 (1983).

[11] CDF collaboration: F. Abe et al., Phys. Rev. D45, 3921 (1992).

[12] S. Gupta and D.P. Roy, Z. Phys. C39, 417 (1988).

[13] H. Baer, V. Barger and R.J.N. Phillips, Phys. Rev. D39, 3310 (1989); V. Barger, J. Ohnemus and D. Zeppenfeld, Phys. Rev. Lett. 62, 1971 (1989); Phys. Rev. D40, 2888 (1989); W.T. Giele and W.J. Sterling, Nucl. Phys. B343, 14 (1990).

[14] N.K. Mondal and D.P. Roy, Phys. Rev. D49, 183 (1994).

[15] R.J.N. Phillips, Higgs Searches and WW Scattering (these proceedings).

[16] We shall not discuss neutral Higgs boson search further since it is covered in the talk of R.J.N. Phillips [15].

[17] V. Barger and R.J.N. Phillips, Phys. Rev. D41, 884 (1990); A.C. Bawa, C.S. Kim and A.D. Martin, Z. Phys. C47, 75 (1990); R.M. Godbole and D.P. Roy, Phys. Rev. D43, 3640 (1991); M. Drees and D.P. Roy, Phys. Lett. B269, 155 (1991).

[18] B.K. Bullock, K. Hagiwara and A.D. Martin, Phys. Rev. Lett. 67, 3055 (1991); Nucl. Phys. B395, 499 (1993).

[19] D.P. Roy, Phys. Lett. B277, 183 (1992); B283, 403 (1992).

[20] V. Barger, R.J.N. Phillips and D.P. Roy, Phys. Lett. B324, 236 (1994).

[22] S. Dimopoulos, L.J. Hall and S. Raby, Phys. Rev. D45, 4192 (1992); V. Barger, M.S. Berger and P. Ohmann, Phys. Rev. D47, 1093 (1993).

[23] Momentum balancing in the longitudinal direction is not possible in a hadron collider due to the loss of particles along the beam pipe.

[24] E. Reya and D.P. Roy, Phys. Lett. 141B, 442 (1984); Phys. Rev. Lett. 53, 881 (1984); Phys. Rev. D32, 645 (1985); J. Ellis and H. Kowalski, Phys. Lett. 142B, 441 (1984); Nucl. Phys. B246, 189 (1984); V. Barger, K. Hagiwara and W.Y. Keung, Phys. Lett. 145B, 147 (1984); A.R. Allan, E.W.N. Glover and A.D. Martin, Phys. Lett. 146B, 247 (1984).

[25] Report of the Supersymmetry Working Group (C. Albarjar et al), Proc. of ECFA-LHC Workshop (CERN 90-10), Vol. II, 606-683 (1990).

[26] D.P. Roy, Phys. Lett. B283, 270 (1992).

[27] H. Dreiner, M. Guchait and D.P. Roy, Phys. Rev. D49, 3270 (1994).

PRAMANA
— journal of
physics

© Printed in India

Supplement to Vol. 45
October 1995
pp. 313-337

The evolution of the quark-gluon plasma

HELMUT SATZ

Theory Group, CERN, CH-1211 Geneva, Switzerland *and* Fakultät für Physik, Universität Bielefeld D-33501 Bielefeld, Germany.

Abstract. We survey the different stages in the evolution of the quark-gluon plasma expected to be produced in high energy nuclear collisions, and we discuss some specific experimental probes for each.

1. Introduction

When we study strongly interacting matter in the framework of statistical quantum chromodynamics, we deal with ensembles of time-independent systems. Adiabatically, quark matter becomes hadronic matter, or vice versa. Our systems are in equilibrium to begin with, and they are transformed, very slowly and by slight of changes in external parameters, into other equilibrium systems. Nevertheless, we hope to test the essential predictions of these studies, quark deconfinement and chiral symmetry restoration, through nuclear collisions, in which our initial system, consisting of two colliding nuclei, is certainly not in any way thermal, and in which whatever matter is eventually produced very rapidly expands and freezes out into non-interacting hadrons. While the basis of what we try to study indeed is given by statistical QCD, our tools must clearly be adopted to the rapidly evolving world accessible to us in high energy nuclear collisions. Whatever we measure will reflect the properties of the system in some stage of its evolution, and we have to learn to associate specific observables and specific stages of the system we are studying. In this survey, I will try to give some examples of how to probe the evolution of the quark-gluon plasma, from two colliding parton beams to the observation of identified hadrons.

Over the past years, three stages in high energy nuclear collisions have attracted particular attention. In the period immediately after the collision, multiple scattering between the primary and secondary constituents is supposed to lead to a rapid generation of entropy and thus eventually to thermalisation. What happens at this stage is of crucial relevance for the subsequent properties of the system, and much important work on this topic has appeared during the past year, based in particular on event generators using parton dynamics [1]. The only tools we have to check this stage directly are hard early phenomena suffering little or no effect by the further

at the time they were formed – i.e., they will tell us about the hadronisation of the quark-gluon plasma [2]. If nuclear collisions do indeed lead to a thermalised system of quarks and gluons, this hadronisation stage, the final state in the evolution, will be independent of the initial thermal state, the primordial plasma. In other words, the *local* hadronisation properties of a plasma initially at a temperature of one GeV should be no different from those of a plasma of two hundred MeV [3]. How can we then probe the primordial plasma, the system we expect to be hotter at RHIC than at the SPS, and much hotter still at the LHC? The tools proposed for this purpose include quarkonium spectra [4], high mass thermal dileptons and hard thermal photons [5], thermal charm [6], and hard jets [7]. Of these, up to now only J/ψ suppression – predicted as a consequence of a hot primordial quark-gluon plasma – was actually observed; the analysis of charmonium spectra is therefore of particular interest.

In the following, I will address some specific aspects of probing each of the three evolution stages. Section 2 will be devoted to pre-equilibrium and thermalisation. In Section 3, quarkonium production will be considered as a probe of the early hot and dense thermal stages in nuclear collisions. Section 4 will then deal with what spectra of thermal hadrons can tell us about the quark-hadron transition and the freeze-out into free hadrons.

2. Pre-equilibrium and thermalisation

Thermal equilibrium can be attained by multiple scattering among the constituents of the incident nuclei and the secondaries produced in these interactions. The primary interactions must trigger a cascade of more and more interacting secondaries, tertiaries, and so on, leading to a rapid entropy increase and with it a (local) loss of memory of the initial state. Computer simulations of such cascades provide estimates of the time t_0 needed to reach local equilibrium, and they tell us what the thermal conditions were at that time. They specify the initial energy density ϵ_0, the initial entropy density s_0, and they can tell us to what extent there is "chemical" equilibrium among the different constituent types, whether hadrons or partons.

In such simulations, a considerable number of input aspects has to be specified in order to arrive at definite predictions.

- What is the nature of the constituents? They can be hadrons, constituent quarks, or the partons (massless quarks and gluons) of perturbative QCD.
- What is the collision dynamics? We can start from a phenomenological picture of hadronic interactions (ARC [8], dual parton model [9]), from string interactions (Venus [10], RQMD [11] Spacer [12]), or from perturbative QCD for partonic interactions, with soft additions both for low P_T processes and for the hadronisation of the partons (Hijing [13], parton cascade model [14]).
- What is the evolution pattern for the collision? Here we can consider independent successive binary collisions, molecular dynamics schemes or a more detailed transport theory description.
- What collective interaction effects should be included? Since all evolution patterns considered are approximative, we have to make sure that such col-

shadowing and jet quenching are correctly taken into account.

It is thus clear that the results of such microscopic evolution studies are necessarily quite model dependent. Therefore an obvious requirement is that before making predictions for nuclear collisions, one has to tune the particular generator to reproduce the available data from hadron-hadron and hadron-nucleus collisions. Beyond this one may hope that in the high energy limit things become less ambiguous: eventually the basic input should be an internetted parton cascade, based on an underlying description in terms of perturbative QCD. The past year has brought a number of interesting studies in this direction. Here we can only summarize their results; for details, we refer to [15] [16].

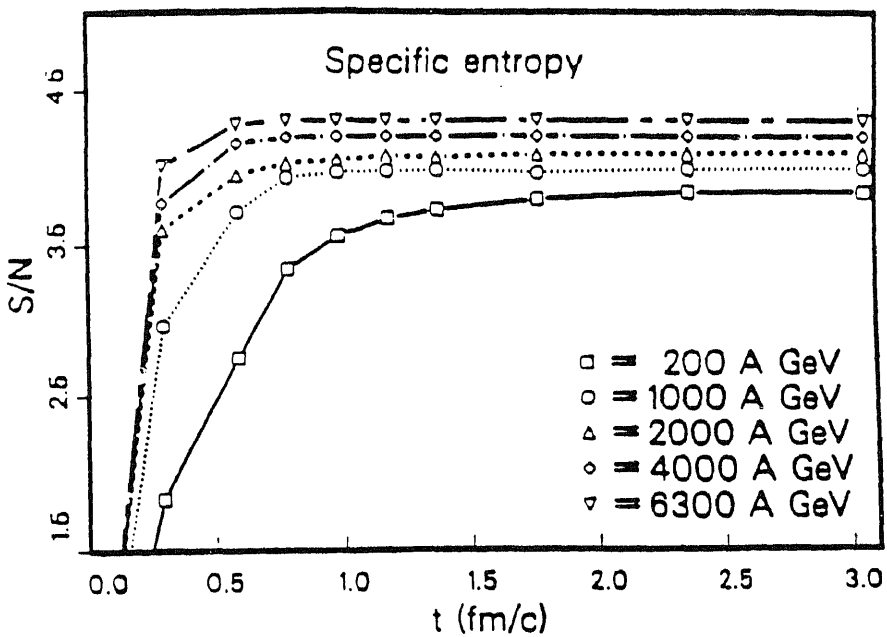

Figure 1. Entropy per parton as function of time after the collision, for different incident CMS energies $\sqrt{s}/A$; from [16].

The specific entropy (entropy per secondary) increases very rapidly at high energies [16], as seen in Fig. 1. While at RHIC energy it is still compatible with the one fermi generally assumed to be the equilibration time at present energies, we approach the expected value $S/N = 4$ in less than 0.5 fm for LHC energy. This rapid equilibration is also reflected in increasingly shorter relaxation times (Fig. 2). As a consequence, the initial temperatures become higher (Fig. 3), since we can now start considering the system as thermal at earlier times.

On the other hand, these high energy considerations do not lead to a corresponding rapid onset of chemical equilibrium. As had been pointed out quite some

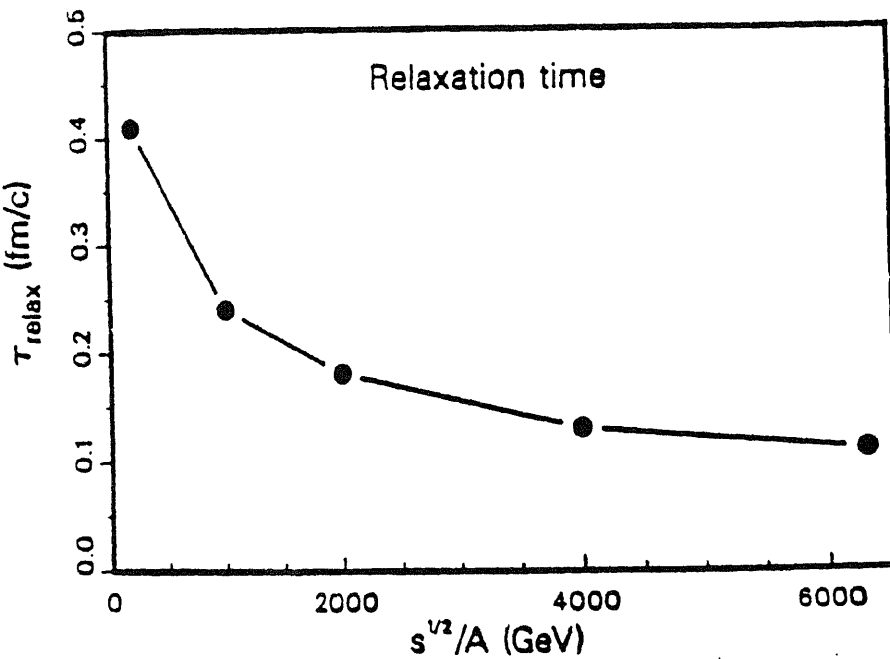

Figure 2. Relaxation time as function of the beam energy $\sqrt{s}/A$; from [16].

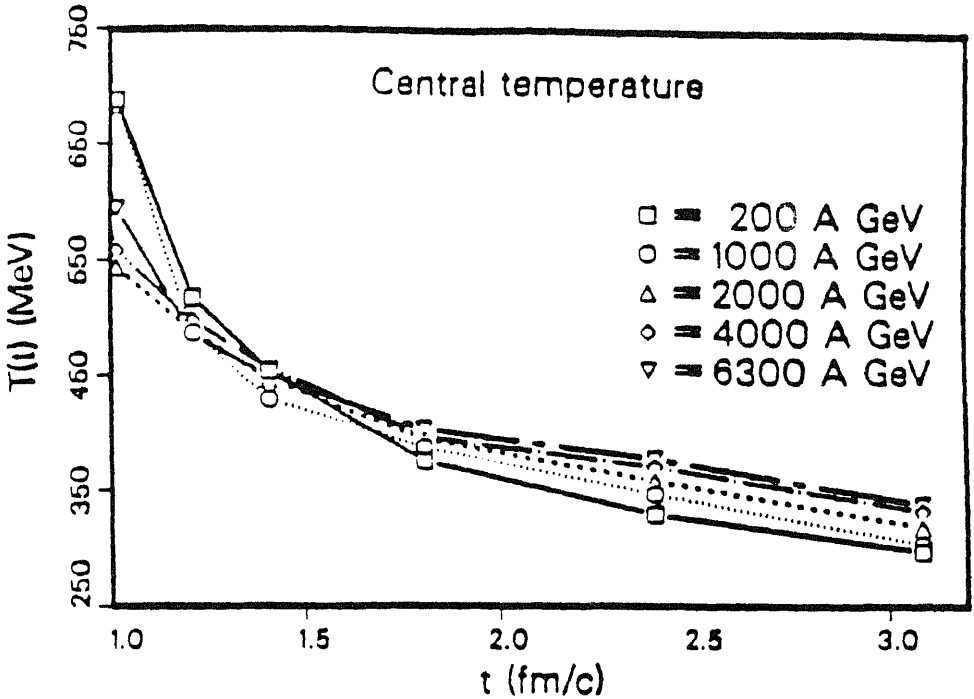

Figure 3. Central temperature as function of time after the collision, for different incident CMS energies $\sqrt{s}/A$; from [16].

time ago [17], the gluon interaction cross sections, including those leading to further gluon production, are considerably larger than their quark counterparts. This results in a perturbative QCD cascade with a very rapid gluon thermalisation, so that the entropy of the gluons soon reaches its equilibrium value. The entropy of the quarks, although it also increases quickly, appears to remain at about 60 - 70% of its equilibrium value for quite some time (Fig. 4). This behaviour has therefore been called the "hot gluon scenario" [6]. We should note, however, that it does not make the early thermal system a *gluon* plasma. A quark-gluon plasma (with 2.5 light quark flavours) in both thermal and chemical equilibrium would contain quarks and gluons in a ratio of about 1.6:1; in the hot gluon scenario we have instead a ratio of about 1:1, so that there are still as many quarks as there are gluons.

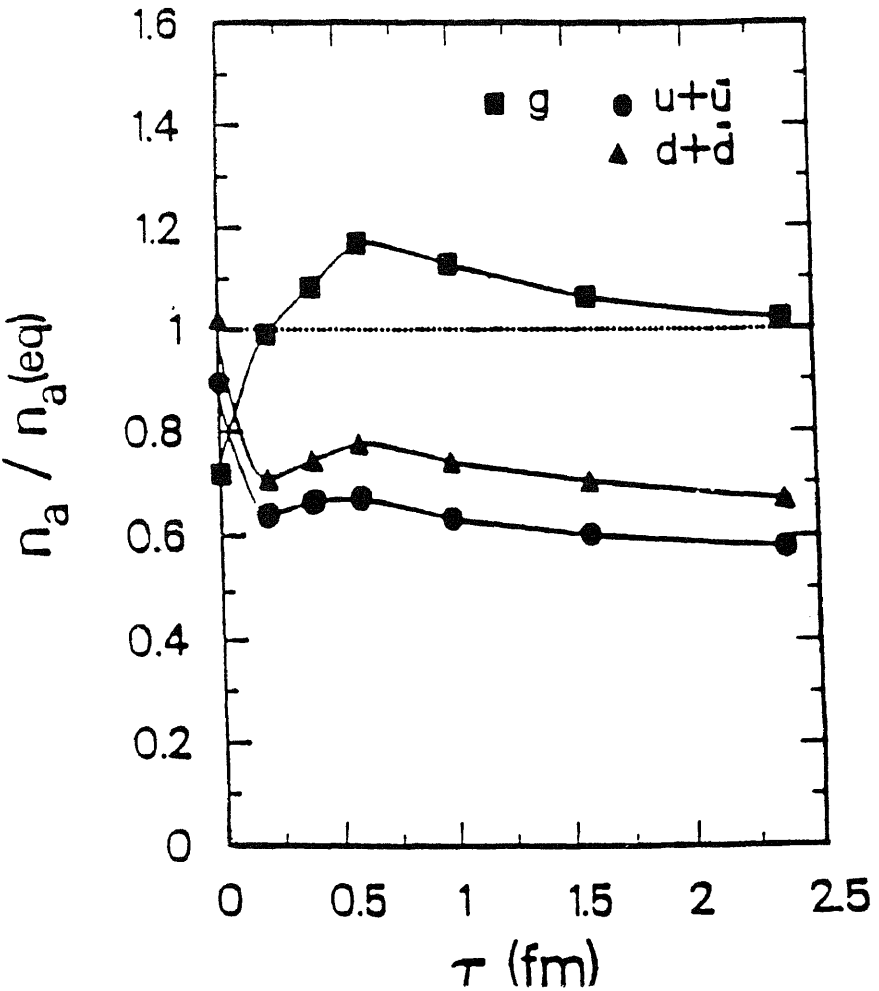

Figure 4. Parton densities, normalised to equilibrium values, for different parton species, as functions of the proper time after the collision; from [16].

The basis of these considerations is a dominance of perturbative QCD processes for the overall behaviour of the system at RHIC and in particular at LHC energies.

How can we test if this is correct? Two basic predictions of the partonic pre-equilibration stage are enhanced open charm [18] and enhanced high mass dilepton production [19]. The former arises because the abundant presence of hard secondary (and tertiary, etc.) gluons, the second since the fewer quarks are therefore harder. Since there are more hard gluons than quarks, open charm production will, however, be enhanced more than that of high mass dileptons.

Here two caveats seem appropriate. First of all, we have to say with respect to what the enhancement is to be measured. With decreasing fractional parton momentum $x \sim (M/\sqrt{s})$, the gluon distributions in *hadrons* are expected to grow more strongly than those for quarks, so that increasing energies will presumably lead to an increase of open charm relative to Drell-Yan productions even in $p-p$ collisions. Hence we will always need hadron-hadron collision data as reference to define the predicted pre-equilibrium enhancement in nucleus-nucleus collisions. Secondly, the high energy predictions for nuclear collisions have not yet been extrapolated down to lower energies where there is data to compare them to. This is obviously not trivial, since at lower energies the soft components are crucial. As long as their role is not checked specifically for the noted processes (open charm, Drell-Yan production), it is not clear how reliable the high energy predictions really are.

We summarize this section by noting that the production of open charm and beauty as well as that of high mass dileptons should provide good tools to probe the pre-equilibrium stage and the onset of thermalisation.

3. The primordial plasma

We now turn to the question of how we can verify if the systems produced in high energy nucleus-nucleus collisions were in their early stages indeed deconfined states of matter. As already noted, for this we need probes which are formed in the primordial stage, and only then, in order to avoid the subsequent "destruction of memory" in a thermal evolution. There are essentially three probes of this type which have so far been considered: quarkonium states (J/ψ, ψ', Υ, Υ'), real or virtual photons (dileptons), and hard jets. We shall here concentrate on the first of these three, since it constitutes the only predicted signature which has in fact been observed experimentally, since it has been studied most extensively (including, in particular, also competing alternative mechanisms), and finally since it illustrates the kind of analysis necessary before we can arrive at any conclusions. The topic of this section thus is quarkonium production as probe of the early quark-gluon plasma; to have a definite process, we shall talk about charmonium (J/ψ and ψ'), but everything is applicable to bottonium production as well.

The basic physics of the probe is quite simple. Charmonium production in hadronic collisions occurs in two stages. We have first a hard process, the fusion of two gluons to form a (coloured) $c\bar{c}$ pair, and then subsequently soft colour neutralisation and resonance binding. The first process, presumably described in terms of perturbative QCD, takes only about $M_c^{-1} \simeq 0.1$ fm or less; the second needs about 0.3 - 0.5 fm [20] [21]. If nuclear collisions lead to the formation of a deconfined medium, then the second step is inhibited in such collisions, the c and the $\bar{c}$ fly apart and eventually form open charm D mesons. In contrast, the overall Drell-

Yan rate is essentially unaffected by the presence of the plasma. In the dilepton spectrum from high energy nuclear collisions, we thus expect a suppression of the J/ψ and ψ' signals relative to the Drell-Yan continuum, if there was quark-gluon plasma production [4]. This suppression should manifest itself in a smaller signal-to-continuum ratio in nucleus-nucleus collisions when compared to hadron-hadron and hadron-nucleus collisions, and it should become stronger with increasing energy density in nucleus-nucleus collisions. Both these effects are in fact observed [22], and we thus have to interpret these observations.

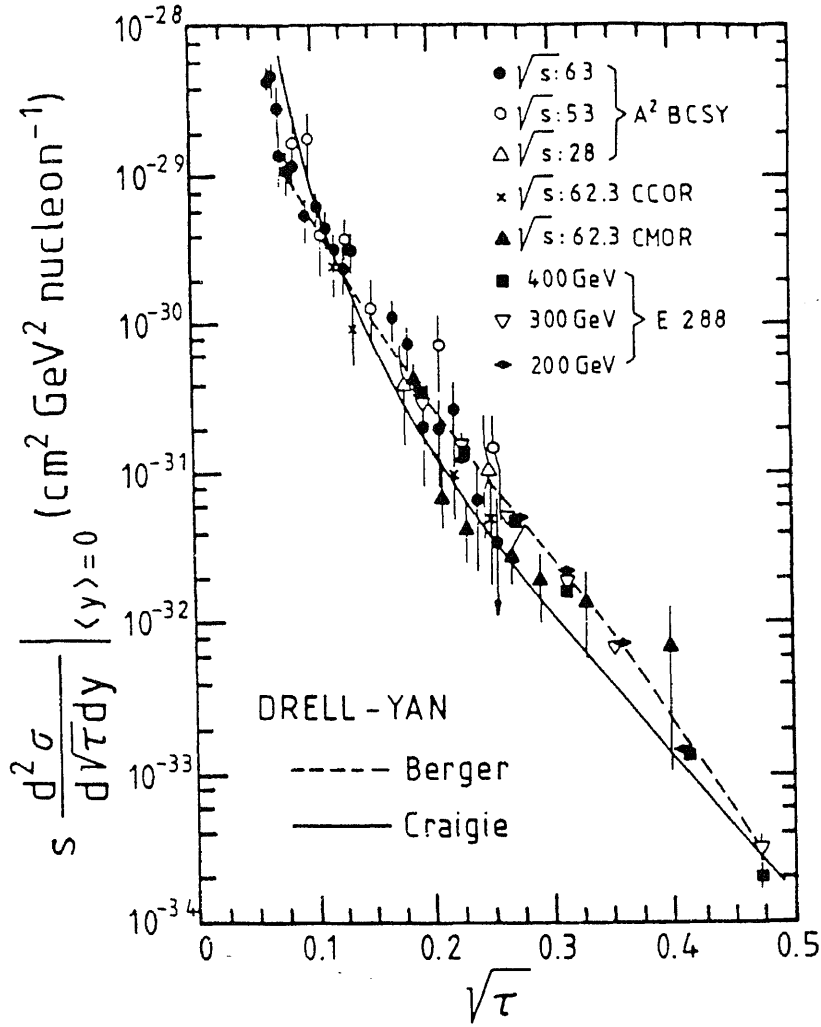

Figure 5. Drell-Yan rates in $p-p$ collisions [45], compared to calculations using quark structure functions (dashed line) [46] and to a fit [47].

Our analysis of experimental results will proceed in several steps. To start with, we show that the overall charmonium and Drell-Yan production rates in hadron-hadron collisions are basically understood, the first in terms of gluon fusion, the

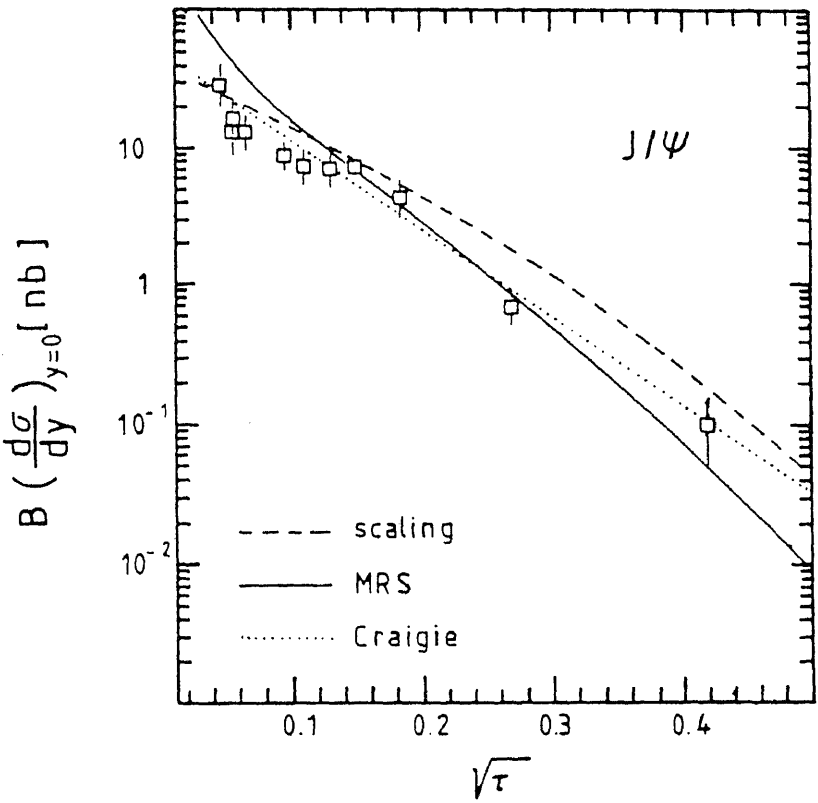

Figure 6. J/ψ production rates in $p-p$ collisions, as obtained for MRS and scaling structure functions [48] and from a fit [47], compared to experimental results [49].

second through quark-antiquark annihilation. In Figs. 5 and 6 we show $p-p$ data for these processes, compared to perturbative predictions using different structure function parametrisations. The data, available at present for CMS energies up to $\sqrt{s} \simeq 100$ GeV, are quite well accounted for. Beyond that energy, we need the structure functions at very small x. HERA will provided this; but it would certainly be good to have independent $p-p$ data at higher energies. We note further that gluon fusion as basic mechanism for charmonium production is nicely supported by recent data comparing results obtained with incident p, π^+, π^- and $\bar{p}$ beams [23].

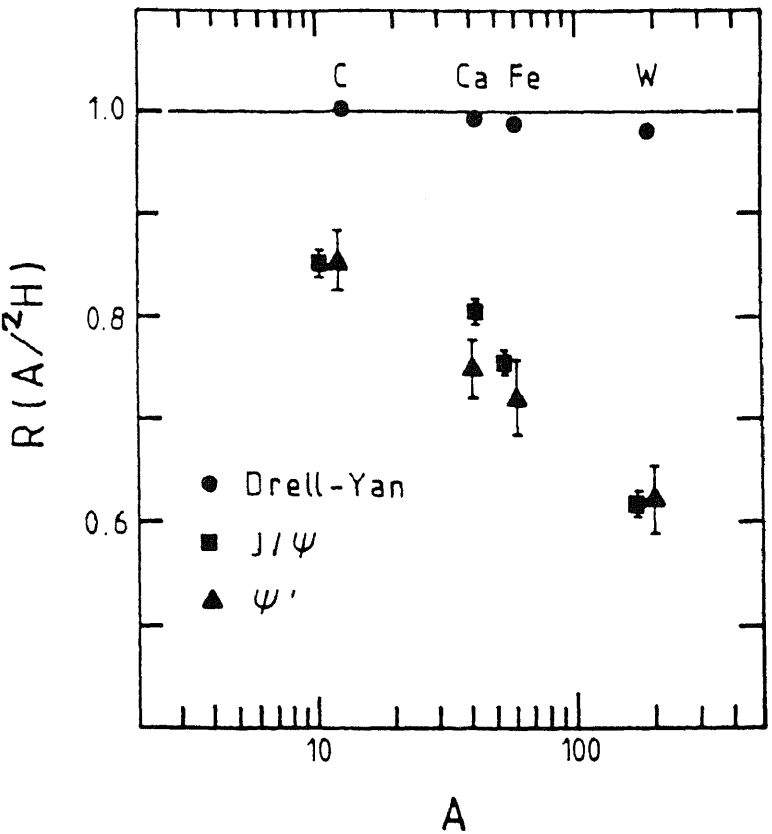

Figure 7. J/ψ and ψ' production in $p-A$ vs. $p-p$ collisions, as function of A [25].

Next we turn to hadron-nucleus collisions. It is found [24] [25] that charmonium production in such collisions (and that of bottonium as well) is suppressed with increasing A, in comparison to the corresponding production on hadrons (Figs. 7 and 8). It thus seems natural to ask if the suppression found in nucleus-nucleus collisions could be due to the same mechanism as in hadron-nucleus reactions; if this were possible, the suppression in nucleus-nucleus collisions could of course not be interpreted in terms of deconfinement. Theoretically, such a common mechanism is difficult to justify. The kinematically accessible region in $h-A$ collisions implies that the produced $c\bar{c}$ pairs leave the nucleus as a small colour octet state and reach

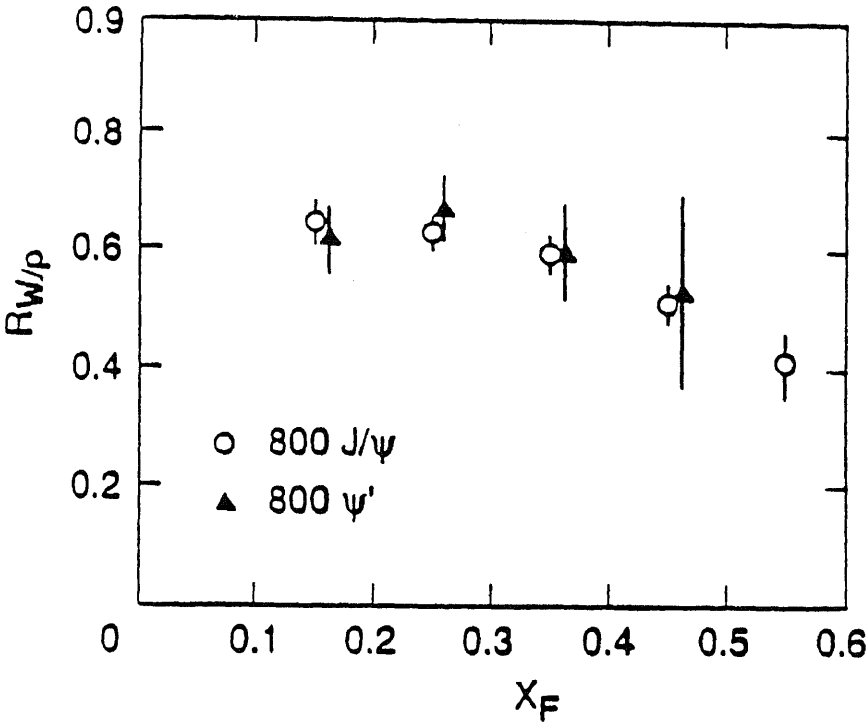

Figure 8. J/ψ and ψ' production in $p-W$ vs. $p-p$ collisions, as function of x_F [25].

physical resonance size only far outside the target; in $A-B$ collisions, on the other hand, fully formed resonances can interact with partially stopped strongly interacting matter. A specific consequence of the pre-hadronic character of the $c\bar{c}$ in $h-A$ collisions is that the suppression of the J/ψ and the ψ' should there be the same; this is in fact observed (see Figs. 7 and 8). The relevant mechanism for the suppression in $h-A$ collisions is thus expected to be a combination of colour interactions [21] [26] and gluon shadowing [27], and this does in fact account for all data in the region $0 < x_F < 1$, as seen in Figs. 9 and 10 [21].

We now return to the suppression in nucleus-nucleus collisions. As already noted, the accessible kinematic region ($0 < x_F < 0.2$) allows the formation of physical resonances in the medium. The observed suppression could thus be due to some type of absorption in confined matter at very high density [28] as well to deconfinement, and we have to find a way to distinguish between the two mechanisms. But whatever the origin of the suppression, the existence of physical resonance states predicts that the ψ' , because of its larger geometric size, will suffer a stronger suppression than the J/ψ. Specifically, this means that the ratio $\psi'/(J/\psi)$ production in $A-B$ collisions should be smaller than in $h-A$ collisions, and that it should decrease with increasing energy density (or equivalently, with E_T). Both predictions are observed [29] [30], as shown in Fig. 11. We therefore conclude that the A-dependent charmonium suppression in $h-A$ collisions and the E_T-dependent suppression in $A-A$ collisions have different origins.

The last step of our analysis should now tell us what the origin of the charmonium suppression in $A-B$ collisions is. We recall that the data [22] shows a J/ψ suppression increasing with E_T, up to a reduction of signal-above-continuum of about 50% at the highest E_T values. While the continuum was up to now mainly determined by the mass range below the J/ψ, the suppression is now established [30] also through the high mass continuum above the ψ', and it persists when the gluon shadowing effects determined in $h-A$ collisions are removed [31]. A similar but stronger suppression is found for the ψ'; moreover, the ratio $\psi'/(J/\psi)$ decreases with E_T. As is known, these features can be accounted for both by deconfinement (quark-gluon plasma formation) and by absorption in a hadronic medium of extreme density [31]. In the deconfinement picture, a charmonium state x survives if the energy density ϵ of the medium is less than the value ϵ_x needed to dissolve it. In nuclear collisions, with a hot inner and a cooler outer interaction region, the survival probability thus becomes

$$S_x^d = \left(\frac{V_{\text{cold}}^x}{V}\right), \tag{1}$$

where V_{cold}^x is that part of the interaction volume V in which $\epsilon \leq e_x$. With ϵ proportional to the nucleon density and with standard nuclear geometry (equidistribution of nucleons in the nucleus), this gives us

$$S_x^d(\epsilon) = \Theta(\epsilon_x - \epsilon) + \left(\frac{\epsilon_x}{\epsilon}\right)^{9/4} \Theta(\epsilon - \epsilon_x) \tag{2}$$

for the survival probability of charmonium state x. In the case of absorption in an expanding medium, on the other hand, this survival probability is given by

$$S_x^a(\epsilon) = \exp\{-\sigma_x n(\epsilon) \tau_o \ln(\tau_o/\tau_f)\}; \tag{3}$$

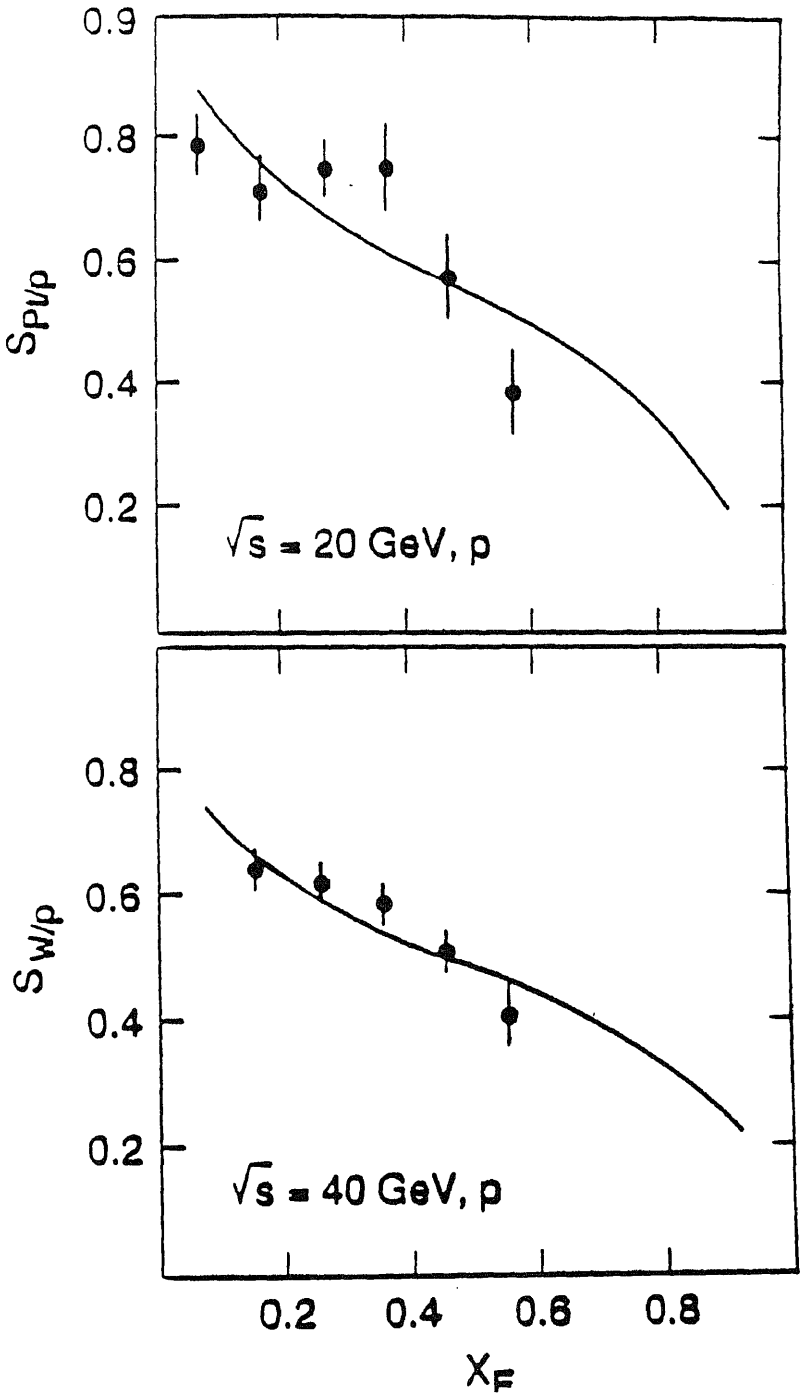

Figure 9. J/ψ production in $p - Pt$ and $p - W$ vs. $p - p$ collisions for different $\sqrt{s}$, as function of x_F [21].

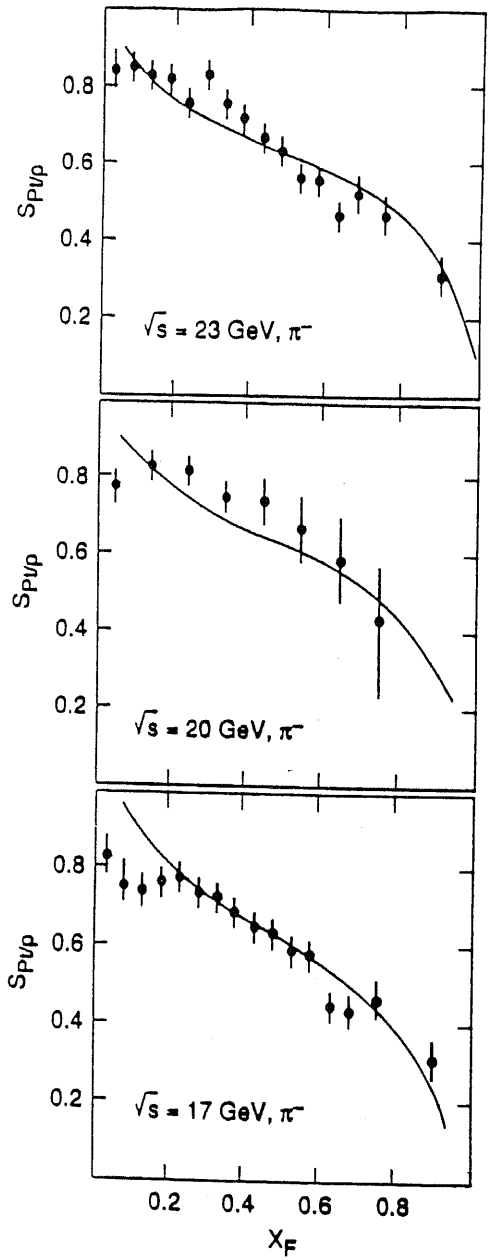

Figure 10. J/ψ production in $\pi^- - Pt$ vs. $\pi^- - p$ collisions for different $\sqrt{s}$, as function of x_F [21].

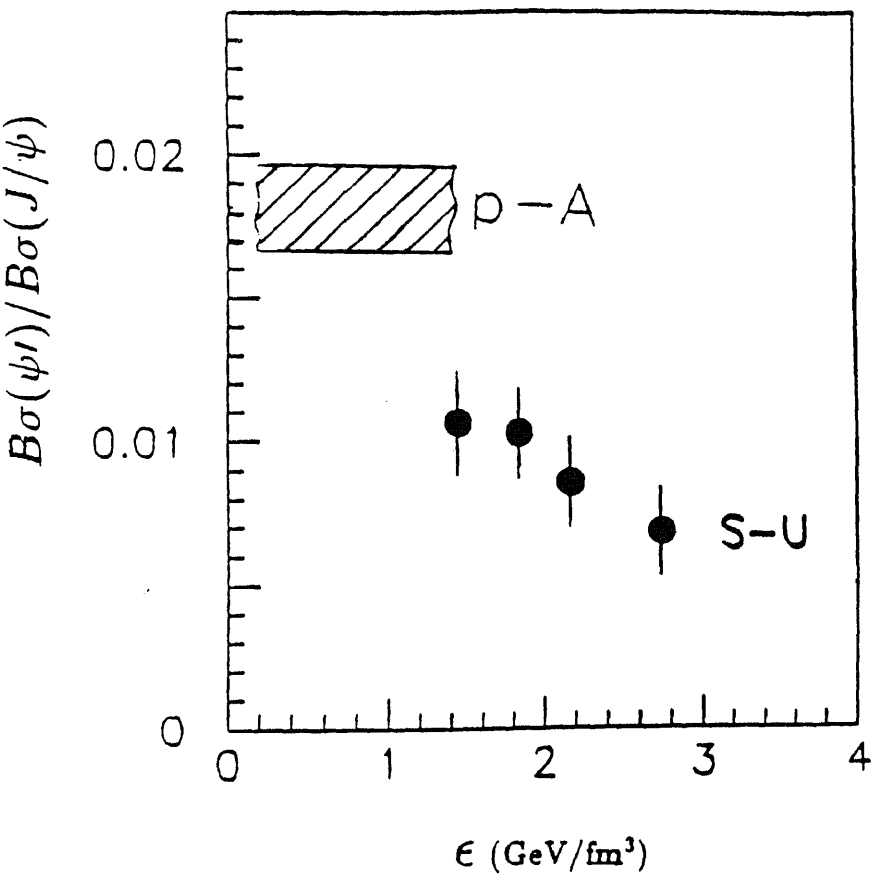

Figure 11. The ratio of ψ' to J/ψ production in $p-A$ and $S-U$ collisions as function of the initial energy density ϵ_0 [30].

at energy density ϵ, τ_o the equilibration time and τ_f the time at which the medium becomes too dilute to provide absorption.

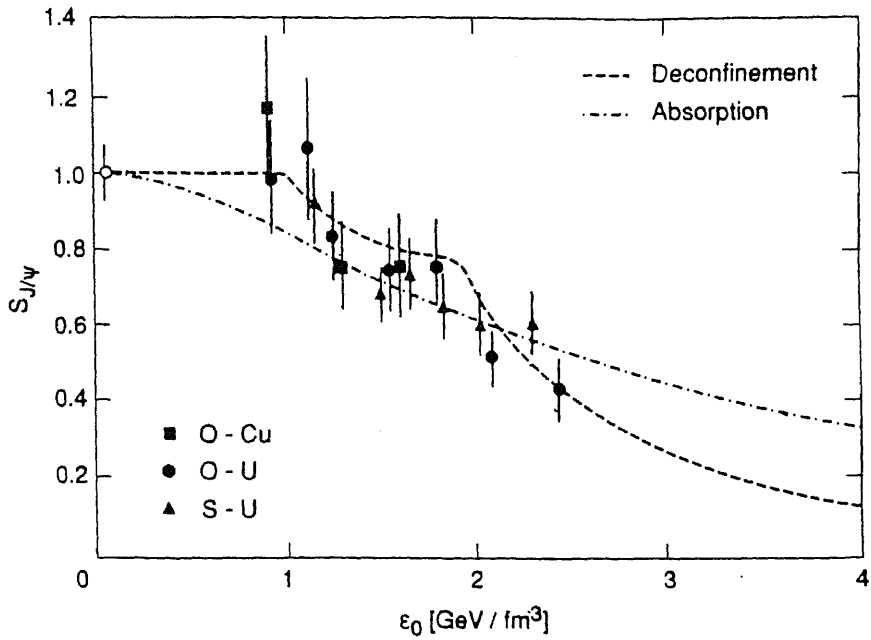

Figure 12. J/ψ suppression as function of the initial energy density ϵ_0 for deconfinement and absorption in dense matter [31].

The two J/ψ suppression patterns resulting from eqs. (2) and (3) are shown in Fig. 12, together with the presently available data [31]. Both are seen to account for the experimental results. We should note, however, that in both approaches the agreement with the data implies an energy density of 2 - 3 GeV/fm^3 at the high end. In the deconfinement picture, such a density results in a quark-gluon plasma and hence charmonium melting. In the hadronic absorption scenario, however, it means a density of four or more hadrons per normal hadronic volume [32], and the J/ψ or ψ' must interact independently with each of these hadrons. It is conceptually not clear how this can take place.

What qualitative differences are there between the two suppression mechanisms? We note two possible effects to look for.

- The pure $1S$ ψ state needs a higher energy density to "melt" than the larger excited χ_c state, which decays into a ψ. The observed J/ψ's are about 70% directly produced and about 30% due to χ-decays. The J/ψ survival proba-

bility thus becomes

$$S_J^d(\epsilon) = 0.3 \left[\Theta(\epsilon_\chi - \epsilon) + \Theta(\epsilon - \epsilon_\chi)\left(\frac{\epsilon_\chi}{\epsilon}\right)^{9/4}\right] + 0.7 \left[\Theta(\epsilon_\psi - \epsilon) + \Theta(\epsilon - \epsilon_\psi)\left(\frac{\epsilon_\psi}{\epsilon}\right)^{9/4}\right], \quad (4$$

where the first term corresponds to the (earlier) suppression of the χ com ponent and the second to that of the direct ψ. As a result, there is th "bump" in the deconfinement suppression pattern seen in Fig. 12, while ab sorption leads to a monotonic decrease in ϵ. It is quite possible that quantur effects will wash out the two-component structure with its resulting diffe ent "melting points"; but if observed, if would certainly provide evidence fo deconfinement.

At any given density, larger resonances are always absorbed more than smalle hence in the absorption scenario, the ratio $\psi'/(J/\psi)$ must vanish with in creasing density. On the other hand, for a sufficiently high given densit deconfinement will melt all resonances; any survivors must come from th cool and hence non-deconfining outer regions of the interaction zone, whic are determined by nuclear geometry. As a consequence, the ratio $\psi'/(J/\psi$ takes on the constant value

$$\left(\frac{S_{\psi'}^d}{S_{J/\psi}^d}\right) = \left(\frac{\epsilon_{\psi'}}{\epsilon_\psi}\right)^{9/4} \quad \text{for } \epsilon \geq \epsilon_\psi \quad (5$$

in the case of deconfinement, while for absorption it vanishes exponentiall in ϵ, as seen in Fig. 13 [31].

At present, the statistics and the energy density range available do not yet allo any decision on the origin of charmonium suppression in $A - B$ collisions. We ca conclude, however, that quarkonium production does give us a tool to probe th primordial state, and this tool has so far indicated the existence of dense primordi matter.

4. The quark-hadron transition

The first goal of high energy nuclear collisions is to produce strongly interactin *matter*. We thus have to find a way to check if the systems produced in suc collisions are indeed in local thermal equilibrium. We hope that a detailed study *thermal* hadrons (i.e., those produced in the break-up of the quark-gluon plasm will provide a tool for this. Such hadrons will give us direct information about th system at the time they were formed: about its equilibration, size, temperatur flow structure, and more. The transition from a quark-gluon plasma to hadron matter is one of the most fascinating features of strong interaction thermodynamic It has attracted much interest, in statistical QCD as well as in the context phenomenological models, and it is clearly of great importance to find ways study it experimentally. If the quark-hadron transition and the final freeze-o

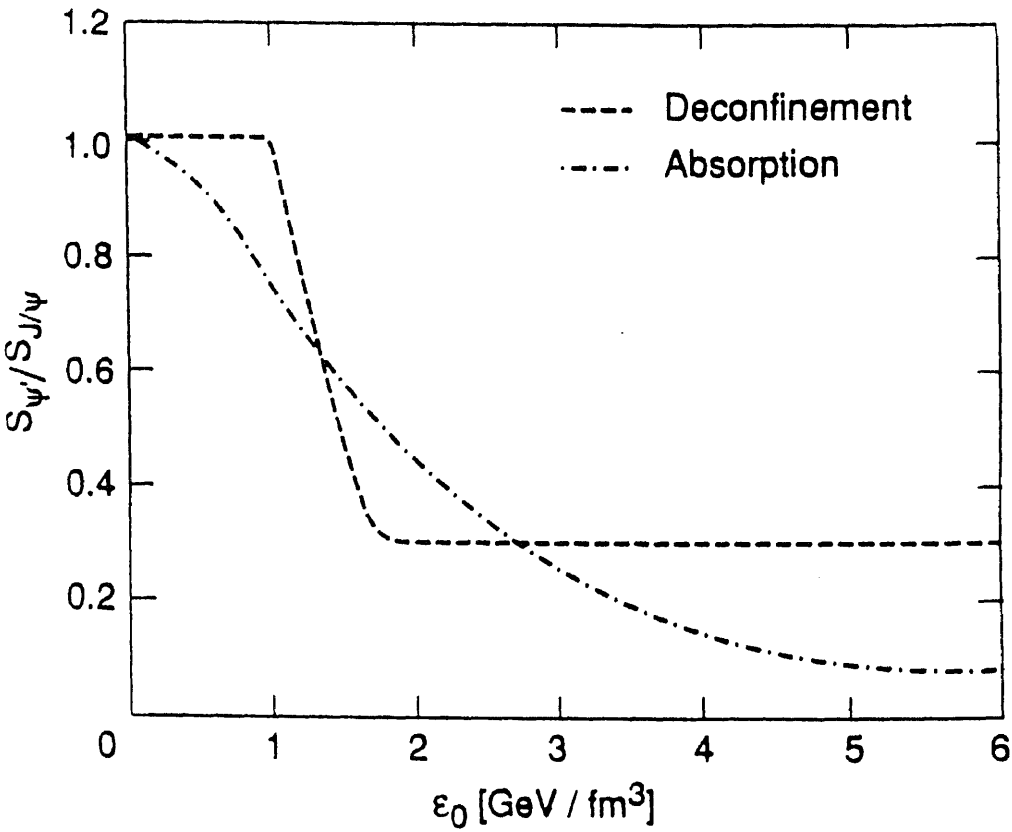

Figure 13. The ratio of ψ' to J/ψ suppression as function of the initial energy density ϵ_0 for deconfinement and absorption in dense matter [31].

are not far apart, it is quite likely that thermal hadrons will retain some transitio features and thus provide us with information about the critical region. In additior thermal hadrons can of course also give us indirect information about prior stages, the evolution pattern of the system is known; we could then use them to determin the initial entropy and energy density or the intial temperature. Here we will no assume the evolution to be known and thus consider thermal hadron production a a way to probe the quark-hadron transition and the freeze-out era.

The basic questions here seem to be these:

- Are the finally emitted hadrons in thermal equilibrium?
- Is there one universal freeze-out point, or do strong interactions stop for som hadrons earlier than for others?

Both questions appearently deal only with hadrons made up of light quarks; char monium and bottonium states, for example, presumably never partake in any ther mal equilibrium. Because of the miniscule Boltzmann factor ($\exp-(M_J/T) \simeq 10^{-}$ for $T \simeq 300$ MeV), the thermal production of these states is ruled out at all mean ingful temperatures.

Thermal equilibrium can appear in two forms. A system containing differen particle species can be in overall thermal equilibrium; this means that each specie has thermal momentum distributions, and that the relative abundance of the differ ent species is governed by their thermal weights, dependent on masses and interna degrees of freedom. Thermal equilibrium for a given species is, curiously enough not so easy to check in high energy nuclear collisions. It implies that the distribu tions of the emitted mesons and baryons should be of Boltzmann form,

$$\frac{dN}{dm_T} \sim e^{-(m_T/T)}, \tag{6}$$

with $m_T = (m^2 + p_T^2)^{1/2}$ denoting the transverse energy of a hadron of mass m It so happens that already the distributions of secondaries in $p-p$ reactions (anc with some caveats, even in e^+-e^- annihilation) have this form. This either in dicates that already these processes lead to thermal behaviour – a point of viev explored a number of times over the past fourty years [33] – or it is due to othe reasons (geometry, uncertainty effects). In either case we have no way to test ther mal behaviour for a given particle species specifically for nucleus-nucleus collisions We can, however, check if the different hadron species are produced according t some thermal weights, and this study has led to very interesting results. It started with the prediction of strangeness enhancement in nuclear collisions and was sub sequently developed into a rather well-defined method to probe thermalisation i this more "chemically equilibrated" sense [2].

If at freeze-out we do indeed have an ideal gas of hadrons and hadronic reso nances, then the system is described by the partition function

$$\ln Z(T, \mu_B, \mu_S) = \left[\sum_i W_i^m + \sum_i \left(l_B^{-B_i} l_S^{S_i} + l_B^{B_i} l_S^{-S_i}\right) W_i\right]. \tag{7}$$

Here W_i is the phase space factor for non-strange mesons of species i, while th

in question. The baryon-number fugacity is defined as $l_B = \exp(\mu_B/T)$ and that for the strangeness as $l_S = \exp(\mu_S/T)$. The phase space factors are given by

$$W_i = \frac{d_i m_i^2 VT}{2\pi^2} K_2\left(\frac{m_i}{T}\right), \tag{8}$$

with d_i denoting the degeneracy, m_i the mass of hadron species i; V is the volume of the system. For the temperature range presently of interest ($T \leq 250$ MeV), it is sufficient to include in the sums in eq. (7) all known hadrons up to a mass of 2 GeV. The partition function (7) then determines all thermal properties of the system in terms of the three parameters T, μ_B and μ_S. One of these, say μ_S, can be eliminated by requiring the overall strangeness of the system to vanish. If there is a one-stage freeze-out of all thermal hadrons, then *all* production ratios ($K/\pi, \pi/\rho, \pi/p, K/Y, Y/\bar{Y}, \Xi/Y, ...$) are given in terms of the two parameters T and μ_B. In other words, we can take two measured ratios, such as $\Lambda/\bar{\Lambda}$ and $\Xi/\bar{\Xi}$, to fix the values of T and μ_B, and all other ratios are then predicted, if the different particle species are indeed present according to their equilibrium weights. Although previous analyses had been in accord with this for all strange baryon and meson ratios at $T \simeq 200$ MeV [34, 38], $\mu_B \simeq 300$ MeV [39], newer and more precise data [40] no longer provide a common equilibrium freeze-out point even for strange hadrons (Fig. 14).

Bringing in non-strange hadrons had always led to disagreement, with lower freeze-out temperatures ($T \simeq 100 - 140$ MeV) as well as lower baryochemical potential ($\mu_B \simeq 200$ MeV). It is possible, however, to retain a common freeze-out for all strange hadrons by introducing partial strangeness saturation, i.e., by assuming that strangeness is not yet fully present in the system to the extent it should be if there was complete chemical equilibrium [41] With this assumption, the fugacities l_S and l_S^{-1} in eq. (7) are multiplied by a strangeness saturation factor $\gamma \leq 1$. This results in $T \simeq 200$ MeV and $\mu_B \simeq 250$ MeV as freeze-out parameters for the (partially equilibrated) strange hadrons [42], as seen in Fig. 15.

The unique freeze-out point for hyperons and cascade particles (and their antiparticles) arises by construction, of course, since we have three independent ratios and three parameters. The freeze-out point is also in accord with present Λ/K_s^o. One basic problem in this type of analysis is the availability of data in the same kinematic regions and for the same collision partners. It will be interesting to follow the further development of the freeze-out study for both strange and non-strange hadrons. All present results do suggest, however, that there is no unique freeze-out point for all hadrons.

It therefore seems reasonable to consider when freeze-out will occur. One possible definition is given by requiring the mean free path of a hadron in the medium to reach the size of the system. This leads to

$$R_F = \left[\left(\frac{3}{4\pi}\right)\left(\frac{dN}{dy}\right)\sigma\right]^{1/2} \tag{9}$$

for the freeze-out radius R_F; here σ denotes the interaction cross-section for the hadron in question. A hadron species with a bigger cross-section should thus undergo a later freeze-out [43]. If we assume strange hadrons to have an interaction cross-section half the size of non-strange cross-sections (this is the case for the Kp

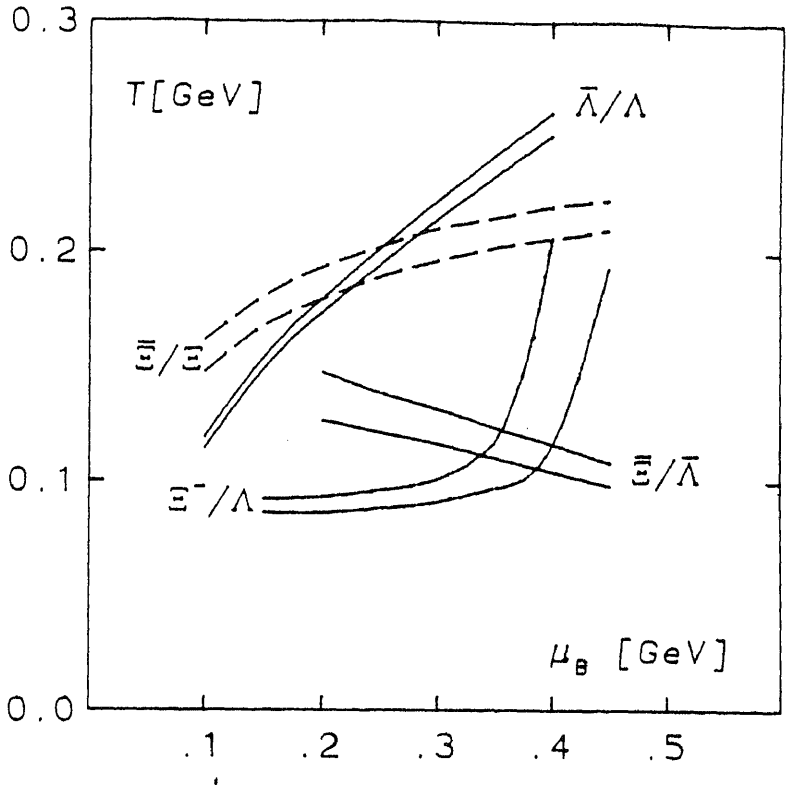

Figure 14. Strange baryon production ratios as function of temperature and baryochemical potential, with full strangeness saturation [42].

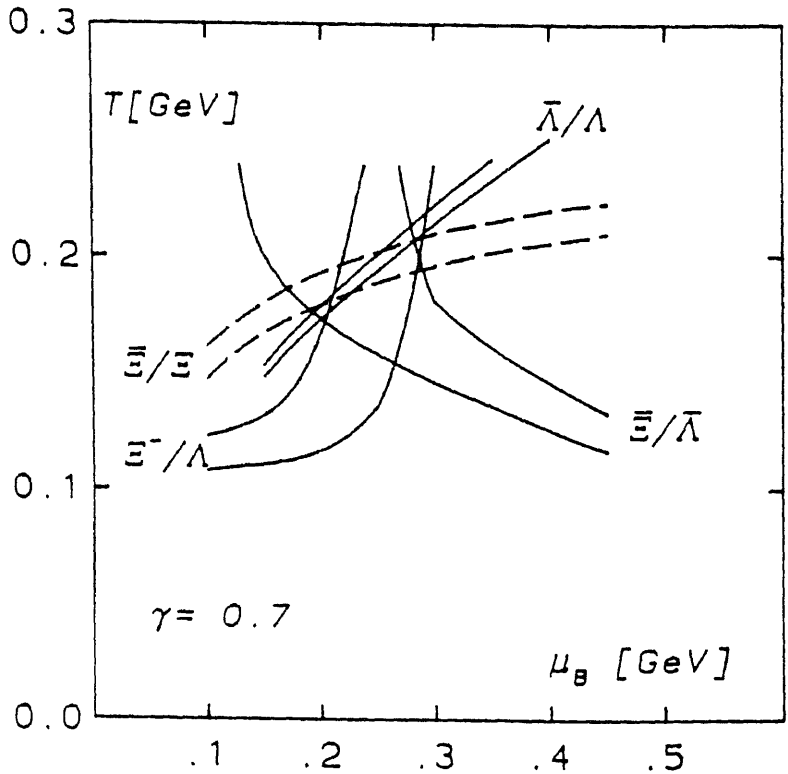

Figure 15. Strange baryon production ratios as function of temperature and baryochemical potential, with partial strangeness saturation [42].

vs. πp cross-sections at 1 GeV/c lab momentum), then we get $R_F^s \simeq 0.7\ R_F^{ns}$. This result can be checked independently by hadron interferometry studies, which determine the freeze-out radii for pions and kaons; new data [44] give at least qualitative agreement. In the case of an isentropic longitudinal expansion, these R_F-values imply $T_F^s \simeq 190$ MeV if $T_T^{ns} \simeq 130$ MeV, in reasonable accord with what we found above. Hadron spectra thus seem to suggest that freeze-out is a sequential process, determined by the different hadronic interaction cross-sections; however, this conclusion is at present still of a very qualitative nature.

Nevertheless, we have seen that hadron spectra and correlations provide us with a good probe for the study of hadronisation and the quark-hadron transition region.

5. Conclusions

We have seen that different signals probe different stages in the evolution of the quark-gluon plasma. It is therefore necessary to clarify what we can learn from any given signal, and from what stage it brings us information. We saw that high mass Drell-Yan pairs and open charm mesons probe the pre-equilibrium stage; the suppression of charmonium and bottonium production provides a tool for the study of the hot primordial QGP; hadronic spectra and correlations give us information about the quark-hadron transition and freeze-out. Clearly they are just some of the possible signals and probes; there are many others – thermal dileptons, direct photons, jet production, hadron mass modifications in media, flow effects, strangelets, to name some that have so far been studied quite extensively. We will certainly need all of them in order to establish the complete evolution pattern of the quark-gluon plasma.

Acknowledgements It is a pleasure to thank J. Cleymans, S. Gupta, D. Kharzeev, K. Geiger, J. Rafelski, K. Redlich, K. Sridhar, E. Suhonen and X.-N. Wang for stimulating discussions on various aspects of this report.

References

[1] D. Boal, Phys. Rev.**C33** (1986) 2206;
R. C. Hwa and K. Kajantie, Phys. Rev. Lett.**56** (1986) 696;
J.-P. Blaizot and A. H. Mueller, Nucl. Phys.**B289** (1987) 847;
for a recent survey see B. Müller in *Particle Production in Highly Excited Matter*, H. Gutbrod and J. Rafelski (Eds.), Plenum Press, London and New York (1993) 11.

[2] J. Rafelski and B. Müller, Phys. Rev. Lett.**48** (1982) 1066;
J. Cleymans and H. Satz, Z. Phys.**C57** (1993) 135;
for a recent survey see U. Heinz in *Proceedings of Quark Matter '93*, Nucl. Phys.**A**, in press.

[3] In contrast, global features such as multiplicities or flow effects on transverse momentum spectra will of course depend on the initial temperature.

[4] T. Matsui and H. Satz, Phys. Lett.**B178** (1986) 416;
for a recent survey see H. Satz in *QCD – 20 Years Later*, P. Zerwas and H. Kastrup (Eds.), World Scientific, Singapore (1993) 748.

[5] E. L. Feinberg, Nuovo Cim. **34A** (1976) 36;
for a recent survey see P. V. Ruuskanen, Nucl. Phys.**A544** (1992) 169c.

[7] M. Gyulassy and M. Plümer, Phys. Lett.**B243i** (1990) 432;
for a recent survey see X.-N. Wang in *Particle Production in Highly Excited Matte*
H. Gutbrod and J. Rafelski (Eds.), Plenum Press, London and New York (1993
387.

[8] Y. Pang, T. Schlegel and S. Kahana, Phys. Rev. Lett.**68** (1992) 2743.

[9] A. Capella et al., Phys. Lett.**B81** (1979) 68.

[10] K. Werner, Z. Phys.**C42** (1989) 85.

[11] M. Sorge, H. Stöcker and W. Greiner, Nucl. Phys.**A498i** (1989) 567c.

[12] T. Csörgö et al., Phys. Lett.**B222** (1989) 115.

[13] X.-N. Wang and M. Gyulassy, Phys. Rev.**D44** (1992) 3501.

[14] K. Geiger and B. Müller, Nucl. Phys.**B369** (1992) 600.

[15] K. Geiger in *Proceedings of Quark Matter '93*, Nucl. Phys.**A**, in press.

[16] K. Geiger, Phys. Rev.**D46** (1992) 4965 and 4986.

[17] A. Krzywicki et al., Phys. Lett.**B85** (1979) 407.

[18] B. Müller and X.-N. Wang, Phys. Rev. Lett.**68** (1992) 2437.

[19] K. Geiger and J. Kapusta, Phys. Rev. Lett.**70** (1993) 1920.

[20] F. Karsch and H. Satz, Z. Phys.**C51** (1991) 209.

[21] D. Kharzeev and H. Satz, Z. Phys.**C60** (1993) 689.

[22] C. Baglin et al. (NA38), Phys. Lett.**B255** (1991) 459.

[23] L. Antoniazzi et al., (E705) Phys. Rev.**D46** (1992) 4828;
L. Antoniazzi et al. (E705), Phys. Rev. Lett.**70** (1993) 383.

[24] J. Badier et al., Z. Phys.**C20** (1981) 101.

[25] D. M. Alde et al. (E772), Phys. Rev. Lett.**66** (1991) 133 and 2285.

[26] G. Piller, J. Mutzbauer and W. Weise, Z. Phys.**A343** (1992) 247.

[27] S. Gupta and H. Satz, Z. Phys.**C55** (1992) 391.

[28] See e.g. J.-P. Blaizot and J.-Y. Ollitrault in *Quark Gluon Plasma*, R. C. Hwa (ed
Singapore (1990) and references given there.

[29] C. Lourenco, in *Proceedings of Quark Matter '93*, Nucl. Phys.**A**, in press

[30] B. Ronceux in *Proceedings of Quark Matter '93*, Nucl. Phys.**A**, in press.

[31] S. Gupta and H. Satz, Phys. Lett.**B283** (1992) 439.

[32] For a recent analysis, see S. Gavin et al., Z. Phys. **C** (1994).

[33] E. Fermi, Progr. Theor. Phys. (Japan) **5** (1950) 570;
I. Ya. Pomeranchuk, Doklad. Akad. Nauk SSSR **78** (1951) 889;
L. D. Landau, Izv. Akad. Nauk SSSR, Ser. Fiz., **17** (1953) 51;
R. Hagedorn, Nuovo Cim. Suppl. **3** (1965) 147.

[34] S. Abatzis et al. (WA85), Phys. Lett.**B259** (1991) 508

[35] M. A. Mazzoni (NA34), Nucl. Phys.**A544** (1992) 623c.

[36] R. Stock et al. (NA35), Nucl. Phys.**A525** (1992) 497c.

[37] E. Andersen et al. (NA36), Phys. Lett.**B294** (1992) 127.

[38] C. Baglin et al., Phys. Lett.**B272** (1991) 449.

[39] J. Cleymans et al., Z. Phys.**C58** (1993) 347.

[40] D. Evans in *Proceedings of Quark Matter '93*, Nucl. Phys.**A**, in press.

[41] J. Letessier et al., Phys. Rev. Lett.**70** (1993) 3530.

[42] K. Redlich in *Proceedings of Quark Matter '93*, Nucl. Phys.**A**, in press.

[43] S. Nagamiya, in *Quark Matter Formation and Heavy Ion Collisions*, M. Jacob and H. Satz (Eds.), World Scientific, Singapore (1982) 281.

[44] E. Beker et al., Preprint CERN-PPE-93-123, June 1993

[45] C. Grosso-Pilcher and H. J. Shochet, Ann. Rev. Nucl. Part. Sci. **36** (1986) 1.

[46] E. L. Berger, as quoted in [45].

[47] N. Craigie, Phys. Rep. **47** (1978) 1.

[48] K. Sridhar, private communication.

[49] From a compilation in M. Glück, J. F. Owens and E. Reya, Phys. Rev.**D17** (1978) 2324.

PRAMANA
journal of
physics

© Printed in India

Supplement to Vol. 45
October 1995
pp. 339-350

Rare K decays

L. M. SEHGAL
III. Physikalisches Institut (A), RWTH Aachen, D-52074 Aachen, Germany

The rare decays of the K meson have had a long tradition as a laboratory for testing the symmetry properties of the weak interactions, and the manner in which these symmetries are broken by higher order effects. Present-day interest is focussed on decays that are suppressed by CP-symmetry or GIM symmetry. Such decays, in the standard theory, are sensitive to effects of the virtual top quark, and could also reveal new interactions transcending the standard model. In addition, the radiative decays of the K meson have become a useful testing-ground for effective Lagrangians describing the low energy interactions of pions, kaons and photons. This talk is a selective review of some rare K processes. For a more comprehensive discussion, we refer to the reviews listed in [1].

1. Charged current rarities

An example of a decay that is rare, yet allowed in the lowest order, is the $\Delta S = 0$ transition $K^0 \to K^+ e^- \bar{\nu}_e$ (Fig. 1a). This is closely analogous to pion β-decay, $\pi^- \to \pi^0 e^- \bar{\nu}_e$. Conservation of the vector current $\bar{u}\gamma_\mu d$ dictates that the relevant matrix element is $\langle K^0|I_-|K^+\rangle = 1$ (in analogy to $\langle \pi^0|I_-|\pi^+\rangle = \sqrt{2}$) and the predicted branching ratio is

$$B(K_L \to K^+ e^- \nu_e) = 3 \times 10^{-9}. \tag{1}$$

A curious analogue of the $\Delta S = \Delta Q$ decay $K^+ \to \pi^0 e^+ \nu_e$ is the hypothetical transition $K^+ \to$ "η"$e^+\nu_e$. The latter is not observable as a real decay process, since $m_\eta > m_K$. The matrix elements for $K^+ \to \eta$ and $K^+ \to \pi^0$ are $-1/\sqrt{6}$ and $1/\sqrt{2}$, respectively. A possible way to probe the $K^+ \to \eta$ coupling is via the decay

$$K^+ \to \gamma\gamma e^+ \nu_e. \tag{2}$$

Some of the relevant diagrams are shown in Fig. 1b. An estimate of this decay would be of interest.

In the second order of weak interactions, it is possible to obtain a $\Delta S = -\Delta Q$ transition $K^0 \to \pi^+ e^- \bar{\nu}_e$ (Fig. 1c). A model based on the parity-conserving vertices $K^0 - \pi^0$ and $K^+ - \pi^+$, combined with the $\Delta S = \Delta Q$ transitions $\pi^0 \to \pi^+ l^- \bar{\nu}_l$ and $K^0 \to K^+ l^- \bar{\nu}_l$ gives [2]

$$\frac{\Gamma(\Delta S = -\Delta Q)}{\Gamma(K_+ \to K_-)} = 0.5 \times 10^{-12}. \tag{3}$$

the transition $\pi^- \to \mu^- \bar{\nu}_\mu$, yields [3]

$$\frac{\Gamma(\Delta S = -\Delta Q)}{\Gamma(\Delta S = +\Delta Q)} = 1.1 \times 10^{-12} \qquad (K_{\mu 3} \text{ only}). \tag{4}$$

This second mechanism produces a $\Delta S = -\Delta Q$ amplitude $K^0 \to \pi^+ \mu^- \nu_\mu$ with a helicity structure and pion energy spectrum that is quite different from that in the $\Delta S = \Delta Q$ transition $\bar{K}^0 \to \pi^+ \mu^- \bar{\nu}_\mu$. To the extent that both mechanisms are possible, the e/μ ratio in $\Delta S = -\Delta Q$ transitions will be different from that in $\Delta S = \Delta Q$ decays.

2. Neutral current decay into $l^+ l^-$ pairs

2.1 Decay $K_L \to \mu^+ \mu^-$

The decay $K_L \to \mu^+ \mu^-$ has a well-known unitarity bound [4]

$$\frac{\Gamma(K_L \to \mu^+ \mu^-)}{\Gamma(K_L \to 2\gamma)} \geq \frac{\alpha^2}{2\beta} \frac{m_\mu^2}{m_K^2} \left(\ln \frac{1+\beta}{1-\beta} \right)^2, \qquad \beta = \sqrt{1 - 4m_\mu^2/m_K^2} \tag{5}$$

associated with the 2γ intermediate state (Fig. 2a). The corresponding branching ratio is

$$B_{abs} = (6.8 \pm 0.3) \times 10^{-9}. \tag{6}$$

If one includes the dispersive part of the 2γ amplitude, as well as the real amplitude induced by the short-distance interaction $s\bar{d} \to \mu^+ \mu^-$ (box and penguin diagrams, Fig. 2b), the full branching ratio is

$$B(K_L \to \mu^+ \mu^-) = B_{abs} + |\sqrt{B_{disp}} \pm \sqrt{B_{short-dist.}}|^2. \tag{7}$$

A theoretical estimate of B_{disp} requires a model for the $K_L \to \gamma^* \gamma^*$ form factor. Vector-meson-dominance models [5], similar to those used for $\pi^0, \eta \to \gamma^* \gamma^*$, tend to give $B_{disp}/B_{abs} \leq 0.1$ (to be compared with the experimental rate of $\eta \to \mu^+ \mu^-$, $B(\eta \to \mu^+ \mu^-) = (1.3 \pm 0.1) \times B_{abs}(\eta \to \mu^+ \mu^-)$). A model for $K_L \to \gamma^* \gamma$ [6], that describes the observed spectrum of Dalitz pairs in $K_L \to \gamma e^+ e^-$ [7], yields an even smaller value of B_{disp}.

The short-distance branching ratio has been calculated to be [8, 9]

$$B_{short-dist.}(K_L \to \mu^+ \mu^-) = 6.4 \times 10^{-3} \cdot \left[P_0(K_L \to 2\mu) + \mathrm{Re}\lambda_t Y(x_t) \right]^2 \tag{8}$$

where

$$Y(x_t) = \frac{x_t}{8} \left[\frac{x_t - 4}{x_t - 1} + \frac{3x_t}{(x_t - 1)^2} \ln x_t \right], \qquad x_t = \frac{m_t^2}{m_W^2}, \tag{9}$$

and

$$\lambda_t = V_{ts}^* V_{td} = -A^2 \lambda^5 (1 - \rho - i\eta). \tag{10}$$

The term $P_0(K_L \to 2\mu)$ denotes a residual charm quark contribution, estimated to be -0.75×10^{-4}, for $m_c = 1.4$ GeV, $\Lambda = 200$ MeV.

$$\frac{\Gamma(\Delta S = -\Delta Q)}{\Gamma(\Delta S = +\Delta Q)} = 1.1 \times 10^{-12} \qquad (K_{\mu 3} \text{ only}).$$

This second mechanism produces a $\Delta S = -\Delta Q$ amplitude $K^0 \to \pi^+\mu^-\nu_\mu$ w a helicity structure and pion energy spectrum that is quite different from that the $\Delta S = \Delta Q$ transition $\bar{K}^0 \to \pi^+\mu^-\bar{\nu}_\mu$. To the extent that both mechanis are possible, the e/μ ratio in $\Delta S = -\Delta Q$ transitions will be different from that $\Delta S = \Delta Q$ decays.

2. Neutral current decay into l^+l^- pairs

2.1 Decay $K_L \to \mu^+\mu^-$

The decay $K_L \to \mu^+\mu^-$ has a well-known unitarity bound [4]

$$\frac{\Gamma(K_L \to \mu^+\mu^-)}{\Gamma(K_L \to 2\gamma)} \geq \frac{\alpha^2}{2\beta}\frac{m_\mu^2}{m_K^2}\left(\ln\frac{1+\beta}{1-\beta}\right)^2, \qquad \beta = \sqrt{1-4m_\mu^2/m_K^2}$$

associated with the 2γ intermediate state (Fig. 2a). The corresponding branchi ratio is

$$B_{abs} = (6.8 \pm 0.3) \times 10^{-9}.$$

If one includes the dispersive part of the 2γ amplitude, as well as the real amplitu induced by the short-distance interaction $s\bar{d} \to \mu^+\mu^-$ (box and penguin diagran Fig. 2b), the full branching ratio is

$$B(K_L \to \mu^+\mu^-) = B_{abs} + |\sqrt{B_{disp}} \pm \sqrt{B_{short-dist.}}|^2.$$

A theoretical estimate of B_{disp} requires a model for the $K_L \to \gamma^*\gamma^*$ form facto Vector-meson-dominance models [5], similar to those used for $\pi^0, \eta \to \gamma^*\gamma^*$, ter to give $B_{disp}/B_{abs} \leq 0.1$ (to be compared with the experimental rate of $\eta \to \mu^+\mu$ $B(\eta \to \mu^+\mu^-) = (1.3 \pm 0.1) \times B_{abs}(\eta \to \mu^+\mu^-)$). A model for $K_L \to \gamma^*\gamma$ [6], th describes the observed spectrum of Dalitz pairs in $K_L \to \gamma e^+e^-$ [7], yields an ev smaller value of B_{disp}.

The short-distance branching ratio has been calculated to be [8, 9]

$$B_{short-dist.}(K_L \to \mu^+\mu^-) = 6.4 \times 10^{-3} \cdot\left[P_0(K_L \to 2\mu) + \mathrm{Re}\lambda_t Y(x_t)\right]^2$$

where

$$Y(x_t) = \frac{x_t}{8}\left[\frac{x_t-4}{x_t-1} + \frac{3x_t}{(x_t-1)^2}\ln x_t\right], \qquad x_t = \frac{m_t^2}{m_W^2},$$

and

$$\lambda_t = V_{ts}^* V_{td} = -A^2\lambda^5(1-\rho-i\eta).$$

The term $P_0(K_L \to 2\mu)$ denotes a residual charm quark contribution, estimated be -0.75×10^{-4}, for $m_c = 1.4$ GeV, $\Lambda = 200$ MeV.

The experimental branching ratio $B_{exp}(K_L \to \mu^+\mu^-) = (7.4 \pm 0.4) \times 10^{-9}$ [10], nly slightly in excess of the unitarity bound (Eq. (6)), and can constrain the ameter $\mathrm{Re}\lambda_t = -A^2\lambda^5(1-\rho)$ appearing in the short-distance contribution. At ent, the uncertainty in the 2γ dispersive rate B_{disp} limits the efficacy of this y in providing a stringent constraint on ρ [11].

Decay $K_L \to \pi^0 l^+ l^-$

ne one-photon exchange approximation, CP-symmetry forbids the decay $K_2 \to l^- l^-$ but allows the decay $K_1 \to \pi^0 l^+ l^-$ [12]. A CP-conserving amplitude for $\to \pi^0 l^+ l^-$ is possible through a 2γ intermediate state (Fig. 2a). The 2γ-induced litude is proportional to m_l if the two photons have $J = 0$; however, dynamical els of $K_2 \to \pi^0\gamma\gamma$ permit also a $J = 2$ component which yields an amplitude $K_2 \to \pi^0 l^+ l^-$ unsuppressed by a factor m_l [13]. It follows that the amplitude $K_L \to \pi^0 l^+ l^-$ will contain three components

$$= \alpha^2 A_{2\gamma} + \alpha\varepsilon A_{1\gamma} + \eta\lambda^4 A_{sd}, \tag{11}$$

re the second and third pieces denote amplitudes associated with indirect and ct (short-distance) CP-violation. The factors α^2, $\varepsilon\alpha$ and $\eta\lambda^4$ express the orders agnitude of these components, and underscore the fact that they are, a priori, parable in size.

The CP-conserving amplitude for $K_2 \to \pi^0 l^+ l^-$ involving a 2γ intermediate e has the form [14]

$$(K_2(p) \to \pi^0(p') + l^-(k) + l^+(k'))_{2\gamma} = -\frac{\alpha}{16} \cdot \bar{u}(k)\Big[\frac{G_{eff}}{M_\rho^2} F_1 \not{q} + F_2\Big] v(k'), \tag{12}$$

e F_2 is proportional to m_l, and is negligible for $K_2 \to \pi^0 e^+ e^-$. The coefficient $/M_\rho^2$ is an effective coupling constant appearing in the $K_2 \to \pi^0\gamma\gamma$ amplitude, metrized as

$$\begin{aligned}(K_2(p) \;&\to\; \pi^0(p')\gamma(q)\gamma'(q')) = 2\frac{G_{eff}}{M_\rho^2}\Big[(\epsilon\cdot\epsilon')(q\cdot p)(q'\cdot p) \\ &+\; (q\cdot q')(\epsilon\cdot p)(\epsilon'\cdot p) - (\epsilon\cdot p)(\epsilon'\cdot q)(q'\cdot p) \\ &-\; (\epsilon\cdot q')(q\cdot p)(\epsilon'\cdot p)\Big] + \cdots\end{aligned} \tag{13}$$

e the ellipsis denote terms that are ineffective for $K_L \to \pi^0 e^+ e^-$. An analysis e data on $K_L \to \pi^0\gamma\gamma$ [15] suggests $G_{eff} \sim 0.15 \times 10^{-7} m_K^{-2}$ [14]. The form r F_1 has an absorptive part

$$\begin{aligned}\mathrm{n}F_1 \;&=\; -\frac{\Delta}{\beta^2}\Big[\frac{2}{3} + \frac{2}{\beta^2} - (\frac{1}{\beta^2} - \beta^2)\frac{1}{\beta}\ln\frac{1+\beta}{1-\beta}\Big] \\ &\overset{\beta\to 1}{\to}\; \frac{8}{3}\Delta,\end{aligned} \tag{14}$$

e $\Delta = -2p\cdot(k-k')$, $\beta = \sqrt{1-4m_l^2/s}$, $s = (k+k')^2$. The corresponding -conserving branching ratio is

$$_{CP}(K_L \to \pi^0 e^+ e^-) = 1.7 \times 10^{-12}\Big(\frac{G_{eff} m_K^2}{}\Big)^2 (1 + \rho_{disp}), \tag{15}$$

ρ_{disp} being the dispersive part, estimated in [14] to be 1.5.

The result (15) has to be compared with the CP–violating rate [16]

$$B_{CPV}(K_L \to \pi^0 e^+ e^-) = \Big[|0.76re^{i\pi/4} + i\tilde{C_V}\frac{\eta}{0.4}|^2 + |\tilde{C_A}\frac{\eta}{0.4}|^2\Big] \times 10^{-11}, \tag{16}$$

where $\tilde{C_V}$ and $\tilde{C_A}$ are coupling constants describing the short–distance interaction $s\bar{d} \to e^+e^-$, with numerical values $\tilde{C_V} = -0.6$, $\tilde{C_A} = 0.7$ for $m_t = 170$ GeV. The parameter r, characterising the indirect CP–violating amplitude, is defined as

$$r = \Big[\frac{\Gamma(K_1 \to \pi^0 e^+ e^-)}{\Gamma(K^+ \to \pi^+ e^+ e^-)}\Big]^{1/2} \tag{17}$$

For $\eta = 0.4$, the CP–violating branching ratio B_{CPV} is $1.2 \times 10^{-11}(2.1 \times 10^{-11})$ for $r = +1(-1)$. Models with much larger and much smaller values of r are possible. These estimates suggest that the CP–violating rate B_{CPV} is somewhat higher than the CP–conserving rate B_{CPC}. A precise measurement of the rate and spectrum of $K_2 \to \pi^0\gamma\gamma$ would help to sharpen the estimate of B_{CPC}, while a measurement of r is needed to predict B_{CPV}. Expectations for the decay $K_L \to \pi^0\mu^+\mu^-$, as well as an estimate of the CP–violating l^+l^- energy asymmetry are given in [14]. Present experimental limits (from the E799 experiment at Fermilab) are $B(K_L \to \pi^0 e^+ e^-) < 4.3 \times 10^{-9}$, $B(K_L \to \pi^0\mu^+\mu^-) < 5.1 \times 10^{-9}$ [17].

2.3 Decay $K_L \to \pi^+\pi^- e^+ e^-$

A study of the photon spectrum in the decay $K_L \to \pi^+\pi^-\gamma$ shows two clear components [18]: (i) bremsstrahlung from the CP–violating decay $K_L \to \pi^+\pi^-$, and (ii) direct photon emission of magnetic dipole nature from the CP–conserving decay $K_2 \to \pi^+\pi^-\gamma$. The simultaneous presence of bremsstrahlung and $M1$ amplitudes implies that the photon in the decay $K_L \to \pi^+\pi^-\gamma$ has a CP–violating circular polarization. The conversion process $K_L \to \pi^+\pi^- e^+ e^-$ may be viewed as a means of probing this polarization, by studying the correlation of the e^+e^- plane relative to the $\pi^+\pi^-$ plane.

An analysis based on the amplitude

$$A(K_L \to \pi^+(p_+)\pi^-(p_-)e^+(k_+)e^-(k_-)) = e|f_S|\Big[g_{Br}\Big(\frac{p_+^\mu}{p_+\cdot k} - \frac{p_-^\mu}{p_-\cdot k}\Big) + g_{M1}\varepsilon_{\mu\nu\rho\sigma}k^\nu p_+^\rho p_-^\sigma\Big]\frac{e}{k^2}\bar{u}(k_-)\gamma_\mu v(k_+) \tag{18}$$

was carried out in [19]. Here $k = k_+ + k_-$, f_S is the amplitude of $K_S \to \pi^+\pi^-$, and g_{Br} and g_{M1} are given empirically by $g_{Br} = \eta_{+-}e^{i\delta_0(m_K^2)}$, $g_{M1} = i(0.76)e^{i\delta_1(s_\pi)}$, $\delta_{0,1}$ being the s– and p–wave $\pi\pi$ phase shifts. A significant CP–violating asymmetry was found in the Φ–distribution of the process, Φ being the angle between the e^+e^- and $\pi^+\pi^-$ planes:

$$A = \frac{\int_0^{\pi/2} d\Phi\frac{d\Gamma}{d\Phi} - \int_{\pi/2}^{\pi} d\Phi\frac{d\Gamma}{d\Phi}}{\int_0^{\pi} d\Phi\frac{d\Gamma}{d\Phi}}$$

$$= 15\% \sin(\Phi_{+-} + \delta_0(m_K^2) - \bar{\delta}_1)$$
$$\approx 14\%, \tag{19}$$

where $\bar{\delta}_1$ denotes an average p–wave phase ($\sim 10^0$). This analysis was extended in [20] to include short–distance CP–violation, contained in the effective Hamiltonian for $s\bar{d} \to e^+e^-$. These direct CP–violating effects were found to be very small ($< 10^{-3}$). The branching ratio of $K_L \to \pi^+\pi^-e^+e^-$ is predicted to be 3×10^{-7}, so that the large asymmetry given in Eq. (19) may well be accessible in the next round of experiments.

2.4 Decay $K^+ \to \pi^+l^+l^-$

The decays $K^+ \to \pi^+l^+l^-$ are dominated by one–photon exchange, and are principally of interest as tests of the $K\pi\gamma^*$ vertex. In chiral pertubation theory, this vertex is calculable in terms of the effective Lagrangian $\mathcal{L}_{eff}(\pi, K, \gamma)$, and the matrix element has the form [21]

$$A(K^+(k) \to \pi(p) + l^+ + l^-) = \frac{\alpha G_8}{4\pi} C^+(z)\bar{u}(\not{k} + \not{p})v,$$
$$z = (k-p)^2/m_K^2, \tag{20}$$

where $G_8 = G_F/\sqrt{2}V_{ud}V_{us}^* g_8$, $g_8 = 5.1$. The function $C^+(z)$ is known, up to an additive constant w_+. In terms of this constant, the branching ratios are calculated to be

$$B(K^+ \to \pi^+e^+e^-) = (3.15 - 21.1w_+ + 36.1w_+^2) \times 10^{-8},$$
$$B(K^+ \to \pi^+\mu^+\mu^-) = (3.93 - 32.7w_+ + 70.5w_+^2) \times 10^{-9}. \tag{21}$$

The recent measurement [22] $B(K^+ \to \pi^+e^+e^-) = (2.99 \pm 0.22) \times 10^{-7}$ implies $w_+ = 0.89^{+0.26}_{-0.14}$, and leads to the prediction $B(K^+ \to \pi^+\mu^+\mu^-) = 3.07 \times 10^{-8}$.

Refinements to the matrix element (20) occur if one takes into account the short–distance interaction $s\bar{d} \to l^+l^-$ [23]. One interesting aspect of these corrections is the addition to the matrix element (20) of a parity–violating term of the form

$$A_{sd}(K^+(k) \to \pi(p) + l^+ + l^-) = \frac{G_F\alpha}{\sqrt{2}} V_{us}\Big[B(k+p)^\mu + C(k-p)^\mu\Big]$$
$$\bar{u}\gamma_\mu\gamma_5 v. \tag{22}$$

The short–distance interaction gives $B = f_+\xi$, $C = f_-\xi$, where

$$\xi = -1.4 \times 10^{-4} - \frac{Y(x_t)}{2\pi \sin^2\theta_W} A^2\lambda^4(1 - \rho - i\eta), \tag{23}$$

f_+, f_- being the two form factors of K_{l3} decay ($f_+ \approx 1$, $f_- \approx 0$). Interference with the leading one–photon exchange amplitude (20) gives rise to a parity–violating longitudinal polarization of the μ^+ [23]

$$|A_{LR}| \equiv \left|\frac{\Gamma_L - \Gamma_R}{\Gamma_L + \Gamma_R}\right| = |2.3\mathrm{Re}\xi|, \tag{24}$$

(20) (which we write as $F_V \bar{u}(\not{p}' + \not{k}')v$) produces a T–odd, P–odd term in the decay rate, of the form $\mathrm{Im}(F_V F_A^*)(\vec{s}_+ \times \vec{s}_-) \cdot \vec{p}$, where $\vec{s}_+$ and $\vec{s}_-$ are spin vectors of the μ^+ and μ^- in the K rest frame, and $\vec{p}$ is the μ^+ momentum. Such a term can probe the CP-violating parameter η of the short–distance interaction. Detection of this term, however, requires measurement of a correlation between the spins of both μ^+ and μ^-, a difficult task.

An important challenge for the low energy effective Lagrangian $\mathcal{L}_{eff}(K, \pi, \gamma)$ is to produce a reliable prediction for the decay $K_1 \to \pi^0 l^+ l^-$. In chiral pertubation theory, the matrix element is determined up to an unknown constant w_S [21]. As discussed in Section 2.2, information on this decay mode is important for determining the magnitude of indirect CP–violation in $K_L \to \pi^0 l^+ l^-$.

3. Neutral current decays into $\nu\bar{\nu}$ pairs

3.1 Decay $K^+ \to \pi^+ \nu\bar{\nu}$

The decay $K^+ \to \pi^+ \nu\bar{\nu}$ is a short–distance dominated reaction, determined by the box and penguin graphs shown in Fig. 3a. The branching ratio is predicted to be [25]

$$B(K^+ \to \pi^+ \nu_l \bar{\nu}_l) = 5.9 \times 10^{-5} |P_0(K^+ \to \pi^+ \nu_l \bar{\nu}_l) + \lambda_t X(x_t)|^2, \tag{25}$$

where

$$P_0(K^+ \to \pi^+ \nu_l \bar{\nu}_l) = \begin{cases} -2.5 \times 10^{-4} & \text{for} \quad \nu_e, \nu_\mu \\ -1.7 \times 10^{-4} & \text{for} \quad \nu_\tau \end{cases} \tag{26}$$

and

$$X(x_t) = \frac{x_t}{8}\left[\frac{x_t + 2}{x_t - 1} + \frac{3x_t - 6}{(x_t - 1)^2} \ln x_t\right]. \tag{27}$$

Summing over all three neutrino flavours, one obtains a typical value $B(K^+ \to \pi^+ \nu\bar{\nu}) = 1.3 \times 10^{-10}$ for $\rho = 0$, $\eta = 0.4$, with a possible range $(0.5 - 5) \times 10^{-10}$ for the presently allowed domain of (ρ, η). The present experimental limit is 5.2×10^{-9} (AGS E787) [26] and a sensitivity of 10^{-10}/event is within reach.

The long–distance contributions to $K^+ \to \pi^+ \nu\bar{\nu}$, symbolised by the diagrams in Fig. 3b, were calculated in [27]. In particular, the hadronic contribution to the $K^+ \pi^+ Z$ vertex was obtained using current algebra arguments. It was concluded that these effects are three orders of magnitude smaller than the short–distance contribution. A more recent calculation [28], using chiral pertubation theory, has found a very similar result. (For additional remarks, see [29]).

3.2 Decay $K_L \to \pi^0 \nu\bar{\nu}$

Finally, an example of a short–distance dominated process, which is at the same time purely CP–violating, is the decay $K_2 \to \pi^0 \nu\bar{\nu}$ [30]. Its branching ratio is given by [31]

$$\begin{aligned} B(K_L \to \pi^0 \nu\bar{\nu}) &= 7.32 \times 10^{-4} \left[\mathrm{Im}\lambda_t\right]^2 X^2(x_t) \\ &= 1.94 \times 10^{-10} \left[\eta^2 A^4\right] X^2(x_t). \end{aligned} \tag{28}$$

While experimentally remote (the present limit is $B(K_L \to \pi^0\nu\bar{\nu}) < 5.8 \times 10^{-5}$ [32]), this reaction is an interesting example of a process that directly measures the CP–violating paramter η, with essentially no hadronic uncertainties.

4. Radiative Decays

The radiative decays of the K mesons, such as $K_{L,S} \to \gamma\gamma$, $K_L \to \pi^0\gamma\gamma$, $K_L \to \pi^+\pi^-\gamma$, $K^+ \to \pi^+\pi^0\gamma$, $K^+ \to \pi^+\gamma\gamma$, $K_L \to \pi^0\pi^0\gamma\gamma$,$K_{L,S} \to \pi^0\pi^0\gamma$ etc. are a source of abundant grist for models, such as chiral pertubation theory [33], that attempt to describe the low energy interactions of pions, kaons and photons. The interplay of chiral symmetry, CP–symmetry and gauge invariance, combined with the weak nonleptonic $\Delta I = 1/2$ rule, produces interesting patterns and hierarchies amongst the various channels. We will limit our remarks here to two reactions,

$$\begin{aligned} K_{L,S} &\to \pi^0\pi^0\gamma, \\ K_{L,S} &\to 3\gamma \end{aligned} \tag{29}$$

that have the piquant feature of being *quadrupole* transitions.

4.1 Decay $K_{L,S} \to \pi^0\pi^0\gamma$

Gauge invariance implies that the $\pi^0\pi^0$ system in $K_{L,S} \to \pi^0\pi^0\gamma$ cannot have $J = 0$ (since that would amount to a $0 \to 0$ radiative transition). Bose statistics implies that the $\pi^0\pi^0$ pair cannot have $J = 1$ (since such a state would not be symmetric under exchange of the two π^0's). It follows that the $\pi^0\pi^0$ state has at least two units of angular momentum, and the associated photon corresponds to quadrupole radiation [34].

CP–invariance implies that the decays $K_L \to \pi^0\pi^0\gamma$ and $K_S \to \pi^0\pi^0\gamma$ are $E2$ and $M2$ transitions, respectively, with matrix elements

$$\begin{aligned} A(K_L \to \pi^0(p_1)\pi^0(p_2)\gamma(k)) &= \frac{g_{E2}}{m_K^3}\frac{(p_1-p_2)\cdot k}{\Lambda^2}\Big[(\epsilon\cdot p_1)(k\cdot p_2) \\ &\quad -(\epsilon\cdot p_2)(k\cdot p_1)\Big], \\ A(K_S \to \pi^0(p_1)\pi^0(p_2)\gamma(k)) &= \frac{g_{M2}}{m_K^3}\frac{(p_1-p_2)\cdot k}{\Lambda^2}\varepsilon_{\mu\nu\rho\sigma}\epsilon^\mu k^\nu p_1^\rho p_2^\sigma. \end{aligned} \tag{30}$$

A qualitative estimate of the decay rates may be obtained by making a comparison with the measured $M1$ transition $K_L \to \pi^+\pi^-\gamma$ [16], parametrized as

$$A(K_L \to \pi^+(p_+)\pi^-(p_-)\gamma(k)) = \frac{g_{M1}}{m_K^3}\varepsilon_{\mu\nu\rho\sigma}\epsilon^\mu k^\nu p_+^\rho p_-^\sigma. \tag{31}$$

Assuming that the dimensionless couplings g_{M1}, g_{M2} and g_{E2} are similar in magnitude, and that the reaction "radius" $1/\Lambda$ is of order $1/m_\rho$, we obtain [34]

$$\begin{aligned} B(K_L \to \pi^0\pi^0\gamma) &\approx 1.0 \times 10^{-8}, \\ B(K_S \to \pi^0\pi^0\gamma) &\approx 1.7 \times 10^{-11}. \end{aligned} \tag{32}$$

pair process $K_L \to \pi^+\pi^-e^+e^-$ could show two components, one associated with $K_L \to \pi^0\pi^0\gamma$ ($E2$; $O(p^6)$), which is strongly peaked at low e^+e^- masses, and one associated with $K_L \to \pi^0\pi^0\gamma^*$ ($O(p^4)$) which shows up as a broad continuum [34].

4.2 Decay $K^0 \to$ Three Photons

Given that $B(K_L \to 2\gamma) = 5.7 \times 10^{-4}$, $B(K_S \to 2\gamma) = 2.4 \times 10^{-6}$ [36] it is interesting to ask what one expects for the decays $K_{L,S} \to 3\gamma$ [37].

First of all, it should be noted that both $K_L \to 3\gamma$ and $K_S \to 3\gamma$ are possible without violating CP or any other general symmetry principle. Gauge invariance dictates that no pair of photons in these channels can have $J = 0$, while Bose statistics forbids any pair from having $J = 1$ (Yang's theorem). It follows that every pair of photons in these decays must have at least two units of angular momentum. A simple model that relates the decays $K_{L,S} \to 3\gamma$ to the other quadrupole transition $K_{L,S} \to \pi^0\pi^0\gamma$ discussed above yields [37]

$$\begin{aligned} B(K_L \to 3\gamma) &= 3 \times 10^{-19}, \\ B(K_S \to 3\gamma) &= 5 \times 10^{-21}. \end{aligned} \tag{33}$$

Thus the 3γ decay mode is suppressed relative to the 2γ mode by *15 orders of magnitude* – a remarkable reminder of the power of Bose statistics in this year of the Bose centenary!

Acknowledgement:

I wish to thank the organizers of the Workshop for their affectionate hospitality, and for the opportunity to discuss physics in a wonderfully congenial and stimulating environment.

References

[1] B. Winstein and L. Wolfenstein, Rev. Mod. Phys. 65 (1993) 1113
L. Littenberg and G. Valencia, Ann. Rev. Nucl. Part. Sci. 43 (1993) 729
J.L. Ritchie and S.G. Wojcicki, Rev. Mod. Phys. 65 (1993) 1149
R. Battiston et al., Phys. Rep. 214 (1992) 293

[2] C.O. Dib and B. Guberina, Phys. Lett. B255 (1991) 113
M. Luke, Phys. Lett. B256 (1991) 265

[3] P. Heiliger and L.M. Sehgal, Phys. Lett. B256 (1991) 410

[4] L.M. Sehgal, Phys. Rev. 183 (1969) 1511; Nuovo Cimento 45 (1966) 785

[5] D.A. Geffen and B.L. Young, Phys. Rev. Lett. 15 (1965) 316
C. Quigg and J.D. Jackson, UCRL-18487 (1968)
L. Bergstrom et al., Phys. Lett. B126 (1983) 117

[6] L. Bergstrom, E. Masso and P. Singer, Phys. Lett. B249 (1990) 141

[7] G.D. Barr et al. (CERN-NA31 collaboration) Phys. Lett. B235 (1990) 356
K.E. Ohl et al. (BNL-E845 collaboration) Phys. Rev. Lett. 65 (1990) 1407

[8] A. Buras and M. Harlander, in "*Heavy Flavours*", edited by A. Buras and M. Lindner, (World Scientific 1992), p. 58

[9] T. Inami and C.S. Lim, Prog. Theor. Phys. 65 (1981) 297, Erratum 1772

[10] T. Akagi et al. (KEK-E137 collaboration) Phys. Rev. Lett. 67 (1991) 2618;
A.P. Heinson et al. (BNL-E791 collaboration) Phys. Rev. D44 (1991) R1

[11] G. Bélanger and C.Q. Geng, Phys. Rev. D43 (1991) 140
P. Ko, Phys. Rev. D45 (1992) 174

[12] M. Baker and S.L. Glashow, Nuovo Cimento 25 (1962) 857
J.F. Donoghue, B.R. Holstein and G. Valencia, Phys. Rev. D35 (1987) 2769

[13] L.M. Sehgal, Phys. Rev. D38 (1988) 808

[14] P. Heiliger and L.M. Sehgal, Phys. Rev. D47 (1993) 4920

[15] G.D. Barr et al (NA31 collaboration), Phys. Lett. B284 (1992) 440
V. Papadimitriou et al. (E731 collaboration), Phys. Rev. D44 (1991) 573

[16] C.O. Dib, I. Dunietz and F.J. Gilman, Phys. Rev. D39 (1989) 2639

[17] D.A. Harris et al. (E799 collaboration), Phys. Rev. Lett. 71 (1993) 3914; ibid (1993) 3918

[18] E.J. Ramberg et al. (E731 collaboration), Phys. Rev. Lett. 70 (1993) 2525

[19] L.M.Sehgal and M. Wanninger, Phys. Rev. D46 (1992) 1035; D46 (1992) 5209(E)

[20] P. Heiliger and L.M. Sehgal, Phys. Rev. D48 (1993) 4146

[21] G. Ecker, A. Pich and E. de Rafael, Nucl. Phys. B291 (1987) 692

[22] C. Alliegro et al. (AGS-777 collaboration), Phys. Rev. Lett. 68 (1992) 278

[23] M. Lu, M.B. Wise and M.J. Savage, UCSD/PTH 92-20

[24] P. Agrawal et al., Phys. Rev. D45 (1992) 2383

[25] G. Buchalla, A. Buras and M. Harlander, Nucl. Phys. B349 (1991) 1, and references therein

[26] M.S. Atiya et al. (BNL-787 collaboration), Phys. Rev. D48 (1993) R1

[27] D. Rein and L.M. Sehgal, Phys. Rev. D39 (1989) 3325

[28] M. Lu and M.B. Wise, CALT 68-1911 (1994)

[29] J.S. Hagelin and L.S. Littenberg, Prog. Part. Nucl. Phys. 23 (1989) 1

[30] L. S. Littenberg, Phys. Rev. D39 (1989) 3322

[31] Buchalla, Buras and Harlander, Ref. [25], and references therein

[32] M. Weaver et al. (E799 collaboration) Phys. Rev. Lett. 72 (1994) 3758

[33] G. Ecker, H. Neufeld and A. Pich, CERN-TH 6920/93

[34] P. Heiliger and L.M. Sehgal, Phys. Lett. B307 (1993) 182

[35] R. Funck and J. Kambor, Nucl. Phys. B396 (1993) 53

[36] Particle Data Group, Phys. Rev. D50 (1994) 1173

[37] P. Heiliger, B. McKellar and L.M. Sehgal, Phys. Lett. B327 (1994) 145

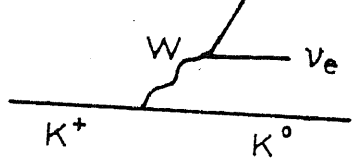

Fig. 1a.

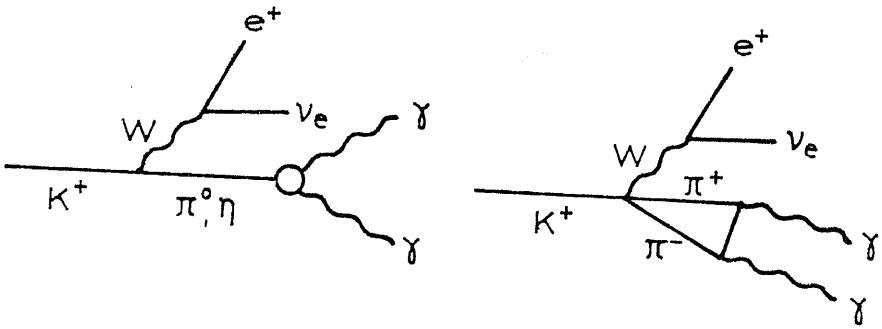

Fig. 1b.

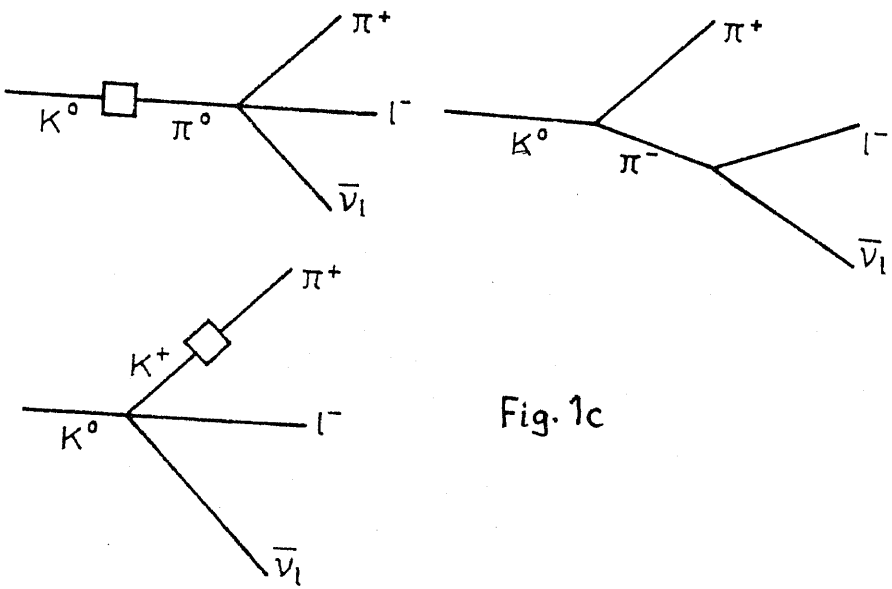

Fig. 1c

Figure 1. Diagrams relevant for the decays (a) $K^0 \to K^+ e^- \bar{\nu}_e$, (b) $K^+ \to \gamma\gamma e^+ \nu_e$, (c) $\Delta S = -\Delta Q$ decays $K^0 \to \pi^+ l^- \bar{\nu}_l$.

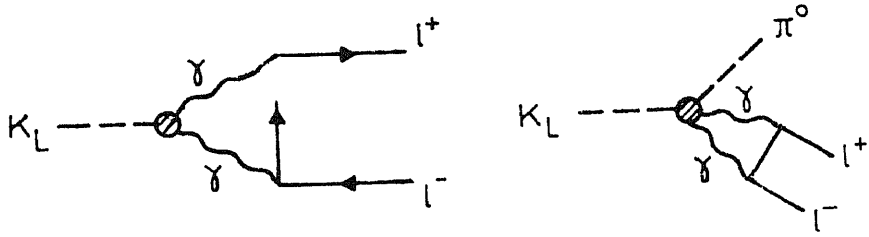

Fig. 2a.

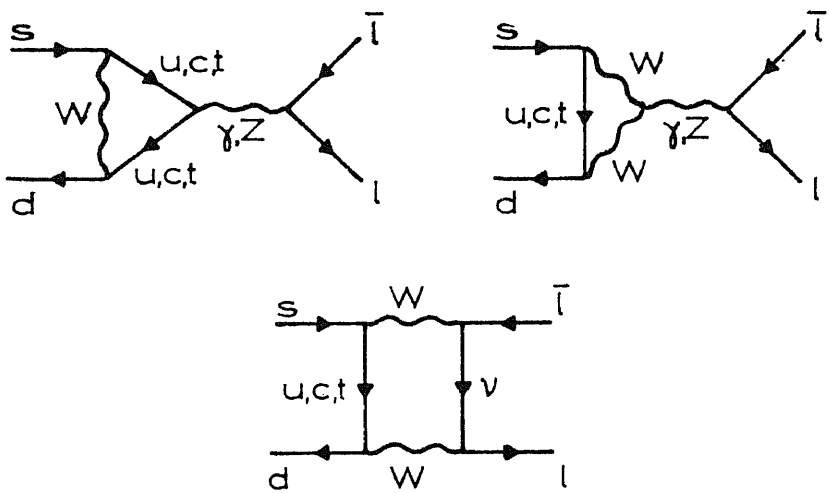

Fig. 2b.

Figure 2. (a) Two-photon contribution to $K_L \to l^+l^-$ and $K_L \to \pi^0 l^+ l^-$. (b) Diagrams describing the short-distance interaction $s\bar{d} \to l^+l^-$.

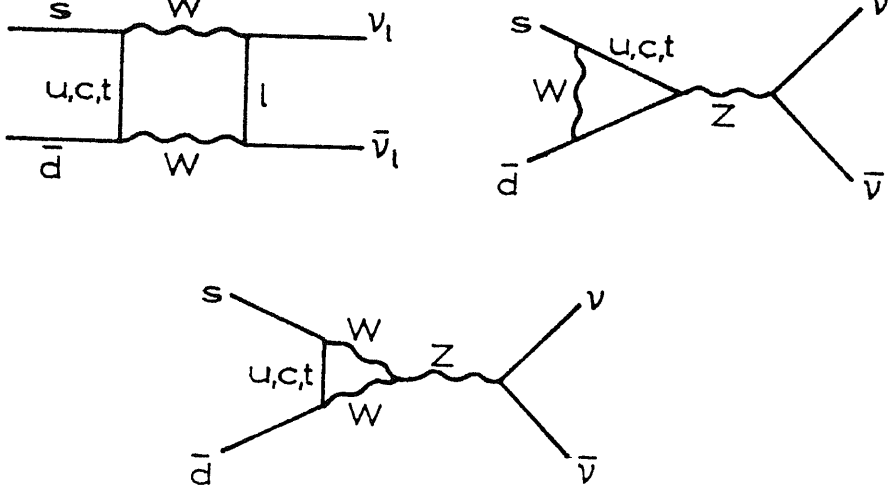

Fig. 3a.

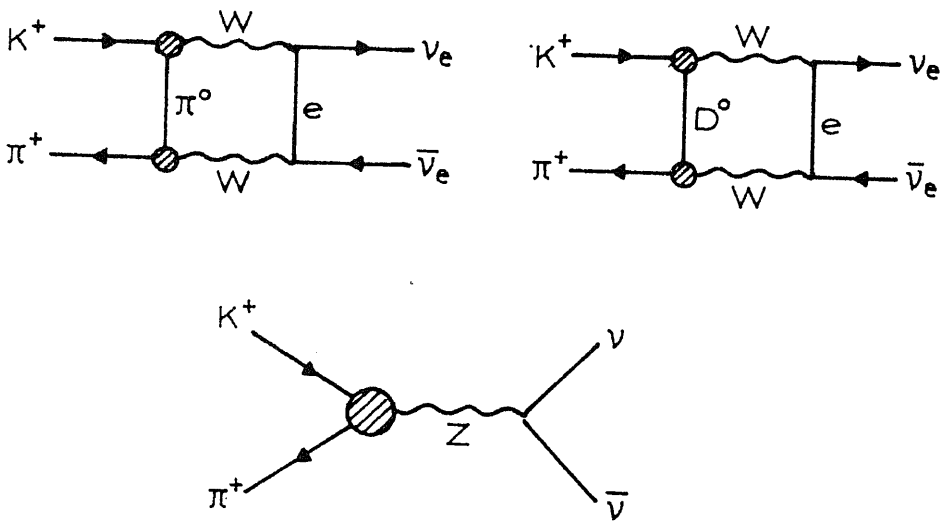

Fig. 3b.

Figure 3. (a) Short-distance diagrams relevant to the interaction $s\bar{d} \to \nu\bar{\nu}$. (b) Long-range contributions to the decay $K^+ \to \pi^+\nu\bar{\nu}$.

Testing electroweak vector boson self interactions

R. SINHA

Institute of Mathematical Sciences, CIT Campus,Taramani, Madras, 600 113.

Abstract. We review anomalous triple electroweak vector boson (TEVB) couplings. The anomalous vertex is written in a model independent way and related to the moments of the W boson. Loop-induced bounds on these couplings are derived, including those obtained from the oblique parameters S, T, U. We show that these bounds from oblique parameters in particular, cannot rule out anomalous couplings even if the oblique parameters are in complete agreement with SM. The importance of testing the TEVB vertex beyond LEPI is thereby demonstrated. We examine direct bounds obtainable from the W-radiative and $W\gamma$ production at CDF and D0 collaborations. However, all the bounds on TEVB to date are too weak to limit most models. It is pointed out that future colliders will be needed to probe loop level SM corrections to the TEVB vertex, as well as examine extensions beyond the SM. A detailed study of the process $e^+e^- \to \ell^+\ell'^-\nu\bar{\nu}'$ is carried out with numerical results pressented for the "Next Linear Collider" (NLC) proposed to run at $\sqrt{s} = 500GeV, 1TeV$. We find that the TEVB couplings can be studied accurately enough to probe regions close the loop level corrections within the SM, and also allow for a possibility of separating the photon coupling from that of the Z using polarized beams at the NLC.

1. Introduction

The $SU(2)_L \otimes U(1)_Y$ theory of electroweak interactions, which is a part of the standard model (SM), has had dramatic confirmations in the last decade. Experiments at LEP are currently able to measure the mass of the Z and its couplings to fermions at a less than 1% level and they agree with the theory considered up to one loop. This success of the SM has generated a feeling that even those of its parameters that have not been tested directly are likely to be in good agreement with observation. While present precision measurements do constrain new physics *vis-a-vis* the parameters of the SM, such constraints need not be as restrictive in some sectors as in others. In fact, the gauge boson couplings of the standard model of electroweak interactions are only just beginning to be directly measured. There has now been observation of the process $p\bar{p} \to e\nu\gamma X$, presumably representing $W\gamma$ production and radiative W decay, at the Collider Detector at Fermilab (CDF), the D0 collaboration at Fermilab [1, 2, 3] and at UA2 at CERN.[4] Recently a lot of work has been devoted to a global analysis of low energy data and LEP data, in order to extract bounds on the gauge boson couplings.[5]. Extensive studies[6] have also been undertaken to determine the possibilities of detecting such deviations at

future colliders.

2. The general triple electroweak vector boson vertex

The vector boson self interactions are uniquely fixed by the gauge structure of the SM. However, new physics as well as higher order corrections will modify these self interactions. The couplings of W bosons to the photon and Z can be described by an effective Lagrangian, the most general form of which may be written down with the minimum requirements– that of Lorentz invariance, global $SU(2)$ and local $U(1)$ symmetry [7, 8] as:

$$\begin{aligned}\mathcal{L}^V_{eff} = & - g_V \left[ig_1^V \left(W^\dagger_{\alpha\beta} W^\alpha - W^{\dagger\alpha} W_{\alpha\beta} \right) V^\beta + i\kappa_V W^\dagger_\alpha W_\beta V^{\alpha\beta} \right. \\ & + i\frac{\lambda_V}{M_W^2} W^\dagger_{\alpha\beta} W^\beta{}_\sigma V^{\sigma\alpha} + i\tilde{\kappa}_V W^\dagger_\alpha W_\beta \tilde{V}^{\alpha\beta} + i\frac{\tilde{\lambda}_V}{M_W^2} W^\dagger_{\alpha\beta} W^\beta{}_\sigma \tilde{V}^{\sigma\alpha} \\ & + \left. g_4^V W^\dagger_\alpha W_\beta (\partial^\alpha V^\beta + \partial^\beta V^\alpha) + g_5^V \epsilon^{\alpha\beta\mu\nu} W^\dagger_\alpha \overleftrightarrow{\partial_\mu} W_\beta V_\nu \right] \end{aligned} \quad (1)$$

In the above equation V represents the neutral gauge bosons either the photon or the Z, $V_{\alpha\beta} = \partial_\alpha V_\beta - \partial_\beta V_\alpha$, $W_{\alpha\beta} = \partial_\alpha W_\beta - \partial_\beta W_\alpha$ and g_V is the WWV coupling strength in the SM with $g_\gamma = e$ and $g_Z = ec/s$, where $c^2 \equiv 1 - s^2 \equiv M_W^2/M_Z^2$. The above Lagrangian consists of five dimension 4 terms and 2 dimension 6 terms and has the corresponding seven parameters or couplings characterizing the couplings of the W to each of neutral gauge bosons. These seven operators exhaust all possible Lorentz structures if it is assumed that $\partial_\mu W^\mu = 0$ and $\partial_\mu V^\mu = 0$. These conditions are automatic if the bosons are coupled to light fermions. Higher dimension operators can be added by the replacement $V_\mu \rightarrow \Box^n V_\mu$. However, contributions from these operators provides only the momentum dependence to the couplings. The SM values for these couplings are $g_1^Z = \kappa_\gamma = \kappa_Z = 1$, and $\lambda_\gamma, \lambda_Z, \tilde{\kappa}_\gamma, \tilde{\kappa}_Z, \tilde{\lambda}_\gamma, \tilde{\lambda}_Z, g_4^\gamma, g_4^Z, g_5^\gamma, g_5^Z$ are all zero. Electromagnetic gauge invariance fixes g_1^γ to be unity and g_4^γ and g_5^γ to be zero. The other couplings $g_1^Z, g_4^Z, g_5^Z, \kappa_\gamma, \kappa_Z, \lambda_\gamma, \lambda_Z, \tilde{\kappa}_\gamma, \tilde{\kappa}_Z, \tilde{\lambda}_\gamma, \tilde{\lambda}_Z$ have to be determined experimentally. Considering that a large number of parameters have to be determined experimentally some assumptions have often been made to reduce this set by making some assumptions. The couplings g_4^Z and g_5^Z violate custodial SU(2) and hence can be assumed to be small or zero. The number of extra parameters is further reduced by taking g_1^Z, the weak neutral charge of the W, equal to unity.

The parameters $\kappa_{\gamma,Z}$ and $\lambda_{\gamma,Z}$ are unique as they can be related to the multipole moments of the W – which can be defined with respect to both neutral bosons γ/Z as follows

$$\begin{aligned} \mu_W &= \frac{e}{2M_W}(1 + \kappa + \lambda) \\ Q_W &= -\frac{e}{M_W^2}(\kappa - \lambda) \\ d_W &= \frac{e}{2M_W}(\tilde{\kappa} + \tilde{\lambda}) \end{aligned}$$

$$Q_W = -\frac{1}{M_W^2}(\tilde{\kappa}+\lambda) \tag{2}$$

where μ_W is the magnetic dipole, Q_W is the electric quadrupole moment, d_W is the electric dipole and $\tilde{Q_W}$ is the magnetic quadrupole of the W boson. Tree level unitarity will restrict the WWV couplings to their SM values at asymptotically high energies. Any deviation from the standard model is thus described by a form factor and depends on a scale for new physics 'Λ'. It is customarily assumed that these form factors are constant for $\sqrt{s} \ll \Lambda$ and start decreasing when Λ is reached or surpassed, in analogy with the nucleon form factors. These form factors will therefore act as regulators for loop corrections.

3. Anomalous couplings in various models

If the W bosons are composite objects, then deviation of the triple gauge boson coupling parameters from their standard model values could be very large indeed; as an example, κ has been calculated to be greater than three in one model[9]. However, within the standard model, upper bounds on the one loop corrections to the tree level values of κ_γ and λ_γ are expected to be [10] $\Delta\kappa_\gamma = 1.7 \times 10^{-2}$ and $\Delta\lambda_\gamma = 0.25 \times 10^{-2}$ for a top quark of about 170GeV. In extensions of the standard model such as those containing extra Higgs doublets, extra heavy fermions [11], the deviations from the tree level standard model values tend to be of about the same order of magnitude as these one loop corrections. For the minimal supersymmetric SM, due to cancellations, the values expected are slightly below the SM ones.Typically, in most renormalizable models, $\kappa_{\gamma,Z}$ are expected to vary by only less than 5% of the SM value. Variations in $\lambda_{\gamma,Z}$ are generally (although not always) further suppressed by an order of magnitude. Hence, variations of, or limits on $\kappa_{\gamma,Z}$ alone are considered usually in literature.

4. Loop-induced constraints on anomalous couplings

Much work has gone into constraining the anomalous couplings in eqn(1),in particular by loop induced processes at low energies. However, questions have been raised on the validity of these bounds. In particular the validity of the Lagrangian itself has been questioned. The Lagrangian is not explicitly gauge invariant, and hence it has been claimed[12] that it is not an valid extension of the SM. However, Burgess and London [13] have argued by an explicit proof that – any Lagrangian that contains W's and Z's which satisfies Lorentz invariance and $U(I)_{em}$ gauge invariance is automatically $SU_L(2) \times U_Y(1)$ gauge invariant–the gauge invariance being realized nonlinearly. Burgess and London, however, agree that most bounds on these couplings are over estimated. The real culprit they point out is not gauge invariance but the improper use of cutoff in estimating the size of the loop diagrams. They point out that the cutoff dependence in low energy theory does not, in general, give an accurate indication of the true dependence on the heavy physics, although it can do so for a logarithmic divergence. The constraints on the anomalous couplings are therefore considerably weakened. Some of the valid bounds –depending at most on

the log of the cutoff scale Λ – are considered here. Bounds from tree level unitarity are based on the assumption of a dipole form factor and provide the limits[14]

$$|\kappa - 1| \leq 7.4\frac{\mathrm{TeV}^2}{\Lambda^2}, |\tilde{\kappa}| \leq 35\frac{\mathrm{TeV}^2}{\Lambda^2} \text{ and } |\lambda, \tilde{\lambda}| \leq 4.0\frac{\mathrm{TeV}^2}{\Lambda^2}.$$

Understandably these limits are too weak to bound any model. The muon magnetic moment is used set the bound [15]

$$\left|(\kappa_\gamma - 1)\ln\frac{\Lambda^2}{M_W^2} + \lambda_\gamma/3\right| < 3.7$$

However, it has been argued [16] that contributions from direct terms such as $\overline{\mu}\sigma_{\mu\nu}\mu F^{\mu\nu}$ which are needed to cancel divergences weaken these limits. Analogously the neutron dipole moment is also used to limit the CP violating couplings giving[17]

$$\left|(\tilde{\kappa}_\gamma)\ln\frac{\Lambda^2}{M_W^2} + \tilde{\lambda}_\gamma/3\right| < 10^{-3}$$

5. Bounds from oblique parameters on anomalous couplings

New physics beyond the SM can be usefully constrained in terms of the "oblique" electroweak correction [18, 19] parameters $\widetilde{S}, \widetilde{T}$, and $\widetilde{U}$ [21] (or $\Delta\epsilon_1, \Delta\epsilon_2$, or $\Delta\epsilon_3$). These are linearly related to $\widetilde{\Pi}_{WW}(q^2)$, $\widetilde{\Pi}_{ab}(q^2)$ (where $a, b = \gamma, Z$), which are the contributions from new physics to the electroweak vector boson self-energies as follows:

$$\begin{aligned}
\alpha M_W^2 T &= \left[\Pi_{WW}(0) - s^2\Pi_{ZZ}(0)\right], \\
\alpha M_Z^2 S &= 4cs\left[cs\left\{\delta\Pi_{ZZ}(M_Z^2) - \Pi_{\gamma\gamma}(M_Z^2)\right\} + (s^2 - c^2)\Pi_{\gamma Z}(M_Z^2)\right] \\
\alpha M_W^2 U &= 4s^2\left[\delta\Pi_{WW}(M_W^2) - s^2\left\{s^2\Pi_{\gamma\gamma}(M_Z^2) + c^2\delta\Pi_{ZZ}(M_Z^2)\right.\right. \\
&\quad \left.\left. + 2\,cs\,\Pi_{\gamma Z}(M_Z^2)\right\}\right]
\end{aligned} \tag{3}$$

where $\delta\Pi(q^2) \equiv \Pi(q^2) - \Pi(0)$. In order to constrain the WWV couplings, we relate them to these oblique parameters and use the known constraints on the latter. The approach presented here is from Choudhury, Roy and Sinha([22]). Analysis of the type discussed here have also been done by Hagiwara *et al.* ([23]) and Burgess *et al.* ([24]), with similar conclusions. Hagiwara *et al.* deal with a linearly realized Lagrangian whereas we and Burgess *et al.* deal with a nonlinearly realised Lagrangian. The major difference between our analysis and that of Burgess *et al.* is that they include vertex corrections ignored by us and include more than the three oblique parameters. However, Burgess *et al.* ignore κ^2, λ^2 and $\kappa\lambda$ terms which have been included by us.

If the anomalous vector boson couplings constitute the sole source of new physics, $\widetilde{T}$ and $\widetilde{U}$ will measure the weak isospin breaking induced by them, while $\widetilde{S}$ arises from their $SU(2)_L \otimes U(1)_Y$ breaking aspect through the involvement of the

longitudnal vector boson modes. One can work out the divergent contributions to the $\widetilde{\Pi}$–functions from the nonstandard WWV vertex by using (1) and dimensional regularization. Defining $\widehat{\Pi}(q^2)$ to be the coefficient of the usual $(2/\epsilon - \gamma_E)$[13] term in $\widetilde{\Pi}(q^2)$, we compute

$$\begin{aligned}\widehat{\Pi}_{ab}(q^2) = -\frac{g_a g_b q^2}{192\pi^2} \quad & \left[(\eta_a+\eta_b)\left(36-4r-r^2\right)+\eta_a\eta_b r(2-r)\right. \\ & +(3\lambda_a+3\lambda_b+\eta_a\lambda_b+\eta_b\lambda_a)(24-4r) \\ & \left.+\lambda_a\lambda_b\left(36+8r-2r^2\right)\right],\end{aligned} \tag{4}$$

where $r \equiv q^2/M_W^2$ and $\eta_{a,b} \equiv 1-\kappa_{a,b}$. For compactness, we introduce the notation:

$$\begin{aligned} C_1 &\equiv 36c^2-4-c^{-2}, & C_2 &\equiv 24c^2-4, \\ C_3 &\equiv 2-c^{-2}, & C_4 &\equiv 36c^2+8-2c^{-2} \end{aligned}$$

With $\widehat{T}$, $\widehat{S}$ and $\widehat{U}$ defined analogously in terms of the $\widehat{\Pi}$'s and denoting $\langle F\rangle \equiv s^2F_\gamma + c^2F_Z$ for any F, we have

$$\widehat{S} = -\frac{1}{12\pi}\left[(\eta_Z-\eta_\gamma)\left\{C_1+\langle\eta\rangle C_3+\langle\lambda\rangle C_2\right\}+(\lambda_Z-\lambda_\gamma)\left\{C_2(3+\langle\eta\rangle)+\langle\lambda\rangle C_4\right\}\right] \tag{5}$$

Since $\widehat{\Pi}_{ab}(0)=0$, only $\widehat{\Pi}_{WW}$ contributes to $\widehat{T}$ and we can write

$$\widehat{\Pi}_{WW}(q^2) = \alpha M_W^2\left[\widehat{T}-\frac{r}{48\pi s^2}\,\mathcal{R}(r)\right], \tag{6}$$

$$\widehat{T} = -\frac{3}{16\pi}\left[\left\{4+\eta_\gamma\right\}\eta_\gamma+\frac{\eta_Z}{c^2s^2}\left\{2\left(2c^4+2c^2-1\right)+\left(c^4+c^2-1\right)\eta_Z\right\}\right], \tag{7}$$

$$\begin{aligned}\mathcal{R}(r) \equiv\ & (4-2r)\left\{5\langle\eta\rangle+\langle\eta^2\rangle\right\}+28\eta_Z+5\eta_Z^2+8(3-r)\left\{3\langle\lambda\rangle+\langle\lambda\eta\rangle\right\} \\ & +24\lambda_Z\left\{3+\eta_Z\right\}+2\left(6+2r-r^2\right)\langle\lambda^2\rangle+4\left(3+3c^{-2}+r\right)\lambda_Z^2 .\end{aligned} \tag{8}$$

Consequently,

$$\widehat{U} = -\frac{1}{12\pi}\mathcal{R}(1)+\frac{1}{12\pi c^2}\left[2C_1\langle\eta\rangle+C_3\langle\eta\rangle^2+2C_2\langle\lambda\rangle(3+\langle\eta\rangle)+C_4\langle\lambda\rangle^2\right] . \tag{9}$$

Since $\widehat{T}$ depends only on $\widehat{\Pi}_{WW}(0)$ and $\widehat{\Pi}_{ZZ}(0)$ and not on their q^2 variations it is unaffected by dimension 6 operators and hence is independent of λ_γ and λ_Z. Also, terms in $\widehat{S}$ are proportional to either $\eta_Z-\eta_\gamma$ or $\lambda_Z-\lambda_\gamma$ as they should, since $\widehat{S}$ originates from the mixing between weak hypercharge (Y) and the third component of weak isospin – the WWY vertex being linear in these differences.

It should be noted that, unlike in the SM and its straightforward extensions, the oblique parameters are not finite quantities here. This is a consequence of the presence of nonrenormalizable terms in the Lagrangian of (1). In a cut–off dependent regularization scheme, this fact would manifest itself through a non–trivial functional dependence on the cut–off scale [23]. As a matching condition between two effective theories [25], we identify $\mu = \Lambda$, the scale at which new physics becomes manifest (assumed to be $\sim 1TeV$). Using the $\overline{\text{MS}}$ scheme of renormalization, we are lead to

$$\widetilde{S}(\Lambda^2) = \widetilde{S}(M_Z^2)+\widehat{S}\,\ln\frac{\Lambda^2}{M_Z^2} \tag{10}$$

translated into S, T and U.

We use [26] $\widetilde{S} = -0.31 \pm 0.49$, $\widetilde{T} = -0.12 \pm 0.34$ and $\widetilde{U} = -0.11 \pm 0.92$, though our results are insensitive to the central values. As pointed out, $\widetilde{T}$ depends only on η_γ and η_Z, being expressed as a sum of quadratic functions of theirs. Thus the measurement of $\widetilde{T}$ alone constrains these parameters to lie on an elliptic band in the $\eta_\gamma - \eta_Z$ plane, the width of the band being given by the errors on M_W/M_Z and $\widetilde{T}$. $\widetilde{S}$ and $\widetilde{U}$ then reduce the allowed region into smaller part of the elliptic band. Since $\widetilde{S}$ is proportional to the differences of γ– and Z–couplings, constraints on it generally (though not always) tend to make those converge. Rather unexpectedly, $\widetilde{U}$ plays a significant role in constraining these anomalous couplings. In conjunction with $\widetilde{S}$ and $\widetilde{T}$, it serves to exclude a large part of the parameter space.

We obtain the (95% C.L.) bounds $-6.1 \lesssim \eta_\gamma \lesssim 4.1$, $-6.0 \lesssim \lambda_\gamma \lesssim 4.5$, $-2.0 \lesssim \eta_Z \lesssim 0.3$ and $-4.5 \lesssim \lambda_Z \lesssim 1.9$, earlier *UA2* analysis [4] had yielded $-8.4 \lesssim \eta_\gamma \lesssim 12.1$ (for arbitrary λ_γ) and $-8.5 \lesssim \lambda_\gamma \lesssim 6.5$ (for arbitrary η_γ). The allowed regions represent solutions to polynomial equations, which are curves that thicken into bands on account of experimental error bars on the coefficients. As the errors shrink to zero, the allowed parameter space collapses into the curves still permitting wide ranges of values for the anomalous couplings. This observation holds even for the SM point *viz.* $\widetilde{S} = \widetilde{T} = \widetilde{U} = 0$, being a consequence of cancellations between various contributions to the $\widetilde{\Pi}$–functions.

The bounds that we have obtained above are still large as compared to the ratio v^2/Λ^2, where v is the electroweak VEV [$v = 2M_W/(e\ s)$]. Arguments based on Naive Dimensional Analysis [27] suggest, for instance, that $\kappa_V - 1 \gtrsim v^2/\Lambda^2$. However, any approximate equality $\kappa_V - 1 \sim v^2/\Lambda^2$ is only a matter of conjecture. This makes phenomenological investigations of these bounds, as performed here, rather important.

6. Direct bounds on anomalous couplings

The bounds mentioned above are to some extent model dependent, in the sense that they are obtained by loop level processes, where 'other new physics' can also contribute. However, there has now been the observation of $p\bar{p} \to e\nu\gamma X$, presumably representing $W\gamma$ production and radiative W decay, at the Collider Detector Facility (CDF) [1] at the Tevatron ($\sqrt{s} = 1.8$ TeV) at Fermilab and at UA2 ($\sqrt{s} = 630$ GeV) at CERN [4]. Such measurement allows for the possibility of directly testing the gauge boson couplings by tree level processes. The best way to detect possible nonstandard gauge boson couplings is to make use of the radiation amplitude zero[28] which occurs in the angular distribution of $d\bar{u} \to W\gamma$ as well as in $W \to d\bar{u}\gamma$.The presence of the zero will be explicitly borne out in equations (12) and (14) below by the factors Z contained therein. The dip which persists in $p\bar{p} \to W\gamma X$, is very sensitive to deviations from the standard model gauge boson couplings.

Preliminary results from CDF[1] quote a limited number of events (6 events corresponding to an integrated luminosity ($\mathcal{L}$) of 4.3pb^{-1}) [29] UA2 has also reported their final results and quote 10 events with an integrated luminosity of 13pb^{-1}.

unless obtain the first direct bounds[30] on κ, from the total number of $W\gamma$ events, as well as the number of radiative W decays, $W^+ \to e^+\nu\gamma$ and $W^- \to e^-\bar{\nu}\gamma$.

The formula for the cross section of $W\gamma$ production is given by

$$\sigma(P\bar{P} \to W^-\gamma X) = \frac{1}{3}\sum_{i=d,s}\int\int dx_A dx_B [P_i^P(x_A)P_{\bar{u}}^{\bar{P}}(x_B)$$
$$\hat{\sigma}(q_i\bar{q_u} \to W^-\gamma) + P_{\bar{u}}^P(x_A)P_i^{\bar{P}}(x_B)\hat{\sigma}(q_i\bar{q_u} \to W^-\gamma)_{\hat{u}\leftrightarrow\hat{t}}] \qquad (11)$$

where,

$$\hat{\sigma}(q_i(k_1)\bar{q_j}(k_2) \to W^-(P)\gamma(k)) = \frac{4\pi\alpha}{\hat{s}}\frac{M_W^2 G_F}{\sqrt{2}}V_{ij}^2\int_{PhaseSpace}$$
$$\left(Z^2\frac{\hat{t}^2+\hat{u}^2+2\hat{s}M_W^2}{\hat{u}\hat{t}} - \eta Z\frac{\hat{u}-\hat{t}}{\hat{u}+\hat{t}} + \frac{\eta^2}{2(\hat{t}+\hat{u})^2}[\hat{t}\hat{u}+(\hat{t}^2+\hat{u}^2)\frac{\hat{s}}{4M_W^2}]\right) \qquad (12)$$

and where $\hat{s} = (k_1+k_2)^2, \hat{t} = (P-k_1)^2, \hat{u} = (P-k_2)^2$ with $\hat{s}+\hat{t}+\hat{u} = M_W^2$, and V_{ij} is the KM matrix element. $Z = (Q_i + \frac{\hat{u}}{\hat{t}+\hat{u}})$ is the zero factor, Q_i is the electric charge of the quark q_i, and $\eta = \kappa - 1$. For this section the subscript γ is supressed, *kappa* is meant to imply κ_γ.

For the radiative W decay case, one obtains the result

$$\sigma(P\bar{P} \to e^-\bar{\nu}\gamma X) = \frac{1}{3}\sum_{i=d,s}\int\int dx_A dx_B \delta(sx_A x_B - M_W^2)\left[P_i^P(x_A)P_{\bar{u}}^{\bar{P}}(x_B)\right.$$
$$\left.\hat{\sigma}(q_i(k_1)\bar{q_u}(k_2) \to e\nu\gamma) + P_{\bar{u}}^P(x_A)P_i^{\bar{P}}(x_B)\hat{\sigma}(q_i(k_2)\bar{q_{\bar{u}}}(k_1) \to e^-\bar{\nu}\gamma)\right]. \qquad (13)$$

where we obtain $\hat{\sigma}$, using the zero-width approximation as,

$$\hat{\sigma}(q_i(k_1\bar{q_j}(k_2) \to W^-(q) \to e^-(p_1)\bar{\nu}(p_2)\gamma(k)) = \frac{48\pi^4\alpha^2}{\hat{s}\,sin^2\theta_w}V_{ij}^2$$
$$B(W^- \to e\bar{\nu})\int_{PhaseSpace}[Z'^2 A - Z'\eta B + \eta^2 C] \qquad (14)$$

where $Z' = (\frac{Q_i}{Q} - \frac{P_1.k}{q.k})$ is the zero factor, and

$$A = \frac{4}{(P_1.k)(P_2.k)}[(P_1.k_2)^2 + (P_2.k_1)^2]$$

$$B = \frac{1}{4(P_1.k)(q.k)}\left[M_W^2(4k_2.P_1 - 2k_1.P_2 - M_W^2) + 4(P_2.k)^2\right.$$
$$+4(k_1.P_1)(k_1.P_1 + 2P_2.k) - 8(P_2.k)(k_1.P_2)(\frac{P_2.k}{M_W^2} - 1)$$
$$+(1 - \frac{2P_2.k}{M_W^2})[4k_1.P_1\, k_1.P_2 + 2P_1.k\, M_W^2]$$
$$-4(k_1.P_1)(k.P_1)(\frac{2k_2.P_1}{M_W^2} + 1)$$
$$\left.-\frac{2k_1.P_2\, k.P_1}{P_2.k}(2\,k.k_2 + \frac{4(P_2.k)(P_2.k_1)}{M_W^2} - \frac{4(P_1.k_1)(P_1.k)}{M_W^2})\right]$$

$$C = \frac{}{4(q.k)^2}[2(P_2.k)(M_W^2 - 2(P_2.k))$$

$$- \frac{4(P_2.k)}{M_W^2}((P_1+P_2).k_1)(2k_2.P_1 - M_W^2)$$

$$-4(P_2.k)(k_1.(2P_1+P_2)) + \frac{8(P_2.k_1)(P_1.k)(k.k_2)}{M_W^2}\Big]. \tag{15}$$

To obtain the total cross sections we perform the integrations over the parton fractions and over the phase space, using Vegas Monte Carlo routines and EHLQ[31] parton distribution functions. The following cuts were also imposed, to agree with the cuts imposed by CDF: (1) the transverse photon energy $E_{T\gamma} < 5$ GeV; (2) the photon pseudo-rapidity $|\eta_\gamma| < 3.0$; (3) the electron-photon angular separation $\sqrt{(\Delta\eta)^2 + (\Delta\phi)^2} > 0.3$

With these cuts, the Wγ production ($W^+ + W^-$) cross section is computed to be

$$\sigma_{W\gamma} = [32.8 - 0.600\eta + 1.42\eta^2]pb. \tag{16}$$

To calculate the number of $p\bar{p} \to W\gamma X \to e\nu\gamma X$ events to be expected at CDF for any given η, we use the the electron and photon acceptances and their detection efficiencies to be $\mathcal{A}_e = 0.41, \mathcal{E}_e = 0.67, \mathcal{A}_\gamma = 0.54$ and $\mathcal{E}_\gamma = 0.50$ respectively, as given by CDF[1]. Also including the Drell-Yan correction factor $K_{DY} = 1.3$, we get $n = \sigma_{W\gamma}\mathcal{L}B(W \to e\nu)K_{DY}\mathcal{A}_e\mathcal{E}_e\mathcal{A}_\gamma\mathcal{A}_\gamma$. Using $B(W \to e\nu) = 0.11$ we get $n = 1.49 - 0.0273\eta + 0.0647\eta^2$. Of the total of six events that are reported by CDF,three events have a large $\eta_\phi \sim 2.4-2.6$ whereas the other three have $\eta_\phi \sim 0.8$ thus they can be clearly classified as $W\gamma$ and W radiative decays.Assuming 3 $W\gamma$ events we get a loose bound

$$-8.6 \leq \kappa \leq 11.0(95\%CL). \tag{17}$$

The cross section for $p\bar{p} \to WX \to e\nu\gamma X$ is

$$\sigma(W^\pm e\nu\gamma) = (18.8 - 0.0758\eta + 0.108\eta^2)pb. \tag{18}$$

Using the same cuts, acceptances, and efficiencies as before we obtain the quadratic equation in η for the number n of $p\bar{p} \to WX \to e\nu\gamma X$ events: $n = 7.79 + 0.0315\eta + 0.0447\eta^2$. For 3 events this gives a bound

$$-2.4 \leq \kappa \leq 3.7(96\%CL). \tag{19}$$

If the events are not separated into decay and radiative ones, the total number of events is $n = 9.28 + 0.0042\eta + 0.109\eta^2$, which gives $-3.9 \leq \kappa \leq 4.8$ (95% CL). UA2 have also set a bound on κ without separating the events to be $-5.4 \leq \kappa \leq 7.9$.

The very loose bounds that one gets in $P\bar{P} \to WX \to e\nu\gamma X$ case compared to the $P\bar{P} \to W\gamma X \to e\nu\gamma X$ considered earlier can be traced directly to the differences in the production mechanisms for the W in the two cases, and to the effect of the cuts imposed on the SM term relative to the non-SM term in the two cases. Note that in Eq.(8), there is a δ function involving parton fractions x_A, x_B which is not there in Eq.(1), whose effect is to reduce the cross section obtained from Eq.(8) relative to that obtained from Eq.(1). The effect of the cut imposed on

when it comes to limiting most models. Direct studies of the TEVB vertices will be possible at Fermilab, and upcoming LEP II or proposed future collider like $\gamma\gamma$ collider or the NLC. New machines will be necessary to probe regions much closer to the SM prediction.

7. Testing TEVB at future colliders

With the Next Linear Collider (NLC) in mind we have investigated[33] a set of processes of four lepton production in e^+e^- collisions with respect to their sensitivity to gauge boson coupling parameters. The processes are all of the general form

$$e^+e^- \rightarrow \ell^+\ell'^-\nu\bar{\nu}'. \tag{20}$$

we include all possible charged lepton combinations, specifically these are $\mu\tau$, μe (τe), $\mu\mu$ $(\tau\tau)$, and ee. The channels given in brackets have the same set of Feynman diagram contributions as their corresponding unbracketed channel and we will henceforth drop reference to them as distinct processes.

For all our processes, we do include the full gauge invariant set of diagrams. the $\mu^+\tau^-$ state can be produced via 9 different diagrams; the μ^+e^- state receives contributions from 18 diagrams. The $\mu\mu$ process has a total of 28 contributing diagrams with most of the extras being γ or Z 'bremsstrahlung' from the initial or final state leptons. The ee process goes via 56 diagrams.. For the $\mu\mu$ and ee final states, in some of the diagrams, all ν species can appear. These diagrams are added incoherently in the calculation. However, for the purpose of counting the number of diagrams, we regard all the ν final states as contributing to a single diagram.

It is important to realize that one needs the full calculation that we discuss here as opposed to the calculations of W pair or single W production. At LEP II energies it is appropriate to calculate W pair production, the processes being dominated by the nearly on-shell W propagators. This is not the case, however, at higher energies unless one is dealing with a final state which allows for the experimental reconstruction of W's. We are considering here the purely leptonic final states. For this case, the W's can be reconstructed (up to a two-fold ambiguity) only under the assumption that they are on-shell. [8] Neither W pair nor single W production can be isolated by experimental cuts for the purely leptonic case. Consequently, we must fully calculate the $\ell^+\ell'^-\nu\bar{\nu}'$ production, as opposed to W pair production only and, in doing so, we aim to unearth a more realistic picture of the sensitivity to the couplings in question.

In order to deal easily with the large number of Feynman diagrams and to readily retain helicity information, we have written the amplitude for each process in the CALKUL helicity formulation [34]. We assume massless spinors describe the fermions although we do retain fermion masses in the propagators; this amounts to neglecting terms proportional to m_f, a good approximation. The matrix element squared for each process is embedded in a Monte Carlo algorithm for integration over the final state four body phase space to yield the cross sections and various

distributions. We sum and average over initial spins and sum over final spins. We use $M_Z = 91.196\,GeV$, $\Gamma_Z = 2.534\,GeV$, $M_W = 80.6\,GeV$, $\Gamma_W = 2.25\,GeV$, $m_e = 0.511\,MeV$, $m_\mu = 0.1057\,GeV$, $m_\tau = 1.7841\,GeV$, and $\sin^2\theta_W = 0.23$.

The experimental signature for the processes under consideration is a clean one, an oppositely charged lepton pair and missing transverse momentum and energy due to the neutrinos. We have made some fairly simple cuts as described below to account for detector acceptance and potential backgrounds. For all the processes, we require a cut on the angle of each of the charged leptons relative to the beam such that $-0.95 \leq \cos\theta_{\ell\pm} \leq 0.95$. This is the only cut we impose for the $\mu\tau$ and μe final states. This angular cut is experimentally motivated however it also serves to regulate the t-channel photon poles, allowing us to neglect the terms proportional to m_f. These diagrams contribute to the μ^+e^- and e^+e^- final states, as described above.

One potential background is τ pair production with each of the τ's decaying leptonically. At $\sqrt{s}$ of $200\,GeV$, each of the four lepton processes and the τ pair production, multiplied by the branching ratios of τ into e or μ of 17.8% each [35], yield about the same rate. At higher energies, the τ pair production cross section is falling like $1/s$ while the cross section for our processes remains large. In addition, the τ pair process should have substantially greater missing energy with four neutrinos in the final state. It seems that this source of background is manageable.

The four lepton processes with one or more τ's in the final state ($\mu\tau$ and $\tau\tau$) could feed down as a background to the processes without any τ if the τ(s) decays leptonically. However, factoring in the τ decay branching ratio and accounting for the higher missing energy keeps this background under control. Another potential background comes from two photon processes with the e^+ and e^- undetected near the beam. This is relevant to the $\mu\mu$ and ee processes and we make a cut on missing transverse momentum to eliminate two photon events as a background source; we require total visible $\not{p}_T > 10\,GeV$. We also require for these two processes that each charged lepton carry a minimum energy, $E_\ell > 10\,GeV$. Finally, again for the $\mu\mu$ and ee processes we make a cut on the invariant mass of the charged lepton pair; we require $m_{\ell^+\ell^-} > 25\,GeV$ in order to eliminate the low invariant mass dileptons corresponding to the photon pole in these processes.

We evaluate the cross sections as a function of $\sqrt{s}$ for the processes $e^+e^- \to \ell^+\ell'^-\nu\bar{\nu}'$ for $\ell^+\ell'^-$ equal to $\mu^+\tau^-$, μ^+e^-, $\mu^+\mu^-$, e^+e^-, respectively, with the cuts as described above imposed. The sensitivity to κ_V increases with increasing center of mass energy. The $\mu\tau$ process exhibits the most sensitivity to κ_V, as might be expected since it has the least number of extraneous contributing diagrams; however, it also has the smallest cross section. Thus, it is useful to consider all the processes.

We make our study of κ_V dependence at two center of mass energies, $500\,GeV$ and $1\,TeV$, motivated by the possibility of future high energy e^+e^- colliders. For each of the four types of four lepton processes, at each of the two energies, we vary κ_γ alone from 0.9 to 1.1, κ_Z alone over the same range, and κ_γ constrained to equal κ_Z over the same range.

At $\sqrt{s}$ of $500\,GeV$, each process is more sensitive to deviations of κ_V below the standard model value of 1 than above it; however at the higher center of mass energy of $1\,TeV$, the sensitivity to κ_V is considerably more symmetric about 1.

a parabola for the cross section as a function of κ and solved for the cross section as a function of the two parameters κ_γ and κ_Z as

$$\sigma \sim |M|^2 = a + b\kappa_\gamma + c\kappa_Z + d\kappa_\gamma\kappa_Z + e\kappa_\gamma^2 + f\kappa_Z^2. \tag{21}$$

We turn these results into limits on the detection of deviations of κ_V from 1 by assuming an integrated luminosity of $50\, fb^{-1}$ for a proposed collider[36]. ¿From the total cross section of the individual processes, we find the following 2σ limits on measurements of κ_γ and κ_Z. At $\sqrt{s}$ of $500\, GeV$, κ_γ could be measured within $-2.5\%\,(\mu\tau)$ to $+9.5\%\,(ee)$ and κ_Z within the range $-6\%\,(\mu\tau,\ \mu e,\ \mu\ mu)$ to $+8\%\,(\mu e)$. At $1\, TeV$, the corresponding limits on κ_γ are $-1\%\,(\mu\tau)$ to $+3.5\%\,(\mu\tau,\ \mu e)$ and on κ_Z we find limits of $-1.5\%\,(\mu\tau)$ to $+2.5\%\,(\mu\tau)$. The channels given in brackets with each limit indicate which of the processes supplies the best bound. These particular limits simply represent the outer bound of the 2σ contour for the various processes. If one makes some assumptions about the relationship of κ_γ and κ_Z, such as that $\kappa_\gamma = \kappa_Z$ or that $\Delta\kappa_\gamma = \frac{2\cos^2\theta_W}{\cos^2\theta_W - \sin^2\theta_W}\Delta\kappa_Z$ [23], better bounds are obtained. In addition, combining the statistics from all the processes considered here would improve the bounds. In fact, one could also combine these four lepton processes with the similar jet channels such as $e^+e^- \to q\bar{q}'\ell\nu$. Combined bounds would necessitate inclusion of detector acceptances and efficiencies for the various particle types. We emphasize that even the bounds quoted above from the cross sections of individual processes are, indeed, approaching the very interesting realm of probing κ_V to within a few per cent of the standard model value. We note that it is particularly important to go to the higher energy in order to probe values of κ_V larger than 1.

We have also generated a number of distributions; these include the differential cross sections with respect to the angle of each charged lepton relative to the beam, the angle between the charged leptons, the energy and transverse momentum of each charged lepton, the total visible energy and transverse momentum and the invariant mass of the charged lepton pair. The charged lepton angular distributions tend to be strongly peaked along the beam line due to the t- channel neutrino exchange; they are generally enhanced somewhat away from the beam direction for nonstandard κ_V values. The energy and transverse momentum distributions of the individual particles tend to be enhanced over most of their range. The total visible transverse momentum is preferentially enhanced where the differential cross section is largest.

It now remains to determine whether we can pinpoint the values of κ_γ and κ_Z individually. There have been a number of approaches proposed for discriminating between deviations of κ_γ and κ_Z. One suggestion is to study processes which only involve one or the other of the γWW and ZWW vertices. The associated production of a W with either a γ or a Z boson, radiative W decay [28], and $e\gamma$ processes such as $e\gamma \to W\nu$ [37] fall into this category. Another suggestion is to make cuts which isolate one of the vertices. For instance,[38] has studied the $\mu^+\mu^-$ production process which we also consider here and have focussed on the ZWW vertex by requiring that the invariant mass of the $\mu^+\mu^-$ pair fall within $5\, GeV$ of M_Z. Here, we emphasize instead the potential usefulness of the helicity structure in providing a determination of κ_γ and κ_Z.

We observe that the $(-++-)$ [39] amplitude is suppressed at $\sqrt{s} \gg M_Z$ for $\kappa_\gamma = \kappa_Z$ as a direct result of the general form of this amplitude, which is given below.

$$M_{(-++-)} = \left[\frac{\kappa_\gamma + 1}{2s} - \frac{\kappa_Z + 1}{2(s - M_Z^2)}\right] A + B \tag{22}$$

Here A and B denote the κ_V dependent and independent factors, respectively, of the amplitude. For large center of mass energies, the cancellation of the κ_γ and κ_Z terms results in a $(-++-)$ helicity contribution of less than about one per cent of the total cross section for the standard model and for $\kappa_\gamma = \kappa_Z$ in general. On the other hand, for nonequal values of κ_γ and κ_Z, this contribution can be as much as 30% of the total. Thus, polarized beams accessing the individual helicity contributions could differentiate between the $\kappa_\gamma = \kappa_Z$ case and the nonequal case. Apart from the general observation described above regarding the case of κ_γ and κ_Z equal, experimental results on the cross sections for the four types of processes we consider with polarized and unpolarized beams could provide a characteristic 'fingerprint' for a $(\kappa_\gamma, \kappa_Z)$ pair. As an example of how this might work,for the $\mu\tau$ process at $1\,TeV$; we note that, for instance, $(\kappa_\gamma, \kappa_Z) = (0.945, 0.945), (1.07, 1.07), (1, 1.095), (1, 0.92)$, and $(0.92, 1)$ all have approximately the same total cross section. The percentage of the cross section supplied by the $(-++-)$ helicity is less than 1% for the two cases quoted with $\kappa_\gamma = \kappa_Z$; it is 3.6% for $(1, 1.095)$, 18% for $(1, 0.92)$, and 27% for $(0.92, 1)$. Since the total cross section for unpolarized beams corresponds to about 1000 events, these cases can possibly be discriminated providing reasonable polarization can be achieved. Similar results from the four types of processes can be combined to narrow in on the actual values of κ_γ and κ_Z, individually. The detailed study of distributions will also be useful as mentioned. We note that the processes considered here offer a very clean experimental signature for excellent sensitivity to κ_γ and κ_Z at a high energy e^+e^- collider.

8. Conclusions

The anomalous electroweak vector boson couplings have just started getting tested. The vector boson vertex can be written in a model independent way and related to the moments of the W boson. We have examined some direct and indirect (loop-induced) bounds on the TEVB couplings. However, these bounds are too weak to limit most models and probe loop level corrections to the standard model. There will be better bounds coming from CDF and D0 collaborations as well as from LEPII when it becomes operational. Bounds obtained from oblique parameters, obtained from LEPI data cannot rule out anomalous couplings even if the oblique parameters are in complete agreement with the SM. Future colliders will be needed to probe modifications to the electroweak vector bosons vertex from loop level corrections within the SM, as well as from most extensions of the SM. In this connection it is found that the Next Linear Collider running at $500GeV$ and $1TeV$ can bound these couplings accurately to probe at this level (less than 5%) and also allow for the possibility of separating the photon couplings from that of the Z using polarized

9. Acknowledgements

Due to time and space constraints justice cannot be done to the vast area of anomalous TEVB coupling in such a short writeup. I have chosen just a few topics that I have been of working on. Several important developments, especially in the area of searches for anamolous TEVB at other future Colliders and HERA have been left out. I would like to thank Nita Sinha for collaborating on most of the work presented here and for reading this manuscript I also thank my several other collaborators with whom parts of the work discussed here have been done. I would like to thank the National/International organizing committee of WHEPP-3 for their kind invitation to present this talk.

References

[1] M. Timko, 'Status of $W\gamma$ Search at CDF', contribution to *The Spring Meeting of the American Physics Society*, Washington, D.C., 16-19 April 1990 (unpublished).

[2] CDF rapportear talk at *Proceedings of the 9th Topical Workshop on Proton-Antiproton Collider Physics*, Tsukuba, Japan,1993.

[3] A. L. Spadoafora (for D0 collaboration),*Proceedings of the 9th Topical Workshop on Proton-Antiproton Collider Physics*, Tsukuba, Japan,1993, Preprint: FERMILAB-Conf-94/016-E (1994).

[4] J. Alitti *et al.*, Phys. Lett. **B277**, 194 (1992).

[5] A list of most papers on this subject may be found in [2] of reference[13].

[6] There are far too many papers on this subject in the literature to attempt to list them here.

[7] J.F.Gaemers and G.J. Gounaris, Z. Phys. **C1**, 259 (1979).

[8] K. Hagiwara, R.D. Peccei and D. Zeppenfeld, Nucl. Phys. **B282**, 253 (1987).

[9] T.G. Rizzo and M.A. Samuel, Phys. Rev. D **35**, 403 (1987).

[10] G. Couture *et al.*, Phys. Rev. D **36**, 859 (1987).

[11] G. Couture *et al.*, Phys. Rev. D **38**, 860 (1988).

[12] A. de Rujula, M.B. Gavela, P. Hernandez and E. Masso, Nucl. Phys. **B384**, 3 (1992).

[13] C.P. Burgess and D. London, Phys. Rev. Lett. **69**, 3428 (1992), C.P. Burgess and D. London, Phys. Rev. **D48**, 4337 (1993).

[14] U. Baur and D. Zeppenfeld, Phys. Lett. **B201**, 383 (1988).

[15] P. Méry *et al.* Z. Phys. **C42**, 263 (1989).

[16] M.B. Einhorn and J. Wudka, ITP, Santa Barbara Report NSF-ITP-92-01 (1992)(unpublished); Michigan U. Report UM-TH-92-25(unpublished); J. Wudka, University of California Report UCRHEP-108 (1993) (unpublished).

[17] W. Marciano and A. Queijeiro, Phys. Rev. D **33**, 3449 (1986); F. Boudjema *et al.*, Phys. Rev. D **43**, 2223 (1991).

[18] M.E. Peskin and T. Takeuchi, Phys. Rev. **D46**, 381 (1992); G. Bhattacharyya, S. Banerjee and P. Roy, Phys. Rev. **D45**, R729 (1992).

[19] G. Altarelli and R. Barbieri, Phys. Lett. **B253**, 161 (1991); G. Altarelli, R. Barbieri

C. P. Burgess, *et al.* Phys. Lett. **B326** 276 (1994).

21] Maksymyk[20] *et al.* have introduced 6 oblique parameters. For details the reader is referred to the talk by Burgess in this proceedings.

22] D. Choudhury, P. Roy, and R. Sinha, TIFR-TH/93-08.

23] K. Hagiwara *et al.* , Phys. Lett. **B283**, 353 (1992); Madison Report MAD/PH/737 (1993) (unpublished); D. Zeppenfeld and R. Szalapski, Madison Report MAD/PH/719 (1992) (unpublished); D. Zeppenfeld *et al.* , Madison Report MAD/PH/729 (1992)(unpublished); P. Hernández and F.J. Vegas, CERN Report CERN-TH 6670 (1992) (unpublished).

24] C. P. Burgess *et al.* Phys. Rev. **D49**, 6115 (1994),Phys. Rev **D**(to be published),(hep-ph/9307223).

25] H.M. Georgi, Nucl. Phys. (Proc. Suppl.) 29**B**, C 1 (1992)

26] J. Ellis, G. Fogli and E. Lisi, Phys. Lett. **B292**, 427 (1992).

27] A. Manohar and H.M. Georgi, Nucl. Phys. **B234**, 189 (1984); H. Georgi, Phys. Lett. **B298**187(1993).

28] K.O. Mikaelian, M.A. Samuel, and D. Sahdev, Phys. Rev. Lett. **43**, 746 (1979).

29] The results discussed in this paper are the best avialable at the time of this talk. CDF have subsequently reported [2] new results with an integrated luminosity of 25pb^{-1}, which can be used to set better bounds set here on kappa, than the ones reported here. D0 [3] has also reported results for 15pb^{-1} and obtain better limits than those reported here.

30] M. Samuel, G. Li, N. Sinha, R. Sinha and M.K. Sundaresan, Phys. Lett. **B280**, 124 (1992);Phys. Rev. Lett. **67**,1991.

31] E. Eitchen *et al.* , Rev. Mod. Phys. **56**,579 (1984).

32] While these proceedings were being written up the author became aware of Ref.[3] where a better limit $-2.5 \leq \kappa \leq 2.7$ have been reported.

33] P. Kalyniak, P. Madsen, N. Sinha and R. Sinha,Phys. Rev. **D48**, 5081 (1993).

34] R. Kleiss and W.J. Stirling, Nucl. Phys. **B262**, 235 (1985).

35] M. Aguilar-Benitez *et al.*, Phys. Rev. D **45**, Part 2 (1992).

36] This estimated integrated luminosity is based on information in *Proceedings of the Third Workshop on the Japan Linear Collider*, KEK, Japan, 1992, edited by A. Miyamoto; *Search for New Phenomena at Colliding Beam Facilities*, New Haven, Connecticut, 1992, to be published.

37] G. Couture, S. Godfrey, and P. Kalyniak, Phys. Lett. **B218**, 361 (1989); Phys.Rev. D **39**, 3239 (1989); D **42**, 1841 (1990).

38] G. Couture, S. Godfrey, and R. Lewis, Phys. Rev. D **45**, 777 (1992).

39] In the following, we will denote the helicities of the particle set $e^+e^-\ell^+\ell'^-$ as $(\bar{\alpha}\alpha\bar{\beta}\beta)$.

journal of physics
October 1995
pp. 365-366

Group report: Collider physics and structure functions

AMITAVA DATTA
Dept. of Physics, Jadavpur University, Calcutta 700 032.

ROHINI M. GODBOLE
Dept. of Physics, University of Bombay, Bombay 400 098.

Participants :
T. Aziz, S. Banerjee, R. Bhalerao, K. Bora, A. Datta (Group Coordinator)
M. Drees, S. N. Ganguli, R. M. Godbole (Group Coordinator), M. Guchait,
V. Gupta, D. Indumathi, P. Kalyaniak, K. Mazumdar, H. S. Mani, P. Mathews,
N. K. Mondal, B. Mukhopadhyaya, M. V. N. Murthy, M. Nowakowski,
P. N. Pandita, R. J. N. Phillips, R. Ramchandran, G. Rajasekaran,
V. Ravindran, S. D. Rindani, R. G. Roberts, D. P. Roy, P.Roy, J. P. Singh,
N. Sinha, R. Sinha, K. Sridhar.

The activities of this group centered round two main topics of current interest. The advent of HERA the e-p collider at DESY led to the measurement of proton structure functions with unprecedented accuracy, in particular, at low values of the Bjorken variable x. Theoretical understanding of these results often demands departures from perturbative QCD. A part of the group activities was therefore devoted to structure functions and related topics. The following topics were discussed in working group sessions(the names of the contributors are given in parenthesis):

1) Determination of $c^{\gamma}(x,Q^2)$ at HERA (M.Drees and R.M.Godbole)

2) Polarised structure functions: possibility of constructing single spin asymmetries (V.Gupta, D.Indumathi, H.S.Mani, P.Mathews, M.V.N.Murthy, R.Ramchandran, G.Rajasekaran, L.Sehgal, J.P. Singh and K.Sridhar)

3) Rise of $F_2(x)$ at small x,fixed poles and Schwinger terms (K.Bora, V.Gupta, D.Indumathi, H.S.Mani, P.Mathews, M.V.N.Murthy, R.Ramchandran, G.Rajasekaran, V.Ravindran and K.Sridhar)

Searches for new particles and interactions indicating physics beyond the standard model are at the focus of attention of all the on going experiments at hadron and $e^+ - e^-$ colliders like LEP 100 at CERN and the TEVATRON at Fermilab. The issues unresolved after the present round of experiments , if any, will continue to dominate the experiments at the future colliders like LEP 200 and LHC at CERN. In view of this a considerable part of the group activity was devoted to the phenomenology of new particle searches at hadron and $e^+ - e^-$ colliders. The following topics were covered in some details(the names of the contributors are given in parenthesis):

1) Virtual LSPs in N = 1 SUGRA models (A.Datta, M.Drees and M.Guchait)

2) Like sign dileptons and SUSY searches in models with conserved and broken R-Parity (M.Guchait, N.K.Mondal and D.P.Roy)

3) Loop Induced gluino decays(M.Drees, M.Guchait, B.Mukhopadhyaya and D.P.Roy)

4) Limit on the lightest neutralino mass in R-parity violating theories (S.Banerjee, R.M.Godbole, K.Mazumdar, D.P.Roy and P.Roy)

5) Tau number violating signals for R-parity violating SUSY at LEP 200 (S.Banerjee, R.M.Godbole, K.Mazumdar and P.Roy)

B) Higgs Physics

1) Production of Charged Higgs in pp collisions via $\gamma - \gamma$ interactions (M.Drees, R.M.Godbole, M.Nowakowski and S.D.Rindani)

2) Implications of a tree level HWZ coupling at $e^+ - e^-$ colliders (R.M.Godbole, B.Mukhopadhyaya and M.Nowakowski)

C) Gauge Boson Physics

1) Faliure of equivalent gauge boson (EVBA) approximation? (G.Rajasekaran, S.D.Rindani and R.Sinha)

2) Single Z production in $e^+ - e^-$ collision, anomalous triple gauge boson coupling and EVBA (S.D.Rindani and J.P.Singh)

3) CP violating tripple vector boson couplings at NLC (P.Kalyaniak, P.Madsen, N.Sinha and R.sinha)

4) Determination of tripple gauge boson vertices at LEP 200 (T.Aziz, S.Banerjee, K.Mazumdar, N.Sinha and R.Sinha)

Summaries of some of the above works were submitted by the authors. They are presented following this.

VLSPs in N=1 SUGRA models

MANUEL DREES

Dept. of Physics, University of Wisconsin, Madison, WI 53706, U.S.A.

AMITAVA DATTA AND M. GUCHAIT

Dept. of Physics, Jadavpur University, Calcutta - 700 032.

The lightest supersymmetric particle (LSP)plays a crucial role in the search for supersymmetry (SUSY) since it carries missing transverse energy ($\not{E}_T$) which is traditionally regarded as the most distinctive signature of SUSY particles. In the currently favoured models, the lightest neutralino ($\widetilde{Z_1}$) is assumed to be the LSP [1].

Recently it has been emphasised [2, 3] that there may exist SUSY particles which, though unstable, **decay dominantly into invisible channels**. This occurs if the sneutrinos ($\widetilde{\nu}$) (the super–partners of the neutrinos) , though heavier than the LSP, are lighter than the lighter chargino ($\widetilde{W_1}$) or the second lightest neutralino ($\widetilde{Z_2}$) and are much lighter than all other SUSY particles. As a consequence, the **invisible two-body decay mode $\widetilde{\nu} \longrightarrow \nu\widetilde{Z_1}$ opens up** and completely dominates over others, being the only kinematically allowed two-body decay of the sneutrinos. The other necessary condition for this scheme to work is that the $\widetilde{Z_1}$ has a substantial Zino component. This, however, is almost always the case as long as the gluino (the super–partner of the gluon) has a mass above the lower bound obtained by the SUSY searches at the Tevatron [4]. In such cases the $\widetilde{Z_2}$, which also has a substantial Zino component, decays primarily through the process $\widetilde{Z_2} \longrightarrow \nu\widetilde{\nu}$. These particles decaying primarily into invisible channels, hereafter called **virtual LSP's** (VLSP's), may act as additional sources of $\not{E}_T$ and can significantly affect the strategy for SUSY searches [2].

Another important consequence is the decay $\widetilde{W_1} \longrightarrow l\widetilde{\nu}, l = e,\ \mu\ or\ \tau$. Since this is the only kinematically allowed two body decay of $\widetilde{W_1}$ it occurs with a branching ratio(BR) ≈ 1.

In Ref 2. sparticle masses were treated as free phenomenological parameters, although it was commented briefly that it is not unlikely that the VLSP scenario can be accomodated in the N=1 SUGRA models with common squark and gaugino masses at the GUT scale [5]. In this work we show in detail that this indeed is the case for a reasonably large region of the SUSY parameter space.

We assume a minimal N=1 supergravity model [5] with a common scalar mass m_0 and a common gaugino mass $m_{1/2}$ at the GUT scale M_X. We also assume minimal particle content. We follow the standard convention for the neutralino and chargino mass matrices [1].

In the following, M_1 and M_2 are SUSY breaking $U(1)$ and $SU(2)$ gaugino masses, μ is the supersymmetric Higgs(ino) mass and $\tan\beta \equiv \langle H_2^0\rangle/\langle H_1^0\rangle$ is the

atio of the vacuum expectation values (vevs). The assumed unification of gaugino nasses leads to the following relation at the weak scale:

$$M_1 = \frac{5}{3}\tan^2\theta_W M_2 \simeq 0.5 M_2, \tag{1}$$

where

$$M_2(M_Z) = 0.82 m_{1/2} \tag{2}$$

gives the connection to the GUT scale gaugino mass. The above parameters also determine the chargino masses.

The relevant slepton masses [5] at the weak scale are determined by M_2, m_0 and $\tan\beta$:

$$m^2_{\tilde{l}_R} = m_0^2 + 0.223 M_2^2 + \sin^2\theta_W D_Z, \tag{3a}$$

$$m^2_{\tilde{l}_L} = m_0^2 + 0.773 M_2^2 + (0.5 - \sin^2\theta_W) D_Z, \tag{3b}$$

$$m^2_{\tilde{\nu}} = m_0^2 + 0.773 M_2^2 - 0.5 D_Z, \tag{3c}$$

where

$$D_Z = M_Z^2 \frac{\tan^2\beta - 1}{\tan^2\beta + 1} > 0 \tag{4}$$

for $\tan\beta > 1$. Notice that $m_{\tilde{l}_L} > m_{\tilde{l}_R}$ always.

Our free parameters are thus m_0, M_2 (which we traded for $m_{1/2}$), μ and $\tan\beta$. There are two sets of constraints on the allowed parameter space: direct experimental constraints (primarily from LEP-I [6]) , and requirements for having VLSP's. We took the following experimental constraints into account [6]:

$$\begin{aligned} & m_{\tilde{l}_R} > 45 \text{ GeV}, \quad m_{\tilde{\nu}} > 40 \text{ GeV}, \quad m_{\tilde{W}_1} > 46 \text{ GeV}, \\ & \Gamma(Z \to \tilde{Z}_1 \tilde{Z}_1) < 12 \text{ MeV}, \quad \sum_{i,j} \Gamma(Z \to \tilde{Z}_i \tilde{Z}_j) < 0.25 \text{ MeV}, \end{aligned} \tag{5}$$

where the sum does not include $(i,j) = (1,1)$.

The defining property of the VLSP scenario is that both the sneutrino and $\tilde{Z}_2$ decay invisibly. This implies the following constraints:

$$\begin{aligned} & m_{\tilde{\nu}} < m_{\tilde{Z}_2} < m_{\tilde{l}_L},\ m_{\tilde{l}_R} \\ & m_{\tilde{\nu}} < m_{\tilde{W}_1} < m_{\tilde{l}_L}. \end{aligned} \tag{6}$$

Notice that eq. 6 implies $m_{\tilde{\nu}} < m_{\tilde{l}_R}$; eqs.(3) then give an *upper bound* on M_2:

$$|M_2| \leq 1.15\sqrt{D_Z}. \tag{7}$$

This in turn requires a gluino light enough to be within the striking range of the Tevatron. For example with $\tan\beta = 2$ (10) the upperbound on the gluino mass is 243.45 GeV (284.29 GeV). For each value of the gluino mass there is an upper bound on the lighter chargino mass (see, for example, Datta, Guchait and Raychaudhuri in ref [6]). The above bounds on the gluino mass implies $m_{\tilde{W}_1} < 95$ GeV (approximately). Then eq. 6 implies that m_0 cannot be too large, either, hence

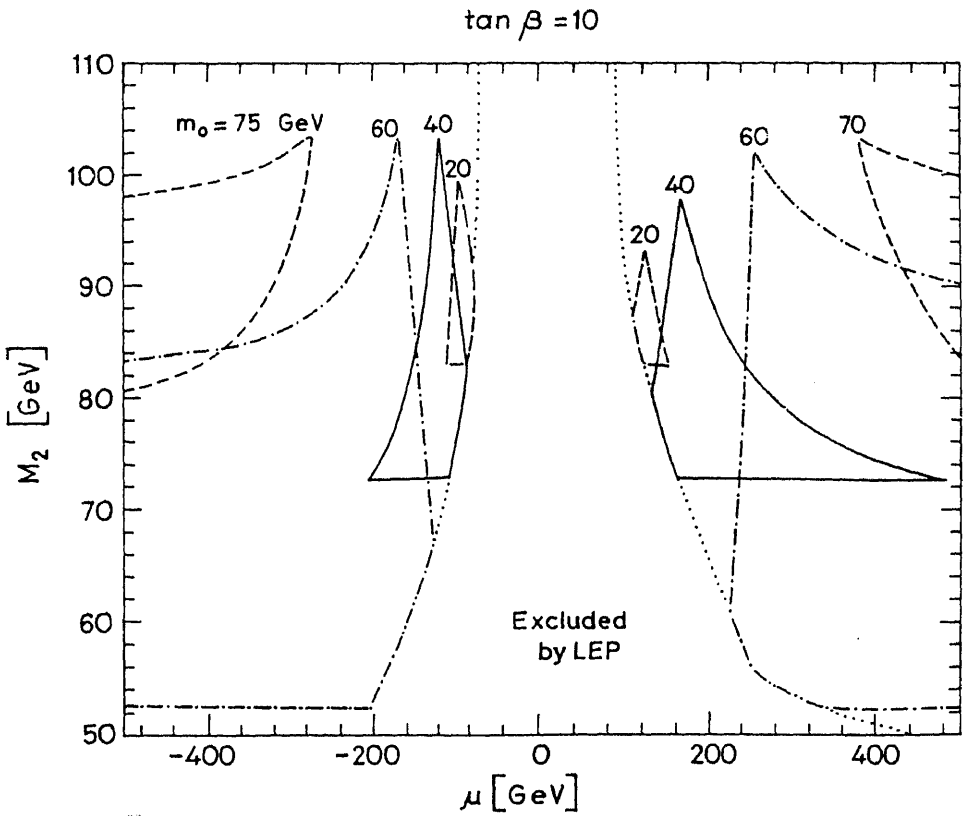
tan β =10
m₀ = 75 GeV
60
40
20
60
40
20
70
Excluded
by LEP
M₂ [GeV]
μ [GeV]
110
100
90
80
70
60
50
-400
-200
0
200
400

Figure 1.

sleptons will also be light. The lightest charged sparticle mass is then expected to be around M_Z. The masses are, therefore, in the region of interest for LEP 200.

Figure 1 shows an example of a allowed region. Here we fixed $\tan\beta = 10$, and plotted the allowed region in the (μ, M_2) plane for various values of m_0. The dotted curve delineates the region excluded by sparticle searches at LEP-I. The allowed region for fixed m_0 is not very large, although the fraction of the plane with a VLSP scenario for *some* value of m_0 is substantial, given only that M_2 satisfies eq 7.

Almost any value of μ can accomodate VLSPs if M_2 and m_0 are chosen properly. In fig.2 we have plotted the allowed region in the (m_0, M_2) plane for $\tan\beta = 2$ (solid

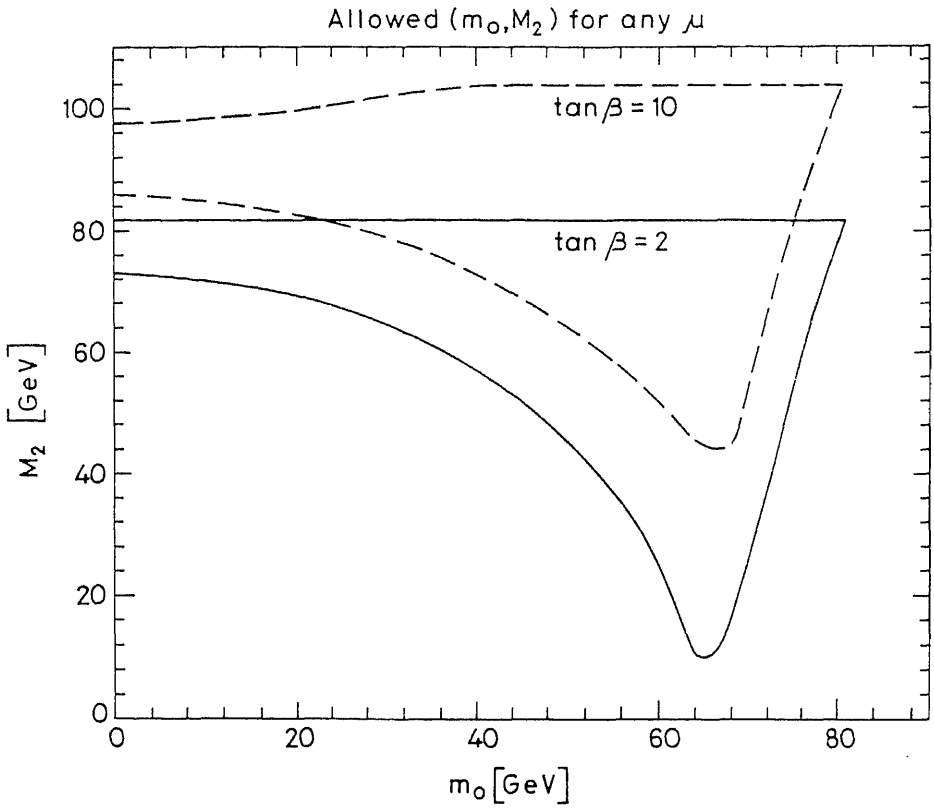

Figure 2.

curve) and 10 (dashed curve), after scanning over all μ; in other words, the curves enclose the region where at least one value of μ can be found so that a valid VLSP scenario emerges.

We now briefly discuss $\tilde{W}_1$ pair production at LEP 200 energies. Our signal is a pair of opposite sign stable dileptons (e or μ) + missing energy, arising from the decay of $\widetilde{W}_1$ s into leptons and VLSPs (sneutrinos).

Since the dilepton final State in this case arises from the decay of spin 1/2 charginos, the distributions of the final state leptons depend on the polarisations

of the charginos. These polarisations can be conveniently taken into account by calculating the dilepton cross-section and the related distributions using the helicity projection technique [7].The calculations are tedious but straight forward and the results will be presented elsewhere [8].

In this scenario with a tightly constrained mass spectrum the lighter chargino is the lightest charged sparticle in certain region of the allowed parameter space discussed earlier. These regions can be most conveniently probed by restricting the beam energy below the threshold for the production of other sparticles . The above dilepton signal consisting of any combination of e and μ, after removing the $\gamma-\gamma$, $\tau-\tau$ and WW backgrounds by appropriate kinematical cuts , then provides an unambiguous signal of chargino pair production. For beam energies above the slepton threshold, only e -μ pairs provide a clean signature of chargino production. Such pairs of course cannot arise from slepton pairs whose decays conserve flavour. In the following we shall present some illustrative examples of chargino signals in the VLSP model.

For m_0 =67.5 GeV ,M_2= 53 GeV ,$tan\beta$ = 2.0 and μ = -150 GeV, the sparticle spectrum of our interest is given by: $m_{\tilde{\nu}}$ = 65.35 GeV, $m_{\tilde{l}_R}$ = 79.58 GeV, $m_{\tilde{l}_L}$ = 89.98 GeV and $m_{\widetilde{W}_1}$ = 72.74 GeV. In this scenario the dilepton cross-section arising out of direct chargino decays at the c.m. energy $\sqrt{s}$ = 160 GeV is $0.15pb^{-1}$ where the kinematical cuts used are as above (the cut against the W-W background of course is irrelevant in this case). Thus for an integrated luminosity of $500pb^{-1}$ we expect about 75 events. Here since 2 $m_{\tilde{l}_R}$ ¿ $\sqrt{s}$, the dilepton final state consisting of any combination of e and μ provides the signal.

Since the charginos can also decay into τ's, stable leptons from the decays $\tau \longrightarrow e($ *or* $\mu)\nu\ \bar{\nu}$ can enhance the signal. The cross-section for this process ,however, turns out to be rather small due to the small leptonic branching ratio of the τ [8].

The end points of the lepton energy spectrum from direct chargino decays are particularly interesting since they determine in principle both $m_{\tilde{\nu}}$ and $m_{\widetilde{W}_1}$. It turns out that the number of stable leptons arising from τ decays is not large enough to obscure completely the characteristics of the above energy spectrum.

We note in passing that in the above example the mass difference between the chargino and the sneutrino is rather small. Yet we get a viable signal. This is to be contrasted with chargino search in this channel at TEVATRON where the signal can be completely washed out if the above mass difference is small [9].

The other case we have considered in some detail consists of the following parameters: m_0 =40 GeV ,M_2= 70 GeV ,$tan\beta$ = 2.0 and μ = -75 GeV. This yields the sparticle spectrum : $m_{\tilde{\nu}}$ = 53.8 GeV, $m_{\tilde{l}_R}$ = 61.9 GeV, $m_{\tilde{l}_L}$ = 82.0 GeV and $m_{\widetilde{W}_1}$ = 79.9 GeV. This case is interesting for two reasons.Firstly, the beam energy has to be above the WW threshold and the cuts against WW background are called for. Secondly , since $m_{\tilde{l}_R} < m_{\widetilde{W}_1}$ only e - μ final states should be considered. A calculation using the standard cuts yields a dilepton cross-section of $0.13pb^{-1}$ from direct decays at c.m. energy $\sqrt{s}$ = 180 GeV .Thus for an integrated luminosity of $500pb^{-1}$ we expect about 65 events.

We have also checked the cross - section for several representative points of the parameter space for tanβ = 10. The number of events for $\sqrt{s} = 150 - 180$ GeV is between 20 - 150 for an integrated luminosity of 500 pb^{-1}.

References

[1] For a review see, for example, H. Haber and G. Kane, Phys. Rep. **117** (1985) 75.

[2] A.Datta, B.Mukhopadhyaya and M. Guchhait, preprint MRI–PHY–11/93, submitted for publication.

[3] Some aspects of VLSPs in the context of SUSY searches at hadron colliders have been considered by H. Baer, C. Kao and X. Tata, Phys. Rev. **D48** (1993) R2978; M. Barnett, J. Gunion and H. Haber, LBL preprint LBL-34106 (1993).

[4] CDF collaboration, F. Abe *et al.*, Phys. Rev. Lett. **69** (1992) 3439.

[5] See, for example, H. P. Nilles, Phys. Rep. **110** (1984) 1.

[6] H. Baer, M Drees, X. Tata, Phys. Rev. **D41** (1990) 3414; G. Bhattacharyya, A. Datta, S. N. Ganguli and A. Raychaudhuri, Phys. Rev. Lett. **64** (1990) 2870; A.Datta, M.Guchait and A.Raychaudhuri, Z.Phys C**54**(1992), 513; J. Ellis, G. Ridolfi and F. Zwirner, Phys. Lett. **B237** (1990) 923; M. Davier in Proc. Joint International Lepton-Photon and Europhysics Conference in High Energy Physics, Geneva, 1992 (eds. S. Hegarty *et al.*, World Scientific, 1992) p151.

[7] See, for example, V. Barger and R.J.N. Phillips, Collider Physics (Addison-wesley, 1987) and references therein.

[8] A.Datta, M.Drees and M.Guchait, paper submitted to the XXVIII International Conference in High Energy Physics, Glasgow, 1994, Contribution code gls 0712, and Madison Preprint MAD-PH-903, Feb. 1995.

[9] S.Chakrabarti, A.Datta and M.Guchait, ICTP pre-print IC/94/303 (1994)- to appear in Z.Phys C.

PRAMANA
journal of
physics

© Printed in India

Supplement to Vol. 45
October 1995
pp. 373-378

$\gamma\gamma$ processes at high energy $p-p$ colliders

MANUEL DREES
University of Wisconsin, Dept. of Physics, Madison, WI 53706, U.S.A.

ROHINI M. GODBOLE
Dept. of Physics, University of Bombay, Bombay 400 098.

MAREK NOWAKOWSKI AND SAURABH D. RINDANI
Physical Research Laboratory, Navrangpura, Ahmedabad 380 009.

The detection of a fundamental charged scalar particle would certainly lead beyond the realm of the Standard Model (SM). These particles can arise either in the context of supersymmetric models, as superpartners of quarks and leptons [2], or in extended Higgs sectors (with or without supersymmetry). In general, the different charged scalars will have different interactions at tree level. Hence a model independent production mechanism is welcome. Such a model independent interaction is clearly given by the scalar QED part of the underlying theory. For example the $\gamma\gamma$ fusion processes:

$$\gamma\gamma \rightarrow H^+H^-,\ \tilde{l}^+\tilde{l}^-,\ \ldots \tag{1}$$

are uniquely calculable for given mass of the produced particles. At pp colliders we also have, however, the possibility of the $q\bar{q}$ annihilation Drell–Yan processes

$$q\bar{q} \rightarrow H^+H^-,\ \tilde{l}^+\tilde{l}^-\ \ldots \tag{2}$$

There has been a claim in the literature that the $\gamma\gamma$ fusion exceeds the Drell–Yan (DY) cross sections at pp by orders of magnitude [3]. This would be an interesting possibility of producing charged heavy scalars at hadronic colliders or for that matter any charged particle which does not have strong interactions.

Apart from the charged scalars mentioned above there exist various candidates for charged fermions. These fermions can be either fourth generation leptons, charginos or exotic leptons in extended gauge theories like E_6 [4]. Current limits on the masses of all exotic charged particles which couple to the Z with full strength are $\sim M_Z/2$. In the case of $H^\pm$ there exist additional constraints (clearly model dependent) from the experimental studies of the $b \rightarrow s\gamma$ decay. The calculation for $\gamma\gamma \rightarrow L^+L^-$ at pp colliders has been done recently [5]. The result in [5] is that the $\gamma\gamma$ cross section is comparable to the corresponding Drell–Yan process at high energies, e.g. at $\sqrt{s} = 40$ TeV for $m_L \sim 100$ GeV. At LHC energies the $\gamma\gamma$ cross section in the same mass range was found to be [5] one order of magnitude smaller than the DY cross section.

We have repeated the calculations for scalar and fermion pair production, and

bution [6]. In what follows we outline briefly the basic tools and approximations in the calculation.

In order to calculate the pp cross section we have used the Weizsäcker-Williams approximation [7] for the inelastic case (γpX vertex) and a modified version of this approximation [8, 9] for the elastic case (γpp vertex). In the latter case the proton remains intact. The inelastic (inel.) total pp cross section for H^+H^- as well as L^+L^- production reads

$$\sigma_{pp}^{inel.}(s) = \sum_{q,\,q'} \int_{4m^2/s}^{1} dx_1 \int_{4m^2/sx_1}^{1} dx_2 \int_{4m^2/sx_1x_2}^{1} dz_1 \int_{4m^2/sx_1x_2z_1}^{1} dz_2 \; e_q^2 e_{q'}^2 \cdot f_{q/p}(x_1,\, Q^2)\, f_{q'/p}(x_2,\, Q^2) f_{\gamma/q}(z_1)\, f_{\gamma/q'}(z_2)\, \hat{\sigma}_{\gamma\gamma}(x_1x_2z_1z_2s) \quad (3)$$

where m is the mass of either $H^{\pm}$ or $L^{\pm}$, $e_u = 2/3$, $e_d = -1/3$ and $\hat{\sigma}_{\gamma\gamma}$ is the production subprocess cross section with the center of mass energy $\sqrt{\hat{s}} = \sqrt{x_1x_2z_1z_2s}$. The structure functions have the usual meaning: $f_{q/p}$ is the quark density inside the proton, $f_{\gamma/q}$ is the photon spectrum inside a quark. We use the the MRSD$'_-$ parameterization for the partonic densities inside the proton [10]. The scale Q^2 has been chosen throughout the paper to be $\hat{s}/4$. We use

$$f_\gamma(z) \equiv f_{\gamma/q}(z) = f_{\gamma/q'}(z) = \frac{\alpha_{em}}{2\pi} \; \frac{(1+(1-z)^2)}{z} \; \ln(Q_1^2/Q_2^2) \quad (4)$$

There is a certain ambiguity about the choice of the scales Q_i^2 in the argument of the log in eq. (4). We choose Q_1^2 to be the maximum value of the momentum transfer given by $\hat{s}/4 - m^2$ and the choice of $Q_2^2 = 1$ GeV^2 is made such that the photons are sufficiently off-shell for the Quark-Parton-Model to be applicable.

The semi-elastic (semi-el.) cross section for $pp \to H^+H^-(L^+L^-)pX$ is given by

$$\sigma_{pp}^{semi-el.}(s) = 2 \int_{4m^2/s}^{1} dx_1 \int_{4m^2/sx_1}^{1} dz_1 \int_{sm^2/sx_1z_1}^{1} dz_2 \frac{1}{x_1} \; F_2^p(x_1,\, Q^2) \cdot f_\gamma(z_1)\, f_{\gamma/p}^{el.}(z_2)\, \hat{\sigma}_{\gamma\gamma}(x_1z_1z_2s) \quad (5)$$

The subprocess energy now is given by $\sqrt{\hat{s}} = \sqrt{sx_1z_1z_2}$. The elastic photon spectrum $f_{\gamma/p}^{el.}(z)$ has been obtained in the form of an integral in [8]. However, we use an approximate analytic expression given in [9] which is known to reproduce exact results to about 10%. The form we use is given by

$$f_{\gamma/p}^{el.}(z) = \frac{\alpha_{em}}{2\pi z}(1+(1-z)^2)\left[\ln A - \frac{11}{6} + \frac{3}{A} - \frac{3}{2A^2} + \frac{1}{3A^3}\right] \quad (6)$$

where

$$A = 1 + \frac{0.71(\text{GeV})^2}{Q_{min}^2} \quad (7)$$

with

$$Q_{min}^2 = -2m_p^2 + \frac{1}{2s}\Big[(s+m_p^2)(s-zs+m_p^2) - (s-m_p^2)\sqrt{(s-zs-m_p^2)^2 - 4m_p^2zs}\Big] \quad (8)$$

At high energies Q^2_{min} is given to a very good approximation by $m_p^2 z^2/(1-z)$. Since the relevant values of the scaled photon energy z_i can in general take smaller values in the elastic case as compared to the inelastic case, eqs. (8),(7) and (6) imply that even in the elastic case there is a logarithmic enhancement of the photon densities.

Finally the pure elastic contribution wherein both the photons remain intact and hence can in principle give rise to clean events, can be written as

$$\sigma^{el.}_{pp}(s) = \int_{4m^2/s}^{1} dz_1 \int_{4m^2/z_1 s}^{1} dz_2 \; f^{el.}_{\gamma/p}(z_1)\, f^{el.}_{\gamma/p}(z_2)\, \hat{\sigma}_{\gamma\gamma}(\hat{s} = z_1 z_2 s) \tag{9}$$

Defining $\hat{\beta}_{L,\,H} = (1 - 4m^2_{L,\,H}/\hat{s})^{1/2}$ the $\gamma\gamma$ subcross sections take the simple form

$$\hat{\sigma}(\gamma\gamma \to H^+H^-) = \frac{2\pi\alpha^2_{em}(M_W^2)}{\hat{s}}\hat{\beta}_H \left[2 - \hat{\beta}_H^2 - \frac{1-\hat{\beta}_H^4}{2\hat{\beta}_H}\ln\frac{1+\hat{\beta}_H}{1-\hat{\beta}_H}\right] \tag{10}$$

and for lepton production

$$\hat{\sigma}(\gamma\gamma \to L^+L^-) = \frac{4\pi\alpha^2_{em}(M_W^2)}{\hat{s}}\hat{\beta}_L \left[\frac{3-\hat{\beta}_L^4}{2\hat{\beta}_L}\ln\frac{1+\hat{\beta}_L}{1-\hat{\beta}_L} - (2-\hat{\beta}_L^2)\right] \tag{11}$$

Note that we have used $\alpha_{em} = 1/137$ in (4) and (6) and $\alpha_{em}(M_W^2) = 1/128$ in the subcross sections (10) and (11).

For completeness we also give here the Drell-Yan $q\bar{q}$ annihilation cross section to H^+H^- including Z^0 exchange, for the case that $H^\pm$ resides in an $SU(2)$ doublet:

$$\hat{\sigma}(q\bar{q} \to H^+H^-) = \frac{4\pi\alpha^2_{em}(M_W^2)}{3\hat{s}}\;\frac{(\hat{\beta}_H)^{3/2}}{4}\left[e_q^2 + 2e_q g_{V_q}\frac{\cot 2\theta_W}{\sin 2\theta_W}\;\frac{\hat{s}(\hat{s}-m_Z^2)}{(\hat{s}-m_Z^2)^2+\Gamma_Z^2 m_Z^2}\right.$$
$$\left. + (g^2_{V_q} + g^2_{A_q})\frac{\cot^2 2\theta_W}{\sin^2 2\theta_W}\;\frac{\hat{s}^2}{(\hat{s}-m_Z^2)^2+\Gamma_Z^2 m_Z^2}\right] \tag{12}$$

In the above g_{V_q} , g_{A_q} are the standard vector and axial vector coupling for the quark. The results of our calculations are presented in Fig. 1 for H^+H^- production and in Fig. 2 for the lepton case. As far as the H^+H^- production in $\gamma\gamma$ fusion is concerned we differ from the results given in [3] by roughly three orders of magnitude: our $\gamma\gamma$ cross section is far below their results and also approximately two orders of magnitude smaller than the DY cross section. The logarithmic enhancement of the photon densities is simply not enough to overcome completely the extra factor α^2_{em} in the $\gamma\gamma$ process. Even if the Higgs is doubly charged (such a Higgs appears in triplet models [11]) the ratio of DY to $\gamma\gamma$ cross section changes only by a factor 1/4 as compared to the singly charged Higgs production. We also find that contributions from elastic, semi-elastic and inelastic processes to the total $\gamma\gamma$ cross section are of the same order of magnitude. The elastic process contributes $\sim 20\%$ of the total $\gamma\gamma$ cross–section at smaller values of m_H going up to 30% at the high end. This can be traced to the logarithmic enhancement of the photon density even in the elastic case mentioned earlier. Assuming the $\tilde{l}_L, \tilde{l}_R$ to be degenerate in mass

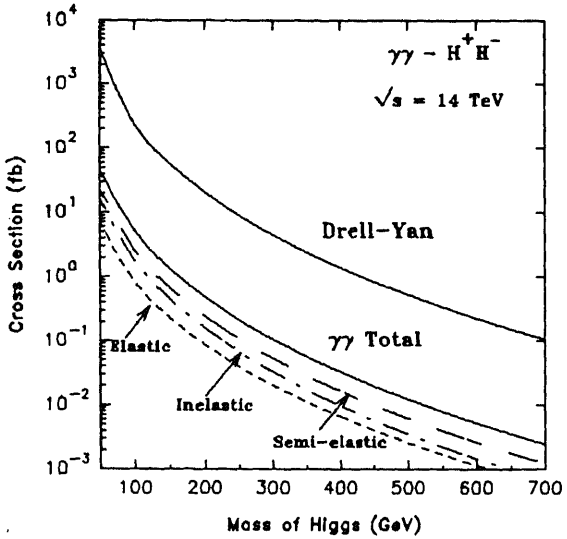

Figure 1. Cross section in fb for DY and $\gamma\gamma$ production of the charged Higgs at LH energies, as a function of the Higgs mass. The dashed, dash-dotted and long-dashed lin show the el., inel. and semi-el. contributions (as defined in the text) to the $\gamma\gamma$ cro sections. The total $\gamma\gamma$ cross section and the DY contributions are shown by the label solid lines.

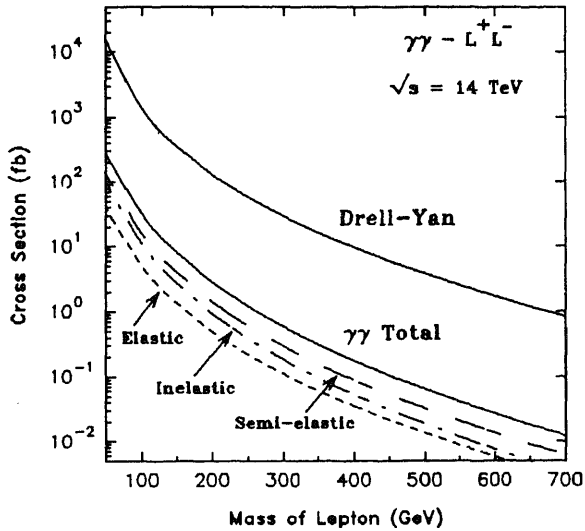

Figure 2. Cross section in fb for DY and $\gamma\gamma$ production of the charged Leptons at LHC energies, as a function of the Lepton mass. The convention is the same as in Fig. 1

masses in the range of $50 - 100$ GeV[6]. In general the L^+L^- cross–sections are higher than the corresponding H^+H^- cross–sections (both for $\gamma\gamma$ and DY) by about a factor of 5–7. This can be traced to the different spin factors and the different $\hat{\beta}$ dependence of the subprocess cross–section for the fermions and scalars. The cross–section for the $\gamma\gamma$ production of charginos will again be the same as that of the charged leptons.

Another process that contributes to the pair production of Higgs bosons and charged leptons is one loop gluon fusion:

$$\begin{aligned} gg &\to H^+H^- \\ gg &\to L^+L^- \end{aligned} \tag{13}$$

These contributions will only be competitive with ordinary DY production if some couplings of the produced particles grow with their mass. Accordingly the first process will be large [12] if $m_t > m_{H+}$ (in which case H^+ production from t decays will have even larger rates) but is expected to decrease for $m_{H+} > m_t$. Since the coupling of chiral leptons to Higgs bosons and longitudinal Z bosons grows with the lepton mass, graphs containing the (1–loop) ggH^{0*} and ggZ^{0*} couplings dominate the production of both charged [13] and neutral [14] chiral leptons of sufficiently large mass.

In summary, we have shown that the cross section for the pair production of heavy charged scalars or fermions via $\gamma\gamma$ fusion amounts to at best a few % of the corresponding Drell–Yan cross section; in many cases there are additional production mechanisms with even larger cross sections. Moreover, at the LHC overlapping events prevent one from isolating $\gamma\gamma$ events experimentally unless the machine is

larger than at LEP200. We do therefore not expect $\gamma\gamma$ fusion processes at the LHC to be competitive with more traditional mechanisms for the production of new particles.

While writing this note we have received a preprint [15] which treats the same subject of $\gamma\gamma$ processes in pp colliders and gets similar results. However we differ somewhat in the details which is most probably due to the different treatment of the photon luminosity functions.

This report is based on the paper *Physical Review* **D 50** *(1994) 2335.*

References

[1]

[2] For a review see J.F. Gunion, H. Haber, G.L. Kane and S. Dawson, "The Higgs Hunter's Guide", Addison-Wesley, Reading, MA, 1990.

[3] S.K. Oh et al., Z.Phys. **C46** (1990)267

[4] J.L. Hewett and T.G. Rizzo, Phys.Rep. **183** (1989) 193

[5] G. Bhattacharya, P.A. Kalyniak and K.A. Peterson, Carleton University preprint, OCIP/C-93-12.

[6] On reexamination the authors of [5] agree with our conclusions for the lepton case (private communication).

[7] E.J. Williams, Phys.Rev. **45** (1934) 729(L); C.F. Weizsäcker, Z.Phys. **88** (1934) 612.

[8] B.A. Kniehl, Phys.Lett.**B254** (1991) 267.

[9] M. Drees and D. Zeppenfeld, Phys.Rev. **D39** (1989) 2536.

[10] A.D. Martin, R.G. Roberts and W.J. Stirling, Phys. Lett. **B306** (1993) 145; Erratum *ibid* **309** (1993) 492.

[11] J.F. Gunion, R. Vega and J. Wudka Phys. Rev. **D42** (1990) 1673 and references therein.

[12] S.S.D. Willenbrock, Phys.Rev. **D35** (1987) 173.

[13] S.S.D. Willenbrock and D.A. Dicus, Phys.Lett. **B156** (1985) 429.

[14] D.A. Dicus and P. Roy, Phys.Rev. **D44** (1991) 1593; A. Datta and A. Pilaftsis, Phys.Lett. **B278** (1992) 162; D. Choudhury, R.M. Godbole and P. Roy, Phys.Lett. **B308** (1993) 394; erratum *ibid* **314** (1993) 482.

[15] J. Ohnemus, T.F. Walsh and P.M. Zerwas, Phys. Lett. **328** (1994) 369.

physics
pp. 379-384

Triplet higgs bosons at e^+e^- colliders

ROHINI M. GODBOLE
Physics Department, University of Bombay, Bombay - 400 098.

BISHWARUP MUKHOPADHYAYA
Mehta Research Institute, 10 Kasturba Gandhi Marg, Allahabad - 211 002

MAREK NOWAKOWSKI
INFN- Laboratori Nazionali di Frascati, Frascati(Roma), Italy

Whereas all the charged fermions must get their masses via Yukawa couplings with Higgs doublets[1] , the vacuum expectation values (vev) of triplets can give Majorana masses to left-handed neutrinos. It is thus natural to consider other phenomenological implications of triplet scalars[2]. However, the vev of the neutral member of the triplet gives additional contributions to the parameter $\rho = m_W^2/(m_Z^2 \cos^2\theta_W)$ (where θ_W is the Weinberg angle) at the tree-level, tending to deviate its value from unity. Since the present experimental value of ρ is $(1.0004 \pm 0.0022 \pm 0.002)$ [3], any scenario with scalar triplets must be constrained accordingly.

One way to avoid this problem is to postulate that the vev of the neutral member of the triplet is small enough so that its contribution to ρ is within the experimental limits. The other option is to assume [4], [5], that there are in fact more than one triplets, arranged in such a manner that their contributions to ρ cancel each other. For this the minimun requirement is one complex (Y=2) and one real (Y=0) triplet, in addition to the Y=1 complex doublet of the minimal standard model. Furthermore the vev's of these two triplet fields must be equal to guarantee $\rho = 1$.

We have examined some testable consequences of triplets in both these situations. using the fact that with triplets, there exists a tree-level coupling involving a charged Higgs, W and a Z. This interaction vertex was studied earlier in the context of LEP-I [6]. We find that in LEP-II and higher energy e^+e^- colliders also, it leads to new types of signals.

In the first of the two cases the complex triplet Δ and a doublet ϕ are of the form

$$\Delta = \begin{pmatrix} \Delta^{++} \\ \Delta^{+} \\ \Delta^{0} \end{pmatrix}, \quad \phi = \begin{pmatrix} \phi^{+} \\ \phi^{0} \end{pmatrix} \tag{1}$$

Taking the vacuum expectation values to be $< \phi^0 >= v$ and $< \Delta^0 >= w$ the ρ parameter in this model is $\rho = (1 + \frac{2w^2}{v^2})/(1 + \frac{4w^2}{v^2})$. The current experimental constraint translates (at 99% confidence level) to

$$\frac{w}{v} \leq 0.066 \tag{2}$$

to be ($s_{H'} \equiv \sin\theta_{H'}$ etc.)

$$s_{H'} = \frac{\sqrt{2}w}{\sqrt{v^2+2w^2}}, \quad c_{H'} = \frac{v}{\sqrt{v^2+2w^2}} \tag{3}$$

It is worth noting here that in this case the H'^+ couples to fermions through the doublet component.

The above scenario causes hierarchy problems because of the large splitting of the two vacuum expectation values. A solution is to add a real triplet field χ ($Y = 0$)

$$\chi = \begin{pmatrix} \chi^+ \\ \chi^0 \\ \chi^- \end{pmatrix} \tag{4}$$

and impose on the Higgs potential a $SU(2)_L \otimes SU(2)_R$ symmetry which at tree level forces the two vacuum expectation values, $< \Delta^0 >$ and $< \chi^0 >$ to be equal. As a result the ρ parameter is one at tree level.

Upon diagonalisation of the mass matrix of the scalar sector, in general one finds, after duly absorbing the Goldstone bosons, a 5-plet, ${H_5}^{++,+,0,-,--}$, a 3-plet, ${H_3}^{+,0,-}$ and two singlets, ${H_1}^0$ and ${H_1}'^0$, as the physical states. The different multiplets charaterise their respective transformation properties under the custodial $SU(2)$. The members of the H_5-plet in this case do not have any overlap with the doublet ϕ, and as such they cannot interact with fermion-antifermion pairs.

Another constraint on the triplet scenario arises from the lepton-lepton couplings of the complex Y=2 triplet. The mass thus acquired by the electron neutrino will be given by

$$M_{\nu_e} = h_{ee}\frac{s_H}{2}\frac{M_W}{g} \tag{5}$$

with

$$s_H = \frac{2w}{\sqrt{v^2+4w^2}} \tag{6}$$

where h_{ab} is the $\Delta L = 2$ coupling strenth of the first generation. The experimental constraints from neutrinoless double beta-decay imply that $M_{\nu_e} < 1eV$. This means that either the doublet-triplet mixing angle or the $\Delta L = 2$ Yukawa coupling is restricted to very small values. Since in this model $\rho = 1$ at tree level a large mixing angle s_H is *apriori* not excluded. Though it still requires fine-tuning to maintain the equality of the triplet vev's at higher orders, the degree of such fine-tuning is not higher than that involved in connection with the naturalness problem within the standard model itself [7],[8].

As has been mentioned before, in both the models discussed above the H^+W^-Z coupling exists at the tree level. The lagrangians are

$$\begin{aligned} \mathcal{L}^{(1)}_{HWZ} &= -\frac{gM_W}{\cos\theta_W} s_{H'}c_{H'}H'^+W^-_\mu Z^\mu + \text{h.c.} \\ \mathcal{L}^{(2)}_{HWZ} &= -\frac{gM_W}{\cos\theta_W} s_H H_5^+ W^-_\mu Z^\mu + \text{h.c.} \end{aligned} \tag{7}$$

lower energies. Here we concentrate upon the final states consisting of the leptonic decay products of the W, i.e. on $e^+e^- \longrightarrow H^{\pm}l\nu_l$. In such cases, the $e\nu_e$ final state also receives contributions from a t-channel diagram with the $H^{\pm}$ emitted from the propagator. For large values of the centre-of-mass energy, this latter diagram is dominant. Fig. 1 shows the cross-sections for $H^{\pm}l\nu_l$-production plotted against

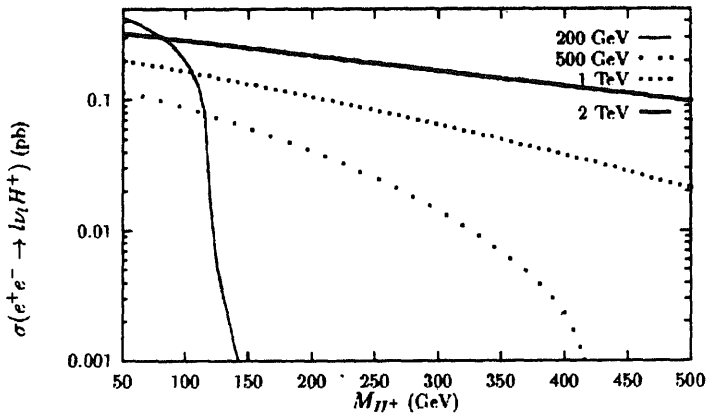

Figure 1. $\sigma(e^+e^- \to l\nu_l H^{\pm})$ (pb) as a function of M_{H^+} (for $s_H(s_{H'}c_{H'}) = 1$) for different values of e^+e^- center of mass energies: the thin solid, dotted, dashed and thick solid line correspond to $\sqrt{s} = 200$ GeV,500 GeV, 1 TeV and 2 TeV respectively. Cross-sections for both charges of the Higgs and muonic as well as electronic channels in the final state are added.

$M_{H^{\pm}}$ for different values of $\sqrt{s}$. The contributions due to the electronic and muonic final states are added. The curves correspond to $s_H = 1$ and $c_{H'}s_{H'} = 1$ for the two cases of $H_5^{\pm}$, $H'^{\pm}$ respectively. The cross-sections for various values of the mixing angles can be read off by multiplying by the appropriate factor. It is clear from the graphs that in the LEP-II case (thin solid line), assuming an integrated luminosity of $10^{39}cm^{-2}$ per year there will be a few hundreds of events for $s_H = 1$ upto at least $M_{H_5} = 110\,GeV$. If now one has only the $Y = 2$ triplet, the restriction from the ρ-parameter allows a maximum s_H^2 of 0.009. This leaves us with about 2 events per year. In such a case, the only reasonable chance of observing this process exists in a higher-energy e^+e^- machine. As can be seen from the plot (dotted line), such a machine with a luminosity of $50fb^{-1}$/year [9] can lead to few tens of events upto $M_{H'} \simeq 300$ GeV even with a value of $s_{H'}$ well within the limits imposed by ρ. On the other hand, since this restriction gets relaxed if one presupposes a complex and a real triplet, at LEP-II itself one can investigate a large area of the $\rho - s_H$ parameter space in the latter scenario.

The signals of the triplet scalars thus produced also depend on their decay channels. For the (complex+real) case, as has been mentioned, $H_5^{\pm}$ do not have

tree-level interactions with fermions. Possibilities of observing them through loop-induced decays into fermion pairs have already been studied [7]. However, there are also the tree-level decays into four-fermions mediated by (real or virtual) W and Z coupling with H_5. We have explicitly calculated such decay widths using methods described in ref. [10] modified appropriately. The decay widths into this channel for leptonic final states (with $s_H = 1$) are as a function of M_{H_5} by the dashed line in

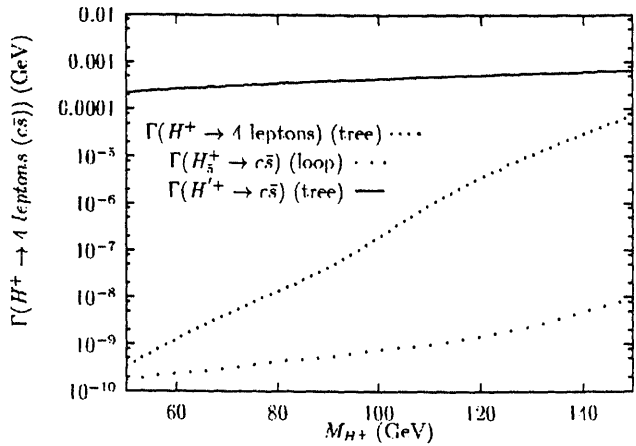

Figure 2. The different possible two body decay widths ($H_5^+ \to c\bar{s}$)at loop level (dotted line), tree level (solid line) and the tree level leptonic four body decay width $\Gamma(H_5^+ \to W^*Z^* \to 4$ leptons) (dashed line) for the charged Higgs. Again the mixing angles are put equal to 1 as in fig. 1. The $\Gamma(H_5^+ \to c\bar{s})$ (loop) has been taken from ref. [7]. The four body decay width is summed over electrons and $\mu's$ in the final state. For four quark final state the numbers are obtained by multiplying the dashed figure by ~ 35

fig. 2. Here we have summed over the muons and the electrons in the final state. For purposes of comparison we also show by the dotted line one of the representative results for the loop induced partial width $\Gamma(H_5^+ \to c\bar{s})$ taken from ref. [7] (also drawn there for $s_H = 1$). The figure clearly shows that the partial decay width for our four-fermion modes is of similar order for $M_{H_5} \sim 50GeV$, and completely dominate for higher values of M_{H_5}. Consequently, the branching ratio for decays into a pair of weak gauge-bosons (WZ) remains close to 100 per cent over most of the parameter space. The 4-lepton ($l\nu_l l'^+ l'^-$) channel then has a healthy branching ratio of $\sim 1.4\%$ The corresponding signal is practically free from standard model backgrounds, and thus it should be considered as the principal technique in looking for triplet Higgs bosons of this type, produced in e^+e^- collider experiments. In addition, with appropriate invariant mass cuts, the signal with four jets in the final states can be used increasing the useful branching ratio to $\sim 50\%$. This would increase the discovery range of $H_5^{\pm}$ even further since the width into four quarks final state will be a factor ~ 35 higher than the four lepton channel. Hence, the discovery range at LEP-200 (NLC) gets extended to 125 (425) GeV, for $s_H = 1$.

For the case of model 1 (i.e. H^+) the two-fermion decay-modes can occur at

tree level. As can be seen from $\Gamma(H'^{+} \to c\bar{s})$ given by the solid line in fig. 2 (and

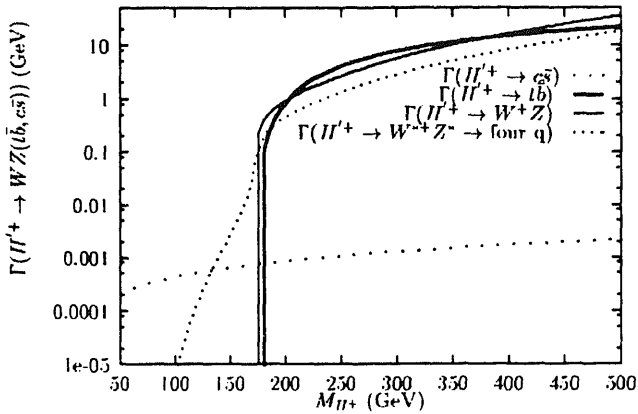

Figure 3. The different possible tree level decay widths ($H'^{+} \to c\bar{s}$) (dotted line), $\Gamma(H'^{+} \to W^{*}Z^{*} \to 4$ quarks) (dashed line), $\Gamma(H'^{+} \to W^{+}Z)$ (thin solid line) and $\Gamma(H'^{+} \to t\bar{b})$ (thick solid line) for the charged Higgs. Again the mixing angles are put equal to 1 as in fig. 1. m_b has been neglected.

dotted line in fig. 3) this decay mode will dominate over the four-lepton decay mode upto $M_{H'^{+}} = 150$ GeV. However, the width for the 4-quark decay mode, shown by dashed line in fig. 3, will be comparable to the two-quark decay mode for $M_{H'^{+}} \geq 120$ GeV.

Another way of detecting a triplet scenario in $e^{+}e^{-}$ machines is to look for production of of a doubly charged scalar via processes such as $e^{+}e^{-} \longrightarrow l^{-}l^{-}H^{++}$. As mentioned before, these involve the $\Delta L = 2$ interactions which are not very tightly constrained when the doublet-triplet mixing angle is small. A detailed investigation is currently under way.

References

[1] The standard reference for extended Higgs sectors is J. Gunion, H. E. Haber, G. Kane and S. Dawson, 'The Higgs Hunter's Guide', Addison-Wesley, 1990; for a recent study of a two Higgs doublet model see for example A. Pilaftsis and M. Nowakowski, Int. J. Mod. Phys. **A9** (1994) 1097

[2] H. M. Georgi, S. L. Glashow and S. Nussinov, Nucl. Phys. **B193** (1981) 297

[3] Review of Particle Properties, Phys. Rev. **D50** (1994).

[4] H. Georgi and M. Machacek, Nucl. Phys. **B262** (1985) 463

[5] S. Chanowitz and M. Golden, Phys. Lett. **B165** (1985) 105

[6] B. Mukhopadhyaya, Phys. Lett. **B252** (1992) 123

[7] J. F. Gunion, R. Vega and J. Wudka, Phys. Rev. **D42** (1990) 1673; **D43** (1991) 2322

[8] P. Bamert and Z. Kunszt, Phys. Lett. **B306** (1993) 335

[9] see, e.g., M. Drees and R. M. Godbole, Z. Phys. **C 59** (1993) 591; P. Chen, T. Barklow and M.E. Peskin, Phys. Rev. **D49** (1994) 3209.

[10] H. Pois, T. J. Weiler and T. C. Yuan, Phys. Rev. **D47** (1993) 3886

PRAMANA
journal of
physics

© Printed in India

Supplement to Vol. 45
October 1995
pp. 385-391

Inclusive charm production at HERA and the charm content of the photon

MANUEL DREES
University of Wisconsin, Dept. of Physics, Madison, WI 53706, U.S.A.

ROHINI M. GODBOLE
Physics Department, University of Bombay, Bombay - 400 098

Measurements of F_2^γ in $\gamma^*\gamma$ scattering at the e^+e^- colliders PEP, PETRA, TRISTAN and LEP [1] have by now yielded a lot of information on the parton content of the photon over a wide range of x and Q^2. However, these measurements give direct information only about the quark content of the photon. The gluon density $g^\gamma(x,Q^2)$ is poorly determined as it affects F_2^γ only through the QCD evolution equations. At the current values of Q^2 the charm quark contribution to F_2^γ is approximated by the quark-parton-model (QPM) matrix elements for the process $\gamma\gamma^* \to c\bar{c}$ and $\gamma^* g^\gamma \to c\bar{c}$. Through the latter process, the effective charm content of the photon becomes sensitive to $g^\gamma(x,Q^2)$. At larger values of Q^2, $c^\gamma(x,Q^2)$ computed using the massive Altarelli-Parisi (AP) evoultion equations, is considerably different from the pure QPM predictions [2]. A study of the charm content of the photon might also help shed some light on the correct treatment of a heavy parton inside a target. The various different available parametrisations of $q^\gamma(x,Q^2)$ and $g^\gamma(x,Q^2)$ [3] treat the charm density $c^\gamma(x,Q^2)$ with varying amount of rigour and care. It is therefore interesting to take a phenomenological approach and think of measurements which will probe $c^\gamma(x,Q^2)$ directly and hence perhaps also yield information about $g^\gamma(x,Q^2)$.

One possibility is to study production of single charm in ep collisions via the excitation processes (the subprocesses being $c^\gamma + q^p \to c + q$ and $c^\gamma + g \to c + g$, here we neglect the contribution coming from charm in the proton) shown in fig. 1. This will give rise to a single high-p_T charm particle whose transverse momentum is balanced by a light q/g jet. Of course the use of structure functions to compute this process is meaningful only for large values of the p_T of the charm quark. Admittedly for lower values of p_T the more reliable computation will be that of the $2 \to 3$ subprocesses (some of which are shown in fig. 2), but at larger values of p_T the structure function language sums up the large $\log(p_T^2/m_c^2)$ terms and hence is more accurate. Another contribution to the inclusive charm signal comes from $c\bar{c}$ pair production, via the 'direct' γg fusion subprocess as well as the 'resolved' processes, where the balancing high-p_T jet is the c ($\bar{c}$) quark jet.

The excitation contribution of diagrams in fig. 1 is given, in the Weizsäcker-Williams (WW) approximation, by

$$\frac{d\sigma^{exc}}{} = \sum \int^{z_{max}} f_{\gamma/e}(z)\, dz \int^1 \qquad \ldots$$

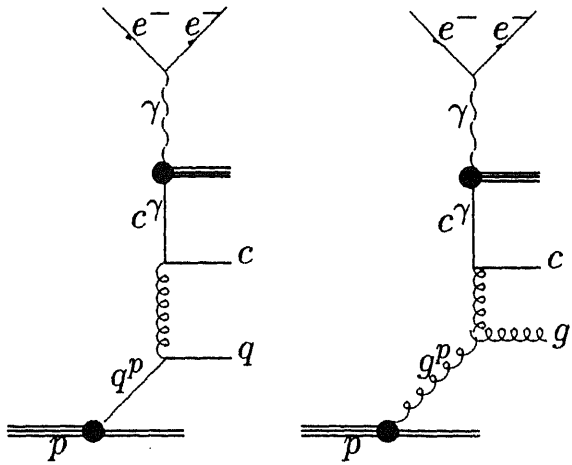

Figure 1. Excitation processes for single charm production in ep collisions

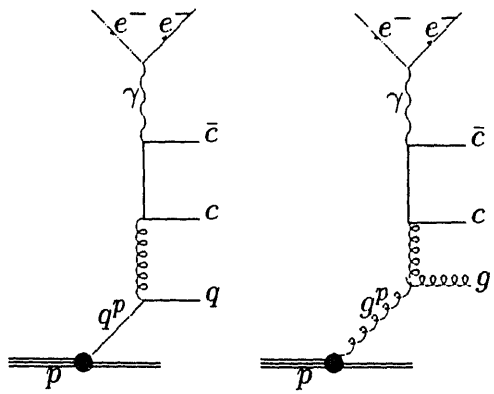

Figure 2. Some of the $2 \rightarrow 3$ diagrams giving rise to single charm production

$$\cdot \int_{x_p^{min}}^{1} f_{P_1|p}(x_p) dx_p \frac{d\hat{\sigma}}{dp_T}(P_1 + c^\gamma \to c + P_1), \qquad (1)$$

e $f_{\gamma|e}$, $f_{c|\gamma}$ and $f_{P_1|p}$ represent the flux factors of the γ in the electron, charm e photon and parton P_1 in proton respectively;

$$z_{min} = \max\{z_{min}^{kin}, z_{min}^{exp}\}$$
$$z_{max} = \min\{z_{max}^{exp}, 1\},$$

e $z_{min(max)}^{exp}$ correspond to the experimental cuts on the outgoing electron (or valently the γ energy) and z_{min}^{kin}, x_γ^{min} and x_p^{min} correspond to the kinematic s on the different momentum fractions. The direct contribution to $c\bar{c}$ pair uction is similarly given by

$$\frac{d\sigma^{pair}}{dp_T} = \int_{z_{min}}^{z_{max}} f_{\gamma|e}(z)\, dz \int_{x_p^{min}}^{1} f_{g/p}(x_p) dx_p \frac{d\hat{\sigma}}{dp_T}(\gamma + g \to c + \bar{c}), \qquad (2)$$

re $f_{g/p}$ represents the gluon flux in the proton, and the 'resolved' contribution ven by an expression similar to eq.(1) where contributions from all the various processes involving all the different partons in the photon are to be included. use LO expressions for all the $2 \to 2$ subprocess cross–sections [3]. The virtuality $-P^2$ of the exchanged photon in figs. 1 and 2 can, in principle, af- its parton content [4]. For the results presented here we impose the requirement < 0.01 GeV^2 and $0.25 < z < 0.70$, following the cuts used in the experimental dy of the photoproduction of jets [5]. This implies that our expression for the oton flux factor is given by

$$f_{\gamma|e} = \frac{\alpha}{2\pi z}[1 + (1-z)^2] \ln\left(\frac{0.01 \text{ GeV}^2}{P_{min}^2}\right) - \frac{\alpha}{\pi}\frac{1-z}{z}, \qquad (3)$$

ere

$$P_{min}^2 = m_e^2 \frac{z^2}{(1-z)}.$$

s a result of the cut on P^2 we can neglect the effect of the virtuality of the γ on s parton content.

The results of our computations are shown in fig. 3 for various photon structure nction parametrisations DG [6], LAC[7], WHIT[2] and different proton structure nctions [8]; we use $\Lambda_{QCD} = 0.4$ GeV for the DG and WHIT parametrizations, nd 0.2 GeV for LAC. We see from this figure that the excitation cross–sections are ndeed comparable to the $c\bar{c}$ production cross–sections. This implies that while the esolved' contribution to $c\bar{c}$ pair production is small (as shown by the long dashed ne) for these large values of p_T, the inclusive charm signal still has a considerable esolved' component due to the excitation contribution. Though we do not show hem separately here, the contribution to σ^{exc} coming from a gluon in the initial tate dominates over most of the p_T range. Apart from the DG parametrisation for which excitation contributions are about a factor 2 higher than the rest, the charm excitation cross–section at HERA seems to be fairly independent of both the photon and the proton structure function parametrisations. Since the DG parametrisations nas $c^\gamma = u^\gamma$ it definitely overestimates the charm excitation and hence this part of

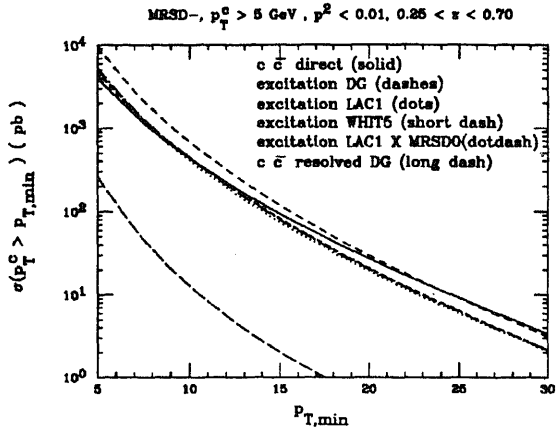

Figure 3. $\sigma(p_T^c > p_{T,min})$ (pb) as a function of $p_{T,min}$ for the excitation as well as $c\bar{c}$ production for different combinations of proton and photon structure functions.

the result is easily understood. In principle, the other parametrisations of $c^\gamma(x, Q^2)$ do also look quite different, both in the small and large x_γ region, but the effective $c-$quark content of the electron, which involves the convolution of this with the WW function is very similar in the end; this is reflected in the similarity of the predictions using the LAC and WHIT parametrizations for $c^\gamma(x, Q^2)$. This can be looked upon as a positive point in that the size of the excitation contribution to the inclusive charm signal, at large p_T, can be estimated quite reliably. However, it is also clear that one needs to devise kinematic cuts to separate the excitation contribution to the inclusive charm signal from that due to $c\bar{c}$ pair production. (This is also necessary if direct $c\bar{c}$ pair production is to be used to study the gluon density in the proton.)

To this end, we next study the kinematic distributions of the decay muon which is used to tag the charm in the final state and also that of the balancing ('away-side') jet. In this calculation we include fragmentation of the $c-$quark into a charmed meson à la Peterson fragmentation function [9] with the parameter ϵ as given in ref.[10], and use the value 0.1 for the semileptonic branching ratio of the charmed hadrons. Since, for our p_T cut, $c\bar{c}$ production is dominated by the 'direct' process, the real kinematical difference between the excitation and $c\bar{c}$ contributions to the charm signal comes from the fact that in the excitation process only a fraction of the γ energy is available for the subprocess, whereas in the 'direct' process all of it goes into the subprocess. As a result, the direct process on the whole receives contributions from smaller x_p values than the excitation process does. Hence the $\bar{c}$ jet in the $c\bar{c}$ case will have much more negative rapidity than the 'light' (q/g) jet in the excitation process (the proton direction is taken as positive z axis); this is very similar to the corresponding situation with the photoproduction of jets [3]. On the other hand, the rapidity distributions of the charm quarks produced in both the excitation and pair production processes are very similar and hence those of the decay muons also. The kinematic distribution in p_T^μ and y_μ therefore are very similar for both contributions. Fig. 4 shows the rapidity distribution of the

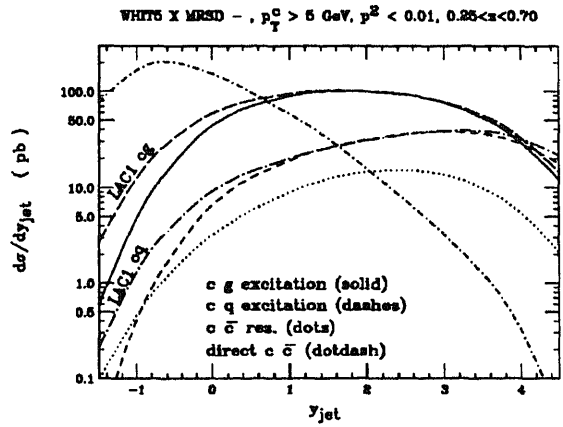

Figure 4. Rapidity distribution for the 'away–side' jet for the excitation and pair production mechanisms.

jet balancing the large p_T charm, with the WHIT5 parametrisations of $q^\gamma(x,Q^2)$ and $g^\gamma(x,Q^2)$ and MRSD- for the proton structure function. As we can see very clearly from the figure, a cut on $y_{jet} < 0.5$ can neatly separate the excitation and the $c\bar{c}$ contribution from each other. The rates presented in the figure include the semileptonic branching ratio of the charm meson. It should also be mentioned that these distributions do have some sensitivity to c^γ, but only for negative values of y_{jet} where the signal is dominated by the $c\bar{c}$ contribution. The figure also tells us that the signal is healthy even after these cuts and hence is measurable. For a clear signal one will have to make an additional cut on p_T^μ as well but that will affect both the excitation and the pair production contribution similarly.

Recently both H1 and ZEUS have reported measurements of inclusive charm production at HERA [11]. ZEUS reports D^* production with $p_T(D^*) > 1.7$ GeV and $|\eta(D^*)| < 1.5$ where η is the pseudorapidity with $P^2 < 4$ GeV^2 and $0.15 < z < 0.86$, whereas H1 reports observation of events with a hard muon with $p_T^\mu > 1.5$ GeV and $30^\circ < \theta(\mu) < 130^\circ$. The ZEUS analysis then uses this measured cross–section to estimate the 'total' $c\bar{c}$ cross–section by extrapolating it outside the measured region and then compare the value so obtained with the QCD NLO calculations. We attempted instead to reproduce the cross–sections measured by ZEUS and H1 by using our LO QCD calculations. Since the p_T cut and m_c are comparable it is not clear whether factorisation of the production and fragmentation of the charm quark is such a good approximation. On the other hand if we include the fragmentation of the $c-$quark in the final state then we must include the excitation contribution which corresponds to the fragmentation of the initial state photon into charm. We therefore run our Monte Carlo with two different options: In one case (A) we fragment the charm using the Peterson fragmentation function and include the excitation contributions whereas in the other case (B) we do not include the fragmentation of the final state c quark and drop the excitation contributions as

comparing with ZEUS results we include a factor of 0.26 which is the probability of a charm quark to fragment into a charged D^* meson.

Table 1. The D^* and μ cross-sections measured at HERA by ZEUS and H1, compared with the LO predictions discussed in the text.

ZEUS (D^*)			H1 (μ)		
Data: $32 \pm 7^{+4}_{-7}$ nb			Data: $2.03 \pm 0.43 \pm 0.7$ nb		
A: Frag and c^γ included			A: Frag and c^γ included		
p str.fn.	γ str. fn.	σ (nb)	p str.fn.	γ str. fn.	σ (nb)
MRSD-	LAC1	27.4	MRSD-	LAC1	1.5
MRSD-	WHIT5	26.0	MRSD-	WHIT5	1.5
MRSD0	WHIT5	21.9	MRSD0	WHIT5	1.48
MRSD-	DG	64	MRSD-	DG	2.9
B: No frag and c^γ not included			B: No frag and c^γ not included		
p str.fn.	γ str. fn.	σ (nb)	p str.fn.	γ str. fn.	σ (nb)
MRSD-	LAC1	26.8	MRSD-	LAC1	1.8
MRSD0	WHIT5	15.4	MRSD0	WHIT5	1.5
MRSD-	WHIT5	37.0	MRSD-	WHIT5	2.4
MRSD-	DG	33.4	MRSD-	DG	2.3

Table 1 gives a summary of our calculations along with the results reported by the two experimental groups. We find that for the ZEUS data, in case A the results become less sensitive to the low-x behaviour of the proton structure function and the excitation contribution actually dominates. In this case both the MRSD- and MRSD0 for the partons in the proton and WHIT5 or LAC1 partons in the photon reproduce the data whereas DG predict too big a cross-section. On the other hand, in case B, the results are more sensitive to the low-x behaviour of the parton densities and we find that we can reproduce the cross-section only for a steeply rising gluon density. In this case all the photonic parton densities combined with MRSD- for the proton are acceptable whereas the MRSD0 gives answers smaller by a factor 2 for all reasonable choices of the momentum scale as well as the photonic parton densities. For the H1 sample, the p_T^μ cut means that the produced charm quark has much higher p_T than for ZEUS. Again, inclusion of fragmentation reduces the sensitivity to the low-x behaviour of the gluon in the proton and results for various combinations of partons in the photon and proton are almost the same. As before, the DG parametrisation predicts a large cross-section, 2.9 nb, but it is not inconsistent with the data.

In conclusion we have studied the contribution to the inclusive charm signal from the excitation of charm in the photon. We find the rates to be comparable to the contribution coming from $c\bar{c}$ pair production. Due to the convolution with $f_{\gamma|e}$ the sensitivity of σ^{exc} of eq. 1 to the region of large x_γ, where the various parametrisations for $c^\gamma(x, Q^2)$ differ most, is reduced. This means that this 'resolved' background to the large p_T, inclusive charm signal coming from the 'direct' process can be predicted quite reliably. Making a cut on the associated jet-rapidity allows a separation of these two contributions. Note that charm excitation events should contain a second 'spectator' charm (anti-)quark in the photon remnant,

which has a large, negative rapidity (close to the electron beam direction). In contrast, $c\bar{c}$ pair production events should contain a second high–p_T charm (anti–)quark. In both cases the presence of a second charmed particle should be visible in some fraction of the events; this could be used as a cross–check of the relative sizes of the two contributions to the inclusive charm signal. Even after all the cuts and folding of the cross–sections with various branching fractions, the rates for inclusive charm production are large and easily measurable. Further, a LO computation including the excitation contributions gives results comparable to the recent measurements of the inclusive charm signal by ZEUS and H1. On the theoretical side, it would be interesting to compare our results with explicit $2 \rightarrow 3$ subprocess calulations and see at what values of p_T do they match.

References

[1] For the recent measurements see: D. Morgan, R. Pennington and M.R. Whalley, J. Phys. **G20**, A1 (1994); OPAL collaboration, R. Akers et al, Z. Phys. **C 61** (1994) 199; TOPAZ collaboration, Phys. Lett. **B 332** (1994) 477.

[2] K. Hagiwara, M. Tanaka, I. Watanabe and T. Izubuchi, Phys. Rev. **D 51** (1995) 3197.

[3] For a summary and further references see, M. Drees and R.M. Godbole, Pramana **41** (1993) 83.

[4] See, for example, M. Drees and R.M. Godbole, Phys. Rev. **D 50** (1994) 3124.

[5] H1 collaboration, I. Abt et al, Phys. Lett. **B 314** (1993) 436.

[6] M. Drees and K. Grassie, Z. Phys. **C28** (1985) 451.

[7] H. Abramowicz, K. Charchula and A. Levy, Phys. Lett. **B 269** (1991) 458.

[8] A. D. Martin, R.G. Roberts and W.J. Stirling, Phys. Lett. **B 306** (1993) 145; Erratum ibid. **B 309** (1993) 492.

[9] Peterson et al, Phys Rev. **D 27** (1983) 105.

[10] Review of Particle Properties, Phys. Rev.**D 50** (1994) 133.

[11] ZEUS collaboration, M. Derrick et al, DESY 95-013; C. Kleinwort for the H1 collaboration, talk given at *ICHEP* Glasgow, August 1994, DESY report 94–187.

Group report: Beyond standard model

A. S. JOSHIPURA
Physical Research Laboratory, Navrangpura, Ahmedabad 380 009

PROBIR ROY
Theory Group, T. I. F. R., Homi Bhabha Road, Bombay 400 005

Abstract. Working group II at WHEPP3 concentrated on issues related to the supersymmetric standard model as well as SUSY GUTS and neutrino properties. The projects identified by various working groups as well as progress made in them since WHEPP3 are briefly reviewed.

Participants:
K.S. Babu, B. Brahmachari, C. Burgess, G. Datta, S. Goswami, A. Joshipura, A. Kundu, Mohan Narayan, S. Nayak, M. V. N. Murthy, M. K. Parida, G. Rajasekaran, S. Rindani, Probir Roy and J.W.F. Valle.

Working group II (WGII) identified definite topics each of which was intensively discussed within the corresponding subgroup during the workshop. Significant progress was made in some of them and some of the projects have been completed in the meantime. The following is the list of the projects addressed by WGII:

- Evolution of R parity violating couplings (*B. Brahmachari and P. Roy*)
- Beyond S, T and U (*A. Kundu and P. Roy*)
- Neutrino masses and proton lifetime in SUSY $SO(10)$ (*K.S. Babu, M.K. Parida and G. Rajasekaran*)
- Degenerate neutrinos(*K.S. Babu, C. Burgess, A.S. Joshipura, S. Rindani, J.W.F. Valle*)
- Solar and atmospheric neutrino problems with three generations (*G. Datta, S. Goswami, A. Joshipura, M.V.N. Murthy, Mohan Narayan, G. Rajasekaran and S. Rindani*)
- Magnetic moments for heavy neutrinos (*K.S. Babu, S. N. Nayak and P. Roy*)
- Extraction of neutrino magnetic moment from experiments (*M.V.N. Murthy, G. Rajasekaran and S. Rindani*)
- Evolution of couplings in SUSY LR model (*B. Brahmachari*)

Brahmachari and Roy [1] studied the evolution of the baryon number and R-parity violating Yukawa couplings in the supersymmetric standard model and derived bounds on them from the requirement of perturbative unitarity. They added the following terms to the superpotential of the minimal supersymmetric standard model (MSSM):

$$\mathcal{L} = \lambda'''_{ijk}(D^c_i D^c_j U^c_k), \tag{1}$$

where U^c, D^c denote the anti quark superfields and i, j, k are generation indices. These terms violate both R parity and the baryon number. Unlike the analogous lepton number violating terms, the presence of the above terms by themselves is not significantly constrained from low energy considerations. Interesting bounds on these couplings can nevertheless be obtained by requiring that all the Yukawa couplings Y remain less than unity till the grand unification scale $M_U \sim 2 \times 10^{16}$ GeV is reached. Assuming only λ'''_{133} and λ'''_{233} to be large, they set up the RG equations for the relevant couplings. The requirement of perturbative unitarity was shown to lead to an upper bound in the range 0.5-0.6 on the baryon number violating Yukawa couplings, the exact value being dependent on the top quark mass as well as on the ratio $\tan\beta$ of the Higgs vevs. It was also shown that the fixed point value of the top Yukawa coupling was somewhat reduced compared to that in the MSSM because of the presence of the additional baryon number violating Yukawa couplings.

2. Beyond S, T and U

A. Kundu and P. Roy examined the q^2-expansion approximation of Peskin and Takeuchi in the context of 1-loop oblique electroweak radiative corrections. They were able to give definitions of the oblique parameters which did not depend on this approximation but kept their symmetry contents intact. In this respect the disagreement with Burgess, Makysmik and London were highlighted. The organizing principle behind the q^2-expansion approximation was found — namely that it was needed in calculating the Z- and W-wavefunction renormalization constants. Measurable ratios, where these were eliminated, could be expressed [2] in terms of S, T and U without reference to this approximate procedure. For other observables, which involved these renormalization constants, the q^2-expansion was generalized upto quadratic terms. The new oblique parameters V, W, X, Y could be bounded [2] experimentally.

3. Neutrino masses in SUSY $SO(10)$

K. S. Babu, M. K. Parida and G. Rajasekaran looked at the issue of obtaining neutrino masses in the experimentally interesting range in the context of supersymmetric $SO(10)$ models. The neutrino masses needed for solving the solar neutrino problem arise naturally in and $SO(10)$ if the Majorana masses of the right handed neutrinos are in the intermediate range $\sim 10^{10}$ GeV [3]. The generation

of such masses through the vacuum expectation values of the chargeless scalars in the $126 + 1\bar{2}6$ representation in SUSY $SO(10)$ models requires [4] some assumptions of the extended survival hypothesis. The aim of the project was to provide an alternative mechanism for generating the right handed neutrino masses in the intermediate energy range.

The following breaking chain was considered:

$$SO(10) \longrightarrow G_I \longrightarrow G_{SM}, \tag{2}$$

where $G_I = SU(3)_c \times SU(2)_L \times SU(2)_R \times U(1)_{B-L}$ or $SU(4)_c \times SU(2)_L \times SU(2)_R$ and was assumed to break at a scale $M_I \sim 10^{14} GeV$. Although the representation $126 + 1\bar{2}6$ was present it did not acquire a vev. The right handed neutrino masses were induced by the presence of the $16 + \bar{16}$ representation to be

$$M_{N_R} \sim \frac{M_I^2}{M_U}. \tag{3}$$

This could be significantly lower than the value $M_{N_R} \sim M_U \sim 10^{16}$ GeV permitted in a single step breaking.

4. Degenerate neutrinos

It has recently been realized [5, 6] that simultaneous solutions of the solar and atmospheric neutrino deficits as well as of the dark matter problem with a hot component of about 30% require almost degenerate masses for the three neutrinos. Such a spectrum was shown to arise in a natural manner in left right symmetric models augmented with a suitable generation symmetry [5, 6]. The aim of the working group was to discuss issues related to the construction of realistic grand unified models following the scenario proposed in refs. [5, 6]. In particular one should obtain (a) the common degenerate mass in the eV range (b) mass splittings appropriate for the solar and the atmospheric neutrino problems and (c) the right mixing pattern. The required mass splitting arise naturally [6] if the Dirac masses for the neutrinos coincide with the up quark masses as in the simplest $SO(10)$. In this case, one obtains

$$\frac{|\Delta_{21}|}{|\Delta_{32}|} \approx \left(\frac{m_c}{m_t}\right)^2 \approx (1-3) \times 10^{-4}. \tag{4}$$

This nicely reproduces the hierarchy required to simultaneously solve the solar and atmospheric neutrino problems. The problem to be addressed was to obtain this prediction in a complete model based on $SO(10)$ preserving other successful features.

While a complete model is still lacking, significant progress was made by the members of the working group [8, 7, 10] as well as others [9] in the construction of realistic models. In particular, Valle and Ioannissyan constructed a model based on $SO(10)$ with a horizontal $SU(2)$ symmetry. In their model, the up quark mass

proposed by Caldwell and Mohapatra [9]. Bamert and Burgess worked out a scenario which contained a singlet fermion in addition to the three left and right handed neutrinos. A horizontal SU(2) symmetry was introduced to obtain the degenerate spectrum. The couplings involving the singlet fermion break the horizontal symmetry and lead to a departure from the degeneracy in neutrino masses. The singlet fermion was moreover used in the context of the left right symmetric theory [10] in order to understand the difference between the quark and leptonic mixing angles in scenarios with almost degenerate neutrinos. The singlet also played a crucial role in generating the required mass pattern among neutrinos in this scenario.

5. Solar and atmospheric neutrino problems with three generations

The understanding of the solar and atmospheric neutrino deficits in terms of neutrino oscillations seems to require two vastly different values for the $(\text{mass})^2$ difference among neutrinos. Thus at least two neutrinos need to be massive and analysis of the solar and atmospheric neutrino data in terms of three generations becomes interesting. Such an analysis was carried out earlier [11, 12] assuming the MSW mechanism to be responsible for the solar neutrino conversion. This working group looked at a complimentary scenario in which two of the neutrinos were assumed to be almost degenerate with very small $(\text{mass})^2$ difference $\sim 10^{-10}$ $(\text{eV})^2$ while the other $(\text{mass})^2$ difference was assumed to be in the range $\sim 10^{-2} - 10^{-3}$ $(\text{eV})^2$. Thus the vacuum oscillations are responsible for both the solar and the atmospheric neutrino deficit. Since two of the relevant $(\text{mass})^2$ differences show hierarchy, the oscillation probabilities involve only one more mixing angle compared to the case of two generations [11, 12]. Fixing this mixing angle ($\theta_{\mu\tau}$) to be in the range appropriate for the atmospheric neutrino problem, restrictions on other mixing angle (namely $\theta_{e\mu}$) and the $(\text{mass})^2$ difference $\Delta_{e\mu}$ were determined from the data on solar neutrino deficit.

6. Neutrino magnetic moment

Two different problems were analyzed in connection with the neutrino magnetic moment. One was the issue of a large magnetic moment of a very heavy neutrino. Since the magnetic moment of fermion turns out to be proportional to its mass in a number of situations, it is interesting to ask if the magnetic moments of heavy singlet neutrinos can be large enough to dominate over their point couplings to W and Z induced by mixing with the light neutrinos. The typical magnetic moment of a very heavy right handed neutrino N was estimated from the one-loop graph and the mass-dependence was seen to come through the factor $m_L M_N (M_N^2 + M_W^2)^{-1}$, where the W couples to ℓ and N, so that there was no enhancement for $M_N \gg M_W$. Thus it was found that, contrary to naive expectation, the point couplings always dominated over the magnetic moment couplings.

The conventional procedure of extracting information on the neutrino magnetic moment coupling from the data on ν e scattering was questioned. In order to extract the magnetic moment from the data, one conventionally writes an effective

tering. An analogous treatment of the $e-p$ scattering has been shown to lead to a drastic overestimation of the QED radiative corrections [13]. By the same token, the inclusion of the neutrino magnetic moment term through the Pauli term must lead to wrong results at some energy scale. The main issue was to determine the relevant scale where the Pauli approximation breaks down. The suggestion was to do a detailed calculation of νe scattering in specific model which leads to large magnetic moment and compare it with the phenomenological result obtained assuming the Pauli term as is conventionally done.

7. Evolution of couplings in SUSY LR model

B. Brahmachari studied the 1-loop evolution of Yukawa copulings in the minimal supersymmetric left-right model. He found [14] a fixed point behaviour in the top Yukawa coupling that was rather analogous to the one one in the MSSM. He was able to explicitly exhibit the dependence of the fixed point solution of $Y_t(m_t)$ on the right-symmetry breaking scale. The predicted top mass value in this scheme was between 168 and 174 GeV. Brahmachari was also able to fix the value of the Majorana Yukawa coupling which is otherwise a free parameter.

References

[1] B. Brahmachari and P. Roy, Phys. Rev. **D50** (1994) R39.

[2] A. Kundu and P. Roy, Saha Institute Report No. SINP-TNP/94-07, hep-ph/9411225.

[3] See for example, S. Bludman,D. Kennedy and P. Langacker, Nucl. Phys. **B374** (1992) 373.

[4] N. G. Deshpande et al, Phys. Rev. Lett.**70** (1993) 3189.

[5] D. Caldwell and R.N. Mohapatra, Phys. Rev. **D 48** (1993) 3259.

[6] A. S. Joshipura, Physical Research Lab. Report, PRL-TH/93/20 (1993), to appear in Zeits. Phys. C.

[7] A. Ioannissyan and J.W.F. Valle, Phys. lett. **B332** (1994) 93.

[8] P. Bamert and C. P. Burgess, Phys. Lett. **B329** (1994) 289.

[9] D. Caldwell and Rabindra N. Mohapatra, Univ. of Maryland report, UMD-PP-94-90 (1994); D. G. Lee and R. N. Mohapatra, Univ. of Maryland Report, UMD-PP-94-95 (1994).

[10] A.S. Joshipura, Physical Research Lab. Report, PRL-TH/94/08 (1994), to appear in Phys. Rev. **D**

[11] A.S. Joshipura and P. Krastev, Phys. Rev. **D50** (1994) 3484.

[12] G.L.Fogli,E.Lisi and D. Montanino,Phys. Rev.**D49** (1994) 3626.

[13] R. Basu et al, Journal of Phys. **G17** (1991) 401.

[14] B. Brahmachari, ICTP report, hep-ph/9411357.

Group report: Heavy ion physics

SOURENDU GUPTA
Theory Group, T. I. F. R., Bombay 400 005.

Participants:
Rahul Basu, Avijit Ganguly, Rajiv Gavai, Rohini Godbole, Sourendu Gupta, N.D.Haridass, Prakash Mathews, Hiranmay Mishra, J. Pasupathy, J. C. Parikh, Hiranmay Mishra, J. Pasupathy, J. C. Parikh, V. Ravindran, Helmut Satz and Vikram Soni.

This working group discussed several aspects of heavy ion physics. Several projects were found to be interesting enough to pursue further. The specific projects chosen for further work are listed below.

1. Braaten-Pisarski Resummation: Hiranmay Mishra and Avijit Ganguly will try to use Braaten-Pisarski resummation to compute the pressure in pure QCD at three loop order. There is some interest in computing the pressure to as high an order in perturbation theory as possible, so that the result can be compared with lattice gauge theory measurements.

2. J/ψ Transverse Momentum: R. M. Godbole, Prakash Mathews, V. Ravindran, S. Gupta and R. V. Gavai have started a project to use resummed perturbative QCD in order to predict the transverse momentum distribution of J/ψ and Υ in the heavy-ion collider mode of LHC. Deviations from such predictions are among the signals of the plasma.

3. Disoriented Chiral Condensates: N. D. Haridass outlined a computation of the critical exponents of the $O(4)$ sigma model in three dimension. R. Basu and S. Gupta plan to compute the dynamics of disoriented condensates after quenching. This has been suggested recently as a mechnism for Centauro events.

PRAMANA
journal of
physics

© Printed in India

Supplement to Vol. 45
October 1995
p. 401

Group report: Heavy flavour physics

S. UMA SANKAR
Institute of Mathematical Sciences, Madras 600 113.

Participants:
Tariq Aziz, Amitava Datta, N. G. Deshpande, P. H. Frampton, U-G. Meissner, J. Pasupathy, Sreerup Raychaudhury, L. M. Sehgal, Gurpreet Kaur Sidana, S. Uma Sankar

This working group discussed several topics of heavy flavour physics. Some of them are listed below.

1. Tariq Aziz gave a talk on the decay time measurements of the B_d and B_s mesons at LEP. These measurements can be used to determine Δm_{B_d} and Δm_{B_s}. The ratio of these mass differences can provide a sensitive test of the three generational unitarity of CKM matrix.

2. Ulf-G. Meissner gave a talk on the application of the techniques of chiral perturbation theory to the non-leptonic decays of kaons.

3. L. M. Sehgal gave a talk on the issue of final state interactions in the non-leptonic B meson decays. In the two pion decay of neutral kaons, the final state contains only two isospin states which can interact with each other via strong interactions. Therefore these decays can simply be parametrized by two amplitudes and two phases. But in B meson decays, a large number of intermediate non-leptonic states, which can interact with one another via strong interactions, are kinematically accessible. It is impossible to take into account all of them. It is desirable to develop ways of parametrizing how the final state interactions (FSIs) affect the two meson decays of the B mesons. This will be extremely useful in CP violation measurements in B mesons.

4. J. Pasupathy gave a talk on the relation between QCD sum rules and the Isgur-Wise Heavy Quark symmetry.

5. Sreerup Raychaudhury gave a talk on a four generational model in which one can make the fermions of the first three generations light without much fine-tuning. The fourth generation, however, will be very massive.

List of Participants

Ramesh Anishetty	I. M. Sc., Madras
S. Arunagiri	Madras University
Tariq Aziz	T. I. F. R., Bombay
K. S. Babu	University of Delaware
K. Bandyopadhyay	Santiniketan
S. Banerjee	T. I. F. R., Bombay
Rahul Basu	I. M. Sc., Madras
Rajiv Bhalerao	T. I. F. R., Bombay
Kalpana Bora	Gauhati University
Biswajoy Brahmachari	P. R. L., Ahmedabad
C.P. Burgess	McGill University
R. Chakrabarti	Madras University
Amitava Datta	Jadavpur University, Calcutta
Gautam Datta	P. R. L., Ahmedabad
Binayak Datta-Roy	S. I. N. P., Calcutta
N. G. Deshpande	University of Oregon
V. Devanathan	Anna University, Madras
Manuel Drees	University of Wisconsin
Ranabir Dutta	Santiniketan
P. H. Frampton	University of North Carolina
S. N. Ganguli	T. I. F. R., Bombay
Avijit Ganguly	P. R. L., Ahmedabad
Rajiv Gavai	T. I. F. R., Bombay
Partha Ghose	S. N. Bose Centre, Calcutta
Rohini Godbole	Bombay University
M. Golterman	Washington University
Srubabati Goswami	Calcutta University
T. R. Govindarajan	I. M. Sc., Madras
Manoranjan Guchait	Jadavpur University, Calcutta
Sourendu Gupta	T. I. F. R., Bombay
N. D. Hari Dass	I. M. Sc., Madras
D. Indumathi	P. R. L., Ahmedabad
Anjan Joshipura	P. R. L., Ahmedabad
P. Kalyniak	Carleton University

S. G. Kamath	I. I. T., Madras
A. K. Kapoor	University of Hyderabad
Indra Bahadur Karki	Tribhuvan University, Khatmandu
Sudhakar Katta	T. I. F. R., Bombay
Romesh Kaul	I. M. Sc., Madras
Anirban Kundu	S. I. N. P., Calcutta
S. Lakshmi Bala	I. I. T., Madras
Uma Mahanta,	M. R. I., Allahabad
H. S. Mani	M. R. I., Allahabad
Prakash Mathews	I. I. Sc., Bangalore
Parthasarathi Majumdar	I. M. Sc., Madras
Kajari Mazumdar	T. I. F. R., Bombay
U.-G. Meissner	Strasbourg
Hiranmay Mishra	P. R. L., Ahmedabad
S. P. Misra	I. O. P., Bhubaneshwar
Subhendra Mohanty	I. O. P., Bhubaneshwar
N. K. Mondal	T. I. F. R., Bombay
Biswarup Mukhopadhyaya	M. R. I., Allahabad
M. V. N. Murthy	I. M. Sc., Madras
Mohan Narayan	I. M. Sc., Madras
Surya Narayan Nayak	I. I. Sc., Bangalore
Marek Nowakowski	P. R. L., Ahmedabad
P. N. Pandita	NEHU, Shillong
M. K. Parida	NEHU, Shillong
J. C. Parikh	P. R. L., Ahmedabad
R. Parthasarathy	I. M. Sc., Madras
J. Pasupathy	I. I. Sc., Bangalore
R. J. N. Phillips	Rutherford Appleton Lab
R. Premanand	Madras University
K. Raghunathan	Madras University
G. Rajasekaran	I. M. Sc., Madras
M. Rajasekaran	Madras University
R. Ramachandran	I. M. Sc., Madras
P. Ramadevi	I. M. Sc., Madras
R. Ramamoorthy	Madras University
Lisa Randall	M. I. T.
V. Ravindran	T. I. F. R., Bombay

Asim Ray	Santiniketan
Sreerup Raychaudhuri	S. I. N. P., Calcutta
Saurabh Rindani	P. R. L., Ahmedabad
R. G. Roberts	Rutherford Appleton Lab
D. P. Roy	T. I. F. R., Bombay
Probir Roy	T. I. F. R., Bombay
K. Sakthi Murugesan	Madras University
Tapobrata Sarkar	I. M. Sc., Madras
K. S. Sateesh	M. R. I., Allahabad
H. Satz	CERN
M. Seetharaman	Madras University
J. Segar	Madras University
L. M. Sehgal	Aachen
Goran Senjanovic	ICTP
H. S. Sharatchandra	I. M. Sc., Madras
Gurpreet Kaur Sidana	M. R. I., Allahabad
J. P. Singh	Jiwaji University, Gwalior
Nita Sinha	I. M. Sc., Madras
Rahul Sinha	I. M. Sc., Madras
Vikram Soni	N. P. L., New Delhi
K. Sridhar	CERN
C. Srinath	I. M. Sc., Madras
M. S. Sriram	Madras University
P. R. Subramaniam	Madras University
S. Uma Sankar	I. M. Sc., Madras
J. W. F. Valle	University of Valencia

re functions and parton distributions
..... *R G Roberts* 277

s prospects at the hadron colliders
..... *D P Roy* 293

olution of the quark-gluon plasma
..... *Helmut Satz* 313

decays ..... *L M Sehgal* 339

electroweak vector boson self interactions ..... *R Sinha* 351

report: Collider physics and structure functions
..... *Amitava Datta and Rohini M Godbole* 365

in N=1 SUGRA models
..... *M Drees, A Datta amd M Guchait* 367

sses at high energy p-p colliders
..... *M Drees, R M Godbole, M Nowakowski and S D Rindani* 373

higgs bosons at e^+e^- colliders
..... *R M Godbole, B Mukhopadhyaya and M Nowakowski* 379

ve charm production at HERA and the charm content of the photon
..... *M Dress and R M Godbole* 386

report: Beyond standard model ..... *A S Joshipura and Probir Roy* 393

report: Heavy ion physics ..... *Sourendu Gupta* 399

report: Heavy flavour physics ..... *S Uma Sankar* 401

participants 403

d in CURRENT CONTENTS ISSN 0304-4289

and published by V K Gaur for the Indian Academy of Sciences, Bangalore 560 080.
-ready text prepared using TEX software and printed at Lotus Printers, Bangalore-560 044.

Regd. No. KRN-A 64

Pramana journal of physics

Supplement to Vo

October

CONTENTS

Proceedings of the Third Workshop on High Energy Particle Physics, 1994

B-physics at LEP ..... *Tariq Aziz*

Limits on 3 boson vertex parameters from LEP200 ..... *S Banerjee*

The effective use of precision electroweak measurements ..... *C P Burgess*

CP violation in a multi higgs doublet model
..... *N G Deshpande and Xiao-Gang He*

Phenomenology of the minimal supergravity SU(5) model ..... *Manuel Drees*

Spontaneous CP violation and neutral B meson decays
..... *Paul H Frampton*

Family symmetry ..... *Paul H Frampton*

Determination of mass and width of W at LEP200
..... *S N Ganguli*

How good is the quenched approximation of QCD?
..... *Maarten F L Golterman*

Polarized structure functions
..... *D Indumathi*

Oscillating neutrinos: Theory vs experiment
..... *Anjan S Joshipura*

Topics in chiral perturbation theory
..... *Ulf-G Meissner*

Threshold effects in SUSY and non-SUSY GUTs
..... *M K Parida*

Higgs searches and WW scattering
..... *R J N Phillips*

The inclusive semileptonic *B* decay lepton spectrum
from B ——> Xe ν ..... *Lisa Randall*

CP violation at colliders
..... *Saurabh D Rindani*

(Continued on the inside bac